ESB2022

27th Congress of the European Society of Biomechanics

26 - 29 June 2022, Porto, Portugal

ABSTRACT BOOK

European Society
of Biomechanics

PERSONALIZED MODELING OF ALZHEIMER'S DISEASE

Ellen Kuhl

Department of Mechanical Engineering, Stanford University, Stanford, CA 94306, United States

Motivation

For more than 25 years, the amyloid hypothesis—the paradigm that amyloid is the primary cause of Alzheimer's disease—has dominated the Alzheimer's community. Now, increasing evidence suggests that tissue atrophy and cognitive decline in Alzheimer's disease are more closely linked to the amount and location of misfolded tau protein than to amyloid plaques[1]. However, the precise correlation between tau pathology and tissue atrophy remains unknown. Here we integrate multiphysics modeling and Bayesian inference to create personalized tau-atrophy models[2] using longitudinal clinical images. For each subject, we infer three personalized parameters, the misfolding rate, transport coefficient, and tau-induced atrophy rate from consecutive annual tau positron emission tomography scans and structural magnetic resonance images[3]. Our study reveals a strong correlation between tau pathology and tissue atrophy[4]. Once calibrated with a larger set of longitudinal images, our model has the potential to serve as a diagnostic and predictive tool to estimate atrophy progression from clinical tau images on a personal basis.

Results

We explore tau-atrophy interactions by integrating a multiphysics brain network model and longitudinal neuroimaging data for n = 61 subjects from the Alzheimer's Disease Neuroimaging Initiative[4]. Using Bayesian inference with hierarchical priors, we personalize subject-level parameter distributions for each subject and infer group-level parameter distributions for amyloid positive and negative groups, Fig. 1.
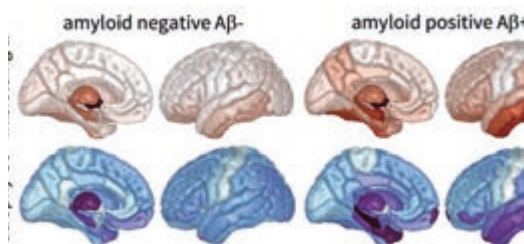
Fig... ...eraged ac... ...group Aβ+ (right) and amyloid negative healthy controls Aβ− (left).

Our results show that the group-level tau misfolding rate for the amyloid positive Alzheimer's group of 0.0165/year is significantly larger than for the amyloid negative control group of 0.1922/year, Fig. 2, top. Similarly, the group-level tau-induced atrophy for the amyloid positive group of 0.0151/year is significantly larger than for the amyloid negative group of 0.0108/year, Fig. 2 bottom. These findings support the

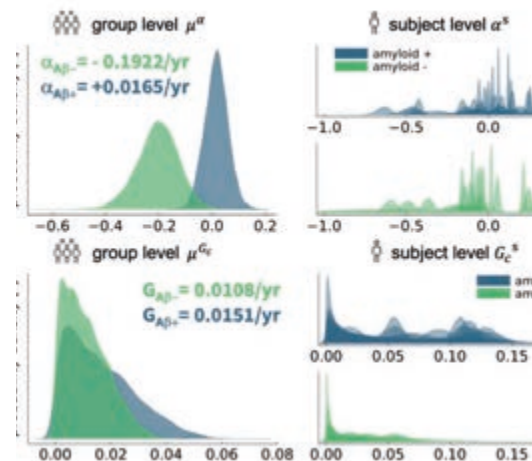hypothesis that amyloid pathology has a magnifying ef...

Figure 2: Group (left) and subject (right) level misfolding rate α (top) and brain atrophy rate Gc (bottom) for amyloid positive Alzheimer's group Aβ+ (blue) and amyloid negative healthy controls Aβ− (green).

References

1. Fornari S, Schafer A, Jucker M, Goriely A, Kuhl E. Prion-like spreading of Alzheimer's disease within the brain's connectome. J Royal Soc Interface. 2019; 16:20190356.
2. Schafer A, Chaggar P, Thompson TB, Goriely A, Kuhl E. Predicting brain atrophy from tau pathology: a summary of clinical findings and their translation into personalized models. Brain Multiphysics. 2021; 2:100039.
3. Schafer A, Peirlinck M, Linka K, Kuhl E. Bayesian physics-based modeling of tau propagation in Alzheimer's disease. Front Physiology. 2021; 12:702975.
4. Schafer A, Chaggar P, Goriely A, Kuhl E. Correlating tau pathology to brain atrophy using a physics-based Bayesian model. Eng Comp. 2022; doi:10/1007/s00366-022-01660-3.

Acknowledgements

META-BIOMATERIALS

Amir A. Zadpoor

Delft University of Technology, The Netherlands

Introduction

In this plenary talk, I will present the recently introduced concept of meta-biomaterials [1] and review some of their latest developments. I coined the term "meta-biomaterials" in 2015 to describe biomaterials that exhibit unprecedented or rare combinations of geometrical, physical, and biological properties. These unusual properties are relevant for tissue regeneration, infection prevention, and the other important functions of biomedical materials. The effective properties of meta-biomaterials at the macroscale result from their small-scale design. The small-scale design features include complex geometries as well as spatial distributions of multiple types of materials with dissimilar properties.

Background

There are three primary challenges in the meta-biomaterials research. While the first challenge is design related, the second is manufacturing focused. The last challenge concerns the demonstration of the improved performance achieved using the developed meta-biomaterials. When designing meta-biomaterials, a "rational design" process is often followed in which computational models, analytical solutions, artificial intelligence, as well as several other quantitative and qualitative techniques from physics, mathematics, and mechanics are deployed to find the small-scale geometries and spatial distributions of materials that give rise to the desired set of (macroscale) properties. Given the complexity of such designs, they often cannot be realized using conventional or even modern manufacturing techniques. One, therefore, needs to apply a combination of custom-made manufacturing techniques, including 3D printing, 4D printing (3D printing of objects whose shape changes with time upon triggering by an external stimulus), origami, and kirigami techniques. Finally, a host of *in vitro*, *ex vivo*, on-chip, and *in vivo* assays are needed to evaluate the performance of the developed meta-biomaterials. In this talk, I will address all the challenges mentioned above within the context of the meta-biomaterials aimed for the treatment of complex bony diseases. Such meta-biomaterials should improve the bone tissue regeneration and osseointegration of implants while preventing implant-associated infections.

Recent Advances

The talk is organized in four sections. The first three sections concern the developments taking place at three different length scales, namely macro-, micro-, and nanoscale. The final section focuses on the integration of all the relevant length scales with the help of origami,

Amir Zadpoor is Antoni van Leeuwenhoek Professor and Chaired Professor of Biomaterials & Tissue Biomechanics at Delft University of Technology as well as Professor of Orthopedics at Leiden University Medical Center. He develops advanced 3D and 4D printing techniques for the fabrication of meta-biomaterials with unprecedented properties. Moreover, he is a world recognized expert in origami- and kirigami-based biomaterials that combine shape shifting with additive manufacturing. Prof. Zadpoor has received many awards including an ERC grant, a Vidi grant, a Veni grant, the Jean Leray award of the European Society of Biomaterials, and the Early Career Award of JMBBM.

kirigami, and 4D printing. At the macroscale, I will discuss the application of meta-biomaterials in the design of patient-specific implants, deployable implants, and the implants developed based on the metallic clay concept. At the microscale, I will cover the use of auxetic meta-biomaterials, multi-material 3D printing, and hyperbolic geometries for the design of meta-biomaterials as well as the importance of bone curvature in this regard. At the nanoscale, I will address the use of nanopatterns to simultaneously enhance osteointegration, induce bactericidal properties, and modulate the immune response.

Future directions

Going back to the three major challenges in the development of meta-biomaterials, the first two challenges (*i.e.*, design and fabrication) have been thoroughly addressed during the last seven years. In particular, all the important aspects of design and fabrication have been studied at least at the individual level. The third challenge, regarding the biological performance of these materials, therefore, remains the main aspect to be studied in the coming years particularly to clarify how these biomaterials interact with multiple cell types (osteoimmunomodulatory pathways) and perform *in vivo* under realistic biomechanical conditions.

References

1. Zadpoor, AA, Biomaterials Science, 8:18-38, 2020.

Acknowledgements

MODELLING THE NEUROMUSCULAR SYSTEM FOR HUMAN-ROBOT INTERFACING

Massimo Sartori

University of Twente, Department of Biomechanical Engineering, The Netherlands

Background

Preserving the ability to move as we age or in response to injury is an essential human need. Physical inactivity is the fourth leading cause of global mortality [1]. Preserving recommended levels of physical activity decreases the risk of cardiovascular diseases, enhances quality of sleep, and mitigates symptoms of depression and anxiety [1]. Therefore, developing robotic technologies that can preserve human mobility as we age, or restore movement following neuromuscular injuries is a key target [2].

However, although research has led to sophisticated mobility enhancing robots (e.g., exoskeletons or bionic limbs), which are small, lightweight and composed of soft materials, we are not yet capable of interfacing them to the human, so that they become a natural extension of the own body, i.e., so that they operate in concert with skeletal muscles and are fully integrated in natural neural control loops [2]. Our main limitation in interfacing humans with wearable robots is due to an incomplete understanding of how to synthesize the key neuro-muscular processes underlying movement into numerical models that we can use for control [2].

Recent Advances

To address these challenges, we have been proposing a specific roadmap that is based on three research pillars: (1) measuring the activity of neural cells involved in the control of movement *in vivo* in the intact moving human, (2) predicting the mechanics of the musculoskeletal system as controlled by the nervous system and (3) controlling wearable robots based on estimates of an individual's neuromuscular function, thereby closing the loop between robots and the human body.

We previously showed the possibility of recording high-density electromyograms (HD-EMGs) from > 250 recording sites over five leg muscles in healthy subjects performing large repertoires of isometric plantar-dorsi flexion contractions (ranging from 20% to 90% MVCs) [3, 4]. We demonstrated the possibility of decoding the underlying activity of alpha motor neurons in populations of 56.7 ± 10.2 neurons across all muscles and subjects [3]. More recently, we extended current decomposition techniques with an automated quality-check assuring decomposition of physiologically relevant sources in four incomplete spinal cord injury patients (injury levels C4-C8) receiving transcutaneous electrical stimulation [4]. By estimating coherence in the delta band between multiple pairs of spike trains we found statistically significant decrease ($p < 0.05$) in z-transformed coherence peak i.e., from $z = 5.06$ (standard error = 0.93) before stimulation to $z = 3.85$ (standard error = 0.75), thereby providing a potential biomarker for spinal neuron response to stimulation [4].

We showed the possibility to translate decoded spike trains into resulting innervated muscle force and joint moments [4].

Finally, we demonstrated the integration of the full chain of EMG-based interfacing and EMG-driven modelling into real-time exoskeleton controllers [5-7]. This enabled healthy individuals to voluntarily control bilateral ankle exoskeletons during a large range of "unseen" walking conditions and transitions that were not used for establishing the control interface. Torque and EMG reductions in novel walking conditions indicated that the exoskeleton operated symbiotically, as exomuscles controlled by the operator's neuromuscular system. The proposed paradigm was also demonstrated on individuals who underwent spinal cord injury and stroke, thereby supporting dynamic joint rotations with reduced EMG activity [5].

Future directions

Supporting the developments of technologies that can be used to interface directly with biological structures in the nervous system and the muscular systems is a key challenge for the future. This is crucial to enable robust neural decoding of biomechanical function. Developments in this direction will enable robust control of complex robots in large variety of movements, by making virtually no assumptions on the motor task to be carried out.

The approach outlined here will also open new avenues for creating digital twins that we can use for predicting injury likelihood throughout highly dynamic tasks or throughout ageing stages.

References

1. Slade et al., Nat. Commun. 12:4312, 2021.
2. Sartori & Sawicki, Prog. Biomed. Eng. 3:023001, 2021.
3. Gogeascoechea et al., Front. Neurol., 11:493, 2020.
4. Sartori et al., Sci. Rep., 7: 13465, 2017.
5. Durandau et al., J. Neuroeng. Rehabil., 16:1, 2019.
6. Lotti et al., IEEE Robot. Autom. Mag., 2020.
7. Durandau, et al., IEEE Trans Robot. 2022.

Acknowledgements

PHYLOGENIC AND ONTOGENIC DETERMINANTS OF MECHANOTRANSDUCTION IN THE HUMAN AORTA

Jean-Baptiste Michel

Lorraine University, INSERM U1116, DCAC, FF-54000 Nancy, France

Although mechanotransduction in highly pressurized arteries has been known since William Harvey (1578-1553), there is still a pressing need to unify the many roles of biomechanics in cardio-arterial pathologies. To address this need, we revisit paradigms related to the evolution of cardiovascular systems and we propose a new general perspective for biomechanicists.

Phylogenesis

The evolution of the circulation from invertebrates to mammals has involved the passage from an open, to a closed in-parallel system via a closed in-series system, accompanying the increasing efficiency of life's biological functions. The archaic heart enables pulsatile motion waves of hemolymph in invertebrates, and the in-series circulation in fish occurs with only an endothelium. We try to address why this evolution took place from a closed, flowing, longitudinal conductance at low pressure to a flowing, pressurized and bifurcating arterial compartment in mammals.

Ontogenesis

Each evolutionary stage imprints the circulatory development in the fetus: early heartbeats, predominance of flow, intracardial shunts, and low arterial pressure. The transition to viviparity thus introduces an entirely transient event, energetically and dynamically fueled by placental function. This allows for the development of organ function by an adapted energetic support. VEGF plays a pivotal role in the specific development of placental angiogenesis and chorionic villi. Oxygenated blood and nutrients are transported to the fetus by the single umbilical vein and conversely more mixed blood and fetal metabolic products are transported back to uteroplacental vein by the umbilical arteries. The final development of the arterial system is only controlled by flow at low blood pressure in fetus until birth.

Birth tsunami

At birth, the increase in arterial pressure is due to an acute rise in arterial resistance. The initiation of the pulmonary circulation increases left atrial pressure, rapidly closing the foramen ovale associated with the gradual closing of the ductus arteriosus in response to vasoconstrictive prostaglandins of lung origin. Likewise, the peripheral frictional force rapidly rises in left side in response to the catecholamine rush and SMC

Jean-Baptiste is currently Research Director Emeritus at the French Institute of Health and Medical Research, Inserm U1116 at Lorraine University at Nancy. He graduated as a Medical Doctor in 1980, as a cardiovascular (CV) Surgeon in 1984, and has obtained his PhD in CV physiology in 1987. His surgical activity allowed him to directly observe the features of human arterial lesions and raised interest for the questions of biological processes involved in atherothrombotic disease progression in humans. In particular he focused on aneurysms of the aorta, thoracic and abdominal. He is the author of more than 500 publications in peer-reviewed journal. He was the coordinator of several EU projects including "Fighting Aneurysmal Diseases" (2008-2012).

tonic contraction, under control of the CNS. Therefore, birth induces a complete change in hemodynamic load, involving not only flow as in fetal life but also arterial pressure and loss of umbilical flow. The adaptation of the wall to the pressure load is not instantaneous but is a progressive process, which takes place during growth in humans from infancy up until the end of puberty. The immature circulation continues to evolve throughout growth to adapt to the pressure load in the arteries, to gravity due to upright posture, to the increase in specifications and activities of organs, and finally to dynamically and permanently equilibrate the energy transfer and dissipation between flow and pressure dependent on mechanotransduction in matrix-rich conductance arteries, and on SMC connections in resistance arteries. However, although arterial pressure was the latest acquired hemodynamic variable, the general teleonomy of the evolution of species is the differentiation of individual organ functions, supported by specific fueling allowing and favoring partial metabolic autonomy. This was achieved via the establishment of an active contractile tone in resistance arteries, which permitted the regulation of blood supply to specific organ activities via its localized function-dependent inhibition. Conductance arteries support this distal part through specific mechanotransduction involving both ECM and SMC interactions.

Consequently, the arterial pressure gradient from circulating blood to the adventitial interstitium generates the unidirectional outward radial advective conductance of plasma solutes across the wall of conductance arteries. This hemodynamic evolution was accompanied by important changes in arterial wall structure, supported by smooth muscle cell functional plasticity, including contractility, matrix synthesis and proliferation, endocytosis and phagocytosis, etc. These adaptive phenotypic shifts are due to epigenetic regulation, mainly related to mechanotransduction.

References

1. Michel JB. Phylogenic determinants of cardiovascular frailty, focus on hemodynamics and arterial smooth muscle cells. Physiol. Rev. 2020; 100:1779-1837 (614 references)

QUANTITATIVE FUNCTIONAL ASSESSMENT IN THE SETTING OF ADULT SPINAL DEFORMITY USING 3D MOVEMENT ANALYSIS

Ayman Assi (1,2), Virginie Lafage (3), Wafa Skalli (2)

1. *Laboratory of Biomechanics and Medical Imaging, Faculty of Medicine, St-Joseph University, Beirut, Lebanon*
2. *Institut de Biomécanique Humaine Georges Charpak, Arts et Métiers Institute of Technology, Paris, France*
3. *Orthopaedics Surgery, Lenox Hill Hospital, New York, USA*

Background

Degenerative diseases increase with ageing, leading to musculoskeletal disorders, especially in the spine [1]. Adult Spinal Deformity (ASD) consists of alterations of the lumbar or thoracolumbar spine [2], leading to compensatory mechanisms in the pelvis and lower limbs that are necessary to maintain a balanced posture where the head is kept above the pelvis, along with a horizontal gaze [3]. Clinical assessment is usually based on full body frontal and sagittal X-rays in standing position. Compensatory mechanisms can have severe consequences on the patient, causing increased back pain, muscle fatigue, accelerated joints degeneration, and most importantly, a limitation of numerous daily life activities such as walking. Clinicians rely mostly on health-related quality of life (HRQoL) and disability questionnaires for the assessment of deformity repercussions on functionality. Since these techniques lack objectivity and quantification, the aim of our research is to evaluate the function of ASD patients using 3D motion analysis during daily life activities.

Recent Advances

We have enrolled more than 120 ASD patients and 70 controls who underwent 3D motion analysis for several daily life activities such as: walking at self-selected speed and fast speed, sitting and standing movement and stairs climbing. The kinematics of the trunk, pelvis and lower limbs were calculated as well as segmental spine motion [4,5]. Biplanar X-rays were performed in both standing and sitting positions, while the reflective markers were kept in place, with subsequent 3D reconstructions of skeletal segments and calculation of classic radiographic parameters. Image registration techniques were applied in order to calculate postural radiographic parameters during movement. All subjects filled HRQoL questionnaires. Patients are followed 3 months and 2 years after surgery or medical treatment.

The findings to date show that quantitative functional assessment in the setting of ASD are better related to HRQoL outcomes than radiographic parameters [6]. Moreover, movement patterns differ between patients depending on the type of spinal deformity: patients with sagittal malalignment have more altered gait with different compensatory mechanisms [7,8]. Image registration techniques showed that some patients have altered balance during gait and are more prone to falls [9]. Some patients use different spinopelvic strategies to acquire a balanced sitting position [10,11]. Moreover,

Ayman Assi is a professor and director of the Laboratory of Biomechanics and Medical Imaging at the Faculty of Medicine, University of Saint-Joseph in Beirut, Lebanon. He is also an invited professor at the Institut de Biomécanique Humaine Georges Charpak, Arts et Métiers Institute of Technology in Paris, France. His research focuses on 3D musculoskeletal models in static and movement in the setting of cerebral palsy, down syndrome, adolescent idiopathic scoliosis and adult spinal deformity, with several publications in this field.

Ayman is also the president of the European Society for Movement analysis in Adults and Children (ESMAC) and ambassador and member of the program committee at the EUROSPINE society.

this research contributed to better understand the hip-spine syndrome in these patients [12,13].

Future directions

The work is in progress to enlarge the database and to analyze patients' data after their medical or surgical treatment. The follow-up data will help clinicians in evaluating treatment outcomes, thus allowing them to choose the optimal treatment in order to restore a normal function during daily activities in these patients and to improve their quality of life.
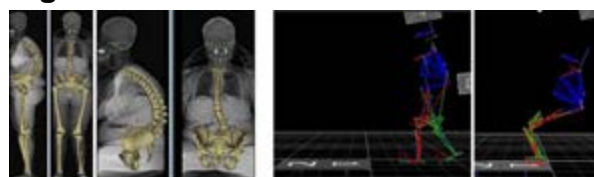
Figures

Figure 1: Data acquisition in static (standing and sitting) and during motion for ASD and controls.

References

[1] M.G. Fehlings, et al., Neurosurgery 2015; [2] F. Schwab, et al., Spine 2005; [3] J. Dubousset, et al., Spine. 1994; [4] A. Leardini, et al., Clin. Biomech. 2011; [5] R.B. Davis, et al., Hum. Mov. Sci. 1991; [6] R.M. Saliby, et al., Gait Posture 2020; [7] G. Kawkabani, et al., Gait Posture 2021; [8] K. Semaan, et al., Gait Posture 2021; [9] G. Rebeyrat, et al., Gait Posture. 2021; [10] E. Saad, et al., Gait Posture 2021; [11] A. Massaad, et al., Gait Posture 2021; [12] M. Mekhael, et al., Eur. Spine J. 2021;[13] R. Rachkidi, et al., Gait Posture 2021.

OPPORTUNITIES IN MULTISCALE AND MULTIPHYSICS HUMAN HEART MODELING

Mathias Peirlinck

Delft University of Technology, Netherlands

Background

From an engineering perspective, the human heart beats any man-made hydrodynamic machine in its combined efficiency, size, and longevity. At the same time, this biological pump is one of the most complex and least understood organs in the human body. Throughout the past three decades, our understanding of the human heart has become much more quantitative, made possible by the close collaboration between medical scientists, biologists, and mathematical modelers. Following this improved understanding, the next natural question that arises is which role human heart modelling can play in the clinic, both now and in the future.

Recent Advances

We have come to a point where human heart modelling can really start to benefit the patient, for improved diagnosis, prognosis, treatment planning, and medical device design[1]. The development multiscale patient-specific heart models equipped with realistic Purkinje networks provides accurate predictions of the heart's electrophysiological behavior under both physiological and pathological conditions. Moreover, it allows us to characterize the effects of drugs in cardiac electrophysiology and develop novel population-specific in silico drug risk stratification[2]. Similarly, we can now confidently and robustly model the physiology and mechanical behavior of the healthy beating human heart. Such a simulation tool provides inexhaustible opportunities to probe pathological conditions and guide device design and treatment planning in health and disease. We can now predict the long-term response of the heart to various forms of pressure and volume overloading and show that our predictions qualitatively match pathophysiological remodeling at the cell, tissue and organ scale[3]. Additionally, we use these tools to simulate the consequences of myocardial infarction and compute how the non-contracting scar region leads to mitral regurgitation. The resulting diseased digital twin of the patient-specific heart forms an interesting in silico bench test to quantify the potential success of various treatment strategies. Particularly, we have used these models to optimize novel mitral annuloplasty rings, predict the coaptation of the mitral valve following edge-to-edge repair, quantify the mechanical loads on pacing leads and the effects of left ventricular assist devices on myocardial dynamics. With a view toward translational medicine, our models also provide a clinical perspective on virtual imaging trials and a regulatory perspective on medical device innovation.

Mathias Peirlinck is an Assistant Professor at the Department of Biomechanical Engineering, Delft University of Technology. He obtained his PhD in Biomedical Engineering at Ghent University in 2019. He was a post-doctoral fellow at Stanford University in 2019-2021. His present research mainly focuses on the biophysical behavior of the human heart, building data-driven modeling frameworks that bridge the cell, tissue, and organ scale. He authored over 20 publications in peer- reviewed journals, and more than 30 contributions to International and National Conferences.

Future directions

Clearly, the ultimate objective of human heart modeling is the individualized prediction of different treatment outcomes with the goal to virtually select the most promising strategy within the paradigm of precision medicine. Cardiac simulations are algorithmically challenging and computationally expensive. With the rapid developments in machine learning, data-driven modeling, and physics-based simulation, we can now risk-stratify large patient groups and improve tailored cardiovascular therapies using machine learning strategies. Intriguingly, precision medicine in cardiac health does not necessarily require a fully personalized, high-resolution whole heart model with an entire personalized medical history. Instead, a population-based library with geometric, biological, physical, and clinical information can already have high clinical value. Ultimately, these steps will pave a translational path towards clinical decision making in full alignment with and endorsed by the regulatory agencies and guidelines.

References

1. Peirlinck, M et al., Biomech. Model. Mechanobiol. **20** (3), 803 (2021).
2. Peirlinck, M et al., Front. Physiol. **12** (1245) (2021).
3. Peirlinck, M et al., Biomech. Model. Mechanobiol. **18** (6), 1987 (2019).

Acknowledgements

HARNESSING 3D PRINTING TO OPTIMISE MEDICAL DEVICE INTERACTION WITH SOFT TISSUE

Eoin D. O'Cearbhaill

School of Mechanical & Materials Engineering, UCD Centre for Biomedical Engineering, University College Dublin, Ireland

Background

The UCD Medical Device Design Group is focused on developing platform medical device technologies, offering smart ways to deliver next-generation therapeutics through minimally invasive approaches. A key aspect to this is research is to optimise the interaction, including penetration and/or adhesion of medical devices to soft tissue. 3D printing is used as an enable technology, due to inherent design freedom that it offers.

The interface between host and implant is a key predictor of device performance. When seeking to attach or integrate medical devices with host soft tissue, current methods of fixation and integration can lead to suboptimal results. There is a reliance on (1) chemical-based adhesives, which require tissue-specific reactive chemistry and subsequent risk of an inflammatory response, or (2) mechanical methods of fixation (sutures or staples) which can induce significant local tissue damage and associated increased risk of infection.

Recent Advances

Here, we present examples of novel interfacing geometries optimised for tissue adhesion and integration respectively. Firstly, microneedle technologies under development in the UCD Medical Device Design Group are described [1-3], including configurations that achieve robust and reversible mechanical adhesion to skin. These platforms can be used for 'click-on' drug delivery and biosignal sensing applications. Secondly, utilising a novel direct ink additive manufacturing approach, we have produced soft flexible silicone-based implants with a unique surface topography designed to minimise fibrosis and control the wound-healing response. These geometrical conformations create platforms for optimal tissue fixation and integration for a broad range of medical devices.
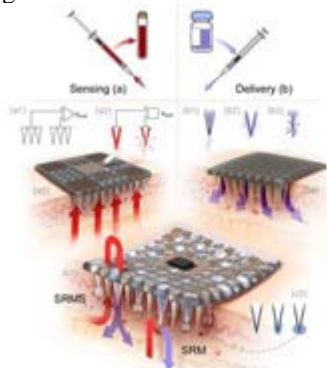

Figure 1: Future Direction of Microneedle Technology towards biofunctional systems.[4]

Dr. Eoin O'Cearbhaill, Associate Professor in Biomedical Engineering, is a former Marie Skłodowska-Curie Fellow, and a Funded Investigator in CÚRAM, SFI Centre for Research in Medical Devices, I-FORM, SFI Advanced Manufacturing Research Centre and AMBER, SFI Advanced Materials & Bioengineering Research Centre. Dr. O'Cearbhaill is a biomedical engineer focused on the development of medical devices, with a particular emphasis on platform technologies, offering smart ways of delivering next-generation diagnostics and therapeutics through minimally invasive approaches. He is a graduate of NUI Galway (BE, PhD) and undertook postdoctoral training under the supervision of Prof. Jeff Karp, Brigham & Women's Hopsital, Harvard Medical School.

Figure 2: Example of a silicone 3D printed device with a tissue integrating surface topography. [5]

Future directions

We predict a convergence of microneedle technologies towards biofunctional systems with inbuilt sensing and therapeutic delivery capacity [4]. In this, and other implantable applications, optimising methods of medium to long-term tissue integration are crucial. Towards this goal, 3D printing has transformative potential, not just as a prototyping tool, but as a method of fabricating medical devices with unique architectures

References

1. Cahill et al., Acta Biomater, 2018. **80**: p. 401-411.
2. Krieger et al., Microsyst Nanoeng, 2019. **5**: p. 42.
3. Shu et al., Acta Biomater, 2021. **135**: p. 403-413.
4. Cahill et al.,. Bioconjug Chem, 2015. **26**(7): p. 1289-96.
5. Coulter et al.. Adv Health Mater, 2021. **10**(14): p. e2100229.

Acknowledgements

MODELLING MECHANICAL DEMANDS ARISING FROM CLINICAL REQUIREMENTS FOR FRACTURE FIXATION

Pankaj Pankaj

Institute for Bioengineering, School of Engineering, The University of Edinburgh, Edinburgh EH9 3BF, UK

Background

Implants used for treatment of fracture need to satisfy three key clinical requirements and consequent mechanical demands arising from them: they must support fracture healing; they must not fail during the healing period; and they should not loosen or cause patient discomfort [1]. This talk examines these mechanical demands via modelling with reference to some commonly used fixation devices such as external fixators and plates and screws. The challenges associated with determining the optimum fixation device and its configuration are discussed.

Recent Advances

There have been numerous past studies, both numerical and experimental, to determine the stiffness of the bone-implant systems which then provide the inter-fragmentary motion (IFM) or fracture gap strain required for healing at the time of treatment [2,3]. Our recent studies have shown that *in vitro* testing incorrectly predicts the performance of different devices due to two reasons. Firstly, depending on the boundary and loading conditions used in the lab, IFM predictions can vary by several orders of magnitude [3]. Since stresses in the implants are correlated with IFM these are incorrectly predicted as well. As lab experiments are simulated to validate models this problem is also carried over to *in silico* models. Starting from sophisticated models and by reducing complexity parameters our studies have found representative boundary and loading conditions that can be readily incorporated in models. The second reason for incorrect performance prediction is that lab tests do not incorporate healing. Our studies show that bone-implant behavior changes drastically even in the early stages of healing; implants that were ideal at the time of treatment no longer remain so when healing begins, which needs to be considered in treatment planning.

Our studies also show that IFM predictions are not strongly influenced by bone quality – so if the aim of the simulation is to merely predict IFM, complex nonlinear models of bone are not required. However, bone quality and its modelling has a major impact on implant loosening. We have considered linear isotropic and orthotropic elasticity [4], strain-based plasticity [5] and nonlinear viscoelasticity and viscoplasticity [6,7] to model bone. Our studies have shown that while all these models can predict implant loosening to varying levels of accuracy, only time-dependent models (e.g. involving viscoelasticity) are able to incorporate accumulation of

Pankaj Pankaj is Professor of Computational Biomechanics at Edinburgh University. He leads the Orthopaedic Biomechanics research group which comprises of clinicians, scientists and engineers. His principal expertise is in the area of nonlinear computational solid mechanics and his research has focused on the solution of real clinical problems using principles of mechanics. Research supervised by him has received a number of awards, such as: best PhD thesis in *in silico* Medicine (from Virtual Physiological Human institute); best medical engineering PhD (from Institution of Mechanical Engineers, UK); and Robertson Medal from the Carnegie Trust in Scotland. Pankaj is a co-chair for ESB2024.

the implant-bone gap due to cyclic loading. Our studies show that loosening is accentuated by this gap which increases with increasing number of cycles and is larger in bone of poor quality [6].

Future directions

Fractures require immediate treatment and leave little time for sophisticated modelling. Currently there appears to be no accepted methodology for selecting a fixation device and its configuration for different fracture types and bone properties to achieve the best possible clinical outcome. Studies have shown that the way a device is selected and configured by different surgeons varies significantly even for similar fractures. So our ongoing research focuses on development of a decision support system that can be used by clinicians in conjunction with the information they obtain from imaging modalities.

References

1. MacLeod et al., Injury, 49, Sup 1:S12-S18, 2018.
2. Claes, J Biomech, 115:110148, 2022.
3. MacLeod et al., Bone Joint Res, 7:111-20, 2018.
4. MacLeod et al., J Orthop Res, 34:1856-164, 2016.
5. Donaldson et al., J Orthop Res, 30:726-32, 2012.
6. Xie et al., Bone Joint Res, 7:580-86, 2018.
7. Manda et al., Biomech Model Mechanobiol, 16:173-89, 2017.

Acknowledgements

CHALLENGES OF VALIDATING COMPUTATIONAL THROMBOSIS MODELS

Keefe B. Manning[1,2]

[1]*The Pennsylvania State University, Department of Biomedical Engineering, University Park, USA*
[2]*Penn State Hershey Medical Center, Department of Surgery, Hershey, PA, USA*

Background

Thrombosis remains a significant clinical issue manifesting in heart attacks and strokes. However, the challenges extend to the success of cardiovascular devices. Given the complex process associated with thrombosis, developing an accurate computational model is not a trivial matter particularly validating the model in an effective and efficient manner. Current models range in complexity from tracking particles in a Lagrangian method to considering bulk concentrations in a more Eulerian frame as reviewed for device-induced computational thrombosis models in [1]. However, the models depend on a variety of data from multiple sources to predict thrombosis effectively. This approach can lead to limited interpretation. As such, developing canonical experiments that acquire a breadth of data will be crucial to leverage for validation of further computational models.

Recent Advances

Our group has been active in acquiring experimental data sets for thrombosis model validation and developing new experimental approaches that includes more robust data. Our initial data focused on macroscopic measurements using magnetic resonance imaging [2,3]. These data have been used by other researchers to assist in validating their models. However, to examine the microscopic behavior and interactions, more experiments are needed. Currently, we are using a sudden-expansion to collect blood samples to measure concentrations of different cellular species (e.g., platelet activation, factor XIIa, etc.) to observe changes over time. We are also leveraging microfluidic platforms and a swine model to collect additional data to inform our computational model.

Future directions

By providing a more robust experimental data set for canonical flows, we believe we will have a more accurate computational thrombosis model. Furthermore, we can provide these data sets for researchers to validate their models as they see fit. By increasing the validation of these models and thus, the complexity of that validation, our thrombosis model will be able to incorporate embolization. The predictions for embolization will be able to provide more insight into stroke and heart attack events. The model can also be used as a tool for cardiovascular device design in an

Prof. Manning is currently Professor of Biomedical Engineering and Surgery at the Department of Biomedical Engineering, The Pennsylvania State University and the Penn State Hershey Medical Center, respectively. He obtained his PhD in Biomedical Engineering at Virginia Commonwealth University in 2001. He was a post-doctoral fellow at The Pennsylvania State University in Bioengineering. He is a member of the ESB, ASME (Fellow), AHA, BMES, AIMBE (Fellow), ASEE, and Biorheology. His present research mainly focuses on Cardiovascular Fluid Dynamics, Cardiovascular Devices, Stroke, and Thrombosis. He is an author of nearly 85 publications in peer- reviewed journals, 4 book chapters, and more than 500 contributions to International and National Conferences.

effort to reduce ideally the need for more animal, benchtop, and clinical studies.

References

1. Manning KB, Nicoud F, Shea SM. Curr Opin Biomed Eng, In Press, 2021.
2. Yang L, Neuberger T, Manning KB. Magn Reson Mater Phy, 34(2):285-295, 2021.
3. Taylor JO, Witmer KP, Neuberger T, Craven BA, Meyer RS, Deutsch S, Manning KB. ASME J Biomech Eng, 136(7): 071012, 2014.

Acknowledgements

BIOMECHANICS OF CRANIOFACIAL GRROWTH

Mehran Moazen

Department of Mechanical Engineering, University College London, WC1E 7JE, UK

Background

The physical-mechanical interactions that shape our skulls during growth are poorly understood. This lack of fundamental knowledge limits our ability to advance treatment of a wide range of craniofacial conditions mostly affecting children. This is a significant engineering challenge due to the complexity of this system. For example, craniosynostosis (CR) is a condition cause by early fusion of cranial joints, affecting 1 in 2000 births, with its prevalence having increased by 2-3x in recent years where its optimum management is still subject of controversy. Here I will give an overview on our work in this area in the past 10 years on characterising craniofacial growth in an animal model and human and developing a validated computational approach that we developed and used to optimise management of most prevalent type of craniosynostosis.

Recent Advances

I carried out a detail morphological and material property characterisation of normal and a craniosynostotic mouse model during the growth in 2015 [1]. These data enabled us to develop a validated finite element (FE) model of calvarial growth in mouse. Here we used intracranial volume to drive the calvarial growth, and developed a strain based tissue differentiation algorithm to predict the bone formation at the cranial joints [Fig. 1A,B - 2,3]. We applied the same approach to develop a validated FE model of normal calvarial growth in human [Fig 1C - 4], having characterised morphological changes during the human craniofacial growth in n=241, aged 0-4 years. We then applied our approach to 2 patient-specific models of CR [5,6] predicting calvarial growth following the surgery. We are currently using our methodology to compare the biomechanics of 9 different treatment options for sagittal CR [Fig 1D - 7]. Our results highlight that different surgical techniques can constrain the growth of the brain in different ways that can potentially have an impact on the neurodevelopment of these children.

Future directions

Further work is required to expand our calvarial approach to predict the whole craniofacial growth i.e. including the facial growth. Moreover, the proposed approach can be used to optimize management of various forms for craniosynostosis as well as other conditions affecting the growth of craniofacial system such as cleft lip and palate. Combination of the approach proposed here together with geometric morphometric and artificial intelligence will unfoundedly transform the future of craniofacial surgery.

Figure 1: [A] validating modelling approach in mouse; [B] validating pattern of bone formation at the sutures; [C] predicting human skull growth; [D] comparing 9 treatment options for sagittal craniosynostosis.

References

1. Moazen et al., PloS One, 12;10:e0125757, 2015.
2. Marghoub et al., J Anat, 232:440-448, 2018.
3. Marghoub et al., Phys Rev Lett, 122:048103, 2019.
4. Libby et al., J Roy Soc Int, 14:20170202, 2017.
5. Malde et al., Sci Rep, 10:3, 2020.
6. Cross et al., Fron Cell Dev Biol, 26:9:621249, 2021.
7. Cross et al., Sic Rep, 11, 21216, 2021.

Acknowledgements

REAL WORLD MONITORING OF GAIT: CHALLENGES AND SOLUTIONS FOR A COMPREHENSIVE TECHNICAL VALIDATION

Claudia Mazzà

Department of Mechanical Engineering and Insigneo Institute for in silico Medicine, The University of Sheffield, Sheffield, UK

Background

Integrating a supervised assessment of mobility (mobility capacity) with its continuous, unsupervised monitoring in daily life (mobility performance) is a key need in a number of disease states [1]. Established clinical tools, based on patient self-reporting and one-off assessment are resource-intensive and lack sensitivity, and do not allow for a satisfactory response to this need. Wearable devices including inertial measurement units (IMUs) allow the quantification of digital mobility outcomes DMOs (e.g. walking speed, regularity, intensity, etc.), but the validity of IMU-based methods to characterise real-world mobility, is still limited, especially in diseased gait. This is because measuring real-world gait is made highly complex by concurring factors influencing the outcome measures, including disease characteristics, patient specific habits, and context and purpose of walking. Furthermore, any suggested solution should include considerations of the participants perception and acceptability of the device, as well as aspects related to wearability and usability.

Recent Advances

The IMI2-JU-funded Mobilise-D (www.mobilise-d.eu) is a multidisciplinary consortium of 34 institutions from academia and industry. Mobilise-D established a comprehensive roadmap [1] to inform the development, validation and approval of DMOs in Parkinson's disease, multiple sclerosis, chronic obstructive pulmonary disease and recovery from proximal femoral fracture. Within this context, the technical validation study (TVS [2]) was designed to: (a) verify the metrological performance of the sensors included in a IMU-based monitoring device, using a procedure that could be replicated on any device; (b) establish the validity and reliability of the DMOs estimated by the algorithms using data from an IMU-based device, taking into accounts the effects of populations (e.g, healthy adults, patients with various conditions), locomotor activities (simple straight walking vs complex walking tasks), contexts (lab based vs real world), durations (device wearing time, DMOs hourly and daily fluctuations, etc) and contextual confounding factors (such as location of walks, weather, use of walking aids, etc); and (c) establish participants' and assessors' opinions on the usability and acceptability of the monitoring devices that will be deployed.
In this talk I will address the significant complementary advances that have been made in association with the TVS development and deployment in the cohorts of interest. Examples will include the implementation of:

proposals for standardization of DMO definitions and data sharing [3]; suitable signal processing algorithms [4]; spot-checks for ensuring the quality of multicentric data collections [5]; gold standard tools for validation in the real world [6]; and objective criteria for device selection and algorithms' concurrent evaluation [7].

Future directions

The ambition of the Mobilise-D consortium is to support significant advances in the field by sharing tools, data and lessons learnt from the TVS and the subsequent clinical validation study. At the end of this journey, we expect to finally see clinical and regulatory [8] adoption of Digital Mobility Outcomes.

References

1. Rochester et al., Digital Biomarkers, 4(1), 13-27, 2020
2. Mazzà et al., BMJ Open, 11(12), 2021
3. Kluge et al., Plosone, 16(8), 2021
4. Soltani et al. IEEE TNSRE, 29, 2021
5. Scott et al., Sensors, 21(24), 2021
6. Salis et al., J Biomech, 127, 2021
7. Bonci et al., Sensors, 20(22), 2020
8. Viceconti et al., Sensors 20(20), 2020

Acknowledgements

MINERALIZED FIBROCARTILAGE AS A HIGHLY TUNABLE TISSUE ALLOWING THE INTEGRATION OF TENDON INTO BONE

Davide Ruffoni

Mechanics of Biological and Bioinspired Materials Laboratory, University of Liege, Belgium

Background

The biomechanical and biological integration of tendon and ligament into bone is crucial for joint health The strong differences in composition, microstructure and material behavior between the soft tissue and the hard bone make attachment regions vulnerable to high stresses, which may cause failure. The tendon-bone interface features several strategies to enhance strength and damage resistance [1], including the presence of a thin layer of mineralized fibrocartilage (FC) having the critical task of anchoring tendon to bone. Although FC is the target of several pathologies and injuries, this tissue is much less understood than bone and tendon, one reason being its heterogeneous behavior and tiny dimensions (i.e., less than 100 μm in thickness). Unsolved fundamental questions on FC include the structure-function relationship and the corresponding biomechanical properties at different locations and length scales, as well as the possible communication between bone and tendon cells with FC cells.

Recent Advances

Using the Achilles tendon insertion into calcaneus bone in rats as a model representative of tendon attachment in humans, we have investigated several aspects of FC and subchondral bone (Figure 1). The chosen location features two contiguous types of FC which have to solve different tasks: the so-called enthesis FC anchors tendon to bone while the periosteal FC facilitates tendon sliding. Firstly, we focused on microstructural porosity measured with high resolution micro-computed tomography. We highlighted a strong anisotropy of fibrochondrocyte lacunae and channel network at enthesis FC with pores oriented towards the tendon insertion. Conversely, periosteal FC features a more random architecture [2]. Moving to material properties, we explored the relationship between mineral content, matrix organization and mechanical properties by combining quantitative backscattered electron imaging, second harmonic generation imaging and nanoindentation. This analysis emphasized a considerable tuning in local mechanical behaviour within mineralized FC provided by matrix organization beyond mineral content. The anisotropic microstructure of enthesis FC is mirrored into highly aligned fibres, enhancing tissue stiffness and strength to anchor the tendon.

Future directions

FC is populated by fibrochondrocytes which are supposed to have limited communication abilities, whereas osteocytes are highly interconnected through

Davide Ruffoni is Professor of Biomechanics at the University of Liege since 2013. He obtained his MSc from Politecnico di Milano and was awarded a Marie Curie Fellowship to carry out his PhD at the Max Planck Institute of Colloids and Interfaces, supervised by R. Weinkamer and P. Fratzl. He did a postdoc at ETH, working with H. van Lenthe and R. Müller. He received two postdoctoral fellowships from the European Calcified Tissue Society and from the International Osteoporosis Foundation for his work on bone remodeling around implants. His current research focuses on mineralized tissues and on interfaces between soft and hard tissues. He is an author of 30+ publications in peer-reviewed journals, 2 book chapters and 60+ conference contributions.

the lacunocanalicular network (LCN). Using confocal laser scanning microscopy on stained samples, we are investigating possible communication paths between bone and FC. Mechanobiological aspects allowing maintenance and adaptation of soft tissue to bone attachments will be explored by simulating fluid flow across channels and nanopores crossing the bone-FC interface. These findings may indicate new targets in drug development to fight interface pathologies.
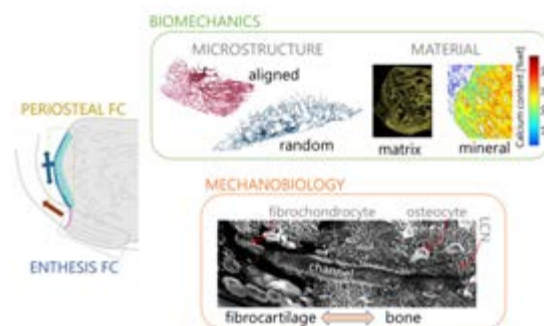

Figure 1: Biomechanical and mechanobiological aspects of fibrocartilage (FC) and subchondral bone at the tendon-bone attachment.

References

1. Tits and Ruffoni, Bone Rep, 14: 1-17, 2021.
2. Tits et al., Sci Rep, 11: 16534, 2021.

Acknowledgements

CELLULAR FORCE EXERTION DURING VASCULAR INVASION: MEASUREMENT AND APPLICATION TO DISEASE

Hans Van Oosterwyck

KU Leuven, Department of Mechanical Engineering, Biomechanics section, Belgium

Background

Cells actively apply forces to change shape, to migrate and to self-organise. This is e.g. the case during angiogenesis, the formation of new blood vessels from pre-existing ones. While force exertion and transmission are known to modulate cell signalling in a process called mechanotransduction, unravelling the exact mechanisms and demonstrating their importance in specific disease contexts remain challenging. In order to tackle these challenges we need methods that can quantify cellular forces under conditions that are representative for particular diseases. In this perspectives talk, I will summarise our work on Traction Force Microscopy (TFM), one of the main techniques for cellular force quantification. I will highlight our efforts in improving TFM accuracy, efficiency, user-friendliness and compatibility with 3D in vitro models of sprouting angiogenesis, as well as its potential for the study of microvascular disease mechanisms.

Recent Advances

We have developed a 3D in vitro model of vascular invasion into extracellular matrix (ECM)-mimicking hydrogels, compatible with live cell optical microscopy imaging and 3D TFM [1]. These methods enable to come up with highly detailed 3D hydrogel deformations and cellular tractions, thereby providing quantitative readouts of cell mechanical functionality and its importance for invasion.

A novel 3D TFM algorithm was developed and implemented into a nonlinear continuum mechanical framework [2]. The method calculates tractions at the cell-ECM interface that lead to a hydrogel deformation field that is as similar as possible to the measured deformation field and that is constrained by stress equilibrium. The accuracy and robustness with respect to measurement errors was assessed by setting up an in silico validation framework and applying this to our 3D invasion model [3]. Average traction error was found to be 23% (for conditions, representative for real TFM experiments), which was superior compared to a forward method (50% average error). The novel algorithm is part of TFMLAB, an open-source software package that streamlines the entire TFM workflow [4]. By providing user-friendly graphical user interfaces, we make 3D TFM accessible to a larger user group.

We are currently applying our in vitro and in silico methods to the study of Cerebral Cavernous Malformations (CCMs), which are malformations of the brain microvasculature that are caused by mutations in the so called CCM genes. Interestingly, these mutations have a number of cell mechanical implications. We

---

Hans Van Oosterwyck is a professor at KU Leuven, and heads a research group focused on the role of cellular forces for microvascular growth (mainly angiogenesis), function and disease. The group combines techniques such as computer modelling, in vitro microvascular models, hydrogels and optical microscopy, among others to innovate Traction Force Microscopy methods and their application. He has (co-) authored 89 journal publications on topics that have evolved from dental biomechanics over bone regeneration and engineering towards cell mechanics and angiogenesis.

recently demonstrated that silencing of the CCM2 gene leads to an increase of vascular invasion, which we could associate to higher cellular tractions (Figure 1).

Future directions

Future efforts should aim at applying TFM to elucidate the role of (abberant) cellular force exertion in disease progression, e.g. by studying the interplay between force exertion and genetic programs. The accuracy and applicability of TFM can be further improved by combining TFM with situ ECM (micro)mechanical characterization and how this evolves over time.
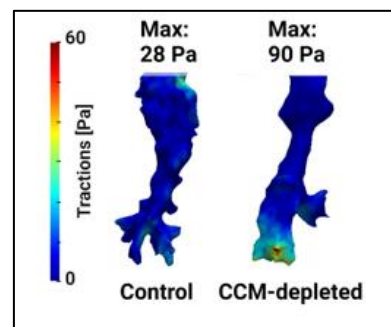

Figure 1: Cellular tractions around control and CCM-depleted invading angiogenic sprouts.

References

1. Vaeyens et al., Angiogenesis, 23:315-324, 2020.
2. Sanz-Herrera et al., Soft Matter, 17:10210-10222, 2020.
3. Barrasa Fano et al., Acta Biomaterialia, 126:326-338, 2021.
4. Barrasa Fano et al., SoftwareX, 15:1-9, 2021.

Acknowledgements

MECHANOSENSING IN BONE USING FLUID FLOW THROUGH NETWORKS

Richard Weinkamer

Max Planck Institute of Colloids and Interfaces, Department of Biomaterials, Potsdam, Germany

Background

Bone's ability to adapt its structure to a changing mechanical environment require bone cells to act as mechanosensors. However, due to the high stiffness of bone, strains are assumed too small to be directly sensed by cells. To resolve this dilemma, Weinberg and coworkers proposed the Fluid Flow Hypothesis [1], which states that load-induced fluid flow through the lacunocanalicular network (LCN) acts as mechanical stimulus. The LCN forms an intricate porosity, which permeates the bone and accommodates the cell network of osteocytes. It is thought that the fluid flow through this network creates shear and drag forces on the surface of the osteocytes, which the cells sense.

Recent Advances

Recently, a critical test of the Fluid Flow Hypothesis could be performed due to advances in experimental techniques. First, it is possible to measure the mechanoresponse in terms of newly formed and resorbed bone in small animals. Here, controlled loading of the bone is combined with time-lapsed in vivo µCT [2]. Second, confocal microscopy and image analysis allows for imaging of the 3D architecture of the lacunocanalicular network [3]. The fluid flow through the LCN can then be computed using circuit theory [4]. This new methodology was applied to the tibiae of three mice to compare the measured mechanoresponse with a prediction based on fluid flow calculations. In contrast to predictions based on strain alone, also considering the LCN architecture predicted correctly that (i) the mechanoresponse is similar on the outer periosteal and the inner endocortical surface of the tibia and (ii) individual differences in the mechanoresponse between mice [5]. An earlier study on fluid flow through the LCN in human osteons showed that load-induced fluid flow results in flow velocity patterns that run counter the intuition, which is usually based on flow resistance [4].

Future directions

The new approach to predict the mechanoresponse of bones based on fluid flow through the LCN should be applied to different skeletal sites and species to determine the influence of the network architecture. Changes in the LCN with age or disease allow now a mechanobiological interpretation. With the possibility to image macroscopic portions of the LCN containing millions of canaliculi, a connectomics approach [6] can be applied, which aims at relating network architecture with the multiple network functions.

Figure

Figure 1: Lacunocanalicular network (LCN) in a cross-section of a mouse tibia imaged using confocal microscopy after rhodamine staining.

References

1. Weinbaum et al., J Biomech, 27: 339-360, 1994.
2. Birkhold et al., Bone, 75: 210-221, 2015.
3. Repp et al., Bone reports, 6: 101-108, 2017.
4. van Tol et al., Biomech Model Mechanobiol, 19: 823, 2020.
5. van Tol et al., Proc Natl Acad Sci 117: 32251, 2020.
6. Weinkamer et al., Curr Osteoporos Rep, 17: 186-194, 2019.

Acknowledgements

X-RAY BASED 3D HISTOLOGY OF BIOLOGICAL TISSUES

Greet Kerckhofs (1,2,3,4)

1. Biomechanics lab, Institute of Mechanics, Materials, and Civil Engineering, UCLouvain, Belgium; 2. IREC – Institute of Experimental and Clinical Research, UCLouvain, Belgium; 3. Dept. Materials Engineering, KU Leuven, Belgium; 4. Prometheus, Division of Skeletal Tissue Engineering, KU Leuven, Belgium.

Background

Biological tissues are highly complex in their composition and microstructural organization. The 3D spatial organization of the tissue substituents, such as proteins, cells, extracellular matrix (ECM) or functional units, is crucial for a proper *in vivo* functioning. To better understand the effect of a pathology on the functioning of a tissue, visualizing and characterizing the 3D microstructure and composition of these tissue substituents would, thus, be crucial. Measurements made in 2D, however, only partially reveal the full 3D microstructure. Indeed, conventional and even digital 2D histological assessment are largely unsatisfactory for spatial assessment of biological tissues, because the restricted sectioning orientation and the limited depth resolution only partially reveal their full 3D morphology, but also because they lack reproducibility on a large scale (sample destruction). In this overview, the potential and added value compared to conventional 2D imaging techniques of contrast-enhanced X-ray microfocus computed tomography (CECT) are presented. CECT is a very recent development in the microCT imaging field and allows **X-ray-based 3D histology** of both soft and mineralized tissues.

Development of novel staining agents

Over the past decade, different contrast-enhancing staining agents (CESAs) have been recently reported for CECT of specific soft tissues [1]. However, both the CESA staining protocol and the image acquisition setup should be non-destructive, having no effect on the tissue integrity. As most of the currently applied CESAs are destructive (acidic, toxic, dehydrating), in our research we focus on the development of non-invasive tissue-specific CESAs. We reported the simultaneous visualization of mineralized and soft structures within bones utilizing an in-house Hafnium-substituted Wells-Dawson polyoxometalate (Hf-WD POM) [2]. Hf-WD POM allowed visualizing, apart from bone, the bone marrow adipocytes at the single cell level, as well as the vascular network allowing full 3D blood vessel network assessment (i.e. branching analysis and spatial distribution).

In a follow-up study, we explored whether similar POM formulations could also be efficient CESAs for soft tissue visualization [3]. We screened different POM formulations, including the much less expensive precursors of the metal-substituted Hf-WD POM, for their potential as CECT CESA. Based on their staining capacity and speed of diffusion, as well as on their fate after tissue staining experiments, we concluded that monolacunary POMs provide a faster staining, but a lower specificity than the 1:2 Hf-WD POM.

Prof. Greet Kerckhofs is full-time Associate Professor at the Institute of Mechanics, Materials & Civil Engineering (UCLouvain, Belgium) and has founded her own biomedical lab at the Institute of Experimental and Clinical Research (UCLouvain). She is also 10% Assistant Professor at the Dept. of Materials Engineering (KU Leuven, Belgium). She is Scientific Committee member of Prometheus, the Division of Skeletal Tissue Engineering (KU Leuven). She obtained her PhD in Materials Engineering (KU Leuven) in 2009, and was a postdoc at the Université de Liège (2012-2014) and the KU Leuven (2009-2011; 2014-2017). Her present research mainly focuses on 'X-ray-based 3D Histology using Contrast-Enhanced microCT'. She is author of 57 peer-reviewed publications, two book chapter and more than 130 contributions to international/national conferences. She has an h-index of 27 with over 3500 citations.

Relevant applications

We have successfully used the POMs for several applications: developmental changes of murine placenta and embryo [4], effect of an anti-angiogenic drug on tumour angiogenesis [5], quantitative analysis of the fibre orientation in tendons and the bone-tendon interface, quantitative description of the microstructure of blood vessels, heart tissue and heart valves (yet unpublished data), and many others.

Future directions

We are currently focusing on the further development and validation of novel, tissue-specific CESAs, on the combination with deep learning image analysis for improved quantitative 3D analysis of the CECT datasets and on 4D CECT, which combines in-situ mechanical testing with CECT imaging; this all to further improve the knowledge on the link between the microstructure of a tissue and its functional behavior.

References

1. de Bournonville *et al.* Contrast-Enhanced MicroCT for Virtual 3D Anatomical Pathology of Biological Tissues: A Literature Review. Contrast Media & Molecular Imaging (2019) 1-9. **2.** Kerckhofs, G. et al. Simultaneous three-dimensional visualization of mineralized and soft skeletal tissues by a novel microCT contrast agent with polyoxometalate structure, Biomaterials 159 (2018) 1-12 **3.** de Bournonville & S., Vangrunderbeeck *et al.*, Exploring POMs as non-destructive staining agents for contrast-enhanced microfocus computed tomography of biological tissues. Acta Biomaterialia (2020). 105, 253-262. **4.** De Clercq, K. *et al.,* High-resolution contrast-enhanced microCT reveals the true three-dimensional morphology of the murine placenta. PNAS doi: 10.1073/pnas.1902688116 **5.** Kerckhofs, G. *et al.* Contrast-enhanced microCT to visualize and quantify the 3D vasculature in biological tissues without the need for perfusion. Bruker User Meeting Brussels 2017.

VISCOSITY AND NONLINEAR ELASTOGRAPHY WILL BECOME THE NEXT GENERATION BIOMARKERS IN CLINICAL DIAGNOSIS

Inas H. Faris, Guillermo Rus

Ultrasonics Lab, Dept. Structural Mechanics, University of Granada + Biosanitary Research Institute, Spain.

Elastic changes in a tissue are associated with a broad spectrum of pathologies, which stems from the tissue microstructure, histology and biochemistry [1]. This presentation aims to elucidate the potential of viscous and nonlinear elastic parameters as conceivable diagnostic mechanical biomarkers. First, by providing an insight into the classic role of soft tissue microstructure in linear elasticity; secondly, by understanding how viscosity and nonlinearity could enhance the current diagnosis in elastography; and finally, by compounding preliminary investigations of those elastography parameters within different technologies.

Background

Ultrasonnic elastography characterization and understanding of soft tissue has been developed as a clinical diagnostic tool over the last two decades [2] and evolved through different technologies: quasi-static, dynamic elastogra-phy, based acoustic radiation force: ARFI, vibroacous-tography or pSWE, or on direct excitation: sonoelasto-graphy and the emerging torsional wave principle [3]. New elastography sensor technologies to characterize soft tissue biomechanics, from hardware to algorithms, are bound to endow a new class of biomarkers that quantify the mechanical functionality and abnormalities in the structural architecture of soft tissues are intimately linked to a broad range of pathologies including tumors, atherosclerosis, brain ageing, gestational disorders, liver fibrosis or osteoarticular syndromes, to name a few. These higher order mechanical parameters may become key discriminating biomarkers since: (1) the physics of wave propagation is explaining how dispersion is a compound expression of the rheological, poroelastic, and microstructural scattering phenomena governed by the complex fibrous multiscale microarchitecture of the stroma, which undergoes characteristic changes during pathologies [4]; and (2) the extreme hyperelasticity that soft tissue exhibits clearly manifests as quantifiable harmonic generation, hypothesized to strongly depend on the unfolding of its collagen fibres, which again controls the tissue's mechanical functionality.

Recent Advances

Existing ultrasonic techniques are restricted to map first order tissue stiffness. In contrast, recent advances covering:

a) new mechanical wave-based sensing technologies ranging magnetic resonance elastography, ultrasonic shear wave elastography or torsional wave elastography,
b) wave propagation models and multiscale interaction with michroarchitectural changes, and

c) patient testing, are allowing to quantify the mechanical functionality through relevant parameters beyond linear: dispersive and nonlinear.

Future directions

a) To understand how structural architecture of soft tissue is intimately linked and controls a broad range of pathologies, which underpins the foundation of a new diagnostic technology.
b) To develop new sensor technologies capable of effectively sensing tissue elasticity, and yield simple and robust diagnostic tests and instruments.
c) To ground a new generation of biomarkers of physical nature based on the mechanical micro-architecture and properties of the tissue.

In conclusion, evidence of the diagnostic capability of elastic parameters beyond linear stiffness is gaining momentum as a result of the technological and imaging developments in the field of biomechanics. The unexplored nature and applicability span of viscous and nonlinear mechanical biomarkers endow a foundational diagnostic technology.

References

1. Rus G., et al. 2020. Sensors, 20, 2379
2. Barr R. G., et al. 2012. *Ultrasound Quarterly* 28 13-20.
3. Melchor J and Rus G. Ultrasonics, 54(2014): 1950-1962.
4. Peralta L., et al. 2015. *J. of Biomechanics* 48 1557-1565.

Acknowledgements

MULTISCALE BIOMECHANICAL AND STRUCTURAL PROPERTIES OF LUMBAR INTERVERTEBRAL DISCS: MECHANISMS OF INJURY

John J. Costi

Medical Device Research Institute, College of Science & Engineering, Flinders University, Australia

Background

Poor vascularity and slow repair of the disc renders it susceptible to developing tears. Circumferential tears are present from the teenage years and arise from delamination of adjacent lamellae within the annulus fibrosus [1]. These tears are associated with disc degeneration [2-3] and likely increase the risk of herniation during lifting [4]. The major underlying microstructural components contributing to these are collagen, elastin, and proteoglycans, which are found within the extracellular matrix (ECM). However, there is limited understanding of how degeneration affects the mechanical properties of collagen type I individual fibre bundles (microscale), and of isolated fibrils (nanoscale). Furthermore, there are significant gaps with respect to both the ultrastructural organisation and mechanical properties of the elastic fibre network between adjacent lamellae (i.e., interlamellar matrix: ILM). Taken together, it is crucial to develop a new understanding of the role that the ILM plays during progressive loading to disc herniation.

Recent Advances

We found that the tensile modulus of human collagen type I fibres and fibrils were not affected by disc region or degeneration [5]. The lack of sensitivity to region and degeneration suggested that tissue properties are influenced by the assembly of collagen type I into composite structures (i.e., lamellae/ILM), together with their composition. These findings led to investigations that focused on the assembly of the collagen and elastic fibre network in the sheep ILM.

Partial digestion techniques were developed and validated to remove collagens and other ECM components from the ILM to isolate the elastic fibre network. Studies were then conducted on the contribution of the elastic network to both the ultrastructural and the micro-tensile/shear viscoelastic properties of intact and digested ILM (i.e. isolated elastic fibres) [6-8]. Key findings revealed a complex network of elastic fibres within the ILM, where the majority of thicker 1-2 µm diameter fibres were oriented parallel to the lamellae, with thinner 0.1 µm fibres symmetrically oriented at ±45° to the lamellae.

The tensile and shear micromechanical properties of the intact and digested ILM revealed viscoelastic behaviour, with differences in failure stress between loading directions for the intact and digested ILM [7,8]. These differences suggested that the ECM plays an important role in imparting isotropic failure properties to the intact ILM, compared to orthotropic behaviour for the elastic fibres only. We hypothesised that a breakdown of the

John J. Costi is an Associate Professor at Flinders University. He earned his PhD in Experimental Biomechanics at Flinders University in 2004. He was a post-doctoral fellow at the University of Vermont, USA in 2004-2005. He is Fellow of the Institution of Engineers Australia (Biomedical & Mechanical Colleges), Fellow of International Orthopaedic Research (FIOR), Associate Editor for the Journal of Biomechanical Engineering, and Scientific Secretary of the Spine Society of Australia. He leads a research program aimed at understanding the multiscale, multiaxial properties of normal, degenerated and injured discs, and their failure mechanisms. He has authored 57 peer-reviewed journals articles, several book chapters and more than 160 contributions to International and National Conferences.

ECM within the ILM could lead to an increased risk of delamination and herniation injury during overloading, which led to the following study.

During compressive loading to herniation in flexed sheep lumbar discs, we identified that local disruption and microstructural disorganisation of the ILM was present at a compressive displacement that was half of that required to cause macroscopic herniation [9]. These are important findings that suggest the presence of a threshold of loading that may initiate a cascade of injury towards herniation and degeneration.

Future directions

Future research on determining the threshold of compressive displacement that places human discs at greater risk of herniation injury would result in a paradigm shift in our understanding towards developing strategies to avoid lifting events that may initiate progressive damage accumulation.

References

1. Vernon-Roberts et al, Spine 22:2641-2646, 1997.
2. Fazzalari et al., Spine 26:2575-2581, 2001.
3. Haefeli et al., Spine 31:1522-1531, 2006.
4. Veres et al., Spine 33:2711-2720, 2008.
5. Pham, Shapter, Costi, J. Biomech, 67:24-31, 2018.
6. Tavakoli, Elliott, Costi, Acta Biomater, 58:269-77, 2017.
7. Tavakoli, Costi, Acta Biomater, 71:411-19, 2018.
8. Tavakoli, Costi, Acta Biomater, 77:292-300, 2018.
9. Tavakoli et al., Ann Biomed Eng, 46:1280-91, 2018.

Acknowledgements

INVESTIGATING THE BIOMECHANICS OF THE SPINE WITH DIGITAL IMAGE CORRELATION (DIC)

Luca Cristofolini

Dept. of Industrial Engineering, Alma Mater Studiorum – University of Bologna, Bologna, Italy

Background

Investigating spine biomechanics poses a number of challenges, because of its complex structure that includes hard (the vertebrae) and soft tissue (ligaments, cartilages and intervertebral discs, IVD). Research in this area covers both basic science and clinical applications. In many cases, one would need to measure the displacements of the different parts, but also the state of stress-strain. Great progress has been made in the understanding of kinematics [e.g. 1,2], in measuring the strain on the vertebra [3] or the pressure within the IVD [4]. However, simultaneous measurement of different quantities is challenging. Specifically, it is difficult to measure the strain distribution in the different tissues.

Recent Advances

Digital image correlation is a contactless technique that allows measuring the full-field displacements and strains on the surface of an object [5]. Its application in biomechanics entails several methodological problems, including preparation of a suitable surface speckle pattern, reducing measurement errors, and optimizing the correlation analyses settings [6].

If properly tuned, it allows to measure at the same time the 3-dimensional displacements and the strain (including principal strains and directions) on the entire surface, including the vertebra, the ligaments, the IVD and implantable components (Fig. 1).
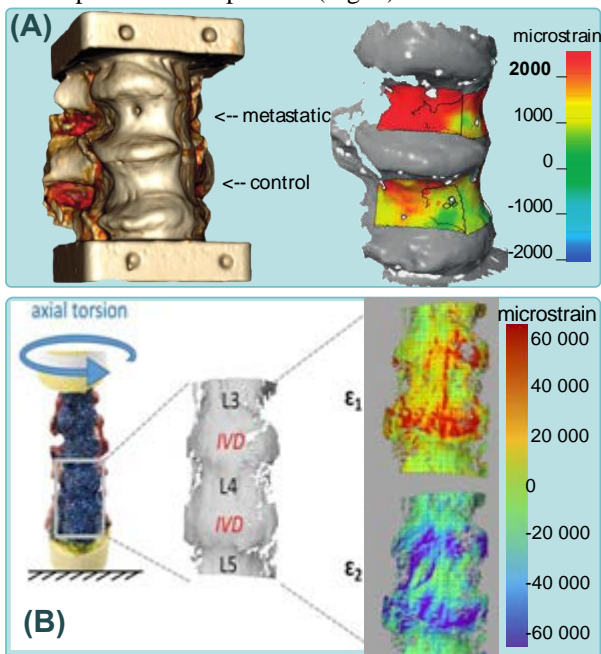
Fig. 1: Applications of DIC to the spine: (A) localized strains due to vertebral metastases [9]; (B) behaviour of the anterior longitudinal ligament, including stretch of the fibers, and concentrations near the osteophytes [10].

Luca Cristofolini is a Professor of Biomechanics at the Dept. of Industrial Engineering, University of Bologna, where he leads the Experimental Biomechanics group. He obtained his PhD in Biomechanics in 1996. He was a research assistant in Experimental Stress Analysis in 1996-2004, and associate professor of biomechanics from 2004 to 2012. His research is in the field of musculoskeletal biomechanics, focusing on implantable devices, fracture and spine. He is acknowledged for his work combining mechanical tests and *in silico* models. He pioneered the use of Digital Image Correlation in Biomechanics since 2007. He authored 200+ papers in peer- reviewed journals, 11 book chapter (including one on DIC) and 350+ Conference papers.

Future directions

DIC is excellent for investigating the specimen surface, but cannot measure internal strains. Digital Volume Correlation (DVC) relies on high-resolution medical imaging to compute strains inside a structure [9]. DVC can achieve similar precision to DIC inside, but is very imprecise on the surfaces. Combining DIC and DVC would allow better addressing complex problems.

Another challenge is to combine DIC and finite element modeling (FEM): DIC can provide a validation to FEM, while FEM allows more extensive investigations, e.g. sensitivity analyses to explore multiple scenarios [10].

References

1. Panjabi MM (2007) "Hybrid multidirectional test method…" Clin Biomech 22: 257–65
2. Wilke,HJ *et al* (1994) "A Universal Spine Tester for in Vitro Experiments …" Eur Spine J 3,2: 91–7
3. Cristofolini L et al (2013) "Strain distribution in the lumbar vertebrae …" The Spine J 13(10):1281–92
4. Wilke J *et al* (2001) "Intradiscal pressure together with anthropometric data…" Clin Biomech;16(S1):111-26
5. Cristofolini L (2015) "Overview of Digital Image Correlation" in "Experimental Stress Analysis" Springer
6. Palanca M et al (2013) "Full-field strain distribution in multi-vertebra spine segments…" Med Eng Phys52:76–83
7. Palanca et al (2021) "Type, size, and position of metastatic lesions…" Bone 151: 116028
8. Palanca et al (2020) "The strain distribution in the lumbar anterior longitudinal ligament…" PLOS ONE: 0227210
9. Palanca M et al (2016) "DVC to estimate local strains in natural and augmented vertebrae" J Biomech 49:3882–90
10. Cristofolini et al (2010) "Positive synergy of FE models and in vitro experiments" Phil Trans A.368:2725–63

Acknowledgements

COMPUTATIONAL SIMULATION TO UNRAVEL CELL MECHANOTRASDUCTION IN PATHOLOGICAL AND PHYSIOLOCIGAL PROCESSES

María José Gómez-Benito

Multiscale in Mechanical and Biological Engineering (M2BE), Aragón Institute of Engineering Research (I3A), Aragon Institute for Health Research (IIS Aragón), University of Zaragoza, Zaragoza, Spain

Background

Cell are able to sense their mechanical environment and translate it into mechanochemical signals. How cells sense and translate this environment is not completely known. The current measurement techniques are not able to determine the exact mechanical environment in the cell and surrounding it. Many uncertainties should be faced, ie. the change of cell mechanical properties depending of the extracellular matrix (ECM). Computational models (CMs) combined with experimental measurements fill this gap. CMs assist in determining the mechanical environment inside the cell and hypothesize on the possible mechanotransduction mechanisms used by cells in different physiological and pathological processes.

Recent Advances

In the last two decades, much effort has been done to understand mechanotransduction mechanisms through CMs at different scales (tissue, cell, subcellular) which have helped to understand the mechanical interplay of the cell with its environment. In our work we try to unravel these mechanotransduction mechanisms behind different biological process from tissue to cell level formulating biophysical laws and implementing then into discrete or continuum CMs [1-6], the models help us to design new in vitro experiments that support the validity of our CMs. (Fig. 1). At the tissue level we have formulated mechanotransduction laws through CMs which help to explain how cell differentiation, proliferation, contraction and ECM remodelling is connected to the mechanical environment, in processes such as bone and wound healing [2]. At the cell scale, we have used CMs to identify possible mechanical stimuli which make a cell choose among different migration modes (lobopodial or lamellipodial) depending on the ECM mechanical properties [3], we have also shown how the mechanical environment in the cell is critical for mesenchymal migration in 3D ECMs [4]; CMs has also allowed us to identify a possible mechanotransduction mechanism which makes uninfected cell reacts to bacterial infection in infected cell monolayers [5]; finally, we have analysed in CMs the mechanical feedback in the extravasation of cancer or inmune cells through endothelial cell contraction and weakening of cell-cell adhesions [6].

Future directions

Future work should formulate hybrid (continuum-discrete) models to go deeper into our understanding of mechanotransduction mechanisms at different scales (tissue, cell and subcelullar) and their interactions.

María José Gómez-Benito is Associate Professor at the University of Zaragoza, Spain, and researcher at Engineering Research Institute of Aragon. She obtained her PhD in Computational Mechanics, 2005. She was a postdoctoral fellow at the Institute of Orthopaedic Research and Biomechanics and at the Max Planck Institute of Colloids and Interfaces (Germany). In the last ten years, she has focused on Computational Cell Mechanics with special emphasis in pathological processes. She is a member of the European Society of Biomechanics since 2007. She has authored around 40 publications in peer- reviewed journals, and more than 100 contributions to Conferences.

Moreover, the advance of experimental disciplines at lower scales will increase the accuracy of measurement techniques to determine the mechanical variables involved in cell processes and provide tools for more accurate mechanotransduction hypothesis.
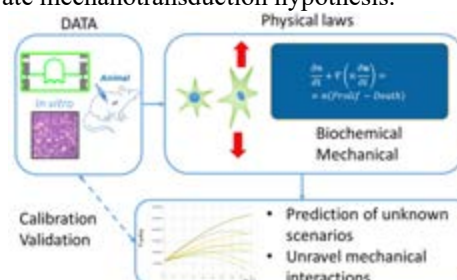
Figure 1: Scheme of a generic mechanochemical model to formulate the mechanotransduction hypothesis.

References

1. Hervás-Raluy et al, Biomech Model Mechanobiol., 18(4), 1177-1187.
2. Valero et al, PloS one. 2014. (3), e92774.
3. Serrano-Alcalde et al., Comput Methods Biomech Biomed Engin 2021 24 496-505.
4. Merino-Casallo et al., Front Physiol. 2018, 9:1246.
5. Bastounis et al., Dev Cell., 56(4), 443-460.e11.
6. Nieto et al., Eng Fract Mec, 2020, 224, 106718.
7. Juste-Lanas et al, J Biomech Eng, 2022, 10.1115/1.4053143

Acknowledgements

C⁴BIO: COMMUNITY CHALLENGE TOWARDS CONSENSUS ON CHARACTERIZATION OF BIOLOGICAL TISSUE

Nele Famaey

Department of Mechanical Engineering, KU Leuven, Belgium

Background

Credible numerical simulations require reliable input parameters and associated acquisition methods[1]. With the advent of simulation-based medical device development and *in silico* trials, there is a strong, industry-driven need for a quality label for the input parameters of these simulations. Focusing on biological tissue properties, not every numerical analyst has access to the experimental facilities and expertise to perform his/her own tests, nor does he/she always have the expertise to assess the quality and uncertainty of material parameters used.

Literature abounds with studies on experimental characterization of the material behavior of various types of biological tissue, but meta-analysis suggests a disconcerting degree of variability in results as well as in methodology. Indeed, there are currently no standards available for testing the material properties of biological tissue, be them mechanical, thermal, electrical or other. Nevertheless, a quantitative analysis of the degree of methodological variability has, to our knowledge, never been attempted and is an essential step towards proper uncertainty quantification (UQ) in model credibility assessment.

Recent advances

The Virtual Physiological Human institute together with the Avicenna Alliance and FIBEr are taking the first steps to quantify the degree of methodological variability and work towards a community consensus of methods for biological tissue characterization, in the so-called C⁴Bio initiative. A pilot testing campaign initiated in 2021, focused on uniaxial tensile testing of porcine aorta. 25 expert labs from all around the globe were asked to perform uniaxial tensile tests using their preferred methodology, on equivalent sets of porcine aorta and synthetic material, prepared at FIBEr (KU Leuven core facility for biomechanical experimentation). All participants also filled in a questionnaire indicating the various design choices they made. Statistical analysis of this first phase yielded coefficients of variation of 71-126% for relevant output parameters.

In a second phase, a consensus methodology was defined with all participants and the same type of material was distributed to the expert labs, who now performed the experiments using the consensus methodology. The results of this second phase are currently under investigation.

Nele Famaey is currently Professor at the Department of Mechanical Engineering, KU Leuven, heading the Soft Tissue Biomechanics group. She obtained her PhD in Biomechanics at KU Leuven in 2012. Since 2017, she is the coordinator of FIBEr (KU Leuven core facility for biomechanical experimentation). Since 2018, she holds a visiting professorship at the University of Ghent in the BioMMeda group. She is currently coordinating the C⁴Bio initiative as a co-chair of the VPHi Tissue Characterization task force. She is an author of 60 publications in peer-reviewed journals and more than 80 contributions to International and National Conferences.

Future directions

Even for a relatively simple method like uniaxial tensile testing, the methodological variation between expert labs is staggering. This first C⁴Bio campaign serves as a proof of concept, as well as a wake-up call, that proper UQ is essential for credible simulations, and that through community effort we should aim to increase the quality and reduce the uncertainty to a workable level, for various tissue types and characterization methods.

Figure 1: C⁴Bio around the globe. The green markers indicate the locations of the expert labs participating in the pilot campaign.

References

1. ASME V&V 40 (2018). Assessing Credibility of Computational Models Through Verification and Validation: Application to Medical Devices. Washington, DC: Standard, American Society of Mechanical Engineers.

Acknowledgements

TRANSLATIONAL COMPUTATIONAL STUDIES TOWARD PREVENTING POST-TRAUMATIC OSTEOARTHRITIS AFTER JOINT INJURY

Rami K. Korhonen[1] and Donald D. Anderson[2]

[1]*University of Eastern Finland, Finland;* [2]*University of Iowa, United States of America*

Background

Traumatic joint injuries trigger a biological response that either leads to restoration of a healthy joint or to post-traumatic osteoarthritis (PTOA). Altered joint biomechanics (pathomechanics) after injury contribute to PTOA risk [1-3], both through mechanobiological pathways and through frank tissue failure. Translational computational studies of articular joints aim to reliably predict PTOA risk after a specific joint injury [4-8]. However, the challenges of modeling such a complex system span scales ranging from whole-joint to tissue and cellular levels. A better understanding of the interplay between biomechanics and biochemical processes affecting cell death, tissue failure, and whole joint degeneration is crucial for predicting early disease progression and identifying ways to prevent PTOA.

Recent Advances

Considerable progress has been made in prospectively modelling tissue-level failure mechanisms in articular cartilage [5,7], including not only the articular joint biomechanics but also the biological processes triggered by and in turn influencing the mechanical state. These studies typically leverage a <u>physics-based forward analysis</u> of important processes (Figure 1) in a small number of subjects. Recent advances have utilized MRI and other imaging modalities to derive patient-specific material property assignments to fuel the analysis. [9] Concurrent progress has been made using retrospective expedited patient-specific computational stress analysis to deduce gross pathomechanical factors that influence PTOA risk in patients after a joint injury. These studies involve what amounts to a <u>reverse engineering strategy</u> to identify critical deleterious mechanical factors in a much larger number of subjects. Recent advances have included integration of low-dose weight bearing CT (WBCT) to provide models in a weight bearing pose, as well as more sensitive early imaging indicators of joint health that provide a basis for shorter and more efficient clinical studies linking joint mechanics to PTOA [10].

Future directions

We have come to recognize that future progress in this area hinges on finding ways to effectively bridge these two computational modelling approaches. Atlas-based methods have been proposed as an alternative to patient-specific modelling, but much work remains to be done here. Efforts to utilize tissue-level failure estimates in larger groups of subjects offers promise for identifying specific targets for new targeted interventions, both biological and mechanical in nature.

Rami is currently Professor in the Department of Applied Physics, University of Eastern Finland. He obtained his PhD in Applied Physics at the University of Eastern Finland in 2004. His present research mainly focuses on developing a basic computational modeling framework for predicting cartilage failure by incorporating tissue-relevant mechanobiological factors. Don is Professor in the Department of Orthopedics and Rehabilitation, University of Iowa. He obtained his PhD in Mechanical Engineering at the University of Iowa in 1989. His research focuses on translational studies that use clinical data sources to deduce pathomechanical factors contributing to post-traumatic osteoarthritis risk after joint injury.
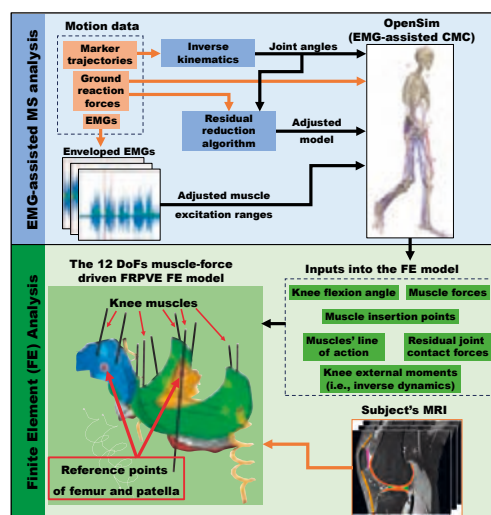
Figure 1: Example of physics-based forward analysis framework for studying joint mechanics/tissue failure.

References

1. Anderson et al., J Appl Biomech, 26:215-23, 2010.
2. Li et al., J Orthop Res, 26:1039-45, 2008.
3. Bolcos et al., Clin Biomech, 79:104844, 2020.
4. Mononen et al., Ann Biomed Eng, 47:813-25, 2019.
5. Liukkonen et al., Comput Methods Biomech Biomed Engin, 20:1453-63, 2017.
6. Tanska et al., J Biomech, 48:1397-406, 2015.
7. Kern & Anderson, J Biomech, 48:3427-32, 2015.
8. Anderson et al., J Orthop Res, 29:802-9, 2011.
9. Orozco et al., J Orthop Res, 39:1064-81, 2021.
10. Willey et al., J Bone Joint Surg Am, 102:796-803, 2020.

Acknowledgements

IN SILICO TRIALS TO ASSESS THE SAFETY AND EFFICACY OF NEW TREATMENTS FOR MUSCULOSKELETAL DISEASES

Marco Viceconti

Department of Industrial Engineering, Alma Mater Studiorum - University of Bologna, and Medical Technology Lab, IRCCS Istituto Ortopedico Rizzoli, Bologna (IT)

Introduction

In Silico Trials are subject-specific predictive models that are used to assess the safety or the efficacy of new medical products, whether drugs or medical devices, before their introduction in the market.

In this perspective talk we will describe four In Silico Trials solutions currently under development in our team and use them as guiding examples of the barriers we need to overcome in the development and deployment of In Silico Trials solutions to assess new treatments for musculoskeletal diseases.

BBCT surrogate biomarker

The Bologna Biomechanical Computer Tomography (BBCT) is the most mature of the four solutions described here. BCT are CT-based patient-specific finite element models that predict the force required to fracture a patient's bone when loaded in a given direction; while BBCT is intended as a research tool, other BCT implementations are sold commercially (SimFini, PerSimiO, IL; VirtuOst, OnDiagnostics, USA), it is now being validated as a surrogate biomarker for proximal femur fracture (PFF) in drug trials for new osteoporosis drugs.

BoneStrength In Silico Trials

Building on the basis of the BBCT solution we developed two cohorts of 500 virtual patients each, one at high risk of PFF and one at lower risk. Using a High-Performance Computing implementation, we simulate hundreds of random falls and the progression of the osteoporosis disease over ten years. We can then predict how any new treatment of known response in term of mineral density is effective in reducing the risk of hip fracture over ten years. We are currently working on the second layer of clinical validation, that pertinent to the modelling of the disease progression.

ForceLoss stratification tool

Dynapenia (the loss of muscle force) is a complex condition related to aging but also secondary to other diseases, such as cancer. There is currently a number of new drugs under development aimed to slow down the loss of muscle mass (sarcopenia). However, dynapenia can be cause by sarcopenia, activation inhibition, or pathological neuromuscular control. The ForceLoss solutions fuse MRI imaging, dynamometry, and EMG data in a patient-specific model that can assist the differential diagnosis of dynapenia, simplifying the stratification in recruitment, so include in a study only

Marco Viceconti is full professor of Bioengineering at the Alma Mater Studiorum – University of Bologna, and Director of the Medical Technology Lab of the Rizzoli Orthopaedic Institute. Before he led the Insigneo Institute at the University of Sheffield, UK. In the last 20 years he focused primarily on In Silico medicine, where patient-specific physics-based computer models are used as clinical decision support systems or to evaluate the safety and efficacy of new medical products. He served in the Council of the ESB, including a term as President. He is currently one of 25 members of the World Council of Biomechanics. In 2021 he received the Huiskes Medal for Biomechanics.

patients with sarcopenia-cased dynapenia. We are currently working on the first layer of clinical validation, that pertinent to the physiology layer (e.g. predicting the maximal voluntary isometric contraction in knee extension in normal healthy adults).

IST4JR

The BBCT technology is also the basis for the In Silico Trials for Joint Replacements (IST4JR) solution. This is a long-term project aimed to develop a complete In Silico Trial for new total joint replacement designs, which can help assessing the risk associated with each of a list of well-known failure modes. Currently we are developing a predictor of the risk of intraoperative fracture for cementless hip stems, a predictor of massive wear for soft bearing knee replacements, a predictor of the risk of recurrent dislocation, and a predictor of the risk of aseptic loosening in cementless implants. We are currently in the early implementation phase or working on the technical validation using outcome results from joint replacement registries.

Conclusions

Considering all these developments, it is possible to identify recurrent barriers that slow down the development, validation, certification, and ultimately the adoption of In Silico Trials for musculoskeletal diseases.

Acknowledgements

DIGITAL TWINS AND COUPLED APPROACHES FOR MANAGEMENT OF TIBIAL PLATEAU FRACTURE

Arnaud Germaneau

Institut Pprime, UPR 3346 CNRS – Université de Poitiers, France

Background

Since several years, trauma surgery has moved toward less invasive approaches that consider the specific pathology, morphology, and life habits of patients. Recently, a new Minimally Invasive Surgery (MIS) named Tuberoplasty [1] has been developed to treat the two most common types of tibial plateau fractures [2]: Type II (depression and separation of bone fragments) and Type III (depression of a bone fragment). MIS offers numerous advantages such as reduced time of surgery, bleeding and risk of infection and soft tissue lesions. These benefits are at the expense of direct visualization of the fractured bones during the surgery due to limited skin incision. Furthermore, the quality of fracture reduction is essential to guarantee the best patient outcome. MIS requires precise per-operative surgical analysis and quantification of bone fragment displacements during the surgery remains complex (reduction and stabilization steps). In addition, many of the common complications following MIS (cement leakage or adjacent fractures) have been postulated to be related to the quality of the cancellous bone–bone cement interface, which is also a function of its mechanical response and fracture resistance.

Recent Advances

Developments and optimization of trauma surgery require an advanced understanding of biomechanical behaviours with combined multi-scale approaches in order to build relevant predictive patient digital twins. We developed and evaluated numerical methods to assist preoperative planning of TPF management, integrating personalized morphological and behaviour data. The first numerical approach, based on statistical shape analysis, was developed to predict the healthy shape of a fractured tibial plateau. The second one concerned the Finite Element (FE) modelling of TPF reduction with balloon inflation by patient-specific modelling using CT scans. The third approach referred to the FE simulation of TPF stabilization to characterize the influence of the type of stabilization and recovery time [3] (Figure 1).
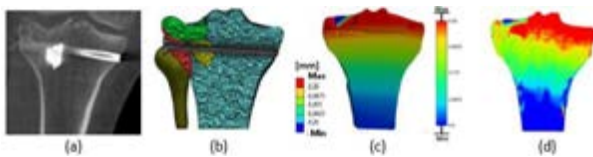
Figure 1: Workflow for digital twin for a tibial plateau fracture. (a) CT scan; (b) Personalized FE model; (c) Displacement from FE model; (d) Displacement field from DVC measurements

Arnaud Germaneau is currently Associate Professor in biomechanics and engineering at the Pprime Institute, University of Poitiers, where he obtained his PhD in mechanics in 2007. His main interest concerns patient specific modelling from surgery to resumption of activity by developing coupled experiments-numerical approaches. He is heading a research group in biomechanics between researchers from Pprime Institute and clinicians from University Hospital of Poitiers. He is an author of ~40 publications in peer-reviewed journals and regularly contributions to International and National Conferences.

Simultaneously, to validate these numerical approaches, adapted experimental methods, like Digital Volume Correlation (DVC) coupled with a medical CT scan, were implemented for the measurement of volume displacement fields associated with bone fragments during fracture reduction and weight loading after stabilization (Figure 1). To identify local mechanical behaviour, we performed experiments at the trabecular scale. An inverse identification technique (Finite Element Method Updating) based on DVC coupled with X-ray µCT was developed to predict the elastic properties of the cancellous bone. An integrated methodology was developed using the Wedge Splitting Test (WST) and Heaviside based Digital Image Correlation (H-DIC) to evaluate the fracture properties of the cancellous bone, PMMA cement, and the interface of cancellous bone and PMMA cement [4].

Future directions

The three coupled numerical approaches, validated from adapted multiscale experiments and full field measurement methods, offer solutions for complete numerical simulation of the surgical procedure to assist in surgical planning.

Developed postoperatively, the workflow we outline to work with relevant digital twins for trauma surgery, provide worthwhile information for pre-operative planning tasks. These digital twins have to be further improved, e.g. integrating soft tissues mechanical interactions with bones, to provide solutions to clinicians to choose the optimal stabilization method and the best post-operative treatment depending on the patient characteristics.

References

1. Vendeuvre et al., Orthop Traumatol Surg Res 99, 267–272, 2013
2. Kfuri and Schatzker, Injury, 49, 2252–2263, 2018.
3. Aubert et al., Frontiers Bioeng Biotech, 9, 2021
4. Bokam et al. JMBBM, 122, 2021

MODELLING BLAST INJURY; FROM CLINICAL DATA TO PATHOPHYSIOLOGY AND PROTECTION

Spyros Masouros

Department of Bioengineering, Imperial College London, United Kingdom

Background

Injuries sustained due to attacks from explosive weapons are multiple in number, complex in nature, and not well characterized. Blast may cause damage to the human body by the direct effect of overpressure, penetration by highly energized fragments, and blunt trauma by violent displacements of the body or of structures against the body. The ability to reproduce the injuries of such insults in a well-controlled fashion is essential in order to understand fully the unique mechanism by which they occur, and design better treatment and protection strategies to reduce mortality and alleviate the resulting poor short and long-term outcomes in survivors. This talk focuses on two common blast-injury patterns; severe pelvic injury in dismounted (on-foot) casualties, and foot-and-ankle injury in mounted (in-vehicle) casualties. The talk will demonstrate how clinical data are used to inform experimental and computational testing, will discuss experimental and computational models of the injuries, and demonstrate their use to evaluate mitigation systems and parameters that affect injury severity.

Recent Advances

Foot and ankle injuries have been shown to be common in the mounted casualty and associated with poor long term outcomes [1]. In order to replicate this severe injury mechanism in a controlled environment, laboratories around the world, including ours [2], developed blast-injury simulators. These have been used to generate injury-risk curves [3] and to validate computational models [4] developed in tandem. These tools are being used now for evaluation of relevant protective strategies.

In the dismounted setting, we identified that pelvic trauma is one of the most severe injuries and is associated with traumatic amputation and mortality when vascular injury is present [5]. We developed equipment and protocols to study separately the two main mechanisms of blast injury; the shock-wave effect [6] and the effect of being impacted by energised fragments [7] on pelvic fracture and traumatic amputation. These helped us describe fully the injury mechanism of traumatic amputation in the dismounted casualty. We then used our testing protocols to evaluate for the first time in a laboratory setting proof-of-concept and established protective equipment [8].

Spyros is Reader in Injury Biomechanics in the Department of Bioengineering at Imperial College London. He obtained his PhD in orthopaedic biomechanics from Imperial in 2008 and – with a small break to work in industry – worked as a post-doctoral research assistant until 2013 when he became Lecturer at Imperial. He sits on the Board of the International Research Council for the Biomechanics of Injury (IRCOBI) and on NATO Human Factors in Medicine panels relevant to injury due to blast and military-vehicle operation. His research has been largely focused on severe musculoskeletal injury and in human tissue material characterization at high loading rates.

Future directions

Blast injury assessment is lagging very much behind injury assessment in other sectors such as sport or commercial automobiles. Much has been done in the last 10 years unfortunately due to conflicts that brought this injury to the fore. Injury biomechanics research can help substantially in establishing new, evidence-based standards for the evaluation of mitigation strategies and protective designs. Diversity not only in terms of anthropometry but also in terms of platform and insult, human tissue behavior at high loading rates, and standardization for certification are challenging areas where work is much needed.

References

1. Ramasamy et al., JBJS 95(5), e25 2013
2. Masouros et al., Ann Biomed Eng, 41(9):1957-67, 2013
3. Chirvi et al., Stapp Car Crash J 61:157-73, 2017
4. Rebelo et al., Front Bioeng Biotech 9, 410
5. Rankin et al., J Trauma 88(6), 832-8, 2020
6. Rankin et al., Front Bioeng Biotech 8, 960, 2020
7. Rankin et al., Front Bioeng Biotech 9, 2020
8. Rankin et al., J Biomech Eng, 143(2), 021004

Acknowledgements

PRESENT AND FUTURE OF COMPUTER-AIDED DIAGNOSIS, PLANNING AND SURGERY

María Angeles Pérez

Multiscale in Mechanical and Biological Engineering (M2BE), Aragón Institute of Engineering Research (I3A), Aragon Institute for Health Research (IIS Aragón), University of Zaragoza, Zaragoza, Spain

Background

Computer-aided bone surgery planning and implant design applications have been used in the past and it is still a growing field, incorporating new tools or technologies every day. In fact, computer-aided diagnosis is increasing its importance and we are encouraged to provide as much personalization as possible not only in the diagnosis but also during the surgery planning or illness treatments. Cancer diagnosis and prognosis is also taking advantage of the new advances in computer-aided technology.

Recent Advances

In orthopaedic surgery, many computer-aided tools have been developed for diagnosis and surgery planning. In our CURABONE project (Figure 1), computer-aided helped in the development of patient-specific treatments for the knee, mandible and shoulder arthroplasty [1-3] and for bone regeneration treatments using bone scaffolds [4-5]. A clear example was generated for total shoulder arthroplasty, where a fully automated method for measuring deltoid and rotator cuff elongation was proposed. This new development will be used by surgeons to refine their surgical plan [3].

In cancer framework (PRIMAGE project), we are changing the field of application. We are working in the development of an open cloud-based platform that will offer precise clinical assistance for phenotyping (diagnosis), treatment allocation (prediction), and patient endpoints (prognosis), based on the use of imaging biomarkers, tumour growth simulation, advanced visualization of confidence scores, and machine learning approaches [6]. The computer-aided decision support tool is constructed and validated on two paediatric cancers: neuroblastoma and diffuse intrinsic pontine glioma.

Future directions

Where is the future of this technology going? It is clear that we move towards personalization. We need a personalized diagnosis of our pathologies and then a personalized treatment is requested. Additionally, computer-aided technology needs to be combined with the machine-learning techniques. There is an increasing demand on using artificial intelligence in the health care system. Every day we have more data and this data may help in the development of better and more precise computer-aided tools.

María Angeles Pérez is Professor at the School of Engineering and Architecture at University of Zaragoza (Spain) and researcher at Engineering Research Institute of Aragon (I3A). She obtained her PhD in Computational mechanics (2004), afterwards she was a postdoctoral fellow at the Trinity College Dublin (Ireland) and at the Ecole de technologie supérieure Montreal (Canada). She is a member of the European Society of Biomechanics since 2007. Her present research and collaborations mainly focuses on computational biomechanics and mechanobiology, design of prostheses and implants and experimental and computational tissue engineering. She is an author of more than 50 publications in peer- reviewed journals, and more than 150 contributions to International and National Conferences.

Figure 1: CURABONE: patient-specific treatments for bone regeneration.

References

1. Vautrin et al., J Mech Behav Biomed Mater, 121, 104641, 2021.
2. Pitocchi et al., Comput Methods Biomech Biomed Eng. 23(10), 642-648, 2020.
3. Pitocchi et al., J Shoulder Elbow Surg, 30,561-571, 2021.
4. Nasello et al., Bone, 144, 115769, 2021.
5. Nasello et al., Front Bioeng, 8:336, 2020.
6. Marti-Bonmati et al., Eur Radiol Exp, 4: 22, 2020.

Acknowledgements

BIOMECHANICS OF THE EYE LENS AND ACCOMMODATIVE SYSTEM: CLINICAL OPPORTUNITIES AND BIOMECHANICAL CHALLENGES

Barbara K. Pierscionek

Faculty of Health, Education, Medicine and Social Care, Medical Technology Research Centre, Anglia Ruskin University, Chelmsford Campus, United Kingdom

Background

The human eye is a biological, optical and biomechanical system designed to meet visual demands of the individual. Up to the sixth decade of life, the eye can alter focusing ability to see objects clearly over a range of distances. This function is provided by the eye lens by changing its shape, a process called accommodation. This is mediated by the ciliary muscle that transmits forces to the lens through a ring of suspension ligaments called collectively, the zonule. With age, the ability of the lens to alter shape decreases; the mechanism of this loss of function is still not fully understood.

Recent Advances

The opto-mechanical relationship within the eye lens has been investigated using correlational analysis and Finite Element modelling (FEM) [1] from optical measurements on human lenses over a wide age range [2]. Following the gradient distribution of refractive index (Figure 1), models were developed with each one assigned linearly changing material properties in the cortex (Figure 2). A large number of different combinations of force distributions to simulate shape change have also been considered to demonstrate applications of computational simulations in assessing optomechanical relationships within the eye lens and the influence of the zonular apparatus in lens accommodation [3]. Whilst shape change of the lens is determined by the biomechanical properties of the lens, which work in synchrony with its optics, both of these functional parameters are dependent on the biological structure of the lens, namely the elegant distribution of crystallin proteins [4]. Links have been made between the optics of the lens ie the refractive index gradient, and the crystallin distributions [4]; the effect of the biological material constituted by the structural proteins on lens biomechanics remains elusive [5].

Future Directions

Insight is needed into how the biological material of the lens affects its opto-mechanical properties and how these alter with age and vary among individuals. This talk will describe the challenges and opportunities for creation of advanced physiologically relevant models of the lens and the complex accommodative system that take into account the biological material of the lens.

Barbara Pierscionek is currently Deputy Dean (Research and Innovation) in the Faculty of Health, Education, Medicine and Social Care and a Professor in the Medical Technology Research Institute at Anglia Ruskin University. She obtained her PhD on the topic of optics and biochemistry of the eye lens at the University of Melbourne and has worked in Universities in Australia and UK. Her current research is focused on the anterior eye and the links between structure and functional parameters of optics and biomechanics. She is an author of over 160 peer-review publications, five book chapters, an encyclopaedia article and one book and has made over 60 contributions to International and National conferences.

Figures
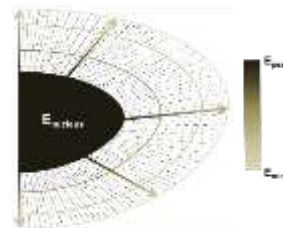
Figure 1: Gradient distribution of Young's moduli.
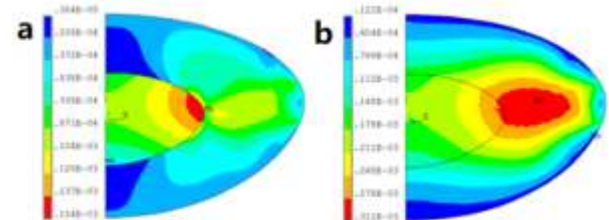
Figure 2: Comparison of stress distributions in a 35-year-old lens model with a)uniform cortical modulus and b) gradient distribution of Young's moduli.

References

1. Pierscionek et al., Oncotarget, 31, 30532-30544, 2015.
2. Wang et al., IEEE TBME, 10.1109/TBME.2019.2927390
3. Wang, K et al., Sci Rep, 6:31171, 2016.
4. Pierscionek & Regini, Prog. Ret. Eye Res, 31: 332-349, 2012.
5. Wang & Pierscionek. Prog. Ret. Eye Res. 17, 114-131, 2019

Acknowledgements

HEMODYNAMICAL STUDY OF A NOVEL PERCUTANEOUS LEFT VENTRICLE ASSIST DEVICE

Idit Avrahami, PhD

Dep. Mechanical engineering and Mechatronic, Ariel University, Ariel, 40700, Israel

Background

A novel percutaneous Left Ventricular Assist Device based on an axial impeller is designed to treat patients with acute heart failure. The novel design is intended to reduce known complications of the assist device, including blood damage and thrombus formation due to contact of blood with the impeller's blades and the non-physiological flow field due to the high rotational speed of the impeller. The suggested design is based on increasing the impeller's inlet-to-outlet area ratio and thus improve pump performance and reducing the rotational speed required for sufficient flow and pressure conditions.

Recent Advances

In this study, we use a combined method of experimental and numerical analyses.
In-vitro experiments combined with machine-learning algorithms (Figure 1) are used to examine and optimize the pump performance at different pump design and rotational speeds.
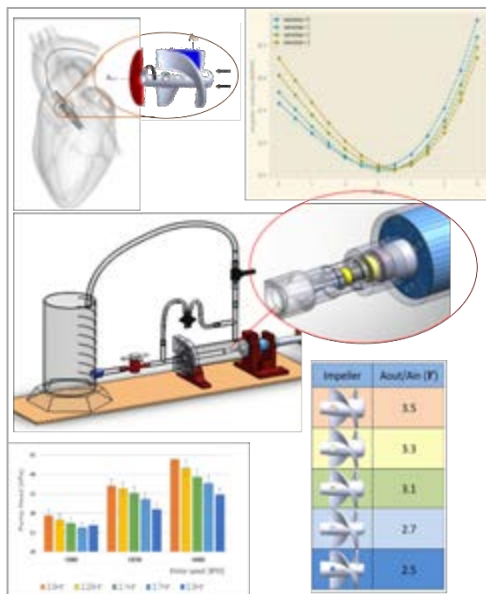
Figure 1: In-vitro experiments and machine learning algorithms of the pump performance to optimize the pump performance.

Particle image velocimetry (PIV) methods (Figure 2) are used to analyze the flow downstream of the impeller and in the ascending aorta. Turbulence intensity, helical flow, flow patterns and jet distributions were examined at different rotation directions and flow conditions.
Computational fluid dynamics (CFD) simulations (Figure 2) are used to analyze the blood damage at

Idit Avrahami is currently Professor at the Department of Mechanical Engineering at Ariel University, Israel. She obtained her PhD in Biomechanics at Tel Aviv University in 2004. She was a post-doctoral fellow at Caltech, CA in 2004-2006. Her present research mainly focuses on Biomechanics and Energy Systems. She is an author of 62 publications in peer-reviewed journals, 7 chapter books and more than 160 contributions to International and National Conferences.

different designs and flow conditions. CFD analysis included estimation of risk for shear-induced thromboembolism (using probability analysis of accumulated shear over streamlines) and hemolysis (using hemolysis index).
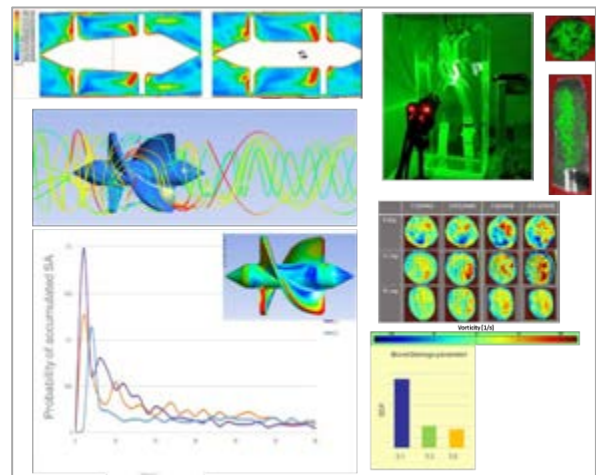
Figure 2: CFD of the blood flow over the impeller.and PIV analyses of the flow downstream of the impeller and in the ascending aorta.

Results show improvement of pump performance and reduction of parameters for blood damage (thromboembolism and hemolysis) for impellers with a larger inlet-to-outlet area ratio. The effect of rotation direction on the helical flow and jet intensity was demonstrated, with respect to turbulence intensity and thrust on the aortic wall.

Acknowledgements

KNEE JOINT LOADING IN OSTEOARTHRITIS

Vasilios Baltzopoulos

Liverpool John Moores University, UK

Background

Knee osteoarthritis (KOA) is a degenerative joint disease that affects a number of different tissues within the knee joint including the cartilage, menisci, subchondral bone and synovial fluid. Abnormal biomechanics at the knee are known to play a role in the initiation and the development of the disease [1]. A number of studies have sought to develop an understanding of the changes in the biomechanical environment of the knee during the early stages of KOA using inverse dynamics approaches [e.g. 2]. The issue with these methods is that they extract measures of whole joint loading, rather than measures of localized stresses in the cartilage tissues that are known to lead to degenerative changes.

Recent Advances

Our recent work as part of the OACTIVE project sought to overcome these limitations of previous attempts to quantify tissue loads in KOA. We used finite element techniques based on subject-specific imaging in combination with musculoskeletal modelling to identify changes in knee joint loading during gait in patients with early KOA and healthy subjects. These advances allowed us to calculate subject-specific stresses in the femoral and tibial cartilage. The musculoskeletal modelling pipeline includes a scaled OpenSim model [3] used to process the gait data and MRI scans were used to build 3D reconstructions of the knee for each subject with finite element models developed using FEBio. There were no differences in knee joint kinematics, moments and joint contact forces (JCF) between the healthy and osteoarthritic groups at the time of 1st and 2nd peak JCF. However, peak medial compressive and shear stresses in the tibial and femoral cartilage (Fig. 1) were found to be significantly larger than those in the healthy group at both 1st and 2nd JCF peaks.
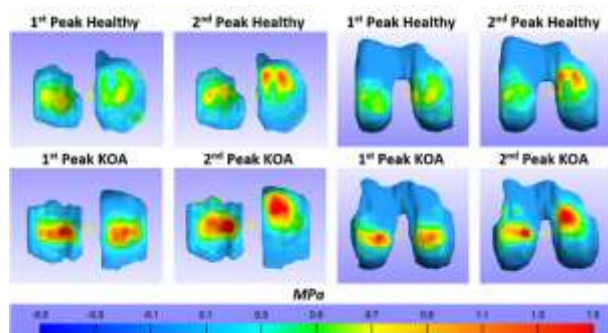
Figure 1. Tibial and femoral cartilage shear stresses between a healthy and a KOA subject at the 1st and 2nd peaks of the knee JCF during gait.

On the lateral side, both compressive and shear tibial and femoral cartilage stresses were higher although these differences were not statistically significant. This is the first time that a combined musculoskeletal and finite element approach has been used to evaluate differences in cartilage stresses between KOA and healthy subjects. These methodological advances in our recent work allowed us to show that medial femoral and tibial cartilage stresses in the knee increase even in the absence of any changes in joint moments or contact forces that are the typical joint loading measures in standard gait biomechanics analyses.

Future directions

This work has demonstrated the utility of subject-specific finite element models in identifying changes in localized tissue loading in early KOA populations. These results also highlight that caution should be taken in the future when using traditional musculoskeletal modelling-based approaches that do not take into account changes in the person's joint morphology. Although these techniques are computationally intensive, they are nevertheless essential for the accurate assessment of tissue and joint loading in KOA.

References

1. Felson, Osteoarthritis Cartilage, 21: 10–15, 2013.
2. Kumar et al., Osteoarthritis Cartilage, 21: 298–305, 2013.
3. Lerner et al., J. Biomechenics, 48, 644–650, 2015.

Acknowledgements

TAILOR-MADE POLYMERS: AN ADDITIONAL DEGREE OF FREEDOM IN THE TUNING OF MECHANICAL PROPERTIES IN TISSUE MODELING

Gianluca Ciardelli

Department of Mechanical and Aerospace Engineering, Politecnico di Torino, Torino, Italy

Background

Polymers have recently attracted widespread interest in the biomedical field. The design and selection of the proper polymer for each application strongly depend on the material capability to fulfill specific demands concerning their manufacturing and physicochemical and biological properties. In this scenario, the possibility to finely tailor polymer properties at different length-scales holds a great promise, opening the way towards the possibility to custom-design and process the best polymer for each envisaged application. For instance, the design of polymeric blends or composites allows fine-tuning of material properties by properly selecting the constituents and their weight ratio. Another possibility relies on the synthesis of multiblock copolymers that allows the ad-hoc design of the optimal polymer for each specific application. In this context, a segment of the research activities conducted in my group is devoted to the ad-hoc synthesis of poly(urethane)s (PUs) as constituent biomaterials of tissue engineering (TE) scaffolds and bioengineered tissue/organ models.

Recent Advances

PUs are versatile biomaterials for a wide spectrum of biomedical applications. Their high potential relies on their LEGO-like chemical structure that usually comprises a diisocyanate, a macrodiol, and a chain extender (CE).[1] A proper selection of PU building blocks can thus be exploited to adapt each newly synthesized material to the specific demands of the investigated application. In TE, poly(ε-caprolactone) (PCL) diol is usually used to synthesize biodegradable thermoplastic PUs (PCL-PUs). Fine-tuning of PCL-PU physico-chemical properties can be achieved by changing the CE used for their synthesis. CE chemical structure affects PU crystallinity, mechanical properties and nano-scale morphology [2,3]. For instance, the use of 1,8-octanediol gave a PU with higher elongation at break ($\varepsilon\%$, $\approx$ 30-40%), while 1,4-butanediol and 1,12-dodecanediol resulted in more brittle and stiff PUs. Conversely, N-Boc serinol gave a PU with around 150 MPa Young's Modulus (E) and $\varepsilon\%$ of ca. 150%, and L-lysine ethyl ester provided the resulting PU with an elastomeric-like behavior (E and $\varepsilon\%$ of around 10 MPa and 700%). The inclusion of poly(ethylene glycol) (PEG) into the backbone of PCL-PUs was also exploited to modulate the mechanical properties and wettability: by increasing the PEG content E decreases, while wettability and $\varepsilon\%$ increase [4]. Due to this wide diversity of available chemical formulations, PUs have been investigated as forming materials of scaffolds for

Gianluca (h-index 42) graduated in chemistry at the University of Pisa (1994) and obtained a PhD in Natural Sciences (1997) from the Swiss Federal Institute of Technology of Zurich. Then, he worked at a private company and at the University of Pisa as assistant professor. In 2004 he joined Politecnico di Torino as associate professor, becoming full professor in 2011. His group carries out research in the design of biomedical polymers, scaffolds, drug carriers, and organ models. He has authored over 150 articles, 8 book chapters and 12 patents.

both hard and soft TE. In hard TE, PUs have been used as coating materials of bioactive glass (BG) scaffolds, resulting in hybrid structs with improved mechanical properties and stability compared to BG scaffolds and unaltered bioactivity [5]. PU scaffolds with adequate mechanical and geometrical features have also been designed for cardiac TE and in vitro cardiac tissue modeling [6-8]. For instance, we have microfabricated PUs into multi-layered constructs with mechanical properties matching those of the native cardiac tissue through melt extrusion additive manufacturing [8]. In this regard, being newly designed biomaterials, PUs have been thoroughly characterized for their thermal and rheological properties to optimize the printing parameters while avoiding undesired degradation.

Future directions

Biomaterial tailoring represents one of the current challenges in the biomedical field. The ad-hoc synthesis of biomaterials represents one of the more promising approaches towards achieving the ultimate goal of engineering biomaterials best matching the demands of each targeted application and the progressive and effective translation of basic research from the bench to the bedside.

References

1. Sartori et al., J. Mater. Chem. B 2:5128-44, 2014.
2. Sartori et al., React. Funct. Polym. 73:1366-76, 2013.
3. Grivet-Brancot et al, *in preparation*.
4. Silvestri et al., J. Biomed. Mater. Res. 102:1002-13, 2014.
5. Boffito et al., *under review*.
6. Boffito et al., J. Biomed. Mater. Res. 103:162-9, 2015.
7. Vozzi et al., Biomed. Mater. 13:055006, 2018.
8. Boffito et al., Plos One 13:e0199896, 2018.

Acknowledgements

SKIN – AN ACCESSIBLE WINDOW TO HEALTH

Michael Crichton

Soft Tissue and Biomedical Devices Lab, School of Engineering and Physical Sciences, Heriot-Watt University, Edinburgh, EH27 8BU

Skin: a microcosm of our body

In the past decade, skin has received a substantial research focus due in part to the surge in wearable technologies and potential for technologies such as microneedle vaccines. Researchers developing sensor technology focused on skin's accessibility; those developing vaccines honed in on skin's rich immune composition. 'Pain free', 'non-invasive', 'personalised medicine' and 'wearable' are the frequent attributes trumpeted by these technologies, but in this perspective talk we highlight that this is just the start of what skin can provide for us.

Our recent work and that of others shows just how abundant the opportunity is for skin. Starting by highlighting the biological context of this, Figure 1 shows how skin's complex composition provides multiple opportunities for sensing.
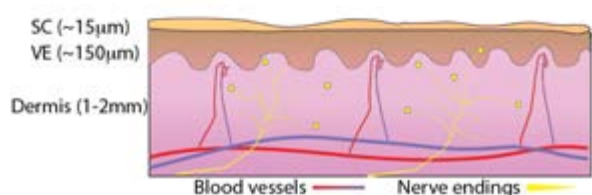
Figure 1: A schematic of skin's layers, blood vessels and nerve endings

First, the cellular composition of skin presents an opportunity for immune access via dendritic cells and lymphatic vessels. Then the cascading scales of capillaries provide a way to understand what type of vascular changes may be occurring as a result of different health or disease states. The nerves that weave through the dermis and into the epidermis then provide a link to the neurological system. And each one of these can then be further explored in the context of health conditions or external stimuli – whether wound healing, cancer, allergies or dermatitis. To that end, if we want to understand what is happening in the body then there is a huge opportunity in the skin. But to exploit this tissue's benefit we must turn to how we engage with the skin. How do we exploit it as an interface with our technologies?

Recent Advances

In recent years we have taken the approach that we can extract much more than has been done previously from skin. Key areas that we have sought to understand include the immune response (allergic and vaccine-driven [1, 2]), the diffusion behaviours of skin [3] and the mechanical challenges in interfacing with tissue [4].

Michael is an Associate Professor in Biomedical Engineering at Heriot-Watt University. He obtained his PhD in the Biomechanics of skin at the University of Queensland in 2012. He then worked in Vaxxas Pty Ltd, a company established to commercialise skin-based microneedle vaccine technology as a medical device engineer, before returning to academic. He joined Heriot-Watt University where he now leads the Soft Tissue and Biomedical Devices lab, working with clinical collaborators to develop skin-based diagnostics and monitoring technologies. He is the author of 29 peer-reviewed publications, 2 book chapters and holds 3 licensed patents.

We are now working on a range of devices that take a biomechanics focussed approach to the engagement and interfacing with skin tissue. We then expand that by seeking to assess how skin changes over time in health and disease. This is particularly relevant as it provides an opportunity for diagnosis and monitoring using wearable technologies.

Future directions

Whilst the opportunities to use skin to understand our health is clearly present, our challenge is now linking the different clinical parameters to skin's inherent properties. Looking forward, technologies need to be patient-centred and therefore capable of adapting to the wide variety of skin properties that are present across our populations – particularly important as the biomechanics of skin change with age, gender, race and environmental factors (among others).

The question we need to be asking now is: how we can develop our understanding of skin tissue biomechanics to enable patient-centred minimally invasive healthcare devices? In this talk we will highlight that a key way forward is a more cohesive model of skin including biomechanics, electrical, chemical and biological parameters for the benefit of human health.

References

[1] Meyer, B. K., et al. (2019). Vaccine: X **2**.
[2] van der Burg, N. M. D., et al. (2019). Journal of Controlled Release **302**: 190.
[3] Wei, J. C. J., et al. (2018). Scientific Reports **8**.
[4] Meliga, S. C., et al. (2017). Acta Biomaterialia **48**: 341.

Acknowledgements

EMMA4DRIVE - DIGITAL HUMAN TWINS FOR EVALUATING ERGONOMICS AND SAFETY IN NEW MOBILITY SOLUTIONS

Joachim Linn[1], Jörg Fehr[2],

1. Fraunhofer Institute for Industrial Mathematics (ITWM), Mathematics for the Digital Factory, Kaiserslautern, Germany;

2. Institute of Engineering and Computational Mechanics (ITM) and Stuttgart Research Cluster of Excellence (SimTech), Stuttgart, Germany

Background

New mobility solutions are necessary to free cities with traffic from large vehicles and to decrease their heavy environmental burden. Trust in the vehicle and its safety concepts are crucial factors for automated driving and new mobility solutions. Nevertheless, these solutions will increase the variability of driving situations, postures and body sizes (variation) for ergonomic and safety-critical protection in automated vehicle concepts. So far, there are separate development processes for vehicle ergonomics and safety, as well as for active and passive safety development procedures. This slows down iteration loops and hinder optimized results. The decisive tool for evaluating comfort and safety in human-centered design is the digital human twin.

Recent Advances

The muscle actuated multibody-model Ergo-dynamic Moving Manikin (EMMA4Drive) combines nonlinear finite element human body models from vehicle safety with human body models from ergonomics, i.e. HBMs for posture optimization and production planning [1].

The model can calculate new postures and human-like movement sequences with the corresponding muscle activities utilizing optimization methods. The reasonable degrees of freedom (<300) and the variational integration methods used for the time integration / optimization provide a very efficient model for stable dynamics.

To implement the EMMA4Drive interaction with the environment, a surrogate interaction model is implemented. This surrogate model is learned from an aggregation of interactions in nonlinear FE-simulations. We combine model order reduction techniques with machine learning techniques [2] to learn the interactions forces and pressures in the reduced space, which makes the process of surrogate modeling more efficient.

Two examples showcase the possibilities of the EMMA4Drive framework to predict and analyze critical driving situations:

(i) the take-over from autonomous driving to active driving in critical situations, i.e. how long does it take to reach the steering wheel from a zero-gravity position? And how helpful is an active backrest to improve the take-over time and to assist handicapped people?

(ii) the stabilization of a standing occupant during braking scenarios in public transport systems: comfort analysis based on kinematic response, muscle and joint forces.

Dr.-Ing. Joachim Linn is currently the head of Mathematics for the Digital Factory, at Fraunhofer Institute for Industrial Mathematics in Kaiserslautern, Germany. One research focus are biomechanic multibody models and the numerical basics and methods for the IPS software suite.

Prof. Dr.-Ing. Jörg Fehr is a Professor at the Institute for Engineering and Computational Mechanics and Cluster of Excellence Simulation Technology (SRC SimTech) of the University of Stuttgart. He research focuses on simulation strategies for active human body models for new mobility solutions and the speedup of simulations using surrogates.

The advantage of the Emma4Drive framework is that it provides human-like motions by optimization instead of replicating observed experimental motions. This allows the generation of knowledge for a larger number of (currently unknown) occupant postures and dimensions and load directions in autonomous driving without increasing the duration of the process.

For the validation of the model, experiments with the RODOS Driving simulator are performed. Of particular interest are the passenger kinematics and the seat pressure distribution in various highly-dynamic driving situations. Here, the experiments with a driving simulator have the following advantages: (i) the safe and replicable environment, (ii) the fast application and testing of different new actuation systems and seating postures under dynamic loading. (iii) kinematic feedback in all six degrees of freedom reducing the risk of motion sickness and allowing multi-directional trajectories and (iv) the visual feedback of a virtual driving environment.

References

1. Roller, et al, Advances in Transdisciplinary Engineering 11, 269 – 276, 2020..
2. Kneifl et al, Int J Numer Methods Eng, 122: 4774-4786, 2021.

Acknowledgements

Figure 1: The Emma4Drive model in a dynamic driving event
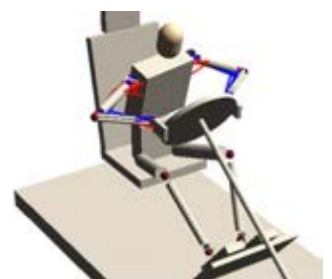
EXPERIMENTAL AND BIOMECHANICAL MODELING INVESTIGATIONS FOR UNDERSTANDING SEATING DISCOMFORT

Xuguang Wang

Univ Lyon, Université Claude Bernard Lyon 1, Univ-Eiffel, UMR_T9406, LBMC, F69622, Lyon, France

Xuguang is a research director at Université Gustave Eiffel. He obtained his PhD in solid mechanics from Ecole Centrale de Lyon in 1991 and his HDR (Habilitation à Diriger des Recherches) from University Claude Bernard – Lyon 1 in 2008. His current research focuses seating comfort, postural monitoring, automotive ergonomics, digital human modeling. He organized the first IEA (International Ergonomics Association) Digital Human Modeling Conference in Lyon in 2011. He is associate editor of International Journal of Human Factors Modelling and Simulation since 2016.

Background

People spend more and more time seated in transportation, at home, and at an office. Comfort is not only an important sales argument for the seat manufacturers, but is also well recognized as an important health factor for sitters. Long-term sitting may lead to discomfort and even to pressure sores for wheelchair users. Despite the large number of existing seating (dis)comfort studies, there is a lack of objective methods for assessing seating discomfort.

Human seat interaction is highly complex and seating comfort/discomfort depends on many factors such as sitter's anthropometry, posture, seat geometry, material proprieties and their interactions. As most of existing studies were carried out using a real seat or an experimental seat with limited possibilities of varying design parameters, it is difficult to isolate the effects of one particular seat parameter and to look at its interaction with other variables. Most of objective variables susceptible to explain discomfort such as internal load at joint, soft tissue deformation cannot be measured directly experimentally. Computational human body models are needed.

In this paper, recent efforts in both experimental and biomechanical modeling investigations on seating comfort at LBMC (Biomechanics and Impact Mechanics Laboratory), a mixed research unit from Université Gustave Eiffel and Université Claude Bernard Lyon1, will be presented.

Recent Advances

Thanks to the multi-adjustable experimental seat recently built at LBMC [1], we collected a large amount of data from a sample of differently sized people testing different seating configurations. Parametric models have been obtained for predicting preferred seat profile [2] and contact force distribution [3] in function of anthropometric dimensions, seat pan and back angles. We showed that a new airplane passenger seat with the preferred seat profile and pre-shaped foam could result in smaller shear force and more uniformly distributed pressure on the seat pan as well as less postural changes involving pelvis shift during a long sitting [4].

In parallel to experimental investigations, we also carried out a preliminary study aiming to relate internal loads estimated by a musculoskeletal (MSK) model and sitting discomfort [5]. Results suggested that lower discomfort rated postures might be associated with lower muscle activities and lower shear force. We also developed detailed finite element (FE) buttock thigh models for assessing soft tissue deformation [6]. For validation purpose, we investigated the effects of foam and seat pan inclination on the deformation of seated buttocks using MRI imaging technique [7]. We observed that the gluteus maximus (GM) muscle displaced away from the ischium tuberosity (IT) once seated and higher shear force led to larger soft tissue compression.

Future directions

The data about preferred seating parameters contribute to define quantitative guideline for improving seat design. Further efforts are needed to develop parametric full human body models to investigate the effects of body size and posture on biomechanical response under different seating conditions. A hybrid approach combing MSK and FE models could be appropriate. Validation of these models under realistic seating conditions is needed before their application in seating discomfort assessment.

References

1. Beurier et al., SAE Technical Paper 2017-01-1393, 2017.
2. Wang et al., App Ergo, 73, 13-21, 2018
3. Wang et al., Ergonomics, 62:7, 891-902, 2019
4. Wang et al., Work, 68(s1):S257-S271, 2021
5. Theodorakos et al. Proceedings of the 20th IEA 2018
6. Savonnet, L., PhD thesis, https://hal.archives-ouvertes.fr/hal-01844866/
7. Wang et al., IISE Trans Occup Ergon Hum Factors, 9(1):23-32, 2021

Acknowledgements

INDIVIDUALIZED VS. POPULATION-BASED MUSCULOSKELETAL SIMULATION FOR MEDICAL AND PRODUCT ENGINEERING

Jörg Miehling

Engineering Design, Friedrich-Alexander-Universität Erlangen-Nürnberg (FAU), Germany

Background

Musculoskeletal simulations hold high potentials by revealing the processes and inner strain conditions of the human body for a wide range of areas. The computed physiological parameters can give insights for the engineering of medical and rehabilitation technology, exoskeletons, mobility products and sports equipment [1]. For reliable and physiological simulation results, a musculoskeletal model suitable for the application as well as a way to measure or predict the human motion and if applicable the interaction with the environment or product are necessary [2].

The conventional approach uses observations from optical marker tracking. This is still the gold standard for motion measurement. However, it requires preparation, data acquisition and post-processing effort. More importantly, often just anthropometric scaling is performed based on the marker data to adapt a generic model to a specific person. Other crucial factors such as muscle strength or mobility are regularly disregarded.

Recent Advances

Patient-specific models, however, mostly rely on 3D MRI/CT data. Using parameters extractable from the imaging data, a generic model is adapted to the specific patient, usually in a restricted area of interest [3]. These models are usable for observational and predictive simulations, but only in very specific situations, such as for surgery planning. In most other applications, it is not feasible to access the necessary data, not least due to ethical issues as well as the time and cost involved.

Population-based approaches bridge the gap towards predictive simulations even further. Modelling relies on empirical population data to adapt a generic model to a desired statistical representative of the population.

Based on this direction, a procedure to create consistent groups of musculoskeletal models across different domains (e.g. range of motion, strength) was set up [4]. Such a model group was used in the ergonomic optimization of bicycles and skiffs [2]. These examples as well as the ergonomic optimization of trikes [5] indicate the strength of predictive musculoskeletal simulations for (bio)engineering applications.

In order to increase data consistency between computer-aided-design applications and human models, we work on a computer-aided-ergonomics tool integrating user, product/environment and interaction models by a feature-based description of physical interactions [6, 7]. Current research also focuses on a co-simulation model integrating a musculoskeletal model with exoskeleton and power tool models to optimize support systems [8].

Jörg Miehling is currently principal investigator and research division leader at the Chair of Engineering Design, FAU Erlangen-Nürnberg, Germany. He completed his doctorate in 2018. His research focuses on musculoskeletal modelling and simulation, computer-aided-ergonomics and user-centered-design. He successfully obtained research grants from the German Research Foundation (DFG), including two projects in a Collaborative Research Centre (CRC/SFB), one of the most competitive and prestigious funding sources in Germany. He is author of more than 50 publications in peer-reviewed journals, book chapters and contributions to international and national conferences.

Future directions

Our goal is to provide methods for the assessment of human behavior in order to support (bio)engineering processes. We work on tracking methods integrating multimodal motion measurement data of novel sensor technology leading to more efficient and accessible workflows. We individualize musculoskeletal human models in multiple domains considering subject-specific kinematic and dynamic movement capabilities. Beyond, the extension of human models with sensorimotor regulation offers potentials to deepen the understanding of bodily processes in order to increase the insights of biomechanical simulation results. Moreover, we address a methodology integrating finite element and musculoskeletal models as well as the phenomenological characterization of human behavior for proactive simulation of user-product-interactions.

References

1. Wartzack et al., Proc. ICED19, 3989-3998, 2019.
2. Miehling, VDI, 445, 2018.
3. Scherb et al., CMBBE Conf., 2021.
4. Miehling, Comput. Methods. Biomech. Biomed. Eng., 22(15):1209-1218, 2019.
5. Meißner et al., Konstruktion, accepted.
6. Wolf et al., IISE Trans. Occup. Ergon. Hum. Factors, 2021.
7. Wolf et al., Ergonomics, 63(11):1442-1458, 2020.
8. Molz et al., CMBBE Conf., 2021.

Acknowledgements

COMPUTER MODELLING AND INVESTIGATIONS OF CAPSULE DYNAMICS IN FLOWS: MEMBRANE VISCOSITY EFFECT

Junfeng Zhang

Bharti School of Engineering and Computer Science, Laurentian University
935 Ramsey Lake Road, Sudbury, Ontario P3E 2C4, Canada

Background

Continuously circulating through the body, blood performs many crucial biological functions, including supply of oxygen and nutrients to and removal of metabolic waste from tissues, circulation of white blood cells, antibodies and platelets for immunization and self-repair, and regulation of body pH and temperature. These functions are mainly accomplished in the microvascular network composed of microvessels and capillaries. As observed in fundamental studies and clinical observations, abnormal microscopic blood flow behaviors are often associated with various diseases and disorders. Among the several blood components, red blood cells (RBCs, also called erythrocytes) paly determinant roles in blood functions and flow behaviours [1]. The RBC membrane viscosity, although being recognized for decades, has not been investigated adequately compared to other RBC properties (morphology, elasticity, aggregation, etc) [1,2]; and its influences on RBC dynamics and functionality are not clear yet.

Recent Advances

In this presentation, we first introduce the finite-difference method we recently developed for incorporating the membrane viscosity in immersed boundary simulations of capsule and RBC dynamics. Unlike previous attempts., our method has a simple and efficient algorithm and a realistic representation of the membrane viscosity consistent with its physical definition [2]. Our method has also been carefully validated and its accuracy, efficiency, and stability have been thoroughly verified [2].

Using this method, we have examined the influences of the interior fluid and membrane viscosities on capsule dynamic characteristics (deformation index, inclination angle, and rotation frequency) in shear flow. Our results show that, although similar, the capsule responses to increases in membrane viscosity and interior viscosity differently, and the membrane viscous effect cannot be replaced by an elevated interior viscosity, which is contradictory to those suggested in the literature [2].

Furthermore, we have studied the lateral migration process of a capsule with viscoelastic membrane in tube flows with various flow and membrane parameters. The lateral migration is of great importance for understanding the cell free layer development in microvessels and cell separation in microfluidic devices. Our results show that, in general, the migration process

Dr. Zhang is currently a Professor at the Bharti School of Engineering and Computer Science, Laurentian University (Canada). He obtained his PhD in Mechanical Engineering at the University of Alberta (Canada) in 2005, and he was a post-doctoral fellow at the Johns Hopkins School of Medicine (USA) during 2005-2007. His research mainly focuses on numerical modelling and studies of red blood cell dynamics in various flow situations, with particular attention to the underlying mechanisms. He is the author of 67 articles in peer-reviewed journals, 8 book chapters and more than 70 invited talks and conference presentations. He also served as the Guest Editor for a special issue in *Micromachines* in 2021.

can be described as the initial transient phase with sudden increase in deformation, followed with the migration phase as the capsule gradually moves toward the tube centreline (Figure 1). A higher membrane viscosity can slow down the capsule rotation and migration, and may introduce significant oscillations in the capsule deformation, inclination, and migration velocity. Moreover, empirical correlations are proposed for the migration velocity and rotation period [3].
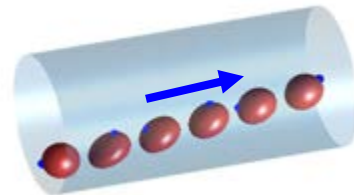
Figure 1: Simulated capsule migration process in tube flow. The blue arrow indicates the flow direction and the blue circles on the capsule surface are used to illustrate the capsule rotation.

Future Directions

Next, we will apply this method to study RBC dynamics in shear and tube flows, and compare our results with available experimental data. Also it would be interesting to examine the membrane viscosity effects on the bulk blood rheology (viscosity, yield stress, shear-shinning behavior, etc) by simulating RBC suspensions.

References

1. A. Popel & P. Johnson, *Annu. Rev. Fluid Mech.* 37:43, 2005.
2. P. Li & J. Zhang, *Int J Num Methods Biomed Eng* 35:e3200, 2019; *Biomech Model Mechanobiol* 19:2667, 2020; *Cardiovasc Eng Tech* 12:232, 2021.
3. A. Rezghi & J. Zhang, submitted, 2021.

ASSESSING THE PERFORMANCE OF THROMBECTOMY DEVICES WITH IN SILICO MODELS

Sara Bridio (1), Giulia Luraghi (1), Praneeta R. Konduri (2,3), Nerea Arrarte Terreros (2,3), Henk A. Marquering (2,3), Charles B.L.M. Majoie (3), José F. Rodriguez Matas (1), Francesco Migliavacca (1)

1. Dept. of Chemistry, Materials and Chemical Engineering "Giulio Natta", Politecnico di Milano, Italy;
2. Dept. of Biomedical Engineering and Physics, Amsterdam UMC, location AMC, The Netherlands;
3. Dept. of Radiology and Nuclear Medicine, Amsterdam UMC, location AMC, The Netherlands.

Introduction

Stent-retriever thrombectomy is the main treatment for acute ischemic stroke when a thrombus obstructs large cerebral vessels. Despite good clinical results there are still causes of failure of the procedure requiring the optimization of the design of the devices. In silico trials based on high-fidelity computational simulations of the clinical procedure [1-3] will have in the near future an important role in refining the usual clinical trials, reducing times and costs. In this work, a comparison of the performance of two commercial devices is carried out in patient-specific vascular models with a methodology oriented towards in silico trials.

Methods

One hundred patient-specific vascular models were reconstructed from images of stroke patients collected at Amsterdam University Medical Centers as described in [2]. In each model, a thrombus was placed in the middle cerebral artery (MCA), the most frequent thrombus location (Fig.1A). The length and composition of the thrombi were different in each model and varied in ranges derived from the literature [4,5]. The created models were used to run finite-element simulations of the thrombectomy procedure, using the settings in [1]. The simulation replicates the crimping of the stent-retriever inside the catheter and positioning at the occlusion location, the deployment of the stent to entrap the thrombus and the retrieval of the stent-thrombus complex. The stent was optimally positioned with respect to the occlusion, following the clinical guidelines [6]. A procedure is considered to have positive outcome if the thrombus is removed from the vessels, otherwise the outcome is negative. For each vascular model, the procedure was simulated with two different stent-retrievers, a TREVO ProVue (Stryker, USA) and an EmboTrap II (CERENOVUS, Ireland), allowing to compare the performance of the devices.

Results

Of the 100 models with the TREVO ProVue, 96 of them were admissible for simulation, whereas in 4 of them a particularly difficult vascular geometry caused numerical instability. Of the 96 simulations, 13 (14%) had a negative outcome. For the EmboTrap II, also 96 models out of 100 were admissible for simulation. Of these, 10 (10%) had a negative outcome. The causes for the negative outcomes were either the thrombus got stuck in the anterior cerebral artery or it was lost in the carotid siphon (Fig.1B). The EmboTrap II shows a stronger interaction with the thrombus, reducing the number of cases where the thrombus was lost in the carotid (Fig.2).
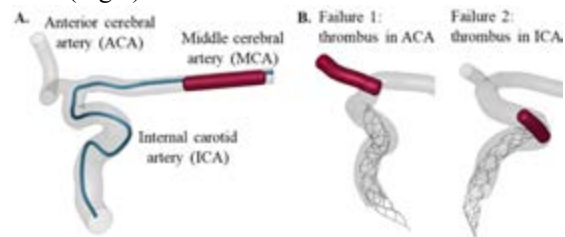
Figure 1: A) Reconstructed patient-specific vasculature with thrombus and catheter; B) causes of negative outcome of the thrombectomy simulations.

Figure 2: Example of different outcomes with the two tested stent-retrievers for the same patient anatomy.

Discussion

A total of 96 high-fidelity simulations of the thrombectomy procedure were executed with two different commercially available stent-retrievers allowing to compare the performance of these two devices. The high success rate associated with both devices (over 80% in both cases) is certainly due to the choice of the optimal stent positioning, as demonstrated in [2]. This methodology can be used in the future to evaluate the performance of new thrombectomy devices in optimal and non-optimal scenarios.

References

1. Luraghi et al, Interface Focus, 11(1):20190123, 2021.
2. Luraghi et al, J Biomech, 126:110622, 2021.
3. Bridio et al, Front Med Technol, 3:1-13, 2021.
4. Boodt et al, Stroke, 51(6):1727-1735, 2020.
5. Duffy et al, Stroke, 50(5): 1156-1163, 2019.
6. Ospel et al, Exp Rev of Med Dev, 16(11): 955-963, 2019.

Acknowledgements

PREDICTING SURGICAL OUTCOMES ACROSS NINE CORRECTIVE TECHNIQUES FOR SAGITTAL CRANIOSYNOSTOSIS

Connor Cross[1], Roman H Khonsari[2], Giovanna Patermoster[3], Eric J Arnaud[4], Dawid Larysz[5], Lars Kölby[6], David Johnson[7], Yiannis Ventikos[1], Mehran Moazen[1]

[1] Department of Mechanical Engineering, University College London, UK

[2] Department of Maxillofacial Surgery and Plastic Surgery, Necker – Enfants Malades University Hospital, Paris, France

[3] Department of Neurosurgery, Craniofacial 16 surgery unit, Necker – Enfants Malades University Hospital, Paris, France

[4] Department of Pediatric Neurosurgery, Necker-Enfants Malades University Hospital, Paris, France

[5] Department of Head and Neck Surgery for Children and Adolescents. University of Warmia and Mazury in Olsztyn, Poland

[6] Department of Plastic Surgery, Sahlgrenska University Hospital, Gothenburg, Sweden

[7] Oxford Craniofacial Unit, Oxford University Hospital, Oxford, UK

Introduction

Craniosynostosis is a medical condition caused by the premature fusion of one or more cranial joints i.e. sutures. The most prevalent form of this condition is called sagittal craniosynostosis. Craniofacial surgeons have developed several corrective techniques to manage this condition with ongoing debates on its optimum treatment option [1]. Computational modelling has been utilized to provide a wider understanding of the biomechanics of craniosynostosis correction [e.g. 2]. The aim of this study was to replicate the calvarial growth under a total of 9 surgical techniques with the goal of optimising sagittal craniosynostosis correction.

Methods

A previously validated patient-specific 4-month-old sagittal synostosis patient model [1] was used in this study to compare the biomechanics of all treatment options virtually. Figure 1 illustrates the simulation workflow. In brief, a linear thermal analogy was applied to the intracranial volume (ICV) to simulate skull growth up to 76 months of age in 6 load steps. A bone formation algorithm based on the level of hydrostatic strain across the sutures and distance from the bony borders was implemented. Meanwhile, contact elements were used at the ICV-inner cranial interfaces.
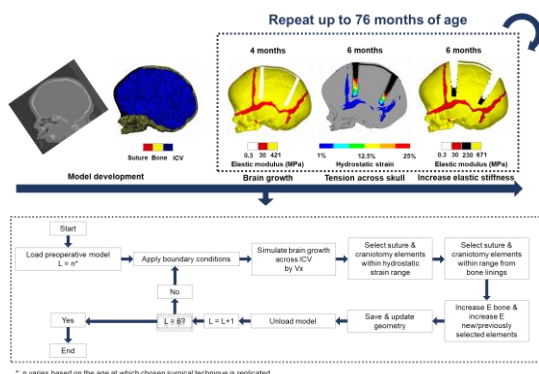
Figure 1: Workflow for simulating calvarial growth and for replicating bone formation.

A total of five strip craniectomy, two spring-assisted cranioplasty (SAC) and two total calvarial remodelling (TCR) techniques were replicated.

Cephalometric measurements and contact pressure levels were measured across all techniques.

Results

Figure 2 highlights the pattern of bone formation and contact pressure predictions across all techniques. The highest and lowest cephalic index were seen in the strip cranioplasty and 3 SAC techniques, respectively. While the lowest contact pressure was captured in both TCR techniques and the highest seen in Renier's 'H' technique performed at 6 months of age.

† Procedure performed at 6 months of age.
‡ Procedure performed at 12 months of age.
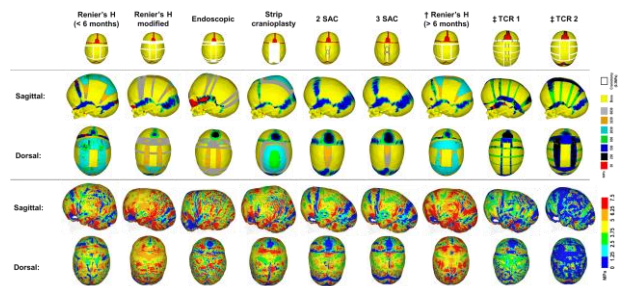
Figure 2: Bone formation & contact pressure predictions at 76 months of age.

Discussion

An extensive investigation into the biomechanics of sagittal craniosynostosis correction was performed. This work is the first in predicting contact pressure levels which may correlate with various defect levels found across different treatment methods [3]. Such methodologies using a FE approach have a large potential in optimising postoperative outcomes, with an emphasis on aesthetic appearance and neuro-functionality years after correction.

References

1. Thomas et al, J Craniofac, 26:19-25, 2015.
2. Cross et al, Sci Rep, 11:21216, 2021.
3. Hashim et al, Plast Reconstr Surg, 134:491-501, 2014.

Acknowledgements

ANGIOGRAPHY-DERIVED WALL SHEAR STRESS TOPOLOGICAL SKELETON VARIABILITY PREDICTS MYOCARDIAL INFARCTION

Maurizio Lodi Rizzini (1), Alessandro Candreva (1,2), Diego Gallo (1), Jean-Paul Aben (3), Claudio Chiastra (1), Carlos Collet (4), Umberto Morbiducci (1)

1. *Dept. of Mechanical and Aerospace Engineering, Politecnico di Torino, Italy; 2. Dept. of Cardiology, USZ, Switzerland; 3 Pie Medical Imaging BV, The Netherlands; 4. Cardiovascular Center Aalst, Belgium.*

Introduction

The hemodynamic stimuli experienced by coronary atherosclerotic lesions have been linked to lesion progression and destabilization [1]. Among them, specific wall shear stress (WSS) features have been associated with the vulnerable transformation of atherosclerotic lesions and their rupture [2], implying that an accurate evaluation of WSS could allow the identification of lesions prone to cause myocardial infarction (MI). Since WSS profiles in coronary arteries can only be quantified through computational fluid dynamics (CFD) simulations, to accelerate the clinical translation of WSS as a biomechanical biomarker of disease we assessed the feasibility and efficacy of a pipeline for WSS analysis in a clinical setting aiming at identifying lesions culprit for future MI.

Methods

Patients presenting with acute MI were retrospectively screened to identify those who had (1) a previous coronary angiography performed between 1 month and 5 years before the event, (2) a mildly stenosed lesion (i.e., $\leq$ 50% diameter stenosis) culprit for MI (future culprit, FC) at the baseline angiography, and (3) at least one additional lesion non-culprit for MI (non-future culprit, NFC) in the other major epicardial vessels. This selection resulted in a total of 188 vessels, with 80 FC lesions and 108 NFC lesions. The workflow of the study was reported in Figure 1. Using three-dimensional vessel reconstructions obtained from two angiographic projections, transient CFD simulations were performed with two approaches: (1) the coarser one denoted as "clinical CFD", using a finite element-based code (CAAS Workstation WSS software, Pie Medical Imaging), with simulations performed by clinicians within a standard clinical setting; (2) the one denoted as "expert CFD", using a finite volume-based code with simulations performed by a CFD expert team with a greater accuracy and resolution to verify the reliability of clinical CFD. The WSS-based analysis was focused on the time average WSS (TAWSS) and on the topological shear variation index (TSVI) [3]:

$$\text{TSVI} = \left\{ \frac{1}{T} \int_0^T \left[\nabla \cdot \left(\frac{\mathbf{WSS}}{\|\mathbf{WSS}\|_2} \right) - \overline{\nabla \cdot \left(\frac{\mathbf{WSS}}{\|\mathbf{WSS}\|_2} \right)} \right]^2 dt \right\}^{\frac{1}{2}} \quad (2)$$

where T is the cardiac cycle period. TSVI, a quantity based on WSS divergence, is a feature of the WSS topological skeleton measuring the variability of the local contraction/expansion action exerted by the WSS on the endothelium along the cardiac cycle. The WSS-based descriptors were then averaged over the lesion region, identified using the standard clinical approach based on quantitative coronary angiography [4].
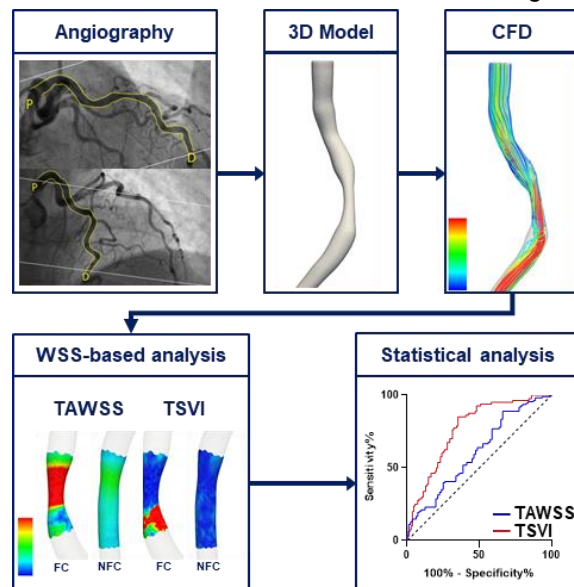
Figure 1: Workflow of the study

Results

The analysis of the ROC curves (Figure 1) highlighted that TAWSS was a moderate MI predictor (AUC=0.61; 95% CI: 0.53 to 0.69, p=0.011), while that TSVI was a strong MI predictor (AUC=0.77; 95% CI: 0.70 to 0.84, p<0.001). The clinical CFD-derived WSS profiles, obtained with computational times around 15 minutes per patient, exhibited discriminatory capability between FC and NFC groups comparable to the expert CFD (TAWSS: p=0.0323 and p=0.011 for expert and clinical CFD, respectively; TSVI: p<0.0001).

Discussion and conclusion

The here presented results confirm that: (1) CFD simulations performed within a clinical framework can provide reliable WSS values able to predict MI; (2) TSVI represents a relevant hemodynamic cue in coronary atherosclerosis. The emergent predictive power of TSVI for future MI expands its association with early atherosclerosis in coronary arteries [3]: high temporal variability of the WSS contraction/expansion action may result in fibrous cap fragility, accelerated disease progression, plaque fatigue, ending in plaque rupture and subsequent MI [4]. In conclusion, high TSVI resulted as a strong predictor of MI, encouraging further clinical trials to enforce the presented results and to translate this concept into clinical practice.

References

1. Lee JM et al., *JACC Cardiovasc Imag*, 12:1032-43, 2019.
2. Kumar A et al., *J Am Coll Cardiol*, 72(16):1926-35, 2018.
3. Mazzi V et al., *Ann Biomed Eng*, 49:2606-21, 2021.
4. Candreva A et al., *Atherosclerosis*, 342: 28-35, 2022.

BIOMECHANICS AND MECHANOBIOLOGY OF MINERALIZED FIBROCARTILAGE AT THE TENDON-BONE ATTACHMENT

A Tits (1), S Blouin (2), M Rummler (3), JF Kaux (1), P Drion (1), GH van Lenthe (4), R Weinkamer (3), MA Hartmann (2), D Ruffoni (1)

1. University of Liege, Belgium; 2. Ludwig Boltzmann Institute of Osteology, Vienna, Austria; 3. Max Planck Institute of Colloids and Interfaces, Potsdam, Germany; 4. KU Leuven, Belgium.

Introduction

The challenging task of integrating soft tissues such as tendon, ligament and cartilage into bone is solved thanks to many remarkable adaptation strategies [1], including the presence of a thin layer of fibrocartilage (FC) between soft tissues and bone. Despite the clinical evidence that FC is involved in numerous joint pathologies in humans, there are several unresolved but yet fundamental aspects of FC, including the interaction between FC and the surrounding tissues. In this work, we combine high resolution material characterization methods to understand the structure-function relationship in FC and to unravel the communication pathways between bone and FC cells. Specifically, we analyze the tendon-calcaneus bone insertion in adult male Sprague-Dawley rats. This location, considered as a model for human-related enthesis diseases, features two types of FC solving specific mechanical functions: enthesis FC anchors tendon to bone whereas periosteal FC facilitates tendon sliding. Previously, we highlighted a strong anisotropy of fibrochondrocyte (FCC) lacunae and channel network at enthesis FC with pores oriented towards the tendon insertion. At the periosteal FC, a more random porosity was observed [2]. Here, we explore structure-function relationship by correlating mechanical properties with mineral content and matrix organization. Focusing on mechanobiological aspects, we investigate possible communication strategies, enhanced by loading, between osteocytes (OCs) and FCCs through porosity present at different length scales.

Methods

Two-dimensional mineral content maps of bone and mineralized FC (mFC) were obtained with quantitative backscattered electron imaging (qBEI). Indentation modulus and hardness were measured extensively (~1000 indents per sample) using nanoindentation (nIND). Second harmonic generation (SHG) imaging was then performed to visualize collagen orientation. The functional porosity (including the lacunocanalicular network, LCN) was investigated on rhodamine stained samples, imaged with confocal microscopy.

Results

At the insertion, mFC displays more even distribution of indentation modulus (a measure of stiffness) and hardness (a proportional measure of strength) than periosteal mFC and bone, despite having similar mineralization (Fig. 1). Such tuning in local mechanical behaviour beyond mineral content is probably provided by the arrangement of the fibers, that are more ordered in enthesis than periosteal FC.
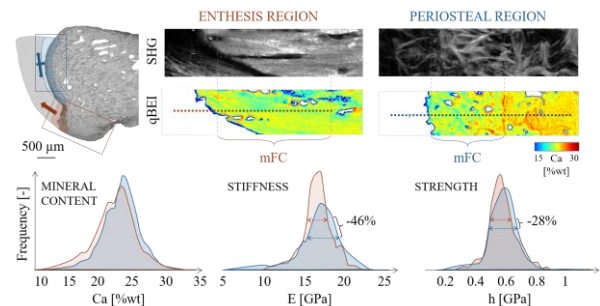
Fig. 1: SHG, mineral content, indentation modulus and hardness at enthesis and periosteal FC.

Considering the interaction between FC and bone, we have unravelled that several FCCs buried inside mFC, although lacking a communication network (like the LCN), still got stained (Fig. 2). Further quantification revealed the presence of channels running through the bone-FC interface and connecting the LCN with FC cells, especially at the insertion region.
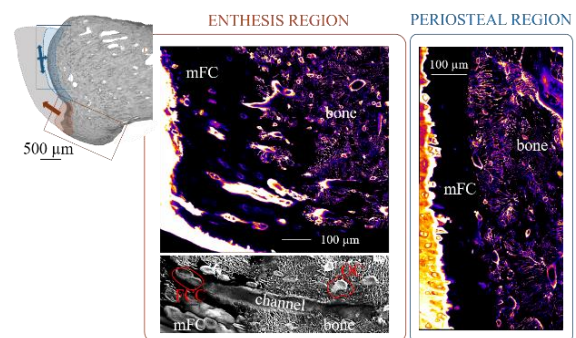
Fig. 2: OC and FCC interactions at the FC-bone interface at the enthesis and periosteal regions.

Discussion

At the material level, the anisotropy of the rat enthesis FC microstructural porosity [2] is mirrored into highly aligned mineralized collagen fibers, likely enhancing tissue stiffness and strength at tendon insertion. The specificities of FC biomechanical behaviour in two adjacent regions demonstrate the adaptability of this tissue. The illustrated communication paths between FC and bone will be further explored by quantifying the permeability of the bone-FC interface, through fluid flow simulations [3]. Such analysis may suggest new avenues to access FCC with the long-term goal of treating fibrocartilage rheumatic pathologies in humans.

References

1. Tits and Ruffoni, Bone Rep, 14: 1-17, 2021.
2. Tits et al., Sci Rep, 11: 16534, 2021
3. van Tol et al., PNAS 117: 32251–32259, 2020.

BIOMECHANICS INDEX FOR DIABETIC FOOT RISK CLASSIFICATION

Annamaria Guiotto (1), Gianmarco Bortolami (1), Alfredo Ciniglio (1), Fabiola Spolaor (1), Gabriella Guarneri (2), Angelo Avogaro (2), Federica Cibin (3), Francesco Silvestri (1), Zimi Sawacha (1,2)

1. BiomovLab, Dept. of Information Engineering, University of Padua, Italy; 2. Dept. of Medicine, University of Padua, Italy; 3. BBSoF s.r.l., Padova, Italy.

Introduction

Diabetic foot ulceration is widely considered a challenge [1]. Several guidelines and recommendations are proposed for the prevention and treatment of diabetic foot, however, a classification of the risk of wound prior to its appearance is desirable, in order to prevent the dramatic consequences of ulcerations and possible subsequent amputations [1]. In terms of diabetic foot biomechanics, diabetic subjects demonstrated higher loads at push-off associated with reduced ankle dorsi-plantar flexion during the stance and push off phases [2]. The aim of this study was to automatically define a diabetic foot risk index obtained by applying machine learning (ML) algorithms to a dataset composed of standard gait analysis data combined with finite element and musculoskeletal modelling data and routine diabetic neuropathy screening scores [4].

Methods

Eighty subjects were retrospectively involved in this study (26.3% healthy subjects, 37.5% diabetics without neuropathy and 36.3% diabetics with neuropathy). Diabetic patients were clinically assessed as reported in [3], according to the ADA guidelines [4]. All subjects performed several gait cycles and kinematic, kinetic and electromyographic (EMG) data were acquired through a modified version of the IORgait protocol [3,5]. Moreover, muscle forces were estimated with the Opensim gait 2392 model and internal stresses were determined using a foot finite element foot model [6]. The following biomechanical parameters were considered: joint angles and moments, ground reaction forces, plantar pressures, EMG envelopes and timing of activation, muscular forces and internal stresses. The clinical features selected for the ML algorithm were the presence or absence of: peripheral and autonomic neuropathy, retinopathy, microalbuminuria, vasculopathy, knee-hallux-toes deformities, plantar callosity. The chosen database program was MongoDB. The data extractions were performed through the library Pandas. The values of different gaits were merged using an arithmetic mean, in order to obtain a narrower dataset and more stable values of the features. Due to the size of the dataset, 'simple' and linear models were adopted. Among these Logistic Regression, Linear Model and Perceptron were chosen. For completeness, some more complex classifiers like Kernel Support Vector Machine, Random Forest, Gradient Boosting Tree and eXtreme Gradient Boosting Tree were also adopted but showed lower performances.

Results

The model achieving the best results was Logistic Regression with the adoption of 4 features: 83% of precision and 83% of accuracy (Figure 1). Once the model was developed, a React Native mobile application was implemented with a relative Application Protocol Interface (API) to produce an environment to host and exploit the model. The results in terms of diabetic foot risk were compared with the state of the art classification provided by ADA based on clinical features [4].
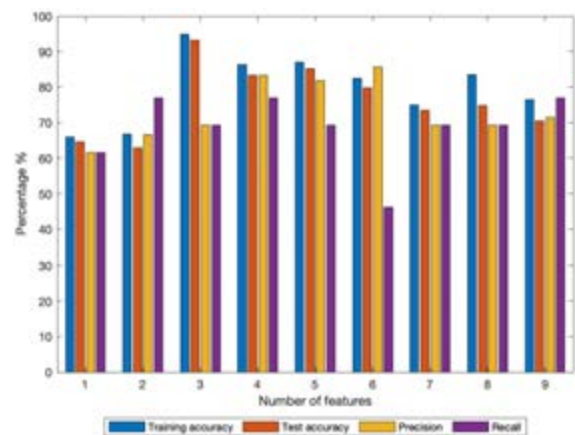
Figure 1: Logistic Regression - Accuracy, Precision and Recall vs n. of features.

Discussion

Although the performances of the model cannot be considered optimal, the results are encouraging in terms of diabetic foot risk index. Future development will include expanding the database and exploring other ML algorithms.

References

1. Cassidy B, et al. Lecture Notes in Computer Science, 90–105, 2022, doi: 10.1007/978-3-030-94907-5_7.
2. Guiotto A et al. Gait Posture, 37(4): 603-610.
3. Sawacha Z. et al, Clinical Biomechanics, 24(9): 722-728, 2009.
4. ADA, Diabetes Care, 37(S1): S5-S13, 2014.
5. Leardini A. et al, Gait Posture, 26(4): 560-571, 2007.
6. Guiotto A. et al. J biomech, 47(12): 3064-3071, 2014.

BIOMECHANICAL EVALUATION OF DIAGNOSTIC TESTS FOR ROTATOR CUFF LESIONS

Johanna Menze (1), Tomas Rojas (2,3), Matthias A. Zumstein (2,3), Stephen J. Ferguson (3),
Kate Gerber(1)

1. sitem Center,University of Bern, Switzerland, 2.University Hospital Bern, Switzerland; 3.Shoulder, Elbow and Orthopaedic Sports Medicine, Orthopaedics Sonnenhof, Switzerland, 4. ETH Zürich, Switzerland

Introduction

Numerous diagnostic shoulder tests have been established in the clinical routine to determine size and location of rotator cuff (RC) tears. Shoulder positions for the RC diagnostic tests aim at maximizing the affected RC muscle activity while minimizing supporting muscle involvement such that a failure to perform particular motion suggests tearing of the tested RC. Multiple clinical studies have analyzed the sensitivity and specificity of the different tests, however, results vary strongly [1-3]. To help explain discrepancies in the effectiveness of diagnostic tests, assessment of the muscle force distribution using musculoskeletal models could provide understanding of the underlying biomechanics.

Thus, the aim of this numerical study was to investigate the underlying biomechanics of six standard diagnostic tests for RC lesions by comparing the tested RC muscle activity with compensatory effects.

Methods

Musculoskeletal modeling based on inverse dynamics was applied to calculate shoulder muscle force and activity (Anybody 7.3, repository AMMR v.2.3.1)[4]. Six diagnostic shoulder arm positions were modeled to test supraspinatus (SS), subscapularis (SubS), infraspinatus (IS) and teres minor (TMin) lesions. As a TMin tear rarely appears alone, it was simulated in conjunction with an IS tear. Each test was modeled as a static position with an external force of 15N. Muscle activity of the tested RC was extracted from the healthy model and an agonist to synergist Ratio (A/S ratio) was calculated by dividing the tested RC force by all synergistic muscles for this motion (see Table 1). Subsequently, a lesion was simulated by setting the strength of the affected RC muscle to zero. The accumulated activity increase of the compensatory muscle was then be determined.

Results

The Jobe and Lift Off test in the healthy model showed a significantly higher SS (29.5%) and SubS (37.9%) activity compared to the Full Can (SS: 13.3%) and Bear Hug test (SubS: 6.9%), respectively. Both SubS-tests showed an A/S ratio of above 70% while both SS-tests demonstrated a ratio below 20%. The TMin activity is a fourfold higher in the Hornblower test compared with the External Rotation Lag test, while the IS activity is a twofold higher in the Hornblower test. Synergistic activity increase is smallest in SS-tests and highest in tests of the external rotators, IS and TMin. Unphysiologically high synergistic activity (%) resulted in the Hornblower test with IS and TMin lesions.

Discussion

Our results confirm the clinical finding of the Hornblower test being the most sensitivity to diagnose TMin dysfunction in posterior RC tears [1]. While the high A/S ratio in the Bear Hug and Lift Off test verifies that they maximize SubS activation, the low overall SubS activity in the Bear Hug test explains why clinicians increase the applied load and compare strength to the contralateral healthy shoulder[2]. A similar explanation applies to both SS tests (Jobe and Full Can). Differences in results among clinical studies likely result from variabilities in patient populations where tested RC tears are present alone or together with other RC lesions. Therefore, future work should involve additional simulations of combined RC lesions in each of the presented tests.

References

1. Walch et al, J. Bone Jt. Surg, 80.4:624-628, 1998
2. Jain et al, Am J Phys Med Rehabil. 2, 96.3:176-183, 2017
3. Miller et al, Arch.Phys.Med.Rehabil,89.6:1162-1168, 2008
4. Nolte et al., J Biomech, 41: S492, 2008.

Test	RC Tear	RC Activity (%)	RC Agonist to Synergist Ratio (%)	Synergist	Summed synergist activity increase (Δ%)
Full Can	SS	13.3	7.9	DA, DL, DP	4.1
Jobe	SS	29.5	15.1	DA, DL, DP	12.8
Lift Off	SubS.	37.9	63.9	PM, LatD, TMa	84.6
Bear Hug	SubS.	6.9	70.1	PM, LatD, TMa	22.5
Ext. Rot. Lag	IS	24.7	45.7	TMin, SS, DP	92.9
	IS + TMin.	24.7 + 10.2	64.6	DP, SS	107.4
Hornblower	IS	53.8	50.8	TMin, DP, SS	132.7
	IS + TMin.	53.8 + 40.1	88.8	DP, SS	791.6

Table 1: Simulated tests for supraspinatus (SS), subscapularis (SubS), infraspinatus (IS) and teres minor (TMin). RC muscle activity and agonist to synergist ratio (A/ S ratio) were calculated in the healthy model. The overall activity increase of all synergists was determined with rotator cuff (RC) tearing. Listed synergists are deltoid anterior (DA), -lateral (DL) and -posterior (DP), pectoralis major (PM), latissimus dorsi (LatD), teres major (TMa), SS and TMin.

EFFECT OF ALENDRONATE ON BONE FRACTURE TOUGHNESS IN OSTEOGENESIS IMPERFECTA

Asier Muñoz and Alessandra Carriero

The City College of New York, NY

INTRODUCTION

Brittle osteogenesis imperfecta (OI) bone has disorganized collagen matrix and abnormal mineralization [1], with reduced resistance to crack initiation and propagation [2]. OI has no cure, and current treatments rely primarily on the use of bisphosphonates, a class of antiresorptive drugs, to enhance bone mass. While bisphosphonates have been proven to increase bone mineral density and improve mobility in children with OI, its effect on the fracture rate and its long-term efficacy and safety use to treat OI children remains unclear and needs further research [3]. In this study, we analyze whether long-term use of alendronate is effective in restoring toughness in OI brittle bones. We further characterize the mechanical environment on bone during loading and crack progression using digital image correlation (DIC).

METHODS

Femurs from B6C3fe-a/acolla2$^{oim/oim}$ (*oim/oim*) mice model of OI, and wild type (WT) counterpart were considered for the characterization of the bone toughness and crack growth. Mice received either alendronate (ALN 0.21 mg/kg/week) or saline in equal volume of 0.1 ml/1g BW [4] starting at 2 weeks of age till sacrifice at 14 weeks. All mice (N=2-3/group) were male. Fresh frozen bones were machine-notched at their mid-diaphysis and immersed in PBS for 24 hrs. Bones were then covered with a thin layer of water-based white paint and speckled with acrylic black paint using a high precision airbrush. Femurs were tested in 3-point bending at a displacement rate of 0.01 mm/s till failure while two CCD cameras (100 mm focal lenses, GOM) recorded images at 32 Hz. Strains distributions engendered by load application were calculated by Aramis SRX System (GOM). Following mechanical testing, fracture surfaces of fully broken bones were imaged in back-scattered mode in an environmental scanning electron microscope (ESEM, Zeiss Supra 55) a Bone fracture toughness was calculated in terms of stress-intensity factor [5].

RESULTS

Oim/oim bones from our sample cohort exhibited a drastic decrease in fracture toughness compared to WT counterparts (Fig. 1). ALN treatment did not enhance *oim/oim* bone fracture toughness, and actually reduced the fracture resistance of WT bone. The extent of stable crack growth was decreased in *oim/oim* bone vs. WT ones, and was further reduced in ALN-treated bone. Only WT bone showed clear crack deflections. WT bones resisted higher strains both ahead and behind the crack tip before fracturing (Fig. 2). Major principal strains ahead of the crack tip were 5.9%, 2.4% for WT and *oim/oim* bone, respectively, and 1.9%, and 0.6% for their ALN-treated counterparts.
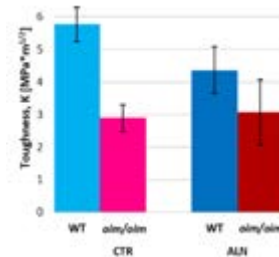
Figure 1: Bone fracture toughness of healthy (WT) and oim/oim mice treated with saline (CTR) or alendronate (ALN).
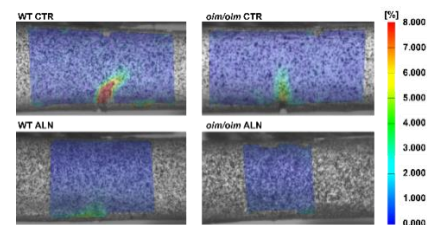
Figure 2: Major principal strain maps on the bone surface during loading at the full extent of the stable crack for saline (CTR) and ALN-treated WT and oim/oim bone. The red color covers a crack extent.

DISCUSSION

Results from this study suggest that the low fracture resistance of *oim/oim* bone is not improved following long term ALN treatment, although the increase in bone mass [4]. Full-field DIC principal strains, although only on the external bone surface, are able to predict the direction of crack growth, in both WT and *oim/oim* bones, with higher values for WT. A larger cohort of samples is currently being tested to statistically determine the effect of ALN on OI bone toughness and understand effects on their mechanical environment. Furthermore, bones from female mice are being examined to assess possible sexual dimorphism in responding to ALN therapy.

REFERENCES

1. Muñoz et al, Curr Osteop Rep, 19(5):510-531, 2021
2. Carriero et al, JBMR, 29(6):1392-1401, 2014
3. Battle et al, Bone Rep, 15 101108, 2021
4. McCarthy et al, Pediatric research, 52.5:660-670,2002
5. Carriero et al, JMBBM, 39:38-47, 2014

Acknowledgments

APPLICATION OF COG THREADS FOR VAGINAL WALL PROLAPSE REPAIR: EX-VIVO STUDY

Rita Rynkevic (1), Catarina Soares (2), Lucie Hympanova (3), Elisabete Silva (1), Teresa Mascarenhas (4), Pedro Martins (1, 5)

1. LAETA, INEGI, Faculty of Engineering, University of Porto, Portugal; 2. Faculty of Engineering, University of Porto, Portugal; 3. Institute for the Care of Mother and Child, Third Faculty of Medicine, Charles University, Czech Republic; 4. LAETA, Faculty of Medicine, University Hospital S. João, Portugal; 5. ARAID, i3A, University of Zaragoza, Zaragoza, Spain

Introduction

Pelvic organ prolapse (POP) is a pelvic floor dysfunction that dramatically influences women's quality of life. It is believed that the number of women suffering from POP increase more than 40% by 2050 [1]. Treatment by native tissue repairs have a relatively high failure rate (19%), presenting as recurrence or POP in other compartments. It can be addressed by a new operation, which may then use an implant for weakened or damaged tissue repair. The reason was that, the use of vaginal mesh have been associated with a high risk of graft-related complications (GRCs) due to insufficient biocompatibility and inappropriate mechanical properties of old-fashion materials [2]. Those inconvenient characteristics needs to be overcome by novel approaches. In 2019, the Food and Drug Administration ordered manufacturers of surgical mesh intended for transvaginal repair of anterior compartment prolapse to stop selling their products [3]. Therefore, this research aims to study an alternative surgical technique for POP correction. The reinforcement of vaginal wall provided by biodegradable cog threads. Technique is inspired by current use for face lifting procedures.

Materials and Methods

Commercially available 360°-4D cog threads (PCL-19G-100), made of polycaprolactone (PCL) (Yastrid, China) were used in this research. Sow' posterior vaginal walls (control n=5, cog n=5) were used to study threads reinforcement effect ex vivo by ball burst testing. Two threads were inserted into the tissue via cannula at 90° angle, creating a non-rigid reinforcement. Explant tensiometry was done using ball burst testing with an 11.5mm plunger at 10mm/min speed until the rupture.

Result

Thread reinforced vaginal tissue could withstand 68N of additional load than untreated tissue ($p<0.05$), showing its strengthening effect (Figure 1). Stiffness in a comfort and stress zone was significantly higher in the tissues reinforced with cog threads ($p<0.05$; $p<0.05$). The deformation was similar in both groups, and no significant differences in the comfort zone length were observed, indicating that threads do not affect tissue compliance.

Discussion

Injectable biodegradable cog threads were used for vaginal wall reinforcement, as a novel POP treatment concept. Results showed that cog threads provide immediate additional strength to the vaginal wall and don't interfere with physiological compliance. This technique has several advantages:1/treatment of early POP stages 2/ the transvaginal access (local anesthesia) 3/the possibility to have a vaginal delivery after threads insertion (not recommended with conventional meshes) 4/ no additional anchoring points and 5/ degradability reducing the material burden decrease chronic inflammatory reaction. The procedure could be personalized, by the injected threads number, material choice and thread type. We hypothesize this new technique will contribute in preventing prolapse progression, avoiding major surgeries and GRCs. Further research will follow to investigate short and long-term response of the vaginal wall in vivo.
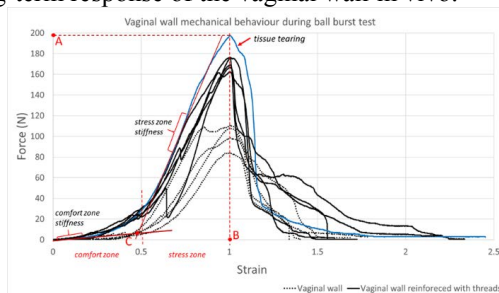
Figure 1: Mechanical behavior of the sow vaginal wall with and without cog threads. A blue colored curve - an example to highlight studied tissues characteristics: comfort and stress zone stiffness; A- ultimate load, B- the maximum change in length at ultimate force; C- comfort zone length.

References

1. Wu JM, et al. Obstet Gynecol 2014;123:141–8.
2. FDA,http://www.amiform.com/web/documents-risques-op-coelio-vagi/fda-notification-about-vaginal-mesh.pdf.
3. FDA,:https://www.fda.gov/news-events/press-announcements/fda-takes-action-protect-womens-health-orders-manufacturers-surgical-mesh-intended-transvaginal

Acknowledgements

MECHANICAL PROPERTIES OF 3D-PRINTED GLASS-CERAMIC SCAFFOLDS ASSESSED THROUGH MICRO-CT-BASED FINITE ELEMENT MODELS

Luca D'Andrea (1), Francesco Baino (2), Enrica Verné (2), Dario Gastaldi (1), Pasquale Vena (1)

1. Politecnico di Milano, Italy; 2. Politecnico di Torino, Italy

Introduction

Bone is a self-healing tissue, but some pathologies, aging, genetic diseases, and trauma may cause a critical size defect precluding the healing process. Due to their biocompatibility and bioactivity, glass-ceramic materials seem to be ideal candidates as bone scaffolds. However, the brittle nature of glass-ceramic materials requires a proper design of the scaffold from a mechanical point of view. This study aims to assess the stiffness and the strength of the scaffolds by using a microCT-based Finite Element approach.

Materials and Methods

An experimental formulation of a SiO_2-based glass-ceramic has been used to robocast the scaffolds [1]. In order to take into account the role of the micro and macro defects in the mechanical response real geometries of the 3D-printed scaffolds have been used by measn of microCT, with a pixel size of 5 µm. The scaffold's architecture shows a distribution of parallel fibres on each printing plane, with a tilting angle of 90° between two adjacent planes. The microCT-based Finite Element solver ParOSol has been used to perform both the elastic and strength simulations. First, the elastic mechanical properties have been obtained by imposing a unitary strain along with the six tensor components of strain. In this case, the whole domain of the scaffold has been analyzed. Then, through a damage-based algorithm, the strength of the scaffold along the direction perpendicular to both the families of fibres has been assessed [2]. In order to match the tension-compression strength mismatch of the material, the Drucker-Praguer criterion has been used. Due to the high computational cost of this approach, the strength analyses have been performed on subdomains of the scaffold, namely on Representative Volume Elements (RVEs).

Results and Discussion

Figure 1 shows the homogenized elastic moduli of the scaffolds along with the three directions of load.
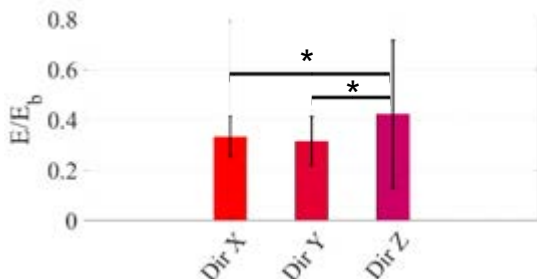
Figure 1: Normalized (E/E_b) elastic moduli.

The elastic modulus normalized with respect to the Young modulus of the bulk material (E_b) is reported. No statistical differences have been found between the two directions parallel to the fibers, namely E_x and E_y (p-value<0.05); while, the homogenized elastic moduli in the z-direction exhibited a third order polynomial relationship with the porosity (φ) [2], namely:

$$\frac{Ez}{Eb} = 1.57(1 - \varphi)^3 \qquad (1)$$

where E_z/E_b is the normalized elastic modulus and φ the porosity. Scaffolds exhibiting defects resulting from the printing process, exhibited elastic properties substantially lower than that predicted by (1). The strength of the scaffold shows the same trend of the elastic modulus with the porosity. Fractures typically occur in the unsupported segments of the rod, where the stress is highest. The fracture pattern obtained through the Finite Element Analysis is shown in Figure 2. It is comparable with the experimental fractures generated on scaffolds of brittle material exhibiting the same architecture [3].
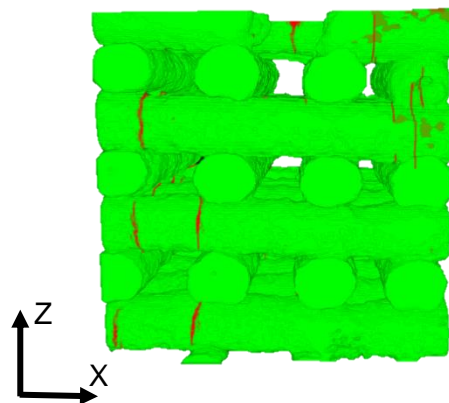
Figure 2: Geometry of a RVE used for strength Finite Element analysis. The fracture pattern is highlighted in red.

References

1. Fiume et al, Acta Biomaterialia, 405-418, 119, 2021.
2. Farina et al, Acta Mechanica Sinica, 37(2):290–301, 2021.
3. Miranda et al, Journal of Biomedical Materials Research - Part A, 646-655, 83(3), 2007.

DESIGN AND FUNCTIONAL EVALUATION OF A 3D PRINTABLE CUSTOM PROSTHESIS FOR TALUS REPLACEMENT

Francesca Danielli (1), Francesca Berti (1), Luigi La Barbera (1), Adelaide Nespoli (2), Chiara Giulia Fontanella (3), Sofia Pettenuzzo (3), Tomaso Villa (1), Lorenza Petrini (4)

1. Dept. of Chemistry, Materials and Chemical Engineering "G. Natta", Politecnico of Milano (Italy); 2. CNR ICMATE, Lecco (Italy); 3. Dept. of Industrial Engineering, Centre for Mechanics of Biological Materials, University of Padova (Italy); 4. Dept. of Civil and Environmental Engineering, Politecnico of Milano (Italy)

Introduction

Additive Manufacturing (AM) is a viable option to conventional manufacturing technologies in the production of custom implantable devices, resulting in a higher impact on patient care. This is relevant when dealing with morphologically complex anatomical sites, such as the ankle joint. Namely, standard implants for talus replacement are invasive, affected by a high failure rate, and require technically demanding surgeries [1]. The current work proposes a coupled experimental-numerical workflow that leads to the design and functional analysis of a talus prosthesis, exploiting AM.

Materials and Methods

A resurfacing prosthesis is conceived to provide a more conservative solution as compared to standard implants. Notably, it involves an external solid layer and an inner trabecular core to reduce implant weight and enhance osteointegration. Within this scenario, Finite Element (FE) modeling is a robust tool for investigating different design solutions, but AM products require a specific approach. This project involves the following tasks.

i) Design requirements. Looking at the literature, morphological, biomechanical, and manufacturing constraints were defined. A nominal strut diameter of 0.6 mm and an overall porosity of 80% were assessed for the trabecular core. An average thickness of 0.45 mm was identified for the cortical shell [2].

ii) Trabecular characterization. The influence of AM process parameters and the miniaturized struts dimensions are crucial factors affecting the morphology and the mechanical properties of AM lattice structures [3]. Thus, Ti6Al4V dogbone samples resembling the trabeculae were printed to characterize the material and to evaluate the morphology of the cross-section (Fig.1a).

iii) Lattice structures selection. According to the design requirements (i), two lattice structures (BCC and Kelvin) were designed to reproduce the trabecular core (Fig.1b). To assess their performance, FE models were built using the results of (ii) and discretized with 1D elements. For validation purposes, lattice samples were printed and tested under compression.

iv) Prosthesis design. Based on clinical images, preliminary prosthesis designs involving the selected lattice structures (iii) were developed exploiting the FE analysis (Fig.1c).

v) Prosthesis functional evaluation. The implantation of the prostheses in the ankle joint was simulated to evaluate stress-strain distribution both on the implant and the surrounding bones. The use of a validated FE model of the joint [4] allowed to reproduce functional loading conditions (e.g. static standing condition, ankle movements) and clinical tests to estimate the ankle joint stability coupled with the talus prosthesis (Fig.1d).
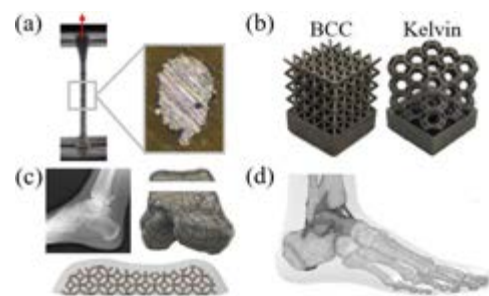
Figure 1: (a) Trabecular characterization; (b) Lattice structures selection; (c) Custom prosthesis design; (d) Prosthesis functional evaluation.

Results

The FE models of the lattice structures, built using data obtained from trabecular characterization (ii), were found to be reliable, exhibiting experimental-numerical differences below 8%. Given the significant variability of the struts morphology, the 1D discretization allowed a versatile assignment of the struts cross-section in the FE models. Simulations under functional loading conditions showed that both prosthesis designs have good biomechanical stability, with more evenly distributed loads when Kelvin structure is used as the inner trabecular core.

Discussion

This work proposes a pipeline to develop validated FE models of lattice structures, considering the uncertainties in manufacturing thin struts. Once the reliability of the developed models was assessed, two prosthesis designs were developed and coupled with a FE model of the ankle joint to simulate realistic scenarios of increasing complexity. This numerical tool allowed to identify the best biomechanical solution for a talus prothesis among the proposed ones.

References

1. Lee et al., Sci Rep, 11(1):1901, 2021
2. Tsegai et al., Am J Phys Anthropol, 163(4):784-805, 2017.
3. Murchio et al., J. Mech Behav Biomed Mater, 119:104495, 2021.
4. Forestiero et al., Australas Phys Eng Sci Med, 40:289-295, 2017.

MATRIGEL COAXIAL BIOPRINTING FOR IN VITRO CANCER MODELS

Paola De Stefano (1), Elena Bianchi (1), Melissa Basha (1), Romeo Bianchi (1), Gabriele Dubini (1)

1. Laboratory of Biological Structure Mechanics, Department of Chemical, Materials and Chemical Engineering "G. Natta", Politecnico di Milano, Italy;

Introduction

Cancer is the second leading cause of death worldwide. Despite the huge efforts to find effective treatments, failure rate is still high [1]. Bioprinted cancer models represent a significant improvement for drug discovery by mimicking the complex physiological 3D architecture. Matrigel™ is the most common basement membrane used in vitro as substrate for 3D cell culture, as it is very similar to the physiological one [2].

However, 3D bioprinting of free-standing Matrigel™ constructs is still an open point: it is hardly bioprinted pure because it needs to be combined to other bioinks because of its complex rheological behavior and low mechanical properties. Nonetheless, the use of other materials introduces additional variabilities, which limits their usage. In our previous work, we presented a custom-made bioprinter able to produce Matrigel™ scaffolds [3]. This method, improving what is reported to the previous literature, allowed us to obtain free-standing structures with good shape fidelity. However, it was possible only to obtain millimeter scale fibers. To scale down the constructs, reduce costs and improve printability process, we have designed a coaxial needle to bioprint diluted Matrigel™ core (1:1 ratio with PBS) inside an Alginate shell.

Materials and Methods

Bioprinting was performed using a custom-made volumetric bioprinter [3] and a custom coaxial needle. In particular, the printhead was designed to accommodate commercial needles of variable dimensions (from 30 to 22G), while the outer part was conceived with two inlets to obtain uniform distribution of the supporting shell (Figure 1). For the optimization of fiber bioprinting, we performed two major steps: a) definition of optimal flow rate and b) printing speed for both internal and external layer. We also evaluated both pre-reticulated and non- reticulated Alginate followed by spraying crosslinking with Calcium Chloride solution as alternatives for the outer layer. Finally, to further characterize hydrogels capability to retain their structures over short and long time culture periods, we will evaluate swelling/degradation properties within one week.

Results

To define the optimal bioprinting parameters, serpentines and grids were printed at different flow rates. Fiber diameters range from 1 to 1.8 mm with a
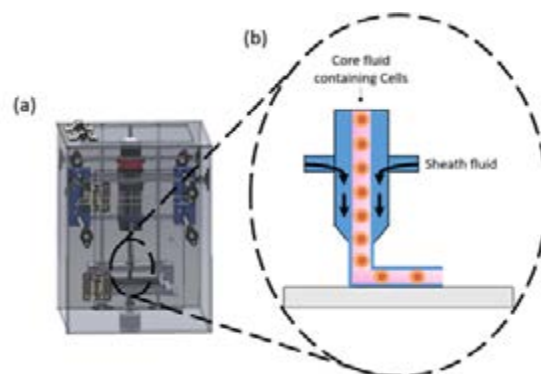
Figure 1: (a) Custom made bioprinting instrumentation, designed to bioprint matrixes by means of a volumetric control of the extruded material. (b) In the circle the detail of the coaxial needle: blue is the shell material and pink is the matrix seeded with cells. The fiber is laid down on the plate (grey), then observed and measured under an optical microscope.

core fiber of around 300 - 800 μm accordingly to the needle and the printing parameters used.

Discussion

Matrigel™ coaxial bioprinting is a very powerful strategy to obtain well defined constructs, while avoiding the seeding of cells in blends. The use of the pre-crosslinked Alginate produces thinner and more stable fibers, but suffers from needle clogging and high pressure related circuital problem compared to non-crosslinked Alginate. After crosslinking, constructs are able to retain their structure and maintain over time up to one week. Moreover, by using this approach, it is also possible to substitute pure Matrigel™ with diluted counterparts without impairing final results and improving bioprinting process.

References

1. Maeda et al., Clinical Translation Medicine, 7, 11, 2018;
2. Benton et al., Advanced Drug Delivery reviews, 79-80, 3, 2014;
3. De Stefano et al., Polymers, 13:12, 2021;

Acknowledgements

BIOMECHANICAL FAILURE BEHAVIOUR OF 3D PRINTED FEMORAL BONES COMPARED TO ARTIFICIAL AND HUMAN BONES

Katharina Nägl (1,2), Andreas Reisinger (1,2), Dieter H. Pahr (1,2)

1. Division Biomechanics, Karl Landsteiner University of Health Science, Austria
2. Institute for Lightweight Design and Structural Biomechanics, TU Wien, Austria

Introduction

The limited amount of human tissue donors makes it organizationally hard to investigate the biomechanical behavior of human femoral bones. To circumvent the problem, artificial bones are often used [1]. Currently a broad range of different casted artificial bones are commercially available, ranging from polyurethane-based foam models to more complex composite materials. However, these models are only generic representations of the geometry and the biomechanical behavior of human bones. In previous studies, fused deposition modelling (FDM) was successfully used to mimic natural bones [2]. The aim of this study was to use 3D printing for the fabrication of artificial human femoral bones with biomechanical behavior resembling that of their real counterparts. One group of samples is based on the geometry and infill properties of commercial artificial femurs to validate and optimize the process. For the second group, patient specific computed tomography scans (CT-scans) were used for the geometry. All printed bones are then mechanically tested and compared to their geometrical analogue commercial and human donor bone.

Methods

Initially, CT-scans of commercial and donor bones were performed to obtain 3D representations. Spongiosa and cortex were separated using medtool 4.5 (Dr. Pahr Ingenieurs e.U., Pfaffstätten, Ausria) allowing for the replacement of the spongiosa with a specific infill pattern (Figure 1 A). The mechanically correct infill density was obtained from a side study.
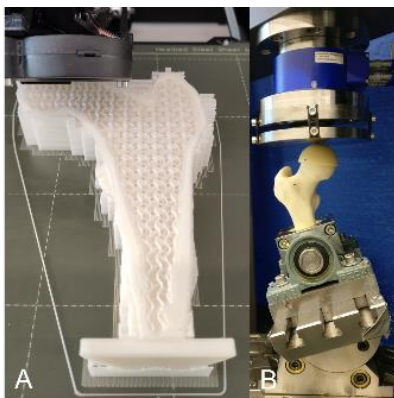
Figure 1: (A) shows the printing process of one femur (B) biomechanical test set-up, stance load case

After FDM printing, compression tests are performed (Figure 1 B) such as to resemble a stance position and loaded until failure. Overall, four different commercial bones - Orthobone (OB) and Orthobone_Standard (OBS) from 3B Scientific GmbH, SYNBONE® (SYN) from SYNBONE AG, SAWBONE® (SAW) from A Pacific Research Company - and three human bones from a previous study were used. They showed different bone densities where Femur 1/2/3 corresponds to high/medium/low bone density.

Results

The average FDM printing time was 15 hours. Figure 2A shows the ultimate loading forces of the commercial (red) compared to the 3D printed samples (green). Figure 2B shows results from human femoral bones (blue) in comparison to the 3D printed bones (green).
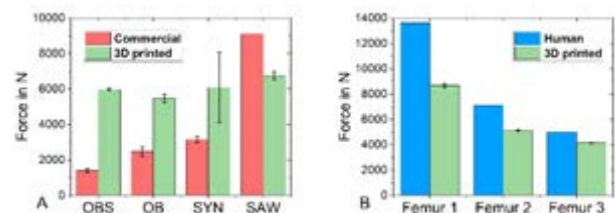
Figure 2: (A) Comparison of the ultimate loading force of commercial (red) and 3D printed bones (green) (B) comparison of the ultimate loading force of donor (blue) and 3D printed bones (green)

Discussion

Ultimate forces showed that FDM printing can be used as quick and comparable cheap method to manufacture artificial femoral bones. The 3D printed samples endure more ultimate load in comparison to polyurethane based commercial bones. Only the composite bone (Figure 2A SAW) withstands more load. Furthermore, FDM printed samples also closely resemble the mechanical properties of genuine samples, especially if the bone density of the femur is lower (Figure 2B Femur 2 and 3). These results show that 3D printing could be a feasible method to fabricate bone samples in the own lab which closely resembling the biomechanical behavior of human femurs.

References

1. Papini et al, Journal of Biomechanical Engineering, 129(1): 12-19, 2006
2. Xu et al, ACS Applied Materials & Interfaces, 6(17): 14952-14963, 2014
3. Dall'Ara et al, Bone, 52 (2): 27-38, 2013

3D BIOPRINTING OF ECM-BASED MULTI-LAYERED SEGMENTS OF TUBULAR CONSTRUCTS

F. Potere (1), G. A. Croci (2,3), P. Petrini (1), F. Boschetti (1), and S. Mantero (1)

1. Department of Chemistry, Material and Chemical Engineering 'Giulio Natta', Politecnico di Milano, Italy;
2. Division of Pathology, Fondazione IRCCS Ca' Granda Ospedale Maggiore Policlinico, Milan, Italy;
3. Department of Pathophysiology and Transplantation, Università degli studi di Milano, Milan, Italy

Introduction

3D bioprinting is the evolution of additive manufacturing techniques in the biomedical field and leads to the realization of tridimensional customized constructs to reproduce the structural complexity [1]. Moreover, the new technological challenge focuses on obtaining a 3D structure with several distinct layers to replicate the hierarchical organization of tissues. This work aims to reproduce tracheal and coronary substitutes compliant with the shape, functionality, and integrity requirements of the original tissues, combining the advantages of the 3D bioprinting and decellularization process and accounting for the presence of different cellular species.

Methods

All the experiments were performed on tracheas and aortas of 6-months pigs, kindly provided by the local abattoir, previously instructed on how to harvest and preserve tissues. The cellular and nuclear materials were removed from tissues through the decellularization process, after optimization. The treated samples were tested to evaluate the decellularized extracellular matrix (dECM) and produced as a powder by cryomilling under N_2. Then, tissues were solubilized by pepsin digestion. To produce bioinks, several solutions, based on gelatin, alginate, and digested dECM, were studied.

3D Bioprinting. After designing the trachea and aorta structures by SolidWorks, the constructs slicing was done using the software CELLINK HeartWare, which allows generating the G-Code.

Results

Decellularization. The decellularization process is validated through DNA quantification. In particular, the quantity of DNA must be less than 50ng/mg of tissue and the DNA fragment length less than 200 bp (base pairs). Moreover, the DNA and RNA components must be not visible in DAPI or hematoxylin and eosin staining.

3D Bioprinting. It was necessary to optimize the composition of a bioink able to withstand the printing of a segment of tubular construct up to 10 mm and to reproduce the multicellular complexity. Among the several compositions tested, the suspension resulting from 8% w/v gelatin, 7% w/v alginate, and 5% w/v dECM combined with a post-printing crosslinking with $CaCl_2$(1M), was able to produce the desired structures. With this bioink, it was possible to print structures made up to 20 layers (*Figure 1*). The dimensions of the printed structures are very close to those established in the design phase (*Table 1*).
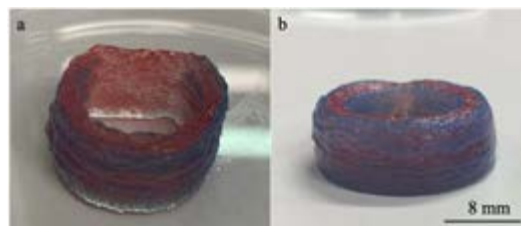
Figure 1. Structure of the trachea (a) and aorta (b) characterized by 20 layers of 8% w/v gelatin, 7% w/v alginate, and 5% w/v decellularized ECM.

Table 1 Comparison of the theoretical (model) and the real (bioprinted) dimensions of the constructs. A: Aorta; T: Trachea; D_i: Internal diameter.

(mm)	Dimension	Thickness	D_i	Height
T	Theoretical	2.41	20	9.91
	Real	2	16	9
A	Theoretical	4.64	20	9.91
	Real	4	16	9

Discussion

With the bioink described in this study, it is possible to print tubular structures capable of maintaining the desired structure avoiding the overlap of the double ink in the thickness, despite the increase in the number of layers. The parameters optimization allows the gain of structures characterized by a height of 20 layers corresponding to 9 mm. Comparing the theoretical and the real structures, they are very close to each other. In fact, the difference consists of 4 mm in the internal diameter, 0.91 mm in height, and 0. 41mm and 0.64 mm in the thickness of the trachea and aorta constructs respectively. Moreover, by tailoring the printing parameters and the amount of dECM the desired mechanical properties can be met. The next step includes the use of endothelial cells (blue bioink) and smooth muscle cells (red bioink).

References

[1] Moghaddam AS. et al, ACS Appl Bio Mater, 4(5): 4049-4070, 2021

FINITE ELEMENT MODELING OF BIPHASIC CALCIUM PHOSPHATE BONE SCAFFOLDS: AN EXPLORATORY STUDY

Natacha Rosa (1), S.M. Olheiro (2), P.M.C. Torres (2), Renato Natal (1,3), Marco Parente (1,3)

1. INEGI – Institute of Science and Innovation in Mechanical and Industrial Engineering, Portugal; 2. Department of Materials and Ceramic Engineering (DEMaC) – CICECO Aveiro Institute of Materials, University of Aveiro, Portugal; 3. Department of Mechanical Engineering, Faculty of Engineering of the University of Porto, Portugal

Introduction

Craniomaxillofacial bone defects are challenging due to their complex anatomical structure, such as sensory transduction pathways and sophisticated tissue structures [1]. To overcome the limitation associated with conventional treatment options, substantial research effort has been recently devoted to the development of cell- and growth factors-seeded synthetic tissue scaffolds which is an innovative fast-growing field in which additive manufacturing has proved its value [2][3]. Nowadays, biphasic calcium phosphate (BCPs) are definitely considered as the gold standard of bone substitutes in bone reconstructive surgery by combining the excellent bioactivity of hydroxyapatite (HA) with the good bioresorbability of beta-tricalcium phosphate (β-TCP) [4][5]. The objective of the present study was to develop a finite element (FE) model for a recently developed printable biomaterial scaffold containing a mixture of HA and β-TCP elastic mechanical capability assessment to withstand compressive stress.

Methods

Different mechanical elastic models for the BCP material were evaluated by comparing the scaffold's predicted FE models in Abaqus with results obtained from mechanical testing. Considering there was no data regarding the bulk BCP material mechanical properties, the linear and hyperelastic models' strain energy potential coefficients were determined incrementally by trial and error approach.

Results
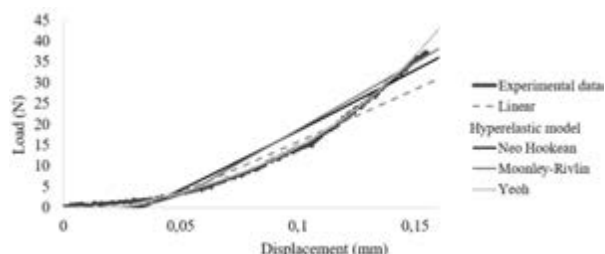
Figure 1: The BCP mechanical models for the characterization of the scaffold elastic behavior
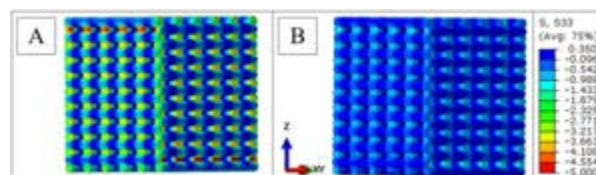
Figure 2: Stress distribution in Z for a 3% axial strain application considering an (A)linear elastic model and a (B) Yeoh hyperelastic model

Discussions

Based on previous demonstrated good cell adhesion provided by the BCP scaffolds [6], different BCP material elastic models were evaluated. A strong congruity was observed between experimental and numerically predicted values for the BCP material Yeoh strain energy potential model while linear elastic, Neo-hook, and Mooney-Rivlin models were incapable to capture the "upturn" in the scaffold load-deformation curve. The hyperelastic material model was capable to predict the mechanical behavior of the printed scaffolds. The developed FE model could be used as a tool for scaffold mechanical behavior assessment and structure improvement in order to mimic the implantation site morphology.

References

1. Ma et al, Chem Eng, 411: 128541, 2021.
2. Abbasi et al, ACS Biomater Sci Eng, 5: 3448–3461, 2019.
3. Wu et al, Someone et al, J Biomech, 117:110233, 2021.
4. Gregori et al, J Eur Ceram Soc, 26:1473-1479, 2006
5. Bouler te al, Acta Biomater, 15:1-12, 2017
6. Rodrigues et al, Biomed Mater, 16 015011, 2021

Acknowledgments

AN IN-SILICO MODEL FOR CELLS EXTRUSION IN BIOPRINTING

Gianluca Santesarti (1), Giuseppe Vairo (1), Francesco Viola (2),
Roberto Verzicco (3), Michele Marino (1)

1. Department of Civil Engineering and Computer Science, University of Rome "Tor Vergata", Italy;
2. Gran Sasso Science Institute, L'Aquila, Italy;
3. Department of Industrial Engineering, University of Rome "Tor Vergata", Italy;

Introduction

In extrusion bioprinting the final outcome of the process and the quality of the printed scaffold are highly influenced by several process variables, such as the dispensing pressure, the bio-ink properties, and the nozzle dimensions [1, 2, 3]. The introduction of the in-silico (computational) models would allow to reduce the experimental optimization costs and to increase the innovation of the bioprinting process.

So far, the theoretical and numerical models used are not specific enough to give a quantitative assessment of the main cell damage causes such as the shear stress and exposure time [4]. The aim of this work is to present a computational model for the non-Newtonian fluid extrusion which considers the presence of the cells and the interaction between the two phases.

Methods

Owing to the complex fluid-structure interaction (FSI) between the hydrogel flowing in the nozzle and the cells, as well as among the cells themselves, we have realized a multi-physics solver based on the immersed boundary technique [5]. In particular, the unsteady cell deformations are solved using a spring-network structural model based on the Fedosov's interaction potential approach [6].

Results

As a first study, a convergent-shaped nozzle with multiple immersed cells has been considered.
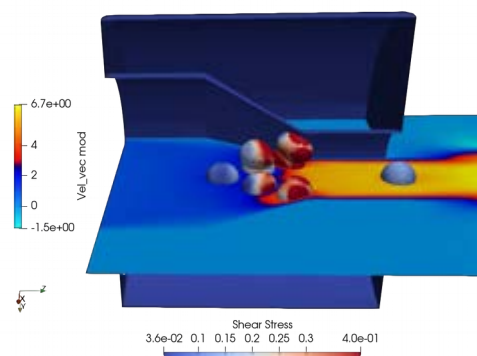
Figure 1: Velocity field along a symmetry plane and shear-stress field in the nozzle at time $t^* = 17.5$.

In Fig.1 the velocity magnitude field of a nozzle

symmetry plane and the shear-stress acting on the cell surface at adimensional time $t^* = 17.5$ are reported. It is observed that the cells locally modify the velocity field of the fluid, and simultaneously the shear-stress and the deformation of cells are highly influenced by the presence of the other cells.
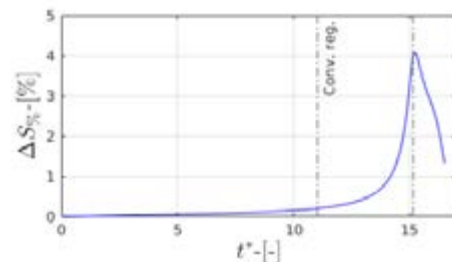
Figure 2: Evolution of the percentage surface variation of a single cell during the extrusion.

Furthermore, by considering a cell flowing along the nozzle axis, in Fig. 2 it is possible to quantify the maximum deformation of the cell surface, occuring in the nozzle throat section at the end of the convergent region.

Discussion

This in-silico model opens then for a systematic optimization of the hydrogels material properties and of the nozzle geometries, in order to achieve a balance between the biological requests of high cell density and viability and the engineering constraint of bio-inks printability.

References

1. Ozbolat, I. T., Hospodiuk, M., Biomaterials, 76, 321-343, 2016.
2. Chang, R. et al., Tissue Eng., Part A 14.1, 41-48, 2008
3. Emmermacher, J. et al., Biofabrication 12.2, 025022, 2020.
4. Ning, L. et al., ACS Biomaterials Science & Eng. 4.11, 3906-3918, 2018.
5. Fadlun, E. A. et al,, J. of Comp. Physics 161.1, 35-60, 2000
6. Fedosov, D. A. et al. (2010). Comp. Meth.s in App. Mechanics and Eng., 199(29-32), 1937-1948, 2010.

MECHANICAL REPLICA OF SOFT TISSUES: A STRUCTURAL APPROACH

Vincent Serantoni, Corinne Rouby, Jean Boisson

Unité de Mécanique (UME), ENSTA Paris/Institut Polytechnique de Paris - 828 Boulevard des Maréchaux, 91762 Palaiseau cedex, France

Introduction

Nowadays, 3D printing enables high fidelity geometrical reconstruction of human part. However, as the haptic feedback on these 3D printed replicas is still far away from living tissues, it is no use for surgeon except for anatomic purpose. Here we propose an alternative approach to the direct reproduction of material properties [1, 2]: working with classical printable material but acting on the shape of the structure to influence the global mechanical response.

To mimic the response of biological tissues by acting on the structure, many works focused on bio-mimicry [3, 4]. However, the stiffening of the curve generally appears for high strain or is not enough to match biological tissues. Here, we focus on a simple double sinus form. Preliminary results indicate that this form is able to reach an important stiffening strongly matching with an experimental tensile-test done on a human mandibular periosteum.

Methods

The geometry of the structure is the sum of a cosine with one large period and another cosine with shorter periods. This function is defined as follows:

$$f_1 = -A_1 \cos(2\pi x)$$
$$f_2 = -A_2 \cos(N\, 2\pi x) \qquad (1)$$
$$f_{tot} = f_1 + f_2$$

depending on 3 parameters : A_1, A_2 and N. To exclude the length of the structure of this study, x was defined between 0 and 1.

The Finite Element (FE) model will be solved using Cast3m [5]. Each FE simulation was defined as follows: an imposed displacement corresponding to the maximum strain obtained on the experimental periosteum test and the extracted forces are normalized with respect to the maximum force.

The parameters optimization uses the gradient descent to minimize the least squares difference. Convergence is assumed when the length of the change in parameter are under a threshold.

Results

Imposed final displacement extracted from experimental data was 0.15. Values tested of N goes from 1 (special case were $f_{tot} = f_1$) to 6. This limit was set by the difficulty to generate a shape with a constant thickness, set to 0.05. The value of best parameters A_1 and A_2 for each N, fitting the experimental curve, are summary in table 1. Result for N = 5 is shown in figure 1.
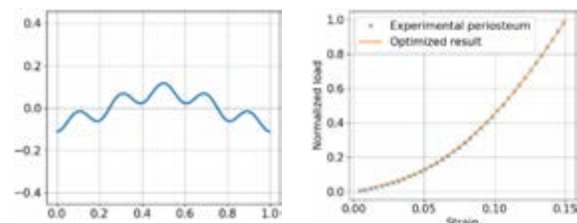
Figure 1: for N = 5, left) structure geometry fitting the experimental test after convergence; right) comparison of the experimental and numerical load/strain curve.

	N=1	N=2	N=3	N=4	N=5	N=6
A_1	0.156	0.132	0.075	0.073	0.073	0.078
A_2	0	0.052	0.559	0.045	0.04	0.039
Ls	0.850	0.767	0.235	0.068	0.010	0.002

Table 1: value of parameter A1 and A2, depending on N, for each convergence. The parameter Ls represents the least squares score.

Discussion

The best optimized structure is obtained for N = 6. The simulated behavior matches very well the periosteum objective curve. In our opinion, the addition of a second shorter cosine function is crucial. Indeed, collagen fiber mechanical behavior can be assimilated to a cable, i.e. working only under tension. The 3D printed polymer acts as beams so it has a compression contribution involved in flexion. In order to diminish the flexion effect while flattening the structure, the curves generated by the second function aims to minimize the rotational energy stored in the structure. Enabling the softening of the curve and generate a toe region similarly to bio-tissues.

Next steps will be to 3D print this shape and compare experimental results with the simulated one. Also, the contribution of the load/stress curve on the parameters has to be precisely identified to be able to adapt the geometry to the variability of soft tissues. Finally, the question of the soft matrix surrounding the structure will be treated.

References

1. A. L. Khalfa et al, J Am Chem Soc, 143, 42:17510–17516, 2021.
2. A. Foerster et al, Materials & Design 205, 109681, 2021.
3. Wang et al, Additive Manufacturing, 12:31-37, 2016.
4. Ma et al, J Mech Phys Solids, 90 :179-202, 2016.
5. Cast3m, http://www-cast3m.cea.fr/index.php

DEVELOPING A FRAMEWORK FOR GENERATING MITRAL VALVE SCALABLE MODELS

Diana Oliveira[1], Daniel Espino[1], Luca Deorsola[2], Jonathan Mynard[3], Vijay Rajagopal[4], Keith Buchan[5], Dana Dawson[5], Duncan Shepherd[1]

1. University of Birmingham, UK; 2. Regina Margherita Children's Hospital, Italy; 3. Murdoch Children's Research Institute, Australia; 4. University of Melbourne, Australia; 5. Aberdeen Royal Infirmary, UK

Introduction

The mitral valve (MV) is a complex anatomical structure, whose shape is key to several traits of its function [1]. Computational methods accounting for a subject's MV shape can be used to evaluate MV biomechanics in pre- and post-operative scenarios, having the potential to improve surgical planning [2]. The accuracy of these models is sensitive to valve geometry and obtaining image-based patient-specific geometries is usually time-consuming. Parametric MV models can therefore be developed and employed in a comprehensive study of MV dynamics. MV shape is important for the long-term outcome of valvular surgical procedures [1], and so there is a need to develop frameworks to generate customisable MV geometries. Our study focuses on developing a computational tool enabling the quick generation of anatomically accurate and clinically useful parametric models of the MV.

Methods

The valve was parameterised using MATLAB: landmark points and relevant MV boundaries were used to parameterise the annulus and leaflets using polynomial fitting. Geometric parameters describing the annulus, leaflet shape and papillary muscle position were implemented and used to scale the geometry. The developed model, available as a toolbox, allows to generate a population of models from (1) patient-specific dimensions obtained from medical imaging or (2) averaged dimensions evaluated from empirical equations, based on the golden ratio [3]. A MATLAB script was written to automatically obtain the MV mesh and use it in the creation of an input file for finite element simulations using LS-Dyna; the mesh file itself is compatible with a range of modelling software [4].

Results

The MV scalable model based on averaged dimensions accurately represents MV shapes (relative errors relative to clinical data: < 10% for annular and leaflet length dimensions; < 24% for leaflet surface areas), with a sample model displayed in Figure 1. This framework was used to generate a range of MV models, including a healthy model based on averaged dimensions and a diseased, patient-specific model incorporating annular dilation and flattening. Finite element simulations representing valve closure were run using LS-DYNA. Valve configurations associated with disease exhibit greater tissue stress in comparison with healthy ones (Figure 2), indicating greater damaging to the tissue.
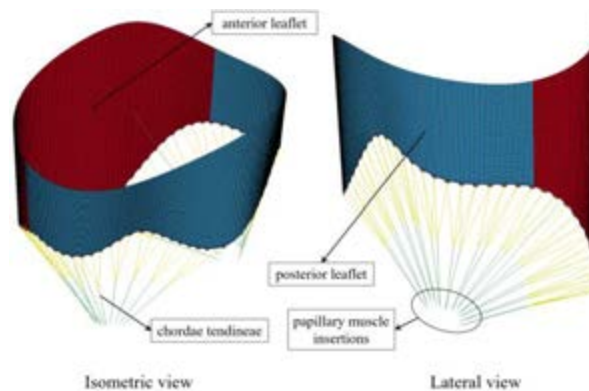
Figure 1: Sample 3D MV model with all components included, ready for computational simulations.
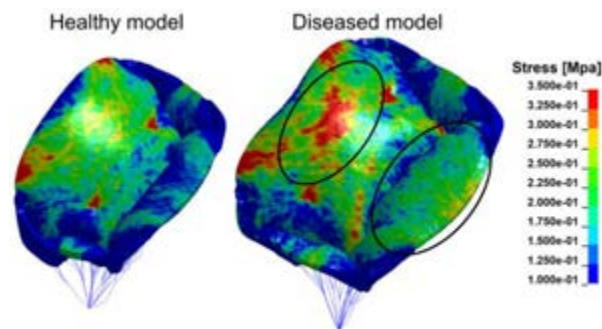
Figure 2: Maximum principal stress [MPa] associated with healthy and diseased MV models.

Discussion

This framework allows for the automatised and user-controlled generation of tailored MV geometries, and the creation of input files for finite element analysis in less than 5 minutes. From a clinical perspective, the toolbox can be used to study the influence of morphological MV parameters on its function. Inputted patient-specific parameters can be used to create a range of diseased scenarios and the respective biomechanics can be evaluated through computational simulations. Following the incorporation of surgical techniques, the toolbox will also aid clinicians when choosing the best patient-specific clinical intervention and improve the design process of new medical devices.

References

1. Al-Atabi et al, Proc Inst Mech Eng H, 226: 275-87, 2012.
2. Kohli et al, Ann Biomed Eng, 49: 1449-1461, 2021.
3. Deorsola et al, Echocardiography, 36: 1028-1034, 2019.
4. C. de Oliveira et al, Comput Biol Med, 135: 104628, 2021.

A Non intrusive data-driven reduced order model framework for cardiovascular problems

Michele Girfoglio (1), Pierfrancesco Siena (1), Nicola Demo (1), Michele Conti (2), Gianluigi Rozza (1), Ferdinando Auricchio (2)

1. Mathematics Area, mathLab, SISSA, via Bonomea 265, 34136 Trieste, Italy;

2. Department of Civil Engineering and Architecture, University of Pavia, Via Ferrata 3, 27100 Pavia, Italy

Introduction and motivation

The relevant improvement of High Performance Computing (HPC) infrastructures occured recently has allowed to obtain a significant reduction of the computational cost associated to the numerical simulation of Partial Differential Equations (PDEs). Nevertheless, when there is the need to investigate several working conditions of the system at hand related to different geometrical features and/or physical setting, the classic discretization methods (often referred as to Full Order Models (FOMs)), such as Finite Volume (FV) and Finite Element (FE) methods, could not be adequate at the aim to provide real-time results. The introduction of Reduced Order Models (ROMs) (see [1] for a recent review) allows numerical simulations at a very high efficiency without a significant loss in terms of accuracy. In particular, non intrusive data-driven ROM approaches are currently a highly active area of research. They have several advantages with respect to the classic intrusive projection-based ROM strategies: they are based only on data and do not require knowledge about the original governing equations describing the problem at hand, therefore no modification of the simulation software is carried out.

Methodology

In this work, the FOM is represented by the incompressible Navier-Stokes equations discretized by using a FV method. The ROM is developed by using the PODI method where Proper Orthogonal Decomposition (POD) is adopted for the computation of reduced basis functions whilst for the evaluation of the modal coefficients we consider two different Interpolation (I) techniques: Radial Basis Functions (RBF) [2] and Artificial Neural Network (ANN) [3].

Test cases

We test the performance of our approach through the investigation of two different bioengineering problems: (i) POD-RBF is used for the efficient simulation of the aortic blood flow patterns induced by the presence of the outflow cannula of a Left Ventricular Assist Device (LVAD) (see Figure 1) [4, 5]; (ii) POD-ANN is used for the modeling of the blood flow in the coronary system when an isolated stenosis of the left main coronary artery occurs [6]. In the case (i) physical parameterization with respect to the LVAD flow rate is considered. On the other hand, in the case (ii) we build a geometrical parametric setting with respect to the stenosis degree. In both cases, the accuracy and efficiency of the ROM is assessed against results obtained with the FOM.
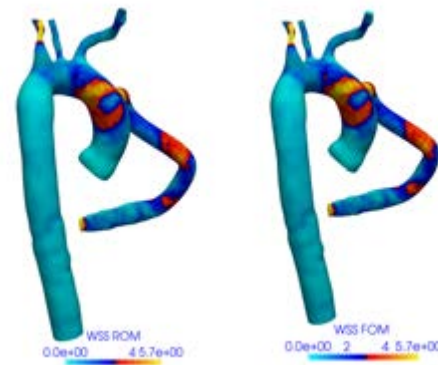
Figure 1: Comparison between ROM (left) and FOM (right) for wall shear stress (WSS).

Perspectives

This study has been conducted on a single patient-specific geometry. With the aim to overcome this limitation, we are interested in efficiently handling geometrical parametrization in the context of patient-specific geometries to different applications and different reduced order model strategies. Moreover, in order to perform more realistic numerical simulations of the cardiovascular flow, a follow-up of the present work is to couple the CFD model with an elasticity model to simulate fluid-structure interaction as well as to consider for the enforcement of realistic pressure outlet boundary conditions by using lumped element models.

References

1. P. Benner et al., De Gruyter, Berlin, Boston, 2020.
2. D. Lazzaro et al., J. Comput. Appl. Math, 140:521-536, 2002.
3. J.S. Hesthaven et al., J. Comput. Phys., 363:55-78, 2018.
4. M. Girfoglio et al., arXiv:2007.03527.
5. M. Girfoglio et al., Acta Mech. Sin., 37:1183-1191, 2021
6. P. Siena et al., arXiv:2201.01804

CFD MODELLING OF THE AIRFLOW IN THE HUMAN NASAL CAVITY

Sverre Gullikstad Johnsen

SINTEF Industry, Trondheim, Norway

Introduction

Computational Fluid Dynamics (CFD) has become a popular tool in assessing patient specific airflow in the upper airways. Very few publications demonstrate validation of simulation results against experimental data, however. This is a paradox since it is well known that CFD modelling requires validation to be trustworthy. Active anterior rhinomanometry (RMM) is one of few clinical measurements that can be used for validation of human airways CFD models. It has been documented by several authors that there exists an unexplained, severe discrepancy between RMM measurements and CFD simulations, see e.g. [1,2]. This work investigates if such discrepancy can be caused by modelling inaccuracies caused by poor computational mesh resolution, transient effects, or transitional flow not captured by simplified models.

Methods

Pre-operative, patient specific Computed Tomography (CT) images and RMM data was obtained from St. Olavs hospital, the university hospital in Trondheim. The patient was a 67-year-old male with a BMI of 28. Segmentation was done with ITK-SNAP 3.4.0 using a HU threshold of -300, to obtain the CFD geometry [3,4]. Using ANSYS Meshing with default settings, coarse and fine computational meshes were generated with 900k and 45M tetrahedral cells, respectively. CFD simulations were performed in ANSYS Fluent 2019R2. Steady-state simulations were performed on the coarse mesh, employing laminar flow model with a pharyngeal velocity inlet boundary condition (BC). Transient simulations were performed on the fine mesh using the WALE Large Eddy Simulation (LES) turbulence model, time-steps of 10^{-5}s, and a homogeneous, sinusoidal velocity inlet BC. The peak volumetric flowrate was 600ml/s and the period was 5s. The airway geometry was considered rigid, and no-slip wall BC was employed. Simulating RMM, one nostril was kept closed (wall) while the other had a total pressure BC. Three periods were simulated and the pressure difference between right and left nostril was recorded (Fig. 1).

Results and Discussion

Fine mesh, transient LES simulations produced RMM data similar to those obtained with the coarse mesh, steady-state laminar model (Fig. 2). The flow resistance reported from clinical RMM is approximately one order of magnitude higher than that obtained from CFD. The fine temporal and spatial resolution (CFL≲1, y^+≲1) ensures that the LES is well within the recommended range for pipe-flow and is expected to represent the flow
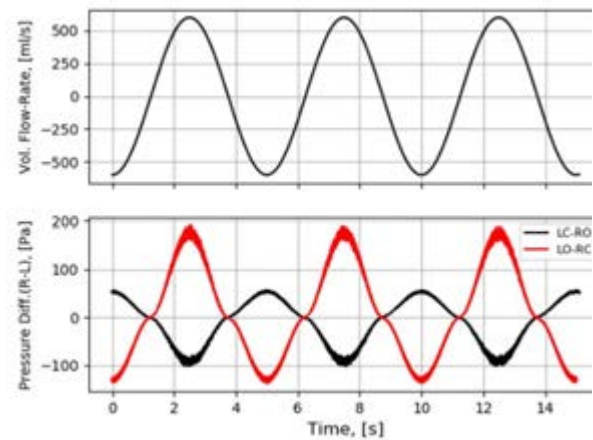
Figure 1: Transient flowrate and pressure difference between right and left nostril (Black: left nostril closed, right open. Red: left nostril open, right closed).
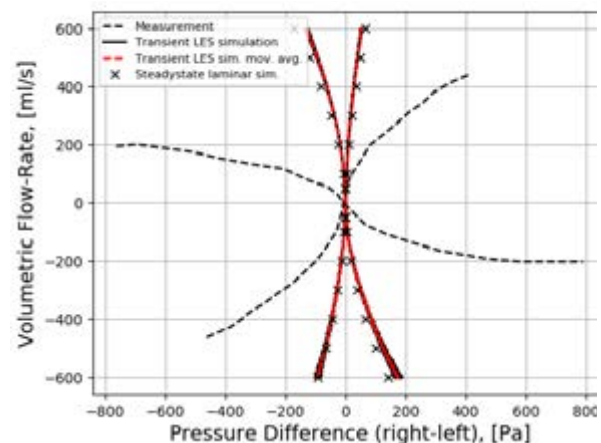
Figure 2: Measured and modelled RMM data.

field accurately. It is concluded that the observed discrepancy between measured and computed RMM data is neither due to mesh resolution, transient effects nor inaccurate turbulence modelling. The airflow in the nasal cavity can be accurately predicted by a laminar flow-model on a relatively coarse computational mesh.

References

1. J. Osman, et al, Current Dir. in Biomed. Eng. 2, 2016.
2. G.B. Cherobin, et al, PLOS ONE 13(11), 2018.
3. P.A. Yushkevich et al, NeuroImage 31, 2006.
4. M.R. Jordal et al, Proc. 12th Int. Conf. CFD, Norway, 2017.

Acknowledgements

ASSESSING PROSTHETIC HAND DESIGNS THROUGH A NEW GRASPING SIMULATION BENCHMARK

Immaculada Llop-Harillo, José L. Iserte, Antonio Pérez-González

Universitat Jaume I, Spain

Introduction

In the last decades, the design of anthropomorphic hands has become popular improving cosmesis and functionality. Experimentation, simulation, and combined approaches have been used with artificial hands in the literature to assess the effect of design alternatives (DAs) on its final performance. However, establishing standard benchmarks for grasping and manipulation is a need recognized among the research community. Experimental approaches allow assessing the grasping ability of artificial hands with realistic information about the final performance, but are costly, time-consuming, and inconvenient in early design stages. Alternatively, computer simulation can be useful in assessing and ranking DAs.

This study presents a new approach based on grasping simulation and assessment within the framework of the OpenRAVE simulation tool [1]. The new methodology involves the use of human knowledge for the generation of efficient grasp hypotheses (GHs) and the definition of a new metric to assess human-likeness of the achievable grasps with the artificial hand. To this end, we propose to adapt to a simulation environment, the Anthropomorphic Hand Assessment Protocol (AHAP) [2], an experimental benchmark that quantifies the grasping ability of anthropomorphic artificial hands, including human-likeness and grasp stability, through grasping actions on several everyday objects. To exemplify the methodology, a comparison of 28 different DAs for the IMMA hand, an anthropomorphic prosthetic hand developed by the authors [3], was performed.

Methods

Twenty-eight different combinations of the orientation angles of the carpometacarpal (CMC) and metacarpophalangeal (MCP) joints of the thumb of the IMMA hand [3] were analyzed in order to find the best combination to improve its performance.

For the simulations, the objects used in the experimental AHAP were modelled in SolidWorks by the authors [4]. For the sake of simplicity, only the two most frequently used grasp types (GTs) were covered in this study: pulp pinch and cylindrical grip.

For the new grasping simulation approach, the OpenRAVE Grasping Module was extended by the authors with phyton scripting. For each object, a set of GHs was automatically generated trying to simulate how the object is usually grasped with the intended GT. Then the grasp process was simulated to reach a grasping posture. Finally, each final grasping posture was automatically assessed according to the anthropomorphic criteria for GT correctness defined in the experimental AHAP [2]. In order to compare the human-like grasping and the stability of the grasps performed with the different hand DAs, a new index is proposed, named Simulated Grasping Ability Score (S_{GAS}), adapted from the Grasping Ability Score (GAS) defined in the AHAP [2].

Results

The best DA was found to be that with orientation angles CMC 30º and MCP 75º. Figure 1 shows, for this DA, one of the grasps accomplishing GT correctness for each of the six simulated objects.
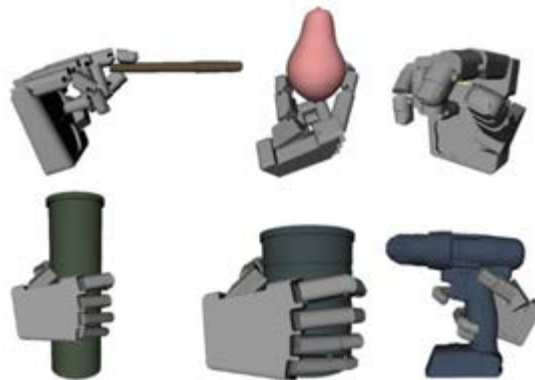
Figure 1: Correct grasps performed with the best IMMA hand design alternative.

Discussion

A new simulation benchmark has been proposed which follows an anthropomorphic approach for defining the GHs and for assessing prosthetic hand designs. The main contributions of this approach with respect to the existing methods in OpenRAVE are: 1) It reduces the computational cost taking profit of the human experience for limiting the number of GHs; 2) Its principles are adapted from the experimental benchmark AHAP; 3) It resulted in more anthropomorphic and realistic grasps; 4) The metric associated to the benchmark allows the comparison of different hand DAs in order to obtain optimal solutions.

References

1. Diankov, PhD, 2010.
2. Llop-Harillo et al, Rob Auton Syst, 121:1-12, 2019.
3. Llop-Harillo et al, Int Biomech, 4(2):50-59, 2017.
4. Pérez-González et al, Zenodo, 2019.

Acknowledgements

COMPUTATIONAL INVESTIGATION AND VERIFICATION OF THE IN-VITRO PERFORMANCE OF BIORESORBABLE BRAIDED STENTS

Agnese Lucchetti (1), Thomas Gries (1), Ted J. Vaughan (2)

1. Institut für Textiltechnik of RWTH Aachen University, Germany; 2. Biomechanics Research Centre (BMEC), School of Engineering, National University of Ireland Galway, Ireland

Introduction

Bioresorbable stents are a promising alternative to permanent metallic devices since they may provide vessel support only for the time require and are subsequently naturally degraded. However, there are still challenges with polymeric bioresorbable stents since they show lower mechanical properties compared to their metallic counterparts [1]. The use of finite element models (FEM) is now widespread, since it allows to obtain a wide understanding of the stent mechanical properties and performance in relative time and cost effective way. Each model however needs to be validated through appropriate comparison with in-vitro test results, which has rarely been carried out for bioresorbable braided stents [2]. The present work aims to build a verified computational model of different in-house manufactured braided polymeric stents with the final goal to have a framework allowing the stent mechanical optimization.

Methods

Different stent geometries were reconstructed with the Matlab code by Zaccaria et. al [3] and imported into Abaqus/Explicit software as orphan meshes of Timoshenko beam elements (Fig 1a). All the stents featured a 5-mm internal diameter, a 100-µm wire diameter and a 20-mm length. Two different braiding patterns were reconstructed: 1:1-1 and 2:2-1 [4] (Fig 1b). Also, different braiding angles were implemented, namely 30° and 20°. Both parallel plate and the radial compression tests were simulated. Two and ten rigid plates were modeled as rigid bodies to resemble respectively the two setups. In both tests, the stents were compressed/crimped to reach circa the 50% of their initial diameter. The poly-L-lactic acid (PLLA) was modelled as an elastoplastic material and its mechanical properties were determined from tensile testing of filaments. The wire-wire and stent-setup friction coefficients were assigned as a penalty after a fitting process. The computational outcomes were then verified by comparison with experimental curves derived from the in-house performed mechanical tests.

Results

From the friction coefficient analysis, it could be observed that the curve hysteresys mainly depends on friction between the stent and the plates, while internal friction between the stent wires has a minimal effect. It was found that for a stent-stent and a stent-setup friction coefficient of 0.3 and 0.25, respectively, the developed computational model accurately matched the mechanical behaviour of the PLLA braided stents for the parallel plate (Fig 1c). With the same coefficients, a satisfingly result was also reached for the crimping model in which the radial stiffness, the chronic outward force and the force at maximum compression are well represented while the radial resistive force is just slightly overhestimated (Fig 1d).
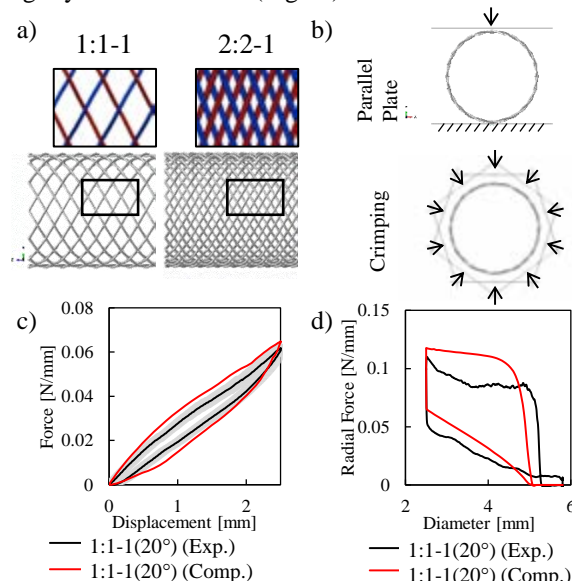
Fig 1: (a) Representation of the braiding pattern reconstructed; (b) Parallel plate (top) and crimping test (bottom) schematics; (c) Example of the parallel plate test results; (d) Example of the crimping tests results.

Discussion

This study developed and experimentally-validated a computational model that could provide an additional insight on the mechanical properties and potentialities of PLLA bioresorbable braided stents. This could be also used as a framework for further mechanical properties optimization to decrease the performance gap between the current bioresorbable braided stents and their metallic counterparts.

References

1. Wu et al, Expert review of medical devices, 18 (4): 351–365, 2021.
2. Zhao et al, JMBBM, 2019.
3. Zaccaria et al, J Biomech, 2020.
4. Kyosev, 2015.

Acknowledgements

MODELLING THE BIOMECHANICAL BEHAVIOR OF THE LIVER IN REAL TIME USING ML MODELS TRAINED ON FE SIMULATIONS.

Oscar J. Pellicer-Valero (1), María J. Rupérez (2), and José D. Martín-Guerrero (1)

1 Intelligent Data Analysis Laboratory, Department of Electronic Engineering, ETSE (Engineering School), Universitat de València (UV), Av. Universitat, s/n, Burjassot, Valencia 46100, Spain, Oscar.Pellicer@uv.es; jose.d.martin@uv.es; https://idal.uv.es

2 Instituto Universitario de Investigación de Ingeniería Mecánica y Biomecánica (I2MB), Universitat Politècnica de València (UPV), Camino de Vera, s/n, Valencia 46022, Spain, mjrupere@upvnet.upv.es; https://i2mb.upv.es/

Introduction

Modelling of human soft tissue biomechanics is the basis for the development of new clinical applications that will improve diagnosis and treatment of some diseases, as well as the planning and guidance of some surgical interventions. The most popular technique used to predict the deformation of the human soft tissue is the finite element method (FEM) due to its high accuracy and robustness. However, FEM has a high computational cost, which makes it unfeasible to integrate in real-time computer-aided surgery systems. An alternative for simulating the mechanical behavior of human soft tissues in real time comes from the use of machine learning (ML) techniques, which can be trained to provide much faster simulations than FEM.

Methods

In this work, a relatively novel approach for developing a biomechanical model of the liver is presented. The model employs a neural network (NN) to provide real-time inference. It was trained on tens of thousands of FEM simulations of the biomechanical behavior of the liver on more than 100 different liver geometries. Considering a target accuracy threshold of 3 mm for the Euclidean Error, four different scenarios were assessed: a single liver with an arbitrary force applied, a single liver with two simultaneous forces applied, a single liver with different material properties and an arbitrary force applied. Finally, a much more general model capable of modelling the behavior of any liver with an arbitrary force applied [1].

Results

The results show that ML models perform extremely well on all the scenarios, being capable to keep the Mean Euclidean Error under 1 mm in all cases [1]. For a single liver with an arbitrary force applied, 99.96% of samples were within the accepted error range; for a single liver with two simultaneous forces applied, 99.84% of samples; for a single liver with different material properties and an arbitrary force applied, 98.46% if samples. Finally, for the model capable of modelling the behaviour of any liver with an arbitrary force applied, 99.01% samples were within the accepted error range for the median liver [1].

Furthermore, the proposed model achieves working frequencies above 100Hz on modest hardware (with frequencies above 1000Hz being easily achievable on more powerful GPUs), which implies that they can work in real-time. These results constitute a remarkable improvement in this field and may help introduce them in clinical practice.

Discussion

The main objective of building a general model able to simulate the mechanical behavior of any liver, given an arbitrary force, with sufficient accuracy and in real time has been achieved. However, other options exist too. For instance, the model in the first scenario achieves higher levels of accuracy, as compared to any liver in the last scenario. In practice, for applications requiring such precision, it would be sensible to simulate a particular liver geometry under a few hundred forces and train a NN on top of it, as part of the pre-operative process.

Furthermore, the capability of the method to generalize from situations where multiple forces or different material properties are at play has been shown.

Finally, a novel geometry parametrization algorithm has been developed, which allows the NN model to generalize to unknown geometries. Moreover, a simple but effective modification to the coherent point drift algorithm has been employed, which enables this algorithm to achieve excellent registration results even when the registered geometries are drastically different.

References

1. Oscar J. Pellicer-Valero, María J. Rupérez, Sandra Martínez-Sanchis, José D. Martín-Guerrero, Real-time biomechanical modeling of the liver using Machine Learning models trained on Finite Element Method simulations. Expert Systems with Applications, Vol. 143, pp. 113083, 2019.

Acknowledgements

PARAMETRISATION SETTING AND GENERATION ALGORITHM FOR ABDOMINAL AORTIC ANEURYSMS

G. Ravon (1), L. Saccaro (1), F. Bernard (3) and A. Iollo (1,2)

1. Inria - Bordeaux Sud-Ouest, Team MEMPHIS, 33405 Talence, France; 2. IMB, UMR 5251, Université de Bordeaux, Talence, France; 3. Nurea, 33000 Bordeaux, France

Introduction

The abdominal aortic aneurysm (AAA) is a pathological enlargement of the section of the aorta, between the renal and iliac arteries. When not surgically treated, the AAA may result in the rupture of the aneurysm sack, a condition that carries a high mortality rate. The clinically established criterion to undergo surgery is when the maximum diameter is above 5cm. However, this criterion does not ensure the rise of premature life-threatening development of the aneurysm before that threshold. In this setting, to correlate hemodynamics, mechanical and biological characteristics of the aneurysm, along with the geometry of the sack and the risk of rupture, is essential to provide reliable indicators of rupture potential. However, large datasets of aneurysms are needed to assess the reliability of a new risk indicator. We describe a data augmentation methodology to generate aneurysm shapes that are statistically relevant, starting from a dataset of 53 patients.

Method

A dataset of 53 CT-based models of AAA is segmented. Subsequently the 3D models are reconstructed using the software PRAEVAorta (https://www.nurea-soft.com). A suitable parametrisation is then devised. We identify a centreline $\mathbf{P}$, and S sections of the aortic wall, perpendicular to the centreline. The profile of each section s is approximated using a Fourier series, as in figure 1:

$$R_s(\theta) = a_0^s + \sum_{i=1}^{N} a_i^s \cos(i\theta) + a_{-i}^s \sin(i\theta)$$

Each aneurysm of the dataset is then be identified by the set of parameters: $\{\mathbf{P}, \mathbf{a}_0, \mathbf{a}_1, \mathbf{a}_{-1}, ..., \mathbf{a}_N, \mathbf{a}_{-N}\}$, where $\mathbf{a}_i = [a_i^1, ..., a_i^S]$.
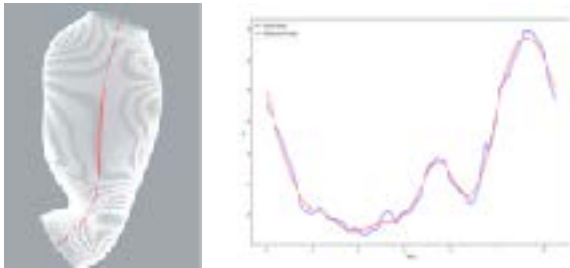
Figure 1: Left: Aneurysm from the dataset parametrised. Right: in red the Fourier approximation of the aortic wall, in blue.

Then we introduce a reduced basis technique to build low-dimensional spaces where each aneurysm of the initial dataset is projected. To take into account the heterogeneity and inherent variability, for each space an appropriate energy threshold is chosen, based on an in-sample and out-of-sample convergence analysis. Projecting onto the low-dimensional spaces, the following approximations holds:

$$\mathbf{P} \approx \sum_{j=1}^{\mathscr{P}} c_{\mathbf{P},j} \phi_{\mathbf{P},j}, \quad \mathbf{a}_i \approx \sum_{j=1}^{\mathscr{N}} c_{i,j} \phi_{i,j} \quad \mathscr{P}, \mathscr{N} \ll 53.$$

See figure 2 for a progression of the aneurysm approximation in reduced spaces with increasing level of energy.
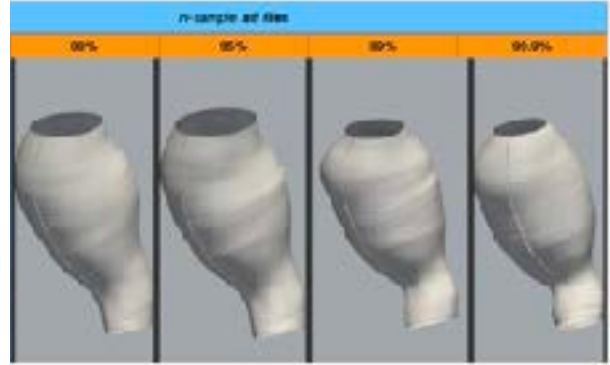
Figure 2: Reconstruction of an aneurysm from the dataset. The parameters are projected onto the reduced dimensional spaces that capture 90%, 95%, 99% and 99.9% of energy.

This low-dimensional space allows us to employ unsupervised learning approaches based on Gaussian mixture models. In particular, we first build multivariate normal distributions on the coefficients $\mathbf{c} = [c_1, ..., c_M]$, and then draw samples of coefficients $\tilde{\mathbf{c}}$, that finally allow us to build new aneurysm's parameters, namely:

$$\tilde{\mathbf{P}} = \sum_{j=1}^{\mathscr{P}} \tilde{c}_{\mathbf{P},j} \phi_{\mathbf{P},j}, \quad \tilde{\mathbf{a}}_i = \sum_{j=1}^{\mathscr{N}} \tilde{c}_{i,j} \phi_{i,j}.$$

Results

To explore the AAA shape variability different energy thresholds are used to build the reduced spaces, and up to four gaussians are employed in the construction of the unsupervised learning model. Examples are shown in figure 3.

Figure 3: Aneurysms generated with unsupervised learning.

References

1. Arzani et al., Phys Fluids, 24, 2012.
2. Caradu et al, J Vasc Surg, 74(1):246-256, 2021.
3. Updegrove et al, Ann. Biomed Eng, 45(3):525-541, 2016.
4. Shum et al, Ann. Biomed Eng 39.1 (2011): 277-286.
5. Cosentino et al Journal of personalized medicine 10.2 (2020): 28.
6. Shalev-Shwartz et al, *Understanding machine learning: From theory to algorithms*. Cambridge university press, 2014

HOW OXYGEN AND GLUCOSE INFLUENCE CELL GROWTH: A COMPUTATIONAL SIMULATION STUDY

Maria Inês Barbosa (1), Jorge Belinha (2), Renato Natal Jorge (3), Ana Xavier (4)

1. Institute of Mechanical Engineering and Industrial Management (INEGI), Portugal; 2. School of Engineering Polytechnic of Porto, Portugal; 3. Faculty of Engineering, University of Porto, Portugal; 4. Institute for Research and Innovation in Health (I3S), Portugal

Introduction

The process of cell proliferation is essential to maintain a balance between cell generation and cell death. This process is characterized by its complexity and leads to the growth and division of cells [1, 2]. Under some circumstances, abnormal proliferation can occur, for example, when tumour cells appear, and then, several tissues can be compromised [3]. Both healthy and tumour cell proliferation are dependent on, for example, oxygen, glucose, or growth factors and, if their supply is affected, the process can be compromised [4, 5].

To study biological phenomena like cell proliferation, it is possible to use several different computational models. With these, various hypotheses can be explored faster [6].

The objective of the present work is to analyze the influence of oxygen and glucose in the process of proliferation of a healthy and a tumorous cell. Thus, a previously created algorithm, combining the Radial Point Interpolation Method (RPIM) with a new phenomenological cell growth law, was used. Moreover, different normal and abnormal ranges of oxygen and glucose concentration were assumed.

Methods

The algorithm proposed in this work uses specific input data and the new cell growth law to establish and initiate the process of cell growth. This growth continues until the cell doubles its initial volume if the concentration of oxygen and glucose are adequate and then, the growth stops and the cell divides into two new cells. If not, the cell does not grow and might initiate the process of apoptosis and die. This algorithm is solved by the RPIM. The main steps of this method are the definition of the geometry of the problem, the solid domain, its limits, and of its boundary conditions, the discretization of the domain using a nodal set, the imposition of the nodal connectivity by overlapping influence-domains, and the creation of shape functions through the combination of radial basis and polynomial basis functions [7].

Results

Twenty-five different curves representing the growth of the cells, in terms of volume, were obtained both for healthy and tumor cell, by combining the different defined states of oxygen (extreme hyperoxia, hyperoxia, normal oxygen concentration, hypoxia and extreme hypoxia) and glucose concentration (extreme hyperglycemia, hyperglycemia, normal glucose concentration, hypoglycemia and extreme hypoglycemia for glucose). Thus, normal, abnormal and extreme concentrations of glucose and oxygen were considered in order to study their influence in the two types of cells. For both cells, their growth occurs in almost all cases, with different velocity rates, with the extreme states of concentrations being the exceptions. In these last cases, the cells started the process of apoptosis.

Discussion

Under normal concentrations of oxygen and glucose, the healthy cell grew in 24 h and the tumor cell in 18 h, which correspond to the normal duration for a human cell cycle. When these concentrations are increased or decreased, the time of growth is affected, tending to be slower in all cases, mainly under hyperoxia, hypoxia, and hypoglycemia. In extreme states, the apoptosis process is initiated, as expected, since cells tend to protect themselves from the aggressiveness of the medium and die to avoid mutations.

The main difference between healthy and tumor cells is the time of the process of proliferation and the effect of hyperglycemia. In tumor cells, this process is faster and, in healthy cells, hyperglycemia slows their proliferation.

References

1. Sandal, T., Molecular aspects of the mammalian cell cycle and cancer. The oncologist, 2002. 7(1): p. 73-81.
2. Tortora, G.J. and B.H. Derrickson, Introduction to the human body. 2017: John Wiley & Sons, Incorporated.
3. Ruddon, R.W., Cancer biology. 2007: Oxford University Press.
4. Casciari, J.J., S.V. Sotirchos, and R.M. Sutherland, Variations in tumor cell growth rates and metabolism with oxygen concentration, glucose concentration, and extracellular pH. Journal of cellular physiology, 1992. 151(2): p. 386-394.
5. Cristini, V. and J. Lowengrub, Multiscale modeling of cancer: an integrated experimental and mathematical modeling approach. 2010: Cambridge University Press.
6. Alfieri, R., et al., Modeling the cell cycle: From deterministic models to hybrid systems. Biosystems, 2011. 105(1): p. 34-40.
7. Belinha, J. (2014). Meshless Methods in Biomechanics. Lecture Notes in Computational Vision and Biomechanics (1. ed.), Springer.

Acknowledgements

A TWO-PHASE GENETIC ALGORITHM TO MODEL THE MENISCAL HORN REPAIRED WITH SUTURE

Estebanez B. (1), Peña-Trabalón A. (1), Moreno-Vegas S. (1), Espejo-Reina A. (1, 2), Nadal F. (1), García-Vacas F. (1), Perez-Blanca A. (1), Prado-Novoa M. (1)

1. *Clinical Biomechanics Laboratory of Andalusia, University of Malaga, Spain*
2. *Vithas Malaga Hospital, Spain*

Introduction

Menisci suturing is a common surgical technique nowadays. Menisci have been modeled with different degrees of complexity in finite element models (FEM) of the human knee [1], but there are few works focused on simulating the meniscus subjected to traction loads in its longitudinal direction [2], such as those produced by sutures after repair. Moreover, there are no models that include the effect of the orifice for the suture. This study develops a material model of the meniscal horn when it is pulled by the thread used to reattach its root.

Methods

For the experimental data, the anterior horn of a human medial meniscus pierced by a Nº2 suture was used. Its surface was marked with 4 ink dots, 2 at the thread insertion and 2 far from this area. A displacement-controlled load-to-failure test was performed on a uniaxial testing bench, as shown in Figure 1a, with the traction load aligned with the meniscal fibers and with the suture. The displacements of the dots were recorded by a videogrammetric system synchronized with the machine load cell, which computed the distances between the ink marks as a function of the traction force until the beginning of the tissue cut-out.
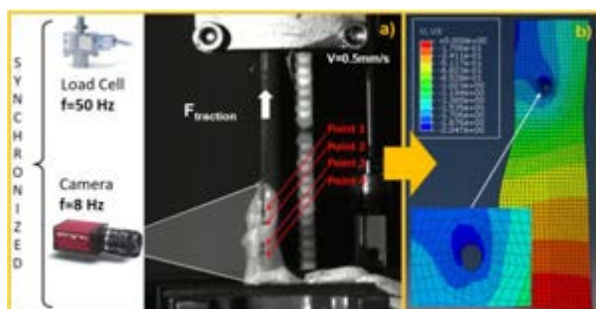
Figure 1: Specimen on the testing bench and its model.

A FEM of the meniscal horn reproducing the boundary and load conditions of the test was developed in Abaqus (Figure 1b). Hyperelastic incompressible Mooney-Rivlin models of 2 and 3 parameters [3] were used for the tissue. To identify the model parameters, a two-phase genetic algorithm was developed. In the first phase, the engineering stress (σ) was computed as a function of the experimental strain ratio (λ) assuming homogenous isotropic material, thus disregarding the orifice, and uniaxial traction [3]:

$$\sigma^{theo} = 2C_{10}(\lambda - \lambda^{-1}) + 2C_{01}(1 - \lambda^{-3}) + 6C_{11}(\lambda^2 - \lambda - 1 + \lambda^{-2} + \lambda^{-3} - \lambda^{-4}) \quad (1)$$

While the experimental stress was estimated as:

$$\sigma^{exp} = F/A \quad (2)$$

F being the measure traction force and A the initial meniscal cross-section at the suture point. The parameter set, $\{C_{10}, C_{01}\}$ for the 2-parameter model or $\{C_{10}, C_{01}, C_{11}\}$ for the 3-parameter model, were found minimizing the RMS between σ^{theo} and σ^{exp} searching in a wide domain ($\pm 10^6$ MPa for all parameters). In the second phase, the model parameters were recomputed by minimizing the RMS between λ^{exp}, the strain ratio experimentally measured in the orifice area, and λ^{theo}, the value simulated for the same points by the FEM of the meniscus. For this phase, with a much higher computational cost, the parameters of the first phase acted as seeds narrowing the search domain around them (first phase results ± 5 MPa for all parameters).

Results and Discussion

The model parameters found by each phase of the material optimization algorithm are shown in Table 1 for the 2- and 3- parameter Mooney-Rivlin models, respectively. The computational time and RMS in the orifice area achieved by each phase are also detailed. The 3-parameter model was more suitable to simulate the strain near the meniscal orifice. However, the RMS for the marks far from the orifice was greater than 0.01, suggesting that a different material model is needed for each tissue area. Not including the first optimization phase was checked with a relatively small initial domain (± 500MPa for all parameters), but after 12 hours the RMS still made it unfeasible.

Phase	C_{01}	C_{10}	C_{11}	RMS	Time
Mooney-Rivlin model of 2 parameters					
1	1.8450	-0.9801	-	0.00016	1.0s
2	0.6131	-0.0948	-	0.0204	4.8h
Mooney-Rivlin model of 3 parameters					
1	1.7468	-0.8775	0.0892	0.00018	0.8s
2	2.2866	-18706	1.3968	0.00012	6.8h

Table 1: Material optimization results.

References

1. Seyfi B. et al, J Mech B of Biomed Mat, 77: 337-346, 2018.
2. Abraham A. C. et al, J Biomech, 44:413-418, 2011.
3. Kumar N. et al, MIT Int J of Mech Eng, 6:43-46, 2016.

BIORESORBABLE LATTICE STRUCTURES FOR TIME-DEPENDENT STIFFNESS IN FRACTURE FIXATION DEVICES

Barnaby Hawthorn (1), Andrew Triantaphyllou (2), Farhan Khan (2), Rosemary Dyson (3), Lauren E. J. Thomas-Seale (1)

1. School of Engineering, University of Birmingham, UK; 2. The Manufacturing Technology Centre Ltd, UK; 3. School of Mathematics, University of Birmingham, UK

Introduction

Designing for variable stiffness within fracture fixation implants could be the key to providing the next generation of fracture healing. It is well established that modern fracture fixation devices can suffer from being over-stiff, which inhibits the bone healing process [1]. Small amounts of motion at fracture site stimulates callus formation, leading to quicker healing, stronger bone formation, increased bone density and stiffness [2]. Implementing time-dependent stiffness to biomedical implants to better suit the requirements of bone-healing could offer enhanced healing rates.

Finite element analysis (FEA) on full lattice structures is very computationally expensive [3]. To predict the mechanical performance of an implant incorporating a bioresorbable lattice region such as the concept shown in Figure 1, at multiple points in time during the healing process, would be beyond the capability of industrial computation. In this study, homogenisation is investigated as a method of simplifying the model.

Methods

Homogenisation numerically calculates macroscopic mechanical properties from a meso-scale geometry input by applying predefined amounts of strain to a representative volume element and extracting resultant stresses. In this work a body centred cubic (BCC) lattice structure is investigated using Ti6Al4V material properties so that workflow can be experimentally validate in future work. A $5\times5\times5$ mm^3 BCC unit cell with 1 mm strut diameter is designed within ABAQUS and meshed with C3D8R elements. EasyPBC [4] and Micromechanics plugins are used for homogenisation, then homogenised mechanical properties are outputted and used to create an equivalent macroscopic material. A $25\times25\times25$ mm^3 lattice model and a solid model of same dimensions with homogenised material properties are tested in compression (Figure 2).

Results

Number of elements reduced by 80% in homogenised test model, reducing computational cost. Homogenised model performs within 7% of the lattice (Figure 3).
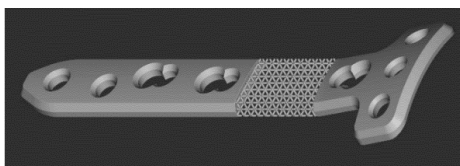
Figure 1 – Concept implant design, incorporating lattice structure to TomoFix^{TM} [5] implant
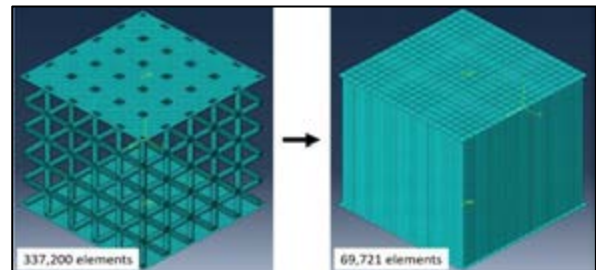
Figure 2: Comparison of mesh and element number for full lattice and homogenised model
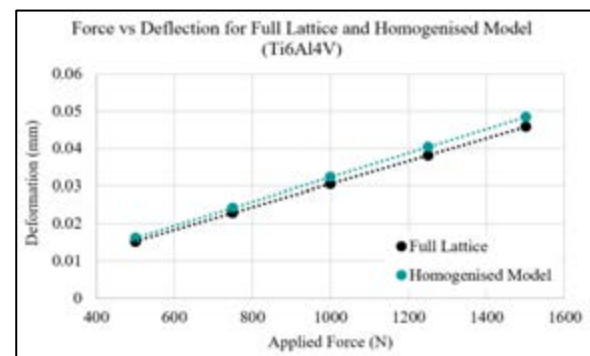
Figure 3: Comparison of deflection in FEA compression tests for full lattice and homogenised model

Discussion

Lattice structures in conjunction with bioresorbable materials, such as zinc-magnesium alloys, could be used in fracture fixation devices to enable tailored and predictable variation in stiffness over time. To achieve this it is crucial to model the implant at different time points throughout the healing process, varying the implant and lattice geometry as a function of the degradation rate of the resorbable material. As the implant - namely the lattice structure - resorbs, its stiffness will reduce and therefore allow increased amounts of micromotion. Homogenisation successfully reduces the computational cost of this problem.

References

1. Röderer et al., Injury, 45:1647-1652, 2014
2. Goodship et al., J Bone Joint Surg Br, 67:650-655, 1985
3. Alwattar et al, J. Compos. Sci., 3:33, 2019.
4. Omairey et al., Eng Comput, 35:567–577, 2019
5. DePuy Synthes., TomoFix^{TM} Application Notes, 2015

Acknowledgements

THE INFLUENCE OF CROSS-LINKING ON THE MECHANICAL PROPERTIES OF COLLAGEN: A BOTTOM-UP APPROACH

Julia Kamml (1), Chun-Yu Ke (1, 2), David Kammer (1)

1. ETH Zurich, IfB, Computational Mechanics of Building Materials, Switzerland; 2. Pennsylvania State University, Department of Engineering Science and Mechanics, University Park, PA, USA

Introduction

Collagen fibrils are the main building constituent of many human tissues, e.g. tendon, bone, skin and the cornea. Their specific building pattern with cross-links connecting collagen molecules to a fibril provides them with unique mechanical properties: high elasticity, large strength and a substantial energy dissipation during deformation. It has been observed that aging and the augmented glycation level in diabetic patients triggers an increased formation of non-enzymatic cross-links, so-called Advanced-Glycation-Endproducts (AGEs) between tropocollagen molecules in bone, but also in soft tissues with a long half-life of collagen. The increased occurrence of AGEs correlates with an increased fracture risk in diabetic bone and deterioration of mechanical properties in tissues. Since the shearing of collagen is responsible for plasticity and toughness, any restriction of this might make the material more brittle. However, it is unknown how AGE accumulation affects collagen sliding mechanisms and damage. We study the mechanisms leading to inferior material properties in diabetic patients, e.g. brittleness, reduced strength and toughness, using a computational bottom-up approach. On the nano-scale level, we are able to investigate the influence of different parameters like cross-link type (enzymatic and non-enzymatic), cross-link density, cross-link mechanical properties, cross-link distribution, collagen molecule stiffness, fibril diameter etc., using a coarse-grained molecular dynamics model of a representative part of the collagen fibril. In this way, we can provide a comprehensive study of collagen fibrils and their mechanical behavior influenced by various factors.

Methods

We implemented a computational 3D model of a collagen fibril segment presenting five gap and overlap zones, the typical basic building unit of collagen fibrils. Velocity controlled tensile tests were performed until fracture and beyond, using steered molecular dynamics. Tropocollagen molecules are represented by particles arranged in a chain of "beads" and interacting according to multi-body potentials. This procedure is commonly referred to as coarse-grained modelling. The mechanical interactions between the particles are obtained from literature [2] [3] [4] and full-scale molecular dynamics simulations using a reactive force field and performing tensile tests on AGEs cross-links (glucosepane and pentosidine) until fracture. Parameters obtained from glucosepane modelling were used as representative parameters for AGEs cross-links, since its levels of

occurrence have been found to be up to 1000 times higher than of any other non-enzymatic cross-link [5]. Enzymatic cross links were inserted at the respective ends of the tropocollagen molecules, whereas AGEs crosslinks are randomly distributed along their helical backbones. This approach allows to reach length scales of several hundred nanometers and time scales of microseconds, where tensile tests are performed with a constant velocity of 10m/s with a time step of $\Delta t = 10$fs.

Results
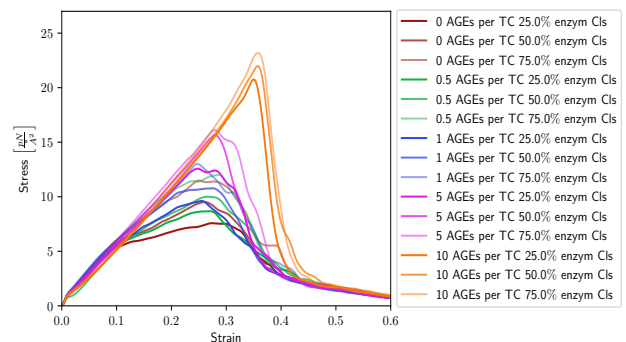
Figure 1: Stress versus strain of a collagen fibril: We vary the densities of enzymatic and AGEs cross-links. An increase in cross-link density leads to increased yield stresses and strains, as well as fracture stresses and strains. We also see that an increased number of cross-links leads to a more brittle fracture behavior. Further, with higher AGEs cross-link content, enzymatic cross-links have less influence on the increase of fracture stresses. For larger cross-link densities, a second regime (steeper curve) is activated.

Discussion

Our model is in good agreement with other data from the literature, but does not show the specific three phase behavior as observed in previous in-vitro studies [6]. Therefore, we will further implement the "hairpin" telopeptide-end as observed by Uzel et al. [7], which has been hypothesized to cause an additional "plateau" phase. We believe we can provide a comprehensive insight into collagen mechanics by investigating the influence of different parameters.

References

1. Depalle et al, J Mech Behav Biomed Mater, 52:1-13, 2015
2. Buehler et al, J Mater Res, 21: 1947-1961, 2006
3. Buehler et al, PNAS USA, 103: 12285-12290, 2006
4. Sell et al, J Bio Chem, 208: 12310-12315, 2005
5. Svensson et al, Acta Biomater, 70: 270-280, 2018
6. Uzel et al, J Mech Behav Biomed Mater, 4: 153-161, 2011

NUMERICAL MODELLING OF A POLYMERIC ANEURYSM IN SUPPORT FOR DIMENSIONNING A MECHANICAL CHARACTERISATION DEVICE

Jolan Raviol (1), Guillaume Plet (1), Hélène Magoariec (1), Cyril Pailler-Mattei (1,2)

1. Laboratoire de Tribologie et Dynamique des Systèmes, CNRS UMR 5513, Université de Lyon, École Centrale de Lyon, France.

2. Université de Lyon, Université Claude Bernard Lyon 1, ISPB-Faculté de Pharmacie, Lyon, France.

Introduction

Intracranial aneurysms (ICA) are a structural and residual deformation of the arterial wall. The estimated prevalence of unruptured ICA is 2-5 % in the world population [1]. ICA rupture leading to subarachnoid haemorrhage has a fatality rate of 30-40 % [2]. None method currently exists to accurately predict the rupture risk. The aim of the MECANEV project is to quantify the *in vivo* mechanical behavior of unruptured ICA and provide a decision support tool to clinicians. This project encompasses the design of an experimental arterial wall deformation device and of a numerical tool to quantify the wall stress state by inverse analysis.

This device is a guidance flux system that has been calibrated on an experimental bench with a polymeric phantom artery. We present in this study the associated numerical model and its use to estimate the best ratio thickness/stiffness wall linked to the issues of 3D printing or molding process in designing both thin and soft materials and evaluate the distance device/aneurysm wall effect.

Materials and Methods

The numerical model developed on COMSOL Multiphysics included solid mechanics elements considered as isotropic elastic linear materials: the artificial phantom artery (reconstructed 3D geometry) and the deformation device (PTFE). 2 parameters were studied: the thicknesses of the aneurysm wall and of the artery wall (600,1500 μm for the artery and 400 μm for the aneurysm,) with Young's modulus between 0.2-3 MPa. Several impact locations and several distances of the device to the wall (1-5 mm) were considered.

The model included 2 laminar flows: one for the static artery outer environment, and one for the miscible artery flow and device pulsed flow (water for both flows for calibration purposes). The associated flow rates were 500 mL/min and 150 mL/min respectively. The fluid-structure interaction (FSI) between the aneurysm arterial wall and the artery/device flow was computed using the arbitrary Lagrangian-Eulerian technique (ALE) and considering the loading of the fluid on the surface [3].

Results and Discussion

The center of the impact location on the aneurysm wall was considered, the displacement and the strain tensor norms for the couples 600-400, 1500-400 μm were compared for all the Young's modulus between 0.2-3 MPa. For the same aneurysm area wall thickness and a same Young modulus, the displacement norm was not comparable unlike the strain tensor norms differences which were between 2 % and 3 %. It has been observed for all the Young's modulus (figure 1).
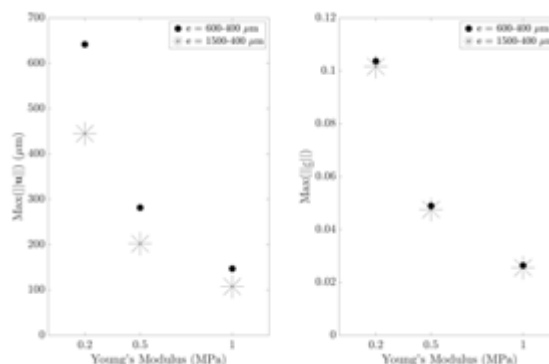
Figure 1: Strain tensor and displacement norms in the center of impact location on aneurysm wall for 600-400 µm and 1500-400 µm and E between 0.2 and 1 MPa.

It was possible to quantify the device position influence on the displacement and strain norms. As it was difficult to target a specific position in the experimental bench, a range of value regarding the position was valuable.

Conclusion

The developed numerical model was useful for the calibration phase of the device with support in (1) designing the phantom artery: for a strain study, it is important to target the appropriate aneurysm thickness but we have flexibility in other part of the artery and (2) quantifying the uncertainties of the experimental bench to help the further numerical/experimental comparisons.

References

1. Rinkel GJ, Djibuti M, Algra A, Van Gijn J. Prevalence and risk of rupture of intracranial aneurysm: a systematic review. Stroke, 1998; 29:251-6.
2. Van Gijn J, Kerr RS, Rinkel GJ. Subarachnoid haemorrhage. Lancet 2007; 369:306-318.
3. COMSOL, Models sme Fluid-structure interaction in a network of blood vessels.

Acknowledgements

SPINADOID AND DUAL-LATTICE BASED ALGORITHMS FOR GENERATING BIOMIMETIC TRABECULAR BONE STRUCTURES

Mahtab Vafaeefar (1), Kevin M. Moerman (1), Ted J. Vaughan (1)

1. Biomechanics Research Center (BioMEC), School of Engineering, College of Science and Engineering, National University of Ireland, Galway, Ireland

Introduction

Trabecular bone microarchitecture is optimized for load-bearing capacity [1]. Computational modeling has been used extensively to investigate relationships between trabecular bone mechanics and its micro-architectural features. Among these models, a range of idealized units cell geometries, such as open-cell foam [2] or hexagonal columnar structure [3] have been proposed. While these idealized structures may adequately represent certain features of bone micro-architecture, they fail to capture more intricate morphological features. To produce biomimetic scaffolds of trabecular bone, this study proposes two separate mathematical algorithms producing computational models of trabecular bone based on spinodoid and dual-lattice based approaches.

Methods

The two algorithms were developed and implemented within the MATLAB-based Gibbon toolbox [4]; (i) a spinodoid [5] stochastic microstructure was derived from the phase-separation process using Gaussian random field; (ii) a dual-lattice structure was built on Delaunay triangulation of tetrahedron elements and thickening struts with desired thickness. As a comparison, the well-known gyroid-based structure was also included in the analysis, which was built using periodic unit-cells to create iso-surfaces boundaries for the solid/void sections. Sensitivity analysis was performed to determine the representative volume element (RVE) size. Using image processing tools [6], morphometric and topological indices were evaluated, quantitatively describing structures, and compared to porcine bone, as the reference structures (Figure 1). Finally, finite element analysis on the optimized structures as well as bone samples was applied, and their mechanical responses were analysed.

Results

Comparison of studied morphometric and topological parameters, as well as elastic mechanical behaviour, is shown in Table 1. It was found that bone volume fraction (BV/TV), trabecular thickness (Tb.Th), trabecular separation (Tb.Sp), and degree of anisotropy (DA) are reproduced close to the reference values. Despite this, the predicted mechanical properties along the primary loading direction (E_{33}) of the gyroid and spinodoid are lower than the reference bone. This arises from differences in other parameters, whereby higher connectivity density (Conn.D.) and ellipsoid factors (EF), and lower SMI values were found in the

computational models. It was found that both the gyroid and dual-lattice performed better than the spinodoid in reproducing mechanical behavior besides morphomtric indices.
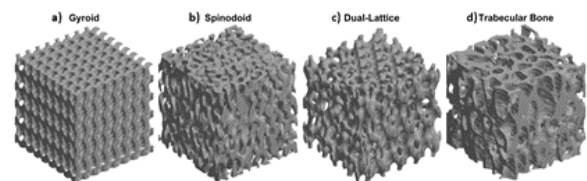
Figure 1: Computationally generated structures, a) gyroid, b) spinodoid, c) dual-lattice and a d) realistic trabecular bone sample.

Parameter	Bone Sample (n=19)		Gyroid	Spinodoid (n=5)		Dual-Lattice
	Mean	Std. dev.	Mean	Mean	Std. dev.	Mean
BV/TV	0.36	0.04	0.37	0.37	0.002	0.38
BS/BV (mm^{-1})	19.83	2.15	24.06	25.86	0.130	22.03
Tb.Th (mm)	0.16	0.02	0.17	0.16	0.003	0.17
Tb.Sp (mm)	0.39	0.05	0.24	0.21	0.001	0.29
DA	0.60	0.08	0.51	0.64	0.007	0.62
Conn.D. (mm^{-3})	16.55	4.50	47.44	37.70	0.453	47.74
SMI	0.10	0.27	1.43	1.77	0.022	1.32
EF	-0.17	0.02	-0.06	-0.04	0.006	-0.02
E11	599.41	246.61	527.79	172.39	19.50	485.61
E22	740.06	182.46	526.23	204.50	22.90	465.33
E33	1187.86	222.31	886.55	713.51	19.94	1312.69

Table 1: Realistic bone, in comparison with the computationally generated structures.

Discussion

This work presents two new efficient computational techniques for producing trabecular bone-like structures using spinodoid and dual-lattice based algorithms. Both approaches algorithms are highly versatile and can capture many of the morphometric and topological parameters of trabecular bone tissue, as well as simulate their anisotropic elastic behaviour. These techniques have potential applications for as candidate biomimetic scaffolds for bone tissue engineering and to further our understanding of trabecular bone biomechanics.

References

1. Basaruddin, K. S. et al, Medical and Biological Engineering and Computing, 50: 1091–1103, 2012.
2. Gibson, L. J., J. Biomech, 38:377–399, 2005.
3. Kim, H. S. et al, J. Biomech, 35:1101–1114, 2002.
4. Moerman, M. K., Journal of Open Source Software, 3:506, 2018.
5. Kumar, S. et al, npj Computational Materials, 6:1–10, 2020.
6. Doube, M. et al, Bone, 47:1076–1079, 2010.

CFD SIMULATION OF THA FOR DIFFERENT FEMUR POSITIONS INCLUDING MICROMOTION BETWEEN BONE AND IMPLANT

Ales Hrouda (1), Maarten Vanierschot (1), Lukas Capek (2,3), Michiel Mulier (4), Kathleen Denis (1)

1. KU Leuven, Department of Mechanical Engineering, Belgium; 2. TU Liberec, Faculty of Textile Engineering, Czechia; 3. Regional hospital of Liberec, Department of Clinical Biomechanics, Czechia; 4. KU Leuven, Locomotor and Neurological Disorders, Belgium

Introduction

Total hip arthroplasty (THA) is one of the most common surgeries that is done worldwide with an increasing trend. [1] Although it is a successful surgery in some cases it still requires a revision surgery mostly due to bone resorption caused by wear particles. [1] There are three hypotheses about the wear particle transportation into the bone i.e., high pressure theory, implant micromotion and the Brownian motion. [2-4] The intracapsular pressure for different activities was measured e.g., during walking, standing, climbing stairs [5] Alidousti et al. [6] performed a simulation including femur and implant with a micromotion definition and the study showed that the micromotion and high pressure affect the transport of the wear particles.

The aim of this study is to show the influence of the hip joint position on the velocity flow field. Firstly, steady-state simulations for three different femur-pelvis positions (FPP) were performed. Secondly, the position that showed the worst flow field conditions (highest velocity) was taken into a time-dependent simulation that included micromotion definition between implant and bone.

Methods

A 3D geometry of a hip joint was imported in the Space Claim software (ANSYS Inc., USA). Next, the implant (MATHYS Twinsys size 12, MATHYS Medical, Switzerland) with a femoral head diameter of 32 mm and the acetabular cup with a diameter of 60 mm was imported into the assembly and positioned in line with the positioning of implants using X-ray images. Finally, a 2D model of a THA was created by a plane cut, this geometry was transferred into the meshing software Pointwise V18 (Pointwise Inc., USA).

The computational mesh was imported into the Ansys Fluent software (Ansys Inc., USA) and the flow field was obtained by solving the Navier-Stokes equations. During stair climbing the capsular pressure reaches up to 60 kPa [5], this value was assigned to the pressure inlets. The bones were defined as a porous zone with a permeability of 10^{-14} m^2.[6] The gap interface between the implant and femur was set at 35 µm [7] and between the acetabulum and the femoral head was set at 95 µm [8]. The mesh convergence study was done according to Roache [9], by discretization of the maximal velocity in gap and interface locations.

Three different FPP were defined neutral position (N) and 20° ab/adduction (AB/AD), although the hip is capable of greater motion [10]. The position showing the worst scenario was further analysed by adding periodical micromotion between the bone and implant. The micromotion was defined as rotational with a centre of rotation in the centre of the femoral head.

Results

The final computational mesh consisted of 460k elements and the computational time for the steady-state simulation was 2910 seconds on single CPU of 2.3 GHz. The pressure drop is noticeable in the bone areas, it is due to the bone definition as a porous zone (see Figure 1a). The micromotion behaves as a pump. Figure 1b shows the effect of implant position if closer to the gap-femur interface the pressure locally increases.
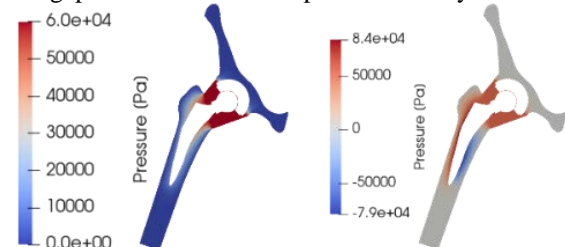
Figure 1 Pressure field a) Steady-state b) Micromotion flow time of 0.14 seconds

The greatest maximal velocity was reached for the abduction (see Table 1) at the gap entrance at the upper part of the acetabulum .

Position	AB	N	AD
Velocity*10^{-10} [m/s]	7.02	0.88	4.87

Table 1 Highest velocity value for different positions in the gap area between the acetabulum and femoral head

Discussion

Three different FPP were simulated. It has been shown that the greatest influence is in the femoral head area where the velocity increases. For the worst scenario of the flow field the micromotion was applied and the effect on the flow field was studied. Also it has been shown that micromotion affects the flow field inside the THA. This study can be further used as a better understanding of the effect of micromotion on the particle trajectories and the bone penetration.

References

1. Kurz et al, Jbjs, 65:575-584, 2007.
2. Aspenberg P. et al., AOS, 69: 1-4, 1998.
3. De Man F et al., JBJS,87:1522-1533, 2005.
4. Bauer W. et al, Skeletal radiology,28: 423-432.
5. Robertsson O et al, AOS, 68:231-234, 1997.
6. Alidousti H. et al., Jbe, 133:121001-1--10, 2011.
7. Erivan R. et al., IO, 44:45-51, 2020.
8. Lundberg J. et al., Jb, 40: 1676-1685, 2007.
9. Roache J.P., JFE, 116:405-413,1994.
10. Weinhandl J. et al., JB, 43:2633-2633.

Acknowledgement

FLUID-STRUCTURE INTERACTION ANALYSIS OF DESCENDING AORTA AFTER VSRR SURGERY: THE EFFECTS OF GRAFT STIFFNESS

Guido Nannini [1], Maria C. Palumbo [1], Simone Saitta [1], Alessandro Caimi [1], Jay D. Humphrey [2], Yadong Wang [3], Leonard N. Girardi [4], Mario Gaudino [4], Jonathan W. Weinsaft [4], Emiliano Votta [1,5], Alberto Redaelli [1]

1. Politecnico di Milano, Italy; 2. Yale School of Engineering and Applied Science, New Haven,CT, USA; 3. Cornell University, Ithaca, USA; 4. Weill Cornell College, New York, USA; 5. IRCCS, P.S.Donato, Italy

Introduction

Thoracic aortic aneurysm (TAA) can be a lethal cardiovascular disease, often consisting of a focal dilatation of the ascending aorta due to structural alteration of the wall. Surgical valve-sparing root replacement (VSRR) is a definitive therapy for TAA treatment, but the risk of post-surgical complications persists in the non-grafted area. The mechanisms leading to such events remain uncertain; it has been speculated that these problems stem from the compliance mismatch between the grafted region and the natural aorta, as grafts are significantly stiffer than native tissue [1]. To test this hypothesis, we quantified the hemodynamics in the descending aorta (DAo) after VSRR with differentially stiff grafts by means of an image-based, patient-specific fluid-structure interaction (FSI) model [2].

Methods

Pre- and postoperative magnetic resonance imaging (MRI) (3TGE SIGNA™) was segmented to reconstruct the aortic lumen, which was complemented by a 2 mm thick aortic wall. Two pre-op model variants were generated, characterized by an elastic modulus of the dilated ascending aorta of 1 or 5 MPa, respectively. Four post-op variants were generated, characterized by a graft elastic modulus ranging from 1 MPa (i.e., physiological aortic stiffness) to 12 MPa (i.e., the typical stiffness of an implanted graft). For each model variant, based on time-resolved phase contrast magnetic resonance imaging (4D flow), we defined a three-dimensional inlet velocity profile and tuned the three-element Windkessel models coupled to the model at the outlets [2]; intramural wall stress (IS) and the wall shear stress (WSS) were quantified in the DAo. FSI simulations were run in ANSYS 21.1 (ANSYS Inc, USA).

Results

FSI results in the DAo were verified against 4D flow data, finding a good matching ($p>0.05$) between velocity patterns. As compared to the post-op model with a hypothetical graft material with a pseudo-physiological elastic modulus (E=1 MPa), the models with graft material elastic modulus equal to 5.25 and 9 MPa showed no statistically meaningful difference in WSS in the DAo; when the graft material elastic modulus was set to the realistic value of 12 MPa, evident and statistically significant increments in DAo WSS were observed (*Figure.2*). IS was significantly higher vs. pre-op conditions for each tested graft stiffness.
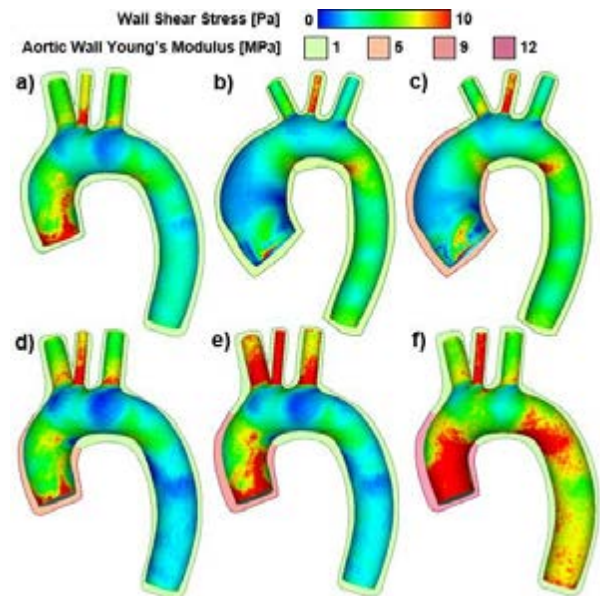
Figure.1. WSS map at systolic peak of: physiological aorta (a); pathological aorta with homogenous E=1 MPa (b) and stiffer aneurysm region E=5 MPa (c); post-VRSS aorta reconstructed with a graft with E equal to 5.25 MPa (d), 9 MPa (e), 12 MPa (f).
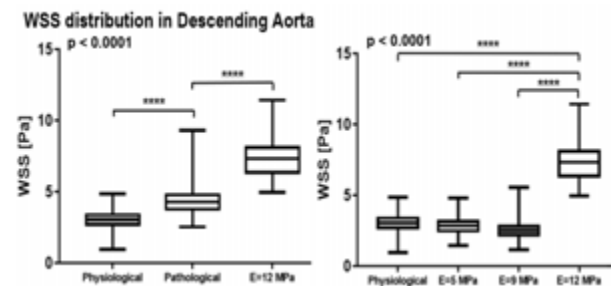
Figure 2. ANOVA of WSS distribution in DAo in cases (a), (c), (f) on the left and (a), (d), (e), (f) on the right.

Discussion

WSS and IS are potentially crucial parameters in the adverse remodeling mechanism [3]. Our results indicate that WSS and IS increase in DAo from physiological to pathological and post-grafting conditions. In the latter case, the stiffness of currently available grafts leads to increased WSS in the DAo; this effect may be mitigated by producing more deformable graft materials.

References

1. Palumbo et al., *PLoS One*, 2020
2. Nannini et al., *Comut. Biol. Med.*, 2021
3. Humphrey, *Hypertension* AHA, 2008

TESTING SIMULATED CARTILAGE BIOMECHANICS TO PREDICT KNEE OSTEOARTHRITIS: DATA FROM THE OSTEOARTHRITIS INITIATIVE

Alexander Paz (1,2), Rami K. Korhonen (1), José J. García (2), Mika E. Mononen (1)

1. Department of Applied Physics, University of Eastern Finland, Finland; 2. Escuela de Ingeniería Civil y Geomática, Universidad del Valle, Colombia

Introduction

Understanding the mechanisms behind the initiation and progression of knee osteoarthritis (OA) would elucidate effective preventive treatments for this disease. In vitro and in silico research have studied how substantial mechanical stimuli yield cartilage damage, establishing relationships between the stimulus magnitude and tissue response (strains, stresses) [1,2]. For clinical purposes, the simulated response needs to correlate with common clinical measurements used to identify OA, like the Kellgren-Lawrence (KL) grading system. Via finite element (FE) modeling, Mononen et al. [3] found that the volume of simulated overstressed cartilage tissue correlates with the KL grade of the knee, i.e., the larger the volume, the higher the KL grade. Although, more subjects are needed to increase the reliability of the approach, and the authors focused on tissue tensile stresses to define weakening in cartilage collagen fibrils. Thus, in this study, we implemented the approach developed by Mononen et al. with numerous knees. We also tested the hypothesis that strain-based volumes correlate with KL grades since previous studies have defined strain-based damage mechanisms for the cartilage non-fibrillar matrix [1].

Methods

We utilized a FE template-based approach [3] implemented in FEBio to simulate the biomechanics of knee articular cartilage in the medial compartment of 248 knees under a simplified gait loading condition (Figure 1). All knees were healthy at baseline and with KL grades at 8-years of follow-up: KL0 N = 131, KL1 N = 30, KL2 N = 56, KL 3 and 4 N = 31. FE models used the information of 126 subjects from the Osteoarthritis Initiative database and fibril-reinforced biphasic formulations for cartilage. We considered bones, ligaments, and menisci in the models through boundary conditions. We correlated knee KL grades with tissue volumes that overpassed thresholds for the maximum principal solid stress, defined in an age-dependent function in [3], the maximum shear and deviatoric strains, in the range of 5%-30%, as well as a combination of both. We used Kruskal-Wallis and Dunn tests to evaluate the differences between volumes of KL groups and ROC curves and AUC values to quantify the classification capabilities of the approach.
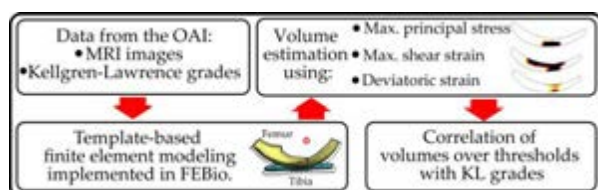
Figure 1: Workflow of the present study.

Results

Using the 248 knees and the maximum principal solid stress criterion, we observed statistically significant differences in volumes (p<0.05) between severely affected (KL3,4) and healthy knees (KL0). Furthermore, when we restricted the analysis to subjects younger than 70 years, and weight loss below 10 kg during the 8-year follow-up (KL0 N = 88, KL1 N = 15, KL2 N = 36, KL3,4 N = 15), we observed significant differences and acceptable classification powers between KL3,4 and KL0 groups (AUC = 0.72) and KL3,4 and KL1 groups (AUC = 0.77) (Figure 2).
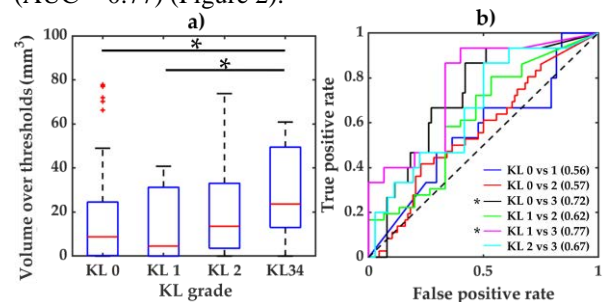
*Figure 2: Results from the best classification approach (using the maximum principal solid stress). a) predicted volumes according to the KL grade. b) ROC curves and AUC values. *p<0.05.*

On the other hand, results (not shown) suggested that none of the other approaches, using strain thresholds or stress/strain threshold combinations, overperformed the classification capabilities of using the maximum principal solid stress.

Discussion

The stress-based approach, which suggests volumes for possible damage of collagen fibrils, showed promising classification capabilities for further development.

We only concentrated on the instantaneous response of a fibril-reinforced biphasic model of articular cartilage, further creep analyses under different loading conditions may result in larger effects of strains. The strain-based predictions explored in this study did not include an age-dependent criterion, which has not yet been proposed and may influence current conclusions.

References

1. Hosseini S. M. et al., Osteoarthr. Cartil., 22:95-103, 2014.
2. Zevenbergen L. et al., Osteoarthr. Cartil., 26:1710-1721, 2018.
3. Mononen M. et al., Ann Biomed Eng, 47:813-825, 2018.

Acknowledgments

IMPLEMENTATION OF SMOOTHED SURFACE, SLIDING CONTACT IN THE VOXEL BASED FINITE ELEMENT SOLVER PAROSOL

Frederik Trommer (1,2), Pinaki Bhattacharya (1,2)

1. Insigneo Institute for in silico Medicine, University of Sheffield, UK
2. Department of Mechanical Engineering, University of Sheffield, UK

Introduction

Micro finite element analysis (uFE) is a validated tool for non-invasively quantifying bone mechanics using high resolution computed tomography (CT) images. uFE solvers for Cartesian mesh (or voxel) models, such as ParOSol [1], can efficiently solve problems with billions of degrees of freedom. As yet, ParOSol avoids unrealistic stress-concentrations due to the jagged Cartesian mesh surface by employing bonded contact. However, this approach itself can lead to large errors. A previous study introduced the so-called simulated smoothed surface, sliding contact (SS-SC) formulation [2] where penalty contact interaction between jagged surfaces was defined by a smooth representation of the voxelized surface. It was shown that errors in predicting contact-induced stresses reduced from 42% (bonded-contact) to 2% (SS-SC). The present study aims to implement the SS-SC contact formulation in ParOSol.

Methods

As a precursor to SS-SC implementation, a previous study [3] implemented the so-called staircase, sliding contact (SC-SC) formulation in ParOSol. There, an incremental solution strategy was adopted such that intermediate contact states leading to the final state of deformation were computed in successive increments. Within each increment, the inherently nonlinear contact boundary conditions were solved iteratively. In each iteration, the global stiffness matrix and the global load vector were updated by contributions from the tangent contact stiffness and the contact reaction forces. These contributions were based on a previous penalty contact formulation that considered slave nodes of a deformable body to be in contact with quadrilateral master facets on another deformable body [4]. In [3], hard, frictionless contact between two elastic blocks using this implementation was investigated.

The present study extends the above implementation to the SS-SC formulation as follows. Slave nodes in any slave–master pair are projected onto a simulated smooth surface. Data structures are defined to store the locations of the projected "smooth nodes" in the ParOSol input file. Following [2], the "smooth nodes" are used to calculate the contact gap and the resulting contact reaction forces. The contact reaction forces are then applied to the original Cartesian mesh nodes, retaining all the computational advantages of the voxel-based approach.

The implementation is used to analyse the problem of a linear elastic, homogeneous and isotropic hemisphere in contact with a rigid plane (Figure 1). The hemisphere is displaced downward towards the rigid plane to achieve 1% apparent compressive strain, and restricted in the lateral directions to prevent rigid body translation and rotation. Coordinates of the smooth nodes are defined by projecting the surface nodes of the voxel mesh on the analytical (smooth) sphere.

The SS-SC model predictions are compared to that of the SC-SC model (both implemented in ParOSol) and of a "benchmark" smooth mesh model implemented in the commercial solver Abaqus.

Results

Figure 1 shows von Mises stress contours, normalized to the homogenous elastic modulus of the sphere, on a plane passing through the hemisphere centre, as obtained using SC-SC and SS-SC models implemented in ParOSol and the Abaqus benchmark model.
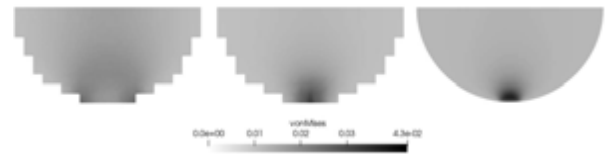
Figure 1: von Mises stresses – normalized to sphere elastic modulus – predicted using standard penalty contact on voxel meshes (left), the SS-SC formulation (middle) and the Abaqus benchmark (right).

Discussion

While the standard penalty contact implementation shows unrealistic stress concentrations due to the voxel geometry, the SS-SC formulation produced results comparable to the Abaqus benchmark. These results agree with those of [2] where the same problem was investigated using an in-house FEA solver which did not possess the excellent scalability of ParOSol. To conclude, the present study provides assurance of an implementation of SS-SC contact in ParOSol.

References

1. Flaig (2012) PhD Thesis ETH Zürich.
2. Bhattacharya et al. (2018) Int J Numer Meth Eng, 115(4):411–26.
3. Trommer, et al. (2021) ESB Congress, Milan:536
4. Parisch (1989) Int J Numer Meth Eng, 28:1803–12.

Acknowledgements

INTEGRATING ANN-BASED REAL-TIME JOINT FORCE PREDICTION WITH DEEP AUTO-REGRESSIVE GOAL-DRIVEN MOTION SYNTHESIS

Iliana Loi (1), Evangelia I. Zacharaki (1), Konstantinos Moustakas (1)

1. Dep. of Electrical and Computer Engineering, University of Patras, 26500 Patras, Greece;

Introduction

Most recent works in human biomechanical variable estimation are developing data-driven models, which are using motion capture, movement history data and motion dependent variables (e.g. GRFs, EMGs etc.) as input to predict joint position [1] and joint forces [2], or to synthesize [3] pose sequences of a virtual human character. By combining musculoskeletal estimation techniques like force prediction and motion modeling approaches, we are taking a step towards physics-based computer graphics' character animation [4], as well as ergonomically-adjusted motion estimation (e.g. fatigue modeling) [5]. With the use of machine learning to produce surrogate models for human biomechanical function estimation, such methods provide more automated as well as real-time solutions.

Inspired by the capability of artificial neural networks (ANNs) to estimate knee joint kinetics from kinematics variables [6], in this work we integrated a joint force estimation network into a deep auto-regressive algorithm for goal-driven motion synthesis, known as *Neural State Machine* (NSM) [7]. Our model predicts the medial and lateral knee contact forces of a 3D character in real-time, while the character moves and interacts with virtual scene objects.

Methods

Our force estimation model is based on an alternative version of the feed-forward ANN described in [6], with less neurons at each hidden layer (121 instead of 400) and modified network hyperparameters (activation functions, batch size etc.). The network was implemented in C++ for Unity [9] (NSM's runtime virtual environment). However, training was carried out in Python Keras [8]. A visualization of the medial and lateral knee contact forces on the virtual character's avatar while performing tasks in real-time was also developed in Unity as shown in Fig.1.

Two models were trained using gait (of variable speed) [6] and sit-to-stand human motion capture datasets [10], respectively, and used (either one) according to the action label estimated by the NSM. Each model was evaluated with cross-validation across all subjects ($n = 54$ for the gait dataset and $n = 19$ for the sit-to-stand dataset). The sit-to-stand dataset was preprocessed following the pipeline described in [11], using the OpenSim software [12]. During training only joint angle measurements were used and no ground reaction forces.

Results

The Normalized Root Mean Square Error (NRMSE) for the gait and sit-to-stand dataset is shown in Table 1. The lateral force in the *x*-axis, is practically negligible, therefore it was not evaluated. The low NRMSE values indicate that our network performs well and produces valid predictions.

NRMSE	x	y	z
Gait			
Medial	2.07	6.31	4.28
Lateral	-	5.25	5.26
Sit-to-stand			
Medial	0.75	3.49	5.86
Lateral	-	3.02	3.48

Table 1: The NRMSE values for x, y and z components of medial and lateral knee contact forces.

Figure 1: Visualization of the medial and lateral knee contact forces during running state. The sphere's color indicates the magnitude of the force based on a cyan to red heatmap (minimum to maximum force). Green and red lines, which are parallel to the axis of the thigh, represent the direction of the force.

Discussion

The motivation behind our work is to optimize and apply an ANN model for knee contact force estimation in a real-time virtual environment and test its performance during different actions. As continuation to our work, we intend to extend our machine learning approach for prediction of knee contact forces for more than one action classes (running, jumping, dancing etc.), overcoming the limitation of the current model being action class-specific. In addition, future work may include the prediction of contact forces in more joints, other than the knee.

References

1. Liu et al, 2019 IEEE CVPR, 9996-10004, 2019.
2. Matijevich et al, Human Movement Science, 74, 2020.
3. Starke et al, ACM Trans. Graph., 40, 2021.
4. Lee et al, ACM Trans. Graph. 40:1-13, 2021.
5. Cheema et al, ACM CHI'20 Conference, 1-13, 2020.
6. Giarmatzis et al, Sensors, 20: 6933, 2020.
7. Starke et al, ACM Trans. Graph, 38, 2019.
8. Chollet et al, https://github.com/fchollet/keras, 2015
9. Haas, J. K, A history of the unity game engine, 2014.
10. Mandery et al, IEEE ICAR Conference, 329-336, 2015
11. Loi et al, Front Bioeng Biotechnol, 9:648356, 2021
12. Seth et al, Procedia IUTAM, 2:212-232, 2011

EXAMINATION OF 2D MARKERLESS MOTION CAPTURE FOR SAGITTAL AND FRONTAL JOINT ANGLES OF THE KNEE AND HIP

Logan Wade (1), Laurie Needham (1), Murray Evans (1), Polly McGuigan (1), Steffi Colyer (1), Darren Cosker (1), James Bilzon (1)

1. Centre for Analysis of Motion, Entertainment Research and Applications, University of Bath, United Kingdom

Introduction

Markerless motion capture using open-source deep learning-based pose estimation, has recently produced reliable identification of 2D joint centre locations and angles (sagittal plane) from a single camera [1]. Such methods could facilitate fast and cost-effective biomechanical analysis in clinical and sports settings. Interestingly, open-source pose estimation algorithms have been trained to detect both visible and occluded joints [2], which if accurate, could enable identification of sagittal joint angles from both sides of the body, instead of just the side closest to the camera.

Alternatively, frontal plane joint angles are yet to be assessed with 2D markerless methods. Movement in this plane during walking is minimal and therefore, methods with low measurement variability and high precision are required to detect meaningful changes. The aim of this study was to compare marker-based and markerless knee and hip joint angles in the frontal and sagittal planes during walking.

Methods

Fourteen healthy participants performed over-ground constant speed walking while motion capture data was recorded (200 Hz) from fifteen Qualisys cameras and two synchronised machine-vision cameras (sagittal and frontal plane). Image data from each machine-vision camera were processed using OpenPose [2]. Multi-person tracking and smoothing of joint centre locations using Kalman filtering [3] was performed to reduce joint centre noise. We employed novel reprojection of 3D marker-based joint centre coordinates into each 2D machine-vision camera image plane to eliminate parallax error between machine-vision and marker-based cameras. 2D marker-based and markerless joint centre locations for the right and left, ankle, knee, hip and shoulder were used to calculate knee and hip joint angles in the frontal and sagittal plane during one stride. Knee and hip angles between systems were compared using Bland-Altman analysis. In the sagittal plane, left joints were on the occluded-side and right joints were on the camera-side.

Results

In the sagittal plane, camera-side joint angle variability (STD of bias) was lower than all occluded-side joints, with the occluded hip producing the highest variability (Table 1). Sagittal plane joint angle range of motion (RoM) from marker-based methods were $45.3 \pm 5.7°$ and $65.8 \pm 5.02°$, thus markerless variability accounted for less than 6.5% of camera-side joint RoM and over 10% of occluded-side joint RoM. Markerless frontal plane joint angles had relatively consistent variability across all joints (Table 1). Joint RoM from the marker-based data of the knee was $11.5 \pm 5.31°$ while the hip was $8.39 \pm 2.70°$. Thus, markerless variability accounted for ~22-24% of the total RoM of the hip and knee.

	Joint	Bias (°)	STD of Bias (°)
Sagittal	Camera-side Knee	-1.5	2.6
	Occluded-side Knee	-1.8	4.7
	Camera-side Hip	-3.6	2.7
	Occluded-side Hip	-4.8	6.0
Frontal	Right Knee	0.7	2.5
	Left Knee	2.5	2.1
	Right Hip	4.7	3.1
	Left Hip	3.9	2.4

Table 1: Sagittal and frontal plane bias and STD of bias (variability) for markerless hip and the knee joint angles, relative to marker-based results.

Discussion

This is the first study to employ reprojected marker-based data to compare aligned markerless and marker-based 2D joint angles. Markerless sagittal plane knee and hip joint angle bias and variability (STD of bias) were worse for the occluded-side compared to the camera-side joints. Thus, while markerless methods can calculate joint centres of occluded joints, variability was almost double camera-side joints. Markerless variability in the frontal plane accounts for over 20% of the total marker-based RoM at the knee and the hip, indicating that the signal-to-noise ratio in the frontal plane may be too high to extract meaningful joint angle data. Current open-source 2D markerless motion capture methods have not been trained on biomechanically informed data sets and therefore do not have sufficient accuracy and reliability to detect occluded joints in the sagittal plane, or any joints angles in the frontal plane.

References

1. Cronin, N.J., et al. *J Biomech*, 87:75-82, 2019
2. Cao, Z., et al. *IEEE Trans*. 43(1):172-186, 2019
3. Needham, L., et al. *Sensors*, 21(8): 2889, 2021

Acknowledgements

Neural Network Finite Element Modeling of the Heart Mechanics

Wenbo Zhang and Michael S. Sacks

Oden Institute and the Department of Biomedical Engineering
University of Texas at Austin, Austin TX USA

Introduction

All high-fidelity cardiac simulations require a comprehensive image-based finite element modeling pipeline [1]. While quite accurate, such traditional approaches cannot be used in practical for time-sensitive clinical evaluations. In this work we developed a neural network surrogate modeling method to generate fast online predictions while frontload the computational cost to model training. Due to the complex geometry of the cardiac models, the finite element discretization is used and integrated with the neural network. To train the neural network model without the need to generate finite element solutions, we developed a physics-based training scheme using differentiable finite elements to backpropagate the gradients from residuals of partial differential equations (PDEs) to the neural network. We considered active contraction and spatially varying fiber structures, all incorporated into a prolate spheroidal model of the left ventricle (LV) as a first step scenario.

Methods

The neural network surrogate model [2] generate trial a solution for given input parameters, active contraction parameters and pressure level. To train the neural network model we employed a physics-based approach. The active stress generally cannot be derived from a potential, so we cannot use the potential formulation as the passive behavior. To address this challenge, we develop the training algorithm that drives the PDE residuals to zeros. The variations of the virtual work δW with respect to the nodal values of the test function yield the residual force vector $\boldsymbol{R}$. Our aim is to drive the residual to zero for all instances of the input parameter $\boldsymbol{M}$. We sample N realization of the input parameter $\boldsymbol{M}$. This means solving the nonlinear equations corresponding to the stationary equations for the variational problem. Evaluation of the Jacobian of the residual becomes intractable, so that we solve the stationary conditions using a matrix-free approach. We then implemented a differentiable finite element library using Jax to streamline the computational pipelines with neural network surrogate model.

RESULTS

We consider a prolate spheroidal model of the left ventricle (Figure 1). The domain is discretized using unstructured tetrahedron elements. The fiber geometry was based on a rules-based approach to approximagte the -60 to 60 degree transmural gradient, and a Fung-type material model with constants taken from the ovine heart used. The entire pipeline was then trained against a represented pressure-volume loop (Figure 1). To verify our differentiable implementation of finite elements, we utilized the same boundary conditions and use FEniCS [3] for verification. The relative error of the gradients is 3.9154565×10^{-7} for a given random initialized displacement field (Figure 1).
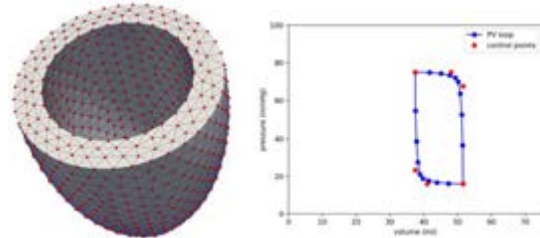
Figure 1: The prolate spheroidal LV model using a Fung-based constitutive model showing the deformed configurations: NNFE mdoel (blue wire frame) against the FENICS (DOLFINx) solution (red points), showing very close accuracy. Also shown is the matched P-V loop used to train the NNFE LV model.

Discussion

In this work, we have developed a novel differentiable finite elements which is ready to integrate with neural network surrogate model for the organ-level model of the heart. We verified our implementation with widely used finite element library and obtained good matches. We also developed a physics-based training algorithm based on weak form to train the neural network surrogate model. The present surrogate modeling method is extensible to incorporate advanced material model of myocardium and complex geometry and boundary conditions. The current studies include investigation of the neural network architecture to faithfully reproduce the responses of the left ventricles and the mathematical analysis to guide the performance improvement of the neural network surrogate model.

Reference

[1] Liu, H et al., Scientific reports, 11.1 (2021): 1-15.
[2] Zhang, W, et al. International Conference on Functional Imaging and Modeling of the Heart. Springer, Cham, 2021.
[3] Logg, et al., Automated solution of differential equations by the finite element method: The FEniCS book. Vol. 84. Springer Science & Business Media, 2012.

Acknowledgements

SUPER-RESOLUTION OF CLINICAL CT DATA: TOWARDS IMPROVING THE STRENGTH OF FRACTURE RISK ASSESSMENTS

Lance Frazer (1), Jay Vaishnav (2), Nathan Louis (1), Daniel Nicolella (1)

1. Southwest Research Institute, USA; 2. Canon Medical Systems, USA

Introduction

Osteoporotic fractures are a primary cause for concern in our aging population. In 2018, osteoporotic fracture costs were estimated to be $57 billion and is projected to be $95 billion in 2040. The current gold-standard for identifying at-risk individuals relies on measurements of bone mineral density. However, bone mineral density only accounts for 30% of fracture incidence indicating its poor predictive capabilities. New fracture risk paradigms are required to improve these bleak statistics. Over the last two decades, significant progress has been made in understanding bone strength and the factors that influence its resistance to fracture. Of these factors, bone microarchitecture has been identified as a significant predictor of fracture risk. However, this information has not been clinically accessible on a large scale. Certain techniques exist, such as high-resolution peripheral quantitative computed tomography, to assess microarchitecture, but this technique is limited in scope and can only assess a few millimeters of bone length at specific locations. To address this limitation and expand microarchitectural measures to whole-bone scales, we propose the use of deep learning to take whole-bone clinical CT images (250-750 micron) as input and output a predicted set of microCT-level (60 micron) resolution images in a process called Super-Resolution (SR).

Methods

Twelve cadaveric femurs were imaged via two different computed tomography (CT) methods: 1) an ultrahigh-resolution CT (UHRCT) scan using the Aquilion Precision (250/350 micron in-plane/out-of-plane resolution), and 2) a MicroCT (NorthStar Imaging) (60 micron). For each femur, the two scans were registered to each other, and the UHRCT data was upsampled to the same voxel spacing as the microCT to create image-to-image correspondence (~3000 images per bone in the axial plane). The microCT image data was segmented via deep learning (UNET). Nine of the femurs were used to train a neural network for super-resolution image processing with the UHRCT as input and the segmented MicroCT data as output. We used a pretrained Super Resolution Generative Adversarial Network [1,2] and trained for 20 epochs with a batch size of 16. We saved the model weights with the highest PSNR (Peak Signal-to-noise ratio) and applied them on the remaining three femurs. Average trabecular thickness, trabecular spacing, cortical thickness, and bone volume fraction were reported as comparative metrics between the SR image data and microCT.

Results

Average trabecular thickness was 0.38 mm for microCT and 0.4 mm for SR. Average trabecular spacing was 0.75 mm for microCT and 0.73 mm for SR. Cortical thickness was 1.66 mm for microCT and 1.70 mm for SR. Bone volume fraction was 0.36 for microCT and 0.38 for SR.
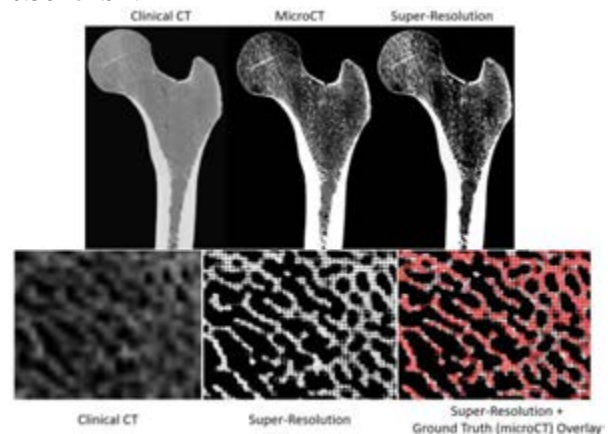
Figure 1: Top row: comparative frontal plane slices of the original, unseen clinical CT, the ground truth microCT, and the super-resolution image data. Bottom row: 5x5 mm of image data in the femoral head. Left: unseen clinical CT image data. Middle: clinical CT processed with our Super-Resolution algorithm. Right: SR image data with microCT ground-truth overlay in red.

Discussion

We have successfully demonstrated the capability of predicting microCT-level quality image data from lower-resolution clinical CT image data at the whole bone level. This ability enables a wider breadth of fracture-risk prediction approaches, as well as greater fidelity of image-based finite element models. Future work will involve implementing physics-based constraints to the neural network and apply the technique to lower resolution image data.

References

1. Wang et al, ECCV, Proceedings, 2018.
2. https://github.com/idealo/image-super-resolution

Acknowledgements

TEMPORALLY OPTIMIZED INVERSE KINEMATICS FOR 6DOF HUMAN POSE ESTIMATION

Kevin Gildea (1), Clara Mercadal-Baudart (1), Richard Blythman (1) , Ciaran Simms (1)
1. Department of Mechanical, Manufacturing & Biomedical Engineering, Trinity College Dublin, Ireland

Introduction

The recent emergence of deep learning and computer vision-based 3D human pose estimation presents opportunities for a form of markerless motion-capture. State-of-the-art approaches have achieved remarkable accuracy in predicting global and relative joint positions [1], however, many potential applications require information on joint orientations, e.g., in the fields of biomechanics. Furthermore, methods that do include joint orientations are incompatible for applications with predefined *incongruent kinematic chains*, i.e., chains with differing limb lengths and proportions. Therefore, we propose a temporal inverse kinematics (IK) optimization technique to infer joint orientations in a user customizable kinematic chain from a position-based 3D pose input. This technique may be particularly useful for sports/injury biomechanics, and telehealth applications.

Methods

Due to the ambiguous joint 'twist' angle around links, the problem of mapping a kinematic chain to a hierarchical 3D position set ($[P]$) is indeterminate. Therefore, optimization is needed. A sequential least squares programming procedure [2] is developed to solve the minimization problem for a 16-joint kinematic chain (G) expressed using the Denavit-Hartenberg convention [3] as a hierarchical set of 4×4 transformation matrices ($\{T_j\}^{e_{j\,parent}}$) with parent-relative positions ($\{\vec{r}_{a_j}\}^{e_{j\,parent}}$) and orientations ($[A^{e_j,e_{j\,parent}}]$) for each joint ($j$) (Eqn.s 1&2), with sequential Cardan angle rotation parameterization bounded joint ranges of motion (ROMs).

$$\{T_j\}^{e_{j\,parent}} = \begin{bmatrix} [A^{e_j,e_{j\,parent}}] & \{\vec{r}_{a_j}\}^{e_{j\,parent}} \\ 0 \quad 0 \quad 0 & 1 \end{bmatrix} \quad (1)$$

$$G = \{\{T_1\}^{e_{j\,parent}}, \cdots, \{T_{16}\}^{e_{j\,parent}}\} \quad (2)$$

Two IK algorithms are developed, 1) a frame-by-frame approach with local and global losses for pose (Eqn. 3), and 2) a 5-frame batch temporal approach including weighted losses for joint angular difference and positional difference (for links with missing joints) across frames ($2_{\text{5-frame}}$) (Eqn. 4).

$$L_{frame} = E_{\angle(\hat{a},\hat{b})} + \lambda_1 E_{\angle(\hat{p}^a,\hat{p}^b)} \quad (3)$$

$$L_{temporal} = E_{\angle(\hat{a},\hat{b})} + \lambda_1 E_{\angle(\hat{p}^a,\hat{p}^b)} + \lambda_2 E_{\Delta\vec{\theta}} + \lambda_3 E_{\Delta\vec{s}} \quad (4)$$

For assessment, we generate a series of motion sequences for the kinematic chain with 1) congruent, and 2) incongruent configurations, and applied both IK algorithms to the resulting joint pose sequences, i.e., with joint orientations hidden (see Fig. 1). Agreement was assessed using a 10-joint Mean Per Joint Angular Separation (MPJAS$_{11}$) between inferred and ground truth joint orientations. Randomly drawn rotations within joint ROMs average approximately 1.18 radians MPJAS$_{11}$ error (68 degrees/joint).
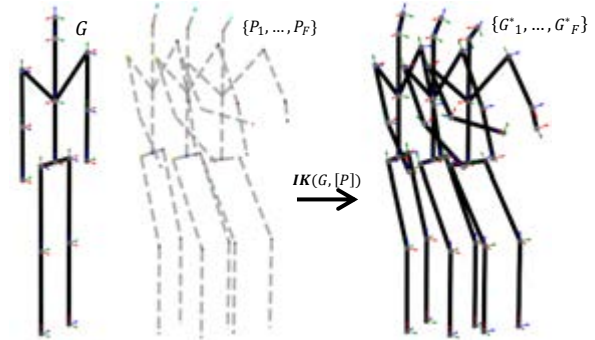
Figure 1: IK approach for 6-Degree of Freedom (DOF) pose from 3DOF pose.

Results

Table 1 shows a comparison of average angular errors. Where algorithm 1 is initialized with random weights for each frame ($1_{\text{rand\_w}}$) or fed weights from previous frames ($1_{\text{prev\_w}}$).

Algorithm	Skeleton					
	congruent			incongruent		
	e	b	tot	e	b	tot
$1_{\text{rand\_w}}$	1.2×10^{-1}	0	4.0×10^{-2}	2.5×10^{-1}	3.5×10^{-2}	9.8×10^{-2}
$1_{\text{prev\_w}}$	6.0×10^{-2}	0	1.8×10^{-2}	1.9×10^{-2}	3.4×10^{-2}	8.2×10^{-2}
$2_{\text{5-frame}}$	1.7×10^{-2}	0	5.0×10^{-3}	1.7×10^{-2}	3.5×10^{-2}	7.5×10^{-2}

Table 1: Accuracy of IK algorithms 1 and 2. MPJAS$_{11}$ (radians) per frame for e: frames with extended/straight limbs, and b: frames with bent limbs, for both congruent and incongruent skeleton types.

Discussion

With frame-by-frame IK and congruent skeletons ($1_{\text{rand\_w}}$, $1_{\text{prev\_w}}$) we obtain uniquely optimal solutions in the case of bent elbows and knees, however, for extended/straight limbs the solution space is non-unique. With our temporal approach ($2_{\text{5-frame}}$) we reduce ambiguity for these poses, resulting in lower overall errors for both congruent and incongruent skeletons, with negligible errors associated with the former (0.3 degrees/joint), and low errors for the latter (4.3 degrees/joint). This technique allows for accurate prediction of joint orientations, for convenient post-processing of 3D pose estimates (e.g., Fig.2).

2D Pose　　　**3D Pose**　　　**6DOF Pose**
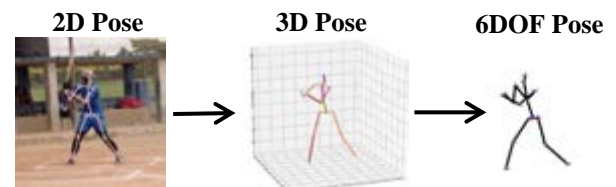
Figure 2: Example application using 3D predictions from [4].

References

1. Zheng et al, J. ACM, 37, 2022.
2. Kraft, 1998.
3. Denavit et al, J. Appl. Mech, 22: 215–221, 1955
4. Liu et al, ICCV, 2272–2281, 2019

Acknowledgements

AUTOMATED SEGMENTATION AND LANDMARKING OF SCAPULAE TO ASSESS THE OUTCOME OF TOTAL SHOULDER ARTHROPLASTY

Osman Berk Satir (1), Alexandre Terrier (2), Arnaud Meylan (3), Fabio Becce (3), Patrick Goetti (3), Robin Diot (3), Philippe Büchler (1)

1. ARTORG Center for Biomedical Engineering Research, Switzerland; 2. Ecole Polytechnique Fédérale de Lausanne, Switzerland; 3. Lausanne University Hospital (CHUV), Switzerland

Introduction

Total shoulder arthroplasty (TSA) is a common surgical procedure to relieve pain and disability associated with glenohumeral osteoarthritis. Despite satisfactory results and a relatively good long-term survival rate, there is a lack of indicators to predict the long-term success and revision risk of TSA [1]. The biomechanical configuration of the glenohumeral joint could influence the implant survival rate and explain possible causes of the observed complications, such as the preoperative condition of the rotator cuff muscles or the shape and orientation of the acromion. Manual quantification of these parameters is a repetitive and time-consuming process that depends on the subjective assessment and expertise of the rater. Therefore, this study aims to develop image analysis and deep learning-based approaches to automatically quantify multiple potential preoperative morphologic markers and to provide an objective assessment of the patient's shoulder anatomy.

Methods

The first step was to segment the scapula and humerus from shoulder CT scans using a Convolutional Neural Network (nnU-Net) [2]. The network was trained on 3D patches of 60 healthy and 56 pathological shoulder CTs. Landmarks identified on the scapula were used to quantify its 3D anatomy (Fig. 1). These landmarks allow, for example, quantification of glenoid version, inclination, or measurement of the position of the glenoid relative to the acromion. We developed an algorithm for the automatic positioning of the predefined landmarks based on a U-Net architecture. Training was performed on the same dataset as the one used for bone segmentation, which was manually annotated by 4 different raters.
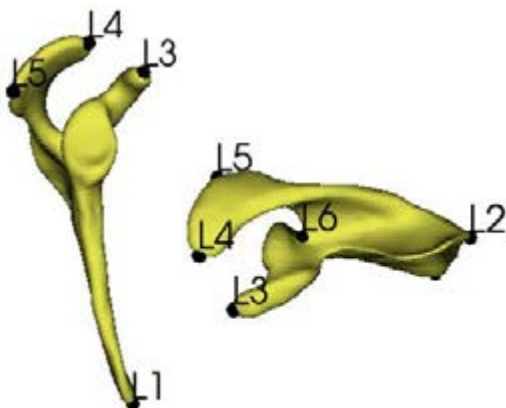
Figure 1: Positions of the landmarks on the scapula.

Results

The 5-fold cross validation showed excellent segmentation accuracy for both the scapula and humerus. For the scapula, the Dice coefficient of segmentation exceeded 0.97 for both healthy and pathological cases, whereas for the humerus it was approximately 0.99.

For landmark detection, validation showed that the error is at a desired level. It can be observed that the prediction error is similar and comparable to the inter-rater error (Fig. 2). When the error was compared between healthy and pathological subjects, it was observed that the error was slightly higher for pathological cases.
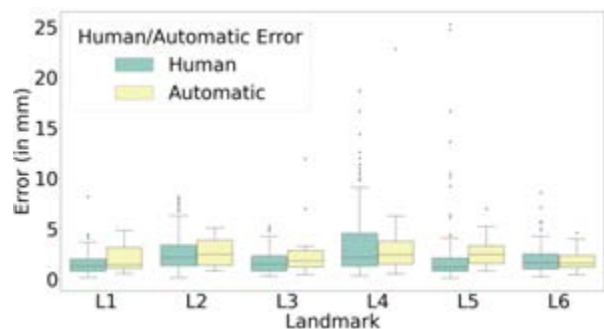
Figure 2: Comparison of the error in the position of the landmarks for the human raters and automatic method.

Discussion

In this work, we proposed deep learning-based algorithms for segmenting scapula and humerus, and predicting specific landmarks of interest for computing morphological markers associated with TSA outcome. Our validation showed high segmentation accuracy of the scapula and humerus. In addition, validation of the automatic landmark detection yielded a low error, comparable to that of human raters. In the future, we will combine this information to automatically determine morphological markers, which will allow retrospective analysis of a large cohort of patients and correlation of the morphometric measurements with clinical outcomes.

References

1. Schoch et al, J Shoulder Elbow Surg. 2015 May;24(5):705-10.
2. Isensee et al, Nature Methods, 1-9.

CORRECTION OF MOTION ARTEFACTS IN HR-PQCT USING CYCLE-CONSISTENT ADVERSARIAL NETWORKS

Philipp Y. Steiner (1), Matthias Walle (1,2), Mattia Rigotti (2), Danielle E. Whittier (1), Cael McLennan (1), Penny R. Atkins (1), Ralph Müller (1), Caitlyn J. Collins (1,3)

1. Institute for Biomechanics, ETH Zurich, Zurich, Switzerland; 2. IBM Research Zurich, Rüschlikon, Switzerland, 3. Department for Biomedical Engineering and Mechanics, Virginia Tech, Blacksburg, USA.

Introduction

High-resolution peripheral quantitative computed tomography (HR-pQCT) can provide important information about age-related changes in bone microstructure and strength [1]. However, in elderly patients, uncontrollable tremors often induce motion artefacts that affect the accuracy of HR-pQCT measurements [2]. Repeat acquisition protocols are commonly used to address this issue; nevertheless, they are ineffective in these patients, resulting in motion-blurred and streaked images. Deblurring these scans computationally is a severely ill-posed inverse problem. Therefore, we present a deep learning approach to suppress motion-induced artefacts in HR-pQCT scans.

Methods

HR-pQCT scans of 13 patients scanned biweekly for five weeks (XtremeCT II, Scanco Medical, 60.7 μm, 68 kV, 1470 μA, 43 ms) were obtained from a previous study [3]. Motion scores of all scans were assessed on a scale of 1 (no visible motion artefacts) to 5 (major streaks) [1]. Scans with a score of 1 were classified as high-quality (HQ), while those with a score 2 or less were classified as low-quality (LQ). 15 LQ-HQ scan pairs were 3D registered and divided patient-wise into 80% train, 10% test, and 10% validation datasets. Our filtering approach used a generative adversarial network (cycle-GAN) as the building block [4]. It enforced the cycle consistency using the least absolute deviation (L1) to establish a nonlinear end-to-end mapping from LQ input images to denoised and deblurred HQ outputs. To quantify the signal recovery after motion-filtering, we calculated a signal-to-noise ratio (SNR) by fitting two Gaussian distributions to values corresponding to bone (signal) and soft-tissue (noise). Further, a peak-SNR and structural similarity index were calculated between LQ, HQ and filtered LQ pairs to assess degradations of structures within the image. Finally, three blinded operators evaluated motion scores of the validation dataset in random order. Fleiss' kappa (κ) was used to assess inter-rater reliability between operators before and after filtering.

Results

We found structural similarity index (0.67±0.03) and peak-SNR (21.43±1.03) were not significantly different between LQ and HQ images. However, the mean SNR was significantly higher in HQ (15.83±1.10) compared to LQ (13.49±0.91, p<0.01), promoting SNR as an evaluation target. Our motion-filtering approach consistently improved the SNR of LQ images to 15.39±0.92 (p<0.01, Fig. 1A), comparable to that of HQ (15.83±1.10). Visually, images were denoised and deblurred; yet, the network failed to resolve severe artefacts (cortical breaks). Finally, operators graded LQ images better (Fig. 1B) and more consistently after motion-filtering, with κ increasing from 0.162 to 0.237.
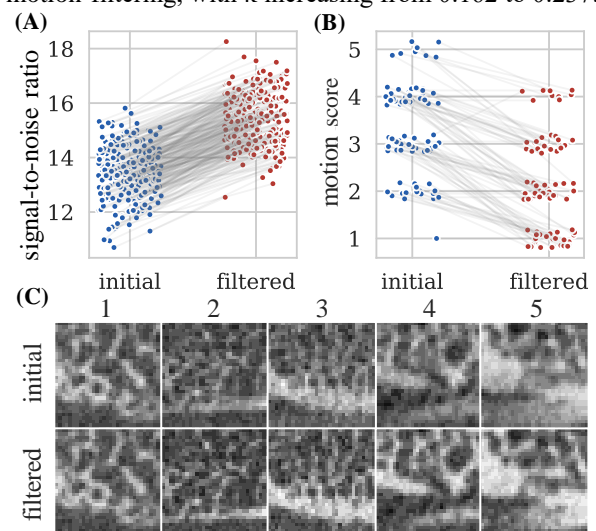
Fig. 1: SNR (A), motion score (B), and visual (C) improvement of validation data after motion-filtering.

Discussion

Using paired *in vivo* scan-rescan data, the proposed cycle-GAN method produced promising results in preserving anatomical information and suppressing moderate motion artefacts in HR-pQCT images after acquisition. Severe degradations, causing breaks in the cortex, were not fully resolved, but visual evaluations confirmed that our proposed method improves image quality. Future studies should assess how this method impacts the diagnostic quality of density and morphology measures. Overall, this work offers stakeholders a realistic methodology for improving current HR-pQCT datasets such that tools for analysing trabecular structure can be used more effectively.

References

1. Whittier DE et al., Osteoporos Int. 31(9):1607-27, 2020.
2. Crawford CR, King KF, Med. Phys. 17(6):967-82, 1990.
3. Atkins PR et al., JBMR Plus 5(6):e10493, 2021.
4. Zhu JY et al., IEEE Comp. Vis. pp. 2223-2232, 2017.

LAMENESS INFLUENCES BREAKOVER DURATION IN HORSES

Eloise Briggs (1), Claudia Mazzà (2)

1. Department of Mechanical Engineering and INSIGNEO Institute for in silico Medicine, University of Sheffield, Sheffield, United Kingdom; 2. Department of Mechanical Engineering and INSIGNEO Institute for in silico Medicine, University of Sheffield, Sheffield, United Kingdom

Introduction

Breakover is the phase of the gait cycle from the heel being lifted off the ground (*onset of breakover*) to the toe leaving the ground (*hoof-off*). During breakover, the hoof experiences maximum ground reaction forces [1]. Lameness is widely regarded as the most prevalent problem affecting equines globally and refers to the adjustment of a horse's posture to relieve loading from a painful limb. While little is known on the topic, it can be hypothesised that lameness influences the duration of breakover. The aim of this research was to verify this hypothesis.

Methods

A varied cohort of sixteen horses (ages 13(6)years, heights 163(9)cm; five sound, five with acute lameness and six with chronic lameness) were included in the study. Shimmer3 IMUs (Dublin, Ireland) were firmly attached to the lateral aspect of the hooves and collected data using triaxial gyroscopes (range ±2000deg/s, 200Hz). Horses were led at walk along a 20m stretch of hard ground for 3 passes. The instants of onset of breakover (b_{over}) and hoof-off (h_{off}) were detected from the resultant of angular velocity (Fig 1) [2,3].
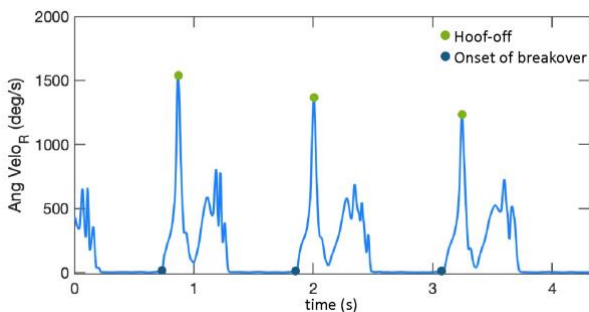
Figure 1: illustration of methods to detect onset of breakover and hoof-off

Breakover durations (T_{BO}, ms) were calculated as the time from b_{over} to the subsequent h_{off} (Eq 1).

$$T_{BO} = h_{off} - b_{over} \qquad (1)$$

The differences (Δ_{BO}, ms) in breakover duration of the left (T_{BOL}) and right (T_{BOR}) limbs of each contralateral limb pair were calculated (Eq 2) and Student's t-tests were used to determine whether differences were statistically significant.

$$\Delta_{BO} = T_{BOR} - T_{BOL} \qquad (2)$$

Results

The absolute mean Δ_{BO} of sound limb pairs was small and comparable to that of opposite pairs (Fig 2). Both were substantially smaller than Δ_{BO} of lame pairs. No differences were seen in any other temporal features of gait (such as stride, step and stance durations). This suggests that the breakover duration alone is affected by lameness.
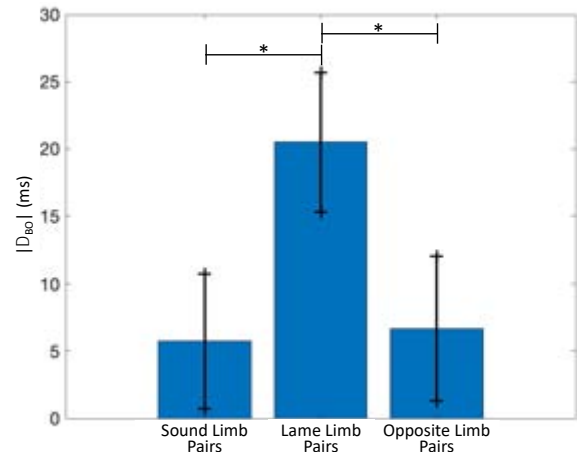
Figure 2: absolute mean values of Δ_{BO} for limb pairs with no lame limbs (sound), one lame limb (lame) and those which were opposite to a lame limb pair (opposite)

Discussion

The small Δ_{BO} of sound limb pairs (Fig 2) indicates a high degree of symmetry in T_{BO} of sound horses. The high Δ_{BO} of lame pairs confirms that lameness affects the contralateral symmetry of T_{BO} while the value for opposite pairs suggests that it does not induce a compensatory effect in the unaffected limb pair. A prolonged T_{BO} in a lame limb may reduce the jerk, increasing comfort, while the reduced T_{BO} of the contralateral enables the horse to maintain the overall gait symmetry [4]. In summary, lameness has been proven to impair the contralateral symmetry of breakover and, hence, the methods promise to be a valuable tool for detecting and assessing lameness in horses.

References

1. Merkens & Schamhardt, Equine Vet. J., 1988
2. Tijssen et al, PLoS ONE, 2020
3. Briggs & Mazzà, PLoS ONE, 2021
4. Buchner et al, Equine Vet. J., 1995

Acknowledgements

A COMPUTATIONAL MODEL OF THE ZEBRAFISH HEART ELECTROPHYSIOLOGY

Ludovica Cestariolo (1), Giulia Luraghi (1), Pierre L'Eplattenier (2), Jose F. Rodriguez Matas (1)

1.   *Politecnico di Milano, Italy; 2. Livermore Software Technology Corp., USA.*

Introduction

In recent years, a rising interest has involved the use of zebrafish due to its human-like physiology, showing similar spontaneous heart rate, a heart rate dependent QT-interval, similar action potential (AP) shape and duration, and the presence of orthologues of human genes leading to a functional similarity in cardiac ion channels. Thus, the zebrafish has been suggested as a potential model for genetic and pharmacological screenings for all factors affecting heart functions.

Although the growing interest, few studies have been dedicated to the development of a computational model of the zebrafish heart. This work aims to create a reliable computational model of the electrophysiology of the zebrafish embryo heart. This work represents the first step towards the development of a digital twin of the zebrafish's heart.

Methods

A full-electrophysiological model of a 3 days post fertilization (dpf) zebrafish was developed. The geometry is composed of the body, heart chambers, and heart myocardium [1]. The latter is, in turn, divided into four regions: the sinoatrial region (SAR), atrial wall, atrio-ventricular band (AV band), and ventricular wall. Other parts were created to assign different conductance values to reproduce the experimental activation pattern of the 3 dpf zebrafish [2]. The Bueno-Orovio four variables minimal model [3] has been adjusted to fit zebrafish's atrial and ventricular experimental APs at a basic cycle length of 500 ms. Then, the extended monodomain equations were solved using a semi-implicit numerical scheme with a fixed time step of 0.02 ms in the multiphysics finite element solver LS-DYNA (ANSYS, Canonsburg, PA, USA) to determine the propagation of the electric signal in the tissue.

Results

The results were analyzed in terms of: i) the activation times at different instants during a single heart beat, ii) AP morphology, and iii) the *in silico* ECG signals as compared with the corresponding experimental results [1,2,4,5,6].

The atrium was activated in 36 ms starting from the SAR where the stimulus is delivered. A delay of 25 ms occurred at the AV band, and finally, the ventricle activated with an apex-to-base pattern in 73 ms. These activation times compared well with the 35 ms, 25 ms, and 75 ms respectively reported in [2]. We also found good agreement with the activation sequence reported in the same study. Regarding the AP morphology, the APD_{90} was found to be 111.70 ms for the atrium and

183.82 for the ventricle, the AP amplitude was 86.42 mV and 102.24 mV, and maximum and minimum upstroke were 6.67 V/s and -2.38 V/s for the atrium and 6.36 V/s and -1.94 V/s for the ventricle, which were found to be in good agreement with results from [1,4].

Monopolar ECGs (*Figure 1*) have been assessed by selecting two electrodes located in the AV band and ventricular regions coincident with the electrode location in [1]. Both signals have been found to be in line with the *in vivo* recordings [1].
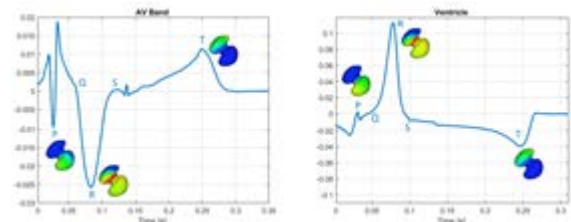
Figure 1: Monopolar ECGs with their respective activation sequence frames.

A bipolar ECG computed between two electrodes located in correspondence with the ventricular base (+) and apex (-) is in good agreement with similar records reported in literature [5] (*Figure 2*).
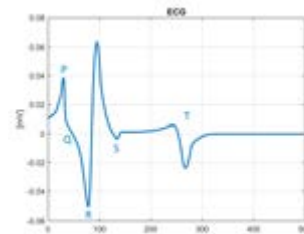
Figure 2: Bipolar ECG computed between electrodes located at the ventricular base (+) and apex (-).

Discussion

This study developed a full-electrophysiological *in-silico* model of the zebrafish's heart and body, allowing the evaluation of the main electrophysiological parameters and involving a significant improvement with respect to the previous model developed in [1] in terms of activation sequence and resulting ECG. In general, in comparison with the experimental data [1,2,4,5,6], we can consider the results as encouraging.

References

1. J. Crowcombe et al., PloS One, 11(11):1-10, 2016.
2. D. Pánákova et al., Nature, 466:874-878, 2010.
3. A. Bueno-Orovio et al., J Theor Biol, 253:544-560, 2008.
4. R. Aranout et al., PNAS, 104(27):11316-11321, 2007.
5. S. Quian et al., Phys Biol, 17, 2020.
6. P. Nemtsas et al., J Mol Cell Cardiol, 48:161-171, 2009.

HISTOMORPHOMETRIC ANALYSIS OF CANINE TRABECULAR BONE IN THE OSTEOPOROTIC CONTEXT

Ernest Kostenko (1), Alius Pockevičius (2), Algirdas Maknickas (3)

1,3. Department of Biomechanical Engineering, Vilnius Gediminas Technical University (VilniusTech), Vilnius Lithuania; 2. Department of Veterinary Pathobiology, Veterinary Academy, Lithuanian University of Health Sciences, Kaunas, Lithuania

Introduction

The mechanical properties of bone are determined by its size and by structural elements – such as the cortical thickness or the number of trabeculae – within the bone. Like humans, animals can suffer from bone fractures due to existing structural changes. We therefore performed a histomorphometric analysis to determine structural alterations in bones.

Bone histomorphometry is an essential technique for examining the processes of bone disease [1]. Osteoporosis is the most common bone disease and is associated with an increased risk of fractures [2]. This analysis may provide valuable information regarding bone structure.

The purpose of this research was to examine the lumbar vertebrae of dogs using histomorphometric analysis and to compare findings with previously published human histomorphometry data.

Methods
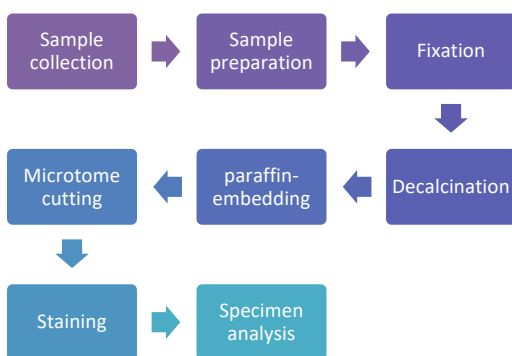
Figure 1: Experiment protocol

In our investigation, we examined the lumbar vertebrae (L1 and L2) of five castrated females without musculoskeletal disorders. All necessary bioethical permissions were received. The protocol for the experiment is included in Figure 1. Following preparation work, we used *OsteoidHisto* software to conduct this research [3]. You can see how the calculations were done in Figure 2. We measured and calculated the following structural parameters: bone volume/tissue volume (BV/TV); trabecular number (Tb.N); and trabecular width (Tb.Wi) [4]. Following our calculations, we compared our values with findings from other research using human osteoporotic vertebrae.

Results
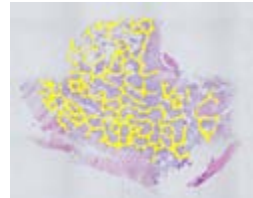
Figure 2: OsteoidHisto software BV/TV calculation

Following analysis, we determined that BV/TV (%) was 16.12 ± 3.06 and 16.08 ± 2.1 in L1 and L2, respectively, while Tb.Th was 25.49 ± 2.93 μm and 25.04 ± 2.28 μm in L1 and L2, respectively. We estimated Tb.N of 6.3 and 6.4 in L1 and L2 vertebrae, respectively. The widths of L1 and L2 were nearly identical at 2.55 μm and 2.50 μm, respectively.

Discussion

The term osteopenia is used more frequently than the word osteoporosis in the animal literature [5]. However, since decreasing bone density increases the risk of fractures, it is critical to assess structural bone alterations. A study of the human medical literature suggests that while risk factors for osteoporotic fractures such as hypoestrogenism or an unbalanced diet are relevant, risk factors vary in animals [6].

References

1. Helfrich, M. H. & Ralston, S. H. (2012). *Bone Research protocols*. S.H. Ralston (Ed.). Humana Press.
2. Sözen, T., Özışık, L., & Başaran, N. Ç. (2017). An overview and management of osteoporosis. *European Journal of Rheumatology*. 4(1), 46–56.
3. Van 't Hof, R. J., Rose, L., Bassonga, E., & Daroszewska, A. (2017). Open-source software for semi-automated histomorphometry of bone resorption and formation parameters. Bone. 99, 69–79.
4. Dempster, D.W., Compston, J.E., Drezner, M.K., Glorieux, F.H., Kanis, J.A., Malluche, H., Meunier, P.J., Ott, S.M., Recker, R.R. & Parfitt, A.M. (2013), Standardized nomenclature, symbols, and units for bone histomorphometry: A 2012 update of the report of the ASBMR Histomorphometry Nomenclature Committee. *J Bone Miner Res.* 28(1), 2–17.
5. Turner A. S. (2001). Animal models of osteoporosis--necessity and limitations. *European cells & materials*. 1, 66–81.
6. Reinwald, S., & Burr, D. (2008). Review of nonprimate, large animal models for osteoporosis research. *Journal of bone and mineral research : the official journal of the American Society for Bone and Mineral Research*, 23(9), 1353–1368.

AN IN-SILICO PIPELINE FOR PATIENT-SPECIFIC HAEMODYNAMIC ANALYSIS OF THE AORTA

Scott M. Black (1), Craig Maclean (2), Pauline Hall Barrientos (3), Konstantinos Ritos (4,5), Asimina Kazakidi (1)

1. Department of Biomedical Engineering, University of Strathclyde, Glasgow, UK
2. Research and Development, Terumo Aortic, Glasgow, UK
3. Clinical Physics, Queen Elizabeth University Hospital, NHS Greater Glasgow & Clyde, Glasgow, UK
4. Department of Mechanical and Aerospace Engineering, Glasgow, UK
5. Department of Mechanical Engineering, University of Thessaly, Volos, Greece

Introduction

Vascular stent-grafts are frequently used to treat aortic pathologies by replacing the function of the vessel wall. For surgical treatment planning and long-term success, detailed understanding of the aortic geometry and blood flow regime is essential. With computational fluid dynamics (CFD), versatile models can be created to investigate aortic haemodynamics *in-silico*. This study introduces a pipeline for patient-specific CFD model generation in healthy, diseased, and post-surgical cases, integrating 4D flow-magnetic resonance imaging (4D Flow-MRI) and computed tomography (CT) for geometry reconstruction and boundary condition (BC) optimization.

Methods

Three-dimensional (3D) aortae were reconstructed from CT and 4D Flow-MRI images. For healthy and stented cases, a novel approach was utilized generate a dataset from 4D Flow-MRI images for model reconstruction (Figure 1). Here, a temporal composite image at each axial slice was created from multiple cardiac time-steps, where luminal signal intensity, and therefore contrast, was proportional to blood velocity magnitude. To generate patient-specific BCs, a zero-dimensional (0D) three-element Windkessel model (3EWM) was coupled to each terminal branch in a reduced order, one-dimensional (1D) model. In this coupled 0D-1D numerical framework, the 3EWM parameters were optimized with respect to *in-vivo* blood flow waveforms extracted from 4D Flow-MRI. Thereafter, these 3EWM BCs were coupled to the terminal branches of the CT and 4D Flow-MRI-derived 3D models. The MRI-obtained velocity profile at the ascending aorta was then prescribed at the inlet, thereby generating a fully patient specific, coupled, 0D-3D CFD model.

Results

4D Flow-MRI derived composite images yielded high contrast within the vessel lumen of the aorta and main branches. From the reconstructed models, vessel radius, curvature, and tortuosity were successfully validated ($p<0.05$) against the corresponding CT gold standard. CT based reconstruction was required for regions of complex dissection. Reduced order modelling permitted rapid optimization of the 3EWM parameters, thus generating BCs which yielded a perfusion distribution throughout the aortae which was comparable with *in-vivo* data. Quantification of clinically relevant near-wall hemodynamic parameters including time-averaged wall shear stress (TAWSS) and oscillatory shear index (OSI) was possible from the 0D-3D coupled models [1].

Discussion

The multi-modality, multi-dimensional combination of 4D Flow-MRI, CT, and CFD granted unparalleled visualization and quantification of blood flow in healthy, diseased, and stented cases. These CFD models may be used to generate healthy reference data, enhance diagnostic capabilities, and predict the post-surgical blood flow regime and haemodynamics following stent-graft deployment. Further, the outlined pipeline for CFD model creation may be utilised in cases where CT is not available, not possible, or avoided where feasible, for example when screening for aortic disease, pregnant women, or children.

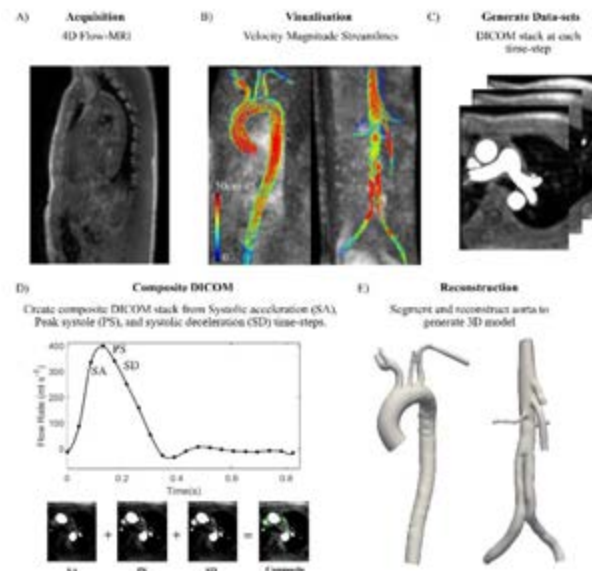*Figure 1: 4D Flow-MRI based CFD model generation pipeline, illustrating A) Acquisition, B) Velocity streamline visualization, C) DICOM image extraction at multiple cardiac time-steps, D) Temporal composite image creation from systolic acceleration, peak systole, and systolic deceleration, E) 3D model reconstruction.*

References

1. C. Celestin et al, Paediatric Cardiology 36:600-615, 2015.

NEAR WALL DYNAMICS OF A TILTED LIGHTHOUSE RETURN CANNULA

Francesco Fiusco (1), Lars Mikael Broman (2,3), Lisa Prahl Wittberg (1)

1. FLOW, Dept. Engineering Mechanics, KTH, Sweden; 2. ECMO Center Karolinska, Karolinska University Hospital, Sweden; 3. Dept. Physiology and Pharmacology, Karolinska Institutet, Sweden.

Introduction

Extracorporeal membrane oxygenation (ECMO) is a life-saving therapy for the critically ill providing heart and/or lung support. The circuit is comprised of a blood pump, membrane oxygenator with heat exchanger, cannulae for drainage and reinfusion of blood from/to the patient, and tubing with connectors. However, its use is associated with risk of both hemolysis and mechanically driven platelet activation[1]. Thus, a detailed knowledge of the flow structures developing in the various components and their sensitivity to boundary conditions, fluid modelling and geometrical features is required to improve treatment and clinical outcomes. In this work, the influence of positioning of the return cannula is investigated.

Methods

The geometry consisted of an external tube representing the blood vessel and a lighthouse tip (single stage) rigid cannula placed in a tilted position towards the vessel wall to simulate a non-centered cannula. Computational Fluid Dynamics (CFD) using Large Eddy Simulation (LES) was applied to investigate the flow structures developing in the domain, especially in the near-wall region. The simulations were carried out using both water and a Newtonian blood analog with different boundary conditions, as shown in Table 1.

Fluid	Cannula flow (L/min)	Co-flow (L/min)
Water	2.6	1.3
Blood analog	3.9	3.9
Blood analog	6.0	3.9
Blood analog	7.8	3.9

Table 1: Investigated flow cases

Results

A time-averaged flow field is shown in Figure 1. The results showed that a large recirculation zone developed downstream of the cannula (red arrow), on the opposite side from the jet. Moreover, small recirculation cells were visible between the side holes and the vessel wall (red circles), creating counter-rotating vortices. The amount of volume flow reinfused through the side holes was small compared to the end hole. Similar levels of shear were achieved as for a centered cannula case. When tilted, a force in the crossflow direction was created (black arrow), indicating that if allowing the cannula to move with the flow-imposed stresses, this force can act to bring the cannula back to a more central position.

Discussion

The results showed that levels of shear rate compatible with platelet activation were reached in parts of the domain. In both the centered and tilted case, the amount of fluid reinfused through the side holes was minor compared to the end hole. However, the presence of the side holes is hypothesized to provide a beneficial effect, inducing a normal force preventing the cannula from attaching to the wall. The small recirculation zones between the side holes and the vessel wall may lead to prolonged residence times of particles caught in that motion. A strong backflow was observed downstream of the cannula in the opposite direction with respect to the jet. Platelets caught in such flow structures are at higher risk of activation due to the prolonged exposure to shear stresses.
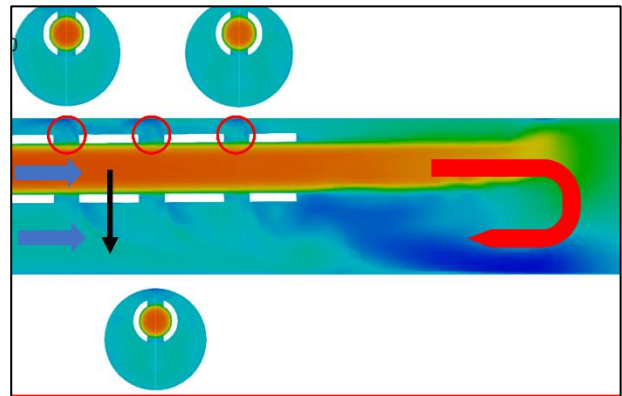
Figure 1: Time averaged flow field of a case using water. The red arrow highlights the backflow region downstream of the cannula, whereas the red circles show the small recirculation zones at the side holes. The black arrow shows the direction of the stabilizing force; the blue arrows indicate the incoming flow direction.

References

1. Olson, S.et al., ASAIO, 67:290–296, 2021.

Acknowledgements

UMBILICAL CORDS ABNORMALITIES CLASSIFICATION BASED ON FLOW SIGNALS FROM DOPPLER ULTRASOUND SIMULATOR

Sara Naftali (1), Yuval Nareznoy Ashkenazi (1), Anat Ratnovsky (1)

1. School of Medical Engineering, Afeka Academic College of Engineering, Israel;

Introduction

Doppler Ultrasound (DUS) provides two-dimensional cross-sectional real time images of an observed two-dimensional flow field. It is used to measure blood velocity inside umbilical cords (UC) to diagnose abnormalities in terms of blood flow and vessel's morphology. However, a professional reading of DUS screening is highly relying on physician skills and experience. A dynamic simulator for practicing DUS monitoring has been conducted with varied vessel models. The objective of this study was to examine the feasibility of using machine learning methods to classify DUS signals derived from normal and abnormal UC models to its appropriate morphology.

Methods

Flow signals obtained within a dynamic simulator, a system which produces controlled pulsatile flow within different vessel models for DUS. The flow was measured at four locations inside normal and abnormal UC models: A-straight, B-coiled, C-inside a knot and D-at an exit of a knotted UC (Figure 1).
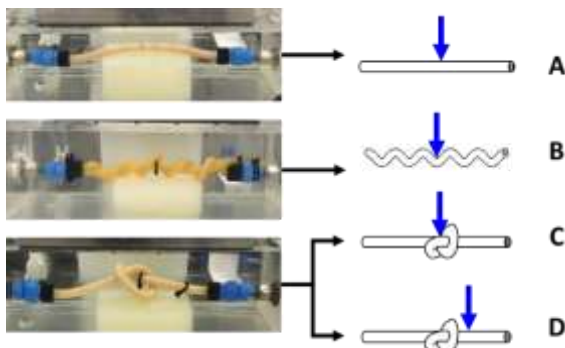
Figure 1: A dynamic Doppler ultrasound simulator that capture the flow field within an UC model applied by controlled pulsatile pump with a circular flow in a pipe connected to a vessel model placed inside a water tank.

DUS images were acquired followed by image processing to extract flow signals which were then segmented into full cycles (Figure 2). A dataset of 250 flow waveform segments for each case was collected. Three feature spaces were tested, the raw signal, its calculated frequency domain, and a set of 12 extracted features per segment.

Dimensionality reduction by principle analysis component (PCA) of the dataset (Figure 3) followed by three classifiers K Nearest Neighbours (KNN), Support Vector Machine (SVM) and Logistic Regression classifiers were conducted. All classification models were 10-fold cross-validated. For each iteration, the test set was composed of 10% of dataset. Two forms of classification were investigated, binary between pairs and multi between all four cases.
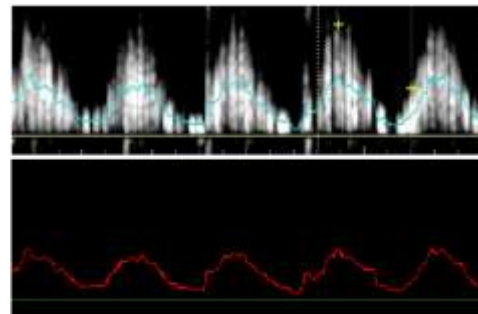
Figure 2: An example of Doppler flow with its average signal and the cleaned extracted average signal after signal processing.
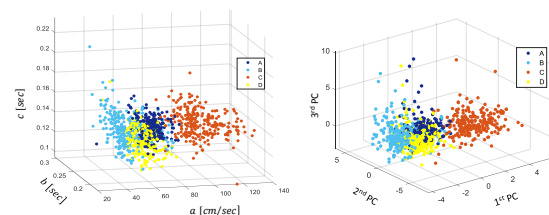
Figure 3: An example of feature mapping before (left) and after (right) PCA.

Results

High classification rates range (93% to 100%) obtained when classifying between case C and other cases, individually. Low (65%-81%) and mild (70%-82%) classification rates found between B and D, and between A and D, respectively. In the multi classification, high results were obtained for C (92%-97%), while low classification rates were obtained for D (32%-68%). Cases A and B achieved mild results of 70%-81% and 52%-69%, correspondingly.

Discussion

DUS signatures can be used to identify UC models to their appropriate morphologies. High classification rates were found when comparing inside knot case to the other cases. Features associated with signal's amplitude were found to have a significant effect on classification. The dynamic simulator may be used to generate data base of flow signals for varies abnormal UC models. The resulted classification accuracy is such that the proposed method shows promise as a decision support system.

STUDY OF THE FLUID BEHAVIOUR IN 3D PRINTED MACROSCAFFOLDS USING CFD ANALYSIS AND PIV

Theresia Baumgartner (1), Tsvetan Yorov (1), Markus Bösenhofer (2,4), Olivier Guillaume (3,5), Aleksandr Ovsianikov (3,5), Michael Harasek (2), Margit Gföhler (1)

1. TU Wien, Institute of Engineering Design and Product Development, Austria, 2. TU Wien, Institute of Chemical Engineering, Environmental and Bioscience Engineering, Austria, 3. TU Wien, Institute of Materials Science and Technology, Austria, 4. K1-MET GmbH, Linz, Austria, 5. Austrian Cluster for Tissue Regeneration (*https://www.tissue-regeneration.at*), Austria

Introduction

Damages affecting bone structures are frequent in modern societies, caused by trauma, diseases or prolonged physical activities. Bones can heal by itself as long as the defects are small [1]. In case of more severe bone damage, scaffolds can be used to provide a template that supports seeded cells to get an optimal environment for their proliferation [2] to re-build the structure. The geometry of the pore network of the scaffold has to provide an appropriate pore size, sufficient permeability and suitable mechanical properties [2,3]. The evaluation of biocompatible properties, such as permeability and wall shear stress (WSS), is challenging because of their influence on cell bioactivity within scaffolds and the micro-size of the scaffold [4]. Therefore, in this work, computational fluid dynamics (CFD) simulations were used to investigate the WSS and to analyse the flow field at different velocities along the scaffold model surface. The numerical results were experimentally validated with µ-particle image velocimetry (PIV) measurements.

Methods

Scaffold geometries, which have a 6 mm long sinusoidal channel with a characteristic length of 0.5 mm, an amplitude of 0.1 mm and different frequencies ($f=3.5$ mm^{-1}, $f=7$ mm^{-1}), were designed using CATIA®. The CFD simulations were performed using the software OpenFOAM®. The scaffolds were meshed using snappyHexMesh. A steady laminar fluid flow was simulated using the solver icoFoam with different inlet velocities, zero pressure outlet and non-slip wall condition. An incompressible Newtonian fluid with a viscosity of 0.000001 m^2/s was assumed. The fluid flow is described by the three-dimensional Navier-Stokes equation. For the µ-PIV experiments, scaffolds were printed by using the Two-Photon polymerisation technique (2PP) based on cross-linking of photosensitive polymers induced by femtosecond laser pulses. The scaffolds were composed of ethoylated trimethylolpropane triacrylate, trimethylolpropane triacrylate (ETA:TTA) and 5 mM of M2CMK photoinitiator.

Results

Two meshes were used to evaluate the mesh dependence of the solution. The surface cell size was reduced by a factor of four in the finer mesh compared to the coarser
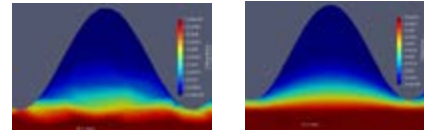
Figure 1: Result of (a) coarse and (b) fine mesh.
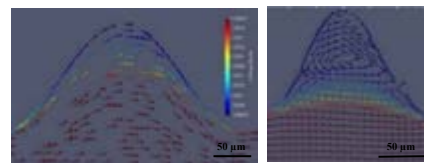
Figure 2: Velocity vector field for an inlet flow of 5 mm/s with a frequency of (a) f=3.5 mm^{-1} *(b) f=7* mm^{-1}.

one. The comparison of the meshes shows a difference in the transition of the velocity profile as depicted in Fig. 1. Changing the frequency also changes the flow field as shown in Fig. 2. The printed 2PP scaffold was used for the µ-PIV experiments to validate the results of the CFD simulations as shown in Fig. 3. A backflow on the top of the cavity with a higher velocity than in the numerical result (Fig. 2b) was observed.
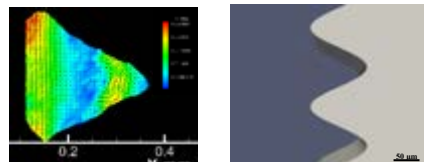
Figure 3: Result of (a) µ-PIV measurement (b) scaffold model surface.

Discussion

The results illustrate the use of CFD to characterise scaffold design and get valuable information on the fluid dynamics for different geometric variations. This is important because changes in the flow field, especially in the regions near the wall, can directly affect the cell behaviour [5].

References

1. Wang et al., Chin. J Mech Eng, 32:19, 2019.
2. Campos Marin et al, Interface Focus, 5(2):20140097, 2015.
3. Singh et al, Mater Today-Proc, 5:18879-18886, 2018.
4. Ali et al, Annals Biomed Eng, 46(12):2023-2035, 2018.
5. Bancrof et al, Tissue Eng, 9(3):549-554,2003.

Acknowledgements

THROMBUS FORMATION IN A STENOTIC CHANNEL; A VISCOELASTIC MATERIAL MODEL

Mohammad Rezaeimoghaddam[(1)], Odyssée Dhaenens[(2)], Antoine Germain[(2)] and Frans van de Vosse[(1)]
1. Department of Biomedical Engineering, Eindhoven University of Technology, Eindhoven, The Netherlands;
2. Department of Biomedical Engineering, Polytech Lyon, Claude Bernard University of Lyon I, Lyon, France

Introduction

Excessive thrombus formation, thrombosis, is a serious clinical condition due to the obstruction of blood flow in a vessel. The prediction of thrombus characteristics under elevated shear rates are important in identifying risks related to thrombus formation [1]. The aim of this study is to introduce a novel coupled scheme using a continuum model of thrombus formation together with the rheological changes of the blood clot as a viscoelastic material model.

Methods

A schematic of the biochemical model [2] which is used in the current study is shown in Figure 1.
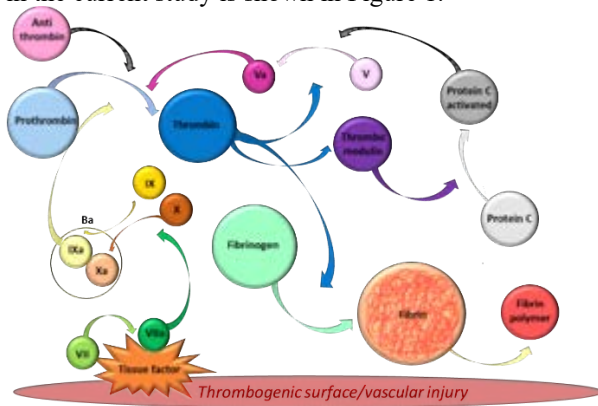
Figure 1: Coagulation cascade used in the model

The transport of fibrinogen and its cleavage to fibrin due to thrombin generation are included in this model. The biochemical model can be described by the convection diffusion and reaction of biochemical agonists into a series of a coupled equations.

$$\frac{\partial [C_i]}{\partial t} + (v.\nabla)C_i = D_i \Delta C_i + S_i(C_j), \qquad (1)$$

Where $[Ci]$ is the concentration of species i, v is the velocity vector, D_i is the diffusivity of species, and $S_i(C_j)$, are the source terms, production/consumption, for the i species. The concentration of prothrombin, thrombin, antithrombin, the total concentration of factor IX and X and their activated form, protein C and its activated form, fibrinogen, fibrin and fibrin polymer are solved. The model is implemented into FLUENT 2021 R1 (ANSYS Inc. PA) Computational fluid dynamics (CFD) software. The computational domain consists of a 2D channel with a height of 40 μm, length of 480 μm and two semi-ellipses which represents stenosis. The stenotic walls (top and bottom) serve as a surface flux boundary condition representing tissue factor coated surface. The Robin boundary condition is applied for adhesion or release of each species on entire the wall. Model parameters, initial concentrations, diffusion coefficients and descriptions can be found in [2]. A

physiologic inflow at the inlet and three-element Windkessel model are prescribed as boundary conditions. The CFD is used to calculate the velocity and pressure fields. The blood is considered as a Newtonian fluid, and fibrin polymer is considered as a viscoelastic material using Oldroyd-B model [3]. Four additional scalar transport equations are used to represents polymer contribution in the Oldroyd-B equation. The value of Deborah number is selected such that the elasticity dominates the stress field. The extra polymeric stresses are introduced as the momentum source terms in the momentum equations.

Results

Thrombus development at t=50s and t=200s colored with velocity magnitude are given in Figure 2. The agonists concentrations and scalar transport of τ_{xx} are demonstrated in Figure 3.
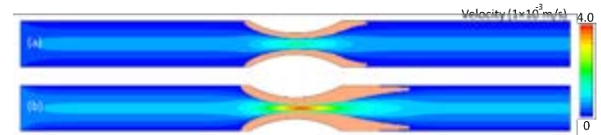
Figure 2: Spatial and temporal evolution of thrombus at (a) t=50s and (b) t=200s.
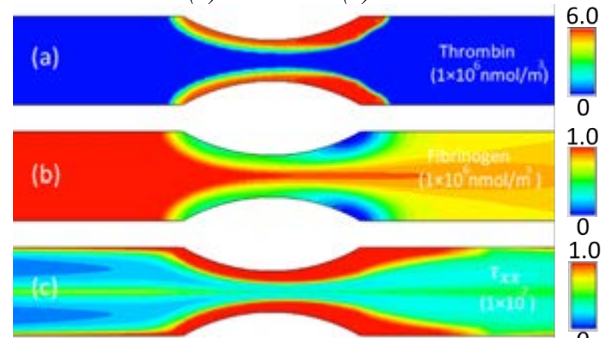
Figure 3: Visualization of (a) thrombin concentration, (b) fibrinogen and (c) Scalar τ_{xx} of Oldroyd-B model.

Discussion

A novel coupled continuum biochemical model to simulate fibrin rich clot has been developed. The kinetics of fibrin formation is shown to be highly related to hemodynamic and Deborah number.

References

[1] M. Rezaeimoghaddam et al. *J. Biomech.*, 2022, doi: 10.1016/j.jbiomech.2021.110915.
[2] A. Bouchnita et al. *Appl. Math. Lett.*, vol. 51, no. 2015, pp. 74–79, 2016, doi: 10.1016/j.aml.2015.07.010.
[3] A. Sequeira et al. *Math. Model. Nat. Phenom.*, vol. 9, no. 6, pp. 34–45, 2014, doi: 10.1051/mmnp/20149604.

Acknowledgements

HIGH DENSITY MICROFLUIDIC TRAP ARRAY GEOMETRIC OPTIMIZATION VIA COMPUTATIONAL FLUID DYNAMICS STUDY

Nicolas Ruyssen (1), Jacques Fattaccioli (2,3), Marie-Caroline Jullien (4), Rachele Allena (5)

1. Institut de Biomécanique Humaine Georges Charpak, Paris, France ;

2. UMR 8640 PASTEUR, Département de Chimie, Ecole Normale Supérieure, 75005 Paris, France ;

3. Institut Pierre-Gilles de Gennes (IPGG), 6 rue Jean Calvin 75005 Paris, France ;

4. Univ. Rennes 1, CNRS, IPR (Institut de Physique de Rennes) UMR 6251 F-3500 Rennes, France ;

5. LJAD, UMR 7351, Université Côte d'Azur, 06100, Nice, France.

Introduction

Microfluidic Trap Arrays (MTAs) appear as very promising tools for the understanding of complex biological phenomena at the single cell scale like cancer development and treatment or immune synapse formation. The MTAs principle is the following: micro-sized objects are diluted inside a fluid going through a microfluidic chamber composed of an array of many traps. While following the fluid flow, objects can encounter traps that isolate them each other. However, it often appears that many traps stay empty even after a long time which can drastically reduce the number of exploitable samples. In this study we built a Computational Fluid Dynamic (CFD) model to optimize MTA's geometry for trapping efficiency.

.

Method

The MTA's nominal geometry is built from parametrized geometric primitives. In the fluid domain, we define the Stokes and continuity equations with the shallow channel approximation. We quantify trapping efficiency (E) by the ratio between the number of traps crossed by at least one streamline and the total number of traps considering 200 streamlines uniformly located on the inlet.

The geometric optimization is performed on 6 parameters: the 5 first parameters modify the chamber's and/or the trap network's geometry keeping regular distances between traps as usual in experimental MTAs. The last parameter modifies trap's relative positions with randomized translations of them. Three studies are conducted: (i) single parametric optimization, (ii) multiparametric optimization and (iii) single optimization with randomized translations on traps positions.

Results

Single parametric studies reveal that every parameter has a strong influence on E (30% variation) but combining the single parameters optimized values leads to a very inefficient geometry.

Multi-parametric optimization results are exposed Figure 1 in terms of stagnation points and streamlines . E is 46% for the non-optimized geometry versus 81% for the optimized geometry.

Randomized translation study results are shown Figure 2. Trapping efficiency is about 81% too.
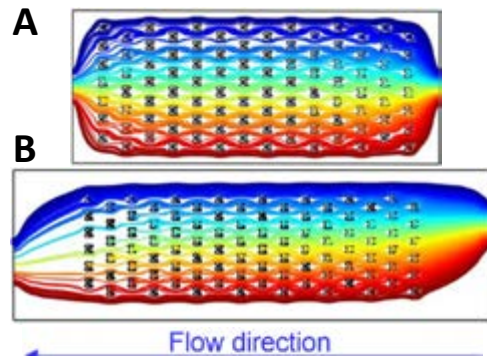
Figure 1: streamlines and stagnation points in the MTA **A:** *before optimization, and* **B:** *after optimization.*
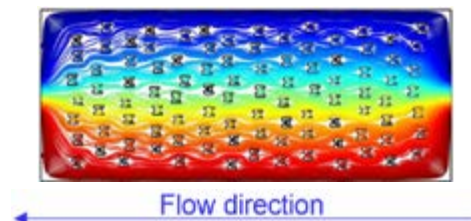
Figure 2: streamlines and stagnation points in the MTA's geometry optimized with randomized trap translations only.

Discussions

Single parametric results suggest that a strong interdependence between parameters exists that justifies the need of a multi-parametric approach.

The multi-parametric optimization geometry creates a thick oblique beam of streamlines that deviates them from their upstream-downstream pattern between traps (Figure 1) that corresponds to an improved version of classique oblique chamber we described previously [2]. We earlier explained that breaking symmetry of the chamber helps trapping [2], this result is here extrapolated by breaking symmetry of the trap network which helps streamlines to invade the chamber (Figure 2) and drastically increases trapping efficiency.

References

1. Mesdjian, O., Ruyssen, N., Jullien, M. C., Allena, R., & Fattaccioli, J. (2021). *Microfluidics and Nanofluidics*, *25*(11), 1–11.

CORRODED MAGNESIUM-BASED SCAFFOLDS FATIGUE STRAIN ACCUMULATION AND MECHANICAL BEHAVIOUR UNDER CYCLIC LOADING

Roxane Bonithon (1), Sarah Davis (2), Mark Morgan (1), Gordon Blunn (2), Aikaterina Karali (1)

1. School of Mechanical and Design Engineering, University of Portsmouth; 2. School of Pharmacy and Biomedical Sciences, University of Portsmouth, UK.

Introduction

Magnesium (Mg) based implants are very promising degradable and osteopromotive materials for regenerative treatment of critical-sized bone defects. Additionally, they must exhibit sufficient mechanical and morphological resemblance to the native bone to provide adequate support and enable initial bone bridging. Digital volume correlation (DVC) combined with high-resolution X-ray computed tomography (XCT) offers a powerful tool to assess the 3D full-field strain [1]. DVC has been used to investigate the initiation and progression of microdamage in bone tissue and Mg scaffolds under compression [2]. However, the relationship between microdamage, residual strain accumulation and corrosion has yet to be investigated. This study aims at employing XCT-based mechanics coupled with DVC to provide insight into the deformation and damage mechanisms under cyclic loading conditions applied to corroded Mg scaffolds.

Methods

Cylindrical fluoride-coated Mg implants (n = 10) dynamically corroded in Hank's balanced solution (0.3 mL/min, 37°C and 5% CO_2) for 2, 8 and 14 days and bovine femoral trabecular bone specimens (n = 2) (Ø6 mm x H6 mm) were prepared and enclosed into brass endcaps. Ten preconditioning cycles were applied at 1-1.5Hz and 0.2% apparent compression. σ/E_0 was calculated where σ is the maximum peak stress and E_0 is the secant modulus at the tenth cycle. The specimens were then cyclically loaded at 0.5Hz for 50, 100 and 200 cycles. The test was performed *in situ* with a loading stage (CT500, 500N, Deben) placed into an XCT system (20μm voxel size, XT H 225, Nikon). Two tomograms were taken after each cyclic step with the specimen loaded and unloaded. 3D full-field strain was computed using DVC (DaVis10, LaVision), with a multipass scheme (110 to 20) and 0% overlap (SDER always < 200μɛ [3]).

Results

Accumulation of corrosion products was clearly visible after 2 days and more pronounced after 14 days (Fig 1). The residual shear strain accumulated was higher after 2 days of corrosion (~ 5000 μɛ maximum; Fig 2) compared to non-corroded scaffolds (~ 500 μɛ maximum), however, a decrease was observed after 14 days (~ 1000 μɛ maximum).
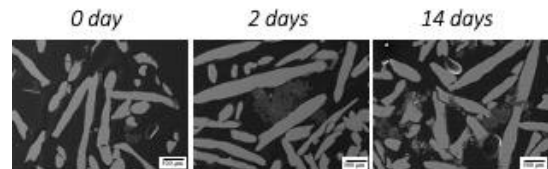
Figure 1: 2D XCT images of the Mg-based scaffolds before and after 2 and 14 days of in vitro corrosion. Scale bar 500 μm.
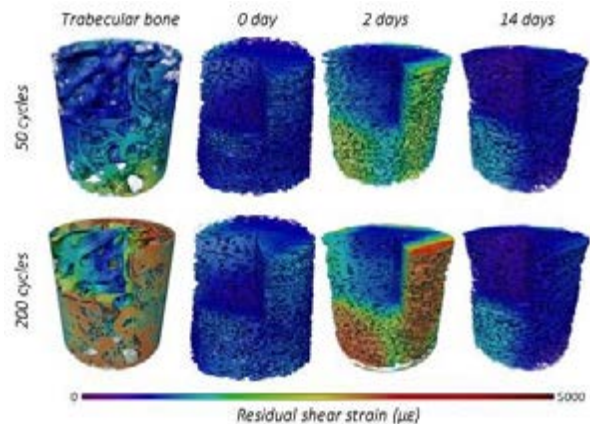
Figure 2: Full-field residual shear strain distribution after 50 (top) and 200 cycles (bottom).

Discussion

The fluoride coating displayed corrosion protection abilities leading to lower *in vitro* corrosion rate (0.6 ± 0.1 mm/year at 14 days) close to the range reported *in vivo* [4]. The corrosion induced mass loss mainly localized at the periphery of the scaffolds. However, no global failure was observed, and the mass loss appeared to be partially counterbalanced by the accumulation of corrosion products trapped in the inner pores at 14 days (Fig 1) which strengthened the global structure (Fig 2). Additionally, hard callus tends to form after 14 days which will further contribute to maintain the mechanical integrity and fatigue resistance of the injured site [5].

References

1. Roberts et al., J Biomech, 47:923-934, 2014
2. Bonithon et al., Acta Biomaterialia 127:338-352, 2021
3. Palanca et al, J Biomech, 58:27-36, 2017.
4. Martinez et al, Acta Biomaterialia, 13:16-31, 2015.
5. Wang & Yeung, Bioactive Materials, 2:224-227, 2017.

BIOREACTOR EVALUTION OF AN ANTIBACTERIAL AND OSTEOGENIC SILICON NITRIDE REINFORCED CRYOGEL SYSTEM

**Seunghun S. Lee[1], Leanid Laganenka[2], Xiaoyu Du[1],
Wolf-Dietrich Hardt[2] and Stephen J. Ferguson[1]**

[1]*Institute for Biomechanics, ETH Zurich, Switzerland,* [2] *Institute of Microbiology, ETH Zurich, Switzerland*

Introduction

Silicon nitride (SiN, [Si_3N_4]) is a promising bioceramic for use in a wide variety of orthopedic applications. Over the past decades, it has been mainly used in industrial applications such as the space shuttle engines, but not in the medical field due to scarce data on the biological effect of SiN. More recently it has been increasingly identified as an emerging material for dental and orthopaedic implant applications. Although a few reports about antibacterial properties and osteoconductivity of SiN have been published, to date, there have been limited studies of SiN-based scaffolds for bone tissue engineering. Here, we developed a silicon nitride reinforced gelatin/chitosan cryogel system (SiN-GC) by loading silicon nitride microparticles into a gelatin/chitosan cryogel (GC), with the aim to produce a biomimetic scaffold with antibacterial and osteogenic properties. In this scaffold system, the GC component provides a hydrophilic and macroporous environment for cells while the SiN component not only provides antibacterial properties and osteoconductivity, but also increases the mechanical strength of the scaffold, to provide enhanced mechanical support for the defect area and a better osteogenic environment.

Methods

First, we analyzed characteristics of SiN-GC groups with different SiN concentrations such as interconnected porosity, mechanical properties and swelling ratio, then we checked apatite forming capacity in simulated body fluid (SBF), protein adsorption capacity and hemolysis rate. Next, we started *in vitro* experiments and investigated an antibacterial effect of SiN-GC against *Escherichia coli* (*E. coli*) and *Staphylococcus aureus* (*S. aureus*) by checking bacterial proliferation rate and attachment to the scaffold. Then, we seeded MC3T3-E1 pre-osteoblast cells to study the cellular activity by examining viability, cell proliferation and morphology. Also, we seeded cells on SiN-GC to investigate mineralization and osteogenic gene expression (*ALP*, *COL1*, *RUNX2* and *OCN*) by Alizarin Red S (ARS) staining and RT-qPCR. Finally, we developed a bioreactor to culture cell-laden scaffolds under cyclic loading (1 hour/day of cyclic compression with 1 Hz of frequency and 10% of strain) to mimic physiological conditions and analyze the osteogenic effect of SiN-GC with ARS staining and RT-qPCR.

Results and Discussions

Incorporation of SiN in the scaffold led to higher elastic modulus, apatite formation in SBF and protein adsorption capacity while keeping the similar level of highly interconnected porosity as GC has, which allows easier cell migration and nutrient flow. We confirmed that all SiN-GC groups showed significantly reduced bacterial proliferation and attachment compared to GC and an increase of SiN concentration in SiN-GC groups led to improved anti-bacterial effect. In addition, for the *in vitro* experiment with MC3T3-E1, the groups with higher SiN concentrations exhibited improved cell proliferation and enhanced morphology. Finally, results from ARS staining and RT-qPCR showed the improved mineralization and upregulated osteogenic gene expressions from SiN-GC compared to GC under both static and cyclic loading conditions in the bioreactor. Furthermore, we confirmed that scaffolds with higher SiN concentrations resulted in higher mineralization and enhanced osteogenesis.

Conclusions

Overall, we confirmed the antibacterial and osteogenic effect of a silicon nitride reinforced cryogel system and the results indicate that silicon nitride has a promising potential to be developed further for bone tissue engineering applications.

Acknowledgements
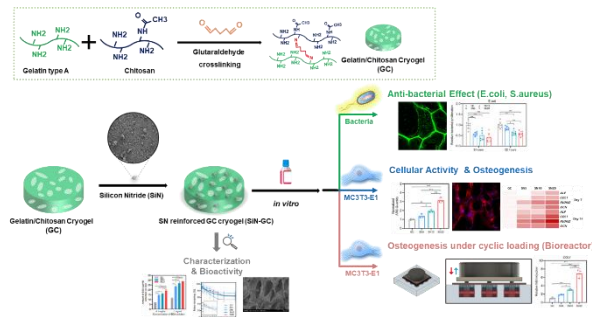
Study summary of silicon nitride reinforced cryogel system.

DYNAMIC MECHANICAL ANALYSIS OF COLLAGEN FIBRILS AND ELECTROSPUN PLLA NANOFIBERS

Mathis Nalbach (1), Alberto Sensini (3), Naoki Motoi (2), Manuel Rufin (1), Orestis G. Andriotis (1), Andrea Zucchelli (3), Georg Schitter (1), Luca Cristofolini (3), Philipp J. Thurner (1)

(1) TU Wien, Austria (2) Kobe University, Japan (3) University of Bologna, Italy

Introduction

Collagen is a ubiquitous structural protein and by that the most abundant protein in human bodies. At the nanoscale, collagen forms the collagen fibrils (CF) with diameters between 50-500 nm. Collagen fibrils show time-dependent material behavior, which suggests that they are viscoelastic. Current available tools and methods are not able to measure the viscoelastic material properties in a reproducible manner. With this study, we present a new method to perform force-controlled dynamic nano-mechanical analysis (DMA) in tension. The method is applied to both individual CFs, as well as, electrospun PLLA nanofibers (PLLA). Electrospinning is an emerging technique for fabrication of nanofibrous biomaterials similar to CFs of musculoskeletal tissues [1, 2].

Methods
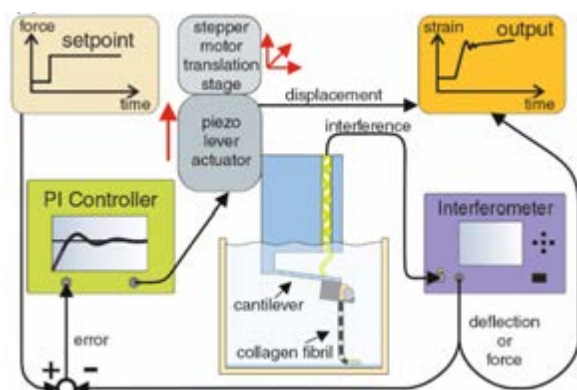
Fig. 1: Schematics of the NanoTens [3] in closed-loop configuration. A CF or another nanofiber is tethered between the cantilever of the force probe and a microscope slide. The piezo position is controlled by a PI controller to maintain a force setpoint.

Tensile tests were conducted with the NanoTens (Fig.1) [3]. Two types of nanofibers, mouse tail tendon collagen fibrils and electrospun PLLA nanofibers (16% (w/v) dissolved in DCM:DMF=65:35 (v/v), spun on a high-speed rotating drum collector [4]), were deposited on microscope slides, glued on one end to the slide and a magnetic bead was attached to the other end. After immersion in PBS, the magnetic bead was lifted together with the fiber by magnetic force and picked up by a microgripper attached to a force probe. Force-control was achieved by controlling the piezo position with a PI controller such that a setpoint force was reached and maintained. NanoDMA was conducted applying a sinusoidal force with 1 µN and 2 µN mean, 200 nN amplitude at 0.1 Hz and 1 Hz. After nanoDMA,

all fibers were tested at 5% strain/s until failure or reaching a maximum force of 10 µN.

Results
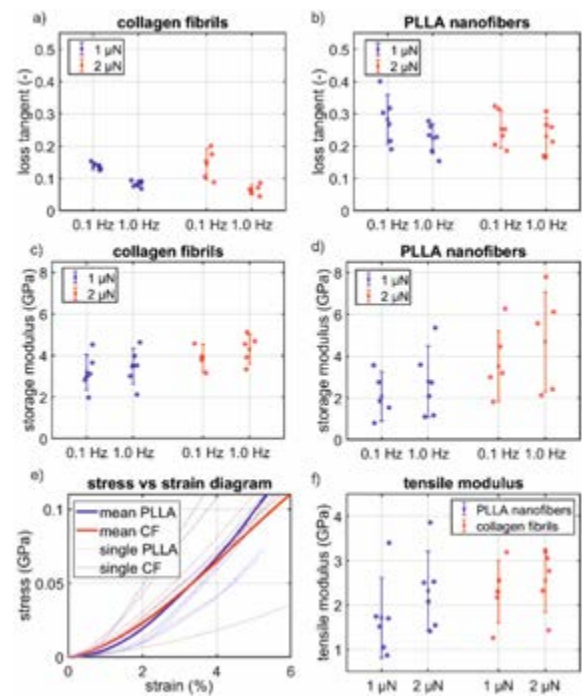
Fig. 2: a) and b) depict the loss tangent of CFs and PLLAs. The loading frequency affected the loss tangent in CFs and was significantly lower for CFs than for PLLA. The elastic response (storage modulus) was similar as seen in c) and d). Monotonic tensile tests result in a qualitatively similar behavior (e)) and no significant differences of the tensile modulus at 1 µN and 2 µN load (f)).

We observe similar elastic behavior in monotonic tensile tests and elastic response in nanoDMA for CFs and PLLAs. However, the loss modulus and tangent of PLLAs is significantly higher compared to CFs (Fig. 2).

Discussion

Differences in dynamic material behavior may arise due to the molecular structure and arrangement. In PLLA, organization of the molecules is rather amorphous in contrast to highly organized structure in CFs. The PLLA organization may result in elevated molecular friction and thus energy dissipation in the force regime investigated here.

References

1. Sensini and Cristofolini, Materials, 11(10), 2018.
2. Sensini et al., Front Bioeng Biotech. 2(9), 2021.
3. Nalbach et al., Rev. Sci. Instrum., 2022. Submitted.
4. Sensini et al., Biofabrication, 11(3), 2019.

NATURE-INSPIRED MEMBRANES FOR ARTIFICIAL RESPIRATION – PRODUCTION OF MICRO-STRUCTURED POLYMER HOLLOW FIBERS

Markus Pekovits (1,2), Paul Ecker (1,2), Fatima Imran (2), Julia Agnieszka Kalarus (3), Michael Harasek (2), Margit Gfoehler (1)

1. Institute of Engineering Design and Product Development, TU Wien, Vienna, Austria; 2. Institute of Chemical, Environmental and Bioscience Engineering, TU Wien, Vienna, Austria; 3. Institute of Applied Synthetic Chemistry, TU Wien, Vienna, Austria

Introduction

Modern respiratory support devices such as extracorporeal membrane oxygenators use state-of-the-art technology to provide the best possible support for the weakened human lungs of patients suffering from severe forms of respiratory disease. However, the survival rate after ECMO treatment is still low at 60-70 % [1]. Part of this mortality rate can be attributed to hemodynamic complications caused by the blood prime volume, which is a critical limiting factor for the design and size of oxygenators [2].

A promising approach to making such devices more efficient is demonstrated by nature using the example of fish. Micro-ridges in gills increase the respiratory surface area and lead to transverse flows, promoting oxygen diffusion, resulting in a decreased mass transfer resistance [3]. Recent CFD simulations utilize this biomimetic approach and show that micro-structuring hollow fiber membranes is a viable way to increase the volume to gas exchange area ratio but may also carry the risk of increased thrombus formation [4].

This work presents the production of micro-structured hollow fiber membranes via the non-solvent induced phase separation (NIPS) technique and evaluation of separation performance and flow characteristics.

Methods

Spinnerets with differently designed outlet openings were integrated into our self-developed hollow fiber membrane spinning plant at TU Wien. The plant's design allows for varying all crucial parameters of the NIPS manufacturing process, which ensures that the spun membrane's geometrical structure and consequently the gas separation properties can be influenced. Light and scanning electron microscopy provided a first impression of the geometrical properties of the hollow fiber membranes (Fig. 1).

To quantify the increase in separation performance of the micro-structured fiber, bundles of fibers are assembled into modules and compared with modules prepared from cylindrical fibers with respect to their gas permeance properties. The flow of the deoxygenated blood around the micro-structured shell side of the fiber in the module bundle is investigated using micro-particle measurement technology. For this purpose, an optically accessible, 3D printed flow channel with staggered fiber arrangement is used (Fig. 2), which reveals possible areas of increased thrombus formation.

Results

Fibers were fabricated at room temperature from a 16.6% PES, 4.9% PVP K30, 4.9% PVP K90, 7.2% H_2O polymer blend, dissolved in 66.4% NMP. Deionized water was used as internal bore fluid and external coagulation bath. A spinneret with four flanks arranged as a cross-slot shape served as the contouring structure of the hollow fiber membrane. Fig. 1 shows the most pronounced microstructure observed at 1.8 ml/min flow rate for dope and bore fluid and an air gap length of 5 mm. All flanks are uniformly shaped.

Figure 1: Micro-structured PES-PVP hollow fiber membrane spun with a self-developed spinning plant.

Figure 2: Staggered arrangement of 3D-printed micro-structured fibers in a flow channel.

Discussion

Preliminary spinning trials with micro-structured hollow fiber membranes show that geometry optimization of the outer surface is a promising approach to increase mass transfer in membranes and thus to increase the efficiency of blood oxygenators. Further spinning experiments and variations of parameter settings are required for the manufacturing process.

References

1. Makdisi et al., J Thorac Dis., E166-E176. 2015.
2. Evseev et al., Membr. Membr. Technol. 1, 201-211, 2019.
3. Maina, Journal of Anatomy 201, (4): 281-304, 2002.
4. Ecker et al., Membranes, 11(5):374, 2021.

NANOFIBRE CAPPED MELT ELECTROWRITTEN GRID STRUCTURES MIMICKING THE ARCHITECTURE OF ARTICULAR SURFACES

Matthias X. T. Santschi (1), Lukas Bienz (1), Michael Leunig (2), Stephen J. Ferguson (1)

1. ETH Zurich, Institute for Biomechanics, Zurich, Switzerland
2. Schulthess Clinic, Department of Orthopaedic Surgery, Zurich, Switzerland.

Introduction

Articular surfaces, such as cartilage or the acetabular labrum, act to distribute contact pressure and provide low friction gliding surfaces. Several studies have revealed a strong similarity of the structure of articular surfaces, a network of fine collagen fibrils organized parallel to the joint surfaces [1], overlaid on a distinct deeper structure. Melt Electrowriting (MEW) and Solution Electrospinning (SES) are established methods in the field of tissue engineering to fabricate micro- and nanofibrous constructs [2]. This study aims to recreate the typical characteristics of the structure of articulating surfaces, by creating well defined micro-grid structures using MEW, covered with a fine SES nanofiber mesh, and to evaluate relevant functional parameters.

Methods

Melt Electrowriting. A custom-built MEW device was used to fabricate MEW constructs consisting of microfibres between 15 and 20 µm in diameter and with interfibre distances of 1mm, 500µm and 250µm. Briefly, PCL (PC12, Corbion, NED) was melted at 80°C and extruded using pressurized air at 1bar through a 22G blunt needle. A total of 5.3kV was applied to stabilize and guide the molten polymer towards a glass-covered translating aluminum collector

Sample Preparation. By directly electrospinning a 12% PCL polymer solution onto the prefabricated melt electrowritten scaffold, a thin layer of nanofibers was deposited on top of the well-defined grid. The hybrid scaffolds were cut to rectangular shapes for testing.

Adhesion Force. In a T-peel test adapted from ASTM D1876, two open ends of the hybrid structures were pulled apart at a peel rate of 0.5mm/s, while the required peel force was measured.

Mechanical Properties. A uniaxial tensile test was performed under quasi-static displacement at (0.1mm/s) until a strain of 100% was reached.

Friction. 6 mm discs were mounted in sample holders and loaded against a rotating stainless steel pin with an applied pressure of 0.6 MPa and a rotational speed of 135 RPM. The COF was derived from the recorded normal force and torque using Eq. 1, with µ being the COF, τ the torque and F_N the normal force acting on the tissue surface.

$$\mu = \frac{3 \times \tau}{2 \times F_N \times r} \qquad (1)$$

Results & Discussion

The adhesion force between the SES and the MEW structures was 3.5±0.75N/m. No significant differences were found between the different underlying structures. Visual post-peeling inspection revealed remaining nanofibers on the MEW-construct, suggesting internal failure of the nanofiber membranes being the main contributor to the delamination mechanism.
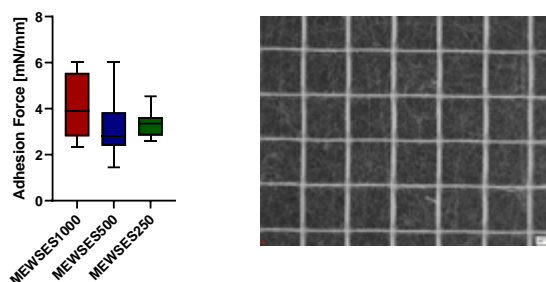
Figure 1: Left: Adhesion force between the electrospun nanofibre and the underlying MEW construct with three different fibre densities. Right: Remnants of nanofibers on the MEW structure after T-peel testing.

Capping MEW structures with a thin layer of nanofibers resulted in a significant increase of the E-Modulus. In addition, nanofibre capped constructs exhibited a significantly reduced coefficient of friction, from 0.203 ± 0.005 to 0.115 ± 0.003, in range with values found for similarly prepared and tested specimens of cartilage, meniscus and the acetabular labrum (work in progress).
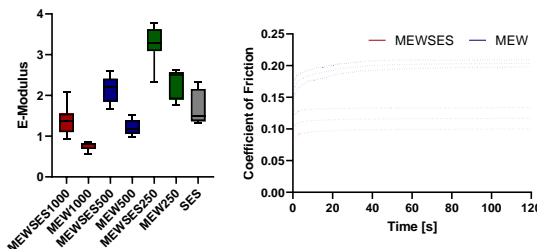
Figure 2: Left: E-Moduli of combined structures as well as MEW and SES samples. Right: Coefficient of friction over 120s for combined and MEW structures.

In summary, this study provides further insight into potential benefits of combining well established methods in tissue engineering in terms of interlayer adhesion, tensile properties and the influence of the surface structure on tribological properties.

Acknowledgment

References

1. Boettcher, K. et al. (2016) Acta biomaterialia, 29, 180-187.
2. Muerza-Cascante, M. L. et al. Tissue Engineering Part B: Reviews, 21(2), 187-202.

MULTISCALE PERFORMANCES OF ELECTROSPUN BIOSTABLE DEVICES FOR TENDON AND LIGAMENT REPLACEMENT

Alberto Sensini (1), Carlo Gotti (1), Chiara Gualandi (1), Maria Vittoria Ricioppo (1), Gregorio Marchiori (2), Nicola Sancisi (1), Milena Fini (2), Maria Letizia Focarete (1), Luca Cristofolini (1), Andrea Zucchelli (1)

1.University of Bologna, Italy; 2. IRCCS Rizzoli Orthopedic Institute, Italy

Introduction

Tendons and ligaments (T/L) are connective tissues with a complex multiscale structure and mechanical properties [1]. Electrospinning can replicate T/L from the fibrillar-level up to the whole tissue [2]. Electrospun nylon6,6 (NY) and polyurethane (PU) are suitable polymers for the musculoskeletal tissue replacement [3, 4]. In this study, we produced electrospun NY fascicle-inspired bundles, grouping them with electrospun membranes of NY or PU (simulating the collagen sheath covering the natural tissues) in different T/L levels of hierarchical complexity. The aim of the study was to identify the relationship between the structure and mechanics of these devices when their hierarchical complexity was increased, and the materials of membranes was changed.

Methods

Two solutions were electrospun: a) 15% (w/v) of NY dissolved in TFA:AC=50:50 (v/v); b) 25% (w/v) of PU dissolved in THF:DMF=70:30 (v/v). Mats of aligned NY nanofibers were electrospun on a drum collector and wrapped up on the drum to obtain ring-shaped bundles (RB). To mimic the different levels of aggregation of T/L (i.e. fascicles, tertiary fiber bundles and whole tissue), the NY bundles were grouped with electrospun membranes of NY or PU (replicating the endotenon/endoligament and epitenon/epiligament) using a custom-made machine. This made it possible to obtain: i) Tertiary Structures (TS); ii) 1-Level Structures (1LS); iii) 2-Level Structures (2LS). The orientation of nanofibers (bundles and membranes) was investigated using ImageJ on SEM images, and the morphology of the structures were investigated using SEM and microCT (voxel size = 9 μm) (Fig.1). The mechanical properties were investigated (bundles: n=10; TS, 1LS, 2LS: n=3) with a monotonic tensile test to failure (strain-rate of 0.33%s^{-1}). The strains of membranes (ε) (axial and transversal) were manually calculated on high-resolution images (at 0%, 25%, 50%, 75% and 100% of the failure force of each specimen) using a camera synchronised with the testing machine.

Results & Discussion

The nanofibers (diameters = 250-150 nm), bundles (diameters = 650-550 μm) and hierarchical structures (diameters: TS $\cong$ 1.5 mm; 1LS $\cong$ 3 mm; 2LS $\cong$ 4 mm) showed a morphology similar to the T/L counterpart. The nanofibers were preferentially axially aligned in the bundles (range 0°-15° $\cong$ 64%) and showed an incremental degree of circumferential orientation in the membranes, depending on the material used and the hierarchical complexity of the structures (Fig.1).
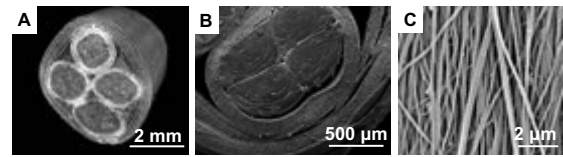
Figure 1: A) MicroCT of a 2LS-NY; B) SEM image of a 2LS-NY; C) Nylon6.6 aligned nanofibers of bundles.

The mechanical properties of the structures showed nonlinear biomimetic behavior with strong dependence on the material used for the membranes (Fig.2). PU membranes, being more deformable than NY membranes, allowed a reduction of stress concentrations, increasing failure force. Moreover, the stresses and elastic moduli calculated using volume fraction (σ_{net}, E_{net}) were significantly higher than those calculated using cross-sectional area (σ_{app}, E_{app}), the latter not considering the contribution of material porosity (Table 1).
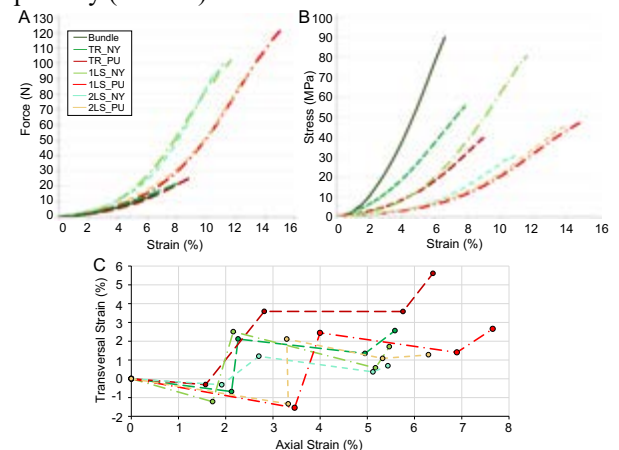
Figure 2: Mechanical behavior of structures: A) force-strain curves; B) net stress-strain curves; C) transversal-axial strain of the membranes.

	RB	TS NY	TS PU	1LS NY	1LS PU	2LS NY	2LS PU
F_F (N)	13.9 ±2.8	21.4 ±3.7	32.1 ±5.2	94.7 ±7.6	127 ±6	82.7 ±12	111 ±6
σ_{Fapp} (MPa)	23.9 ±5.9	13.4 ±2.6	12.6 ±2.3	13.9 ±1.2	22.1 ±5.0	5.9 ±0.4	8.7 ±2.4
σ_{Fnet} (MPa)	82.6 ±6.7	54.2 ±9.1	39.6 ±1.5	62.1 ±17.4	66 ±16	25 ±4.7	35.1 ±10.8
ε_F (%)	6.7 ±0.7	7.7 ±0.7	9.3 ±0.4	10.3 ±1.2	16.1 ±1.1	10.4 ±0.5	12.9 ±1.6
E_{app} (MPa)	475 ±90	256 ±45	208 ±40	226 ±18	272 ±78	104 ±7	122 ±47
E_{net} (MPa)	1773 ±112	1018 ±127	635 ±45	976 ±184	782 ±204	400 ±93	452 ±110

Table 1: Mechanical properties of the electrospun structures.

References

1. Goh et al., J Biomed Nanotechnol, 10(10):2464-507, 2014.
2. Sensini and Cristofolini, Materials, 11(10), 1963, 2018.
3. Sensini et al., Med Eng & Phys, 71:79-90, 2019.
4. Gotti et al., Frontiers Bioeng Biotech, 8:767, 2020.

ALIGNED ELECTROSPUN FIBRES GUIDE COLLAGEN DEPOSITION TO SUPPORT A LAMELLA-LIKE TWISTED ORIENTATION BY MSCS

Alice J Hann[1,2], Gifty Tetteh[2], Nicola H Green[1,2], Frederik Claeyssens[1,2], Gwendolen C Reilly[2,1]

*Science and Engineering, Kroto Research Institute, University of Sheffield, Sheffield, United Kingdom[1],
Department of Materials Science and Engineering, INSIGNEO Institute for in silico Medicine, University of
Sheffield, Sheffield, United Kingdom[2]*

Introduction

In cortical bone, collagen is organised into a lamellar structure, with highly aligned collagen sheets packed into a "twisted plywood" configuration, contributing to its strength and toughness. However, reproducing this structural anisotropy in laboratory-grown bone-like matrices is highly challenging. In a previous unpublished study within our laboratory, it was seen that when mature late-osteoblast-like cells, MLO-A5, were cultured on aligned polyurethane fibres, collagen grew initially along the direction of the fibres. Above the scaffold, collagen was deposited in a direction offset to the initial substrate layer, and continued in subsequent layers, creating a lamellae-like twisted-plywood structure. In this study we aimed to test whether human cells at an early stage of osteogenic differentiation would deposit collagen exhibiting a twisted plywood deposition behaviour and therefore be able to provide a model system of laboratory-grown lamellae for use as a 3D model system of bone formation.

Methods

Aligned and non-aligned polycaprolactone (PCL) nanofibers were fabricated by electrospinning and resulting fibres treated with air plasma. hTERT Y201 immortalised human MSCs [1] were seeded directly onto the scaffolds and after 3 days of culture were supplemented with osteogenic induction media and cultured for a further 28 days. On days 14, 21 and 28 samples were stained for calcium deposition using Alizarin Red stain (ARS) and collagen deposition using Sirius Red stain (SRS). Collagen was also imaged using second harmonic generation (SHG) to obtain z-stack images of each sample. Z-stacks were segmented into 5µM sub-sections and the directionality of fibres in each section was analysed using the ImageJ "Directionality" Plug-in.

Results

As expected, collagen deposition was initially shown to orientate along the direction of the aligned PCL fibres. At D21, however, a new orientation could be observed, with collagen layers having a twist in the anti-clockwise direction compared with their substrate layer with an average change in orientation of $16.53° \pm 13.22$. By D28, the change in orientation had further progressed from the initial direction of the PCL fibres by 53.1 ± 15.6. For non-aligned scaffolds there was no noticeable collagen directionality within the scaffolds at any time point.

Mineral and collagen stains showed that there were no significant differences in quantities of matrix produced within either scaffold type.
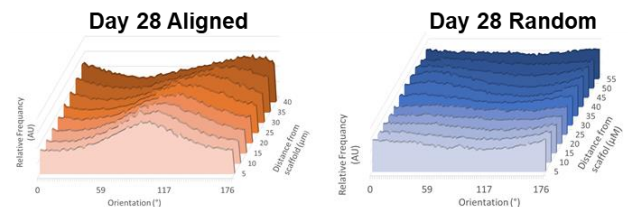
Figure 1: 3D histograms highlighting shifts in the peak orientation of collagen fibres in relation to depth for each 5µm stack of SHG slices. Each histogram is of a single Z-stack that is deemed representative of 4 fields of view and 6 scaffolds examined for each condition.

Discussion

Within this work, we demonstrated a change in collagen direction comparable to that seen within *in vivo* human lamellae, which shows a gradual change in fibril direction between 10-60° from the initial orientation of the fibrils closest to the osteon's centre. However, lamellae are generally shown to have a periodicity of about 5-7µm, which is much more compact than the depth of 35-45µm which was observed within this study. Further work is needed to explore the mechanisms behind this, as this may provide an insight into how collagen organizes into tissue-specific structures. A method to produce a more cortical bone like structure may be valuable for a variety of applications, including the development of more accurate models of bone for high throughput drug testing, bone graft substitutes and barrier membranes.

References

[1] S. James *et al.*, "Multiparameter Analysis of Human Bone Marrow Stromal Cells Identifies Distinct Immunomodulatory and Differentiation-Competent Subtypes," *Stem Cell Reports*, vol. 4, no. 6, pp. 1004–1015, Jun. 2015.

Acknowledgements

A FRAMEWORK TOWARDS THE DESIGN OF TUNABLE AND GRADED OPEN-CELL BONE SCAFFOLDS WITH ANISOTROPIC PROPERTIES

K. Cheikho (1), C. Laurent (1), J.-F. Ganghoffer (1)

1. *Université de Lorraine, CNRS, Arts et Métiers ParisTech, LEM3, Nancy, France*

1. Introduction

The selection of a suited scaffold geometry requires the definition of a scaffold with adapted morphology and properties, since these factors condition cell colonization and bone tissue generation [1]. Triply Periodic Minimal Surfaces (TPMS) have gained a growing interest due to their high surface-to-volume ratio and easy structural modulation [2]. However, they are often associated with isotropic mechanical properties while native bone tissue is far from being isotropic [3,4] and they are limitedly compatible with large pore sizes gradient suited for new tissue growth [5]. In a recent study [6], we have presented an original framework to design graded cylindrical scaffold cross-sections by mapping a perfectly periodic reference domain in 2D onto a circular domain. In the current contribution, we explore the design of a 3D open-cell scaffold from 2D cross-sections issued from the quasi-periodic mapping of a hexachiral unit cell (UC). This UC was selected based on a previous study [6], due to its associated low radial properties suitable for mini-invasive positioning. We test the assumption that a periodic repetition of these cross-sections in the longitudinal direction allows to create versatile reachable apparent anisotropic mechanical properties matching the native bone properties.

2. Methods

The generation of 3D scaffolds is done in two successive steps. First, a conformal circular transformation is applied to a given periodic UC to create a porous cross-section (x-y) with graded pore size from the core to the periphery of the macrostructure, as illustrated in Fig. 1.a. The second step is to create a sequence of Connecting Elements (CE) in the (z) direction that will link the cross-sections together towards an open-cell structure. As an illustration in Fig. 1.a, we present three scaffolds based on a hexachiral UC called HCN-PT (Periodic transformation in x-y direction with vertical CE), HCN-CT (Circular transformation in x-y direction with vertical CE) and HCN-HCT (Circular transformation in x-y direction with helicoidal CE) respectively. These three selected designs exhibit the same porosity of 74%. The mechanical apparent properties are computed from a FE method, by deriving the internal energy associated with elementary virtual strain fields as described in [7].

3. Results and discussion

In Fig. 1.b, we show the range of radial bulk modulus K, axial elastic modulus E_z and apparent Poisson's ratio of the three geometries selected as a particular illustration of this type of scaffolds. As Fig 1.c shows, the

configuration HCN-CT offering the pore size gradient results in the same axial properties as the periodic unit cell HCN-PT, with an axial modulus E_z=250MPa, while the helicoidal configuration has an axial modulus reduced to E_z=65MPa (PLA is selected as the base material). This methodology offers a tunable parameters to be added to the large versatility of reachable cross-sectional properties.
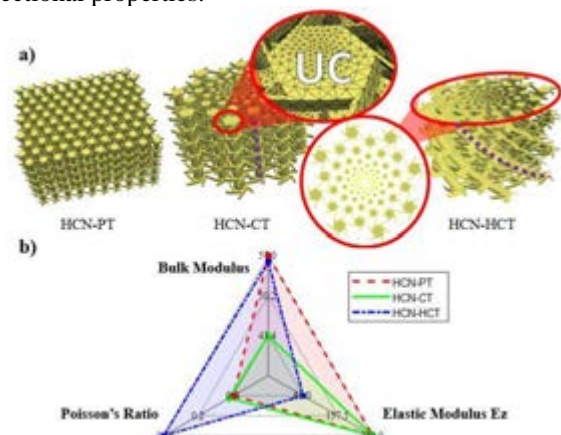
Figure 1: Design of 3D open-cell scaffolds, a) HCN-PT, HCN-CT and HCN-HCT configurations, b) Apparent mechanical properties

4. Conclusion

The present work reports a general framework to generate tunable open-cell graded scaffold geometries from the mapping of a periodic reference UC, and to calculate the apparent properties in the quasi-periodic domain. Configurations based on a hexachiral UC are explored as an illustration, and results emphasize the versatility of the reachable apparent mechanical properties that may be tuned independently in the cross-sectional and longitudinal directions.

References

1. Bobbert et Zadpoor, J. Mater. Chem. B 5, 6175-6192, 2017.
2. Afshar et al, J. Mech. Behav. Biomed. Mater. 62, 481-494, 2016.
3. Li et al, J. Mech. Behav. Biomed. Mater. 21, 109-120, 2013.
4. Ruegg et al, Current Dir. in Biomed. Eng. 3, 607-611, 2017.
5. Sobral et al, J. Acta Biomateriala 7, 1009-1018, 2011
6. Cheikho et al, J. Mech. Behav. Biomech. Mater. 125, 104887, 2022.
7. Goda et Ganghoffer, Comp. Struct. 141, 292, 2016.

Acknowledgements

SURFACE MODIFICATIONS TO PROMOTE THE IN VITRO OSTEOCONDUCTIVITY OF UHMWPE FABRICS FOR THE BIOAID

C.A.M. Jacobs (1), E.E.A. Cramer (1,2), A.A. Dias (3), H. Smelt (3), S. Hofmann (1,2), K. Ito (1,2)

1. Orthopaedic Biomechanics, Dept. of Biomedical Engineering, Eindhoven University of Technology, the Netherlands; 2. Institute for Complex Molecular Systems, Eindhoven University of Technology, the Netherlands; 3. DSM Biomedical, Chemelot Brightland Campus, the Netherlands

Introduction

A novel biomimetic artificial intervertebral disc (bioAID) for the cervical spine was developed containing a hydrogel core representing the nucleus pulposus, an ultra-high molecular weight polyethylene (UHMWPE) fiber jacket as annulus fibrosis and titanium endplates with pins for mechanical fixation (Fig. 1). Osseointegration of the UHMWPE fibers to adjacent boney structures is required to achieve proper biomimetic behavior and to provide long-term stability [1]. Therefore, the aim of this study was to assess the effect of plasma treatment and hydroxy apatite (HA) particle embedment on the osteoconductivity of fabrics made of UHMWPE yarns.
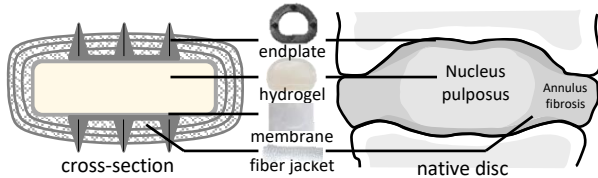
Figure 1: Schematic representation of bioAID design.

Materials and Methods

2D weft-knitted UHMWPE fabric groups were: non-treated (N), plasma-treated (PT), 10% HA loaded-fibers (10%HA), plasma-treated 10% HA fibers (PT-10%HA), 15% HA loaded-fibers (15%HA) and plasma-treated 15%HA fibers (PT-15%HA) [2]. A '2.5D' culture using mesenchymal stromal cells for 14 days was performed. After 2, 7 and 14 days, cell adherence on the surface was assessed using scanning electron microscopy (SEM), quantifying DNA content and cell viability with PrestoBlue assay. After 14 days, osteoblast differentiation was verified using alkaline phosphatase activity assay. Mineralization was assessed with SEM images and EDX analysis.

Results

On day 2, both metabolic activity and DNA content was increased for groups that were plasma treated (PT, PT-10%HA and PT-15%HA) compared to the same surfaces without treatment (Fig. 2AB). This was verified by SEM on day 2 for all groups (not shown). However, at day 7 and 14, the difference in metabolic activity and DNA content became non-significant (data not shown). At day 14, ALP activity of HA loaded and PT groups (PT-10%HA, PT-15%HA) were highest (Fig. 2C). SEM/EDX analysis at day 14 also demonstrated the presence of mineralization nodules for all groups (Fig. 2D).
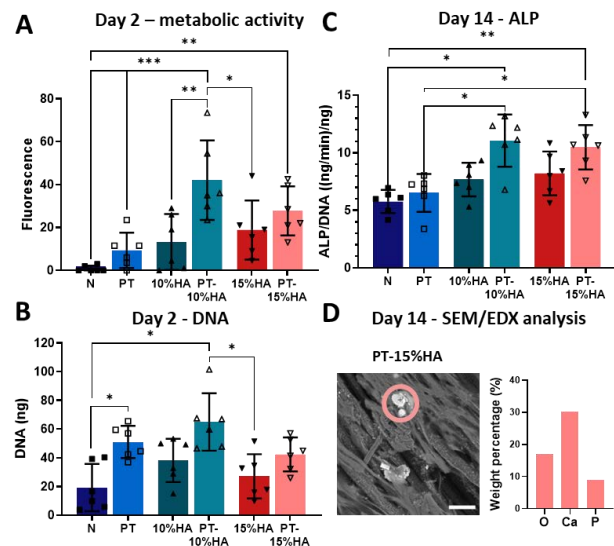
Figure 2: A: Metabolic activity (fluorescence, mean ±SD) on day 2. B: DNA content (ng) on day 2. C: ALP normalized to DNA on day 14. D: representative SEM/EDX result of PT-15%HA group.

Discussion

Plasma treated samples showed increased initial cell adherence, indicating importance of hydrophilicity for cell attachment [3]. However, only the groups that contained HA loaded fibers and were plasma treated resulted in both an increased cell adherence and increased ALP activity. This indicates a combined effect of applying plasma treatment on the HA containing fabrics resulting in increased hydrophilicity, more HA particles being exposed at the surface and therefore also increased surface roughness which are known factors to increase osteoconductivity [4]. Based on these results, combination of HA loaded UHMWPE fibers and plasma treatment provide the most promising fabric surface for facilitating bony ingrowth.

References

1. Van den Broek et al., J Biomech, 45:134-140, 2012
2. Dias et al., US Patent 2021/0299332 A1, 2021
3. More et al., Appl Surf Sci., 144665, 2019
4. Blatt et al., J. Craniomaxillofacial Surg., 46:453-460, 2018

Acknowledgements

OSTEOARTHRITIC KNEES CAN BE QUANTIFIED WITH IN VIVO SCANNERS

Paolo Antonacci (1), Jan Dauwe (1, 2), Peter Varga (1), Daniel Ciric (1), Dominic Gehweiler (1), Boyko Gueorguiev (1), Karen Mys (1)

1. AO Research Institute Davos, Switzerland; 2. UZ Leuven, Belgium

Introduction

Cartilage diseases, such as osteoarthritis, rheumatoid arthritis and posttraumatic arthritis after intra-articular fractures and osteochondral defects have an important impact on the patient's quality of life and are a heavy burden for the healthcare system [1]. Better understanding, early detection and proper follow-up could improve quality of life and reduce healthcare related costs. Imaging is a valuable tool for detecting and monitoring these cartilage-related diseases and how they progress. Therefore, the aim of this study was to evaluate the potential of improved imaging techniques of these medical conditions by quantifying cartilage and subchondral bone.

Materials & Methods

Two osteoarthritic (OA) (n = 2, mean age = 88.3 years) and three non-OA (n = 3, mean age = 51.0 years) human cadaveric knees were scanned three times (Figure 1). A high-resolution peripheral quantitative computed tomography (HR-pQCT) scan (XtremeCT, Scanco Medical AG, Switzerland) was performed to visualize the bone microstructure. A contrast-enhanced clinical CT scan (GE Revolution Evo, GE Healthcare, USA) was made to visualize the cartilage. A microCT scan (VivaCT40, Scanco Medical AG, Switzerland) served for validation. Visipaque 320 (60 ml) was used as contrast media for the contrast-enhanced clinical CT scan and a layer of BaSo4 was added on the joint to visualize the cartilage with microCT scans. Afterwards, the regions of interest (ROI) were identified automatically. Finally, these ROI were segmented using adaptive thresholding [2]. Bone microstructural parameters, namely bone volume fraction (BV/TV), trabecular thickness (Tb.Th), trabecular separation (Tb.Sp), trabecular number (Tb.N) and cartilage thickness were quantified.

Results

The microCT results highly correlated with the XtremeCT and clinical CT results. For all microstructural parameters, the accuracy range (R^2) was between 0.79 and 0.95. Differences in bone microstructure and cartilage thickness were observed on the XtremeCT and clinical CT scans between the OA and non-OA knees.

Discussion

Bone microstructural parameters and cartilage thickness of knees were quantified with high accuracy on *in vivo* available scanners and apparent differences between the OA and non-OA knees were detected. Those results may improve OA follow-up and detection and lead to a better understanding of OA. However, further *in vivo* studies are needed to test these findings in clinical practice.

References

1. Hunter et al., Nature Review Rheumatology, 10:437-441, 2014.
2. Mys et al., Bone, 114:206-214, 2018.

Acknowledgements

1. Scanning   2. Selection of ROI   3. Quantification of trabecular parameters   4. Quantification of cartilage parameters
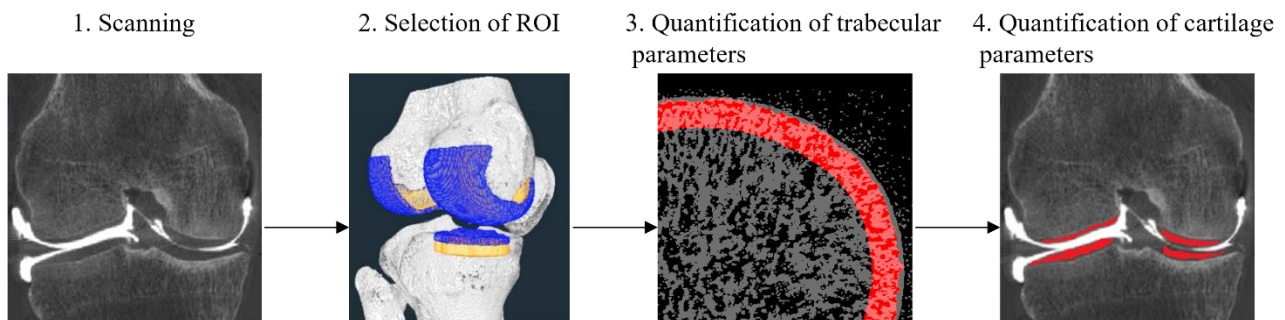
Figure 1: Overview of the technique: (1) the bones were scanned with the three scanners, (2) the ROI were defined automatically, (3) the bones were segmented, and the trabecular bone was quantified, (4) the cartilage was defined and quantified.

AN *IN SILICO* METHOD TO EVALUATE BONE REMODELLING AFTER TOTAL HIP ARTHROPLASTY: A SIX YEARS LONGITUDINAL STUDY

Valentina Betti[1], Halldór Jónsson Jr[2], Luca Cristofolini[1], Magnus Kjartan Gislason[3], Paolo Gargiulo[3]

1. Dept of Industrial Engineering, Università di Bologna, Italy; 2. Landspitali University Hospital, Dept of Orthopaedics, Iceland; 3. Institute of Biomedical and Neural Engineering, Reykjavik University, Iceland

Introduction

Research on bone remodelling after total hip arthroplasty (THA) is a key element to (i) improve THA design by locating where the changes in bone mineral density (BMD) occur, and (ii) investigate the mechanisms of bone remodelling in the long term [1]. Existing studies use DXA scans and look at the density in two dimensions, which can lose some pivotal features of how bone remodels since it is a 3D mechanism [2,3]. The aim of this work was to develop a method to quantitatively assess femur's BMD evolution in the long-term after THA based on CT scans, localising the changes in the seven standard Gruen zones (GZs).

Methods

Spiral CT scans of THA patients were taken 24 hours, 1 year and 6 years post-operatively. Scans were calibrated using a phantom to convert the Hounsfield unit (HU) to BMD. A segmentation (*Mimics*) with threshold [300-2999] HU was performed to isolate the region of interest, creating a mask from the greater trochanter to 2 cm below the implant. In order to assess the inter-operator variability in the segmentation, ten operators were recruited. The error in the volume of the mask was calculated as:

$$Err_\% = \frac{|Vop - Vr| + |Vr - Vop|}{Vr} \cdot 100, \qquad (1)$$

where V_{op} and V_r are respectively the volume of the mask of each operator and the volume of the mask of the author set as the reference mask. To identify the GZs, each mask was set to the frontal view and the planes identified as per protocol [4]. The average value of BMD was calculated in each GZ, for each subject at the three timepoints, to assess the gain/loss in BMD over time. To better assess any change from the previous dataset, post-1y data were normalised by post-24h; post-6y data by post-1y ones. To test the method, twelve subjects (six males, six females), five with a cemented implant, seven with an uncemented one, were analysed.

Results

The $Err_\%$ between operators was on average 1.75%. The mean time spent to create the mask was 1 hour. Changes in BMD [%] grouped and averaged according to the type of fixation are reported in Table 1. No statistically significant changes over time were observed in the cemented group. For the uncemented one, variations were statistically significant only in few regions (GZs 4-6 after one year, GZs 1 and 4 after six years).

GZs	BMD CEMENTED $\mu_{\frac{1-24}{24}}$ [%]	BMD CEMENTED $\mu_{\frac{6-1}{1}}$ [%]	BMD UNCEMENTED $\mu_{\frac{1-24}{24}}$ [%]	BMD UNCEMENTED $\mu_{\frac{6-1}{1}}$ [%]
1	1.01	0.96	1.02	-2.11*
2	-1.85	-2.30	-1.41	0.12
3	-2.00	-0.80	-2.15	1.77
4	-0.75	0.49	-1.05*	1.00*
5	-0.40	1.53	-2.77*	3.29
6	-1.73	-1.25	-3.29*	1.84
7	-1.05	0.70	-2.27	0.10

*Table 1: Average BMD gain/loss [%] in each GZ for the cemented and uncemented groups. Negative values state for an average loss, positive values for an average gain. *statistically different from previous dataset (p<0.05).*

Discussion

The *in silico* method presented in this study can be easily employed as a tool to evaluate long-term bone remodelling in the femur. The protocol showed good results in terms of reproducibility ($Err_\%$) and efficiency (time) [5].

While the BMD changes for the cemented group were not statistically relevant, our findings for the uncemented one in GZs 4-6 one year post-op are in line with other prospective studies, which reported a bone loss of BMD in the medial part of the femur, more pronounced in the proximal area [6]. The significant changes in GZs 1 and 4 after six years are likely caused by load transfer being shifted from the proximal part of the femur, through the rigid implant to the distal area.

These results may depend on the small number of subjects analysed. Future analyses on more data will be performed to assess (i) the potential statistical significance of other areas, and (ii) the relationship between BMD gain/loss and several features (e.g. age, sex, pathologies).

References

1. Gislason et al, *Clin Biomech*, 78:105092, 2020.
2. Kröger et al, *JMBR*, 11:1526-1530, 2009.
3. Albanese et al, *Hip Int*, 16:9-15, 2006.
4. Gruen et al, *Clin Orthop Relat Res*, 141:17 - 27, 1979.
5. Patijn, *Man Med*, 57:451-479.
6. Nyström et al, *Acta Ortho*, 93:206-2011, 2022.

A CORRELATIVE MULTIMODAL IMAGING APPROACH FOR MULTISCALE ANALYSIS OF BONE REGENERATION AND ADAPTATION

Francisco C. Marques (1), Bryant Schroeder (1), Dilara Yilmaz (1), Esther Wehrle (1), Ralph Müller (1)

1. Institute for Biomechanics, ETH Zurich, Zurich, Switzerland

Introduction

Bone is a hierarchical tissue with mechanobiological processes spanning several temporal and spatial scales. Likewise, new correlative multimodal imaging (CMI) approaches enable holistic analyses of complex multiscale biological systems [1]. However, few CMI approaches have been proposed to study bone and are often limited in their throughput and the samples that can be analysed. This work introduces a CMI approach to correlate time-lapsed *in vivo* 3D micro-computed tomography (micro-CT) images with *ex vivo* 2D histological sections from the same sample at the study endpoint, quantitatively characterising the Local *in vivo* Environment (LivE) of embedded bone cells with unprecedented detail. The results will focus on bone regeneration in a mouse femur defect model, and we expect this tool to be generalisable to other preclinical models used in bone research.

Methods

The data used in this work was collected in a previous study [2]. In short, 20-week-old C57BL/6J mice underwent femur defect surgery and were imaged weekly with *in vivo* micro-CT (10.5μm, 55kV, 145μA, 350ms; vivaCT 40) over seven weeks. Images were Gauss-filtered (sigma 1.2), binarised at 395 mgHA/cm^3, and the greatest connected component was isolated. *Ex vivo* histological sections (10μm thick) were collected from one paraffin-embedded femur from day 49 and stained for Safranin-O (Saf-O) and Sclerostin (Sost), and the bone was segmented using QuPath [3]. A graphical user interface was designed in Python to visualise and perform an interactive affine registration of both modalities and included an iterative optimizer (based on Powell's method and Bayesian optimization with Gaussian processes) to identify the best registration parameters in the neighbourhood of the current transformation, according to a score function. Additional features allow pre-processing the images and exporting the output efficiently. The result was assessed visually and by computing Dice scores (DSC), average (ASD) and Hausdorff (D$_H$) surface distance metrics.

Results

Six histological sections (interval of 100 μm) were aligned with high DSC values under 1h, highlighting the accuracy and throughput of the tool (Table 1). Figure 1 shows how artifacts in histological sections can affect registration quality and prevent better alignment.

Figure 1: Representative A) Saf-O and B) Sost stained sections; C-D) Overlay (yellow) of binarised micro-CT
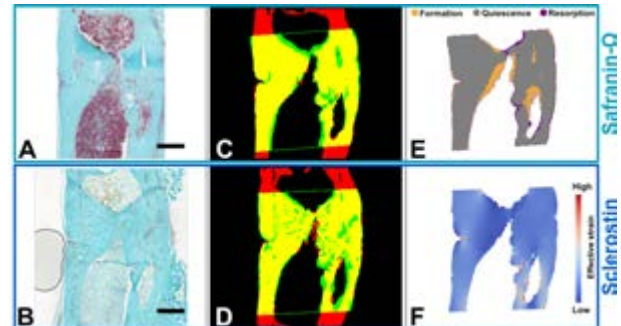
(green) and histological sections (red). E) Bone remodelling regions and F) micro-FE analysis from time-lapsed micro-CT. Scale bar: 400μm.

Type	Time (min)	DSC	ASD (μm)	D$_H$ (μm)
Saf-O	18	0.833	63.2	62.1
Sost	11	0.805	50.0	64.7
Sost	5	0.819	44.7	63.0
Sost	6	0.806	37.8	62.1
Sost	4	0.842	28.0	65.6
Sost	11	0.894	24.1	59.4

Table 1: DSC, ASD and D$_H$ scores for six histological sections aligned to the corresponding micro-CT image.

Discussion

Since the registration step is based on binary images, histological sections stained for different markers can be analysed if the mineralised bone can be identified reliably. Furthermore, we greatly improved the throughput and achieved functional registration accuracy over existing approaches by designing a novel iterative semi-automated registration method, making it an efficient tool for LivE charactisation in multiple sections and larger regions of interest. Also, this correlative approach is complemented by pipelines to process histological sections and micro-finite element analysis (Fig. 1F) of the micro-CT images, effectively integrating tissue-level strains and morphometry (Fig. 1E) with cellular activity data. Ongoing work is focusing on validating the registration step and techniques to compensate for deformations in histological sections. We expect this tool to enable uncovering multiscale mechanobiological pathways ruling bone regeneration and adaptation.

References

1. Walter et al., Front. Phys. 8:47, 2020.
2. Wehrle et al., Sci Rep 11**,** 23037, 2021.
3. Bankhead et al., Sci Rep 7, 16878, 2017.

Acknowledgements

LONGITUDINAL CHANGES IN THE SUBCHONDRAL BONE IN A MOUSE MODEL OF KNEE POST TRAUMATIC OSTEOARTHRITIS

Sara Oliviero (1,2,3), Zhengqi Chen (1), Alexandra Rayson (1), Bryant C Roberts (1,2), Heba MS Ismail (4), Ilaria Bellantuono (1,2), Enrico Dall'Ara (1,2)

1. Department of Oncology and Metabolism, University of Sheffield, UK; 2. INSIGNEO Institute for In Silico Medicine, University of Sheffield, UK; 3. Department of Industrial Engineering, University of Bologna, Italy; 4. Department of Infection, Immunity and Cardiovascular Disease, University of Sheffield, UK

Introduction

Osteoarthritis (OA) is one of the most common diseases of the musculoskeletal system and mouse models are used to investigate it. Destabilization of the medial meniscus (DMM) is one of the most used models of post-traumatic OA (PTOA) [1]. Most commonly, *ex vivo* micro-Computed Tomography (microCT) is used for high resolution characterization of the subchondral bone micro architecture. However, a longitudinal design with *in vivo* microCT would provide better insight into the early stages of the disease and its progression, as well as reduce the number of animals used [2,3].

The aim of this study was to use *in vivo* microCT to analyse spatio-temporal changes in the subchondral bone in a mouse model of PTOA.

Materials and methods

Sixteen male C57BL/6J mice received DMM surgery or sham operation at 14 weeks of age (N=8 per group). The right knee of each mouse was microCT scanned *in vivo* (VivaCT80, Scanco Medical; 55kVp, 145μA, 10.4μm voxel size) every 4 weeks until the age of 26 weeks, when mice were sacrificed. The microCT grey levels were converted into tissue mineral density using a densitometric calibration phantom.

Each image of the proximal tibia was aligned to a reference image using rigid registration (Amira). The subchondral trabecular bone was manually contoured and segmented using single level threshold. Standard morphometric parameters were measured including trabecular bone volume fraction (BV/TV), thickness (Tb.Th), separation (Tb.Sp) and number (Tb.N).

A region of interest including the cortical and trabecular bone between the growth plate and the articular surface was selected. This region was divided into eight quadrants (Fig1A) and the bone mineral content (BMC) was calculated in each compartment.

Results

Increased trabecular thickness (Fig1B) and decreased trabecular number were observed in DMM mice compared to SHAM. Interestingly, the largest variation in Tb.Th (+11%) was observed 4 weeks after surgery, while at subsequent time points the change rate was comparable to the SHAM group. Similarly, the largest variations in local BMC (up to +35% in the postero-medial compartment) were observed at week4 (Fig1C). At early stages of the induced disease, a local increase in BMC was observed at the medial side.

At later time points, the effect partially extended to the lateral side with smaller differences between DMM and SHAM groups (Fig1C).
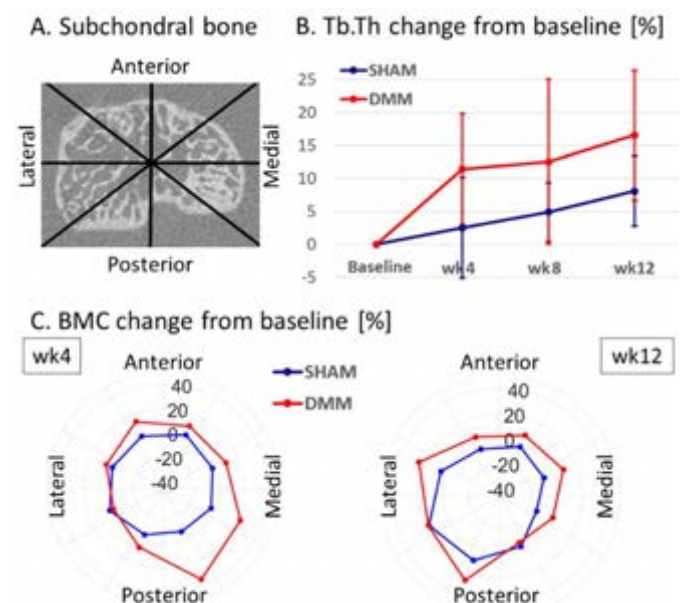
Figure 1: (A) Cross-section of subchondral bone of the tibia. (B) Temporal changes in trabecular thickness (Tb.Th) normalized by baseline values. (C) Spatial changes in bone mineral content (BMC) at week 4 and 12 with respect to baseline (week 14 of age).

Discussion

In this study longitudinal microstructural assessment of subchondral bone and subregional analyses of BMC have identified early effects of PTOA in a mouse model. The observed heterogeneity of spatio-temporal bone changes in OA is important to gain insight on the disease onset and progression, and for future assessment of treatments for PTOA. Future analyses will be performed to identify the relationship between these changes and biomechanical properties of the knee joint in PTOA.

References

1. Ramos-Mucci et al, Arthritis Res Ther, 22:171, 2020.
2. Bouxsein et al, JBMR, 25:1468–1486, 2010.
3. Lu et al, JBiomech, 49:2095-2099, 2016.

Acknowledgements

THE OSTEOCYTE LACUNO-CANALICULAR NETWORK AT THE BONE-IMPLANT INTERPHASE IMAGED WITH FOCUSED ION BEAM – SCANNING ELECTRON MICROSCOPY

Elin Törnquist (1), Guillaume Haïat (1), Yoann Hériveaux (2), Hugues Albini-Lomami (1), Elsa Vennat (2), Sophie Le Cann (1)

1. CNRS, MSME UMR 8208, France; 2. Université Paris-Saclay, CentraleSupélec, ENS Paris-Saclay, CNRS, LMPS, France

Introduction

The biomechanical properties of the interphase between an implant and the host bone determine long-term stability of the implant. The compositional, structural and mechanical properties of the bone-implant interphase (BII) evolve during healing and vary at different length scales due to the hierarchical arrangement of bone tissue [1]. In particular, bone nano- and microstructure orientation and arrangement are important predicators of key mechanical properties such as bone strength [2]. However, these structural features at the BII are not fully understood [3], especially the spatio-temporal evolution during healing, and the impact on the resulting BII strength. This study aims at investigating the microstructure of the BII using electron microscopy techniques.

Methods

Specimen. A standardized coin-shaped implant (TiAl6V4, Ø5mm, H3mm, Fig. 1A) was osseointegrated for 7 weeks in the cortical bone of a rabbit tibia. The extracted specimen was embedded into PMMA, cut transversely into a $2 \times 5 \times 2 mm^3$ cube and polished to expose the mineralized tissue at the BII (Fig 1B).

Imaging. A FIB-SEM (FEI Helios NanoLab 660) in back-scattered electron (BSE) mode was used to image a $20 \times 30 \times 30 \mu m^3$ region close to the implant (Fig 1B). 3D images were obtained using the "Slice and View" mode (Fig 1C) with 20nm distance between two slices. Image analysis was done using ImageJ (v.1.53f51).

Results

Ellipsoidal osteocyte lacunae (~10μm long axis, ~5μm short axis) were observed and appeared aligned parallel with the implant surface (Fig 1D). Multiple canaliculi (Ø 100-300nm) were seen connected to the lacunae, permeating the bone matrix. Collagen fibrils were found to alternate in orientation within 2-3μm thick lamellae, also aligned parallel with the implant surface (Fig 1D).

Discussion

The utilised implant model allows access to a bone-implant interphase where the tissue is certain to be newly formed. This enables investigation of the lacuna-canalicular network (LCN) in young bone close to an implant, and comparison to mature bone. Alternating orientation in collagen fibrils within lamellar structures was found to be consistent with previous observations in mature bone [4] and osteocyte lacunae were observed to align along the implant as seen previously for screw-type implants [5]. Further work will focus on extending the image analysis to investigate porosity distribution and alignment of the collagen fibrils within the LCN. Structural specificities of the newly formed tissue will be compared to a mature region in the same specimen.
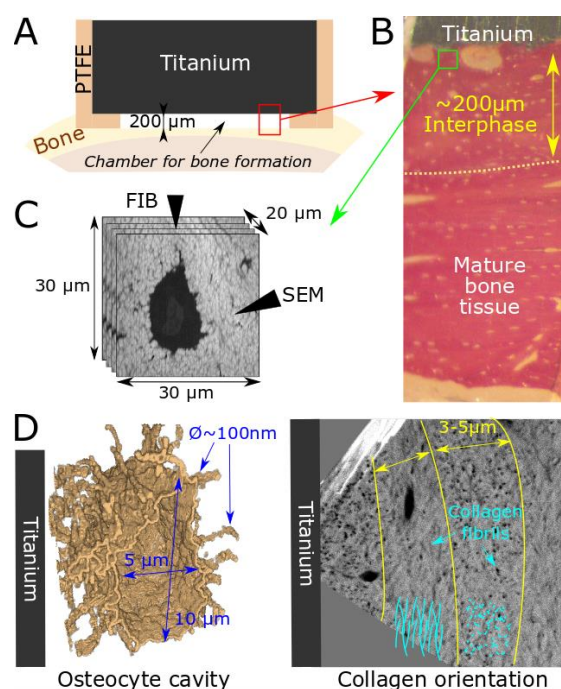
Figure 1: Standardized implant (A), specimen with bone tissue stained red with Picrofushin (B), FIB-SEM "slice and view" (C); osteocyte cavity and lacuna-canalicular network in immature bone tissue (D, left) and changes in collagen fibrils orientation (D, right).

References

1. Shah et al., Acta Biomat., 84 :1-15, 2019
2. Georgiadis et al. J. R. Soc. Interface 13, 20160088 (2016)
3. Gianuzzi et al., J Oral Maxillofac Surg 65:737-747, 2007
4. Reznikov et al., Bone, 52: 676-683, 2013
5. Shah et al., ACS Biomater. Sci. Eng. 1:305−313, 2015.

Acknowledgements

AUTOMATIC MUSCLE SEGMENTATION WITH DEFORMABLE IMAGE REGISTRATION OF LOWER LIMB MAGNETIC RESONANCE IMAGES

William Henson (1,3), Claudia Mazzà (1,3), Enrico Dall'Ara (2,3)

1. The University of Sheffield, Department of Mechanical Engineering, United Kingdom; 2. The University of Sheffield, Department for Oncology and Metabolism, United Kingdom; 3. INSIGNEO institute for in silico medicine, The University of Sheffield, United Kingdom

Introduction

Identification of muscle volume and geometry from Magnetic Resonance (MR) images is useful in the assessment of muscle health metrics, estimation of muscle strength, and building of image-based musculoskeletal models [1]. Typically, muscle segmentation is performed either manually or semi-automatically, incurring both operator variability issues and interaction time. The aim of this study was to assess the accuracy of an automatic segmentation method based on automatic image preprocessing and deformable image registration.

Methods

Lower limb T1-weighted MR images were acquired from five women (Age: 67 – 83 y.o., Height: 156 – 164 cm, BMI: 21.2-32.1) after gaining informed consent. The Sheffield Image Registration Toolkit [2] was employed as a segmentation tool for 25 lower limb muscles which were compared to the outputs of semi-automatic segmentation using Mimics (Materialise), considered as gold standard after manual corrections [3]. Two tests were performed: 1) registration of left and right limbs of the same subjects, to find the optimal registration parameters; 2) registration of the right limb from different subjects to evaluate the accuracy of the approach. To homogenize the appearance of the subjects within the images automatic morphological processes were used to remove the skin and homogenize the fat layer (Figure 1).
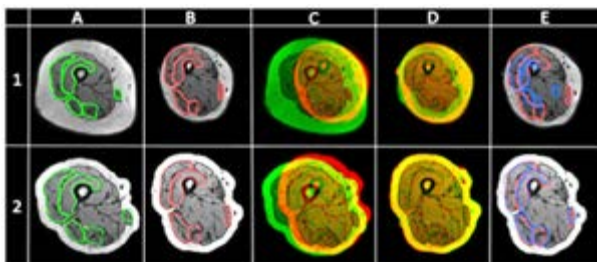
Figure 1: Stages of segmentation with (2) and without (1) pre-processing. The reference data (A) was registered to the target data (B) (pre- and post-registration in C and D respectively), giving segmentation results (E), semi-automatic and automatic shown in red and blue respectively.

The resulting 25 automatically generated segmentations (M_{auto}) were compared to the corresponding semi-automatic segmentation (M_{ref}). The Dice similarity score (Equation 1) [4] was measured to account for the differences in shape and volume of the segmentation. Muscle volumes were also computed and compared.

$$D = 100 \times \frac{2(M_{auto} \cap M_{ref})}{|M_{auto}| + |M_{ref}|} \quad (1)$$

Results

The left-right test resulted in a high Dice similarity score and low relative volume error across the 25 muscles considered and with all subjects (Table 1). The among-subjects test resulted in a significantly lower Dice similarity score and higher relative volume, error with a wide large range in the accuracies of segmentation.

Dice similarity score		Relative volume error (absolute %)	
mean $\pm$ standard dev. [range]		mean $\pm$ standard dev. [range]	
Test 1	Test 2	Test 1	Test 2
87.4$\pm$6.3 [69.7, 96.0]	64.5$\pm$15.4 [25.1, 87.5]	6.0$\pm$3.8 [0.3, 15.1]	14.3$\pm$11.4 [2.5, 44.3]

Table 1: Quantification of segmentation accuracy.

Discussion

The variability of the muscle architecture between the subjects is far greater than that between the left and right limb of one subject [3], causing the expected disparity in the accuracy of segmentation between the two tests. Further, this shows that through image registration the variability in muscle geometry between subjects cannot be captured for every muscle to a level comparable to the confidence level of the semi-automatic process [3].

In conclusion we have shown the limitations of an automatic deformable image registration approach to segment muscles from MRI. Nonetheless, this approach can be used to computationally generate new sets of credible images. These are currently being added to our datasets to enable alternative methods based on deep learning.

References

1. Blemker S.S., et al., J MRI 2007
2. Barber D.C., Hose R., J Med Eng. Technology 2005
3. Montefiori E. et al., PLOSONE 2020
4. Dice L.R., Ecological Society of America 1945

Acknowledgements

AUTOMATION OF MRI-BASED SPINAL MUSCLE SEGMENTATION

Birgitt Peeters (1), Thomas Overbergh (1), Dario Farotto (2), Erica Beaucage-Gauvreau (1), Lennart Scheys (1,3)

1. Institute for Orthopaedic Research and Training (IORT), Faculty of Medicine, KU Leuven, Belgium; 2. Materialise HQ, Leuven, Belgium; 3. Division of Orthopaedics, University Hospitals Leuven, Belgium

Introduction

Adult spinal deformity (ASD) is a spectrum of three-dimensional (3D) spinal abnormalities, often resulting in pain and disability [1]. Currently, ASD surgical care primarily relies on static two-dimensional radiographic parameters to assess spinal alignment, neglecting associated changes in muscle structure and function. Post-operative complication (42.6%) and revision rates (35%) are high [2,3], showing the limitations of the current approach towards clinical decision-making. Evaluation of the impact of ASD on musculoskeletal dynamics, using subject-specific musculoskeletal models (MSM) and simulations, has the potential to improve ASD care by quantifying functional impairment [4]. Obtaining subject-specific muscle paths in the MSM, currently requires slice-by-slice manual muscle segmentation from 3D medical images. This procedure is time-consuming and error-prone, and can greatly benefit from automation. To our knowledge, no automated magnetic resonance imaging (MRI)-based muscle segmentation methods have been developed for ASD patients. This work aims to automate MRI-based spinal muscle segmentation in ASD patients and define muscle paths for future integration in a MSM (Fig. 1).
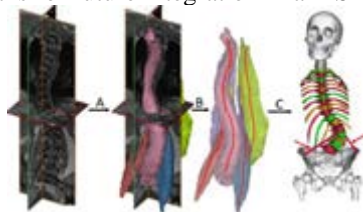
Figure 1: Schematic of the segmentation process. (A) Automatic segmentation. (B) Segmented muscle volume reduction to muscle path (red lines). (C) Muscle paths (red lines indicated by arrows) in a MSM (future work).

Methods

MRI images of 3 control and 13 ASD subjects (different degree of deformation) were used. Ground truth (GT) segmentation of the spine, erector spinae, multifidus, and psoas muscles was manually annotated by two operators. An automatic and semi-automatic atlas-based segmentation workflow were developed (Mimics v22 with python interface, Materialise, Leuven), Fig. 2. The segmented muscle volumes were automatically reduced to their muscle paths (i.e., the line through the centroids of each axial muscle area). Mask and muscle path accuracy were evaluated against GT segmentations and their associated muscle paths. The segmented mask accuracy was evaluated in a leave-one-out experiment using the Dice Similarity Coefficient (DSC), a measure for overlap of segmented volumes [5]. Since muscle path accuracy affects simulation results of forces and loads in a MSM, it was additionally evaluated with the axial in-plane moment arms, defined as distances between muscle path and the spine centerline, using the root-mean-squared-error (RMSE) against GT.
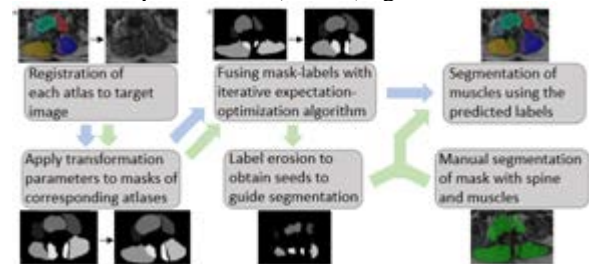
Figure 2: Schematic of the automatic (blue path) and semi-automatic (green path) segmentation workflows.

Results

Manual segmentation required on average 2h52min, compared to 30min (83% reduction) and 1h3min (63% reduction) for the automatic and semi-automatic workflows, respectively. The median DSC of the spinal structures varied between 0.44-0.62, and 0.82-1.00 for the automatic and semi-automatic workflows, respectively. The median RMSE of the in-plane moment arms of the muscle paths varied between 4.53-6.89 mm and 0.344-3.82 mm for the automatic and semi-automatic workflows, respectively.

Discussion

Both workflows notably reduced the segmentation time compared to manual segmentation. The semi-automatic workflow outperformed the automatic and other state-of-the-art methods [6,7], even considering that the latter were evaluated in a less challenging, healthy population. The muscle path accuracy was well within defined acceptable criteria, even at muscle attachment sites. The automatic workflow favored automation over accuracy, and can benefit from further improvement. Thus, the developed workflows contribute to the automation of spinal muscle segmentation, reduce segmentation time, and show potential to implement the resulting muscle paths in a MSM to quantify functional impairment.

References

1. Ailon et al, Neurosurgery, 77(suppl_1):S75–S91, 2015.
2. Scheer et al, Neurosurg. Spine, 19, 464-470, 2013.
3. Sánchez-Mariscal et al, Spine J., 14, 1629-1634, 2014.
4. Haddas et al, Spine J., 21, 1193–1204 (2021)
5. Dice, Ecology, 26:297–302, 1945.
6. Karlsson et al, Magn. Reson. Imaging,41:1558–1569,2015.
7. Meesters S. et al, IFMIA, 16–17, 2012.

A NON RIGID REGISTRATION ALGORITHM TO BUILD STATISTICAL SHAPE MODEL OF THORACIC AORTA, TOGETHER WITH AORTIC ARCH AND SUPRAORTIC VESSELS

Martino A. Scarpolini (1,2,3), Marilena Mazzoli (4), Francesco Bardi (1,5), Katia Capellini (1,4), Vincenzo Positano (1,4), Simona Celi (1)

1. Fondazione Toscana G. Monasterio, Italy; 2. TechneValue GmbH, Switzerland; 3. University of Rome "Tor Vergata", 4. University of Pisa, Italy; 5. Mines Saint-Etienne, Université de Lyon, France..

Introduction

Cardiovascular diseases (CVDs) are accounted for 45% of all deaths in Europe [1]. Among these casualties, ascending Thoracic Aortic Aneurysm (aTAA) is the 19th common cause of human death [2]. In this work we present a novel non rigid registration algorithm specifically designed for vessel-like structures. The application of this algorithm to the human thoracic aorta allowed us to build a surface-based Statistical Shape Model (SSM) of the ascending and descending aorta, together with the arch and supra aortic vessels. Computational Fluid Dynamic (CFD) features are computed and a correlation study is performed with respect to the anatomical features extracted through the SSM.

Methods

Non rigid registration algorithms for shape alignment are usually based on a point cloud correspondence procedure together with a deformation method. However, due to the complexity of the vessel tree, the point correspondence can represent a difficult problem. To overcome this limitation the vessel tree correspondence is ensured by optimizing an objective function of the distance between the surfaces of the two shapes, plus some domain specific constraints. A preconditioned gradient descent-based optimization procedure [3] is implemented in python, using Pytorch and pyvista libraries. 80 patient specific aortas, affected mainly by aTAA, are manually segmented and the obtained surface meshes are aligned using the developed algorithm. The segmentation starts from the aortic root and includes 18 mm of each supra aortic vessel and 140 mm of the descending aorta (see Figure 1). The aligned surfaces are used to build a SSM via Generalized Procrustes analysis (GPa) and Principal Component Analysis (PCA). Transient CFD simulations (with lumped parameter models for pressure boundary conditions) are performed on each patient specific model and clinically relevant biomarkers for aTAA are extracted and correlated with PCA modes (i.e. with anatomical features).
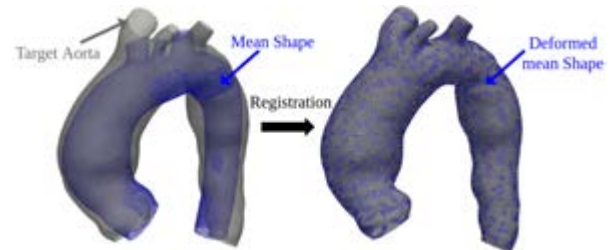
Figure 1: Representation of non rigid registration between a source aorta (mean shape) and a target one.

Results

A dataset of 80 patient specific aortas was successfully aligned to a mean shape determined through GPa (see Figure 1). A final Chamfer distance under 0.5 mm was achieved between each aorta and the deformed mean shape. A SSM of the aligned dataset has been built and 98% of its variance is captured by the first 40 modes of the PCA. A correlation study is carried out between PCA modes values and clinically relevant CFD-based Biomarkers for aTAA.

Discussion

Statistical Shape models are a powerful tool to analyze and model the geometric variability of anatomical structures. The main difficulty of SSM is the non rigid registration required to build an aligned dataset of shapes. While with relatively simple anatomical structures the problem can be easily solved, with complex geometries (e.g. vessel trees with many branches) the solution is often to simplify the shape either by modifying it or by removing secondary structures. To our knowledge, this is the first surface based SSM of the whole thoracic aorta.

References

1. Group, A.W. et al, Eur. Heart J. 39(7), 508–579 (2017).
2. Chau, K.H. et al, Prog. Cardiovasc. Dis. 56: 74–80 (2013).
3. Nicolet, B. et al, ACM Trans. Graph. 40, 6, Article 248 (2021).

Acknowledgements

IN-VIVO 3D MUSCLE MORPHOLOGICAL MEASUREMENT BASED ON 3D FREEHAND ULTRASOUND AND DIFFUSION TENSOR IMAGING

Zhongzheng Wang (1), Francesco Cenni (2), Antea Destro (1), Sven Petersson (3), Ruoli Wang (1)

1. KTH MoveAbility Lab, Department of Engineering Mechanics, KTH Royal Institute of Technology, Stockholm, Sweden; 2. Faculty of Sport and Health Sciences, University of Jyväskylä, Jyväskylä, Finland; 3. Department of Medical Radiation, Physics and Nuclear Medicine, Karolinska University Hospital, Stockholm, Sweden

Introduction

3D muscle morphological parameters, such as fascicle length (FL) and pennation angle (PA) are important characteristics to muscle-force production capacity [1]. To reconstruct in-vivo muscle fascicles, methods based on Diffusion Tensor Imaging (DTI) were proposed [2]. In recent years, 3D freehand ultrasound (3DfUS), which is combination of 2D ultrasound and 3D motion capture system, has become another tool to study in-vivo muscle structures [3]. However, whether 3DfUS can accurately measure 3D muscle FL or PA remains unknown. The objectives of this study were: (1) to evaluate the 3DfUS measurement accuracy of FL, PA, and muscle volume in tibialis anterior (TA) and gastrocnemius medialis (GM) compared to DTI measurement; (2) to evaluate the inter-session and sensitivity performance of 3DfUS measurement.

Methods

Seven healthy subjects (3M/4F, 54.9 ± 5.9 years, 70.8 ± 9.2 kg, 170.8 ± 11.0 cm) were recruited in this study. Randomized side of the legs were scanned using a diagnostic ultrasonography system with a 38 mm wide linear transducer. A 10-camera optical motion capture system was used to record the position of four reflective markers rigidly fixed on the transducer. Three-dimensional ultrasound images of TA and GM were reconstructed based on a previously published method [3]. The muscle volume was calculated according to manual muscle segmentation. Three fascicles were manually picked in an image section where the fascicles were clear (Figure 1). Mean FL and PA of these fascicles were calculated. Inter-session analysis was performed by repeating the FL and PA identification procedures at two different occasions. Sensitivity analysis was performed by evaluating the effect of choosing three or five fascicles in the selected image section. Intraclass correlation coefficient (ICC) was used to evaluate the agreement of inter-session and sensitivity analysis.
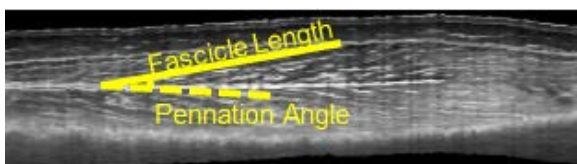
Figure 1: Illustration of FL and PA measurement. The fascicles were clear and intact in this section. Fascicles in muscle belly region were selected.

Subjects were scanned using a 3.0-Tesla MR scanner in the same alignment as the 3DfUS measurement. T1-weighted and DTI images were acquired. The reconstruction of muscle fascicles and identification of the FL and PA were based on a previous report [4]. Mean differences of muscle FL, PA, and volume measured by 3DfUS and DTI were calculated.

Results

Compared to DTI measurement, 3DfUS measurement overestimated the FL of TA and GM for 2.2 mm and 0.7 mm. Regarding PA, 3DfUS measurement overestimated PA of TA for 1.5 degree, and underestimated PA of GM for 0.3 degree. Also, 3DfUS measurement underestimated the muscle volume of TA and GM for 3.7 cm^3 and 5.7 cm^3. Both inter-session and sensitivity analysis showed excellent agreement of 3DfUS measurement (Table 1).

		FL	**PA**
Inter-session *Measurement in two different days*	TA	0.999	0.956
	GM	0.994	0.978
Sensitivity *Choosing 3 fascicles vs 5 fascicles*	TA	0.996	0.958
	GM	0.994	0.977

Table 1: ICC of the inter-session and sensitivity analysis (excellent agreement, ICC above 0.9).

Discussion

In this study, the FL and PA of GM measured by 3DfUS had errors within 1 mm or 1 degree compared to DTI measurement. Errors in TA structure were higher than GM. The reason maybe that TA is longer than GM, thus making the TA morphological parameters had a bigger distribution. Also, 3DfUS measurement had good inter-session reliability and sensitivity.

References

1. Nordin et al. Lippincott Williams & Wilkins, 2001
2. Bolsterlee et al. J Biomech, 2015
3. Cenni et al. Comput Meth Prog Bio, 2016
4. Korting et al. Sci Rep, 2019

GENERATING 3D PERSONALISED RESPIRATORY DOMAINS FOR DEPOSITION MODELS FROM CT AND CHEST X-RAYS

Josh Williams (1), Haavard Ahlqvist (1), Alex Cunningham (1), Andrew Kirby (2), Steve Cunningham (3), Ali Ozel (1), Uwe Wolfram (1)

1. Heriot-Watt University, School of Engineering and Physical Sciences, Edinburgh, United Kingdom;
2. Royal Hospital for Children and Young People, Radiology Department, Edinburgh, United Kingdom;
3. University of Edinburgh, Centre for Inflammation Research, Edinburgh, United Kingdom

Introduction

Respiratory patients frequently have poor inhaler technique which impacts their disease management. Treatment efficacy could be improved using predictive models for drug deposition based on airway shape and patient inhalation technique [1]. Widely applying personalised models requires a rapid and cost-effective image processing approach. Segmentation of airways and lungs from volumetric computed tomography (CT) has been well-developed [2,3]. Chest X-rays have not previously been used to extract patient-specific respiratory systems for deposition models, although statistical shape and appearance models (SSAMs) have been used to reconstruct 3D bones from 2D X-rays [4]. Here, we present our image processing pipeline for generating patient-specific respiratory systems from 2D or 3D images. We assess its performance by comparing morphometric properties and deposition results.

Methods

For SSAM training data, we used 50 CT scans from the LUNA16 dataset with radiologist-verified lung and airway segmentations. We generated digitally reconstructed radiographs with ray-tracing, which were used to train appearance in our SSAM and test the model accuracy. We performed principal component analysis on the landmark position and gray-value to parameterise the SSAM. To reconstruct lungs and airways from X-rays, we optimised the SSAM parameters by minimising differences between the X-ray and SSAM outline and gray-value. To segment lungs from CT, we used a U-Net which was pre-trained on CT slices 231 patients (mean DICE 0.97) [3]. We trained a U-Net which segmented the airways [2]. We generated complete conducting airway trees [5] using diameter and length from the central airways. We implemented our imaging framework in Python 3.7. Computational fluid dynamics (CFD) simulations were performed in OpenFOAM with particle tracking to compare deposition [1].

Results and discussion

Our airway U-Net yielded a DICE value of 0.93 on the LUNA16 scans set aside for model validation (10 out of 50). We found our SSAM to reconstruct the lung volume to a median error of 7% (maximum error 24%). Additionally, the SSAM could reconstruct the trachea and main bronchi diameter to a median error of 7% (95th percentile 22%). In the segmental bronchi, the airway diameter error increased to 12% (95th percentile 34%).

This is as the airways lower than the main bronchi are not visible on an X-ray. Preliminary CFD simulations showed upper airway deposition hotspots were similar in all imaging methods.

To understand error propagation to the generated distal airways, we compared diameter for the U-Net and the SSAM X-ray reconstruction with the ground truth (Fig. 1). We see the SSAM and U-Net lie within the ground truth airway diameter range. Mean SSAM diameter error grew from ~20% in the first 3 bifurcations grew to a factor of 2 at generation 10. The maximum U-Net mean diameter error was 20% at generation 7.

Our results show that imaging, morphological and deposition metrics in airways using SSAMs or U-Nets are consistent with ground truth. Our future study will compare deposition models to experimental deposition data. Validation of such models will provide clinicians with trust that our framework is suitable to trial various treatments *in silico* to optimise patient treatment.
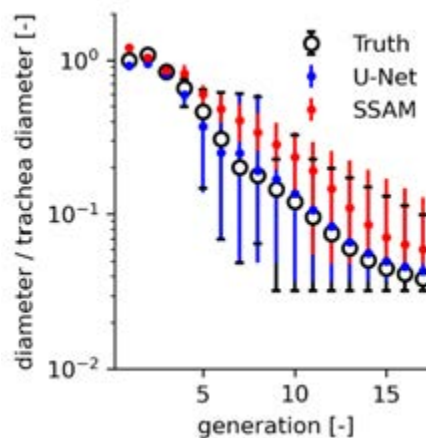
Fig. 1: Airway diameter with generation, comparing image processing techniques, shown for the patient where SSAM diameter error was 22% (population's 95th percentile). Points show mean with minimum to maximum range.

References

1. Williams, J. et al., 2022. *Int. J. Pharm.*, *612*, p.121321.
2. Juarez, A.G.U. et al., 2019. In MLMI (pp. 583-591).
3. Hofmanninger J. et al., 2020. *Eur. Radiol. Exp*, *4*(1), pp.1-13
4. Väänänen, S. et al., 2015. *Med. image. anal.*, *24*(1), pp.125-134.
5. Bordas, R. et al., 2015. *PloS one*, *10*(12), p.e0144105.

Acknowledgements

IN-VIVO DETERMINATION OF REGION-SPECIFIC MATERIAL PARAMETERS OF HEALTHY AND OSTEOARTHRITIC MENISCI

Jonas Schwer (1), Fabio Galbusera (2), Mirco Sgroi (3), Martin Faschingbauer (3), Anita Ignatius (1), Lutz Dürselen (1), Andreas M Seitz (1)

1. Institute of Orthopaedic Research and Biomechanics, Trauma Research Centre, Ulm University Medical Centre, Ulm, Germany; 2. Spine Center, Schulthess Clinic, Zürich, Switzerland; 3. Department of Orthopedics, Ulm University Medical Centre, Ulm, Germany

Introduction

Studies have shown that meniscal pathologies, including meniscal tears and degenerative changes, contribute to the evolution of osteoarthritis (OA) in the knee joint [1]. It seems that degeneration-related mechanical changes are probably first detectable in the menisci before the articular cartilage is affected [2]. Thus, identifying mechanical changes in the meniscus associated with progressive degeneration is of particular interest for OA research. Hence, the aim of this *in-vivo* study was to identify material parameters in different anatomical regions of the lateral meniscus of healthy subjects and OA patients based on magnetic resonance imaging (MRI) and inverse finite element analysis (FEA).

Methods

After IRB approval and written informed consent 12 healthy volunteers and 12 osteoarthritic patients were placed in a customized MRI compatible loading device at approximately 5° knee flexion. Each individual was MRI-scanned both in unloaded condition and under simulation of 25% subject-specific body weight. According to the method described in [3,4], patient-specific finite element (FE) models and 3D displacement fields of the lateral menisci were assessed (Fig 1). The FE models were divided into 5 anatomical
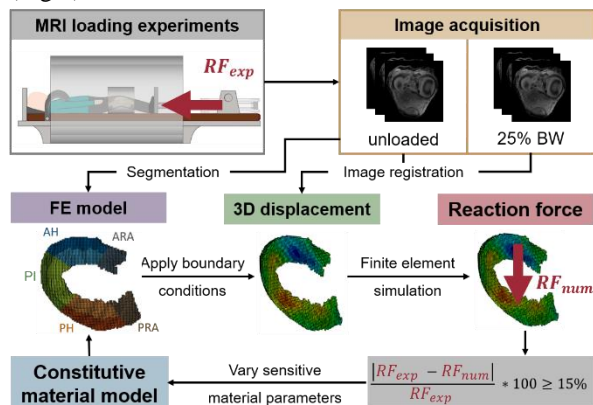
Fig 1: Schematic illustration of the parameter optimization procedure.

regions: anterior and posterior root attachment (ARA, PRA); anterior horn (AH); pars intermedia (PI); posterior horn (PH). To model the anisotropic and viscoelastic properties of the meniscus, the strain energy density function proposed by Holzapfel [5] was utilized in a poroelastic model. The superficial displacements, estimated by non-rigid registration were applied as boundary conditions. By running a FE simulation, the femoral reaction force that is needed to cause the applied

displacement was calculated. During a particle swarm optimization, the difference between the numerically calculated reaction force and the experimentally applied force was minimized by varying four sensitive material parameters in a physiologically range for each region (Fig 1). The varied parameters described the stiffness (C10) and compressibility (D) of the matrix as well as the nonlinear fiber stress (k1) and the permeability (k).

Results

The optimized parameters showed a significant increase in the compressibility of the meniscus matrix (D, $p \leq 0.05$) in all regions. Further, the stiffness of the meniscus matrix (C10) tended to decrease, while the permeability (k) tended to increase with progressive degeneration.
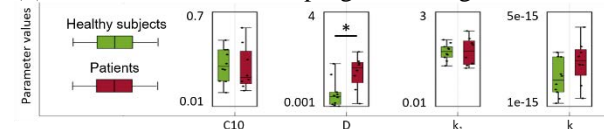
Fig 2: Box-Plots of the four optimized global parameter sets.

Discussion

In summary, the feasibility of our previously presented *in-vitro* approach [3,4] for applications in the clinic has been demonstrated. The most important finding of the study indicates that progressing knee joint degeneration leads to a softening of the meniscus matrix. This is in accordance with the findings of Fischenich et al. [6], who found in their *in-vitro* investigations a significant decrease in the compressive properties of the meniscus with progressing degeneration. In addition, Warnecke et al [7] reported that the permeability increases with progressive meniscus degeneration, which was also observed as a trend in our results. In conclusion, local material parameters of lateral menisci of both, healthy subjects and OA patients were successfully determined based on MRI loading experiments and inverse FEA.

References

1. Guermazi et al, Radiology, 268: 814-821, 2013.
2. Seitz et al, Front Bioeng Biotechnol, 9, 2021.
3. Schwer et al, Front Bioeng Biotechnol, 8, 2020.
4. Freutel et al, J Biomech, 48:1343-49, 2015.
5. Holzapfel et al, J Elast, 64: 1-48, 2000
6. Fischenich et al, J Biomech, 48: 1407-11, 2015
7. Warnecke et al, Osteoarthr Cartil, 28: 1482-91, 2020

Acknowledgements

AGE-RELATED DEGENERATION AFFECTS THE STRUCTURE–FUNCTION RELATIONSHIP OF HUMAN MENISCI

Graciosa Q. Teixeira, Jonas Schwer, Anita Ignatius, Lutz Dürselen, Andreas M. Seitz
Institute of Orthopaedic Research and Biomechanics, Ulm University, Germany

Introduction

The elastic and viscoelastic properties of degenerated menisci seem to change before alterations are detectable in the adjacent articular cartilage [1]. However, despite its high clinical relevance, the age-related degeneration process of the meniscus is not yet fully understood, especially with regard to the structure-function relationship. Therefore, the goal of this work was to identify changes in the structure-function relationship of lateral and medial menisci during ageing/degeneration.

Methods

Based on Kellgren-Lawrence (KL) classification, 12 mild (KL: 1-2; donor age: 47 ± 11 years) and 12 severely (KL: 3-4; donor age: 82 ± 9 years) degenerated human knee joints were investigated [1,2]. Stress-relaxation tests were performed on axial explants from lateral and medial menisci to assess the permeability (k) and the equilibrium modulus (E_{eq}) [3], whereas tensile tests were performed on circumferential explants to determine the Young's modulus (E) and the failure load (F_{max}). Sulphated glycosaminoglycan (sGAG) content was determined after tissue enzymatic digestion using a biochemical assay and the collagen tissue area was determined by histological analysis of meniscus sections stained with picrosirius red [4]. Mann-Whitney U and Kruskal-Wallis tests were used for statistical analysis, while $p<0.05$ was generally considered significant.

Results

The compression-relaxation tests showed an increase of E_{eq} with degeneration, particularly for the lateral meniscus ($p<0.05$, Fig. 1A), without affecting k (Fig. 1B). The tensile properties (Fig. 1C,D) of the menisci were not altered with degeneration ($p>0.16$).
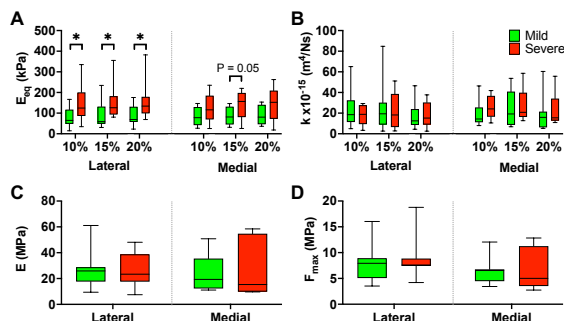
Fig. 1: Results of the confined compression stress-relaxation tests: A) Equilibrium modulus (E_{eq}); B) permeability (k), and for the tensile tests: C) Young's modulus (E) and maximum force (F_{max}) for mild and severely degenerated lateral and medial menisci. n=10-12; *p<0.05.

Moreover, while the sGAG content increased with degeneration (Fig. 2A,B), the percentage of collagen area decreased (Fig. 2C,D), both in the lateral ($p<0.05$) and medial ($p=0.06$) menisci. Qualitative histological evaluations showed a progressive destruction of the otherwise hierarchically arranged fibrous collagen structure, increasing tissue microcracks, calcium deposits, blood vessel infiltration and hypertrophic chondrocytes with progressing degeneration.
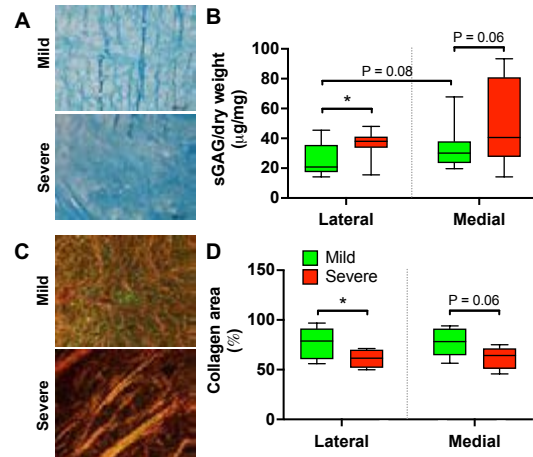
Fig. 2: A) Representative alcian blue staining of lateral meniscus for mild and severe degeneration. B) Sulphated glycosaminoglycan (sGAG) content in lateral and medial menisci for mild and severe degeneration normalized to the dry weight (µg/mL). C) Picrosirius red staining of lateral meniscus under polarized light depicting young (green), and mature (yellow to red) fibers. D) Collagen area (%). n=10-12, *p<0.05.

Discussion

In order to gain a more detailed insight into the etiology of gonarthrosis, the biomechanical behavior, as well as tissue composition and cellularity were investigated for the same menisci. On a structural level, the increase in E_{eq} can be explained by a disturbed relationship in the biphasic meniscus structure which may be resulting from changes in matrix composition, namely an increase in sGAG accompanied by tissue calcification, particularly observed in lateral menisci. This indicates that structural changes in the matrix composition may be detectable at protein level, before changes can be observed in biomechanical investigations. In conclusion, our data contributes to a better understanding of the structure-function relationship during age-related meniscus degeneration. It can be used to validate *in silico* determination of meniscus material parameters, with special focus on the early detection of osteoarthritis [2,5].

References

1. Seitz et al, Front Bioeng Biotechnol, 9:659989, 2021.
2. Schwer et al, Front Bioeng Biotechnol, 8:582055, 2020.
3. Seitz et al., J Mech Behav Biomed Mater, 26:68-80, 2013.
4. Pereira et al, Sci Rep, 6:33836, 2016.
5. Freutel et al, J Biomech, 48:1343-49, 2015.

Acknowledgements

INFLUENCE OF AGEING ON MICROMECHANICAL PROPERTIES OF THE FEMORAL NECK USING THE INVERSE METHOD

Benjamin Voumard (1), Pia Stefanek (2), Michael Pretterklieber (3), Dieter Pahr (2), Philippe Zysset (1)

1. ARTORG Center for Biomedical Engineering Research, University of Bern, Switzerland 2. Institute of Lightweight Design and Structural Biomechanics, Vienna University of Technology, Austria 3. Gottfried Schatz Research Center, Division of Macroscopic and Clinical Anatomy, Medical University of Graz, Austria

Introduction

People worldwide are living longer, and the incidence of hip fracture risk increases exponentially with age. Loss of bone mass and falls are the primary causes of hip fractures, but bone mechanical integrity at the microscale was also reported to increase with mineralisation and decline with age. Macroscopic tests of the proximal part of the femur are prone to errors, and corresponding μFE models become exceedingly large. In contrast, compressive testing of bone sections was shown to be accurate. Therefore, we performed compressive tests of femoral neck sections and simulated the same tests with non-linear μFE [1]. We hypothesised that the micromechanical parameters of the μFE models must decrease with age in order to match the macroscopic experimental response.

Methods

Eighty-four fresh-frozen human femurs were obtained with the consent of the donors and cut plane-parallel at the neck to obtain 10 mm thick sections. The samples were compressively loaded with a servo-hydraulic testing machine [*Figure 1*] with a displacement in the elastic range of 0.5 mm/min for stiffness calculation, followed by a monotonic loading until failure. An optical extensometer (d, lighting) recorded deformations while a load cell (c) recorded forces. The sections were scanned at 16 μm resolution with μCT, and the images subjected to standard morphological analysis, including BMC, BMD, and TMD. The grayscale images were downscaled to 32 μm and 65 μm for the linear and non-linear analysis respectively and segmented. The μFE solver ParOSolNL [2] was finally used with the same material properties for all samples to compute stiffness, ultimate force and the corresponding intrinsic variables, elastic modulus and strength.
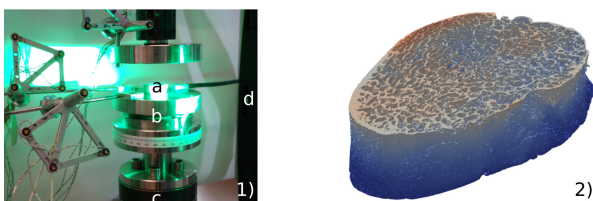
Figure 1: 1) experimental setup, a) sample, b) ball-joint, c) load cell, d) extensometer 2) μFE voxel-based mesh.

Results

As expected, the femoral neck's BMD decreased with age (p=0.006). The μFE outperformed BMC for both ultimate force prediction (R²=0.68 vs R²=0.19) and stiffness prediction (R²=0.83 vs R²=0.66) [*Figure 2*]. Strength was also well correlated with μFE (R²=0.85) but less with BMD (R²=0.51). The gap was smaller with the elastic modulus (μFE: R²=0.78, BMD: R²=0.72). TMD was constant with age (p = 0.068). The strength and elastic modulus errors between μFE and experiment were neither TMD- (p=0.57, p=0.13, resp.) nor age-dependent (p=0.75, p=0.8, resp.).
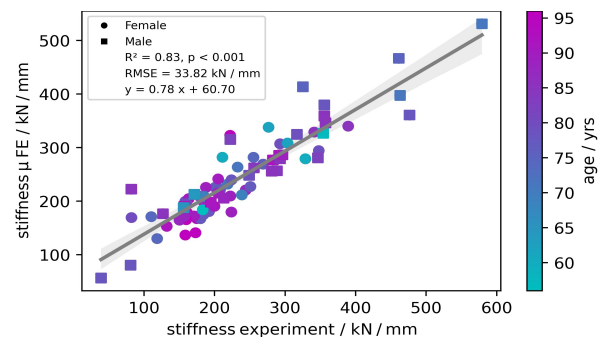
Figure 2: μFE stiffness correlates highly with stiffness measured in the experiment. However, the remaining variations correlate neither with TMD nor age.

Discussions

The μFE was the better predictor for both extensive (ultimate force, stiffness) and intensive (strength, elastic modulus) variables. The resolution of the μFE mesh, both linear and non-linear (32μm and 65μm, resp.), is expected to cover most morphological changes induced by ageing. The errors between the simulation and the experiment for both strength and elastic modulus were neither TMD- nor age-dependent, suggesting that the tissue material parameters can be assumed constant. The evaluation of further aspects of bone quality on these proximal femora is ongoing.

References

1. Rietbergen et al, J Biomechanics 28(1):69-81, 1995
2. Stipsitz et al., Biomech Mod Mech, 19:861-874, 2020.

Acknowledgements

IMPACT OF THE TIME SCALE OF MUSCLE ACTIVATION DYNAMICS ON REACHING PERFORMANCE

Tiina Murtola, Christopher Richards

Royal Veterinary College, United Kingdom

Introduction

Muscle activation dynamics causes a delay between neuromuscular control signals and the generation of muscle force. This delay must be accounted for by the motor control system to achieve desired movement. The time scale of the activation dynamics, hereafter called *activation speed*, depends on the fiber type composition of the muscle, which may change due to, for example, exercise, disease, or ageing. Our aim is to investigate how changes in the activation speed affect reaching performance.

Methods

An anatomically simplified planar model with four links and three hinge joints is used [1]. The arm moves in the horizontal plane, and its movement is controlled via excitation of three antagonistic muscle pairs, each pair crossing one joint. A Hill-type model with third-order activation dynamics [2] and nonlinear force-length-velocity properties represents each muscle.

For the reaching tasks, four targets at different directions and an equal distance from a fixed initial position are used. Muscle excitations are computed using a predictive PD controller to track a pre-planned straight, minimum-jerk [3] trajectory from initial to target position. Prediction time and PD gains are optimized numerically to minimize the average error in the final position over the four targets.

The three time constants of the activation dynamics are scaled to achieve five different activation speeds. The resulting muscle twitch responses have time-to-peak (TTP) values in the range 54-86 ms, and they are also characterized by half-relaxation times that increase with TTP and peak amplitude that decrease with TTP.

Results

Simulation results indicate that slow muscle activation dynamics leads to less accurate reaching, both in terms of average tracking error and average final position error (Figure 1, top). However, while the errors vary by over 50%, the reaching movements remain so accurate that the deterioration in performance makes little difference for most applications.

High performance can only be maintained when the control parameters are re-tuned for each activation speed. With slow muscle activation dynamics, the prediction time of the controller must be increased and the positional gains generally decreased (Figure 1, middle) while velocity gains remain roughly unchanged.

Co-contraction of the antagonistic muscle pairs in the model tracks, to some extent, the changes in the positional gains, but without a clear decreasing trend for slower activation speeds (Figure 1, bottom).
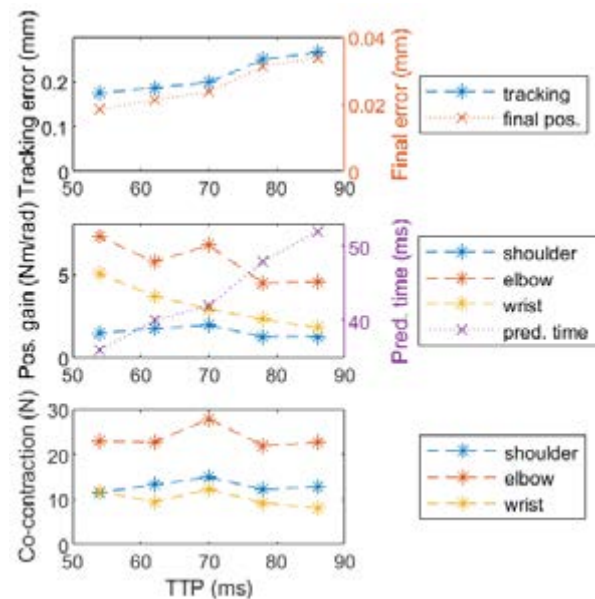
Figure 1: Average tracking and final position errors (top), positional PD gains and prediction time (middle), and joint-wise co-contraction (bottom) vs activation speed characterized by TTP.

Discussion

The observed deterioration in reaching performance with slower muscle activation speed can mainly be attributed to diminished accuracy of the longer predictions (to account for the longer delays between muscle excitation and contraction). To increase the robustness of the system, positional gains decrease for slower activation muscles, consequently decreasing the controller's sensitivity to predicted deviation from the planned trajectory. Given the apparent absence of other stabilization mechanisms, such as co-contraction, the compensation mechanism that relies on the re-tuning of the PD gains appears to be sufficient for achieving dynamical stability in reaching.

References

1. Murtola and Richards, AMAM 2021.
2. Lee et al, J Electromyogr Kinesiol, 21:557-565, 2011
3. Flash and Hogan, J Neurosci, 5:1688-1703, 1985.

Acknowledgements

UPPER LIMB FUNCTIONAL EVALUATION OF A COMPLEMENTARY THERAPY IN PARKINSON'S DISEASE: A PRELIMINARY STUDY

Elena Pegolo (1), Marco Romanato (1), Chiara Riccò (1), Alberto Cucca (2), Fabiola Spolaor (1), Daniele Volpe (2), Sawacha (1,3)

1. Department of Information Engineering, University of Padova, Italy; 2. Fresco Parkinson Center, Villa Margherita, S. Stefano, Vicenza, Italy; 3. Department of Medicine, University of Padova, Italy

Introduction

Parkinson's Disease (PD) is a progressive disease that mainly affects the movement causing impairments in both the upper and lower limbs. Upper limbs (UL) functional disorders may cause loss of dexterity, accuracy, speed, and smoothness in PD subjects [1]. Impairments in the UL kinematics highly affect patients' quality of life. Physicians usually employ clinical scales and timed tests in order to assess impairments at the UL. However, these evaluations might not be sufficient to provide precise information on spatial and temporal features of UL tasks [2]. The aim of the present preliminary study is to quantitatively explore the potential benefits of a complementary therapy based on experimental artistic interventions on PD's UL functionality through an ad hoc designed reaching test.

Methods

Eight PD subjects (age = 70.0±4.4 years old, BMI = 25.5±4.5 kg/m^2) were enrolled in the present study. Data collection took place before and after the therapy. Nineteen retroreflective markers were applied on UL and trunk anatomical landmarks to track their trajectory in space [3] with an 8-camera optoelectronic system (Vicon Motion System, Oxford, UK, 120Hz). Participants were comfortably seated in front of a white blank board and were asked to point firstly at the self-jugular incision, then at the board center with the forefinger of the dominant hand. Each task was performed 5 times. From the acquired data, jerk was computed for the index finger trajectory (marker positioned in the tip of the finger) in the mediolateral (x), anteroposterior (y) and vertical (z) directions. Jerk was considered as a measure of task smoothness and defined as the third derivative of the displacement in the three directions. Finally, normalized jerk (NJ) was extracted [4] in order to compare results across task length and treatment time frames:

$$NJ = \sqrt{\frac{1}{2} \int jerk(t)^2 \times \left(\frac{duration^5}{length^2}\right) dt}$$

where duration was defined as the movement duration in seconds and length as the difference between the maximum and the minimum position of the marker along the considered direction.

Results

Figure 1 reports the obtained results for the NJ before and after the therapy. Lower values of NJ indicate increased smoothness in the considered task.
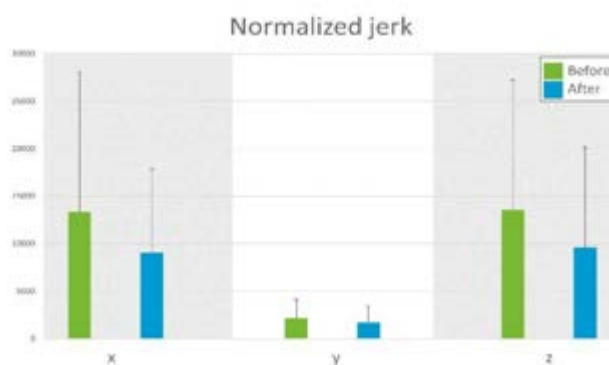
Figure 1: Normalized jerk before (green) and after (blue) the therapy for the index finger trajectory in the mediolateral (x), anteroposterior (y) and vertical (z) directions. Data are reported as mean ± standard deviation.

Discussion

Although preliminary, the obtained results might suggest an influence of the complementary artistic experience over UL functional abilities. Indeed, after the treatment, lower values of NJ were revealed, which are associated with an increased smoothness of the UL movement. Further studies should focus on the correlation of the obtained results with the clinical scales.

References

1. Proud E. et al, Archives of Physical Medicine and Rehabilitation. 96:540-551, 2015.
2. Corona F. et al, Clinical Biomechanics. 57:137-143, 2018.
3. Kontaxis A. et al, Clinical Biomechanics.24:246-253, 2009.
4. Choi A. et al, BioMedical Engineering OnLine. 13:20, 2014.

Acknowledgements

A SLOUCHED OR ERECT SPINAL POSTURE MODIFIES UPPER LIMB KIMENATICS

Aurélie Tomezzoli (1), Alexandre Naaïm (1), Bertrand Fréchède (1), Sonia Duprey(1)

1. *Univ Lyon, Univ Claude Bernard Lyon 1, Univ Gustave Eiffel, LBMC UMR_T9406, F69622, Lyon, France*

Introduction

Upper limb musculoskeletal disorders (MSDs) are a major public health issue [1]. The main biomechanical risk factors for MSDs are forceful exertions, repetitiveness and awkward joint angles [1]. Current treatments often remain unsatisfactory [2,3]. Empirical treatments based on spine curvature modifications [4] are used for shoulder, elbow and wrist MSDs. The impact of spinal curvatures on upper limb kinematics has been assessed only at the shoulder level: scapula position and humerus axial rotation were modified [5]. The goal of this study is to assess the impact of two spinal postures (erect and slouched when seated) on the wrist, elbow and shoulder joint angles, in relation to the risk thresholds defined by international standards [6].

Methods

Twenty-two healthy participants (14 women, 23.6 ± 4.4 years) were recruited after ethical endorsement (CPP N°2020-A00573-36). Spinal curvatures were modified using oral instructions and light touch, to reach erect and slouched sitting postures, in a random order. Participants performed 3 times 3 MSD risk-related tasks [1]: moving a box as far forward as possible, screwing against resistance, painting above the shoulder level. Instructions were standardized. Tasks were personalized according to participants' anthropometry and wrist isometric maximal voluntary force. Cutaneous marker trajectories were recorded using a Vicon motion capture system at 100 Hz, then filtered using a 4th order low-pass Butterworth filter with a cutoff frequency of 10 Hz. Angles for the shoulder, elbow and wrist were computed according to ISB definitions of local coordinate systems and rotation sequences [7], except at shoulder level, where the rotation sequence was Z-X-Y [8]. Maximal angles were computed during two task stages (TS) of each trial, the reaching and the task completion, then plotted along with risk thresholds [6]. After visually checking for normality, mixed effect models were computed using R lmer function [9], the participant effect being modeled as a random intercept.

Results

Maximal angle levels were modified by spinal posture during at least one TS for shoulder forward flexion (6 TS, $p<0.001$), retropulsion (6 TS, $p<0.001$) and abduction (4 TS, $p<0.05$ to 0.001) (Fig 1), elbow flexion (1 TS, $p<0.01$), extension (1 TS, $p<0.001$), pronation (1 TS, $p<0.01$) and supination (3 TS, $p<0.05$ to 0.01), wrist flexion (1 TS, $p<0.001$) and extension (1 TS, $p<0.01$). Wrist abduction and adduction were not. Shoulder forward flexion and elbow extension reached the risk threshold [6] during 2 and 4 TS, respectively.
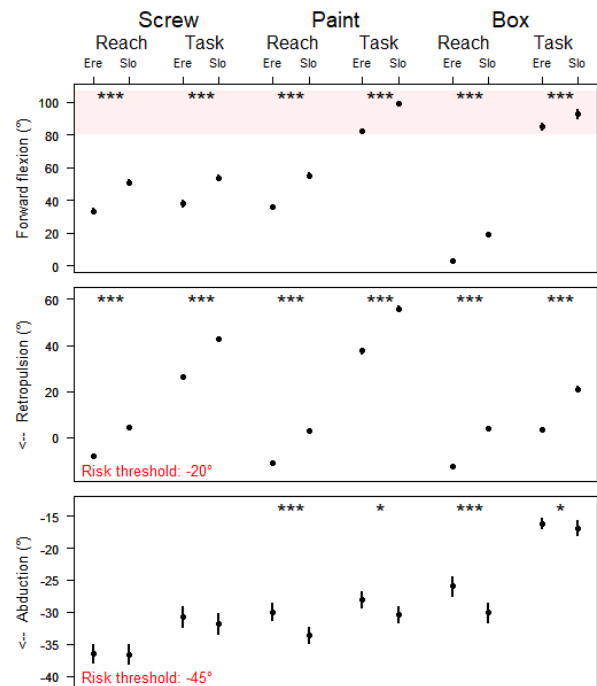
Figure 1. Thoraco-humeral maximal angles for each task and spinal posture (Ere-Slo): mean, SE. In red: risk threshold [6]. *** p <0.001, ** p <0.01, *p <0.05.

Discussion

Spinal postures affect upper limb kinematics, mostly at the shoulder level but also at the elbow and wrist. As tasks and outcomes were chosen to be relevant in terms of MSD risk, spinal posture may modify this risk, including remotely for some tasks. The main limitation of the study is the differences of angles computation methods used in the ergonomic standards [6] and in biomechanics [7]: threshold values must be considered with caution. As the risk of MSD increases with joint angle levels and also depend on the time of exposure [1], SPM statistics could complement these results.

References

1. Brière et al, Saint-Maurice: INVS, 2015, 51p.
2. Marik et al. Am J Occup Ther. 2017;71:7101180020p1–11.
3. Roll et al, Am J Occup Ther. 2017;71:7101180010p1–12.
4. de Alcantara, AleXitère, 2006.
5. Finley et al, Arch Phys Med Rehabil, 84:563-8, 2003.
6. NF ISO 11228-3, 2009.
7. Wu et al, J Biomech, 38(5), 981-992, 2005.
8. Senk et ak, Clin Biomech, 21 Suppl 1:S3-8, 2006.
9. Bates et al. JSS, 2015.

A NOVEL METHOD TO QUANTIFY PSEUDO-KINEMATICS OF THE RIB CAGE OVER THE VITAL CAPACITY RANGE

Claudio Vergari (1), Wafa Skalli (1), Louis Clavel (1,2), Michel Demuynck (1), Rémi Valentin (1,2), Baptiste Sandoz (1), Thomas Similowski (2,3), Valérie Attali (1,2,4)

1. Arts et Métiers Institute of Technology, Institut de Biomécanique Humaine Georges Charpak, Paris, France; 2. Sorbonne Université, INSERM, UMRS1158 Neurophysiologie Respiratoire Expérimentale et Clinique, Paris, France; 3. AP-HP, Groupe Hospitalier Universitaire APHP-Sorbonne Université, site Pitié-Salpêtrière, Département R3S, Paris, France; 4. Groupe Hospitalier Universitaire APHP-Sorbonne Université, site Pitié-Salpêtrière, Service des Pathologies du Sommeil, Département R3S, Paris, France

Introduction

Several pathologies can affect the relationship between breathing function, rib cage morphology and kinematics, and spinopelvic alignment. For instance, chronic respiratory pathologies and trunk deformities, such as scoliosis. Rib movements have previously been quantified experimentally, usually by acquiring sagittal radiographic images or CT scans of the chest at different lung volumes [1,2]. However informative, these techniques are either limited to 2D (radiography) or to the lying position, and induce high radiation dose (CT). The aim of this work was to determine the feasibility of functional analysis of the rib cage and the spine at rest and at minimal and maximal lung volumes using biplanar radiography.

Methods

Forty-seven healthy adults with normal respiratory function were included prospectively. Subjects were 21 female and 26 males, aged between 20 and 83 years (33 [25; 48] years old, median [1st, 3rd quartile]). Median height was 1.72 [1.65; 1.76] m, and median weight 71 [61; 78] kg. Subjects underwent low-dose biplanar radiographs and 3D reconstructions of the spine and rib cage using validated methods [3]. Acquisitions were performed at rest (functional residual capacity, FRC), and in apnea at total lung capacity (TLC) and full expiration (residual volume, RV). T1-T12 kyphosis was computed from the 3D model, as well as the orientation of each pair of ribs in the subject's anatomical sagittal plane ("pump-handle angle"). The ribs absolute orientation was measured relative to the horizontal. Results are reported as median [1st, 3rd quartile].

Results

T1-T12 kyphosis increased significantly on expiration (from 51° at FRC to 63° at RV, p<0.001) and decreased on inspiration (from 51° to 47° at TLC, p<0.001). Figure 1 shows the sagittal absolute angle at the three lung volumes. Significant differences were present at all rib levels and between all three lung volumes (p < 0.05). The median change between FRC and TLC (inspiration) was -16° while the change from FRC to TLC (expiration) was only -5°. Uncertainty of sagittal absolute angles was lower than 3.5° at all rib levels.

Discussion

In this work, pseudo-kinematics of the rib cage was acquired using biplanar radiography, giving an insight into rib cage function. Results were consistent with Wilson et al. [4], who measured sagittal angles in 2D, from rib 2 to 9, between 40 and 50° at FRC and 25° to 40 at TLC. The main limitation of this work is the pseudo-kinematic character of the acquisition, which might not reflect the rib cage conformation during continuous breathing. Nevertheless, results confirm that both the spine and the rib cage are largely involved in maximal inspiration and expiration, but also that their action is asymmetrical: inspiration mostly mobilized the ribs and costo-vertebral junction, while expiration was driven more by the spine. Further studies should apply the method to compare healthy subject and patients, to determine how the pattern of breathing function can be altered by the pathology.
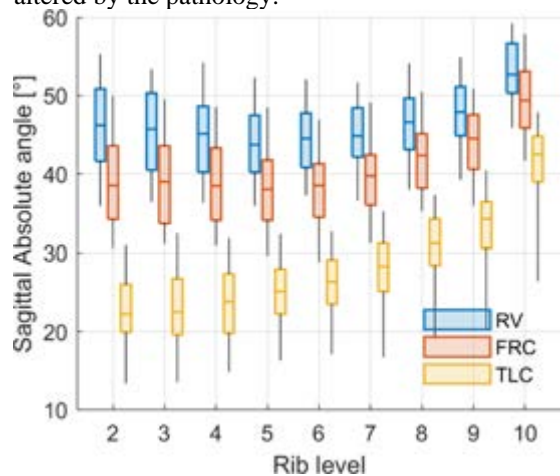

Figure 1: Sagittal angle of the ribs in RV, FRC and TLC.

References

1. Sharp et al, J. Appl Physiol, 61:2050–2059, 1986.
2. Beyer et al, Respir Physiol Neurobiol, 232:57–65, 2016.
3. Vergari et al., CMBBE Imaging Vis, 8: 15-23, 2020
4. Wilson et al., J Physiol, 530: 319–330, 2001

Acknowledgements

EXPLORING MINIMUM TOE CLEARANCE AS A PREDICTOR FOR RISK OF STUMBLES AND FALLS IN OLDER ADULTS

Marco A Avalos, Noah J Rosenblatt

Rosalind Franklin University of Medicine and Science, North Chicago, IL, USA

Introduction

Falls are the leading cause of unintentional injuries in older adults [1]. People who self-report multiple stumbles (i.e., balance losses without falls) are more likely to report a fall [2]. The possibility of stumbling over an obstacle during gait (i.e., tripping) may be greatest when the swing foot is at its' lowest point [3], defined as minimum toe clearance (MTC). While lower, more variable MTC may theoretically increase the risk of stumbling [4], prospective studies linking these measures and stumbles in community-dwelling older adults do not exist. In addition, metrics related to MTC distribution may also be relevant to predicting stumbles [4,5]. The purpose of this study was to provide initial evidence regarding the extent to which MTC, MTC variability and distribution, based on laboratory assessment, may serve as measures to predict the risk of community-based trip-related stumbles in healthy older adults. Identifying people at increased risk of stumbling, and in turn falling, may provide a means to reduce fall risk through targeted interventions to improve MTC [5].

Methods

We analyzed data from 50 older adults with BMI of 18.5-24.9 kg/m^2 or BMI $\geq$ 30 kg/m^2 recruited as part of a larger study on obesity and falls. Participants self-reported the number of falls in the prior year. They then walked across an 8 m walkway at a comfortable pace while the motion of a marker on the second metatarsal head ("toe marker") was tracked using motion capture. We normalized the vertical trajectory of the toe marker during swing phase to its value at the prior midstance, and MTC was identified in each swing phase as a local minimum in the trajectory. We calculated median MTC (MED), interquartile range (IQR), skewness, and kurtosis from each participant.

Participants reported their stumbles, including causes of stumbles, biweekly for one year following the collection of MTC data. We categorized participants as "stumblers" if they reported two or more trip-related stumbles during the year (N=14); otherwise, we defined them as "non-stumblers" (N=36). We used a multivariate analysis of covariance (MANCOVA) to compare group differences in the set of five variables, covarying for any demographics found to differ between groups.

Results and Discussion

The only demographic difference between groups was fall history, where "stumblers" were more than twice as likely to report a fall in the prior year (Table 1). A total of 107 trip-related stumbles were reported by stumblers (8.2 ± 9.4 per stumbler; maximum of 29).

	Non-Stumblers (n=36)	Stumblers (n=15)	p
Sex (F/M)	19/17	9/6	.870
Fall History (%)	33.3	71.4	.034
Age (years)	70.5(9)	69.0(6)	.468
Mass (kg)	79.3 ± 21.7	80.2 ± 15.5	.880
Height (cm)	168.9(17.8)	165.1(14.6)	.450
BMI (kg/m^2)	24.5(10.9)	30.3(10.9)	.577
Walking Speed (m/s)	1.03 ± 0.16	1.02 ± 0.19	.963

Table 1 *Demographics and anthropometrics of participants Note.* Normally distributed data are presented M ± SD, otherwise presented as MED (IQR).

Although group differences failed to reach significance in the MANCOVA, the stumbler group showed decreased median MTC with a platykurtic and less skewed MTC distribution. MTC-IQR was similar between groups (Table 2).

	Non-Stumblers (n=36)	Stumblers (n=14)	p
Median MTC (cm)	1.58 ± 0.62	1.44 ± 0.46	0.493
MTC-IQR (cm)	0.79 ± 0.27	0.77 ± 0.23	0.888
Skewness	0.53 ± 0.44	0.32 ± 0.32	0.213
Kurtosis	0.29 ± 0.93	-0.20 ± 0.70	0.107

Table 2 *Summary of average outcomes of the stumble groups Note.* Data is presented as M ± SD.

the absence of group differences may reflect a lack of ecological validity between MTC during level-ground walking in the laboratory and MTC in the community where people encounter and adapt MTC in response to complex environments (e.g., uneven surfaces). In addition, activity level may mediate the relationship between lab-based MTC and community-based stumbles; high risk of stumbling during gait may poorly predict the actual occurrence of stumbles if an individual is highly sedentary.

Conclusions

Although no significant differences were found between groups, the stumbler group had a more centralized and flatter distribution. Collectively, this suggest that stumblers may be less likely to have higher MTC values. Additional work is needed to understand the extent to which activity and MTC adaptability relate to stumbles.

References

1. Moreland et al, MMWR, 69:875-881, 2020.
2. Srygley et al, Arch Phys Med Rehabil, 90:786-792, 2009.
3. Barrett et al, Gait Posture, 32:429-435, 2010.
4. Begg et al, Gait Posture, 25(2):191-198, 2007.
5. Begg et al, Front Hum Neurosci, 8:1-6, 2014

WALKING IN CHILDREN WITH HEMIPLEGIA USING DIFFERENT TYPES OF ANKLE FOOT ORTHOSIS

Federica Camuncoli (1), Alessia Barbonetti (1), Luigi Piccinini (2), Eugenio Di Stanislao (3), Claudio Corbetta (2), Lucia Donno (1), Manuela Galli (1)

1. Department of Electronics, Information and Bioengineering, Politecnico di Milano, Milan, Italy;
2. Scientific Institute IRCCS Eugenio Medea, Bosisio Parini, Lecco, Italy;
3. ITOP SpA Officine Ortopediche, Palestrina, Rome, Italy;

Introduction

In cerebral palsy three main problems can be distinguished. The primary problems pertain tone abnormality (hypertone, hypotone or dystonia), selective motor control deficit, coordination and balance deficits, muscle weakness and sensory problems. Over time, primary problems also determine secondary ones consisting in muscular retractions and skeletal deformities. Finally, tertiary problems are all the compensatory strategies that children use to compensate for the abovementioned problems [1]. Ankle foot orthoses (AFOs) are prescribed to compensate for these complications and therefore are used on a daily basis. Thus, this study aims to compare the kinematics and kinetics of a new AFO, which is designed to support the patient during sport activities, with respect to the common devices currently available on the market in children with hemiplegia.

Methods

Seventeen children (11 males and 6 females, age: 8.6 ± 1.7 years, height: 1.31 ± 0.1 m, weight 28.5 ± 5.9 kg (mean ± SD)) aged between 6 and 11 years old with a diagnosis of right or left hemiparesis belonging to GMFCS I-II were recruited and provided with a custom made AFO designed by ITOP Officine Ortopediche SpA. The device was an evolution of the Carbon Modular Orthosis (Ca.M.O) [2], made of thermoplastic (polypropylene) calf containment, a foot shell with flexible tip and a composite posterior leaf spring (carbon-fibre mat pre-impregnated with acrylic resin) specifically designed to support motor activities such as running and/or jumping.

The experiments were conducted with the approval of the Ethical Committee at IRCCS Eugenio Medea (Bosisio Parini, Lecco, Italy).

Walking was evaluated in four conditions at self-selected speed: (i) barefoot (ii) wearing the commonly used AFO (iii) wearing the new AFO on the delivery (iv) wearing the new AFO after an adaptation period of about one month. Kinematic and kinetic data were acquired by an optoelectronic motion analysis system and four coupled force platform (8 cameras, BTS Smart DX 700, P-6000, Bioengineering, Milano, Italy).

For each subject three valid gait trials were averaged and then analysed through a custom-made script in Matlab®. SPM was used to detected statistical differences among the conditions. A one-way repeated measure ANOVA (α = 0.05) followed by post hoc test (two tailed paired t-test with Bonferroni correction) was applied.

Results

The graphs (Figure 1) show the effects of orthoses on children's gait at the level of the ankle.
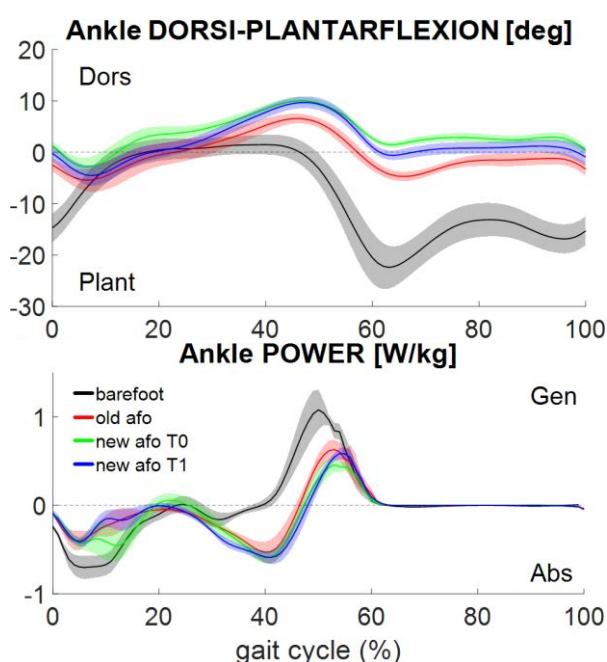
Figure 1: ankle kinematic and power of the affected side during the gait cycle. Mean and SD of four conditions are represented.

Discussion

For both ankle kinematics and kinetics the post hoc tests highlighted statistically significant differences ($p<0.01$) in all trial conditions with respect to each other.

Even if it is designed for use in high impact activities, the new AFO determines ankle biomechanics in walking that is quite similar to that of the common devices (effective in the correction of the 1st and 2nd rockers). The graphs also depict that it is essential to allow children time to adapt to the use of the device, as the curve at the delivery (in green) improves at timepoint T1 (in blue).

References

1. Armand et al., *EFORT Open Rev*, 1(12):448-460, 2016.
2. Tavernese et al., *NeuroRehabilitation*, 40(3):447–457, 2017.

LONG TERM EFFECTS OF AN ACL RECONSTRUCTION ON KNEE JOINT KINEMATICS AND LOADING

Johannes Eichwalder (1), Willi Koller (1), Arnold Baca (1), Patrick Weninger (2), Hans Kainz (1)

1. *Centre for Sport Science and University Sports, University of Vienna, Vienna, Austria*
2. *Sports Medical Center, Vienna, Austria*

Introduction

Rupture of the anterior cruciate ligament (ACL) is one of the most common sports injuries, and despite advance reconstruction surgery, only 55% reach their pre-injury level of sports [1]. Rehabilitation programs aim to restore typical symmetrical joint kinematics and loading. Contralateral differences in joint angles, joint moments, and muscle activations affect the knee joint loading[2]. A previous study showed that asymmetrical gait patterns lead to asymmetrical, higher loading of the tibiofemoral joint [2]. In the long run, atypical joint loading can lead to degenerative joint diseases such as osteoarthritis [3]. Hence, it is of utmost importance to know if people with a reconstructed ACL manage to restore typical and symmetrical joint kinematics and loading.

The twofold aim of this study was 1) to determine if asymmetric movement pattern and joint loading are maintained in people with a reconstructed ACL even after completing the rehabilitation program, and 2) assess if the asymmetry in movement pattern and joint loading depends on the intensity of the movement. We hypothesized that 1) people with a reconstructed ACL have larger asymmetries in joint kinematics and loading compared to people without a previous ACL injury and 2) the asymmetry in joint kinematics and loading increases with the intensity of the movement. The findings of this study are intended to increase our insights into the functional long-term consequences of an ACL reconstruction.

Method

Data (walking, forward lunge, star excursion balance test) were collected and analyzed from eight male participants with a unilateral reconstructed ACL (age: 24.4 ± 2.7 years; weight 78.8 ± 7 kg; height 1.79 ±0.1 m; injury 5-right 5-left, time since reconstruction surgery 36.6 ±14 months) and compared with a control group (n=8; age: 24.1 ± 2.5 years; weight 80.4 ± 9.5 kg; height 1.83 ± 0.1 m). Three movements with increasing intensity (walking, forward lunge, and star test) were recoded via a three-dimensional motion capture system (10 cameras, Vicon Motion Systems, Oxford, UK, five force plates, Kistler Instruments AG, Switzerland).

Musculoskeletal modelling was performed using the model from Lenhart et al.[4]. This model includes a 6 degrees-of-freedom tibiofemoral joint and includes the ligaments of the knee joint. After scaling the model to the anthropometry of each participant, joint kinematics, joint kinetics, muscle and joint contact forces, and ligament strains were calculated using OpenSim 4.1 [5].

We compared knee kinematics and ACL strains between the injured and uninjured leg, as well as between the ACL and control group.

Results

So far, we analyzed the walking trials and therefore these results are presented in this abstract. The difference in knee joint angles, ACL bundle length, and strain between the injured and uninjured leg did not significantly differ to the left-right differences of our control group.
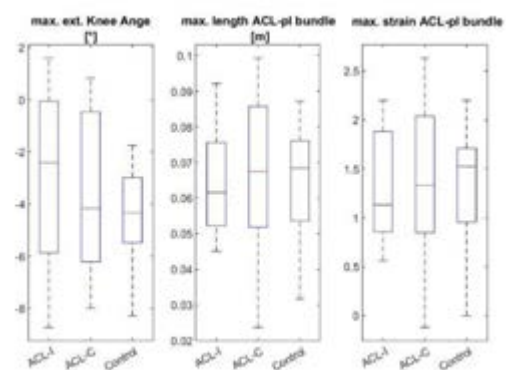
Figure 1: Boxplots showing the maximum knee extension angle, length and strain of the ACL for the operated (ACL-I) and non-operated knee (ACL-C), and the control group (Control).

Discussion

Against our hypothesis, we did not find any significant difference in knee joint angles and ACL strain between the ACL and control group. However, it is noteworthy that the ACL group included a higher variability in the injured and uninjured leg compared to the control group (Figure 1), indicating that some people have problems returning to a symmetric walking and loading pattern.

We only analyzed the walking trials of our participant so far. Next, we will investigate if more intense movements, i.e., forward lunge and star excursion balance test, lead to the same results.

References

1. Ardern et al., Br. J. Sports Med, 48:1543–1552, 2014.
2   Capin et al., J. Orthop. Res, 36:2364–2372, 2018.
3   Dare et al., Curr. Rheumatol. Rep, 16:1–5, 2014.
4   Lenhart et al., Ann. Biomed. Eng, 43:2675–2685, 2015,
5   S. L. Delp et al., Delp2007, 54:1940–1950, 2007.

A VECTOR FIELDS ANALYSIS TO INVESTIGATE FOOT-GROUND INTERACTIONS IN INFANCY DURING WALKING

Eleonora Montagnani (1), Stewart C Morrison (1), Carina Price (2)

1. University of Brighton, UK; 2. University of Salford, UK

Introduction

Center of pressure (COP) data in infancy is scarce, limited to small samples and low-resolution analysis approaches that extrapolated scalars from medio-lateral (ML) and anterior-posterior (AP) components of COP trajectories (1). As a result, analysis of continuous fields has been simplified and COP trajectories have not been treated in their original forms, thereby sacrificing data quality. This work aimed to provide a comprehensive investigation of foot-ground interactions in infants mastering walking. This was achieved by implementation of a robust processing framework to analyze ML and AP components of the COP using Statistical Parametric Mapping (SPM), in addition to analysis of stability indices (1).

Methods

Thirty-nine infants walked across an EMED-xl platform at walking onset, and again when confidently walking. Frames of 468 pressure steps were exported as ASCII files in Matlab 2019b. Frames for each participant and stage were embedded in standardized matrices and aligned vertically along the foot axes using principal component analysis (PCA). COP trajectories were exported from frames (2) and AP and ML treated as separate vectors given: $v(q) = \{v_x(q)\ v_y(q)\}$, where q is the time domain. After being temporally normalized, within-subjects ML and AP trajectories were estimated for each participant and stage of walking. Comparison between stages was undertaken using nonparametric SPM1d paired t-test. Foot stability indices (R_x and R_y) (1) were calculated as averaged scalars from the ML and AP trajectories and compared between stages using Wilcoxon-Signed Rank tests.

Results

AP trajectories differed significantly between 0 and 10% of the stance (Fig.1). No differences were detected with respect to the ML trajectories, although an accentuated shift of medio-lateral loading was evident in confident walkers, who also showed significantly decreased R_x and R_y (p=0.001).

Discussion

After 2.3 months of walking experience, significant increase in posterior loading at the beginning of stance highlighted the initial heel contact. Despite the robustness of our processing framework, high inter-individual variability in origin of AP trajectories was visible in both stages. This highlights sensitivity of AP trajectory to the large inter-individual variability of plantar pressure and contact pattern. No significant changes were present for ML trajectory, but our analysis suggested a more accentuated medial-to-lateral loading transfer in confident walking over stance. These findings objectively demonstrated, for the first time, the presence of a typical yet immature rollover pattern of the foot. With R_x and R_y decreasing, this work also showed that changes in foot-ground interactions occur with increasing stability. As a result, improved foot-ground interactions occur at an early stage of development, underpinning changes of gait dynamics in the transition to confident walking.
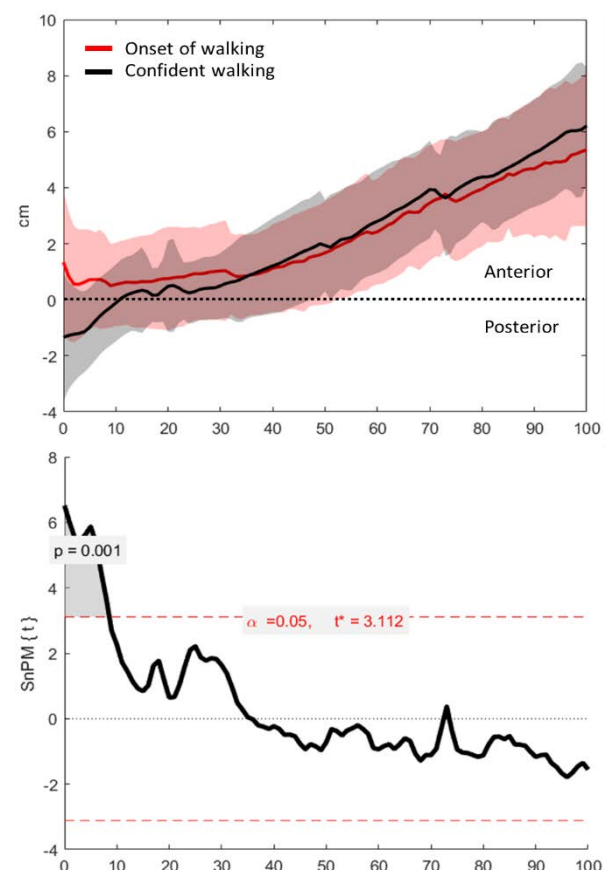

Figure 1: (Top) Mean and SD (cm) of temporally-normalizes AP trajectories. Zero is the mean origin value of AP trajectories calculated between stages. (Bottom) Nonparametric SPM1d Paired t-test for comparison of AP trajectories between walking stages.

References

(1)Hallemans A., et al. (2003); F&AI 23: 142-148;
(2)Rashid U., et al. (2018); B&B, 21:361-364.

DEVELOPMENT OF GROSS MOTOR CONTROL IN SCHOOL-CHILDREN: INFLUENCE OF AGE, SEX, AND ANTHROPOMETRY

Rita Stagni (1), Alice Masini (2), Stefania Toselli (2), Sofia Marini (2), Laura Bragonzoni (3), Andrea Ceciliani (3), Marcello Lanari (4), Alessandra Sansavini (5), Alessia Tessari (5), Davide Gori (2), Laura Dallolio (2), Maria Cristina Bisi (1)

1. Department of Electrical, Electronic and Information Engineering "G. Marconi", University of Bologna, Italy; 2. Department of Biomedical and Neuromotor Science, University of Bologna, Italy; 3. Department of Life Quality Studies, University of Bologna, Italy; 4. Department of Medical and Surgical Sciences; University of Bologna, Italy; 5. Department of Psychology "Renzo Canestrari", University of Bologna, Italy

Introduction

Timely motor development in childhood is the foundation of healthy adult life and aging, affecting not only physical, but also mental health, and social participation. Nevertheless, how intrinsic and extrinsic factors influence this development is still not clear. Several approaches have been proposed for the monitoring of motor development, but recently, wearable inertial sensors allowed to develop a quantitative longitudinal assessment approach, exploitable in ambulatory conditions [1]. The present study is comprised in the I-MOVE study [2], a school-based intervention trial, with a quasi-experimental design, performed in a primary school, and aims to analyze gross motor development in school children with respect to age, sex, and anthropometric characteristics.

Materials and Methods

One hundred and fifty children from an Italian primary school participated in the study, 72 first- (38M, 34F; age 75±5 months) and 78 third grade (48M, 34F; age 108±6 months). The study was approved by the University of Bologna Bioethics Committee, on the 18th of March 2019 (Prot. n. 0054382 of 18/03/2019). The study was conducted following the Declaration of Helsinki and approved by the school board. Anthropometric characteristics (height, weight, triceps and subscapular skinfold thicknesses) were collected according to standardized procedures. Children walked along a 20m straight path 3 times back and forth at self-selected speed (NW) and once in tandem (TW) wearing three inertial sensors (OPAL, APDM, Usa) on the lower back and on the shanks. Temporal parameters, short- and long- term variability, and nonlinear metrics of trunk kinematics (i.e. recurrence quantification analysis, multiscale entropy) were calculated and statistically analyzed (Kruskal-Wallis test 5%) with respect to age, sex, and anthropometric characteristics (i.e. weight, height, BMI, and triceps and subscapular skinfold thicknesses).

Results

Stance and double support duration increased during NW and decreased during TW with age independently from sex, while their variability decreased in both NW and TW. Automaticity (i.e. recurrence indexes) increased with age during NW more in female than in males, while it decreased during TW independently from sex. Complexity (i.e. entropy) increased with age during TW, but not in NW. No dependency on height or weight alone was identified independently from age, while overweight (i.e. BMI and skinfold thicknesses) was associated to a reduction in the development of automaticity during NW independently from age and sex.
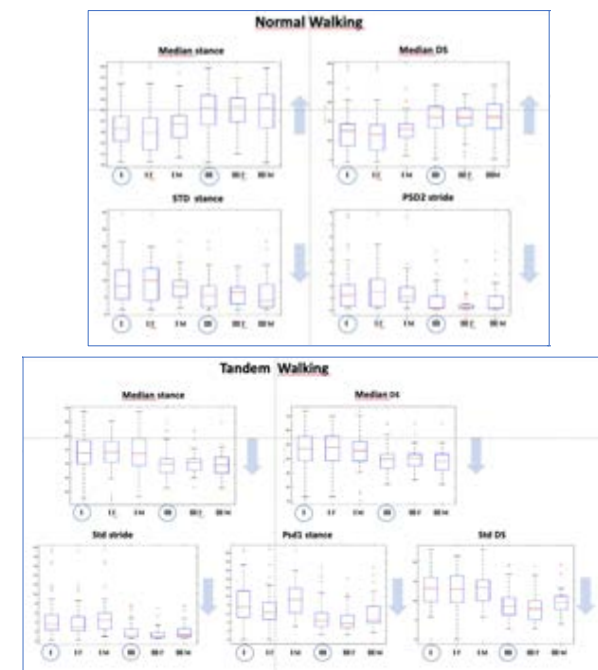
Figure 1: Temporal parameters (stance and double support) and variability (standard deviation, Std, short- and long-term variability, PSD1 and PSD2) as related to age (first grade, I, third grade, III) and sex (F, M)

Discussion

Both sex and anthropometry resulted to influence motor development in the target population, in particular overweight appears to delay the maturation of automaticity.

References

1. Bisi et al. Gait&Posture. 68:232–237, 2019.
2. Masini et al., Environmental Research and Public Health, 17:1-16, 2020

SINGLE IMU BASED OPEN-SOURCE AND LOW-COST GAIT EVENT DETECTION WEARABLE DEVICE

Nitzan Breitman (1), Arielle Fischer (1)

1. Department of Biomedical Engineering, Technion, Israel Institute of Technology, Israel

Introduction

Ankle sprains are common injuries that without proper treatment and rehabilitation can cause aberrant movement patterns and pain [1]. Laboratory motion-capture systems are recognized as the gold standard for movement quantification that are limited to controlled environments due to the lack of portability and technical expertise required. Rehabilitation may benefit from real-time gait event detection for use in event-dependent feedback wearable devices that can be used in and outside of the lab [2,3]. Gait event assessment in real life walking conditions is needed while using few sensors to allow easy reproducibility. We propose an inexpensive, lightweight, wireless design and validation of an open-source gait event detection wearable device. A custom developed system software performed adaptive real-time gait detection algorithms based on a single gyroscope mounted on the shank.
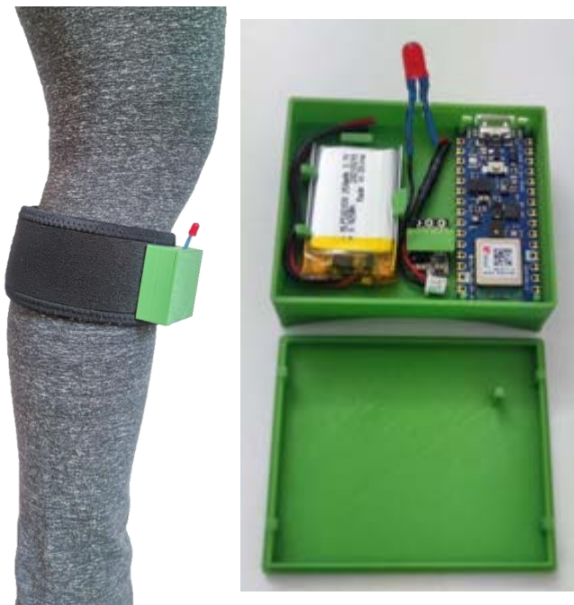
Figure 1: Right, gait event detection system components overview. Left, device attachment location on shank.

Methods

The developed device is based on an Arduino Nano 33 BLE Sense, a 3.7 Volt 250 mAh Li-Po battery and a 3.7 to 5 Volt step-up voltage regulator. All components were strategically placed in a custom designed enclosure (45x55x21 mm) 3D printed of polylactic acid (PLA) (figure 1). Total cost was less than $45. The device sits on the shank with an elastic strap.

We developed an algorithm that records the change in angular velocity and detects two distinct gait events i.e., Mid-Swing (MS) and Heel-Strike (HS), by calculating the local minima, maxima, and zero-crossing. We incorporated a patient specific gait pattern self-correcting adjustment of MS and HS thresholds.

Results

The device was designed based on readily available low-cost off-the-shelf components. We validated our gait event detection algorithms by capturing a LED signal indicating HS using a slow-motion camera. Onboard algorithms then calculated when MS and Toe-Off occur. The device was tested on six healthy subjects and successfully showed consistent gait event detection. Additionally, we developed an app that records and displays the data collected in real-time and sends it to the cloud. Data were then analyzed offline using MATLAB. The gait detection algorithm and device were designed to be an open-source.

Discussion

Motion capture systems are the bread and butter of biomechanical gait analysis research but many times limits researchers/experiments settings to the physical dimension of the lab. We developed a system that accurately captures gait events from one inertial measurement unit (IMU) sensor, records the data, and displays it in real-time. The system is not confined to the lab and can be modulated to researcher's needs by adding sensors and functions, such as surface electromyography for muscle function monitoring, vibration for biofeedback and video capture. This system will enable us to assess the capacity of a wearable inertial-based system to detect gait events and evaluate the effectiveness of interventions and quantify rehabilitation progress. Future studies will show the effect of intermittent stimulation of cutaneous afferents and muscle spindles on lateral ankle sprain patients.

References

1. Wikstorm EA et al, Sport Med 43(6):385-393, 2013.
2. Aminian K et al, J Biomech, 35(5):689-699, 2002.
3. Bötzel K et al, J Biomech, 49(3):332-337, 2016.

KINEMATIC CHANGES DURING WALKING WITH WHOLE-BODY VIBRATION AND PSYCHOMOTOR TESTING

Alex P. Moorhead[1,2], Andrea Mazzoleni[1], Alessandra Goggi[2], Stefano Marelli[1], Giuseppe Lorenzini[1], Marco Tarabini[1]

1. *Department of Mechanical Engineering, Politecnico di Milano, Italy*
2. *Department of Electronics, Informatics, and Bioengineering, Politecnico di Milano, Italy*

Introduction

Human locomotion is achieved through complex coordination of the musculoskeletal and cognitive systems in which there are constant adjustments to the continually changing environment. In daily circumstances, humans are very adept at responding to unlevel ground, obstacles, or unforeseen variables. The responses are typically brief, and natural gait is resumed quickly. However, if either of these systems are out of sync, it would, at a minimum, lead to inefficient and uncoordinated movement, and at worst, be hazardous for tripping or falling [1]. The cognitive response in these situations is rarely even considered if there aren't other cognitive factors which require attention. However, in many working and recreational activities, humans are exposed to extended bouts of whole-body vibration (WBV) which create an abnormal amount of stress to the musculoskeletal and cognitive systems [2]. This is particularly important to consider workers such as on planes and trains who must respond not only to daily WBV exposure but also interact with clients. By measuring the kinematic changes in gait during WBV exposure and cognitive testing, we can start to understand how the functional changes in human behavior are related to the biodynamic responses to WBV and potentially begin formulating new standards for safety.

Methods

Twenty-one male participants (31 ± 7 years old, 27.75 ± 1.75 cm foot length, 178 ± 13 cm tall, 70.5 ± 15.5 kg; mean $\pm$ SD) were asked to perform two 7-minute trials of walking at 1.4 m/s on a treadmill mounted to a lateral shaker. One trial without vibration, one with 1 m/s^2 rms acceleration. After 2 minutes of walking, subjects performed a 5 minute Psychomotor Vigilance Test (PVT). Kinematic data were gathered using an Xsens Link sampling at 240 Hz during the 2nd and 7th minutes resulting in four data sets per subject. Strides were cut based on consecutive heel strikes of the same foot. Kinematic stride parameters were then compared using statistical parametric mapping (SPM) to determine at what percentage of the stride that gait kinematics were significantly different between walking with and without PVT or vibration.

Results

Differences in joint abduction were shown to be statistically significant in the hip and both knees when comparing the kinematics of walking with and without vibration.
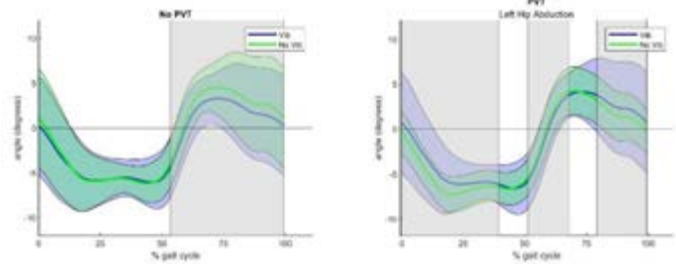
Figure 1: SPM analysis of all subjects left hip abduction time curves with vibration (blue) and without vibration (green) during the course of a mean stride without PVT (left) and with PVT (right). Grey bars show moments of significantly different abduction.
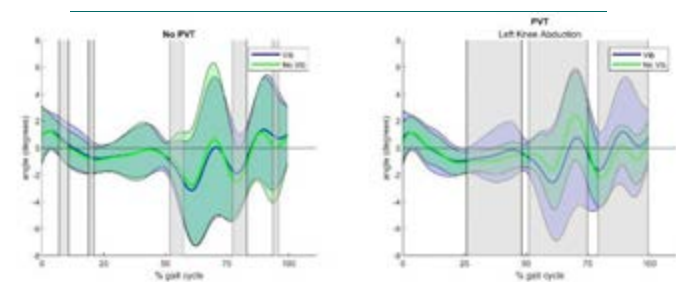
Figure 2: SPM analysis of all subjects left knee abduction time curves with vibration (blue) and without vibration (green) during the course of a mean stride without PVT (left) and with PVT (right). Grey bars show moments of significantly different abduction.

Discussion

Aside from right elbow flexion and neck flexion, there were no statistically significant differences found in walking kinematics due to PVT. Both were attributed to the posture required to perform the PVT and not due to cognitive strain. In contrast, lower limb joint abduction showed significant differences in both the knees and the hips when walking with and without vibration. Results suggest that psychological testing does not affect gait whereas vibration leads to more unstable gait.

References

1. Yang F, Munoz J, Han L zhu, Yang F (2017) Effects of vibration training in reducing risk of slip-related falls among young adults with obesity. J Biomech 57:87–93
2. Bovenzi M, Hulshof CT, Hulshof MBCTJ (1999) An updated review of epidemiologic studies on the relationship between exposure to whole-body vibration and low. IntArchOccupEnvironHealth 72:351–365

VALIDATION OF AN INERTIAL-BASED GAIT ANALYSIS SYSTEM USING A SIX DEGREES-OF-FREEDOM JOINT SIMULATOR

Ariana Ortigas Vásquez (1, 2, 3), Allan Maas (1, 3), William R. Taylor (2), Thomas M. Grupp (1, 3)

1. Research and Development, Aesculap AG, Tuttlingen, Germany
2. Laboratory for Movement Biomechanics, Institute for Biomechanics, ETH Zürich, Switzerland
3. Department of Orthopaedic and Trauma Surgery, Musculoskeletal University Center Munich (MUM), Campus Grosshadern, Ludwig Maximilians University Munich, Munich, Germany

Introduction

State-of-the art in gait analysis includes optical motion capture and dynamic fluoroscopy, both of which require considerable expense, time and infrastructure. Consequently, the demand for an affordable mobile alternative has been recently addressed with inertial motion units (IMUs) [1]. IMU-based gait analysis systems, however, are highly heterogenous, differing in hardware components, algorithms and biomechanical models. There is therefore a need for a standardised validation protocol with which to assess the accuracy of these systems. In a first analytical validation step, the inherent error of the algorithm used to obtain joint angle estimates should be determined. The options currently available (e.g., manually operated mechanical rigs or commercially available robot arms) are subject to limitations, including unrealistic joint geometry, lack of soft tissue modelling, and incompatible coordinate frames. This study thus aims to test a potential validation protocol which employs a six-degree-of-freedom hydraulically actuated joint simulator to generate realistic motions based on actual patient data.

Methods

To avoid a separate extensive calibration procedure and the use of magnetometer data, as well as to allow arbitrary sensor placement, a specific implementation of an extended Kalman filter and smoother was employed to estimate knee joint angles from angular velocity and linear acceleration [1]. The joint simulator (VIVO, AMTI, Watertown, MA) was programmed to replicate a custom gait profile based on previously published patient data [2], such as to replicate level walking.
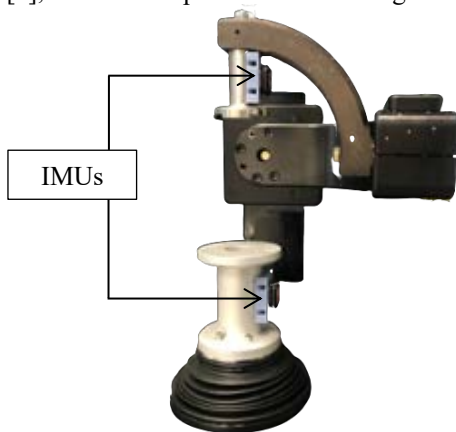
Figure 1: Six degrees-of-freedom joint simulator setup with IMU sensors attached.

Two IMUs (Xsens DOT, Movella, San Jose, CA) were adhered to the joint simulator using mounting strips: one on the condylar adapter and the other on the tibial adapter. Data were sampled during each simulation trial at a rate of 60 Hz. Finally, root-mean-square error (RMSE) for a representative gait cycle was assessed to measure the difference between IMU-estimated kinematics and simulator-generated ground truth data.

Results
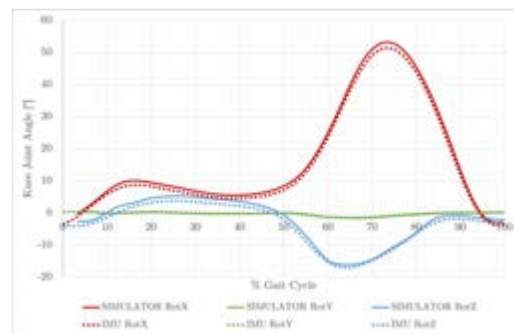
Figure 2: Knee joint angles as per Grood and Suntay [3] in the sagittal (red), frontal (green) and transverse (blue) planes, according to joint simulator (solid) and IMU (dashed) data.

As shown in Figure 2 and Table 1, joint angles are estimated with less than 2° error. While the maximum absolute error on x-axis and z-axis rotations has a magnitude of 1.9° and 1.7°, respectively, the error on rotations around the y-axis never surpasses 0.3°.

	Sagittal	Frontal	Transverse
RMSE (°)	1.32	0.13	1.17

Table 1: RMSE for the knee joint angles estimated based on IMU data versus joint simulator.

Discussion

Using a six degrees-of-freedom joint simulator offers a reliable way to generate realistic ground truth data for validation of new gait analysis systems. A comparison between simulator and IMU-based measurements is possible, thus assessing the inherent error of a system prior to the introduction of soft tissue artefact.

References

1. Versteyhe et al, Sensors, 20(6):1683, 2020.
2. Bergmann et al, PLoS ONE, 9(1): e86035, 2014.
3. Grood & Suntay, J Biomech Eng, 105(2):136-44, 1983.

BIOMECHANICS IN THE WILD: VALIDATION OF A WEARABLE KINETIC MEASUREMENT SYSTEM

Huawei Wang*, Akash Basu, Guillaume Durandau, and Massimo Sartori
University of Twente, the Netherlands

Abstract

Current conventional setup (optical motion capture + force plate) for human motion measurement requires participants to stay in a restricted capture region, which limits the testable movement types as well as the duration of measurements. In this study, we built a fully wearable system, based on available systems (initial measurement units + pressure insoles) that has the ability to measure both kinematic and kinetic motion data. In addition, its capability and accuracy in estimating joint angles and moments were tested against a conventional 8-camera based motion capture system.

Introduction

Most studies in evaluating wearable measurement systems mostly focus on testing single-type sensor: either kinematic or force sensors [1], which prevents estimation of musculoskeletal internal states, such as joint torques and muscle forces. Previous studies estimated movement kinetics using kinematic measurement sensors, however, the underlying machine learning methods used have shown limits in extrapolating to untrained motion types [2]. In this work, we built a fully wearable system based on available inertial measurements unit and pressure insole systems and tested its ability of directly estimating internal motion states.

Methods

An experiment was conducted, with 12 healthy participants (age: 26 ± 3 years; weight: 69.8 ± 12.0 *kg*; height: $1.71 \pm 0.07m$) wearing the wearable measurement system and performing 13 daily movement types, from slow walking to fast running, together with vertical jump, squat, lunge and single leg landing, inside the capture space of the conventional system. Then, the recorded motion data were post-processed to obtain the information of joint angles, ground reaction forces (GRFs), and joint torques, of both measurement systems

Results

Comparing to the conventional system (optical mocap and instrumented treadmill data), the established wearable measurement system was able to measure sagittal plane lower limb joint angles (Pearson's r = 0.929), vertical GRFs (Pearson's r = 0.954), and ankle torques (Pearson's r = 0.917). Center of pressure (CoP) at the anterior-posterior direction and knee joint torques are fairly matched (Pearson's r = 0.683 and 0.612, respectively). Hip joint torques and medial-lateral CoP are not matched (Figure 1).
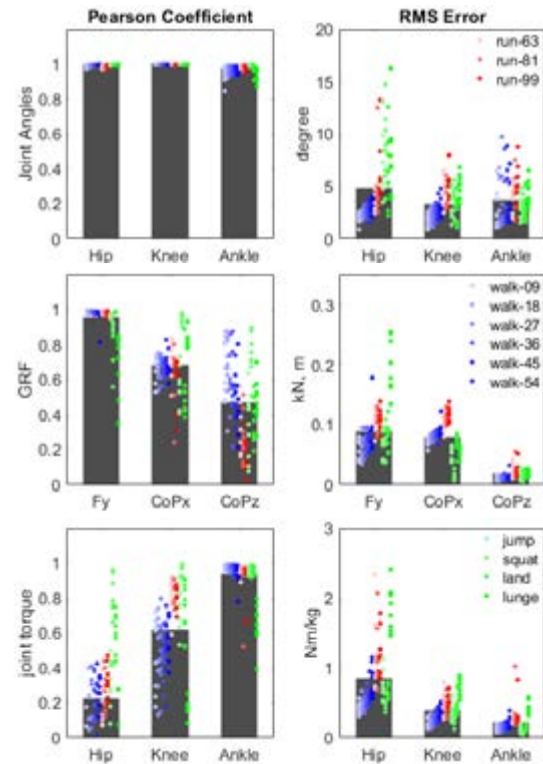
Figure 1. Pearson coefficients and root mean square error of joint angles, GRFs, and joint torques. The bar values are averaged among all subjects and experimental trials. Colored dots represent the value for each subject at each movement trial (bule indicates walking; red indicates running, and green indicates jump to lunge.) The grey level of each color separates the motion speeds and movement types. The different dots at the same vertical column are in the same movement trial, but different subjects.

The calculated joint torques of the wearable system did not depend on the estimation of the horizontal GRFs. Future work will test whether the validation results shown in this study apply to other movements that were not included in the validation testing, such as sit-to-stand, stepping stairs, and so on.

In conclusion, the established wearable measurement system can provide accurate kinematic data at lower limb and good kinetic data at ankle joint without the need of estimation horizontal GRFs.

References

1. Al-Amri et al, Sensors, 18:719, 2018.
2. Karatsidis et al, Sensors, 17(1):75, 2016.
3. Farber et al, J Biomechanics, 70: 235-241, 2018

Acknowledgements

CAN WALKING SPEED BE ACCURATELY ESTIMATED USING A MARKER-BASED GAIT EVENT DETECTION METHOD?

Tecla Bonci (1), Francesca Salis (2), Kirsty Scott (1), Lisa Alcock (3), Clemens Becker (4), Andrea Cereatti (5), Eran Gazit (6), Clint Hansen (7), Jeffrey Hausdorff (6), Walter Maetzler (7), Palmerini Luca (8), Lynn Rochester (3), Basil Sharrack (9), Ioannis Vogiatzis (10), and Claudia Mazzà (1), on behalf of the Mobilise-D consortium

1. Dept of Mechanical Engineering & INSIGNEO Institute for in silico Medicine, The University of Sheffield, UK; 2. Dept of Biomedical Sciences, University of Sassari, IT; 3. Translational and Clinical Research Institute, Newcastle University, UK; 4. Dept for Geriatric Rehabilitation, Robert-Bosch-Hospital, DE; 5. Dept of Electronics and Telecommunications, Politecnico di Torino, IT; 6. Centre for the Study of Movement, Cognition and Mobility, Tel Aviv Sourasky Medical Centre, IL. 7. Kiel University and University Hospital Schleswig-Holstein, DE; 8. Dept of Electrical, Electronic, and Information Engineering, University of Bologna, IT; 9. Dept of Neuroscience, Sheffield Teaching Hospitals, UK; 10. Dept of Sport, Exercise and Rehabilitation, Northumbria University Newcastle, UK.

Introduction

Quantifying gait metrics during complex motor tasks is of interest when aiming to a discriminative assessment of patients in early stages of a given condition [1]. The accuracy of such metrics is affected by the correct identification of foot-to-ground initial contacts (ICs). Indirect IC identification from stereophotogrammetric (SP) data is a convenient solution to monitor consecutive ICs during complex tasks, but SP-based IC methods have been limitedly validated in curvilinear walking [2]. This study aims to validate a new method for IC detection during different performance tests that include turning while walking, evaluating its impact on walking speed quantification both in healthy and mobility impaired participants.

Methods

Ten participants from six cohorts were included in this study (young healthy adults (YHA): 4 F, 27.1 ± 5.3 yr., 21.8 ± 2.3 kg/m^2; older healthy adults (OHA): 5F, 72.4 ± 6.8 yr., 25.6 ± 4.2 kg/m^2; chronic obstructive pulmonary disease (COPD): 5F, 72.1 ± 8.7 yr., 25.5 ± 5.2 kg/m^2; multiple sclerosis (MS): 4F, 53.1 ± 9.6 yr., 31.9 ± 7.8 kg/m^2; Parkinson's disease (PD): 1F, 69.3 ± 6.0 yr., 26.1 ± 4.3 kg/m^2; proximal femur fractures (PFF): 3F, 82.9 ± 7.7 yr., 24.3 ± 4.5 kg/m^2) and performed three tests: Timed Up and Go, L-Test and shuttle walk. Reference IC (*rIC*) were identified using sixteen force-sensing resistors embedded in two pressure insoles (PI) [3]. SP (10-camera Vicon T160) and PI signals were acquired in a synchronised fashion (f_s = 100 Hz) [3]. Marker-based ICs (*mIC*) were detected when the 3D velocity of the maker placed on the heel fell below test-specific 0.5*walking speed thresholds. For each participant and test, using heel marker trajectories and relevant time instants (i.e., IC), reference (*rWS*) and marker-based (*mWS*) walking speeds were calculated as average stride speed using *rIC* and *mIC*, respectively. For each cohort, mean IC temporal errors (Δt) and differences between *rWS* and *mWS* (ΔWS) were evaluated and compared using paired t-tests (Matlab R2021a; p<0.05).

Results

Figure 1 shows the IC temporal identification inaccuracies and their relevant impact on walking speed quantification (ΔWS) as calculated for each cohort. No significant statistical difference was observed between *rWS* and *mWS* (p>0.05) in any of the cohorts.
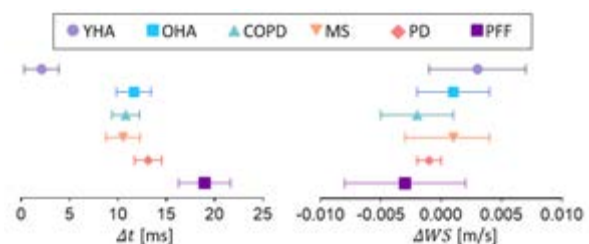
Figure 1: Mean differences and confidence intervals for Δt and ΔWS.

Discussion

The proposed method accurately identified ICs in all the cohorts, while existing methods have been verified only on impaired straight-line walking or on small curvilinear portions in YHA and OHA ($\Delta t \approx 11\,ms$) [2]. ICs inaccuracies did not significantly affect WS estimations, either in the healthy (YHA and OHA) or in the impaired cohorts. Moreover, the observed mean differences and their confidence intervals were always lower than clinically meaningful changes in speed previously reported for older adults (0.05 m/s) [4]. Overall, the proposed method can be used to accurately measure IC and WS also when walking while turning is included.

References

1. El-Gohary M et al, Sensors, 14(1):356–69, 2014.
2. Ulrich B et al., J Biomech, 91:69–78, 2019.
3. Salis F et al, J Biomech, 127:110687, 2021.
4. Perera S et al, J Am Geriatr Soc, 54(5):743–749, 2006.

Acknowledgements

PROPRIOCEPTION, MUSCLE ACTIVITY AND TIBIAL TRANSLATION DURING HEEL STRIKE IN RUNNING: ROLE OF ACL SURGERY TYPE

Linda Bühl (1,2), Niklas Bleichner (1), Corina Nüesch (1,2), Sebastian Müller (1), Geert Pagenstert (3), Christian Egloff (1), Annegret Mündermann (1,2)

1. University Hospital Basel, 2. University of Basel and 3. Clarahof Orthopedics, Basel, Switzerland

Introduction

Anterior cruciate ligament repair with InternalBrace augmentation (ACL-IB; Arthrex Inc., USA) after proximal ACL ruptures is an alternative to gold-standard ACL reconstruction (ACL-R). Preservation of the native ACL after ACL repair is believed to maintain neuromuscular integrity, provide more natural joint mechanics [1], and thereby retain dynamic stability. Here, we compared proprioception, muscle activity and tibial translation (TT) between ACL-IB, ACL-R and healthy controls.

Methods

Knee proprioception, TT and muscle activity (Root Mean Square in functional intervals before [-200;-100], at [-100;0] and after [0;100] ms of heel strike) during treadmill running at self-selected speed were compared among sex- and age-matched groups (N=19 each): ACL-IB (13m/6f; age 37±11years; body mass index 24±3kg/m²; 25±4months postoperatively); ACL-R using semitendinosus tendon (13m/6f; 38±12years; 25±2kg/m²; 25±4months postoperatively); healthy controls (13m/6f; 37±11years; 24±4kg/m²). Knee proprioception was assessed in active-active joint position reproduction tests (JPS) at 60° and 30° knee flexion. Muscle activation was measured via electromyography (Myon AG, CH) and normalized to maximal voluntary contraction on a dynamometer (MVC; vastus medialis, vastus lateralis, and semitendinosus muscles). Range and velocity of anterior/posterior TT were measured using motion capture (VICON, UK) and the Point Cluster Technique for 15 gait cycles. Group differences (operated (patients) vs non-dominant (controls)) were detected using Kruskal-Wallis and Dunn-Bonferroni Post Hoc tests (P<.05).

Results

Self-selected speed, JPS (deviation in all groups <5°), range of TT, knee flexion and muscle activity did not differ between groups (P>.190). Compared to controls, no ACL group differed in TT velocity (P>0.80). Between patients, ACL-IB had slower anterior (P=.019) and posterior TT (P=.017) (Fig. 1A). Overall, ACL-IB had the lowest and ACL-R the highest values in TT.

Discussion

Surprisingly, the ACL groups did not differ in JPS and did not have clinically relevant deficits [2]. Although proprioception seems to improve during the acute rehabilitation after ACL-R, reported results 2 years after surgery are controversial [2].
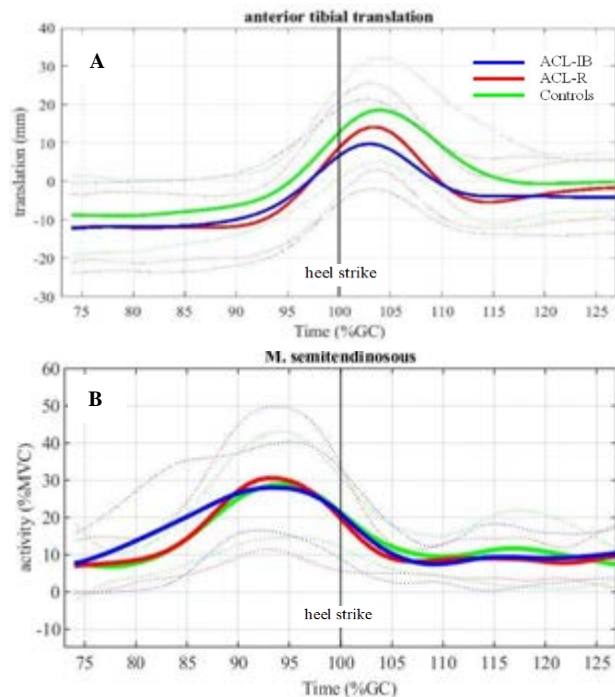
Figure 1: Tibial translation (A) and activity of the semitendinosus (B) in patients after ACL-IB, ACL-R and controls.

Because knee flexion angles and range of TT did not differ between groups, differences in TT velocity of the ACL groups might indicate different adaptations between patient groups. In ACL-IB the semitendinosus muscle (ACL agonist) tended to be earlier and more (but not significantly) activated (Fig. 1B) indicating more controlled translation compared to ACL-R. Preservation of an intact semitendinosus muscle-tendon complex could be advantageous. However, it is still unclear whether range or velocity of TT is more relevant for good long-term outcome (e.g. lower risk of osteoarthritis), and if this pattern is present in ACL-R using other tendon grafts. Further studies concerning this aspect and the biomechanical knee function after ACL repair with augmentation are necessary and desirable.

References

1. DiFelice et al, Arthrosc, 5:1057-1061, 2016.
2. Busch et al, PLoS ONE, 16: e0253503, 2021.

Acknowledgements

MUSCLE CONTRIBUTIONS TO CENTER OF MASS ACCELERATION IN SIMULATED CROUCH GAIT BY HEALTHY CHILDREN

C. Cardadeiro[1,2], F. João[1], R. Mateus[1], A. P. Veloso[1]

1. Faculty of Human Kinetics, University of Lisbon, Cruz Quebrada, Portugal
2. Faculty of Sciences and Technology, Nova University, Lisbon, Portugal

Introduction

Neurologic dysfunctions, like cerebral palsy (CP), lead to serious disorders of movement, being walking really affected. Nowadays, the causes associated to crouch gait (CG) are not clearly identified, so being able to differentiate the several gait deviations associated to crouch, may provide guidance for more precise clinical decision-making. Comparing healthy children simulating this pathological gait with CP children with real crouch gait may provide new insight into what is behind the crouch gait pattern. The purpose of this study was to investigate and compare the muscle forces required to walk in simulated crouch and real crouch gait, and to determine how the individual muscle contributions to vertical and fore-aft acceleration of the mass center differ between simulated crouch, real couch, and unimpaired gait, considering just the single support phase of the stance

Methods

There were considered three study groups: 3 children with cerebral palsy walking in severe crouch gait, 6 typically developing children (TDC) simulating crouch gait, and the same TDC children performing unimpaired gait. Kinematic and kinetic data were collected using 14 infrared cameras (Qualisys) 200 Hz and 3 force plates (Bertec corp). Muscle forces were attained through OpenSim [1]. The musculoskeletal model was manually scaled to match each subject's anthropometry. A residual reduction algorithm (RRA) step was used to minimize errors related to kinematic inconsistencies and modelling assumptions. Muscle forces were estimated using a Computed Muscle Control (CMC) optimization technique. The forces obtained from CMC and the adjusted kinematics from RRA were used for this analysis. Muscle contributions to forward and upward accelerations of the Center of Mas (CM) were estimated based on [2].

Results

The results indicate that simulated and real crouch gait show a similar muscle behavior throughout single support in stance phase, relying mostly on the same muscle groups. The gastrocnemius produced greater muscle forces during unimpaired gait compared with both simulated and real crouch. It was previously suggested that weakness of the gastrocnemius and the hip abductors could contribute to crouch gait [3]. Furthermore, by comparing the TD children simulating crouch with the CP children, the results indicate that the diminished capacity to generate force from the gastrocnemius may be more related to the posture adopted in crouch gait than muscle weakness.
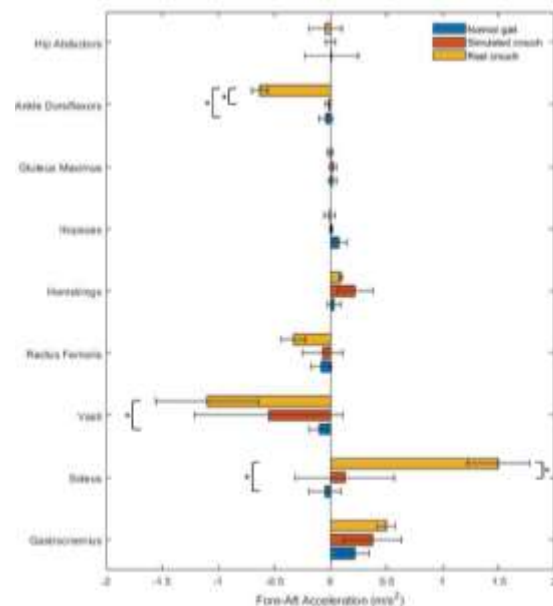
Figure 1: The average fore-aft accelerations of the CM during stance produced by each muscle. Error bars are ±1 SE

Discussion

Our results showed that the ankle dorsiflexors produced significantly greater backward acceleration of the mass center in real crouch than simulated crouch and unimpaired gait, which seems to be compensated by the forward acceleration produced by the soleus. These results suggest that surgically weakening or reducing force-generating capacity of the soleus in CP children may disable them to walk or reduce their capacity to progress during gait.

References

1. S. L. Delp et al.(2007), IEEE Trans. Biomed. Eng.,**54**: 1940–1950.
2. K.M. Steele, et al. (2013). Gait and Posture. 38(1), 86–914.
3. K.M. Steele, et al. (2012) Journal of Biomechanics. 45(15), 2564–2569.

Acknowledgements

PATELLAR TENDON LOADING AND STIFFNESS DERIVED FROM IN VIVO LOADS AND KINEMATICS

Paul F. Kneifel (1), Philippe Moewis (1), Philipp Damm (1), Pascal Schütz (2), Jörn Dymke (1), William R. Taylor (2), Georg N. Duda (1), Adam Trepczynski (1)

1. Berlin Institute of Health at Charité – Universitätsmedizin Berlin, Julius Wolff Institute, Berlin, Germany;
2. Institute for Biomechanics, ETH Zürich, Zürich, Switzerland

Introduction

The mechanical properties of the patellar tendon (PT) have been linked to disease progression [1], and are key to investigating potential mechanical causes of anterior knee pain. The values reported so far have a large range, and rely on *in vitro* tests or on parameters with a high uncertainty. In particular, the magnitude of the PT force is difficult to assess *in vivo* due to the unknown antagonistic co-contraction, and unknown flexion axis, which is key for the effective PT lever arm. Based on the hypothesis that previous studies might have overestimated the force in the PT and thus its stiffness, the aim of this study was to use a unique dataset of directly measured internal TF loading and knee joint kinematics (CAMS-Knee) [2] to derive the stiffness of the PT *in vivo*.

Methods

Four male patients (aged 65 -78 years) with an instrumented total knee arthroplasty performed 5-6 repetitions each of activities known to produce high PT forces: sit-stand-sit and squat. *In vivo* TF forces were measured by an instrumented tibial component, while a video-fluoroscope synchronously captured the internal kinematics [2] (Fig. 1A). Combined with PT attachment sites from CT-data, the PT length was calculated for each time point. Using musculoskeletal modelling, PT forces were computed using the *in vivo* measured TF forces as a boundary condition to account for the unknown level of antagonistic co-contraction. The effective lever arm of the PT was based on the patient specific functional flexion axis derived from the relative motion of the implant components during the high flexion phase of motion. Patient specific PT stiffness was determined as the slope of the linear regression between PT elongation and PT force across the combined data of both activities.

Results

For the sit-stand-sit and squat activities respectively, the peak *in vivo* measured TF forces were 2.92 ± 0.33 BW (mean $\pm$ SD) and 2.84 ± 0.43 BW, while maximal knee flexion angles were $87 \pm 5°$ and $85 \pm 9°$. The peak PT forces were 2.37 ± 0.33 BW and 2.29 ± 0.48 BW, while the maximal PT elongations were 2.19 ± 0.35 mm and 2.57 ± 0.31 mm for sit-stand-sit and squat respectively (Fig 1B). The patient specific PT stiffness ranged from 625 to 1010 N/mm (Fig. 2).
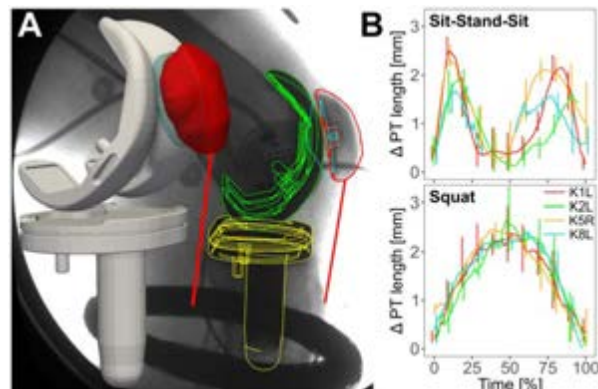
Figure 1: Reconstruction of 3D joint kinematics from fluoroscopy with the patellar tendon (PT) indicated in red (A). Elongation of the PT for the two activities (mean value lines and range bars) (B).
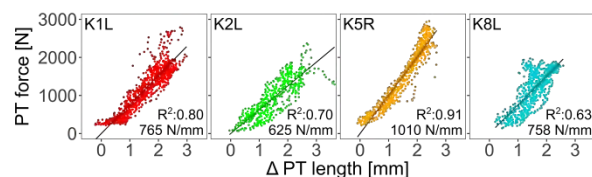
Figure 2: Linear regressions between the elongation and the transmitted force for the patellar tendon (PT) with the stiffness (slope) given for each patient.

Discussion

For the first time, *in vivo* mechanical properties of the patellar tendon have been assessed based on direct measurements of internal knee kinematics and loading conditions. The PT stiffness' found in this study are lower than those reported in literature [3] by a factor of about 1/2. This might be due to overestimated PT forces in previous studies. In this study we minimized this uncertainty by employing *in vivo* measured joint loads and flexion axes. Despite the low number of subjects our results present considerable inter-subject variability. Our results offer a unique direct assessment of the mechanical parameters of the PT, which is key for understanding conditions like anterior knee pain.

References

1. Wiesinger HP et al, Front Physiol, 11: p. 704, 2020
2. Taylor WR et al, J Biomech, 65:32-39, 2017
3. Kösters et al, Scand J Med Sci Sports, 25:67–73, 2015

Acknowledgements

ASSESSING THE IMPACT OF A REHABILITATION TREATMENT WITH EXOSKELETON IN PD: A MUSCULOSKELETAL MODELLING APPROACH

Marco Romanato (1), Fulvia Fichera (2), Fabiola Spolaor(1), Daniele Volpe (2), Zimi Sawacha (1)

1. Department of Information Engineering, University of Padova, Padova, Italy; 2. Fresco Parkinson Center, Villa Margherita, S. Stefano, Vicenza, Italy

Introduction

Gait and postural alterations are the most disabling symptoms affecting people with Parkinson's disease (PPD) quality of life [1]. PPD who underwent robotic-assisted gait training experienced a significant enhancement in spatiotemporal parameters of gait [2]. Overground wearable exoskeletons (OWE) are gaining attention in the rehabilitation field for their capacity to combine the advantages delivered from the grounded robotic devices with the ability to make the users range in a real-world environment. Benefits of adopting gait analysis and musculoskeletal modelling (MSM) for treatment planning and assessment has been recently reported in literature [3]. However, to the best of the authors knowledge, there is no study investigating gait effects from an OWE in PPD. Furthermore, no evaluations using comprehensive gait analysis and MSM to reveal mechanistic changes as a result of therapy has never been reported. Thus, preliminary results of a randomized clinical trial designed with those aims are reported in the following.

Methods

Three people with PD (age=72±12.1years, BMI=25.8±3.1kg/m^2) have been enrolled (ClinicalTrials.gov Identifier: NCT04778852). Gait analysis was performed before and after a 4-weeks gait training intervention (Table 1).

PD1	PD2	PD3
12 sessions	6 + 6 sessions	12 sessions
OWE	OWE + FKT	FKT

Table 1: Gait training intervention per each subject. (FGT = functional kinematic training)

Several gait cycles were collected with an 8-camera optoelectronic system (120Hz, Vicon, USA), synchronized with two force plates (960Hz, AMTI, USA). Three left and three right representative gait cycles were extracted. The MSM pipeline presented in [4] was adopted. Inverse kinematics, inverse dynamics, and static optimization were performed in OpenSim using a muscle-optimized scaled model [5]. Results from the sum of the musculotendon forces composing the anterior and posterior kinetic chains for each participant were compared with healthy controls normative bands (age = 57.8±5.6 years, BMI = 27.3±3.9 kg/m2).

Results

Results are reported in Figure 1.
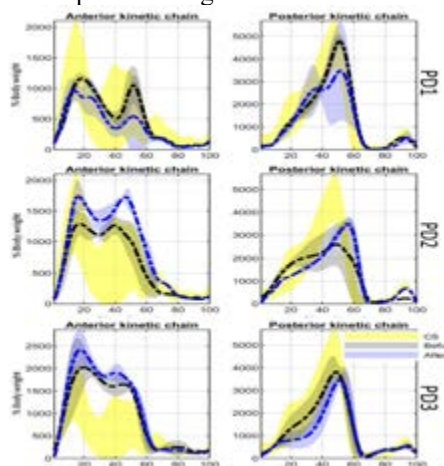
Figure 1: Before(black) and after(blue) the treatment: mean(solid-dashed line)±standard deviation(shaded area).

Discussion

Using a stable kinetic chain (KC) of multiple limb segments is pivotal for an energy-efficient locomotion [6]. Our preliminary results showed how after OWE, in a crucial phase for KC stability as the load acceptance, PD1 reached a functional muscle force profile in the range of the healthy controls, while this was not the case of the other peers who did not complete the protocol. Those results, yet preliminary, might lay the basis to establish a quantitative assessment of the therapy outcomes.

References

1. Morris et al. Mov. Disord. 1(20):40–50, 2005.
2. M. Galli et al, Functional Neurology. 31 (3):163-70, 2016.
3. M. Bortole et al, JNER. 54(12), 2015.
4. Romanato et al. CMBBE. 17;1-13, 2021.
5. Modenese et al. J Biomech. 49:141-48, 2016.
6. Karandikar et al. PM&R. 3, 739-745. 2011.

Acknowledgements

A QUALITY CHECK TO ENABLE RELIABLE MULTICENTRIC STEREOPHOTOGRAMMETRIC DATA COLLECTION

Kirsty Scott (1), Tecla Bonci (1), Lisa Alcock (2), Clint Hansen (3), Lars Schwickert (4), Eran Gazit (5), Andrea Cereatti (6), Claudia Mazzà (1)

1. Dept of Mechanical Engineering & INSIGNEO Institute for in silico Medicine, The University of Sheffield, Sheffield, UK; 2. Translational and Clinical Research Institute, Newcastle University, Newcastle, UK; 3. Kiel University and Dept of Neurology, University Hospital Schleswig-Holstein, Kiel, Germany; 4. Dept for Geriatric Rehabilitation, Robert-Bosch-Hospital, Stuttgart, Germany; 5. Center for the Study of Movement, Cognition and Mobility, Tel Aviv Sourasky Medical Center, Tel Aviv, Israel; 6. Dept of Electronics and Telecommunications, Politecnico di Torino, Torino, Italy

Introduction

Camera set-up, capture volume, as well as calibration procedures influence the accuracy of Stereophotogrammetric (SP) systems [1]. Assessing measurement accuracy is crucial to ensure satisfactory data quality and comparability. The many methods previously proposed to this scope, are often underutilised due to their complexity [2]. This study demonstrates the use of a simple quality control (QC) check and the relevant results obtained from its validation and use in different laboratories.

Methods

Using the SP systems proprietary calibration object, which comprises of markers attached to a rigid body, two trials were recorded for the QC check: 1) Static: a 5 s recording of the object placed in the centre of the capture volume and 2) Dynamic: a recording of the operator moving the object exploiting the full capture volume.

After reconstructing and labelling the marker data, the expanded uncertainties ($Uncertainty = SD_E \times k$,where SD_E is the standard deviation of the error and k is the coverage factor, k=3) for the distances and angles between markers were calculated for the static trials to isolate random errors. Subsequently the systematic error was quantified as the root mean square errors (RMSE) of each distance and angle for the dynamic trials [3].

The reliability of the proposed QC check was assessed through a validation that included varying: the calibration object used, the operator performing the trials and the system calibration/session.

The suitability of the QC for deployment in a multicentric study, was investigated including data collected from four different SP systems in different locations, with varying laboratory and system setups, SP system manufacturers and operators.

Results

In all reliability testing, the random errors, as calculated by the expanded uncertainty, were below 0.1 mm for the inter-marker distances and below 0.1° for the angles. The systematic errors, as calculated by the RMSE, were all at submillimetre and sub-degree level.

Figure 1 summarises the results of the QC checks performed on each system on 20 different days of data collection. Errors observed both within and between systems were low overall, with all errors for distances and angles under 1.9mm and 1.8°, respectively.
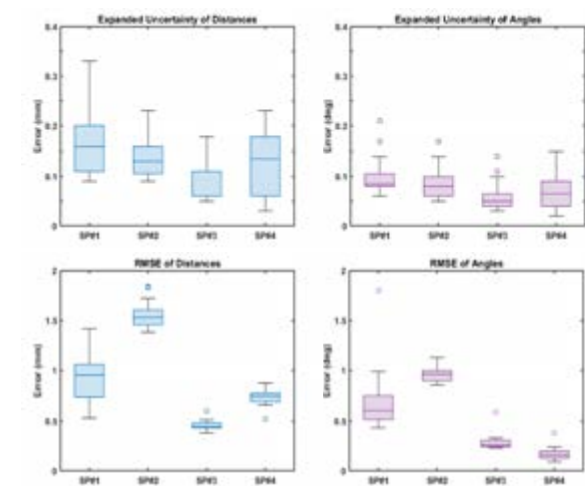
Figure 1: Box charts of the expanded uncertainty and RMSE calculated for the distances and angles of the 20 QC checks completed by the four sites.

Discussion

This study demonstrates the adoption of a simple and time effective QC check to estimate the random and systematic errors of different SP systems as part of the routine data collections. The validation of the QC check demonstrated its reliability regardless of the calibration object used, the operator performing the trials and the system calibration/session, indicating its suitability in multi-session and multi-centric studies. The code to implement the check is available in [4].

References

1. Windolf et al. (2008). *J.Biomech*, **41**: 2776-2780.
2. Conconi et al. (2021). *J. Biomech.l* **114**: 110-162
3. DiMarco et al. (2017). *Meas.J*. **101**: 265-271
4. Scott et al. (2021), *Sensors*, 21(24)

Acknowledgements

THE EFFECT OF FOOT ORIENTATION MODIFICATIONS ON KNEE JOINT BIOMECHANICS DURING DIFFERENT ACTIVITIES

Yi Wan (1), Logan Wade(1), Polly McGuigan (1), James Bilzon (1)

1. Department for Health, University of Bath, Bath, United Kingdom

Introduction

Foot position during daily activities can influence the magnitude and rate of knee joint loading [1]. Over time, increased loading can cause cumulative damage to the articulating surfaces of the knee joint, especially in people with existing knee osteoarthritis [2]. Knee joint loading is difficult to measure in vivo as the majority of knee loading is distributed on the medial compartment of the knee joint, therefore, knee adduction moment (KAM) is commonly used as a surrogate measure for knee joint loading [3].

Foot orientation is believed to have an impact on knee loading during daily activities such as walking and standing from a chair, altering the direction of the ground reaction force vector to reduce the adduction moment arm, relative to the knee joint [4]. However, limited studies have systematically explored the effect of foot orientation on KAM in activities other than walking, which is crucial for improving functional mobility and quality of life in this population beyond the lab. Therefore, this study aims to evaluate the effect of different foot orientations (toe-in, parallel and toe-out) on knee loading across several daily activities (walking, sit-to-stand, and stair climbing).

Methods

Twenty-nine participants (56 ± 5 years, 170 ± 8 cm, 74 ± 14 kg) performed over-ground walking, stair climbing and sit-to-stand movements at their preferred constant speed under three foot conditions, 10° toe-in, 10° toe-out, neutral (0°). Participants performed walking and sit-to-stand on overground force plates, and stair climbing on a portable force plate embedded within the stairs. Each condition within each activity was repeated until five successful trials were obtained.

Three-dimensional kinematic (200 Hz) and kinetic data (1000 Hz) were recorded to obtain knee joint moments and foot progression angles. Foot progression angle was identified using the frontal angle of foot (defined as a 6DOF rigid body) to the global coordinate system (QTM). KAM was computed using inverse dynamics (Visual 3D) and normalised to body mass. Mean within-participant values were calculated for statistical analysis, with repeated measures ANOVA and Bonferroni post-hoc analysis used to compare the KAMs of three foot orientations across all activities.

Results

KAMs during toe-in foot position were significantly lower than those under neutral foot position during walking (P = 0.011), stair climbing and sit-to-stand (P < 0.001), while the KAMs during neutral foot position were significantly lower than those in toe-out foot position across all activities (P < 0.001) (Fig 1).
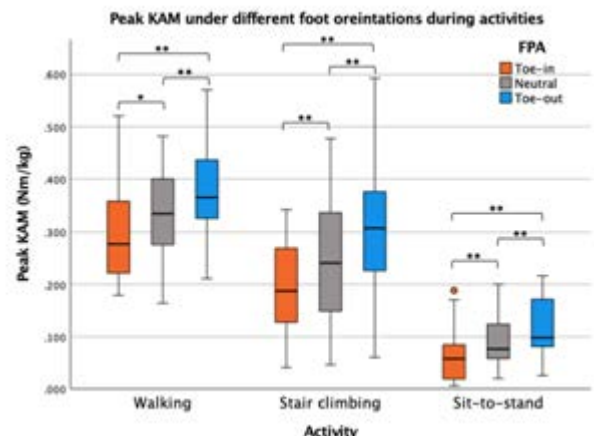
Figure 1: Median and interquartile, peak KAM for toe-out, toe-in and neutral foot position conditions during walking, stair climbing and sit-to-stand.

Discussion

All results showed a significant decrease in peak KAM during the toe-in foot position condition compared to toe-out and neutral foot positions, which is consistent with previous gait studies. The results of this study indicate that toe-in gait can reduce knee joint loading not only during walking, but also in stair climbing and sit-to-stand activities.

The results of this study will be of help in gait retraining programme in clinics and rehabilitation aimed at minimising knee loading and joint pain to slow the progression of the disease. They may provide a range of clinical guidance for injury prevention in a healthy older population under the common contexts of stair climbing and sit-to-stand, taking the technique outside the lab. Future studies should explore the effectiveness of altered foot orientation modifications on knee loading and pain reduction, in a patient population such as knee osteoarthritis.

References

1. Valenzuela et al, J Sports Sci. Med, 15:50-56, 2016.
2. Lynn et al, Clin Biomech, 23: 779-786, 2008.
3. Manal et al, Osteoarthr. Cartil, 23:1107-1111, 2015.
4. Rutherford et al, Osteoarthr. Cartil, 16:883-889, 2008.

Acknowledgements

HIGH FIDELITY SIMULATION OF CEREBRAL ANEURYSM WITH FLOW-DIVERTER

Elie Hachem (1), Ramy Nemer (1), Pablo Jeken-Rico (1), Aurèle Goetz (1), Philippe Meliga (1), Augusto Sanches (2), Yigit Özpeynirci (2), Thomas Liebig (2), Aurélien Larcher (1).

1. PSL Mines Paris, CFL Research Group at CEMEF, Sophia Antipolis, 06904, France; 2. Institute of Neuroradiology, University Hospital, LMU, Munich.

Introduction

Fluid-Structure Interaction (FSI) is used in many healthcare applications. In the present work, we are interested in the interaction between a deformable brain aneurysms, the stent and the blood flow. In other terms, the present work aims to tackle the complexity of the involved physics and the complexity of the numerical methods used to achieve such a simulation. Modeling such a complicated biomechanical system with accuracy and precision can subsequently be used as a diagnostic tool and to assess the risk of rupture in aneurysms.

Methods

We propose a new FSI framework for the analysis of cerebral aneurysm. It is based on an Adaptive Immersed Mesh (AIM) method combining finite element solid dynamics solver with a fully Eulerian fluid-solid framework. It easily handles the insertion of a stent which finally allows us to accurately describe the mechanical exchanges between the blood flow, the surrounding vessel tissue, and the flow-diverter (see Figure 1). The Navier-Stokes equations are solved for the fluid, with the appropriate blood rheology. Hyperplastic solid dynamics equations are solved for the solid, which can handle both compressible and incompressible material [2].

Results

The Variational Multi Scale (VMS) [3] stabilization method is used for both methods. It helps stabilize the advection dominated regime for the fluid flow, and damp out spurious pressure oscillations for the solid problem. The hybrid FSI framework with dynamic mesh adaptation is relevant to account accurately for complex interactions between the blood flow, the surrounding vessel tissue, and the flow-diverter at the same time. Several 3D patient specific test cases are simulated, and their results show on the one hand the flexibility of the approach handling the deformation of the aneurysm with the immersion implementation of the stent and on the other hand the robustness of the proposed approach.

Discussion

The main discussion will focus on the role of the stent by computing the Wall-Shear Stress (WSS) with and without its implementation. It will be followed by a discussion on the role of the fluid-structure interaction solver compared to the rigid modeling of the aneurysm. Finally, we highlight the main challenges that could be needed to complete such a numerical framework for complex biomechanical system to become an important tool for the diagnostics and the analysis of cerebral aneurysms.

(a)   (b)
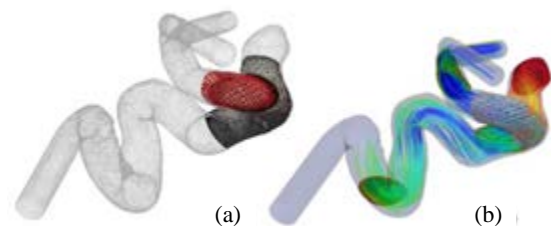
Figure 1: (a) Anisotropic mesh of a patient-specific aneurysm geometry along with its generated stent (in red). (b) Fluid-structure interaction simulation result showing the relative distribution of maximum wall shear stress over one cardiac cycle (red is higher).

References

1. Ryo Torii et al. "Fluid-structure interaction modeling of a patient-specific cerebral aneurysm: influence of structural modeling". Computational Mechanics 43 (Dec. 2008), pp. 151–159.
2. R. Nemer, A. Larcher, T. Coupez, E. Hachem, Stabilized finite element method for incompressible solid dynamics using an updated Lagrangian formulation. Computer Methods in Applied Mechanics and Engineering, 384, 113923, 2021
3. P. Meliga and E. Hachem. "Time-accurate calculation and bifurcation analysis of the incompressible flow over a square cavity using variational multiscale modeling". Journal of Computational Physics 376 (2019), pp. 952–972.

A COMPUTATIONAL METHODOLOGY FOR STUDYING THE MURINE BLOOD-BRAIN BARRIER HEMODYNAMICS

Santiago Mañosas (1), Aritz Sanz (1), Cristina Ederra (2), Ainhoa Urbiola (2), Elvira Rojas de Miguel (3), Ainhoa Ostiz (3), Iván Cortés (2), Natalia Ramírez (3) Carlos Ortiz de Solórzano (2), Arantxa Villanueva (1,3), Mauro Malvè (1)

1. Public University of Navarre (UPNA), Spain; 2. Center for Applied Medical Research, University of Navarra, Spain; 3. Navarrabiomed, Hospital Universitario de Navarra, UPNA, IdiSNA, Spain.

Introduction

The blood-brain barrier (BBB) is a physiological filter for molecules that reach the brain through the blood stream. Despite its importance, very little is known about its functional properties. In recent years, mixed cell culture, animal and computational models have been used with the aim of mimicking the human BBB [1]. Unfortunately, these models are not individual specific and do not reflect its characteristics and behavior. With the aim of improving the existing knowledge of the barrier, we present a novel methodology for the analysis of the BBB hemodynamics based on tissue clarification, advanced microscopy, image analysis of the murine BBB and one-dimensional (1D) modeling of its hemodynamics.

Materials and Methods

To prepare mouse brain samples for image acquisition, we followed the following steps: 1. *Fixation*: Mice samples were fixed using paraformaldehyde (PFA) perfused transcardially before dissection of their brains and post-fixation with PFA; 2. *Sectioning*: 500 μm-thick brain slices were sectioned using a vibratome; 3. *Clarification*: sections were cleared using CUBIC protocol. This technique reduces the difference between refractive index and tissue molecules by removing all lipids; 4. *Staining*: delipidated sections were stained with FITC-Lectin and an arteriole-specific dye Alexa Fluor 633 hydrazide; 5. *Imaging*: 500μm slices were analyzed using an advanced two-photon microscopy system. Image datasets were acquired and further treated using an in-house MatLab code. The volume coming from the images was filtered using Gaussian and non-local means filters. The latter helps reducing the Poisson noise resulting from the acquisition with the microscope. Further morphological filters were used for enhancing vessel patterns. Furthermore, a binarization of the volumes was carried out using an adaptive threshold and Gaussian statistic. A morphological closing was applied for cleaning the 3D region. The 3D geometrical volume of the BBB obtained using the images coming from the tissue clarification was used for creating a 1D model in MatLab. This model is composed by a collection of interconnected nodes and segments of the BBB geometry. In this vascular network, the nodes represent locations where vessels bifurcate or end, and the segments represent the vessels.

Results

The 1D model was used for discretizing and solving the Stokes equations. The BBB 1D flow was obtained using pairs of adjacent nodes with different blood pressures. The blood flow magnitude depends on the pressure difference and the conductance of the vessels. In Figure 1, the entire methodology is summarized, from the clarification to the blood flow distributions in a microvasculature region, represented by average values in each segment.
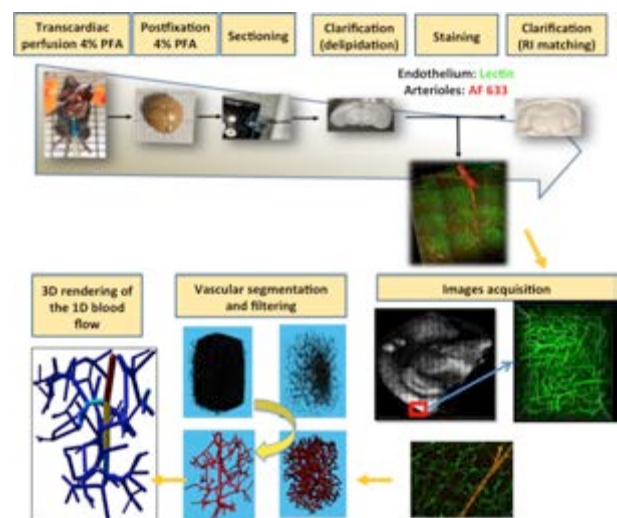
Figure 1. Adopted methodology: tissue clarification, images acquisition and treatment, 1D simulation.

Discussion

The presented methodology can provide detailed information about the murine cerebral microvascular morphology, flow regime, pressure field and wall shear stress among other variables. Although it is a simplified model, it allows a first insight on the BBB hemodynamics and offers several related scenarios for the systematic quantitative analysis of the microcirculatory processes and morphological changes in the mouse BBB.

References

1. A. Linninger et al, Mathematical synthesis of the cortical circulation for the whole mouse brain-part I. theory and image integration. Computers in Biology and Medicine 110:265-275, 2019.

Acknowledgements

HOW MACROSCOPIC TISSUE DEFORMATION AFFECTS THE BRAIN'S MICROSTRUCTURE

Nina Reiter (1), Friedrich Paulsen (2), Silvia Budday (1)

1. Institute of Applied Mechanics, Friedrich Alexander University Erlangen-Nürnberg, Germany, 2. Institute of Functional and Clinical Anatomy, Friedrich Alexander University Erlangen-Nürnberg, Germany

Introduction

The devastating consequences of traumatic brain injuries show that brain tissue is extremely sensitive to mechanical impacts. Brain injuries are often characterized by diffusely distributed axonal and vascular damage that is invisible to the imaging techniques used in medical diagnosis. Therefore, computational simulations of brain injury are a valuable tool to provide more insights into the spatial distribution of harmful stresses and strains during head impacts. Still, the latter alone cannot explain the diffuse distribution of brain lesions: it is still unclear how the forces acting on the brain are transferred from the organ to the cell scale and why some cells are damaged while neighboring cells remain unaffected.

Methods

To investigate mechanically induced microstructural changes in human and porcine brain tissue, we subjected histologically stained fresh tissue specimens to compressive loading and simultaneously observed the resulting displacements of cells and blood vessels through an inverse microscope integrated into the testing setup.

Results

At the microscopic level, we observed that the cells moved with the network of intercellular connections and extracellular matrix when it was deformed under loading [1]. In most samples, cell displacements were homogeneous across the entire field of view of the microscope, i.e., relative movements between adjacent cells were small compared to the total displacement of the cells, as shown in Figure 1.
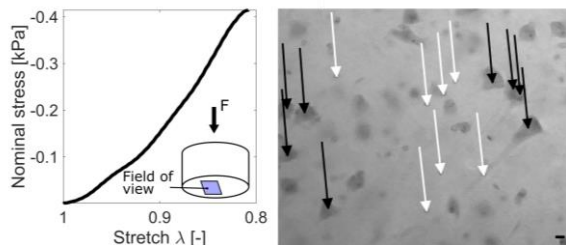
Figure 1: Homogeneous displacements of neurons (black arrows) and glia (white arrows) in a sample from the porcine cerebrum. Arrows start at the original location of cell nuclei and point to their final location in the loaded state. The microscope image shows the loaded state. Scale bar = 10 µm.

However, at the interfaces between gray and white matter, the displacement field was inhomogeneous, and the distances between cells changed under loading, as shown in Figure 2.
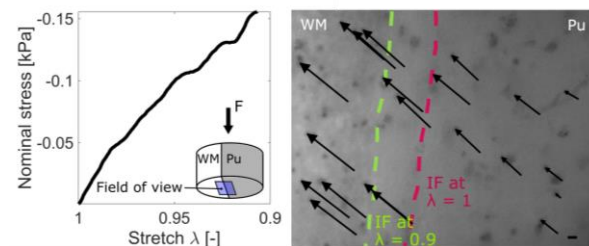
Figure 2: Inhomogeneous cell displacements at the interface (IF) between putamen (Pu) and cerebral white matter (WM) in a human brain sample. Arrows start at the original location of cell nuclei and point to their final location in the loaded state. The microscope image shows the loaded state. Scale bar = 10 µm.

In a small number of samples with homogeneous cell displacement fields, a single neuron was displaced over a smaller distance than the surrounding neurons, and the shape of its soma changed.

We further observed that blood vessels appear to be stiffer than the surrounding brain tissue and can strongly influence tissue deformation in their vicinity.

Discussion

Our results indicate that brain tissue deformation is inhomogeneous at gray and white matter interfaces and near blood vessels, which may lead to greater axonal stretching and thus greater susceptibility to axonal damage in these regions. We observed cell body deformations that could not be explained by the local tissue deformation and may instead be a consequence of stretched axons or dendrites. These insights are a valuable basis to develop new microstructure-based material models for brain tissue and to refine existing computational models of traumatic brain injury to assist injury prevention, diagnosis, and treatment.

References

1. Reiter et al, J Elast, 145:99–116, 2021.

Acknowledgements

FLUID MECHANICS OF THE ZEBRAFISH EMBRYONIC HEART TRABECULATION

Adriana Gaia Cairelli[1], Renee Wei-Yan Chow[2], Julien Vermot[1,2], Choon Hwai Yap[1]

[1] *Dept of Bioengineering, Imperial College London, London, United Kingdom*

[2] *Institut de Génétique et de Biologie Moléculaire et Cellulaire (IGBMC), Strasbourg, France*

Introduction

The formation of trabeculae in the embryonic heart is a mechanosensitive process that is important for cardiac function and defective trabeculation is associated with embryo-lethality. It is thus important to accurately quantify embryonic heart trabeculation fluid forces. To do so, careful consideration of the fine-scale geometry and motion dynamics of trabeculation surface structures is necessary. Here, we do so via image-based computational fluid dynamics (CFD) simulations, using a zebrafish embryonic fish line expressing fluorescence at the endocardial cell membrane (the very boundary with blood) and high-resolution confocal microscopy to capture trabeculated endocardial geometry and motion more accurately.

Methods

4D confocal imaging of zebrafish embryonic hearts at 3 days post-fertilization (dpf) was performed. Motion tracking was performed with a validated algorithm [1], followed by image-based, dynamic-mesh CFD on both individual inter-trabecular spaces and whole ventricles, using previous methods [2].

Results

First, our results showed that by using a fish line with fluorescence at the endocardial cell membrane boundary, rather than with fluorescence in the myocardium like conventionally used in the literature, endocardial wall shear stress (WSS) results were significantly higher. Second, simulations of single inter-trabecular spaces (ITS) under various scenarios (with and without translational or deformational motions, without and without connection to the main ventricle chamber) demonstrated that a squeeze-flow effect was responsible for most of the endocardial WSS magnitude, rather than the interaction with flow in the main ventricular chamber (Figure 1A). Third, simulations with and without trabeculation structures showed that trabeculations caused high spatial variability and oscillatory nature of WSS, and reduced endocardial deformational burden. Fourthly, since blood cells were unlike to enter the ITS, we propose a mixed-viscosity scenario (plasma viscosity within trabecular spaces and blood viscosity in the main chamber) to be more realistic estimate of endocardial WSS. Finally, single or groups of fli1 and gata1 positive cells were found within the inter-trabecular spaces, and were thus likely hematopoietic cells. These cells were observed to increase endocardial WSS magnitudes (Figure 1B). Previous studies suggested that these cells rely on fluid forces stimuli to undergo the haematopoiesis process.
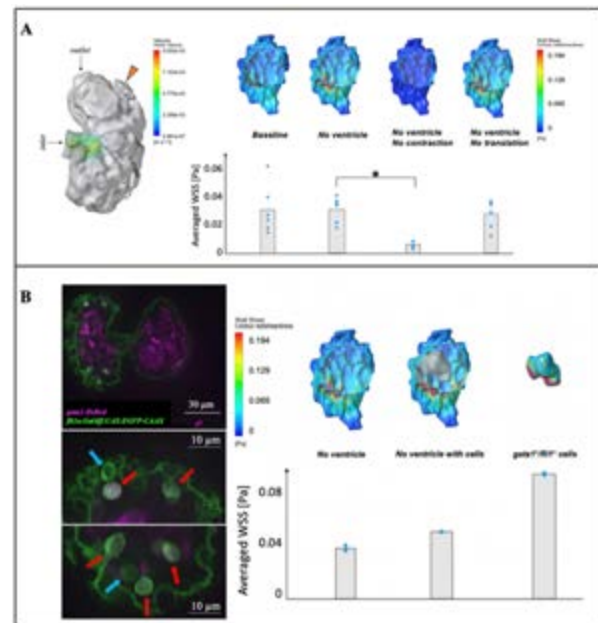
*Figure 1: (A) CFD results: WSS for single ITS (orange arrow) extracted from simulations of the whole ventricle ("baseline" case) was compared to simulations of the same space but without linkage to the rest of the ventricle ("no ventricle" case); and to simulations of the de-linked ITS without translation ("no translation" case) or without contractile/deformational motions ("no contraction" case). This demonstrate that contractile deformational motions are the most important for WSS generation. (n=6, * p<0.05). (B) Confocal image of a 3 dpf zebrafish embryonic heart showed some cells within the ITS expressing both fli1 and gata1, suggesting that they are maturing hematopoietic cells. These cells increased endocardial WSS, and they experienced about twice as much WSS as the endocardium. (n=2).*

Discussion

Our results showed the importance to have detailed anatomic and motion information of endocardial-blood boundary for endocardial WSS estimates. We also showed that the ITS space has a squeeze-flow motion that actively generates its own flow and WSS, and should not be thought of as a passive space. Further, complex considerations for the hematopoietic cells were also necessary for accurate WSS quantifications. Since mechanobiological processes are important for the embryonic heart development, our findings may be useful for future investigations on heart development.

References

1. Wiputra et al,*Scientific Reports*, 10(1):1-4,2020
2. Foo et al,*Biomech Model Mechanobiol*, 19(1):221-32,2020

HEMODYNAMICS-DRIVEN AORTIC GROWTH FOR GENETICALLY MODIFIED MICE MODELS

Marisa S. Bazzi(1), Jessica E. Wagenseil (2), Victor H. Barocas (3)

1. Chemical Engineering and Materials Science Department, University of Minnesota, Minneapolis, MN, USA;
2. Department of Mechanical Engineering and Materials Science, Washington University, St. Louis, MO, USA
3. Department of Biomedical Engineering, University of Minnesota, Minneapolis, MN, USA

Introduction

Thoracic aortic aneurysms (TAAs) affect approximately 15,000 people in the US per year and can be fatal in 80% of the cases when ruptured[1]. Genetic connective tissue disorders as well as blood flow dynamics have been associated with the disease[2–4], the latter driving intense interest in the development of computational models. However, models of aortic growth and remodeling often ignore the variability of the hemodynamically-driven stresses along the aorta[5]. This simplification can lead to inaccuracy in longitudinal and axial growth, since it does not account for heterogeneous growth of the tissue resulting from heterogeneous fluid stress fields.

We studied hemodynamically driven hetero-geneous growth in the aortic wall of Fbln4[SMKO] mice. To perform the study, we used a combination of subject-specific fluid-solid-interaction (FSI) models, longitudinal data from medical scans during the mouse lifetime, and a local stress-driven growth model.

Methods

Mouse-specific FSI models: Five mice lacking expression of the fibulin-4 gene in smooth muscle cells (Fbln4[SMKO]) were used in the study. Magnetic resonance angiography (MRA) images for two-, four- and six-month old mice were used to monitor the *in vivo* TAA growth. FSI models were built from 2-month scans. The aortic wall was described using the Holzapfel-Gasser-Ogden (HGO) model, where the parameters were specified for each mouse based on postmortem measurements. Simulations were performed for ten cardiac cycles using SimVascular [7] at the Minnesota Supercomputer Institute (MSI).

Finite Element Growth: Aortic growth was defined by a local growth tensor given by $G=diag(\lambda_r, \lambda_\theta, \lambda_z)$ at time relative to the reference state, t=T0. For this study, T0 was taken to be at age 2 months. The geometry was prestressed during the FSI simulations to account for any residual stress caused by the initial growth of the aorta. The
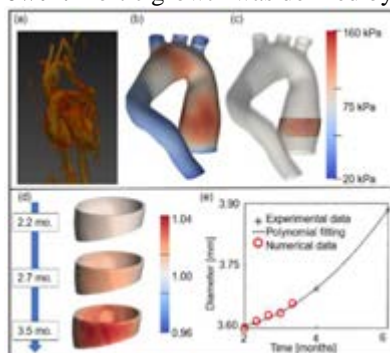
Figure 1: (a) MRA scans of FBLN[SMKO] mice taken at age two months. (b) Von Mises stress distribution from the FSI simulations. (d) Aortic ring around the largest diameter region used to solve the (e) local growth or the aortic tissue and validate the model.

growth model was based on that of Alford and Tabor[6]. The macroscale change in the geometry is solved using Prestrain plugin[7] of FEBio Studio 3.5.

Model tuning and validation: FSI simulation were performed on the geometry extracted from MRA scans, and the stress distribution was calculated (Fig1a-b). For simplicity, the G&R model was solved in a ring around the maximum diameter region (Fig 1c-d). The time constants were found by matching the radial growth to the experimentally-observed trends (Fig 1e).

Results

Five Fbln4[SMKO] mice were analyzed in this study. Fig 2a shows the adjusted time constants for all five mice. As expected, smaller values of the radial and tangential time constants were observed for geometries with a larger growth in the first weeks. Figures 2b-c show the the computed growth along the aorta due to the inhomogeneous stress distribution. As expected, more growth occurred in the ascending aorta.
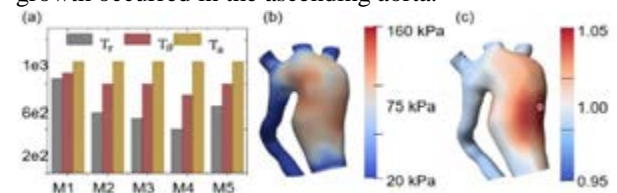
Figure 2: (a) Time constants from tuning the G&R model for each mouse model. (b) Stress distribution from the FSI simulations (c) Total aortic growth.

Discussion

A hemodynamically-driven G&R model based on mouse-specific FSI simulations was implemented. The radial growth was compared to the trend measured *in vivo.* The model results qualitatively matched the experimentally-observed radial growth for the first 3-12 weeks following the initial state. Results for full aortic growth show substantial heterogeneity of the growth process as a direct consequence of the inhomogeneous stress distribution along the aortic wall.

References

1. Zhou, B. et al. Lancet 389, 37–55.
2. Kim, J., Procknow, et al. Hear. Circ. Physiol., 2015.
3. Howard, D. P. J. et al. Br. J. Surg. 102, 907–915.
4. Bazzi, M. S. et al J. Cardiovasc. Eng. Technol., 2022
5. Mahutga, R. R. et al. J. Biomech. Eng. 2020.
6. Alford, P., et al Biomech. Model. Mechanobiol.2009
7. Maas, S. A., et al J. Mech. Behav. Biomed. Mater. (2016).

Acknowledgements

BIOMECHANICAL MODELLING OF THE AORTA IN ADULT ZEBRAFISH

Matthias Van Impe (1), Marco Stampanoni (2), Patrick Sips (3), Julie De Backer (3), Patrick Segers (1)

1. IBiTech-bioMMeda, Ghent University, Belgium; 2. Paul Scherrer Institute, Switzerland;
3. Center for Medical Genetics, Ghent University Hospital, Belgium

Introduction

Zebrafish models are used to study the fundamental mechanisms of cardiovascular disease [1]. The importance of mechanobiology in development and (patho)physiology suggests that it might be crucial to integrate biomechanical aspects of the zebrafish circulation. A few recent studies exploit the optical transparency of developing zebrafish and describe the cardiovascular biomechanics at this stage [1,2]. Imaging options in adult zebrafish, no longer transparent, are more limited and models to evaluate the cardiovascular biomechanics at adult stages are lacking. We combine high-frequency echocardiography and synchrotron X-ray imaging to demonstrate the feasibility of finite element modelling of the aorta in adult zebrafish.

Methods

First, *in vivo* high-frequency ultrasound measurements (VEVO 2100 ultrasound machine and VEVO MS 700 probe) of n=5 wild-type, 13 months old adult zebrafish were acquired. Afterwards, *ex vivo* phase-contrast synchrotron X-ray imaging of the same samples was performed at the Paul Scherrer Institute in Villigen, Switzerland. Synchrotron scan settings were based on [3]. Starting from the resulting synchrotron image stacks, Mimics 24.0 was used for semi-automatic segmentation and 3D reconstruction of blood and vessel wall volumes. Three cardiac cycles were simulated in finite element software COMSOL Multiphysics v5.6, both in computational fluid dynamics (CFD) and fluid-structure interaction (FSI) studies. Blood was modelled as an incompressible, Newtonian medium (ρ=1060 kg/m³, μ=2.2 cP) and in FSI studies, the vessel wall was modelled as an incompressible, Neo-Hookean material (ρ=1000 kg/m³, μ=30 kPa). Inlet flow profiles were based on the ultrasound measurements while resistive outlet conditions were tuned to approximate equal outflow from all gill branches.

Results

Accurate, sample specific aorta geometries could be obtained from the synchrotron scans. Other structures such as the bulbus arteriosus (the pear-shaped buffer in between the ventricle and aorta) could also be segmented and 3D reconstructed form the synchrotron images. The semi-automatic aorta segmentation is illustrated in Figure 1 (top). Computational results such as velocity (max. $\pm$200 mm/s), pressure (max. $\pm$6 mmHg), wall shear stress (max. $\pm$30 Pa) and first principal stress (max. $\pm$30 kPa) were fairly consistent across all five samples. For one sample, wall shear stress at systolic peak is presented in Figure 1 (bottom).
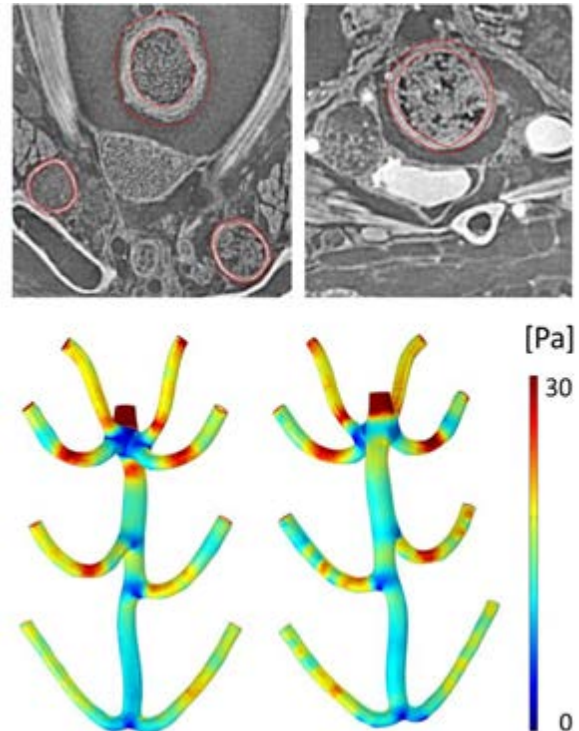
Figure 1: Top - Synchrotron images of the aorta region. Red tracings indicate the segmentation of blood and vessel wall areas for a proximal (left) and distal (right) cross section of the aorta. Bottom - Wall shear stress results from an FSI study at systolic peak. A ventral (left) and dorsal (right) view is provided (the vessel wall is not visible). The diameter of the aorta is about 0.1 mm.

Discussion

For the first time, biomechanics in the aorta of adult zebrafish can be evaluated. For now, most emphasis should be put on overall patterns rather than exact absolute values. Note for example that the region of lowest wall shear stress, i.e., the ventral side of the most proximal branching region, is also the location of highest principal stress in the vessel wall for all samples. The same modelling workflow can be applied in zebrafish models of cardiovascular disease and the wild-type results provide a baseline in such studies.

References

1. Bowley et al, Br J Pharmacol, 1-18, 2021
2. Salman et al, J Cardiovasc Dev Dis, 8(2), 14, 2021
3. Logghe et al, Sci Rep, 8, 2223, 2018

Acknowledgements

FLUID MECHANICS OF FETAL AORTIC VALVULOPLASTY IN FETAL AORTIC STENOSIS AND EVOLVING HLHS

Hong Shen Wong[1], Hadi Wiputra[2], Andreas Tulzer[3], Gerald Tulzer[3], Choon Hwai Yap[1]

1. Department of Bioengineering, Imperial College London, UK; 2. Department of Biomedical Engineering, University of Minnesota, USA; 3. Department of Pediatric Cardiology, Kepler University Hospital, Austria

Introduction

Hypoplastic Left Heart Syndrome (HLHS) can occur due to mid-gestational cardiac abnormalities. One example is fetal aortic stenosis with abnormal flow characteristics such as retrograde systolic transverse arch flow and left-to-right atrial shunting. Most such fetuses will progress to HLHS by birth [1], and are thus called evolving HLHS (eHLHS). In such cases, a catheter-based intervention in the fetal heart, fetal aortic valvuloplasty (FAV) can resolve aortic obstruction, allow better growth for the remainder of gestation, and prevent progression to HLHS at birth [2]. In both disease and intervention, biomechanical stimuli and loading conditions have important consequences to fetal heart development, but the precise biomechanical environment in eHLHS and biomechanical effects of FAV has not been investigated in detail.

Methods

Patient-specific echocardiographic-based simulations of left ventricles (LV) using computational fluid dynamics (CFD) were done for five feHLHS fetuses before and after FAV. Comparisons were made with five healthy fetuses.

Results

The eHLHS LV had narrowed and faster monophasic diastolic mitral inflow due to impaired valve opening dynamics, which resulted in a narrow but fast-moving diastolic vortex ring that moved quickly to the LV apex and impinged at the apical region. Consequently, high wall shear stress (WSS) and low oscillatory shear index (OSI) was seen in the apical region. In contrast, healthy LVs demonstrated high WSS and low OSI primarily in the mid-ventricular region due to greater interaction of a wider and slow-spreading diastolic ring. After FAV intervention, an additional narrow and fast-moving vortex ring manifested due to the aortic regurgitation. This aortic vortex ring interacted with the mitral vortex ring to generate complex flow structures. It increased the overall WSS magnitude but did not significantly alter the spatial WSS patterns from before FAV. Due to aortic stenosis and impaired mitral valve dynamics, systolic and diastolic energy losses per volume of flow was significantly elevated in eHLHS cases. However, this was partially resolved after FAV. Calculations of mass fraction of initial versus freshly introduce blood showed that turnover of blood could be drastically reduced in feHLHS LVs, suggesting hypoxia in the LV, but this improved after FAV, due to acute improvements in ejection fraction and flow rates through the valves.
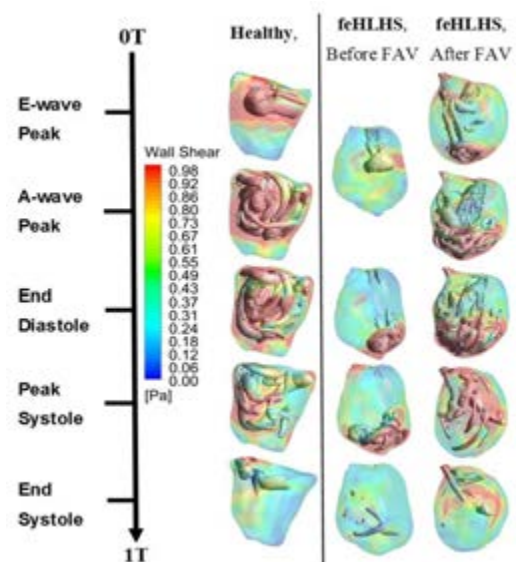
Figure 1: WSS color contour and λ^2 iso-velocity surfaces in healthy fetal LV and a feHLHS before and after FAV.

Discussion

A combination of high LV pressure and excessive energy losses were consistently observed in all diseased cases and were likely to impose an excessive burden on feHLHS LVs. Relieving this burden with the FAV intervention was thus likely to be a reason why FAV could prevent some eHLHS hearts from progressing to actual HLHS at birth. The aortic stenosis in eHLHS LV prevented adequate exchange of blood in the LV, and was likely to cause hypoxic stress to the inner lining of the LV, which prevailing literature suggests will lead to endocardial fibroelastosis that is often observed in eHLHS [3]. Although there were differences in the spatial pattern of WSS between normal and eHLHS LVs, there were no overall WSS magnitude difference between the two, and there was a large variability of WSS magnitude in the disease cohorts. It was thus unlikely that WSS was a contributing factor to whether the LV progresses to malformation at birth.

References

1. Mäkikallio, K. et al, Circulation 113: 1401-1405, 2006
2. Freud, L. R. et al, Circulation *Circulation* 130: 638-645, 2014.
3. Peserski, Z. et al, *Developmental Dynamics* 247: 509-520, 2018.

Acknowledgements

"GLOBAL AND LOCAL STIFFENING OF HUMAN THORACIC AORTAS UNDERGOING TEVAR IN VITRO: A MOCK-LOOP STUDY"

Emmanouil Agrafiotis (1), Gerhard Sommer (1), Christian Mayer (2), Martin Grabenwöger (3), Peter Regitnig (4), Heinrich Mächler (2), Gerhard A. Holzapfel (1,5)

1. Institute of Biomechanics, Graz University of Technology, Austria; 2. Department of Cardiac Surgery, Medical University of Graz, Austria; 3. Department of Cardiac Surgery, Klinik Florisdorf, Vienna, Austria; 4. Institute of Pathology, Medical University of Graz, Austria; 5. Department of Structural Engineering, Norwegian University of Science and Technology (NTNU), Trondheim, Norway.

Introduction

Patients undergoing thoracic endovascular aortic repair (TEVAR) face graft-related pathophysiological complications such as hypertension, aortic stiffening, and others [1]. Such complications are driven by biomechanical events within the aortic wall [2] and the presence of a stiffer prosthesis creates an elastic gap, known as the "compliance mismatch". This study aims to provide a better understanding of how the stent-graft affects the elastomechanical behavior of the aorta.

Methods

Non-pathological human thoracic aortas (n=9) were subjected to long-standing perfusion (8h) within a mock circulation loop (Fig. 1A) [3], with pre- and post-TEVAR test periods under physiological conditions. Pressure (p_{aorta}) measurements of the ascending and descending aorta were compared. Permanent markers were placed on both concave and convex locations of the proximal landing zone (Fig. 1B) to track the cyclic circumferential stretch ($\lambda_{circ.}$) during the periods without stent and with stent. Then the compliance variations were compared by plotting p_{aorta}-$\lambda_{circ.}$ to examine the mismatch between the stented and the non-stented aortic wall. After perfusion, biaxial tension tests (stress-stretch) were carried out to investigate the stiffness profile on stented and non-stented samples. Further investigations of possible local damage by the stent-graft were assessed histologically.

Results

The experimental results demonstrate two main findings: (i) a significant reduction (>50%), in the global aortic elasticity after TEVAR, indicating aortic stiffening and compliance mismatch, and (ii) a stiffer local behavior of the stented samples compared to the non-stented samples with earlier entry into the nonlinear part of the curve, which implies an early loss of elastic fibers [4].

Discussion

For the first time, TEVAR-induced damage to the human thoracic aortas was artificially created under physiological conditions. The biomechanical and histological comparison of the conditions without stent and stent enables new insights into the interaction between stent and the aortic wall. The gained knowledge could refine the stent design in order to minimize its damage to the aortic wall and its subsequent complications.

Figure
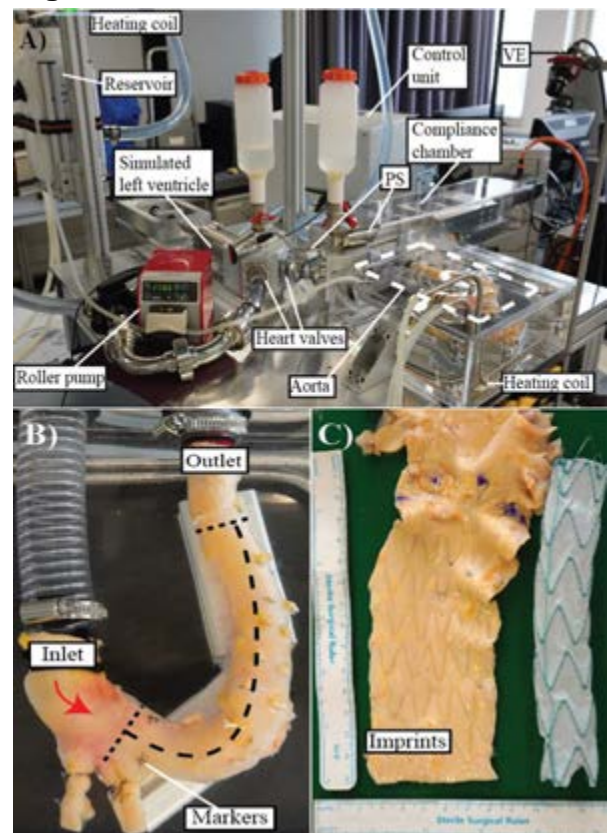
Figure 1: Overview of the mock loop (A). Pressure sensors (PS) recorded the pressure (p_{aorta}) and the video-extensometer (VE) to track the cyclic circumferential stretch (λ_{circ}). Perfused stented aorta with markers (B). Dashed lines indicate the stented area. Post-perfusion stent-induced imprints on the lumen surface (C).

References

1. Grabenwöger M et al, Eu Heart J, 33:1558-63, 2012.
2. Humphrey JD et al, J Biomech, 45:805-14, 2012.
3. Agrafiotis E et al, Artif Ograns, 45:1562-75, 2021.
4. Weisbecker H et al, J Biomech, 46:1859-65, 2013.

INVESTIGATING LOCAL PROPERTIES OF ATHEROSCLEROTIC PLAQUE CAPS USING A TISSUE-ENGINEERED MODEL

Hanneke Crielaard (1), Tamar Wissing (1,2), Su Guvenir Torun (1), Pablo de Miguel (1,3) Ranmadusha Hengst (1,3), Gert-Jan Kremers (1), Frank Gijsen (1,3), Kim van der Heiden (1,2), Ali Akyildiz (1,3)

1. Erasmus Medical Center, The Netherlands; 2. Eindhoven University of Technology, The Netherlands; 3. Delft University of Technology, The Netherlands;

Introduction

Stroke is commonly initiated by rupture of the atherosclerotic plaque fibrous cap in a carotid artery. However, cap rupture mechanisms are not well understood yet. Understanding the impact of the structural components of the cap on its local mechanics may provide critical insights into plaque rupture. Various limitations within studying plaques *in vivo* and *ex vivo* highlight the need for additional methods to investigate rupture mechanics. Therefore, we created collagenous tissue-engineered plaque cap analogs [1]. In the current study, we present our pipeline for visualizing collagen orientation and obtaining local mechanical properties in these analogs.

Methods

Ten collagenous cap analogs with a soft inclusion (SI), mimicking the plaque lipid core, were created [1]. Afterwards, the analogs were exposed to multiphoton microscopy (MPM) with second harmonic generation (SHG) to visualize the collagen architecture. From the SHG images, the local fiber orientations were measured using a fiber orientation analysis tool (FibLab). After imaging, the analogs were exposed to uniaxial tensile tests until full rupture. Local (Green-Lagrange) strains under tensile stretching were measured through DIC analysis using the software Ncorr [2].

Results

The local predominant fiber angles (θ, in degrees) and standard deviations (SD, in degrees, an indicator of fiber dispersion level) within a representative sample are presented in Fig 1. The fibers were mostly oriented in the y-direction (θ ± SD, average of ten samples: 91±22°), which is the stretch direction during culturing of the analogs and corresponds to the circumferential direction in real plaque tissue.
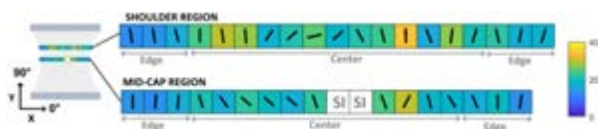
Figure 1: θ (black line) and SD (background color).

Fibers at the edges of the sample are oriented closer to the y-direction than fibers in the center of the sample. The difference of the predominant fiber orientation with the y-axis (Δθ) averaged over the ten analyzed samples is 13° at the edges and 35° in the center. Center sections show a more dispersed fiber distribution compared to edge sections (SD, average of ten samples: 24° vs. 18°). In the mechanical tensile tests, five samples ruptured at the clamping site and were therefore excluded from strain analysis. The rupture in the other five samples initiated in the SI and propagated in a -slightly tilted-horizontal direction (Fig 2A) and after crossing the SI-fibrous tissue interface, propagated in the fibrous tissue, in a rupture over the full width of the analog. Fig. 2B shows the DIC-derived local tensile strains (E_{yy}) at the timepoint of rupture initiation in the SI. The figure shows a region of elevated tensile strain near the rupture location. (Maximum vs mean strain, average of ten samples: 60% ± 20% vs 15% ± 5%)
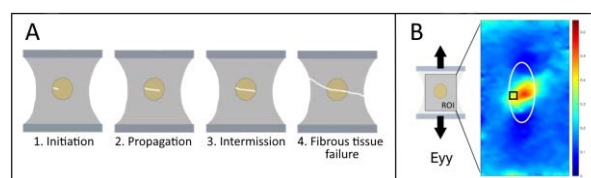
Figure 2: A) Rupture phases in cap analogs. B) DIC-derived local tensile strains. (White oval = SI-fibrous tissue interface, Black square = rupture initiation locus)

Discussion

We successfully visualized the collagen orientation and obtained local mechanical (strain) properties in tissue-engineered cap analogs. Our results showed that collagen fibers in the analogs are mainly oriented in the circumferential direction (y-direction). In the center of the samples, larger deviations of the predominant fiber orientation from the circumferential direction and a more dispersed fiber architecture were found compared to the edges. Rupture initiated near high tensile strain regions within the SI and propagated in the fibrous tissue towards the edge (luminal surface). As the next step, we will investigate the intra- and inter-sample variations in the fiber orientations in a larger sample set, and study the association of this local structural information to the rupture propagation path and the local strain pattern. We will also further study our new hypothesis that rupture initiation is not always at the luminal surface to gain more insight in underlying plaque rupture mechanisms.

References

1. Wissing TB et al. BioRxiv. Preprint 2021
2. Blaber J et al. Exp. Mech., 55: 1105-1122, 2015

Acknowledgements

LOCAL RUPTURE ANALYSIS OF ATHEROSCLEROTIC HUMAN CAROTID PLAQUES BY STRUCTURAL IMAGING, DIC AND UNIAXIAL TESTING

Su Guvenir Torun (1), Pablo de Miguel Munoz (1,2), Hanneke Crielaard (1), Hence J.M. Verhagen (1), Aad van der Lugt (1), Gert-Jan Kremers (1), Ali C. Akyildiz (1,2)

1. Erasmus Medical Center, Rotterdam, Netherlands; 2. Delft University of Technology, Delft, Netherlands

Introduction

Atherosclerotic plaque rupture, primary cause of cardiovascular events, is the local mechanical failure of the plaque tissue. However, the failure characteristics of the tissue and the link of the underlying microstructure are not well established yet [1]. In this work, we characterized local rupture properties of human carotid plaque tissue by using uniaxial testing and digital image correlation (DIC), and explored their correlation with the tissue's collagen structure assessed by second harmonic generation (SHG) imaging.

Methods

Nineteen atherosclerotic human carotid endarterectomy (CAE) samples were collected at Erasmus Medical Center. They were scanned with a micro-CT (Quantum GX 2), and at the non-calcified areas, rectangular shaped plaque tissue strips (long axis in circumferential direction) (n=31) were obtained. Their fibrillar collagen structure was imaged with SHG microscopy imaging (Leica SP5). By using the Fiblab software [2], SHG images were analyzed, and the predominant angle (pDA), standard deviation (SD), and the anisotropic fraction (AF) of the local fiber orientations were measured. Then, the samples were mechanically tested under tensile loading in circumferential direction until rupture. Traditional gauge length (GL) based global strains at the rupture were calculated, and Ncorr DIC software [3] was used to obtain local tensile strains.

Results

Structural imaging and mechanical testing of all 31 strips were successfully conducted. The preliminary analysis of 5 strips were completed, and demonstrated the necessity of local strain assessment for plaque rupture investigation as the DIC measurements revealed the local, non-uniform, heterogenous strain distribution over the tissue (Fig.1(A)).
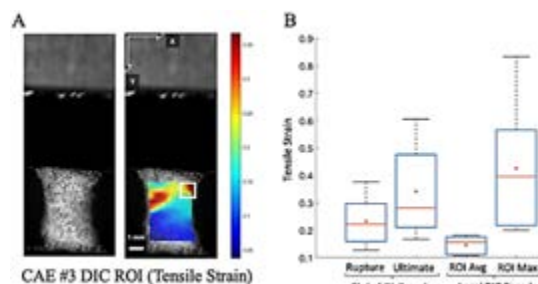
Figure 1:(A)DIC strain patterns of representative CAE #3. The white square indicates the rupture area. (B) GL based and local DIC strains compared. (ROI: Region of interest)

Ruptures mainly occurred at the global max or a local max tensile strain spot, where the DIC measurements showed the median [range] of 40% [20 to 83%]. Meanwhile, the traditional GL based gross tissue strain assessment underestimated the rupture strain as 22% [13 to 38%] (Fig.1(B)). Collagen imaging results of a representative sample is given in Fig.2(A). In overall, for the analyzed five samples, the predominant collagen orientation was circumferential (mean pDA±SD of 1°±30°, range: -75° to 68°). The SDs of the local fiber angle distribution (range:14° to 48°, mean:26) and AFs (range:0.10 to 0.82, mean: 0.53) demonstrated quite variable local fiber dispersion in the samples. At rupture areas, the measured pDA ± SD were 16°±29°, 44°±21°, -29°±26°, -12°±26°, and 30°±23°, and AFs were 0.72, 0.43, 0.44, 0.59 and 0.26 for CAE # 1, 2, 3, 4 and 5, respectively (Fig.2(B)).
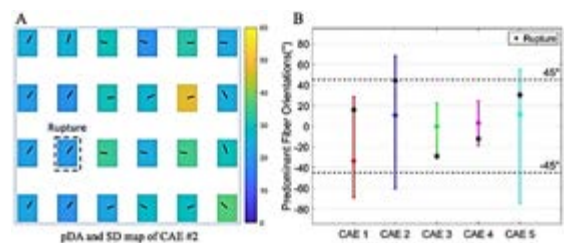
Figure 2: (A) pDA (black arrows) and SD (colormap) distribution of representative CAE #2. (B) The pDA ranges of the analyzed five CAE samples. Black diamonds indicate the pDA at the rupture area.

Discussion

In this work, we performed structural and mechanical analyses of human carotid plaque tissue samples to reveal the plaque rupture properties. The preliminary analysis of five samples revealed that global GL based strains (homogeneous) greatly underestimated the local (heterogeneous) tissue rupture strains. Structural analyses showed circumferential collagen fiber alignment in the plaque tissue in overall, as well as the rupture areas, with varying level of fiber dispersion locally. For future work, all tested strips (n=31) will be analyzed to obtain the complete picture of mechanical and structural CAE rupture characteristics. This essential information will provide great insights for understanding plaque rupture mechanism(s) and for developing plaque rupture prediction tools.

References

1. Akyildiz et al., *J Biomech*,47.4:773-783,2014.
2. van Haaften et al., Tissue Eng Part C, 24:418-429,2018.
3. Blaber et al., Exp Mech, 55.6:1105-1122,2015.

MECHANICAL CHARACTERIZATION OF PASSIVE MYOCARDIAL TISSUE PROPERTIES IN HEALTHY AND INFARCTED PORCINE HEARTS

Nicolás Laita (1), Miguel Ángel Martínez (1,2), Manuel Doblaré (1,2), Estefanía Peña (1,2)

1. Aragón Institute of Engineering Research (I3A), University of Zaragoza, Zaragoza, Spain
2. Biomedical Research Networking Center in Bioengineering, Biomaterials and Nanomedicine (CIBER-BBN), Spain

Introduction

Cardiovascular diseases are the main cause of death worldwide. Focusing on the heart, due to its complex electromechanic behaviour is essential to fully understand its mechanical properties and its electrophysiology. From the mechanical point of view, the heart undergoes very specific conditions during the cardiac cycle including biaxial extension and compression and shear stress [1,2]. Furthermore, this study is focused on the myocardium infarction, which provokes a great impact into the behaviour of the tissue, making the infracted tissue stiffer and considerably thinner.

It is widely accepted that the cardiac tissue presents an orthotropic behaviour [3,4]. Hence, it is necessary considering different loading scenarios in order to accomplish a complete three-dimensional characterization. Following this line, several mechanical tests considering different loading scenarios were performed into porcine specimens, including healthy porcine hearts and infarcted ones. The obtained experimental results were used to estimate the Costa material model parameters [5]. This is one of the most widely used material models to in silico reproduce the cardiac tissue behaviour.

Methods

Porcine left ventricular transmural biopsy specimens were obtained from 14 white pigs. 7 animals were used for control purposes, and 7 animals were infarcted in the anteroapical region (IAA) by temporal occlusion of the left anterior descending coronary artery employing a balloon catheter.

Following the experimental procedures observed at the literature [2,6], cyclic biaxial extension tests (i) and triaxial shear tests (ii) were performed both in the healthy and infarcted hearts in samples from the central area of the anterior wall of the left ventricle, close to the left circumflex coronary artery area (LCAA). Furthermore, cyclic biaxial (iii) and uniaxial (iv) extension tests were performed at the IAA of the infarcted hearts to analyse the influence of this episode on the tissue behaviour (data not shown). A total of 33 biaxial tests, 96 tangential tests, and 14 uniaxial tests were performed.

For the Costa parameters estimation, individual mean animal results and global mean results were considered. Least-squared minimization method was used for the estimation. For the validation of the experimental fit, we used two different statistical errors: coefficient of determination (R2) and Normalised Root Mean Square Error (NRMSE).

Results
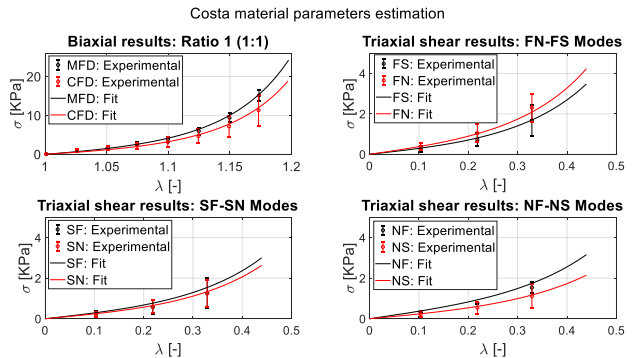
Figure 1. Experimental and Costa simulated results comparison. Healthy hearts global mean results

In Figure 1, healthy hearts mean results are shown. The tissue has proved to have a transversely isotropic behaviour, obtaining greater stress values at Mean Fiber Direction (MFD) than in Cross Fiber Direction (CFD) for the biaxial results and also a stiffer response in FN-FS modes than the others for the triaxial shear results. Regarding the Costa simulated response demonstrated a great fit of the experimental behaviour, with values of $R^2>0.9$ and NRMSE<0.1 at every scenario.

Conclusions

Aiming at characterizing the passive mechanical properties of healthy and infarcted cardiac tissue, cyclic biaxial extension, triaxial shear and uniaxial extension tests were performed into 7 healthy porcine hearts and 7 infarcted ones. This set of experiments allows us to fully characterise the orthotropic nature of the tissue. Consistent results were obtained according to literature in every test. Costa material model parameters were estimated and a great reproduction of the experimental response was obtained.

Acknowledgements

References

1. Holzapfel G.A. et al, Philos. Trans. R. Soc. A. 367 (2009) 3445–3475.
2. Dokos S. et al, Am. J. Physiol. 283 (2002) H2650-H2659.
3. Yin F.C.P. et al, J. Biomech. 20 (1987) 577–589
4. Sacks M.S. et al, J. Biomech. Eng. 115 (1993) 202–205.
5. Costa, K.D et al. Philos. Trans. R. Soc. A. 359 (2001), 1233-1250
6. Sommer G. et al, Acta biomaterialia, 24, (2005) 172-192

CHARACTERISING DISSECTION IN AORTIC TISSUE: EFFECT OF LOCATION AND DISSECTED LAYER

Itziar Ríos-Ruiz (1), Miguel Ángel Martínez (1,2), Estefanía Peña (1,2)

1. Aragón Institute of Engineering Research (I3A), University of Zaragoza, Spain; 2. CIBER-BBN: Centro de Investigación Biomédica en Red en Bioingeniería, Biomateriales y Nanomedicina, Spain

Introduction

Aortic dissection is a relevant cardiovascular disease that can have a fatal outcome. This pathology consists in the generation of a tear that propagates through the different layers of the vessel wall, causing clogging or even the rupture of the vessel. It can happen throughout the entire aorta, with different outcomes depending on the location. Dissection in the ascending part of the aorta tends to be more severe and need surgical intervention in contrast to other sites, where it can be treated medically and become chronic [1].

In order to better understand the progression of this disease and the reason for these differences, some studies are currently focusing on determining the dissection properties of the aortic wall via delamination tests. These are usually performed only on the medial layer [2, 3] or focusing on a specific location of the vessel when considering different layers [4]. Therefore, in this study, we perform a complete dissection study in porcine aortas that includes the dissection of the two interfaces (intima-media and media-adventitia), as well as the medial layer, all through the different locations of the aorta.

Methods

A total of 9 healthy porcine aortas were harvested, including the three zones of study: the ascending thoracic aorta (ATA), the descending thoracic aorta (DTA) and the infrarenal abdominal aorta (IAA). The arteries were kept frozen at -80ºC and brought to 4ºC 24 hours before testing.

20 x 5 mm strips were cut in both the longitudinal and circumferential directions. An initial incision was performed in order to assure the separation between the layers of interest. In these specimens, two different dissection tests were carried out: a T-peel test, which reproduces a mode I of fracture, and a 180º peel test, involving a mixed mode of fracture that includes modes I and II, see Fig. 1.

(a)   *(b)*
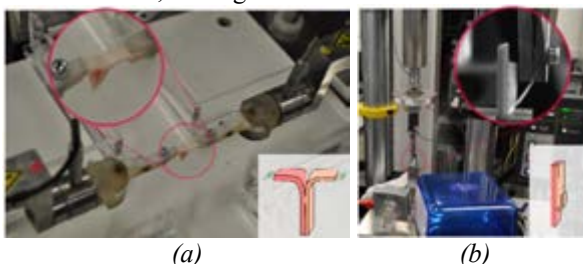
Figure 1: Experimental setup and outline of the T-peel test (a) and the 180º peel test (b).

In both tests, the tongues of the specimens are fixed by two clamps. In the peel test, both clamps move at a speed of 1 mm/min, whereas in the mixed test, only one clamp moves at that speed while the other is fixed. The force-displacement curves are recorded and subsequently processed.

Results

Dissection in the ATA required higher force in both delamination tests, see Fig. 2.

The dissection of samples in the longitudinal direction usually required more force and results were more disperse than the same layer dissection in the circumferential direction, probably due to collagen fibers being mostly oriented circumferentially, so a longitudinal tear would need to rupture this fibered structure.

In all locations, the dissection of the intima-media required the least force of all layers. This result can explain the rapid initial development of the disease and the subsequent slowing down when reaching the medial layer.

(a)   *(b)*
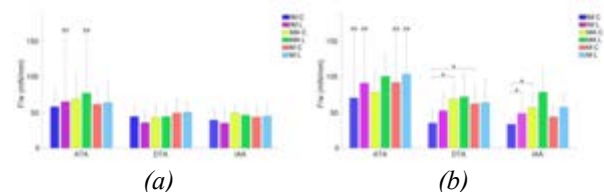
Figure 2: Averaged mean force and standard deviation of the T-peel test (a) and the 180º peel test (b).

Discussion

A complete study of the dissection in the aorta was carried out. This study highlighted the anisotropy of the aorta and the need to characterise the dissection properties as function of the location and layer of the vessel.

References

1. Nienaber et al, Nat Rev Dis Primers, 2(1), 2016.
2. Sommer et al, J Biomech Eng, 130(2): 021007, 2008.
3. Leng et al, J Mech Behav Biomed Mater, 77:321–330, 2018.
4. Kozun, J Theor Appl Mech, 54(1):229, 2016.

Acknowledgements

AORTIC MEDIA UNDER RADIAL TENSION: GLOBAL AND LOCAL EFFECTS OF RELAXATION

Selda Sherifova (1), Stéphane Avril (1,2), Gerhard A. Holzapfel (1,3)

1. Institute of Biomechanics, Graz University of Technology, Austria; 2. Mines Saint-Étienne, Univ Lyon, Univ Jean Monnet, INSERM, France; 3. Department of Structural Engineering, Norwegian Institute of Science and Technology, Norway

Introduction

The radial tensile strength of the aorta can be significantly reduced due to some pathological conditions that predispose patients to dissection, which is one of the most devastating complications of thoracic aortic disease [1]. However, the mechanical behavior of arteries under radial tension has rarely been investigated [1-6]. Here we report the first results of radial tensile tests using optical coherence tomography (OCT) and digital volume correlation (DVC).

Methods

Specimens of the porcine aortic media were divided into 2 groups and tested using the OCT set-up described in [6], with the circumferential-radial section facing the camera. After the specimen was glued to the holders, a volume of $4 \times 1 \times 1.6$mm (radial $\times$ circumferential $\times$ axial) was imaged with the OCT. After 5 preconditioning cycles, the radial displacement was applied in increments of 100µm. In both groups, the volume was imaged immediately after each loading step. In group 2, an additional volume was acquired after allowing the specimen to relax for 10 minutes at each step. DVC was then applied on the volumetric images using DaVis 8.4 (LaVision) to derive the displacement fields and Green-Lagrange strain fields were derived using a custom Matlab code.

Results

In both groups, the force curves showed a plateau during earlier loading steps, and in group 1, the force increased continuously to failure with subsequent loading steps; see Fig. 1(a). Voids that merged into larger defects appeared before the peak force was reached, Fig. 1(b)-(c). DVC analyses revealed complex deformations, including hot spots of strains, indicating early localization effects in both groups. Relaxation experiments showed that the specimen relaxed by absorbing fluid that induced local strain gradients, see Fig. 1(d), slightly dispersing the sharp localizations.

Discussion

Aortic media can resist significant radial stretches by absorbing fluid. Increasing radial stretches induce strain concentrations and mechanical damage that bear similarities to the localized effects of GaG pooling in dissected tissues [5]. The methodology will be extended to healthy and dissected human aortas to better understand the biomechanical implications of the disease.
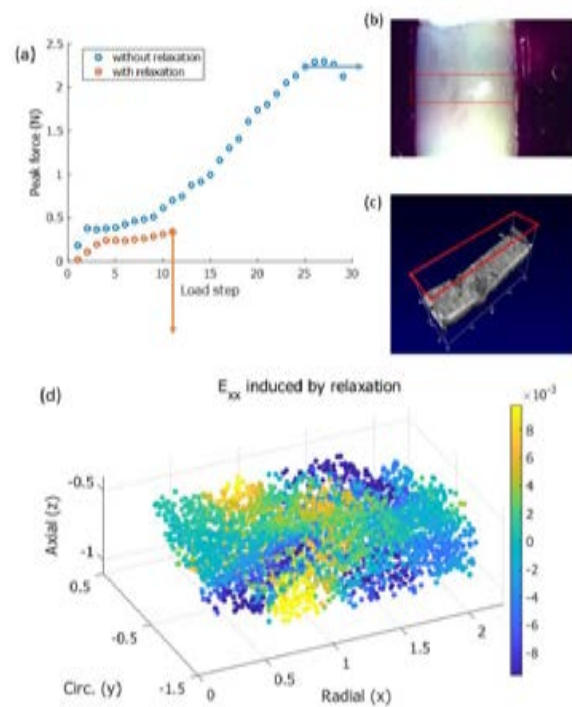
Figure 1: (a) Peak force vs. load step during the radial tensile test with (blue) and without (orange) relaxation; (b) camera view and (c) OCT rendering showing voids at the load step indicated by the blue circle; and (d) changes in the Green-Lagrange strain component E_{xx} induced by relaxation at the final load step, indicated by the orange circle.

References

1. Sherifova & Holzapfel, Acta Biomater, 99:1-17, 2019.
2. Roach & Song, Clin Invest Med, 17:308-318, 1994.
3. Sommer et al, J Biomech Eng, 130:021007, 2008.
4. Sommer et al, J Biomech, 49:2374-2382, 2016.
5. Roccabianca et al, Biomech Model Mechanobiol, 13:13-25, 2014.
6. Di Giuseppe et al, Exp Mech, 61:119-130, 2021.

Acknowledgements

NON-HOMOGENEOUS GEOMETRICAL INFLUENCE ON RING-OPENING STRESS RECONSTRUCTION

Andrés Utrera (1), Matías Inostroza (1), Eugenio Rivera (1), Diego J. Celentano (2), Claudio García-Herrera (1)

1. Departamento de Ingeniería Mecánica, Universidad de Santiago de Chile, Chile; 2. Departamento de Ingeniería Mecánica y Metalúrgica, Pontificia Universidad Católica de Chile, Chile.

Introduction

Residual stress in arteries is a well-studied behavior of blood vessels relevant to normal and pathological conditions inside the arterial wall [1]. These stresses play an essential role in pressure distribution along the vessel and homogenize the stress distribution inside the wall thickness [2]. Several authors have used the so-called ring-opening test to measure the residual strain state of arteries. This test consists of radially cutting a ring-shaped vessel specimen to measure its final opening angle at an assumed stress-free state to quantify some degree of strain indirectly.

Authors have shown that a unique deformation parameter isn't enough to describe the complexity of the residual stress and strain problem [3,4]. It has been demonstrated that it is a non-homogeneous field. Nevertheless, it is still a straightforward method to characterize possible homeostatic changes inside the arterial wall under effects such as aging, diseases, or pathological conditions.

This study describes how the non-homogeneous resulting geometry after the ring-opening test cut impacts the assumption of homogeneous stress. A sheep-specific aortic segment is used to perform uniaxial tensile and ring-opening tests from the abdominal aorta region. The resulting anisotropic material characterization, along with image-based geometric quantification and posterior FE analyses, is used to quantify potential errors in the classical and straightforward ring-opening test.

Methods

A tensile test is used to characterize the anisotropic behavior of the vessel. A Holzapfel-Gasser-Ogden constitutive model is fitted to the experimental stress-strain relationship in both circumferential and longitudinal directions. On another side, a classical and straightforward ring-opening test is assessed, taking photographs of the vessel in its closed shape and then, in its opened condition, with a 15-minute interval since the opening cut. Both procedures are performed with the tissue submerged in Krebs buffer at 38°C. Once the geometry of the tissue is successfully captured, the 2D transverse geometry of the vessel is reproduced in its opened image, using a spline function, allowing further to measure the sample-specific curvature and thickness variation along the vessel wall perimeter. Three scenarios are analyzed: shape idealization, variable curvature and constant thickness, and finally, variable curvature and thickness. A displacement-based finite element closing and pressurization procedure is carried out to estimate how important the assumption of uniform shape is in this experimental test.

Results

From the comparisons between the three analyzed scenarios, the presence of a non-uniform-shaped specimen in a residual stress study will be highly biased from the optimal scenario. The main findings suggest that thickness variation inside a range of 50% variation wouldn't excessively affect the results. However, the opened curvature variation along the vessel is a good estimator of the non-homogeneity of the internal stress field.

Discussion

We have demonstrated how biased is the stress field considering a severe case of non-homogeneous residual strains visible to the naked eye. Result suggests that although the residual stress field is highly heterogeneous, it is not far from the raw values obtained in the homogeneous case. However, the most severe bias could be in a pre-stretched and pressurized vessel. With all this information, we have assessed a possible quantitative criterion to discard vessel samples of this experimental test when they present a non-homogeneous shape.

References

1. C. J. Chuong, Y. C. Fung. *J Biomech Eng*. May 1986, 108(2): 189-192.
2. Chandran, K.B., Mun, J.H., Chen, J.S. *et al. KSME International Journal* **15,** 965–973 (2001).
3. Holzapfel GA, Sommer G, Auer M, Regitnig P, Ogden RW. Ann Biomed Eng. 2007 Apr;35(4):530-45.
4. Badel, P., Genovese, K. and Avril, S. (2012). Strain, 48: 528-538

Acknowledgements

A PHENOMENOLOGICAL DEGRADATION MODEL TO PREDICT THE LONG-TERM PERFORMANCE OF A POLYMERIC SCAFFOLD

Constantino Fiuza (1), Katarzyna Polak-Krasna (2), Gianluca Poletti (3), Luca Antonini (3), Giancarlo Pennati (3), William Ronan (1), Ted J. Vaughan (1)

1. Biomechanics Research Centre, School of Engineering, National University of Ireland Galway, Ireland; 2. Institute of Active Polymers, Hemlholtz-Zentrum Hereon, Germany; 3. Laboratory of Biological Structure Mechanics, Department of Chemistry, Materials and Chemical Engineering "Giulio Natta", Politecnico di Milano, Italy

Introduction

Bioresorbable scaffolds (BRS) are capable of being completely absorbed into the body through metabolic processes, thus avoiding some late stage complications associated with drug eluting stents (DES) [1]. Difficulties in BRS development include understanding physical degradation processes and prediction of long-term behaviour once implanted. Modelling efforts to capture the performance of polymer BRS have focused on capturing short-term performance. The objective of this study is to develop a phenomenological elasto-viscoplastic framework that can predict short- and long-term degradation behaviour of a polymer BRS.

Methods

The constitutive framework describing degradation was based on the Johnson-Cook (JC) elastic-plastic model (see Eqs. 1-2). Degradation was controlled by varying the A parameter of the JC plastic model and the strain to failure over time.

$$\bar{\sigma} = [A(t) + B(\bar{\varepsilon}^{pl})^n]\left[1 + Cln\left(\frac{\dot{\bar{\varepsilon}}^{pl}}{\dot{\varepsilon}_0}\right)\right][1 - \hat{\theta}^m] \quad (1)$$

$$\varepsilon_f^{pl} = \frac{\varepsilon_{max} - \varepsilon_{min}}{1 + e^{\left(t - \frac{t_{max}}{2}\right)c}} + \varepsilon_{min} \quad (2)$$

The constitutive model was used to capture the experimental long-term performance of a polymer BRS undergoing thermally accelerated degradation, whereby 36 BRS devices were immersed in phosphate buffered saline at 50°C for 181 days. Radial compression testing was performed at consecutive timepoints. Parameters of the JC degradation model was calibrated to match the measured radial force of the degraded timepoints, with the A and ε_f^{pl} varied through time using a USDFLD subroutine to capture the mechanical response at degraded timepoints. A model consisting of two circumferential rings was used for computational efficiency.

Results

The degradation model predicted the radial response at day 0 capturing the point of yield and the plateau region. After the initial timepoint, the model captured the increase in strength until day 77. Beyond day 112, the model was able to accurately capture the brittle failure seen in the experimental samples, with fracture happening soon after yield strength was reach. Figure

1(c) shows a summary of the calibrated model's prediction of both radial stiffness and strength of the BRS device.
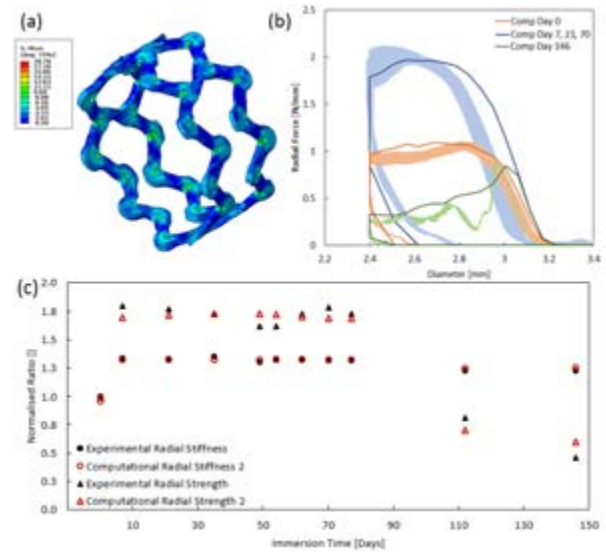
Figure 1: (a) Contour plot of BRS (b) Experimental and computational radial force vs diameter. (c) Calibrated material versus experimental radial strength and stiffness.

Discussion

Degradation of the polymer BRS resulted in a decrease in the strain to failure of the scaffold, with radial strength and stiffness maintained after 77 days of immersion in PBS at 50°C. The loss of radial strength is evident from day 77 in figures 1(b-c) with the plateau region greatly reduced. The degradation model is shown to accurately capture the changes in strength and stiffness of the scaffold over the degradation period. The inclusion of the ductile damage model is shown to accurately capture the brittle behavior at later timepoints.

References

1. Serruys et al. Lancet 373:897-910, 2009

Acknowledgements

ON THE RELATIONSHIP BETWEEN KINETIC ENERGY AND HELICITY IN PROSTHETIC HEART VALVES HEMODYNAMICS

Diego Gallo (1), Marco D. De Tullio (2), Umberto Morbiducci (1)

1. PoliTo^{BIO}Med Lab, Department of Mechanical and Aerospace Engineering, Politecnico di Torino, Italy;
2. Department of Mechanics, Mathematics and Management Politecnico di Bari, Italy

Introduction

Previous studies have revealed distinct signatures of prosthetic heart valves (PHVs) hemodynamics and their relations with long-term clinical performance [1]. Risks of complication in both biological or mechanical heart valves (BHV and MHV, respectively) have been linked to high levels of turbulence (and consequent energy dissipation), or to the formation, interaction and decay of the complex vorticity patterns and helical flow developing downstream of the PHV [1]. To date, there has been no detailed investigation on the interactions among these fluid structures, despite their role in determining PHVs success or failure. In this study, we used fluid-structure interaction (FSI) *in silico* models to investigate the interplay between the production of (phase-averaged and fluctuating) helicity, energy dissipation and transition to turbulence in the presence of MHV or BHV, to expand the understanding of PHV hemodynamics with potential translation into improvements of PHV design.

Methods

An idealized aortic root geometry was adopted. Two PHVs were considered, one reproducing a BHV St. Jude Trifecta model, with three deformable pericardial tissue leaflets, the other the bileaflet MHV St. Jude Regent model. Direct numerical simulations of the FSI problem were conducted by applying the immersed boundary method [2]. A strong coupling scheme was adopted for the FSI, using a validated implicit approach [2]. The MHV leaflets motion was obtained by integration of the rigid body dynamics equations. A mass-spring model was employed for the dynamics of the BHV, with a non-linear anisotropic model for the deformable leaflets [2]. A cardiac output of 5 L/min was prescribed at 70 beats/min (peak Reynolds number: 6200). The role of helicity and kinetic energy downstream of the PHVs is investigated using the Reynolds decomposition of the instantaneous velocity $\mathbf{u}$ into its phase-averaged and fluctuating component ($\overline{\mathbf{u}}$ and $\mathbf{u}'$, respectively). In detail, we denote the kinetic helicity density, derived by the phase-averaged or fluctuating velocity component, as $\overline{H_k}$ and H'_k, respectively:

$$\overline{H_k} = \overline{\mathbf{u}} \cdot \overline{\boldsymbol{\omega}} = \overline{\mathbf{u}} \cdot (\nabla \times \overline{\mathbf{u}}) \qquad (1)$$
$$H'_k = \mathbf{u}' \cdot \boldsymbol{\omega}' = \mathbf{u}' \cdot (\nabla \times \mathbf{u}') \qquad (2)$$

where $\boldsymbol{\omega}$ is vorticity vector. The kinetic energy E can be decomposed into mean kinetic energy (KE) and turbulent kinetic energy (TKE) as:

$$KE = 1/2 \ \overline{\mathbf{u}}\,\overline{\mathbf{u}} \qquad (3)$$
$$TKE = 1/2 \ \overline{\mathbf{u}'\mathbf{u}'} \qquad (4)$$

Results

A clear PHV-type dependence of the helicity production and decay emerged, with MHV hemodynamics presenting larger phase-averaged and fluctuating helicity than BHV (Fig. 1a,b). The relation between phase-averaged and fluctuating quantities along the cardiac cycle was further investigated by using a loop representation (Fig. 1c,d), highlighting how the generation of volume-average TKE or H'_k for both valves is not associated with a large overall change in their phase-averaged counterpart (Fig. 1c,d). For both PHVs, strong correlations emerged between volume-average kinetic energy and helicity when based on phase-averaged or fluctuating quantities (Pearson's correlation coefficient r ranging from 0.88 to 0.98, $p<0.001$). The production of TKE or H'_k for both PHVs was delayed with respect to the inflow waveform or the production of KE and $\overline{H_k}$ (up to 5.4% and 2.6% of the cardiac cycle, respectively for BHV and MHV).
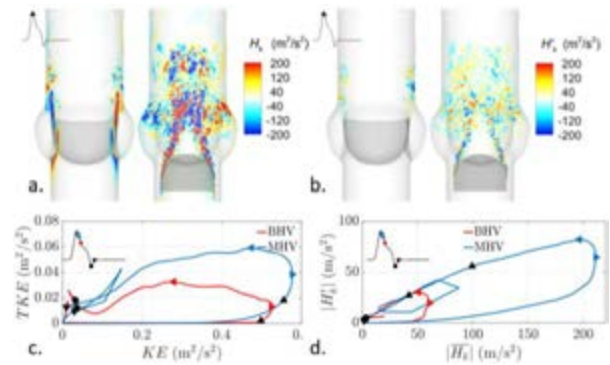
Figure 1: contours of $\overline{H_k}$ and H'_k (a,b); loop representation of KE vs. TKE (c) and $|\overline{H_k}|$ vs. $|H'_k|$ (d).

Discussion

The hemodynamics of PHVs is characterized by a strong interplay between kinetic energy and helicity. Although the dynamical significance of helicity is still matter of debate in relation to PHVs, these findings suggest a relevant role of both phase-averaged and fluctuating helicity in the evolution of turbulence downstream of the implantation site. The present characterization may prove useful to measure the restoration of physiological hemodynamics, optimize the leaflets design, evaluate the hemodynamic performances of PHVs and estimate the risk of complications.

References

1. Sotiropulos et al, Annu Rev Fluid Mech, 48:259-283, 2016.
2. De Tullio et al, J Comp Phys, 325:201-225, 2016.

FINITE ELEMENT SIMULATIONS OF THE CARDIOBAND PROCEDURE FOR THE TREATMENT OF THE REGURGITANT MITRAL VALVE

Emanuele Gasparotti (1,2), Emanuele Vignali (1), Massimiliano Mariani (3), Sergio Berti (3), Simona Celi (1)

1. BioCardiolab, Fondazione Toscana Gabriele Monasterio, Massa, Italy; 2. Information Engineering Department, University of Pisa, Pisa, Italy; 3. Dept. Interventional and Diagnostic Cardiology, Fondazione Toscana Gabriele Monasterio, Massa,

Introduction

Mitral valve regurgitation disease is one of the most common heart valve pathology [1]. Cardioband® (Edwards, Irvine) system is a surgical-like direct annuloplasty adjustable device, implanted via transcatheter on beating heart [2]. This procedure is based on the fixing of the device polyester sleeve (PS) around the mitral annulus through insertion of metal anchors. The annulus is contracted by pulling a guidewire sewed at sew points on the PS (cinching phase). Currently, the implant size (anchors number) and the anchors position are defined on the basis of the CT dataset by analyzing the site of access and measuring the commissure to commissure distance on the posterior annulus. The aim of this study is to present a numerical method integrating image processing and Finite Element (FE) method to simulate the Cardioband procedure and evaluate its effect on the mitral valve dynamic and on the surround cardiac structures.

Materials and Methods

The method consisted of three main structural simulations: the simulation of the regurgitant mitral valve before the procedure (i), the simulation of the device activation (ii), and the simulation of the mitral valve after the procedure (iii). The simulations were performed using patient-specific geometries obtained by segmenting both computed tomographic (CT) and transoesophageal echocardiographic (TEE) datasets from a patient treated with Cardioband. In the first part of the study, the software LS-DYNA was employed to set up the structural simulation of the patient's mitral valve before the procedure. A transvalvular time-dependent pressure was applied on the leaflets of the valve. The motion of the mitral annulus during the cardiac cycle was imposed with nodal time-dependent displacements based on the CT dataset.

In the second part, the contraction of the device was simulated by developing a specific FE environment in Matlab® [2] that reproduces the behaviour of the Cardioband device, the whole structures of the left heart and their mutual interactions during the cinching phase. The resulting nodal contraction was transferred to the structural model as mitral annulus motion and, in the third part, the mitral valve was simulated in the cinched configuration by applying a time-dependent transvalvular pressure to the leaflets.

Results

Figure 1(a-b) shows the axial and radial displacements of the cardiac structures. Maximum contraction is achieved in the mitral annulus and atrium. The effects of the device on systolic function of MV are assessed by the area of the leaflet contact areas (CoA), as shown in Figure 1(c). Activation of the device increases CoA values from 123 mm^2 to 231 mm^2. The changes in valve behavior during diastole are studied using the Geometric Orifice Area (GOA), which is described by the free edges of leaflets. The Cardioband treatment reduces the MV GOA from 390 mm^2 to 370 mm^2.
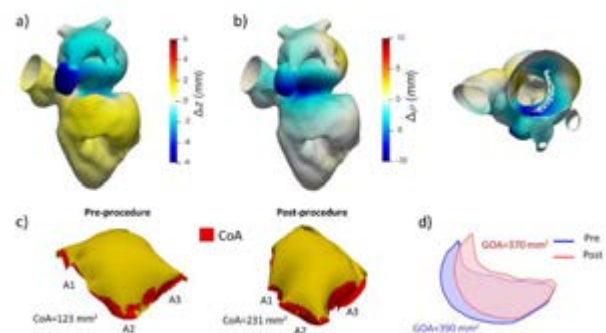
Figure 1: Axial a) and radial b) displacements of the cardiac structures. MV Coaptation Area c) and Geometric Orifice Area d) in pre- and post- procedure.

Discussion

Simulation results have shown that the Cardioband procedure can induce contraction of cardiac structures surround to the device, promoting improvement of leaflets coaptation and restoration of valve tethering without compromising the diastolic function of the valve. In this way, it will be possible to perform preoperative planning to evaluate the postoperative parameters and increase the overall performance of the procedure in the treatment of mitral regurgitation.

References

1. Ferrero Guadagnoli, A. et al, Expert Rev. Med. Devices, 15.6: 415-421 (2018).
2. Gasparotti, E. et al, Proc. ESB2021, 121 (2021).

Acknowledgements

MYOCARDIAL BIOMECHANICS OF LEFT ATRIAL LIGATION CHICK EMBRYONIC MODEL OF HYPOPLASTIC LEFT HEART SYNDROME

S.Samaneh Lashkarinia (1), Wei Xuan Chan (1), Zheng Yu (2), Hummaira banu Siddiqui (3), Mervenur Coban (3), Bortecine Sevgin (3), Kerem Pekkan (3), Choon Hwai Yap (1)

(1) Department of Bioengineering, Imperial College London, UK

(2) Department of Biomedical Engineering, National University of Singapore, Singapore

(3) Department of Mechanical Engineering, Koc University, Turkey

Background

Left atrial ligation (LAL) of the chick embryonic heart at early developmental stage is a model of the hypoplastic left heart syndrome (HLHS) disease. LAL relies on mechanical intervention without genetic or pharmacological manipulations [1]. Therefore, it is a good model for understanding the biomechanics origins of such HLHS malformations. However, the mechanical properties and behavior of the embryonic heart myocardium has not been investigated in detail, and neither is the mechanobiological mechanism of how LAL can lead to HLHS. In the present study we analyzed the biomechanics of the LAL myocardium via image tracking and finite element modelling (FEM) and reveal single cell RNA sequencing to obtain gene expressions potentially linked to myocardial mechanics abnormalities.

Methods

4D ultrasound imaging was performed on White Leghorn chick embryos at HH25 (ED 4.5) for both LAL (n=3) and normal (n=3) embryonic hearts, using a high frequency ultrasound system (Vevo2100, Visual Sonics Inc., Canada). 3D segmentation of the embryonic ventricle myocardium was conducted via a lazy-snapping algorithm and vascular modelling toolkit (VMTK) software (Figure1A). A validated cardiac motion estimation algorithm was applied to track wall motion [2], and calculate 3D myocardial strains. Myofiber directions were estimated at mid-ventricular wall by seeking the smallest eigenvector of the strain tensor (direction of maximum strain). FEM was conducted by adapting a previous model, and featured subject-specific ventricular geometries and myofiber architecture obtained from images, the Guccione active tension model, and a fung-type transversely isotropic passive stiffness model [3]. FEM models were tuned to match literature reported ventricular pressures. Single-cell RNA sequencing of chick embryonic heart ventricles for normal and LAL embryos (at ED6.5 days, HH31) was performed and differentially expressed gene with >log2(1.0) fold change were identified.

Results

Morphological analysis indicated that LV thickness decreased from 0.153±0.021 mm in normal samples to 0.098±0.032 mm in LAL sample. Image analysis showed no specific differences in the spatial pattern and averaged myofiber directions between normal and LAL hearts. However, the mean compressive strains in myofiber direction were larger in LAL compared to normal by 48%. FEM produced pressure-volume curves showed in Figure1B, and indicated that LAL myocardium has reduced 42% lower stresses (in the myofiber direction) than normal myocardium (136.5 Pa vs 236.7 Pa), which was due to a lower peak systolic pressure. RNA-seq data revealed a number of differentially expressed genes in myocytes related to their biomechanical conditions, including several that are relevant to mechanosensing (eg., focal adhesion genes, Cadherins, NOTCH1), and to myosin contractility (eg., CALM, MLCK, MLCP) and calcium signalling (eg., PI3K, SERCA, STIM2).
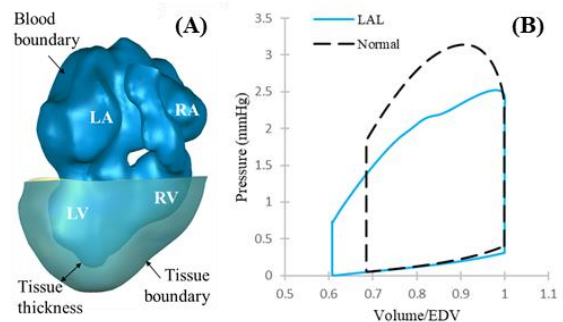
Figure 1: (A) Tissue-blood boundaries and ventricle myocardium segmentation at HH25 for a normal embryonic heart. (B) PV loop obtained from FEM for a normal and a LAL ventricle at HH25.

Conclusions

We find that LAL brings about specific changes to the myocardial biomechanics. Due to the atrial ligation that restricted inflow from the left atrial (LA) to the LV, LV has decreased pressure, and there were higher strains, but overall myocardial stresses were decreased. These changes to the stresses and strains could have led to abnormal development to reach HLHS. RNA-seq showed that many genes related to myocardial contraction, deformation, and ECM remodelling were differentially expressed, corroborating with the biomechanical analysis that altered myocardial biomechanics could be a causative factor in the HLHS outcome in the LAL model.

Acknowledgements

References

1. Kowalski, W. J., *Developmental Dynamics*, *243*: 652, 2014
2. Wiputra, H., *Scientific Reports*, *10*: 18510, 2020
3. Ong, C. W., *ABME*, *49*: 1364, 2021

A NOVEL MODEL FOR THE HEMODYNAMICS OF CEREBRAL ANEURYSMS TREATED WITH ENDOVACULAR COILS BASED ON SYNCHROTRON IMAGING AND EXPERIMENTAL VALIDATION

J. ROMERO BHATHAL[A], SYED FAISAL[B], F. CHASSAGNE[C], L. MARSH[B], M. LEVITT[C,D], C. GEINDREAU[A], AND A. ALISEDA[C,D]

[A] Univ. Grenoble Alpes, CNRS, Grenoble INP, 3SR, Grenoble, France; [B] Dpt. Mechanical Engineering, Univ. Washington, Seattle, WA, USA, [C] Mines Saint-Etienne, Univ Lyon, Univ Jean Monnet, Etablissement Français du Sang, Inserm, U 1059 Sainbiose, F - 42023 Saint-Etienne France, [D] Dpt. Neurological Surgery, Univ. Washington, Seattle, WA, USA

Introduction

Cerebral aneurysm (CA) hemodynamics have been related to aneurysm progression. Computational fluid dynamics (CFD) has been used to assess the relationship between the effect of treatment on hemodynamics and its clinical outcome. To determine the failure or success of the treatment through CFD, it is important to have patient-specific anatomic models and realistic boundary conditions. The state of the art to model the coils deployed inside the aneurysmal sac is a homogeneous and isotropic porous medium. Comparing this approach against coil-resolved simulations has shown that the homogenous isotropic approximation represents a significant compromise in accuracy [1]. The objective of the present work is to create a porous model representative of the heterogeneous porosity of the coils deployed in the aneurysm and that reproduces accurately the effect of coils on intracranial hemodynamics

Methods

Virtual 3D models of the aneurysm and parent vessels were built from seven patients having a CA treated with coil embolization. Computed tomography scans were 3D printed (1:1 scale) in a clear polyester resin (PDMA). The surgeon who performed the endovascular surgery on the patient inserted the same coils on the 3D printed model, using the same procedure used on the patient. The coiled PDMA models were imaged at the European Synchrotron Radiation Facility (Grenoble). Coil 3D geometries were positioned in the aneurysm models and the porosity distribution was analyzed radially. Two parameters define the porous medium that slows down flow in the aneurysm, defined predominantly tangentical to "crowns" concentric with the aneurysm sac: permeability (α_i) and inertial coefficient C_2. 3 models were compared to validate the permeability used in the model: the coil-resolved, and two homogeneous isotropic porous models with α_{mean} and α_{crowns} respectively, under steady Stokes flow. To validate the complete porous model, 3 different models were studied: coil-resolved, and two homogeneous isotropic porous models with (α_{mean} and C_{2mean}), and with (α_{crowns} and $C_{2crowns}$), under unsteady high Reynolds number. Planar Laser Induced Fluorescence (PLIF) experiments were used to the residence time in the aneurysmal sac for each patient and compare to the computational models, coil-resolved and porous media.

Results

All patients show a similar distribution of porosity: higher in the external crowns near the wall than in the core. Between x=0.5mm and x=0.75mm from the aneurysm wall, porosity becomes constant and close to the mean porosity. It is important to consider the heterogeneity of the porous media in the first 0.5mm while modelling the flow in the coiled aneurysm.

The low Reynolds number simulation shows that the parallel porous media model is an improvement for modelling flow compared to only considering the mean porosity in the aneurysm. However, the parallel model needs to take in account the patient-specific anatomy, modelling it as a bilinear porosity distribution.
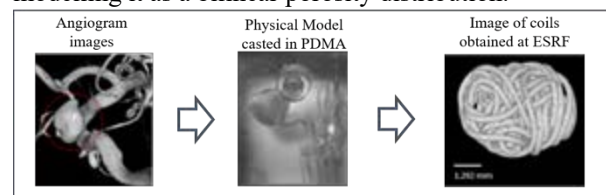
Figure 1: Coiled Aneurysm modeling workflow: patient CTA, physical 3D printed model treated with the same coils as patient (validation of the coil-resolved model in terms of Residence Time in the sa)c and reconstruction of the coils in the aneurysm for computational model. The coil synchrotron images serve as both a source of data for porous model development and as the "gold-standard" coil-resolved computational model.

Conclusion

The crown method for porous characterization of coils in a cerebral aneurysm captures the heterogeneity of the porous distribution. The parallel porous media model seems to be an optimum approximation for modelling flow in the aneurysm, as it takes into account the heterogeneity of the coil distribution near the aneurysm wall. Comparison of the Residence Time in experiments and simulations for the same coiled aneurysm allows to validate the numerical models, not only in for Eulerian metrics, such as WSS, OSI, etc. but also for Lagrangian metrics that may be more accurate to predict thrombus formation in the aneurysmal sac after treatment.

References

1. Levitt MR, et al. 2016. Computational fluid dynamics of cerebral aneurysm coiling using high-resolution and high-energy synchrotron X-ray microtomography: comparison with the homogenous porous medium approach. JNIS 0:1-6.

IMPACT OF HYPERTENSION AND ARCH MORPHOLOGY ON AORTIC HEMODYNAMICS: A PRELIMINARY NUMERICAL ANALYSIS

Maria Antonia D'Attimo (1), Alessandro Caimi (1), Massimiliano Marrocco-Trischitta (2), <u>Francesco Sturla</u> (2,1), Alberto Redaelli (1).

1. Politecnico di Milano, Milano, Italy; 2. IRCCS Policlinico San Donato, San Donato Milanese, Italy

Introduction

Abnormal helical flow (HF) in the aortic arch, secondary to specific anatomical arch features (e.g., curvature and tortuosity), has been proposed as a causative factor for the onset of aortic disease (AD) [1]. Concurrently, aortic wall stiffening associated with hypertension is a major risk factor for ADs with age and high blood pressure, as established in terms of pulse wave velocity (PWV), being the main determinants [2]. However, the interplay between arch morphology and hypertensive conditions in triggering aortic bulk flow derangements, has been poorly explored and time-expensive fluid-structure interaction (FSI) models are required [3].

Herein, we sought to investigate aortic arch HF alterations which may result from the combination of hypertensive conditions, i.e., due to increased PWV and ageing, with definite anatomical patterns of the aortic arch.

Methods

One-way FSI simulations [4] based on the coupled momentum method (CMM), were employed to compare HF features associated with type I to III aortic arches (Figure 1). Each anatomy was segmented from computed tomography in ITK-Snap, and subsequently meshed and simulated in SimVascular [5].
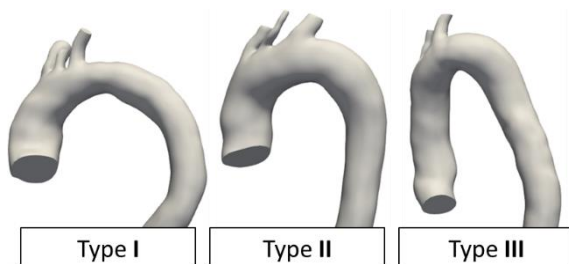
Figure 1: simulated anatomical aortic arch models.

To reproduce the effect of hypertension (normotensive *vs.* hypertensive) and age (<30 *vs.* >70 years), the aortic wall elastic modulus was estimated from reference PWV values [2], through the Moens-Korteweg equation, and pressure boundary conditions were prescribed with 3 element Windkessel circuits at each outflow. A physiological aortic flow waveform was imposed on the inflow. Bulk flow pattern was regionally assessed, i.e., from zone 0 to 3 along the aortic arch [1]. Aortic flow pathlines were computed at systole and used to extract local normalized helicity (LNH), helical flow index (HFI), shape indexes of curvature (κ) and torsion (τ), and normalized residence time (RT).

Results

LNH, HFI and τ remained comparable between aortic arch types with no significant variations due to hypertension or age. Conversely, κ and RT revealed significant changes from arch type I to III and, in particular, in zone 3 (Figure 2). In this region (i.e., 3/III), hypertension and age exacerbated both κ and RT, both reporting the highest values (κ and RT up to 0.2 mm^{-1} and 0.06 s/cm, respectively) in the hypertensive elderly (>70) model. Hence, these HF features of pathlines' curvature and residence time proved to be sensitive markers of the aortic bulk flow alterations associated with hypertension.
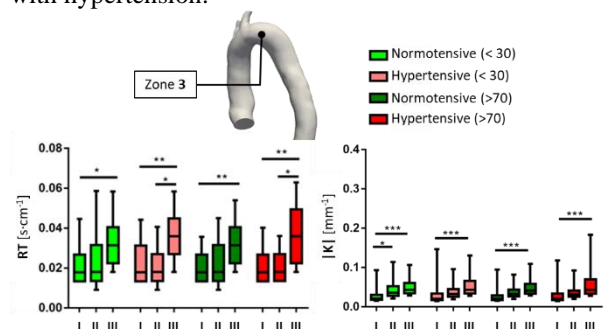
Figure 2: absolute κ and RT box and Whiskers plots in zone 3 for each arch type (I, II and III) under the different conditions tested for both hypertension and age (*P≤.05, ** P≤.01, *** P≤.001).

Discussion

Our proof-of-concept FSI analysis effectively reproduced aortic arch HF under the different conditions of PWV and blood pressure associated with arterial hypertension, detecting arch-type regional differences in aortic bulk HF. The significant exacerbation of aortic HF localized in Zone 3 of Type III arch configuraiton, which is prevalent in patients with type B aortic dissection, deserves further investigation.

References

1. Marrocco-Trischitta *et al*, EJCTS, 61(1):132-139, 2022.
2. Arterial Stiffness' Coll., Eur Heart J 31, 2338–2350, 2010.
3. Campobasso *et al*, CVET, 9: 707–722, 2018.
4. Figueroa *et al*, Comput Methods Appl Mech Eng, 195: 5685-5706, 2006.
5. Updegrove *et al*, Ann Biomed Eng 45:525-541, 2016.

Acknowledgements

USING THE DIGITAL TWIN OF HUMAN FETAL HEART TO PREDICT OUTCOMES OF A FETAL HEART INTERVENTION

Laura Green (1), Wei Xuan Chan (1), Andreas Tulzer (2), Gerald Tulzer (2), and Choon Hwai Yap (1)

1. Imperial College London, UK; 2. Children's Heart Centre Linz, Austria.

Introduction

Most fetuses with critical aortic stenosis with evolving hypoplastic left heart syndrome (eHLHS) will progress to a univentricular birth outcome, but a type of minimally-invasive fetal heart intervention, fetal aortic valvuloplasty (FAV) can prevent this, reducing the risks of single ventricle birth from 72-74% to 28-34% [1]. However, we do not understand the biomechanical and functional effects of the disease and intervention and cannot accurately predict outcomes. Investigations are thus needed on this, to help accurately select patients for the procedure, to help with prognosis and inform patient and clinician decisions, and to provide hints on how to optimise the intervention. We developed a digital twin of the human fetal heart, which can reconstruct a patient-specific fetal heart model based on echo images and use it here to evaluate the post-interventional scenarios of FAV on eHLHS, to achieve outcome prediction and precision medicine in future.

Methods

We first constructed the pre-intervention digital twin of the fetal left ventricle (LV), and subsequently used it to simulate post-interventional scenarios to predict possible outcomes. The 3D anatomy of the fetal LV was reconstructed from 3D echocardiography images, and its 3D motion extraction with a validated motion estimation algorithm. A Finite Element model (FEM) of the LV was then constructed, with spatially varying fibre orientation, Guccione active tension model and a Fung-type transversely isotropic passive stiffness model. The FEM was linked to a Windkessel lumped parameter model which is scalable to the specific fetal gestational ages. Optimisations were subsequently carried out where: (1) the valve flow resistances in the diseased LV were determined via matching the valve pressure gradients in the model with Doppler valve velocity measurements; and (2) the myocardial contractility was determined by matching LV stroke volume of the model to that obtained from the images. Post-interventional scenarios were investigated for various extent of relieving the aortic valve obstruction (AV recovery ratio, 1=full recovery, 0=obstructed), and various extents of aortic regurgitation. FEM for Normal fetal LVs were used as controls.

Results

The pre-FAV model showed that eHLHS diseased LVs were overloaded (elevated systolic and diastolic pressures) and had contractile dysfunction (reduced myocardial strains and high work burden) compared to normal LVs. In the simulated post-intervention scenarios (Figure 1), systolic depressurisation was typically observed, and myocardial strains and LV stroke volume typically increased. End-diastolic LV depressurisation, which indicates depressurisation of the left atria (LA), was observed for cases where aortic regurgitation was low to none, but with severe aortic regurgitation, the LA failed to depressurise.
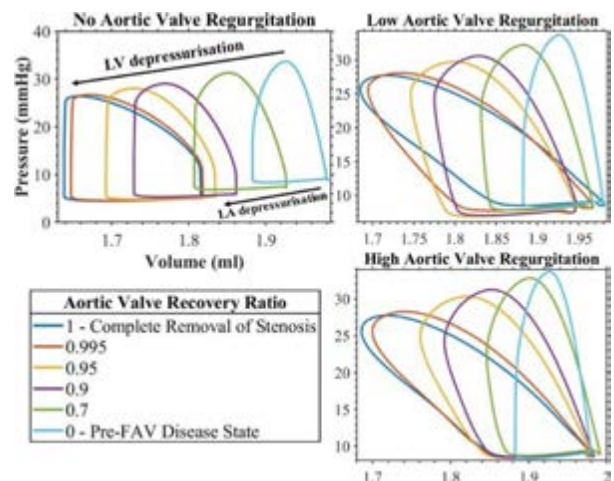
Figure 1: PV loops of pre- and post-FAV scenarios. Increasing aortic valve recovery ratio (increasing extent of stenosis relief) increases LV depressurisation and the stroke volume. However, LV end-diastolic pressure (indicative of LA pressure) could only depressurise without significant aortic regurgitation.

Discussion

We successfully developed a digital twin of the fetal LV, specifically matched to an eHLHS patient, in terms of anatomy, function, and motion, and used it to make interventional outcome predictions, thus moving closer towards achieving precision medicine with the digital twin. Simulation results showed that the LV biomechanics, and its flow and strain function were severely compromised, and that FAV can restore some of the lost function, likely contributing to increased chances of biventricular birth. However, our simulations suggest that care must be taken, as excessive relief of the stenosis, which likely leads to severe aortic regurgitation, could prevent LA depressurisation, and impede a biventricular outcome.

References

1. Pickard S, et al, Circulation, 13(4), 2020.

Acknowledgements

THE INFLUENCE OF THE ORTHOTROPIC TISSUE IN AN ELECTROMECHANICAL HEART MODEL

David Holz (1), Denisa Martonova (1), Emely Schaller (1), Minh Tuan Duong (1,3), Muhannad Alkassar (2), Sigrid Leyendecker (1)

1. Institute of Applied Dynamics, Friedrich-Alexander-Universität Erlangen-Nürnberg, Germany;
2. Department of Cardiac Surgery, Friedrich-Alexander-Universität Erlangen-Nürnberg, Germany;
3. School of Mechanical Engineering, Hanoi University of Science and Technology, Vietnam

Introduction

A large variety of approaches is existing in order to assign the orthotropic tissue structure to computational heart models. Many studies in the field of cardiovascular biomechanics investigate on multiple levels (e.g. cell, tissue, organ) the function of the heart to improve diagnosis, therapy as well as drug development. The orthotropic tissue structure decisively influences the mechanical and electrical properties. However, there are not many studies existing which are investigating to what extent the different approaches, which lead to a different orthotropic tissue structure, are influencing the subsequent cardiac simulation. In detail, we are utilising three existing Laplace-based approaches and compare the results of the electromechanical simulations on the basis of specified global characteristics (ejection fraction; wall thickening in the base, middle and apex region; generated peak pressure; apex shortening; myocardial volume reduction) as well as local characteristics (active fibre stress; fibre strain).

Methods

We utilise a fully-coupled electromechanical computational heart model including a Windkessel model to represent the hemodynamics. The fully-coupled computational heart model is based on an experimentally derived geometry (left ventricle (LV)) of a healthy subject via magnetic resonance imaging. The orthotropic tissue structure is based on three previously published Laplace-based approaches [1,2,3]. On the one hand, the methodological differences between the approaches [2,3] lie in the computation of the transmural thickness. On the other hand, approach [1], in contrast to the approaches [2,3], directly utilises the Laplace equation to transmurally interpolate the assigned vector components (e.g. fibre and sheet vectors) on the endocardium and epicardium. Subsequently, based on the different orthotropic tissue structure obtained from the different approaches, we systematically investigate the differences based on the defined global and local cardiac characteristics w.r.t. the cardiac function.

Results

In Fig. 1, we exemplarily show the result for the local characteristic of strain in fibre direction. We see that the local strain measure significantly differs for the different approaches [1,3] w.r.t. the reference solution [2].
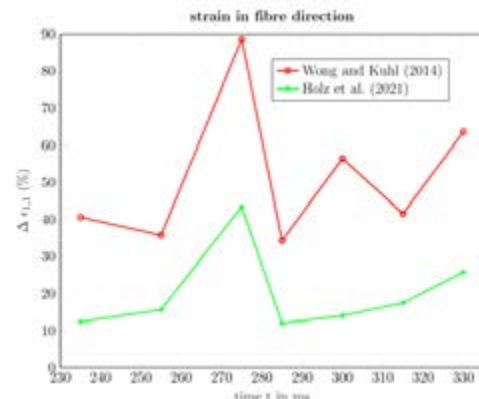
Figure 1: Averaged deviation of the local strain measure in fibre direction during the cardiac cycle for [1,2,3].

In this study, we additionally show that the obtained orthotropic tissue structure for the same LV from the three different approaches leads to a clearly different fibre orientation. The results coincide with the observations presented in [3]. The local material orientations by [1,2,3] lead to comparable results in the electromechanical simulation with moderate differences w.r.t. all specified global characteristics, especially for the maximum values of the quantities during systole. Nevertheless, the local material orientation decisively influences the temporal shift of the quantities, e.g. time shift of maximum wall thickening among the different methods as well as the local characteristics, see Fig. 1.

Discussion

The orthotropic tissue structures for the different approaches have a moderate influence on the global characteristics but a significant influence on the local measures.

References

1. Wong, J. et al, Computer methods in biomechanics and biomedical engineering, 17(11):1217-1226, 2014.
2. Bayer, J. et al, Ann Biomed Eng., 40:2243-2254, 2014.
3. Holz D. et al, J Biomech Eng., 144(3):031002, 2022.

Acknowledgements

COMPUTATIONAL STUDY ON TWO IDEALIZED MODELS OF THE LEFT VENTRICLE WITH DIFFERENT MYOFIBER ARCHITECTURES

Kasra Osouli (1), Francesco De Gaetano (1), Paolo Zunino (2), Maria Laura Costantino (1)

1. Department of Chemistry, Materials and Chemical Engineering "Giulio Natta", Politecnico di Milano, Italy
2. Department of Mathematics, Politecnico di Milano, Italy

Introduction

The arrangement of cardiomyocytes (CM) in the compact left ventricular wall has been described as a crossing double-helical pattern with myocytes in the sub epicardium having a left-handed and those in the sub endocardium a right-handed helix angle, whereas those in the mid myocardium are circumferential [1,2]. A common approach to assigning the myocardial orientation in computational rule-based models of the idealized geometries of the heart is to view the ventricles as nested ellipsoids. As a result, the fibers congregate at the apex of the left ventricle (LV) to produce a singularity [3]. Alternatively to the previous model, we describe the LV as a nested set of tori with fiber running on the closed geodesics with the possibility that a fiber running on the external surface can pass through the bottom of the left ventricle (the apex) in order to run on the internal surface [4,5]. In this study, we exploit a unique method for assigning myocardial orientation based on the nested tori conjecture.

Methods

The LV was modeled by a Truncated Ellipsoid (TE) and the Nested Tori (NT) model. The local coordinate systems aligned with the fiber direction was assigned by a Laplace Dirichlet Rule-Based Method (LDRBM) to the TE whereas a wall distance formulation was used to generate the encapsulated toroidal surfaces and assign the fiber local coordinate aligned with the geodesic curves (figure 1). The simulation contained two steps, diastole and systole, with end-diastolic pressure (10 mmHg) and end-systolic pressure (120 mmHg), respectively, is applied to the endocardial surface. All the nodes at the basal plane were fixed in the longitudinal direction and the endocardial ring was also fixed in the angular direction. SolidWorks was utilized to generate the geometries and the finite element modeling was performed in COMSOL Multiphysics 5.6.

Results

The CM stress distribution and the global deformation of the ventricle were compared in both models. The mean and maximum CM stress in the NT model was about 30 and 120 kPa whereas in the TE model a large stress concentration at the apex region was measured (about 400 kPa) while the average stress was about 40 kPa (figure 2).

Figure 1: The arrangement of the fibers at the apex region in the TE (red) and NT (green) models. From the image It is visible the fibers congregation at the apex of the TE model versus the continuation of the fibers from the endocardium to the epicardium in the NT model
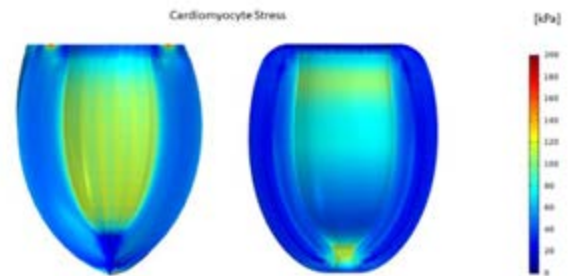
Figure 2: The results of the simulation on the TE (on the left) and NT (on the right) models of the LV. CM stress distribution has been plotted at the end-systolic stage.

Discussion

In this study, we introduced a new approach for modeling the LV fibrous and the influence of the CM's arrangement on the LV regional wall stress distribution and global deformation in diastole and systole. According to the results, in the NT model of the left ventricle CM stresses are distributed more homogeneously. Further studies are necessary to assess the influence of the geodesics and tori's characteristics on the ventricular mechanics.

References

1. Streeter et al, Circulation Research, DOI: 10.1161/01.RES.24.3.339.
2. Jouk and Usson, JCDD, DOI: 10.3390/jcdd8120179.
3. Ahmad Bakir et al, Front. Physiol., DOI: 10.3389/fphys.2018.01259.
4. Mourad, Journal of Geometry and Symmetry in Physics, DOI: 10.7546/jgsp-16-2009-23-37
5. Streeter D., Gross Morphology and Fiber Geometry of the Heart, In: Handbook of Physiology 1979 pp 61-112

4D FLOW MRI & NETWORK-BASED ANALYSIS OF THE HEMODYNAMIC CORRELATION PERSISTENCE LENGTH IN THE HEALTHY AORTA

Karol Calò (1), Andrea Guala (2), Diego Gallo (1), Jose Rodriguez Palomares (2), Stefania Scarsoglio (1), Luca Ridolfi (3), Umberto Morbiducci (1)

1. PoliTo^{BIO}Med Lab, Department of Mechanical and Aerospace Engineering, Politecnico di Torino, Italy;
2. Department of Cardiology, Vall d'Hebron Institut de Recerca, Spain; 3. PoliTo^{BIO}Med Lab, Department of Environment, Land and Infrastructure Engineering, Politecnico di Torino, Italy

Introduction

The approaches currently adopted to characterize the large-scale aortic flow structures are mainly based on integral quantities. Thus, they do not fully capture the complexity of the aortic hemodynamics. To contribute to close this gap, this study proposes a novel network-based approach [1] to characterize the spatiotemporal aortic flow coherence in a 4D flow MRI dataset of healthy human aortas. The correlation between the subject-specific inflow rate $Q(t)$ waveform and the axial velocity waveforms obtained from *in vivo* velocity data at each voxel was used to build a *"one-to-all"* network [2]. The anatomical length of persistence of this correlation was then quantified using an ad-hoc network metric to explore its association with the flow rate waveform cycle-average value and dynamics.

Methods

The study population comprises 41 healthy volunteers. The 4D flow MRI acquisition protocol is described in [3]. For each subject, the thoracic aorta lumen was reconstructed. The inflow rate $Q(t)$ waveform at the sinotubular junction (STJ) section and the axial velocity component $V_{ax}(t)$ waveform in each voxel of the aortic fluid domain were extracted from the measured phase velocity data (**Fig.1**). To study the effect of the subject-specific $Q(t)$ waveform's shape on the large-scale aortic flow, a *"one-to-all"* network was built for each subject. The network nodes are represented by the center of mass of the STJ section (where $Q(t)$ is measured) and by all the voxels of the aortic domain. The link between the STJ node and each voxel i was weighted by the Pearson correlation coefficient R_i^Q between $Q(t)$ and $V_{ax}(t)$ at that voxel. To quantify the length of persistence of the $Q(t)$ *vs.* $V_{ax}(t)$ correlation, the curvilinear distance s_{i-STJ} between the STJ node and each voxel i was calculated along the centerline, weighted by the R_i^Q value and averaged over all the N voxels, obtaining the ad-hoc network metric *Averaged Weighted Curvilinear Distance AWCD* [2] (**Fig. 1**). To account for geometric intervariability, *AWCD* was normalized to the curvilinear length l of the aorta.

Results

The R_i^Q volumetric maps (only values above the median value $\widehat{R^Q} = 0.69$ of the combined distribution of all subjects are visualized), together with *AWCD* values are presented in **Fig. 1** (lower panel) for three explanatory cases. In subject A, the dynamical similarity between

axial flow and inflow rate waveforms only persists for 13% of the aorta full length; in subject B, the anatomical persistence length of the correlation extends to the entire ascending aorta; in subject C, it extends to 39% of the entire aortic length. Notably, *AWCD* was positively associated with the cycle-average flow rate $\bar{Q}$ (R=0.66, $p<0.001$), as well as with $Q(t)$ peak-to-peak amplitude Q_{p-p} (R=0.42, $p<0.01$). Significant differences ($p<0.05$) emerged in *AWCD* values when the 41 subjects were stratified in three groups based on $\bar{Q}$ or Q_{p-p} tertiles (Q_{p-p}: box plot in **Fig.1**).
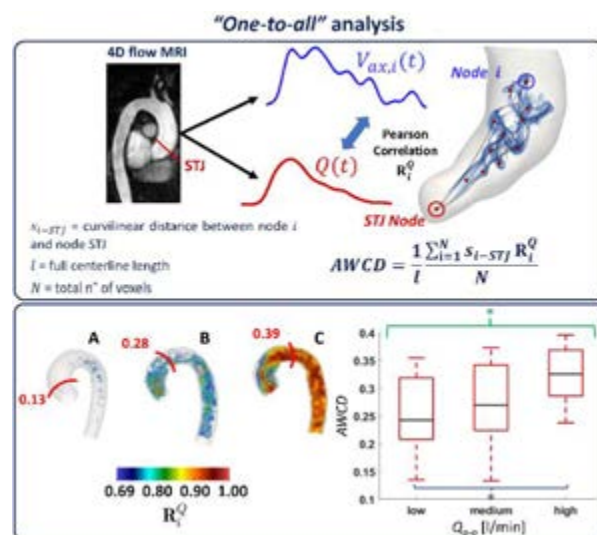
*Figure 1: Overview of methods and results. Lower panel: R_i^Q volumetric maps with AWCD (red line); box plots of AWCD stratified by Q_{p-p}. * p<0.05.*

Discussion

The applied network approach allows to quantify *in vivo* the physiological anatomical length over which the inflow rate waveform markedly shapes the large-scale flow in aorta. Such correlation persistence length is positively correlated with the flow rate waveform cycle-average value and dynamics. In the future, the *AWCD* could be applied to not invasively measure the impact of aortic pathologies or surgical interventions on the spatiotemporal aortic flow coherence.

References

1. Calò et al., Ann Biomed Eng, 49:2441-53, 2021.
2. Calò et al., IEEE Trans Biomed Eng, 67:1841-53, 2020.
3. Dux-Santoy et al., Eur Heart J-Cardiovasc Imaging, 34:1-11, 2019.

PREDICTION OF ANALOG THROMBI MECHANICAL PROPERTIES, COMPOSITION, AND CONTRACTION USING CT IMAGING

Janneke M.H. Cruts (1), Jo-Anne Giezen (2), Kim van Gaalen (1), Robert Beurskens (1), Yanto Ridwan (1), Marcel L. Dijkshoorn (1), Heleen M.M. van Beusekom (1), Nikki Boodt (1), Aad van der Lugt (1), Frank Gijsen (1,2), Rachel Cahalane (1)

1. Erasmus Medical Center, the Netherlands; 2. Delft University of Technology, the Netherlands

Introduction

Endovascular thrombectomy is now the standard of care for patients with acute ischemic stroke (AIS), but is still not effective in 41% of the patients [1]. It has been postulated that the thrombus composition and platelet-driven thrombus contraction affect the mechanical properties of thrombi, which in turn influence the interaction with the thrombectomy device [2]. A pre-interventional estimation of the mechanical properties is hypothesized to aid in selecting the most suitable treatment on a case-by-case basis to improve success rates. Computed Tomography (CT) imaging is the most commonly used imaging modality for diagnosis of AIS and could therefore potentially be useful in predicting the mechanical properties, composition, and contraction of cerebral thrombi.

Methods

Thrombus analogs were made from drawn blood of four healthy donors with five different volumetric red blood cell (RBC) ratios: 0%, 20%, 40%, 60% and 80%. To assess the degree of thrombus contraction, the weight of each thrombus was measured and expressed as a percentage of the weight of the original clotting mixture. The composition of the thrombi was analysed using histology with Hemotoxylin and Eosin stain. To determine the mechanical properties, unconfined compression tests were performed. As a measure for the stiffness, the high strain (approximately final 2%) secant moduli were measured from the non-linear stress-strain curves. The analogs were subjected to clinical CT imaging to measure the thrombus density on non-contrast CT (NCCT) scans. Perviousness, which reflects the permeability of a thrombus, was quantified by measuring the thrombus CT density increase 20 minutes after the administration of a contrast agent.

Results

A strong relationship was found between the degree of contraction and the initial volumetric RBC ratio of the clotting mixture (Fig. 1A). Histological analysis showed that the initial volumetric RBC ratios of 0%, 20%, 40%, 60% and 80% produced thrombi with non-equivalent compositions of 0%, 91%, 94%, 95%, and 98% RBCs, respectively (Fig. 1B). This indicates that only 0% RBC and RBC-rich thrombi (>90% RBC) were produced. The mechanical tests showed that the high strain stiffness decreased with increasing initial volumetric RBC ratio of the clotting mixture (Fig. 1C),

and was associated with the degree of contraction. The NCCT density and the density increase of the 0% RBC thrombi were found to be significantly lower and higher, respectively, compared to the RBC-rich thrombi (Fig. 1D).
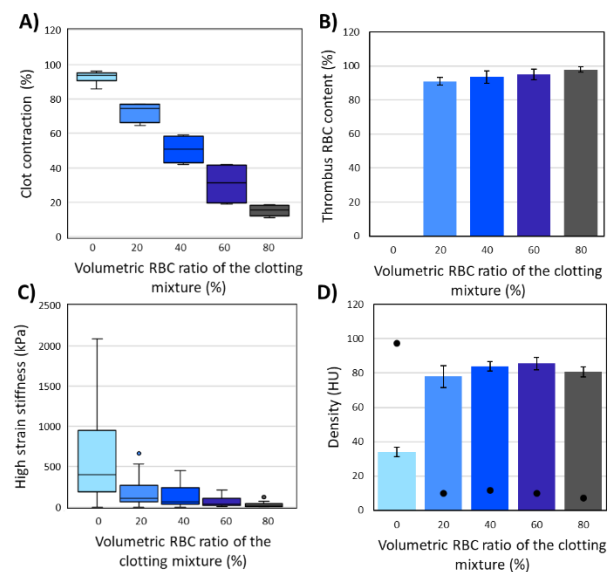
Figure 1: Volumetric RBC ratio of the clotting mixture vs. (A) degree of contraction (B) thrombus RBC content, (C) high strain stiffness, and (D) mean thrombus density on NCCT baseline scans (bars) and 20 minutes after contrast administration (dots).

Discussion

We showed that thrombus mechanics is related to the degree of contraction, as they both decrease with increasing volumetric RBC ratio of the clotting mixture (Fig. 1A and C). However, mechanics was not (strongly) related to the imaging characteristics that were explored in this study. Instead, the imaging characteristics were associated with the thrombus RBC content, as similar patterns were observed for the thrombus RBC content and the CT density (Fig. 1B and D). Future experiments will focus on creating clots with intermediate RBC content and different levels of contraction.

References

1. I. Jansen et al, BMJ, 360:k949, 2018.
2. S. Johnson et al, J Neurointerv Surg, 12(9):853-857, 2020.

UNIVERSAL LEFT ATRIAL APPENDAGE COORDINATES TO COMPARE AND CLASSIFY PHENOTYPIC FLOW PATTERNS

Jorge Dueñas-Pamplona (1), Alejandro Gonzalo (2), Savannah F. Bifulco (3), Patrick M. Boyle (3), Elliot McVeigh (4), Andrew M. Kahn (4), Pablo Martínez-Legazpi (5), Javier García García (1), José Sierra-Pallares (6), Manuel García-Villalba (7), Óscar Flores (7), Javier Bermejo (8), Juan C. del Álamo (2)

1. Departamento de Ingeniería Energética, Universidad Politécnica de Madrid, Madrid, 28006, Spain;
2. Mechanical Engineering Dept., University of Washington, WA 98195, US;
3. Bioengineering Dept., University of Washington, WA 98195, US
4. Division of Cardiovascular Sciences, University of California San Diego, La Jolla, CA 92093, US
5. Departamento de Física y Matemática de Fluidos, UNED, Madrid, Spain
6. Dept de Ingeniería Energética y Fluidomecánica, Universidad de Valladolid, Valladolid, Spain
7. Dept de Ingeniería Aeroespacial y Bioingeniería, Universidad Carlos III de Madrid, Leganés, Spain
8. Hospital General Universitario Gregorio Marañón, Madrid, Spain

Introduction

Atrial fibrillation (AF) is the most common cardiac arrythmia. During AF, the atrium beats weakly and irregularly, causing an increased risk of thrombus formation. These thrombi can travel to the brain causing stroke. Although the left atrial appendage (LAA) is the most frequent site of intra-cardiac thrombosis, the mechanical nexus between the LA/LAA anatomy, flow patterns, and thrombosis risk are elusive. This is in part due to the complexity and variability of the LA geometry, which makes it difficult to compare results between different patients and cardiac conditions.

We propose a new framework to compare hemodynamic variables in the LAA across different patients. Our approach uses Principal Component Analysis (PCA) to reduce the flow dimensionality, identify distinct flow patterns associated with different phenotypes, and classify patients based on their flow patterns [1]. To facilitate this process, we map the LAA surface onto a unified coordinate system (universal left atrial appendage coordinates, or ULAAC), which is an extension of the Universal Atrial Coordinate (UAC) system developed by Roney et al. [2]. To illustrate this approach, we apply it to patient-specific computational fluids dynamics (CFD) flow data from two groups of patients with and without LAA thrombosis, obtaining the hemodynamic signature of clot formation.

Methods

The LAA walls of six patients (three of them with LAA thrombosis) [3] were mapped into the unit square using the ULAAC system. The flow data come from CFD simulations in time-resolved patient-specific anatomies obtained by 4D-CT [2]. The ULAAC transformation uses two coordinates that are determined by solving the Laplace equation. Boundary conditions were assigned using the ostium and the LAA tip as landmarks for the first coordinate, and the superior and inferior LAA paths for the second coordinate.

Hemodynamic variables such as wall residence time expressed in the ULAAC (Figure 1) were fed to a machine learning algorithm based on PCA [1] to identify specific patterns associated with clot formation within the LAA.
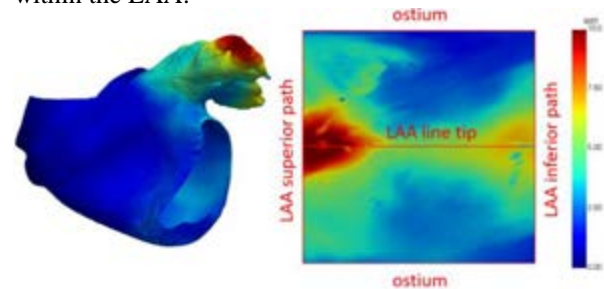
Figure 1: *Residence time mapped to the unit square employing the ULAAC coordinates after solving Laplace equations for the LAA surface.*

Conclusion

We present a new universal LAA coordinate system (ULAAC) to compare and classify phenotypic hemodynamic signatures across patient cohorts. The ULAAC system provided us with a framework to identify patterns related with normal and impaired atrial function, illustrating some features associated with thrombi formation.

References

1. M. G. Borja et al, *APS Division of Fluid Dynamics Meeting Abstracts (pp. W07-018)*.
2. C. H. Roney et al, *Med. Image Anal.*, 55:65-75, 2019.
3. M. García-Villalba et al, *Fron. Physiol.*, 12:596596, 2021.

Acknowledgements

CALIBRATION OF THE MECHANICAL BOUNDARY CONDITIONS OF A THORACIC AORTA MODEL INCLUDING THE HEART MOTION EFFECT

Leonardo Geronzi (1,2), Antonio Martinez (1,2), Marco Evangelos Biancolini (1), Michel Rochette (2), Olivier Bouchot (3), Alain Lalande (3), Pier Paolo Valentini (1)

1. Univ. Rome "Tor Vergata", Rome, Italy; 2. Ansys Lyon, France; 3. Univ. Burgundy & CHU Dijon, France

Introduction

In the study of aortic aneurysm and dissection, the inclusion of the heart motion effect in the thoracic aorta (TA) simulation is of crucial importance. So far, few studies consider the soft tissue (ST) surrounding the aorta and the anatomical and functional relationship between the aorta and the spine. This work shows a procedure (*Figure 1*) to calibrate the TA mechanical boundary conditions (BCs), including the effect due to the heartbeat, using Model Order Reduction techniques.

Methods

A 4D-Flow MRI dataset (25 phases per cardiac cycle) with spatial resolution of 2 x 2 x 2 mm^3 of a 71-year-old man is selected. 5 cardiac phases φ are segmented, and the end-diastolic frame is used to obtain a starting shell mesh of the vessel wall. To reproduce the interaction of the TA with the vertebrae and the surrounding ST, each node i is connected to a damper (damping coefficient c = 1 Ns/m) and three springs, each for a J-direction of the 3D space. The stiffness K of each spring is calculated as:

$$K_{J_i} = K_{ST} + W_{d_i} W_J K_{SPINE} \qquad (1)$$

with K_{ST} in the range [0.8; 1.2] N/m, the weights W_J in the range [0.5; 1.5], $K_{SPINE} = 100$ N/m [1] and:

$$W_{d_i} = 1 - \alpha \frac{d_i}{d_{MAX}} \qquad (2)$$

where $\alpha = 0.95$, **d** is the vector containing the Euclidean distance of each TA node from the spine and d_{MAX} the maximum distance. An optimal space filling method is used to combine the 4 parameters to be optimized and get 81 Design Points. To reproduce the fluid-dynamic BCs, a patient-specific 0-D closed loop [2] is used. Imposing these, 3 cardiac cycles are run in *ANSYS Fluent* to evaluate the aortic wall pressure (WP). On the mechanical side, the wall thickness is set to 2 mm and a 3-parameters Mooney–Rivlin model is adopted. Through an iterative method [3] and using the diastolic WP as load, the stress-free model is obtained. By means of cine-MRI acquired in apnea in axial and oblique sagittal orientations, the aortic annulus motion is tracked and its displacement detected. A Multi-Point Constraints BC is used to apply the rigid motion to the nodes connected to the inlet. The whole WP field is then applied to the inner wall and the full set of transient structural simulations is run using *LS-DYNA* (ANSYS). For each phase, a deformed aorta is stored and used to build the Reduced Order Model (ROM). By changing the input parameters (W_J and K_{ST}), the ROM is able to return a new deformed configuration. The patient-specific coefficients are obtained through a Least Square Method minimizing the following function:

$$f(K_{ST}, W_x, W_y, W_z) = \sum_{t=1}^{\varphi-1} \sqrt{\frac{1}{n}\sum_{i=1}^{n} d_{t_i}^2(K_{ST}, W_x, W_y, W_z)} \qquad (3)$$

where n is the number of nodes and d_{t_i} is the smallest Euclidean distance between each node i and the vertices of the segmented models.
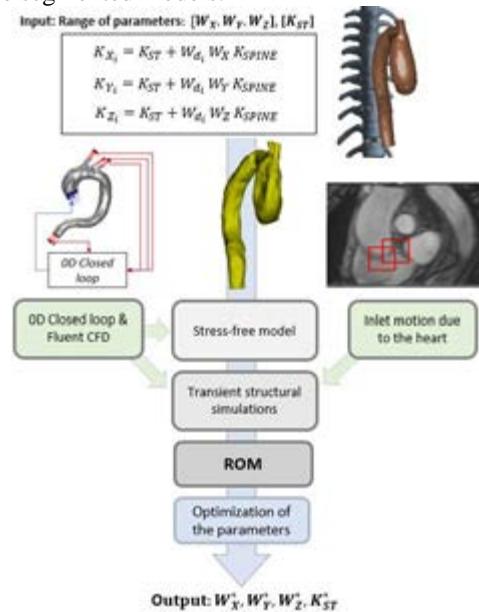
Figure 1: Overview of the calibration procedure.

Results and Discussion

After the optimization, the TA deformation and displacement due to blood pressure and heart motion are obtained. The ROM and Reduction maximum absolute errors respectively are 0.2 mm and 0.4 mm. The maximum Hausdorff distance between the simulated model and TA segmentations is 1.8 mm; it is detected in the region of the Valsalva sinuses. As next steps, this procedure will be extended to more patients and a full fluid-structure interaction simulation will be performed.

References

1. Moireau et al, Biomech Model Mechanob, 11,1 1-18, 2012.
2. Tomasi et al, Med hypotheses, 135, 109477, 2020.
3. Rausch et al, J Biomech, 58:227-231, 2017.

Acknowledgements

DECIPHERING VORTICITY IN THE ABDOMINAL AORTIC ANEURYSM

Valentina Mazzi (1), Karol Calò (1), Diego Gallo (1), Angelo Iollo (2,3), Umberto Morbiducci (1)

1. Polito^{BIO}Med Lab, Department of Mechanical and Aerospace Engineering, Politecnico di Torino, Italy; 2. IMB, UMR 5251, Université de Bordeaux, Talence, France; 3 Inria - Bordeaux Sud-Ouest, Talence, France

Introduction

Abdominal Aortic Aneurysm (AAA) is a vascular disease characterized by a localized enlargement of the abdominal aortic lumen. It has been highlighted that local blood flow disturbances may contribute to disease progression [1]. Therefore, the characterization of the local hemodynamics within AAAs is essential to better understand the risk associated with aneurysm progression. In this context, a variety of hemodynamic descriptors have been proposed to visualize and quantify flow disturbances. However, these measures often fail in describing the structure that hides behind the flow field. Here, we propose a quantitative analysis of the complex vortical structures produced/transported in the AAA based on the terms of the vorticity transport equation, applied to patient-specific computational hemodynamics models of AAA, offering a different perspective to decipher the AAA flow complexity.

Methods

A dataset of 20 CT-based models of AAA was here considered. Image segmentation and 3D model reconstruction was carried out using the software PRAEVAorta (https://www.nurea-soft.com) [2]. Transient CFD simulations were performed using the finite element-based open-source code SimVascular [3] to solve the governing equations of fluid motion. The AAA resolved flow fields were used to calculate the terms of the vorticity transport equation:

$$\partial\boldsymbol{\omega}/\partial t + (\boldsymbol{u} \cdot \nabla)\,\boldsymbol{\omega} = (\boldsymbol{\omega} \cdot \nabla)\,\boldsymbol{u} + \nu\Delta\boldsymbol{\omega} \tag{1}$$

where $\boldsymbol{u}$ is the velocity, $\boldsymbol{\omega}$ is the vorticity and ν is the kinematic viscosity. The first two terms on the left side of eq. (1) are the vorticity acceleration and advection term, quantifying the rate of change of vorticity due to unsteadiness and convection, respectively, while the two terms on the right side are the stretching term, describing the vortex lengthening due to velocity gradients (vorticity production), and the term quantifying vorticity diffusion due to viscosity.

Results

Instantaneous volumetric maps of the single terms of the vorticity transport equation are presented in Figure 1 for two representative AAA models (AAAI, presenting a marked expansion, and AAAII, where intraluminal thrombus formation has led to a quasi-physiological blood canalization). The time-histories of the volume-average value of the vorticity transport equation terms are also presented. The analysis clearly shows differences in vorticity production, stretching and dissipation between the models ($\frac{\overline{\partial\omega/\partial t}_{AAAI}}{\overline{\partial\omega/\partial t}_{AAAII}} = 1.2$, $\frac{\overline{(u \cdot \nabla)\,\omega}_{AAAI}}{\overline{(u \cdot \nabla)\,\omega}_{AAAII}} = 1.9$, $\frac{\overline{(\omega \cdot \nabla)\,u}_{AAAI}}{\overline{(\omega \cdot \nabla)\,u}_{AAAII}} = 1.7$, $\frac{\overline{\nu\Delta\omega}_{AAAI}}{\overline{\nu\Delta\omega}_{AAAII}} = 1.02$).

In detail, AAAI presents a flow pattern at the sac inflow that rolls up into a large vortex ring when it enters the expansion region. This vortex ring undergoes a marked stretching and splitting and dissipates in the proximal part of AAA sac leading to a strong stirring/mixing during diastole. Contrarily, in AAAII vorticity is mostly produced in the near-wall region due to viscosity and velocity gradients and diffused out into the flow.
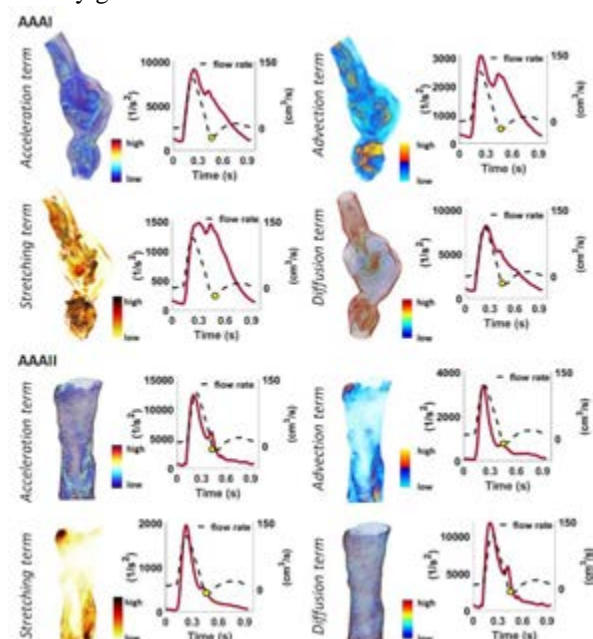
Figure 1: Instantaneous (yellow dot in the flow rate waveform) volumetric maps and time-histories of volume-average values of the vorticity equation terms (red line) in two representative AAA models.

Discussion

Here the vorticity transport equation is applied to decipher the complex hemodynamics in AAA models, interpreting the contribution of each single term of eq. (1) in light of its physical meaning. The presented approach might contribute to a deeper understanding of the hemodynamics-driven processes underlying AAA progression, providing a quantitative tool to link identifiable and quantifiable vorticity features involved in e.g., biochemical transport and fluid-wall interaction to aggravating biological events.

References

1. Arzani, A. et al., Phys Fluids, 24, 2012.
2. Caradu, C. et al, J Vasc Surg, 74(1):246-256, 2021.
3. Updegrove et al, Ann. Biomed Eng, 45(3):525-541, 2016.

PATIENT-SPECIFIC FLOW SIMULATIONS OF A DISSECTED AORTA INFORMED BY 4D FLOW MRI: THE IMPACT OF SEGMENTAL ARTERIES

Catriona Stokes (1), Fabian Haupt (2), Daniel Becker (3), Vivek Muthurangu (4), Hendrik von Tengg-Kobligk (2), Stavroula Balabani (1), Vanessa Diaz-Zuccarini (1)

1. Department of Mechanical Engineering, University College London, United Kingdom; 2. Department of Diagnostic, Interventional and Pediatric Radiology, Inselspital, University of Bern, Switzerland 3. Clinic of Vascular Surgery, Inselspital, University of Bern, Switzerland 4. Centre for Translational Cardiovascular Imaging, University College London, United Kingdom

Introduction

Segmental arteries, including the intercostal, subcostal and lumbar arteries, branch from the posterior descending aorta. Although small, 4D Flow MRI data indicates that they accept 5-10% of the descending aortic flow (1). These branches are almost always neglected in aortic flow simulations. Previous studies have used idealized geometries to assess flow dynamics near the segmental bifurcations (2) and in rabbit aortae (3). Some Fluid-Structure Interaction studies use intercostals structurally to tether the aorta in place, but the haemodynamic impact of these branches has not been studied in a patient-specific human aorta.

Haemodynamic metrics have been linked to the development and progression of aortic diseases. For example, false lumen (FL) pressure has been linked with FL growth in Aortic Dissection (AD). Without patient-specific human studies of the impact of the segmental arteries, it is not yet understood whether the inclusion of these branches and their associated flow loss will affect these metrics. This understanding will be critical if simulations are to be used in a clinical context.

This work demonstrates the very first *in silico* assessment of a patient-specific human aorta with all pairs of segmental arteries, along with patient-specific inlet and outlet boundary conditions informed by 4D Flow MRI (4DMR). It is also the first study of this kind in an AD patient.

Methods

After manually segmenting CT images from a 56yo male patient with chronic Type-B AD, we extracted the centrelines and bifurcation points of all segmental arteries and used these to reconstruct all branches with a 1.5 mm diameter (4). We registered this domain to the 4D Flow MRI domain and produced an identical segmentation without segmental arteries.

We extracted a three-dimensional, three-component inlet velocity profile from 4DMR and dynamically mapped this to the static CFD inlet. Using 4DMR data, we calibrated three-element Windkessel outlet boundary conditions independently for both segmentations at each major aortic branch using a previously developed method (1). Constant diastolic pressure outlet conditions were used at the distal end of each segmental artery. Transient, rigid-wall simulations were performed in ANSYS CFX and results were validated by comparing CFD velocity data with 4DMR.

Results

The use of constant diastolic pressure outlets at the segmental arteries resulted in a 7% total flow loss along the descending aorta, in line with previously measured values (1). As a result of this flow loss, inclusion of the segmental branches reduced false lumen (FL) pressure by 1.5 mmHg, as observed in Fig. 1A.

The inclusion of segmental arteries led to elevations of instantaneous WSS in regions surrounding each bifurcation. Due to the loss of flow, WSS was also reduced in the abdominal aortic branches when the segmental arteries were included, as indicated in Fig. 1B.
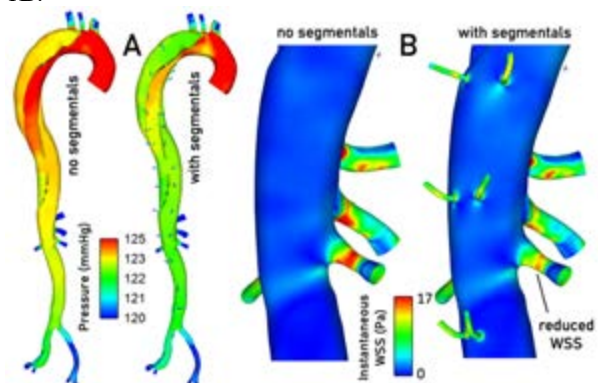
Figure 1: Instantaneous contours of pressure (A) and wall shear stress (B) during systole in simulations with and without intercostal branches, as indicated.

Discussion

This work represents the first patient-specific simulation of a human aorta with all segmental arteries and is the first study of its kind in an AD patient. Our results demonstrate notable differences in pressure and wall shear stress distributions when the segmental branches are included, which may impact the clinical conclusions made from simulations. As such, these effects should be considered in future haemodynamic studies of the aorta, particularly in AD patients where metrics such as FL pressure are of utmost clinical importance.

References

1. *Stokes et. al., J. Biomech (2021) Vol. 129; 110793*
2. *Kazakidi et. al., J. R. Soc. Interface (2011) 8, 1594–1603*
3. *McElroy et. al., J Engineering in Medicine (2018) Vol. 232 (2) 103–113*
4. *Jacques et. al., Ann Thorac Surg (1993) 56:1078-81*

ARTIFICIAL NEURAL NETWORK FOR PREDICTION OF MECHANICAL PROPERTIES OF ATHEROMA PLAQUE

Ricardo Caballero(1), Miguel Ángel Martínez(1,2), Estefanía Peña(1,2)

1. Aragón Institute of Engineering Research (I3A). University of Zaragoza, Spain; 2. Biomedical Research Networking Center in Bioengineering, Biomaterials and Nanomedicine (CIBER-BNN), Spain

Introduction

Nowadays, cardiovascular diseases have become the first cause of death around the world and, in particular, atherosclerosis affects 50% of cardiopathic patients [1]. Therefore, having a quick and reliable diagnostic is crucial in order to mitigate the effects of this pathology. Different approaches to detect the vulnerability of a plaque have been explored, such as virtual histology [2] and iMOD elastography [3], but all of them are characterized by a too high waiting time, incompatible with nowadays hospital day care examinations. For this reason, an accurate and quick estimation of the mechanical properties of patient-specific atheroma plaques, starting from image-based techniques, may help treating and preventing the disease.

Materials and Methods

For the purpose of this study, an Artificial Neural Network (ANN) has been developed to perform accurate estimations of Young's moduli of the necrotic core (E_{core}) and the plaque (E_{plaque}). First, a large database has been built, starting from nine idealized 2D geometries of coronary artery with atheroma plaque, characterized by different stenosis ratio (SR), ranging from 40% to 80%. All models were developed in ABAQUS (version 6.14, Dassault Systems Simulia Corp., Providence, RI, USA).

As inputs of the ANN the candidate variables were: maximum principal strain (ε_1), minimum principal strain (ε_2), core thickness strain (ε_{core}), fibrous cap thickness strain (ε_{cap}), variation of lumen diameter (ε_{theta}) and SR. A Neo-Hookean incompressible model has been assumed for the material characterization.

Given that the ANNs' predictive capacity is mainly based on statistics, a sensitive analysis of candidate variables was performed. The resulting database was pre-processed and given as the input of the ANN. Then, the structure of the ANN was explored using the try-and-error methodology. Once the hyperparameters of the ANN were determined, the ANN was validated with data from real IVUS [4].

Results

The analysis showed that the relationship between the candidate variables and the response was nonlinear, following a quadratic pattern. Moreover, by analyzing the most influential variables in the prediction of Young's moduli of the necrotic core and plaque, it has been determined that the model made of SR (%), $\varepsilon_{core-cuad}$, and $\varepsilon_{cap-cuad}$ was able to predict the goal variables with an accuracy of 92.8% and 97.67%, respectively. After a comprehensive examination of multiple configurations of hyperparameters, a competitive configuration was obtained. The main characteristics of the ANN were the number of layers (eight), the activation function (softplus) and the batch size (eight elements). The error in the prediction of Young's moduli performed with this ANN can be seen in figure 1.
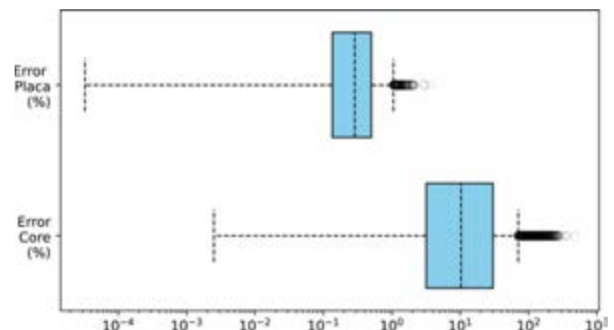
Figure 1: Error (%) obtained in prediction of necrotic core and plaque Young's moduli

Discussion

The nonlinearity observed during the statistical analysis concluded that it was advisable to use second-order input variables. Moreover, multiple regression analyses showed that the most influential variables in the output variables were SR (%), $\varepsilon_{core-cuad}$ and $\varepsilon_{cap-cuad}$. Due to the high variability of Young's moduli found in literature, obtaining accurate predictions became a challenging task. Therefore, the database created in this study is a good proposal to face such variability and observing the results, it can be considered enough to be treated as input of an ANN.

References

1. Roth G. et al., The lancet, 392 (10159): 1736 – 1788, 2018
2. Thim T., Danish Medical Bulletin, 57(7):B4161, 2010
3. Tacheau A, et al., Ultrasound in Medicine and Biology, 42(3): 727-741, 2016
4. Le Floc'h et al., IEEE Transactions on Medical Imaging, 28(7):1126-1137, 2009

Acknowledgements

PULSE WAVE VELOCITY AS A GUIDE TO REDUCE THE MATERIAL PARAMETERSPACE IN ARTERIAL COMPUTATIONAL BIOMECHANICS

Lise Gheysen (1), Lauranne Maes (2), Nele Famaey (2), Patrick Segers (1)

1. Ibitech-Biommeda, Ghent University, Belgium; 2. Biomechanics section, KU Leuven, Belgium

Introduction

Computational arterial biomechanics models most often rely on an extended parameter set to describe the constitutive behavior of the arterial wall using, e.g. the commonly used Gasser-Ogden-Holzapfel (GOH) formulation [1]. Parameters are typically derived from ex-vivo tissue experiments and fitting the model to mechanical tests on tissue samples, which yields ranges for individual parameters. When setting up models for patient-specific simulations from clinical data, however, it is not trivial to choose parameter sets that adequately lead to the desired mechanical behavior of the arterial wall. Therefore, this study investigates whether Pulse Wave Velocity (PWV), a widely available and easily measurable parameter that reflects functional stiffness at diastolic pressure, can be used as a guide to narrow down the material parameter space in computational arterial biomechanics.

Methods

Based on a literature study, physiological parameter ranges were selected and discretized in 5 levels for each GOH parameter (c_{10} = 0.005-0.025 MPa , k_1 = 0.0002-1.0 MPa, k_2 = 4.0-35.0, α = 0-90°, κ = 0-1/3). The levels were equally spaced within the range, except for k_1 and k_2 where a logarithmic step size was applied in order to represent all orders of magnitude for these parameters. For all parameter combinations, PWV was calculated using the Bramwell-Hill equation for a (pre-stretched) reference tube that represents the aortic wall, including a medial and adventitial layer, at a physiological diastolic pressure of 80 mmHg. For the 78125 parameter combinations, it was analyzed which combinations lead to predefined target PWV values, over the physiological range of 4 to 12 m/s (with steps of 1 m/s and a tolerance of 5%). The relation between PWV and the pair-wise combinations of GOH parameters was considered as well.

Results

From all 78125 parameter combinations, 10724 resulted in a PWV between 4 and 12 m/s ($\pm$ 5%). The number of combinations that lead to a PWV within a tolerance of 5% from the target PWV ranged from 1.15 to 13.9% of the total number of combinations in the PWV range, as shown in figure 1. Most of the pair-wise combination plots indicated a narrowed parameter space for higher PWV values, as e.g. illustrated in figure 2 for the parameter combination k_1 - κ_M and for PWV values of 5 to 11 m/s.
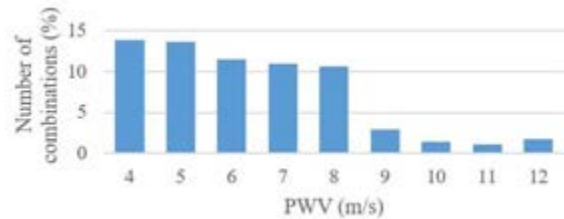
Figure 1: Number of combinations with a PWV that deviates < 5% from the target, relative to the number of combinations with a PWV of 4-12 m/s ($\pm$ 5%).
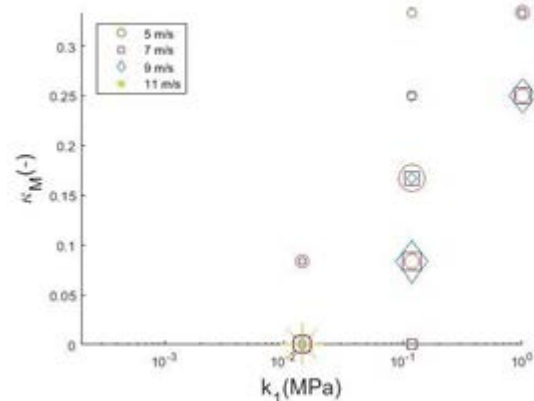
Figure 2: Combination plot of material parameters κ_M and k_1 for PWV from 5 to 11 m/s, with a marker size proportional to the frequency of appearance.

Discussion

Many parameter combinations corresponded to the target PWV, with the number of combinations decreasing for an increasing target PWV and with a remarkable drop at 8-9 m/s. This might indicate that PWV is able to strongly reduce the number of parameter combinations for larger PWV, although the logarithmic step size used for material parameters k_1 and k_2 could play an important role too. These preliminary results suggest that PWV can provide guidance in the parameter selection process when developing a computational arterial model, in particular for stiffer arteries. However, the relation between the limited number of material combinations with a PWV close to the target PWV and the narrowed parameter space needs to be further elucidated.

References

1. Gasser T. C. et al, in J. R. Soc. Interface, 3:15-35, 2006.

Acknowledgements

COMPUTATIONAL MODELLING OF THE EFFECT OF INFARCT STIFFENING ON LOCAL MYOFIBER MECHANICS

Koen Janssens, Maaike Kraamer, Peter Bovendeerd

Eindhoven University of Technology, The Netherlands

Introduction

Adverse ventricular remodelling following acute myocardial infarction (MI) may induce ventricular dilation, fibrosis and loss of global contractile function, possibly resulting in heart failure (HF). Large collagen fibres deposited in infarcted myocardial tissue during the healing process are a primary determinant of its mechanical properties and play an important role in the depression of pump function. [1] Understanding the relation between the time-dependent changes of these properties and the contractile function of the heart may further our understanding in the development of HF post-MI and subsequently the development of novel therapies.

In this abstract, we employ computational models of MI in order to analyse the relation between infarct stiffening and cardiac function on both a global and local scale.

Methods

We extend a previously presented finite-element model of acute MI from [2] by locally increasing material stiffness. An ellipsoidal thick-walled geometry was assumed in favour of patient-specific geometry to exclude any geometric effects. Subsequently, a region of infarcted tissue was defined based on experimental data of four mongrel dogs after occlusion of the left-anterior descending coronary artery. A border zone was included by means of a linear transition from healthy to infarct tissue over a distance of 0,5cm. The overall size of this region composed 11.2% of the entire LV volume.

Acute infarction was simulated by locally restricting active stress generation within the infarct. Subsequently, passive material properties were multiplied with a factor of 5 and 100 to simulate the effects of infarct stiffening. Both global hemodynamics as well as local stress and strain patterns during the cardiac cycle were analysed in four different locations (Fig 1a) throughout the left ventricle to assess cardiac function.

Results

On a global level, simulations showed the relative loss in pump function exceeded loss in the amount of healthy tissue about two-fold (Fig 1b). In acute MI, the end-diastolic volume remained largely unaffected whilst end-systolic volume increased by 25% compared to the healthy heart. Both volumes were found to decrease proportionally to the degree of infarct stiffening.

Locally, different behaviour was observed in healthy fibres within the border zone in series or parallel arrangement with the infarct region. In acute MI, fibres located in parallel (Fig 1c, AL) were able to produce more stress during contraction but did not shorten as much compared to the healthy case. Fibres in series (Fig 1c, AM) showed an opposite effect, presenting reduced stress generation and higher fibre shortening overall.

With increasing stiffness, stretching of infarct tissue during systole is reduced. This was reflected in a reduction of end-diastolic sarcomere length and stress generation in parallel fibres. Serial fibres show less sarcomere shortening during isovolumetric contraction phase and more stress generation overall.
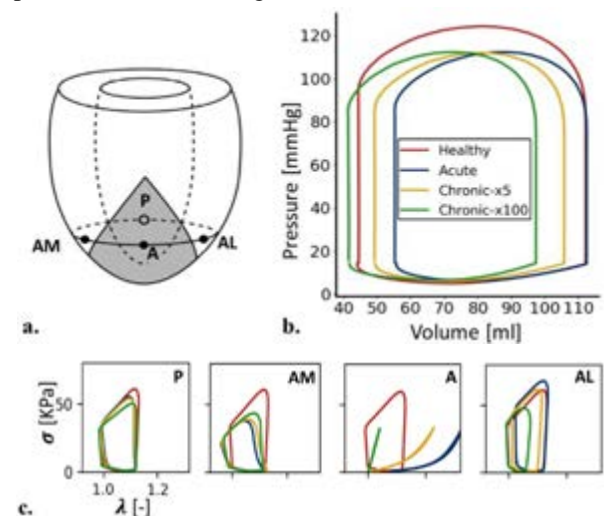
Figure 1a: Ellipsoidal geometry including posterior (P), anterior-medial (AM), anterior (A) and anterior-lateral (AL) sites for analysis of local fiber mechanics. b: Pressure-volume loops for healthy and infarcted heart. c: Cauchy stress vs. fiber stretch over the course of a cardiac cycle in infarcted and normal ventricle.

Discussion

The amount of pump function lost due to MI exceeded the loss in healthy tissue by about two-fold, irrespective of the degree of infarct stiffening. In the case of acute MI this additional loss in work may be attributed to fibres adjacent to the infarct region whose mechanical environment changes and limits their efficiency. In chronic MI, the increased infarct stiffness allows serial fibres to deliver more work due to an improved afterload. In parallel fibres however, this change is reflected in a reduced end-diastolic sarcomere length and subsequently decrease in performed work, resulting in an overall limited change in pump function.

References

1. Clarke et al., J Mol Cell Cardiol., 93:115-24 , 2015.
2. Bovendeerd et al, AM. J of Physiol, 270(1):H398-H410, 1996.

ON THE CFD MODELLING OF HEMODYNAMICS IN UNRUPTURED INTRACRANIAL ANEURYSMS

Pablo Jeken-Rico (1), Aurèle Goetz (1), Ramy Nemer (1), Philippe Meliga (1), Jonathan Viquerat (1), Aurélien Larcher (1), Augusto F. Sanches (2) Yigit Özpeynirci (2), Thomas Liebig (2), Elie Hachem (1)

1. PSL Mines Paris, CFL Research Group at CEMEF, Sophia Antipolis, 06904, France;
2. Institute of Neuroradiology, University Hospital, LMU, Munich, Germany;

Introduction

Intracranial Aneurysms (IAs) are thought to be caused by abnormalities in the Wall-Shear-Stress (WSS) and other related flow indicators in the brain arterial system [1]. To aid the decision-making of neurosurgeons on whether to operate a patient or not, Computational Fluid Dynamics (CFD) simulations could be run on patient-specific vessel geometries to bring empirical evidence on the flow conditions. Some of the modeling assumptions of CFD simulations of IAs are however unclear [2] and require a more precise physiological and numerical assessment. Therefore, the present work will provide an extensive analysis on different fluid modeling assumptions, such as blood rheology, the inflow and outflow boundary conditions, among others.

Methods

The used vasculature geometries stem from angiography images of patients with saccular IAs. The flow profiles have been computed using stabilized finite elements with anisotropic adaptive remeshing for and increased computational efficiency and proper resolution of boundary layers. The simulations have been run on two different scales, to evaluate the influence of boundary conditions. First, a simulation of the brain's arterial network using patient-specific waveforms has been run in order to retrieve the flow distributions. Afterwards, a local simulation of the surroundings of the aneurysm has been executed to extract detailed flow profiles at the region of interest. Using both scales, a detailed comparison has been made to determine the modeling effects and the influence of numerical tools.

Results

The first results show that the use of a variational multi scale stabilization method [3] that considers both fine and coarse scales of the velocity field is well suited to handle complex blood flow simulations. Moreover, the compatibility of several blood rheology models is straightforward using this type of finite element resolution. The two steps proposed strategy highlights the impact of multiple modeling assumptions such as the boundary conditions, while using the complete network compared to only a selected part of it that contains the dome. Several 3D patient specific test cases are simulated, and their results show on the one hand the flexibility of the approach handling large- and small-scale simulations and on the other hand the impact of considering only an isolated reduced model.

Discussion

The results have been analyzed with a special interest in the pressure, WSS and OSI (Oscillatory Shear Index) distributions both at the aneurysm's dome and neck. To capture all the deterioration indicators, the previously mentioned quantities have been monitored during peak systole and diastole. The obtained results provide information about varying viscosity models and the impact of fixed boundary conditions. Other factors, such as the influence of elastic vessels or the influence of turbulence have been neglected. A full study should be conducted including these factors to draw more generalizable conclusions. The patient-specific waveforms are a subject of debate since their measurement is conducted under circumstances that can alter the vital constants from their normal state.

References

1. H. Meng et al. "High WSS or Low WSS? Complex interactions of hemodynamics with intracranial aneurysm initiation, growth, and rupture: Toward a unifying hypothesis". American Journal of Neuroradiology 35, 1254–1262, 2014.

2. P. Berg et al. "A review on the reliability of hemodynamic modeling in intracranial aneurysms: Why computational fluid dynamics alone cannot solve the equation". Neurosurgical Focus 47.1, 2019.

3. P. Meliga and E. Hachem. "Time-accurate calculation and bifurcation analysis of the incompressible flow over a square cavity using variational multiscale modeling". Journal of Computational Physics 376, pp. 952–972, 2019.

SEGMENTATION AND MECHANICAL CHARACTERIZATION OF ATHEROSCLEROTIC PLAQUES.

Álvaro T. Latorre (1), Miguel A. Martínez (1,2), Myriam Cilla (1,2,3), Jacques Ohayon (4,5), Estefanía Peña (1, 2)

1. Instituto de Investigación en Ingeniería de Aragón (I3A), Universidad de Zaragoza, Spain; 2. CIBER-BBN, Centro de Investigación en Red en Bioingeniería, Spain; 3. Centro de la Defensa (CUD), Spain; 4. Laboratory TIMC-IMAG, CNRS UMR 5525, France; 5. Savoie Mont-Blanc University, France

Introduction

Detection and characterization of the atheroma plaque are vital steps for an early diagnosis of vulnerable patients. In coronary arteries, the most common technology to see the cross section is the Intravascular Ultrasound (IVUS), which also allows to get the estimated strain map of the arterial walls. In this work, we have developed a new methodology to segment the geometry of the plaque and to obtain the mechanical properties of the tissues.

Methods

This process consisted of four different steps: 1st Simulating IVUS data. Three human coronary plaques [1], were used as geometry for the finite element (FE) models. The models had fibrotic tissue, lipid core and a calcification (in third plaque); tissues were modelled as Neo Hookean [1] as shown in *Table 1*. The calcification was considered as isotropic liner elastic (E=5000 kPa). The results corresponding to an increment between 110-115mmHg were analyzed, simulating the acquisition of two consecutive pictures taken by an IVUS [3].

Tissue	C10 [kPa]	D1
Fibrotic Tissue	103.62	0.0001
Lipid Core	1.85	0.0109

Table 1: Parameters for Neo Hook materials.

2nd Segmentation Process. In this step, the modulus of the strain gradient variables (SGVs) like $|\nabla \varepsilon_{rr}|$ or $|\nabla \varepsilon_{vMises}|$ were computed. The representation of one or two SGVs enabled to mark the contour of the different tissues. Then, a Gradient Vector Flow and Watershed techniques were applied getting the lipid core and the fibrotic tissue segmented. 3rd Segmented FE Model. New FE models were built with the segmented parts. The pressure imposed was 5mmHg and materials were modelled as linear elastic. 4th Mechanical Properties Optimization. The linear elastic properties of the tissues were achieved with an optimization process. The Poisson Coefficients were fixed as quasi-incompressible (v=0.49), except for the calcification (v=1/3).

Results

The segmentation process was performed with 105 possible SGVs combinations. The performance was affected by the geometry, however, there were some SGVs with accurate results regardless the geometry like: $|\nabla \varepsilon_{III}|$, $|\nabla \varepsilon_{rr}|$ or $|\nabla \varepsilon_{yy}| + |\nabla \varepsilon_{vMises}|$. This procedure provided important morphological information such as the lipid core area and the fibrous cap thickness (e_{cap}).

Plaque	e_{cap} [μm]		Lipid Area [mm²]	
	Actual	Results	Actual	Results
# 1	247	221	0.81	0.89
# 2	214	200	3.25	3.09
# 3	170	144	1.29	1.30

Table 2: Geometrical features of the simulated IVUS data and the segmented results.

The mechanical optimization obtained the young modulus of each tissue with low errors, 3-13% for the fibrotic tissue and 4-15% for the lipid core. In the calcification, the errors were higher (24%). The simulated IVUS strain map and the results of each geometry are represented in the *Figure 1*.
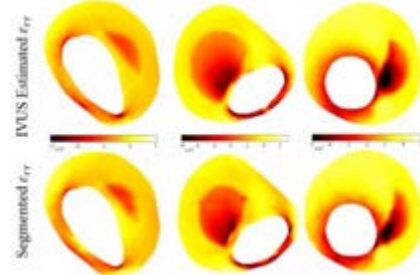
Figure 1: Simulated IVUS ε_{rr} and segmented-optimized results of the first, second and third plaque.

Discussion

A new segmentation technology was presented with good results regardless geometrical features. This process obtained important measures as the lipid area and the fibrous cap thickness. Besides, after an optimization procedure the mechanical properties could be estimated accurately. In the case of the calcification, due to the low strains that produced, was estimated as highly rigid with more error.

References

1. Le Floc'h et al. IEEE Trans Med Imag, 28:1126-37, 2009.
2. Porée J. et al. IEEE Trans Ultrason Ferroelectr Freq Control, 64:1805-17, 2017.

Acknowledgements

FLUID STRUCTURE INTERACTION MODELING OF COMPLIANT AORTIC VALVES USING THE LATTICE BOLTZMANN CFD AND FEM METHODS

Adi Morany (1), Karin Lavon (1), Ricardo Gomez Bardon (2), Brandon Kovarovic (3), Ashraf Hamdan (4), Danny Bluestein (3), Rami Haj-Ali (1,3)

1. School of Mechanical Engineering, Tel Aviv University, Tel Aviv, Israel 2. Dassault Systemes España, SIMULIA XFlow, Madrid, Spain 3. Department of Biomedical Engineering, Stony Brook University, Stony Brook, NY, USA 4. Department of Cardiology, Rabin Medical Center, Petach Tikva, Israel

Introduction

The Lattice Boltzmann Method (LBM) has been increasingly used as a CFD solver in various applications. In this study, we integrated two commercial software to introduce a new fluid-structure interaction (FSI) co-modeling approach using LBM and Finite-Element (FE) methods. The suitability of the proposed approach was examined for compliant aortic valve (AV) biomechanical simulations. Towards that goal, LBM-FE hemodynamic FSI models were generated for healthy tricuspid aortic valves (TAV) and bicuspid aortic valve (BAV). A multiscale structural approach has been employed for the leaflets that differentiate between the collagen network of fibers embedded within the leaflets. Different parameters have been examined, and both structural stresses on the valve and resulting hemodynamics are analyzed.

Methods

The parametric geometry of the AV describes a 3D geometry of TAV [1], [2] ,[3] and elaborated to present BAV [4], considering the heterogeneous structure composed of collagen fibers embedded in the leaflets. In this study, the XFlow (Dassault Systemes, Simulia Corp., Madrid SLU, Spain) commercial code was utilized for the fluid part using LBM approach in a 3D cartesian velocity set using D3Q27 uniform lattice. Representative FSI test cases utilizing LBM-FE approach of healthy AV and pathological compliant BAV using normotensive physiological pressure realistic conditions. The flow simulation was discretized with ~1M unity D3Q27 lattices and a coarsest spatial length of 1 mm. FSI partitioned approach was used to conduct all the simulations in this study using XFlow solver Abaqus (Dassault Systemes, Simulia Corp., Providence, RI) solver for the structural analysis.

Results

Figure 1 presents the flow velocity field evolution using FSI LBM-FE at representative instants for TAV and BAV models through the cardiac cycle. Moreover, the mechanical maximum principal stresses and WSS are shown at systole peak and mid diastole instants.

Discussion

The TAV orifice area at systole peak was calculated 3.38 cm^2 and the max velocity was 1.0 m/s. It corresponds adequately with the published range of values (0.9-2.3 m/s and 3.38-4.13 cm^2, respectively) in the literature from in-vivo, in-vitro and in-silico studies and clinical guides. The predicted maximal principal stresses along the surface of the leaflets are calculated

~150 kPa. The wall shear stress has a high value is shown around the leaflets' coaptation region and gradually decreases towards the belly. By a similar argument for all the above, the BAV model, as a test case of a pathological valve with irregular geometry was evaluated. We have shown that LBM-FE FSI model can decently predict the flow and structural properties of TAV, and adequately handles irregular geometries such as BAV.
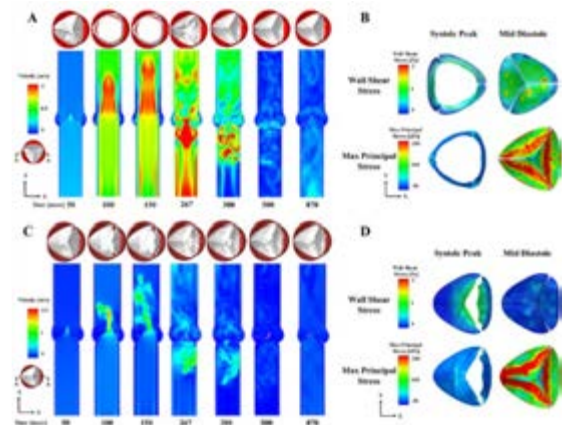
Figure 1: FSI models using coupled LBM-FE: (A) Flow velocity of TAV (B) Flow wall shear stress (upper row) and mechanical stress (lower row) distributions on TAV cusps (C) Flow velocity of BAV (D) Flow wall shear stress (upper row) and mechanical stress (lower row) distributions on BAV cusps.

References

[1]   Haj-Ali *et al. J. Biomech.*, vol. 45, no. 14, pp. 2392–2397, 2012.

[2]   Marom *et al. Med. Biol. Eng. Comput.*, vol. 50, no. 2, pp. 173–82, Feb. 2012.

[3]   Morany *et al. Ann. Biomed. Eng.*, vol. 49, no. 1, pp. 441–454, 2021

[4]   Lavon *et al.*, *J. Biomech. Eng.*, vol. 140, no. March, pp. 1–7, 2017.

Acknowledgements

THE EFFECT OF SIZE AND PROXIMITY OF MICRO-BEADS ON THE RUPTURE THRESHOLD OF ATHEROMA CAP LABORATORY MODELS

Andrea Corti (1), Daniel Khalil (1), Sheldon Weinbaum, PhD (1), Luis Cardoso, PhD (1)

1.Department of Biomedical Engineering, The City College of New York, New York, USA

Introduction

The mechanical vulnerability of the atherosclerotic cap is a crucial risk factor in asymptomatic fibroatheromas. Our research group demonstrated using numerical modeling that microcalcifications (μCalcs) located in the fibrous cap can multiply the tissue background stress by a factor 2-7[1-3]. We showed how this effect depends on the size and the ratio of the gap between particles pairs (h) and their diameter (D) along the tensile axis. In this context, we studied the impact of micro-beads of varying diameters and concentration on the rupture of human fibroatheroma laboratory models.

Methods

We created silicone-based (DowsilEE-3200, Dow Corning) dumbbell-shaped models (80%-scaled ASTM D412-C) of arterial tissues. Samples were divided into three groups: (1) without μBeads (control, n=12), (2) with μBeads of varying diameter (D=30,50,100μm) at a constant concentration of 1% weight (n=36), (3) with μBeads of constant diameter (D=50μm) at different concentrations (3% and 5% weight) (n=24). Before testing, samples were scanned under Micro-CT, at a resolution of 4μm. Images were then reconstructed in NRecon (SkySCan, v.2014) and structural parameters obtained in CTan (SkyScan, v.2014). These data were used to calculate the number of beads and their respective h/D ratio in a custom-made MATLAB script. We tested the samples using a custom-made micro material testing system equipped with real-time control and acquisition software (LabVIEW, v. 2018, NI). The reaction force and displacement were measured by the system and images of the sample were recorded by a high-resolution camera. The true stress and strain profiles of each sample were obtained by means of Digital Image Correlation (DIC).

Results

Samples with and without μBeads exhibited a distinct hyperelastic behaviour typical of arterial tissues **(Fig1)**.
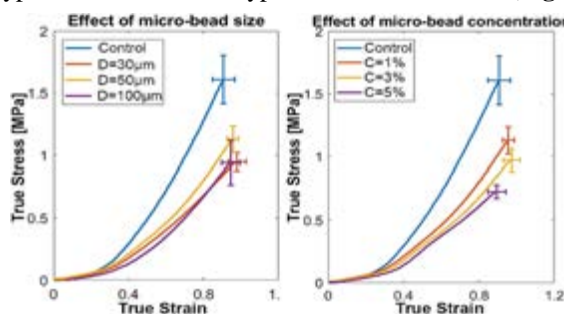
Figure1: True stress-strain curves of samples with μBeads of varying diameter (Left) and concentration (Right) against control group. Error bars represent ±SD of ultimate stress and strain.

Comparison of the mean ultimate stress (UTS) between groups was performed by one-way ANOVA test followed by post-hoc pairwise comparison. Regardless of the group, the presence of μBeads determined a statistically significant reduction in UTS **(Fig2)**. Increasing the μBeads concentration was also positively correlated with lower stresses at rupture as more clusters formed resulting in lower values of h/D **(Table1)**.
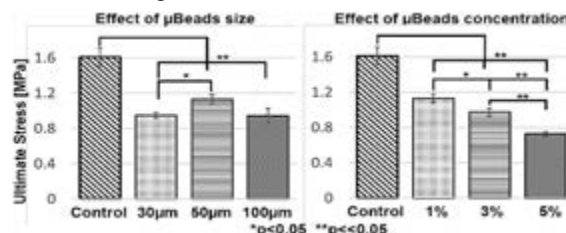
Figure2: Bar-charts of UTS±SD for each group.

	30	**50**	**100**	**1%**	**3%**	**5%**
# Beads	4348	302	13	302	876	1526
# Close Beads	22	6	0	6	59	81
h/D	3.1	3.4	>4	3.4	2.5	2.3
UTS Drop	41%	30%	42%	30%	40%	55%

Table 1: List of the average number of μBeads, the number of μBeads close to each other (h/D<4), the lowest h/D value and the amount of UTS reduction for each group with μBeads.

Discussions

Our results clearly capture the influence of μBeads on the rupture threshold of a vascular tissue mimicking material. In fact, samples with μBeads exhibit levels of UTS that are around two times lower than the control group. This effect appears to be dependent on the μBeads proximity, as lower h/D correlates with higher UTS reductions. On the other hand, the effect of particle size is not apparent for the diameters considered in this study. The plausible explanation for the observed change in rupture threshold is the increase in stress concentration around spherical μBeads, which we have previously shown in analytical and numerical studies [1-3]. Our experimental observations support our previous studies suggesting that μCalcs located within the fibroatheroma cap may be responsible for significantly increasing the risk of cap rupture that precedes myocardial infarction and sudden death.

References

1. Vengrenyuk et al, PNAS, 103 (40) 14678-14683, 2006.
2. Kelly Arnold et al., PNAS110 (26) 10741-10746, 2013.
3. Cardoso et al, Ann Biomed Eng, 42(2):415-431, 2015.

Acknowledgements

WALL SHEAR STRESS TOPOLOGICAL SKELETON VARIABILITY PREDICTS PLAQUE GROWTH IN HUMAN CORONARY ARTERIES

Giuseppe De Nisco (1), Eline Hartman (2), Valentina Mazzi (1), Diego Gallo (1), Claudio Chiastra (1), Joost Daemen (2), Jolanda Wentzel (2), Umberto Morbiducci (1)

1. PoliTo^{BIO}Med Lab, DIMEAS, Politecnico di Torino, Italy; 2. Department of Cardiology, Biomedical Engineering, Erasmus MC, Netherlands

Introduction

Although low wall shear stress (WSS) has become the consensus hemodynamic mechanism for coronary atherosclerosis, the exact biomechanical stimulus affecting atherosclerosis evolution is still undetermined [1]. Aiming at bridging this gap of knowledge, recently the WSS topological skeleton (TS) is receiving increasing interest, because of (1) its link with flow features that have been associated with vascular dysfunction [2], and (2) its capability to concur to the description of the complex biomechanical stimulus affecting atherosclerosis evolution [3]. Briefly, the WSS TS is composed by fixed points, where the WSS vanishes, and unstable/stable manifolds connecting them, where WSS exerts a contraction/expansion action on the endothelium [4]. Here we test the ability of WSS TS to predict the temporal evolution of coronary artery plaque burden (PB), a hallmark of atherosclerosis development, in 49 patient-specific computational models of human coronary arteries.

Methods

A non-culprit coronary segment for 48 hemodynamically stable patients was imaged at baseline (T1) and at 1 year follow-up (T2). Vessel geometries were reconstructed at T1, and computational hemodynamic simulations were carried out prescribing patient-specific boundary conditions. Widely adopted descriptors of WSS magnitude and multidirectionality were tested (i.e., TAWSS, OSI, RRT, and transWSS). Additionally, a Eulerian method was applied to analyse the WSS TS [4], identifying WSS contraction/expansion regions at the coronary luminal surface by the divergence of normalized WSS vector field (DIV_{WSS}). The amount of variation in WSS contraction/expansion action along the cardiac cycle T was quantified by the Topological Shear Variation Index (TSVI) [2]:

$$\text{TSVI} = \left\{ \frac{1}{T} \int_0^T [\text{DIV}_{WSS} - \overline{\text{DIV}_{WSS}}]^2 dt \right\}^{1/2} \quad (1)$$

PB growth was evaluated as the difference between PB measurements (100*plaque area/total vessel area) at T2 and T1 averaged over 3mm/45° luminal sectors. Hemodynamic descriptors were averaged over 3mm/45° luminal sectors and divided into artery-specific low, mid and high tertiles to perform a statistical analysis on the associated PB growth measurements.

Results

Figure 1 reports (1) the luminal distribution of TAWSS and TSVI for two explanatory cases (panel A), and (2)

the average PB growth values for low, mid, or high values of these two hemodynamic descriptors (panel B). Overall, sectors exposed to high TSVI at T1 exhibited PB growth in the T2-T1 time interval significantly higher than sectors exposed to low or mid TSVI at T1. A significant association emerged also for the exposure to low TAWSS at T1 and PB growth. An association also emerged between PB growth in the T2-T1 time interval and WSS multidirectionality at T1. However, the very low values of OSI (<0.01) and transWSS (<0.15 Pa) suggest a secondary role of the WSS multidirectionality in promoting aggravating biological events.
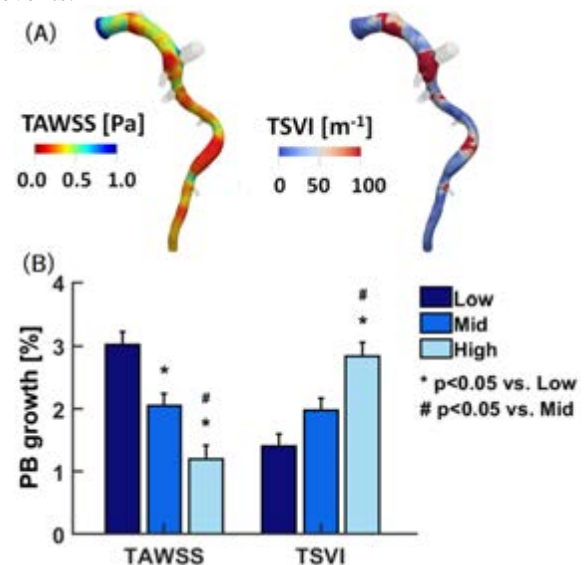
Figure 1: (A) TAWSS and TSVI luminal distributions; (B) TAWSS and TSVI vs. estimated PB growth.

Discussion

Here we demonstrate that luminal exposure to high TSVI was associated with significant PB growth. Physically, TSVI quantifies the variability of WSS contraction/expansion action on the endothelium, describing a different hemodynamic stimulus with respect to low TAWSS. This study confirms recent findings on TSVI as biomechanical marker of vascular disease, encouraging further clinical trials for a translation of this concept into clinical practice.

References

1. Brown AJ et al., Nat Rev Cardiol, 13:210-220, 2016.
2. Morbiducci U et al., Ann Biomed Eng, 48:2936-49, 2020.
3. Candreva A et al., Atherosclerosis, 2021.
4. Mazzi V et al., Biomech Model Mechanobiol, 19(5):1403-23, 2020.

ON THE INFLUENCE OF THROMBUS PERMEABILITY ON FLUID DYNAMICS IN THORACIC AORTIC ANEURYSM: IN SILICO MODELS

Carine Guivier-Curien (1), Valérie Deplano (1)

1. Aix-Marseille Université, Ecole Centrale, CNRS, IRPHE UMR 7342, France

Introduction

In pathologies of aorta, such as aneurysm, intraluminal thrombus (ILT) can form and grow. ILT is a 3D fibrin structure comprised of blood cells and proteins, leading to a network of canaliculi permeable to fluids [1]. During the evolution of the aneurysm, the thrombus progressively thickens and is then composed of three layers of variable permeability. To understand the key role of fluid dynamics in thrombus evolution could help in a better management of pathologies. The way to consider the ILT in the current *in silico* models differs from authors. Few model a porous medium. In this study, *in silico* models are developed to tackle the question whether and how a thrombus model should be included in CFD simulations when focus is done at macroscale level of fluid dynamics.

Methods

Based on CT-angioscans of a 72-year-old man suffering from a descending thoracic aorta aneurysm, a geometrical model was build focusing on the aneurysm zone. Straight tubes were added upstream and downstream to ensure fully developed flow conditions. Meshes were refined in the boundary layer. At the inlet, a fully developed unsteady velocity profile was implemented from a thoracic aorta flow rate described by [2]. At the outlet, an outflow condition was imposed. Walls were rigid with a no-slip condition. Flow was assumed to be laminar and the fluid Newtonian. Cardiac period was 1s. The mean Reynolds number was 1450. The whole geometrical and physical models are intentionally degraded compared to the reality since the objective is to perform relative comparisons between different ILT modeling saving computational time.

Three different models were developed: M0, ILT is fully impermeable; M1, ILT is a porous medium with a constant and isotropic permeability $k=10^{-9}$ m²; M2, ILT is a porous medium with a gradient of permeability from 10^{-7} (interface with lumen) to 10^{-11} m² (arterial wall). Porous medium was governed by the Darcy's law including as a source term in Navier-Stokes equations. All simulations were performed on Ansys Fluent Software (R2020). Convergence was reached at the third cycle and results presented are from this cycle.

Results

Major differences in luminal velocity and pressure patterns are found during the deceleration phase especially for M2 compared to the other ones. Within ILT, velocity values are more than one order greater in M2 than in M1 due to higher permeability value at the ILT/lumen interface (Figure 1).
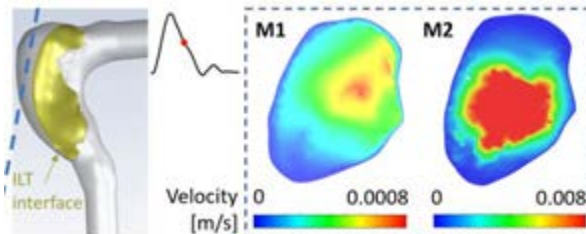
Figure 1: Velocity contour in a plane (blue dashed line) within ILT for M1 and M2 during deceleration phase

At the end of the deceleration phase, the wall shear stress (WSS) at the arterial wall covered by ILT is about 5-fold higher in M2 than in M1, especially where ILT thickness is low. In addition, WSS is about 2 orders of magnitude lower than in M0 (Figure 2). No difference on pressure patterns is observed at the arterial wall whatever the model, as it was also previously shown *in vitro* [3].
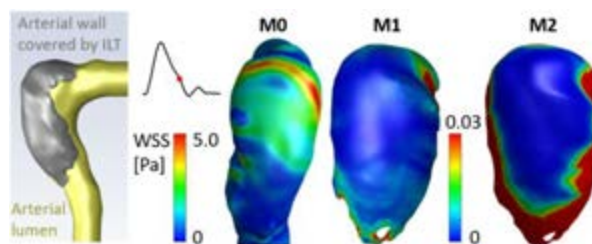
Figure 2: WSS at arterial wall (covered by ILT for M1 and M2) at the deceleration phase (colormap for M1 and M2 differs from M0 one for readability)

Discussion

Although ILT integration shows little influences on fluid dynamics at a macroscale level in the whole lumen part once $k<10^{-9}$ m², it plays a significant role on diminishing WSS at the arterial wall known to be involved in wall remodeling. It clearly appears that k value controls a part of macroscale mechanisms within ILT. Given the limited amount of *in vivo* data about ILT permeability, experimental measurements coupled with histological analyses are currently in progress to go further in the model. Modeling ILT as a porous medium seems all the more appropriate as we know that at the micro scale, biochemical transport phenomena take place and could have an impact on the thrombus evolution and role in the pathology [4].

References

1. Adolph et al, J Vasc Surg, 25:916–926, 1997.
2. Olufsen et al, Ann Biomed Eng, 28:1281-1299, 2000.
3. Thubrikar et al, J Cardiovasc Surg, 44:67-77, 2003.
4. Behr Andersen et al, Arterioscl Thromb Vasc Biol, 38:2254-2267, 2018.

IMAGE-BASED SIMULATION OF FLOW IN A PLATELET AGGREGATE

Yue Hao (1), Gábor Závodszky (1)(2), Claudia Tersteeg (3), Alfons Hoekstra (1)

1. Computational Science Lab, University of Amsterdam, the Netherlands; 2. Department of Hydrodynamic Systems, Budapest University of Technology and Economics, Budapest, Hungary; 3. Laboratory for Thrombosis Research, IRF Life Sciences, KU Leuven Campus Kulak Kortrijk, Kortrijk, Belgium

Introduction

The formation of a platelet aggregate is the initial step in the formation of thrombi. The mechanical properties of such aggregate are significantly influenced by its microstructure and its interaction with the flow during formation. A large number of computational models have been developed to study the intrathrombus flow, but these models either were done in 2D [1] or ignored the microstructure of the thrombus [2].

In this work, a 3D blood flow computational model is proposed based on the in vitro structure of a platelet aggregate measured under a physiological shear rate. The structure of the platelet aggregate is inferred from microcopy images of labelled platelets.

Methods

In the platelet aggregation experiments, blood with labelled platelets was perfused over Horm-collagen at a wall shear rate of 1600 s^{-1} for 5 minutes. The images in Figure 1 were captured under differential interference contrast (DIC) microscopy with 100 times magnification for each z-stack. The intensity of the fluorescence in these images was matched to the porosity values [1] of the platelet aggregate.
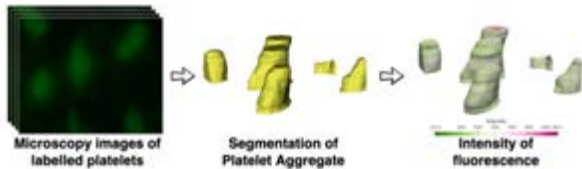
Figure 1: Flow diagram for the image-based modeling methodology of the platelet aggregate. Each image represents a $125\mu m \times 100\mu m$ domain. The volume of the perfusion channel was reconstructed by the stack of images and the platelet aggregates were segmented by the intensity of fluorescence.

In the computational model, the platelet aggregate is modelled as a porous medium. To describe the incompressible blood flow through it, the Navier-Stokes equations including an external Darcy force term are applied

$$\rho \left(\frac{\partial \mathbf{u}}{\partial t} + \mathbf{u} \cdot \nabla \mathbf{u} \right) = - \nabla p + \mu \Delta \mathbf{u} - \frac{\mu}{k} \mathbf{u}, \qquad (1)$$

$$\nabla \cdot \mathbf{u} = 0. \qquad (2)$$

Here, $\mathbf{u}$ denotes the velocity of the fluid, p is the pressure, ρ is the fluid density, and μ represents the dynamic viscosity. The last term is the interaction force between the fluid and the platelet aggregate, that is defined by Darcy's law. In this term, k is the permeability, which is estimated by the Kozeny-Carman equation:

$$k = \Phi_s^2 \frac{\epsilon^3 D_p^2}{150(1 - \epsilon)^2}, \qquad (3)$$

where Φ_s is the sphericity of platelets, ϵ is the porosity of the platelet aggregate, and D_p is the platelet diameter.

Results

The system above was solved using finite element method and implemented with FreeFEM. Selected results are presented in Figure 2. Figure 2(a) and 2(b) show the permeability of the platelet aggregate and the velocity profile of the blood flow on a cross-section of one of the aggregates respectively. Figure 2(c) shows the interaction force between the flow and the platelet aggregate on the cross-section. Most of the force interaction between the flow and the aggregate happens on the surface of the aggregate, and the flow induced forces are much smaller inside.
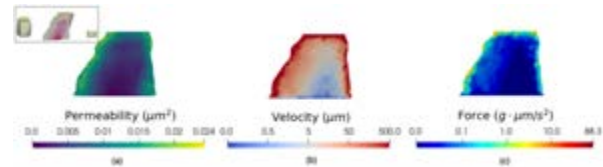
Figure 2: (a) The permeability of the platelet aggregate. The small figure on the top left shows the intensity of fluorescence on the cross-section. (b) The velocity profile of blood flow around the platelet aggregate at logarithmic scale. (c) The interaction force between the flow and the platelet aggregate at logarithmic scale.

Discussion

Using the presented method, the accurate shape and porosity of early stages of platelet aggregates can be represented in detailed flow simulations. This allows the investigation of the flow inside the aggregate and yields information on the flow-induced force distribution, which in turn will be used to model the mechanics of the aggregate in the future.

References

1. Tomaiuolo M, Stalker T J, Welsh J D, et al. A systems approach to hemostasis: 2. Computational analysis of molecular transport in the thrombus microenvironment[J]. Blood, The Journal of the American Society of Hematology, 2014, 124(11): 1816-1823.
2. Kadri O E, Chandran V D, Surblyte M, et al. In vivo measurement of blood clot mechanics from computational fluid dynamics based on intravital microscopy images[J]. Computers in biology and medicine, 2019, 106: 1-11.

THE INFLUENCE OF PLAQUE STRUCTURAL STRESS AND WALL SHEAR STRESS ON HUMAN CORONARY PLAQUE PROGRESSION

Aikaterini Tziotziou (1), Eline Hartman (1), Suze-Anne Korteland (1), Antonius F.W. van der Steen (1), Joost Daemen (2), Jolanda Wentzel (1), Ali C. Akyildiz (1,3)

1. Department of Biomedical Engineering, Erasmus Medical Center, Rotterdam, the Netherlands;
2. Department of Cardiology, Erasmus Medical Center, Rotterdam, the Netherlands;
3. Department of Biomechanical Engineering, Delft University of Technology, Delft, the Netherlands

Introduction

Atherosclerosis is one of the most widespread diseases in our cardiovascular system and a primary cause of death as its progression and rupture can lead to myocardial attack or stroke [1]. Atherosclerotic plaque progression over time in coronary arteries is affected by local hemodynamic and biomechanical factors, such as the Wall Shear Stress (WSS) and the Plaque Structural Stress (PSS) [2]. Low WSS is known to be associated with plaque progression but the association between PSS, and its combination with WSS, towards plaque progression has not been well-established yet [2]. In this work, we study the effect of PSS and WSS on human coronary plaque progression.

Methods

Forty-nine non-stented, non-culprit coronary arteries (IMPACT study) [3] were imaged at two time points (baseline and one-year follow-up) using combined near infrared spectroscopy intravascular ultrasound (NIRS-IVUS) and optical coherence tomography (OCT). The 2D plaque geometries and 3D lumen surfaces were extracted from the combined imaging data. PSS (max principal stress) in patient-specific cross-sections was calculated via ABAQUS, by using the material properties of individual plaque components reported previously [2,4]. The backward incremental method [4] was applied to quantify and incorporate the initial stresses, that were present within the plaque structure when the artery was imaged, in the finite element simulations. The individual and combined impact of PSS and WSS on plaque progression was studied using Linear Mixed Models in SPSS. For this purpose, the time averaged WSS (TAWSS), calculated previously for these coronary arteries [3], were combined with the PSS, computed in the Fcurrent study. The 3D artery geometries were divided into 1,5mm/45° sectors and the statistical analyses were sector-based. The plaque thickness change was used as the parameter to quantify plaque progression in the analyses.

Results

So far, the analyses of 17 patients have been finalized. Greater PSS was observed in the thin wall and in the plaque cap regions with the non-uniform stress distribution. For the statistical analysis, the arterial sectors were divided into three tertiles (low, mid, high) with respect to PSS and WSS. The effect of PSS and

TAWSS individually, as well as when combined, on the plaque thickness change were statistically significant. Specifically, low PSS associated with plaque regression while high PSS associated with plaque growth (Fig 1). The analysis of the combined effect of PSS and WSS on plaque thickness showed that sectors of high PSS and low TAWSS had the greatest plaque progression whereas the ones of low PSS and high TAWSS the greatest plaque regression (Fig 1) .
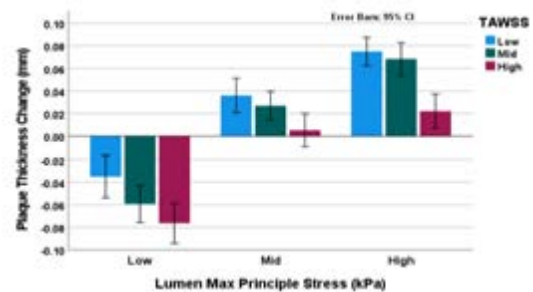
Figure 1: Impact of PSS and TAWSS combined on plaque thickness change.

Discussion

In this work, we have generated 2D and 3D patient-specific coronary computational models to investigate the influence of PSS and WSS on atherosclerotic plaque change over time, from a unique data set of IVUS and OCT combined. Our analysis of the first 17 coronaries already showed the statistically significant impact of PSS and WSS on plaque change over time individually and combined. Next immediate step of our study is to finalize the analyses of the entire data set of 49 coronaries. We also plan to further analyze the healthy and the diseased sectors separately. These will provide great insights for better understanding the plaque growth mechanisms and developing plaque progression prediction models.

References

1. Shah, P et al., Thrombosis, 2015:634983, 2015.
2. Costopoulos, C et al., Eur Heart J., 40:1411-1422, 2019.
3. Hartman, E et al., J. of Cardiovasc. Trans. Res., 14:416–425, 2021.
4. Akyildiz, A C et al., Computer. Methods in Biomech. and Biomed. Eng., 19: 771–779, 2016.

Acknowledgements

A HIGH-POWER LED ILLUMINATED PIV SETUP TO CHARACTERIZE THE FLOW BEHAVIOUR IN ABDOMINAL AORTIC ANEURYSM MODELS

Francesco Bardi (1,2), Emanuele Gasparotti (1), Emanuele Vignali (1), Miquel Aguirre (2), Stéphane Avril (2), Simona Celi (1)

1. BioCardioLab, Fondazione Toscana Gabriele Monasterio, Italy; 2. Mines Saint-Etienne, Université de Lyon, France

Introduction

Experimental circulatory loops are acquiring an increasing importance, given their possibility to be used as tools to deepen the knowledge of cardiovascular pathologies. In the context of *in-vitro* hemodynamics, Particle Image Velocimetry (PIV) is a well-established technique to measure the spatial and temporal evolution of the velocity and the Wall Shear Stress (WSS) inside anatomical phantoms. The aim of this work is to assess the feasibility to use a high-power LED illumination system [1] instead of a laser, to characterize the flow field and the WSS in large blood vessels.

Methods

The setup is shown in Figure 1. Two phantoms were manufactured using Sylgard 184: a cylinder (inner diameter of 20 *mm*) and an idealized symmetric abdominal aortic aneurysm (inner diameter ranging from 30 *mm* to 50 *mm*).
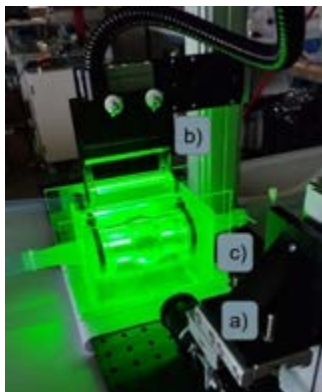
Figure 1: 2D PIV setup: a) camera b) line light and cylindrical lens c) abdominal aortic aneurysm phantom

A Mock Circulatory Loop consisting of a piston pump [2], a gear pump and a compliance chamber was used to impose the desired flow rate at the inlet of the phantoms. The flow rate and the pressure were measured upstream and downstream of the test section. A mixture of glycerol and water (61:39), matching the refractive index of the phantoms, was used as working fluid and the flow was seeded with 10 *μm* – diameter hollow spherical particles. A pulsed high-power LED (HardSOFT) and a line light were used to create a light sheet. The LED was operated with a pulse width of 20 *μs* and a pulse separation time of 200 *μs*. The illumination system was synchronized with a camera (acA1920-155um - Basler Ace) fitted with a f=35 *mm*

f#=1.8 lens, via a cRIO controller. Both phantoms were characterized under steady and pulsatile flow conditions with varying the flow rate from 3 *l/min* to 20 *l/min*.

Results

The flow rate measured with the ultrasonic flow meters was compared against the one obtained via the integral of the longitudinal velocity at the middle section of the cylindrical geometry (assuming axial symmetric flow), and for each flow condition the difference between the two was less than 5%. The flow behaviour in the abdominal aortic phantom was in agreement with previous studies [3]. The characteristic recirculation region is at the beginning of the deceleration phase for a pulsatile flow rate (period 1 *s* and peak flow rate 6 *l/min*) is clearly visible in Figure 2.
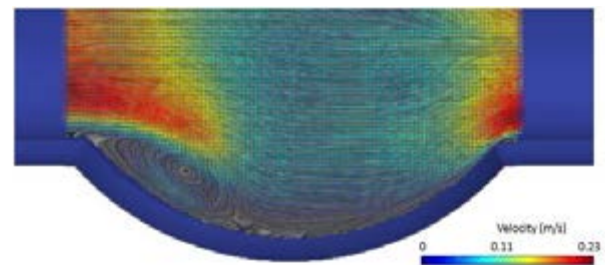
Figure 2: Instantaneous velocity vectors with velocity magnitude colormap

Discussion

A cost-effective setup to perform 2D PIV studies of large blood vessels has been evaluated. We found that the system can be used to measure the instantaneous velocity field for a region of interest of 25 *mm* x 50 *mm*. Future works will include a comparison between the measured velocity fields and the results of Computational Fluid Dynamic and Fluid Structure Interaction simulations.

References

1. C Willert *et al, Meas. Sci. Techno,* 21 075402, 2010.
2. Vignali et al, ASAIO, January 12, 2022.
3. Salsac et al, J Fluid Mech, *560* 19-51 , 2006.

Acknowledgements

INTEGRATING IN-SILICO AND EX-VIVO ANALYSIS FOR BIOMECHANICAL ASSESSMENT OF AORTIC ENDOGRAFTING

Michele Conti, Daniele Bianchi, Santi Trimarchi, Maurizio Domanin, Daniele Bissacco, Ferdinando Auricchio

1DICAr, University of Pavia, Italy
2 Fondazione IRCCS Ca' Grande Ospedale Maggiore Policlinico Milano, Milan, Italy

Background. Although Thoracic endovascular repair (TEVAR) is widespread in clinical practice for treating aortic disease, it has relevant systemic complications, such as the increase of the cardiac work load due to post TEVAR aortic stiffening, and local issues such as re-entry tears due to the tissue damage caused by endograft interaction. Such considerations are particularly important when considering the use of TEVAR in young patients or to treat ascending thoracic aorta, that is close to the heart. For this reason, the assessment of the biomechanical impact of TEVAR on the arterial systemic circulation is vital from many perspectives: procedure planning, device design, and follow-up analysis. Such analysis is often performed from a single perspective (e.g., stent-graft apposition [1], pre- vs post-op hemodynamics [2], etc.) using a single methodology (e.g., in-silico – FEA [3] or CFD [4], in-vivo [5], or ex-vivo [6]) lacking the capability to provide a biomechanical comprehensive analysis.

Recent Advances. Given such considerations, the present study aims to elucidate these biomechanical mechanisms by coupling ex-vivo analysis related to the measurement of the pulse wave velocity and performing uni-axial tensile test on porcine tissue samples, and the in-silico analysis of the wall stress though finite element (FE) analyses of stent-graft deployment and the sample pressurization. The ex-vivo results highlight an increase of baseline PWV by a mean 0.78 m/s or 12% after TEVAR with a 100 mm stentgraft (P<0.013). In the in-silico analysis, the average von Mises stress in the landing zone increases of about 15 % and 20% using respectively stent-graft with radial oversizing of 10% and 20%. The work shows the effectiveness of integrated framework to analyse the biomechanical mechanisms post TEVAR. Moreover, obtained results highlights the key aspect of prosthesis choice showing the stiffening after TEVAR and the increasing of wall stress proportionally to the stent-graft oversizing.

Future directions Use 3D printing for both surgical planning purposes [7] and manufacturing mock aortic models, assessing the performance of printed materials to mimic materials features of the aorta.

Figures
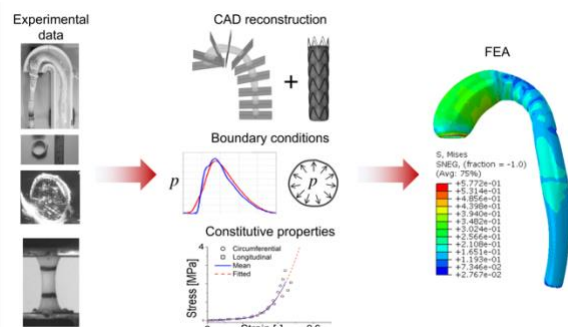
Figure 1: In-silico modelling. from left to right: ex-vivo analysis of porcine aortic sample; computational modelling integrated with experimental data; FEA analysis of deployment and pressurization

References

1. Auricchio, **MC**, et al. (2013). *Patient-specific aortic endografting simulation: From diagnosis to prediction*, CBM 43 (4) 386–394.
2. Auricchio, **MC**, et al. (2014) *Patient-specific analysis of postoperative aortic hemodynamics: a focus on thoracic endovascular repair (TEVAR),* Computational Mechanics, 54(4), 943-953.
3. Romarowski, **MC** et al. (2018). *Computational simulation of TEVAR in the ascending aorta for optimal endograft selection: A patient-specific case study*. Computers in biology and medicine, 103, 140-147.
4. Romarowski, Faggiano, **MC**, et al. (2018). *A novel computational framework to predict patient-specific hemodynamics after TEVAR: Integration of structural and fluid-dynamics analysis by image elaboration.* Computers & Fluids. doi.org/10.1016/j.compfluid.2018.06.002
5. de Beaufort, Nauta, **MC** et al. (2017) *Extensibility and Distensibility of the Thoracic Aorta in Patients with Aneurysm*. EJVES, 53 (2), 199–205.
6. de Beaufort, **MC**, et al. *Aortic stiffness Increases After Thoracic Endovascular Aortic Repair in an Ex-vivo Porcine Model* [Annals of vascular surgery, 43, 302-308.
7. Marone, Rinaldi, Marconi, **MC**, et al. (2018). *A 3D-printed patient-specific model to assist decision making in endovascular treatment of thoracoabdominal aortic aneurysm.* The Journal of cardiovascular surgery, 59(2), 291.

PREDICTING 1-YEAR IN-STENT RESTENOSIS IN FEMORAL ARTERIES THROUGH MULTISCALE COMPUTATIONAL MODELING

Anna Corti (1), Monika Colombo (1,2), Jared M Rozowsky (3), Stefano Casarin (4,5,6), Yong He (3), Francesco Migliavacca (1), Jose F. Rodriguez Matas (1), Scott A. Berceli (3,7), Claudio Chiastra (1,8)

1. Politecnico di Milano, Italy; 2. ETH Zürich, Switzerland; 3. University of Florida, FL, USA; 4. Houston Methodist Hospital, Houston, TX, USA; 5. Houston Methodist Research Institute, Houston, TX, USA; 6. Houston Methodist Academic Institute, Houston, TX, USA; 7. Malcom Randall VAMC, FL, USA; 8. Politecnico di Torino, Italy

Introduction

In-stent restenosis (ISR) is an inflammatory-driven response of superficial femoral arteries (SFAs) to stent placement, characterized by exacerbated cellular proliferative and synthetic activities, leading to lumen re-narrowing and failure of the procedure [1]. Although multiple systemic, biological and biomechanical drivers are known to promote ISR, a thorough understanding of its underlying mechanisms is lacking. Computational multiscale frameworks of ISR, integrating continuous- and agent-based approaches, have recently emerged as promising tools to decipher the mechanobiological processes governing the post-stenting arterial wall remodeling [2]. However, patient-specific applications including multi-omics data have never been proposed yet [2]. This work presents a patient-specific multiscale agent-based modeling framework of ISR that integrates the effects of the hemodynamics and monocyte gene expression, accounting for systemic inflammation, on the cellular dynamics, to replicate the long-term response after stent placement in SFAs.

Methods

Two SFA lesions from the left and right legs of a patient who underwent self-expanding stenting were considered. Computer tomography, doppler ultrasound and monocyte gene expression were gathered at multiple time points within 1-year post-intervention.

The framework receives as input the patient-specific stented SFA 3D geometry (baseline), the blood flow velocity waveform and the monocyte gene expression data, and generates as output a 3D arterial lumen geometry at 1-year follow-up. The framework consists of 2 cyclically coupled modules (Fig. 1A): (i) a 'hemodynamics' module, in which the wall shear stress profile along the lumen is computed through computational fluid dynamics; (ii) a 'tissue remodeling module', in which first a 2D ABM replicates the arterial wall remodelling at several arterial cross-sections by simulating cell and extracellular matrix dynamics in response to the post-operative hemodynamic input and the inflammatory-related monocyte gene expression, and second a follow-up 3D arterial geometry is reconstructed from the ABM output. The ABM parameters were calibrated based on the data of the left SFA lesion at months 1 and 6. The calibrated framework was then used to simulate the arterial wall remodelling for both the SFA anatomies from baseline to 1 year.

Results

The framework successfully captured the patient-specific post-operative lumen area change from baseline to 1 year (Fig. 1B). Specifically, (i) no significant differences were found between the patient's and the simulated lumen area of the stented portion at the available follow-ups, and (ii) both the patient's and simulated cases presented the greatest lumen area reduction at 1-month follow-up (p<0.05). However, the framework was not fully able to capture the local heterogenous response of the artery to stenting in the left SFA (Fig. 1C), suggesting that additional local factors may play a role in the remodeling process.
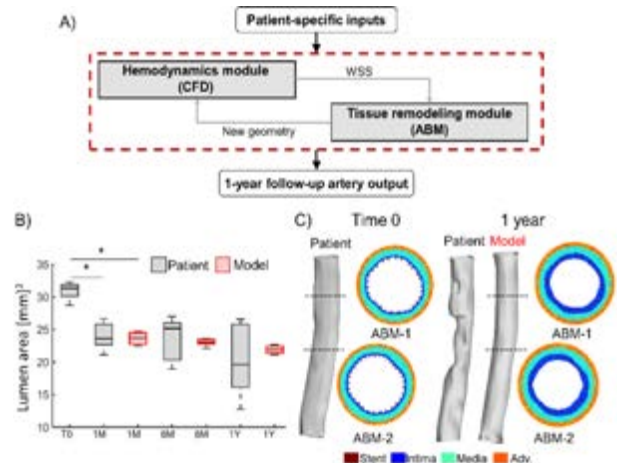
Figure 1: A) Multiscale framework of ISR; B-C) Results of the framework applied to the left SFA lesion.

Discussion and conclusions

The multiscale framework predicted the overall patient's lumen area reduction from baseline to 1-year follow-up, thus highlighting the potentialities of the developed approach in deciphering patient-specific pathological pathways in the context of ISR. Future efforts will be focused on the inclusion of additional local inputs (e.g., the local arterial wall damage) to improve the predictive power of the framework.

References

[1] Chaabane, C. et al. *Cardiovasc. Res.* 99: 353–363, 2013.
[2] Corti, A. et al. *Front. Bioeng. Biotechnol.* 9: 744560, 2021.

Acknowledgements

IN VITRO INVESTIGATION OF THE IMPACT OF ANEURYSMAL SAC ASPECT RATIO AND NECK SIZE ON HEMODYNAMICS OF CEREBRAL ANEURYSMS TREATED WITH FLOW DIVERTING STENTS

Fanette Chassagne (1), Michael C. Barbour (2), Michael R. Levitt (3), Alberto Aliseda (2)

1. *Mines Saint-Etienne, Univ Lyon, Univ Jean Monnet, Etablissement Français du Sang, INSERM, U 1059 Sainbiose, F - 42023 Saint-Etienne France; 2. Department of Mechanical Engineering, University of Washington, Seattle, USA; 3. Department of Neurosurgery, University of Washington, Seattle, USA*

Introduction

Flow diverting stents (FDS) are one of the leading methods for endovascular treatment of cerebral aneurysms. These high porosity meshes aim to provide a scaffold for healing of the parent vessel, redirecting the flow along it and reducing the flow into the aneurysmal sac, thus promoting the formation of a stable thrombus in the sac. However, 25% of treatments fail and need to be re-treated [1], with the thrombus not completely filling the sac and the aneurysm wall still being subjected to flow-induced mechanical stresses. This *in vitro* study investigates the impact of aneurysm geometry (sac aspect ratio and neck size) and vessel curvature on the hemodynamics of cerebral aneurysms treated with FDS, via Particle Image Velocimetry (PIV) measurements.

Methods

The experimental plan was divided in two steps. First, we investigated the effect of the Reynolds, Dean and Womersley numbers (parent vessel flowrate and curvature, Q =100, 200, 300, 400 ml/min, $\kappa = 1/r_C$: 0.0, 0.06, 0.14, and 0.22 mm^{-1}) on intra-aneurysmal flow. Then, the effect of the aspect ratio of the sac (AR = 0.4 and 1.6) and the neck size (3 and 5 mm) is studied for selected values of the Dean and Womersley numbers. 12 idealized geometry flow phantoms were casted in optically clear silicone. These phantoms were connected to a flow loop reproducing physiological flowrates and cardiac frequencies. A blood mimicking fluid (water/glycerin/salt mixture), with the same viscosity as blood and refraction-index-matched to the silicone models, was used. Stereo-PIV measurements were performed at 2 cardiac frequencies (50 and 100 BPM) and 4 flowrates in the parent vessel ([100-400] mL/min). The models were then treated with an FDS (4 x 20 mm Pipeline, Medtronic), and measurements were repeated.

Results

Measurements showed a single counter-rotating vortex in the sac before treatment for all experimental conditions, in all but one geometry. The circulation in the sac was found to correlate strongly to the curvature of the parent vessel and the mean flow rate (Dean number scaling). Increases in neck size led to a strong increase in the circulation in the aneurysmal sac: +380% for a neck increase of 67% (from 3mm to 5mm), showing injection of vorticity from the parent vessel with wider necks. After treatment, the flow topology was identical to pre-treatment for the conditions with

higher Dean numbers. For the low curvature cases, the circulation in the sac changed sign over the cardiac cycle, and flow reattached fully for larger neck size and larger aspect ratio. To assess the effect of treatment, the post-treatment velocity fields were compared to the pre-treatment results. Depending on the curvature, neck size and aspect ratio, the post-treatment circulation decreased to values ranging from 65% to a few percent of the pre-treatment circulation. A linear model with interactions was used to assess the relative influence of the different parameters on the flow reduction due to treatment. This method revealed that some parameters, such as frequency, have very little influence on the treatment effect, while the curvature of the parent vessel played an outsized role. Sac aspect ratio had a complex influence when the injection of vorticity into the sac exceeded the formation number limit and induced break down of the main central vortex core.

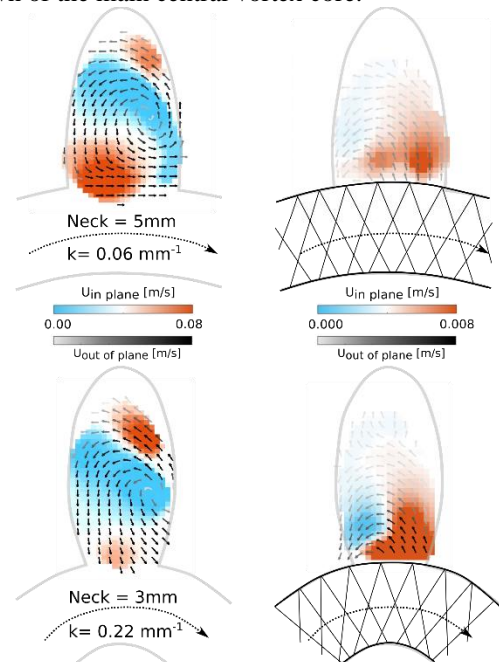*Figure 1: Velocity fields in idealized aneurysm flow phantoms (aspect ratio=0.4) pre- and post-treatment at peak systole for a mean flow rate = 300mL/min.*

Conclusion

This *in vitro* investigation identified that curvature, aspect ratio and neck size dominate the efficiency of FDS treatment, and enable failure predictions.

References

1. Brinjikji W. et al, J Neurointerv Surg, 5(1):45-8, 2013.

FINITE ELEMENT STUDY ON THE PROXIMAL FIXATION OF A STENT-GRAFT: IMPACT OF THE AORTIC ARCH ANGULATION

Anna Ramella (1), Laura Iannetti (2), Jose Felix Rodriguez Matas (1)
Francesco Migliavacca (1), Giulia Luraghi (1)

1. Politecnico di Milano, Milan, Italy; 2. Beta CAE Systems

Introduction

The Thoracic Endovascular Aortic Repair (TEVAR) is a minimally invasive technique to treat thoracic aorta pathologies and consists of inserting a self-expandable stent-graft into the pathological region to restore the correct vessel lumen. A crucial risk factor that affects the outcome of the procedure is the high aortic arch angulation in the proximal landing zone which may lead to inadequate stent-graft sealing. This could cause other device-related complications like bird-beak, device migration, or endoleaks [1]. In this context, Canaud et al. [2] experimentally investigated the proximal fixation of commercial stent-grafts in healthy human aortas by increasing the aortic arch angulation. The proposed study aims at proposing an *in-silico* methodology to evaluate the impact of aortic arch angulation on virtual stent-graft deployment.

Methods

The Valiant Captivia (Medtronic Inc, Santa Rosa CA) thoracic stent-graft model (*Fig.1a*) is created using Solidworks (Dassault Systemes) and discretized with ANSA (BETA CAE System). The stent is discretized with beam elements and the graft with triangular membrane elements. The Nitinol is modeled as a superelastic material, the PET as a linear elastic fabric material. Also, the stent prestress is included in the complete sutured model [3].
Following the procedure proposed by Canaud et al. [2], eight different aorta configurations are realized by increasing the arch angulation from 70° to 140° adopting the morphing tool available in the ANSA pre-processor, as reported in *Fig.1b*. Each aorta is discretized with triangular shell elements with a thickness of 1.5 mm and modeled as a hyperelastic material.
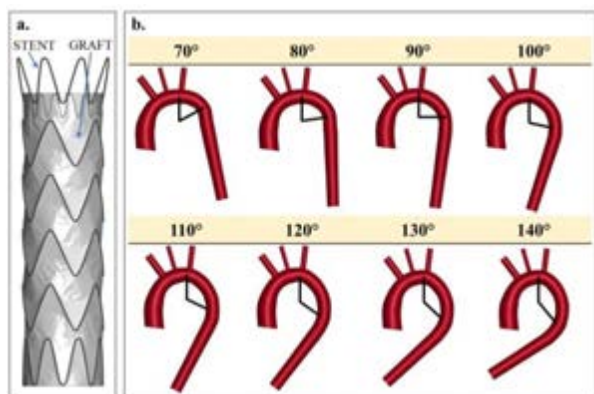
Figure 1. (a) stent-graft configuration; (b) aorta configurations changing the arch angulation.

The deployment simulations are performed using the explicit FE software LsDyna (ANSYS) and consist of crimping, morphing, and deploying the stent-graft in each vessel.

Results

The deployment simulation results for the 70° and 140° configurations are depicted in *Fig. 2*.
In the second case (*Fig.2b*), despite the arch angulation is higher, the proximal fixation of the stent-graft is assured, in line with the literature results [2]. The radial force distribution exerted by the stent on the aorta is also reported.
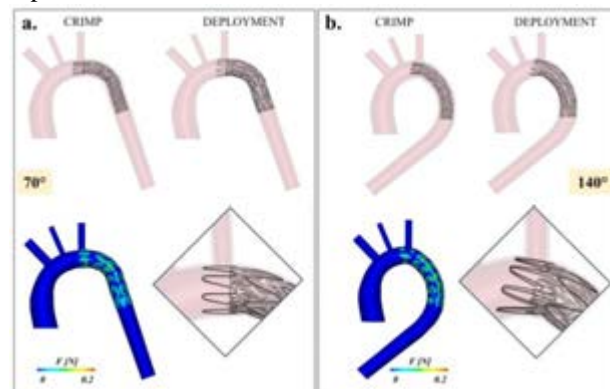
Figure 2. Crimp and deployment simulation results for the 70° (a) and 140° (b) aorta configurations with details on the radial force distribution on the aorta.

Discussion

The correct stent-graft apposition plays a significant role in the clinical outcome of the TEVAR procedure. The FE methodology here proposed may be followed by clinicians in the pre-operative planning to correctly position the stent-graft in the aorta. Furthermore, it can support the manufacturers to improve the device design to specifically address this problem.

References

1. Daye et al, Cardio Diagn & Ther, 8:S138, 2018.
2. Canaud et al, J Vasc Surg, 57:1084-1089, 2012.
3. Concannon et al, Biom Mod M.biol, 20(6):2373-92, 2021.

Acknowledgements

A SMART PARTICLE IMAGE VELOCIMETRY SYSTEM FOR THE IN VITRO ASSESSMENT OF CORONARY ARTERY HEMODYNAMICS

Elena Torta (1), Giuseppe C. A. Caridi (1), Claudio Chiastra (1), Diego Gallo (1), Umberto Morbiducci (1)

(1) Polito*BIO*Med Lab, Department of Mechanical and Aerospace Engineering, Politecnico di Torino, Italy

Introduction

Particle Image Velocimetry (PIV) has become a reliable measurement technique for the in vitro characterization of the local fluid dynamics. It plays a fundamental role in verifying/validating in silico models and/or in the design/optimization of cardiovascular devices [1]. However, the use of PIV is hampered by the high costs of its components (order of magnitude of 100 k€), and by the safety procedures required by the high-power lasers. Recently, alternative test benches that adopts solutions such as cameras embedded inside commercial smartphones [2] and low-power light sources, just to mention a few, have been proposed, thus reducing the costs to an order of magnitude of 1 k€. The present study explores the feasibility of adopting a test bench for cardiovascular applications, referred to as smart-PIV approach in the following, based on the use of smartphone cameras and low energy light source. In detail, (1) smart-PIV is adopted to analyze the flow field in realistic phantoms of healthy and stenotic left circumflex coronary arteries (LCX), and (2) the hemodynamic results are compared with those obtained from standard PIV measurements.

Methods

The study was conducted in two 3D-printed phantoms (Elastrat, Geneva, Switzerland). The first one represents a patient-specific replica of a healthy LCX reconstructed from angiographic images; the second one a diseased condition, through an artificially generated 67% diameter stenosis obtained by locally reshaping the healthy model. Measurements were carried out under steady-state flow conditions. The flow rates were monitored with an ultrasonic flow meter (Transonic, Ithaca, NY, USA) and set within the range (80-100 mL/min for the healthy model and 10-80 mL/min for the stenotic one), according to in vivo measurements [3]. The working fluid (glycerin-water, 40:60) was seeded with polyamide particles (density 1030 kg/m^3, diameter 60 μm). In the smart-PIV set-up, the camera of a Samsung Galaxy S9+ (12800x720 pixels, 960Hz) and a low-power continuous laser were used for time-resolved image acquisitions. In the standard PIV set-up (Dantec Dynamics A/S, Denmark), one HiSense Zyla camera (CMOS, 2560x2160 pixels) and a dual pulsed Nd:YAG laser were adopted. The MATLAB (MathWorks, Natick, MA, USA) toolbox PIVlab was employed to post-process the acquired images using the ensemble-correlation method.

Results

The comparison between smart-PIV and standard PIV 2D axial velocity fields in the healthy and stenosed coronary phantoms is shown in Figure 1. The smart-PIV approach was capable to capture the main flow features identified by the standard PIV approach in the healthy vessel phantom (dictated by the main geometric attributes of the vessel, Fig. 1-a) as well as the in stenotic vessel (Fig. 1-b). In particular, (1) the increase in fluid velocity caused by the area reduction in the stenotic region with the classical jet-like flow configuration, and (2) the typical post-stenotic recirculation region were properly detected. Moreover, the smart-PIV was able to detect the expected expansion/stretching of recirculation region distal to the stenosis in consequence of an increasing flow rate (data not shown).
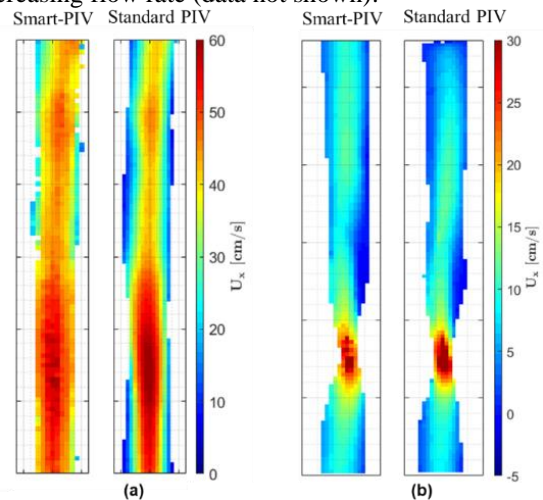
Figure 1: Axial velocity maps in (a) healthy LCX phantom (Q_{inlet}= 80 mL/min) and (b) stenotic LCX phantom (Q_{inlet}= 30 mL/min).

Discussion

An easily reproducible and maneuverable, secure, low-cost and low-energy consumption set-up for the in vitro characterization of healthy and stenotic coronary flows was proposed. The main limitation is related to the smartphone camera image acquisition frame-rate, which restricts the examinable flow regimes. However, the decrease in terms of costs and the increase in terms of security allow the smart-PIV system to be used for educational and research purposes for low-cost practical investigations.

References

1. Freidoonimher, N. et al., Fluids, 62:133, 2021.
2. Cierpka, C. et al., Fluids, 57(6):1-10, 2016.
3. Kessler, W. et al., Int J Card Imaging, 14(3):179-186, 1998

VASCULAR ADAPTATION FOLLOWING ENDOVASCULAR AORTIC ANEURYSM REPAIR

Shaojie Zhang (1), Joan Laubrie (1), S. Jamaleddin Mousavi (1), Stéphane Avril (1)(2)

1. Mines Saint-Etienne, INSERM, U 1059 Sainbiose, France; 2. Institute of Biomechanics, Graz University of Technology, Austria

Introduction

Endovascular aneurysm repair (EVAR) has become a standard treatment of abdominal aortic aneurysm (AAA), given that EVAR is associated with superior intraoperative outcomes and similar long-term survival compared with open repair. EVAR consists in implanting an endograft, or stent-graft (stent covered with an impermeable fabric) into the aneurysm sac through endovascular navigation, only requiring a small incision in the femoral artery. Once the stent-graft is successfully positioned and deployed, the impermeable fabric works as a pressure isolation barrier, preventing the transmission of systemic pressure to the weakened aneurysm wall. For this reason, shrinkage of the aneurysm sac is commonly accepted as clinical evidence for a successful EVAR [1,2].

Methods

We studied post-EVAR AAA shrinkage using numerical simulation, as shown in Figure 1. We set up a 3D finite-element model of post-EVAR vascular adaptation within an open-source finite-element code, which was initially developed for growth and remodelling (G&R). We modelled the endograft with a set of uniaxial prestrained springs that apply radial forces on the inner surface of the artery. Constitutive equations, momentum balance equations, and equations related to the mechanobiology of the artery were formulated based on the homogenized constrained mixture theory. We performed a sensitivity analysis by varying different selected parameters, namely oversizing and compliance of the stent-graft, gain parameters related to collagen G&R, and the residual pressure in the aneurysm sac. This permitted us to evaluate how each factor influences post-EVAR vascular adaptation [3].

Results

It was found that oversizing, compliance, or gain parameters have a limited influence compared to that of the residual pressure in the aneurysm sac, which was found to play a critical role in the stability of aneurysm after stent-graft implantation. An excessive residual pressure larger than 50 mmHg can induce a continuous expansion of the aneurysm while a moderate residual pressure below this critical threshold yields continuous shrinkage of the aneurysm. Moreover, it was found that elderly patients, with relatively lower amounts of remnant elastin in the arterial wall, are more sensitive to the effect of residual pressure.
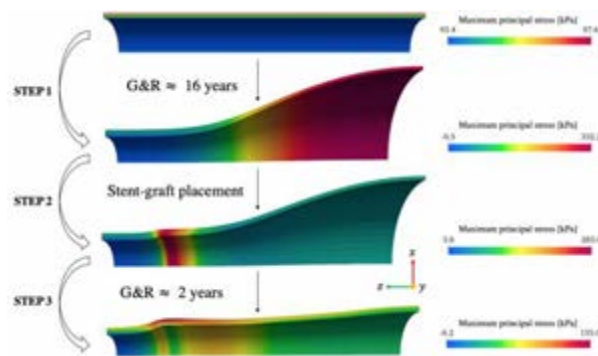
Figure 1: Simulations showing geometrical and maximum principal stress evolutions over the different simulation steps: formation of aneurysm, implantation of stent-graft and post-operative adaptation of aneurysm.

Discussion and conclusion

Ideally, implanting a stent-graft should avoid the aneurysm sac being subjected to systemic blood pressure, hence reducing the risk of aneurysm rupture. However, it was reported that aneurysm rupture may occur with a rate of 1%~3% of patients treated with EVAR. Our results show that elderly patients may present higher potential risk of aortic sac expansion due to intra-aneurysm sac pressure after EVAR than for younger patients. This indicates that elderly patients with AAA may be more susceptible to endoleaks-related complications after EVAR. The main perspective of this work will be the extension of the present model with layer-specific arterial wall models, and with applications to more relevant patient-specific cases

References

1. Ellozy SH, et al. Abdominal aortic aneurysm sac shrinkage after endovascular aneurysm repair: correlation with chronic sac pressure measurement. Journal of vascular surgery; 43(1): 2-7 (2006).
2. O'Donnell TF, et al. Aneurysm sac failure to regress after endovascular aneurysm repair is associated with lower long-term survival. Journal of vascular surgery; 69(2): 414-422 (2019).
3. Zhang, S., et al. 3D finite-element modelling of vascular adaptation after endovascular aneurysm repair. International Journal of Numerical Methods in Biomedical Engineering, in press (2021).

Acknowledgements

USING 4D ULTRASOUND IMAGING TO QUANTIFY ARTERIAL WALL PROPERTIES IN VIVO

Christopher Blase (1,2), Andreas Wittek (1), Achim Hegner (1), Wojciech Derwich (3), Armin Huß (1)

1. *Personalized Biomedical Engineering, Frankfurt University of Applied Sciences, Germany; 2. Biosciences, Goethe University Frankfurt, Germany, 3. Vascular and Endovascular Surgery, University Hospital Frankfurt, Germany*

Introduction

The biomechanical properties of the cardiovascular system are an important factor for its physiological function as well as pathological changes. The in vivo analysis of the changing individual biomechan-ical properties is of special interest for a better un-desrstanding of the pathophysiology of the cardio-vascular system. Based on these findings, additional biomarkers for the diagnosis of cardiovascular dis-eases can be established.

The cyclic deformation of blood vessels, caused by the pulsatile activity of the heart, can be used to determine the elastic properties of blood vessels in vivo. This requires a high temporal resolution which is currently not available from most medical imag-ing modalities providing 3D data (MRI / CT). Ultra-sound imaging provides a high temporal resolution but has been limited to 2D data. Recently, time re-solved 3D ultrasound imaging (4D US) has become available. In combination with speckle tracking algorithms it provides full field deformation data of vascular walls. These data can be used to investigate the spatiotemporal deformation pattern of vascular walls and to determine their constitutive behavior in vivo [1].

Recent Advances

4D US imaging with wall motion tracking provides information on the deformation of vascular seg-ments of up to 8 cm length as motion functions of discrete areas of the arterial wall. These can be un-derstood as material points in a continuum mechan-ics sense and thus be used to calculate in plane strain for wall areas of 2 to 10 mm². Based on these data and diastolic and systolic blood pressure, we have developed a finite element updat-ing approach to determine the individual, non-linear, anisotropic elastic properties of arterial walls [2]. This approach was applied to identify the con-stitutive behavior of healthy and diseased aortic walls from non-invasive in vivo measurements [3].

In another approach, we have used the measured deformation data to calculate a linear approximation of the locally varying elastic properties of healthy and diseased aortic walls [4]. This approach is based on non-invasive measurements (4D US, pulse pres-sure) alone and does not require, e.g. homogenizing, assumptions.

Future directions

We have developed different approaches to charac-terize the elastic behavior of arterial walls, based on data which is available by non-invasive measure-ments. We are currently applying these methods to volunteers and patients with and without aortic an-eurysms, to find caracteristic changes in the elastic properties and ther spatial variation which correlate with the progression of the disease.
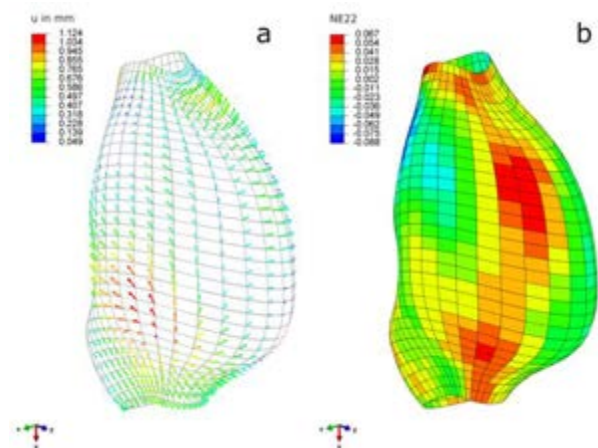
Figure 1: Processing of 4D US data. Diastolic-systolic dis-placements plotted on the diastolic geometry (a) and derived circumferential strain field (b) from an aneurysmal segment (diameter 48 mm, length 65 mm).

References

1. Karatolios, Wittek et al., Ann Thorac Surg, 96:1664–1671, 2013.
2. Wittek et al., JMBBM, 27:167–83, 2013.
3. Wittek et al., JMBBM, 58:122-138, 2016.
4. Wittek, et al., Z Angew Math Mech, 98:2275-2294, 2018.

AAA MECHANICS DURING ULTRASOUND PROCEDURES: A PATIENT-SPECIFIC COMPUTATIONAL STUDY

Marta I. Bracco (1, 2), Marco E. Biancolini (2), Laurence Rouet (3), Stephane Avril (1)

1. Mines Saint-Étienne, Univ Lyon, Univ Jean Monnet, INSERM, France; 2. Department of Enterprise Engineering, University of Rome Tor Vergata, Italy; 3. Philips Research, France.

Introduction

In current clinical practice, 2D ultrasound imaging (2D-US) is the first choice for abdominal aortic aneurysm (AAA) patients' follow-up. Abdominal US is commonly used to assess the maximum antero-posterior (AP) AAA diameter with a semi-standardized procedure. Possible advanced application of (time-resolved) 2D-US consists in assessing the stiffness of the aortic wall under pulsatile blood pressure through strain quantification [1]. However, mechanical models of AAA rarely take into account the surrounding tissues [2, 3]. Moreover, existing literature pays little attention to the effect of the pressure exerted on the patient by the operator during abdominal US scans. Previous attempts to quantify the inter-operator variability in transducer push resulted in very large ranges [4].

Our goal is to evaluate how significantly 2D-US probe pressure affects AAA morphology and mechanics via finite element models.

Methods

A 3D finite-element model of patient-specific AAA, spine and intra-abdominal tissues was developed via the following steps: semi-automatic segmentation of a CT scan, surface smoothing and meshing.

The surface mesh of the AAA, considered as the diastolic configuration, was subsequently imported in the ABAQUS/CAE software. The behavior of the AAA wall was linearized across the physiological pressure range, as shown in [5], with a Young's modulus of 1 MPa and a Poisson ratio of 0.495. A pressure of 5kPa, corresponding to the pressure increase between diastole and systole in a cardiac cycle, was applied to the inner walls of the AAA. To include the effect of surrounding tissues, the segmented volume of the abdominal soft tissues was meshed and modelled as a homogeneous hyperelastic material (shear modulus of 20 MPa, as in [2]). In addition, a portion of the spine was included and modelled as linear elastic material (Young's modulus of 17 GPa and Poisson's ratio of 0.3). Contacts were modelled as tie constraints and the spine and AAA extremities were fixed to complete the FEM model, comprised of 465287 elements and 380362 nodes (Figure 1.A). The output strains and diameter changes were evaluated on a plausible scanning plane (i.e. the maximum AP diameter plane) at the peak systolic pressure without and with US probe pressure. The US probe was simulated as an external pressure of 5 kPa (taken from [4]) applied on a rectangular area (17 mm x 34 mm) of the patient abdomen based on the US probe geometry and the scanning plane position.

Results

In Figure 1, maximum principal strains computed for the model without (1.B) and with probe pressure (1.C) are mapped onto the initial (dotted) and deformed (solid) cut views. From the initial to the deformed configuration, the AP diameter increased by 1.47%, and 0.63% respectively.
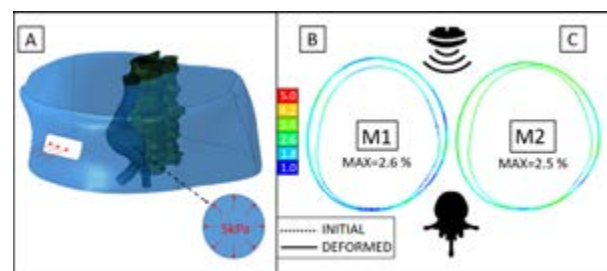
Figure 1: Complete FEM model (A). Strain maps (max principal) due to internal pressure only (B) and with the added probe pressure (C). Deformation scale factor is set to 5 for better visualization.

Discussion

This work shows the impact of including ultrasound probe pressure in patient-specific structural simulations of AAA wall under pulsating blood pressure. Previous studies focused on deriving AAA mechanical properties from images without taking into account the complexity of the mechanical environment [1]. Our results show that a structural model complete of surrounding tissues allows to capture the effect of a probe pressure: the maximum strain is located in the anterior wall and the AP diameter experiences a diminished expansion that is compensated by a lateral dilation.

The presented results suggest that probe pressure can significantly influence the AAA biomechanical environment during a US scan. The next steps will focus on including more realistic material models, loads, and boundary conditions in our model.

References

1. Mix et al, Ultrasound Med Biol, 43:2372-2394, 2017.
2. Petterson et al, J Biomech, 85:126-133, 2019.
3. Moireau et al, Biomech Model Mechanobiol, 11:1-18, 2012
4. Svendsen et al, Ultrasonics, 116:106484, 2021.
5. Zelaya et al, PLoS One, 9:101353, 2014.

Acknowledgements

MONITORING MECHANICAL AND GEOMETRICAL PROGRESSION OF ABDOMINAL AORTIC ANEURYSMS USING 3D+T ULTRASOUND

Esther Maas (1,2), Arjet Nievergeld (1,2), Judith Fonken (1,2), Mirunalini Thirugnanasambandam (1), Marc van Sambeek (1,2), Richard Lopata (1)

1. *Eindhoven University of Technology, Netherlands; 2. Catharina Hospital Eindhoven, Netherlands*

Introduction

In current clinical practice, the rupture risk of an abdominal aortic aneurysm (AAA) is assessed from its maximal diameter. Previous research has shown the added value of other parameters in estimating the rupture risk, such as AAA volume, curvature and elasticity [1-3]. These studies were typically based on computed tomography (CT) imaging, which is unsuitable for longitudinal studies because of the use of radiation and nephrotoxic contrast. Therefore, this study focusses on the use of time-resolved 3D ultrasound (3D+t US) imaging, which provides the complete geometry of the AAA during the cardiac cycle, in a non-invasive and inexpensive way. The goal of this study is to monitor the progression of geometrical and mechanical AAA parameters during the growth of the AAA, using 3D+t US.

Methods

For 22 AAA patients, 3D+t US images were acquired while the blood pressure was measured with an arm cuff. The AAA wall was automatically segmented on each time frame of the US images using an adaptation of a Star-Kalman algorithm. A centerline was created using a Dijkstra shortest path algorithm. The segmentations were resampled to obtain slices perpendicular to the centerline, from which the maximal diameter (D_{max}) of the time-average geometry was determined. The point-wise curvature of the aortic inner wall was determined with a finite differences approach, from which the median value was taken. Furthermore, the elasticity (Ep) of the aortic wall was determined from the systolic and diastolic diameter (D_{sys} and D_{dia}) and the pulse pressure (Δp):

$$Ep = \frac{133.3 \cdot \Delta p}{(D_{sys} - D_{dia})/D_{dia}} \qquad (1)$$

Box-and-whisker plots of the elasticity were created for different D_{max} groups, and groups were compared with a Wilcoxon rank sum test. Furthermore, linear regression between D_{max} and curvature was studied, in which differences between slow (<3mm/y) and fast-growing AAAs (>3mm/y) were investigated.

Results

An example of a segmentation on the ultrasound data is given in Fig 1a, showing good correspondence with the image features. In Fig 1b, the elasticity is shown for the different diameter groups, showing a difference between the smallest aneurysms and the other groups (p=0.016

for medium and p=0.029 large AAAs). Fig 2 shows (a) the spreading in growth rates and (b) a negative correlation between D_{max} and the curvature (R^2 =0.73, p<0.01), with no clear relation to the growth rate.
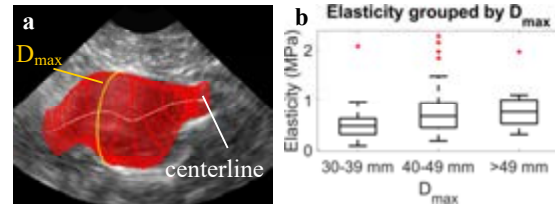
Figure 1a: Geometry plotted on the ultrasound data. b: Box-and-whiskers plots of elasticity grouped by D_{max}.
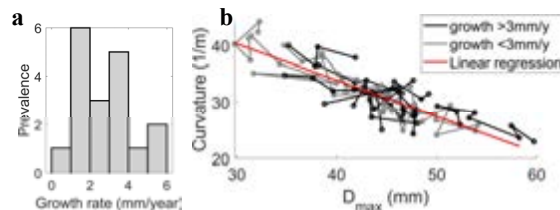
Figure 2a: Growth rates for the different patients. b: Relation between D_{max} and curvature. Datapoints of the same patient are connected.

Discussion

A tool to automatically determine the maximal diameter, curvature, and elasticity of a AAA from a 3D+t US image has been developed. With this, a positive correlation between D_{max} and Ep was found, which corresponds to previous research [4]. Furthermore, a decrease in curvature with the progression of D_{max} is shown, which can be explained by the AAA growing in all directions. Next steps are analyses of aortic wall stresses, AAA volume and thrombus volume, for which in-house tools are available. The promising results show the feasibility of our tool to monitor mechanical and geometrical AAA parameters in a longitudinal study, to relate these parameters to growth and rupture risk.

References

1. Lindquist Liljeqvist et al, *J Vasc Surg*, 63:1434-1442, 2016.
2. Lee et al., *Ann Biomed Eng*, 41:562-576, 2013.
3. Wilson et al., *J Vasc Surg*, 37:112-117, 2003.
4. Wilson et al, *Eur J Vasc Endovasc Surg*, 15:472:477, 1998.

Acknowledgements

US-BASED VOLUME-TIME CURVES OF THE AAA FOR ESTIMATING IN-VIVO THROMBUS COMPRESSIBILITY AND WALL STIFFNESS

Arjet Nievergeld (1,2), Esther Maas (1,2), Judith Fonken (1,2), Marc van Sambeek (1,2), Frans van de Vosse (1), Richard Lopata (1)

1.   *Eindhoven University of Technology, Netherlands; 2. Catharina Hospital Eindhoven, Netherlands*

Introduction

Rupture risk of abdominal aortic aneurysms (AAAs) is currently estimated based on the maximum diameter, which has been proven to be a non-optimal criterion [1]. Biomechanical models can improve rupture risk prediction using patient-specific geometries obtained from imaging modalities such as computed tomography (CT) and ultrasound (US). US is safe, cheap and adds temporal information for mechanical characterization. Previous studies have shown that intraluminal thrombus (ILT) affects the rupture risk [2], and should therefore be included in rupture risk assessment. Imaging ILT using US is challenging, due to the limited contrast between lumen and thrombus. In this study, we investigate the feasibility of US-based mechanical characterization of both the thrombus and AAA vessel wall.

Methods

The US images of 10 AAA patients (volume rate 4-8 Hz) were acquired in the Catharina Hospital Eindhoven. After the US exam, the brachial blood pressure was measured. The thrombus and vessel wall geometries were segmented using an in-house developed fully automatic segmentation algorithm, which was validated using CT. The segmentations of the lumen and inner vessel wall were used to determine the volume-time curves. The systolic and diastolic thrombus volumes ($V_{ILT,sys}$ and $V_{ILT,dia}$) were used to calculate the in-vivo relative thrombus volume change during the cardiac cycle. The shear modulus (G) was calculated using equation 1, with the Finger strain (ε_F) and the diastolic and systolic circumferential stress (σ_{dia} and σ_{sys}), calculated using Laplace's law.

$$G = \frac{(\sigma_{sys} - \sigma_{dia})}{2 \cdot \varepsilon_F} \qquad (1)$$

Results

Figure 1 shows an example of an US image with the difference between the systolic and diastolic geometry of both lumen and vessel wall in blue.
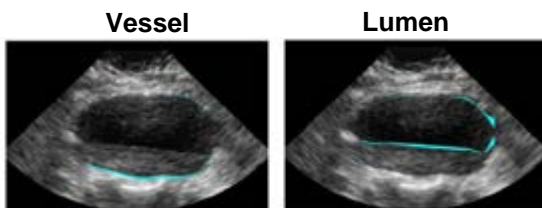
Figure 1: US images with displacements of the lumen and vessel between diastole and systole

Figure 2 shows an example of the volume-time curves. The volume-time curves for the lumen and vessel show a clear pulsatility. However, for the thrombus volume no clear pulsation is seen.
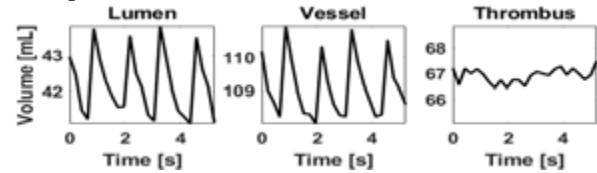
Figure 2: Volume-time curves of the lumen, total artery, and intraluminal thrombus.

The thrombus volume change (Figure 3) for all patients has a median of 0.4 %, with an IQR of 1.5%. The median shear modulus of the vessel wall is 1.12 MPa, with an IQR of 0.8 MPa (Figure 3).
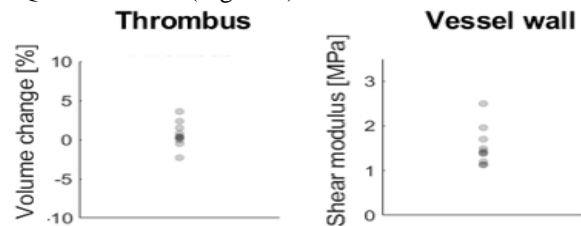
Figure 3: Compressibility of the thrombus and shear modulus of the vessel for 10 AAA patients

Discussion

The pulsatility in the volume-time curves show feasibility for mechanical characterization. The thrombus volume change was comparable to the ones of Kontopodis on ECG-gated CT (median 0.4% , IQR 3), showing that the assumption of incompressibility is valid[3]. The stiffness found in this study is higher compared to the ones in van Disseldorp et al [4] (median 1.1 MPA, IQR 0.7-1.4). Those deviations might be explained by the assumptions in Laplace's law. Future research will focus on thrombus and vessel wall stiffness estimation using inverse FEA. The patient-specific geometry in combination with the patient-specific stiffness of both thrombus and vessel wall can ultimately be used for FE-based stress analysis for more accurate, patient-specific rupture risk prediction.

References

1. vande Geest et al. Annals of Biomedical Engineering, 34(7):1098-1106, 2006
2. Riveros et al. Ann Biomed Eng. 43(9):2253-6, 2015
3. Kontopodis, et al. EJVES Extra, 26(1):e4–e6,2013
4. van Disseldorp et al., JVES, 52(5):635-642, 2016

MECHANICAL CHARACTERIZATION OF ABDOMINAL AORTIC ANEURYSMS USING 4D ULTRASOUND AND VIRTUAL FIELDS METHOD

Mirunalini Thirugnanasambandam (1), Esther J Maas (1,2), Arjet HM Nievergeld (1,2), Marc RHM van Sambeek (1,2), Stephane Avril (3), Richard Lopata (1)

1. Eindhoven University of Technology, The Netherlands.
2. Catharina Hospital Eindhoven, The Netherlands. 3. Mines Saint-Étienne, France.

Introduction

To reduce the uncertainties associated with estimating biomechanical rupture risk indices of abdominal aortic aneurysms (AAAs), it is crucial to first evaluate their personalized mechanical properties. The main aim of this study is to identify the constitutive material parameters of AAAs *in vivo* using a novel combination of 4D ultrasound (4D US) and a modified virtual fields method (mVFM). Traditional VFM is used to identify unknown material parameters from experimental full-field deformation data [1] by applying the principle of virtual work to a parametric stress field. Since the stress components depend on the constitutive parameters at any point, it is possible to derive a system of scalar equations of the material parameters, which can be solved to evaluate the constitutive model parameters. In this study, instead of full-field deformation data, we use the 3D deformation field derived from 4D-US images of AAAs as input to mVFM.

Methods

4D-US images of a AAA patient were recorded in a supine position during multiple heartbeats at an acquisition rate of 4-8 volumes per second. The US image volumes were segmented in the end diastolic phase. The inner wall and outer wall were tracked over the cardiac cycle using a 3D speckle tracking algorithm [2], and the 3D wall displacement between the diastolic and systolic phases was evaluated as shown in Figure 1. A tetrahedral finite element mesh was generated using the diastolic geometry of the AAA wall. The displacement vector of each node in the mesh was evaluated based on weighted linear interpolation of the displacement vectors of their innerwall and outerwall neighbors. The deformation field was smoothed using an unsupervised discretized spline smoother.

The modified VFM (mVFM) combines the iterative nature of the well-known finite-element model updating (FEMU) technique [2] with a virtual work – based cost function of the traditional VFM. For the implementation of mVFM, two different models of FEA were simulated: (1) Strains were evaluated using the current configuration, where the displacement of each node was solely prescribed based on 3D tracking data derived from US; (2) The virtual fields were derived using a stressed intermediate configuration, where an intraluminal pressure corresponding to the deformation field was applied, an initial guess for the material parameter was provided, and displacements were
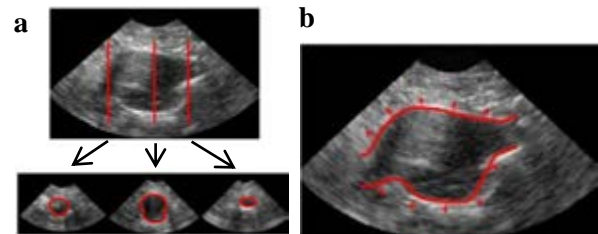
Figure 1a: Automatic segmentation of the US images. b: Speckle tracking of the AAA inner wall

prescribed in every boundary where tractions were unknown.

Results & Discussion

An uncoupled Neo-Hookean model (Mooney-Rivlin formulation with $c_{01} = 0$) was used to describe the material behavior. An initial guess of $c_{10} = 1.24 \cdot 10^6$ Pa was used in the implementation of mVFM. By iteratively minimizing the deviation from the principle of virtual work, c_{10} prediction values converged within 5 to 6 iterations as shown in Figure 2.
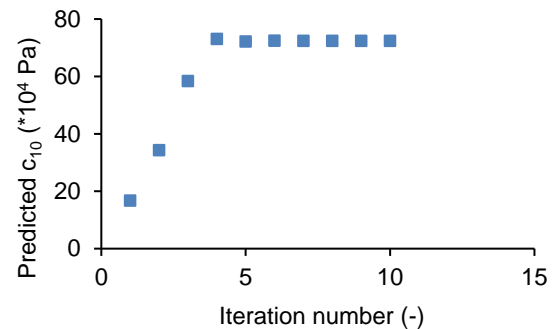
Figure 2: Iterative process for the prediction of c_{10}

Thus, mVFM has allowed us to harvest the advantages of both these methods: (1) setting up the iterative problem automatically based on FEMU, and (2) achieving quick convergence based on VFM. We were able to demonstrate, for the first time, the feasibility of evaluating unknown constitutive model parameters of AAAs using a novel combination of 4D US and mVFM. As the next step, regional variation in material properties will be captured using mVFM.

References

1. Mei Y et al. J Elast, **145**, 265-194 (2021).
2. van Disseldorp EMJ et al. *Eur. Heart J.* **20(2)**, 185-191 (2019).

NOVEL BIODEGRADABLE CAROTID GRAFT: EXPERIMENTAL ASSESSMENT THROUGH AN ANIMAL TRIAL

Amber Hendrickx[1], Milad Ghasemi[2], Thibault Vervenne[2], Tom Langenaeken[1], Hannah Bauer[3], Heleen Fehervary[2], Martijn Cox[3], Piet Claus[4], Filip Rega[1], Nele Famaey[2], Bart Meuris[1]

1. Department of Cardiac Surgery, KU Leuven, Belgium; 2. Department of Mechanical Engineering, KU Leuven, Belgium; 3. Xeltis BV Research and Development, Eindhoven, The Netherlands; 4. Cardiovascular Imaging and Dynamics, KU Leuven, Belgium

Introduction

Cardiovascular disease is a leading cause of death worldwide. Bioresorbable polymeric scaffolds have already shown great promise in treatment of valvular and arterial related diseases [1]. However, there is a lack of information on how scaffold (micro)structure and its surrounding mechanical conditions drive the process of scaffold degradation and endogenous tissue restoration (ETR) *in vivo*. We hypothesized that scaffold characteristics, such as wall thickness and fiber distribution would influence the scaffold degradation and ETR process. Therefore, we examined two designs of a novel polymeric electro-spun scaffold, with different wall thicknesses. The information obtained by this research can inform computational models that simulate the ETR process. This can enable a simulation-based design optimization of the scaffolds in terms of maximizing the biocompatibility and long-term performance of the scaffolds.

Methods

Animal trials: the animal experiments were approved by the Animal Ethics Committee of the KU Leuven (093/2020), similar to [2]. Unilateral carotid interposition scaffolds were implanted in fourteen 1-year old Swifter sheep at the animal facility of KU Leuven (Fig. 1A). Preoperatively, the blood pressure and carotid axial prestretch were measured. After a six month follow-up, the animals were sacrificed and the explants were harvested.
Imaging: ultrasound images and magnetic resonance images (MRIs) were collected at different timepoints, both pre- and postoperatively.
Microstructural analysis: scanning electron microscopic (SEM) images were obtained from the explanted scaffold. Histological analysis, using different stainings was performed to characterize the constituents of the restored tissue.
Mechanical analysis: planar biaxal and ring extension experiments were conducted on native carotid arteries and explanted scaffolds.

Results

Five animals needed to be sacrificed early because of insufficient flow on echo and/or wound problems. The other animals (3 already explanted, 6 still in follow-up) remained well. Fig 1B illustrates one explant with the restored tissue after 6 months. Figure 1C indicates an SEM image from an early explant (8 days post implantation). Here, the restored cells and scaffold can be visualized. Figure 1D represents a histological image with H&E staining (8 days post implantation). Cellular infiltration was observed throughout the scaffold. The follow-up ultrasound and MRI imaging were also performed (not shown).
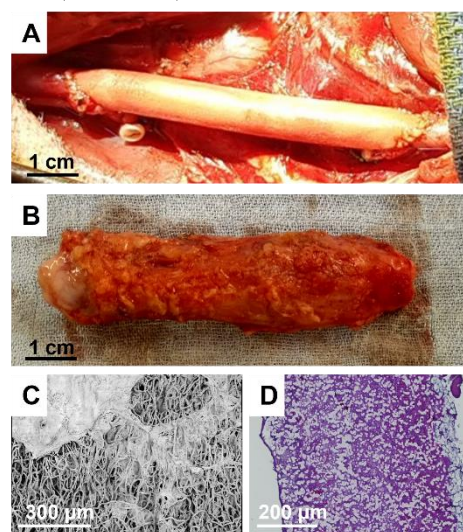
Figure 1: A) implanted scaffold, B) explanted scaffold 6 months after implantation, C) SEM image of an explanted scaffold (8 days post implantation), D) histological image with H&E staining (8 days post implantation).

Discussion

Preliminary histological and SEM data indicate that tissue restoration is initiated already after 8 days of implantation. Ultrasound and MRI imaging are being performed and 6 months data will be available at the time of conference. The preliminary results of ultrasound and MRI imaging show that wall thickness may play an important role in scaffold behavior and could consequently have an important influence on the ETR and scaffold degradation. The results of the histological analysis and mechanical tests will provide more information regarding the influence of the scaffold microstructure and mechanical properties on the ETR and scaffold degradation process, and will be used in future work to inform computational models.

References

1. Prodan et al., Seminars in Thoracic and Cardiovascular Surgery, WB Saunders, 2021.
2. Vanderveken et al., Scientific reports 10, no. 1, 1-12 , 2020.

QUANTITATIVE PHASE MICROSCOPY-BASED CELL VISCOELASTICITY MEASUREMENT BY SHEAR STRESS

Jaromir Gumulec (1), Tomas Vicar (1,2), Jiri Chmelik (2), Jiri Navratil (1), Jan Balvan (1), Radim Kolar (2), Larisa Chmelikova (2), Vratislav Cmiel (2), Michal Masarik (1)

1. Masaryk University, Faculty of Medicine, dept. of Pathological Physiology, Czech Republic;
2. Department of Biomedical Engineering, Faculty of Electrical Engineering and Communications, Brno University of Technology, Czech Republic.

Introduction

Mechanical properties of cancer cells are linked to disease aggressiveness and patient prognosis; measuring cancer cell viscoelasticity is therefore potentially attractive from a perspective of a clinical setting. However, live-cell mechanophenotypisation assays are often limited by low throughput, unphysiological levels of stress, or the necessity of highly expert operators. We describe a quantitative phase microscopy-based approach for shear modulus estimation based on [1]. The system employs a deconvolution-based approach to minimize the influence of the fluidic system and an approach with two perfusion media with different refractive indexes to estimate cell height, a parameter needed for modulus calculation.

Methods

The system consists of a holographic microscope Q-PHASE (Telight), syringe pump as a flow source, shear stress-optimised sample chamber and flow meter, components are connected with PTFE tubing. Two syringes with media of different RIs are connected to the cell chamber, and image $\phi 1(x, y)$ with the first medium with RI $nm1$ and image $\phi 2(x, y)$ with the second medium with RI $nm2$ is measured, the cell height $d(x, y)$ is calculated (described in detail in [2]):

$$d(x,y) = \frac{\lambda(\phi_2(x,y) - \phi_1(x,y))}{2\pi(n_{m1} - n_{m2})} \qquad (1)$$

Consequently, shear strain is calculated from the centre of mass changes in direction of the flow dY(t) and cell height L_{cell}: $\gamma(t) = dY(t)/L_{cell}$ and the whole analysis is shown in figure Fig. 1. Viscoelastic parameters are calculated using a Kelvin-Voight (KV) model. Because the generated flow is distorted by the flow system, the impulse response is not square. The convolution model we describe in [3] enables us to formulate a simple cost function for estimation of the parameters of KV model using a suitable optimization method.

Results

The system was tested on cancer cells of known Young modulus (Fig. 1) and using cytoskeleton-targeting drugs. We determined the cells differ in a stress-strain response and we extracted viscoelastic parameters using parametric deconvolution. The shear modulus of cells was roughly 9fold lower compared to Young modulus determined by AFM and both methods demonstrated to be linearly dependent. The system furthermore enables to study of dynamic processes like actin cytoskeleton recovery after cytochalasin washout. Shear modulus normalisation is observable within 15 min, following actin recovery.
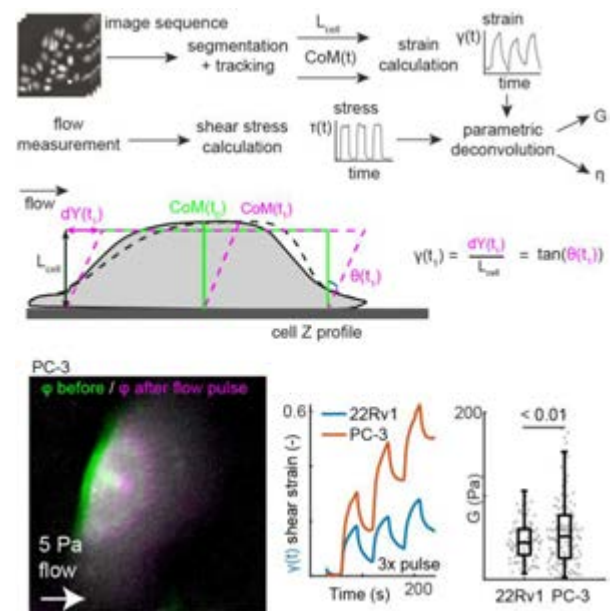
Figure 1: block diagram, calculation of Center of Mass (CoM) and stress/strain response in cancer cell lines.

Discussion

In agreement with our previous study we observed identical trends in stiffness of cancer cell lines. Compared to AFM, this approach is easy to implement on a QPI microscope and enables to measure also refractive index and cell viscosity directly. Because viscosity is influenced by tubing and syringe used, parametric deconvolution is used, making the viscosity measurement independent of fluidics. Viscosity measurement can provide additional information that can be biologically interesting.

References

1. Eldridge, W. J. et al, Biophys J, 117:696–705, 2019
2. Vicar, T. et al, Annu Int Conf IEEE Eng Med Biol Soc, 2021:439-442.
3. Vicar, T. et al, bioRxiv, 2021.08.05.455201

PHOTO-SWITCHABLE BIO-INTERFACES FOR DYNAMIC CELL CULTURES

Francesca Mauro (1,2), Carlo Natale (2), Valeria Panzetta (1,2), Paolo Antonio Netti (1,2)

1. Department of Chemical, Materials and Industrial Production Engineering, University of Naples Federico II, Naples, Italy;

2. Center for Advanced Biomaterials for Healthcare@CRIB, Fondazione Istituto Italiano di Tecnologia, Naples, Italy

Introduction

Cellular microenvironment carries out a crucial role in affecting and dictating cellular functions thus influencing several biological processes such as morphogenesis, tissue regeneration and repair [1]. The bidirectional communication between cells and the extracellular matrix (ECM) occurs through the transmission of biochemical/biophysical signals at sub-micrometric level involving different sub-cellular component such as focal adhesions, cytoskeleton structures and the nucleus. Then a series of events can be activated, eventually affecting cellular fate [2,3]. Moreover, the ECM is a dynamic entity and its properties change during time (i.e. tissue growth, disease progression) representing a fundamental aspect that should be taken into account in order to design more reliable bio-interfaces able to impact cell function and behavior. The aim of this work is to realize a dynamic cell culturing platform, by exploiting the photo-switchable properties of azobenzene molecules, which allow to precisely modulate on demand surface topographic features both in space and time, in order to affect and guide cell response in terms of morphology, migration, proliferation and differentiation.

Methods

pDR1m was spin coated to realize a thin film on glass bottom petri dishes and a micrograting relief was inscribed by using a scanning confocal microscope with 514 nm wavelength and a time exposure of 30s. The removal of the impressed pattern was performed by using a mercury lamp with a rhodamine filter for 2 min. A JPK NanoWizard II was used to measure mechanical properties of living cells. MCF10A cells were grown in DMEM/F12 with 5% horse serum, glutamine and antibiotics. Cells were seeded on pDR1m substrates at 10^3 cells/cm² 24h before pattern inscription. Then, cells were fixed in paraformaldehyde 4% and immuno-stained for paxillin, nuclei and actin. FAs, cells and nuclei area, orientation and shape factor were measured by Fiji software. Nuclear volume was measured by Imaris software.

Results

The dynamic azopolymer platforms were realized to provide cyclic topographical signals to cells. The linear pattern inscription/removal was performed after giving the cells the time to adapt to the new environment.

Results showed the efficacy of the dynamic system to modulate cell and focal adhesions morphology such as area, elongation and orientation (Figure 1). Moreover, MCF10A cell nuclei were affected by the cyclic topographic signal presentation, with nuclear area, elongation and volume increasing from flat-to-pattern and decreasing after pattern-to-flat variations, resembling the flat condition. Finally, cell mechanical properties were influenced by the dynamic stimulus, showing an increase of the cell Young's modulus on pattern and a decrease on pattern-to-flat surfaces.
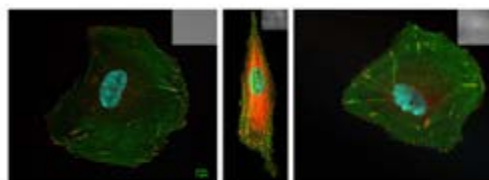
Figure 1: Fluorescence images of MCF10A cells labelled with phalloidin (actin, green), paxillin (FAs, red), Hoechst 33342 (nucleus, cyan) on flat, pattern and erased surfaces (left to right).

Discussion

Topographical signals are known to affect cell behavior at different levels, from adhesion to differentiation. Here, a dynamic photo-switchable platform was realized to transmit cyclic stimuli and to give precise instructions to cells thus controlling their functions, in terms of spreading, alignment, orientation, nuclear shape and volume, and mechanical properties. Indeed, the surface topography of the azopolymer film which undergoes flat-to-pattern-to-flat variation can transmit the cyclic signal to the cells and produce a cyclic cell behavior from cell-scale to submicron-scale.

Conclusion

The ability of azobenzene molecules to induce a reversible surface mass transport has led to the realization of a cell culturing platform for the investigation of cell behavior in a dynamic context. The transmission of specific instructions paves the way to the possibility to control and revert cell functions both in space and time.

References

1. M.Ventre et al, J. R. Soc. Interface (2012) 9, 2017–2032.
2. Frantx et al, J Cell Sci (2010) 123 (24): 4195–4200.
3. Cimmino et al, (2018) Front. Bioeng. Biotechnol. 6:190.

MECHANOREGULATION OF CRISPR/CAS9 MEDIATED BONE CELL REPORTER MICE UNDER CYCLIC MECHANICAL LOADING

Dilara Yilmaz* (1), Francisco C. Marques* (1), Esther Wehrle (1), Gisela A. Kuhn (1), Ralph Müller (1)

(1) Institute for Biomechanics, ETH Zurich, Zurich, Switzerland, *equal contribution

Introduction

Mechanical loading has been shown to significantly increase bone mass in mice. Indeed, osteoblasts and osteoclasts, the cells responsible for bone formation and resorption, respond to cues secreted by osteocytes embedded in the matrix, which assume a crucial role in governing bone mechanoregulation. To elucidate bone modeling processes at the cellular level, our lab has developed a transgenic reporter mouse (bone cell reporter, BCR) which enables identifying and characterizing single osteoblasts (*Ibsp-eGFP* knock-in) and osteoclasts (*TRAP-mCherry* knock-in) in their local *in vivo* mechanical environment. In this project, we explored if the response of BCR mice to mechanical loading is comparable to wildtype (WT) mice, making it a suitable model for subsequent mechanobiological studies.

Methods

At 12 weeks of age, BCR and WT female mice were pinned at 5th and 7th vertebra and 3 weeks later, loading of the 6th caudal vertebra (CV6) was performed for 5 min, 3000 cycles, 10 Hz frequency, 3 days/week for 4 weeks (n=9-10 mice/group). Images were acquired weekly using *in vivo* micro-CT (vivaCT 80, voxel size 10.5 µm). Micro-finite element simulations [1] were performed to compute the effective strain (EFF) distribution in the samples (Young's Modulus: 14.8GPa; Poisson's ratio: 0.3). Mechanoregulation was quantified comparing conditional probability curves and percent differences for mean EFF among the different remodeling regions (formation, resorption, quiescence) [2]. Immunostaining of TAZ, a key mechanoregulator of bone [3], was used to assess mechanosensitivity in 30-µm-thick sections using 3D confocal microscopy (n=3 mice/group). Statistical differences in mechanoregulation data were computed with one-way ANOVA with Dunnett posthoc test for the *in vivo* data and an unpaired t-test for comparison of histological data.

Results

Since the first week of loading, mean EFF at formation sites was higher (not significant) compared to quiescent sites for both BCR and WT mice and lower (mostly significant) for resorption sites (Fig. 1 A-B). A similar EFF distribution between remodeling clusters was visible in the corresponding conditional probability curves. TAZ immunostaining demonstrated higher expression in the loaded (8N) group compared to control (0N) for both BCR and WT mice (Fig. 1 C) and the expression was predominantly observed around resorption cavities. Consistent with immunostaining results, quantification of TAZ intensity accentuated the significantly higher expression of TAZ in loaded mice compared to controls (Fig. 1 D).
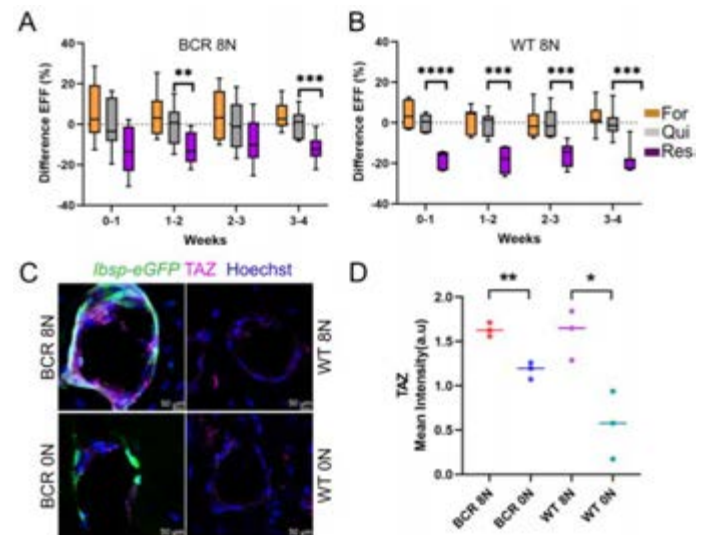
Figure 1: A-B) Mean EFF at formation, quiescent and resorption sites expressed as percentage differences from BCR and WT mice for 8N group. C) Representative images showing endogenous signals of osteoblasts (Ibsp-eGFP), stained Hoechst (nuclear, blue) and TAZ (purple) in BCR and WT mice for 8N and 0N groups. D) Mean intensity (a.u.) of TAZ signals of BCR and WT mice for 8N and 0N groups. Scale bars: 50 µm. *p<0.05, **p<0.001, ***p<0.0001.

Discussion

Our results indicate that BCR mice have a similar response to mechanical loading as WT mice given the similarities in the mechanoregulation analysis and the significant upregulation of TAZ expression between the 8N and 0N loading groups. Additionally, BCR mice allow identifying single osteoblasts and osteoclasts through their fluorescent reporters in native bone. Ultimately, BCR mice can provide valuable insights toward the investigation of bone adaptation and mechanoregulation in the local *in vivo* environment.

References

1. Webster et al., Comput Methods Biomech Biomed Engin, 11(5), 435-441, 2008.
2. Schulte et al., PLoS One, 8(4), e62172, 2013.
3. Kegelman et al., FASEB J, 32(5), 2706-2721, 2018.

Acknowledgments

PERFORMANCE OF LINEAR AND NONLINEAR APPROACHES IN TRACTION FORCE MICROSCOPY FOR COLLAGEN HYDROGELS

A. Apolinar-Fernández (1), J. Barrasa-Fano (2), M. Cóndor (2), H. Van Oosterwyck (2,3), J.A. Sanz-Herrera (1)

1. Escuela Técnica Superior de Ingeniería, Universidad de Sevilla, Spain; 2. Biomechanics section, Department of Mechanical Engineering, KU Leuven, Belgium; 3. Prometheus division of Skeletal Tissue Engineering, KU Leuven, Belgium

INTRODUCTION

Traction Force Microscopy (TFM) constitutes a mixed experimental-computational methodology which allows to estimate forces acting on the surface of cells due to mechanical interaction with the surrounding environment (ECM) during processes like cell adhesion or migration. Taking advantage of available microscopic techniques, measurement of displacements within hydrogels (that mimic the ECM) can be performed. Then, by using an adequate hydrogel's constitutive law cell tractions can be reconstructed. While the accuracy of TFM cellular force reconstruction is crucial to provide precise insight into cell mechanics and its potential role in the development of certain pathologies, many aspects of the methodology remain still unclear. Particularly, the evaluation of the applicability of employing a linear approach in cell traction field reconstruction, due to its simplicity and low computational cost, may be of interest especially when elaborate constitutive hyperelastic laws are to be numerically implemented for nonlinear matrices.

METHODS

TFM can be carried out through two distinct fundamental approaches: the forward method, and the inverse method. The forward method is employed for computation of cell tractions directly from measured displacements through the selected constitutive law for the hydrogel. The inverse method searches for a new displacement field that closely resembles the measured one within a minimization procedure that follows a regularization strategy. Then, tractions are computed from the new displacement field through the constitutive law. Previously, we developed a novel inverse method that enforces the new displacement field to satisfy force equilibrium within the hydrogel [1]. The results provided by our inverse method significantly outperform those produced by the forward method on both linear and nonlinear hydrogels [1,2]. The aim of this study is to present a comprehensive assessment of the accuracy of traction reconstruction with respect to important challenges in 3D TFM, by using synthetically generated (control) ground truth solutions as a reference for comparison purposes. TFM accuracy, via the definition of a specific error indicator, is evaluated in a set of real scenarios such as: mechanical nature of the hydrogel (linear or nonlinear), cell morphology, level of strain achieved within the hydrogel for different cellular pulling forces, and the feasibility of considering a linear material behaviour for collagen in traction recovery. The nonlinear hyperelastic model selected for implementation considers the fibrillar microstructure of collagen hydrogels [3] and was calibrated with shear rheology tests.

RESULTS
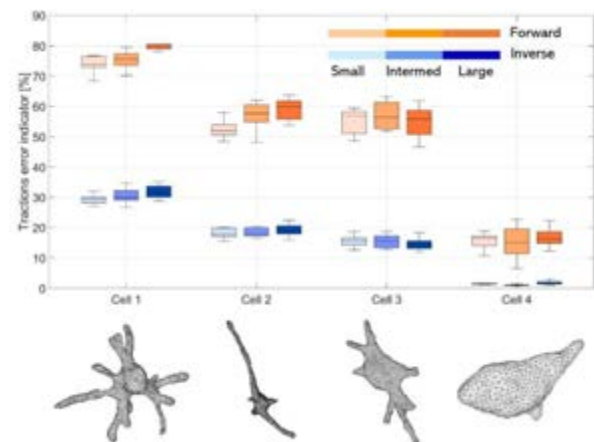
Figure 1: Error of reconstructed tractions solution assuming a linear behaviour of the collagen matrix versus ground truth solution of the considered nonlinear matrix in forward and inverse methods. Small, intermediate and large cellular pulling force cases.

DISCUSSION

The main conclusions to be drawn from the study are the following: (i) cell traction reconstruction becomes more challenging for complex (non-spherical) cell geometries that exhibit multiple large protrusions. (ii) cellular pulling force magnitude does not significantly impact on the accuracy of traction reconstruction. (iii) linear modelling constitutes a poor assumption when compared its performance with that of a nonlinear model that accurately represents the real mechanical nature of the synthetic collagen matrices considered in this paper. This knowledge may be useful to properly design TFM in vitro experiments, and to further investigate new methods and models in mechanobiology.

REFERENCES

1. J.A. Sanz-Herrera *et al*, Soft Matter, 17:10210-10222, 2021.
2. J. Barrasa-Fano *et al*, Acta Biomaterialia, 126:326-338, 2021.
3. J. Steinwachs *et al*, Nature Methods, 13:171–176, 2016.

THEORETICAL AND EXPERIMENTAL MODELLING OF STRESS-DEPENDENT CELL AND TUMOUR GROWTH

Bobby Huxford (1), Vatsal Kumar (1), Laoise McNamara (1), Eoin McEvoy (1)

1. *Discipline of Biomedical Engineering, National University of Ireland Galway, Ireland*

Introduction

Tumour growth is a force-sensitive process, regulated in part by mechanical feedback from surrounding tissue (1). Such mechano-responsiveness can govern tissue-specific risk and progression of cancer, ultimately impacting disease outcomes. However, the underlying biomechanisms by which mechanical loading influences cellular growth and proliferation have not yet been uncovered. In this study, we propose a joint theoretical-experimental framework to determine how the feedback between growth, mechanical loading, and cell-cell exchange flow could restrict tumour cell proliferation.

Methods

Model development: Cell size is regulated by an interplay between energy-consuming pumps, mechanosensitive ion channels, actomyosin tension, and cytosolic proteins that coordinate to manipulate cellular osmolarity and subsequently cell volume V (2, 3). Growth induced by electro-osmotic fluxes of multiple permeable ion species $dc_i(\phi)/dt$ can be driven by impermeable solute (protein) synthesis dX/dt and deviations in membrane potential ϕ, such that the osmotic pressure difference across the cell membrane is given by $\Delta\Pi = RT(\sum \Delta c_i + X/V)$. Assuming a membrane water permeability $L_{p,m}$, single cell growth may be written as $dV/dt = -L_{p,m}(\Delta P - \Delta\Pi)$, where the hydrostatic pressure difference ΔP depends on active cell stress and external mechanical loading. With further consideration of convective and diffusive solute flow between connected cells, we aim to quantify the external pressure p_o required to inhibit cell division by restricting growth below a critical mitotic volume V_{crit} (Fig 1A).

Experimental methods: Hydrogels of varying stiffness (0.58-1.1 kPa) were generated by crosslinking gelatin with transglutaminase. 4T1 mammary carcinoma cells were encapsulated within hydrogels and after 7 days we quantified tumour spheroid size and cell number (DNA).

Computational analysis: A continuum model was developed using *user-defined material subroutines* within Finite Element (FE) software Abaqus to predict tumour cell (c_t) proliferation as dependent on spheroid stress $\boldsymbol{\sigma}$ induced by matrix deformation:

$$\frac{dc_t}{dt} = \left(\frac{c_t}{\tau_t}\right)\left(1 - \frac{\text{tr}(\boldsymbol{\sigma})}{3p_o}\right), \qquad (1)$$

where τ_t is the timescale for tumour proliferation in the absence of other factors. To simulate growth we adopted a multiplicative decomposition of the deformation gradient $\mathbf{F}$ into $\mathbf{F_g}$ (growth tensor) and $\mathbf{F_e}$ (elastic tensor) (4, 5), such that $\mathbf{F} = \mathbf{F_e}\mathbf{F_g}$. Here $\mathbf{F_g} = \lambda_g\mathbf{I}$, where $\lambda_g = c_t/c_o$ is the growth stretch, $\mathbf{I}$ is the second order identity tensor and c_o is the initial number of cells in a spheroid.

Results and Discussion

Our model predictions for electro-osmotic control of division suggests that synthesis during the cell cycle reduces membrane potential and increases cytosolic osmotic pressure to drive cell growth. Simulations indicate that compressive loading and exchange flow through gap junctions in connected cells can restrict osmotically-regulated cell growth and subsequently limit the potential for a cell to surpass the size checkpoint for division (Fig 1B). Our experiments of tumour spheroid growth in hydrogel indeed show that spheroid size reduces with increasing hydrogel stiffness (Fig 2C) and our associated simulations can characterize the stress-dependence of growth using a mechano-sensitive formulation (Fig 2D-E). These results provide new insight into the stress-dependent nature of cell and tumour growth, with broad applications to patient-specific cancer diagnosis and tissue engineering.
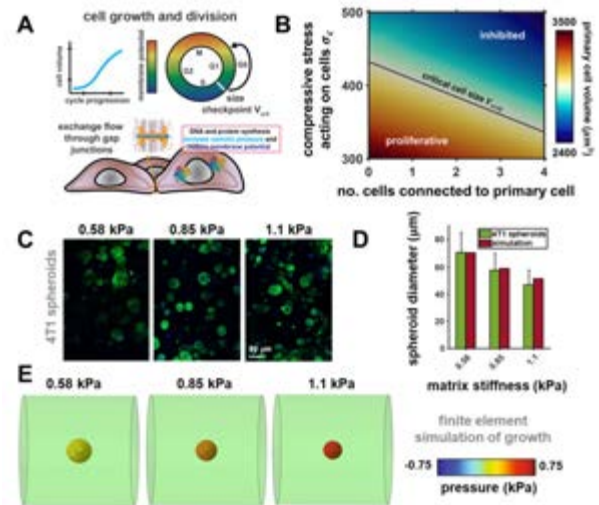
Figure 1: (A) Cells increase in volume and reduce membrane potential during their cycle; (B) Model predictions for cell growth suggest that mitosis can be restricted by stress and cell-cell contact; (C-E) 4T1 spheroid growth can be mechanically controlled by hydrogel stiffness in agreement with model predictions.

References

1. M. Kalli and T. Stylianopoulos. *Front. Oncol.* **8**, 55 (2018).
2. E. McEvoy et al. *Nat. Commun.* **11**, 1–11 (2020).
3. F. Yellin, *et al. Biophys. J.* **114**, 2231–2242 (2018).
4. E. K. Rodriguez et al. *J. Biomech.* **27**, 455–467 (1994).
5. D. Ambrosi et al. *J Elasticity* **129** (2017).

Acknowledgements

CREEP BEHAVIOR OF INDIVIDUAL COLLAGEN FIBRILS IN TENSION IS DEPENDENT ON CROSS-LINKING

Mathis Nalbach (1), Naoki Motoi (2), Manuel Rufin (1), Orestis G. Andriotis (1), Georg Schitter (1), Philipp J. Thurner (1)

(1) TU Wien, Austria (2) Kobe University, Japan

Introduction

Collagen fibrils (CFs) are viscoelastic, nanoscale fibers that make up a large variety of tissues in our bodies and provide the biomechanical scaffold for cell attachment. Despite their major relevance for mechanical integrity and cell function, data on the time-dependent mechanical behavior of CFs is sparse. Currently, there is a debate as to which extent intermolecular cross-linking affects CF stiffness and molecular sliding – a mechanism speculated to be a major contributor to viscoelasticity[1,2]. Creep experiments on individual CFs would be an appropriate method to investigate molecular sliding. However, such experiments were not feasible to date, due to shortcomings in tensile testing methods. We recently developed a nano tensile testing instrument, the NanoTens[3], and implemented force-control enabling us to conduct creep experiments.

Methods
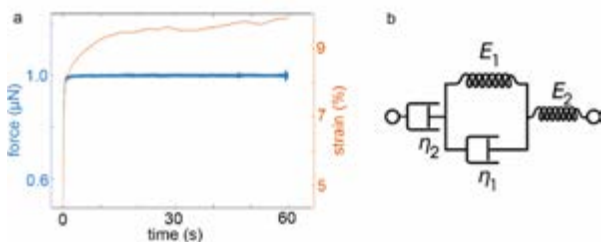
Fig. 1: Results of a creep experiment on an individual collagen fibril in tension (a). Force (blue) is held constant at 1 µN, while strain (red) is measured over time. The Burgers model in Kelvin-Voigt configuration (b) is fitted to the creep data.

CFs from mouse tail tendons were deposited on microscope slides and incubated in methylglyoxal (MGO) or control buffer for 4h at 37ºC in equal number. CFs were then prepared for tensile testing with the NanoTens by gluing to the substrate and application of magnetic beads. Tensile tests were conducted in PBS by lifting each magnetic bead along with the attached CF via magnetic tweezer and placing them in a microgripper mounted on a force probe. Force-control was achieved by feeding probe readout back into the system PI controller. Through this, force probe position is actuated such that force applied to the CFs is following a force setpoint. We applied force step-inputs to 0.5, 1.0 and 1.5 µN and held the force constant for 60s to all CFs, MGO cross-linked and control, while measuring strain. Through this, we conducted a creep experiment (Fig. 1 a). We fitted the Burgers model in Kelvin-Voigt (KV) configuration to the resulting strain, solving it for constant force input (Fig. 1 b).

Results
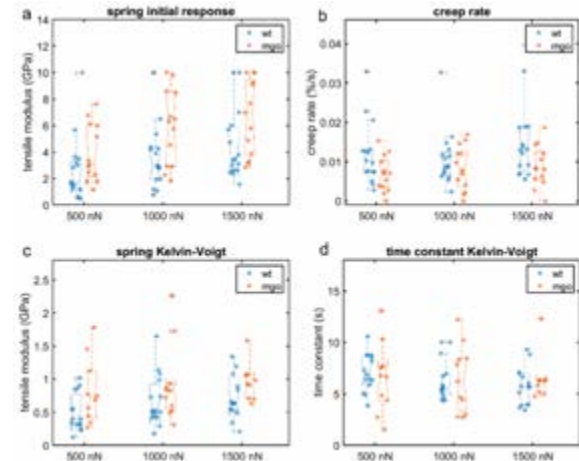
Fig. 2: We find significantly increased elastic response (a - E_2, c – E_1) to force step-inputs and reduced creep per time (b) in cross-linked CFs. The transient response (KV, c and d) shows significantly increased elastic response but no differences in time constant. Significance was tested with the Mann-Whitney U-test.

The elastic response is significantly increased for both spring elements (E_1, E_2) in the Burgers model due to MGO cross-linking. Furthermore, also the long-term viscosity (η_2) is significantly increased, which manifests in reduced creep over time (Fig. 2 b). However, transient viscoelasticity, e.g. the time constant of the KV element, is not affected by cross-linking. Overall, the magnitude of the applied force only affects the elastic response, but not the viscous behavior.

Discussion

To the best of our knowledge, we have for the first time conducted creep experiments of nanoscale fibers and by that studied nanoscale phenomena independent from interaction of the fibers at scales above. The results clearly demonstrate reduced molecular sliding due to intermolecular cross-linking. At the same time, cross-linking evidently increases the elastic response, which combined with the reduced sliding indicates reduced energy dissipation due to cross-linking. Contrarily, transient viscoelasticity seems not to be affected. We therefore contribute the transient viscoelasticity to rearrangements in the water network as well as straightening and uncoiling of collagen molecules that is independent of intermolecular cross-linking.

References

[1] R.B. Svensson et al., Acta Biomater. **70**, 270 (2018).
[2] G. Fessel et al., PloS One **9**, (2014).
[3] M. Nalbach et al., Rev. Sci. Instrum. (2022). Submitted.

COMBINED EXPERIMENTAL AND COMPUTATIONAL STUDY OF TENSIONAL HOMEOSTASIS IN CELL-SEEDED TISSUE-EQUIVALENTS

Daniel Paukner (1,2), Jonas F. Eichinger (1,3), Jay D. Humphrey (4), Christian J. Cyron (1,2)

1. Institute of Continuum and Material Mechanics, Hamburg University of Technology, Germany; 2. Institute of Material Systems Modeling, Helmholtz-Center Hereon, Germany; 3. Institute for Computational Mechanics, Technical University of Munich, Germany; 4. Department of Biomedical Engineering, Yale University, USA

Introduction

Most cells in native soft tissues are subjected to multiaxial loading conditions. To examine how different mechanical boundary conditions influence tensional homeostasis in cell-seeded tissue equivalents, we developed a novel biaxial bioreactor to study and compare this phenomenon in a uniaxial and biaxial setting. In combination with a detailed micromechanical computational model and a simple theoretical mechanical analog model, we are able to identify possible cell-level quantities a cell might regulate that translate into tensional homeostasis on tissue-level on short time scales (hours) where collagen production and removal can largely be neglected.

Methods

The biaxial bioreactor [3] has two highly sensitive force transducers which allow the precise measurement of cell-generated forces in initially stress-free collagen-based tissue-equivalents over a period of up to 2 days. The device is capable of accurately applying static and dynamic strains through the independent control of each axis (Fig. 1A). This allows measuring the cellular response of force generation to external perturbations in a uniaxial and biaxial setting. The experiments were performed with 3T3 fibroblasts and primary cells extracted from murine aortas. In the computational model [1], collagen fibers of the extracellular matrix are modeled as non-linear finite beam elements. A cell can form a connection to a surrounding fiber via integrins which are represented as catch-slip bonds with a force-dependent unbinding rate. This complex system was reduced to a simple theoretical mechanical analog model (Fig. 1B) consisting of springs and a motor element [2].

Results

The experiments with the novel bioreactor showed that the homeostatic force (F_H), established after approximately 24 hours, is higher in a biaxial setting than in a uniaxial setting (Fig. 1C). Additionally, we found that F_H depends on cell density and collagen concentration. After applying a single external step perturbation, we observed that cell-seeded collagen gels cannot exactly restore their homeostatic force, even over periods of several hours (Fig. 1C). Our computational model was able to reproduce these observations for varying cell densities and collagen concentrations. We used the simple mechanical analog model to test different hypotheses of which mechanical

cellular quantity might be regulated on short time scales and found that cells most likely regulate their contractile forces rather than stress or strain in the extracellular matrix or their own shape.
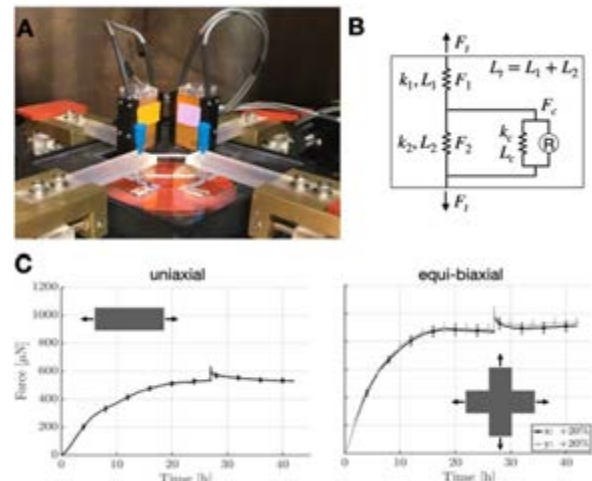
Figure 1: A) Biaxial bioreactor placed in incubator. B) Schematic of mechanical analog model. C) Experimental results of applying an external perturbation to cell-seeded tissue equivalents (3T3 fibroblasts, 1.0E6 cells/ml, collagen concentration 1.5 mg/ml. Mean ± SEM, n = 4.)

Discussion

The results highlight the importance of appropriate boundary conditions when performing experiments with 3D tissue-equivalents. A biaxial setting, which is more natural as almost all tissues and cells are subject to multiaxial loading conditions in-vivo, produces a different homeostatic force under otherwise identical conditions. Combining the experimental and computational results with the mechanical analog model, we were able to confirm that the deviation of the force from F_H after an external perturbation is a consequence of the mechanisms underlying tensional homeostasis such as the catch-slip bond behavior of integrins.

References

1. J. F. Eichinger, et al., Biomechanics and Modeling in Mechanobiology 20, 1851 (2021).
2. J. F. Eichinger, et al., Acta Biomaterialia 134, 348 (2021).
3. J. F. Eichinger, D. Paukner, et al., Journal of Biomechanical Engineering 142, (2020).

Acknowledgements

EXPERIMENTAL INVESTIGATION OF TROPOCOLLAGEN MECHANICS

Andreas Rohatschek(1)*, Patrick Steinbauer(2), Stefan Baudis(2), Philipp J. Thurner(1)

1. Institute of Lightweight Design and Structural Biomechanics (ILSB), TU Wien, 1060 Wien, Austria
2. Christian Doppler Laboratory for Advanced Polymers for Biomaterials and 3D Printing, Institute of Applied Synthetic Chemistry (IAS), TU Wien, 1060 Wien, Austria

* Recipient of a DOC Fellowship of the Austrian Academy of Sciences at the ILSB at TU Wien

Introduction

Collagens are the most abundant and structurally the most important proteins of the human extracellular matrix. Therefore, mechanical properties of collagen molecules (tropocollagen), and the progressively larger structures they form, are crucial for tissue mechanics and function. While there are a number of studies modeling the mechanical behavior of tropocollagen molecules via molecular dynamics (MD) approaches there is little but none experimental data available [2,3]. Due to MD limitations experimental validation of predicted behavior such as molecular uncoiling is needed and will also provide further insight into collagen mechanics.

Here, we present an approach to experimentally characterize adhesion forces between tropocollagen molecules and mica.
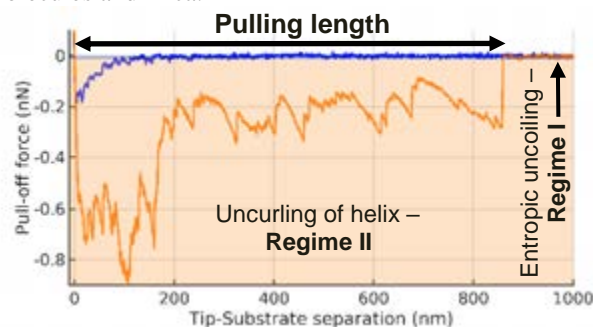
Figure 1: Example force-distance curve. Different force regimes [2] are indicated by background colors.

Methods

Maleimide based surface functionalization [1] is used to tether individual collagen type III molecules onto an AFM tip using a N-hydroxysuccinimide (NHS), polyethylene glycol (PEG), maleimide (MI) linker system.

Table 1: Pulling length and pull-off force results. AFM SMFS measured in HAc and with 4s holding time.

Approach/Retract. Velocity (µm/s)	Pull. length Median (nm)	Pull-off force Mean±Std (pN)
0.1	469	368 ± 209
0.25	506	458 ± 203
0.5	616	540 ± 185
1	448	487 ± 218
1.5	1446	519 ± 202
2	831	633 ± 200

Atomic Force Microscopy (AFM) Single Molecule Force Spectroscopy (SMFS) measurements were conducted in water and acetic acid on mica at different approach and retraction speeds (0.1, 0.25, 0.5, 1, 1.5, 2 nm/s) and at different holding times (0, 1, 2, 4s) to investigate Tropocollagen-substrate interactions.

Results

We detected collagen-substrate interactions on mica and in acetic acid. All detected force-distance curves showed similar behavior.

In a typical force-distance curve (see Figure 1), unspecific adhesion interactions within the first 30 nm are followed by tropocollagen-related interactions with pulling lengths longer than 2 µm and pull-off forces of up to 1.4 nN in acetic acid (0.5 mol/L). More than 38000 force curves were used for analysis.
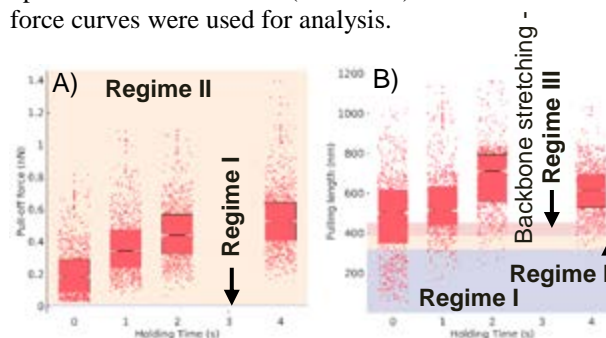
Figure 2: Analysis of 3340 force curves measured in acetic acid, at 0.5 µm/s approach and retraction velocities and four different holding times (0s, 1s, 2s, 4s). Different force regimes [2] are indicated by background colors. A) Pull-off force, B) Pulling length.

Discussion

We report first experimental measurements on collagen molecules reaching deformation-relevant forces. Further, determined median pull-off forces for longer holding times are confirmed by MD simulations of shear-dominant stresses applied which reported a peak force of 621 pN with 12.7% strain [4]. Measured median pulling lengths may indicate even higher strains suggesting even more severe modification, i.e. pulling out of one of the three peptide chains forming the collagen triple helix.

References

1. Kamruzzahan, A *et al, Biocon. Chem.* **17**,1473–81, 2006.
2. Buehler, M. J. et al, *Biophys. J.* **93**, 37–43, 2007.
3. Zitnay, J. L. *et al. Nat. Commun.* **8**, 2017.

Acknowledgements

NANOMECHANICAL SIGNATURE OF FIBROSARCOMA: FROM SINGLE CELLS TO TISSUE LEVEL

Katerina Polemidiotou (1), Fotios Mpekris (2), Triantafyllos Stylianopoulos (2), Andreas Stylianou (1,2)

1. Cancer Mechanobiology and Applied Biophysics Group, Basic and Translational Cancer Research Center, School of Science, European University Cyprus, Cyprus

2. Cancer Biophysics Laboratory, University of Cyprus, Cyprus

Introduction

In many solid tumours, such as sarcoma, a desmoplastic reaction takes place and as a result solid tumors stiffen as they grow in a host's normal tissue. Stiffening is caused by an increase in the structural components of the tumor, particularly in the density of the extracellular matrix fibers and mainly of collagen [1,2]. Although tumor microenvironment stiffening poses a major physiological barrier to the effective delivery of drugs, the underlying mechanisms remain unclear [3].

In this study, we investigated the effect of collagen content / stiffness on fibrosarcoma cells, particularly on specific cytoskeletal properties involved in tumour growth and invasion [2, 4]. Also, the nanomechanical properties and tumor microenvironment alterations during cancer progression were studied in tissue level [1,4]. Atomic force microscopy, optical and fluorescence microscopy, image processing and biological assays were used in order to assess cells cytoskeletal remodeling and tumor microenvironment alterations.

Methods

Cells: Human fibrosarcoma cell line HT1080 and the murine fibrosarcoma cell line MCA205 were maintained in DMEM and RPMI-1640, respectively, supplemented with 10% Fetal Bovine Serum (FBS) and 1% antibiotics. Orthotopic fibrosarcomas were established by implantation of HT1080 and MCA205 into the third mammary fat pad of 6-8-week-old C57BL/6 mice. Tissue biopsies were obtained at 3 different time points during cancer progression. AFM measurements (Molecular Imaging, PicoPlus) on live cells and fresh samples were conducted, with silicon nitride cantilevers (MLCT-Bio, Bruker). The force maps were analyzed by AtomicJ using the Hertz model. Cells' cytoskeleton was assessed by staining F-actin with phallodin and β-tubulin with relevant antibodies. Fibers orientation was evaluated with FilamentSensor tool. Collagen abundance was evaluated via picrosirius red staining and images were acquired using an Olympus BX53 microscope with linear polarizers.

Results

Our results demonstrated that collagen stiffness remodels cells' cytoskeleton (Fig. 1A, B). Cells were becoming softer (Fig. 1C) and with more aligned stress fibers when on stiffer substrates (Fig. 1D). In tissue level, during cancer progression the tumor's collagen content was increased due to desmoplasia (Fig. 1E). AFM analysis of tumor biopsies at different times of tumor growth in fibrosarcoma revealed two distinct characteristics as far as the distribution of elastic modulus is concerned: a lower elasticity peak, due to cancer cell softening and a higher elasticity distribution, due the collagen overproduction (Fig.1F).
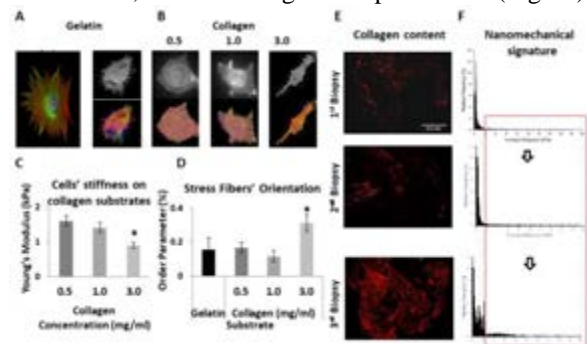
Figure 1: A) Representative MCA205 cell (blue: nucleus, Green: β-tubulin, Red: F-actin) B)MCA205 cells on different substrates. C) F-actin stress fibers orientation, D) MCA205 cells' stiffness, E) Collagen content and F) Nanomechanical signature during cancer progression (HT1080 murine tumor model).

Discussion

Overall, our results demonstrated that collagen stiffness modulates sarcoma cells cytoskeleton remodeling. Furthermore, we found that AFM techniques are sensitive to access small nanomechanical modifications during cancer progression, which are related to cancer desmoplasia and cancer cells' softening. Further research in this area is demanded so as to develop novel nanomechanical biomarkers that can be used for diagnostic and prognostic purposes.

References

1. Stylianou, A., et al., BBA-Gene Subjects, 1862, 2018
2. Stylianou, A., et al., J R Soc Interface, 16, 2019
3. Gkrestsi, V., et al., Front Oncol, 5:214, 2015.
4. Stylianou, A, et al., Nanoscale,10:20930, 2018.

Acknowledgements

MECHANOBIOLOGY-BASED RAPID DIAGNOSIS AND EARLY PROGNOSIS OF METASTATIC RISK IN CANCER

Daphne Weihs

Faculty of Biomedical Engineering Technion – Israel Institute of Technology, Haifa 3200003, Israel

Introduction

The main cause of cancer-related death is metastasis; early detection or prediction are crucial. Metastasis is currently predicted via histopathology, disease-statistics, or genetics, yet those are often-inaccurate, not rapidly available, and require known markers. We have developed a rapid (~2hr) mechanobiology-based approach to rapidly diagnose cancer and provide early prognosis of the in vitro invasiveness of cells [1], which we show here accurately agrees with the clinical likelihood for metastasis [2,3].

Methods

We evaluate the mechanical invasiveness of cells from ten breast and pancreatic cancer cell lines and also from freshly resected, enzymatically degraded, human pancreatic and skin tissue samples [2,3]. Cells are seeded on physiological-stiffness (2.4 kPa) gels with fluorescent beads embedded at their surface as markers. Within 1-hr of seeding, the invasive cell-subsets forcefully push into an indent an impenetrable, physiological-stiffness polyacrylamide gels, while non-invasive/benign cells do not. The fraction of cells that indent the gels and their attained depths are determined by fluorescence microscopy. In cell lines, we compare to trans-well, Boyden chamber, migration assays (8 µm pores, 72 hrs). In tumor samples, clinical histopathology and patient follow-up are used as gold-standard.

Results

We show (Figure 1) that the percentage of indenting cells and their attained depths, together the sample's mechanical invasiveness, agree with the *in vitro* and literature established metastatic potential in cell lines and with the clinically determined invasiveness in tumor samples [2,3].
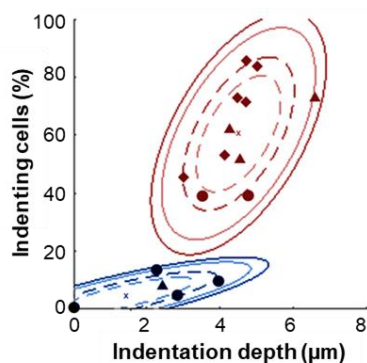
Figure 1: K-means cluster analysis of pancreatic tumor-samples (●) together with breast (▲) and pancreatic (♦) cell-lines demonstrates separation between metastatic and non-metastatic cells. With permission from [2].

We demonstrate, via finite element modeling, the force levels and configurations and cell mechanobiology required to attain invasive indentations [4]. Utilizing the current experimental and clinical database, we have developed machine learning models to automatically predict the invasiveness and metastatic risk. Specifically, 2-class models (distinguishing invasive from non-invasive) provide high sensitivity and specificity, respectively 0.92 and 1, and 5-class models (i.e. normal, benign, non/low/high metastatic-risk) provided sensitivity and specificity of 0.69 and 0.91 [5].

Discussion

The mechanical invasiveness of high or low-metastatic-potential and benign/normal cells are significantly different, allowing determination of cancer-type specific, clinically relevant prognostic thresholds. Our innovative and unique mechanobiology-based approach provides a rapid and accurate cancer diagnosis and prediction of metastatic likelihood in tumors, already during the time of first diagnosis, which can critically affect patient-specific treatment protocols and disease management.

References

1. Weihs & Merkher, Patent pending, WO/2019/207587, 2019.
2. Merkher et al., Ann. Biomed. Eng., 48:2846-2858, 2020.
3. Kortam et al., Biomech. Model. Mechanobiol., 20:1767-1774, 2021.
4. Ben-David & Weihs, Biomech. Model. Mechanobiol., 20: 1187-1194, 2021.
5. Rozen & Weihs, Ann. Biomed. Eng., 49:1774-1783, 2021.

Acknowledgements

IDENTIFICATION OF THE MOST IMPORTANT CELLULAR PROCESSES BEHIND IMPAIRED BONE REGENERATION IN TYPE-2 DIABETES

Mahdi Jaber (1), Georg Duda (1), Sara Checa (1)

1. Julius Wolff Institute, Berlin Institute of Health, Charité - Universitätsmedizin Berlin, Germany

Introduction

Bone has the fascinating ability to self-regenerate. However, under certain conditions, such as Type 2 diabetes mellitus (T2DM), this ability is impaired. T2DM is a chronic metabolic disease known by the presence of elevated blood glucose levels that is associated with reduced bone regeneration, high fracture risk and non-union. Several cellular processes have been shown to be affected in T2DM patients, such as impaired osteoblast (OB) function and slower cell migration [1]. However, it is yet unknown how the T2DM-related alterations at the cellular level contribute to altered bone regeneration. Therefore, the aim of this study was to identify key cellular activities that impact bone regeneration in T2DM, using an *in silico* approach.

Materials and Methods

A previously described computer model able to explain bone regeneration in uneventful conditions of healing [2] was further developed to investigate bone regeneration in T2DM. The computer model combined finite element (FE) analysis, to determine the mechanical environment within the defect region, and an agent-based model (ABM) to characterize biological processes taking place during bone regeneration. To analyze the impact of distinct T2DM-altered cellular activities on the overall regeneration, distinct biological alterations were modulated and compared against non-diabetic healing with a design of experiments (DoE) approach.

Aspects analysed included the presence of stromal cells (MSCs), cellular migration, proliferation, differentiation and apoptosis. To verify the computer model findings an in vivo experimental setup was replicated, in which regeneration was analysed in healthy and diabetic after a rat femur bone osteotomy stabilized with a plate fixation [1]. Two FE models were built having the same gap size (3mm) and overall geometry (Fig.1), but with different loading conditions, to take into account the higher body weight of the diabetic animals. The gap region was initially filled with granulation tissue, while titanium material properties were assigned to the plate and screws.

Fig. 1: Computer model of a rat femur osteotomy, replicating the experimental setup described in [1]. In red, the cross section shown in Fig 2A.

Results

Initially, higher compressive strains were predicted within the defect of the diabetic rat (Fig. 2A). The parametric analysis revealed that alterations in MSC proliferation, MSC migration and OB differentiation had the highest impact on bone defect regeneration. To verify our findings against in vivo data, a downregulation of these cellular activities was simulated and computer model predictions of bone regeneration where compared to experimental μCT data of bone regeneration in diabetic. Under these constrains, in silico predictions of regenerated bone in diabetic and and non-diabetic cases matched qualitatively and quantitatively those from ex vivo microCT at 12 weeks post-surgery (Fig. 2B and C).
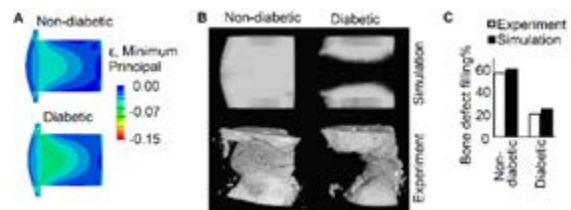
Fig. 2: (A) Minimum Principal Strains within the healing region. Bone defect filling 12th week post-osteotomy in experiments [1] and simulations (B) qualitative and (C) quantitative.

Discussion

Our results suggest that alterations in MSC proliferation, MSC migration and OB differentiation due to T2DM were most relevant to the delay in bone regeneration. In vivo data showed that osteopontin and BMP2, known to affect the cellular activities of MSCs and OB, were considerably down regulated in diabetic animals (1, 3). A down regulation of these specific cellular activities relevant to bone defect healing may be considered as key drivers for an impaired regeneration in diabetics. Future studies should investigate salvage strategies that could tackle these specific cellular processes.

Acknowledgements

References

1. Hamann et al., Am J Physiol Endocrinol Metab, 301(6):E1220-8, 2011.
2. Checa S et al., J Biomech. 44(7):1237-45, 2011.
3. Kahles et al., j. Mol Metab., 3(4):384-93, 2014

EMERGENCE OF BONE REMODELLING BEHAVIOUR FROM A MICRO-MULTIPHYSICS AGENT-BASED MODEL

Jack J. Kendall, Daniele Boaretti, Charles Ledoux, Francisco C. Marques, Esther Wehrle, Ralph Müller

Institute for Biomechanics, ETH Zurich, Zurich, Switzerland

Introduction

Bone (re)modelling is a biological optimisation process whereby the structure is adapted and maintained to meet the demands of mechanical loading. The adaptation is directed by osteocytes and results from a joint effort by osteoblasts and osteoclasts which form the basic multi-cellular unit (BMU). Recently, a micro-Multiphysics Agent-based (micro-MPA) model has been developed to provide unprecedented capabilities at simulating cell mechanobiology and behaviour at the tissue-scale [1]. However, the rules governing the cellular behaviours require calibration. Previous *in silico* studies have investigated and unified the theories of trabecular and cortical remodelling [2], albeit not within the context of an ABM. To this end, we aim to understand the emergence of bone (re)modelling from specific rules pertaining to the cells of the BMU.
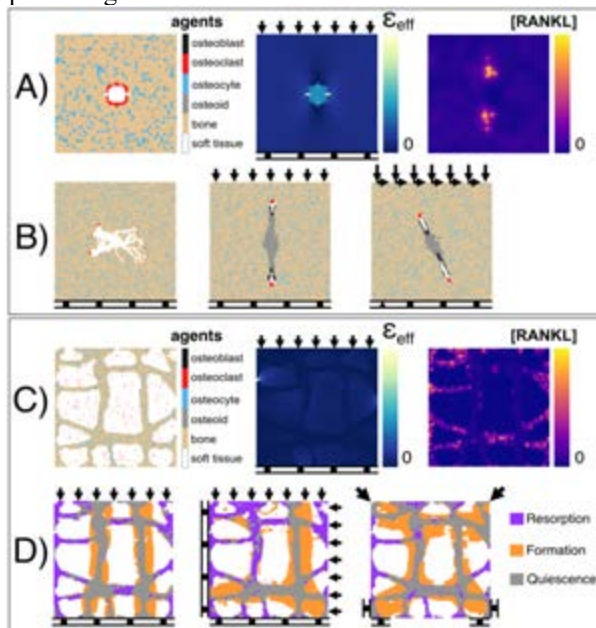
Fig. 1: a) Initial condition of cortical bone under uniaxial compression; b) no load, uniaxial compression, and combined loading. c) Initial condition of the trabecular bone for uniaxial compression. d) Bone formation, resorption, and quiescence for uniaxial, biaxial and 45° rotated biaxial compression.

Methods

Cell behaviours and rules were implemented and investigated using a two-dimensional version of the micro-MPA model [1]. This 2D model relied on the same finite-difference and finite-element solvers for the diffusion and tissue mechanics, respectively. Osteocytes, osteoblasts and osteoclasts were modelled as independent agents on a discrete lattice with square elements of uniform length. Trabecular and cortical bone were discretised as two domains with 150 pixels squared (Fig. 1ac). A timestep consisted of an update of the agents followed by diffusion, whereas tissue strain was updated every 20 timesteps. The osteocytes were responsible for inducing resorption by producing receptor activator of nuclear factor kappa-B ligand (RANKL) in regions of minimal effective strain (ε_{eff}) [3]. RANKL was modelled as a chemoattractant for osteoclasts which resorbed mineral within their Moore's neighbourhood. Whereas the osteoblasts deposited osteoid predominantly in the direction of increasing mineral concentration. Osteoblast motility was governed by an affinity towards regions of higher effective strain. Various loading scenarios were devised for testing the rules governing the BMU's behaviour and capability of (re)modelling. The cortical bone was subjected to no load, uniaxial compression, and combined loading (Fig. 1b). The trabecular bone was loaded uniaxial, biaxial, and rotated (45°) biaxial compression (Fig. 1d). The results were verified by qualitatively assessing the resulting micro-architecture.

Results

The simulations show that the BMU can be guided by mechanosensitive RANKL signalling by osteocytes and reproduce experimentally observed (re)modelling patterns in the cortical (Fig. 1b) and trabecular region (Fig. 1d) for all loading scenarios after 800 iterations.

Discussion

The advantages of studying mechanobiology with this 2D micro-MPA model were its low computational cost and its capability of rapid development cycles and calibration. The emergence of the (re)modelling process from our investigation of the BMU's behaviour with this model aligns with experimental observations and corroborates findings from previous *in silico* investigations [1,2]. The implemented rules are suitable for further investigation with a more refined model that includes pathways targeting bone formation and metabolism.

References

1. Boaretti et al., Abstracts 26th ESB Congress, Italy, 2021
2. Van Oers et al., Bone, 42:250-259, 2008
3. Nakashima et al., Nat Med, 17:1231–1234, 2011

Acknowledgements

A COUPLED FINITE ELEMENT AND SYSTEMS BIOLOGY MODEL TO STUDY THE ROLE OF MECHANICS AND INFLAMMATION IN KNEE OA.

Satanik Mukherjee[1,2], **Raphaëlle Lesage**[1,2], **Liesbet Geris**[1,2,3]

[1]*Prometheus, Division of Skeletal tissue Engineering, KU Leuven, Belgium;* [2]*Biomechanics Section, KU Leuven, Belgium;*[3]*GIGA In silico medicine, University of Liège, Belgium.*

Introduction

Osteoarthritis (OA), a degenerative joint disease is suspected to be triggered by multiple factors, with abnormal mechanics and inflammation being predominant ones. *In silico* models can provide unique insights to unravel the complex interplay between mechanics and pro-inflammatory cytokines in the initiation and progression of OA. One of the novel approaches in this context is to couple finite element (FE) models with systems biology models. In this approach, the mechanics translating across multiple length scales (from joint-level to cell-level) obtained using FE models is coupled with intracellular gene/protein regulatory networks modelling intracellular biochemical processes in a multiscale manner. Using such an approach, the aim of this paper is to delineate the effect of physiological and pathological mechanical signals (post meniscectomy) on the fate of articular chondrocytes in the human knee joint, in combination with pro-inflammatory cytokines.

Methods

The modelling workflow incorporates computer models at 3 different length scales (figure 1) as follows:
A FE model of the right knee of a 70 year old female was developed in FEBio [1]. Hyperelastic material properties were assigned to cartilage, menisci and the ligaments as obtained from literature. Joint kinetics and kinematics for stance phase of the gait was used as input boundary conditions for the knee joint.
FE models of the chondrocyte and its microenvironment (containing the pericellular matrix (PCM) and extracellular matrix (ECM)) for the different zones of the cartilage (superficial zone (SZ), middle and deep zone (DZ)) were developed in Abaqus. The ECM and PCM were modelled as fibril reinforced poro-viscoelastic materials [2]. The cell was modelled as a biphasic material. The maximum compressive and shear strains obtained at the different zones of articular cartilage from simulations of the knee joint were used as input boundary conditions for the cell-level model.
An additive, semi-quantitative regulatory network for chondrocyte mechanotransduction and inflammation was developed using a combination of knowledge-based and inference-based approach. The forces sensed by cells in the cell-level FE model were used as an input to perturb the regulatory pathways.
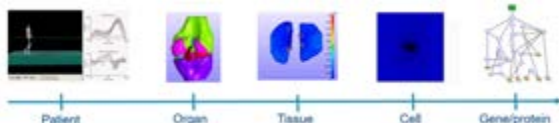
Figure 1. Multiscale model of human knee joint

Results

Meniscectomy led to increased strains in the articular cartilage as compared to a healthy joint, resulting in higher forces sensed by the chondrocytes in all the zones of cartilage. This increased cellular forces led to subsequent build-up of inflammatory cytokines over time, which in tandem with the abnormal mechanical loading led to blocking of relevant mechanotransduction pathways (TRPV4 and YAP/TAZ) in SZ chondrocytes. Furthermore, a phenotypic switch of SZ chondrocytes to a hypertrophy-like state was observed (evidenced by the high activity of the pro-hypertrophic biomarkers RUNX2, Coll-X, MMP13, ADAMTS5). On the contrary, the DZ chondrocytes initially remained in their stable state showing very small degenerative effects due to meniscectomy. However, when the SZ had degenerated considerably at a later stage, the DZ chondrocytes showed hypertrophy-like behaviour. This was due to higher mechanical forces now transmitted to the DZ of the cartilage.
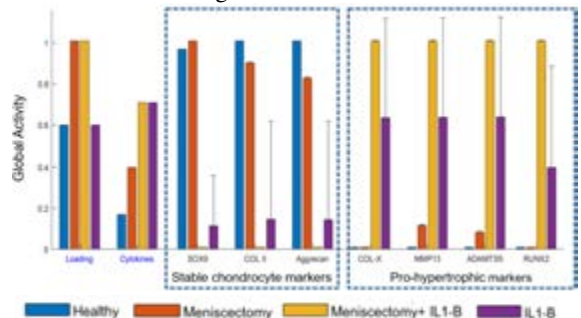
Figure 2: Activity of SZ chondrocyte biomarkers due to meniscectomy and pro-inflammatory cytokine IL-1b.

Discussion

The multiscale model developed (combining FE and systems biology) predicted that meniscectomy induces inflammation and subsequent loss of ECM components in articular cartilage. It also revealed the differential behavior of SZ and DZ chondrocytes, which was due to the difference in mechanics perceived in the different zones. Calibration and validation of the model with respect to an in-vitro setup of dynamic compression of cartilage explants is ongoing, to make it more robust.

References

[1] Erdemir A. J. Med Device.7(4):, 2013.
[2] Wilson W et.al. J. Biomech. 38, 1195–1204, 2005.

Acknowledgements

BIOMECHANICAL MODEL OF BONE REMODELING COUPLED WITH ADVANCED DISCRETIZATION METHODS

Madalena M. A. Peyroteo (1), Jorge Belinha (2), Renato Natal Jorge (3)

1. Institute of Science and Innovation in Mechanical and Industrial Engineering (INEGI), Portugal; 2. School of Engineering Polytechnic of Porto (ISEP), Portugal; 3. Faculty of Engineering, University of Porto, Portugal

Introduction

Bone is a unique tissue due to its remodeling ability. During bone remodeling, new bone tissue is secreted in response to certain mechanical or biological stimuli. Being a mechanically sensitive tissue, bone adapts its structure according to its loading, through the activity of osteoclasts and osteoblasts. Osteoclasts are the bone cells responsible for bone resorption, while osteoblasts are the bone-forming cells. Although the transduction of the mechanical signal into a biological response is still under debate, remodeling algorithms are an important tool to test distinct hypothesis to explain this biomechanical communication. This work presents a new approach to link the mechanical and biological components of bone remodeling, combining a biological model and a mechanical model of bone remodeling previously proposed [1-2].

Methods

The remodeling algorithm begins with a mechanical analysis to calculate the strain energy density (SED) field. Based on the SED level, the nodes discretizing the domain are divided into three groups – resorption, formation and quiescence – with distinct parameters to control bone's biological response. These parameters, here proposed for the first time, regulate osteoclasts and osteoblasts activity, which ultimately affects bone's apparent density.

The algorithm is validated with a benchmark example [3], consisting on a 2D bone patch loaded with an oblique load, as presented in Figure 1a). Simulations are combined with three distinct numerical methods – finite element method (FEM), radial point interpolation method (RPIM) and natural neighbor radial point interpolation method (NNRPIM).

Results

Figure 1b), c) and d) show the trabecular distribution attained at the end of the simulation with FEM, RPIM and NNRPIM. Although bone's apparent density distribution maps differ from each other, the obtained trabeculae reflect the orientation of the applied load, validating the algorithm.
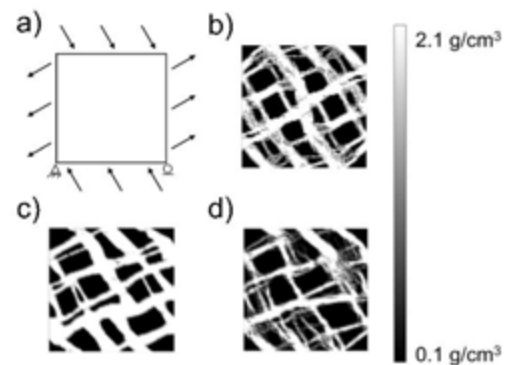
Figure 1: (a) Schematic representation of the benchmark example used; Trabecular bone distribution obtained with (b) FEM, (c) RPIM and (d) NNRPIM. White regions represent bone, while black regions represent non-bone areas.

Discussion

The combination of meshless methods (i.e. RPIM and NNRPIM) with a biomechanical model of bone remodeling was proposed for the first time in this work. As presented in Figure 1, meshless solutions presented highly individualized trabeculae with smooth contours, supporting their use in remodeling algorithms.

References

1. Peyroteo M. M. A. et al, Eng Anal Bound Elem 100:125–139, 2019.
2. Peyroteo M. M. A. et al, Int. J. Numer. Method. Biomed. Eng. 35 (6), e3196, 2019.
3. Mullender MG et al, J Orthop Res, 13(4):503–12, 1995.

Acknowledgements

THE INFLUENCE OF WNT PATHWAY IN BONE REMODELLING AND CALCIUM CONCENTRATION IN MICROGRAVITY CONDITIONS

Andrada Pica (1), Andrea Marinozzi (2), Franco Marinozzi (1), Fabiano Bini (1)

1.Department of Mechanical and Aerospace Engineering, "Sapienza" University of Rome, Italy;
2. Orthopedy and Traumatology Area, "Campus Bio-Medico" University, Italy

Introduction

Bone is characterized by a continuous process of remodelling driven by complex actions of biological cells, biochemical and mechanical factors. Conditions of altered mechanical loading, e.g. microgravity, present an adverse effect on bone homeostasis, associated with increased bone resorption [1]. Mathematical modelling represents a complementary method to investigate cells interconnections and their influence on the mechanobiology of bone remodelling. In this study, we extend a previous computational model of bone remodelling [2] to take into account recent biological evidence, i.e. Wnt pathway. Wnts are secreted glycoproteins that promote osteoblast proliferation and bone formation [3]. Conversely, sclerostin inhibits Wnt signaling by binding with Wnt receptors LRP5/6, leading to a decrease of bone formation. Using this novel model, we investigate the effects of microgravity on mineralized bone area and calcium concentration.

Methods

The mathematical framework consists of ordinary differential equations that take into account mechanical stimulus, endocrine regulation and local biochemical mediators [1-2]. Mechanotransduction is considered through the response of osteocytes subjected to a mechanical stress [4]. Biochemical regulations involve signaling molecules of RANK-RANKL-OPG pathway regulated by nitric oxide and prostaglandin E2, transforming growth factor β, parathyroid hormone and Wnt signaling [1, 4-5]. Wnt pathway is described via competitive binding reactions between Wnt, sclerostin and LRP5/6. It is integrated in the previous model [2] adopting the implementation proposed by [3]. We used average values of the model parameters in line with [2]. In 1g gravity, the load is set to obtain a strain ε=1500 με in the trabecular sample and in microgravity the theoretical mechanical stimulus is F= 0N. The simulation is performed considering initial 30 days of 1g gravity, followed by 180 days of microgravity, while the last 40 days are defined by 1g gravity.

Results

We analysed the microgravity effects on the temporal evolution of mineralized bone area and on the calcium concentration in bone fluid. In Figure 1 we compare the outcomes of the current model with the results achieved with the previous model [2], showing good agreement. The incorporation of the Wnt pathway leads to a slightly accentuated diminution of bone area in microgravity
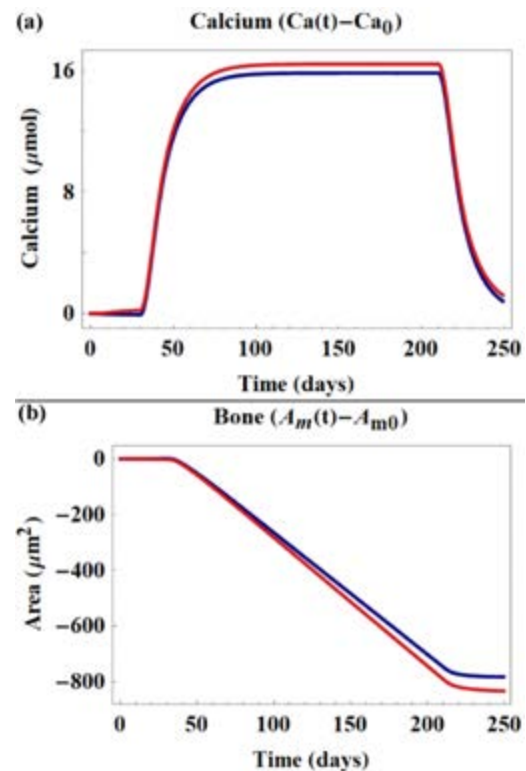
Figure 1: Variation of calcium in bone fluid (a) and bone area (b) achieved from previous model [2] (blue line) and current model (red line).

conditions and to a subsequent increase of calcium concentration in bone fluid.

Discussion

With respect to the current model, the previous one [2] underestimates calcium concentration in bone fluid and subsequently overestimates bone area. The incorporation of Wnt pathway contributes to the development of a more accurate equation system. The novel computational framework paves the way for a more predictive model in order to investigate the microgravity conditions that influence long term space missions.

References

1. Pennline, NASA/TM—2009-215824, 2009.
2. Pica et al., Abstract book 26th Congress of the European Society of Biomechanics, pp. 229, 2021.
3. Martin et al., Biomech. Model Mechanobiol. 18:1475-1496, 2019.
4. Maldonado et al., Conf. Proc. 28th IEEE EMBS Conference, pp. 3154-3157, 2006.
5. Lemaire et al., J. Theor. Biol., 229:293-309, 2004.

DISRUPTED OSTEOCYTE CONNECTIVITY AND MECHANOSENSATION IN BONE WITH AGING AND DEFECTIVE TGF-B SIGNALLING

Stefaan W. Verbruggen (1, 2, 3), Charles A. Schurman (4, 5), Tamara Alliston (4, 5)

1. Mechanical Engineering & Insigneo Institute for In Silico Medicine, University of Sheffield, UK; 2. Institute of Bioengineering, Queen Mary University of London, UK; 3. Department of Biomedical Engineering, Columbia University, New York, USA 4. Department of Orthopaedic Surgery, University of California, San Francisco, USA; 5. UC Berkeley-UCSF Graduate Program in Bioengineering, USA;

Introduction

Aged bone presents several osteocyte-specific defects including a lack of mechano-responsiveness, uncoupling of bone deposition and resorption, and increased bone fragility attributed to poor bone quality [1]. However, the mechanisms underlying the concurrent decline in bone mass, quality, and mechano-sensitivity with age remain unclear. The important role of osteocytes in these processes and the age-related degeneration of the intricate lacuna-canalicular network (LCN) in which osteocytes reside point to a primary role for osteocytes in bone aging [2]. However, the extent to which LCN defects impact osteocyte mechano-transduction, intercellular communication, and solute transport remains unclear.

Methods

Given technical constraints in experimentally dissecting these processes, we applied two *in silico* approaches to investigate the functional impact of LCN disruption resulting from either systemic aging or from osteocyte-intrinsic defects in TGF-β signaling (TβRII$^{ocy-/-}$) in C57BL/6 mice. Using 3D reconstructed confocal images of fluorescently-labelled osteocyte networks, we applied Connectomic Network Analysis to model solute transport and computational fluid dynamics (CFD) to model LCN fluid flow and mechano-sensation [3].
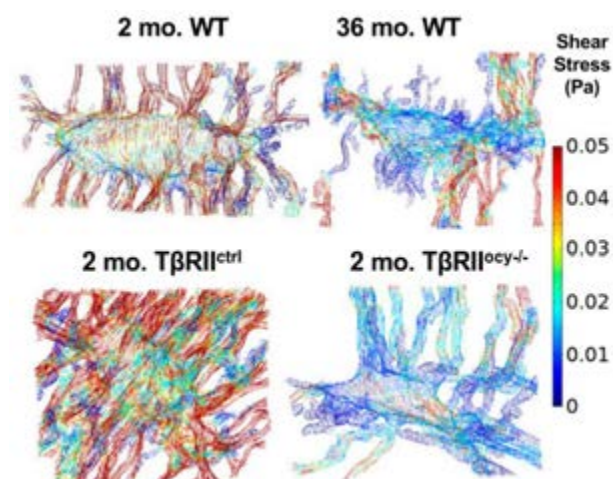
Figure 1: CFD streamlines demonstrated significantly lower fluid velocity and shear stress around individual osteocytes from both aged wild-type (36 mo. WT) and young TGF-β receptor knockout mice (2 mo. TβRII$^{ocy-/-}$) compared with young healthy controls (n = 5).

Results

We found that osteocytes from aged and TβRII$^{ocy-/-}$ mice had 33 to 45% fewer, and more tortuous, canaliculi. Connectomic network analysis revealed that diminished canalicular density is sufficient to impair diffusion even with intact osteocyte numbers and overall LCN architecture. Computational fluid dynamics predicted that the corresponding drop in shear stress experienced by aged or TβRII$^{ocy-/-}$ osteocytes is highly sensitive to canalicular surface area [4]. Simulated expansion of the osteocyte pericellular space to mimic perilacunar/canalicular remodeling [5] restored predicted shear stress for aged osteocytes to young levels.

Discussion

In this work, we identify canalicular loss as a driver of declining mass transport and mechano-stimulation within the LCN of aged bone and of bone with osteocyte-intrinsic defects in transforming growth factor beta signaling. Overall, these models show how loss of LCN volume through LCN pruning may lead to impaired fluid dynamics and osteocyte exposure to mechano-stimulation. Furthermore, osteocytes emerge as targets of age-related therapeutic efforts to restore bone health and function. We identify the ability to restore physical stimulation to osteocytes through expansion of the pericellular space. Future studies will determine if therapeutic stimulation of osteocyte function can improve bone health with age.

References

1. Razi et al., J Bone Miner Res, 30(10):1864-73, 2015.
2. Schaffler et al., Calcif Tiss Intl, 94:5-24, 2014.
3. Verbruggen, et al., Biomech Model Mechanobio, 13, 2014.
4. Schurman et al., PNAS, 118(25), 2021.
5. Dole et al., Cell Reports, 21(9):2585-96, 2017.

Acknowledgements

AGENT – BASED MODEL OF VASCULOGENESIS INCLUDING CELL – ECM INTERACTIONS

Ana Carrasco-Mantis (1), Tomás Alarcón (2), José A. Sanz-Herrera (1)

1. School of Engineering, University of Seville, Seville, Spain; 2. Institució Catalana de Recerca i Estudis Avançats (ICREA) and Centre de Recerca Matemàtica (CRM), Barcelona, Spain.

Introduction

For blood to travel from the heart to the different parts of the body, blood vessels, i.e., arteries and veins, are essential for the delivery of nutrients, oxygen and the removal of cellular waste. If these originate for the first time, the process is called vasculogenesis, while if they are created from existing ones, angiogenesis. In this work, from an *in-silico* point of view, the influence of the stiffness and viscoelasticity of the extracellular matrix (ECM) is modeled. For this purpose, a discrete 3D agent-based model has been developed, based on previous studies [1], in which the vascular network grows immersed in the ECM.

Methods

The mathematical model contemplates the subsequent forces: angular (F^a), random (F^r), chemotactic (F^c), directional persistent (F^p), mechanical (F^m) and viscoelastic (F^v). Depending on their location, a distinction is made between Tip cells ('t'), located at the tip and Vessel cells ('v'), positioned inside the vessels. Additionally, there are the cells of the ECM ('g'), which has been modeled as a spatial distribution of particles forming a sphere, interconnected with their neighbors. Regarding the cell type, a certain set of forces is applied (see eqs. 1 and 2) and when the Vessel cells complete their cell cycle, they proliferate, giving birth to a daughter cell and increasing the size of the vascular network:

$$\mu \frac{dx_i}{dt} = F_i^{m,nn} + F_i^{m,tg} + F_i^r + F_i^c + F_i^p + F_i^{v,tg} \quad (1)$$

$$\mu \frac{dx_j}{dt} = F_j^{m,nn} + F_j^{m,vg} + F_j^r + F_j^a + F_j^{v,vg} \quad (2)$$

Results

The results have been structured in three parts: (i) constant ECM stiffness, (ii) ECM stiffness gradients and (iii) ECM viscoelasticity (see Figs. 1 and 2):
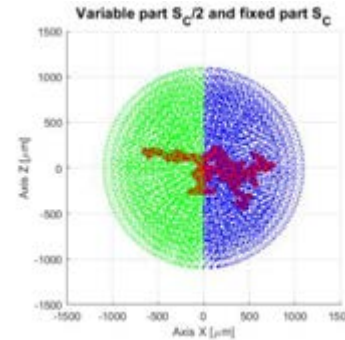
Figure 1: In the positive part of the X-axis a nominal stiffness is maintained ($S_c = 5,56 \cdot 10^{-5} \frac{nN}{\mu m}$) while the negative part is tested with different values of this stiffness, in this case $S_c/2$.
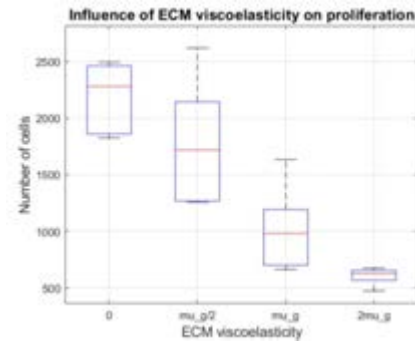
Figure 2: Representation of the cell number versus the cases of ECM viscoelasticity considered (referred to different viscoelastic coefficients). Five realizations were performed for every case.

Discussion

The main findings are: first, increased proliferation is observed with increasing spring elastic constant; second, stiffer zones have higher cell concentration because there is a tendency for the cells to migrate to more rigid zones; and third, the network becomes less dense as the value of the viscoelastic coefficient of the ECM increases. Qualitatively, these results are aligned with experimental data available in the literature [2-4].

References

1. Perfahl, H. et al., Journal of theoretical biology, 414, 254-268, 2017.
2. Bonnans, C. et al., Nature reviews Molecular cell biology, 15(12), 786-801, 2014.
3. Sunyer, R. et al., Current Biology, 30(9), R383-R387, 2020.
4. Chaudhuri, O. et al., Nature communications, 6(1), 1-7, 2015.

AGENT-BASED MODEL OF LONG-TERM DISEASE PROGRESSION IN DUCHENNE MUSCULAR DYSTROPHY

Katherine Crump (1), Silvia Blemker (1), Shayn Peirce-Cottler (1)

1. Department of Biomedical Engineering, University of Virginia, Charlottesville, VA, USA

Introduction

Duchenne muscular dystrophy (DMD) is a severe muscle wasting disease that affects 1 in every 3,500 boys [1]. DMD is caused by a lack of dystrophin, a protein essential in maintaining the strength of the muscle fiber membrane. The weak membrane is susceptible to damage by muscle contractions during everyday movements, initiating a cascade of muscle fiber necrosis, and chronic inflammation [2]. However, despite extensive research and knowing the cause of DMD, there is no cure for DMD and current treatments have had limited efficacy.

Computational modeling provides a powerful to tool to investigate complex behaviors in skeletal muscle that may not be accessible through experiments. In this abstract, we present a computational model of chronic muscle degeneration in the *mdx* mouse model of DMD. The new model combines the strengths of other previously developed computational models ([3],[4],[5],[6]) to offer a more comprehensive simulation of repetitive injury, cellular interactions, inflammatory cues, and muscle repair.

Methods

To simulate chronic injuries and disease progression in the *mdx* mouse, a previously published agent-based model of acute injury response in *mdx* skeletal muscle was adapted utilizing Repast Simphony [3]. Cell "agents" behaviors included migration, growth factor secretion, division, differentiation, and apoptosis.

Key changes made to the prior model included infliction of multiple injuries, inflammatory cell migration, and chemokine diffusion. New dystrophic conditions were defined by literature-derived rules. Damage was defined as % of fiber area replaced with necrotic tissue.

To mimic how damage changes during disease progression in the mdx mouse [7], we simulated decreasing levels of damage over time: 2% for the first 2 weeks, 1% until 3 months old, 0.5% until 6 months old, and finally 0.25 % for 6 months.

Daily constant microinjuries of 0.25%, 0.5%, and 1% were inflicted to simulate the responses to chronic injury in healthy and dystrophic mouse muscle.

Simulations were run for 1 year. The model was validated using published literature data on change in cross-sectional area (CSA), fibrosis, satellite stem cell (SSC) count, and macrophage cell count.

Results

With the variable damage protocol, the model captures the peak onset of muscle fiber damage that levels off after 3 months leaving some increased fibrotic tissue, followed by a relatively stable period up until 8 months
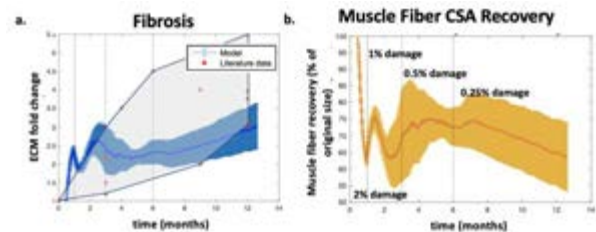
Figure 1. (a) Fibrosis/extracellular matrix (ECM) fold change and (b) Muscle fiber recovery predictions from variable damage schedule in an mdx mouse.

when muscle fiber recovery declines and fibrosis begins to increase at a much faster rate (Fig. 1). SSC counts follow a similar trend to literature data, peaking at 3-4 months and declining steadily with age. Starting at 4 months, there is a steep decline in M1 macrophages and at 6 months, M2 becomes the predominant phenotype.

Daily infliction of a constant level of damage to both healthy and dystrophic muscle caused degeneration and increased fibrosis. Lower levels of daily damage (0.25% and 0.5%) allowed dystrophic and healthy muscle to maintain their fiber size and extracellular matrix until ~6-8 months. Dystrophic and healthy mice differ significantly in muscle fiber recovery when daily damage is increased to 1%, but are similar at lower damage levels. Unexpectedly, the simulated mdx mouse does not degenerate as rapidly as the healthy mouse.

Discussion

Through low-level, daily injuries, the model simulations capture the peak damage before the *mdx* mouse is 3 months old and the switch from a pro-inflammatory environment to an anti-inflammatory, pro-fibrotic environment after 6 months. As the only change in the model is inflicted damage, this transition is an emergent behavior based on the altered cell behaviors and growth factor and chemokine secretions.

One key finding from the simulations was that sustained, repetitive injury, even as low as 0.25% of the muscle fibers, results in impaired regeneration. This suggests that this amount of damage is not viable over time and implies that the amount of damage likely decreases, possibly through protective measures, such as increased stiffness to minimize strain or through altered cellular mechanisms not included within this model.

References

1. Emery et al. *Neuromuscul Disord.* 1991.
2. Ervasti et al. *Nature,* 345(6273):315-9, 1990.
3. Virgilio et al. *J Appl Physiol*, 125(5):1424-1439, 2018.
4. Martin et al. *J Appl Physiol,* 118(10):1299-309, 2015.
5. Houston et al. *Bull Math Biol,* 81(10):3976-3997, 2019.
6. Jarrah et al. *Biomed Res Int*, 2014:871810, 2014.
7. Pessina et al. *Skelet Muscle*, 4:7, 2014.

THE ROLE OF OUTER-VASCULAR MECHANICS ON SPROUTING ANGIOGENESIS: AN *IN SILICO* STUDY

Chiara Dazzi (1), Julia Mehl (1), Georg N. Duda (1), Sara Checa (1)

1. Julius Wolff Institute, Berlin Institute of Health, Charité - Universitätsmedizin Berlin, Germany

Introduction

Angiogenesis is the process by which new blood vessels sprout off from existing vasculature. Sprouting angiogenesis plays a major role during many physiological and pathological processes, including bone regeneration. Insufficient re-vascularization is a major clinical challenge leading to non-unions of fractures or other injuries. During sprouting, endothelial cells (ECs) are known to be sensitive to local mechanical signals and to interact with outer-vascular stromal cells (SCs) through cellular traction forces (intrinsic loads). However, also outer-vascular mechanical cues impact tissue deformation during sprouting (extrinsic loads) and affect patterning [1]. How these different mechanical cues impact sprout patterning remains, however, largely unknown. This study aimed to investigate the relative role of extrinsic and intrinsic mechanical signals on sprout patterning, using a computer modeling approach.

Methods

In silico multi-scale models of the mechano-regulation of sprouting angiogenesis and SCs organization were developed to represent two different experimental setups: 1) the healing region of a mouse osteotomy subjected to physiological loading and stabilized with a rigid or a semirigid fixator [2] (***angio_vivo***) and 2) a gelatin substrate subjected to either static or cyclic uniaxial loading [1] (***angio_vitro)***. Finite Element Models (FEMs) at the tissue scale, to compute mechanical strains, were coupled to Agent-Based Models (ABMs) at the cellular scale, describing ECs and SCs activity in response to local mechanical signals (e.g. *durotaxis*) [3] (Fig.1).
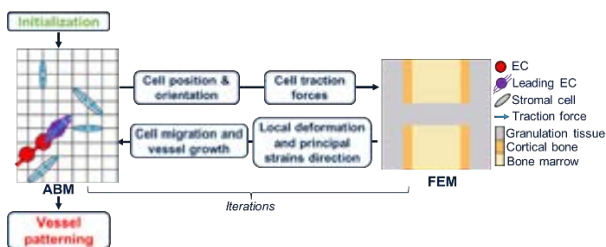
Figure 1: Schematic representation of the coupling between ABMs and FEMs. Exemplarily, the FEM for angio_vivo is shown.

The iterative nature of the model allowed to obtain results at discrete time points. Vessel patterning predictions were compared to dedicated histological data of the *in vivo* (***angio_vivo***) and *in vitro* experiments (***angio_vitro***) [1].

Results

Vessels fragments, consisting of multiple ECs, were predicted to gradually align towards the lateral direction (i.e. perpendicular to the bone long-axis) while approaching the osteotomy gap, as observed experimentally (Fig.2). Furthermore, the lack of vascularity within the gap observed for the semi-rigid fixator was mimicked by the *in silico* analyses and could be explained by high mechanical strains locally, which were the result of extrinsic mechanical loads (Fig.2).
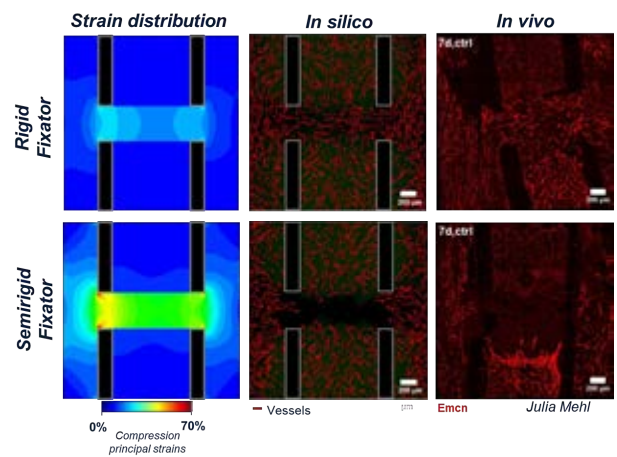
Figure 2: Healing region 7 days post-fracture. Emcn=Endomucin stained.

The same computer model was also able to describe vessel patterning in the *in vitro* experimental setting.

Discussion

Our results suggest that high extrinsic mechanical loading is capable to overrule intrinsic mechanical cues on a cell-matrix and cell-cell mechanical communication level. Taking the macro-mechanical constraints into account will enable the development of strategies to modulate angiogenesis through mechanics.

References

1. Rosenfeld et al, Proc Natl Acad Sci USA, 12:3215-20, 2016.
2. Borgiani et al, J Bone Miner Res., 10:1923-37, 2019.
3. Checa et al, Biomech Model Mechanobiol., 1:1-3, 2015.

Acknowledgements

A 3D COMPUTATIONAL MODEL OF AORTIC VALVE INTERSTITIAL CELL CONTRACTILE BEHAVIOR WITHIN A PEG HYDOGEL MEDIUM

Alex Khang and Michael S. Sacks

James T. Willerson Center for Cardiovascular Modeling and Simulation, The Oden Institute and Department of Biomedical Engineering, The University of Texas at Austin, Austin, Texas, USA

Introduction

Aortic valve interstitial cells (AVICs) oversee extracellular matrix (ECM) maintenance and turnover in the aortic valve (AV) and take on an activated phenotype in diseases such as bicuspid AV (BAV) disease, in which the AV has two instead of the normal three leaflet tissues. AVIC activation is characterized by increases in ECM production, remodeling, and contractility via expression of alpha-smooth muscle actin stress fibers (SFs). Currently, we have a limited understanding of the intrinsic differences between AVICs from structurally normal AVs and BAVs and how these differences contribute toward an increased rate of disease progression in the BAV population. Herein, we used experimental and computational methods to estimate AVIC SF architecture and contractile forces in tissue-emulating 3D hydrogels.

METHODS

Porcine AVICs and fluorescent microbeads were seeded in peptide-modified, poly (ethylene glycol) hydrogels for 72 hours before experimentation. The sample was incubated in Tyrode's Salt before obtaining an image stack of a single AVIC and surrounding fluorescent microbeads. Afterwards, Cytochalasin D was added to elicit cell relaxation through actin depolymerization and a second z-stack of the same FOV was obtained. The images were analyzed with our software FM-track, which outputted an AVIC surface mesh and field displacements. The displacements were interpolated onto the AVIC surface mesh, resulting in a 1:1 mapping between the initial and final AVIC shapes. The hydrogel, AVIC cytoplasm, and AVIC nucleus were modeled. AVIC geometry and spatial position was informed by 3DTFM data. Average nuclear geometry and spatial position was informed by immunostaining images from prior studies. The mesh consisted of ~50,000 linear tetrahedral elements. The hydrogel domain was modeled as a Neo-Hookean solid. To account for cell-induced degradation or strengthening of the gel, μ was allowed to vary spatially from the experimentally measured value of 108 Pa. The cytoplasm and nuclear domains were modeled as Neo-Hookean using eq. 1 with shear moduli of 750 and 7500 Pa, respectively, as informed by literature values [3,4]. SFs were modeled in the cytoplasm with total Cauchy stress given as:

$$\boldsymbol{T}^{sf} = \mathrm{H}(I_4 - 1)\left(2\frac{I_4}{J}\frac{\partial \psi_p^{sf}}{\partial I_4}\boldsymbol{m}\otimes\boldsymbol{m}\right) +$$
$$\mathrm{f}\bar{\phi}_{sf}\frac{I_4}{J}\boldsymbol{m}\otimes\boldsymbol{m}, \qquad (2)$$

where the first and second terms account for the passive and active stress produced by the SFs, respectively, $H()$

is a Heaviside step function that ensures SF passive stress arises only in tension ($I_4 > 1$), I_4 is the SF stretch, ψ_p^{sf} is the SF strain energy density function $\psi_p^{sf} = \frac{\mu_{sf}\bar{\phi}_{sf}}{2}(I_4 - 1)^2$, where μ_{sf} and $\bar{\phi}_{sf}$ are the SF modulus and expression level, respectively, $\boldsymbol{m}$ is the SF orientation, and f is the contractile strength per unit SF. Parameters μ_{sf} and f are set to 390 and 1590 Pa, respectively [3,4]. We backed out $\boldsymbol{m}$ and $\bar{\phi}_{sf}$ by minimizing the error between the simulated and experimental hydrogel displacements.

RESULTS.

The model successfully predicted SF orientations ($\boldsymbol{m}$) within the AVIC cytoplasm (Fig. 1). In addition, the model successfully predicted SF expression levels ($\bar{\phi}_{sf}$) and total stress ($\boldsymbol{T}^{sf}$), which showed that the highest SF expression level, and therefore total stress, was localized at the AVIC protrusions (Fig. 1A&B). The simulated AVIC shape in the final configuration (red) showed good agreement with experiment (green) (Fig. 1C).
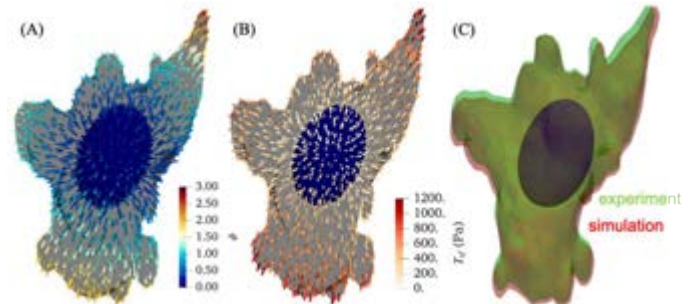
Figure 1: SF orientation depicted by lines. (A) SF expression level. (B) Total SF stress. (C) The simulated (red) and experimental (green) AVIC shapes in the final configuration.

DISCUSSION

To our knowledge, we present for the first time the ability to predict 3D SF architecture and contractile strength in AVICs embedded within a 3D medium. This novel experimental and computational approach allows for unprecedented insight into AVIC SF structure, expression levels, and contractile forces in full 3D, which reflect AVIC biophysical state and phenotypic activation level. Moreover, our simulation was able to predict that AVICs strengthen and do not meaningfully degrade the hydrogel, contrary to previous reports in the literature. This is likely a result of the AVICs excreting nascent ECM components that reinforce the PEG hydrogel material, leading increased in local moduli.

MAGNETO-ACOUSTIC INTERACTION IN MAGNETIC NANOSYSTEMS

R. Marqués (1,2), Ashofteh Yazdi A (2), J. Melchor (2,4,5), R. Ibarra (1), G. Rus (3,4,5)

1. Instituto de Nanociencia y Materiales de Aragón, Universidad de Zaragoza, España; 2. Departamento de Estadística e Investigación Operativa, Universidad de Granada, Granada, España; 3. Departamento de Mecánica de Estructuras e Ingeniería Hidráulica, Universidad de Granada, España; 4. Instituto de Investigación Biosanitaria, ibs.GRANADA, España; 5. Unidad de Excelencia Investigadora "Modeling Nature" (MNat), Universidad de Granada, España.

Introduction

Energy absorption by Magnetic Nanoparticles (MNPs) under alternating magnetic fields is the source of the heating properties used for magnetic hyperthermia. These experiments are usually performed at frequencies f = 100-800 kHz and field amplitudes up to 50 kA/m. In a simple description, the basic mechanisms for energy absorption are related to relaxation of magnetic moments within single-domain nanoparticles. Relaxation can occur by Néel relaxation between the hard and easy magnetization axes of the magnetic material, and by physical rotation of the MNPs if they are immersed in a carrier liquid (Brown relaxation). The work carried out by the UNIZAR group over the last few years has shown that, when energy absorption by NPMs occurs within magnetically charged cells, biological membranes (cells and endosomal membranes) can suffer physical damage as a consequence of the energy released by the particles. [1,2]

This membrane damage cannot be explained by considering only the effects of temperature. Recently, Carrey et al. [3] have proposed that the generation of ultrasonic waves, in the range of W/cm2 (sufficient to cause damage to the membrane in eukaryotic cells) due the mechanical oscillation of NPMs under a magnetic field gradient could explain the observed results.

Materials and methods

The main objective is the development of a valid experimental methodology for the study of mechanical waves generation by MNPs under magnetic fields. Hence, an experimental setup has been developed combining the emission/reception of US and the possibility of emitting high-frequency alternating magnetic fields. The samples are contained in the botton of a glass tube filled with water. The bottom is surrounded by the coil which applies the field and in the top of the tube we put the hydrophone for the acoustical signal acquisition.

In turn, a multiphysics computational model has been made, emulating the experimental configuration under certain hypotheses.

Results

In the preliminary results, when applying an alternating magnetic field to the MNPs we can see an increment on the signal received in the hydrophone. (figure 1.a)

Attending to the FFT of the 'control' and 'sample' signals (figure 1.b), the amplitude in the first harmonic for the sample signal is greater than the control one. The signal received in the control sample has been proved to be caused by interferences caused by the coil when applying the field. This 'noises' has been almost deleted by moving the hydrophone away from the coil but a signal post-processing method is going to be applied for better results.
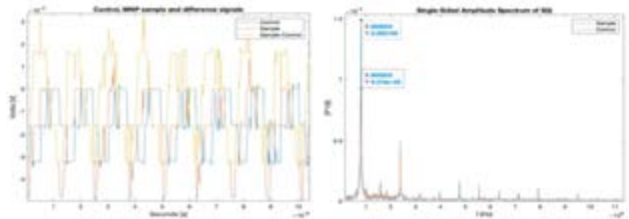
Figure 1: a. Control, MNP sample and difference adquired signals; b. Fast Fourier Transform (FFT) of the control and sample signals.

Attending to the computational results, when applying a field of the same characteristics to the MNPs, we can observe maximum displacements of *20E-12 m*.

Conclusions

In short, this effect could make it possible to generate ultrasound in cells that have magnetic nanoparticles. An efficient targeting of NPMs would also lead to the possibility of performing ultrasound therapy at the cellular level, for example targeting MNP aggregates in lysosomes [3]. The new phenomenology that could potentially be discovered in the event of a positive outcome of this hypothesis could include new therapeutic and detection strategies such as mechanical intracellular actuation, new imaging protocols, and selective biomolecular detection.

References

1. L Asín, MR Ibarra, A Tres, and GF Goya. Controlled cell death by magnetic hyperthermia: effects of exposure time, field amplitude, and nanoparticle concentration. Pharmaceutical research, 29(5):1319–1327, 2012.
2. Beatriz Sanz, M Pilar Calatayud, Teobaldo E Torres, Mónica L Fanarraga, M Ricardo Ibarra, and Gerardo F Goya. Magnetic hyperthermia enhances cell toxicity with respect to exogenous heating. Biomaterials, 114:62–70, 2017.
3. Julian Carrey, Vincent Connord, and M Respaud. Ultrasound generation and high- frequency motion of magnetic nanoparticles in an alternating magnetic field: toward intracellular ultrasound therapy? Applied Physics Letters, 102(23):232404, 2013.

Developing *in silico* avatars of cells to predict and drive cell migration on travelling waves

Jean-Louis Milan[1], Maxime Vassaux[2], Laurent Pieuchot[3], Karine Anselme[3], Ian Manifacier[1]

1. *Aix Marseille University, CNRS, ISM, Marseille, France*
2. *Univ Rennes, CNRS, IPR, Rennes, France*
3. *Institut de Science des Matériaux de Mulhouse, University of Haute Alsace, 68057 Mulhouse, France*
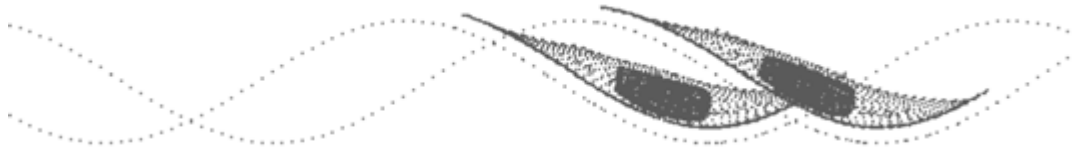
Introduction

We showed previously that cell migration is guided towards concave areas by a curvature gradient [1]. We called this phenomenon *curvotaxis* that is not induced by gravity. We showed that curvotaxis is a mechanobiological process involving the cytoskeleton and nucleus. The nucleus, is pushed by apical cortex pressure and is consequently displaced toward concave areas where the stress is lower [2, 3]. Influenced by the repositioning of the nucleus, the cell migrates to concave areas until a more relaxed mechanical state is reached. Nonetheless static curved surfaces guide cell migration only locally. We hypothesize that changing curvature dynamically by generating travelling waves at the surface of the substrate should stimulate and drive cell migration over large distances. Verifying our hypothesis directly by in vitro methods would require a long-time to develop the working prototype of a dynamic wavy substrate able to stimulate and drive cell migration. We proposed to verify it first using in silico with cell avatars.

Methods

We have developed in silico cell avatars that reproduce the mechanisms by which the cells sense the curvature of the substrate dynamically during cell migration [2, 3]. Cell model is a network of mechanical interactions that reproduce the contractile and dynamic structure of the cytoskeleton bound to the extracellular environment via focal adhesions. The cell model, in open access [4] is developed using LMGC90, a computational framework dedicated to non-smooth contact dynamics and multi interaction systems. Waves of 10μm of amplitude and 160μm of wave-length were simulated at the surface of a virtual substrate at a speed of 4μm/iteration. Migration of the cellular model was then initiated and driven by curvotaxis.

Results

The cell model follows the progression of the wave and migrates indefinitely as long as the wave exists. Influenced by the travelling wave, the nucleus moves towards the concavity and the cell migrates in that direction. When retaining the same wavelength and velocity parameters, the speed of the cellular avatar decreased by a third when we lowered the amplitude of the wave 5 μm. But, with a wave amplitude of 20μm, cell model migrated 1.5 times faster.

Discussion & Conclusion

Using the model, concerning the impact of travelling waves on cell migration, we answer a question that would otherwise be hard to directly address by experimental means. We propose the first in-silico proof-of-concept to guide cell migration by generating travelling waves. This will help in the designing of dynamic substrates to stimulate cell migration in vitro. Our in-silico avatar of migrating cells can later be implemented for cell engineering and lab-on-chip technology, as a live augmented reality tool to drive smart substrate actuation and control cells in vitro.

[1]   Pieuchot *et al.*, *Nature Commun.*, 2018, https://doi.org/10.1038/s41467-018-06494-6.
[2]   Vassaux et al., *Biophys. J.*, 2019, https://doi.org/10.1016/j.bpj.2019.07.022.
[3]   Vassaux et al., *Adv. Struct. Materials*, 2020, https://doi.org/10.1007/978-3-030-50464-9_12
[4]   Vassaux et al., *Zenodo available in Github* https://doi.org/10.5281/zenodo.1187087

NUMERICAL AND EXPERIMENTAL APPROACH TO STUDY THE RESPONSE OF YAP AND NPC TO DIFFERENT MECHANICAL SIGNALS

Stefania Saporito (1,2), Carlo F. Natale (2), Costantino Menna (3), Paolo Antonio Netti (1,2), Maurizio Ventre (2)

1 Department of Chemical, Materials and Industrial Production Engineering, University of Naples Federico II, Italy,

2 Center for Advanced Biomaterials for Health Care@CRIB and Istituto Italiano di Tecnologia, Naples, Italy

3 Department of Structures for Engineering and Architecture, University of Naples Federico II, Italy

Introduction

Mechanical forces, acting on eukaryotic cells, are responsible for cell shape, cell proliferation, cell polarity and cell differentiation thanks to two cells abilities known as mechanosensing and mechanotransduction [1]. These signals propagate from the extracellular matrix to the nucleus with different well known physical connections, but how the mechanical signals are transduced into biochemical one remains an open challenge [2].

Recent findings showed that the cell-generated forces affect the translocation of transcription factors (TFs) from the cytoplasm to the nucleus. Along these lines, nuclear pore complexes (NPCs) features play an important role during this process [3]. Owing to the complex patterns of strains and stresses of the nuclear envelope caused by cytoskeletal forces, it is likely that the morphology of NPC changes as cytoskeleton assemblies' change. This may ultimately affect molecular transport through the nucleus, hence altering cell functions.

Among the various TFs, Yes-associated protein (YAP) is able to activate specific pathways when entrapped into the cell nucleus [3].

Methods

A multiscale finite element (FE) model aimed to simulate the macroscopic cell spreading and consequent changes in the cell mechanical behaviour was developed. In this way the intracellular stress states and YAP nuclear transport can be related.

The model was supported by an experimental campaign designed to control cell shape and thus the intracellular stress states. Particularly, adipose stem cells were cultivated for 24h on circular or rectangular fibronectin micro-islets patterned surfaces having size 1300 μm² or 5000 μm².

The FE modelling strategy consisted in the definition of two numerical models representing two different scales of observation: (i) a full 3D non-linear mechanical model that reproduced the stretching/spreading of the whole-cell lying on the substrate and based on a proper experiment-derived displacement field as function of micropattern geometry; and (ii) a specific 2D periodic meso-model of the nuclear envelope subjected to pattern-related displacements derived from the full 3D FE simulations.

Results

Micropatterned substrates possessing small or large adhesive islets were employed to precisely control cellular spreading area. Furthermore, different micropattern shape dictated for peculiar actin stress fibres assemblies. Our results showed that such cytoskeleton organization differently impact nucleus morphology and YAP nuclear/cytoplasm trafficking. Moreover, different stresses distribution is observed with the 3D FE model on cellular and nuclear surfaces which correspond to different NPCs responses (Fig. 1).

Discussion

Nuclear translocation requires the crossing of the nuclear membrane through NPCs, so the altered morphologies of NPCs affect the YAP translocations.

Since it is difficult with electron microscopy acquire the representative regions of interest of NPCs, the numerical models are useful to partially overcame this technical limitation, providing a valuable insight on how nanoscale nuclear pores change their morphology features according to deformations occurring at the whole nucleus level.

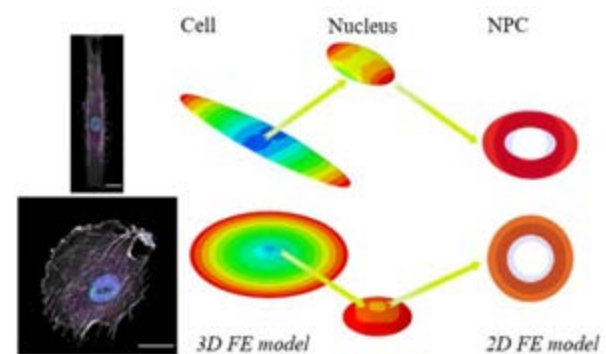*Figure 1: Representation from experimental based 3D FE model to the 2D FE model scheme with a zoom on NPC structure. Scale bar 20 μm. Cell displacement field: 0-60μm; Nucleus displacement field 0-8.5μm; NPC displacement field:0-0.75μm*

References

1. B. Enyedi, et al., Nucleus. 8(2):156-161, 2017
2. N. Wang, et al., Nat Rev Mol Cell Biol. 10, 75–82, 2009
3. A. Elosegui-Artola, et al., Cell. 171(6):1397-1410, 2017

INVESTIGATION OF LIMITED CT SCAN COVERAGE IN BIOFIDELIC SIDEWAYS-FALL MODELS FOR CLINICAL COHORTS

Alexander Baker (1), Ingmar Fleps (1), Pierre Guy (2), Stephen J. Ferguson (1), Benedikt Helgason (1)

1. Institute for Biomechanics, ETH Zürich, Zürich, Switzerland;

2. Division of Orthopaedic Trauma, Department of Orthopaedics, University of British Columbia, Canada

Introduction

Sophisticated biofidelic finite element (FE) models of sideways falls are an emerging tool for predicting hip fracture. These models can predict the fracture results of a sideways fall [1]; however, they often require femoral geometry beyond what is typically acquired during clinical scans. As such, there exists a large body of femoral data that cannot currently be utilized in sideways-fall FE models.

We aim to validate our femoral extension methodology in a fully automated biofidelic pipeline against experimentally validated models for use in large clinical cohorts.

Methods

Six preexisting validated biofidelic FE fall models [1] were used as a reference for this study. In these, the femur was cut 175mm distal to the greater trochanter, and strain-rate-dependent nonlinear material properties were assigned based upon CT gray levels [2]. In each new model, the original CT scan was truncated, and the femur was extended using a hollow tube (ρ=1.8g/cm^3) to the original femur length. The model was subsequently built in the same manner as the reference models.

Truncation distances ranged from 5mm to 150mm. This was split into 20 equally spaced bins and a random distance was chosen from each bin for each of the 6 specimens. This resulted in 120 simulations. For easier interpretation, the truncation distances were converted to scan coverage distal to the lesser trochanter (SC).
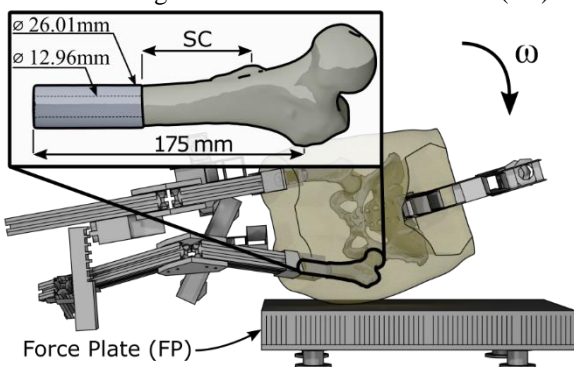
Figure 1: Biofidelic FE fall simulation with the femur truncated and extended.

For each simulation, the peak force on the force plate (FP$_{error}$) and the angle orientation of left femur (S$_{error}$) was compared to the corresponding reference model. Association between metrics was measured using Kendall's rank correlation coefficient (τ).

Results

Two simulations did not solve correctly and were discarded. Across all simulations, FP$_{error}$ ranged from -0.118 kN to 1.56 kN. In general, truncated models had lower peak forces (positive FP$_{error}$) as SC decreased ($\tau =$ 0.44, p<0.001 Fig 2). S$_{error}$ magnitudes ranged from 0.60° to 9.29° and was correlated with both SC ($\tau =$ 0.39, p<0.001) and FP$_{error}$ ($\tau = 0.20$, p=0.002)
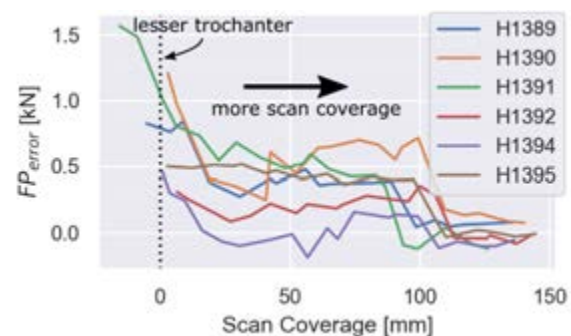
Figure 2: FP$_{error}$ decreases as scan coverage past the lesser trochanter (SC) increases for each of the 6 specimens.

Discussion

SC influenced FP$_{error}$ at all coverages, however scans covering only the lesser trochanter showed largest FP$_{error}$. In most cases, the connection between the femur extension and the bone failed; this is not representative of the experiment or reference models and resulted in a larger than expected FP$_{error}$. This may be alleviated by different connection methods and should be the focus of future work. Additionally, as S$_{error}$ was associated with FP$_{error}$ and SC, S$_{error}$ likely contributes to the FP$_{error}$ and reducing S$_{error}$ through better femur orientation methods may reduce FP$_{error}$. This reduction is likely to be secondary to error from femur connection methodology. Insufficient CT scan coverage can introduce large model errors and care should be taken when interpreting models built using extended femurs from especially short CT scans.

References

1. Fleps et al. J Bone Min Res, 34:1837–1850, 2019.
2. Enns-Bray et al, J Mech Behav Biomed Mater, 78:196-205, 2018.

Acknowledgements

RELIABILITY OF FLUOROSCOPIC ASSESSMENT OF GLENOHUMERAL TRANSLATION DURING A 30° SHOULDER ABDUCTION TEST

Eleonora Croci (1,2), Marina Künzler (1,2), Sean Börlin (2), Franziska Eckers (2), Corina Nüesch (1,2,3,4), Daniel Baumgartner (5), Andreas Marc Müller (2), Annegret Mündermann (1,2,3,4)

1. Department of Biomedical Engineering, University of Basel, Switzerland; 2. Department of Orthopaedics and Traumatology, University Hospital Basel, Switzerland; 3. Department of Clinical Research, University of Basel, Switzerland; 4. Department of Spine Surgery, University Hospital Basel, Switzerland; 5. Institute of Mechanical Systems, Zurich University of Applied Sciences, Switzerland

Introduction

Although rotator cuff tears are often clinically linked to a superior translational instability possibly because of insufficient joint centering, to date a thorough understanding of glenohumeral motion in patients with rotator cuff tear is lacking. The clinical manifestation of rotator cuff tears varies largely among patients: some patients have no complaints and the diagnosis is an incidental finding, while other patients have severe pain and limited range of motion that can be marginally restored with conservative treatment [1].

The aim of this study was to assess the reliability of fluoroscopically measured glenohumeral translation during a 30° shoulder abduction test.

Methods

Ten patients with rotator cuff tear and asymptomatic contralateral side participated in this study (6 men and 4 women; mean (standard deviation), age: 65.6 (10.3) years; height: 175 (8) cm; body mass: 79.5 (15.8) kg; body mass index (BMI): 26.2 (5.5) kg/m^2).

Single plane fluoroscopic images were acquired for each shoulder, with a pulse rate of 3Hz during 30° abduction and adduction in the scapular plane with extended elbows and hands in neutral position without additional weight and with handheld weights of 2kg and 4kg.

All images were manually labelled (Figure 1) once by one rater and twice by another rater. Inferior (-) - superior (+) glenohumeral translation during the entire motion was calculated.
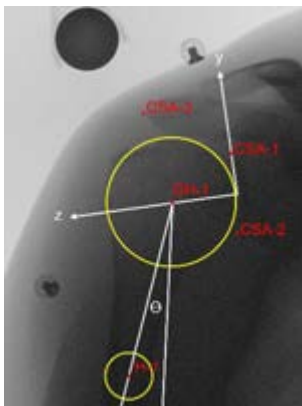
Figure 1: Example of a labelled image at initial position with glenoid coordinate system [2]. GH1— Glenohumeral head joint center (as a best-fit circle); Ɵ—Abduction angle; CSA—Critical shoulder angle; H1—center of humeral shaft.

Intra-class correlations (ICC) with their 95% confidence interval (CI), limits of agreement and paired t-tests of the translation range during abduction and adduction for interrater and intrarater reliabilities were computed.

Results

Moderate to good interrater and intrarater reliabilities of the translation range during abduction (ICC [95% CI]; interrater: 0.803 [0.691; 0.877]; intrarater: 0.817 [0.712; 0.887]) and adduction (ICC [95% CI]; interrater: 0.705 [0.551; 0.813]; intrarater: 0.688 [0.529; 0.801]) were found.

Differences in the translation range between repeated measurements were not statistically significant (mean difference, interrater: abduction, -0.1mm, p=0.686; adduction, -0.1mm, p=0.466; intrarater: abduction 0.0mm, p=0.888; adduction, 0.2mm, p=0.275).

Limits of agreement for the glenohumeral translations were found to be within 3mm, for both interrater and intrarater reliabilities during abduction and adduction.

During abduction, glenohumeral translation (average between the two raters) ranged from 3.3mm to 3.8mm and to 4.1mm and from 2.3mm to 3.9mm and to 3.8mm for the asymptomatic and symptomatic side for 0kg, 2kg and 4kg, respectively. During adduction, glenohumeral translation ranged from -3.4mm to -3.5mm and to -3.9mm and from -1.9mm to -3.1mm and to -3.4mm for the asymptomatic and symptomatic side for 0kg, 2kg and 4kg, respectively.

Discussion

The proposed method is suitable for measuring inferior-superior glenohumeral translation in the scapular plane and further exploring shoulder joint kinematics in loaded abduction tests. In addition, differences in glenohumeral translation during abduction and adduction within a subject (e.g., between sides or conditions, or before or after treatment) or between subjects (e.g., patients versus controls) exceeding 3mm should be considered relevant.

References

1. Moosmayer et al, J. Bone Jt. Surg. - Ser. B 92, 83–91, 2010
2. Teyhen et al, J. Biomech. 43, 1380–1385, 2010

Acknowledgements

ASSESSING CREDIBILITY OF A MULTISCALE MODEL FOR JOINT REPLACEMENTS SOLUTIONS

Cristina Curreli (1,2), Sylwia Huebner (2), Andrea Di Pietro (2) Giorgio Davico (1,2) and Marco Viceconti (1,2)

1. Department of Industrial Engineering, Alma Mater Studiorum - University of Bologna, Italy
2. Medical Technology Lab, IRCCS Istituto Ortopedico Rizzoli, Bologna, Italy

Introduction

Multiscale modeling is a widely used approach in computational biomechanics. The combination of different spatial and temporal scale models and simulation strategies can provide a more in deep understanding of the complex biological system. Applications of this strategy were also recently presented in the field of In Silico trials for joint replacement solutions (IST4JR) where computational models are used to assess the safety of new implant designs. For example, in [1], body-level simulations provided knee joint loading for tissue-based analyses that estimated contact pressure and wear in Total Knee Replacements (TKRs). The combination of musculoskeletal (MSK) multibody-dynamics and finite element (FE) analyses proved to be a promising solution to realistically simulate the in vivo loading conditions during specific tasks of induvial patients and predict the surface damage process of the implant. However, one critical question that to the author's best knowledge has never been answered is how to assess model credibility of such multiscale models. This study aims to investigate this aspect, of fundamental importance in the context of regulatory acceptability for the adoption of the methodology in clinical practice.

Methods

A multiscale platform was developed coupling a MSK model of a subject implanted with an instrumented Zimmer NK-II cruciate-retaining knee prosthesis and a FE wear model of the specific implant. Experimental data obtained from the fifth edition of the KGC Competitions [2] were used to scale the generic MSK model and run the walking simulations. Kinematic and dynamic results obtained from the MSK analyses performed in OpenSim v3.3 were provided as inputs to the FE simulations that were run using Ansys Workbench: the relative pose of the TKR components during one gait cycle together with the load history defined the boundary conditions for the FE model. Wear simulations were performed to estimate the volume lost and the wear depth on the surface of the tibial insert during the service life of the device.

A two layer model credibility assessment framework was proposed to account for the different modelling approaches, spatial and temporal scales (Fig. 1). The first layer was designed based on the guidelines described in the VV&40 standard [3] and includes typical verification, validation and uncertainty quantification (VV&UQ) activities that are specific for the two modelling approaches; the second layer referred to the whole system-level predictions and investigated the possible source of errors that can arise when the sub-models interact (e.g., propagation and reiteration of model uncertainties through the pipeline).
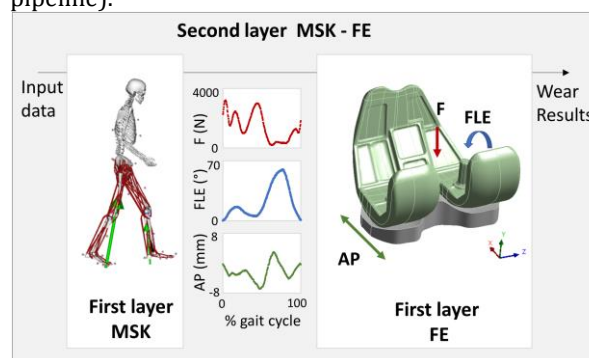
Figure 1: Two layer model credibility assessment framework for the multiscale MSK- FE model.

Results

Among the model form assumptions investigated in the first VV&UQ layer related to the MSK model was the kinematic definition of the knee joint. A maximum variation range of about 4 mm, 1° and 100 N was found for anterior- posterior translation, flexion-extension rotation and axial force respectively when different knee spline functions were implemented. Predicted and experimental joint reaction forces and moments acting on the tibial insert component and measured by the instrumented knee implant showed a good level of agreement ($R^2 \sim 0.8$). Regarding the first credibility layer related to the FE model, typical verification activities aimed at reducing the numerical error were defined and performed (e.g., mesh convergence analysis on the maximum contact pressure). FE model results in term of volume lost estimated after 10^6 wear cycles were compared to experimental data available in the literature and percentage difference were found of about 7 %.

Discussion

In this study, a new framework to assess model credibility of a multiscale model was developed and applied to a combined simulation approach where MSK and FE analyses are used to evaluate the risk associate to a typical failure mode in TKR.

References

1. Viceconti et al, Ann Biomed Eng. 49:3349-3355, 2021.
2. Fregly et al, J. Orthopeadic Res., 30:503-513, 2012.
3. ASME Standard Subcommittee V&V 40, 2018.

A MODELING FRAMEWORK TO ENABLE THE DIFFERENTIAL DIAGNOSIS FOR THE LOSS OF MUSCLE FORCE

Giorgio Davico (1,2), Luciana Labanca (3), Francesca Bottin (1,2), Fabio Baruffaldi (2), Maria Grazia Benedetti (3,4), Marco Viceconti (1,2)

1. Department of Industrial Engineering, University of Bologna, Italy; 2. Medical Technology Lab, IRCCS Istituto Ortopedico Rizzoli, Italy; 3. Physical Medicine and Rehabilitation Unit, IRCCS Istituto Ortopedico Rizzoli, Italy; 4. Department of of Biomedical and Neuromotor Sciences, University of Bologna, Italy.

Introduction

Naturally, with aging, human muscles become weaker [1]. However, this process can be accelerated or aggravated by ongoing pathological processes. Recently, the loss of muscle force, namely dynapenia, has been associated to (1) sarcopenia (i.e., the loss of muscle mass/volume), (2) poor (suboptimal) muscle control and/or (3) innervation problems. While quantitative measures (e.g., dynamometry, medical imaging) exist and enable to acquire important pieces of information, what is currently missing is a way to fuse such information in one diagnosis. Consequently, the decision is often left to the clinicians' own experience. To this end, we hereby propose a modeling (in silico) framework to conduct the differential diagnosis for dynapenia, aiming to provide clinicians with a tool to identify the cause of the loss of muscle force.

Methods

Magnetic Resonance Imaging (MRI), surface electromyography (sEMG) and dynamometry data will be fused to develop the Digital Twin of a patient. This will be employed to conduct a series of *in silico* simulations, specifically designed to test various scenarios and rule out, one by one, those that do not explain the observed loss of muscle force (Figure 1). Sarcopenia will be implicitly accounted for, as the muscle parameters of the Digital Twin will be derived from each patients' own MRI data. Suboptimal muscle control will be tested implementing different optimization functions and using various modelling approaches (e.g., EMG-assisted [2] approaches and Static Optimization). Reduced muscle activation (due to innervation problems) will be determined via in vivo superimposed neuromechanical electrical stimulation measures, acquired on the patient in the lab. Model verification and validation will be performed to ensure the predictions are physiologically plausible. The clinical validity of the framework and outcome assessment will be tested on a healthy adult (normative) cohort and a cohort of candidate for total hip arthroplasty patients.

Results

Preliminary tests have been run to optimize the experimental protocol, to define a pipeline to efficiently develop the Digital Twins and to test the simulation environment (i.e., model-to-experiment registration, methods and parameters to run the simulations). The developed modeling pipeline, that employs the novel STAPLE toolbox [3], is currently being validated using an independent and publicly available validation data collection [4].
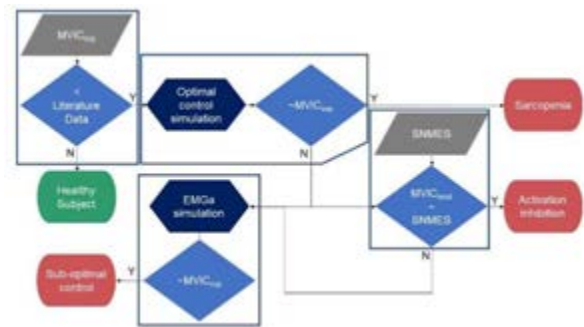
Figure 1: Proposed framework to determine the primary cause of dynapenia (red), combining experimental measures (gray) and in silico simulations (dark blue). Exp = experimental, mod = model predictions, EMGa = EMG-assisted, MVIC = maximal isometric voluntary contraction torque, SNMES = superimposed neuromuscular electrical stimulation.

Discussion

Once validated, the proposed framework has the potential both to inform clinical decision making and to be used as stratification tool in the enrollment phase for clinical trials aiming to test drugs for sarcopenia, where the inclusion of dynapenic (not sarcopenic) patients may be a confounding factor.

References

1. Danneskiold-Samsøe et al, Acta Physiol 197: 1–68, 2009.
2. Pizzolato et al, J Biomech, 48: 3929-3936, 2015.
3. Modenese and Renault, J Biomech, 116: 110186, 2021
4. Fregly et al, J Orthop Res, 30:503–513, 2011.

Acknowledgements

A PARAMETRIC STUDY TO IMPROVE SURGICAL PLANNING OF SPRING-ASSISTED POSTERIOR VAULT EXPANSION

Lara Deliège (1,2), Karan Ramdat Misier (1,2), Gregory James (2), Juling Ong (2), David Dunaway (2), Noor ul Owase Jeelani (2), Silvia Schievano (1,2), Alessandro Borghi (1,2).

1. University College London, UK; 2. Great Ormond Street Hospital, London, UK

Introduction

Spring-Assisted Posterior Vault Expansion (SAPVE) has been adopted at the London Great Ormond Street Hospital for Children (GOSH) to treat raised intracranial pressure in patients affected by syndromic craniosynostosis (SC), a congenital calvarial anomaly causing the premature fusion of skull sutures [1]. SAPVE involves elastic distractors used to dynamically reshape the skull and increase the intracranial volume (ICV). The surgical outcome is uncertain due to the complexity of the procedure and the lack of knowledge of the interaction between spring and skull. Finite Element (FE) modelling was proved suitable to accurately predict the outcome of spring expansion in syndromic and non-syndromic populations [1, 2]. We developed, tested and validated a patient-specific model able to predict the ICV increase for SC patients, using information retrievable from Computed Tomography (CT) scans and improved the current understanding of the effect of surgical correction.

Methods

Eighteen patients, who underwent SAPVE at GOSH (age at surgery = 2.6 ± 1.8 years) and had preoperative (74 ± 106 days before surgery) and postoperative (257 ± 234 days after surgery) CT data (fig.1A, B) were selected and classified by type of SAPVE performed (2 springs implanted on top or side of the skull and 4 springs implanted). Osteotomy dimensions, spring models and location were recorded from postoperative CT scans and notes. Expanding on a previously validated methodology [1], the 3D model outer surface was extracted and smoothed. The location and size of the surgical cuts were parametrised using 3 parameters (fig.1C) and replicated on the surface model. A constant thickness (equal to the patient's average calvarium thickness) was applied to the geometry in ANSYS 2020 (Canonsburg, Pennsylvania, US) before simulating the spring expansion [1]. A Design of Experiment (DoE) was performed to assess the parameters impact on the surgical procedures' outcome i.e., the post-expansion ICV (automatically estimated in ANSYS using a computational tool developed in Python language [version 3.9]). Each parameter was assigned with a parametric range and an Optimal Space-filling Design was selected for the DoE. For each patient, the predicted postoperative skull shape was retrieved and compared with the respective postoperative CT model. Predicted and postoperative ICV (ICV_{FE}, ICV_{CT}) were also compared. The local sensitivity of ICV_{FE} to each parameter was analysed for each patient of each group

(i.e., variation of ICV_{FE} when a single input parameter varies with all the other inputs to their current value).
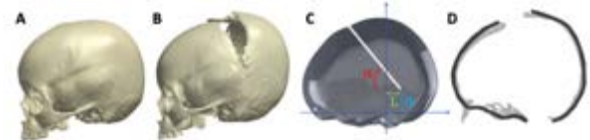
Figure 1. (A) Preoperative, (B) Postoperative CT models, (C) FE model with osteotomy and parameters, (D) comparison of end-of-expansion FE model (dark grey) and postoperative CT model (light grey).

Results

The average postoperative ICV_{CT} recorded was 1394 ml ± 216 ml and the FE model yielded comparable values (fig.1D) with an average of 1484 ml ± 267 ml ($R^2 = 0.76$, $p < 2.10^{-6}$). The results of the sensitivity analysis showed a consistency throughout the cohort but highlighted some differences in terms of intensity depending on the type of procedure performed (fig.2). The ICV of patients in the 4 springs group appears to have a statistically higher local sensitivity to the parameter L compared to the two others groups (*p = 0.0312*).
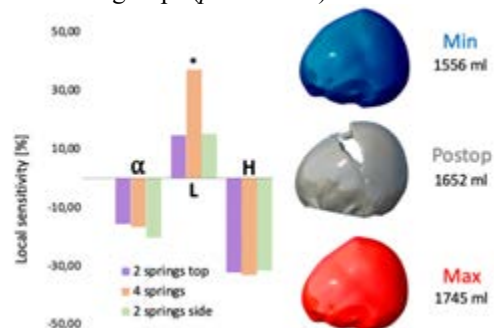
Figure 2. Local sensitivities of ICV_{FE} to osteotomy's position (i.e., parameters) for each procedure (left). On the right, minimal (top) and maximal (bottom) volumes estimated by Ansys after the DoE compared to relative postoperative CT (middle). (*) = statistically different.

Discussion

This work shows that our FE model can reliably predict the effect of spring insertion on SC patients and allows for parametric optimization of surgical cuts. The study indicates how to optimize the ICV increase according to the type of procedure and provides indication on the most robust surgical strategy.

References

1. Deliège et al., Clinical Biomechanics 88, 2021
2. Borghi et al., Med Eng Phys 53:58–65, 2018

USE OF ASME V&V-40-2018 STANDARD AS METHODOLOGICAL FRAMEWORK FOR THE QUALIFICATION OF DIGITAL TWINS

Alessandra Aldieri (1,2), Cristina Curreli (1,2), Antonino A. La Mattina (1,2), Marco Viceconti (1,2)

1. Department of Industrial Engineering, Alma Mater Studiorum - University of Bologna, Italy 2. Medical Technology Lab, IRCCS Istituto Ortopedico Rizzoli, Bologna, Italy

Introduction

Evidence of safety and efficacy is necessary to obtain marketing authorization for a new medical product from regulatory agencies. Historically, efficacy and safety are established through *in vivo* or *in vitro* controlled experiments, but In Silico methods, referred to as In Silico trials, are increasingly being included in regulatory submissions. In many cases there is no clear pathway for regulatory approval of In Silico Trials [1]. In 2018, the ASME VV-40-2018 standard was published [2], designed to assess the credibility of computational models adopted for the regulatory evaluation of new medical devices. Here, the VV-40 standard is adopted to assess the credibility of the Bologna Biomechanical Computed Tomography (BBCT)-hip, a digital twin technology for which we sought qualification advice from EMA for its use surrogate biomarker of the fracture endpoint.

Methods

BBCT-hip is a digital twin model that calculates a surrogate biomarker of the risk of fracture, called Absolute Risk of Fracture at time zero (ARF0). To do so, it predicts 1,000,000 possible fall impact forces for a body of the height and weight equal to those of the patient and compares them to the loads to failure for each possible impact direction predicted by a patient-specific Finite Element (FE) model of the femur based on the patient's QCT data. ARF0 is calculated as the ratio of the number of fall impact forces causing a fracture divided by their total number. ARF0 is a better surrogate biomarker of fracture than areal Bone Mineral Density (aBMD) [3, 4] and might be employed in Clinical trials Phase II and Phase III to assess new antiresorptive treatments efficacy. In this framework, BBCT-hip credibility is demonstrated conducting a technical validation plan inspired by ASME VV-40:2018:

1. *Definition of Context of Use* (CoU): ARF0 is used as a surrogate biomarker of the primary endpoint proximal femoral fracture in phase II and phase III clinical trials to evaluate the efficacy of a new antiresorptive drug, in place of DXA-based aBMD.
2. *Risk Analysis*: combining model influence and consequence BBCT-hip risk is determined to be high for the established CoU.
3. *Verification and Validation activities* carried out with rigor (credibility level) commensurate to model CoU and risk: *Code verification* evidences are provided by the vendors (Ansys Inc; MathWorks Inc) of the simulation frameworks used to implement BBCT-hip.

Calculation verifications are conducted on all components of the model that can contribute to the numerical approximation error. The influence of the *Model form* and *Model inputs* on the quantity of interest (load to failure) was evaluated. *Validation* was conducted on predicted deformations and load to failure, as well as on classification accuracy. Prediction accuracy was evaluated comparing the FE analyses with *in vitro* experimental tests [5,6]; stratification accuracy was assessed *in vivo* using a pair-matched retrospective cohort of post-menopausal women [4].
4. *Applicability:* the relevance of the quantities of interest and of the validation activities to the CoU was analysed.

Results

Verification and Validation activities allowed to establish the numerical approximation error ($< 5\%$) and the extent uncertainties in BBCT-hip inputs affected load to failure prediction to (differences $< 7\%$). The strain prediction accuracy was characterized by a Root Mean Squared Error (RMSE) of 7%. The load to failure prediction produced a Standard Error of the Estimate normalised by the average measured failure load between 15% and 16%. The area under the ROC curve AUC=0.852 was significantly higher for ARF0 than AUC=0.750 corresponding to DXA-based T-score at the femoral neck.

Discussion

A pathway to assess the credibility of an In Silico Trial methodology to be used in regulatory submissions is here proposed and adopted for BBCT-hip. It has recently been included with a clinical validation plan in a qualification advice request submitted to EMA. This work fosters the adoption of standardized pathways for In Silico Trials qualification in EU.

References

1. Viceconti et al., *Methods*, 2021
2. ASME, *'Assessing Credibility of Computational Modeling through Verification & Validation: Application to Medical Devices'*, 2018
3. Altai et al., *Clin Biomech*, 2019
4. Bhattacharya et al., *Biomech Model Mechanobiol.*, 2019.
5. Cristofolini et al., *Philos. Trans. Royal Soc.*, 2010
6. Viceconti et al., *Curr. Osteoporos. Rep*, 2018

Acknowledgements

THE USE OF MOBILE EYE TRACKING TO ASSESS COGNITIVE LOAD IN LOWER LIMB AMPUTEES: A PILOT STUDY

Sabina Manz (1,2), Strahinja Dosen (2), Jose Gonzalez-Vargas (1)

1. Ottobock SE & Co. KGaA, Duderstadt, Germany;
2. Department of Health Science and Technology, Aalborg University, Aalborg, Denmark

Introduction

Lower limb amputation can have significant impact on the patients' quality of life and physical abilities [1], and has also been shown to have social [2] and cognitive effects [3]. The literature reports that the use of a prosthetic device is associated with increased cognitive load [3]. The limited research which exists has demonstrated that more advanced prosthetic knee joints (e.g., microprocessor-controlled knees, MPK) have been able to reduce the cognitive burden on the users compared to non-microprocessor-controlled knees (NMPK) [4]. However, current methods (e.g., EEG) are cumbersome and can only be used in controlled settings. Recently, eye trackers have become of interest with respect to assessing cognitive load in amputees. One pilot study looked at the transitions from stairs to level ground and vice versa and found that amputees spend more time focusing on the transition area compared to the able-bodied population [5].

The use of eye trackers, however, is fairly new in this field and its relevance for the assessment of cognitive load is still unknown. Therefore, the purpose of this study was to investigate the use of gaze data obtained from a mobile eye tracker in patients with lower limb amputation to estimate the cognitive load in different motor tasks.

Methods

A mobile eye tracker (Tobii Pro Glasses 3, Stockholm, Sweden) was used to record the gaze location in a patient with unilateral transfemoral amputation and an able-bodied participant. The participants were asked to wear the eye tracker, similar to regular glasses, while performing different activities of daily living. The experiment was performed in a laboratory environment that allowed stair and ramp ascent/descent, walking on different terrains, and tight turns. A preliminary qualitative analysis of the gaze data obtained during stair ascent was performed. For this evaluation, the gaze data was mapped to a screenshot of the stairs.

Results

The qualitative gaze analysis can be seen in Figure 1. The left and right image show the results for the able-bodied participant and the subject with transfemoral amputation, respectively. On the left, the visual sampling is spread out equally across the stairs, whereas on the right, the sampling is concentrated in the areas of visual interest to safely ascend the stairs when using a prosthesis. In the latter case, there are clearly visible "hot spots" associated to the steps taken with the prosthetic leg (i.e., 2nd and 4th stair).

Figure 1: Gaze locations during stair ascent, accumulated from two trials for an able-bodied participant (left) and a participant with transfemoral amputation (right). The colors indicate the duration of each fixation, i.e., the redder the spot, the longer the fixation.

Discussion

The preliminary analysis showed clear differences in the gaze patterns of the able-bodied participant compared to the subject with transfemoral amputation. The next step in this research is to perform a more extensive data collection that will include more participants, wearing different prosthetic devices, and a larger set of tasks (e.g., dual-tasking). This will show whether eye tracking could be used to assess the cognitive burden while using a prosthesis. Furthermore, it is of interest to investigate whether eye tracking can determine the assumed differences in the cognitive burden between different types of devices, for instance, NMPK versus MPK systems.

References

1. Jordan et al, Prosthet Orthot Int, 36:430-434, 2012.
2. Burger et al, Prosthet Orthot Int, 21:35-39, 1997.
3. Miller et al, Arch Phys Med Rehab, 82:1031-1037, 2001.
4. Möller et al, Prosthet Orthot Int, 43:257-265, 2019.
5. Li et al, IEEE Engineering in Medicine and Biology Society - Annual Intern. Conference, 3163–3166, 2019.

Acknowledgements

MARKOV CHAINS WITH PATIENT-SPECIFIC FE MODELS FOR IN SILICO TRIALS OF ANTIRESORPTIVE DRUGS

Antonino A. La Mattina (1,2), Marco Viceconti (1,2)

1. Department of Industrial Engineering, Alma Mater Studiorum – University of Bologna, Italy
2. Medical Technology Lab, IRCCS Istituto Ortopedico Rizzoli, Bologna, Italy

Introduction

Population ageing in western countries leads to the increasing prevalence of fragility fractures due to osteoporosis, that causes bone mineralization loss and microarchitecture degradation. To demonstrate efficacy of new antiresorptive drugs in phase III clinical trials, thousands of patients need to be enrolled for several years [1]. Patient-specific finite element (FE) models have been developed and demonstrated to be a better predictor of femur fracture with respect to the clinical standard, i.e., absorptiometry [2].

However, to validate an In Silico Clinical Trial technology it is of chief importance to obtain an output comparable with that of real past clinical trials, typically the number of observed fractures, but the current models usually give physics-based results (e.g., fracture load, fracture risk).

Here we report our preliminary convergence results of a stochastic clinical trial simulator (placebo arm) based on FE models orchestrated by a simple Markov chain.

Materials and Methods

The starting cohort was composed by 94 patient-specific proximal femur FE models from the Sheffield cohort of post-menopausal women [3], from which a statistical anatomy atlas was derived and used to generate 150 synthetic models.

The 150-patients synthetic cohort was simulated for an observation timespan of 10 years, with a timestep of 1 month: briefly, every month each patient mineralization was updated (1% areal bone mineral density loss per year [4]) and she fell (also multiple times) or not (Poisson distribution, 0.65 falls per year [2]); for each falling, a load orientation was randomly chosen (uniform distributions) in the intervals -30:30° in antero-posterior and -30:0° in medio-lateral directions, respectively [2]; the estimated fracture load was compared with a stochastically-generated patient-specific falling load magnitude [2]; if the stochastic load exceeded the fracture load, the patient was classified as fractured at that year, and excluded from further simulations. The same simulations were performed with mineralization updates every 2, 4, 6, and 12 months; the number of fallings and the associated stochastic parameters were kept the same as the 1-month timestep, to isolate the effects of bone remodelling frequency.

To explore convergence of the stochastic realizations of the Markov-chain, the starting 94 femurs were simulated 25 times for a 10-years timespan with a timestep of 12 months, and the number of fractured patients was monitored at the end of year 1, 5, and 10. Convergence was assumed when the relative difference of the cumulative coefficient of variation was under 0.01 for at least 5 realizations [5].

Results

In the bone remodelling timestep convergence study only one patient fractured at a different year (9th instead of 7th, from 4-months step on), because of a difference of a few Newtons in the estimated failure load (2274 [2-months step] vs 2277 [4-months step], with a falling load of 2275 N). A timestep of 12 months was therefore considered adequate.

The convergence of the fraction of patients fractured within 1, 5, and 10 years was achieved after 16, 20, and 10 realizations at 27.8%, 78.8%, and 93.8%, respectively.

Discussion

This work demonstrated a simple orchestrator to simulate real-like clinical trials with a Markov chain model. The fast convergence of the mineralization update of such stochastic models will be of chief importance if FE models will be coupled with a computationally intensive bone remodelling simulation. Also, some works [6] reported a slower mineralization decay, so our research has possibly explored a worst-case scenario.

If validated, this simple approach can be used for the simulation of phase III clinical trials with an efficient use of computation time.

References

1. Van Norman, J Am Coll Cardiol Basic Trans Science, 1:399–412, 2016.
2. Bhattacharya et al., Biomech Model Mechanobiol, 18:301–318, 2019.
3. Taylor et al., J Mech Behav Biomed Mater, 118:104434, 2021.
4. Paggiosi et al., Osteoporos Int, 22(2):721–729, 2011.
5. Curreli et al., Int J Numer Methods Biomed Eng, 37(7):e3470, 2021.
6. Cummings et al., JAMA, 280(24):2077–2082, 1998.

Acknowledgements

CHANGES IN GAIT PATTERNS AFTER HIP ARTHROPLASTY – COMPARING IMU- AND MARKER-BASED DATA

Corina Nüesch (1,2,3,4), Petros Ismailidis (1,3,4), David Koch(1,2,5), Karl Stoffel(1), Annegret Mündermann (1,2,3,4)

1. Department of Orthopaedics and Traumatology, 2. Department of Spine Surgery, University Hospital Basel, Switzerland; 3. Department of Biomedical Engineering, 4. Department of Clinical Research, 5. Department for Sport, Exercise and Health, University of Basel, Switzerland

Introduction

Inertial measurement units (IMUs) have become increasingly popular in assessing gait parameters in patients suffering from osteoarthritis (OA) [1]. We have previously shown that differences in gait patterns between patients with hip OA and healthy controls measured with IMUs are comparable to those assessed using marker-based methods reported in the literature [2,3].

The aim of this study was a direct comparison of an IMU- with a camera-based system for assessing gait patterns in patients with hip OA before and changes after total hip arthroplasty (THA).

Methods

Fifteen patients (10 male, 5 female; age, 64.4 (SD: 12.7) years; body mass index, 27.2 (2.5) kg/m^2) with unilateral hip OA scheduled for THA participated in this study. Measurements were performed pre- and 1 year postoperatively. At both visits, participants performed a gait analysis in a 20m hallway with seven inertial sensors placed on the pelvis, thigh, shank and foot (RehaGait, Hasomed, Magdeburg, Germany) and a gait analysis on a 10m laboratory walkway using retroreflective markers placed according to the PlugIn Gait model and 10 high-speed cameras (Vicon, Oxford, UK).

Walking speed, cadence and hip flexion/extension trajectories were calculated and extracted from the respective software and hip range of motion (ROM) during stance was calculated. For each system, differences in pre- and postoperative discrete parameters were tested using paired t tests (P<0.05) and in hip angle trajectories normalized to gait cycle (GC) using statistical parametric mapping (SPM) with paired t tests (P<0.05).

Results

Walking speed increased postoperatively with both systems (Table 1), but this increase was not significant (P>0.09). Hip flexion/extension ROM measured with RehaGait increased postoperatively by 10.8° (P<0.001) and measured with Vicon by 7.2° (P=0.005, Table 1). Similarly, hip flexion increased postoperatively on average by maximally 8.9° (0-29%GC; P<0.001) and 8.4° (84-100%GC; P=0.007) when measured with RehaGait and by 6.9° (0-22%GC; P=0.009) and 6.4° (67-100%GC; P=0.001) when measured with Vicon (Figure 1).

Table 1: Mean (SD) of discrete gait parameters measured with IMUs (RehaGait) and Vicon for patients with hip OA before (pre) and after (post) THA.

Parameters	IMU pre	IMU post	Vicon pre	Vicon post
Walking speed (m/s)	1.13 (0.17)	1.18 (0.14)	1.19 (0.19)	1.27 (0.13)
Cadence (steps/min)	111.3 (9.4)	111.8 (7.1)	109.4 (9.6)	110.7 (7.4)
Hip ROM stance (°)	25.5 (6.3)	36.3 (7.7)	32.5 (9.5)	39.7 (5.1)
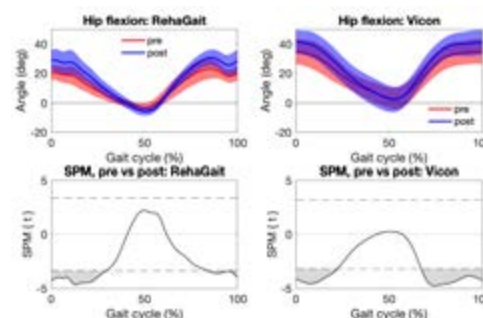
Figure 1: Mean (±1SD) hip flexion in patients before (red) and after (blue) THA with corresponding SPM statistics (grey areas indicate significant differences).

Discussion

Both systems detected similar improvements in hip kinematics of patients with hip OA who received THA. Differences in definition of the pelvic segment (IMU overlying the 5th lumbar vertebra vs markers on anterior and posterior iliac spines) and definition of neutral hip angles might have contributed to differences in absolute joint angles and time periods with significant differences. Nevertheless, gait assessments using IMUs have a huge clinical potential because they allow to assess pre- and postoperative changes in gait in a short time and are suitable for application in large clinical trials.

References

1. Kobsar et al, Sensors, 20:7143, 2020
2. Ismailidis et al, Gait Posture, 81:49-55, 2020.
3. Ismailidis et al, J Orthop Res, 39:1253-1261, 2021.

Acknowledgements

Simulation of piezoelectric scaffold for bone regeneration

Vahid Badali (1), Melika Mohammadkhah (1), Sara Checa (2), Manfred M. Zehn (1)

(1) Department of Structural Analysis, Institute of Mechanics, Technische Universität Berlin, Germany; (2) Julius Wolff Institute, Berlin Institute of Health, Charite – Universitaetsmedizin Berlin, Germany

Introduction

The treatment of large bone defects remains a clinical challenge, where current treatment strategies present many limitations. Tissue engineering scaffolds appear as a promising treatment strategy, where scaffolds are used to support tissue growth. Due to the intrinsic piezoelectric properties of biological tissues, piezoelectric scaffolds have recently attracted a lot of attention [1]. These scaffolds generate electrical signals under mechanical deformation. Experimental studies have shown the benefits of piezoelectric materials in scaffold-supported bone regeneration [2], however, the influence of scaffold design on the electro-mechanical coupling remains largely unknown. The objective of this study is to investigate the influence of scaffold design on the generated electrical signals under external mechanical loading.

Methods

Finite element models of cuboid scaffolds, with overall dimensions of 40×20×20mm and porosities of 65 and 85%, were created in ABAQUS/CAE 2020. Scaffold dimensions were based on experimental studies of a large bone defect in a large animal model [3]. Piezoelectric patches with a thickness of 0.03mm were tied to the scaffold walls to create electric potentials. Titanium properties were assigned to the scaffold and piezoelectric PVDF and barium titanate properties were used for piezoelectric patches (Table 1). A compressive load that simulated mechanical conditions during daily walking [4] was applied to both top and bottom faces of the scaffold. The electric potential of the face of the patches in contact with the titanium scaffold was set to be zero. Due to symmetry, only 1/8 of the scaffold was modelled (Figure 1a). The model was meshed using quadratic hexahedral elements with size of 0.1mm.

	Titanium	PVDF	Barium titanate
Young's modulus (GPA)	104	2.7	112
Poisson's ratio	0.3	0.35	0.3
d_{31} (pC/N)	-	21	-60
d_{32} (pC/N)	-	1.5	-60
d_{33} (pC/N)	-	-32.5	140
d_{15} (pC/N)	-	-27	260
d_{24} (pC/N)	-	-23	260
Relative permittivity	-	8.5	1450

Table 1: Material properties [5-7]

Results

Figure 1b shows the voltage distribution generated by the piezoelectric patches made of barium titanate in the scaffold with porosity of 65%. Patches attached on the vertical walls exhibit higher voltage values since they are subjected to higher compression. In addition, scaffolds with higher porosity produced higher voltages due to higher stresses.

The voltage obtained using different piezoelectric materials and scaffold porosities are summarized in Table 2.
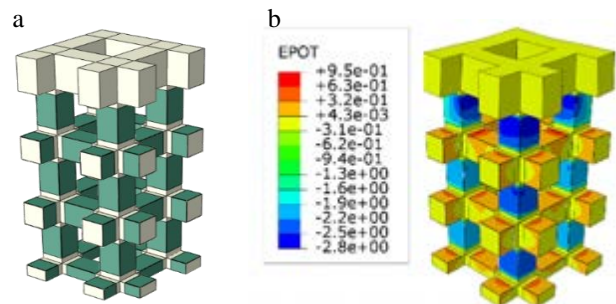
Figure 1: a) 1/8 of the scaffold's model with piezoelectric patches (green), b) Voltage distribution generated by piezoelectric patches (Porosity: 65%, Patches material: barium titanate)

Material	Scaffold porosity	Voltage (V)
Barium titanate	65 %	+0.9 to -2.8
Barium titanate	85 %	+4.9 to -4.2
PVDF	65 %	+1.2 to -1.3
PVDF	85 %	+1.3 to -2.3

Table 2: Voltage results for different piezoelectric materials and scaffold porosities

Discussion

The designed scaffolds produced a voltage range which has previously been reported to enhance cell proliferation [8]. and osteogenic differentiation [2], making our results suitable for bone regeneration purposes. In the future, the relevance of these electrical signals for bone regeneration will be investigated.

References

1. Mohammadkhah, M., et al., Bone, 2019. **127**: p. 544-555.
2. Damaraju, et al.,. Biomaterials, 2017. **149**: p. 51-62.
3. Pobloth, et al., Sc. trnsl medicine, 2018. **10**(423).
4. Duda, G.N., et al., J biomech, 1997. **31**(3): p. 201-210.
5. Perier-Metz, et al, Frontiers in bioeng and biotech, 2020. **8**.
6. Nix, et al, Ferroelectrics, 1986. **67**(1): p. 137-141.
7. Narita, F. et al, Int. J. Metall. Mater. Eng, 2015. **1**: p. 103.
8. Dubey, et al, J of Biomed Mat, 2011. **98**(1): p. 18-29.

Acknowledgements

A NOVEL TOP-DOWN NETWORK MODELLING APPROACH TO ESTIMATE CELL ACTIVITY IN MULTIFACTORIAL ENVIRONMENTS

Laura Baumgartner (1), Miguel Ángel González Ballester (1, 2), Jérôme Noailly (1)

1. BCN MedTech, BMMB, DTIC, Univ. Pompeu Fabra, Spain; 2. ICREA, Spain

Introduction

Slowly developing tissue disorders are often caused by adverse cell responses. Bottom-up (intracellular) network modeling is a common way to estimate such responses. However, it requires extensive experimental research, and network feedback is often highly sensitive to the network topology. Moreover, the capacity to integrate time sensitivity to chronic stimulus exposure is limited. In this work, we present a novel top-down network modeling approach, reflecting a comprehensive methodology to estimate cell activities (CA) over long time periods including dose-dependent time sensitivity. The methodological workflow is illustrated by predictions of intervertebral disc Nucleus Pulposus (NP) cells, based on which this approach was developed.

Methods

A system of interest was initially determined, consisting of key relevant external stimuli and CA for NP cells. Chosen stimuli are glucose (glc) and pH and load magnitude (mag) and frequency (freq). CA of interest were the mRNA expression (expr) of tissue proteins (Aggrecan (Agg), Collagens Type I & II (Col-II, Col-II)) and proteases (MMP3 and ADAMTS4) (Fig.1).

Fig. 1: System of interest (A) systematically approached (B) and calculated with the PN-equation (C). Effects of mechanical load are dose- and time-dependent (D).

In this top-down network modelling approach, the cell is considered as a black box and each individual CA (ω_{CA}) is interpreted as an individual, parallel network (PN), regulated by their surrounding stimuli (Fig.1, B). The relat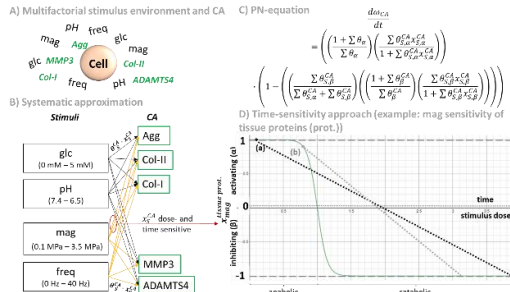ionship between a stimulus and a CA is determined by the sensitivity of a CA to the given stimulus (subscript s) (x_S^{CA})[1] and the relative impact of a stimulus to a CA (θ_S^{CA})[2]. Eventual CA was further influenced by inflammation in the cell neighborhood (not shown in Fig.1). Time sensitivity was integrated for loading parameters. Values were estimated by a constant adaptation of x_S^{CA}, depending on the initial, user-defined stimulus dose. In case of anabolic stimulus doses (Fig.1, C), hourly decay was obtained by utilizing the dose dependent difference between x_S^{CA} and 1, which led to faster decays at higher initial stimulus doses

(illustratively shown for doses (a) and (b), Fig.1, C). PN environments were calculated with the PN-equation, an ordinary differential equation uniquely developed for the hereby presented time-dependent parallel networks (PN$_t$) methodology. It provided interrelated outputs for each CA, reflected as PN-activity. Subsequently, results were presented for 4h jogging (mag: 0.65 MPa [3], freq: 2.75 Hz) and six months microgravity exposure (0.25 MPa (estimated from [3]), 0 Hz), assuming an optimal cell nutrition environment (5 mM glc, pH 7.1).

Results

Whilst one hour of jogging was predicted to be highly anabolic, an important catabolic shift after two hours of jogging was observed (Fig.2, left). In contrast, microgravity exposure led to a less pronounced but continuous catabolic shift in the NP cells.
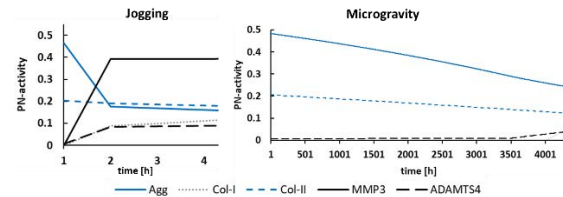
Figure 2: CA during 4h of jogging (left) and six months of microgravity exposure (right).

Discussion

Predictions indicate that beneficial effects of jogging seem to be strongly time-sensitive, with important downregulation of Agg and upregulation of MMP3 after 2h of activity. Such results might help to shed light on contradicting findings about the benefit of jogging [4,5]. The absence of load as experienced in microgravity led to constant downregulations of Agg and Col-II mRNA expr, whilst protease mRNA expr were predicted to remain low within the first months in space. Results are in good agreement with literature and provide explanations to both, disc swelling as found in bedrest studies [6] or disc desiccation, as found in astronauts [7]. The PN$_t$-Methodology reflects a brand-new network modeling approach that uniquely allows to estimate CA over time for user-defined conditions.

References

1. Baumgartner et al, Bioinformatics, 37(9):1246-53, 2020.
2. Baumgartner et al, Front. Bioeng. Biotechnol. 9:1-17, 2021
3. Wilke et al., Spine, 24(8):755-62, 1999
4. Takatalo et al. Scand J Med Sci Sports 27: 1993-2001, 2017
5. Belavý et al. Sci. Rep. 7: 45975 2017
6. Koy et al., PLoS ONE 9(11): e112104, 2014
7. Garcia et al. J Ultrasound Med 37(4):987-99, 2018

Acknowledgements

CELLULAR SENESCENCE IN A MECHANOBIOLOGICAL MODEL OF LONGITUDINAL BONE GROWTH OF THE FEMUR

Andreas Lipphaus (1), Andreas Wegener-Panzer (2), Ralf-Bodo Tröbs (3), Ulrich Witzel (1)

1. Biomechanics Research Group, Ruhr-University Bochum, Germany; 2. Dept. of Radiology, Children's Hospital Datteln, Germany; 3. Dept. of Pediatric Surgery, Helios Hospital St. Johannes Duisburg, Germany

Introduction

Longitudinal bone growth is influenced by various mechanical, hormonal, and genetic factors. While mechanobiological models of the fetal or early postnatal growth plate model the hormonal gradients in a differentiated manner, in growth models of the older child or adolescent this biological component is usually represented by a fixed baseline [1]. In particular, the growth spurt during puberty and the declining growth rate due to cellular senescence are not taken into account. The addition of these factors is necessary to model long-term growth and catch-up growth after temporary epiphysiodesis [2] or glucucocorticoid administration [3].

Methods

The growth rate *gr* results from cellular senescence *cs*, a biological baseline ε_b, a mechanically stimulated component ε_m, a theoretical generalized hormonal factor *h* and the additional accelerated and later diminished growth rate due to sex hormones during puberty *p(x)*:

$$gr = cs\left[h\left(\varepsilon_b + \varepsilon_m + p(x)\right)\right] \qquad (1)$$

Reference measurements of the femur in boys between 1 and 18 years by Anderson and Green [4] were used for calibration. Regression of growth in the first ten years of life before puberty using a logarithmic function and values normalized to growth in the first year is used to calculate the decline in growth due to chondrocyte senescence:

$$cs = a\ln(growth_{cumulative}) + b \qquad (2)$$

The peak growth rate representing the pubertal growth spurt is isolated by subtracting the values obtained by equation (1) from the growth measurements and analyzing them with the Curve Fitting Tool in Matlab (Version R2018b, The Mathworks, Natick, USA) using the Gaussian function:

$$p(x) = a_1 e^{-\left(\frac{x-b_1}{c_1}\right)^2} + a_2 e^{-\left(\frac{x-b_2}{c_2}\right)^2} \qquad (3)$$

The functions are compared with the original growth chart for validation. Catch-up growth is examined after *h* has been reduced to 50% in the first five years.

Results

The regression yielded coefficients a=-0.1558 and b=0.9894 and an R-squared of 0.9992, and a1=-3.314; b1=-7.079; c1=2.482; a2=0.7852; b2=2.626 and c2=1.1502 with an R-squared of 0.9993 and agrees well with the original growth diagram. Catch-up growth modeling was able to compensate for about 35% of the reduced growth in the first five years.
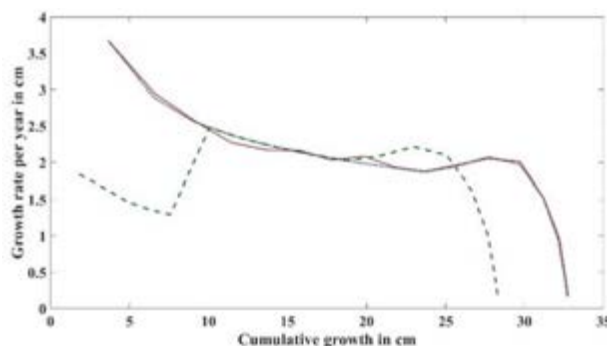
Figure 1: Green-Anderson growth chart (red, solid). Growth predicted by the present model (blue, dotted). Growth reduced to 50% for the first five years with following catch-up (green, dashed).

Discussion

Consideration of cellular senescence and pubertal growth spurt in mechanobiological models of longitudinal bone growth is necessary to study catch-up growth. However, in the present model, cellular senescence alone cannot fully explain the rebound phenomenon sometimes observed in children, and additional effects of hormones on cellular senescence should be investigated and included in theoretical modeling. Further research will aim to combine finite element modeling with the mathematical models presented here.

References

1. Yadav et al., Med Eng Phys, 90:83-91, 2021
2. Corominas-Frances et al., Bone Joint J, 97:862-8, 2015
3. Baron et al, Endocrinology, 135:1367-71, 1994
4. Anderson et al., J Bone Joint Surg, 46:1197-202, 1964

Acknowledgements

IN SILICO ANALYSIS OF THE INFLUENCE OF THE SUBSTRATE STIFFNESS ON THE EVOLUTION OF 3D CULTURES OF GLIOBLASTOMA.

Marina Pérez-Aliacar (1), Lucía Palos (1), Clara Bayona (1,2), Jacobo Ayensa-Jiménez (1,2), Ignacio Ochoa (1,2,3) and Manuel Doblaré (1,2,3)

1. Aragón Institute of Engineering Research (I3A), University of Zaragoza, Spain
2. Aragón Institute of Health Research (IIS Aragón), Zaragoza, Spain
3. Centro de Investigación Biomédica en Red en Bioingeniería, Biomateriales y Nanomedicina (CIBER-BBN)

Introduction

Tumours are not only composed of cancer cells, but also comprise a wide variety of different cells (e.g., epithelial, immune or host cells), as well as non-cellular components such as chemical substances or extracellular matrix (ECM) components. All these are collectively designated as Tumour Microenvironment (TME). The mutual interaction between tumoural cells and their TME greatly influences the evolution of the disease. In particular, the mechanical properties of the ECM have demonstrated to play a key role on cell behaviour, in terms of proliferation and migration [1]. Hence, understanding the crosstalk between cells and their TME seems crucial to advance in cancer research.

In this sense, mathematical models are invaluable tools to check hypotheses or isolate effects, thus allowing a better grasp of the phenomena governing cancer progression. Mathematical models and simulation tools (*in silico* models) are therefore considered as optimal complements of *in vitro* experiments, especially of 3D models such as microfluidic devices, currently considered as the most biomimetic, since they are able to reproduce the complex environment of cells, including their mechanical interactions [2].

This work focuses on the influence of the substrate mechanical properties on the evolution of glioblastoma (GBM), the most common and lethal primary brain tumour. Previous studies with *in vivo* animal models have shown that ECM stiffness influences growth, migration, and drug resistance in this tumour [3].

Methods

We present a continuum mathematical model to describe the evolution of tumour cells interacting with their TME. We model the cell populations C_i and chemical species S_i by means of transport equations with a source term, that is, by the system of partial differential equations:

$$\frac{\partial C_i}{\partial t} = \nabla \cdot F_i(\boldsymbol{C}, \boldsymbol{S}, \boldsymbol{P}) + A_i(\boldsymbol{C}, \boldsymbol{S}, \boldsymbol{P})C_i, \qquad (1)$$

$$\frac{\partial S_i}{\partial t} = \nabla \cdot F'_i(\boldsymbol{C}, \boldsymbol{S}, \boldsymbol{P}) + A'_i(\boldsymbol{C}, \boldsymbol{S}, \boldsymbol{P})C_i, \qquad (2)$$

where, in general, both the flux terms $\boldsymbol{F}, \boldsymbol{F}'$ and the source terms $\boldsymbol{A}, \boldsymbol{A}'$ can depend on the field variables and some external parameters $\boldsymbol{P}$, such as the mechanical properties of the ECM. The model has been previously validated [4] with different experiments reproducing the evolution of GBM under hypoxic conditions.

The main goal of the present work is to extend this model to consider the effect of the substrate mechanical properties. To do this, we fit the model to experimental results of GBM in microfluidic devices. These results reproduce the formation of necrotic cores, characteristic of GBM evolution, under different substrate stiffnesses. Statistical analyses are also performed to determine the behavioural differences in each experimental condition.

Results

The presented mathematical model reproduces the formation of necrotic cores in GBM for different values of the ECM stiffness, which allows us to derive relationships between the mechanical properties and the different phenomena involved in GBM evolution in microfluidic devices.

Discussion

We have developed a framework to simulate tumour evolution incorporating the effect of the mechanical properties of the ECM. The presented model allows to incorporate the effect of the substrate stiffness on cell growth and migration and yields good results when reproducing experimental data of tumour progression in microfluidic devices, enabling a better understanding of GBM evolution.

References

1. Cavo et al, Sci Rep, 6:35367, 2016.
2. Sontheimer-Phelps et al, Nat Rev Cancer, 19: 65-81, 2019.
3. Zhu et al, J Biomed Mater Res A, 109.6:1027-1035, 2021.
4. Ayensa-Jiménez et al, Sci Rep, 10:21193, 2020.

Acknowledgements

MODELLING THE MECHANO-INFLAMMATORY REGULATION OF CHONDROCYTE IN EARLY OSTEOARTHRITIS

Maria Segarra-Queralt, Gemma Piella, Jérôme Noailly
BCN MedTech (Universitat Pompeu Fabra), Spain.

Introduction

Knee articular cartilage (AC) chondrocytes (CC) respond to mechanical loads through a process known as mechanotransduction (MT). Moderate mechanical stimulations maintain normal tissue function, whereas injurious loads may promote AC degradation and increased expression of pro-catabolic mediators, which likely influences the early progression of osteoarthritis. Network-based models (NBM) can integrate detailed biological information for CC regulation [1], in contrast to tissue-scale mechanobiology models [2]. They allow to predict steady states (SS) of CC behavior, according to different micro-environments imposed as nodal initial conditions. A novel NBM was developed as a continuous dynamical system, including important mechano-sensors, downstream MT cascades and the regulation of inflammatory processes.

Methodology

A corpus of 44 peer-reviewed articles from indexed journals was retained to map mechanoregulatory molecular interactions of CC. The interactome (simplified in Fig.1) consisted of 115 nodes, related to each other through 263 directed edges. It was converted into a semi-quantitative mathematical model through a system of differential equations [3]. A physio-osmotic (PO) initial condition was simulated through TRPV4 and $\alpha_5\beta_1$ nodal perturbation. We further assessed whether our model could predict expected SS under inflammation (INF) and injurious mechanical loads, i.e., static compression (ST) and static hydrostatic compression (SHC) through PIEZO and PTCH activation, respectively. The ability of the model to predict semi-quantitatively reasonable changes in CC activity, depending on physico-chemical environments reported in the literature, was used for evaluation.
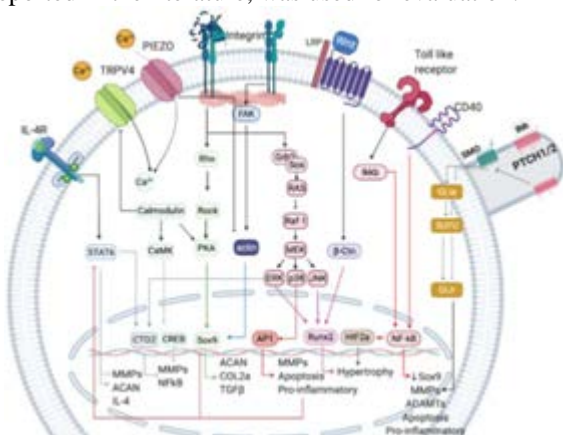
Figure 1. Schematic representation of MT events.

Results

Under PO conditions, the NBM model evolved towards an anabolic SS (Fig. 2, blue): expression levels were low for enzymes and high for anabolic factors. INF and HS led to a catabolic SS, (Fig. 2, orange; yellow): pro-inflammatory mediators and enzymes were fully expressed. SHC promoted intermediate anti-inflammatory and pro-anabolic responses, but proteases and transcription factors indicated possible undue AC turnover (Fig.2, purple).
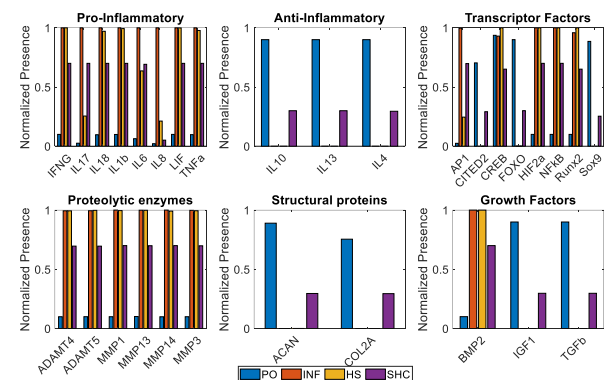
Figure 2. SS for the Physio-osmotic stimuli (*PO*-blue), Inflammation (*INF*-orange), High Strain (*HS*-yellow) and Static Hydrostatic Compression loads (*SHC*-purple).

Evaluation showed that the model could replicate 94,12% of the conditions selected (Table 1).

Table 1. Evaluation details. $\Uparrow$ the response should increase, $\Downarrow$ means the opposite. If green, the response is correct, if red not.

Nodal activation		Expected response			
Connexin	$\Uparrow$	ATP			
TRPV4	$\Uparrow$	Ca²⁺	COL2A	ACAN	TGFβ
	$\Downarrow$	NO	ADAMT5	IL1β	
$\alpha_5\beta_1$	$\Uparrow$	ACAN			
$\alpha_v\beta_3$	$\Uparrow$	ACAN			
PIEZO	$\Uparrow$	Ca²⁺			
PTCH	$\Uparrow$	GLIr	Ihh		
PTHrP	$\Uparrow$	CITED2	ACAN		
	$\Downarrow$	MMP1	MMP3		

Discussion

MT links associated with PO loading regimes appeared cornerstone to activate anti-inflammatory cytokines. This result highlights the importance of proteoglycans to protect the AC against daily fluctuations of low-grade inflammation. SHC seemed less harmful than high strain, but with limited ability to preserve AC integrity, reflecting potential deleterious effects of persistent static postures. Hypertrophy was favoured by high strain rather than SCH. In conclusion, a MT NBM coupled with inflammatory complexity has been successfully developed, revealing a unique potential to reflect load-induced chondroprotection or AC degradation in different mechano-chemical-environments.

References

1. Kerkhofs Jet al, PLoS One. 11: e0162052–e0162052,2016.
2. Marc R et al, PLoS One. 13: e0200899–e0200899, 2018.
3. Mendoza et al, Theor Biol Med Model. 3: 13. 2006.

Acknowledgements

IN SILICO IMMUNOFLUORESCENCE: A NOVEL APPROACH TO CALIBRATE MECHANOREGULATORY MODELS OF EARLY BONE FRACTURE HEALING

Edoardo Borgiani (1,2), Gabriele Nasello (1), Claudia Schlundt (3), Katharina Schmidt-Bleek (3), Liesbet Geris (1,2)

1. Prometheus, division of Skeletal Tissue Engineering, KU Leuven, Belgium;
2. Biomechanics Research Unit, GIGA In Silico Medicine, University of Liège, Belgium;
3. Julius Wolff Institut, Charité Universitätsmedizin Berlin, Germany

Introduction

Early bone fracture healing is a complex phase that has an intrinsic importance in the generation of an adequate reparative callus environment. Due to its complexity, the early stage of bone fracture healing, typically called the inflammatory phase, could benefit from the support of computational analysis [1]. Therefore, we present the COmputational Mechano-biological Model of Bone INjury Immunoresponse (COMMBINI): a multiscale *in silico* approach that simulates the early bone fracture process with the support of finite element analysis and agent-based model (ABM). An original methodology to calibrate the model, which employs *in vivo* immunofluorescence images, is hereby presented.

Methods

The innovation behind COMMBINI is the introduction of a discrete ABM to describe the biological dynamics at the cellular level. While other models of immune response in bone healing were using a continuous domain of investigation [2], the presented model is simulating each individual cell. All cells migrate, proliferate and secrete cytokines according to specific rates. For calibration of the *in silico* model, we use a deep learning algorithm to segment cell nuclei from immunofluorescent images (DeepCell [3]) of the murine standardized fracture model callus at post fracture day 3 (PFD3) [4].
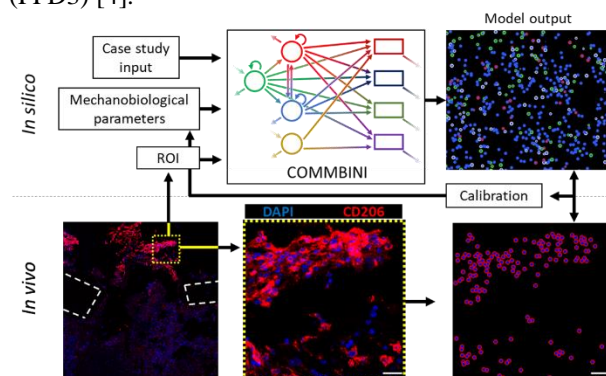
Figure 1: Top: in silico immunofluorescence (model output); Bottom: immunofluorescent image at PFD3 showing cell nuclei (blue) and CD206-positive cells (red). The latter is used as a marker for the anti-inflammatory cells (M2) to calibrate the model. For a direct comparison, a COMMBINI-like image within the same Region of Interest (ROI) is generated to show the position of M2 cells in vivo. Scale bar: 50 µm.

The algorithm extracted information about cellular quantification and distribution, focusing on the M2 anti-inflammatory macrophages. The comparison with the ABM output (also named *in silico* immunofluorescence) ensures a parametric adjustment of the model to guarantee a more close-to-reality outcome (Figure 1).

Results

In first instance, the calibration process showed that the original *in silico* model was characterized by a low macrophages recruitment ratio. This was highlighted by a reduced number of cells predicted by COMMBINI, when compared with the immunofluorescence images. An iterative adaptation of the parameter value was observed to lead to a more realistic output (Figure 2).
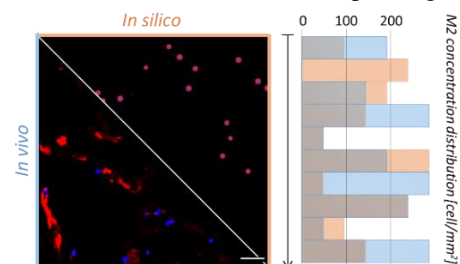
Figure 2: Qualitative (left) and quantitative (right) comparison between in vivo (orange, avg:156,6 cells/mm^2) and in silico (blue, avg: 138.8 cells/mm^2) M2 cell distribution post calibration. Scale bar: 50 µm.

Discussion

The *in silico* immunofluorescence is a powerful calibration instrument to use in the model building stage, easing the path towards full experimental validation. However, due to its intricacy, COMMBINI will necessitate further iterations to obtain a global calibration that takes into consideration all the parameters and variables involved. The model calibration will surely lead to a more realistic algorithm, assisting the creation of a tool that can help to shed light on the complexity and importance of the early inflammatory stage on the whole of the regeneration process.

References

1. Lafuente-Gracia et al, Front Bioeng Biotech, 9:2296, 2021.
2. Trejo et al., Math Comput Appl. 24:12, 2019.
3. Bannon et al., Nature Methods 18:43-45, 2021.
4. Schlundt et al., Bone 106:78–89, 2018.

UNRAVELLING THE IMPACT OF PRENATAL MUSCLE FORCES ON THE DYNAMIC CELL BEHAVIOURS DRIVING JOINT GROWTH IN MICE

Josepha Godivier (1), Yuming Huang (1), Andrew J. Bodey (2), Chrissy L. Hammond (3), Hanna Isaksson (4), Niamh C. Nowlan (1, 5)

1. Imperial College London, UK; 2. Diamond Light Source, Oxfordshire, UK; 3. University of Bristol, UK; 4. Lund University, Sweden; 5. University of Dublin, Ireland

Introduction

During embryogenesis, complex synovial joint shapes emerge through growth and morphogenesis. Fetal movements have been shown to be critical for the healthy development of joints [1]. The cell-level dynamics underlying joint shaping, particularly the effects of mechanical loading on such dynamics, are still poorly understood. In this research, we quantified the individual contributions of the main cellular dynamics involved in growth and morphogenesis of the murine distal humerus over time using a predictive computational simulation of joint development. We assessed the impact of absent muscular contraction on these cell-level dynamics.

Methods

Embryonic mouse limbs at three different developmental ages were imaged at the Diamond Light Source synchrotron using phase contrast X-ray microtomography. Both wild type and muscleless-limbs from the Splotch delayed (Sp-d) line were studied. Cells in the distal humerus were segmented and their shapes and centroid positions extracted. Local growth rates in the distal humerus between two consecutive ages were estimated based on the change in cell volume, ECM volume and cell number using equations from [2] which were adapted to the type of data gathered in this study. These growth rates were integrated into a finite element model of the murine distal humerus with which growth between ages was predicted. The impact of each of the three considered drivers for growth—cell volume, ECM volume and cell number changes—was explored by successively simulating growth when each of these drivers was kept constant or was the only active one.

Results

Accurate shape predictions were obtained for both wildtype and muscleless-limb distal humeri between each ages demonstrating the reliability of our growth rate estimations. For example, Theiler Stage (TS) 24 to TS25 wild type growth predictions are shown in Fig. 1. Assessment of individual contributions revealed a pronounced time evolution: in wild type mice, from TS23 to TS24, ECM volume increase was the main driver for growth, but it played no role from TS24 to TS25 where increases in cell number and volume were the main growth factors (Fig 2). In muscular dysgenesis mice from TS23 to TS24, cell and ECM volume decreased promoting tissue contraction which was compensated by a pronounced increase in cell number.
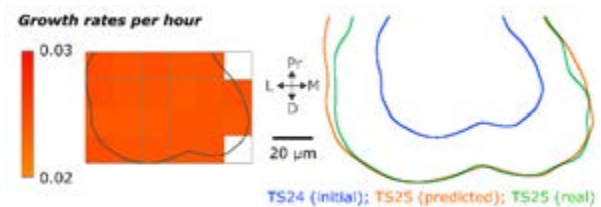
Figure 1: Distal humerus growth maps and predictions from TS24 to TS25 wild type when cell volume, ECM volume and cell number changes are all included. L: Lateral, M: Medial, D: Distal, Pr: Proximal.
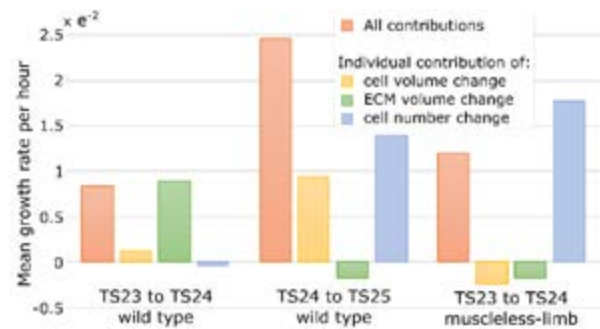
Figure 2: Distal humerus growth rate estimations when cell volume, ECM volume and cell number changes between consecutive ages are all included (orange bar), or when only one of these factors was active. Negative growth rates would promote tissue contraction.

Discussion

Accurate shape predictions in the murine distal humerus were obtained from integration of cell expansion, ECM volume increase and cell proliferation data, suggesting that these behaviours are the main drivers of murine distal humerus growth and morphogenesis. The temporal patterns of these three drivers were revealed. When muscle contractions were absent, the contribution of these growth factors were altered, demonstrating the influence of mechanical stimuli on the dynamic cell behaviours driving growth and morphogenesis.

References

1. Nowlan, Eur Cell Mater, 29: 1-21, 2015.
2. Graner et al, Eur Phys J E Soft Matter, 25:349-369, 2008.

Acknowledgements

COMPUTATIONAL EVIDENCE FOR A MULTI-LAYER CROSSTALK BETWEEN CADHERIN-11 AND PDGFR SIGNALING

Zeynep Karagöz (1), Fiona Passanha (1), Lars Robeerst (1), Martijn van Griensven (1), Vanessa L. S. LaPointe (1), Aurélie Carlier (1)

1. Department of Cell Biology–Inspired Tissue Engineering, MERLN Institute for Technology-Inspired Regenerative Medicine, Maastricht University, Maastricht, Netherlands

Introduction

Human mesenchymal stem cells (hMSCs) have been at the center of regenerative medicine research due to their ability to differentiate into various cell types and to self-renew. It is known that various cell surface receptors play an important role in their differentiation and self-renewal. One such receptor is the cadherin, which maintains the cell–cell adhesion and mechanically couples cells together.[1] Recently, cadherin-11, which is a member of the type II classical cadherin family, has been shown to be involved in the fate commitment of hMSCs.[2] Interestingly, cadherin-11 has no known intrinsic signaling activity and is thought to affect cell behavior via interactions with other cell surface receptors. Members of the platelet-derived growth factor receptor (PDGFR) family are hypothesized to be interaction partners of cadherin-11.[3] Experiments confirmed that PDGFR-α can bind to extracellular cadherin-11 regions and its activity increases upon binding[4], whereas the interaction between PDGFR-β and cadherin-11 suppresses the activity of the growth factor receptor. Cadherin-11 knockdown experiments also decreased in cell proliferation.[3] These interactions between cadherin-11 and PDGFRs indicate a crosstalk between these receptors and their downstream signaling activities.

In this study, we used a computational model to represent the experimentally proven interactions between cadherin-11 and the two PDGFRs and we inspect whether the crosstalk also exists downstream of the signaling initiated by the two receptor families. We compared our predictions to experimental observations on receptor activity and cell proliferation.

Results

We developed a standardized qualitative dynamical model of the PDGFR and cadherin-11 signaling pathways (Figure 1) using ordinary differential equations described by Mendoza and Xenarios.[5] This framework allowed us to monitor the relative activity levels of each molecule in the system. We performed model simulations to mimic the conditions in previous experimental studies (i.e. cadherin 11 knockdown and inhibiting the extracellular domain of cadherin-11) and to predict the effect of crosstalk on cell proliferation.

Overall, our predictions suggest the existence of a third layer of crosstalk, namely between the β-catenin (downstream to cadherin-11) and an ERK inhibitor (e.g. dusp1 or MKP1, downstream to PDGFRs, referred as "crosstalk protein" in Figure 1), in order to match the experimental data, or in other words, for cadherin-11 to influence the proliferation of hMSCs.
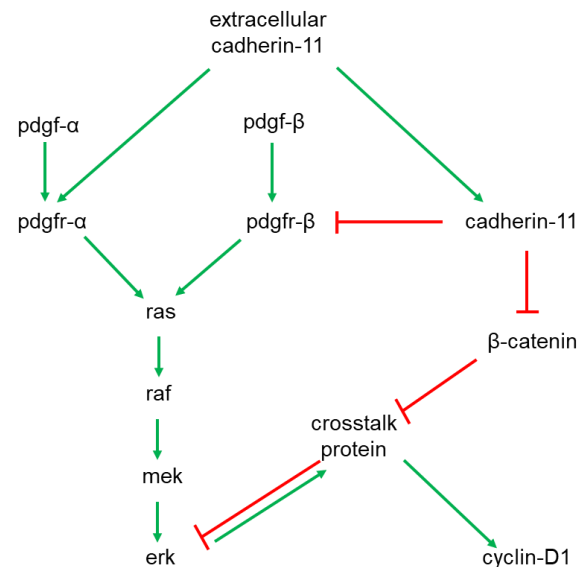
Figure 1: Overview of the cadherin 11–PDGFR crosstalk model. Green arrows represent activation, red connections represent inhibition.

Discussion

Our results provide computational evidence for a multi-layer crosstalk between cadherin-11 and PDGFR receptors, which ensures dynamic control over the proliferation in hMSCs. We believe computational models such as ours are crucial for the discovery of many more possible crosstalks between signaling pathways controlled by cell surface receptors. Elucidating these crosstalks will eventually contribute towards a better understanding of cell decision-making in response to physical, chemical and mechanical changes in the extracellular environment.

References

1. Lecuit T, Yap AS. *Nat Cell Biol,* 2015
2. Passanha FR, *et al., Biomaterials,* 2020
3. Passanha FR., Maastricht University, 2021.
4. Madarampalli B, *et al., Biochim Biophys Acta - Mol Basis Dis.* 2019
5. Mendoza L, Xenarios I., *Theor Biol Med Model.* 2006

Acknowledgements

AGENT-BASED SIMULATIONS OF BONE REMODELLING INCLUDING OSTEOMORPHS PREDICT RAPID BONE LOSS POST DENOSUMAB

Charles Ledoux (1), Daniele Boaretti (1), Jack J. Kendall (1), Ralph Müller (1), Caitlyn J. Collins (2)

1. *Institute for Biomechanics, ETH Zurich, Zurich, Switzerland*
2. *Biomedical Engineering and Mechanics, Virginia Tech, Blacksburg, Virginia, USA*

Introduction

Incidence of osteoporosis (OP) is increasing with our aging population. Denosumab, a common treatment for OP, is a monoclonal antibody that binds to RANKL and thus reduces osteoclastogenesis, osteoclast-mediated bone resorption and remodelling rates. Upon cessation of treatment, however, resorption rises quickly to levels even higher than baseline and thus rapid bone loss occurs (i.e. rebound effect) [1]. This has been attributed to: (a) accumulation of osteoclast precursors due to blocked differentiation to osteoclasts (i.e. the gate-blocking effect) [2] or (b) osteomorphs, cells in the marrow originating from the fission of osteoclasts on the bone surface. Osteomorphs can survive low RANKL conditions as occur during treatment with denosumab [3]. In this work, we used an in-house micro-multiphysics agent-based (micro-MPA) model to explore mechanisms responsible for the rebound effect following cessation of denosumab treatment.

Methods

For the micro-MPA model, bone and marrow cells are represented as agents on a voxel-based lattice and are motile and capable of producing or resorbing tissue and signaling molecules [4]. Osteomorphs were implemented as an additional cell type with a half-life of 6 months, residing in the marrow and moving towards higher RANKL faster than osteoclasts on the surface. The probability of an osteoclast fissioning to osteomorphs is inversely proportional to its RANK binding site occupancy and the probability of osteomorphs fusing to osteoclasts on the surface is proportional to their RANK binding site occupancy. A micro-multiphysics solver is used to determine the diffusion and reactions of signaling molecules. Concomitantly, the bone mechanical environment is simulated using micro-finite element analysis to determine the internal strains, which serve as stimulus for the osteocytes and osteoblasts. Micro-computed tomography (micro-CT) data serves as input for the baseline model structure. Starting from 7 micro-CT scans of iliac crest biopsies from postmenopausal women (age: 72±5 years) [4], simulations with and without osteomorphs were run for 2 years of denosumab treatment with an additional 2 years of follow-up without treatment and for 3 years of treatment.

Results

In *in vivo* trials and the simulated iliac crest micro-MP models with and without osteomorphs, bone volume fraction dropped rapidly starting 6 months after the last denosumab injection and stabilized below baseline but above placebo levels by month 48.

After 3 years of simulated denosumab treatment, the mean ratio of osteoclast precursors in the marrow in the treatment and placebo cases was 1.84 in clinical patient data [2], 2.43 in simulations without osteomorphs and 1.78 in simulations with osteomorphs.
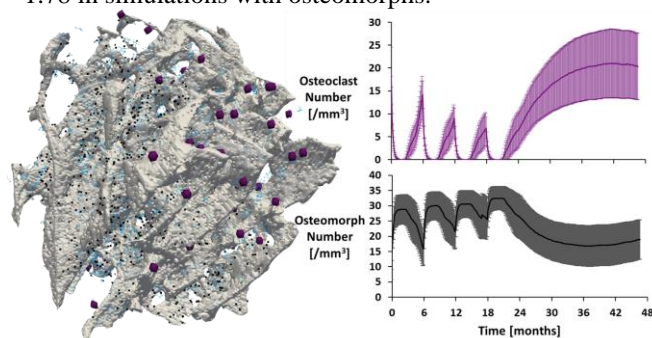
Figure 1: micro-MPA simulation showing osteoclasts (violet), osteoclast precursors in the marrow (blue) and osteomorphs (black) after 3 years of denosumab (left) and average and standard error in osteoclast and osteomorph numbers during 2 years of denosumab followed by 2 years without treatment (right)

Discussion

With and without osteomorphs, the micro-MPA model reproduced trends in bone mineral density observed experimentally after withdrawal of denosumab. The accumulation of preosteoclasts more closely matched *in vivo* measurements when osteomorphs were explicitly included as an additional cell type in the model. These simulations suggest that both accumulation of preosteoclasts and osteomorphs play a key role in causing the rapid bone loss following denosumab discontinuation, with accumulation of preosteoclasts contributing approximately twice as many resurgent osteoclasts as osteomorphs. Micro-MPA models may provide a fast and inexpensive tool to computationally test hypotheses relating to bone mechanobiology and OP treatment sequence and assist in formulating *in silico* trials to help reduce and refine human clinical trials.

References

1. Bone et al. (2011) J Clin End & Met 96(4):972-80
2. Fontalis et al. (2020) Bone Reports 13:100457
3. McDonald et al. (2021) Cell 184(5):1330-1347
4. Tourolle et al. (2021) JBMR Plus 5(6):e10494

Acknowledgements

UMBRELLA SAMPLING FOR THE ESTIMATION OF THE FREE ENERGY BARRIER OF PI RELEASE IN MYOSIN

Robin Manevy (1), Matthieu Caruel (2), Fabrice Detrez (1), Isabelle Navizet (1)

1. Univ Gustave Eiffel, Univ Paris Est Creteil, CNRS, UMR 8208, MSME, F-77454 Marne-la-Vallée, France;
2. Univ Paris Est Creteil, Univ Gustave Eiffel, CNRS, UMR 8208, MSME, F-94010 Creteil, France

Introduction

At the molecular scale Myosin and Actin proteins interact in a cycle and form a molecular motor at the origin of muscular contraction. During this metabolic process the energy comes from the hydrolysis of adenosine triphosphate (ATP):

An ATP molecule, initially coordinated to a magnesium cation, is broken into ADP and inorganic phosphate (Pi) inside the active site of the Myosin molecule (see Figure 1). This hydrolysis is accompanied by the conformation change of the Myosin that leads to the working stroke of the muscle in link with Pi release.

The mechanisms behind this key biochemical-mechanical coupling are still under intense investigation both experimentally and with simulation. In the present work we used Molecular Dynamics and Umbrella Sampling simulation to study the energetics of the departure of the Pi from the active site and describe the associated structural pathways.

The goal is to give a detailed description and give an estimation of the free energy barrier of Pi release

Methods

After preparation of the relaxed all atoms' models hydrated in explicit water boxes and using appropriate forces field, we performed Umbrella Sampling simulations with AMBER to obtain the associated free energy barrier with two different initial conformations preceding phosphate release, called Pre-Powerstroke (PPS) and Pi-Release (PiR). For each state, the simulations were also started with 2 different initial hydrations of Magnesium, resulting in four initial conditions. The potential of mean force (PMF) as well as the different interactions along the release of the Pi along the protein cavity are compared.

Results

The comparison of the structural motion within the active site along the four trajectories was done in parallel with the study of the PMF. For this, new analytical tools to extract information on most important interactions are proposed. Important residues involved in the trajectory are highlighted.

Our simulations suggest that the release of phosphate is favored in PiR compared to PPS which is in accordance with previous studies on Pi release. [1]

Moreover, all escapes were observed along the backdoor exit, which is the most probable escape route, without explicit bias.

Finally, our detailed analysis of the molecular interactions along this escape route brings new elements to explain the difference between the energetic costs in each process. [2]

Discussion

Our results confirm the role of the hydration of magnesium for an easier release of phosphate which was proposed using unbiased simulations.[3]

However the coupling between Pi release and working stroke remains debated. [4]
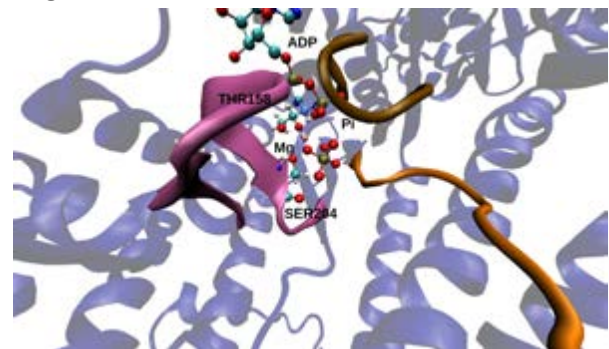
Figure

Figure 1 : Representation of the active site with Pi, Mg and some important residues represented.

References

1. M. L. Mugnai and D. Thirumalai, J. Phys. Chem. A B, 125.4:1107-1117, 2021
2. M. Cecchini, Y. Alexeev and M. Karplus, Structure, 18.4:458-470, 2010.
3. Manuscript in preparation.
4. M. Caremani, et al., J. Physiol 591.20:5187-5205, 2013

A MULTISCALE, MECHANOBIOLOGICAL MODEL OF CORTICAL BONE ADAPTATION DUE TO PTH AND MECHANICAL LOADING

Corey Miller (1), Edmund Pickering (1), Enrico Dall'ara (2), Vee San Cheong (2), Peter Pivonka (1)

1. Queensland University of Technology, Australia; 2. University of Sheffield, England

Introduction

Osteoporosis (OP) is among the most prevalent bone diseases, causing significant health concerns and potential injury to those affected. PTH(1-34) is used to treat severe OP, however exercise is well known to provide anabolic benefits; combining these two treatments has shown to provide synergistic benefits to overall bone health [1].

Significant experimental work has been undertaken to understand how PTH and mechanical loading (ML) therapies influence bone formation. Currently, efforts have been made in creating computational models capable of predicting bone's adaptive response to these stimuli. However, these models either consider PTH as a simple mechano-regulated system [1] or investigate adaptation at the organ level [2], and thus don't accurately represent the mechanobiological regulation of bone.

Here, we present a multiscale mechanobiological model for combined PTH and ML. This model combines beam theory (BT) with a bone cell population model (BCPM) to biologically describe the adaptive response in the mouse tibia. The objectives of this work are to:

1. Numerically determine a mechanistic link between ML, PTH and the adaptive response
2. Provide a platform to explore treatment dosage combinations and subsequent adaptive changes

Methods

Longitudinal data used in the calibration/validation of this model was collected by Roberts et al. [3]. This data covers three treatment types: ML monotherapy, PTH monotherapy, and a dual PTH + ML therapy. Mouse tibiae were longitudinally scanned using μCT and rigidly registered in AMIRA. Image analysis and modelling being conducted in MATLAB.

Cortical bone adaptation is investigated at a cross-sectional level, where the periosteal and endosteal envelopes are mapped as discrete x/y coordinates. The algorithm follows four steps: 1) cross-sectional mechanical properties are calculated using BT, 2) external ML is converted into an adaptive signal (Ψ) at the cortical surface, 3) Ψ and PTH concentration are used as regulatory functions for the BCPM which calculates osteoblasts (OB) and osteoclasts (OC) numbers at cortical surfaces. 4) formation or resorption events occur at a given cortical point based on bone volume fraction, determined as the difference in OB and OC activity. Subsequently, the x/y coordinates of the cortical surface envelopes are updated. These four steps are iteratively run at a time step of one day and terminated at the endpoint of the experiment.

Results

Preliminary results of the simulations have focused on mechanical-based adaptation using a Wolff type adaptation law. Results show that longitudinal strain is a good mechanical signal (Ψ) to drive bone adaptation response. The adaptive response could be predicted to within one pixel (~10μm) of error for ~87% of the periosteum, as shown in Figure 1.
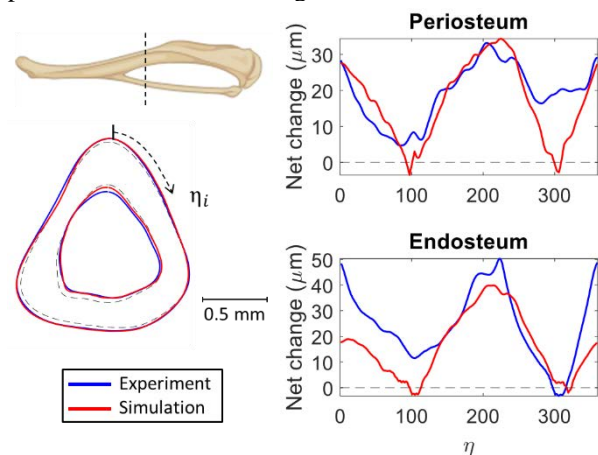
Figure 1: Comparison of experimental (blue) and simulated (red) adaptive changes across the periosteal and endosteal surfaces in the midshaft of the mouse tibia [3].

Discussion

Strains calculated through BT have been shown as effective drivers of mechanical adaptation on the cortical surface. Work has begun on modifying a previously proposed BCPM [2] into a surface-based representation for use in mouse tibiae studies. Once completed, the BT + BCPM will provide the means for rapid investigation of the adaptive response, allowing for exploration into optimizing patient-specific treatments for those suffering from OP.

References

1. Cheong et al, Acta Biomat., 136:291-305, 2021.
2. Lavaill et al, Biomech Model Mechanobiol, 19(5):1765-1780, 2020.
3. Roberts et al., Sci Rep, 10:8889, 2020.

Acknowledgements

Agent-based *in-silico* model for Multiple Myeloma tumor growth analysis

Pau Urdeitx [(1),(2)], Mohamed H. Doweidar [(1),(2)]

1. Mechanical Engineering Department, School of Engineering and Architecture (EINA), University of Zaragoza, 50018 Zaragoza, Spain;

2. Aragon Institute of Engineering Research (I3A), University of Zaragoza, 50018 Zaragoza, Spain;

Introduction

Multiple myeloma (MM) is a heterogeneous cancer, which is the second blood-associated cancer with a particularly high mortality rate and being incurable in most cases. Mechanical conditions on the extracellular matrix (ECM), as well as the interactions with other resident cells, seem to play a key role in MM growth, drug resistance, and cancer metastasis [1, 2]. The development of new effective therapies is not straightforward due to the complex conditions in tumor microenvironment. In this sense, computational models can offer us new perspectives and support conclusions to improve *in-vitro* models. To adequately identify the specific tumor conditions, the use of agent-based models can offer a wide possibility, which can focus on each individual cell conditions. Here, we present a new model where MM cell behavior can be defined in a Discrete Particle Model (DPM), which has been validated with previous results from the bibliography and previous models [3].

Methods

Cell motion is considered through the cell acting forces:

$$m\frac{dv}{dt} = F_{drag} + F_r + F_{grav} + F_{ij}, \qquad (1)$$

where, m is the cell mass, F_{drag}, F_r, and F_{grav}, corresponding to the contributions of the drag forces, domain motion, and gravity, respectively. Finally, F_{ij} are contact forces, due to the cell interaction with the ECM and other cells as:

$$F_{ij} = \sum[[K\,\delta^{\frac{3}{2}} + \gamma(v_{ij}e_{ij})](e_{ij} + \mu\widehat{e_{ij}})], \quad (2)$$

where, K is the contact stiffness, δ is the cell penetration distance, γ is the loss factor, v_{ij} is the collision relative velocity, μ is the cell friction coefficient. Finally, e_{ij} and, $\widehat{e_{ij}}$ are unit vectors, which define the normal and tangential contact direction, respectively.

The effect of the cell is transmitted to the fluid flow through the momentum exchange, F_{ex}, as:

$$F_{ex} = \sum\left[\frac{18\,\mu_f C_D Re}{\rho_p(2r_p)^2 24}(v_p - v_f)\right]\dot{m}\Delta t, \quad (3)$$

being, μ_f is the ECM viscosity, C_D is the drag coefficient, Re is the Reynolds number, ρ_p is the cell density, r_p is the cell radius, v_p and v_f are the difference of the particle and fluid velocity, respectively.

Results

Cell and ECM properties/behavior have been calibrated via obtained data/results from the bibliography [4, 5].
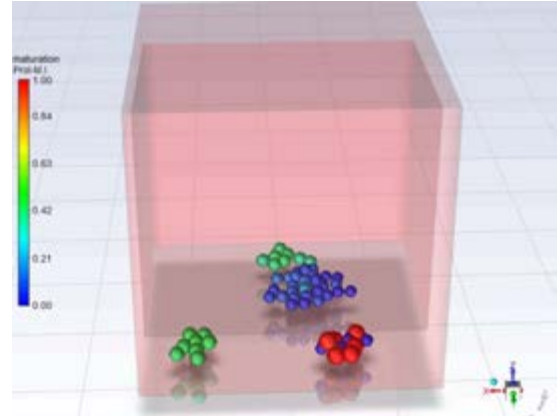
Figure 1: Cell maturation index after 6 days of cells in culture with initial cell concentration of 5×10^5 cell/ml. Tumor aggregates are considered for a minimum of 30 cells.

Cell sedimentation has been studied for 4.5 mm height ECM. Cell proliferation has been calibrated for 6 days of simulation. Then the formation of cell aggregates has been studied for 21 days of cells in culture.

Discussion

A computational model to study MM in a liquid microenvironment has been developed. With this model, we have studied the formation of MM tumor aggregation in MM-like ECM conditions. Results for cell sedimentation and cell proliferation are consistent with those obtained from the bibliography [4, 5, 6]. The cells remain attached once they proliferate, increasing cell numbers and forming tumor aggregates, which are proportional to the initial cell concentration. Moreover, cell-cell interaction increases cell maturation and, consequently, cell proliferation and tumor growth.

References

1. Qiang et al, Blood, 106(5), 1786–1793.
2. Wu et al, (BBA) Mol Cell Res 1853(2), 338–347.
3. Urdeitx et al, Math, 8(11), 1875.
4. Hamburger et al, J. Clin. Investig. 60(4), 846–854.
5. Lambert et al, Mol. Biol. Cell, 22(9), 1463–1472.
6. Urdeitx et al, Biol, 10(2), 135.

Acknowledgments

PREDICTION OF GUIDEWIRE INDUCED AORTIC DEFORMATIONS DURING EVAR: FEA AND IN VITRO STUDY

Monica Emendi (1) (2), Karen-Helene Støverud (1), Geir Arne Tangen (1), Håvard Ulsaker (3), Sigrid Kaarstad Dahl (1), Victorien Emile Prot (4), Thomas Langø (1)

1. SINTEF Medical Technology, Trondheim, Norway; 2. University of Tor Vergata, Rome, Italy; 3. St.Olavs Hospital, Trondheim, Norway; 4. NTNU, Trondheim, Norway

Introduction

The introduction of stiff guidewires during the endovascular treatment of aortic aneurysm (EVAR) causes deformations on the vessel wall, thus leading to a mismatch with the pre-operative aortic configuration. This lowers the accuracy of image fusion used for intra-operative navigation and affects the selection of the stent graft [1]. Thus, a prediction of the intra-operative deformations has the potentiality to improve EVAR and assess its feasibility [2]. Previous studies [2], [3], [4] used finite element analysis (FEA) to predict these deformations and compared their results with intra-operative imaging data.

This work aims to predict the aortic deformations and the guidewire's path using FEA and validate the results with in vitro experiments.

Methods

Eight patient-specific aortas with abdominal aortic aneurysm (AAA) were segmented from CT angiographies and 3D printed (PolyJet technology, material: Agilus30). Ten radiopaque markers (Tantalum Beads 0.8 mm, Tilly Medical Products AB, Sweden) were placed on the models in positions of anatomical interest (e.g., iliac bifurcation, ostia of renal arteries and visceral branches, AAA, iliac arteries). FEM simulations were carried out using the commercial finite-element solver LS-DYNA Explicit (ANSYS, USA). The aortic wall was modeled with shell elements, while the guidewire with beam elements. A velocity of 0.5 m/s was applied to the lower node of the guidewire, as suggested by Gindre et al [2]. A rigid introduction tube was modelled to prevent the buckling of the guidewire outside the vessel. A frictionless contact algorithm was applied. Experiments were performed acquiring cone beam CT (CBCT) scans of the 3D printed models, before and after inserting a Lunderquist Extra-Stiff Wire Guide (Cook Medical, USA).

Results

Figure 1 (left) shows the deformed aortic configuration, obtained from FEA, for a patient when the guidewire is fully inserted from the left iliac artery. Figure 1 (right) shows the comparison between the CBCT acquisitions and the FEA results, after the insertion of the guidewire, in an axial and sagittal plane.
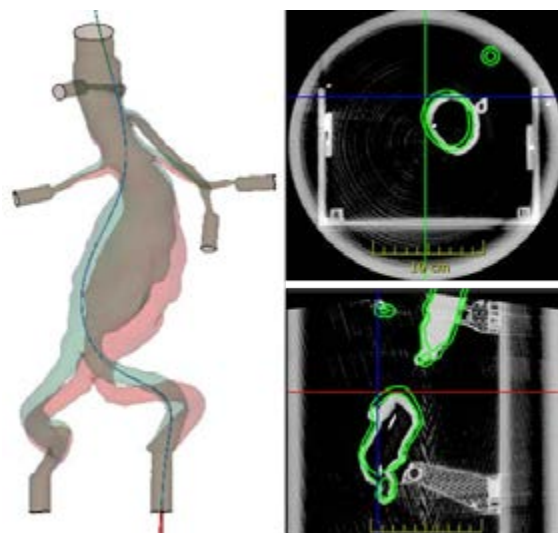
Figure 1: FEA results: deformed configuration with fully inserted guidewire (green) vs initial (red), left side. Experimental (CBCT, grey) vs FEA results (green) in axial and sagittal planes, right side.

Discussion

Both in experiments and FEA, in agreement with literature [1], the main effect of the guidewire insertion is a straightening of the vessel along with a decrease in tortuosity of the iliac arteries. Further developments of this work include the mechanical testing of the material of the phantoms and a sensitivity analysis to better assess the impact of uncertainties, e.g., velocity and direction of guidewire's insertion, on FEA results. The present analysis will be extended to a larger cohort of patients. Furthermore, the effect of the thrombus and calcification patterns on aortic deformations will be investigated. The future aim is towards more realistic in vivo boundary conditions and vessel mechanical properties, comparing the results with intra-operative data, to assess the potential use of the present experiments for clinical training purposes.

References

1. Koutouzi et al, Vascular, 27:511-517, 2019.
2. Gindre et al, Int J Numer Meth Biomed Engng, e02716, 2015.
3. Kaladji et al, Comput Med Imaging Graph, 37:142-9, 2013.
4. Mohammadi et al, Ann Biomed Eng, 46:2148-2161, 2018.

Acknowledgements

AN INVESTIGATION OF SPARSE 3D POINT CLOUD REGISTRATION COST FUNCTIONS FOR ESTIMATING 3D POSE OF HUMAN BONE

Dennis Christie[1], René Fluit[1,2], Guillaume V. Durandau[1], Massimo Sartori[1], Nico J.J. Verdonschot[1,3]

1. University of Twente, The Netherlands; 2. University of Groningen, The Netherlands
3. Radboud University Medical Center, The Netherlands

Introduction

Ultrasound together with a motion capture (*MoCap*) system has the potential to reconstruct the skeletal kinematics in a non-invasive and non-radiative manner. Multiple A-mode transducers produce multiple bony landmarks. With *MoCap* system, a point set in 3D-space is obtained, thus, the bone 3D-pose can be recovered.

The proof of concept to obtain 3D tibiofemoral kinematics was provided by [1]. However, their proposed registration algorithm struggles to recover z-rotation (Rz) and translation (tz) of bone pose. This inaccuracy is highly related to the noise and the cylindrical shape of the Femur and Tibia bone.

Registration algorithm performs by (1) estimating local transformation to (2) minimize a cost function. Root Mean Square Error (RMSE) is a broadly common cost function as it is used by ICP and its variants, and filtering-based registration. In contrast, Gaussian Mixture Model (GMM)-based registration, which treated the point cloud as Gaussian Mixture centroids, uses GMM L2-distance [2] or Neg-Loglikelihood [3] for its cost function. However, assuming we have a perfect global optimizer to search the global minimum, there is still no direct observation and comparison of how these cost functions behave in the presence of noise.

In this work, we evaluated the mentioned cost functions in the case for estimating the 3D pose of a human bone.

Method

15 points are selected based on [1] from Tibia and Femur bone model. To simulate noise, a random normal noise, ranged from [0, 1) and [0, 2) is applied to each point. A transformation which combines *Rz* & *tz*, ranged from (-10, +10) degrees and mm, respectively, is applied to the bone models. We expect the (0,0) combination is the global minimum from the cost functions (see Fig. 1). 1000 trials are repeated on each noise level and the global minimum is obtained using `min` function.
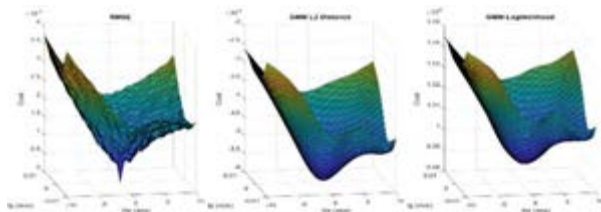
Figure 1: Cost function's search space. Left to right, RMSE, GMM L2-distance, GMM Neg-Loglikelihood.

Tibia and Femur bone is used, as this research is directed towards tibiofemoral joint kinematics. 2-DoF (*Rz* and *tz*) out of 6-DoF is investigated as they are the most difficult DoF to recover in this case.

Results

Every trial produces one global minimum and is plotted to an XY-plane, (*Rz* and *tz* as x- and y-axis; see Fig. 2). The closer the distribution to origin, the better they are estimating the true transformation regardless the noise.
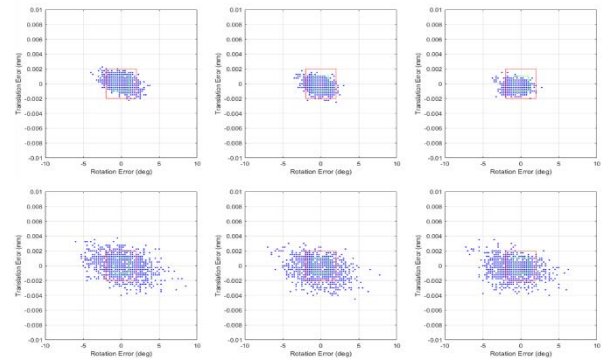
Figure 2: Global minimum on 1000 trials. Each row represents level-1 and -2 noise. Each column represents cost functions, from RMSE, GMM L2-distance, GMM Neg-Loglikelihood. Tibia bone is used in this figure.

Quantitively, GMM L2-distance performs better in estimating Rz, both for Tibia and Femur, in the presence of level-1 and -2 noise (see Tab 1, column 3-5). However, in rare occasions for femur trials, outliers are observed in GMM cost functions, which makes standard deviations larger than RMSE (see Tab. 1, row 4).

Bo-ne	RMSE		GMM L2-distance		GMM Neg-Likelihood	
	Rz (°)	tz (mm)	Rz (°)	tz (mm)	Rz (°)	tz (mm)
$T_{n=1}$	1.04±0.74	**0.6±0.4**	**0.86±0.64**	0.6±0.4	0.90±0.69	0.5±0.4
$T_{n=2}$	1.85±1.40	**1.1±0.8**	**1.72±1.30**	1.1±0.8	1.78±1.31	1.0±0.8
$F_{n=1}$	0.66±0.48	**0.5±0.4**	**0.59±0.42**	0.5±0.4	0.68±0.47	0.7±0.5
$F_{n=2}$	1.31±0.96	**1.1±1.0**	**1.13±1.01**	1.1±1.2	1.13±1.00	1.2±1.2

Table 1: Mean and standard deviations of absolute errors from expected global minimum cost functions. T=Tibia, F=Femur, n = level of noise.

Discussions

GMM L2-distance gives better results than the other two, especially in estimating Rz. Other benefit, compare to RMSE, is the smoothness of cost function surface (see Fig. 1), which will ease the optimizer to find global minimum. Although, in rare occasions, outliers are observed, it can be solved by tuning the σ parameter.

References

1. Niu, K., et al., N., 2018. A novel ultrasound-based lower extremity motion tracking system. In Intelligent Orthopaedics (pp. 131-142). Springer, Singapore.
2. Jian, B. et, al., 2010. Robust point set registration using gaussian mixture models. IEEE transactions on pattern analysis and machine intelligence, 33(8).
3. Myronenko, A. and Song, X., 2010. Point set registration: Coherent point drift. IEEE transactions on pattern analysis and machine intelligence, 32(12), pp.2262-2275

IN-SILICO BIOMECHANICAL DESCRIPTORS TO STRATIFY REAL WORLD CASES OF PROXIMAL JUNCTION FAILURE IN SPINE SURGERY

Morteza Rasouligandomani (1), Alex del Arco (3), Ferran Pellisé (4), Miguel González Ballester (1,2), Fabio Galbusera (5), Jérôme Noailly (1)

1. BCN MedTech, DTIC, Univ. Pompeu Fabra, Spain; 2. ICREA, Spain; 3. Hospital del Mar, Spain; 4. Univ. Hospital Vall d'Hebron, Spain; 5. Lab. of Biological Struct. Mech., IRCCS Istituto Ortopedico Galeazzi, Italy

Introduction

Adult Spinal Deformity (ASD) is an abnormal alignment of the spine in elderly patients. Proximal Junction Failure (PJF) is one of the most serious complications of ASD spinal surgery [1]. The Global Alignment and Proportion (GAP) score was proposed to predict PJF [2]. It uses morphological parameters, but does not explicitly include biomechanical descriptors. Therefore, the objective of this study is to explore biomechanical descriptor associated with PJF. Finite Element Models (FEM) have been proposed as effective tools to study the biomechanical aetiology of ASD but require structured meshes that are difficult to generate automatically. Hence, we propose a new tool to generate Patient-Specific (PS) FEM models of the thoracolumbar spine, based on Statistical Shape Modelling (SSM) and mesh transformation. PS simulations were used to explore biomechanical descriptors able to categorize PJF and tested the use of these descriptors for prognosis.

Methods

42 operated patients were selected. Inclusion criteria were age 50-75, Pelvic inclination> 20°, SVA> 5cm, PJF post-op complications [3]. Pipeline of modelling and FE steps are introduced in Fig.1.
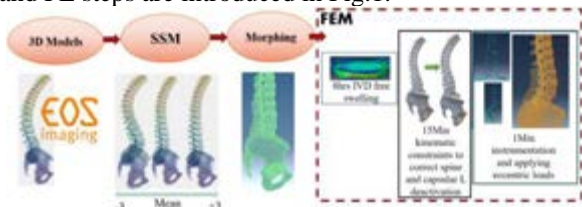
Fig.1. Modeling and FEM pipeline

3D thoracolumbar surfaces were obtained through the sterEOS software. Principal Component Analysis (PCA) allowed to learn the main modes of shape variation of the SSM. Thanks to the SSM, virtual P-S 3D geometrical models were recreated by activating different mode shapes. Structured FEM meshes were morphed to the unstructured surface meshes of the geometrical models. Thin Plate Spline and Coherent Point Drift algorithms were used for vertebras and intervertebral discs (IVD), respectively [4]. Tissue models and boundary conditions are shown in Table1.

Table1: Material properties and boundary conditions

Material properties	Intervertebral disc	Vertebras	Ligaments
	Anisotropic hyperelastic model [5]	Linear elastic [6]	Hypoelastic model [7]
Boundary Conditions	Eccentric load in vertebra center; Sacrum is fixed		

Control and PJF cases were further compared to find computed biomechanical descriptor able to discriminate PJF cases through the analysis of the Area (AUC) under the Receiver Operating Characteristic (ROC) curve. Cut-off analyses, based on Youden Index calculations further provided quantitative thresholds to characterize the control and failure groups.

Results and discussion

Among the calculated biomechanical descriptors, the fibre maximum principal strain in the IVD adjacent to the Upper Instrumented Vertebra differed consistently in the PS PJF compared to control models (Fig.2).
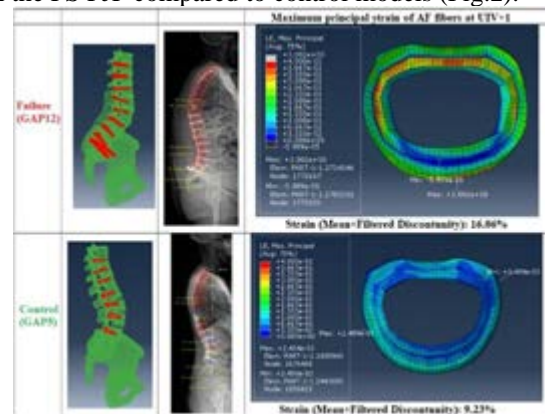
Fig.2. Maximum principal fibre strain for a control and a PJF case

The mean value of the fibre strain in the failure cases was 73.99% higher than in the controls (16.06% vs 9.23%). The ROC-AUC analyses confirmed that the fibre strain discriminated possible PJF cases, with about 10% improvement compared to GAP score (Table 2).

Table 2: ROC analysis for GAP and fibre strain

	AUC	Confidence interval	Threshold based on maximizing Youden Index
Fiber strain	0.9875	0.80 to 0.9923	10.56%
GAP score	0.8856	0.71 to 0.93	7

The calculated PS fibre strains suggest that incremental degeneration of the IVD cranial to the instrumentation might play an important role in PJF and serve the prognosis of ASD surgery. These results proved the power of computational biomechanical analyses, to discriminate PJF. The modelling pipeline allows the further testing of a larger number of FEM, and further boundary conditions should be studied in the future.

References

1. Hyun SJ, et al., Korean J Spine, 14(4), 2017
2. Yilgor C, et al., The Spine J, 17(10), 2017
3. Hart, R., et al., Neurosurgery Clinics, 2013
4. Rasouli, M, et al., 26th ESB congress, 2021
5. Malandrino, A., et al., Front. Bioeng., 2015
6. Galbusera, F., et al., Med. Eng., 2011
7. Noailly, J., et al., Eur. Spine J., 2012

Acknowledgements

A NUMERICAL STUDY OF THE IMPACT ON GRAFT LONGEVITY FROM CORONARY ARTERY BYPASS GRAFTS' BULK-BODY GEOMETRY.

Charlie Bright (1), Amin Deyranlou (2), Stuart Grant (3,4), Amir Keshmiri (1)

1. Department of Mechanical, Aerospace and Civil Engineering, The University of Manchester, UK;
2. Department of Medical Physics and Biomedical Engineering, University College London, UK;
3. Division of Cardiovascular Sciences, The University of Manchester, UK;
4. ERC, Manchester University NHS Foundation Trust, UK

Introduction

Coronary artery bypass graft (CABG) surgery is an effective treatment for severe and multi-vessel cardiovascular disease [1]. With time, the additional vessels suffer the same damage and disease for which they were implemented to treat. Graft complications require additional medical intervention, decreasing the patient's quality of life whilst increasing the costs of treatment and care [1–3]. Building upon the previous work in the field of haemodynamic analysis using computational fluid dynamics (CFD) simulations [4–6], the aim of this work is to assess the impact of CABG geometry on the local haemodynamics that dictate its long-term performance.

Methods

A patient-specific anatomical model was digitally recreated for a quadruple heart-bypass patient, to which we applied clinically accurate flowrates and boundary conditions (BCs). A healthy comparative case was generated by altering the anatomy and BCs to remove the disease and existing bypasses. Returning disease to an isolated vessel, virtual surgery was then performed. Several novel bypass designs were generated through modifications to the length, shape, and anastomosis location of an idealised bypass. Figure 1 demonstrates six of the bypass designs shown in yellow across two anatomical models. 3D CFD simulations were used to evaluate select haemodynamic metrics for these 9 configurations and were compared against each other and the patient's in-situ bypass.
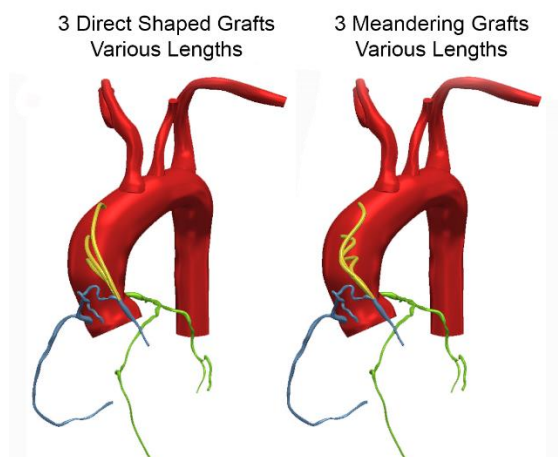
Figure 1: Merged illustrations of several bypass shape and length variations on 2 cardiovascular geometries.

Results

The distal coronary run-off was minimally impacted by shape, with variation <5% between designs. The longer bypasses experienced reduced outflows due to increased vascular resistance. CABG shapes with minor deviations performed more favourably, whilst all 9 novel designs out-performed the in-situ bypass. Bypass shape profoundly impacted the velocity flow profile and axial velocity distribution through the length of the bypass. At curvatures, flow redirection resulted in amplified extreme values of time averaged wall shear stress (TAWSS) by up to 145% percentage difference. For a given bypass, the surface area at risk to early failure due to pathological TAWSS (defined as $<4 \, \mathrm{dyn \cdot cm^{-2}}$ & $>25 \, \mathrm{dyn \cdot cm^{-2}}$) was summed and normalised against the total surface area. The maximum and minimum values for percentage surface area at-risk were 59% and 28% respectively. Oscillatory shear index (OSI) measurements were also highly varied. The normalised at-risk area due to pathological OSI (defined as >0.15) expressed a maximum of 81% and minimum of 44% between designs.

Discussion

Our findings align with the current understanding of coronary bypass haemodynamics [3], whilst evidencing the untapped research of bulk-body geometry as a predictor for early bypass failure. At present, cardiothoracic surgeons decide a bypass' configuration from intuition and experience, testament to lacking surgical guidance. This study aims to expand its findings to provide guidance and optimisation for improved patient outcomes.

References

1. Y. Abu-Omar and D. P. Taggart, Medicine (UK), vol. 42, no. 9, pp. 527–531, 2014.
2. C. Spadaccio and U. Benedetto, Ann. Cardiothorac. Surg., vol. 7, no. 4, pp. 506–515, 2018.
3. D. N. Ghista and F. Kabinejadian, Biomed. Eng. Online, vol. 12, no. 1, 2013.
4. A. Deyranlou, et al., Ann Biomed Eng, vol. 48, no. 4, pp. 1291–1308, 2020.
5. A. Ruiz-Soler, et al., Sci Rep, vol 7, no. 1, pp. 1865-1879, 2017.
6. F. Kabinejadian, et al., PLOS ONE, 2018

A WEB PLATFORM FOR DATA-DRIVEN REAL-TIME MODELING AND VISUALIZING CARDIOVASCULAR PROBLEMS

Nicola Demo (1), Pierfrancesco Siena (1), Michele Girfoglio (1), Michele Conti (2), Gianluigi Rozza (1), Ferdinando Auricchio (2)

1. Mathematics Area, mathLab, SISSA, via Bonomea 265, 34136 Trieste, Italy;

2. Department of Civil Engineering and Architecture, University of Pavia, Via Ferrata 3, 27100 Pavia, Italy

Introduction and motivations

In the last decades, the improvements in numerical algorithms and the increasing computational availability have produced a huge amount of scientific data. To properly exploit such data, Reduced Order Modeling (ROM) [1] gained large popularity in many engineering and applied science fields, especially using the data-driven approach, since it allows building real-time models by recycling such (pre-computed) data.

Despite its potentiality, ROM application is still quite limited in several fields, in particular the ones less used to computational simulations – e.g. the biomedical sector. Although its successful employment [2], the absence of consolidated user-friendly and ready to use applications to perform ROM simulations, strongly limits nowadays the dissemination of this method.

The real-time web platform ATLAS

We propose the computational interface ATLAS [3], accessible directly through a web browser, aiming to intersect the demand of ready-to-use real-time tools by exploiting the recent developments in ROM. We are then able to encapsulate real-time models in graphical applications for the final users, allowing dissemination of numerical simulations to a vast audience of institutions. In this way, the less technical users have the possibility to interact with the web interface using sliders or forms, changing the parameters of the simulation of interest - e.g. the boundary conditions, the flow/structure properties -, not only modeling the physical phenomena but also directly rendering the solution in real-time.
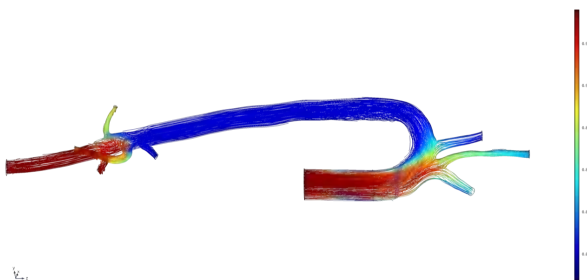
Figure 1: Streamlines of cardiovascular flow in a numerical VA-ECMO simulation.

The interface via web and the exploitation of ROM allow in principle to use it in any devices with internet connection, without constraints related to the hardware, thanks to the low computational cost of ROM. With these features, we imagine ATLAS as the portal which brings numerical simulations in several medical contexts, like for example an interactive and patient-specific medical records, or a real-time monitoring system to be placed in the operating room.

The VA-ECMO application

Still in a prototypal status, ATLAS already contains different testing applications providing possible use cases.

Beyond these, we propose in this contribution the first "*real-world*" application related to the Veno-arterial Extracorporeal Membrane Oxygenation (VA-ECMO). Such medical therapy is an artificial circulation supporting patients with severe cardiac and respiratory failure.

As demonstrated in [4], the technique is complex even in numerical simulation settings, since it has to be calibrated for the specific patient to optimize its effectiveness. The issues of the state-of-the-art methodologies could be mitigated by the described computational interface. The application we present allows us to deal with parametric boundary conditions in an intuitive way, enabling a real-time prediction and visualization capable of guiding the doctors to the optimal setting of the VA-ECMO.

Conclusion

The contribution concerns a novel and innovative technological platform that aims to disseminate ROM in the medical fields. We develop a computational interface to study VA-ECMO technique, with the final goal of introducing a valuable tool for supporting doctors' decisions.

References

1. P. Benner et al, *De Gruyter*, Berlin, Boston, 2020.
2. M. Girfoglio et al, Acta Mech Sin, 37:1183–1191, 2021
3. ATLAS web page: https://argos.sissa.it/atlas
4. M.C. Stevens et al, J. Biomechanics, 55:64-70, 2017

INFLUENCE OF PLATE DESIGN ON SUBCONDYLAR FRACTURE FIXATION: A COMPARATIVE FINITE ELEMENT ANALYSIS

Anoushka Gupta, Abir Dutta, Kaushik Mukherjee

*Department of Mechanical Engineering, Indian Institute of Technology Delhi, Hauz Khas,
New Delhi – 110016, India*

Introduction

Subcondylar fractures are the most common condylar fractures [1], accounting for 25-35% amongst all mandibular fractures [2]. 10-30% of all mandibular fracture reconstructions suffer from various post-operative complications including revision surgeries [3]. Although various finite element (FE)-based studies have compared different plates for subcondylar fracture reconstructions [4], most of them have simplified either the mandibular model or the mastication cycle or both [4]. To address this limitation, the present study is focused on performing a thorough comparative *in silico* evaluation of five subcondylar fracture fixation plates (trapezoid, strut, lambda, double and single miniplate) while considering both the complex mandibular model and the mastication cycle to understand the influence of miniplate configurations on condylar fracture reconstructions.

Methods

The patient-specific FE model of intact mandible with details of teeth, periodontal ligament, condylar fibrous cartilage, cancellous and cortical bone was developed from the CT-scan dataset. The titanium (Ti) plates and screws were modelled based on the commercially available plates and were used to virtually fix the simulated subcondylar fracture created at an angle of 40° from the sigmoid notch to the posterior border of ramus. Region-specific orthotropic material properties were assigned to the cortical bone, and isotropic material properties were assigned to the cancellous bone, teeth, and soft tissues [5,6]. All the models were simulated under a complete mastication cycle [5]. The plate-bone and the subcondylar fracture interfaces were modeled with frictional contact while the screw-bone and screw-plate interfaces were assumed to be bonded.

Results

In intact mandible, high principal tensile strains were observed around the condyle region and from the coronoid region towards the lower anterior sides of the cortical bone. (Fig.1(a)). Strains were higher in fractured mandibles (Fig 1(b to e)) as compared to the intact mandible (~ 860µε) [5]. The trapezoidal plate induced the least strains (913µε) and stress in the mandible, among the other plates, and the strain distribution was closest to those of the intact mandible. The lambda, strut and single miniplate caused high strains of 940-970µε in the cortical bone and teeth (Fig 1(d,f)). Amongst all the plates, highest von Mises stresses were generated in single-miniplate. However, the peak von Mises stresses in all the plates were lower than the yield strength of Ti (~900MPa).
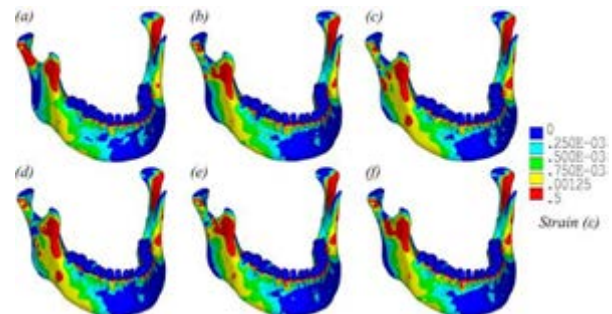
Figure 1. Principal tensile strain distributions:(a) intact and reconstructed mandibles with, (b) trapezoid (c) strut (d) lambda (e) double and (f) single miniplate
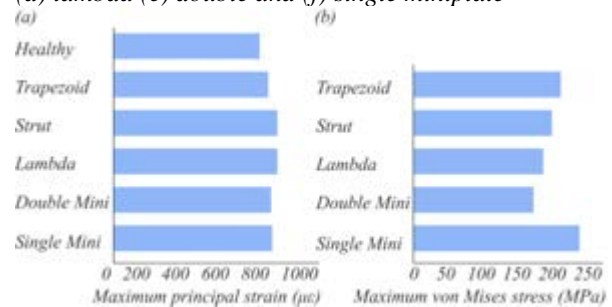
Figure 2: Comparison of (a) maximum principal tensile strains in reconstructed mandibles, and b) maximum von mises stresses in different plates

Discussion

The study shows the trapezoid and double miniplates to be the most favorable plate configurations for fixation of subcondylar fractures. This might be influenced due to the structural advantage of these plates, having the anterior arms providing support to both the buccal anterior and posterior sides of the fracture. The presence of bridges and the large surface area between two arms in the trapezoidal plate, resulted in the load transfer around the condylar neck, very close to those of an intact mandible. As observed earlier [7], subcondylar fracture reconstructed with single-miniplate exhibited high strains and stresses in the mandible and plate, and therefore, should not be preferred for reconstruction.

References

1. Lindahl et al, Int J Oral Surg, 6:12–21, 1977
2. Adhikari et al, Int J Oral Maxillofac Surg, 50(6):756-62, 2021
3. Nasser et al, Cochrane Database Syst Rev 7:CD006087, 2013
4. Ergezen et al, J Oral Maxillofac Surg, 78(9)1596, 2020
5. Dutta et al, Proc Inst Mech Eng J Eng Med Part H, 234(5):486-495, 2020
6. Dutta et al, Comp Bio Med, 108:31-41, 2019
7. Murakami et al, J Oral Maxillofac Surg, 75(6):1239-e1, 2018

TOLERANCE ANGLE DETERMINATION FOR PEDICULAR SCREW INSERTION

Lugdivine Leblond (1), Yves Godio-Raboutet (1), Yann Glard (2), Morgane Evin (1)

1. Aix Marseille Univ, Univ Gustave Eiffel, LBA, Marseille, France; iLab-Spine: International Laboratory on Spine Imaging and Biomechanics, Marseille-Montreal, France-Canada; 2. Department of Paediatric Orthopaedics, Saint Joseph Hospital, Marseille, France.

Introduction

One of the most used technics for pedicle screw insertion [1], [2] is free-hand insertion technic based on anatomical landmarks to choose an entry point and determine the trajectory by feeling intraosseous differences inside the pedicle [3]. When colliding with the cortical shell and to reach the trajectory defined during the planning phase, the surgeon adapts the axis of the tool motion during perforation.

The aims of this work are 1) to reproduce the perforation of the pedicle by the perforation tool in a synthetic model of pedicle; 2) To mimic pedicle material using different types and density of foams; 3) To quantify forces necessary to apply during the trabecular-cortical transition perforation.

Methods

A simplistic model was designed by cylinders using 1) single synthetic component (3 solid rigid polyurethane foams with short fiber filled epoxy (1mm) from Sawbone) 2) bi-synthetic components (solid rigid polyurethane Sawbone foams glue to Creaplast foam) to simulate trabecular and cortical bones (Table1). 7 samples were tested.

Sawbone PCF 20 foam	0.32 g/cm3
Sawbone PCF 10 foam	0.16 g/cm3
Sawbone PCF 5 foam	0.07 g/cm3
Creaplast foam	0.25 g/cm3
Epoxy sheet	1.64 g/cm3

Table 1: Foams density references

Perforation tests were performed on an MTS Acumen 3 A/T electrodynamic tester and were monitored by a triaxial load sensor (Kistler 9317S – range $\pm2000N$) installed at the top of the medical perforation tool.

The test procedure was mimicking the surgeon's movement and was composed of three rotations coupled with three translations insuring a constant perforation velocity. A circular positioning table (Norelem, 21161-10-08) is enabling rotation of the cylinder according with the expected angle between perforation tools and transition surface (Fig1). 10,15,20,25 and 30° were tested for each material.

Figure 1 : Simplistic model positioning of the sample under the MTS Acumen device

A home-made Matlab (Matlab®, version R2020b) code was used to post-process the data. The force's signal was divided into three sections for each translation and rotation where one or two elastic moduli, if there was or was not perforation of the cortical wall respectively, was determined by computing the slope curve. CTscan images were made after the tests to validate if there was or was not perforation of the cortical wall. Statistics and boxplot representations were performed using R (R Core Team (2012)).

Results and Discussion

Reproductible tests were performed by testing the 10° tolerance angle five time in a row. No perforation was observed on the reproducibility tests of Sawbone foams with epoxy. When testing the reproducibility by comparing bi-material foams, the influence of the difference between the two materials can be highlighted due to the differences between compressive strength of Creaplast foam and Sawbone foams. Perforations of the epoxy were assessed using post-experimentation CTscan images. Changes in section 3 in elastic modulus can be observed compared to previous two sections. According to these results, a threshold is found between 20° and 25° tolerance angle.

When studying the influence of angle perforation on bi-materials samples, changes in elastic modulus is highlighted in section 2. An inversion in elastic modulus measurements appears around 25° in all cases.

Conclusion

Experimental tests on synthetic materials show that the angle of insertion has indeed a threshold value, between 20 and 25°, at which the trajectory become critical for the patient. Further tests should be conducted on *ex-vitro* materials to consider the morphology of vertebrae, the bone density and the inter-individual's anatomical differences. Furthermore, values of the angle of perforation need to be refined between 20 and 25° to determine a minimal angle accuracy. This study offers a reliable protocol to characterize trajectory and minimal angle for insertion of the pedicle screw.

Acknowledgments

References

[1] L. Liu, X. Hong, J. Li, et S. Zhang, « Delayed Presentation of Thoracic Aortic Pseudoaneurysm Following Pedicle Screw Implantation: A Case Report », *Orthop. Surg.*, vol. 13, nº 1, p. 338-341, janv. 2021, doi: 10.1111/os.12793.

[2] W. Du, D. Zou, J. Zhang, J. Liu, W. Qu, et S. Zhang, « Guide wire displacement in robot-assisted spinal pedicle screw implantation », *Videosurgery Miniinvasive Tech.*, vol. 16, nº 3, p. 526-535, sept. 2021, doi: 10.5114/wiitm.2021.103952.

[3] Y. J. Kim, L. G. Lenke, K. H. Bridwell, Y. S. Cho, et K. D. Riew, « Free hand pedicle screw placement in the thoracic spine: is it safe? », *Spine*, vol. 29, nº 3, p. 333-342; discussion 342, févr. 2004, doi: 10.1097/01.brs.0000109983.12113.9b

LEFT VENTRICULAR ASSIST DEVICE SURGICAL OPTIMISATION USING COMPUTATIONAL FLUID DYNAMICS

Gabriela Lopez-Santana (1), Alessandro De Rosis (1), Amir Keshmiri (1)

1. Department of Mechanical, Aerospace and Civil Engineering, The University of Manchester, UK

Introduction

A Left Ventricular Assist Device (LVAD) is a battery-powered mechanical pump with an external controller surgically inserted below the heart. It acts as a bridge that connects the left ventricle with the aorta and is needed by patients who have reached an advanced stage of heart failure to improve the blood flow until a compatible heart donor is available.

The positioning of the outflow cannula in the ascending aorta is one of the factors to consider for increasing the life expectancy of a patient with LVAD. This research will focus on the study of the different combinations of angles and positions for the anastomosis of the graft and its side effects after implantation, such as aortic valve regurgitation and irregular blood flow perfusion.

Methods

The healthy aorta of a 31-year-old male volunteer which has been subject to a Magnetic Resonance Imaging (MRI) and 4D flow analysis was first used to validate the model by neglecting the presence of the cannula [1]. Then, 3D models are created with different combinations of geometrical parameters for the attachment of the outflow cannula of the magnetically levitated centrifugal-flow LVAD.

Star CCM+ is used to simulate the unsteady blood flow and to find salient hemodynamic parameters, such as mean velocity and time-average wall shear stress (TAWWS). Making reference at Figure 1, boundary conditions consisted of 2 inlets (*i.e.*, the aortic root, AR, and the outflow cannula, OC) and 7 outlets (*i.e.*, the right coronary artery, RCA, left coronary artery, LCA, right subclavian artery, RSA, right common carotid artery, RCCA, left common carotid artery, LCCA, left subclavian artery, LSA, and descending aorta, DA.
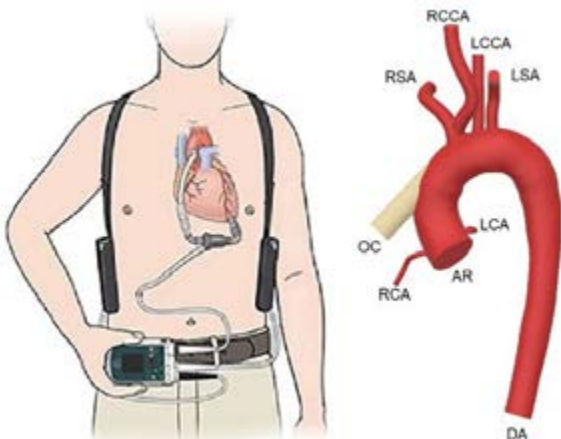
Figure 1: Boundary conditions of the aortic 3D model with the outflow cannula. Modified from Ref. [2].

The three-element Windkessel model is applied to account for the outlet pressure [3].

Results

Our simulations show the best combination of geometrical parameters, aiming to limit the wall shear stress and improve the flow perfusion. We find that angles of attachment between $40^{\circ}\pm10^{\circ}$ are better than $20^{\circ}\pm10^{\circ}$. Moreover, this optimal angle manifests a dependence on the shape of the aorta. The position of the outflow cannula compromises the flow intake of some arteries. It also induces higher stresses in sections close to the location of the attachment, as well as in critical points such as the branching of the arteries.

Discussion

CFD analysis can help to enhance the surgical planning procedure for the anastomosis of the outflow graft to the aorta, decreasing the effects of aortic valve regurgitation.

This research demonstrates the potential of using patient-specific data before surgical procedures to determine the optimal choice for the position of the cannula in each patient. In this way, the accuracy of the intervention can be definitely improved.

References

1. A. Deyranlou, C. A. Miller, A. Revell, and A. Keshmiri, 'Effects of Ageing on Aortic Circulation During Atrial Fibrillation; a Numerical Study on Different Aortic Morphologies', *Ann Biomed Eng*, vol. 49, no. 9, pp. 2196–2213.
2. Abbott Cardiovascular, "HeartMate 3™ Left Ventricular Assist System - Device setup guide in the operating room using the system monitor", 2019.
3. N. Westerhof, N. Stergiopulos, and M. I. M. Noble, 'The Arterial Windkessel', in *Snapshots of Hemodynamics: An Aid for Clinical Research and Graduate Education*, 2010, pp. 173-181.

Acknowledgements

A BONE-REMODELING DRIVEN NUMERICAL FRAMEWORK FOR HIP PROSTHESIS DESIGN

Francesca Rotini (1), Stefania Marconi (1,2), Gianluca Alaimo (3)

1. University of Pavia, Department of Civil Engineering and Architecture, Italy; 2 IRCCS Policlinico San Matteo Hospital

Introduction

Total hip arthroplasty (THA) represents a successful treatment for several diseases like arthritis, arthrosis or complex joint fractures and it consists in removing the damaged bone and cartilage tissues and replacing them with prosthetic components. However, a joint replacement is not a permanent solution since a revision surgery is required after 15/20 years, according to current prostheses lifespan. One of the principal causes of failure is the bone loss due to the so-called *stress shielding*, a phenomenon caused by the difference in stiffness between the metal prosthesis (usually titanium alloy) and the bony tissue. When the hip is loaded during daily activities, the stiffer prosthesis absorbs most of the stress, transferring only a smaller portion of the load to the adjacent bone, which in turns results underloaded with respect to the natural condition. Since those regions are considered no more useful for mechanical support functions, a bone resorption process is induced. In the literature, many works propose Topology Optimization (TO) techniques with the aim of improving the implant's geometry. Nevertheless, those formulations don't consider directly the bone resorption process: for example, in the work proposed by Pasini et al. (1), authors try to reduce the bone loss acting on the maximization of the prosthesis compliance, to make it less stiff. Another example is the work of Hessan et al (2), where authors reduce the weight of the implant, minimizing the prosthesis compliance, to ensure mechanical properties according to the current standard ISO.

In the present work we proposed a new formulation for the objective function of hip joint stems TO, to define a patient specific prosthesis that minimize the bone loss due to stress shielding.

Methods

We adopted the model developed by Kuiper (3) that describes the bone remodeling with the following formulation:

$$\frac{d\rho}{dt} = \begin{cases} B\big(S - (1 - C_s)S_{ref}\big) & if \ S < (1 - C_s)S_{ref} \\ 0 & if \ S_{ref} \le S \le (1 + C_s)S_{ref} \\ B\big(S - (1 + C_s)S_{ref}\big) & if \ S > (1 + C_s)S_{ref} \end{cases} \quad (1)$$

Where B is the Bone remodeling rate, C_s is a coefficient allowing for the definition of "dead zone", a threshold that defines the minimum stimulus needed to start the bone remodeling process. S is the mechanical signal for bone remodeling:

$$S = \frac{U}{\rho} \quad\quad (2)$$

where U is the strain energy density and ρ is the local density, and S_{ref} is the reference value of S such as, for example, the one in the pre-operative case.

Following the model in 1), we developed an in-house code in Ansys framework to predict the bone remodeling after a defined time from THA surgery.

Analyzing the quantities that play an important role in bone remodeling, we choose the bone's compliance as objective function for the TO. This function has to be maximized because, in this way, the Strain Energy Density (SED), which represent the mechanical signal for bone remodeling, increases, leading to a reduction of the bone resorption. The objective function we propose is:

$$max_{\rho \epsilon \Omega_p} C = \sum_{i=1}^{N_{bone}} SED_i \, v_i \quad\quad (3)$$

Where ρ is the design variable, Ω_p represents the prosthesis design domain, SED_i is the Strain Energy Density calculate on the bone's elements, v_i is the bone's element volume and N_{bone} is the number of elements that represent bone in the volume mesh used in the simulation.

Results

We developed simple examples, intended to prove the feasibility of the proposed approach. We verified how it is actually possible to modify the compliance value of a body acting on the material distribution of an adjacent body, thanks to the interface regions that they share.

Discussion

The aim of this work is to present a numerical framework for the hip prosthesis TO in which bone remodeling guides design improvements. The results suggest the feasibility of the formulation we proposed. Further development is required to build the entire optimization architecture, where we must take into account also the mechanical constraints of the implant.

References

1. Pasini D., et al.: Hip implant design with three-dimensional porous architecture of optimized graded density. Journal of Mechanical Design, Journal of Mechanical Design, 2018, Vol. 140.
2. Hessan M, et al: A novel design, analysis and 3D printing Ti-6Al-4V alloy bio-inspired porous femoral stem. Journal of Materials Science: Materials in Medicine, 2020
3. Kuiper J. H. Numerical optimization of artificial hip joint designs. 1993.

EVALUATION OF PHARMACOLOGICAL TREATMENTS FOR OSTEOPOROSIS USING DXA-BASED 3D FINITE ELEMENT MODELS

Carlos Ruiz Wills (1), Muhammad Qasim (2), Renaud Winzenrieth (2), Silvana Di Gregorio (3), Luis Del Rio (3), Ludovic Humbert (2), Jérôme Noailly (1)

1. BCN MedTech, Universitat Pompeu Fabra, Spain; 2. 3D-Shaper Medical, Spain; 3. CETIR Grup Mèdic, Spain

Introduction

Osteoporotic hip fractures in elderly people stand for a high social and economic burden in western countries. Hence, pharmacological treatments for osteoporosis are of high interest for clinicians. The areal bone mineral density obtained through dual X-ray absorptiometry (DXA) can monitor osteoporosis drug treatments in clinical practice. Advanced imaging techniques like DXA-based 3D modelling provide volumetric BMD (vBMD) distribution and quantification of cortical thickness [1]. Recently, 3D finite element (FE) models based on DXA showed high potential for fracture discrimination [2]; yet, its capability to capture the effects of pharmacological treatments on bone strength remains unexplored. We aim to use DXA-based 3D FE analysis to evaluate the changes in bone strength in patients with different osteoporosis treatments.

Methods

A database of 155 patients was obtained from CETIR Grup Mèdic to generate 3D femur models. The patients were stratified by treatments: alendronate (AL, n=54), denosumab (DMAB, n=33), teriparatide (TPTD, n=31), and naive of treatment (NAÏVE, n=37). Patient's baseline and follow-up femur anatomy and vBMD were estimated using 3D-Shaper® software (version 2.6) [3]. The bone anatomy was converted into 8-node hexahedral FE mesh using mesh morphing algorithm. vBMD was mapped onto the mesh and converted into Young's modulus using empirical relationships [2]. Sideways lateral fall was simulated by applying displacement on the femoral head in the direction of the fall, while the nodes on the trochanter surface were allowed to move only in the plane normal to the imposed displacement. The distal end of the femur was fully constrained (Fig. 1). Elastic perfectly plastic failure mode was simulated using density-dependent yield stress values [4]. Femur strength was calculated as the force at 4% deformation of the femoral head with respect to the greater trochanter (Fig. 1).
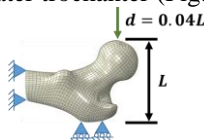

Figure 1: 3D FE model with boundary conditions.

The femur strength at baseline was calculated. "Integral" strength models mapped follow-up density on the follow-up geometry. "Cortical" strength models mapped baseline trabecular density and follow-up cortical density on the follow-up geometry, and "Trabecular" strength models mapped baseline cortical density and follow-up trabecular density on the follow-up geometry. Changes in Integral, Cortical and Trabecular strengths were computed relative to baseline. The major principal stresses (MPS) were also evaluated

Results

DMAB led to the highest increase in strength for the Integral, Cortical, and Trabecular models (Table 1). For AL, the strength increased mostly for the integral and cortical models. TPTD increased the strength only for trabecular models. The NAÏVE group strength decreased for integral, trabecular, and cortical models.

Treatment	Integral	Trabecular	Cortical
AL	+2.50	+0.40	+1.28
DMAB	+3.98	+2.51	+1.81
TPTD	+1.09	+1.99	-1.00
NAÏVE	-1.19	-0.76	-2.41

Table 1: Femur strength percentage changes between follow up and baseline, for each treatment arm.

Discussion

The FE-derived strength changes obtained with the different treatments were consistent with previous vBMD assessments [2]. Bone strength changes with DMAB ($p < 0.05$) were consistent with the expected effect of the treatment. MPS mapping showed that AL reinforced the neck of the femur, which resulted critical to increase the global strength of the organ. Such local effect might reflect interactions with the natural bone mechanobiology. In contrast, DMAB led to more uniform increments of MPS, explaining the largest strength increase under simulated lateral fall.

Overall, this study translated the pharmacologically induced bone turnover in osteoporotic patients into a mechanical descriptor, i.e. femur strength. It reveals the value of 3D-Shaper DXA-based FE models to provide valuable information to the clinicians for the evaluation and management of osteoporosis patients under therapy, as a low radiation alternative to QCT based models.

References

1. Humbert L. et al., IEEE TransMed Imaging 36:27-39 2017.
2. Ruiz Wills C. et al., Bone 121:89-99, 2019.
3. Winzenrieth R. et al., Osteoporos. Int. 29:2323-2333, 2018.
4. Morgan E. and Keaveny T., J. Biomech. 34:569-577, 2001.
5. Orwoll E. et al., J. Bone Miner. Res. 24(3):475-483, 2009.

Acknowledgements

NUMERICAL AND EXPERIMENTAL ASSESSMENT OF MULTIROOTED ROOT ANALOG IMPLANTS

Mostafa Aldesoki (1), Ludger Keilig (1,2), Istabrak Dörsam (1,2), Christoph Bourauel (1)

1. Oral Technology, University Hospital Bonn, Germany;

2. Department of Prosthodontics, University Hospital Bonn, Germany

Introduction

Conventional threaded implants (TI) have been successfully used for the replacement of missing teeth. However, they have limited designs in terms of diameter, length, and emergence profile when compared to customized root analogue implants (RAI) [1]. The benefits of RAI over TI are decreased number of surgeries, less initial bone loss, and uncomplicated placement [2]. Although the accuracy of milled and 3D printed dental models has been discussed in several studies [3,4], there is still lack of enough data regarding RAIs, especially for multi-rooted teeth. The aim of this study was to compare the biomechanical behavior of different RAIs experimentally and numerically to the conventional TIs.

Methods

A 3D model of a multi-rooted RAI was generated from a patient's cone-beam computed tomography (CBCT). Four RAI series (two materials: titanium, zirconia; two manufacturing techniques: milling, 3D printing, each N = 5) were produced. All RAIs were optically scanned to check the manufacturing dimensional accuracy. RAIs and conventional TIs (as control) were inserted into bone replacement blocks (Sawbones, Vashon, USA) and loaded up to 100 N in a hexapod biomechanical measurement setup (HexMeS) [5]. Furthermore, finite element (FE) models of the examined RAIs and TIs were created and loaded with and without osseointegration with up to 200 N in different directions.

Results

In particular, the milled titanium RAIs showed the least trueness result with local deviations of up to 610 µm in the furcation area. The in-vitro measurements showed a slightly lower deflection and thus an increased primary stability for the RAIs compared to the TIs. This could also be reproduced in the FE simulations. There were only minor differences between the various RAIs in both experimental and numerical investigations. In the FE simulations, the induced equivalent stresses on the TI were drastically higher than the stresses induced on the RAI (Figures 1 and 2). Furthermore, the healing status had a positive effect on the RAI model reducing the stresses from 23.7 MPa in the immediate loading to 13.2 MPa in complete osseointegration.
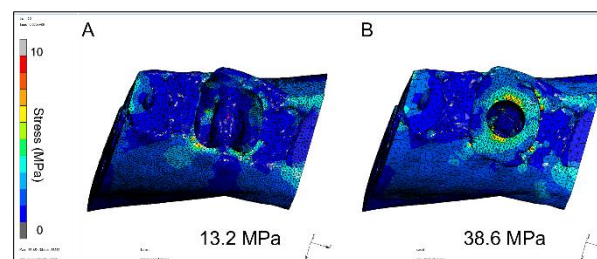
Figure 1: Equivalent of stress in bone. A) RAI, B) TI
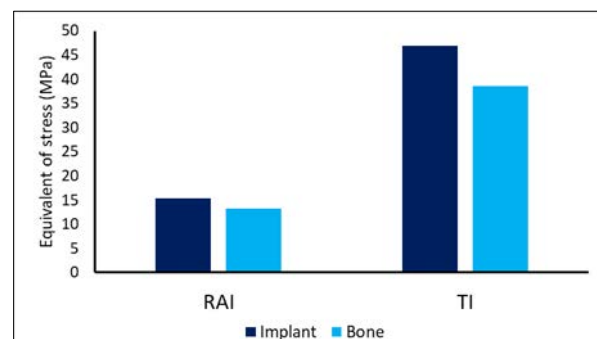
Figure 2: Comparison of equivalent of stress values in different components of RAI and TI models

Discussions

The in-vitro studies have shown that the initial mobility of the RAIs is comparable to that of the TIs. Printed zirconia showed the highest precision. Milled zirconia showed the highest trueness followed by printed titanium. The numerical simulations clearly showed, from a biomechanical point of view, that the RAI produced a more favorable stress distribution compared to the TI. The influence of osseointegration on the bone bed's stresses is greater than that of the choice of the material and the manufacturing method for the RAIs.

References

1. Chen et al, J Prosthet Dent, 112:1088-1095, 2014.
2. Mangano et al, Lasers Med Sci, 29:1321-1328, 2014.
3. Jeong et al, J Adv Prosthodont, 10:245-251, 2018.
4. Choi et al, Materials (Basel), 12:1-10, 2019.
5. Keilig et al, Biomed Tech, 49:208-215, 2004.

Acknowledgements

THE EFFECT OF TRIMMING LINE GEOMETRY ON FORCE TRANSMISSION BY ORTHODONTIC ALIGNERS (A FINITE ELEMENT STUDY)

Tarek M. Elshazly (1), Ludger Keilig (1), Ahmed Ghoneima (2),
Moosa Abuzayda (3), Christoph Bourauel (1)

1. Oral Technology, Bonn University, Bonn, Germany;

2. Department of Orthodontics, Hamdan Bin Mohammed College of Dental Medicine, MBRU, Dubai, UAE;

3. Department of Prosthodontics, Hamdan Bin Mohammed College of Dental Medicine, MBRU, Dubai, UAE.

Introduction

Due to the complexity of teeth movements by clear aligners [1], use of finite element methods (FEM) may facilitate understanding their biomechanical behaviour [2]. The aim of our study was to investigate the influence of the geometry of the trimming line and the thickness of an aligner on the force transmission from the aligner to the teeth using FEM. A 3D FE model was developed. The initial forces generated during bodily 0.2 mm movement of upper central incisor tooth were calculated.

Methods

Using Mimics software, a realistic 3D model of upper jaw was imported to design full cast, Bone, PDL, and aligners with different thicknesses (0.6, 0.5, 0.4 mm). Different trimming line designs (Fig. 1) were also modelled similar to Cowley et al. [3]. The model (Fig. 2) was exported to Marc/Mentat FE software. 10-noded tetrahedral elements were used for meshing of the aligner, while 4-noded tetrahedral elements were used for the cast. Material parameters of all structures were chosen as shown in Table 1. A touching frictionless mode was established in contact interfaces between the aligner and the tooth surfaces, with an interference closure of -0.04. The forces generated at 0.2 mm bodily facio-lingual movement of the tooth 21 were calculated.

Results

The initial transmitted forces were in the range of 0.5 – 1.5 N. The findings are compatible with the reported ideal orthodontic movement (0.5 -1.0 N). The straight trimming line showed higher forces than the scalloped. The forces increased by increasing the thickness of the aligner and the extension of the trimming line.

References

1. Elkholy et al, American Journal of Orthodontics and Dentofacial Orthopedics, 151:407 – 415, 2017.
2. Lee et al, Comput. Methods Biomech. Biomed. Engin., 16:1143–1149, 2013.
3. Cowley DP et al, Journal of Clinical Orthodontics, 46: 697-702, 2012.

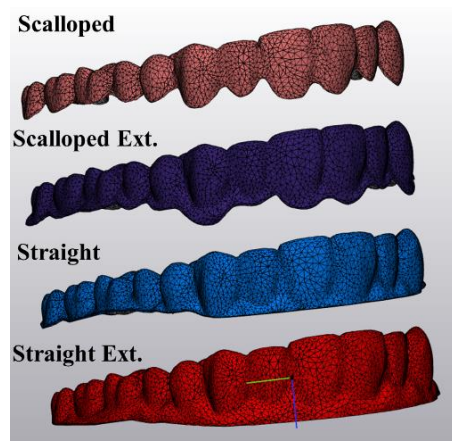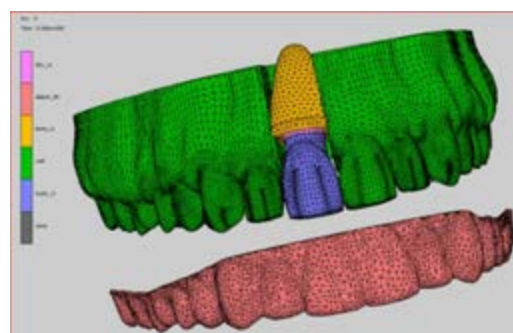*Figure 1: Different designs of aligners with different trimming line.*

Figure 2: A 3D finite element model of a cast, a separated upper central incisor, PDL, Bone, and an aligner.

Structure	Young's Modulus (MPa)	Poison's ratio
Aligner	1500	0.3
Teeth	80000	0.3
Bone	1000	0.25
PDL	0.1	0.35

Table 1: Material parameters of all structures.

Acknowledgements

DESIGN EVALUATION OF SIMPLIFIED CERAMIC CANTILEVER SINGLE-RETAINER RESIN-BONDED FIXED DENTAL PROSTHESES USING FEA

Nicoline Hjort (1), Philippe Boitelle (1,2), Irena Sailer (3), Jean-Pierre Attal (1), Aurélie Benoit (1)

1. URB2i, Faculty of Dental Surgery, Université de Paris, France; 2. Oral rehabilitation Department, Faculty of Dental Surgery, University of Lille, Lille University Hospital Center, France; 3. Division of Fixed Prosthodontics and Biomaterials, University Clinic of Dental Medicine, University of Geneva, Switzerland.

Introduction

Ceramic cantilever single-retainer resin-bonded fixed dental prostheses (RBFDP) provide excellent clinical outcome for the replacement of single missing teeth in the anterior region and is now considered as a valuable treatment option in the posterior region, especially with the use of zirconia ceramics [1]. This minimally invasive treatment approach allows numerous advantages as it preserves healthy dental tissue with very little tooth preparation, is esthetic, low cost, reversible, presents no risk of pulp irritation and does not require anesthesia. Primary complications are debonding, failure or chipping in the connector regions and secondary carries.

Among the variety of configurations proposed by the clinicians, finite element analysis is an interesting tool to optimize the design of RBFDPs on a mechanical point of view [2]. The objective of our study is to characterize the influence of different design parameters on stress distribution using a simple finite element model, in order to draw general clinical recommendations for the design of RBFPDs.

Methods

Simplified 2D finite element models of RBFDPs are created with COMSOL Multiphysics® (V6.0) to analyze stress distribution in the adhesive layer and in the prosthesis (Figure 1).
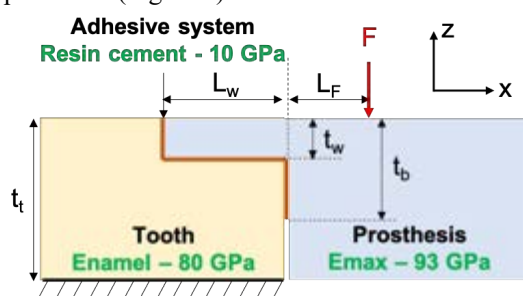
Figure 1: 2D Finite element models of RBFPDs

All materials are modeled as homogeneous, linear elastic. The bottom of the tooth is fixed, a concentrated force F is applied at a distance L_F from the tooth. The influence of several parameters is evaluated: the position of the force characterized by L_F, the thickness t_w and the length L_w of the retainer, the bonding length along the loading axis t_b, and the depth of the tooth and the prosthesis, d_t, along y-axis.

To correlate with clinical data, fractographic analysis of a fractured RBFDP in lithium disilicate Emax replacing a lateral incisor is performed to identify the origin and the mode of failure.

Results

In the prosthesis, results are in accordance with the mechanical theory of bending beams. The first principal stress is proportional to $\frac{FL_F}{d_t t_b^2}$. For a chosen bonding length t_b, the length and the thickness of the retainer have little influence on the observed stress distribution in the prosthesis. In the adhesive layer, stress is strongly influenced by the length of the retainer: a 50% reduction of the first principal stress is observed for a retainer length L_w equal to 2 mm compared to 0.5 mm.

The fractography analysis reveals that crack initiated from surface roughness created by repeated impacts of the antagonist tooth. The connection failed due to an excessive load in bending. The model predicts a maximal stress equal to 25% of Emax strength and the failure of the prosthesis can be attributed to a combination of surface defects and mechanical loading.
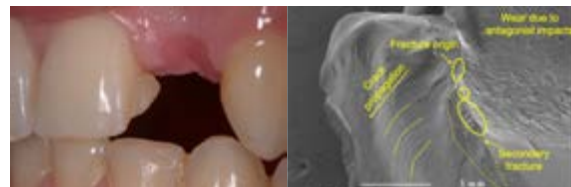
Figure 2: Clinical view (left) and fractographic analysis (right) of a fractured RBFDP.

Discussion

This simple model shows that RBFDP design greatly influences tensile stress in the prosthesis and in the adhesive layer.

Clinical recommendations regarding connectors and bonding surface areas should take into account the orientation of occlusal forces. Indeed, the bonding length along the loading direction has more influence than the thickness of the retainer or the depth of the prosthesis. In the posterior region, occlusion on the prosthesis should be tuned in order to bring the contact points closer to the connection and reduce the lever arm. To prevent debonding, longer retainers (>1.5 mm) should be preferred.

References

1. Yazigi et al, J Dentistry, 116:103907, 2022.
2. Chen et al, J Prosthetic Dentistry, in press, 2022.

EFFICENCY AND LEARNABILITY OF MAGNETIC MALLET AS A RETRIEVAL TOOL FOR DENTAL CROWNS: A PRELIMINARY STUDY

Andrea T. Lugas (1,2), Giulia Caraceni (1,2), Gianmario Schierano (3), Alberto L. Audenino (1,2), Domenico Baldi (4), Cristina Bignardi (1,2), Mara Terzini (1,2)

1. Polito^{BIO}Med Lab, Politecnico di Torino, Italy; 2. Department of Mechanical and Aerospace Engineering, Politecnico di Torino, Italy; 3. Department of Surgical Science, c.i.r. Dental School, University of Turin, Italy; 4. Division of Prosthetic Dentistry, Department of Surgical Sciences, University of Genoa, Italy

Introduction

Implant-supported dental prostheses are commonly used in the treatment of edentulous patient. Sometimes, due to implant sites diseases or other failure causes, such as poor fit or cementation, the retrieval of the crown may be necessary, and a conservative disassembly would be ideal [1]. There are various types of tools which allow an intact removal of permanently cemented restorations, most of which apply percussion to break the luting agent bond [2]. Impulsive instruments for crown retrieval have already been compared in previous works [3]. This study aims to determine the influence of the user experience and the selected power level on the forces applied on the dental implant by means of Magnetic Mallet (Meta Ergonomica, Milan, Italy), a device designed for oral surgery which bases its functioning on magneto-dynamic technology.

Methods

During this study the generated force and the corresponding energy of impulses performed with Magnetic Mallet were computed. For this purpose, a piezoelectric loadcell (Brüel & Kjær, Nærum, Denmark) was secured on a bench vise and connected to an amplifier (Brüel & Kjær, Nærum, Denmark) and a data acquisition board (National Instruments, Austin, Texas, USA). Impulses were delivered on the load cell through a screw with a transversal hole to allocate the crown remover tool.

Four operators (2 experienced and 2 inexperienced) performed 50 impulses on the load cell with each of the four available power level of the Magnetic Mallet. The force trend over time was recorded throughout the procedure at 51.2 kHz. The maximum force reached during a single impulse was considered as the force of the impulse, and the area under curve (AUC) in the force trend over time as the energy dissipated during each impulse (Figure 1).
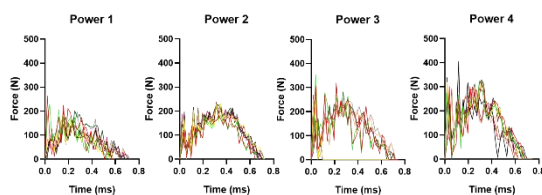
Figure 1: Superimposed force trends over time of different impulses obtained with different power levels by the same operator.

The mean force and energy obtained by each operator using each power level of the instrument were computed and used as indicators of the bone stress during the procedure. An analysis of variance (ANOVA) was conducted to investigate the statistical influence of the operator experience and the instrument power on these two indexes.

Results

Figure 2 shows the mean impulsive force measured during the tests. The ANOVA highlighted a significant difference between the operators and the instrument power levels, and a Tukey-Kramer test was performed for the pairwise comparisons. A significative difference ($p<0.05$) was revealed between operator A and the others. Regarding the instrument power, levels 3 and 4 resulted similar, while levels 1 and 2 were significantly different ($p<0.05$) from one another and from levels 3 and 4. Similar results were obtained for the AUC.
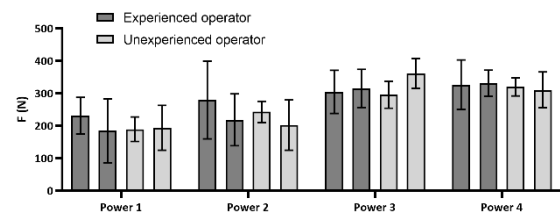
Figure 2: Force generated from each operator at different power levels of the instrument (mean ± SD). At each power level, the bars represent the results obtained by one of the operators (from left to right: operators A, B, C, and D).

Discussion

The results revealed a significant difference between different operators. However, the experience of the operators was not highlighted from the statistical analysis, suggesting a valuable learnability of the instrument use. Furthermore, power levels 3 and 4 showed a higher force and energy of the impulses compared to levels 1 and 2, but were similar to each other, which could be interpreted as a similar efficiency in crown removals.

References

1. Addy et al, Dent Update, 34:140-150, 2007.
2. Bajunaid, Gen Dent, 65:48-53, 2017.
3. Bignardi et al, Open Biomed Eng J, 12:27-35, 2018.

IMPACT OF SIMULATED TOOTHBRUSHING AND THERMOCYCLING ON SURFACE ROUGHNESS OF CAD/CAM RESIN MATRIX CERAMICS

Liliana Porojan (1), Roxana Diana Vasiliu (1), Flavia Roxana Toma (1), Sorin Daniel Porojan (2)

1. Department of Dental Prostheses Technology (Dental Technology), Center for Advanced Technologies in Dental Prosthodontics, Faculty of Dental Medicine, "Victor Babeş" University of Medicine and Pharmacy Timişoara, Romania; 2. Department of Oral Rehabilitation (Dental Technology), Center for Advanced Technologies in Dental Prosthodontics, Faculty of Dental Medicine, "Victor Babeş" University of Medicine and Pharmacy Timişoara, Romania

Introduction

From clinical point of view, a stable appearance can increase the longevity of esthetic dental restorations. Therefore the surface properties should be preserved during their lifetime. Dental restorations with smooth surfaces are less prone to plaque accumulation and superficial staining [1]. In the last decade, a new category of dental materials has been promoted for esthetic CAD/CAM restorations, resin-matrix ceramics or hybrid ceramics, consisting of an organic matrix highly filled with ceramic particles [2]. The physical properties related to resin matrix ceramics are very close to those of natural teeth, and between ceramics and composites. Several in vitro ageing protocols have been proposed to simulate the conditions that restorative materials are subjected in the oral cavity which could alter the surface properties. The objective of the study was to evaluate the surface properties by microroughness, before and after simulated ageing procedures.

Methods

A total of 80 specimens (5 materials: Vita Enamic [E] Lava Ultimate [L], Cerasmart, [C], Shofu HC [S], Hyramic Upcera [H] × 4 specimens × 3 techniques: water storage [w], toothbrushing [tb], and thermocycling [tc], and 1 control group [b]) were prepared. Rectangular-shaped plates (1 mm thick) were sliced, polished using silicon carbide papers (600-2000 grit) and finally polished with a low-speed handpiece and diamond polishing paste. For water storage a 37°C distilled water bath was chosen. A toothbrush simulating machine was used with medium tooth-brushes, a 2:1 glycerin:toothpaste slurry and a 2 N vertical load. For thermocycling distilled water baths at 5°C and 55°C with a 30-second dwell time in each bath were used. All specimens were aged with 10000 cycles, which represent one year of clinical service. Specimens' surface roughness was analyzed with a contact profilometer SurftestSJ-201 (Mitutoyo, Kawasaki, Japan). The sampling length was 0.3 mm. Ra values were calculated. IBM SPSS Statistics software (IBM, New York, USA) was used to perform the statistical analysis.

Results

No significant differences were observed among the material groups regarding roughness. The water storage alone decreases roughness, but did not lead to any significant difference. Ageing by thermocycling and toothbrushing did increase roughness. After toothbrushing roughness values increased significant (p=0.024 for [b]-[tb], and p=0.001 for [w]-[tb]), as expected, because toothpastes contain abrasive components [3]. Calculated average roughness values are: Ra= 0.05 µm for [b], 0.04 µm for [w], 0.10 µm for [tb], and 0.60 µm for [tc].
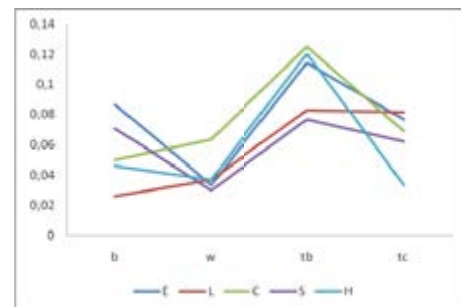
Figure 1: Mean Ra values [µm] of sample groups.

Discussions

The surface roughness of all specimens before and after ageing was below the suggested threshold of 0.2 µm for substantial increase in bacteria colonization [4]. The effect of dentifrice abrasiveness on restorative material and tooth structure has been documented [3, 4] and the results of this research confirm other studies. The wear resistance attributed to resin-matrix ceramics, with smaller filler sizes could be related to their small inter-filler spacing, which decreases as filler size decreases [1]. Further studies will be needed to investigate the effect of different brushing systems. Withal validating simulated toothbrushing and thermocycling models using longitudinal in vivo and in vitro comparative studies would be helpful to improve and estimate the clinical performance of these materials [1, 4].

References

1. Salgado VE, Cavalcante LM, Moraes RR, Davis HB, Ferracane JL, Schneider LF. J Dent, 59:48-53, 2017.
2. Al Amri MD, Labban N, Alhijji S, Alamri H, Iskandar M, Platt JA. J Prosthodont, Apr;30(4):318-328, 2021.
3. Garza LA, Thompson G, Cho SH, Berzins DW. J Prosthet Dent, 115(4):489-94, 2016.
4. Yuan JC, Barão VAR, Wee AG, Alfaro MF, Afshari FS, Sukotjo C. J Prosthet Dent, 119(6):1000-1006, 2018.

DIFFERENCES IN TMJ LOADING BETWEEN MEDIOTRUSIVE AND LATEROTRUSIVE TOOTH GRINDING

Benedikt Sagl (1), Martina Schmid-Schwap (1), Eva Piehslinger (1), Xiaohui Rausch-Fan (1), Ian Stavness (2)

1. Medical University of Vienna, Austria; 2. University of Saskatchewan, Canada

Introduction

Previous literature has often reported a potential connection between increased temporomandibular joint (TMJ) loading and the onset and progression of temporomandibular joint disorders (TMD) [1]. An often-debated topic in this realm is the possible role of sleep bruxism in the onset of TMD. Due to the small size and complex composition of the joint, *in vivo* investigations of its biomechanics are virtually impossible, leaving *in silico* investigations as one of the few available tools. We previously published an investigation of the effect of tooth facet inclination during laterotrusive bruxing on TMJ loading [2] and the presented project aims to expand our previous work to include laterotrusive as well as mediotrusive tooth grinding and investigate the effect of the different grinding movements on TMJ loading.

Methods

We based our investigation on our previously developed computer model and forward-dynamics tracking approach for tooth grinding tasks [2]. In short, we used a combined rigid body- finite element model of the jaw region together with a movement and grinding force goal to compute the muscle activations necessary to fulfill the optimization goals. Muscles were modeled as Hill-type line actuators. To enable the use of a grinding force target, the grinding facet of the respective upper jaw tooth was idealized using a bilateral, planar constraint. For this study, we focused on grinding on the first molar and used a facet inclination of 8.1°, which represents the lateral guidance inclination of the first molar [3]. Due to a lack of literature values, and to allow for easy comparison of results, the same inclination was used for mediotrusive grinding. All simulations were performed with a grinding force target (part of the input of the forward-dynamics tracking simulation) of 280N and a movement target leading to 3mm lateral/ medial excursion along the grinding plane. Differences in computed muscle excitation, grinding force as well as TMJ loading will be reported.

Results

All simulations were able to successfully compute a tooth grinding motion with a grinding force target of 280N. There are clear differences in TMJ loading as well as muscle activations between the laterotrusive and mediotrusive grinding simulations (Figure 1). The laterotrusive grinding simulation rotates the working side condyle, while protruding the non-working side condyle, as is to be expected for a laterotrusive

movement. This leads to a higher mechanical load in the non-working side disc. Mediotrusive grinding on the other hand facilitates a protrusion of the working side condyle to rotate the mandible towards the non-working side. The condylar protrusion in combination with closing force application leads to a high mechanical loading of the working side TMJ disc. The differences in mandibular movement also lead to differences in computed muscle activations (e.g. strong vs. no activation of working side temporal muscle and non-working side posterior temporal muscle).
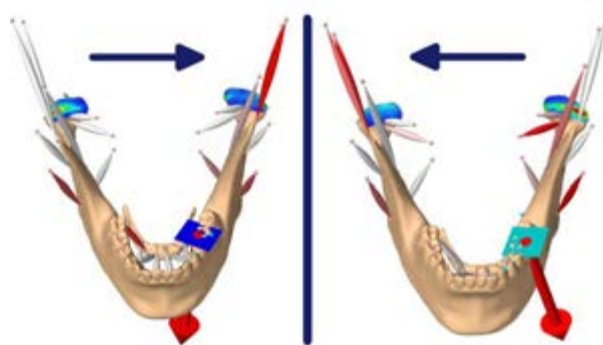
Figure 1: Comparison of laterotrusive (left) and mediotrusive (right) tooth grinding simulations. Activated muscles turn red and the disc colormaps depict von Mises stress. TMJ capsule not shown.

Discussion

This project presents a dynamic, muscle-driven *in silico* investigation of differences between laterotrusive and mediotrusive tooth grinding. Our preliminary results show clear changes in muscle activation patterns, caused by the differences in mandibular movement. These changes consequently lead to differences in loading, with a trend towards highest TMJ loading on the working side disc during mediotrusive grinding tasks. The presented results are a starting point for a series of investigations into TMJ loading differences between various tooth grinding patterns that can potentially help to better understand the connection between tooth grinding and mechanical TMJ loading. These results can possibly aid in the identification of risk factors for high TMJ loading and consequently TMD onset and progression.

References

1. Ingawalé et al. Ann Biomed Eng, 37:976-996, 2009.
2. Sagl et al. J Adv Res, 35:25-32, 2022
3. Kulmer et al. J Oral Rehabil, 26:650-660, 1999.

MOTION ANALYSIS OF THERAPEUTIC CLIMBING: A REHABILITATION TOOL FOR CHILDREN WITH CEREBRAL PALSY

Cecilia Monoli (1,2), Greta Simoni (3), Jeffrey A. Tuhtan (1), Eduardo Palermo (3), Manuela Galli (2) and Alessandro Colombo (2)

1. Department of Computer Systems, Tallinn University of Technology, Tallinn, Estonia; 2. Department of Electronics, Information and Bioengineering, Politecnico di Milano, Milan, Italy; 3. Department of Mechanical and Aerospace Engineering, Sapienza University of Rome, Rome, Italy.

Introduction

Cerebral Palsy (CP) is estimated as the most common cause of motor disabilities in children [1], requiring continuous rehabilitation to improve and preserve the quality of life [2]. Therapeutic climbing has been identified as a favorable exercise for both psychological and physical purposes [3]. The potential positive effects on coordination, strength and motion ability in general are highlighted by previous studies of sport climbing as a rehabilitation tool for children affected by CP [1,2]. The overall therapeutic value of climbing is known, but the unstructured environment limits the possibility of traditional quantitative motion analysis methods. To address this limitation, standard video-based methods preferred for highly dynamics tasks are combined with interaction forces of the climber, including custom holds equipped with force sensors [4-6]. Despite the increasing popularity of therapeutic climbing, there remains a lack of studies performing active measurements and motion analysis through wearable sensors in a clinical framework. The aim of this project is to simultaneously exploit wearable Inertial Measurement Units (IMUs) and load cells to quantify the effectiveness of climbing as a therapeutic tool. This was done by monitoring the climbing subject's maximum elbow extension.

Methods

10 CP children from 7 to 11 years old affected by hemiplegia caused by perinatal stroke were involved in the study. The subjects performed sport climbing, assisted via a rope and by trained personnel, on three consecutive days. The wall was equipped with 10 sensorised holds, which recorded the force intensity and direction independently of the contact location between limb and hold (3 axis, 0-240KgF, 80Hz). The subjects wore 5 IMUs (50Hz, Xsens Enschede, Netherlands) positioned between the scapulae, and on each arm and forearm. Prior to climbing, three calibration poses were performed: orthostatic standing with arms relaxed, parallel to the ground, and upward facing. All inertial data were filtered with a Butterworth lowpass filter at 10Hz, and data from the arm and forearm IMUs were combined to estimate the elbow angle measure.

Results

Preliminary results in this work are focused on the kinematics of motion. Fig. 1 shows for each subject and trial, the maximum elbow extension measured during upwards calibration (Calibration) and while climbing (Wall) for both hemiplegic and unaffected arms. The maximum elbow extension is higher in 93.1% of the cases (median 10.3, iqr 16.5) for the unaffected arm, while for the hemiplegic arm it increases in 72.4% of the cases (median 7.5 iqr 13.9).

Discussion

Overall, a greater elbow extension was observed while climbing, both in the hemiplegic and the unaffected arm. This may indicate increased involvement of the subject in the task, as they are motivated by the playful environment, supporting the use climbing as a therapeutic tool. Further analysis of the statistical significance of the measurement data is in progress. Future works will compare the kinematic information collected by the IMUs to the data of the custom force sensors to provide a more complete understanding of the climber's elbow extension and the performed exercise.
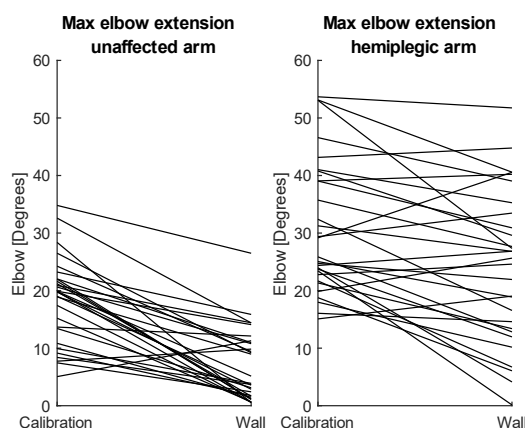
Figure 1: Maximum elbow extension measured during calibration task (Calibration) and while climbing (Wall) for unaffected and hemiplegic arms for each trial.

References

1. Christensen M.S. et al, BMC Neurology, 17, 2017.
2. Kock H.G. et al, Acta Fisiatr., 22(1): 30-33, 2015.
3. Frühauf A. et al, Int. J. Environ. Res. Public Health, 18, 2021.
4. Donath L. et al, J. App. Biomech., 31(5): 377-382, 2015.
5. Bauer F. et al, Sports Technology, 7(3-4): 120-127, 2014.
6. Iguma H. et al, Int. Symposium on System Integration, 1002-1007, 2020.

Acknowledgements

MUSCLE ACTIVITY ASSOCIATED WITH PERFORMING ROBOTIC-ASSISTED AND CONVENTIONAL LAPAROSCOPY

Abdul Shugaba (1), Joel E. Lambert (1), Helen E. Nuttall (2), Daren A. Subar (3), Christopher J. Gaffney (1) & Theodoros M. Bampouras (1)

1. Lancaster Medical School, Lancaster University, UK; 2. Department of Psychology, Lancaster University, UK. 3. East Lancashire NHS Hospitals Trust, UK;

Introduction

Minimally invasive surgery offers excellent benefits to patients [1] and one of its modalities; Robotic-assisted laparoscopic surgery (RALS) is increasingly being adopted to perform more complex procedures [2]. One of the claimed benefits is reduced musculoskeletal stress, which is important as surgeons are amongst the most at risk profession of work-related musculoskeletal decline [3]; with a high prevalence of work-related pain [4-6], and musculoskeletal injuries [7], predominantly affecting the neck, arm, shoulder, and back. The study aimed to compare electromyogram (EMG) activity in four relevant muscle groups during live laparoscopic surgery (LS) and robot assisted laparoscopic surgery (RALS).

Methods

Muscle activation during surgery was measured using a wireless EMG device during 80 surgeries (45 RALS, 35 LS). Root mean square (RMS) EMG activity was obtained bilaterally from four muscle groups (biceps, deltoid, upper trapezius, and latissimus dorsi), normalised to a previously recorded maximum contraction. Recordings were obtained at three time points: non-critical dissection, critical vessel dissection, and dissection after vessel control. The percentage changes normalised to a Maximal Voluntary Contractions (%MVC) in the four muscles compared to baseline was used to determine musculoskeletal demand.

Results

There was greater muscle activation in the LS group except in the biceps muscle. This was significant in bilateral upper trapezius (P = 0.006 & P = 0.001) and bilateral latissimus dorsi (P = 0.09 & P = 0.0009) across all 3 time points. Only the left deltoid (P = 0.026), had higher activation in LS when surgeons performed dissection around critical blood vessels and post vessel-control dissection.

In both RALS (P = 0.08) and LS (P = 0.001), comparative muscle activation was significantly greater in the right biceps. Similar greater activation in the right deltoid and right upper trapezius was observed in both groups.
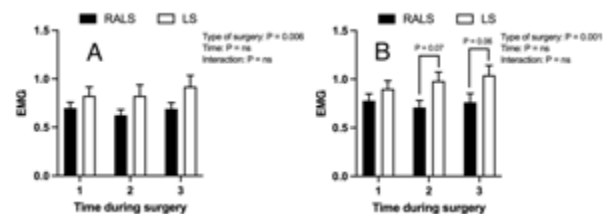
*Figure 1: RMS EMG data of muscle activation of the left (Panel A) and right (Panel B) **upper trapezius** between robotic (filled bars) versus laparoscopic (empty bars) surgery.*

Discussion

The differences found bilaterally for LS are reflective of the different tasks the arms are performing during a surgery with one arm needed to 'hold' while the other is needed to 'perform' (e.g., dissect tissue planes, make incisions etc). This increased level of muscle activation could predispose to injury, suggesting that robotic surgery might be more beneficial for surgeons' long-term health. The lower muscle activation seen in RALS could assist in reducing muscular strain during surgeries and thus contributing to reducing the risk of work-related musculoskeletal injuries in surgeons. This finding offers some mechanism to a recent meta-analysis suggesting that robotic surgery is ergonomically superior to laparoscopic surgery [8].

References

1. Patankar et al, Diseases of the colon & rectum, 46(5):601-611, 2003.
2. Schreuder et al, BJOG: An International Journal of Obstetrics & Gynaecology, 119(2):137-149, 2012.
3. Money et al, Estimation from THOR surveillance data, 2019.
4. Adams et al, Journal of minimally invasive gynecology, 20(5):656-660, 2013.
5. Dalager et al, Journal of surgical research, 240:30-39, 2019.
6. Stucky et al, Annals of Medicine and Surgery, 27:1-8, 2018.
7. Epstein et al, JAMA surgery, 153(2):e174947-e174947, 2018.
8. Hislop et al, Surgical endoscopy, 34(1): p. 31-38, 2020.

Acknowledgements

FE MODELING AND SIMULATION OF THE CUPULA DEFORMATION OF A SEMICIRCULAR CANAL IN A CLINICAL ROUTINE

Manon Blaise (1), Daniel Baumgartner (1), Anne Charpiot (1,2)

1. University of Strasbourg, ICube UMR 7357, France; 2. University of Strasbourg, University Hospital, ENT Department, France

Introduction

In vertebrates, sense of balance is vital and primitive. The vestibule contained in the inner ear constitutes one of the main component of this sensory system. Itself filled and immersed in waterlike fluids, this soft membranous labyrinth is comprised of two saclike structures and three semicircular canals (SCC) dedicated to linear and angular acceleration measurement of the head. The smallness and the fragility of the vestibular organ make the understanding of the interactions between the fluids and the thin tissue structures incomplete, delicate and challenging. The present work aims at studying these interactions by the development of a finite element (FE) model of a human vestibule part. While several models in the literature use an approach with rigid SCC [1-3], the present work explores the influence of the surrounding structures –the boundary conditions of these membranes– on the mechanical behaviour of the areas of interest, in particular the part overlaying the sensory hair cells called the cupula.

Methods

A 3D FE model of a 50-μm slice of lateral SCC is built using Altair Hyperworks™ software. Six continuously meshed parts describe the two fluids –endolymph and perilymph– and four tissue structures –labyrinth membrane, cupula, crista and bone– of a human SCC (Fig. 1). Solid tissue are assumed to be linear elastic, except the cupula modeled as a viscoelastic material [4]. All nodes are constrained in the Z direction. The model is subjected to simulation of Head Impulse Test (HIT) considered as a clinical test of reference and consists of an axial rotating of the head at a speed of π rad.s^{-1} followed by an abrupt interruption in 100 ms.

Absence of perilymph component, offset positions of the rotation axis from the foramen magnum and Arbitrary Lagrangian-Eulerian (ALE) formulation are studied and compared with conditions of reference. In the absence of perilymph, the membrane part is either let free of constraints, made stiffer or embedded in the bone part. For each case, cupula transversal displacement following nodes of interest as well as pressure and shear stress are recorded.

Results

Depending on the model distance from the rotation axis, (X=0, 20, 40 (foramen magnum), 60 mm), no significant variations of maximal pressure (P=0.83-1.82 Pa) or maximal Von Mises stress (VM=1.22-1.26 Pa) are recorded and values are comparable to those in [5]. The transversal displacement at the cupula base is slightly higher when X=0 (D=56 vs 48 μm for the other distances). Without perilymph, cupula deformation greatly increases or tends to be cancelled if membrane is soft (D=101 μm, P=2.7 Pa, VM=2.6 Pa) or rigid (D=13 μm, P=2.2 Pa, VM=0.2 Pa) respectively. Results with ALE are equivalent to those with pure Lagrangian formulation, but computation time is doubled.
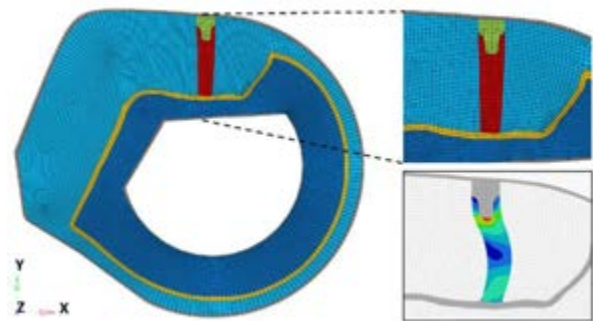
Figure 1: FE model of SCC 3D slice (10,338 hexahedral elements): endolymph (blue sky), perilymph (dark blue), cupula (red), crista (green), membranous (orange) and bone (grey) components. Right: close-up on the cupula (top) with VM stress repartition (max 1.2 Pa as expected in hair cells layer at cupula base) during HIT (bottom).

Discussion

A remaining challenge in understanding the fluid-structure interaction phenomena in the inner ear is to develop an accurate and complete model that could take into account the dynamic boundary conditions of the structures. However, such model would increase the computation time. As well as modeling a single 3D slice of SCC, pure Lagrangian instead of ALE formulation shows in this case an interest for preliminary results before enhancing the computations on a global 3D model. Furthermore, acting on labyrinth membrane stiffness could be a solution to mimic the surrounding perilymph space.

While validation by experimental data may be considered, such FE modeling is a useful approach to answer some clinical needs, when direct measurements are delicate by either surgery or medical imaging techniques.

References

1. Goyens, Hear Res, 396:108071, 2020.
2. Santos et al, Adv Biomech Tissue Regen, 21-32, 2019.
3. Shen et al, Biophys J, 118:729-741, 2020.
4. Selva et al, J Vestib Res, 19:95-110, 2009.
5. Baumgartner et al, Comput Methods Biomech Biomed Engin, 22:S84-S86, 2019.

TOWARDS THE LEARNING OF HUMAN-SEAT INTERACTIONS FOR RUNTIME-EFFICIENT HUMAN MODELS BASED ON PRESSURE DISTRIBUTIONS

Daniel Niklas Fahse (1), Michael Roller (2), Fabian Kempter (1), Jörg Fehr (1)

1. Institute of Engineering and Computational Mechanics (ITM), University of Stuttgart, Germany;
2. Fraunhofer ITWM, Germany

Introduction

Human body models (HBM) are an important tool for developing safety systems and evaluating ergonomics. Especially in accident scenarios, detailed Finite-Element-Models (FEM) are used to investigate the injury risk of the passengers. The high computational cost of these simulations prevents the analysis of the wide range of future crash scenarios and varying human behaviors inside the vehicle. These aspects and the requirements arising from the foreseeable increase of automated driving situations motivate the creation of runtime-efficient human models with active musculature. Multibody systems (MBS) modeling the human body with discrete mechanics and optimal muscular control show promise for predicting human-like motion [1]. However, for the application in a vehicle interior, the human-seat interaction is crucial to obtain valid results. In this contribution, we propose an approach to learn a surrogate model which describes the interaction between human and seat by processing force distribution data of simulations with detailed FE-HBMs. This leads to a run-time efficient active human body model that can interact with the car interior and enable simulations of longer, more complex traffic scenarios including realistic occupant movement.

Methods

The interaction between the HBM and the vehicle interior is learned in an offline phase. Therefore, contact regions for the different body parts are defined and the pressure (force) distributions of the detailed FE-simulations are processed in an automatic fashion to obtain the resultant forces and torques. Subsequently, model order reduction (MOR) and machine learning (ML) algorithms are combined for pre-processing and training the surrogate model representing the interaction [2]. Figure 1 shows a schematic of this procedure.
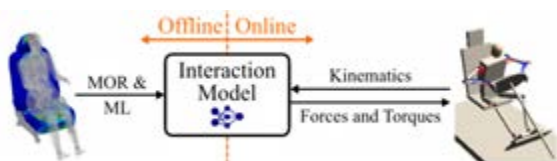
Figure 1: Schematic of the methodology to formulate the human-seat interaction with a separation in an offline learning phase with detailed FE simulations (left) and an online interaction phase (right).

Results

Suitable coordinate systems (COS) are introduced in both FE and MBS human models to describe their kinematics and to allow the transfer of the identified interaction model. A decisive factor there is, to find a suitable translation between the kinematics of the FE model and the low-degree of freedom MBS model which combines several anatomical bodies, e.g. vertebrae, into one lumbed rigid body segment. Thus, the resultant interaction forces f_i^{res} and torques τ_i^{res}, at the COS i can be formulated as a function of the human kinematics of the corresponding body r_i relative to the seat

$$f_i^{\mathrm{res}} = f_i^{\mathrm{res}}(r_i) \text{ and } \tau_i^{\mathrm{res}} = \tau_i^{\mathrm{res}}(r_i) \; \forall \; i \in \mathrm{I} \quad (1)$$

So far, we have categorized the body into 8 contact-regions and learned the interaction properties based on force-controlled virtual experiments performed in nonlinear FE simulations.

Discussion

As shown, the relevant characteristics of the human-seat interaction are extracted from the virtual FE-simulations to an interaction model which can be applied to a MBS simulation. This will allow the runtime-efficient human model to interact with different interiors without the need to model them as an MBS and perform a contact-based approach to calculate the corresponding interaction forces. The normally expensive interaction procedure is replaced by simple matrix vector multiplications.

Furthermore, the approach is formulated in a way that additional experimental data can be easily integrated into the training data of the interaction model. Thus, the data basis for training is enlarged and real-world transferability is improved.

References

1. Roller et al, Adv Transdiscipl Eng, 11:269-276, 2020.
2. Kneifl et al, Int J Numer Methods Eng, 122: 4774-4786, 2021.

Acknowledgements

How does kinematic alignment influence femorotibial kinematics in medial stabilised TKA compared to mechanical alignment?

L. Bauer, M. Woiczinski, C. Thorwächter, PE. Müller, BM. Holzapfel, TR. Niethammer, J.-M. Simon
Department of Orthopaedics and Trauma Surgery, Musculoskeletal University Center Munich (MUM), University Hospital, LMU Munich

Introduction

An increasing number of primary total knee prosthesis implantations are being performed every year and, at the same time, the need for a good and satisfying functional outcome after total knee arthroplasty (TKA) for the patient is growing. The more and more used kinematic alignment (KA) as the choice of surgical positioning method for a TKA [1] has shown very good patient satisfaction [2, 3] compared to the mechanical alignment (MA), which has been established for years. Whether the KA method has an influence on the knee joint kinematics has not yet been investigated. It is assumed that the KA has a more physiological outcome/movement pattern compared to the MA. The aim of the present in vitro study was to compare a KA with a MA in terms of femorotibial kinematics.

Method

Eight fresh frozen human knee joints were tested on a knee rig during active, muscle-controlled knee flexion (weight-bearing) from 30° to 120°. For this purpose, in each specimen, a TKA with a medial stabilized (MS) design (GMK Sphere, Medacta International, Castel San Pietro, Switzerland) was implanted and tested first with a KA and then with an MA. Femorotibial kinematics were recorded using an optical measuring system (ARAMIS 3D camera 2.3M, GOM GmbH, Braunschweig, Germany) and the relative femorotibial knee joint kinematics were calculated and evaluated.

Result

During flexion in the knee joint, the tibia rotated more internally with a KA compared to a MA in the same specimen. From approximately 90° of flexion, internal rotation decreased slightly. With MA, the tibia rotated less internally. The curve flattened for MA from 80° and the tibia hardly rotated via deep flexion (80–130°). With a KA, the tibia was already more anterior at the beginning than with the MA (2.9 mm). During flexion of the knee joint (30–130°), a similar trend of KA and MA could be observed for the anterior-posterior movement. Both implantation techniques lead to an anterior movement of the tibia during flexion, thus a femoral rollback. A more constant femorotibial medial rotation point (less standard deviation) up to approximately 70–80° flexion could be shown for the KA. From 80° flexion, a posterior translation of the medial rotation point could be observed. A medial rotation point could also be shown for the MA. However, this was less distinct since less movement was visible on the lateral side.

Discussion

The main findings of the present study were a greater tibial internal rotation and femoral rollback (AP translation of the tibia) during flexion within KA TKA compared to MA TKA. In this regard, it can be concluded that a KA TKA using a MS inlay design may support the reproduction of physiological, patient-specific knee joint mechanics.
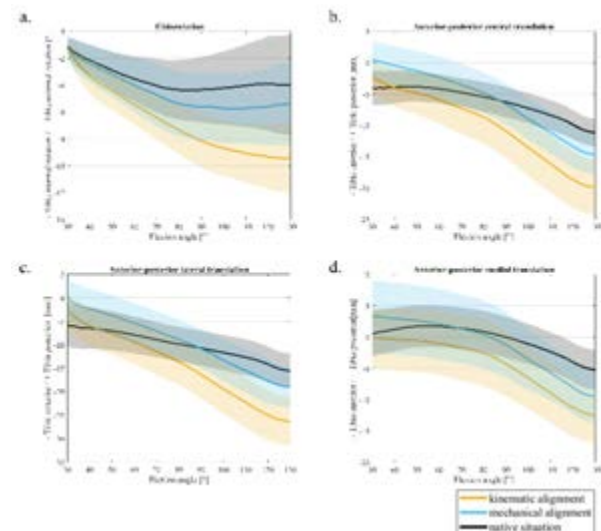
Figure 1: Mean values (n = 8) and 95 % confidence interval for femorotibial kinematics of MS prosthesis for deep knee bend from 30° to 130°: a. Tibial rotation; b. Anterior-posterior central translation; c. Anterior-posterior lateral translation; d. Anterior-posterior medial translation, of kinematic alignment (orange), mechanical alignment (blue) and native situation (black)

References

1. Calliess T, Ettinger M, Stukenborg-Colsmann C, Windhagen H (2015) Kinematisches Alignment in der Knieendoprothetik. Der Orthopäde 44:282-289
2. Courtney PM, Lee G-C (2017) Early outcomes of kinematic alignment in primary total knee arthroplasty: a meta-analysis of the literature. The Journal of arthroplasty 32:2028-2032. e2021
3. Dossett HG, Swartz GJ, Estrada NA, LeFevre GW, Kwasman BG (2012) Kinematically versus mechanically aligned total knee arthroplasty. Orthopedics 35:e160-e169

MECHANICAL PERFORMANCE OF HYBRID FIBROUS STRUCTURES FOR TENDON REPAIR

Tânia Peixoto (1,2), Maria Lopes (2), Raúl Fangueiro (3), Rui Guedes (4)

1. REQUIMTE-LAQV, Departamento de Engenharia Metalúrgica e Materiais, Faculdade de Engenharia, Universidade do Porto, Portugal; 2. Instituto de Polímeros e Compósitos, Departamento de Engenharia de Polímeros, Universidade do Minho, Portugal; 3. Centro de Ciência e Tecnologia Têxtil, Universidade do Minho, Portugal; 4. LABIOMEP-INEGI, Departamento de Engenharia Mecânica, Faculdade de Engenharia, Universidade do Porto, Portugal

Introduction

This work analyzes hybrid braids based on polyethylene terephthalate (PET) and polylactic acid (PLA) yarns. These braids comprise 16 multifilament yarns of different PLA/PET ratios. Varying the number of braids and the PET/PLA ratio in the final structure allows tuning the load and strain at failure, as well the stiffness. This is crucial to attaining mechanical compatibility with different tendons/ligaments. PET and PLA yarns are preferred since multifilament scaffolds are usually stronger and have better elastic recovery than monofilament. This effect is linked to the load sharing between the yarn filaments. Another benefit of implantable multifilament scaffolds is their lower flexural stiffness more complaint with surrounding tissues than the monofilament devices.

The tensile properties of fibrous structures depended upon their architecture assembled in braid formation. Different methodologies have been proposed to model the tensile mechanical response of braids consisting of multi-layered structures [1-4].

Materials & Methods

The fibrous structures with different proportions of yarn type (PET or PLA), produced samples labelled in accordance as 16PET, 12PET4PLA, 10PET6PLA, 8PET8PLA, 6PET10PLA, 4PET12PLA, and 16PLA. For example, 10PET6PLA is a braided structure with 10 PET yarns and 6 PLA yarns. The braid angle, measured by optical microscopy images as the angle between the intertwining yarn with the braid axis, was similar for all structures, i.e. ≈13o.

The mechanical characterization until failure employed a Shimadzu EZ-LX Long-Stroke Model tensile testing machine (Shimadzu, Japan) with a 500 N load cell, a gauge length of 235 mm, and a crosshead speed of 8.5 mm/s. These conditions reproduce the average length of the Achilles tendon at a physiologic displacement rate.

Results& Discussion

The force at failure and stiffness decreased significantly as the number of PLA yarns increased, although strain at failure remained the same. The PET yarns are crucial for the mechanical strength of hybrid structures. Higher PET content correspond to superior tensile performance, in Table 1 and Figure 1.

A simply structural model based on the geometrical properties of the braid and the constitutive behaviour of individual components is proposed to predict the tensile behaviour of the hybrid braided structures. The experimental data is used in the analytical model to test its predictive accuracy.

Sample	Force at Failure (N)	Strain at Failure (%)	Stiffness (N/mm)
16PET	1116.3 ± 68.9	19.2 ± 1.2	28.7 ± 0.3
12PET4PLA	958.8 ± 28.7	20.4 ± 1.1	25.8 ± 1.9
10PET6PLA	845.4 ± 45.3	19.7 ± 1.8	25.5 ± 1.4
8PET8PLA	766.8 ± 35.1	20.7 ± 2.5	24.0 ± 1.2
6PET10PLA	662.0 ± 21.2	21.9 ± 1.0	22.7 ± 0.7
4PET12PLA	513.3 ± 8.20	20.4 ± 1.0	21.0 ± 0.5
16PLA	529.7 ± 34.7	50.8 ± 3.0	18.7 ± 0.9

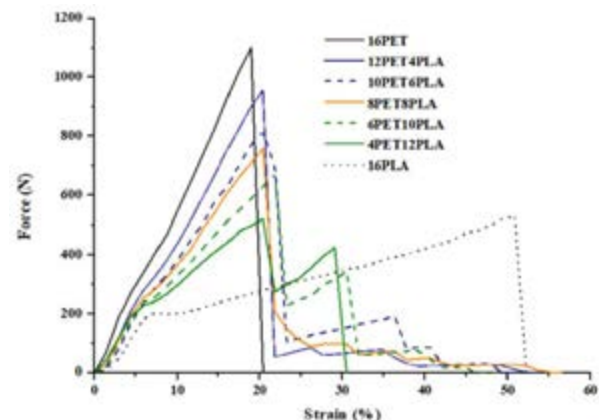*Table 1: Tensile properties of the braided structures.*

Figure 1: Experimental Stress-Strain curves.

References

1. Rawal et al. Textile Research Journal 85(19):2083-2096, 2015.
2. Rawal et al. Mechanics of Materials 91(P1):277-289, 2015
3. Laurent et al. Ligament Reconstructions 2021, pp. 321-369.
4. Laurent et al. Lecture Notes in Computational Vision and Biomechanics, 2013, pp. 1-44.

Acknowledgements

DIGESTION OF COLLAGEN FIBRILS TROUGH MMP-1: LIVE TRACKING OF MECHANICS THROUGH NANOINDENTATION

Manuel Rufin (1), Simon Jaritz (2), Gerhard J. Schütz (2), Philipp J. Thurner (1) , Orestis G. Andriotis (1)

1. Institute of Lightweight Design and Structural Biomechanics, TU Wien, Austria; 2. Institute of Applied Physics, TU Wien, Austria

Introduction

Collagen fibrils (CFs) are the structural backbone of most tissues in the human body and subject of constant remodeling with new fibrils assembled and existing ones being enzymatically digested by Matrix Metallo-proteinases (MMPs). In this study, we show how the digestion process of isolated fibrils from tendonous collagen can be morphologically and mechanically monitored through nanoindentation using an atomic force microscope (AFM). Results obtained so far indicate significant variation in digestion behavior between different fibrils.

Methods

CFs from mouse tail tendon (OT1, m, 12 weeks) were prepared on round coverslips [1] and mounted in a heated fluid cell (BioCell, Bruker-JPK) in buffer (25 mM HEPES, 2mM $CaCl_2$, 50 mM NaCl) at 34°C. Indentation data was acquired on a Nanowizard 3 AFM (Bruker-JPK) in Quantitative Imaging™ mode at a resolution of 256x256 pixels and a setpoint of 1 nN in 20-30 minute intervals using a Bruker MSCT-F cantilever (nominal spring constant, 0.6 N/m). After the first measurement, activated recombinant human MMP-1 (BioLegend) was added to the buffer to achieve an enzyme concentration of 10nM. Overall digestion time was 3 hours. Force-distance curves were analyzed with the Hertz-Sneddon method to yield an indentation modulus. Individual fibrils were characterized using modulus and height pixel values from the crest points of each fibril. Only valid crest points (excluding spots with several fibrils on top of each other) were used. They ensure smallest systematic error for indentation modulus and were determined via automated segmentation.
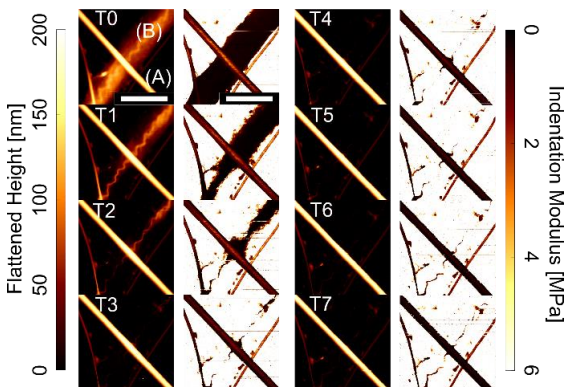
Figure 1: Digestion of collagen fibrils in 8 time steps T0-T7: Pairs of AFM images - flattened height (column 1 & 3) and indentation modulus (column 2 & 4) - reveal evolution in structure and mechanics (A) typical intact

fibril, with stark decrease in modulus but no detectable change in height. (B) typical overstrained fibril, almost completely digested after one hour T2 . Scalebars 2 μm.

Results

AFM live monitoring of the enzymatic digestion process of collagen fibril through MMP-1 reveals a large variability in digestion characteristics of individual fibrils in the same region of interest. Despite being exposed to the same concentration of MMP-1, the different fibrils in our measurements show diverse behavior during digestion, especially looking at the rate of height loss (see Fig. 1). The biggest difference is observed between intact (Fig. 1 (A)) and overstrained (Fig. 1 (B)) fibrils. The latter is easily spotted as they exhibit a wavy pattern, in contrast to the straight D-banding of intact collagen fibrils.

Figure 2: Indentation moduli along the crest of the largest intact fibril (A) in Figure 1 (running from top left
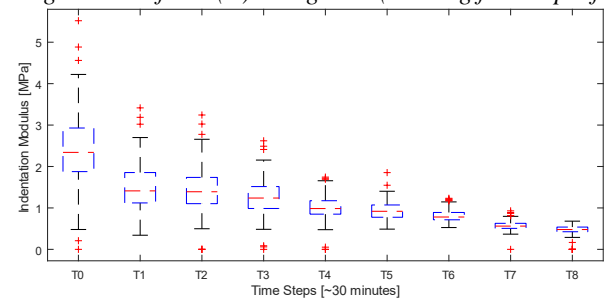
to bottom right). The modulus steadily decreases in each time step with intervals of 20-30 minutes.

Discussion

While studies on collagen digestion have been carried out on bulk material at the macroscale and others on very low concentrations at the molecular scale [2] we present this process here at the level of the fundamental building block, the collagen fibril. First findings show the digestion rates to be negatively correlated with fibril stiffness and fibril swelling. Both of these relations might be tied to the confounding variable of the amount of fibril cross-linking.

References

1. Andriotis et al, JMBBM, 39:9-26, 2014.
2. Saffarian et al, Science, 306:108-111, 2004.

Acknowledgements

DESIGN OF BIOMECHANICAL TESTING DEVICE FOR THE PELVIS INCLUDING GAIT MUSCLE FORCES

Ahmed Soliman[1], Pierre-Louis Ricci[1], Slawomir Kedziora[1], Jens Kelm[2], Torsten Gerich[3], Stefan Maas[1]

[1] University of Luxembourg, Luxembourg; [2] Chirurgisch-Orthopädisches Zentrum Illingen, Germany; [3] Centre Hospitalier de Luxembourg, Luxembourg

Introduction

Associated bone diseases due to aging are rising with the increasing number of elderly people in modern societies. Traumas in the pelvic ring have a significant negative influence on the human mobility and may lead in worst cases to lethal complication. Hence, developing realistic testing protocols with clinical relevance is vital in order to provide reliable testing of the pelvic reconstructive implants and restore pelvic ring stability and functionality. The novel test stand developed in the current study is designed numerically to reproduce more realistically the stress states in the pelvis compared to literature [1-3].

Methods

A biomechanical test stand to emulate physiological gait loading of the pelvis was developed numerically and then built (ref. to Figure 1).
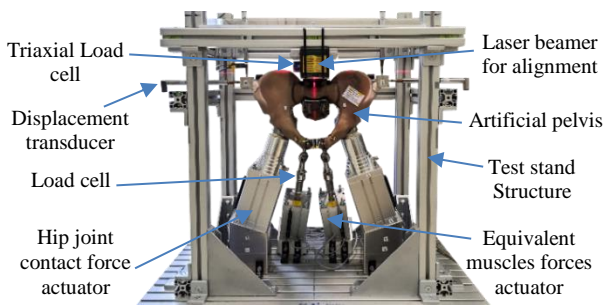
Figure 1: Experimental pelvis test stand replicating the stress states of gait loading cycle.

Starting with inverse dynamics, all muscles and hip joint contact forces applied to the pelvis were calculated using software AnyBody [4] to simulate normal gait movement. These forces were then applied to a realistic finite element model of the pelvis. A numerical model of the test stand including the pelvis was developed in order to investigate iteratively the possibility of reducing the high number of acting muscles and joint contact forces. These forces were reduced to only 4 actuators: two for the hip joint contact forces and another two for equivalent muscles forces. The design objective is to match as close as possible the simulated stress-distribution at critical location for important moments of the gait [5]. Then 3 pelvises of Sawbones 4th Generation reproducing mechanical behavior of human bone [6] are tested and strain was measured at 8 critical locations together with the lumbosacral joint reaction force and the pelvis displacement. All measurements could validate the preceding simulations, thus demonstrating high repeatability.

Results

The simulated test with only 4 actuators is able to reproduce a similar stress state compared to a pelvis with all muscles and joints contact forces. This finding is presented in Figure 2 for the moment of Left Heel Strike (LHS) as an example.
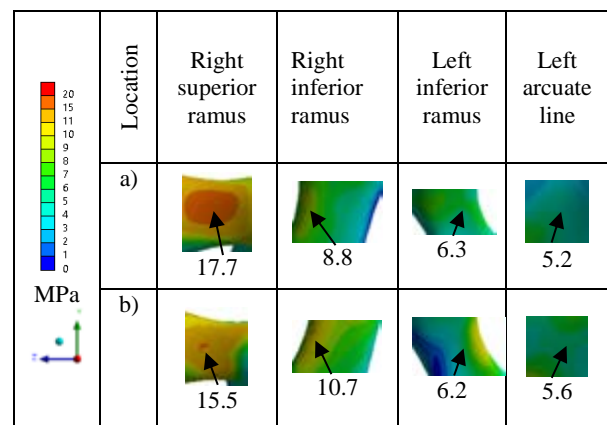
Figure 2: von Mises stress distribution at some location of interest in the pelvis. a) Pelvis with all muscles, hip joint and SIJ contact forces. b) Simulated test stand with only four actuators

Globally, the stress states at superior and inferior rami and at sacral iliac joint show the same magnitude and spatial distributions in both configurations.

Discussion

The experimental set-up is designed numerically with only 4 actuators and validated by strain, displacement, force measurements versus the complete numerical model. Furthermore, clinical observations confirm simulations and experiments, therefore strengthening the study. The developed test stand is currently used for real implant-testing for rami fractures.

References

1. M. Ramezani et al., BioMed Research International, 2019, 2019.
2. D. Liu et al., J. Mech. Behav. Biomed. Mater., 90:626–634, 2019.
3. G. Osterhoff et al, Eur J Trauma Emerg Surg. 42:197–202, 2016.
4. AnyBody. The AnyBody Modeling System. Aalborg, Denmark: AnyBody Technology A/S; 2017.
5. P.L. Ricci, PhD thesis, University of Luxembourg, 2019, ISBN 978-3-8440-6823-8, Shaker Verlag, Germany.
6. Sawbones USA, "Sawbones Product Catalogue," A Pacific Research Company, 2021.

DEVELOPMENT OF A PHYSICAL TWIN FOR CARDIOVASCULAR LIFE-SUPPORT DEVICES ANALYSIS AND COMPARISON

Emanuele Vignali (1), Emanuele Gasparotti (1), Francesco Bardi (1), Serena Prizio (2), Dorela Haxhiademi (2), Paolo Del Sarto (2), Simona Celi (1)

1. BioCardioLab, Fondazione Toscana Gabriele Monasterio, Italy 2. Anesthesiology and Intensive Care Unit, Fondazione Toscana Gabriele Monasterio, Italy

Introduction

Cardiogenic shock is a life-threatening condition linked with heart flow output insufficiency. Currently, different clinical procedures are available to manage this pathology. The Extracorporeal Membrane Oxygenation (ECMO) and the Impella device are possible solutions. Nevertheless, the effects on the circulatory system remain a matter to clarify. It is, in fact, well established that ventricular afterload is modified by support devices [1], as left ventricle (LV) pressure is increased. To deepen the investigation on these effects, the contribution of experimental fluid dynamic setups can be highly valuable [2].

Given this context, the aim of the current work is to present a physical-twin fluid dynamic system to analyze the effect of both ECMO and Impella support devices. Both single and combined (ECMELLA) configuration are tested.

Methods

A fluid dynamic mock circulatory loop (MCL) was developed. A piston pump was adopted to impose a physiological aortic flow profile within the MCL (Figure 1 a) system [3]. The pressure conditions are maintained by imposing three-element Windkessel models at the outlets via pressurized chambers. A 3D printed patient-specific phantom of the aortic complex with supra-aortic and iliac arteries was manufactured. In addition, a centrifugal pump to simulate the ECMO support with femoro-femoral access and an Impella device (Abiomed) at the aortic valve level were included. Three conditions of aortic stroke volume were tested: healthy (70 ml) as a reference, severe (SVR - 70% reduction) and mild (MLD - 30% reduction) shock. The level of ECMO support was ranged from 1 l/min to 7 l/min for both the MLD and SVR cases to be compared with the healthy condition. The same test procedure was repeated by also enabling the Impella support (ECMELLA configuration) with speed fixed at 5 at the device console level.

Results

The plot in Figure 1 b represents the effect of ECMO support on the average supra-aortic vessels flow for the SVR and MLD shock levels. It can be noted that the physiological healthy condition could be reestablished in both cases. The effect on left ventricular pressure was established as well. As it is possible to detect in Figure 1 c, ECMO and ECMELLA systems influence the LV pressure differently. In particular, the ECMELLA produces a lower pressure load on the LV if compared with the single ECMO. The same trend was established on both MLD and SVR shock conditions.
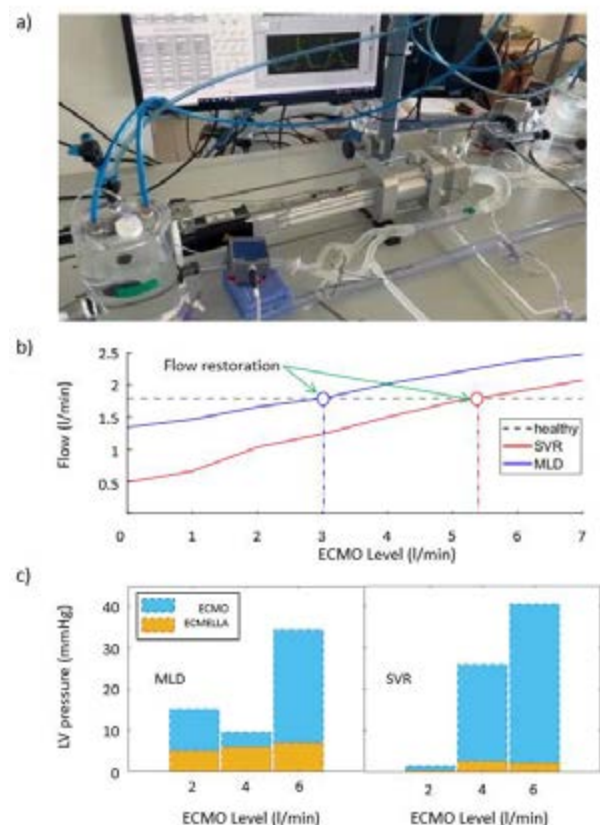
Figure 1: MCL setup for the experimental evaluation of ECMO and ECMELLA a). Flow restoration trend b) and LV pressure increase comparison c)

Discussion

The experimental system was successfully developed for the analysis of support devices in cases of cardiogenic shock. It was possible to assess the possibility to reestablish flow conditions in both simulated shock conditions. It is interesting to note how the ECMELLA device was able to maintain low levels of LV afterload increase.

References

1. Donker, et al, Perfusion, 2019, 34.2: 98-105.
2. Mariotti et al, Proc. of AIMETA Conf. Springer, Cham, 2019. p. 898-907.
3. Vignali et al, ASAIO Journal, 2022.

REPRODUCIBLE GENERATION OF PREDEFINED TIBIA FRACTURES

Kerstin Wickert (1), Michael Roland (1), Annchristin Andres (1), Stefan Diebels (1)

1. Saarland University – Chair of Applied Mechanics, Germany

Introduction

An individual approach to fracture therapy requires not only knowledge of trauma surgery but also expertise in mechanical aspects. In order to understand and optimise the process of fracture healing, it is necessary to deal with the origin of the fracture.

Only with the help of experimentally supported material models can the mechanical behaviour of bones be meaningfully simulated and corresponding predictions made possible. The basis is the fracture generation and the behaviour of the bone under different loading conditions. Therefore, a testing device was designed and built to generate reproducible and predefined human cadaveric tibiae fractures.

Methods

The specimens come from body donations. Before the experiment is performed, a computer tomography (CT) scan including a 6-rod calibration phantom for bone density is made from the lower leg. The segmentation of the CT stack forms the basis to build the 3D model for the simulation and is equipped with the bone mineral density information based on the calibration phantom. The model is passed to a high-quality finite element meshes generator. The image processing was done in Simpleware ScanIP[TM].

The fracture events are performed on the self-designed testing device (see Figure 1 a) and the fracture event takes place due to superimposed compressive and torsional loads. Two six-axis force sensors (3) are measuring the forces during the experiment.

After soft-tissue removal and foot exarticulation, the human tibiae are equipped with a so-called Speckle pattern for the evaluation via digital image correlation (DIC). All experiments are performed on the testing device and recorded by corresponding high-speed cameras including real-time triggering.

The specimens are clamped into an individual complex clamping system (4). To generate realistic fractures data from Orthoload[TM] [1] are applied to the testing device and are scaled with the body weight of the donors. Longitudinal loads are applied by pre-compressing one axis with the stepper motor and the screw drive (1&6). The spiral fracture is caused by the torsion axis with the direct drive and the leading bellow coupling (1&2). The axial loading corresponds to the maximum forces acting during a step forward based on the scaled Orthoload[TM] [1] data and then torsion is applied until fracture.

The experiments are evaluated using a combination of the measuring sensors and the DIC evaluation [2]. The DIC process starts with a reference image of the undeformed specimen and calculates the surface displacements and strains with respect to the images of the deformed states.

Results

Reproducible distal tibiae fractures were produced (see Figure 1b & Figure 2) as statistical fractures for the further workflow of testing new trauma implants. It is possible to make a statement about the limit loads before failure. Through the evaluation material parameters of the bones yields additionally.

Discussion

An essential part of fracture healing is the understanding how the event happened and which fracture morphology arises. Information is provided by taking into account realistic load cases on a whole bone.

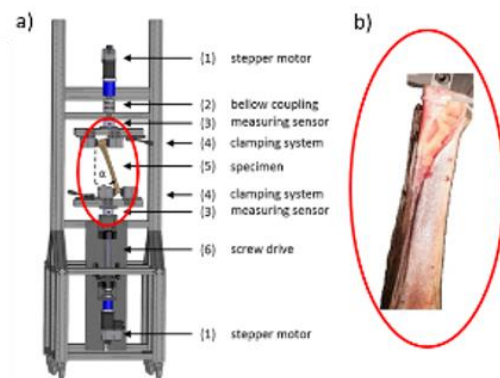*Figure 1 a) Testing device b) Spiral fracture*
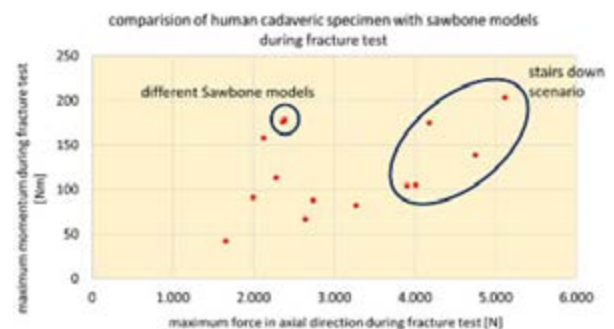

Figure 2 Results for a series of complex distal tibia fractures

References

[1] https://orthoload.com/
[2] https://www.dantecdynamics.com/solutions-applications/applications/biomechanical-biomaterial-testing/

Acknowledgements

EXPERIMENTAL VALIDATION OF A MECHANISTIC MODEL OF THE BERLIN HEART EXCOR USING A MOCK CIRCULATION LOOP

Victoria Yuan* (1), Luca Rompani* (1), Francesco De Gaetano (1), Maria Laura Costantino (1)

1. Laboratory of Biological Structure Mechanics, Politecnico di Milano, Italy

Introduction

Children in need of heart transplants have the highest waitlist mortality of all solid-organ transplant patients [1]. The Berlin Heart EXCOR (BH) is the only licensed ventricular assist device (VAD) for infants and children with heart failure [2]. The BH has successfully bridged children to transplant or to recovery. The device comes in a wide range of volumes, and physicians can control four different settings – device rate, systolic time, and diastolic and systolic pressures. The BH consists of an air chamber and a blood chamber, separated by a thin, flexible member. High pressure in the air chamber displaces the membrane, which drives output to the patient's circulation. Understanding membrane dynamics is essential to modeling the performance of the BH. While an *in-silico* model of the BH based on membrane mechanics has been developed, it has not been experimentally validated, thus limiting its applicability [3]. In this study, we present an experimental test bench to validate an existing computational model of the BH and to investigate device performance under variable settings.

Methods

A 25 mL BH was connected to a 3 parameters resistor-capacitor-resistor mock circulation loop (MCL) to represent the systemic circulation in a 5-month-old infant (Figure 1). The inflow of the BH was connected to a constant pressure of 4 mmHg to reflect pediatric left atrial pressure; the outflow was connected directly to the MCL. Resistive and capacitive values were chosen to reflect the physiologies of infants from 5 to 10 months.
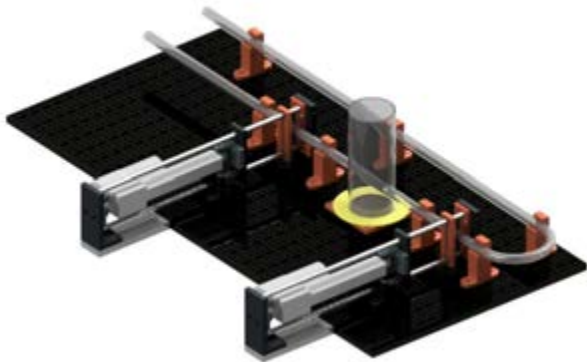
Figure 1: Schematic of the 3 parameter MCL to validate a computational model of the BH in the systemic circulation in a 5-month-old infant.

The MCL is based on a 3-element Windkessel model, which represents the vasculature as two resistive elements and a capacitive element. The resistors consist of pinch valves actuated by spring pressers, which maintain a constant linear relationship between low rates and pressure drops. The capacitive element is designed as closed air chamber whose volume can be varied to simulate a wide range of physiologically realistic compliances. Because the resistive and capacitive elements are electronically driven, their values can be readily changed to reflect diverse physiologies.

The BH was driven at 240/-20 mmHg and 60 beats per minute (bpm). Using flow and pressure sensors, we quantified device output and pressures at the inlet, outlet and internal to the VAD. Experimental results were compared to simulated results, and error was quantified. This procedure is repeated for BHs with volumes of 10 and 60 mL and for device rates of 90 to 120 bpm.

Results

Our in-vitro and initial parametric tests with the BH are extremely promising. After performing experiments, data from the MCL will be compared to the computational model of the BH. If our analysis reveals a sufficiently reasonable error, the model in Yuan, et al. will be successfully validated [3]. With our MCL, we also hope to gain insight into membrane deformations across a wide range of device volumes, rates and pressures. These observations may be leveraged to improve the mechanistic model.

Discussion

We presented an experimental setup that can be readily adjusted to simulate a wide range of adult or pediatric physiologies. Our MCL is uniquely situated to validate a computational model of the BH and study its behavior under different operating conditions [3]. A validated model of the BH can act as both a clinical tool to inform treatments and a training tool for physicians. Our results will investigate the relationship between BH settings and hemodynamics, which can improve clinical understanding of the device. Finally, our results can inform the improvement of existing simulations while informing future models of pulsatile VADs.

References

1. Almond, CSD, et al, Circulation, 119:717-727, 2009.
2. Molfetta, AD, et al, Front Phys, 7, 2016.
3. Yuan, V, et al, Cardiovasc Eng Tech, 2022.

Acknowledgements

INTEGRATING µCT AND INDENTATION PROTOCOLS TO ASSESS STRUCTURE AND MECHANICS OF ARTIFICIAL MENISCUS IMPLANTS

Matteo Berni (1), Gregorio Marchiori (1), Milena Fini (1), Massimiliano Zingales (2), Claudia Trombino (2), Stefano Di Paolo (1), Stefano Zaffagnini (1), Nicola Francesco Lopomo (3), Massimiliano Baleani (1)

1. IRCCS Rizzoli Orthopaedic Institute, Italy; 2 University of Palermo, Italy; 3 University of Brescia, Italy

Introduction

Menisci are porous, fibro-cartilaginous, wedge-shaped structures, which play a key role in redistributing contact stress across the knee joint generated during daily activities. When meniscal lesion occurs, surgical treatment is recommended to reduce the risk of late degenerative sequelae [1]. Reconstruction or replacement can be performed by allogenic, heterologous, or artificial meniscus. Regarding the latter option, the ideal artificial implant should resemble the mechanical and structural features of the native tissue [2]. In this perspective, it is crucial to accurately assess parameters capable of elucidating the fundamental relationships at the base of the implant function. Very recent investigations on native meniscus exploited microcomputed tomography (µCT) to reveal its microstructure [3], and indentation to measure its mechanical response [4]. Accordingly, the purpose of this study is to optimize µCT and indentation approaches aiming to quantitatively and coherently evaluate the main aspects of artificial meniscal implants.

Methods

Artificial menisci (n = 3; 95% collagen fibers, 5% glycosaminoglycans by dry weight) were dry scanned (source voltage 30 kV, current 175 µA; no filter; image pixel size 5 µm) using Skyscan 1172 µCT (Bruker, Belgium), achieving information about implant architecture (*Fig. 1*) – i.e., porosity (*Po*), mean fiber thickness (*Th*) and degree of anisotropy (*DA,* 0 for total isotropy, 1 for total anisotropy).

$Po = 62\%$
$Th = 50\mu m$
$DA = 0.8$
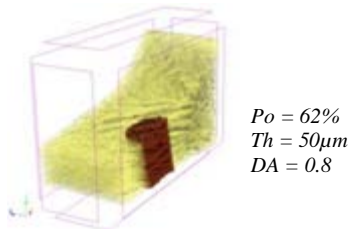
Fig.1: Cross-section of implant architecture (yellow), in which a region interested by indentation was highlighted (red).

Then, specimens were soaked in PBS 1x (7.4 pH, Life Tech., The Netherlands) for 24h, thus to reach a steady rate of fluid sorption. Subsequently, each sample was placed in a testing chamber filled with PBS. A polar system of coordinate was implemented, allowing to perform indentations along two different arcs, R_{int} and R_{ext} (*Fig. 2*). The angular distance between nearby points, β, was set equal to at least three times the radius of the indenter surface, to avoid influence between subsequent indentations.
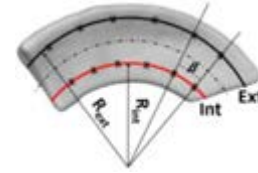
Fig.2: Artificial meniscus partition, highlighting the minimum angular distance, β, between nearby points, and internal, Int, and external, Ext, regions.

Tests were performed by a multi-axis mechanical tester (Biomomentum, Canada) equipped with a multi-axis load cell and with a spherical indenter (Ø = 2 mm). Since meniscus response is strain dependent, specimens were tested firstly by a displacement approach, and then by reproducing *in vivo* conditions, i.e., 10% nominal deformation and $0.10s^{-1}$ strain rate [5]. Elastic and viscous peculiarities of the implant were investigated, considering maximum load (F_{max}), initial viscous response (Et_{20}), and relaxation percentage (ΔF_{relax}).

Results & Discussion

Preliminary analyses highlighted inhomogeneity of the artificial meniscus, i.e., between the internal and the external region. Structural parameters, i.e., *Po* and *DA*, differ between the investigated regions. Further, strain-based indentation protocol seems to be more sensible in detecting variations of the estimated mechanical parameters, showing higher values for the implant external region.

Conclusions

This work lays solid foundations in determining mechanical and structural features of artificial meniscus implants, providing an integrated framework able to monitor the implant performance even in regenerative studies. Future developments will concern the assessment of structure-function relationship, achieving key information capable of improving the implant clinical outcomes.

References

1. Vranckenet et al, Int Orthop, 37(2):291-9, 2013.
2. Pietrzak et al, 978-1-59745-239-7, 2008.
3. Kestila et al, Ost Cart, 27(12):1790-1799, 2019.
4. Seitz et al, Front Bioeng Biotechnol, 9: 659989, 2021.
5. Schwer et al, Front Bioeng Biotechnol, 8: 582055, 2020.

Acknowledgements

SPATIALLY-RESOLVED PROTEOMICS AND MICROMECHANICS OF HUMAN MENISCI

Martin Handelshauser (1)(2), Orestis G. Andriotis (1), Martina Marchetti-Deschmann (2), Philipp J. Thurner (1)

1. Institute of Lightweight Design and Structural Biomechanics, TU Wien, Austria; 2. Institute of Chemical Technologies and Analytics, TU Wien, Austria;

Introduction

A high percentage of the population experiences pain and irritation from meniscal degeneration. The hallmark of meniscal degeneration is degenerative tears, mainly caused by repetitive loads onto fatigued menisci [1]. Structurally, about 75% of the dry mass of menisci consists of collagens. Other proteins, identified in meniscal tissue are, e.g., serum albumin, mimecan and biglycan [2]. To better understand the influence of collagens on the process of meniscus degeneration and resulting tearing, we investigate the distribution of proteins in human menisci samples by mass spectrometry imaging (MSI) and compare this information to the local mechanical properties collected by atomic force microscopy (AFM).

Methods

Degenerated human menisci, were embedded in Tragacanth, cryo-sectioned into 12 µm sections and thaw-mounted on ITO (indium tin oxide) slides. Microindentation experiments [3] were conducted on an AFM (NanoWizard ULTRA Speed, JPK) using a cantilever with a stiffness of 0.028 N/m and furnished with a 10 µm sphere, at a 1nN setpoint, in physiological conditions (Ringer acetate buffer/protease inhibitors). Three 10 x 10 force maps with 1 µm spacing were recorded on the tissue in each of 2 regions of interest (ROI) (Figure 1(**A**)). Consecutively, salts and lipids were removed by washing the sections in ethanol, water and Carnoy's solution as preparation for MALDI-MSI (matrix assisted laser desorption/ionization). Trypsin/Lys-C (50 µg) was applied to the sample by spraying (HTX TM-Sprayer) and incubated at 37° C for one hour at high humidity. 0.25 mg/cm² CHCA (α-cyano-4-hydroxycinnamic acid) matrix was applied via spraying. Samples were measured on a MALDI-TOF/TOF (time of flight) system (ultrafleXtreme, Bruker) at 40 µm lateral resolution.

Results

Figure 1(**B**) shows higher indentation moduli in ROI1 ([4.58 ± 0.99] kPa) compared to ROI2 ([1.54 ± 0.34] kPa). Figure 1(**C**) shows that peptides from the alpha-1 chain of collagen type XI and V were identified. The relative intensities for collagen type XI are higher in ROI2 compared to ROI1, while collagen type V was found in higher intensities in ROI1 compared to ROI2. Correlating results from microindentation to MALDI-MSI shows that regions with a higher abundance of collagen type V show a higher stiffness in comparison to regions with a higher abundance of collagen type XI.
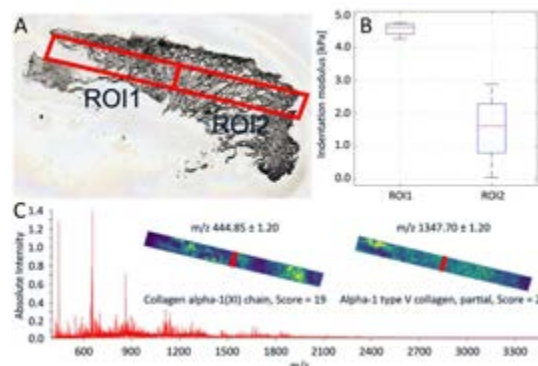
*Figure 1: (**A**) Medial meniscus sample and regions of interest (ROI1, ROI2). (**B**) Indentation modulus calculated from force-indentation curves in ROI1 and 2. ROI1 shows a higher indentation modulus as ROI2. (**C**) Tentative assignment of protein identification for peptides detected in resulting spectra from the enzymatic digestion. Peaks are found for collagens.*

Discussion

In this work, we identified collagens in degenerated menisci by MALD-MSI, while also gathering biomechanical information under physiological conditions by employing AFM from human menisci samples. In our proof-of-concept study different collagen types (i.e. V and XI) were detected at different abundance levels over the tissue sections and these distributions correlated with anatomical regions of the meniscus (white-white, red-white and red-red zone). Through the introduced correlated imaging approaches, we aim to better understand the influence of the meniscus' biochemical composition on biomechanical behaviors under physiological conditions.

References

1. Howell R. et al, World J Orthop., 5:597-602, 2014
2. Folkesson E. et al, BMC Musculoskelet Disord., 19:1-10, 2018
3. Kain L. et al., JMBBM 85:225-236, 2018

Acknowledgements

COMBINING EXPERIMENTAL AND NUMERICAL APPROACHES TO ASSESS THE TANGENTIAL DEBONDING OF COIN-SHAPED IMPLANTS

Yoann Hériveaux (1), Sophie Le Cann (2), Katharina Immel (2,3), Elsa Vennat (1), Vu-Hieu Nguyen (4), Roger A. Sauer (3,5,6) and Guillaume Haïat (2)

1. Université Paris-Saclay, CentraleSupélec, ENS Paris-Saclay, CNRS, LMPS, France ; 2. CNRS, MSME UMR 8208 France ; 3. AICES, RWTH Aachen University, Germany ; 4. Université Paris-Est Créteil, MSME UMR 8208, France ; 5. Faculty of Civil and Environmental Engineering, Gdansk University of Technology, Poland ; 6. Dept. of Mechanical Engineering, Indian Institute of Technology Guwahati, Assam, India.

Introduction

While cementless implants are now widely used clinically, surgical failures still occur and are difficult to anticipate. Assessing the biomechanical strength of the bone–implant interface (BII) may improve the understanding of osseointegration processes and help to prevent failures [1]. The aim of this study is to combine experimental and numerical approaches to investigate the behavior of a BII submitted to torsional loading.

Methods

Specimens. Four standardized 3D-printed coin-shaped implants (TiAl6V4, Ø5mm, H3mm) with an arithmetic average roughness $Ra = 20.8\mu m$ were osseointegrated for 15 weeks in the cortical bone of sheep tarsi.

Torsion tests. A mode III cleavage test was performed on each specimen (Fig. 1a) using a dedicated device (Fig. 1b), similarly as in [2]. The implant was fixed on the device by a wrench screwed to a torque sensor and the bone rotated at 0.03°/s until complete debonding, while recording the normal force and the torque.

Numerical modelling. The torque variation during such tests was simulated using a finite element model previously developed by our group [3]. To describe the adhesion and debonding phenomena, a modified Coulomb's law was introduced, using a varying friction coefficient to represent the transition from an unbroken to a broken BII. All parameters, including the bone Young's modulus and the normal force, were optimized to minimize the difference between experimental and numerical torques; except for the force, directly set based on experimental measurements.
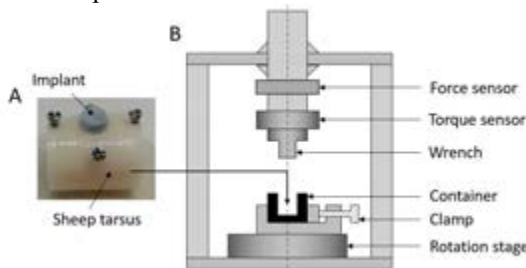
Figure 1: Typical bone-implant specimen (A); Schematic representation of the torsion test device (B).

Results

Experimentally, the torque first increases almost linearly with the twisting angle, then reaches a maximum around 1° (0.48-0.72N.m), and finally decreases to reach a constant value (Fig. 2). The normal compressive force increases from around 10-15N to 30-40N during the debonding, before stabilizing around the same angle as the torque. A good agreement was obtained between numerical and experimental torques, with mean numerical friction coefficients of 8.9 for the unbroken state, and of 1.2 for the broken state.
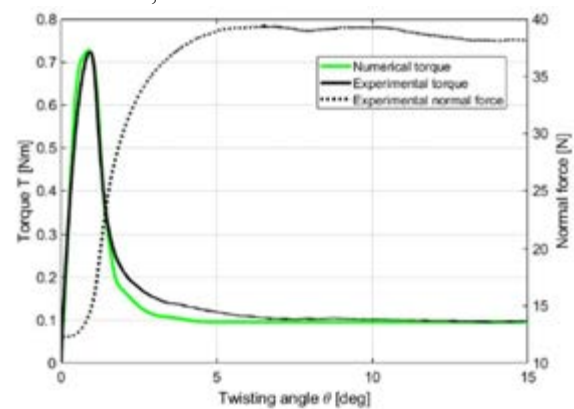
Figure 2: Evolution of the experimental torque and normal force and of the numerical torque as a function of the twisting angle for a typical specimen.

Discussion

The higher values of the maximal torques obtained herein compared to previous tests [2] may be explained by the higher roughness of the implants. Moreover, the significant increase of the normal force during the test and the high numerical friction coefficients suggest the presence of bone debris at the interface, which may be generated by the progressive debonding of the BII. Future studies should consider different BII configurations (*e.g.* implant roughness, healing time) to better understand their influence on the implant osseointegration.

References

1. Mathieu et al, J Biomech 47(1):3–13, 2014.
2. Mathieu et al, J Mech Behav Biomed Mater, 8:194, 2012.
3. Immel et al, Biomech Model Mechanobiol, 19:1091-1108, 2020

Acknowledgements

PERMEABILITY TEST BENCH FOR CHARACTERIZING HARD AND SOFT SCAFFOLDS FOR TISSUE ENGINEERING APPLICATIONS

Beatrice Masante (1,2), Stefano Gabetti (1,2), Chiara Massini (1), Riccardo Tassi (1), Federico Mochi (3), Costantino Del Gaudio (3), Alessandro Schiavi (4), Diana Massai (1,2)

1. Polito^{BIO}Med Lab, Department of Mechanical and Aerospace Engineering, Politecnico di Torino, Italy;
2. Interuniversity Center for the Promotion of the 3Rs Principles in Teaching and Research, Italy; 3. Hypatia Research Consortium, Rome, Italy; 4. INRiM-National Institute of Metrological Research, Turin, Italy

Introduction

Tissue engineering (TE) strategies are based on the active interplay among cells, three-dimensional (3D) scaffolds, and physiological signals in view of developing *in vitro* functional tissue substitutes [1]. Scaffold effectiveness is strongly influenced by its microstructure and ability to be permeated by fluids and species (i.e., the scaffold permeability). Permeability depends on the combination of porosity, pore size, tortuosity, and interconnectivity and its characterization is crucial for an effective evaluation of the overall scaffold performance [2,3]. Several methods were proposed to characterize the permeability of hard and soft scaffolds, however defined protocols are still missing. Moreover, soft scaffolds pose challenging tasks due to their deformability. Inspired by this context, we developed a versatile permeability test bench for characterizing hard and soft scaffolds, and we compared its performance with a reference test bench, previously validated for the measurement of hard scaffolds [4].

Methods

The proposed permeability test bench (PTB) is based on the pump method [2]. The main component is the permeability chamber (PC), consisting of two parts coupled by screws and an internal cylindrical geometry with interchangeable silicone gaskets and a grid for housing hard or soft cylindrical samples (height = 1-14 mm, diameter = 8-27 mm). The PC is part of a closed-loop hydraulic circuit, composed of a reservoir, a peristaltic pump (Masterflex), silicone tubing, two pressure sensors (HJK) upstream and downstream the PC, and 3-way stopcocks. The sensor signals are acquired by a DAQ (National Instruments), which is controlled by a computer running a purpose-built LabView interface (Fig. 1A). Demineralized water (dynamic viscosity $\mu = 1$ mPa·s) is used as test fluid. Upon imposing a defined flow rate (guaranteeing laminar flow), permeability (k) is measured by using the Darcy flow transport model [5]:

$$\Delta P/L = \mu/k \cdot (Q/A) \qquad (1)$$

where ΔP is the pressure drop across the sample, L is the thickness of the sample, Q is the flow rate, and A is the area of the sample cross-section.

Tests are performed without and with the sample, and the pressure drop due to the sample is then obtained as:

$$\Delta P_{sample} = \Delta P_{full} - \Delta P_{empty} \qquad (2)$$

For a preliminary validation of the PTB, a commercial cylindrical hard scaffold (diameter = 10.3 mm, height = 3.3 mm, SmartBone IBI S.A, Fig. 1B) was tested at 5 mL/min for 4 independent repetitions, then the mean permeability value was calculated and compared with the results from a reference test bench (RTB) [4].

Results

Preliminary tests demonstrated that the PC design allows holding effectively the sample, preventing deformations and ensuring watertightness. The permeability values of the scaffold tested within the PTB and the RTB resulted to be $2.9 \cdot 10^{-10} \pm 2.2 \cdot 10^{-10}$ m^2 and $1.1 \cdot 10^{-10} \pm 1.6 \cdot 10^{-11}$ m^2, respectively (Fig. 1C). The normalized error between the measured values was 0.809.
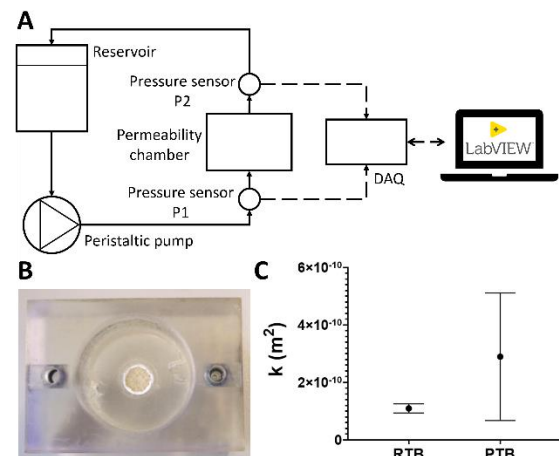
Figure 1: A) Schematic drawing of the PTB; B) Picture of the PC housing the scaffold; C) Permeability test results.

Discussion

A versatile test bench for characterizing the permeability of hard and soft scaffolds under Darcy flow regime has been developed. Preliminary validation tests, performed on a hard scaffold, showed that the permeability values obtained using the PTB and RTB setups were compatible, although the PTB measurements were affected by a higher dispersion. For reducing measurement uncertainty, the optimization of the PTB data acquisition system is in process, and in parallel tests varying the imposed flow rates and using different hard and soft scaffolds are ongoing.

References

1. Amini et al., *Crit Rev Biomed Eng* 40, 363–408, 2012
2. Pennella et al., Ann. Biomed. Eng., 41:2027-2041, 2013.
3. Santos et al., J. Mech. Behav. Biomec. Mater., 110: 103932, 2020
4. Schiavi et al., Meas. Sci. Technol., 23:105702, 2012.
5. Bear, J. Dynamics of Fluids in Porous Media. New York: Dover, 1972.

PRIMARY STABILITY OF A PRESS-FIT CUP COMBINED WITH IMPACTION GRAFTING IN AN ACETABULAR DEFECT MODEL

Ronja A. Schierjott (1), Georg Hettich (1), Marc Baxmann (1), Federico Morosato (2), Luca Cristofolini (2), Thomas M. Grupp (1,3)

1. Aesculap AG, GER; 2. Università di Bologna, IT; 3. Ludwig-Maximilians-University Munich, GER

Introduction

In total hip arthroplasty, the main reason for revision is aseptic loosening [1]. Among others, it can be caused by insufficient primary stability, i.e. excessive relative motion at the bone-implant-interface. Revision surgery is often associated with acetabular bone defects. One possible treatment option is impaction bone grafting (IBG), i.e. a defect filling with compacted cancellous bone chips. However, these have some disadvantages, such as limited supply and remaining infection risk.

Synthetic bone graft substitutes may represent an attractive alternative. The objectives of this study were to (1) assess primary of a press-fit cup in combination with compacted bone chips (gold standard) in an especially therefore developed reproducible surrogate model and to (2) compare it to the primary stability achieved by two different bone graft substitutes.

Materials and methods

A previously developed acetabular test model made of polyurethane foam with a mainly medial defect [2] was used. The defect was filled with either cancellous bone chips (bone chips), bioactive glass granules in a polyethylene glycol-glycerol matrix (b.a.glass+PEG), or β-tricalciumphosphate tetrapods in a collagen matrix (tetrapods+coll) and combined with a press-fit cup (Figure 1).

Figure 1: The three test groups bone chips, b.a.glass+PEG and tetrapods+coll in previously developed defect model and exemplary specimen with press-fit cup and tracking points for optical relative motion analysis, dynamically loaded by a servo-hydraulic testing machine.

Specimens (N=6 in each test group) were loaded in a sinusoidal wave form in direction of the maximum resultant force during level walking, whereby the maximum load was increased stepwise from 600 N to 3000 N. Relative motions (inducible displacement and migration) between cup and acetabular defect model were assessed with the optical measurement system GOM Pontos (GOM GmbH Braunschweig, Germany).

Results

Relative motions increased with increasing loads (Figure 2). At the last load step, inducible displacement was highest for *bone chips* (113 ± 3 µm) and lowest for *b.a.glass+PEG* (91 ± 3 µm), whereas migration was highest for *b.a.glass+PEG* (881 ± 95 µm) and lowest for *tetrapods+coll* (494 ± 12 µm). Difference among the test groups was statistically significant (p<0.05).
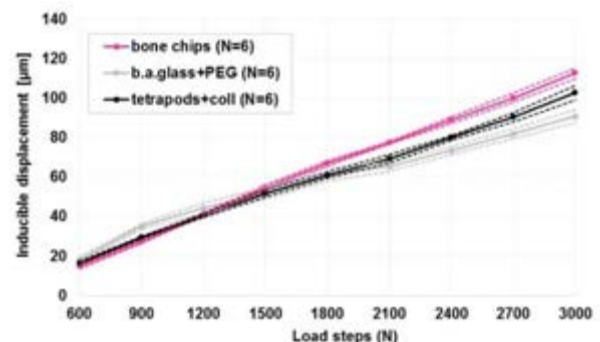
Figure 2: Mean ($\pm$ SD) inducible displacement in the three test groups.

Discussion and conclusion

A comparable behavior of *bone chips* and *tetrapods+coll* was observed, which suggests that this material might be an attractive alternative to the gold standard bone chips. However, primary stability was so far assessed in one specific defect and should be further investigated in additional defect types and complemented by osseointegration analysis.

References

1. Sadoghi et al., The J of Arthroplasty, 28:1329-1332, 2013
2. Schierjott et al., J Orthop Res, 38:1769-17781-10, 2020

Acknowledgements

MINERAL CONTENT AND BIOMECHANICAL PROPERTIES OF FIBROLAMELLAR BONE

Astrid Cantamessa (1), Pauline Muraro (1), Yann Delaunois (1), Philippe Compère (1), Stéphane Blouin (2), Markus A Hartmann (2), Davide Ruffoni (1)

1. University of Liège, Belgium; 2. Ludwig Boltzmann Institute of Osteology, Vienna, Austria.

Introduction

Fibrolamellar bone is a peculiar type of bone found in the long bones of young large mammals, which combines the conflicting requirements of a fast growth with high stiffness and strength, as required to withstand the weight of such large animals [1]. Fast growth is achieved by depositing a primary hypercalcified layer (PHL) of disordered bone, located in between two blood vessels. This central layer acts as a scaffold to direct the formation of parallel-fibered bone (PFB), having mineralized collagen fibers well oriented along the longitudinal direction of the bone. When reaching the blood vessels, PFB is then replaced by lamellar bone (LB), which features a few alternating bone lamellae with collagen fibers oriented in different directions. A so-called fibrolamellar bone unit (FBU) comprises these three different types of bone. Although the microstructure of fibrolamellar bone is known [1], the corresponding biomechanical properties are not well characterized. Specifically, there is no information about the local mechanical behavior of each basic building block. Yet, this tissue is of clinical relevance given the similarity between its deposition and callus formation in bone healing. Here, the correlation between local mechanical properties and mineral content of fibrolamellar bone is investigated by combining standard nanoindentation (nIND), nanoscale modulus mapping (nanoMM) and backscattered electron imaging (BEI), including quantitative analysis (qBEI).
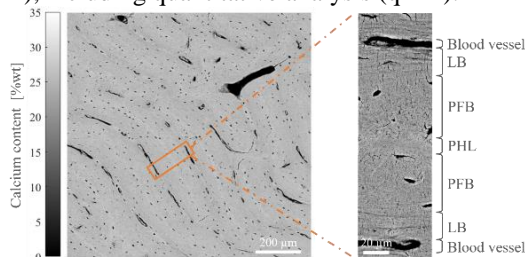
Fig. 1: 2D map of mineral content along with a higher magnification backscattered electron image of a FBU.

Methods

Samples from two femurs of calves were harvested and prepared, considering both longitudinal and transverse sections. A combination of qBEI (1.8 µm pixel size) and BEI at higher magnification (57 nm pixel size) was used to quantify mineral content and highlight nanostructural features. Mechanical properties were measured across FBU using nIND (Berkovitch tip, 6 µm spacing between indents, 3000 µN) and nanoMM. The latter is based on applying a small static force (1 µN) to ensure elastic contact between tip and sample surface; a periodic modulation force (0.6 µN, 275 Hz) is then added to probe local storage modulus without plastically deforming the sample. In the present setting, this approach has a lateral resolution of about 80 nm [2].

Results

Quantitative analysis (Fig. 1) revealed a homogeneous mineral composition across the FBU with the exception of the PHL, which appeared more mineralized. In LB, brighter lamellae can be distinguished from darker ones with high resolution BEI, this contrast being due to different fiber orientation. Indentation modulus profiles highlighted stiffer bone within PFB and lower values within the PHL (Fig. 2). Higher resolution is needed to characterize submicron mechanical behavior within LB. NanoMM showed alternating storage moduli: thicker (2.56±0.24 µm), brighter lamellae are more than 1.5 times stiffer than thinner (2.03±0.43 µm), darker ones. As they have approximately the same mineral content, this difference can probably be explained by the different collagen orientation in neighboring lamellae.
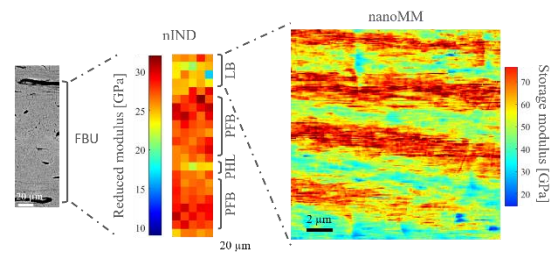
Fig.2: Mechanical properties across a FBU using nIND and nanoMM.

Discussion

We characterized the mechanical heterogeneity of fibrolamellar bone and showed that the PHL, being deposited very fast, has lower stiffness although having a higher mineral content compared to LB and PFB, therefore highlighting the critical role of collagen organization. The weak region is then reinforced by high stiffness PFB. High resolution nanoMM provided sub-micrometer biomechanical information which is not accessible with traditional nanoindentation. Yet, these data are relevant to reach a comprehensive understanding of the structure-function relationship of bone. Indeed, LB shows lamellae with a strong elastic contrast (higher than previously reported in osteonal bone) which may be needed to hamper crack propagation in the presence of only a few lamellae.

References

1. Almany Magal et al, J Struct Biol, 186:253-264, 2014.
2. Zlotnikov et al, Prog Mater Sci, 87:292-320, 2017.

OPTIMISING METHODS OF MODELLING OSTEOCHONDRAL GRAFTS IN HUMAN TIBIOFEMORAL JOINTS

Gavin A Day, Alison C Jones, Marlène Mengoni, Ruth K Wilcox
Institute of Medical and Biological Engineering, University of Leeds, UK

Introduction

Articular cartilage defects in the knee affect a considerable proportion of the population and range from single focal defects to larger areas of diseased hyaline cartilage. Defects arise from a precipitating trauma or osteoarthritis, cause localised knee pain, motion deficits, and lead to further degenerative changes. Autologous osteochondral grafting has demonstrated positive outcomes by replacing the damaged region of cartilage with a graft consisting of a cylinder of bone with a layer of cartilage taken from a non-loadbearing region of the knee [1]. However, the factors that affect the short-term stability of the grafts remain largely unknown with some evidence of graft subsidence or poor integration. The aim of this study was to develop computational models of the tibiofemoral joint to enable the parameters affecting osteochondral graft stability to be analysed. The objectives were to experimentally calibrate the bone material properties and graft-bone coefficients of friction (COF) and then to independently validate the model contact mechanics under different graft conditions.

Methods

Elementwise material properties of the bone were used throughout the study. These were calibrated using six cadaveric human femoral condyles. They were experimentally tested and models were built from μCT scan data. An optimisation of μCT scan voxel brightness to Young's modulus of the elements was carried out, utilising the experimental and computational stiffness.

Twelve push-out tests were carried out on two cadaveric human femurs. The COF values in corresponding FE (Finite Element) models was calibrated to match the experiment.

Changes to the contact pressure shape and area were identified through in vitro tests on a single cadaveric human tibiofemoral joint which was experimentally tested using a materials testing machine and a knee specific loading rig [2]. Six defects were created in the femoral condyles which were subsequently treated with osteochondral autografts or metal pins. Contact pressure measurements were made using a flexible sensor. Loads were applied at three time points: intact, post-defect creation and post-repair. μCT scans were taken prior to each of these loads. Specimen specific FE models were created from the scan data registered together. Calibrated frictional and material properties from the prior tests were used. Graft oversizing and experimental press-fit was mimicked in the simulation. Boundary conditions and loading conditions matched the experimental setup. Pressure maps for the tibial cartilage layers, mean pressure values and contact area, were measured and compared to the experimental data.

Results

Material property optimisation for the bone was successfully achieved and applied. Frictional value optimisation was also achieved, (CCC=0.91, Fig. 1, C). The tibiofemoral joint experiment provided a range of cases to model. These cases were well captured in the resultant pressure maps and were well represented in the FE models. Cartilage defects were measurable in the experimental pressure data with good agreement in the FE model pressure maps (Fig. 1, D).
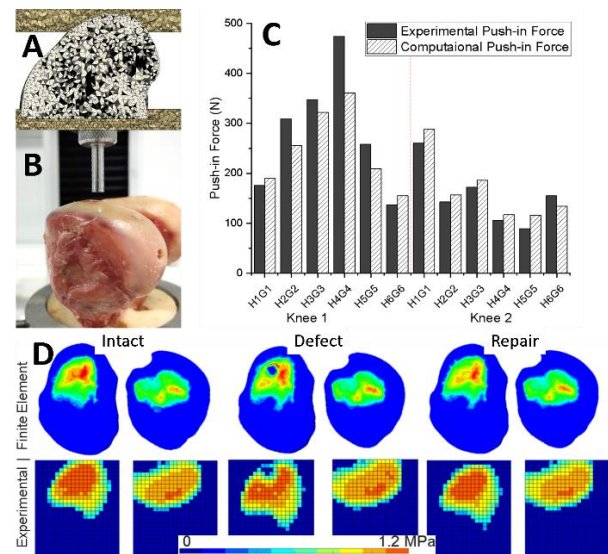
Figure 1: A, FE material property calibration. B, Experimental graft push-in testing. C, Experimental to computational push-in test results. D, FE and experimental contact pressure distributions for intact, defect and repair cases.

Discussion

The extensive validation and calibration testing of the FE models (validation of contact pressure maps, material property calibration, graft push-in tests) has given substantial confidence to the model. Experimentally, the graft depth varied, this positioning and alignment was well replicated in FE and evidenced by good agreement between the in vitro and model contact pressure maps. An extensible method of creating osteochondral graft models within tibiofemoral joints has been developed and is now being used to investigate a wide range of grafting and procedural parameters.

References

1. Pareek et al. 2016. Arthroscopy
2. Cooper et al. 2020 J Mech Behav Biomed

Acknowledgements

DEGREE OF MINERALIZATION AND MINERALIZED COLLAGEN FIBRE ORIENTATION PREDICTS THE ELASTIC MODULUS OF BONE IN OSTEOGENESIS IMPERFECTA

Michael Indermaur (1), Tatiana Kochetkova (2), Daniele Casari (1,2), Bettina Willie (3), Johann Michler (2), Jakob Schwiedrzik (2), Philippe Zysset (1)

1. ARTORG Center for Biomedical Engineering Research, University of Bern, Switzerland;
2. Swiss Federal Laboratories for Material Science and Technology, Thun, Switzerland,
3. Shriners Hospital for Children, McGill University, Montreal, Canada

Introduction

Osteogenesis Imperfecta (OI) known as "brittle bone disease" is a collective term of hereditary, collagen-related bone diseases leading to an increased bone fragility at the organ level. At the lamellar level, OI bone reveals higher degree of bone mineralization (*DBM*), indentation modulus, and compressive strength [1]. In addition, modulus and strength are highly dependent on *DMB* for both healthy and OI bone [1]. However, elastic modulus of healthy human bone is as well dependent on the orientation of the mineral collagen fibers (*MCFs*) [2]. We hypothesized that the elastic modulus of OI bone can be predicted using the information of *DBM* and *MCFs* orientation, using quantitative polarized Raman spectroscopy (qPRS) [3] and nanoindentation.

Materials and Method

Three trans-iliac, human bone biopsies of healthy control (n=1), OI type I (n=1) and OI type III (n=1) were used to perform qPRS measurements and site-matched nanoindentation in osteonal bone (Figure 1). At each position of a qPRS measurement, 12 Raman spectra were collected with an increasing polarization angle of 15° to assess the *DBM* and the out-of-plane angle of the *MCFs* (θ_{MCF}) [3]. Per each osteon, seven Raman measurements were taken with a 3 μm distance in between, resulting in a line-scan of 18 μm. Using the seven measurements, a mean θ_{MCF} and *DBM* per osteon were computed. In total, 23 osteons were analyzed (healthy n=8, OI type I n=7, OI type III n=8).
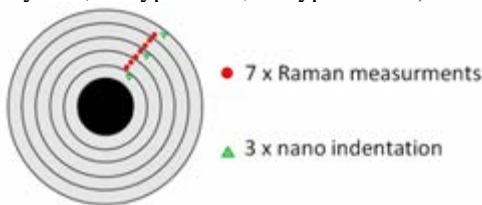
Figure 1: Schematic overview of one osteon with the Raman line scan (red) and the three nanoindentations (green).

In the same osteon, three nanoindentation measurements were taken and indentation moduli (E_{ind}) were extracted and averaged. Finally, a model (eq. 1) was developed to predict the E_{ind} according to the θ_{MCF} and the *DMB*.

$$E_{ind} = \alpha DBM + \beta E_0(\theta_{MCF}) + \epsilon \qquad (1)$$

With $E_0(\theta_{MCF})$ being the indentation modulus computed from the transverse isotropic stiffness tensor with the parameters reported in [2].

Results

The *DBM* and E_{ind} are higher in OI bone compared to healthy bone. Higher θ_{MCF} variation was observed within the osteons of healthy bone (Table 1).

Param.	Healthy	OI type I	OI type III
DBM [−]	2.6 ±0.6	3.1 ±0.3	3.2 ±0.2
θ_{MCF} [°]	39.4 ±14.3	30.2 ±6.3	41.8 ±5.4
E_{ind} [GPa]	15.6 ±2.0	22.6 ±1.4	19.9 ±0.6

Table 1: Mean and standard deviation of the indentation modulus (E_ind), degree of mineralization (DBM) and out-of-plane angle (θ_{MCF}).

Both *DBM* (p = 5.23e-06) and θ_{MCF} (p= 2.13e-05) have a significant influence and can be used to predict the indentation modulus E_{ind} (Figure 2).
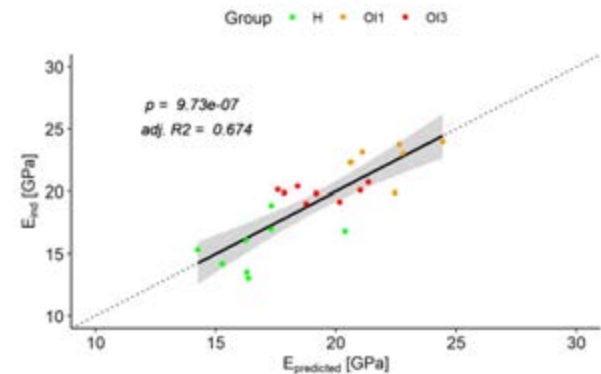
Figure 2: Indentation modulus vs. predicted modulus computed from the Raman measurements.

Discussion

The result of this study showed that the indentation modulus of the healthy control and two different OI types is driven by *DMB* [1] and the orientation of the *MFCs* [2]. Combining the two parameters, the indentation modulus can be predicted with a surprisingly high level of significance and seems independent of OI status. However, the number of osteons and biopsies should be increased to confirm a universal model.

References

1. Indermaur et al. JBMR, 36:1364-1375, 2021.
2. Dall'Ara et al. JMBBM, 25:23-32, 2013.
3. Kochetkova et al. Acta Biomat., 119:390-404, 2021.

Acknowledgements

THERMAL ACTIVATION ANALYSIS OF HYDRATED LAMELLAR OVINE BONE

Cinzia Peruzzi (1), Tatiana Kochetkova (1), Stefan Remund (2), Beat Neuenschwander (2), Johann Michler (1), Jakob Schwiedrzik (1)

1. *Laboratory for Mechanics of Materials and Nanostructures, Empa, Switzerland; 2. Institute for Applied Laser, Photonics and Surface technologies (ALPS), Bern University of Applied Sciences, Switzerland;*

Introduction

Bone, a hierarchically structured composite material, is mainly composed of collagen molecules, calcium phosphate minerals and water. In cortical bone mineralized collagen fibrils are embedded into an extrafibrillar matrix and form 3 to 7 µm thick lamellae that are wrapped around blood vessels forming osteons with a diameter of up to 200 µm. In mammals, bones are subjected to a body temperature of around 37°C[1] as well as mechanical loading at different strain rates, such as during walking (0.005- 0.08 s^{-1}), sprinting (0.05 s^{-1}) and accidental falls (25 s^{-1})[2]. In this study, we investigate the temperature and rate-dependent mechanical behavior of ovine bone micropillars at the length scale of a few lamellae. We tested at four temperatures (24°C, 37°C, 50°C and- 60°C), four strain rates (0.1s^{-1}, 1s^{-1}, 10s^{-1} and 100s^{-1}) and two orientations (along and perpendicular to the main osteon direction).

Methods

Micropillars were manufactured with a femto-second pulsed laser (SATSUMA HPII, Amplitudes Systemes) on eight samples from one ovine tibia. Four samples were oriented parallel (axial) and four perpendicular (transverse) to the main osteon direction. On every sample a total of 70 micropillars were fabricated with a diameter of 22.7+/-0.1 µm and a height of 71.5+/-7.5 µm. To validate the orientation polarized Raman spectrae were taken on every micropillar (NT-MDT, NTEGRA Spectra, Russia)[3]. Compression experiments were performed on 256 micropillars under ambient pressure and with a relative humidity greater than 90% at four strain rates (0.1, 1, 10, and 100 s^{-1}) and four temperatures (24, 37, 50 and 60°C). High resolution scanning electron microscope (HRSEM, Hitachi S-4800, Japan) imaging was conducted on all micropillars before and after compression. The data was then analyzed with a custom Matlab script (R2018a, MathWorks, USA) to determine the activation volume and the thermal activation energy.

Results

The yield stress increases with increasing strain rate for all temperatures and both orientations (Figure 1). The yield stress for the axial orientation is higher than the yield stress for the transverse orientation for all the strain rates and temperatures. The activation volume and the activation energy for the axial and the transverse orientation are v_{ax} = 0.2+/-0.03 nm^3 and v_{tr} = 0.5+/-0.07
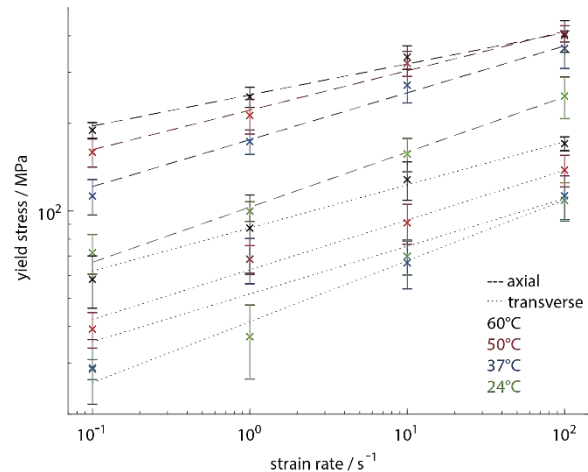
Figure 1: Yield stress extracted from micropillars with axial and transverse orientation compressed at different strain rates and temperatures.

nm^3 and Q_{ax} = 105.6 kJ/mol and Q_{tr} = 85.7 kJ/mol respectively.

Post compression HRSEM images show that axial and transverse micropillars are deformed perpendiculary to the mineralized collagen fibril axis. Axial micropillars fan outwards circularly at the top of the micropillar, transverse micropillars fold out at the two sides of the micropillar perpendicular to the mineralized collaged fibril orientation.

Discussion

In this study temperature and the strain rate dependent yield properties of lamellar bone were measured under hydrated conditions to perform a thermal activation analysis. The experiments were performed at four strain rates (0.1-100 s^{-1}) and four temperatures (24- 60°C). The activation volume and energy are similar to values reported previously for other species and different length scales and are associated to the breaking of bonds in the extrafibrillar matrix between mineralized collagen fibrils [4]. The post compression HRSEM images support the assumption that the deformation is due to interface failure between fibrils.

References

1. PR Morrison and FA Ryser, Science, 1952
2. D.R. Carter et al., Science, 1976.
3. T. Kochetkova, C. Peruzzi, O. Braun et al., Acta Biomaterialia, 2020.
4. H.S. Gupta et al, J. R. Soc. Interface, 2007

Acknowledgements

COLD-WATER CORALS RETAIN OUTSTANDING TISSUE STRENGTH BUT LOSE TISSUE STIFFNESS IN ACIDIFIED WATERS

Uwe Wolfram (1) Marta Peña Fernández (1) Samuel McPhee (1) Ewan Smith (1) Rainer J. Beck (1)
Jonathan D. Shephard (1) J Murray Roberts (2) Sebastian Hennige (2)

1. School of Engineering and Physical Sciences, Institute of Mechanical, Process and Energy Engineering, Heriot-Watt University, Edinburgh, United Kingdom; 2. Changing Oceans Research Group, School of Geo-Sciences, University of Edinburgh, Edinburgh, United Kingdom

Introduction

Ocean acidification is a threat to cold-water corals (CWC) and could lead to dramatic and rapid loss of the reef framework habitat they build. Weakening of structurally critical parts of the coral reef framework can lead to physical habitat collapse on an ecosystem scale, reducing the potential for biodiversity support [1]. The mechanism underpinning crumbling and collapse of CWCs can be described by mathematical and computational models that integrate experimental results. To use computational models to support future conservation and management of these vulnerable marine ecosystems, however, strength parameters at key length scales of the material architecture are currently missing. Therefore, this study aims at identifying CWC skeletal tissue strength exposed to acidified and non-acidified waters.

Material and Methods

Coral samples examined here were from acidified waters in the California Sea bight with an aragonite concentration of $\Omega_{Arag} = [0.71, 1.04]$ and from non-acidified waters in Scotland with $\Omega_{Arag} = [1.67, 2.62]$ [1,2]. After drying, we fabricated $m = 144$ micropillars on $n = 12$ CWC specimens using an ultrashort pulsed laser machining workstation based on a Carbide laser (Light Conversion) with a laser wavelength of $\lambda = 1028$ nm, a pulse length of 6 ps, a repetition rate of 2 kHz and a pulse energy of 10.3 µJ (Figure 1). The ablation process can be considered 'cold' and does not harm the sample [3].
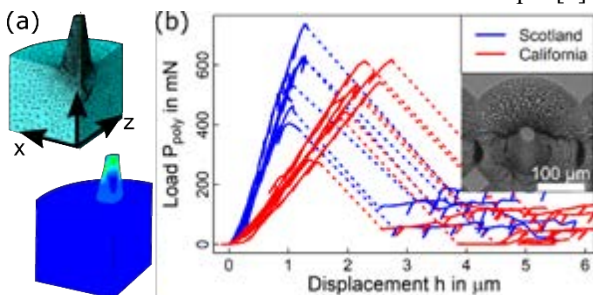
Figure 1: (a) µFE mesh used to interpret micropillar compression tests with qualitative von Mises stress. (b) representative responses for non-acidified (blue) and acidified (red) waters. SEM inlay shows a micropillar.

Micropillars were compressed uniaxially at a rate of 0.05 µm/s to a displacement of 10.25 µm. The probe was retracted 0.25 µm for every 0.75 µm to allow evaluation of potential damage. Load and displacement were recorded simultaneously at 30 Hz.

As laser ablation alone results in tapered micropillars (Figure 1), we utilised a micromechanical elasto-visco-plastic material model implemented as a UMAT in Abaqus (v6.16) [2] to interpret micropillar compression tests (Figure 1). Briefly, the skeletal wall was modelled as a polycrystalline material with randomly oriented aragonite needles using a self-consistent scheme. We used a Mohr-Coulomb criterion to model strength of the aragonite crystal interface and a Drucker-Prager criterion to model strength of the polycrystal. A micropillar was modelled using quadratic elements and loaded like the micropillar experiments. CWC stiffness compared well to experimental results [2]. The µFE models were used to identify the aragonite crystal interface strengths as well as the strength of the polycrystal.

Results

Micropillars featured surface and base diameters of 28.96 µm (27.76-30.51 µm) and 86.5 µm (81.52-90.21 µm), a taper angle of 15.02° (12.16-18.19°), and a height of 110.77 µm (90.20-129.44 µm). Ultimate force of the pillars was not significantly different between acidic and non-acidic environments, but pillar stiffness was (Table 1). Using the *in silico* micropillar compression we identified tensile and shear strengths of the aragonite crystal interface of $\sigma_{int}^{ut} = 294.5$ MPa and $\sigma_{int}^{sh} = 130.2$ MPa and tensile and compressive strengths of the polycrystal of $\sigma_{poly}^{ut} = 177.5$ MPa and $\sigma_{poly}^{uc} = 462.3$ MPa.

Envir.	Acidic	Non-Acidic	p
F_{pillar}^{ult}	516.40 mN	517.86 mN	$\rightarrow 1$
K_{pillar}	633.41 mN/µm	401.98 mN/µm	$\rightarrow 0$

Table 1: Ultimate force F_{pillar}^{ult} and pillar stiffness K_{pillar} from micropillar compression tests.

Discussion

Results indicate that CWCs are 10 times stronger than concrete and twice as strong as nacre [4, 5]. Our results contradict the perception that mineralised CWC skeletons will generally weaken due to climate change. In fact, CWCs seem to retain their strength despite a loss of stiffness, and the threat to the ecosystem comes rather from a loss of material from acidification-induced increases in internal porosity and dissolution.

References

1. Hennige et al. Front Marine Sci 7, 1-16, 2020
2. Wolfram et al. Sci Rep, in review (see arXiv:2110.01701)
3. McPhee et al. Sci Rep 11, 11007, 2021
4. Königsberger et al. Cem Concr Res 103, 77, 2018
5. Barthelat et al. J Mech & Phys Solids 2007, 55(2), 306

Acknowledgements

HIP FRACTURE RISK PREDICTION BASED ON STATISTICAL MODELS INFORMED BY DXA IMAGES

Alessandra Aldieri (1,2), Federica Pagotto (5), Pinaki Bhattacharya (3), Margaret Paggiosi (4), Richard Eastell (4), Cristina Bignardi (5), Alberto L. Audenino (5), Mara Terzini (5)

1. Department of Industrial Engineering, Alma Mater Studiorum - University of Bologna, Italy; 2. Medical Technology Lab, IRCCS Istituto Ortopedico Rizzoli, Bologna, Italy; 3. Department of Mechanical Engineering and INSIGNEO Institute for in silico Medicine, University of Sheffield, UK; 4. Department of Oncology and Metabolism University of Sheffield, UK; 5. PolitoBIOMed Lab, Department of Mechanical and Aerospace Engineering, Politecnico di Torino, Torino, Italy.

Introduction

The rates of osteoporotic hip fracture incidence worldwide will increase in the future, with major economic and social impacts [1]. Considering the adverse impact of hip fracture on patients' lives, the identification of subjects at high risk is pivotal, since it is the gateway to fracture prevention. The areal bone mineral density (aBMD), measured by Dual energy X-ray Absorptiometry (DXA) is currently used in the diagnosis of osteoporosis and as an indication for treatment. The sensitivity and specificity of this test is between 55% and 75%, respectively [2]. We have recently reported the ability of a statistical shape and intensity modelling approach informed by QCT images to predict hip fracture in a British postmenopausal cohort [3]. Nevertheless, QCT is not routinely performed in a clinical setting. Therefore, in this study the performance of an analogous approach informed by DXA images is assessed on the same cohort, focusing preliminary only on shape.

Methods

A retrospective British postmenopausal women cohort of 2D DXA-based proximal femurs was investigated building up Partial Least Square (PLS)-based statistical models. The cohort comprised 49 fracture and 49 control subjects, pair-matched for age, body weight and height [3]. In detail, a Statistical Shape Model (SSM) was built. Its construction relied on *Deformetrica* [4] which, based on the femur geometries segmented from the DXA images, allowed to identify the template, i.e. the mean anatomical shape, and the deformation functions, gathering the subject-specific shape patterns, which map the template to the subject-specific shapes. PLS allowed to identify the space (PLS modes) of maximal covariance between the patients' shape features and their known fracture status. By projecting the original shape features onto the PLS modes, the PLS components could be obtained. The statistical shape model was used to predict the subject-specific hip fracture status. A regression analysis based on the use of a logistic function was carried out between the PLS components, taken as independent predictors, and the fracture status, taken as binary dependent variable. More in detail, a 10-fold cross-validation procedure was adopted.

Results

A total of five shape modes could explain at least 90% of the total shape variance, compared to the 22 modes necessary to achieve an analogous outcome in the 3D case. The first three 2D shape modes, seen as deformations of the template shape, are depicted in Fig. 1 compared to the first three 3D shape modes. The predictive models with the first two, three, four and five 2D PLS components used as predictors resulted in AUC values all settled between 0.59 and 0.61. In the 3D case an AUC value of 0.64 was achieved employing the first two shape components. An AUC of 0.72 was obtained using the gold standard aBMD.
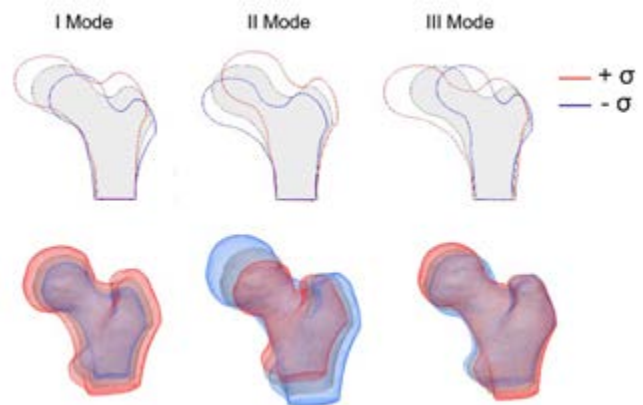
Figure 1: The first three 2D and 3D PLS shape modes, shown as deformation of the template (displayed in grey) along each mode between $\pm \sigma$, where σ^2 represents the mode variance.

Discussion

In this study, shape was not able to outperform aBMD in diagnostic accuracy. As expected, the 3D shape components achieved a better stratification accuracy. The stratification accuracy improvement due to the addition of local density information, which was significant in the 3D case, will be established soon. In this way, the possibility to fully take advantage of the information contained in a DXA image for the purpose of integrating the aBMD value for the hip fracture risk prediction will be better investigated.

References

1. Kanis et al, *Osteoporos Int*., 2019.
2. Kanis et al, *Lancet*, 2002.
3. Aldieri et al., ABME, 2022.
4. Durrleman et al, *Neuroimage*, 2014.

REPLICABILITY OF A FINITE ELEMENT MODEL TO QUANTIFY HUMAN FEMUR FAILURE LOAD

Marc Gardegaront (1, 2), Amelie Sas (3), François Bermond (2), Cyrille Confavreux (4), Jean-Baptiste Pialat (4), G. Harry van Lenthe (3), Hélène Follet (1), David Mitton (2)

1. Univ Lyon, Univ Claude Bernard Lyon 1, INSERM, LYOS UMR 1033, 69008 Lyon, France;
2. Univ Lyon, Univ Eiffel, Univ Claude Bernard Lyon 1, LBMC UMR_T9406, 69622 Lyon, France;
3. Biomechanics Section, Dept. Mechanical Engineering, KU Leuven, Leuven, Belgium;
4. Centre Hospitalier Lyon Sud, Hospices Civils de Lyon, Lyon, France

Introduction

Femur metastases may affect femur strength. Currently, the clinical gold standard for failure risk estimation is the Mirels' score [1]. However, as pointed out several times [2], this score does not allow enough reliability to make an accurate prediction. Recent studies suggest that finite element (FE) methods may provide better estimations when it comes to fracture risk assessment [3, 4]. To our knowledge, none of the currently available FE models were reproduced outside of their original laboratory, thus, none were tested for their replicability. Therefore, the aim of this study is to evaluate the replication of one of the most promising FE models from the literature [5].

Material and methods

Two ex-vivo femur datasets were used. The KU Leuven dataset (8 femurs with lesions), and the Lyon dataset (16 intact + 6 femurs with lesions). All femurs were scanned with a clinical CT-scanner following similar protocols and reconstructed with resolutions of 0.5x0.5x0.2 mm^3 (Leuven) & 0.7x0.7x1.2mm^3 (Lyon). Femurs underwent compressive tests to measure the failure load [6]. CT-scans were used to create a non-linear FE model [5].

Firstly, the reproducibility (*i.e.,* replication with the same dataset) of the model was tested. The FE analyses of the Leuven dataset were done by the original author of the model (Leuven operator) and an operator from Lyon, who transcribed the model from the original paper (same methodology but different tools). The results from both operators were then compared, which hints at the inter-operator and model transcription variabilities.

Secondly, the model was tested for replicability. The Lyon operator did the FE analysis on the Lyon samples. The resulting accuracy was compared with those of the same operator on the Leuven samples to assess the influence of the experimental dataset.

Results

With the Leuven dataset, the difference between simulated and experimental failure loads (cf. Fig. 1A) averages to 549 N (RMSE = 881 N, r^2 = 0.96) for the Leuven operator and 978 N (RMSE = 1118 N, r^2 = 0.98) for the Lyon operator. A high correlation was found between operators (slope = 1.08, r^2 = 0.95).

The accuracy of the model on the Lyon dataset (cf. Fig. 1B) averages to -978 N (RMSE = 1666 N, r^2 = 0.3) for

lesioned femurs and -3989 N (RMSE = 4487 N, r^2 = 0.67) for intact femurs. One of the FE analyses of the Lyon lesioned femurs did not converge; thus, the results are based on five femurs out of six.
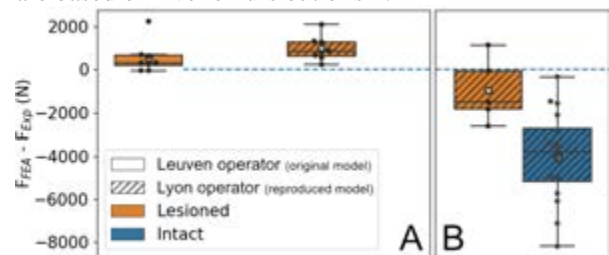
Figure 1: Accuracy of the FE analyses (Failure loads diff.: F$_{FEA}$ - F$_{Exp}$). (A) Leuven dataset. (B) Lyon dataset.

Discussion

When using the Leuven dataset, both operators displayed similar results. Differences could be explained by inter-operator variabilities induced by segmentation or orientation [7], and by different pre-processing algorithms and FE software used.

When applied to the Lyon dataset, the Lyon operator obtained an average accuracy 7 times worse than the original paper [5] on intact femurs, and 2 times worse on femurs with lesions. In addition to the aforementioned causes of variabilities, the lack of replicability questions the influence of the experimental setup, scan parameters, and possible divergences of physiologic femur characteristics between datasets. Overall, this replication study emphasizes the need to have clear and rigorous guidelines for bone FE models [8] and experiments, and assert the importance of model assessment on large datasets.

References

1. H. Mirels, *Clin. Orthop. Relat. Res.*, 249:256-264, 1989.
2. C. Confavreux *et al.*, *CSEA*, 13:5711, 2021.
3. F. Eggermont *et al.*, *Bone Joint Res*, 7:430-439, 2018.
4. A. Sas *et al.*, *Bone Reports*, 12:100286, 2020.
5. A. Sas *et al.*, *Bone Reports*, 12:100263, 2020.
6. A. Sas *et al.*, *J. Mech. Behav. Biomed.*, 104:103648, 2020.
7. A. Levillain *et al.*, *ESB 2021*, 2021
8. M. Viceconti *et al.*, *Methods*, 185:120-127, 2021.

Acknowledgements

THE INFLUENCE OF FORAMINA ON FEMORAL NECK FRACTURES AND STRAINS PREDICTED WITH FINITE ELEMENT ANALYSIS

Joeri Kok (1), Lorenzo Grassi (1), Hanna Isaksson (1)

1. Lund University, Sweden

Introduction

Hip fractures following a low-impact fall are common in the elderly. Finite element (FE) models of the proximal femur can improve the prediction of fracture risk over current clinical standards. Validation against bilateral digital image correlation (DIC) based strain measurements has shown that FE models may fail to accurately predict strains in regions with foramina [1]. It has been suggested that foramina in the femoral neck affect how failure of the femur initiates [2]. This study aimed to show how foramina in the femoral neck affect the fracture line and local strains.

Methods

µCT images were taken of 10 cadaveric proximal femora before and after fracture, following mechanical loading representing a fall to the side [3]. The µCT images post fracture were used to determine where the bones fractured in relation to the foramina (Fig. 1). FE models, representing the *ex vivo* experiment, were created based on µCT and clinical CT scans of the intact femora (Fig. 2A). The superolateral side of the femoral neck was modelled with high detail including foramina (Fig. 2B). Element-specific Young's moduli were assigned and the models were solved quasi-statically. The models were used to predict strains in and around foramina. Additional models were created, where strains in elements with a low modulus were ignored and where strains were averaged over a region with a 3 mm radius.
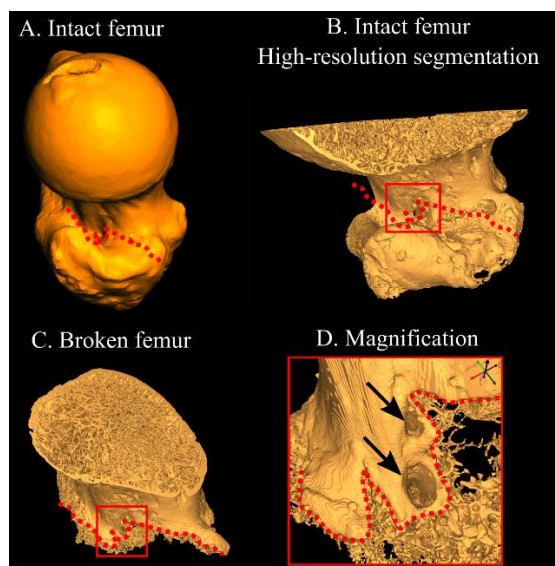
Figure 1: Segmentations of: A) an intact proximal femur; B) the µCT scan of the same intact femur; C) the µCT scan of the broken femur. D) A magnification of the fracture near foramina. The red dotted lines indicate the fracture line. The black arrows point at foramina.

Results

In most cases foramina were present close to the resulting fracture line without the fracture passing through the foramina (Fig. 1D). The models based on µCT images predicted high strains inside foramina (Fig. 2C), agreeing with experimental strain measurements. The high strains inside foramina were often not related to the observed fracture location. Correlation between the measured and predicted fracture force (R^2=0.34) improved when ignoring elements with a low modulus (R^2=0.78) or by averaging of strains (R^2=0.71).
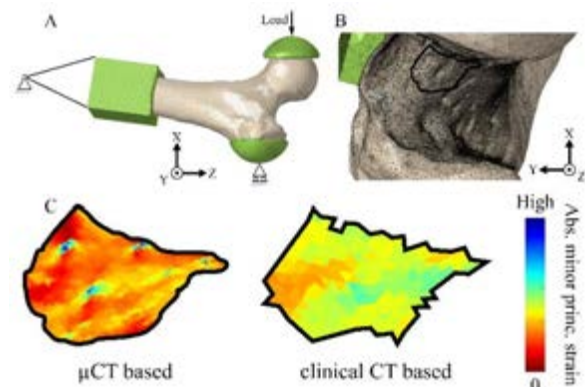
Figure 2: A) Fall loading conditions of the FE models. B) Mesh detail in the femoral neck of an FE model based on µCT images. C) Strains predicted by FE models based on clinical and µCT images in the region where strains were also experimentally measured [3].

Discussion

This study has shown that the presence of foramina influences the fracture pattern. Inclusion of foramina in FE models improves the prediction of local strain concentrations. However, strains concentrated around foramina do not necessarily lead to fracture initiation. This is in agreement with the experimental results, where failure under quasi-static loading could be seen to mostly initiate in the trochanteric fossa [3].

References

1. Kok et al., J Biomech 122, 110445, 2021
2. Bahaloo et al., Ann. Biomed. Eng. 46, 270–283, 2018
3. Grassi et al, J Biomech, 106, 109826, 2020

Acknowledgements

AGE MODULATES BMD AND STRENGTH BUT NOT FORCE RELAXATION IN HUMAN FEMORA

Saulo Martelli (1,2)

1. School of Mechanical, Medical and Process Engineering, Queensland University of Technology (QUT), Brisbane, Australia; 2. Medical Device Research Institute, College of Science and Engineering, Flinders University, Tonsley SA, Australia

Introduction

Age modulate bone viscoelasticity by affecting cross-link concentration [1] and the interface between mineral and collagen phases [2]. However, dynamic properties of whole bones stem from different concomitant mechanisms including the superposition of relaxing stresses, structural heterogeneity, poroelasticity and damage, difficult to observe integrally in isolated bone cores. The aim of the present study was 1) to test the validity of earlier bone stress relaxation theories developed for bone cores in whole human femora and 2) to falsify the hypothesis that aging modulates the femur's relaxation response.

Methods

Force relaxation data of the femur for 12 female donors whose age ranged between 56 and 91 years. Ethics clearance was obtained from the institutional HREC (Project # 6380). Specimens were scanned using a clinical CT scanner (Optima CT660, General Electric Medical Systems Co., USA). The fracture load was calculated using an earlier finite-element procedure (R^2 = 0.89) and a symmetric yield strain criterion [4]. The total hip area, Bone Mineral Content (BMC), Bone Mineral Density (BMD), and the corresponding osteoporosis level (T-score). Data comprised 30 relaxation cycles; 23 cycles where obtained during an earlier imaging study using a custom-made compressive stage step-wise loading the specimen up to fracture [5] while 7 cycles were obtained using a custom-made hexapod robot a a lower initial force below one-fifth of the estimated fracture load. The specimens were instrumented using pre-wired 3 mm stacked rosette strain gages (KFG-3-120-D17-11L2M2S, Japan) (Figure 1).
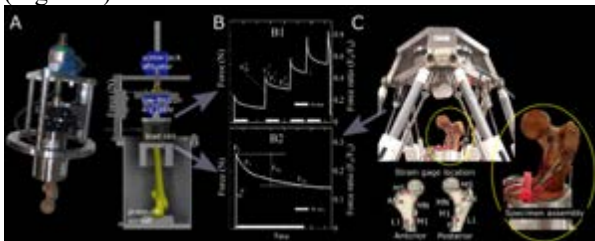
The 30-minute force response to a constant compression generating an initial force, F_0, between 7% and 78% of the estimated fracture load, F_S, was obtained by fitting the stretched decay function by Nakayama et al. [6]

$$F(t) = A \times e^{\left(\frac{-t}{\tau}\right)^\beta} \qquad \text{Eq. 1}$$

The relationship between the A, β, and τ, age, and BMD were analyzed using robust linear regression.

Results

The relaxation function fitted well to all the recordings (R^2 = 0.99). The force relaxation profile was a function (R^2 = 0.83) of the initial force alone for a relative initial force below 0.4 while the shape factor β, which modulates the early force response, was no longer associated with the initial force F0 for F0/FS greater than 0.4. Age and body weight were associated with bone mass and fracture load (R^2 = 0.27 − 0.65, p < 0.05) but not to force relaxation when their effect on bone mass was accounted for.
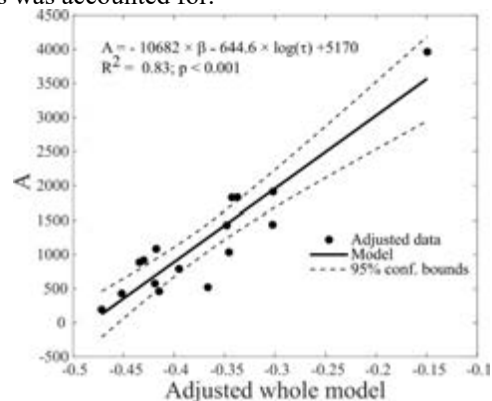
Discussion

The femur's characteristic time is strongly related to the initial compression, relative to the femur's strength, and differs from that measured from bone cores. The effect of age on the femur's force relaxation is negligible as compared to the effect of age on bone mass, strength, and the effect of the initial compression. These results bridge the gap between relaxation experiments in isolated bone cores and entire bone organs.

References

1. Donnelly et al, J. Biomed. Mater. Res. - Part A 92, 2010
2. Lakes et al, J. Biomech. 12, 657–678, 1979
3. Bayraktar et al, J. Biomech. 37, 27–35. 2004
4. Martelli et al, J.M.Behav.Biomed.Mater. 84, 265–72, 2018
5. Nakayama et al, J. Biomech. 26, 1369–1376, 1993.

Acknowledgements

PRINCIPAL COMPONENT ANALYSIS FOR ELUCIDATING IMPORTANT CHANGES IN MOUSE TIBIA GEOMETRY

Stamatina Moraiti (1,4), Vee San Cheong (3,4), Enrico Dall'Ara (2,4), Visakan Kadirkamanathan (3,4), Pinaki Bhattacharya (1,4)

1. Department of Mechanical Engineering, University of Sheffield, UK; 2. Department of Oncology and Metabolism, University of Sheffield, UK; 3. Department of Automatic Control and Systems Engineering, University of Sheffield, UK; 4. Insigneo Institute for in -silico Medicine, Sheffield, UK

Introduction

Preclinical studies have investigated effects of diseases and treatments on mouse bone geometry. These effects are typically reported using scalars (e.g., cortical thickness, area) obtained by morphometric analysis on micro computed tomography (μCT) images. Such parameters describe the three-dimensional (3D) geometric variability of the bone only partially. In contrast, the orthogonal modes obtained from Principal Component Analysis (PCA) capture 3D geometric variability more thoroughly. We hypothesize that the new 3D mode shapes identified by PCA will describe statistically significant geometrical differences between mouse tibia at two different time points during a course of treatment in a mouse model of osteoporosis.

Methods & Materials

Experimental data obtained from a previous longitudinal murine study was used [1]. Therein, six C57BL/6 female mice were ovariectomized at week 14 of age; the right tibia was scanned using *in vivo* μCT (10.4μm/voxel) every two weeks between week 14 and 24 [1]. Mechanical loading was applied *in vivo* at week 19 and 21 (12 N peak load, 40 cycles/day and 3 days/week on alternate days) [1]. In the present study, PCA is performed on images at weeks 18 and 24 (i.e., 12 observations) to identify important shape modes.

The PCA input comprises the coordinates of a fixed number of points on the endosteal and periosteal surfaces of each bone. A landmark-free approach is applied to ensure that each surface point corresponds to the "similar" anatomical location across all bones. The μCT images of the whole tibia were previously aligned with rigid registration [1]. Presently, image slices corresponding to a midshaft section (Figure 1) are cropped (8% of the tibia length [2]), aligned, and binarized. To ensure that each bone is topologically equivalent to an annular cylinder, cortical pores are "filled", and trabeculae are manually deleted. Point correspondence is ensured as follows. Surface points are extracted from the binarized 3D image of the reference bone (one imaging sample at week 18). The reference is elastically registered to the 3D binarized images of each sample using the Sheffield Image Registration Toolkit (ShIRT) and a 10-voxel nodal spacing [3]. Displacement vectors are calculated at the nodes of the ShIRT grid and tri-linearly interpolated to the reference bone surface points. This obtains the coordinates of the surface points on the target bones. Each row of the PCA-input matrix

(MATLAB) corresponds to the coordinates of one sample. PCA modal scores from the two time-points are grouped separately and tested (Wilcoxon paired test) for statistically significant (p < 0.05) differences.
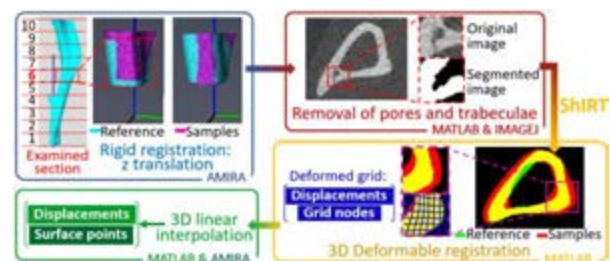
Figure 1: Image processing steps prior to PCA

Results & Discussion

The reference bone surfaces comprised 9125 points in total. The first 3 PCA modes captured 86% of the total shape variance. Concomitant endosteal resorption and periosteal apposition at the anterior crest (1st mode) and to a lesser extent at the medial aspect (2nd mode) (Figure 2) were the main changes between the two time points, as indicated by statistically significant differences in modal scores. In conclusion, this study identified new 3D features that capture the main changes in tibia shape during a course of treatment in osteoporotic mice. This shows the potential for further testing the influence of treatment (e.g., mechanical loading) on future bone strength as mediated through changes in bone shape.
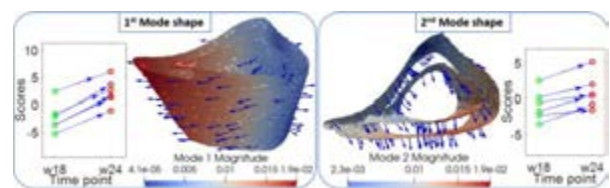
Figure 2: The first two PCA mode shapes are shown as arrows and colour contours plotted on the mean shape. Green and red circles denote differences in modal scores in individual mice before and after treatment.

References

1. Roberts, B.C. et al, Sci Rep, 10:1-16, 2020
2. Cheong, V.S. et al, Acta Biomaterialia, 116:302-317, 2020
3. Barber, D.C., J. Medical Eng. & Techn., 29:53-63, 2005

Acknowledgements

IDENTIFICATION OF STATISTICAL CRITICAL AREA TO DISCRIMINATE PROXIMAL FEMUR FRACTURE DUE TO LATERAL FALL

Nicole Morando[1,2], Carlos Ruiz Wills[1], Jérôme Noailly[1], Simone Tassani[1]

1. BCN MedTech, DTIC, Univ. Pompeu Fabra, Barcelona, Spain; 2. Politecnico di Torino, Italy

Introduction

Osteoporotic hip fracture is a worldwide health problem in the elderly population, with a negative social and economic impact [1]. Although Dual-energy X-ray absorptiometry (DXA) is the gold standard for osteoporosis diagnose, it is not reliable enough for fracture prediction. For this reason, Finite Element (FE) models rise as complementary tools in fracture risk assessments. However, the selection of region of analysis to identify fracture predictors in simulated case-control studies, is often based on visual identification which can lead to noisy detection of discriminant. On the other hand, the simple identification of maximum stress and maximum strain might be misleading since these values might be only partially related to the development of the fracture [2] and the differences between groups might be not significant. For these reasons, the visual evaluation of FE femur model, might present limits of reliability for the discrimination of fractured and non-fractured subjects.

The aim of the present study is to provide an innovative rigorous methodology applicable on FE proximal femur models, to identify statistically significant differences between fractured and control patients for the prevention of hip fracture.

Methods

The investigated groups include 82 osteoporotic female subjects: 45 fractured and 37 controls. Fracture region (trochanter) and type of tissue (trabecular/cortical) were considered in the analyses to explore the impact of these factors on the dependent variables Major Principal Stress (MPS) and Major Principal Strain (MPE) already available from FE simulations. In brief, 3D FE models were built from DXA acquisitions. All model shared the same element ID, and lateral fall was simulated as in [3]. Area with statistically differences were selected through Random Field Theory (RFT) and its topological extension based on Statistical Parametric Map (SPM) using the software "spm1d" [4]. The elements of FE model identified as significant by the SPM were grouped and further analyzed in the second level of analysis through a Two-way ANOVA, to take into consideration the interaction between factors (simultaneous changes in the behavior of cortical and trabecular bone in control and fracture subjects). In the end, the suitability of the selected element regions for the discrimination of a fracture event was validated through the ROC curves and area under the curves (AUC) methods. Statistically significant elements belonging to the regions identified as critical in the current methodology (Fig.1 b) and those obtained analyzing the whole area of the trochanter (Fig. 1 a) as conducted in a previous study [3] without the support of RFT, were considered as reference and discussed.

Results

Elements identified with statistically difference using RFT represented the 16% of the original zones of the trochanter (Fig.1 b). The trochanter showed an AUC of 0.896 for the trabecular MPS, followed by the cortical MPE with 0.855. Interaction between factors presented the highest AUC with 0.898 and 0.834 (Tab.1).
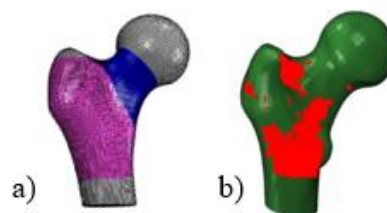
Figure 1: Regions used to identify trochanteric fracture based on (a) anatomical identification of trochanteric region (violet) and (b) Statistically significant elements (marked in red) obtained applying RFT.

Item	Full zone	Reduced zone
MPS-cortical	0.613	0.853
MPS-trabecular	0.825	0.896
MPE-cortical	0.541	0.855
Interaction MPS	0.590	0.834
Interaction MPE	0.310	0.898

Table 1: AUC for each variable taken into consideration, concerning trochanter region.

Discussion

A reduction of the analysis zone allowed to avoid the inclusion of not representative values that might affect the analysis hiding the variation of the critical zone. In fact, with the reduced zone the power of classification of MPS and MPE increases to over 80%. Interestingly, the interaction between factors led to the highest AUC, indicating that the mechanical response of trabecular and cortical tissue seems to change simultaneously but in a non-linear way when a subject pass from control to become at risk of fracture. In conclusion we present a model with good classification capabilities.

References

1. Young-Kyun Lee et al, J KMS, 28(7):976-7, 2013.
2. Tassani Simone et al, Front Mater, 1-9, 2018.
3. Ruiz Wills Carlos et al, J Bone, 89-99, 2019.
4. Todd C. Pataky, J CMBBE, 15:3,295-301, 2012.

Acknowledgements

A MICROMECHANICAL PHASE FIELD DAMAGE MODEL TO INVESTIGATE THE FRACTURE PROPERTIES OF LAMELLAR BONE

Hamid Alijani (1), Ted J.Vaughan (1)

1. Biomedical Engineering and Biomechanics Research Centre, School of Engineering, College of Science and Engineering, National University of Ireland Galway, Galway, Ireland.

Introduction

Bone ultrastructure at lamellar level is a natural composite of mineralized collagen fibrils (MCFs) embedded in the extra-fibrillar matrix which composed of hydroxyapatite minerals and a glue like interface made out of water and non-collagenous proteins. These components are organized in an intricate manner to provide an optimized tissue that exhibits excellent stiffness, strength and resistance to fracture. A wide range of computational models have been proposed to predict the effective elastic properties of lamellar bone [1-3], with recent studies suggesting that the extrafibrillar matrix plays a prominent role in the elastic response of the tissue [4]. However, the post-yield behavior of the bone ultrastructure remains poorly understood and, more importantly, the precise role of the extra- and intra-fibrillar regions is not well established. In this work, we developed a finite element-based homogenisation scheme to investigate the effective failure properties of lamellar bone through a phase-field damage model.

Methods

In this study, a two-dimensional pre-cracked geometry and also a representative volume element (RVE) of lamellar bone are considered that include circular MCFs (elastic-linear plastic material: E_{MCF}, ν_{MCF}, and E_{MCF}^p) distributed through a matrix of granular minerals (elastic material: $E_{HA} = 114\,GPa$, $\nu_{HA} = 0.27$ [5]) bounded by thin interface layer of non-collagenous proteins (elastic-fracture material: $E_{NCP} = 1\,GPa$, $\nu_{NCP} = 0.4$, $G_{NCP} = 0.2\,N/m$, and $S_{NCP} = 64\,MPa$ [2,3]), as shown in Figure (1). These geometries were simulated under several loading conditions using a phase field approach which enables the prediction of elastic and failure properties (such as J-integral ,and strength) of lamellar bone in transverse direction. The phase field model, which is implemented in the Abaqus finite element software through a UMAT subroutine, takes two distinct values of $\phi = 1$ and $\phi = 0$ representing damaged and intact matter, respectively, with a smooth change between both value in the zone around the crack propagation. The J-integral was evaluated through equation (1) where W is strain energy, Γ is a path surrounds the pre-crack tip counterclockwise, $\boldsymbol{\sigma}$ is Cauchy stress, ds is path increment, **n** is normal vector to path increment, and **u** is displacement vector.

$$J = \int_{\Gamma} \left(W dy - (\boldsymbol{\sigma} \cdot \mathbf{n})\frac{\partial \mathbf{u}}{\partial \mathbf{x}} ds\right) \quad (1)$$

This approach predicts differences in the effective properties of lamellar bone in terms of interface thickness, failure properties of non-collagenous proteins (G_{NCP}, S_{NCP}), material properties of MCFs (elastic modulus, yield stress and plastic modulus), and MCFs volume fraction.
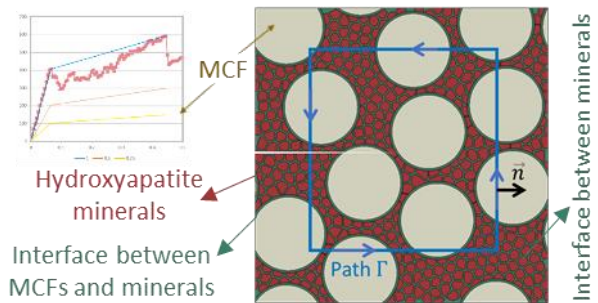
Figure 1: Geometry of lamellar bone with an initial crack surrounded with counterclockwise path Γ.

Results and Discussion

Figure (2) shows both the mechanical behaviour of pre-cracked geometry and RVE of lamellar bone where simulations were carried out under an assumption that the interface between MCFs and minerals are two times stronger than the typical interface between minerals. The results indicate the stiffness of lamellar bone deteriorates with increasing MCFs volume fraction which is in line with the literature [4]. Furthermore, MCFs appeared to block the crack propagation that lead to enhanced bone toughness and ultimate strength. This study suggests MCFs play a pivotal role in post-yield behavior of lamellar bone acting as barriers to crack propagation.
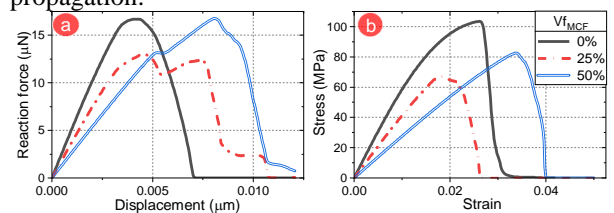
Figure 2: Mechanical response of (a) pre-cracked geometry and (b) RVE of lamellar bone.

References

1. Vaughan et al., J. Mech.Behav.Bio. Mater., 12:50-62:2012.
2. Hamed et al, Acta Mechanica, 154:131-154, 2010
3. Hamed et al, J. Mech. Behav. Bio. Mater, 28:94-110, 2013
4. Alijani et al, J. Mech. Behav. Bio. Mater, *unpublished*.
5. Katz et al, J Biomech, 4:3:227-227, 1971.

Acknowledgements

MEASUREMENT UNCERTAINTIES OF A GLOBAL DVC APPROACH ARE WEAKLY AFFECTED BY THE VERTEBRAL BONE MICROSTRUCTURE

Giulia Cavazzoni[1-2], Enrico Dall'Ara[2], Luca Cristofolini[1], Marco Palanca[1]
1. *Dept of Industrial Engineering, Alma Mater Studiorum – University of Bologna, Bologna, IT*
2. *Dept of Oncology and Metabolism, and INSIGNEO, The University of Sheffield, Sheffield, UK*

Introduction

The microstructure of metastatic vertebrae is characterised by blastic (high density) or lytic (low density) tissues. The mechanical behaviour and strain field inside metastatic vertebrae can be measured only with Digital Volume Correlation (DVC), based on micro-computed tomography (μCT) images. However, the highly heterogenous microstructure (Fig.1A) of metastatic vertebrae may affect the uncertainty of DVC measurements, limiting their reliability, especially at low strain magnitudes (non-destructive testing) [1]. This study aims at exploring the relationship between the microstructure of human vertebrae with and without metastases, and the measurement uncertainties of a global DVC algorithm (BoneDVC) for different measurement spatial resolutions.

Methods

Fourteen human metastatic vertebrae (7 lytic, 5 mixed and 2 blastic) and 15 control vertebrae (radiologically healthy) were obtained from an ethically approved donation program. The vertebrae were μCT-scanned twice (VivaCT80, isotropic voxel size = 39μm) to characterise the microstructure of the tissue and evaluate the measurement uncertainty of BoneDVC at zero-strain [2]. Two volumes of interest were defined: the volume of the vertebral body excluding the cortical shell (VOI1, for all vertebrae), the volume of the vertebral body excluding the cortical shell and the metastatic lesions (VOI2, metastatic vertebrae). 3D microstructural parameters were calculated in each VOI (CTAn): Bone Volume Fraction (BV/TV), Trabecular Thickness (Tb.Th.), Trabecular Spacing (Tb.Sp.). The strain measurement uncertainties were quantified applying the BoneDVC to the repeated scans using four different nodal spacings (NS: 25,50,75,100 voxels [2]). The mean of the absolute values of the six strain component (εm) was evaluated in each node of the DVC grid. The standard deviation of εm across each node (SDER) [3] was calculated for each vertebra.

Results

BV/TV and Tb.Th, in VOI1, in metastatic and control vertebrae were significantly different (p<0.05). Conversely, no significant differences were found in the microstructural parameters between metastatic and control vertebrae in VOI2 (Table1). As expected the median SDER decreased for increasing NS [2] (Table2). The correlation between SDER and BV/TV, SDER and Tb.Th. in VOI1 was not statistically significant (p>0.4). Significant but very weak correlations were found between the SDER and the Tb.Sp. (R^2< 0.23) in VOI1.

	N°	BV/TV [%]	Tb.Th. [μm]	Tb.Sp. [μm]
Ctrl_VOI1	15	10±14	166±76	970±228
Mets_VOI1	14	20±22*	198±53*	1004±307
Mets_VOI2	14	12±5	184±18	849±214

Table1: Microstructural parameters (median±standard deviation) for metastatic (VOI1, VOI2), and control vertebrae (VOI1). *statistically different from controls (p-value<0.05).

NS =	25	50	75	100
Mets	801±428	578±270	415±264	358±232
Ctrl	1005±598	388±187	300±182	258±124

Table2: SDER values[με] for different nodal spacing (NS).

Discussion

These results showed that the bone metastases significantly alter the overall vertebral microstructure, but do not affect the microstructure of the bone surrounding the lesion. The overall DVC uncertainties were weakly affected by the Tb.Sp. Nevertheless, local peaks of error could be related to the lack of microstructural features in the bone for such spatial resolution. The microstructural heterogeneity may explain the variability of the measurement uncertainty within each vertebra (Fig.1B). Future analyses will focus on local gradients of measurement uncertainties and microstructural features.
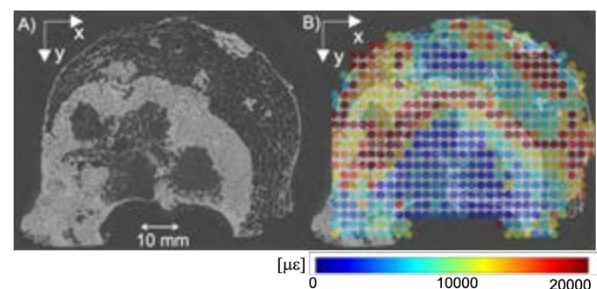

Fig.1: A) μCT cross-section of a mixed metastatic vertebra. B) Distribution of εm [με] (NS=50 voxels) on the same μCT cross-section.

References

1. Liu et al. (2007), *JBiom* **40**: 3516-1520
2. Dall'Ara E. et al. (2014), *JBiom* **47**: 2956-2963
3. Palanca M. et al (2016), *JBiom* **47**: 3882-3890

Acknowledgements

CRACK PROPAGATION IN CORTICAL BONE ANALYZED WITH DIGITAL IMAGE CORRELATION

Giulia Galteri[1-2], Lorenzo Grassi[1], Jonas Engqvist[3], Stephen A Hall[3],
Luca Cristofolini[2], Hanna Isaksson[1] , Anna Gustafsson[1]

1. Dept of Biomedical Engineering, Lund University, Sweden; 2. Dept of Industrial Engineering, Alma Mater Studiorum-University of Bologna, Italy 3. Division of Solid Mechanics, Lund University, Sweden

Introduction

Age and degenerative diseases compromise the integrity of bone and increase the risk of fracture. Bone mineral density, hierarchical structure, accumulation of microcracks and the orientation of the osteons influence the fracture resistance of cortical bone. However, it is difficult to experimentally measure damage properties locally and to distinguish how the fracture resistance is affected by structural local alterations [1]. The aim of the study was to measure the critical strains in cortical bone using digital image correlation (DIC) to understand how the damage evolution is related to the underlying microstructure.

Materials and Methods

Notched beam specimens ($2x4x25mm^3$) of cortical bone were cut from the mid-diaphysis of bovine femurs along three directions: longitudinal (n=5), radial (n=5) and transversal (n=5) (Fig. 1). The notch (1.65 ± 0.2 mm) was sharpened with a scalpel and the initial notch size was measured from micro-computed tomography (μCT) images (RX solution, voxels 29 μm). A speckle pattern was applied to the frontal face of each specimen using an airbrush. Three-point bending tests (span=16mm) to failure were performed (Instron®8511) with a progressive loading protocol (loading +0.045 mm followed by unloading -0.025 mm repeated until failure) at 0.005 mm/s [2] in combination with 2D-DIC (Vic 2D, Correlated Solution, image acquisition at 1 Hz, pixels 5.5 μm). The maximum axial strains (ε_{xxmax}) measured and the strain distribution (ε_{xx}) at the last load cycle before failure, were evaluated in relation to microstructure. Differences between maximum values were tested with Mann-Whitney test ($p<0.05$).

Results

The peak force was higher in the longitudinal specimens than in the radial ($p=0.0079$) and transversal ($p=0.016$) ones. No difference was found in the ε_{xxmax} between the three different groups (Table 1). In longitudinal and radial specimens, the cracks deflected from the initial crack direction, while straight cracks were seen in transversal specimens. Specimens with representative crack patterns are shown in Fig. 1.

	Longitudinal	Radial	Transversal
Force(N)	75 ± 11	49 ± 9	47 ± 6
$\varepsilon_{xxmax}(\mu\varepsilon)$	9010 ± 3413	8150 ± 3778	5090 ± 1117

Table1: Peak force and peak of axial strains (mean±SD) in longitudinal, radial and transversal specimens.
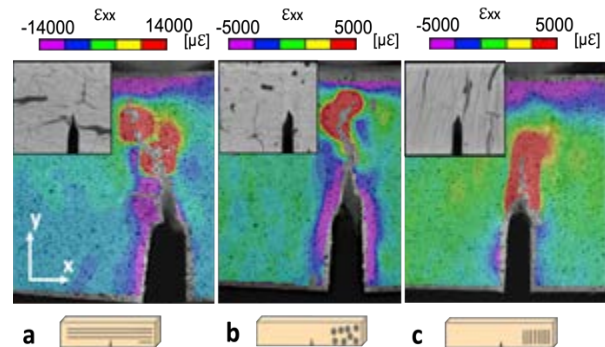
Figure 1: Axial strain field in last load cycle before failure in (a) longitudinal, (b) radial and (c) transversal specimens. The microstructure in the notch area is visualised from the μCT images. Schematic beams show the osteons orientation.

Discussion

The mechanical behaviour of the specimens was similar to previous studies [2]. The DIC analysis showed that the crack propagation in cortical bone seems to be affected by the osteon orientation. Osteons can deflect cracks, which is seen in the irregular crack paths of the longitudinal and radial specimens (Fig. 1 a-b). Conversely, the crack in the transversal specimen grew along the direction of the initial notch (following the orientation of the osteons) which led to faster crack propagation and lower peak load (Fig. 1 c). Future μCT analyses on tested specimens will evaluate the crack path in relation to the local microstructure to elucidate orientation specific toughening mechanisms and their influence on the local strains. Furthermore, the experimental data will be used to validate finite element models of crack propagation in cortical bone [1][3] in order to better understand local damage mechanisms in bone tissue at the microscale.

References

1. A. Gustafsson et al, *BMMB,* 18:1247-1261, 2019
2. R. N. Yadav et al, *Med. Eng. Phys*, 93:100-112, 2021
3. A. Gustafsson et al, *J Biomech*, 112: 110020, 2020

Acknowledgements

NOVEL METHOD TO OBTAIN MECHANICAL PROPERTIES OF ISOLATED TRABECULAE UNDER COMPRESSION IN WET CONDITION

Katja Haslinger (1), Martin Frank (1,2), Dieter H. Pahr (1,2), Philipp J. Thurner (1)

1. *Institute of Lightweight Design and Structural Biomechanics, TU Wien, Vienna, AT*
2. *Division Biomechanics, Karl Landsteiner University of Health Sciences, Krems, AT*

Introduction

Bone as an organ, derives its apparent strength from its inherent mechanical (material) properties, and its hierarchical structural arrangement. To examine the material properties, the structural influence should ideally be excluded. For trabecular bone this suggests to perform mechanical characterization on individual trabeculae. Based on our previous work we here present a compression test of individual trabeculae, that will enable the systematic characterization of trabeculae from healthy and diseased human donors.

Methods

Three human trabeculae were excised from a human femoral head and furnished with a speckle pattern for optical strain measurement. Samples were aligned and glued into a custom-made 3D printed chamber with modified epoxy resin (Best-KL 6009). Compression tests were performed with a servo-electric load frame (SEL-mini, Thelkin), equipped with a 10 N load sensor (S2M-10, HBM), a video camera (Kitocam, Kitotec) and a waterbath. Preparation and compression tests were done in Hank's Balanced Salt Solution (pH 7.4) to mimic physiological conditions. Sample geometry was obtained via micro-computed tomography (μCT100, SCANCO Medical) at a nominal resolution of 3.3 μm (voltage 70kVp, current 145 μA). Calculated stress is based on mean cross-sectional area, strain was calculated by tracking speckle positions at multiple points at the top and bottom of the samples. An overview of the test is shown in Figure 1.
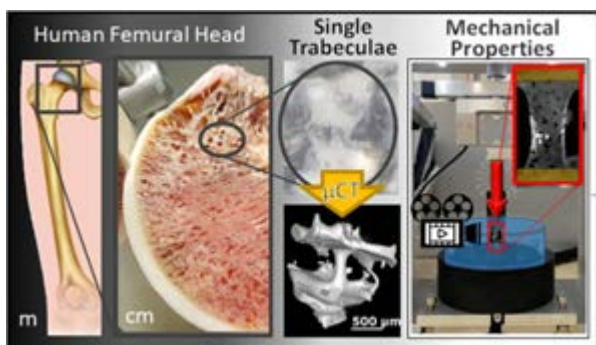
Figure 1: Trabeculae were extracted from a human femoral head and imaged via μCT. The speckle pattern was tracked using a video camera. Mechanical properties were assessed in compression.

Results

Determined mechanical parameters (n=3) are (mean ± std) apparent compression modulus (4.1 ± 2.9)GPa,

maximum compression stress in the fourth cycle (41 ± 26)MPa, maximum compression strain in the fourth cycle (8.1± 5.7)%, (0.2% offset criterion) transition strength (29 ± 14)MPa and transition strain (1.7 ± 1.6)%. Figure 2 illustrates a selected stress-strain curve, indicating a large non-linear region, which was present in all samples.
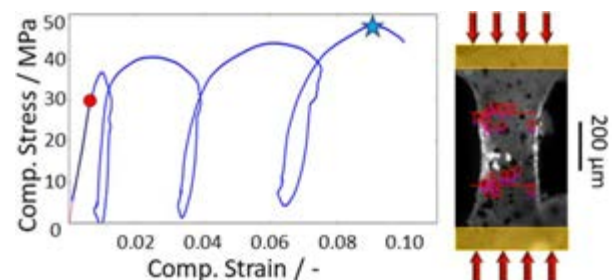
Figure 2: Stress-strain diagram. Measured data in blue, linear region at beginning of curve in black. The red point indicates transition (yield) point. The cyan star shows the max. comp. stress in the fourth cycle.

Discussion

We have established a new test method to obtain mechanical properties of individual trabeculae under compression. Literature reports tensile/compression moduli ranging from 0.75 GPa to 16.85 GPa [1]. However, it is important to note that trabecular bone is not linear elastic [2] and that most studies in literature were conducted in dry conditions. The large variation in material properties reported in literature is likely linked to experimental challenges, limited reproducibility, low sample numbers, varying experimental conditions, e.g. dry/wet, human/animals, different anatomic location. Therefore, systematic, and reliable characterization of individual trabeculae in compression remains to be conducted. Frank et. al [3] have developed a set-up for tensile experiments. In total they have so far reported studies testing well over 300 samples. On this basis, we here present the next development: a novel high-throughput compression test for samples in wet condition to deliver material properties required to simulate physiological loading conditions. This tool enables measurement of visco-elastic properties. This will further enhance our understanding of trabecular bone and improve fracture risk estimation via computer models.

References

1. Wu D., et al, Acta Biomaterialia, 78, 1-12, 2018.
2. Reisinger, et al, Biomech Model Mechanobiol., 19(6):2149-2162, 2020
3. Frank, M., et al, JBMR Plus, 4;5(6):e10503, 2021

FULL-FIELD STRAIN EVALUATION OF BONE TISSUE SUBJECTED TO MICROINDENTATION USING SPHERICAL AND BERKOVICH INDENTERS

Marta Peña Fernández (1), Jakob Schwiedrzik (2), Alexander Bürki (3), Françoise Peyrin (4), Johann Michler (2), Philippe Zysset (3), Uwe Wolfram (1)

1. School of Engineering and Physical Science, Heriot-Watt University, UK; 2. EMPA, Swiss Federal Laboratories for Materials Science and Technology, Switzerland; 3. ARTORG Centre, University of Bern, Switzerland; 4. Université de Lyon, CNRS 5220, INSERM U1294, CREATIS, France

Introduction

Personalized treatment strategies for skeletal diseases rely on the understanding of the mechanical behavior of bone in relation to its structure at different hierarchical levels. At the microscale, microindentation can be used to evaluate elastic and plastic deformation of bone tissue [1]. If combined with high-resolution imaging, it allows to elucidate the microfracture behavior, crack shielding and anisotropic behavior of bone tissue [2]. This study aims at investigating the interplay between crack initiation and plastic deformation underneath spherical and Berkovich indenters in relation to cortical bone microstructure combining *in situ* synchrotron micro-computed tomography (SRµCT) microindentation and digital volume correlation (DVC).

Materials and methods

Cortical bone specimens (~4x4x4 mm) were obtained from ovine femoral diaphysis in axial and transverse directions, with free ends lathed to 3 mm diameter and flattened using an ultramiller. *In situ* step-wise microindentation was performed in beamline ID19 at ESRF using a custom-made microindenter equipped with a 30 µm high Berkovich and a 20 µm diameter spherical indenter. Specimens were loaded with three ~10 µm displacement steps and phase-contrast SRµCT images (670 nm voxel size) were acquired after mechanical relaxation (300 s), and after unloading. Following image reconstruction, the indenter tips were masked, and DVC (DaVis 8.4) was used to evaluate the full-field displacement and strain distribution underneath the indenters using a multipass scheme with a final subset size of 26.80 µm.

Results

DVC-computed strains showed a general increase in strain magnitudes along the radial direction, irrespective of the specimen orientation and indenter tip. Radial strains (ε_r) were essentially axially symmetric, showing a tensile region extending ~200 µm around the indenter and extensive compressive deformation further from the tip (Figure 1a). Hoop strains (ε_φ) reflected the anisotropy of bone, with strains more significant for axially oriented specimens compared to transverse ones. Microcracks ahead of the indenter were accommodated by the hoop strains, with high tensile strain regions associated with mode I cracks (Figure 1b). Strain accumulation was less extensive for specimens oriented in the transverse direction compared to the axial direction which displayed significantly more cracks.
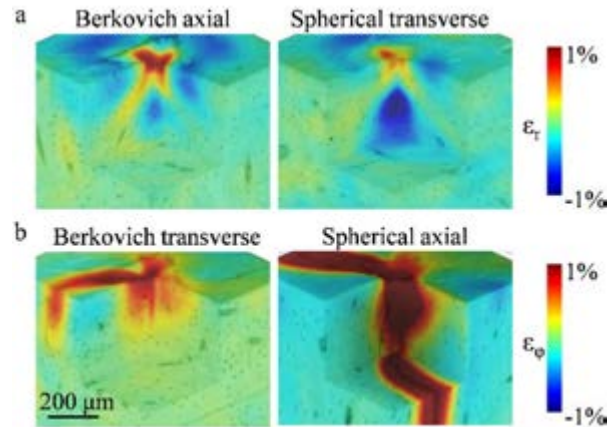
Figure 1. Full-field (a) radial (ε_r) and (b) hoop (ε_φ) strain distribution under the Berkovich and spherical indenters of cortical bone specimens indented ~30 µm in axial and transverse direction.

Discussion

Strains exceeding tissue yielding values were quantified using DVC suggesting extensive plastic deformation under the indenter. For both indenters significant anisotropy was observed ahead of the tip, with lower strains and smaller crack systems observed in transversally oriented specimens, where the underlying fibrillar ultrastructure of ovine bone is largely aligned perpendicular to the indenting direction [3]. Such alignment effectively helps to accommodate the strain energy while providing intrinsic crack-tip shielding in the hoop direction and inhibiting catastrophic failure. Higher tensile hoop strains generally correlated with regions that display significant cracking radial to the indenter, indicating that the tensile hoop and compressive radial stresses serve to open microcracks in the radial direction. This study highlights the anisotropic nature of bone and results may help to validate finite element models for identification of post-yield properties of bone [4].

References

1. Mirzaali et al., Bone, 93:196-211, 2016.
2. Lu et al., Acta Biomat, 96:400-411, 2019.
3. Schwiedrzik et al, Nat Mat, 13:740-747, 2014.
4. Schwiedrzik et al, CMBBE, 18:492-505, 2015.

Acknowledgements

DAMAGE IN SINGLE TRABECULAE UNDER TENSION IDENTIFIED BY INVERSE RHEOLOGICAL MODELLING

Andreas Reisinger (1,2), Martin Frank (1,2), Philipp Thurner (2), Dieter Pahr (1,2)

1. Division Biomechanics, Karl Landsteiner Private University, Krems, Austria
2. Institute of Lightweight Design and Structural Biomechanics, TU Wien, Vienna Austria

Introduction

Recently, we could show that a 2-layer rheological model, can be used to identify elastic, yield and viscous material parameters of individual trabeculae, [1]. In this study, the model is extended by a damage parameter and applied on the same sample set, in order to improve the model fit and to quantify the damage evolution in individual trabeculae.

Methods

Fifteen (n=15) individual trabeculae were dissected from the human femoral head (female, age: 61, no osteoporosis reported) and subjected to cyclic tensile load with increasing amplitude until failure while kept wet, [1] (Fig. 1a)
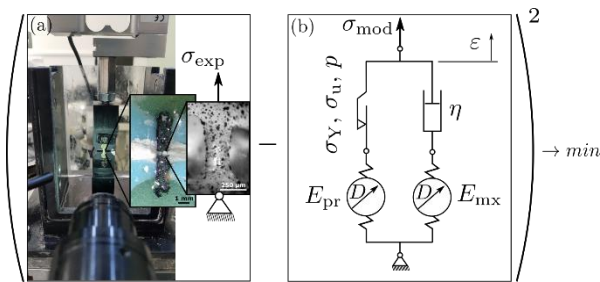
Figure 1: (a) Experimental setup for loading a single trabecula. (b) Rheological model topology. The optimization procedure attempts to reduce the squared difference of (a) and (b) to a minimum.

The 2-layer elastic-visco-plastic rheological model from [1] was extended by a damage parameter, (Fig. 1b). The elasto-plastic Prandtl layer now consists of a degrading elastic spring, with initial Young's modulus E_{pr}, in series with a plastic slider (yield stress σ_Y, ultimate load σ_u, hardening exponent p). The visco-elastic Maxwell layer consists of a second degrading elastic spring (E_{mx}) in series with a viscous damper η. The damage D is driven by the amount of accumulated plastic strain in the slider.

The model parameters were determined by minimizing the root mean square error (RMSE) between the measured stress response from the experiments (σ_{exp}) and the force response of the model (σ_{mod}) for the given strain signal.

Results

The average RMSE value improved from (2.91±1.77) for the model without damage from [1] to (2.34±1.14)

MPa for the current model including damage, (Fig. 2, Tab. 1).
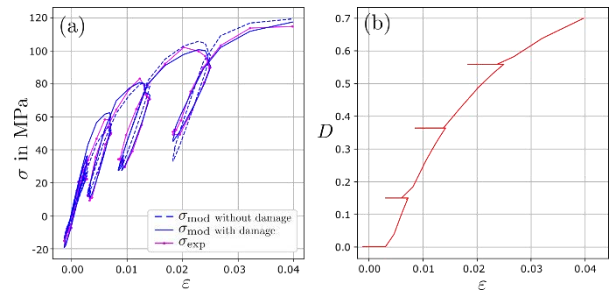
Figure 2: (a) Selected stress-strain behavior of an individual trabecula as measured experimentally (magenta) and as simulated by the 2-layer model neglecting damage (dashed blue) and including damage (solid blue). (b) damage evolution over strain.

Material parameter	No damage [1]	Damage allowed
E_{pr}	3.6±2.0 GPa	5.7±3.3 GPa
σ_Y	17.0±12.7 MPa	17.8±12.4 MPa
σ_u	64.0±25.1 MPa	0.9±1.8 GPa
p	172±114	75±74
E_{mx}	2.0±1.0 GPa	5.8±6.1 GPa
η	3.7±3.5 GPa s	5.3±4.0 GPa s

Table 1: Average identified material parameters of the 15 trabeculae by the two models. (Not filtered for outliers.)

Discussion

The model including damage is resembling the measured trabecular bone material behavior with better accuracy. As shown in the example (Fig. 2b), the damage parameter D is affecting the material stiffness significantly along the loading path. As a side effect, the initial stiffnesses (E_{pr}, E_{mx}) increased and the instantaneous modulus $E_{pr} + E_{mx} > 11$ GPa is now closer to other studies, e.g. [2,3]. In summary, the introduction of the constitutive effect of damage improves the representation of the real behavior of wet trabecular bone.

References

1. A.G. Reisinger et al.: Biomech Model Mechanobiol, 19(6) (2020), 2149-2162.
2. M. Frank et al.: J Mech Behav Biomed Mater, 87 (2018), 296 - 305.
3. R. Carretta et al.: J Mech Behav Biomed Mater, 20 (2013), 6 - 18.

VALIDATION OF LINEAR AND MATERIALLY NONLINEAR µFE PREDICTED DISPLACEMENT FIELDS OF BONE BIOPSIES USING DVC

Pia Stefanek (1), Alexander Synek (1), Enrico Dall'Ara (2), Dieter H. Pahr (1,3)

1. Institute of Lightweight Design and Structural Biomechanics, TU Wien, Austria;
2. Department of Oncology and Metabolism, University of Sheffield, UK;
3. Division Biomechanics, Karl Landsteiner University of Health Sciences, Austria

Introduction

Micro-finite element (µFE) models are able to predict the mechanical behaviour of bone at the tissue level. Their validation on the macro-scale has already been achieved by comparing predicted apparent mechanical properties with experimental measurements. Recently, Digital Volume Correlation (DVC) enabled the validation of µFE models at the meso-scale in the elastic regime [1], but a validation of models including material nonlinearities has not been conducted yet. The goal of this study was to validate the highly efficient µFE solver ParOSol [2] at the meso-scale (~ 1mm) using DVC displacements measured in human trabecular bone specimens tested up to failure. The study compares the predicted displacement fields of different linear and materially nonlinear [2] µFE simulation methods.

Methods

Figure 1 shows the overall study workflow. The study is based on the experimental results of five randomly selected specimens from a previous study [3], where uniaxial compression until failure was applied to human trabecular bone biopsies (~8mm in diameter, ~12mm in height) in a stepwise manner. At every loading step µCT scans were recorded (36µm resolution). They were used as input for the BoneDVC algorithm [4], which measures the displacement field at discrete points of a cubic grid (nodal spacing = 24 voxels). To exclude boundary effects, only the middle part of the specimens was considered. The unloaded 3D images were used to generate voxel-based µFE models. Boundary conditions were imposed using the interpolated DVC displacements. Material parameters for the linear and damage-based nonlinear model were taken from [2] and adapted as described in [3]. For the linear (L) and nonlinear (NL) simulations, the boundary conditions were derived only from the DVC displacement field at the ultimate load step. In another nonlinear simulation (NLS), boundary conditions were applied stepwise using the DVC displacement field of every available loading step (red circles in Fig. 1). The µFE-predicted displacement fields at the ultimate load step were then compared to the DVC displacement fields using linear regression.

Results

Linear µFE models were able to predict more than 84% of the variations in the DVC displacements in z-direction for the five selected specimens ($R^2 = 0.84 - 0.95$). NL and NLS simulations showed a slightly higher correlation with DVC displacements ($R^2 = 0.86 – 0.96$).

NLS did not show an improvement in comparison to the NL simulation method (Fig. 2). The specimen-averaged RMSE in z-direction was largest for the L simulation (0.016mm) and decreased for the NL (0.014mm) and NLS simulations (0.013mm). For x- and y- direction, R^2 was generally lower, but the same trends were observed between the different models.
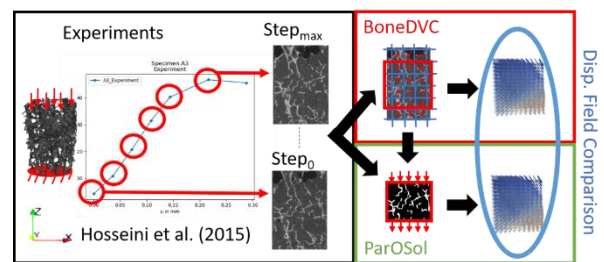
Figure 1: Description of the study workflow.
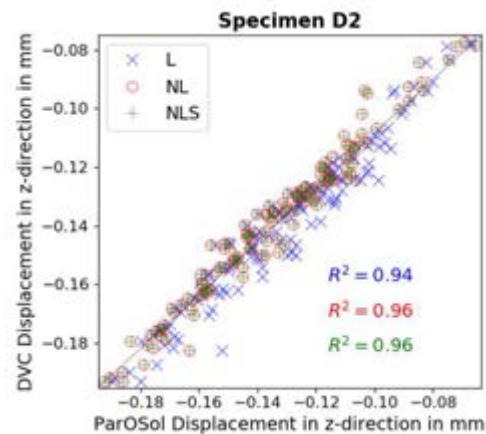
Figure 2: Displacement comparison in z-direction for one representative specimen (D2).

Discussion

Predicted displacement fields of all µFE simulation methods (L, NL, NLS) were in good agreement with the DVC-measured displacement field; NL and NLS only slightly improved the predictions. However, this study was restricted to one material model and only evaluated displacement fields of small bone biopsies. Differences between the simulation methods could be more pronounced for other material models, larger bone samples or different output parameters (e.g. stresses).

References

1. Chen et al, J Mech Behav Biomed Mater 65:644-651, 2017
2. Stipsitz et al, Biomech Model Mechano 19:861-874, 2019
3. Hosseini et al, Int J Numer Method Biomed Eng 31: e02728, 2015
4. Dall'Ara et al, J Biomech 47:2956-2963, 2014.

NEW INSIGHTS INTO HIGH-RESOLUTION STRAIN FIELDS OF TRABECULAR BONE USING DIGITAL IMAGE CORRELATION

Nedaa Amraish (1,2), Dieter Pahr (1,2)

1. Division Biomechanics, Karl Landsteiner University for Health Sciences, Austria

2. Institute of Lightweight Design and Structural Biomechanics, TU Wien, Austria

Introduction

Trabecular bone structures consist of rods and plates [1]. The reduction in bone volume to total volume is a thinning of this network and leads to a higher slenderness ratio, which could cause the trabecula to fail under buckling if it reaches a critical value [2, 3]. The aims of this study were to (a) obtain high resolution full-field strain fields of the trabecular network using DIC and (b) investigate the correlation between the local strain magnitudes on the trabecula level and its orientation.

Methods / Materials

Six cubes of trabecular bone samples (8x8x8 mm^3) were cut from the distal femoral epiphyses of bovine bone. The specimens were subjected to a cyclic (ramp and hold) compression load using a Zwick machine. During the test, 2D high-resolution images (6μm) of the cut surface were captured. Three types of strains are measured. The global strain is computed as the length change of the virtual extensometer divided per its original length, see Fig 1. The local strain is the length change of each trabecula divided by its original length, and the facet strain is the strain computed on the surface of the trabecula. The facet strain (in x,y) was transformed onto a new axis (x',y') which is inclined from the original y-axes at an angle Φ and points along the axis of the network
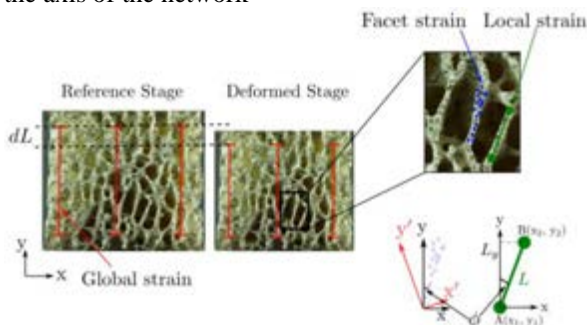
Figure 1: Strain analysis

Results

The global strain obtained from the virtual extensometer is plotted in Fig 3 (black line) The measured noise evaluated at the first five stages captured at zero-strain. Overall, the noise was less than 100 μstrain. High resolution full-field strain maps were obtained on the surface of trabecular specimens, see Fig 2. Seven trabeculae were selected (2 rods and 5 plates), the orientation angle of these trabeculae ranges between 5.66° and 83.81°.
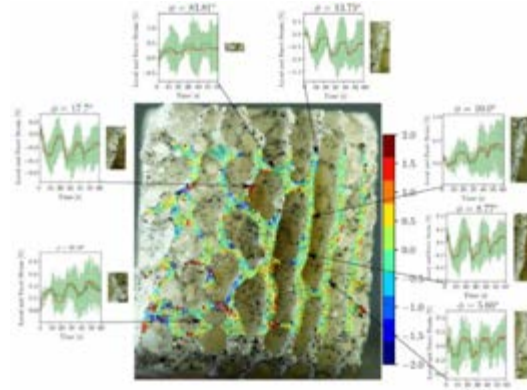
Figure 2: Full-field surface strain (±2%) at 2% global strain (big pictures) as well as facet and local strain over time (small pictures).

This study showed that strain magnification is not prominent for all trabeculae, see Fig 3. No significant correlation was found between the local strain of trabecula and its orientation.
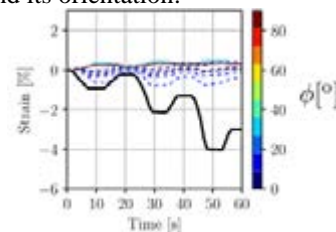
Figure 3: The global strain obtained from the virtual extensometer (in black) and the local strain for different trabeculae rods (solid colours) and plates (dashed line). Colours indicate the inclination angle in °.

Conclusion

This study showed that with high resolution images, it was possible to obtain 2D full-field strain maps of single trabecula or plates within the trabecular network. These maps give a unique insight into the mechanical response at this length scale and can be used to validate non-linear simulation models.

References

1. Stauber et al. J. of Bone and Mineral Research. 2006.
2. Bell et al. Calcified tissue research. 1967.
3. Townsend et al. Journal of biomechanics. 1975.

Acknowledgements / Funding

IN END-STAGE KNEE OSTEOARTHRITIS THE SUBCHONDRAL BONE MICROARCHITECTURE OF THE TIBIAL PLATEAU IS CORRELATED TO THAT OF THE DISTAL FEMUR

Fahimeh Azari (1,*), William Colyn (2,*), Johan Bellemans (3) , Lennart Scheys (1,3,**), G. Harry van Lenthe (1,**)

1. KU Leuven, Leuven, Belgium; 2. General Hospital Turnhout, Turnhout, Belgium; 3. University Hospital Leuven, Leuven, Belgium; * and ** indicate equal contributions.

Introduction

Knee osteoarthritis (OA) is a common and progressive joint disease. Although OA was previously considered a primary disorder of articular cartilage, recent studies suggest that OA involves the whole joint and highlight the crucial contribution of subchondral bone in OA development [1, 2]. Yet, only limited data has been reported on the structural properties of the subchondral bone plate (SBP) and underlying subchondral trabecular bone (STB) in end-stage OA; furthermore, how altered properties in the tibial plateau relate to those in the distal femur is unknown. Therefore, this study aimed to visualize and quantify bone microstructure in the medial tibial plateau and medial distal femur in patients with end-stage OA and varus malalignment.

Materials and methods

The medial part of the tibial plateau and medial part of the distal femur from 23 end-stage knee-OA patients with varus deformities were micro-CT scanned at 20.1 µm/voxel. For the tibia, one cylindrical VOI (10 mm in diameter, a total height of ~3–5 mm, depending on the specimen) was selected within the load bearing region of the medial part of the tibial plateau [2,3]. In the axial image dataset, the largest possible ellipse was indicated within the inner condylar boundary of the medial tibial plateau (software CT Analyzer, v1.19.4.0, Skyscan-Bruker). The cylindrical VOI was located at the center of the anterior half of the medial condyles, defined by the elliptical region (Figure 1). For the femur, a cylindrical VOI was defined in the middle of the medial distal part. Cartilage and SBP were segmented manually by contouring on the coronal cross-section images [2]. The cortical and trabecular bone morphometric parameters were computed using voxel counting
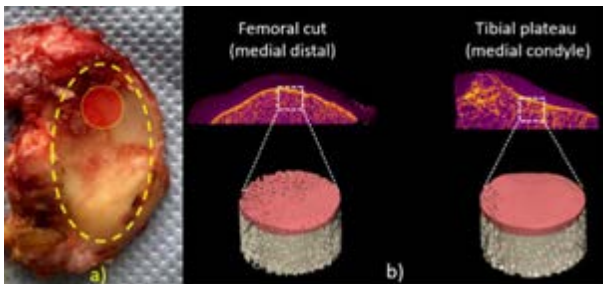
***Figure 1**: a) Photograph of osteoarthritic medial tibial plateau; the red-colored circle within the elliptical region is the investigated VOI. b) 3D rendering of VOIs on the medial tibial plateau and medial distal femur.*

(BV/TV) and sphere fitting (Cart.Th, Pl.Th, and Pl.Po), as implemented in CT Analyzer software.

Results

The microstructural parameters at the tibial plateau were strongly correlated to those of the distal femur. For Cart.Th, BV/TV, Pl.Th and Pl.Po the correlation coefficients were 0.95, 0.82, 0.92 and 0.93, respectively(Fig. 2).
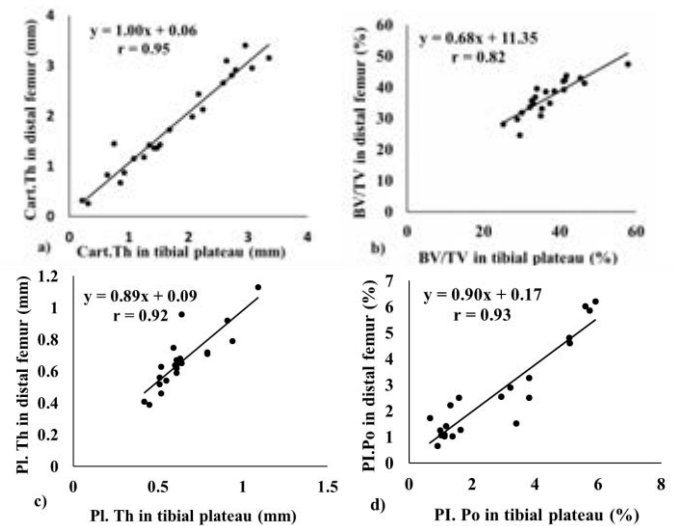
Figure 2: a) Cart.Th, b) BV/TV, c)PI.Th, and d) PI.Po at the medial tibial plateau were correlated highly with those of the medial distal femur.

Discussion

Our data on the tibial plateau are in line with those from OA-induced mice and OA found in humans [2,4], and contribute to a better understanding of the bone changes occurring in varus OA knees. Varus knee are characterized by higher forces medially than laterally [2]. As adaptation of both the subchondral bone plate and subchondral trabecular bone microarchitecture reflects responses to local mechanical factors in the joint, our results demonstrates that varus alignment influences both the medial tibial plateau as well as medial distal femoral distribution of force.

References

1. Rapagna S et al, J Orthop Res, 39:1988–1999, 2021.
2. Roberts BC et al, J Orthop Res, 35:1927–1941, 2017.
3. Adouni M et al, J Biomech, 47:1696–1703, 2014.
4. Botter SM et al, Arthritis Rheum, 63:2690–2699, 2011.

HOMOGENIZED-FE-BASED INVERSE BONE REMODELING: MODIFIED OPTIMIZATION CRITERION AND EVALUATION ON THE DISTAL RADIUS

Sebastian Bachmann (1), Dieter H. Pahr (1, 2), Alexander Synek (1)

1. Institute of Lightweight Design and Structural Biomechanics, TU Wien, Vienna, AT
2. Division Biomechanics, Karl Landsteiner University of Health Sciences, Krems, AT

Introduction

Inverse bone remodeling (IBR) is a method to deduce the external loading from a given bone microstructure [1]. In its essence, it optimally scales a set of unit loads until a homogeneous tissue loading state is reached. Despite its simplicity, it was successfully used to estimate physiological loading conditions [2] or infer habitual hand bone loadings of primates [3]. However, the method was formulated for computationally expensive micro-finite element (µFE) models, limiting its application to smaller bones and requiring high-quality scans. This study aimed to translate the inverse remodeling method to computationally efficient homogenized FE (hFE) models and test it on distal radius sections.

Methods

µFE-based IBR scales a set of unit loads such that the difference of element-wise strain energy density (SED), $U(\boldsymbol{x})$, and a target stimulus $\widetilde{U}$ is minimized [1].

To ensure consistent results between µFE and hFE-based IBR, we propose a continuum-level target stimulus $\widetilde{U}_{hom}$ in the form of a density-dependent power-law: $\widetilde{U}_{hom} = \widetilde{U}_0 \rho(\boldsymbol{x})^d$.

The constants $\widetilde{U}_0$ and d were identified on 701 trabecular bone cubes (5.3mm edge length; Fig. 1, top) [4]. First, µFE-based IBR with six canonical load cases was performed for each bone cube using $\widetilde{U} = 0.02\text{MPa}$ [1]. Then, the continuum-level stimulus $\widetilde{U}_{hom}$ was evaluated for each bone cube, and the was power-law fitted.

µFE and hFE-based IBR was performed on 13 distal radius sections [5] to test the modified criterion (Fig.1, bottom). Only trabecular bone was used to remove bias from the cortical shell. A density-dependent orthotropic material was mapped onto 1mm hex-elements for the hFE models [4] using the method from Pahr and Zysset [6]. Three uniaxial displacement load cases were applied at the distal end, keeping the proximal end fixed. The optimally scaled load cases from µFE and hFE-based IBR were then compared based on the reaction force at the distal end using linear regression.

Results

IBR on the bone cubes showed that the continuum-level target stimulus could be well captured using a power-law with $\widetilde{U}_0 = 0.0208\text{MPa}$ and $d = 1.21$ (Fig. 2a). With this density-dependent target stimulus, hFE-based IBR correlated well ($R^2 = 98.5\%$) with µFE-based IBR in terms of the predicted reaction force magnitude on the distal radius, but hFE-based predictions were systematically larger than µFE (Fig. 2b).
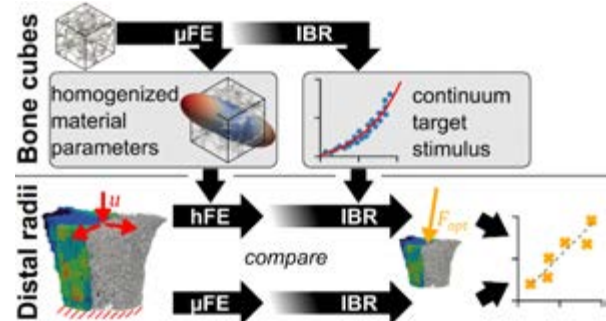
Figure 1: Top row: Material properties and continuum-level target stimulus are inferred from trabecular bone cubes using µFE-based inverse bone remodeling (IBR). Bottom row: comparison of inverse remodeling using µFE and hFE.
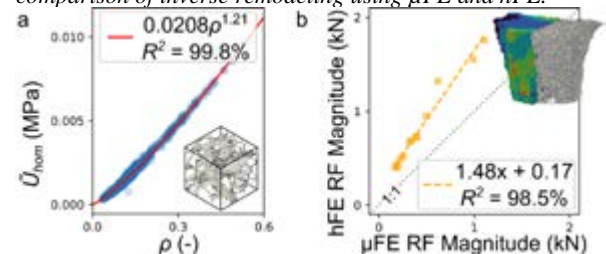
Figure 2: (a) Relative density ρ vs. continuum-level stimuli $\widetilde{U}_{hom}$ and the fitted power-law for 701 trabecular bone cubes. (b) Correlation of the predicted reaction force magnitude using µFE or hFE-based IBR on 13 distal radius sections.

Discussion

The proposed continuum-level target stimulus enabled the use of hFE for IBR and led to a good correlation with µFE-based IBR, while using the unmodified criterion in hFE-based IBR led to a worse prediction. The systematic overestimation of the predicted reaction forces is in line with previously reported overestimation of stiffness in such hFE models of 40-50% [6]. So far, it was only tested on distal radius sections excluding the cortex. Therefore, further studies should investigate optimization procedures with different homogenization methods, calibrated material properties, more elaborate optimization criteria, and other bones typically loaded in a multi-directional way, such as the proximal femur.

References

1. Christen et al. *Biomech Model Mechan* (2011)
2. Christen et al. *J Biomech* (2013)
3. Synek et al. *Biomech Model Mechan* (2018)
4. Gross, Pahr, and Zysset. *Biomech Model Mechan* (2012)
5. Hosseini et al. *Bone* (2017)
6. Pahr and Zysset. *J Biomech* (2009)

Acknowledgments

27th Congress of the European Society of Biomechanics, June 26-29, 2022, Porto, Portugal

MICRO-FE DERIVED MECHANICAL PROPERTIES FOR TRABECULAR BONE REMODELING AND ADAPTATION UNDER LOADING

Daniele Boaretti (1), Francisco C. Marques (1), Jack J. Kendall (1), Gisela A. Kuhn (1), Esther Wehrle (1), Yogesh D. Bansod (1), Ralph Müller (1)

1. Institute for Biomechanics, ETH Zurich, Zurich, Switzerland

Introduction

Micro-Finite Element analysis (micro-FE) has been widely used to investigate the mechanical properties of bone at the tissue level. The most commonly used properties to correlate remodeling to mechanics are the strain energy density (SED) and the norm of the gradient of SED (∇SED). However, it is still not clear which of these properties has the better modeling performance of formation and resorption events in trabecular bone remodeling. To investigate this, we have created micro-FE models of *in vivo* micro-computed tomography (micro-CT) images of the sixth caudal vertebra (CV6) of mice to predict the evolution of these properties over a remodeling period of four weeks.

Methods

We used *in vivo* micro-CT images of mechanically stimulated CV6 vertebrae of 15 week-old prematurely aged female mice (PolgA, n=5) [1]. The vertebrae were subject to a cyclic load of 8 N/10 Hz for four weeks and they showed a continuous increase of bone volume fraction (BV/TV) up to three weeks of loading (+17%). To create the micro-FE models of these images, intervertebral discs were added to the proximal and distal ends of these vertebrae. The bone voxels were identified with a threshold of 580 mg HA/cm^3 and used to compute the SED and ∇SED (Figure 1) using micro-FE as described in [2]. The remodeling regions of formation and resorption were obtained by registration and overlay of subsequent weekly time-lapsed images. The trabecular region was extracted for each sample using masks obtained with an established procedure [3]. To determine the modeling performance of SED and ∇SED, we used a receiver operator characteristic (ROC) analysis. Using this approach, we also computed the area under the curve (AUC), which represents the modeling performance of the predictor, SED or ∇SED, to classify regions of formation and resorption. This analysis was carried out on the trabecular bone surface regions. Additionally, along with AUC, we computed the optimal threshold of formation and resorption by maximizing the differences between the true-positive and false-positive rates.
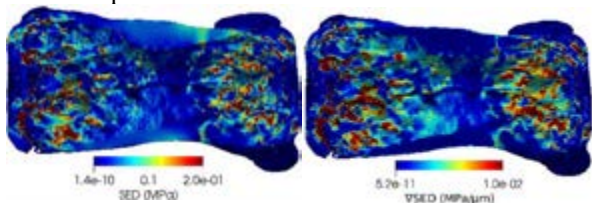
Figure 1: SED and ∇SED distribution in the CV6.

Results

The modeling performance of SED is slightly higher over time compared to ∇SED for both formation and resorption (Figure 2a). The thresholds of formation and resorption are different until the second week (initial mean percentage difference=51% and 80% for SED and ∇SED, respectively) and they tend to overlap afterwards (final mean percentage difference=10% and 25% for SED and ∇SED, respectively) (Figure 2b,c).
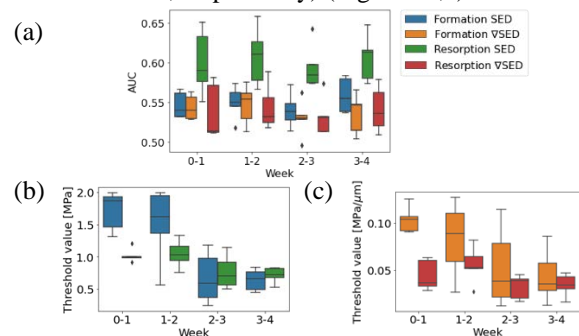
Figure 2: (a) ROC AUCs using SED and ∇SED. Threshold values using (b) SED (c) ∇SED.

Discussion

Based on the results, SED might be chosen as a predictor for modeling bone resorption, whereas little difference was observed between SED and ∇SED for modeling bone formation (average AUC=0.55 and 0.54, respectively). The convergence towards the same range of values for the optimal thresholds of formation and resorption suggests that bone adaptation is initiated from the second week. Hence, at the end of the loading period bone formation and bone resorption occurs at the sites with similar mechanical signal. As a result, bone adaptation starts from the second week with noticeable changes in BV/TV from the third week. To conclude, this work suggests using SED, not ∇SED as hypothesized previously [4], as mechanical stimulus for predicting the presence of formation or resorption events in the PolgA mice during bone adaptation.

References

1. Scheuren et al, J Cachex, 11(4), 1121-1140, 2020.
2. Webster et al, J Biomech, 48:866-875, 2015.
3. Lambers et al, Bone, 49(6), 1340-1350, 2011.
4. Scheuren et al., Front. bioeng. Biotechnol, 8: 566346

Acknowledgements

DAMAGE MECHANICS OF TYPE-2 DIABETIC TRABECULAR BONE SUBJECT TO MONOTONIC AND CYCLIC LOADING

Marissa Britton, Jessica Schiavi, Ted Vaughan
Biomechanics Research Centre, National University of Ireland Galway.

Introduction

Type-2 Diabetic (T2D) patients experience up to a 3-fold increase in bone fracture risk [1]. Paradoxically, T2D patients have a normal or increased bone mineral density (BMD) when compared to non-diabetic patients [2]. The current leading hypothesis is that the hyperglycaemic state leads to non-enzymatic glycation in collagen causing the formation of crosslinks, known as AGEs, stiffening the overall collagen network leading to more brittle behaviour [3]. This implies that T2D has a deleterious effect on bone quality, whereby the intrinsic material properties of the bone matrix are altered. This creates clinical challenges as current diagnostic techniques are unable to accurately predict the fracture probability in T2D patients. To date, the relationship between cyclic fatigue loading, mechanical properties and microdamage accumulation of T2D bone tissue has not yet been examined and thus our objective is to investigate this relationship.

Methods

Ethically approved femoral heads were obtained from patients, which were categorised into two main groups with sub-groups osteoarthritic (OA); non-T2D (n=9) and T2D (n=9), and osteoporotic (OP); non-T2D (n=8) and T2D(n=8). Cancellous cores were removed from along the main trabecular direction. To obtain the mechanical properties, one cancellous bone core underwent a monotonic compression test, the other core underwent a cyclic compression test at a normalized stress ratio. The damage was then stained by forming a $BaSO_4$ [4] precipitate and scanned with microcomputed tomography at a resolution of $10\mu m$.

Results

Monotonic test: For the OA group. the T2D subgroup, when compared to non-T2D subgroup, had a significantly higher apparent modulus (p=0.031), yield stress (p=0.013), max stress (p=0.008), post-yield strain energy (p=0.005), modulus of resilience (p=0.023), toughness (p=0.006) and BV/TV (p=0.008). When normalized against BV/TV the max stress, post-yield strain energy, modulus of resilience and toughness all remained significantly higher in the T2D subgroup. Similarly, the T2D subgroup within the OP group showed no statistical difference in mechanical properties to the non-T2D group, even when normalised against BV/TV. There was also no difference in BV/TV in the OP group.

Cyclic Test: The creep-fatigue curve (Fig.1B) consisted of three phases; the primary phase the secondary phase and the tertiary phase. For the OA cyclic group, the T2D subgroup showed no statistical difference in mechanical properties to the non-T2D group. The T2D had a significantly higher number of cycles to failure (p=0.05)

and a higher BV/TV (p=0.002). For the OP cyclic tests, the T2D subgroup had a significantly higher initial modulus and on average the final modulus and number of cycles to failure were higher but these were not statistically significant.

Microdamage Accumulation: The presence of microdamage was significantly higher for T2D in the monotonic (p=0.041) but not the cyclic. The microdamage accumulation was also higher for the untested T2D samples (p=0.035). There was no statistically significant difference in microdamage accumulation for the OP group.
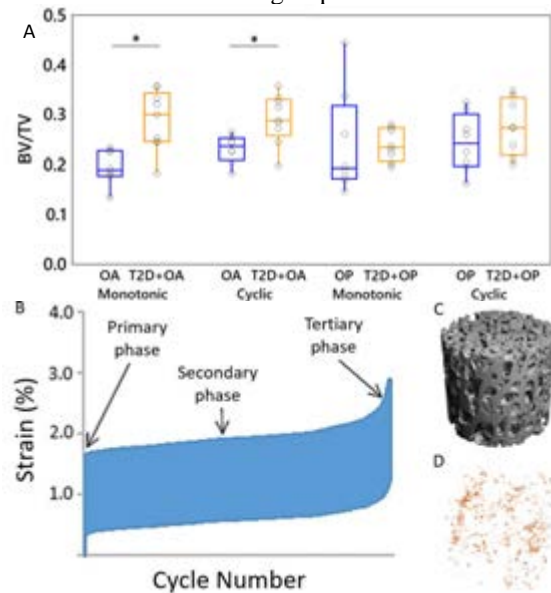
Figure 1: A) Boxplots of BV/TV B) Example of cyclic behaviour of trabecular core C) Example of T2D+OA bone D) BaSO4 labelled microdamage present in T2D+OA bone

Discussion

Previous population-level studies have found that T2D patients have been shown to have an increased fracture risk when compared to non-T2D patients. This research indicates that T2D does not impair the mechanical properties of trabecular bone from the femoral heads of T2D patients, suggesting that other mechanisms may be responsible for the increased fracture risk seen in T2D patients.

References

1. Looker, A. C. *et al.*, Bone 82:9–15, 2016.
2. Heilmeier, U. *et al.* Osteoporos Int 26:1283–1293, 2015.
3. Bank, R. A *et al.* Biochem. J vol. 330:345-351, 1998.
4. Wang, X. *et al*. J. Biomech. 40:3397–3403, 2007.

Acknowledgements

EFFECTIVENESS OF ALTERNATING PTH AND MECHANICAL LOADING TREATMENT IN AN OVARIECTOMISED MOUSE MODEL

Vee San Cheong (1, 2), Bryant Roberts (1,3), Visakan Kadirkamanathan (1, 2), Enrico Dall'Ara (1,3)
1. Insigneo Institute for in silico Medicine, University of Sheffield, United Kingdom, 2. Department of Automatic Control and Systems Engineering, University of Sheffield, United Kingdom 3. Department of Oncology and Metabolism, University of Sheffield, United Kingdom

Introduction

Combined mechanical loading and parathyroid hormone (PTH) treatment has been found to be more effective at slowing the deleterious effects of osteoporosis on bone properties than either monotherapy [1]. However, high cost and poor adherence of PTH impacts the cost-effectiveness of using PTH compared with other pharmacological agents [2,3]. This study uses a combined experimental and computational approach to compare the effectiveness of alternate or concurrent PTH and mechanical loading treatment on bone properties in ovariectomised mice.

Methods

Twelve C57BL/6 female mice were ovariectomised at week 14 of age and the right tibia scanned using *in vivo* micro computed tomography (10.4µm/voxel) at week 14, 16, 18, 20 and 22. Mechanical loading was applied to the right tibia *in vivo* at week 19 and 21 with a 12N peak load, 40 cycles/day and 3 days/week on alternate days. Mice received either injection of PTH at 100 µg/kg/day every week (PTHML group, N=6) or on alternate weeks (week 18 and 20; PTHMLx group, N=6). All micro-CT images were rigidly registered to a reference tibia, before the locations and frequency of apposition and resorption were quantified using bitwise comparison. Densitometric analyses (bone volume fraction; BV/TV, bone mineral content; BMC, bone mineral density; BMD) were performed in the whole bone and across 40 compartments. Voxel-based homogeneous linear elastic microFE models were developed to estimate changes in the strain distribution due to the treatments. The Mann-Whitney U test was used to compare if concurrent and alternate PTHML treatments were significantly different (p<0.05).

Results

At the level of the whole bone, the change in BV/TV between treatments were not significantly different at weeks 18-20 and weeks 20-22. However, PTHMLx resulted in higher increases in BMC and BMD at weeks 18-20, which was correlated to significantly higher tissue mineral density (TMD) at weeks 18-20 in the PTHMLx group. At weeks 20-22, PTHMLx induced a lower increase in BMC and no change in BMD (Figure 1). Spatial analyses revealed that bone remodelling changes between PTHML and PTHMLx were largely similar between weeks 18-20. Periosteal apposition slowed at weeks 20-22, which was significantly lower for PTHMLx than PTHML across 9 longitudinal sections (Figure 2).
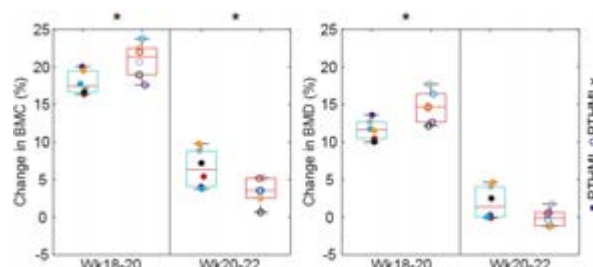
Figure 1: Changes in BMC and BMD after the commencement of treatment.
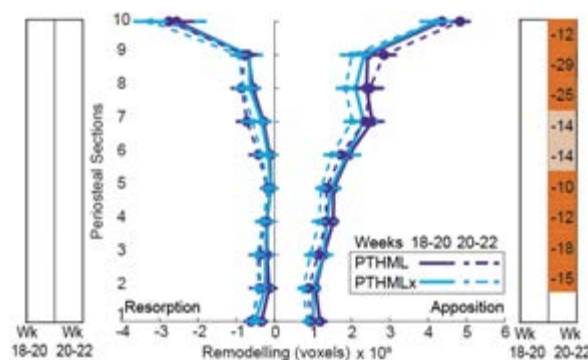
Figure 2: Periosteal bone adaptation at weeks 18-20. Heat maps indicate statistical significant difference. Lighter shade, p<0.05; darker shade, p<0.01. Numbers in heat maps indicate the relative percentage difference.

Discussion

The results show that at weeks 18-20, PTHMLx is a compatible alternative for PTHML. PTHMLx treatment resulted in a faster and higher increase in BMD that peaked at week 20. Moreover, BMC continued to increase between weeks 20-22. Although BMD remained higher in the PTHMLx group than the PTHML group at week 22, the slowing of periosteal apposition at weeks 20-22 for PTHMLx suggests that further optimization may be required to sustain the efficacy of the treatment for a longer period.

References

1. Roberts et al, Sci Rep, 10:8889, 2020.
2. Johnell & Kanis, Osteoporos Int, 17:1726–1733, 2006.
3. Tosteson et al, Am J Manag Care, 14:605-615, 2008.

Acknowledgements

SITE-MATCHED MICROPILLAR COMPRESSION AND RAMAN SPECTROSCOPY TO ASSESS JAW BONE QUALITY

Tatiana Kochetkova (1), Alexander Groetsch (1), Cinzia Peruzzi (1), Michael Indermaur (2), Stefan Remund (3), Beat Neuenschwander (3), Joelle Hofstetter (4), Benjamin Bellon (4), Johann Michler (1), Philippe Zysset (2), Jakob Schwiedrzik (1)

1. Empa, Swiss Federal Laboratories for Materials Science and Technology, Laboratory for Mechanics of Materials & Nanostructures, Thun, Switzerland; 2. ARTORG Center for Biomedical Engineering Research, University of Bern, Switzerland; 3. Institute for Applied Laser, Photonics and Surface technologies (ALPS), Bern University of Applied Sciences, Burgdorf, Switzerland; 4. Institut Straumann AG, Basel, Switzerland

Introduction

Preclinical studies often require animal models for *in vivo* experiments. Particularly in dental research, pig species are extensively used due to their anatomical similarity to humans [1]. However, there is a knowledge gap on the microscale porcine bone properties governing bone quality, which is crucial for implant studies. Here, we examine cortical bone from the jaw of a common animal model used in dental research, the miniature pig. Three minipig genotypes were examined: Yukatan, Göttingen, and Sinclair. We used a multi-modal approach to assess the bone quality at the microscale using a combination of methods for compositional and mechanical analysis.

Material and Methods

Cortical bone samples were extracted along the main jaw axis from the premolars region of three minipig genotypes (Yukatan, Göttingen, and Sinclair); three animals per genotype were used. Micromechanical properties were assessed by micropillar compression [2] at ambient conditions. A novel laser ablation protocol was developed based on femtosecond (fs) laser ablation to prepare a 5×5 micropillar array on each of the bone samples. The average pillar diameter was ~24 µm with an aspect ratio of 2.3 and a taper angle of ~15°. Micropillars were uniaxially compressed using monotonic and cyclic loading protocols, giving access to microscale elastic moduli and yield values. The influence of the taper angle was corrected by means of finite element simulations. Raman spectra were collected from the top of micropillars (Fig. 1) to assess the mineral to matrix ratio and its effect on the compressive microscale bone properties in a site-matched fashion.
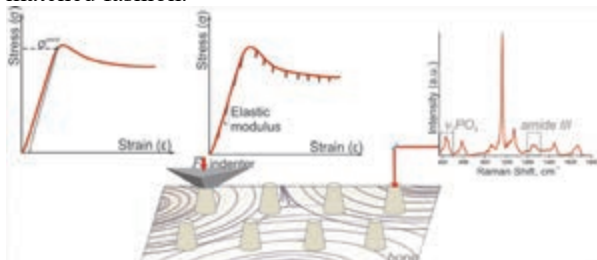
Figure 1: Outline of the site-matched micropillar compression and Raman spectra acquisition.

Results and Discussion

All three genotypes demonstrate significantly different mineralization values (Fig. 2, Top), with the highest and the lowest values for the Göttingen and Yucatan minipigs accordingly. The same trend is observed for the yield stress values, with a non-significant difference between the Yucatan and Sinclair genotypes. The elastic moduli and yield strain values of the Göttingen genotype are similar to the Sinclair minipigs. From the correlation analysis, only yield strain showed a significant correlation with mineralization, primarily due to the high variations within the Yucatan genotype (Fig. 2, Bottom).
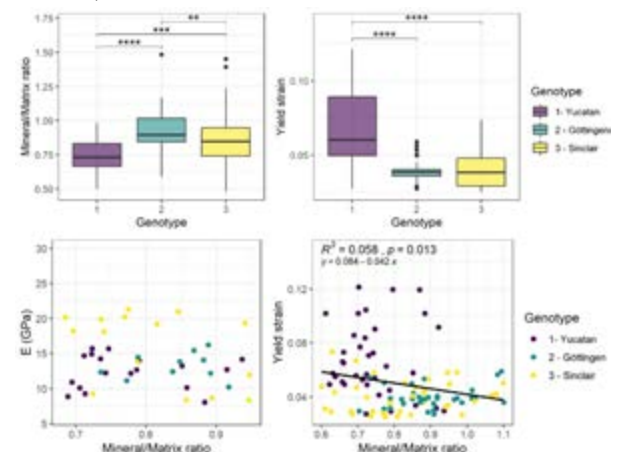
Figure 2: Top: Comparison of bone mineralization and yield strain between the minipig genotypes (**−p≤0.01, ***−p≤0.001, ****−p≤0.0001). Bottom: Elastic modulus and yield strain vs. bone mineralization.

Fs-laser ablation facilitated a high-throughput analysis of bone microscale compressive properties. Observed variations in the output mechanical parameters may be attributed to the structural and compositional heterogeneity of the samples. Measuring local compositional and mechanical properties in a site-matched fashion shed light on structure-property relationships of bone at the microscale. To extend the analysis, mineralized collagen fibril orientation and structural defects like hidden osteocytes and microvascular channels need to be taken into account in the future.

References

1. Pearce et al, *eCM Journal*, 13(0), 2007.
2. Schwiedrzik et al, *Nat Mat*, 13(7), 2014.

Acknowledgements

EXPERIMENTAL STUDY OF CERVICAL SPINE INJURY AND KINEMATICS IN LATERAL HEAD IMPACT

Marie-Hélène Beauséjour (1,2), Nicolas Bailly (1,2), Wei Wei (1), Lucas Troude (3), Paolo Panichelli (1), Pierre-Jean Arnoux (1,2)

1. Aix-Marseille Univ, Univ Gustave Eiffel, LBA, France; 2. iLab Spine : International Laboratory on Spine Imaging and Biomechanics, France & Canada ; 3. Neurosurgery, CHU Nord Marseille, France

Introduction

Lateral head impact occurs in motor vehicles roll-over crashes [1]. Roberts et al [1] have reproduced rollover crashes on post-mortem human surrogates and dummies and have noted that the Nij is ineffective to assess neck injury. Moreover, most previous experimental studies on neck injury have focused on axial compression or sled impact and the cervical spine kinematics during a lateral head impact have not yet been described nor associated with the risk of neck injury. This experimental study objective was to evaluate head kinematics and cervical spine injuries from a lateral head impact on human cadavers.

Methods

Five post-mortem human surrogates (2 males and 3 females) wearing a motorcycle helmet were hit to the lateral side of the head with a 37 kg impactor with a 45 degrees inclined surface at 3,5 (low velocity) or 5,1 m/s (high velocity). The impact conditions were chosen from previous multibody karting rollovers simulations showing that the head impact occurs in average at 4.5 m/s with an important tangential velocity. A previously designed test bench was used [2]. The surrogates were equipped with accelerometers at the sternum, at the vertebra T1, in the mouth and on the helmet. A load cell was placed on the impactor. Markers were positioned on the surrogates' helmet to measure the head kinematics by stereography (figure 1). After the impact, the surrogates were imaged by tomodensitometry and the cervical spine was dissected.
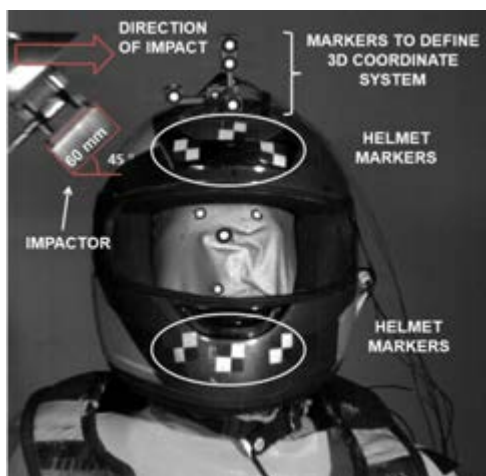
Figure 1: Experimental set-up, impactor and markers position.

Results

The cervical spine injuries found were: rupture of the posterior ligaments (at C1-C2 and C2-C3 for subject 1 and at C5-C6 for subject 4), articular facet fracture at C4-C5 for subject 4 and lamina fracture (at C3 for subject 2 and C7 for subject 1). The injuries were coherent with a previous roll-over experimental study [1]. Head maximal lateral bending during the impact was 35 to 53 degrees (table 1). The reported physiological head lateral bending is 44.5 degrees in each direction [3] which shows that lateral bending under or close to the physiological limit can cause injury. The average maximum resultant impact force was between 1800 N and 5600 N.

Subject number	Sex	Maximum resultant force (kN)	Maximum lateral bending rotation (degrees)	Maximum resultant acceleration (mouth) (g)
1	F	2.1	35	20
2	F	1.8	35	13
3	F	2.4	40	50
4	M	4.7	44	51
5	M	5.6	53	47

Table 1: Impact force, maximum head lateral bending in frontal plane and resultant acceleration recorded at mouth accelerometer.

Discussion

The forces and head kinematics measured in this experimental study are new and important data to understand the cervical spine response to head impact. They will serve as reference for neck injury tolerance and to design more efficient protective devices. This set of data has been used to validate finite elements simulations in an ongoing study which will enable the development of a new neck injury criterion specific for lateral head impact.

References

1. Roberts et al, Clin Biomech, 64, 2019.
2. Beauséjour et al, Clin Biomech, 92 : 105552, 2022.
3. Watier et al, ITBM-RBM, 27, 2006.

Acknowledgements

A MULTIMODAL FRAMEWORK FOR EVALUATING THE EFFICACY OF ORTHOPAEDIC IMPLANTS IN A SIDEWAYS FALL IMPACT

Emily Bliven (1), Anita Fung (2), Ingmar Fleps (3), Alexander Baker (2),
Benedikt Helgason (2), Pierre Guy (1), Peter Cripton (1)

1. University of British Columbia, Canada; 2. ETH-Zurich, Switzerland; 3. Boston University, USA

Introduction

Hip fracture is one of the most disabling and deadly events that an elderly person can experience. This injury is shown to most often occur in a sideways fall from standing height. Orthopaedic implants have been suggested as a preventative option to strengthen the fragile femur and prevent impending fracture in a vulnerable candidate. Despite trends in applied biomechanical test protocols, an appropriate way to comprehensively evaluate the performance of these constructs has yet to be demonstrated. This study presents a multimodal framework for testing orthopaedic implant efficacy in the proximal femur, which are promising candidates for hip fracture prevention in a sideways fall impact.

Methods

We integrated a custom-built biplanar x-ray system [1] into a previously-developed subject-specific fall simulator. The fall simulator has been used in combination with a corresponding finite element model, whose simulations accurately predict impact loading and fracture location [2].
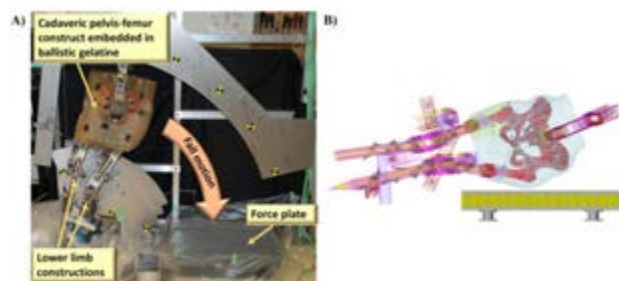
Figure 1: A) Experimental fall simulator, B) corresponding finite element model.

We assessed the feasibility of using the biplanar x-ray system to capture the impact of a femur implanted with orthopaedic hardware. This requires aligning the sources and image intensifiers of each system and taking preliminary images for undistortion and calibration (Figure 2). X-ray data collected using these methods is compatible with software tools for calculating rigid body kinematics such as XMALab and AutoScoper.

Results

We propose that fracture classification, bone structural deformation and impact force-time response can be compared between the experimental (implanted specimen) and computational analyses (native specimen) to gauge implant efficacy.
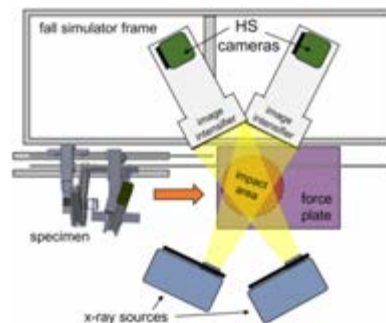
Figure 2: Overhead view of fall simulator with x-ray.

Supplementing the fall simulator with biplanar high speed x-ray offers additional context to the impact, with synchronized data that describes both relative bone-implant motion, fracture initiation, and progression.
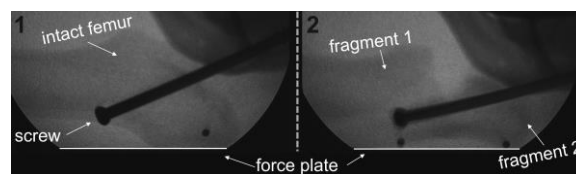
Figure 3: X-ray video frames showing fracture of a surrogate femur (A-P view) implanted with an orthopaedic screw and steel markers.

Discussion

The presented work offers a novel approach for investigating the efficacy of orthopaedic implants under impact loading simulating a sideways fall. This expands current biomechanical practice for evaluating such augmentations. Experimental methods used to date may lack biofidelity in that material testing machines apply loads to the femur as a stand-alone model and fracture is created in each specimen. In contrast, only a small percentage of fall-induced loading results in hip fracture in human subjects [3]. We anticipate that key insights into orthopaedic augmentation will be drawn from future cadaveric tests using this proposed framework. Fracture initiation and progression captured with x-ray may shed light on less-protected areas of the femur and correlate with computational predictions. Observing implant mechanics and fracture phenomena in a model that considers soft tissue effects offers valuable information for studying injury from a sideways fall impact when orthopaedic implants are present.

References

1. Whyte et al, J Biomech, 19:109279, 2019.
2. Fleps et al, J Bone Miner Res, 34:1837-1850, 2019.
3. Nachreiner et al, J Womens Health, 16:1437-1446, 2007.

CHANGE OF DIRECTION BIOMECHANICS AND COORDINATION IN ANTERIOR CRUCIATE LIGAMENT-INJURED FEMALE FOOTBALLERS

Stefano Di Paolo (1), Laura Bragonzoni (1), Alberto Grassi (2), Stefano Zaffagnini (2)

1. University of Bologna, Italy; 2. IRCCS Rizzoli Orthopaedic Institute, Italy

Introduction

The rapid growing of women's football leads to increasing rates and always earlier occurrence of primary of Anterior Cruciate Ligament (ACL) injury. A deeper comprehension of the ACL injury biomechanics in female football players has been advocated to target preventative interventions and mitigate the injury risk [1-2]. The purpose of this study was to investigate the biomechanical predictors of Anterior Cruciate Ligament (ACL) injury during a 90° change of direction (COD) task in a prospective cohort of female football players by means of 3D motion capture and vector coding technique.

Methods

Sixteen female first-division football players (age 19.5 years, range 18-22) were enrolled in this prospective pilot study. Every player performed a series of pre-planned 90° COD tasks. Players' biomechanics was collected through a set of 10 optoelectronic cameras (VICON Nexus, Vicon Motion Systems Ltd, Oxford, UK) in the ultimate foot contact before the change of direction.

In the next 2 consecutive football seasons, 4 ACL injuries (25%, all aged 18 years old) were registered.

Coupling angles through vector cording technique were computed for lower-limb angles. The following angle couples were investigated: hip flexion/knee flexion, hip rotation/knee flexion, knee varus-valgus/knee flexion, hip rotation/knee varus-valgus, knee varus-valgus/ankle inversion-eversion, and knee flexion/ankle flexion. Joint coordination and coordination variability were derived for each angle couple.

The student's t-test in Spm1D (p<0.05) was used to compare continuous biomechanics, joint coordination, and coordination variability between the ACL-injured (ACL-injured leg) and non-injured (dominant leg) players. The frequency of proximal/distal and in-phase/anti-phase coordination was also compared among the groups (Mann-Whitney U-test) for all the joint couples.

Results

The ACL-injured players showed greater (p<0.05) knee valgus and knee internal rotation (weight acceptance), external hip rotation (propulsion), ankle eversion (from midstance to propulsion), and pelvic contralateral drop (entire stance). Different coordination patterns were found both on the frontal and sagittal plane between ACL-injured and non-injured players. Knee dominance was noted in all the hip/knee couples on both the sagittal and frontal/transverse planes. Ankle distal dominance was also noted on both frontal and sagittal planes in knee/ankle couples (Figure 1). Anti-phase coordination was more frequent in ACL-injured players. ACL-injured players showed lower coordination variability for all the joint couples (p<0.001).

Figure 2: Hip flexion/Knee flexion coupling angle according to the different coordination patterns for ACL injury (red) and no injury (blue) players.

Discussion

Significant differences were found in terms of continuous biomechanical data and coordination patterns between ACL injured and non-injured players. The biomechanics and coordination patterns of the ACL-injured players were strongly consistent with the ACL injury mechanism underlined in in elite female players [2]. Due to the complex nature of the movements and the mechanisms leading to the ACL injury, innovative comprehensive approaches, such as the coupled biomechanics/coordination analysis, might inform ACL professionals on preventative strategies in women's football.

References

1. Silvers-Granelli, H., Int J Sports Phys Ther, 2021, 16(4);971:977
2. Lucarno S, et al., Am J Sports Med, 2021, May, 49(7); 1794:1802

Acknowledgements

MECHANICAL CARACTERIZATION OF A KNEE COMPRESSION FRACTURE BY H-DVC ON A CLINICAL CT-SCAN

Mathieu Severyns (1,2), Tanguy Vendeuvre (1,3), Kevin Aubert (1),
Valéry Valle (1), Arnaud Germaneau (1)

1 Institut Pprime, UPR 3346 CNRS – Université de Poitiers – ISAE-ENSMA, France
2 Department of Orthopaedic surgery and Traumatology, University Hospital, Martinique, France
3 Department of Orthopaedic Surgery and Traumatology, University Hospital, Poitiers, France.

Introduction

Compression fractures can occur for an axial weight loading on an articulation during daily movements [1]. The simplest fracture state is an epiphyseal depression of the articular surface. Age-related osteoporosis is a combination of a decrease in bone density and a change in bone microarchitecture [2]. One of the current challenges is to identify the risks of fractures in relation to physiological loads during daily movements. For this purpose, it is necessary to know the conditions of fracture occurrence and the pre-fracture limit parameters. Crack apparition can be identified by mechanical field measurements and from a strain level attained for which bone damage can occur. The use of Digital Volume Correlation (DVC) on physiological CT scan images recorded on patient before and during weight bearing could be a solution to measure strain levels and detect potential risk of fracture. The objective of the present work is to evaluate the ability of Digital Volume Correlation to provide quantified data allowing prevention of crack apparition. For that, we performed in situ loading tests on an anatomical segment up to articular fracture.

Methods

A fresh frozen anatomic specimen of knee (F/81yo) was prepared. In situ compression loading was performed on the specimen in the CT scan by using a specific setup (Figure 1). Several volume images were recorded for various loading steps up to three times the weight bearing. The volume fields were measured at each loading level in volume images by Heaviside based Digital Volume Correlation (H-DVC) [3]. The extended H-DVC proposed to modify the kinematical transformation permitting to address and capture displacements fields in case of apparition and propagation of cracks. The mathematical principle to determine the position $\varphi(X)$ in the deformed state of a point X from the initial one can be written on the entire voxel domain D as:

$$\varphi(X) = X + U + \frac{\partial U}{\partial X}(X - X_0) + U'.H(X - X_0) \quad (1)$$

Figure 1. Anatomic specimen and loading setup specifically developed for in situ testing in the CT scan

Results

Figure 2 shows displacement fields measured at the crack apparition for a loading of 1950N. We can identify a depressed fracture zone on the external condyle. Observation of displacement fields revealed a discontinuity of the cancellous bone area.
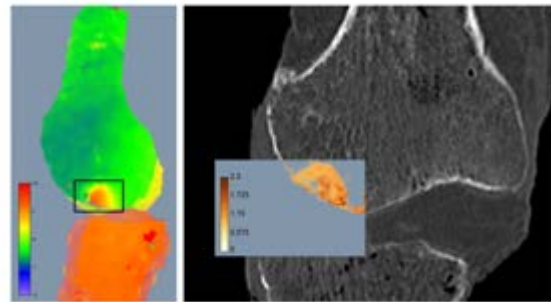
Figure 2. Displacement fields measured by H-DVC at the crack apparition during compression loading.

Discussion

Osteoporotic compression fractures, which can occur without trauma, are a public health issue. Detecting and treating these fractures before they occur remains a complex task. For some years now, we have access to weight bearing CT scans and the use of DVC on loaded and unloaded images would allow us to detect this fracture risk. Our study seems very promising because for a loading corresponding to a physiological stress on this osteoporotic anatomical subject, we were able to identify the pre-fracture kinematic fields of the bone trabeculae. Further studies will be needed on different anatomical segments but this work provides a proof of concept for the use of DVC in this application.

References

1. Chakhtoura M et al, J Bone Miner Res, 36:1942–1956, 2021.
2. McCloskey EV et al, J Bone Miner Res. 31:940–948, 2016.
3. Valle V et al, Exp Mech, 59:1–15, 2019.

SIMULATION OF BICYCLE ACCIDENTS USING HUMAN BODY MODELS

Karin Brolin (1), Victor Alvarez (1), Anna-Karin Säther (2), Dick Olsson (2), Heino Wendelrup (2)

1. Lightness by Design AB, Sweden; 2. Hövding Sverige AB, Sweden

Introduction

Single-bicycle accidents were the most common cycling accidents in Europe [1-4]. Vehicles were involved in a majority of the lethal bicycle accidents. Neck injuries were a small portion of all cycling injuries but associate with a large risk of permanent medical impairment. Hövding is a head protective device that is worn as a scarf around the neck, with sensors that trigger inflation of an airbag in the case of an accident. Theoretically, the portion of the airbag that surrounds the neck could protect from neck injuries (Fig. 1A).

The past ten years have seen drastic increases in research on finite element human body models (FE HBMs) [5-8]. HBMs with detailed neck models are good candidates to study neck injury protection in bicycle accidents. The aim of this study was to evaluate the suitability of two HBMs to predict neck injuries in bicycle accidents.

Methods

The FE code LS-DYNA was used for all simulations. The ViVA average size female HBM [10] and the GHBMC simplified average size male HBM [11] were positioned on an existing FE bicycle model [12]. An FE model of the inflated Hövding was developed (Fig.1B) and compared to experimental drop tests.
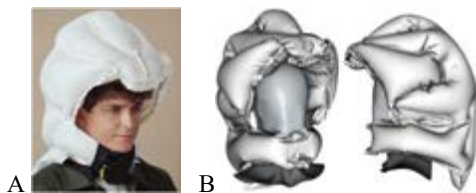
Figure 1: A. The physical inflated Hövding device (www.hovding.com). B. The developed FE model of inflated an inflated Hövding on a head form.

Simulations of a bicycle impact in a concrete pedestrian road barrier (5 m/s) were performed and compared to experiments with stunt persons. The concrete barrier mass was 250 kg and a sliding contact (0.3 friction) was defined to the ground. Constraints were defined for the hands-to-handlebar and feet-to-pedals that were active for 2-20 ms. Finally, varied head impact scenarios were simulated: 1) without protective system, 2) with the inflated Hövding FE model, and 3) with a generic bicycle helmet FE model.

Results

The inflated Hövding model compared well to the experimental drop tests, with similar accelerations of the head form and airbag thickness and pressure.

Fig. 2. illustrates the kinematics of the two HBMs compared to a stunt person. The bicycle kinematics and interaction with the HBMs were relatively similar to the experiments. The largest deviations were seen in the interaction between the legs and the barrier, due to differences in feet-pedal position between the volunteer and the HBMs. During the 'flight phase', the GHBMC's neck did not flex, while the ViVA's neck was very flexible (large extension and flexion). Thus, resulting in very different head impact conditions for the HBMs.

All head impact simulations ran without numerical issues for all three configurations. Both helmet and Hövding reduced the predicted head injury criteria. For the neck, the reductions of injury criteria with Hövding varied for the impact scenarios.

Figure 2: Comparison of kinematics at two instances in time during the barrier collision.

Discussion

Our results indicate that the methodology was promising. Our main conclusions were: 1) the initial position of the legs/feet on the pedals significantly influenced kinematics, 2) the road barrier friction and sliding on the ground was important to capture a realistic bike-barrier response, and 3) more experimental data representing other accident scenarios are needed before assessing personal safety systems.

References

1. Kjeldgård et al., BMC Public Health 19:943, 2019.
2. Rizzi et al., IRCOBI Conference, IRC-13-46, 2013.
3. Amoros et al. Inj. Prev. 18:27–32, 2012
4. Schepers et al. Cycling Res. Int., 2:119 – 135, 2012.
5. Jones et al. Traffic Inj Prev. 20(sup2): S96-S102, 2019.
6. Hu et al. Traffic Injury Prevention 20: S97-S105, 2018.
7. Iraeus et al. J. Mech Beh Biomed Mat. 106, 2020.
8. Östh et al. J. Biomech. 51:49-56, 2017.
9. Östh er al. J. Biomech. Eng. 138(6):061005, 2016.
10. Chalmers Univ. Tech. Downloaded (Jan. 2021) from https://www.chalmers.se/en/projects/pages/openhbm.aspx
11. Global human body model consortium's model, GHBMC-M50-OS. Licensed from Elemance Ltd (Clemmons, North Carolina, USA. https://www.elemance.com/)
12. Hardy et al. APROSYS Deliverable D3.2.3. p.43-44, 2004.

PERIPROSTHETIC FRACTURE MODELLING USING A COMBINED FINITE ELEMENT – SMOOTH PARTICLE HYDRODYNAMIC METHOD

Özgür Cebeci (1)(2), Sara Checa (2)

1. Ingenieurgesellschaft für Automobiltechnik (IAT) mbH, Germany; 2. Julius Wolff Institute, Berlin Institute of Health, Charité – Universitätsmedizin Berlin, Germany

Introduction

Periprosthetic femur fractures (PFFs) remain a major clinical challenge, which often result in patient death or the need for a complex re-operation [1]. Epidemiological studies show a relatively high number of PFFs during the early postoperative (EP) period, especially with cementless stems [2]. Due to the lack of bone ingrowth during this period, the mechanical behavior of the bone-stem interface plays a key role in the implanted femur strength.

Although previous studies have attempted to predict PFFs using finite element simulations, they were limited by using the element erosion criteria to eliminate highly distorted elements during simulation [3-4], which causes unphysical material loss and neglects the bone debris created during implantation [5].

The main objective of this study was to develop and validate a computer model to predict periprosthetic femoral fractures using a combined approach based on finite element (FE) and smoothed particle hydrodynamics (SPH) methods.

Methods

In this study, the trabecular and cortical bone segments were modeled using crushable foam and metal plasticity-based material models, respectively. Additionally, a maximum principal strain-based element erosion criteria was defined. Eroded trabecular bone elements were replaced with SHP particles, where the particles inherited the history variables of the eroded elements. Sliding contact definitions were defined between SPH particles, trabecular bone elements and the stem with the related coulomb friction coefficients.

Bone-stem interaction was validated based on the simplified implanting experiment reported by Ovesy et al. [4], where a conic probe was inserted into the trabecular bone with cyclic displacement.

In addition, two femur models representative of the experimental samples were constructed with statistical femur models and used to determine implanted femur strength in axial compression [6]. Finally, PFF simulations were compared with the experimental data in terms of axial compression strength.

Results

FE simulations combined with the SPH method showed good agreement with the simplified stem insertion experiment in terms of stem reaction forces. In addition, the combined model showed improved model performance in comparison to simulations without SPH method (figure-1).
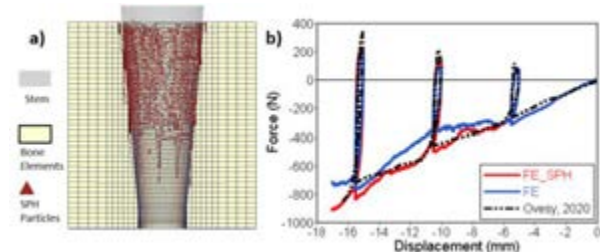
Figure 1: Simplified stem insertion simulation where eroded bone elements were replaced with SPH particles (a); Stem reaction force-displacement curves of the experiment (dash line), and simulations (blue: FE only, Red: combined FE-SPH) (b)

PFF simulations predicted the axial strength of the different groups of femurs with a median age of 65 and 79 years with an average absolute error of 13.95% (Table 1).

Age	Experiments (sd.)	Simulation	Error (%)
65 y.o.	5.02 (1.82) kN	5.53 kN	10.15%
79 y.o.	2.42 (0.64) kN	1.99 kN	-17.76%

Table 1: PFF simulation results in comparison to the experiments in terms of the axial strength.

Discussion

During implant insertion, highly deformed trabecular bone generates bone debris. Combined FE and SPH methods can model the stem-trabecular bone interaction taking the bone debris formations into account.

Using FE and SHP methods, simulation results showed good agreement with simplified implanting experiments. Additionally, PFF simulation results were also within the one standard deviation range of experiments regarding femur strength.

In the future, the modeling strategy presented in this study can help to more accurately predict and mitigate PFFs.

References

1. Drew et al, J. of Arthroplasty 10:01611, 2015.
2. Abdel et al, Bone Joint J, 98-B:468–74, 2016.
3. Miles et al, Med. Eng. & Physics, 37:567–573, 2015.
4. Ovesy, J. of Biomec. 107:109844, 2020.
5. Bätz et al, Clin. Biomech., 73: 234-240, 2020.
6. Jakubowitz et al, Med. Sci. Monit., 15(11): 307-312, 2009.

TOWARDS COMPUTATIONAL MODELLING OF ACTIVE RESPONSE IN CYCLIST FALLS FROM IN-THE-WILD FOOTAGE

Kevin Gildea (1), Ciaran Simms (1)

1. Department of Mechanical, Manufacturing & Biomedical Engineering, Trinity College Dublin, Ireland

Introduction

The self-protective effects of active response in unplanned falls is a well-established, yet under-researched area [1,2]. Our recent study demonstrated how single cyclist falls are prevalent (i.e., cyclist road traffic collisions not involving another road user) [3], and that active response is of particular importance in these cases [4]. This phenomenon has not been considered in previous computational modelling studies involving passive multibody models. Multibody dynamics solvers implement the equations of motion as an initial value problem, and it is known that resulting impact kinematics and dynamics are influenced significantly by initial posture and motion [5].

In recent years, many deep learning and computer vision-based 3D human pose estimation methods have been developed [6]. These techniques allow for inference of joint positions from monocular/stereo camera footage. In this study, we develop a pipeline for applying joint degrees of freedom (DOFs) and their 1st derivatives (linear and angular velocity) to represent active response using Madymo's pedestrian multibody ellipsoid model. As demonstration, we apply this to monocular footage of 30 cases of cyclist falls on railway tracks from [7].

Methods

Footage was spatially calibrated with respect to the ground-plane using the approach from [8], whereby scene points on the ground plane are manually annotated in both camera footage and a satellite image of the recording location (obtained from Google Earth). GAST-Net [9] was applied to obtain 3D poses. This is a regression-based method that employs a 2D keypoint pose estimator [10] (HRNet) as a backbone and lifts these estimates to 3D. To improve accuracy of the 3D pose estimates we manual repositioned 2D poses.

A temporal inverse kinematics (IK) optimization technique was developed to infer joint orientations in the Madymo multibody model to match the pose [11]. Linear and angular velocities were defined using the central difference method, and output as .xml include files for interpretation by the Madymo solver. The pipeline is demonstrated in Fig.1.

Discussion

The findings indicate that the limbs are used to prevent falls, absorb impact energy and protect the head in the case of single cyclist falls. This is supported by findings from our analysis of single cyclist fall types [4]. The kinematic forms characterized in this study can be used to inform initial conditions for computational modelling and injury estimation in single cyclist falls.

We have developed a novel pipeline which allows for semi-automatic inference of human kinematics from in-the-wild video footage for reconstruction in Madymo. This approach can be applied to a variety of impact biomechanics tasks not limited to cyclist falls.

References

1. Feldman et al, J. Biomech., 40: 2612-2618, 2007
2. Hsiao et al, J. Biomech., 31: 1-9, 1997
3. Gildea et al, AAP, 151: 106264, 2021
4. Gildea et al, AAP, 159: 105948, 2021
5. Li et al, AAP, 85: 83-92, 2015
6. Zheng et al, J. ACM, 37, 2022.
7. Ling et al, JTH, 7: 54-63, 2017
8. Tsai , IEEE j. robot. autom., 34: 323–344, 1987
9. Liu et al, ICCV, 2272–2281, 2019
10. Sun et al, CVPR, 2019
11. Gildea et al, ESBbiomech 2022 [**Submitted to AI in Biomechanics track**]

Acknowledgements
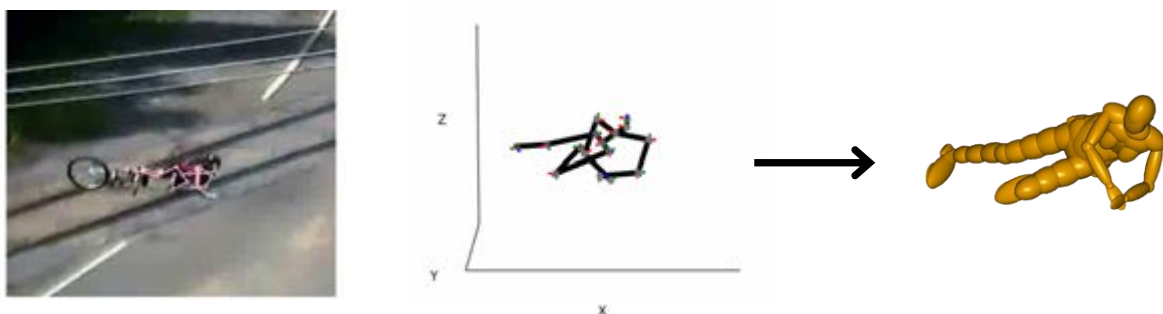
Figure 1: Pipeline for reconstruction of cyclist falls from monocular camera footage.

SIMULATING HEAD-FIRST IMPACT IN SPORT: A HYBRID MULTIBODY AND FINITE ELEMENT HEAD AND NECK MODEL

Thomas Holzinger (1,2), Johannes Martinek (1), Dario Cazzola (3), Benedikt Sagl (2)

1. University of Applied Sciences Technikum Wien, Austria; 2. Medical University of Vienna, Austria
3. University of Bath, United Kingdom

Introduction

Spinal cord injuries can have a severe impact on people's life. Therefore, it is important to investigate the mechanisms responsible for such injuries. Computational models can help to gain insight into the injury mechanisms using theoretical simulations of injurious events. Yet, most multibody muscle-driven models consist of rigid bodies and consequently are not appropriate for fully replicating injuries involving tissue deformation [1, 2]. A potential solution is the use of a dynamic model that combines rigid bones, muscles, and finite element (FE) models of the inter-vertebral discs (IVDs). However, the appropriate material properties for the FE IVDs during impact events are not well known. Thus, we used an experiment-driven approach for optimising the material properties of the IVDs using data collected during simulated head-first injuries. These parameters were included in a human cervical spine model to perform axial impact simulations.
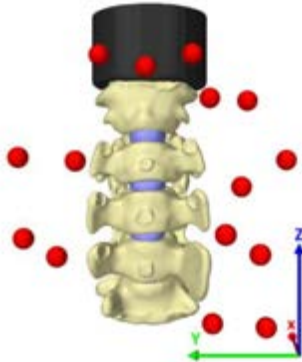
Figure 1: An in silico simulation replicating the experimental test described in [1].

Methods

Impact data of five pig spines (S1-S5) collected by [1], using an impact fixture described in [3], were used for the study. For validation purposes, animal-specific in silico models of the experiments were created in ArtiSynth (www.artisynth.org) (Figure 1). A hyper-elastic Mooney-Rivlin material was used to model the mechanical behavior of the FE IVDs. The strain energy function of the material is described by the equation:

$$W(I_1, I_2) = C_1 (I_1 - 3) + C_2 (I_2 - 3) \qquad (1)$$

where C_1 and C_2 are the material constants and I_1, I_2 are the first and second invariant of the left Cauchy-Green deformation tensor. We computed a total of 2500 simulations with different combinations, varying each constant from 0.1 MPa to 30 MPa. The root means square error (RMSE) between the *in vitro* and *in silico* marker traces was calculated and compared to results

using individually optimized bushing elements [1] ($RMSE_{bushing}$) or stiffness and damping values derived from functional movements [2] ($RMSE_{FM}$). Lastly, a human cervical spine model was created from an existent OpenSim model [1], where the bushing elements were replaced with FE IVDs, and head-first axial impact forward simulations were performed.

Results

The median values over all specimens are 12.56 MPa for C_1 and 0.48 MPa for C_2. Table 1 shows that the RMSE computed in this study is slightly larger than reported by [1], while it is smaller than the RMSE computed in [3].

Specimen Nr.	$RMSE_{bushing}$ [mm]	$RMSE_{FM}$ [mm]	$RMSE_{FE}$ [mm]
S1	0.46	2.59	0.80
S2	0.33	2.28	0.36
S3	0.58	2.08	0.72
S4	0.51	2.60	0.72
S5	0.44	2.30	0.71

Table 1: RMSE over the 15 markers using our material properties (FE), and two comparable models [1,2].

The material properties used for FE simulations provided a kinematics error in the same order of magnitude of the one generated using individually optimized bushings [1], and overperformed the material properties derived from [2].

Discussion

Our approach seems to overestimate the stiffness of the IVDs, when compared to the model including bushing elements. This can be explained by the fact that the material properties were systematically varied rather than optimised using a heuristic algorithm as done in [1] for the bushing parameters. Additionally, the same material properties are used for all IVDs, while the optimisation performed in [1] allowed for different material properties for all IVDs. However, the single combination of material properties generated much better results than the material properties taken from a comparable study [2], highlighting the importance of impact-specific parameters to simulate head-first injurious scenarios. Future work should focus on identifying such parameters for individual IVDs to enable the simulation of injury in sporting and automotive scenarios.

References

1. Silvestros et al. PLoS One, 2019.
2. de Bruijn et al. Multibody Syst. Dyn.,34:1-24, 2016.
3. Holsgrove et al. J. Spine, 15:1856-63, 2015.

BIOMECHANICAL BEHAVIOUR OF THE TRANSVERSE LIGAMENT OF THE ATLAS: AN *IN VITRO* EXPERIMENTAL ANALYSIS

Sébastien Laporte (1), Sylvain Persohn (1), Baptiste Sandoz (1)

1. Arts et Métiers Institute of Technology, Université Sorbonne Paris Nord, IBHGC - Institut de Biomécanique Humaine Georges Charpak, Paris, France

Introduction

The biomechanical behavior of the transverse atlas ligament has been sparsely described in the literature with very various experimental protocols [1,2,3,4,5]. However, a good description of its behavior is necessary both for a detailed understanding of the biomechanical behavior of the craniocervical joint and for the development of geometric and mechanical models of the upper cervical spine.

In order to reduce this knowledge gap, the aim of this study is to investigate the biomechanical behavior until rupture of the transverse atlas ligament, for a quasi-static load close to physiological conditions.

Methods

Ten Atlas vertebrae from PMHS (59 ± 6 yo, 5♀/5♂) were imaged using µCT (0.1x0.1x0.1 mm), fresh-frozen for storage, thawed at room temperature the day before test. An anteroposterior quasi-static traction test (5 mm/min) of the transverse ligament [2] was performed using an 10 mm diameter cylinder on an INSTRON machine model 5566 (Figure 1).

From the force-displacement curves, the anteroposterior stiffness (N/mm), rupture force (N) and rupture displacement (mm) were identified. A digital camera, synchronized with the test machine, was used to identify injury mechanisms.
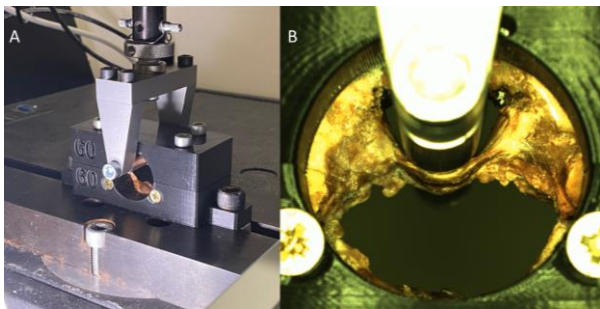
Figure 1: A) Global view of the test bench, the atlas vertebra is fixed in a personalized 3D-printed support. B) View from the digital camera.

Results

For three ligaments, failure was observed for very low loads (<150 N) and were then excluded from the analysis. For the other seven specimens, the same mechanical behavior is observed, with a toe of curve followed by a linear phase until quasi-fragile failure (Figure 2). In six cases, the rupture was associated with delamination of the posterior fibers and in only one case with a bone tear.
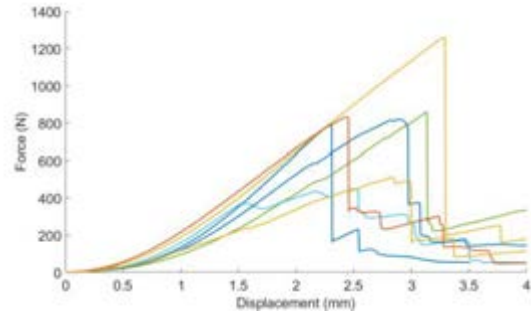
Figure 2: Force Displacement curves for the seven transverse ligament specimens.

The identified stiffness is 412 ± 98 N/mm (mean ± SD), the identified rupture force is 790 ± 245 N and the identified rupture displacement is 2.8 ± 0.3 mm.

Discussion

For the three ligaments with very poor mechanical behavior, the ligaments were injured during sample dissection.

As explained in the introduction, trial protocols are disparate in the literature, making it difficult to compare our results with previous studies. Comparison of our results with those of Heller et al [5] shows that our results for displacement and force to rupture are lower; however, it should be noted that the loading speeds are different (from 60 mm/min to 5.1 m/min) and that the definition of failure by Heller et al. is not clear.

The injury mechanisms obtained are consistent with the type of loading applied, with the posterior fiber bundles being the most loaded for the test conditions in our study.

A more detailed modeling of these tests (Finite Element Modeling for example) should make it possible to determine the mechanical properties of this tissue (Young's modulus, rupture stress and strain, ...) necessary for its mechanical modeling.

References

1. Dvorak et al, J Orthop Res 6:452–461, 1988
2. Heller et al, J Spinal Disord, 6:162-165, 1993.
3. Panjabi et al, Clin Biomech, 13:112-120, 1998.
4. Shim et al, Exp Mech, 46:77-89,2006.
5. Mattuci et al, JMBBM, 23:71-79, 2013.

Acknowledgements

E-SCOOTER CRASH SCENARIO AND KINEMATICS: ANALYSIS OF 112 CRASH VIDEOS

Nicolas Bailly (1,2), Sarah Honore (1), Yvan Petit (2,3,4), Alexandre Naaim (5), Antoine Muller(5), Wei Wei (1,2)

1. Aix-Marseille Univ, Univ Gustave Eiffel, LBA, France; 2. iLab-Spine: International Laboratory on Spine Imaging and Biomechanics, France; 3. École de technologie supérieure, Canada; 4. Research Center, CIUSS Nord de l'île de Montréal, Canada; 5. Univ Lyon 1, Univ Gustave Eiffel, LBMC, France

Introduction

E-scooter practice and consequently E-scooter-related head injuries have dramatically increased the last few years. Several studies have shown that the most frequent type of crash was simple fall (73,5%), followed by the collision with a vehicle (11%) [1]. However, the detailed scenario leading to the injury as well as the head impact conditions is poorly known. The objective of this study is to collect and analyze videos of E-scooter crash in order to identify detailed E-scooter crash scenarios and obtain the kinematics of the accident (initial speed and impact speed of the body).

Method

A systematic research of E-scooter crash videos was conducted on the Google video and YouTube search engines. Every video with an unintentional E-scooter accident was included. The analysis consisted in describing the crash: type, location, causes, part of the body impacted and a fall description with the help of sketches. When it was possible (quality of the video, direction of the fall, angle of the camera), the riding speed before the crash and the impact speed (speed of the body part when impacting the ground or the obstacle) were measured using the software Kinovea according to the method described by Shishov et al.[2].

Results

A total of 112 videos of E-scooter crash were collected and analyzed. Among the e-scooter crashes, 59% were simple falls, 28% collision with another vehicle, 9 % collision against an obstacle and 4% collision against a pedestrian. During simple falls, 57% of the users fell on the side while 36% fell on the front (head first). Falls were mainly due to a loss of control (56%) and irregularities on the road (18%). Collisions with vehicles occurred mainly with a car (36%) or with another E-scooter (36%) mostly due to infringements of the highway code (53%). Overall, the head was the most impacted zone (43%) followed by the hip (40%), upper limb (36%) and shoulder (35%).

Velocity before the crash and at the impact were measured on 12 fall videos, 9 of which involved a head impact against the ground. Figure 1 presents the measured riding speed and impact speed. The mean riding speed before the crash was 4.2 (±1.3) m/s. The mean tangential impact speed was 3.8 (±2) m/s and mean normal impact speed was 3.1 (±1.3) m/s.
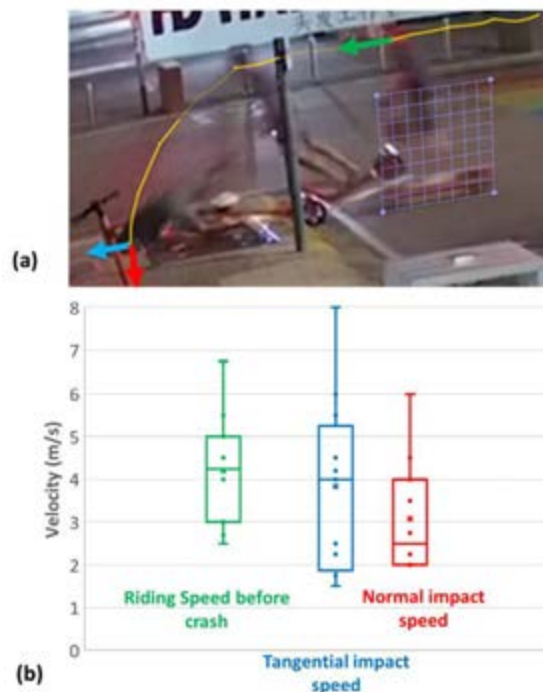
Figure: (a) example of the speed analysis during an E-scooter fall and (b) the riding speed, tangential impact speed and normal impact speed measured in 12 videos of falls. Scattered dots represent measured values and cross represents the mean value.

Discussion

This study is a first biomechanical analysis of E-scooter crashes from real crash videos. It provides new knowledge on the overall scenario of 112 E-scooter crashes as well as detailed impact kinematics in 12 E-scooter falls. Those data are valuable to evaluate and design protections. We found that the normal impact speed measured during falls was consistent with current helmet standards evaluation but we also measured high tangential speed not currently accounted in standard evaluations. Those findings are consistent with the findings of Posirisuk et al [3]. One limitation of this work may be the lack of representativeness of the videos found on the internet compared to epidemiological studies. However, the type of crash and scenario distribution is consistent with previous epidemiological studies[1].

References

1. M. Kim *et al.*, *J. Korean Soc. Traumatol.*, 2021
2. N. Shishov et al. *PLOS ONE*, 2021
3. P. Posirisuk et al., *Accid. Anal. Prev.*, 2022

BIOMECHANICAL STUDY OF ELECTRIC SCOOTER FALLS

Marion Fournier (1, 2, 4), Nicolas Bailly (3, 4), Andreas Schäuble (5), Yvan Petit (1, 2, 4)

*1. École de technologie supérieure, Canada; 2. Research Center, CIUSS Nord de l'île de Montréal, Canada;
3. Univ Gustave Eiffel, LBA, France; 4. iLab-Spine: International Laboratory on Spine Imaging and
Biomechanics, France; 5. DEKRA Automobil GmbH, Germany*

Introduction

In the last few years, e-scooters have shown an increase of popularity as a form of micro-mobility transport in urban areas. However, the risk of accident for e-scooter riders is 167 times more than for car drivers [1]. During these accidents, the head is one of the most injured body parts. Fifty eight percent of hospitalizations are due to head injury according to Trivedi et al [2]. In addition, the use of protective gear remains very low [3]. As e-scooters are a relatively new modality of transport there is a lack of knowledge on the fall kinematics and impact conditions during crashes. The objective of this work is to reproduce numerically an e-scooter crash to evaluate the kinematic and impact conditions of the head.

Methods

A multibody model of e-scooter fall was built using the Madymo software. The pedestrian model of Madymo was used to represent an e-scooter rider and the e-scooter model was based on the ESA 1919 EKFV e-scooter. The scenario of simulation was an e-scooter forward fall induced by the collision with a curb. The model was validated against an experimental e-scooter crash test performed with a Hybrid III dummy (Figure 1): the experimental kinematics of the head was compared to that of the multibody model. A design of experiment was performed to evaluate the effect of fall conditions (initial speed, orientation of the obstacle, size of user, e-scooter inclination) on the head impact kinematics (impact speed and acceleration).
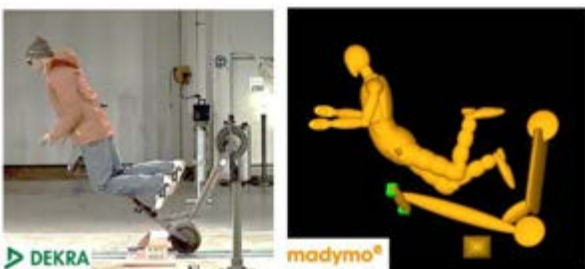
Figure 1: Comparison of the experimental (DEKRA) and the numerical (Madymo) fall for the model validation.

Results

Our results show that the head kinematics of the numerical model is consistent with that of the experimental test. One hundred and sixty two crashes scenarios were simulated. In 62 % of those, the head first hit the ground in the frontal and temporal zone. The average tangential and normal impact speeds were 3,5 m/s and 4,8 m/s respectively. The average peak linear acceleration was 571 g and the average peak rotational acceleration was 25580 rad/s². Nearly 100 % of the simulations identify a risk of concussion (linear acceleration peak>82 g and rotational acceleration peak >6383 rad/s²) (Figure 2) and 90 % of simulations suggest severe head injuries (HIC>700). E-scooter speed (p<0,001) and inclination (p=0,001) are the most significant factors contributing to the head impact speed and the risk of injury.
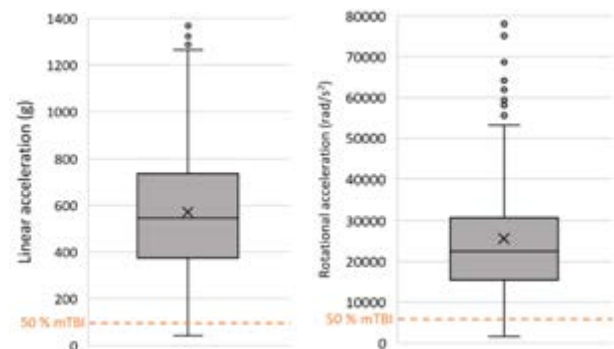
Figure 2: Linear and rotational acceleration distribution and injury threshold.

Discussion

This study is a first step in evaluating the head impact conditions that could occur in an individual e-scooter accident. It provides new knowledge on head acceleration during those crashes. A high risk of head injury was identified which is consistent with epidemiological data. Also, a typical head impact speed during an e-scooter crash was identified. This could be used during helmet standard evaluations.

References

1. Rix et al, The American Journal of Emergency Medicine, 2020.
2. Trivedi et al, JAMA Network Open, 2(1), 2019.
3. PBOT, E-Scooter Findings Report, 2018.
4. Zhang et al, J Biomech Eng, 226:236-126(2), 2004.
5. Rowson et al, Annals of Biomed Eng, 1:13-40(1), 2012.
6. Eppinger et al, Development of Improved Injury Criteria for the Assessment of Advanced Automotive Restraint Systems—II, 1999.
7. Takhounts et al, Stapp Car Crash Journal, 243:266-57, 2013.

Acknowledgements

PELVIC SUBCUTANEOUS ADIPOSE TISSUE THICKNESS AND OUTER SHAPE CHANGE WITH POSITION FOR NUMERICAL MODELING

Daniel Hanesch (1), Julia Muehlbauer (1), Elke C. Sattler (2), Nicholas Moellhoff (3), Riccardo E. Giunta (3), Steffen Peldschus (1), Sylvia Schick(1)

1. *Biomechanics and Accident Analysis, Institute of Legal Medicine, LMU Munich, Germany*
2. *Department of Dermatology and Allergy, University Hospital, LMU Munich, Germany*
3. *Division of Hand, Plastic and Aesthetic Surgery, University Hospital, LMU Munich, Germany*

Introduction

The distribution of soft tissue around the anterior superior iliac spine (ASIS) is hypothesized as critical factor for seatbelt occupant interaction [1]. State-of-the-art Finite Element (FE) Human Body Model (HBM) subcutaneous adipose tissue (SAT) thickness values mostly are based upon supine medical imaging. So far, an increase in SAT thickness above the ASIS from supine to a sitting posture has been observed in a single individual [2]. To improve FE HBM geometry for seating positions more robust SAT thickness transfer data for different sitting postures is needed [3]. This study characterizes SAT thickness above the ASIS in four different body positions through sonography to narrow the gap in current FE HBM morphology.

Methods

Ethical approval was obtained from the Medical Faculty Ethics Committee of the University of Munich LMU. The study included ten healthy 50th percentile male volunteers aged 27.5 years (median) (range 22-31) (body height: 180cm (175-186); body weight: 80.5kg (73.0-86.5); BMI: 24.9 (22.8-25.9). The SAT thickness was measured non-invasively between the ASIS and the skin surface using a linear handheld 9.0 MHz sonographic probe (Logiq P9, General Electric, USA) by the same operator. Four body positions were tested: supine, resting (seat angle 5°, backrest angle 45°), driving (seat angle 5°, backrest angle 15°) and upright standing. For each, three measurements were taken with as little pressure as possible, shortly before losing body contact with the probe. For the supine position, a second measurement series was taken pressing the probe onto the ASIS. Median values per position and volunteer are utilized. Pairwise non-parametric tests for dependent samples with Bonferroni adjustment are applied to detect differences between postures. In addition, 3D surface objects of all subjects in every posture were reconstructed from high-resolution images using 92 cameras simultaneously (Vectra WB360, Canfield Scientific Inc., USA) (Figure 1).

Results

In Figure 1, median values per volunteer and position are presented. Median SAT thickness for ten volunteers each in supine, resting, driving and standing posture in [cm] was 0.56, 0.90, 1.09 and 0.89, respectively. In nine out of ten subjects, ASIS SAT thickness increased with increasing seatback angle. The individual SAT minimum was always found in supine posture. The median transfer factor for SAT thickness above the ASIS from supine to resting posture is 1.54 (range 1.02 - 1.87) and from supine to driving posture 1.81 (range 1.41 - 2.22). The within-subject difference in SAT thickness between with and without pressure for the supine posture was 0.35±0.14 cm. Significant differences between positions was found for driving vs supine (p=0.000) and resting vs supine (p=0.019).
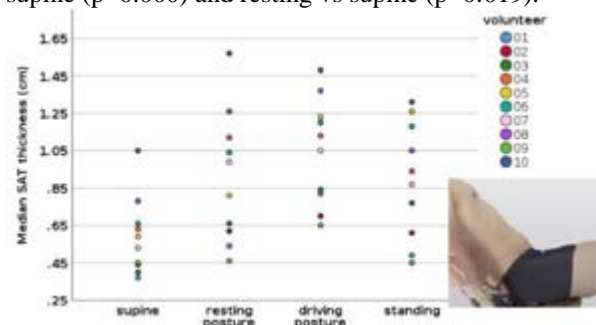
Figure 1 Median SAT thickness (cm) above the ASIS in four body postures (n=10) and a 3D-object of a resting volunteer

Discussion

For the first time, ASIS SAT thickness values for two sitting postures, supine and standing posture are presented. When seated, the more vertical the upper body is positioned, the more SAT thickness tended to increase at ASIS level. As SAT thickness was smallest in supine posture, it might be underestimated in current FE HBM. A transfer factor of 6 from supine to sitting measured based on one post mortem subject in [2] cannot be confirmed within the present cohort. Various factors, e.g. imaging modality, posture, age and post mortem processes, may contribute to this deviation. Combined SAT thickness data and reconstructed 3D-objects may inform design modifications for existing and future FE HBM, ensuring a more biofidelic soft tissue representation in a key region for belt engagement.

References

1. Hartka et al., Traffic Injury Prevention, 2018
2. Schick et al., Traffic Injury Prevention, 2021
3. Gayzik et al., RCCADS workshop, 2021.

Acknowledgements

DEVELOPMENT OF A SIMPLIFIED HUMAN THORACIC FE MODEL FOR BLUNT IMPACT AND RELATED TRAUMA

M. Chaufer (1), R. Delille (2), B.Bourel (2), C. Marechal (2), F. Lauro (2), O. Mauzac (3), S.Roth (1)

1. Interdisciplinary Laboratory Carnot of Bourgogne, site UTBM, UMR 6303, CNRS / Univ. Bourgogne Franche-Comté (UBFC), 90010 Belfort, France; 2. Laboratory LAMIH UMR 8201 CNRS, Univ. Polytechnique Hauts-de-France, 59313 Valenciennes, France; 3. French Ministry of the Interior, CREL/SAELSI, Place Beauveau, Paris, France

Introduction

Several problems of mechanical engineering can be solved by using finite element approach. In the framework of biomechanics, the use of numerical procedures helps dealing with ethical issues when conducting experiments. Thus, for the evaluation of protective device, the use of such models has shown their wide interest. Nevertheless, developing numerical model of protective device, like body armor, has always been complex. Therefore, it would be interesting to develop an instrumented physical surrogate of human thorax for protection assessment. Since materials laws and mechanical properties implemented in the numerical model are not easily manufacturable, simplifications are needed. These simplifications will be considered in a new simplified FE model. This FE model must be validated according to well-known experiments. This study proposes a simplified human thorax finite element model based on HUByx, a finite element model of the human thorax [1]. This model was validated against experimental data of the literature [2]. These data are reused in this study as a reference to validate the simplified finite element model of human torso called SurHUByx for Surrogate Hermaphrodite Universal Body YX. SurHUByx shows consistent and interesting results compared to experimental data.

Methods

The study focuses on the development and the validation of SurHUByx biomechanical model. All the implemented material laws and components must be manufacturable and show a biofidelic behavior. In this way, cortical and trabecular parts of bones and costal cartilage had been merged. New material properties were computed using an equivalence in terms of module of inertia. Parameters are available in table 1.

Parameters	Bones	Cartilage
Density (g/mm^3)	0.0012	0.0010
Young Modulus (MPa)	20226	148
Fracture plastic strain	0.02	-

Table 1: New bones and costal cartilage properties.

SEBS (styrene-ethylene-butylene-styrene) is considered as a good substitute of human soft tissue, with numerous advantages such as mechanical consistency and transparency [3]. Transparency can help during experimentations. SEBS was used to model soft tissues and muscle [4]. The mediastinum was modeled with an elastic law using the properties of a synthetic gelatin E= 0.05MPa. The properties of Hybrid III skin were used to model the skin. Finally, to validate SurHUByx authors proposed a numerical recreation of test conducted on postmortem subjects by Bir et al. [2]. The impact cases consist in three different experimental condition (A, B, C) where various rigid projectiles impacted the mid sternum at different velocities. Experimental corridors were provided in the experimental study, which allow validating the numerical model in terms of sternal deflection time history. These tests are reference tests in ballistic even if significant differences may exist with living tissue experiments. The rear of the projectile had been used to plot curves.

Results

Figure 1 illustrates the different deflection time history in relation with their corresponding experimental corridors for impacts A, B, C.
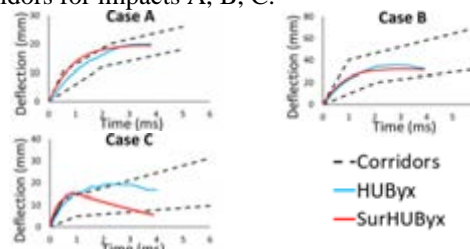
Figure 1: Comparison of Hubyx and SurHUByx deflection time curve.

With the unification of cortical and trabecular parts and new simplified constitutive laws, numerical results are inside the corridors for each impact, allowing using simple and manufacturable material which will be used for further development of the physical surrogate.

Discussion

The model presented in this paper, provide good results and the model can be considered as biofidelic. As a result, a physical surrogate based on SurHUByx with its simplified material properties can be built.

References

1. Chaufer et al, CMBBE, 24: sup1, S310-S311, 2021.
2. Bir and al, J. Biomech, 37:73-7, 2004.
3. Mrozek RA et al, JMBBM 44:109-1.2015.
4. Bracq et al, Int. J. Impact Eng. 118:78-90, 2018.

Acknowledgements

BIOMECHANICAL EVALUATION OF THE SPATIAL CONFIGURATIONS OF STABILIZER USED IN DISTAL HUMERUS FRACTURE TREATMENT

Artur Kruszewski (1), Piotr Piekarczyk (2), Szczepan Piszczatowski (1)

1. Bialystok University of Technology, Poland; 2. Military Institute of Medicine, Department of Traumatology and Orthopaedics, Poland

Introduction

Treatment of complex intra-articular, multifragmental fractures of the distal humerus is still challenging and associated with the high risk of complications. Open Reduction and Internal Fixation (ORIF) with use of two contoured locking plates is nowadays a gold standard in such cases [1]. However, optimal spatial configuration of the stabilizer is still a matter of debate. For this reason, the aim of the presented study was to provide reliable information on the influence of the spatial stabilizer configuration on the biomechanical conditions in the treatment of typical variants of fracture of the distal part of the humerus.

Methods

Physical models (fig.1a) of three types of distal humerus fractures, medial λ, H and Y according to Jupiter and Mehne classification, were prepared with use of composite model of humerus (Sawbone 4th Gen., Composite). Each of them was fixed using Variax Elbow Locking Plate System (Stryker, USA) applied in three different spatial configurations: parallel, posteromedial and posterolateral [2]. Simultaneously, FEM models (fig.1b) of particular variants of the humerus – stabilizer system were prepared using preprocessor of the ANSYS software.
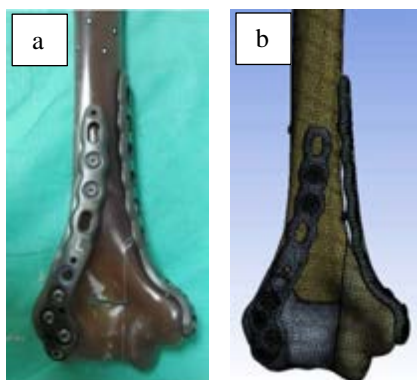
Figure 1: Physical (a) and numerical (b) model of the distal humerus fracture (medial λ) fixed with the Variax stabilizer in posterolateral configuration consisting of the medial and posterolateral plates

Physical models of the fractured humerus - stabilizer system were tested using the MTS Insight 1kN machine under loadings occurring in elbow joint flexed in the range 0 - 145° [3]. The same loadings were applied also in numerical analyses. Additional variants of loadings were analyzed using only numerical simulation.

Results

Global stiffness of the fractured humerus – stabilizer system as well as deformity of particular plates of stabilizer were evaluated using both physical and numerical models. Additionally, mutual displacement between particular bone fragments were calculated basing on results of numerical simulations (fig. 2).
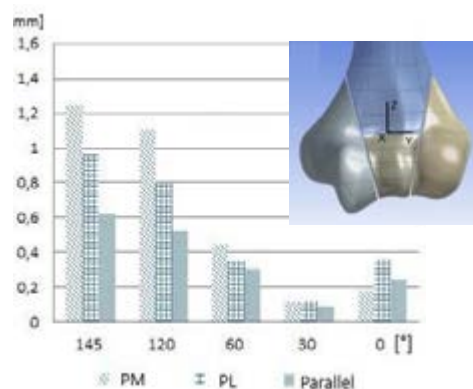
Figure 2: Mutual displacement in x-y plane (tangential component) between distal fragment and the shaft of humerus in the coronoid fossa region for various elbow joint angle (0 - 145°). Exemplary results for H fracture fixed using posteromedial (PM), posterolateral (PL) and parallel configurations of the stabilizer

Discussion

The results obtained for particular variants of the fractured humerus - stabilizer model clearly indicate that stabilizer does not always provide biomechanical conditions for the fracture healing. Spatial configuration of the stabilizer should be carefully fitted to individual fracture characteristics. Numerical modelling could be very helpful in such process, especially in the most complex cases.

References

1. Goel et al, Oper Tech Orthop, 20: 24-33, 2010.
2. Kruszewski et al, Acta Bioeng Biomech, 22(1): 153-163, 2020.
3. Kindcaid and An, J Biomech, 46: 2331–2341, 2013.

Acknowledgements

CHANGES IN LOADING DURING FRACTURE HEALING DO NOT IMPACT BONE MICROARCHITECTURE OF THE CONTRALATERAL RADIUS

Danielle Whittier (1,4), Matthias Walle (1), Patrik Christen (2), Penny Atkins (1), Caitlyn Collins (1), Michael Blauth (3), Kurt Lippuner (4), Ralph Müller (1)

1. Institute for Biomechanics, ETH Zurich, Switzerland; 2. Institute for Information Systems, FHNW, Switzerland; 3. Department Trauma Surgery, Innsbruck University Hospital, Austria.; 4. Department of Osteoporosis, Bern University Hospital, Switzerland

Introduction

The study of fracture healing using high-resolution peripheral quantitative computed tomography (HR-pQCT) has the potential to improve our understanding of bone (re)modelling during healing *in vivo* [1]. The contralateral radius is typically used as a control [1,2], but day-to-day use, and thus mechanical loading, of the contralateral radius, can be temporarily increased due to immobilisation of the fractured wrist. Mechanical loading interventions have demonstrated that bone microarchitecture can adapt to changes in arm loading during a relatively short period (<1 year) and that the magnitude of change is influenced by hand dominance [2]. This study aims to evaluate whether the temporary increase in mechanical stimuli of the unfractured arm during fracture healing is sufficient to induce measurable changes in HR-pQCT parameters.

Methods

Patients who had a distal radius fracture were recruited from two clinical centres in Bern, Switzerland and Innsbruck, Austria. Fractures were immobilised using casts for about 5 weeks as part of standard clinical care. HR-pQCT (XtremeCT II, Scanco Medical AG, 61 µm) scans of the fractured and contralateral distal radii were obtained at 1-, 3-, 5-, 12-, 26-, and 52-weeks post-fracture. Scans with high image motion artefacts were removed prior to analysis [3]. The common region across time points was determined using 3D image registration, and the standard morphological analysis protocol was implemented to measure bone mineral density (BMD), microarchitecture, and cross-sectional areas. The absolute change in bone parameters at each follow-up time point relative to baseline (week 1) were compared against previously reported least significant change (LSC) values to determine whether within-patient changes in the contralateral wrist could be considered significant [4]. Group-level temporal changes in HR-pQCT parameters were evaluated using mixed-effects regression models. Hand dominance, sex, and age were added as fixed effects for assessing whether they significantly (p<0.05) influence temporal changes in bone properties.

Results

Data from 24 patients (63% female, mean age 45.8 ± 17.0 years) were available, where 13 patients had completed all study visits at the time of analysis, and all participants had at least three time points with scans of adequate image quality. Half (n=12) of the patients had fractured their dominant arm. Absolute changes in HR-pQCT parameters showed that cortical BMD, trabecular number (Tb.N), bone volume fraction, and cortical porosity exceeded LSC for more than one patient during follow-up, while all other parameters had no more than one patient temporarily exceed LSC (Figure 1). Tb.N had the highest ratio of patients exceeding LSC at any timepoint, reaching a maximum of 32% of patients with changes above LSC at 3 months post-fracture. However, changes were typically modest and not sustained for the full 52-week follow-up. Mixed-effects models found no significant temporal changes in Tb.N or other HR-pQCT parameters of the contralateral radius (Figure 1, p=0.07), and covariates (age, sex, and hand dominance) had no significant association with temporal changes.
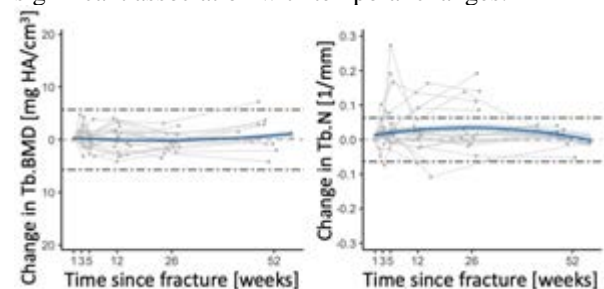
Figure 1: Changes relative to baseline in trabecular BMD (Tb.BMD) and trabecular number (Tb.N) of the contralateral radius during recovery. Individual patient trajectories (n=24) are shown in grey, and mixed-effects regression in blue. The dashed horizontal lines represent thresholds for LSC.

Discussion

Few patients experienced changes in bone parameters of the uninjured radius that exceeded LSC, indicating the possible increase in loading does not induce sufficient mechanical stimuli to cause lasting changes in bone microarchitecture. Temporary increases in Tb.N indicate that mechanical stimuli may induce some remodelling activity, and assessment of local bone morphometry may allow for local structural changes to be observed. Overall, this study shows that the uninjured wrist can be used as a control for evaluating changes in global HR-pQCT parameters during fracture healing.

References

1. Spanswick PJC et al, Bone Reports 14:100748, 2021.
2. Troy KL et al, Bone Reports 14:101012, 2021.
3. Pauchard Y et al, Bone, 50:1304-10, 2012.
4. Manske SL et al, JBMR, 32(7):1514-24, 2017.

BIOMECHANICAL ANALYSIS OF DIFFERENT LEVEL OF CONSTRAINT IN TOTAL KNEE ARTHROPLASTY DURING DAILY ACTIVITIES.

Edoardo Bori (1), Silvia Pianigiani (2), Laurence Rapallo (1), Gianluca Castellarin (3), Bernardo Innocenti (1)

1. BEAMS Department, Université Libre de Bruxelles, Belgium;

2. Adler Ortho, Cormano (MI), Italy

3. II Unit Orthopaedic Department, Ospedale di Suzzara, Mantova, Italy

Introduction

A wide variety of total knee prosthetic implants are currently available on the orthopedic market, and since this variety includes different tibio-femoral interactions (i.e. "levels of constraint") each with its biomechanical consequences on the joint performances, a biomechanical comparative study could represent a helpful tool for the clinical decision-making process.

In order to compare the knee biomechanics induced by different levels of constraint, this study analyzed four configurations from the same family of products (thus avoiding the effects induced by the changes in brand-related design) under three different configurations, representing the typical knee joint daily activities.

Methods

The investigation was performed via finite element analysis, and the knee model used was developed from an already published and validated model [1]. Among the various prosthesis models available, significant role is covered by Cruciate Retaining (CR) prosthesis, Posterior Stabilized (PS) prosthesis and Constrained Condylar Knee (CCK) ones. A further characterization is then made between Mobile-Bearing (MB) and Fixed-Bearing (FB) implants, depending on the insert-tibial tray level of constraint. Among the mobile-bearing implants, a further distinction between standard and ultra-congruent inserts is made depending on the level of conformity between the femoral component and the insert.

The prosthesis family analyzed counts four different types of designs: two MB CR knee prostheses (one with a standard insert and one with an ultra-congruent one), one FB PS prosthesis and one FB CCK prosthesis.

The different designs were therefore incorporated in the 3D finite element model of the lower leg and analyzed in three different configurations, reproducing landing and taking-off phases occurring during the gait cycle and chair-rising.

Implant kinetics (in terms of contact areas and contact pressures, together with polyethylene and tibial bone stresses) were calculated at the three different loading conditions for each design and compared among configurations.

Results

The bone stress distribution in the different regions of interest of the tibia returned to be relatively homogeneous regardless of the type of design used.

The MB CR ultracongruent design presented the highest congruency, with its contact area value being almost 3 times higher than the one of the fixed bearing inserts (as reported in Figure 1), similarly to what found in [2].

The main relevant difference was then observed between the mobile and fixed bearing models, as the contact areas are significantly different between these models in all the analyzed loading conditions; as a consequence, significant changes in the stress distribution are observed at the interface between the prosthetic components and in the poly insert, but no significant stress difference is found on the tibial bone.
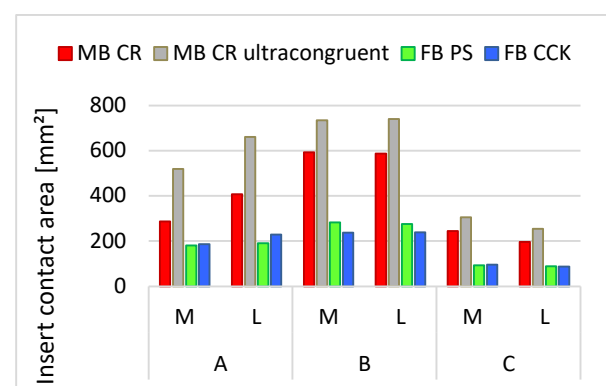
Figure 1 – Medial (M) and Lateral (L) contact areas of the different prosthesis in the three configurations analyzed (A, B, C)

Discussions

Comparing biomechanically the different level of constraint it was possible to highlight differences in terms of implant and bone stress, with the main relevant difference being between the mobile and fixed bearing models. Moreover, the different models exhibited a symmetrical medial and lateral distribution of the contact areas, which is not always common among all the currently available prosthesis (i.e. medial pivot designs). In each configuration, the distribution of the stress on the different zones of the tibia (proximal, distal, cortical, total) is relatively homogeneous between the models. Changing the prosthetic implant would therefore not induce a big variation of the stress distribution in the different regions of the tibial bone, while it would however significantly change the distribution of stress at the interface between the prosthetic components.

References

1. Innocenti et al., J Arthroplasty, 29(7):1491-8, 2014.
2. Innocenti, Knee Surg Sports Traumatol Arthrosc, 28(9):3040-3047, 2020 .

IN VIVO CONTACT MECHANICS IN TOTAL KNEE ARTHROPLASTY IS GOVERENED BY THE IMPLANT CONFORMITY

Seyyed Hamed Hosseini Nasab (1), Barbara Szazi (1), Colin Smith (1), Pascal Schütz (1), Barbara Postolka (1), William R. Taylor (1)

1. Institute for Biomechanics, ETH Zürich, Switzerland

Introduction

Polyethylene wear caused by high contact pressures is one of the main reasons for total knee arthroplasty (TKA) failure [1]. Finite element (FE) modelling has been widely used to estimate tibiofemoral contact pressure in different implant designs. However, a clear understanding of the influence of implant design on the articular contact mechanics during functional activities has been limited by uncertainty in their input implant kinematics.

Using accurate 3D implant kinematics from mobile video-fluoroscopy together with a combined musculoskeletal and FE modelling approach, we aimed to investigate the influence of implant design on the articular contact pressure during level walking.

Methods

Thirty subjects (10 with a posterior-stabilized (PS), 10 with a medial-congruent (MC), and 10 with an ultra-congruent (UC) implant, Medacta International, Switzerland) were measured in our lab. Skin marker trajectories, ground reaction forces, and 3D implant kinematics obtained from mobile fluoroscopy were collected during 5 cycles of level walking [2].

A previously validated musculoskeletal model [3] was scaled to the measured subjects. Skin marker trajectories and ground reaction force data were used to run subject-specific models and estimate knee contact force and moments following a static optimization approach minimizing sum of the squared muscle activations.

3D geometry of the implants was used to develop subject-specific FE models in ANSYS (Ansys Workbench, ANSYS Inc.). The metallic parts were modeled as rigid bodies, whereas the tibial inlay was modeled as a deformable object and meshed with tetrahedral elements (Figure 1A, max. mesh size = 0.8mm).

The tibial component was fixed to the ground, while a six degree of freedom (DoF) tibiofemoral joint allowed reconstruction of the fluoroscopic kinematics. Transient structural analyses were performed where FE models were driven by the input antero-posterior translation, internal-external rotation, and flexion-extension. Other DoFs of the tibiofemoral joint were left open to be driven by the friction-based contact, while superior-inferior force and abduction-adduction moment from musculoskeletal modelling were applied to the joint.

Figure and Tables

UC and PS implants showed very similar medial contact pressure (MCP) patterns with a maximum pressure of around 15 MPa (at around 50% gait cycle, Figure 1B). However, the MC implant showed a very different MCP pattern with its maximum pressure (14 MPa) occurring in early-swing phase. The MC implant experienced the highest lateral contact pressure (LCP) (18 MPa) compared with other implants (14 MPa for UC and 12 MPa for PS, Figure 1C).
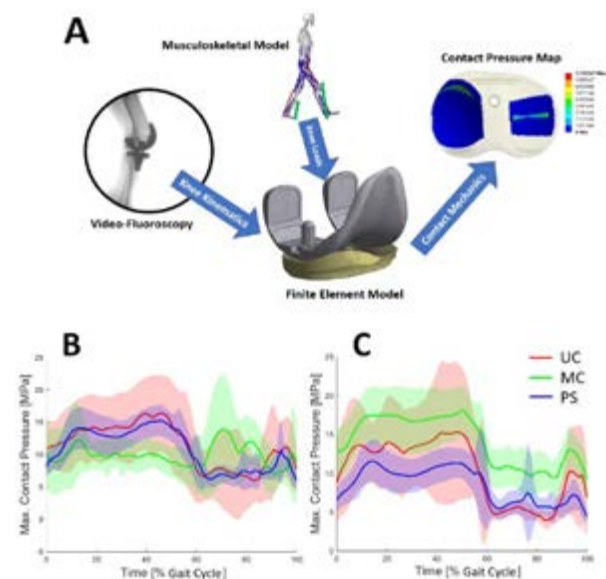
Figure 1: A) The modelling flowchart. B) Mean and std of medial contact pressure during walking. C) Mean and std of lateral contact pressure during level walking.

Discussion

Our findings highlight the relationship between implant conformity and contact pressure distribution in TKA. While the incongruent articular geometry on the lateral side of the MC implant is designed to allow more axial rotational freedom, the very small lateral contact area seems to considerably increase the maximum LCP.

References

1. Kim et al., Knee Surg Relat Res. 2014; 26(1): 13-19.
2. Schütz et al., J Orthop Res. 2019; 37(11): 2337-2347.
3. Rajagopal et al., IEEE Trans Biomed Eng. 2016; 63(10): 2068-79.

Acknowledgements

BIOMECHANICAL ANALYSIS OF FLEXIBLE FEMORAL CONES IN HINGED TOTAL KNEE ARTHROPLASTY

Bernardo Innocenti

1. BEAMS Department, Université Libre de Bruxelles, Belgium;

Introduction

The use of metaphyseal cones is a suitable procedure to manage severe bone loss in revision total knee replacement. Since the metaphysis of such patients could shows important defect, the bone is weak and might be easily damaged during the surgery [1-2].

Nowadays, the cones available in the market are rigid and, unless they are custom-specific designed, are unable to correctly adapt to the shape of the patient's bone. Therefore, flexible metaphyseal cones have been recently introduced to reduce potential bone trauma during implantation surgery as they theoretically improve the interaction between cone and bone, reducing bone stress and relative risk of fracture.

Preliminary clinical study on the use of such devices have shown promising results [3]. However, an in-vitro biomechanical study is required to evaluate and quantify the effects of flexible cones during their surgical implantation and the performance during common daily activities.

Methods

This study is performed using finite element analysis, based on an already validated and published knee finite element model [4].

For the bone, the geometry of a femoral sawbones (right side, size medium) was selected in agreement with previous studies [2,4,5]. The geometries of the orthopedic devices used were selected based on data coming by the industrial manufacturer.

To take into account for different implant designs geometries, two versions were considered for this study: a 2-zones and a 3-zones cone. The 2-zone cone is interacting medio-laterally, while the 3-zones also have a potential interaction on the anterior side of the bone.

Each geometry was modeled as flexible and as rigid; the rigidity of the cones was achieved fixing the two metal posterior flanges to avoid any the relative movements of the cone. With this approaches both rigid and flexible cones are characterized by the same external and internal geometry, therefore the bone-cone interaction is the same, a part of the different flexibility of the two designs.

The cones were mounted on a femoral bone following surgical guidelines provided by the manufacturer and coupled with a hinged revision TKA.

Three activities were simulated in this study: surgical impaction, walking and chair-rise based on previous studies [6,7].

Results

Quantitatively, figure 1, considering the metaphyseal region of the femur, during impaction, the Von Mises stress have been considerably reduced by the use of the flexible cone. In details, comparing the flexible with the rigid cone, the 2-zones reduced the average stress of around 50% anteriorly and 40% posteriorly; while the 3-zones reduced respectively the stress of 6% and 36%.

Moreover, the bone stress resulted also better distributed and more homogenous all over the cortical bone, with lower bone peaks.

The investigation of the two daily loads did not show remarkable differences between the cones and the stress distribution did not represent any risk of bone damaging, and similar implant stability.
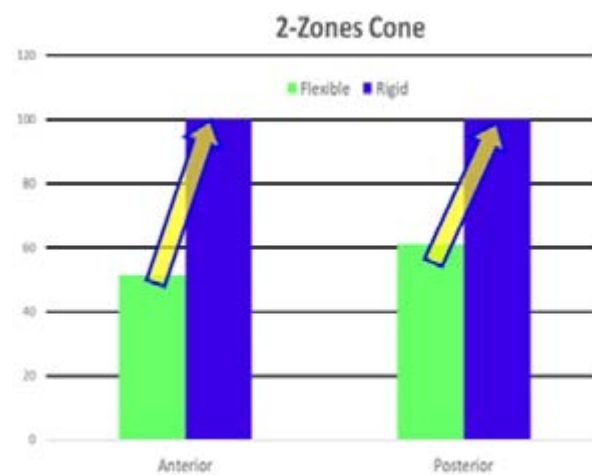
Figure 1 – Average Von Mises stress, normalized with respect to the Rigid outcomes, for the anterior and the posterior cortical bone in the case of 2-Zones cone.

Discussions

As flexible cones are able, during the impact, to deform their geometries, they show a reduced average and max von mises stress and, therefore, a reduced risk of bone damage intra-operatively, with respect to rigid cone.

The comparative investigation of the daily activities showed no major differences between rigid and flexible cone in terms of stress distribution, stress magnitude and implant micromotions. Thus, the performances of the flexible cone are the same of the rigid cone when common activities are performed, and despite their flexibility, the implant stability has not changed.

References

1. Radnay et Scuderi, CORR 446:83-92, 2006.
2. Innocenti, et al., J Biomech Eng: 140(111006): 1-10, 2018.
3. Ohlmeier et al., AOTS 141: 555-60, 2021.
4. Innocenti, et al., JOA: 29(7): 1491-8, 2014.
5. Soenen, et al., JOA: 28(8): 1437-45, 2013.
6. Vanlommel et al., The Knee 17(1):43-7, 2010.
7. Burastero et al., AOTS 140(12):555-60, 2020.

CRUCIATE RETAINING TOTAL KNEE ARTHROPLASTY SYSTEMS MAY BE UNSUCCESFUL IN AVOIDING ANTERIOR FEMORAL SHIFT DESPITE DIFFERENT BEARING GEOMETRY.

Philippe Moewis (1), Hagen Hommel (2), Adam Trepczynski (1), Leonie Krahl (1), Georg N. Duda (1)

1. Berlin Institute of Health at Charité – Universitätsmedizin Berlin, Julius Wolff Institute, Berlin, Germany;
2. Krankenhaus Märkisch Oderland, Wriezen, Germany

Introduction

Although total knee arthroplasty (TKA) is an established procedure with 95% survivorship, around 14-39% of patients report dissatisfaction with the outcome [1]. One of the reported causes is anterior knee pain due to paradoxical anterior shift. Despite a wide number of available TKA designs, there is no clear consensus about the effectivity of specific design geometrical features in combination with cruciate ligaments strategy to achieve a physiological knee joint kinematic pattern during flexion. The aim of this study was to analyze two different TKA designs in both cruciate ligaments strategy during in-vivo conditions to achieve an understanding of the outcome.

Methods

Four cohorts of patients operated with specific TKA designs consisting of; gradually changing radius posterior stabilized (G-Curve PS), gradually changing radius cruciate retaining (G-Curve CR), lateral pivot CR (LP-CR), asymmetric bicruciate stabilized (A-BCS) and asymmetric CR (A-CR) were analyzed in-vivo during unloaded flexion-extension and loaded lunge. Single plane fluoroscopy was used to collect the movement from extension until maximal flexion [3]. Specific medial and lateral distal points relative to the tibia component plateau were determined to conduct a kinematic analysis (Figure 1).

Figure 1: Specific medial and lateral distal points.

Results

A clear tendency towards a paradoxical anterior shift was observed on the medial compartment in all CR cohorts during unloaded flexion-extension (Figure 2, top). Although still present during loaded lunge, the magnitude of the anterior shift was however reduced. Also, certain degree of lateral femoral rollback can be observed. In contrast, the kinematic of both BCS and PS systems was characterized by reduced movement on the medial compartment and femoral rollback on the lateral compartment during unloaded flexion-extension (Figure 2, bottom) and loaded lunge.
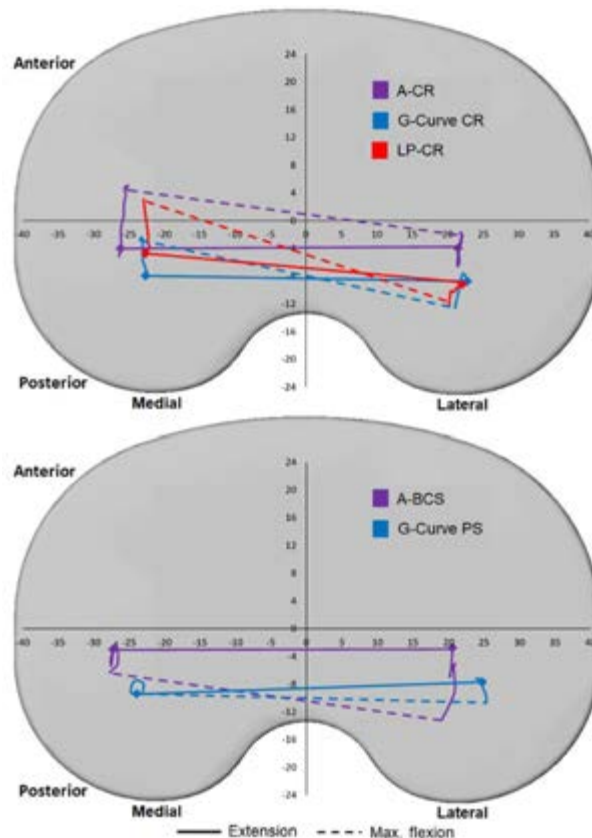
Figure 2: Knee joint kinematics during unloaded flexion-extension in CR (top) and PS (bottom) systems.

Discussion

Although there is undoubtedly an effect of specific design features, the results of this in-vivo study showed that despite geometrical contribution, the kinematical outcome is definitely conditioned by the cruciate ligament strategy selected. Although cruciate retaining systems are very well established, the kinematic of the analyzed CR cohorts indicates that the retained posterior cruciate ligament alone is insufficient to avoid paradoxical anterior shift during flexion. Future designing needs to consider the multifactorial aspect of TKA and as consequence the interaction between ligament tension, loading and geometrical features.

References

1. Maratt et al., J Arthroplasty. 2015
2. Donadio et al., Sports Traumatol Arthrosc. 2015
3. Pfitzner et al., Knee Surg Sports Traumatol Arthrosc. 2017

Acknowledgements

UNDERSTANDING KNEE STABILITY AFTER TKA BY MEANS OF DYNAMIC VIDEOFLUOROSCOPY

Longfeng Rao (1), Nadja Meister (1), Nils Horn (2), William R. Taylor (1), Barbara Postolka (1), Stefan Preiss (2), Pascal Schütz (1)

1. Laboratory for Movement Biomechanics, Institute for Biomechanics, ETH Zurich, Switzerland
2. Department of lower extremities, Schulthess Clinic, Switzerland

Introduction

Knee instability is one of the main factors accounting for poor outcomes after total knee arthroplasty (TKA) [1]. Clinically, assessment of joint instability depends on the surgeon's passive examination and patient reported outcome measures. The relationship between passive laxity and joint stability during activities of daily living is not well understood, which can result in discordance between surgeons and patients [2]. Therefore, to determine whether more objective relationships exist, the aim of this study was to investigate *in vivo* tibiofemoral implant kinematics in subjects with stable and clinically diagnosed unstable knees after TKA during daily activities.

Methods

Two study cohorts (stable:7m,3f; unstable:2m,6f) with the Persona CR implant design and UC inlay (Zimmer Biomet) were recruited from the Schulthess Clinic, Zurich, based on the presence or absence of signs of clinical knee instability. One standing trial and 3-6 complete cycles of level gait, downhill walking as well as stair descent were assessed for each subject using mobile fluoroscopy [3]. The 3D geometries of the implant components were then registered to the 2D X-ray images to provide the 3D tibiofemoral rotations [4] and anterio-posterior (A-P) translation for the medial and lateral condyles [5], which were compared between the cohorts using an independent t-test.

Results

Comparable ranges of A-P translations were observed in the medial as well as the lateral condyle between the stable and unstable group throughout both the stance- and swing phase in all activities (Table 1, Figure 1).

A-P translation [mm]	Stance phase		Swing phase	
	medial	lateral	medial	lateral
level gait stable	5.4±1.4	5.1±1.0	7.0±2.5	5.7±1.9
unstable	4.5±0.9	4.5±0.8	6.2±1.6	5.5±1.5
downhill stable	4.2±0.9	4.0±0.7	5.7±1.5	4.7±1.2
unstable	3.4±1.0	4.5±0.7	5.5±1.5	5.4±2.0
stair stable	5.1±1.6	5.5±1.9	7.7±1.7	6.0±2.1
unstable	4.6±1.2	5.5±1.7	6.9±1.7	7.4±2.9

Table 1: Mean±sd of A-P translation range for stance and swing phase for all activities.

Interestingly, the differences in two condylar A-P translations (lateral RoM - medial RoM) showed a significant difference between groups during stance phase of downhill walking (unstable 1.1±1.3mm, stable -0.2±1mm) and swing phase of stair descent (unstable 0.5±2.4mm, stable -1.7±2.0mm).

For joint rotations, only range of adduction/abduction during stance phase of downhill walking exhibited a significant difference between the cohorts (unstable 3.5±0.3°, stable 2.9±0.4°). All parameters were associated with high inter-subject variability (Fig. 1).
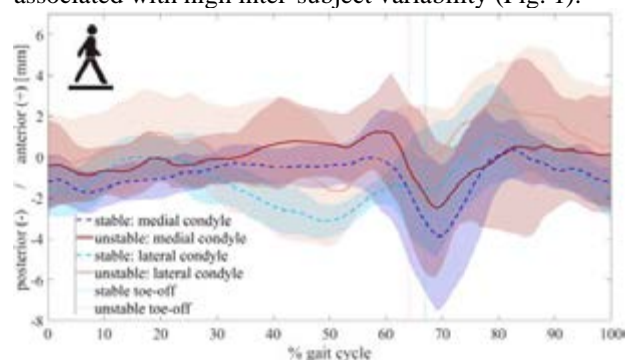
Figure 1: Mean±sd of A-P translations for the medial and lateral condyles over complete gait cycles of level gait, presented relative to the standing trial.

Discussion

The range of adduction/abduction and the difference in A-P translation between the condyles showed some potential for differentiating between stable and unstable cohorts in the more challenging activities. These differences could be explained by increased ligament laxity and more restricted medial condylar movement in the unstable knees possibly resulting from the differences in muscular constraints. The large inter-subject variability demonstrates the challenge in quantifying joint instability *in vivo*. Further analysis into time series of implant kinematics and EMG synergies might offer further discretisation and provide clinicians with a better understanding of knee stability after TKA.

References

1. Schroer et al, J Arthroplasty, 28:116-119, 2013.
2. Harris et al, J Arthroplasty, 28:722–727, 2013.
3. List et al., PloS One, 12:e0185952, 2017
4. Grood et al, J Bioech Eng, 105:136-44, 1983.
5. Schütz et al, J. R. Soc. Interface.1620180678, 2019.

Acknowledgements

DYNAMIC KNEE JOINT LINE ORIENTATION IS NOT A RELIABLE PREDICTOR OF CONTACT LOAD DYNAMICS IN VIVO

Adam Trepczynski (1), Philippe Moewis (1), Philipp Damm (1), Pascal Schütz (3), Jörn Dymke (1), Hagen Hommel (2), William R. Taylor (3), Georg N. Duda (1)
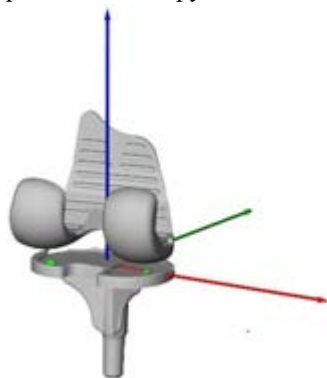
1. Berlin Institute of Health at Charité – Universitätsmedizin Berlin, Julius Wolff Institute, Berlin, Germany; 2. Krankenhaus Märkisch-Oderland, Wriezen, Germany; 3. Institute for Biomechanics, ETH Zürich, Switzerland

Introduction

While mechanical alignment (MA) is most commonly targeted in total knee arthroplasty (TKA), alternatives such as anatomical alignment (AA) have been proposed. Along with improving ligament balancing, AA aims at a horizontal joint line during the stance phase of walking, by means of tilting the joint line medially by ~3° relative to the mechanical leg axis. The hypothesis behind this concept is that this would lead to more uniform load distribution. So far, this link between anatomy and loading has not been analyzed *in vivo*. The aim of this study was therefore to determine how the joint line moves during functional activities, and investigate its relationship with internal joint loading.

Methods

Six TKA patients (aged 65-80y) with instrumented tibial components performed 5-10 cycles of level walking. The *in vivo* tibio-femoral (TF) forces were synchronously measured together with the component kinematics using a mobile video-fluoroscope. *In vivo* kinematics were used to determine the dynamic orientation of the joint line and compared against the subjects' static alignments from postoperative frontal radiographic images.

Results

During stance, the joint line was tilted laterally in reference to the ground by up to 8°. At the peak TF force, the joint line tilt was usually 0°–2° smaller than its maximal value (Fig. 1). The tibial implantation varus had more impact ($R^2=0.50$) on the peak medial TF force than the overall varus alignment (hip-knee-ankle, HKA) ($R^2=0.22$). When the stance phases of all patients were combined, the relation between the dynamic joint line tilt and the medial TF force was weak ($R^2=0.17$). In contrast, the external adduction moment (EAM) correlated strongly with the medial TF force ($R^2=0.85$) (Fig. 1). Similarly, the ratio of medial to total TF force showed a strong correlation with the EAM (pseudo $R^2=0.78$) but less with the dynamic joint line tilt (pseudo $R^2=0.19$).

Discussion

The static and dynamic joint lines differ quite substantially, indicating that an anatomical alignment could indeed make the dynamic joint line more horizontal. However, during the loaded stance phase the dynamic joint line varies substantially and did not dominate the TF force distribution or even the medial

TF force. The variable relationship between the static and the dynamic joint line during the loaded stance phase, and the weak correlation of static HKA to peak medial TF force, are consistent with the findings of other studies: The static radiographic joint line measures are not reliable predictors of the contact load dynamics *in vivo*. In contrast, the external abduction moment is a much stronger predictor.
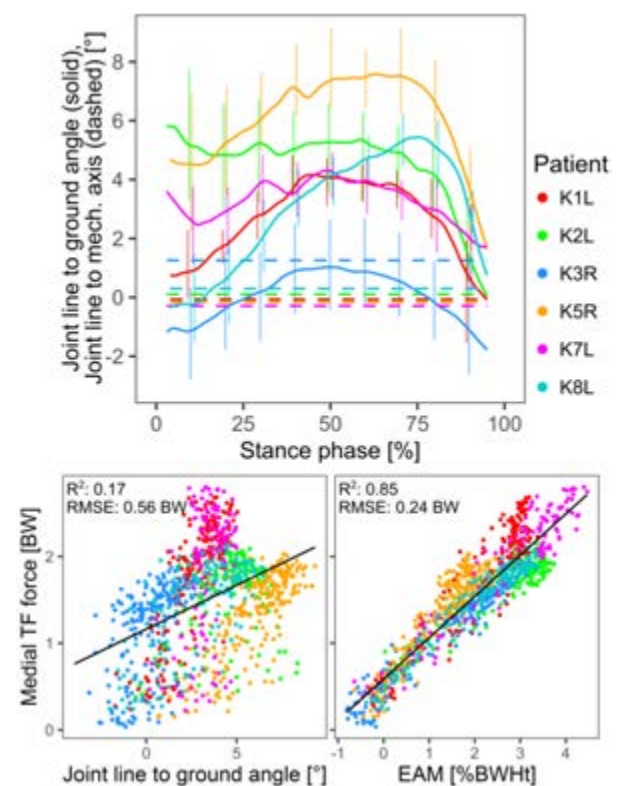
Figure 1: TOP: Lateral tilt of the joint line during the stance phase relative to the ground (solid lines, bars indicate range), and relative to the mechanical axis of the leg (dashed). BOTTOM: Correlations of the medial tibio-femoral contact force with the lateral joint line tilt (left) and the external adduction moment (EAM) (right). Adapted from [3] under CC-BY.

References

1. Cherian et al, Curr Rev Musculoskel Med, 7:89–95, 2014
2. Rivière et al, Orthop Tra Surg Res. 103:1047-1056, 2017
3. Trepczynski et al, Front. Bioeng. Biotechnol. 9:754715, 2021

Acknowledgements

ANALYTICAL MODEL FOR THE MECHANICAL PERFORMANCE PREDICTION OF A BONE-PLATE IMPLANT.

Federico A. Bologna (1,2), Mara Terzini (1,2), Alberto L. Audenino (1,2)

1. Department of Mechanical and Aerospace Engineering, Politecnico di Torino, Italy

2. Polito^BIO Med Lab, Politecnico di Torino, Italy

Introduction

Every osteosynthesis device needs to guarantee the mechanical success of the implant: ASTM F382 is the latest and most widely used test standard for metallic bone plates [1]. ASTM standards establish a test methodology and define the setup condition, but insufficient knowledge is available to predict the success or failure of fixation devices in the first few days after surgery. The main purpose of this work is to develop an analytical procedure to determine the minimum level of performance of a generic bone plate and simplify the experimental tests campaign for regulatory purposes.

Methods

Quasi-static and dynamic four-point bending tests were performed as reported in the ASTM standard to determine the plate fatigue life and the related maximum bending moment. The maximum von Mises stress in the ASTM setup was calculated, and then validated through a Finite Element (FE) model, with a first analytical model (Figure 1a), informed by a parametric FE model (FEM-SCF) able to determine the stress concentration factor (SCF) induced by the hole plate longitudinal curvature. A second analytical model of the implanted plate was created starting from the experimental failure section of the plate (second-order tetrahedral mesh with a size of 1 mm). The femur was modelled with cortical bone only, considered as a rigid body, while the fractured bone was inserted in correspondence with the free length of the plate through a linear spring (stiffness equivalent to 5 % of the axial stiffness of femur cortical bone). Loads measured during normal walking were applied to the femur, according to Bergmann et al., 2001 [2]. The analytical model was finally validated with a FE model of the plate-femur assembly (Figure 1b).

Results

The runout load obtained through the experimental tests was equal to 22800 Nmm. In the ASTM setup, the analytical model of the plate determined maximum equivalent stress equal to 1029 MPa (the standard SCF [3] was increased by 2.25 times because of the curvature, as obtained from FEM-SCF results), while the FE model showed a peak of 1025 MPa in the same zone where the failed specimens exhibited fracture (Figure 1a). The maximum analytical stress calculated on the critical section of the implanted plate was reported in Figure 1b and it was equal to 780 MPa (error with respect to FE model < 5 %).
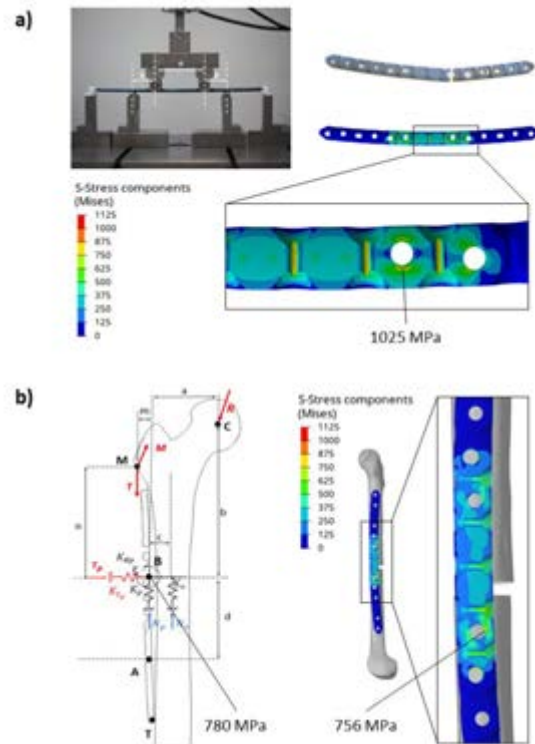
Figure 1: a) Four-point bending setup, fractured zone of a failed specimen, and related FE model results of tested area for model validation; b) analytical model of the femur-plate construct and equivalent stress distribution on the implanted plate.

Discussion

The proposed procedure allows to avoid comparison with a predicate device and reduce the times involved in the experimental tests for regulatory purposes. In addition, the parametrical study for the SCF determination of a curved plate could be extended in order to identify the minimum performance of a wide range of fixation devices.

References

1. ASTM F382-17, Standard Specification and Test Method for Metallic Bone Plates. ASTM International, 1–12, 2017.
2. Bergmann G. et al., Hip contact forces and gait patterns from routine activities. J. Biomech. 34, 859–871.
3. Juvinall RC, Marshek KM (eds). Fundamentals of machine component design. 5th Ed., Wiley & Sons; 2012.

STANDARDIZED IN VIVO KNEE IMPLANT KINETICS AND KINEMATICS AND THEIR APPLICATION TO IMPLANT WEAR SIMULATION

Michael J. Dreyer (1,3), Adam Trepczynski (2), Bernhard Weisse (3), William R. Taylor (1), Philipp Damm (2) and Colin R. Smith (1)

1. Laboratory for Movement Biomechanics, Institute for Biomechanics, ETH Zürich, Zürich, Switzerland;
2. Berlin Institute of Health at Charité – Universitätsmedizin Berlin, Julius Wolff Institute, Berlin, Germany;
3. Laboratory for Mechanical Systems Engineering, Empa, Dübendorf, Switzerland

Introduction

In vivo data on tibio-femoral loads and kinematics is critical for understanding knee biomechanics, developing implants, and performing computational simulations. The extensive CAMS-Knee dataset [1] contains implant kinematics from dynamic fluoroscopy and contact loads from instrumented implants. However, a standardized summary of that data is needed to facilitate use by the research community and for time-intensive testing and simulation tasks. Thus, we present "Stan", the standardized CAMS-Knee subject. One application of Stan's data is knee implant wear prediction. Currently, the model-based ISO 14243 loading and kinematic boundary conditions (BCs) are standardly used to investigate knee implant wear. To demonstrate the importance of using in vivo measured BCs based on Stan compared to existing standards, we use a state-of-the-art computational wear prediction algorithm to investigate the differences in abrasive/adhesive wear due to the applied BCs.

Methods

Using the Orthoload HIGH100 averaging methodology [2], we obtained Stan's standardized tibio-femoral kinematics and associated CAMS-HIGH100 kinetics from the six subjects and five activities of the CAMS-Knee dataset. We then built finite-element models of the ISO force controlled (FC) and displacement controlled (DC) knee implant wear tests. Stan's (FC, DC), and the original Orthoload (FC) BCs for level walking were also applied to otherwise identical copies of the ISO models to enable direct comparison. Polyethylene inlay wear and creep was predicted for 5 million cycles using a cross-shear and contact-pressure dependent wear model and a compressive creep model.

Results

For level walking, Stan's CAMS-HIGH100 loads matched the Orthoload-HIGH100 loads well, whereas the ISO loads and kinematics were objectively different (Fig. 1). The DC Stan model showed the lowest and the ISO FC model the highest wear rate (Fig. 2). Contact was more posterior and less conforming for the DC models compared to the FC models, so much so that the ISO DC model dislocated. Despite differences in the applied loads and resulting kinematics in the FC models, their wear patterns were all similar, with a larger and more anterior medial wear scar. All three FC models incorrectly predicted internal-external rotation to be effectively zero in stance phase, and more anterior contact than observed *in vivo* (Stan DC model).
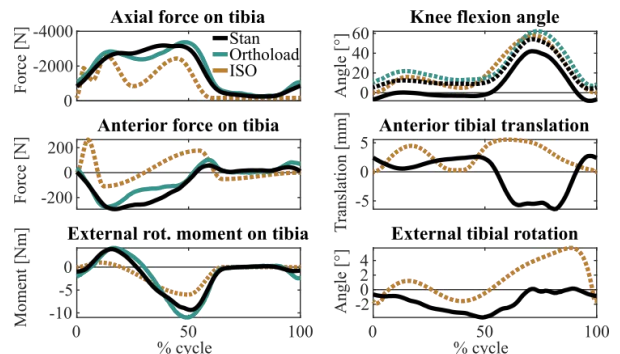
Figure 1: Comparison of applied BCs. Dashed lines: mechanical axes. Dotted lines: implant axes.
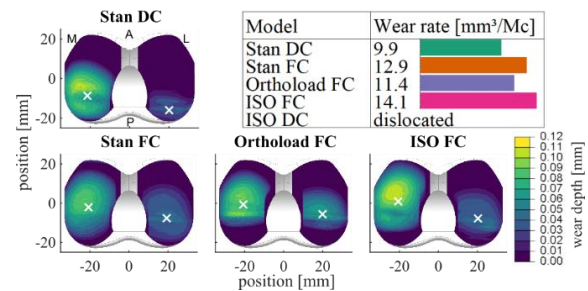
Figure 2: Wear rate, wear scar depth and centroid (X) after 5 million cycles (Mc).

Discussion

We presented Stan's set of standardized tibio-femoral loads and kinematics and demonstrated their applicability to implant wear prediction. The DC Stan model's lowest predicted wear is likely due to the lower contact area, while the FC models' similar wear scars indicate that contact mechanics were principally governed by the highly constrained implant geometry. More generally, the FC-DC mismatch demonstrates the importance of fluoroscopy kinematics such as Stan's for validation and future improvement of knee simulation or testing setups.

References

1. Taylor et al, J. Biomech., 65: 32–39, 2017
2. Bergmann et al, PLoS ONE, 9: e86035, 2014

Acknowledgements

COMPREHENSIVE BOUNDARY CONDITIONS FOR INVESTIGATING TOTAL KNEE REPLACEMENT WEAR DURING WALKING

Míriam Febrer-Nafría (1), Michael Dreyer (2), Ning Guo (2), S. Hamed Hosseini Nasab (2), Colin R. Smith (2), William R. Taylor (2)

1. Universitat Politècnica de Catalunya, Spain; 2. ETH Zürich, Switzerland

Introduction

In vitro experiments and finite element models can provide important insights into implant failure due to wear [1]. While these methods are heavily influenced by the applied boundary conditions (prescribed loads and kinematics), and parameters that have important effects on knee loading (such as limb alignment and muscle coordination) vary across patients, current ISO wear testing standards only specify a single loading condition. Thus, to understand the detrimental *in vivo* conditions that lead to premature implant wear, there is a need to establish a range of wear testing scenarios to cover the full inter-patient kinematic and kinetic variability during activities of daily living. This study applies probabilistic musculoskeletal simulations of full body and joint level mechanics for a range of different implant alignments and muscle coordination strategies to establish their influence on boundary conditions for future investigations of implant wear.

Methods

A full body, muscle-driven model with 6 degrees of freedom tibiofemoral and patellofemoral joints [2] was developed for subject K5R from the CAMS-knee datasets [3]. Probabilistic simulations were performed using the Concurrent Optimization of Muscle Activations and Kinematics approach [4] to predict secondary joint kinematics and knee contact loads using motion capture and ground reaction force data of one level walking cycle. The cost function minimized the sum of the squared difference between the actual muscle activation and an input desired activation function. The varus-valgus implant alignment of the baseline subject-specific model was perturbed to generate 10 models with random alignments. Each model was then combined with 100 sets of randomly determined desired muscle activations. This resulted in 1,000 probabilistic simulations, which allowed us to study the effect of parametric variation of the implant alignment and neuromuscular coordination on the predicted secondary tibiofemoral kinematics and contact loads during walking.

Results

The perturbed alignments and coordination caused the largest variability in medial translation (mean: 4.34 mm) and internal rotation (mean: 4.22 deg), compared to the other secondary kinematics (Fig. 1). For medial translation, this variability remained almost constant throughout the gait cycle. For knee internal rotation, this variability was higher during late stance, when the second vertical knee contact force peak occurred (7.38 deg). Variability in knee contact loads was in general larger during the stance phase compared to swing phase (e.g., for anterior-posterior force, 0.34 BW during stance phase compared to 0.17 BW during swing phase). The vertical force, on the contrary, exhibited a high variability throughout the entire gait cycle (mean: 1.24 BW, maximum: 1.75 BW).
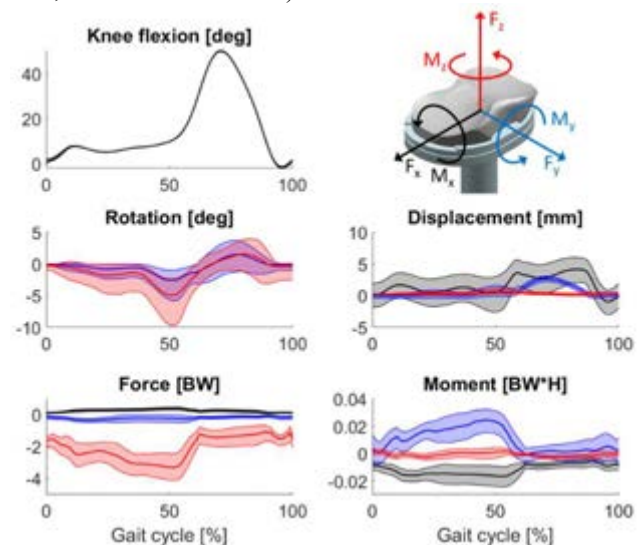
Figure 1: Knee kinematics and knee contact loads (colours according to displayed axes, translations are relative to the initial implant pose at heel strike). The bold centrelines are the mean and shaded regions show the 5th to 95th percentiles of the 1,000 simulations.

Discussion

The presented framework provides a powerful tool to improve our understanding of the *in vivo* kinematic and kinetic behaviour of the knee for a wide range of muscle coordination strategies and different implant alignments, and to establish upper and lower limits on the boundary conditions that should be considered for realistic implant wear testing. Future work will include variation of the implant alignment in all directions and exploration of other activities.

References

1. Pitta, M, et al. J. Arthroplasty 33:407–414, 2018.
2. Lenhart, RL, et al. Ann Biomed Eng 43:11 2015
3. Taylor WR, et al, J Biomech, 65:32-39. 2017.
4. Smith CR, et al, J Biomech, 82:124-133, 2019.

Acknowledgements

A SIMULATION BASED APPROACH FOR KINEMATICS EVALUATION AND WORST-CASE DETERMINATION IN PRE-CLINICAL TESTING

Allan Maas (1,2), Ana Laura Puente Reyna (1), Thomas M. Grupp (1,2)

1. Research and Development, Aesculap AG, Tuttlingen, Germany
*2. Department of Orthopaedic and Trauma Surgery, Musculoskeletal University Center Munich (MUM),
Campus Grosshadern, Ludwig Maximilians University Munich, Munich, Germany*

Introduction

Finite-Element (FE) models are mandatory during preclinical testing of implants to determine worst-case constructs under quasi-static loading conditions according to the corresponding standards. However, in dynamic wear testing of knee-joint prostheses, a medium size combination is tested representatively for a whole system by default [1]. A drawback of this practice is the possibility to overlook design- or combination related issues, which might affect the lifetime of implant components, especially the polyethylene inlay. Aim of this study was the development of a dynamic FE-framework to identify worst-case size combinations and kinematics in a virtual wear simulator setup covering five daily activities and high, dynamic loads [2].

Methods

Two cruciate sacrificing knee designs were tested physically on a wear-testing machine prior the model development using a high demanding, daily activity protocol (HDA) [2]. A simplified FE-setup was generated, reduced to the 3D geometries of the assembly whereas the representation of the mechanical wear simulator conditions and the load transmission was achieved by joint elements. Inertial and other time-related effects of the physical situation were compensated by a system of spring- and damper elements (*Fig.1*).

Fig.1: Simplified FE-representation of a wear-testing machine running an HDA-protocol.

Using a time-series signal optimization approach on the anterior-posterior translation and the internal-external rotation results for each activity, 38 variable parameters were varied in between pre-defined limits in a semiautomatic workflow. For each design, two consecutive cycles of a single activity were analysed and the results of the second cycle were used for the optimization. Based on the determined values, a single set of averaged parameter settings was identified that covers all activity cycles sufficiently.

Results

A total of 1010 dynamic analyses were carried out in order to find a sharable set of parameter values. The resulting kinematics of five dynamic activities, using the determined parameter set, are shown in *Fig.2*.
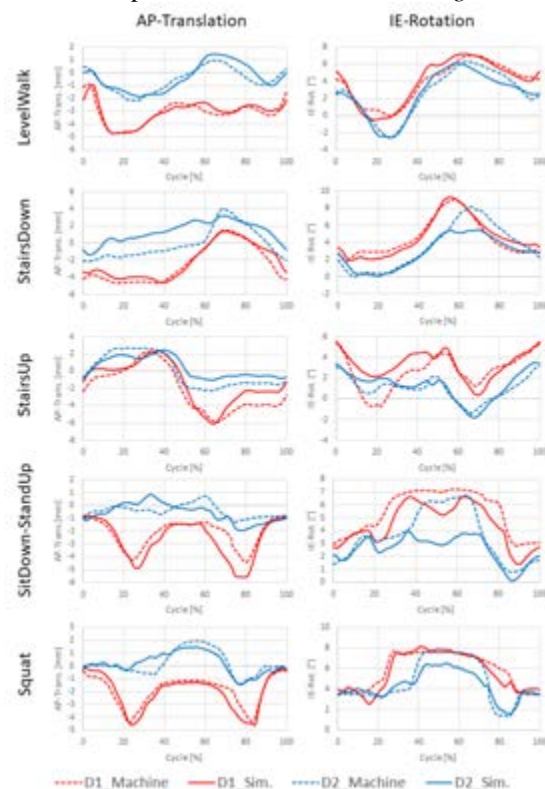
Fig.2: Kinematic results of two designs (D1 & D2) in five daily activities compared to actual HDA test data (dotted lines).

Discussion

In this study, an efficient simulation workflow for design evaluation was developed. Therefore, a HDA wear-testing machine was simplified to boundary conditions and stabilizing elements, using a single set of parameters for all activities. The calculated kinematics were in a comparable range to the machine output. Further applications of the method were found in systematic analyses of entire implant systems to achieve consistent kinematics over the size compatibility range in the design process of new implant systems.

References

1. ISO 14243-1:2009
2. Schwiesau et al., Med. Eng. Phys. 35.5:591-600, 2013.

SYSTEMATIC VALIDATION OF FINITE ELEMENT SIMULATIONS OF LOCKING PLATE FIXATIONS

Dominic Mischler (1), Manuel Knecht (1), Peter Varga (1)

1. AO Research Institute Davos, Switzerland

Introduction

Finite element (FE) modeling is an accepted method to evaluate the biomechanical behavior of fracture fixations, i.e. bone-implant constructs [1,2]. Validated models are required for trustworthy predictions [3]. To achieve reasonable results with a low amount of computation time, assumptions and simplifications are usually made to model geometries, interactions, or loads. Further, material properties are usually taken directly from literature [1]. Experimental validation studies frequently use construct stiffness as the main validation metric [2]. However, in locking plate fixations of diaphyseal fractures, fracture gap movement and plate stress are two important factors determining healing progression and implant fatigue failure, respectively. Stereoscopic digital image correlation (DIC) techniques allow tracking of displacements and deformations and thus offer further metrics for FE validation. Therefore, the aim of this study was to evaluate material and interface properties in a systematic manner and apply the resulting knowledge on a whole construct models to validate fracture gap movement and implant surface strain.

Material and Methods

The construct validation was divided into different stages based on model complexity (Figure 1). First, the material properties of the isolated implant components were determined via four-point bending of the plate and three-point bending of the screw. Second, stiffness of the screw-plate interface was evaluated by means of cantilever bending to determine the properties of the locking mechanism. Third, different configurations of entire fixation constructs were tested on an artificial bone (Canevasit) rod in axial loading, measuring the implant surface strain and the fracture gap movement.
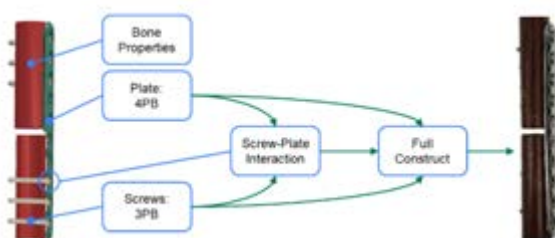
The material and interface properties assessed in these experiments were then implemented into FE models of entire fixation constructs with different configurations corresponding to the third experiments. The computed FE surface strains and fracture gap motions were compared with the experimental results.

Results

The experimentally measured gap motions of the different construct configurations correlated strongly with the simulated results ($R^2>0.99$). Plate surface strains showed tight correspondence with the FE results ($R^2>0.95$, Figure 2). The predictions were quantitively correct but showed slight deviations in large plate working length scenarios.
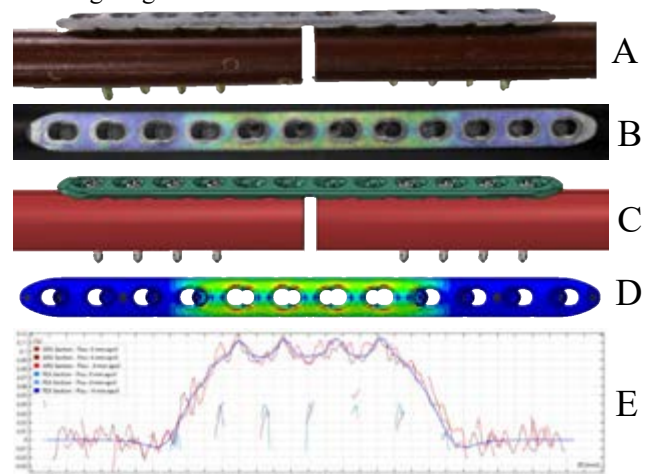
Figure 2: Experimentally tested construct (A) with DIC-measured surface strains on a locking plate (B). Virtually replicated construct assembly (C) and underlying FE strain results (D). Quantitative comparison between measured surface strains (red) and FE results (blue) along the plate cross-section (E).

Conclusion

Successful construct validation with accurate predictions was achieved in a systematic approach by determining material properties and locking mechanism behavior in isolated tests incorporating the newly gained knowledge into simulations of entire fracture fixation constructs. Beyond standard measures, this study showed quantitatively correct results for fracture gap motion and implant deformation. These validated FE models are intended to be utilized in a novel online education tool OSapp [4] to illustrate and explain biomechanical principles of fracture fixations.

References

1. Stoffel et al., Injury, 34:11-19, 2003
2. Lewis et al., Curr Osteoporos Rep., 19:403-16, 2021.
3. Scott et al., Bone Joint J., 102-b:1271-3, 2020
4. https://osapp.ch/

Acknowledgements

THE EFFECT OF INTERFERENCE FIT AND COEFFICIENT OF FRICTION ON THE INTERFACE GAPS OF A PEEK FEMORAL COMPONENT

Corine Post (1), Thom Bitter (1), Adam Briscoe (2), Nico Verdonschot (1,3), Dennis Janssen (1)

1. Radboud University Medical Center, Radboud Institute for Health Sciences, Orthopaedic Research Laboratory, Nijmegen, The Netherlands. 2. Invibio Ltd., Thornton Cleveleys, Lancashire, United Kingdom. 3. University of Twente, Faculty of Engineering Technology, Laboratory for Biomechanical Engineering, Enschede, The Netherlands.

Introduction

Polyetheretherketone (PEEK-OPTIMA™) is of interest as a material for the total knee arthroplasty due to its stiffness properties being comparable to the stiffness of bone. Consequently, aseptic loosening resulting from stress-shielding of the peri-prosthetic bone may be prevented. When introducing a new material for a cementless femoral component, it is necessary to properly test the primary fixation which is required for a successful long-term fixation. Therefore, the micromotions and normal gaps on the bone-implant interface need to be quantified which are both dependent on factors as the interference fit and coefficient of friction. The aim of this finite element (FE) study was to define the effect of interference fit and coefficient of friction of a cementless PEEK femoral component on the micromotions, normal gaps and gap volume change. Secondly, this was compared to a cementless cobalt-chromium (CoCr) femoral component.

Methods

In this study, 24 FE models of the femur and femoral component were created. The femoral component was assigned with a Young's modulus for either PEEK (3.7 GPa) or CoCr (210 GPa). Four interference fit (250, 500, 750 and 1000 µm) and three coefficient of friction (0.5, 1.0 and 1.5) variations were analyzed. Axial forces of a jogging activity from the Orthoload database were applied on the medial and lateral condyles [1]. During each loading cycle, the forces were incrementally increased from an unloaded situation to the maximum force and back to the unloaded situation. This was repeated four times. We analyzed the 95th percentile of the maximum resulting micromotions, the maximum normal gap, and gap volume change to quantify the primary fixation. The gap volume change, defined as the dynamic change in volume between the bone and the implant, is an important parameter as it gives us information about the fluid flow and debris transport caused by repeated opening and closing of the implant-bone interface as this might over time lead to inflammation, osteolysis and loosening of the implant.

Results

The interference fit and coefficient of friction both influence the micromotions, normal gaps and gap volume change. The largest 95th percentile of the maximum resulting micromotions were generated in the PEEK component with low interference fit and low coefficient of friction (Figure 1, Figure 2). The largest normal gaps and gap volume change were seen in the PEEK models with high interference fit and low coefficient of friction.
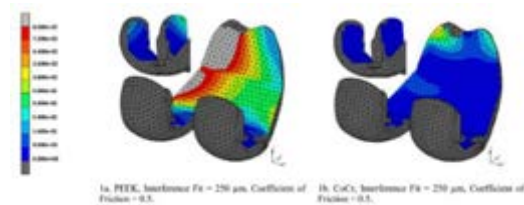
Figure 1: Resulting micromotion distribution (mm) at the implant interface after the 4th loading cycle.
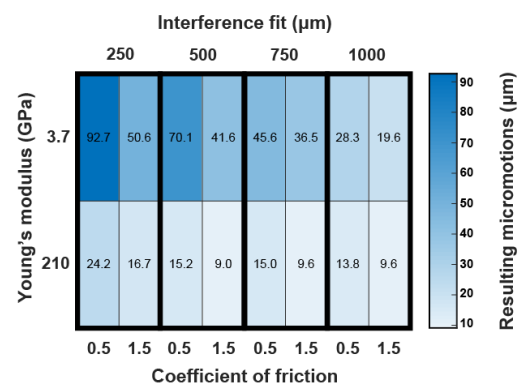
Figure 2: 95th percentile of maximum resulting micromotions (µm) on the implant interface after the 4th loading cycle.

Discussion

Although the cementless PEEK femoral component generated larger micromotions and interface gaps than the cementless CoCr femoral component, a proper primary fixation of the PEEK femoral component can be obtained by coordinating the surface treatment and interference fit. The insights of the current FE simulations may be further studied in mechanical experiments to get more information on the optimal correlation between interference fit and coefficient of friction.

References

1. Bergmann, et al. PLoS ONE 9:1-12, 2014.

Acknowledgements

INFLUENCE OF CERCLAGE WIRE APPLICATION ON THE DYNAMIC BEHAVIOUR OF A FRACTURED IMPLANT-CYLINDER SYSTEM.

Maikel Timmermans (1), George Athanassoulis Makris (1), Laura Van Bel (1), Janne Verhoeven (1), Quentin Goossens (1), Leonard Pastrav (1), Kathleen Denis (1)

1. KU Leuven, Department of Mechanical Engineering, Smart Instrumentation, Leuven, Belgium;

Introduction

Total Hip Replacement (THR) is one of the most common joint replacing procedures with over 500 000 registered THR's in 2020 in the US alone and over 1 million annual cases in the US predicted by 2035 [1]. Primary implant stability in cementless THR is realized by hammering the implant in a broached cavity in the femur until a tight press fit is obtained. During hammering, however, a periprosthetic fracture in the bone can occur. Cerclage wires can be tightened around the fractured femur to increase the load bearing capacity and avoid crack propagation [2]. In this study, the influence of applying a cerclage wire on the vibration properties of a fractured cylinder – implant system, is investigated.

Methods

Two short fibre reinforced epoxy cylinders (length: 500mm, outer diameter: 40mm, inner diameter: 38mm), filled with a PUR foam of 0.160 kg/m³ (3403-32, Sawbones, Malmö, Sweden) were broached to create cavities for the insertion of a H-max S size 13 hip implant (LimaCorporate, Udine, Italy). The implant was inserted by hammering and between each insertion step, consisting of 2 hammer blows, vibration analysis was performed. A single-axis lightweight accelerometer (PCB A352A24, PCB Piezotronics, Depew, NY, USA, weight 0.8 g) was attached to the implant neck using beeswax and the cylinder-implant structure was suspended from elastic bands to simulate free-free boundary conditions. Excitation by hammer impaction was performed on the neck, opposite to the accelerometer. After each insertion step, one measurement was done in the mediolateral direction of the implant and one in the anteroposterior direction. Data acquisition was performed with LMS SCADAS LVLIII (Siemens, Leuven, Belgium). The resonance frequencies of the system were determined from the acquired frequency response function (FRF). When the insertion endpoint was reached, determined based on the method of [3], the cylinder was placed in a lathe. The longitudinal feed of the lathe was used to push a Stanley blade into the cylinder to induce a crack and hence a release of hoop stress. For two out of four insertions however, the cylinder cracked by an insertion hammer blow before the insertion endpoint was reached. In both cases, vibration analysis was repeated according to the methodology above after the fracture was obtained. Then a hose clamp (B44106, Van Marcke NV, Gent, Belgium) was applied around the femur shaft at 9 mm of the proximal end to simulate the effect of applying a cerclage wire. The hose clamp was gradually tightened with a torque screwdriver A.404 (Facom, Mechelen, Belgium) from 1 Nm to 6 Nm with steps of 0,5 Nm. Vibration analysis was performed after each step.

Results

The resonance frequencies after each insertion step, fracture and tightening step were compared. All resonance frequencies increased during implant insertion until the last insertion steps where the FRF's barely changed. Following the methodology of [3], the endpoint was assigned to the insertion step where a Pearson's correlation coefficient of 0.99 between two successive FRF's was acquired. When a fracture occurred, the resonance frequencies dropped approximately 5% over the different experiments. Application of the hose clamp and tightening up to 6 Nm increased the resonance frequencies again by approximately 3% compared to the fractured state. Due to mass loading of the hose clamp, this percentage is slightly lower than the actual increase by tightening.

Table 1: Results for one experiment with measurement in anteroposterior direction - first 6 resonance frequencies in Hz for three key situations.

Insertion endpoint [Hz]	Fracture [Hz]	Hose Clamp 6 Nm [Hz]
381,6	373,6	374,4
969,6	944,8	968,8
1312,8	1207,2	1246,4
1780,0	1752,0	1754,4
2485,6	2408,0	2482,4
3437,6	3086,4	3308,0

Discussion

Application of a hose clamp increases stiffness of the connection between imlant and cylinder and, as a consequence, the resonance frequencies of the fractured cylinder-implant system increase as well. A tightening torque of 6 Nm for the hose clamps largely restitutes the resonance frequencies of the state before fracture.

References

1. Singh et al., J. Rheumatol., 46(9): 1134-1140, 2019
2. Incavo et al., Clin. Orthop. Relat. Res. 272: 175-180, 1991
3. Pastrav et al., J Appl Biomater Biomech, 6(1) : 23-9, 2008

Acknowledgements

FINITE ELEMENT MODELLING OF A CRANIAL IMPLANT DURING IMPACT

Ricardo Alves de Sousa (1), Pedro Santos (1), Fábio Fernandes (1)

1. Center for Mechanical Technology and Automation (TEMA), Universidade de Aveiro, Portugal

Introduction

The human head is sometimes subjected to impact loads which lead to the skull fracture or other injuries that require the removal of part of the skull - craniectomy. Consequently, the removed portion is replaced using autologous bone or alloplastic material. The aim of this work is to develop a cranial implant to fulfil a defect created on the skull and then study its mechanical performance, integrating it on a human head finite element model. The material chosen for the implant was PEEK, a thermoplastic polymer that has been recently in use in cranioplasty. So, a numerical model head coupled with an implant was subjected to analysis to evaluate two parameters: the number of fixation screws that enhance the performance and ensure the structural integrity of the implant and the implant capacity to protect the brain compared to the integral skull. The main findings point to the fact that, among all tested configurations of screws, the model with eight screws presents a better performance when considering the von Mises stress field and the displacement field on the interface between the implant and the skull. Additionally, under the specific analyzed conditions, it is observable that the model with implant offers more efficient brain protection when compared with the model with the integral skull.

Results and Findings

Results are valid only for the implant geometry and location chosen, as well as the impact conditions studied. In this sense, results must be viewed in such context. The numerical simulations involved a finite element human head model [1] with an integrated implant and were divided into two parts:

1. A parametric study which had the purpose of finding out the best configuration of fixation screws, in terms of its number, that optimized the mechanical performance of the model and the structural integrity of the implant;
2. A comparative study between a model with a cranial implant and another with an integral skull to evaluate the implant's capacity to protect the brain against TBI.

Relatively to the first part of the analysis, the structural integrity of the implant was maintained in almost all the configurations, except the one with five screws. Also, the solution with eight and nine screws proved to be the better setups since they could reduce the localized von Mises stress and the displacements at the interface between the implant and skull, one of the critical zones. Also, the evolution of the stresses along the implant interface showed local maximums on the regions nearby the screws' locations. About the second part of the analysis, the model with the implant showed a greater capacity to protect the brain against TBI for all parameters evaluated since less percentage of brain tissue was at risk of suffering moderate or severe injuries. For the particular conditions analysed, the reason is related to the more flexible mechanical properties of the implant material when compared to the cortical bone. Since PEEK has a lower stiffness (resultant of a lower Young's Modulus), a damping effect is verified, reducing the brain motion. Overall, the modelled cranial implant and the options made during the modelling process proved to have a great result since the main goals of the work were accomplished, specifically the development of a cranial implant that, when subjected to impact load, retains its structural integrity and ensures brain protection.
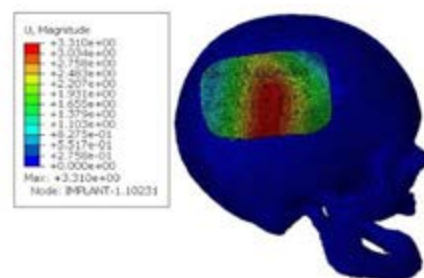

Figure 1: Typical Displacement field after impacting the head with implant
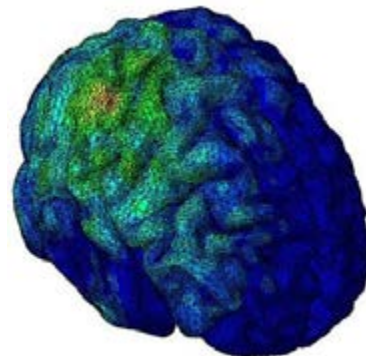
Figure 2: Stresses developed within the brain.

References

1. Fernandes et al, Eng. Comp., *Eng. Comput. (Swansea, Wales)*, vol. 35, no. 1, pp. 477–496, 2018, doi: 10.1108/EC-09-2016-0321.

Acknowledgements

ON THE BIOMECHANICS OF RECONSTRUCTED MANDIBLES WITH CAD/CAM FIXATION DEVICES

Giorgio Biesso (1, 2, 3), Vincenzo Orassi (1, 3), Clarence Janka (4), Carsten Rendenbach (2), Sara Checa (1)

1. Berlin Institute of Health at Charité – Universitätsmedizin Berlin, Julius Wolff Institute, Germany; 2. Charité – Universitätsmedizin Berlin, Freie Universität Berlin, Humboldt-Universität zu Berlin and Berlin Institute of Health, Department of Oral and Maxillofacial Surgery, Berlin, Germany; 3. Berlin-Brandenburg School for Regenerative Therapies, Berlin, Germany; 4. Karl Leibinger Medizintechnik GmbH & Co.KG

Introduction

The optimal reconstruction of mandibular defects remains a clinical challenge. Current reconstruction strategies are based on the mechanical connection of a bone flap harvest from the patient to the mandible. The fixation is ordinarily performed through CAD/CAM plates. Although the approach is highly successful, recent investigations have reported quite cases of osseous non-union [4]. Bone healing is known to be highly dependent on the biomechanical conditions at the healing site. In addition, recent studies revealed that the stiffness and geometry of the fixation system influence the regeneration process [2]. A biomechanics evaluation of the reconstructed mandible is still missing on plate design. Therefore, this study aims to investigate whether the healing outcome in reconstructed patients can be related to postoperative biomechanical conditions.

Methods

Four patients were identified as ideal candidates. The choice of patient was based on the healing outcome (Tab. 1). Subject-specific finite element models (FEMs) were built for each patient (Fig. 1). The bone geometry was reconstructed from clinical Computed Tomography (CT) scans. Homogeneous and linear elastic material properties were assigned to elements representing fibular and mandibular bone tissue. The fixation system consisted of a combination of titanium alloy CAD/CAM load-bearing and load-sharing fixation plates. Plates design and mechanical properties were derived from the individual surgical plan. 24 muscles, modelled as actuators, were added to the FEM through coupling constraints. Insertion points, muscle attachments, and force magnitudes were imported as boundary conditions through a musculoskeletal modelling technique [3]. The mesh and the coordinate system were maintained consistent between the two computational models. To ensure a proper occlusion, condylar processes were assumed locked in the mandibular fossa.

Patient	Healing	Fixation System
1	BC	2MP + 1RP
2	BC	1RP
3	NU	2MP + 1RP
4	NU	1RP

Table 1: Healing outcomes with fixation system: Bone Continuity (BC), osseous Non-Union (NU), Miniplates (MP), and Reconstruction Plates (RP)

Three static clenching tasks were simulated with intercuspal, incisal, and right unilateral biting. The 1st and 3rd principal strains were evaluated for all elements at the bone-defect interface.
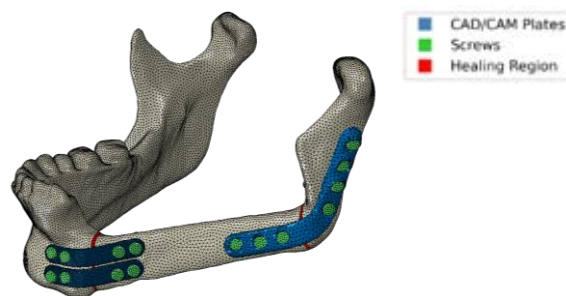
Figure 1: Subject-specific FE model of postoperative reconstructed mandible with CAD/CAM miniplates and reconstruction plates.

Results

The 3D geometry obtained through the segmentation process presented a relatively high accuracy, even though the CT scans were characterized by artifacts. The contact between plates and the mandibular surface was retained within the range of 10^{-2} mm. Preliminary studies revealed that the modelling technique adopted allows modulating muscle forces according to each reconstruction scenario.

Discussion

The present FE model aims to characterize the biomechanics at the bone-defect interface to support clinical practice. Further studies are needed for modelling the remaining samples and measuring the strain distribution. Model verification will be performed through a comparison with experimentally measured bite forces.

Acknowledgements

References

1. de Zee et al., J. Biomech., 2006
2. Lacroix et al., J. Biomech, 2002
3. Orassi et al., Front. bioeng. Biotechnol., 2021
4. Rendenbach et al., J. Oral Maxillofac. Surg., 2018.

FINITE ELEMENT MODELLING OF ACOUSTIC EMISSION FOR DENTAL IMPLANT MONITORING

Gabriel Boron, Robert Reuben, Uwe Wolfram

School of Engineering and Physical Sciences, Institute of Mechanical, Process and Energy Engineering, Heriot-Watt University, Edinburgh, United Kingdom

Introduction

Tooth loss can negatively affect mental health and, in turn, general health [1, 2]. Its causes are old age, poor oral hygiene, gum disease, and tooth trauma [1, 3, 4]. A potential treatment are dental implants with a 95% success rate [5]. However, they cost around £2000 for a single implantation, with £300 for consultations and CT scans in the UK [6]. Wearable or self-deployed devices for continuous implant monitoring could help to lower costs. They require, however, on-board or cloud-based mechanical analyses that are currently not available. To realise such analyses, we propose a framework combining acoustic emission (AE) and finite element (FE) analyses to analyse implant stability. Specifically, our objectives were (i) to develop a poro-viscoelastic material model for acoustic emissions; (ii) to identify and validate this model; and (iii) to investigate AE for monitoring dental implants in FE.

Methods

We developed and implemented a BV/TV and fabric based poro-viscoelastic material model [8, 9, 10] as a VUMAT in Abaqus (v6.16) to simulate AE through bovine rib. It captures the poroelastic behaviour of bone, accounting for the fluid and solid phase, and viscoelasticity as the damping source. We verified that variation in fluid content was negligible at small magnitude loads using in Abaqus SOILS on four Cubic ROI's. Two resembling fully cortical and trabecular conditions, and two representing end-of-rib open conditions with one and three permeable faces. We then performed AE experiments on $n = 15$ bovine rib samples. Ribs were loaded with pencil led breaks and AE was detected using a piezoelectric sensor (Physical Acoustic micro-80D). The frequency and energy of the signals was computed and analysed along with maximum amplitude. We varied source-sensor distance from 10 mm to 20 mm, the volume of ultrasonic couplant gel used (0 mm^3, 15 mm^3, 60 mm^3) and mounting technique (rubber-band stiffness 1691 N/m, 11319 N/m, 29430 N/m). Ribs were fixed in alcohol and μCT scanned (XTekCT) at 25-40 μm voxel size. BV/TV and fabric were determined from these scans using custom code written in Python. We use experimental results on 10 of the experimental ribs to identifying fractional viscoelastic parameters (C_ρ and ρ) and the remaining 5 ribs for validation.

Results

We found variation in fluid content in a porous media to be negligible with low magnitude loads (pencil lead break 2.89 N). Cortical and trabecular cubes had 0% change in fluid content, whereas cubes with 1 and 3 permeable side had 20×10^{-4}% and 22×10^{-4}% change respectively. We found an optimal experimental setup with 20 mm source-sensor distance, 0 mm^3 gel volume, and 29430 N/m rubber-band stiffness. Decreasing source-sensor distance (20 mm – 10 mm) increased signal amplitude (1.4 V – 4.3 V). Increasing gel volume (0 mm^3 – 60mm^3) increased amplitude (0.82V – 5V). Increasing rubber-band stiffness (1691 N/m – 29430 N/m) increased amplitude (0.42 V – 1.03 V).
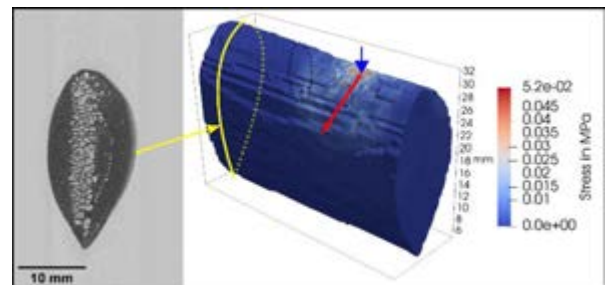
Figure 1: Simulation of a wave propagating (red arrow) through a heterogeneous rib model from pencil led break loading of 2.89N (blue arrow). The model was made from CT scans (left). Dashed black ellipsoid indicates experiment sensor location on the far side of rib.

Discussion

The poro-viscoelastic model adds damping as seen in the experiments to the solely poroelastic model, improving accuracy. The variation in fluid content was assumed to be negligible at our small loads. This assumption allowed a simplified calculation of pore pressure for the poroelastic part of the model. The proposed AE-FE framework may enable analyses and long-term monitoring of bone-implant interfaces using reflection/transmission coefficients of the disturbed interface as metric. It may, therefore, be extendable to other implantation sites.

References

1. Grifin et al, American J Public Health 3:411-418, 2012
2. Allen et al, J Canadian Dental Assoc, 10:662, 2003
3. Dosumu et al, Annals Ibadan Postgrad Med 2014, 1:42-48
4. Mal et al, J American Dental Assoc, 3:252-265, 2013
5. Moraschini et al, J Oral & Maxillofac Surg, 377-388, 2015
6. Aesthetic smiles, http://www.aesthetic-smiles.co.uk/blog/the-cost-of-dental-implants, 2019
7. Mavrogordato et al Med Eng Phys, 33:395–406, 2011.
8. Cowin et al, J Biomech Model Mechanobiol, 1:39-65
9. Alotta et al, J FE in Analysis and Design, 28-41
10. Zysset et al, J Mechanics of Materials, 4:243-250

AN INSTRUMENTED ORTHOSIS PROTOTYPE FOR CRANIAL CORRECTION

Begona Garate Andikoetxea (1), Aitor Zabala (1), Ahmed Elawadly (2), Stephen Taylor (1), N U Owase Jeelani (2), David Dunaway (2), Greg James (2) Silvia Schievano (1,2), Alessandro Borghi (1,2)

1. University College London, United Kingdom; 2. Great Ormond Street Hospital, London, United Kingdom

Introduction

Metopic Craniosynostosis (MC) is a congenital craniofacial anomaly, which involves premature closure of the metopic suture, leading to restricted brain growth and aesthetic problems (abnormal forehead shape). Surgical treatment of MC involves extensive skull reshaping, usually during the first year of life. More recently, minimally invasive endoscopic strip craniectomy (ESC) - involving endoscopic resection of the synostosis suture via a small frontal incision - has been adopted worldwide. ESC in conjunction with the post-operative helmeting (ESCH) has shown very promising results both in terms of aesthetic and functional improvement [1]. Although helmet therapy is a well-established methodology, side effects and complications such as skin irritation, pain and helmet dislodgement remain common A better understanding of the interaction between paediatric calvarium and orthotic helmet would most certainly help address the individual needs of patients treated with ESCH.
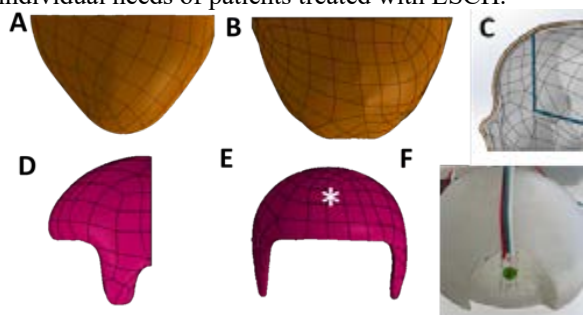
Figure 1. A) PRE model (top view) B) POST model (top view), C) Head model showing skull, soft tissues and sutures, D) Helmet model, side and E) top view (the * shows the location of the rosette); F) helmet 3D printed model with strain gauge rosette.

Methods

A patient affected by MC was treated with EAC (age at surgery= 4.8 months) and – post-operatively – orthotic helmet therapy treatment to improve head shape. The patient 3D scans (Rodin4D®) obtained postoperatively (pre-treatment - PRE) and after three months of treatment (POST) were processed to create 3D models to simulate the effect of helmet remoulding. Solidworks® was used to produce 3D shape of the soft tissue surfaces; these surfaces were offset by an averaged value (2.8mm) to produce a simplified outer skull surface, which was afterwards offset by a constant value (2.49mm) to create the skull model. The sutures for each case were also replicated in the 3D model, as well as the osteotomy size (as recorded on theatre). A moulding helmet model was created using a sample physical helmet available: it was scanned using a clinical CT scanner and reconstructed using Simpleware ScanIP. The helmet model was imported along with soft tissue and skull models in ANSYS. Helmet positioning was simulated for both PRE and POST models using linear elastic properties for both skull (E = 421MPa) and sutures (E=16MPa) and skin (E = 0.42MPa) [2]. The 3D model of the helmet and the PRE head model were then 3D printed on a Stratasys Connect 360 in Vero White plastic. A strain gauge rosette was positioned on the helmet in the area where maximum strain was predicted by the FE model. The helmet prototype was then positioned on the PRE model to simulate helmet insertion. Strains were recorded and the maximum principal strain was derived.

Results

Helmet positioning simulation showed markedly different strain pattern for the PRE and POST models (figure 1A). Positioning of the instrumented helmet model on the PRE model showed a marked and measurable increase in maximum principal strain in the area predicted by the FE model (Figure 1B).
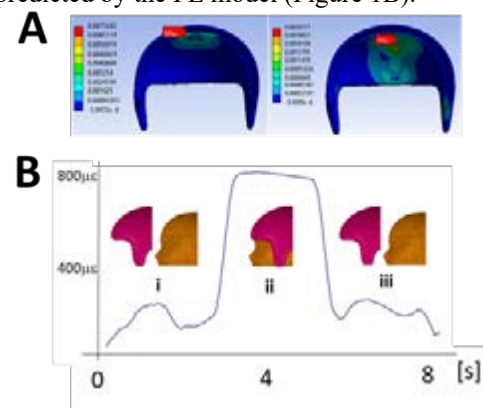
Figure 2. A) Maximum principal strain simulation for the PRE (left) and POST (right) models. B) Maximum Principal strain gauge measurements on the helmet 3D printed model (i, iii = baseline; ii = helmet positioning).

Discussion

This work shows that the interaction between helmet and patient head can be monitored by means of instrumented orthosis and that strain gauge location can be designed using FE modelling.

References

1. Halim et al., BJNeurosurg, 2020, 26(11).
2. Borghi A et al, MedEngPhys 2018, 53(3).

A NOVEL METHOD TO MEASURE DISTRACTION FORCES DURING MID-FACE ADVANCEMENT

Aitor Zabala (1), Begoña Garate (1), Stephen Taylor (1), Juling Ong (2), David Dunaway (2), Owase Jeelani (2), Silvia Schievano (1,2), Alessandro Borghi (1,2).

[1] *University College London, UK,* [2] *Great Ormond Street Hospital, London, UK*

Introduction

The crouzon syndrome is a rare genetic disorder causing premature fusion of cranial sutures, which in some cases lead to severe functional problems, including raised intracranial pressure and airway and visual pathway dysfunction. Surgical treatment includes mid-face advancement (following fronto-facial osteotomy), performed by means of a rigid external distractor (RED FRAME, KLS Martin, figure 1A). The RED frame is composed of a vertical carbon rod (connected to a halo – in red in figure 1B - which is secured to the patient's head) and a horizontal distraction stage where two wire connectors are linked by means of wires to the patient's maxilla and allow for distraction force transmission. The functional outcomes of distraction are acceptable, yet unpredictable. The knowledge of magnitude and directions of such vector would provide an important tool for distraction planning, thus ensuring an improvement in functional and aesthetic outcomes.
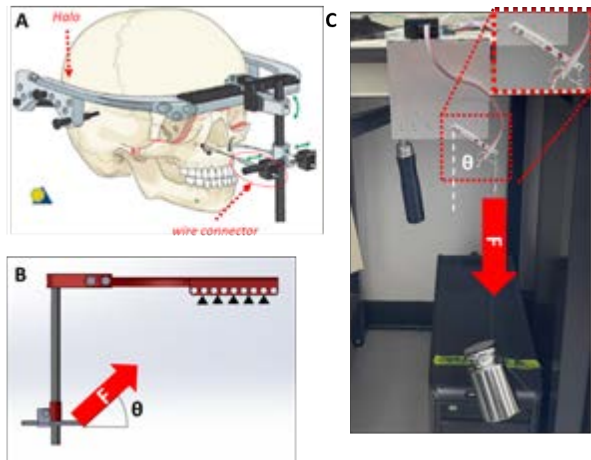
Figure 1: A) Schematic of mid-face distraction using RED-FRAME B) CAD model of RED Frame used for FE modelling, showing the location of the Force F and the boundary conditions C) Experimental set up: a replica of the wire connector is instrumented using strain gauges (see inset) and subject to a calibrated force F.

Methods

A 3D CAD model of the RED frame (figure 1B) was created in Solidworks® and imported in ANSYS 2020 R2® for FE modeling. To assess the displacement and strain pattern it is subject to during distraction, a direct force of 21.25N [1] was applied on each wire connector, at an angle Θ which varied between 0 to 60° . The halo was fixed in all directions to simulate connection with the patient's calvarium. The strain pattern on the wire connectors was estimated in each configuration.

A replica of the wire connector was manufactured using an aluminum bar and instrumented using four strain gauges (SG - two per side: one parallel to the bar, the other at 45 degrees - figure 1C, inset). By means of calibrated weights (figure 1C), the bar was subject to 5 to 20N force at a relative angle ranging from 0° to 60° (figure 1C). The SG were then wired to a conditioning and amplification stage and monitored through a microcontroller. The analogue voltage output was read, convert it into digital signal, recorded and averaged. Multiple linear regression (MLR) was carried out between the sensitivity components and force components - axial (=F·cos Θ) and shear (=F·sin Θ).

Results

FE analysis allowed visualization of the displacement pattern on the RED frame and strain pattern on the wire connector when subject to distraction force (figure 2A). SG measured sensitivity ranged from 0.71 (45 deg) and 1.82 (longitudinal) μstrain/N at for Θ = 0° to -3.9 (45 deg) and 3.8 (longitudinal) μstrain/N. The instrumented bar showed good response linearity (figure 2B) for both 45 degrees SG (R^2 =96.1%±4.3%) and longitudinal SG (R^2 =99.3%±0.1%). MLR allowed for effective separation of the axial (error = 1.2±0.9N) and shear (error = 0.17±0.3N) components of the force.
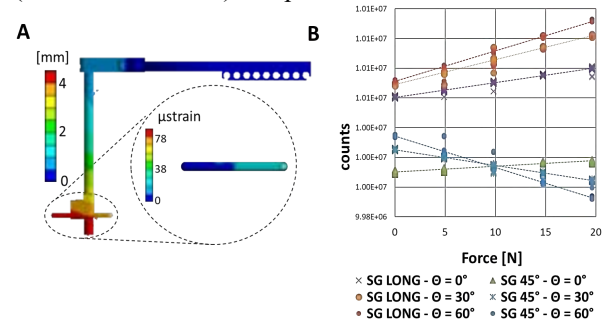
Figure 2: A) FE simulation of displacement pattern on the RED frame and strain pattern on the wire connector. B) Microcontroller output vs force for the 45degrees and longitudinal strain gauges for Θ = 0°, 30°, 60°.

Discussion

Magnitude and direction of distraction force can be measured using an instrumented version of the RED frame. MLR allowed for effective separation of force components with a resolution of ~ 1÷2N.

In the next step, the prototype will be calibrated and validated in-vitro using realistic anatomical phantoms.

References

1. Suzuki et al. JOMS 2009, 67(10).

TOWARDS THE DESIGN OF A NOVEL NITINOL DISTRACTOR FOR CRANIOFACIAL SURGERY

Laura Zabalza (1), Naiara Rodriguez-Florez (3,4), Dulanka Silva (2), Owase Jeelani (2), Greg James (2), David Dunaway (2), Juling Ong (2), Silvia Schievano (1,2), Alessandro Borghi (1,2)

1.University College London, United Kingdom; 2. Great Ormond Street Hospital, London, United Kingdom; 3. Universidad de Navarra, Spain; 4. Ikerbasque, Spain

Introduction

Craniosynostosis is defined by the early fusion of cranial sutures leading to clinical and aesthetic impairments often requiring reconstructive surgery. Unicoronal Craniosynostosis (UC), which affects one side of the coronal sutures, is surgically challenging and current solutions involve an invasive reconstruction of frontal bones to correct the asymmetry. [1] Spring Assisted Cranioplasty (SAC) has become an accepted minimally invasive treatment for patients with craniosynostosis [2]. However, it cannot be directly used in due to the directional limitation of current devices. This is where nitinol is expected to make an impact, as it can be programmed to be shaped to patient-specific anatomy [1]. The objective of this work is to establish a computational framework to design novel nitinol cranial distractors to correct UC.

Method

UC patients (n=19) with preoperative CT scans were retrieved (age = 1.5 ± 0.4 years) and post-processed combining ScanIP (Simpleware) and Meshmixer (Autodesk). 3D head models were created and the average calvarial thickness was obtained by measuring the surface distances between the inner and outer skull for each patient.

Statistical Shape Modelling (SSM) was performed using Deformetrica to get the mean shape and shape variability of the studied population. [3] The resulting mean was then used to simulate surgery by Finite Element Modelling (FEM) (Ansys 2020). In order to select the best virtual surgery strategy, the mean model was 3D printed (Stratasys Connex 3 Objet260V) and given to five expert surgeons to draw the osteotomies which resulted in three different models.

Surgical cuts were replicated in FEM and a spring-like distractor was simulated (based on existing distractors used in SAC (k=0.17, 0.39, 0.68 N/mm) parameterizing the position of the notch for the spring along the osteotomy. Spring expansion and the deformed calvarial shape were recorded. Head shape changes were quantified by measuring the Cranial Vault Assymmetry Index (CVAI; a value of 1 refers to a perfectly symmetric forehead); and visualized by color maps of surface distances from the initial mean 3D model to the post-virtual surgery deformed shape (VMTK and ParaView) (Figure 2C).

Results

SSM resulted in a mean 3D model with a CVAI of 4.17. The surgical cuts suggested by the surgeons led to three osteotomy designs (Figure 2A).
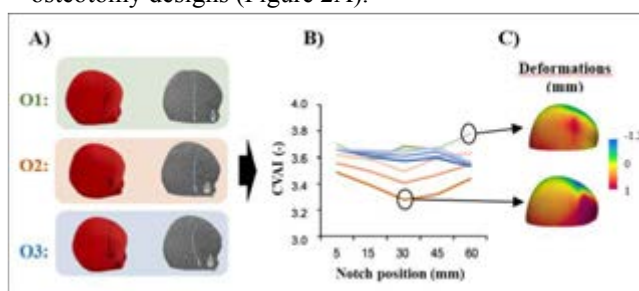
Figure 2: A) Physical and virtual models of the osteotomies (O1-3); B) CVAI according to notch position, osteotomy and spring stiffness (the darker the stiffer); C) Surface distance maps from pre-surgery to the deformed shape showing the worst (above) and best results (below).

In all studied cases the CVAI was improved comparing to the initial value (smaller CVAI). The second osteotomy with the spring located at 30mm from the bottom resulted in the best result in terms of CVAI (Figure 2B). Thus, this would be the selected osteotomy for further steps. However, the deformations obtained using only one spring were not sufficient to correct the asymmetry.

Discussion

In this work, SSM, 3D printing and FEM were combined to establish a framework for virtual surgery for UC as a first step towards the design of a novel distractor. Next steps will investigate the addition of a second distractor and/or increase in the stiffness of the spring in order to correct head asymmetry. The optimal designs will be manufactured in nitinol using additive manufacturing technology and studied using physical and virtual in-silico models of UC.

References

[1]   W. Rodgers *et al.*, *Br. J. Oral Maxillofac. Surg.*, 55, p. e83, 2017.

[2]   A. Borghi *et al.*, *Med. Eng. Phys.*, 53, 58–65, 2018.

[3]   N. Rodriguez-Florez *et al.*, *Int. J. Comput. Assist. Radiol. Surg.*, 12, 1739–1749, 2017.

AN EXPERIMENTAL AND COMPUTATIONAL STUDY ON A PATIENT-SPECIFIC 3D PRINTED TI6AL4V HEMIPELVIS PROSTHESIS

Luca Ciriello (1), Francesca Danielli (1), Riccardo Verga (2), Fabio Alemani (2), Maurizio Cicero (2), Jose Felix Matas Rodriguez (1), Giancarlo Pennati (1), Luigi La Barbera (1)

1. Department of Chemistry, Materials and Chemical Engineering, Politecnico of Milano, Italy
2. Adler Ortho SpA, Milan, Italy

Introduction

3D printing is a rapidly growing industry. Given the complex anatomy of the pelvis, 3D printing has the potential to adapt to complex surgery planning and to improve procedural accuracy [1]. With the development of 3D printing, it is possible to realize metallic implants with different characteristics, such as continuous external solid parts and highly-inhomogeneous lattice structures matching closely the modulus of the bone, thereby reducing problems related to stress shielding. Some studies consider the optimization of the prosthesis implanted. However, most of the computational models rely on different simplifications such as no distinction among continuous solid parts and highly lattice structure present in the additive manufactured prosthesis [2,3,4]. This works aims at investigating the influence of different materials in a validated Finite Element (FE) model of a patient-specific hemipelvis prosthesis, implanted in a pelvis bone. Two different steps have been performed to develop the computational model: (i) experimental validation of the hemipelvis prosthesis, (ii) implementation of functional loadings on the implanted model.

Materials

Experimental validation of the prosthesis model. The patient-specific FE model of the hemipelvis prosthesis was built using Abaqus 2021 (Dassault Systèmes, SIMULIA Corp., RI), assigning different materials in the continuous external solid parts, filling lattice, and interface lattice structures. The materials of different parts were previously characterized through tensile tests on dog-bone specimens manufactured in Ti6Al4V by electron-beam melting (by Adler Ortho SpA). The same boundary conditions of an ad-hoc experimental test were imposed on the numerical model (Figure 1a and 1b). Three different tests were performed in order to validate the FE model in terms of stiffness (K, slope of force-disp. curve) and local strains (ε_{Princ}) using strain-gauge rosette.

Functional loadings on the implanted hemipelvis. The validated prosthesis was coupled with the patient's pelvis bone model and a general contact was defined between them. The fixing screws were considered (Figure 1c) and a tighten force of 160N was defined. The mechanical characteristics of the bone were assigned through Bonemat software using the correlation between the Hounsfield units of the CT images and Young modulus [5]. The implanted pelvis model was loaded through the application of weight and active muscles forces in the stance phase of the gait cycle (Figure 1c) [6].

Results

Experimental validation of the prosthesis model. The numerical model with the characterized materials (77GPa for external parts and 58GPa for filling and interface lattice structures) demonstrated good agreement with experimental static tests (Table 1).

Table 1: In vitro and in silico results from the prosthesis test.

	EXP	FEA	% diff.
K [N/mm]	1037±56	1176	+13%
$\varepsilon_{MAX,Princ}$ (μm/m)	50±5	53	+ 5%
$\varepsilon_{MIN,Princ}$ (μm/m)	-483±6	-422	-15%

Functional loadings on the implanted hemipelvis. With the applied load, the bone fatigue deformation limit (1.95%) and the maximum stress limit (129MPa) were not reached on bone and prosthesis [7]. In particular the bone underwent deformation values equal to about 1.58%, while the prosthesis reached maximum principle stress values equal to 95 MPa on the filling structures.

Discussions

This works shows how an accurate characterization of the different parts within 3D printed prostheses is crucial for the validation of the corresponding FE models. In addition, the different parts of the prosthesis with their associated stiffnesses lead to a different distribution of stresses and strains on the bone and the prosthesis itself, in contrast to literature studies [5,6].
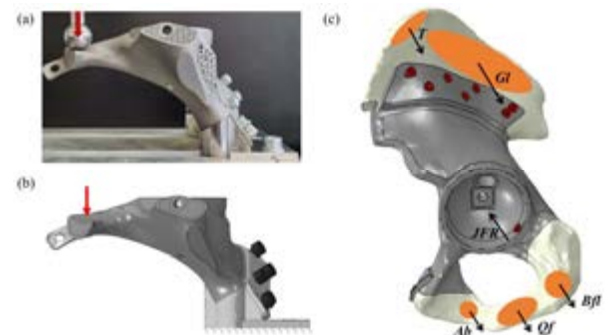
Figure 1: (a)Validation experimental setup; (b) FE model of the test; (c) FE model of the implanted pelvis bone with details of muscles forces directions and attachment zones in orange (JRF=3300N, T=202N, Gl=3246N, Ab=174N, Qf=147N and Bfl=309N) and the screws in red.

References

[1] Liebsch et al. Clin Biomech. 78:105070, 2020.
[2] Iqbal et al., J of Eng.in Med. 231(6), 2017.
[3] Dong et al., J of Bionic Eng. 15(3): 443-51, 2018.
[4] La Barbera et al., Int J Artif Organs. 42(10): 75-85, 2019.
[5] Arkusz et al. Acta of Bioeng&Biomech. 20(1):29-38, 2018.
[6] Dalstra et al., J of Biomech. 26(4-5): 523-35, 1993.
[7] Razavi et al., Addit. Manuf. 36:101426, 2020.

ADDITIVELY MANUFACTURED MICROLATTICE STRUCTURES FOR AN INNOVATIVE INTERVERTEBRAL DEVICE

Fabio Distefano (1), Gabriella Epasto (1), Eugenio Guglielmino (1), Rosalia Mineo (2,3)

1. Department of Engineering, University of Messina, Contrada di Dio, Vill. Sant'Agata, 98166 Messina, Italy;
2. Mt Ortho srl, via fossa lupo sn, Aci Sant'Antonio, 95025 Catania, Italy;
3. Department of Civil Engineering and Architecture, University of Catania, Via S. Sofia 64, 95125 Catania, Italy

Introduction

Degenerative disc diseases are a serious health problem which may result in mechanical back pain, reduced mobility and poor quality of life. Different surgical options for interbody fusion of the lumbar spine have been developed.

The aim of this study is the analysis of the mechanical behaviour of a lumbar cage, made of Ti6Al4V ELI alloy, produced by electron beam melting (EBM) technique, and implanted in the L4-L5 motion segment via transforaminal lumbar interbody fusion (TLIF) approach. A finite element (FE) model was developed for this purpose.

Methods

The intervertebral device object of the research is a partially porous lumbar cage (Fig. 1), which included an external shell made of bulk material (blue part in Fig. 1a), a core (green part in Fig. 1a) and an upper endplate (red part in Fig. 1a) both with rhombic dodecahedron (RD) microlattice structure.

The FE analyses were performed by using Altair Hyperworks® package software.

Following a mesh sensitivity analysis, tetrahedral element with 0.3 mm size was selected for the mesh of the device. The whole lumbar spine was considered in the model, including intervertebral discs and ligaments. The bone and the discs were meshed with tetrahedral elements of 0.6 mm size, while ligaments were modelled by using beam elements. At the interface between cage and vertebrae, a friction coefficient of 0.8 was considered. In Fig. 1b is shown the lumbar spine with the implanted cage. The bone was divided in three parts: cortical, cancellous and posterior; while the intervertebral disc was divided in nucleus pulposus and anulus fibrosus.

The cortical bone was modelled as orthotropic material, while cancellous bone, posterior bone, intervertebral discs and ligaments were modelled as isotropic material. Five different load conditions were simulated: a pure compression physiological load of 650 N and four different combined load conditions including 150 N in compression and 10 Nm moment in flexion, extension, lateral bending and torsion.

Results

The principal stresses at the interface between cage and vertebrae were analysed. These results were compared to those obtained at the interface between intervertebral disc and vertebrae in the intact spine as shown in Fig. 2, which shows the results for compression load. The same considerations were made for the other load conditions. For all the cases, stresses values are lower than the mechanical strength of the vertebral bone 140 MPa.

Discussion

The proposed intervertebral device is an optimal solution for the treatment of the lumbar diseases. The stress distribution was analysed and compared with the model of a non-pathological spine. No overload caused by the device was found on the bone. Such behaviour does not imply pain due to the mechanical damage of the bone.

Figures

Figure 1: (a) TLIF lumbar cage; (b) lumbar spine with the implanted cage
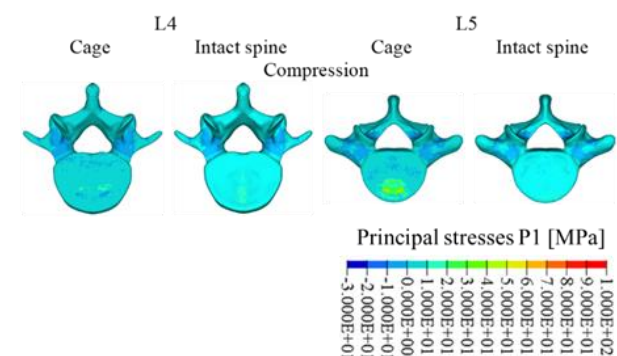
Figure 2: Principal stresses in the L4-L5 motion segment

CAN 3D-PRINTED VORONOI STRUCTURES REDUCE FRICTION IN ORTHOPAEDIC IMPLANTS?

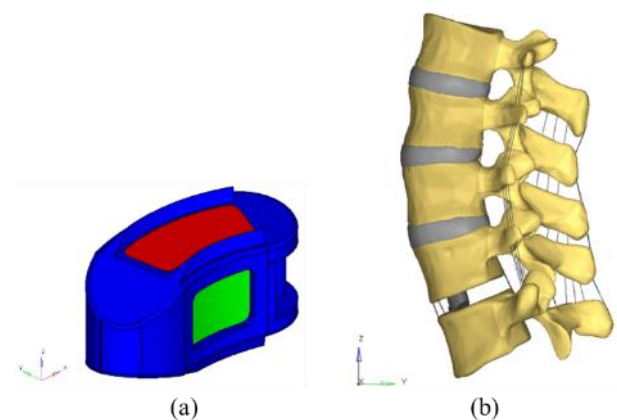**Cong Hou[1], István Nemes-Károly[2], Leonard Pastrav[1], Bey Vrancken[1], Gyorgy Kocsis[3], Kathleen Denis[1], Gábor Szebényi[2,4]**

1. KU Leuven, Department of Mechanical Engineering, Belgium; 2. Budapest University of Technology and Economics, Faculty of Mechanical Engineering, Department of Polymer Engineering, Hungary; 3. Semmelweis University, Department of Orthopaedics, Hungary 4. MTA-BME Lendület Lightweight Polymer Composites Research Group, Hungary

Introduction

With the advent of an ageing society, the number of joint replacements has rapidly increased in recent years. Wear is an important factor limiting the life span for artificial joints. Recent studies indicated that approximately 10% of surgeries each year are revisions [1]. A joint prosthesis typically consists of a polyethylene (PE) versus polished solid metal surface pair. Instead of the solid part, our group uses a porous metal structure. A particular type of Voronoi lattice structure has been studied. The porous structure is helpful for the hydro-dynamic effect, which results in reduced friction [2]. The structure may also filter the synovial fluid and collect wear debris, reducing the risk of abrasive wear. This abstract deals with the manufacturing procedure of Voronoi-type structured porous structures and early stage tribological experiments (pin-on-disk).

Methods

The generation of a Voronoi structure starts from a collection of nodes in a certain space, from which the three-dimensional lattice structure is then generated [3]. Ti6Al4V powder (grade 23, Carpenter Additive, particle size 15-53 µm) was used as material to meet the requirements for orthopaedic implants, such as biocompatibility and relative low E-modulus. Laser powder bed fusion (LPBF, ProX 320, 3D Systems) was used to manufacture the pin-shaped samples, which were subsequently used for pin-on-disk testing. The samples were chemically cleaned (SILC procedure, 3D Systems) to improve surface quality. The procedure consists of acid bath, centrifuge and oven drying. To measure the coefficient of friction (COF) between the samples and PE disks, a pin-on-disk test was performed with a pin-on-disk tribometer (TRB3, Anton Paar GmbH), with three samples in each group. Polished solid Ti pins were used as control group.

Results

Figure 1 represents the surface morphology of a printed lattice structure before and after chemical cleaning. A large number of powder particles are partially sintered to the surface of the as built samples, which is a common feature of LPBF. Even though there are some particles left deep down, most of the particles located on the surface have been removed after cleaning.

The tribological test results are shown in figure 2. The control samples exhibited a COF of 0.21. The dense and porous Voronoi structures resulted in a reduction to 0.18 and 0.16, respectively. Pilot test results indicated the COF between PE and samples further decreased to around 0.14 after chemical cleaning.
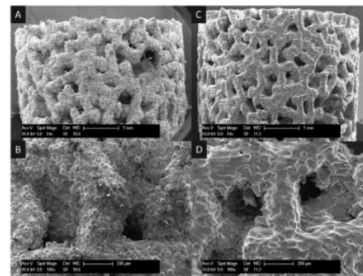
Figure 1: SEM pictures of printed Voronoi structures: as printed (A and B) and after cleaning(C and D).
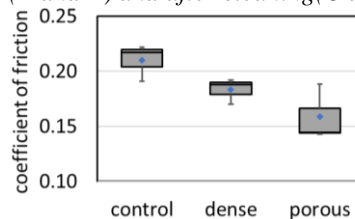
Figure 2: Tribological test results, comparison between solid pins, and two types of Voronoi structures.

Discussion

The results of the pin-on-disk tests showed excellent frictional properties of the Voronoi structure on PE. Further studies will be carried out with the focus of improving manufacturing quality, such as optimizing geometric accuracy and remove surface particles. Its application in artificial articulating surfaces will be explored in subsequent studies.

References

1. Norwegian National Advisory Unit on Arthroplasty and Hip Fractures, Annual Report 2020, 2020.
2. Ito H, Kaneda K, Yuhta T, et al. Reduction of polyethylene wear by concave dimples on the frictional surface in artificial hip joints. The Journal of arthroplasty, 15(3): 332-338, 2000.
3. Hanniel I, Elber G. Computing the Voronoi cells of planes, spheres and cylinders in R3, Computer aided geometric design, 26(6): 695-710, 2009.

Acknowledgements

3D PRINTED SOFT METAMATERIAL FORCE SENSORS FOR GAIT MONITORING USING TPU-GRAPHENE COMPOSITES

Inigo Sanz-Pena* (1), Noelia Rubio Carrero (2), Hang Xu (3), Matthew Hopkins (4)

1. Department of Mechanical and Industrial Engineering, University of Illinois at Chicago, USA; 2. Department of Organic and Inorganic Chemistry, University of Alcala, Spain; 3. Department of Materials, Imperial College London, United Kingdom; 4. Department of Surgery and Cancer, Imperial College London, United Kingdom. *Corresponding author: e-mail: isanzpen@uic.edu

Introduction

Measuring the vertical ground reaction force (VGRF) is fundamental in monitoring gait during rehabilitation. Force plates and inertial sensors are among the most commonly used systems [1], however, such sensors are typically expensive and bulky. Alternatively, wearable pressure sensitive insoles using commercial force sensors have shown potential advantages e.g. low profile, portability, and low-cost [2]. Additive manufacturing (AM) techniques can be used to combine elastomers with electrically conductive materials and inks allowing the fabrication of pressure sensors [3]. Moreover, the geometry of AM can be tailored to create soft metamaterial sensors with the desired force range. The aim of this study was to develop application-specific wearable sensors using mechanical metamaterials with piezoresistive behaviour, where the sensitivity can be defined by the structural and material properties.

Methods

Three sensors were designed using regular lattice structures to measure different compressive force ranges. The sensors were manufactured in two stages. First; the sensors were printed using a SLS 3D printer in Thermoplastic polyurethane. Second; each sensor was immersed in a graphene/ethanol ink solution. Lastly the sensors were dried using a vacuum oven. Two different gradient concentrations were studied to see the effects of the infusion process on the piezoresistive behaviour of the sensors. (1) A concentration of 2.5 mg/mL applied on a single infusion and (2) two consecutive immersions of 0.5 and 2.5 mg/mL with a drying process in between. The sensors were tested using an Instron testing system while measuring the electrical resistance across the top and bottom layer. The graphene deposition was analysed using a scanning electron microscope (SEM).

Results

The stiffness results obtained from the compressive tests for the three prototypes (1.0, 2.0, and 3.0) showed repeatable parallel force range trajectories independent of the compression velocity (Fig. 1). Despite using the same structural stiffness (prototype 1.0 samples), the piezoresistive behaviour was influenced by the graphene concentration, with lower concentrations of graphene leading to substantially greater sensitivity for forces between 0 - 25 N (Figure 2).
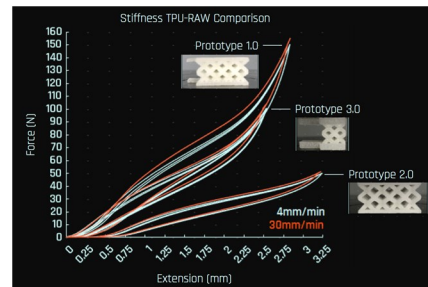
Figure 1: Stiffness of the three lattice designs for three compression cycles (0-50 N, 0-100 N, and 0-150 N).
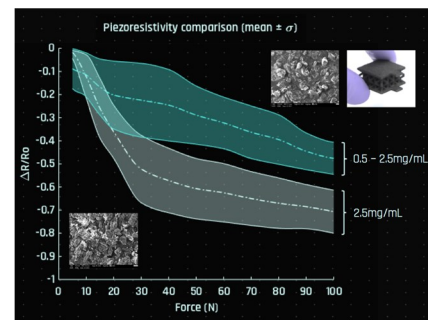
Figure 2: Normalised electrical resistance response for prototype 1.0 (1.1, 1.2, 1.3, and 1.4 samples) classified for the 2.5 mg/mL and 0.5 - 2.5 mg/mL concentrations.

Conclusions

Graphene infusion of the sensors in separate phases reduced the electrical resistance across the sensor more than single infusion deposition. The two-infusion process resulted in a linear behaviour over the tested force range, while the single infusion method produced greater sensitivity at lower forces. These results indicate that 3D printed soft metamaterial sensors can be fabricated using TPU lattice structures coated with graphene inks. The force range results show the potential use as wearable sensors for measuring the VGRF at foot pressure points during gait.

References

1. A.H. Razak et al., *Sensors*, 7: 9884-9912, 2012.
2. I. Sanz-Pena et al., *IEEE H-M. Syst.*, 51:5:484-493, 2021.
3. A. D. Valentine et al., *Adv. Mater.*, 29:40, 2017.

Acknowledgements

ARTICULAR CONTACT VS. EMBEDDING: THE EFFECT OF BOUNDARY CONDITIONS ON VOLAR PLATE FIXATION AT THE DISTAL RADIUS

Laurenz Berger (1), Dieter H. Pahr (1,2), <u>Alexander Synek</u> (1)

1. Institute of Lightweight Design and Structural Biomechanics, TU Wien, Vienna, Austria;
2. Division Biomechanics, Karl Landsteiner University of Health Sciences, Krems, Austria

Introduction

Distal radius fractures (DRF) are among the most common fractures and treatment often involves surgical reduction and internal fixation with a volar locking plate (VLP). Due to their high incidence, fracture treatments are extensively investigated – both with experiments and finite element analyses (FEA). Still, the loading conditions are often highly simplified. In experiments, load is typically applied uniaxially at the radiocarpal joint (RCJ) using embedding materials or indenters of arbitrary shape [1]. In FEA models, either embedding material is used or point loads are applied at the articular surface [2]. Only rarely, carpal bones and articular contact are accounted for [3]. However, the load distribution at the RCJ might be of high relevance for the loading of the VLP system, as the distal screws are positioned just below the articular surface. This study investigates if the effort of implementing complex boundary conditions with articular contact is justified to predict VLP loading parameters accurately.

Methods

A reference FEA model of an extra-articular DRF with VLP treatment was created based on a computed tomography scan. The reference model included carpal bones and articular contact in the RCJ and was loaded uniaxially with 250 N. Four models with simplified boundary conditions were created and compared to the reference model (Fig. 1): One with embedding material instead of carpal bones (EM), one with carpal bones tied to the cartilage of the radius (TM); each loaded either uniaxially (EM_u, TM_u) or with statically equivalent loads with respect to the reference model (EM_m, TM_m). Fracture gap movement (FGM), peak von Mises stresses in the implant plate, loading of each distal screw, and the normalized root mean square error (NRMSE) of the effective stresses in the distal fragment were evaluated.
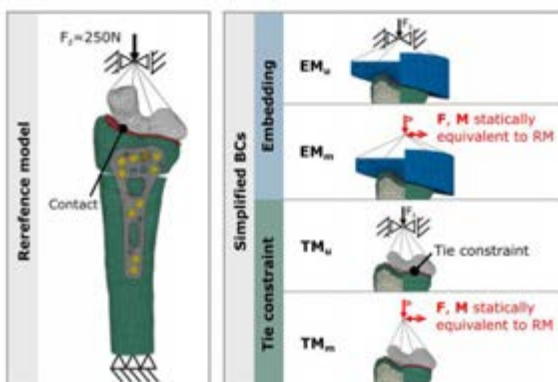
Figure 1: Reference model (RM, left) and models with simplified boundary conditions (right)

Results

The effective stresses at the articular surface showed that local stress peaks are absent in models excluding the carpal bones (Fig. 2, left). Errors of the uniaxially loaded models (EM_u, TM_u), were considerable for all parameters, ranging from 22 to 187% (Fig. 2, right). Even errors in FGM and peak plate stresses were larger than 50%. Using statically equivalent loading greatly reduced errors with respect to the reference model also in the embedded model (EM_m, all below 50%). Including the carpal bones with tied contact and statically equivalent loads further reduced the error to below 10% even for screw loads and stresses in the distal fracture fragment.
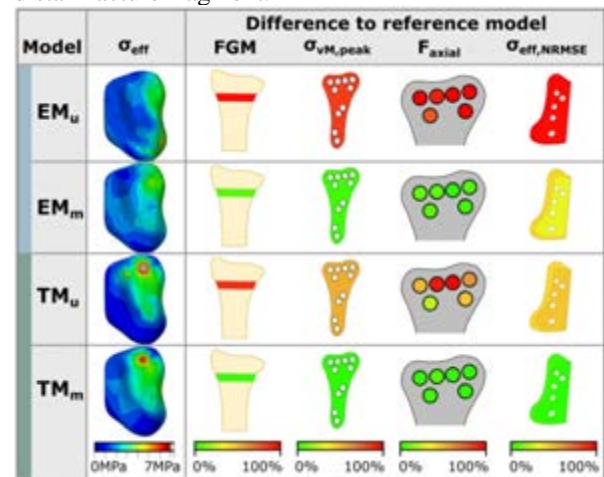
Figure 2: Stress distributions at the articular surface (left) and differences with respect to the reference model in mechanical parameters of VLP treatment caused by simplified boundary conditions (right)

Discussion

The results of this study suggest that realistic multiaxial loading is of highest relevance for accurate loading of VLP implants, irrespective of including carpal bones in the model. These multiaxial loadings could be obtained from experimental measurements or musculoskeletal models. Including carpal bones might only be relevant if screw load distributions or peri-implant bone stresses are investigated. In this case, using carpals with tie constraints and realistic multiaxial loading seems to offer a good trade-off between modelling effort and accuracy for computational models.

References

1. Crosby et al., J Hand Surg Am 38(6):1097-105, 2013
2. Caiti et al., Med Biol Eng Comput 57:1099–1107, 2019
3. Yamazaki et al., CMBBE 24(15):1687-1692, 2021

AFFORDABLE SOLUTION FOR LOW AND MIDDLE-INCOME COUNTRIES: UNILATERAL EXTERNAL FIXATOR

Mehdi Saeidi (1), Spencer Barnes (2), Michael Berthaume (1), Sander R Holthof (2), Anthony M J Bull (1), Jonathan Jeffers (2)

1. Department of Bioengineering, Imperial College London, London; 2. Department of Mechanical Engineering, Imperial College London, London

Introduction

External fixators are the first-line treatment for open fractures to the extremities. Commercial devices are costly and not pervasively available in Low- and Middle-Income Countries (LMICs) due to the lack of advanced resources and healthcare training. The need is even more critical in conflict-affected regions due to the type and severity of injury, damage to the soft tissue [1, 2], and the lack of provision of commercial devices, resulting in a significant shortage. This has resulted in homemade external fixators being used [3]. The aim of this study was to develop an affordable and locally manufacturable unilateral fixator with comparable performance to commercial devices.

Methods

In close collaboration with local partners, the device was designed based on local LMIC needs. The resulting device is lightweight, reusable, and biocompatible, and provides similar stiffness to commercial fixators. Imperial has also developed a toolkit (Figure 1) including a set of jigs to manufacture the device to international standards with conventional techniques. Anyone with basic machining skills would be able to produce an accurate external fixator using this kit.

Figure 1: Toolkit to manufacture imperial external fixator.

The Imperial and Stryker Hoffmann®3 unilateral external fixators were tested on cadaver specimens under 100 N and results were compared. The experimental setup is shown in Figure 2.

Results

The interfragmentary motion of femur specimens measured using a motion tracking system was on average 1.84±0.86 and 1.03±0.29 mm for Stryker and Imperial external fixators, respectively. In other words, the Imperial fixator demonstrated equivalent ability to stabilise the fracture as the Stryker device

Figure 2: Testing setup to measure interfragmentary motion in cadaver specimens.

Discussion

The Imperial fixator is significantly cheaper than the commercial ones, such as Hoffmann 3 because the materials used, aluminum and stainless steel, are low-cost and easily accessible. Also, the design is simple so it can be manufactured using conventional tools and equipment. Accordingly, this affordable solution can match the performance of pricy/commercial devices without sacrificing quality and is a viable solution for LMICs. After performing various testing, including the one explained here, the Imperial unilateral external fixator is currently being piloted in Sri Lanka (with local manufacture) and Gaza for different cohorts. Further engagement with many organisations including WHO, UNDP, MSF, and ICRC is being pursued in order to translate this device to more LMIC countries.

References

1. Whiting PS, et al. Journal of orthopaedic trauma. 2019;33:234-9.
2. Gellman RE.. Current Trauma Reports. 2016;2:100-5.
3. Fouad FM, et al.. The Lancet. 2017;390:2516-26.

Acknowledgements

LIGHT-CURABLE FIXATION COMPARABLE WITH PLATES IN TORSION

Peter Schwarzenberg (1), Thomas Colding-Rasmussen (2), Daniel J. Hutchinson (3), Dominic Mischler (1), Peter Horstmann (2), Michael Mørk Petersen (2), Michael Malkoch (3), Christian Wong (2), Peter Varga (1)

1. AO Research Institute, Switzerland; 2. RegionH, Denmark; 3. KTH Royal Institute of Technology, Sweden

Introduction

Traditional metal osteosynthesis hardware cannot be easily customized for a fracture in the operating theatre. Additionally, metal solutions can lead to debilitating soft tissue adhesions, especially in complex areas such as the hand [1]. A new osteosynthesis method, AdhFix, has been developed to combine metal screws and a light-curable polymer composite for highly customizable fixation solutions that induce no soft tissue adhesions [2]. While the bending performance of AdhFix is advantageous [2], torsion remains unknown. In this study, we investigate how the biomechanical performance of AdhFix compares to metal hardware when loaded in torsion in an ovine phalanx model.

Methods

Twenty-one ovine proximal phalanges were excised and stripped of soft tissue. Specimen-specific 3-D printed guides were used to drill four 1.1 mm pilot holes and perform a 3 mm gap transverse osteotomy between the innermost holes. Next, 1.5 mm cortex screws (DePuy Synthes) were inserted bicortically into each pilot hole. The light-curable polymer composite was then applied using the method developed by Hutchinson et al. [2] to create osteosyntheses mimicking bridge plating in two groups, having either a narrow (6 mm, N = 9) or a wide (10 mm, N = 9) fixation patch. A final group (N = 3) was fixated with conventional metal plates (1.5 mm locking plates with 1.5 mm Locking Screws, DePuy Synthes). Following the osteosyntheses, the epiphyses of each bone were embedded in PMMA with a 10 mm hex cavity centred along the AdhFix or plate axis for biomechanical testing. This cavity was used to position and load the constructs on an electromechanical testing machine (Instron 5943) in torsion at a rate of 6°/second until failure or 45° of rotation was reached. Torque and angular displacement were measured, torsional stiffness was calculated as the slope of the Torque-Displacement curve, and maximum torque was queried for each specimen in MATLAB 2020b (The MathWorks, Inc). Descriptive statistics and One-Way ANOVAs were performed in SPSS 27 (IBM Corp.).

Results

The torsional stiffnesses of the narrow, wide, and metal plate constructs were 39.1 ± 6.2, 54.4 ± 6.3, and 16.2 ± 3.0 Nmm/° respectively (Figure 1). All groups were statistically different from each other ($p < 0.001$). The maximum torques of the narrow, wide, and metal plate constructs were 424 ± 72, 600 ± 120, and 579 ± 20 Nmm respectively (Figure 2). The narrow constructs were statistically different from the wide and metal constructs ($p < 0.05$). The wide and metal constructs were not statistically different from each other ($p = 0.76$).
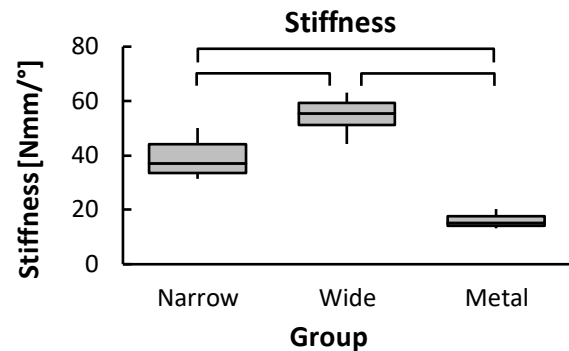
Figure 1: Box plots of the torsional stiffness for each group. Bars show statistical significance (p < 0.05).
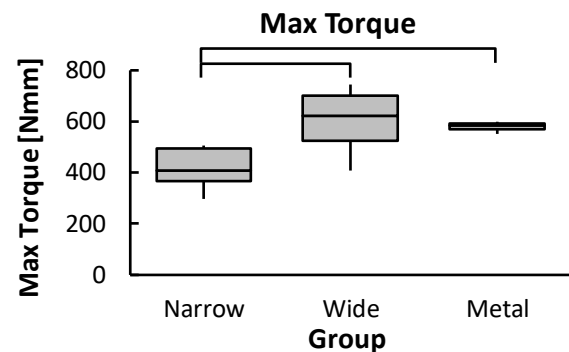
Figure 2: Box plots of the maximum torque of each group. Bars show statistical significance (p < 0.05).

Discussion

This work demonstrated that the torsional performance of the novel light-curable polymeric solution is comparable to traditional metal fixators. As a measure of the functional range, the torsional stiffness in the AdhFix exceeded that of the metal plate, even in the narrow patches which are of comparable dimensions. Furthermore, the wide patches were able to sustain a similar maximum toque as the metal plates. These suggest AdhFix to be a viable, customizable alternative to metal implants for fracture fixation in the hand.

References

1. Brei-Thoma et al, Arch. Orthop Trauma Surg.,2015
2. Hutchinson et al, Adv Funct Mater.,2021

Acknowledgements

BIOMECHANICAL ANALYSIS OF HELICAL VERSUS STRAIGHT PLATING OF PROXIMAL THIRD HUMERAL SHAFT FRACTURES

I. Zderic (1), T. Pastor (1,2), K. van Knegsel (1,2), B.C. Link (2), F.J.P. Beeres (2), F. Migliorini (3), R. Babst (2,4), S. Nebelung (5), B. Ganse (6,7), C. Schoeneberg (8), B. Gueorguiev (1), M. Knobe (2)

1. AO Research Institute Davos, Switzerland; 2. Lucerne Cantonal Hospital, Switzerland; 3. University of Aachen Hospital, Germany; 4. University of Lucerne, Switzerland; 5. University Hospital Aachen, Germany; 6. Saarland University, Germany; 7. Saarland University Hospital, Germany; 8. Alfried Krupp Hospital, Germany

Introduction

Proximal humeral shaft fractures are commonly treated with long straight locking plates endangering the radial nerve distally. The aim of this study was to investigate the biomechanical competence in a human cadaveric bone model of 90°-helical PHILOS plates versus conventional straight PHILOS plates in proximal third comminuted humeral shaft fractures.

Methods

Eight pairs of humeral cadaveric humeri were instrumented using either a long 90°-helical plate (group1) or a straight long PHILOS plate (group2). An unstable proximal humeral shaft fracture was simulated by means of an osteotomy maintaining a gap of 5cm. All specimens were tested under quasi-static loading in axial compression, internal and external rotation as well as bending in 4 directions (Fig.1). Subsequently, progressively increasing internal rotational loading until failure was applied and interfragmentary movements were monitored by means of optical motion tracking.
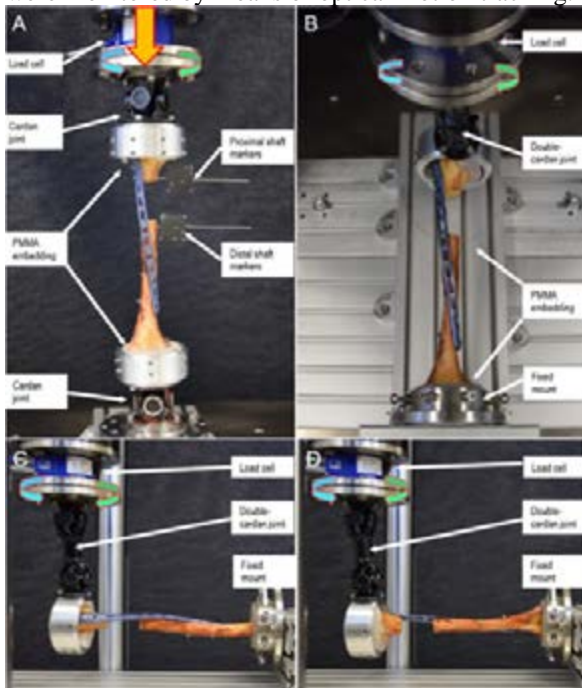
Figure 1: Setup with a right humerus instrumented with 90° helical PHILOS plate and mounted for biomechanical testing. A: Axial compression or internal/external rotation. B, C: Bending loading in varus/valgus in two different views. D: Bending loading in flexion / extension.

Results

Flexion/extension deformation (°) in group1 was (2.00±1.77) and (0.88±1.12) in group2, p=0.003. Varus/valgus deformation (°) was (6.14±1.58) in group1 and (6.16±0.73) in group2, p=0.976. Shear (mm) and displacement (°) under torsional load were (1.40±0.63 and 8.96±0.46) in group1 and (1.12±0.61 and 9.02±0.48) in group2, p≥0.390 (Fig.2). However, during cyclic testing shear and torsional displacements and torsion were both significantly higher in group 1, p≤0.038. Cycles to catastrophic failure were (9960±1967) in group1 and (9234±1566) in group2, p=0.24.
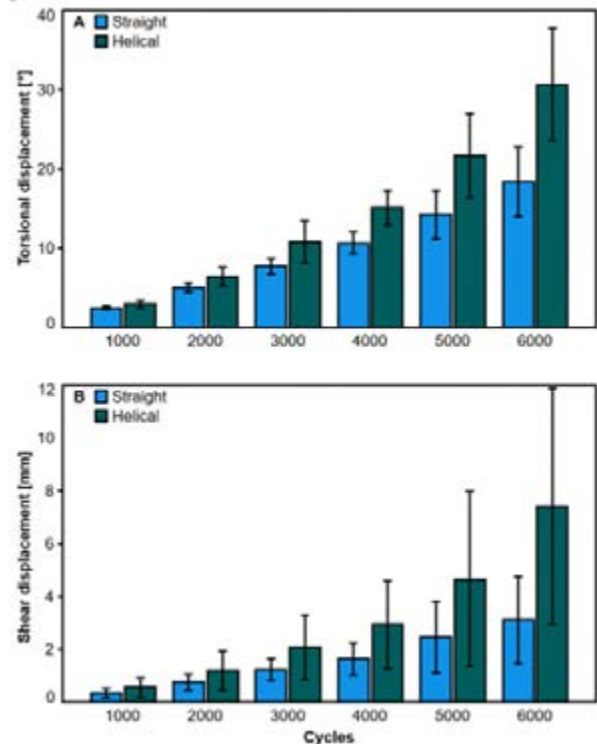
Figure 2: Torsional (A) and shear (B) displacement over the course of selected cycles shown for each group separately in terms of mean and standard deviation.

Discussion

Although 90°-helical plating was associated with improved resistance against varus/valgus deformation, it demonstrated lower resistance to flexion/extension and internal rotation as well as higher flexion/extension, torsional and shear movements compared to straight plates. From a biomechanical perspective, 90°-helical plates performed inferior compared to straight plates and alternative helical plate designs with lower twist should be investigated in future paired cadaveric studies.

FEMORAL FRACTURE PREVENTION VIA VIBRATION ANALYSIS DURING TOTAL HIP ARTHROPLASTY

George Athanassoulis Makris (1), Maikel Timmermans (1), Leonard Pastrav (1), Quentin Goossens (1), Michiel Mulier (2), Georges Vles (2), Wim Desmet (3), Kathleen Denis (1)

1. KU Leuven, Department of Mechanical Engineering, Smart Instrumentation, Belgium; 2. UZ Leuven, Orthopedic Surgery Department, Belgium; 3. KU Leuven, Department of Mechanical Engineering, MSD Section, Belgium

Introduction

A major complication of Total Hip Arthroplasty (THA) is the occurrence of intraoperative periprosthetic fractures. This complication is becoming more prevalent due to orthopedic surgeons increasingly choosing for cementless THA and the increasing number of revision procedures [1]. A periprosthetic fracture currently roughly occurs once in each 50 operations [2]. Pastrav et al. suggested that Vibration Analysis (VA) monitoring techniques can be used to detect problematic implant insertion situations such as implant blockage and consequently prevent impending periprosthetic fractures [3]. Producing a fracture in a controlled manner in an experimental setting can be challenging due to the unpredictable nature of fracture occurrence. This work presents the findings of a VA experiment that led to a periprosthetic femoral fracture.

Methods

An artificial femur (Sawbones 3403, Sawbones) was prepared by the orthopaedic surgeon by cutting and discarding the femoral head, and forming the femoral cavity using the appropriate set of broaches, gradually enlarging the cavity up to broach size 13 (Corail Broach, DePuy Synthes). The femoral stem (Corail, size 13, DePuy Synthes) was inserted into the femoral cavity. Following each insertion hammer hit, the femur was suspended using elastics and FRF measurements were taken in both the Antero-Posterior (AP) and Mediolateral (ML) direction, at the implant's neck. For each direction the measurements were achieved by attaching an accelerometer (PCB 352A24, PCB Piezotronics) on the implant neck and exciting on the opposing side of the implant neck surface using a modal hammer (PCB 086C03, PCB Piezotronics). The seventh insertion hit produced a periprosthetic fracture. The Pearson Correlation Coefficient (PCC) for both directions was calculated from the subsequent FRF's as a distance metric.

Results

The peaks for both AP and ML direction shift to the right with each subsequent insertion hit, as shown in Figure 1. While the shift to the right appears mostly consistent for the measurements in the ML direction, for the AP direction, the shift between step 3 and 4 appears remarkably small.
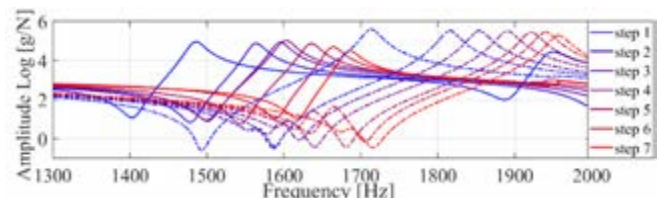
Figure 1: The 1,3 – 2 kHz band of the FRFs obtained in the AP (solid line) and ML (dashed line) direction.

The similarity between insertion step three and four in the AP direction is also reflected in the high value of the PCC corresponding to that transition (Figure 2).
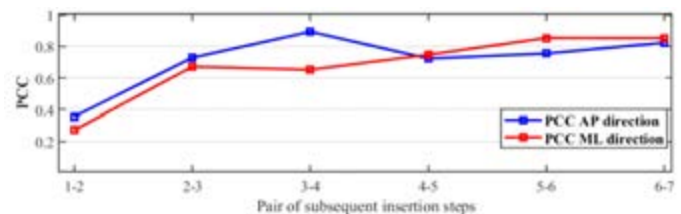
Figure 2: PCC for each subsequent insertion step pair calculated in the range of 1-3500 Hz

Discussion

During a successful implant insertion, the stiffness of the bone–implant structure gradually increases, up to the insertion endpoint. As a consequence, at the insertion endpoint, the FRF's converge, yielding a PCC close to one. In this experiment, however, the higher PCC values and the small FRF shift between step three and four in the AP direction imply that an early press-fit was formed in that direction while no press fit was yet formed in the ML direction, allowing the implant to subside deeper and to eventually fracture the bone. In conclusion, a "premature" convergence in only one direction, either AP or ML, constitutes a warning of a potential implant blockage due to an inconsistency between implant and femoral cavity shape which could lead to a periprosthetic femoral fracture.

References

1. D. Davidson et al. J Bone Joint Surg Am, 90:2000–2012, 2008.
2. M. P. Abdel et al. Bone Joint J, 98-B:461–467, 2016.
3. L. C. Pastrav et al. J Orthop Surg, 4:10, 2009.

Acknowledgements

A FINITE ELEMENT MODEL TO PREDICT THE RISK OF INTRAOPERATIVE FRACTURES IN NEW CEMENTLESS HIP STEM DESIGNS

Maila Petrucci (1,2), Antonino A. La Mattina (1,2), Cristina Curreli (1,2), and Marco Viceconti (1,2)

1. Department of Industrial Engineering, Alma Mater Studiorum - University of Bologna, Italy;
2. Medical Technology Lab, IRCCS Istituto Ortopedico Rizzoli, Bologna, Italy

Introduction

Total hip arthroplasty is one of the most successful orthopaedic procedures, but in the last years the increase in the use of cementless stems has led to a consequently increase in the probability that an intraoperative fracture may occur (3-5%) [1]. Generally, no quantitative measures are available to assess this risk, and, in addition, the incidence of this complication seems to vary considerably depending on the stem design. The aim of the present study is to describe a new approach for the numerical evaluation of the intraoperative femur fracture risk by using a simpler quasi-static Finite Element model able to simulate a crack propagation during stem implantation and to predict the load value causing the femur fracture.

Materials and Methods

Eleven deceased patients were selected by age, gender, and femur length from the HipOp collection, available at the Rizzoli Orthopaedic Institute, and patient-specific models were built from CT-data: the 3D shape of each femur was segmented, using a threshold value of HU=200, and the material properties were assigned using Bonemat software. [2] A non-commercial cementless stem, assumed to be made by a Titanium Alloy (E=105 GPa, v=0.3) [3], was positioned according to a pre-operative planning performed by an expert surgeon, and the bone–implant interface was modelled with an asymmetric face-to-face large-sliding frictional contact (μ=0.3 [3]). Boundary conditions (BC) were defined to simulate the surgeon's hammering: a compressive load with a stepped curve from 1,000 to 14,000 N was applied along the stem axis, while the distal part of the femur was constrained with a fixed support (Fig. 1a). A maximum principal strain criterion was used to deactivate ('kill') elements that exceed the threshold value of 0.73% [4], and the load-and-kill procedure was repeated until the fracture reached bone external surface; the final applied load was considered as the failure load.

Results

A crack propagation was obtained in five of the eleven simulated patients (Fig. 1b), with estimated fracture loads of 3,000 N, 5,000 N (for two of them), 6,000 N and 14,000 N; three femurs mechanically failed at the distal fixed support and other four could not achieve a good primary stability, probably because the size selected was small-to-fit. Considering that a surgeon hammer stroke produces about 6,000-7,000 N [5][6], three of the cracked femurs would have fractured, one certainly would not and one is doubtful.
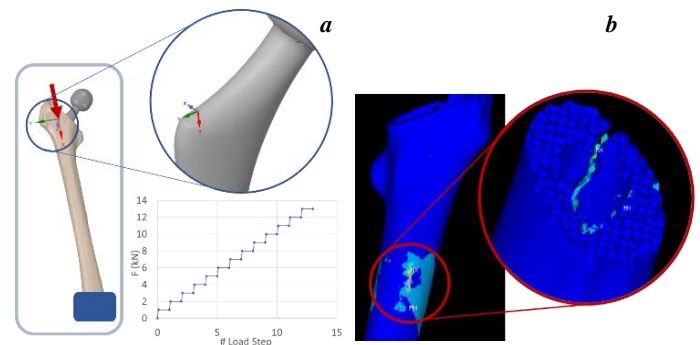
Figure 1: a) BC definition for the press-fit stem implantation; in detail, the local reference system and the applied stepped load graph. b) Crack propagation up to the surface of the femur and killed elements; in detail, section of femur diaphysis shaft, showing fracture propagation up to the outer surface.

Discussion and conclusions

For the present work, a non-commercial, copyright-free conceptual design for a cementless stem was used, to describe the methodology in detail. Perturbations of stem's pose and size, load orientation, and femur mineralization can be used to estimate fracture risk and to identify the worst-case scenario for that femur-stem pairing. In the near future, the goal is to repeat the same workflow by using two femoral stems available on the market, to validate the developed algorithm with clinical data. A faster model makes large scale Monte Carlo simulations feasible.

References

1. Caleb Christos Ioannidis *et al.*, *Appl. Mech. Mater.*, 2014.
2. F. Taddei, *et al.*, *Med. Eng. Phys.*, 29(9):973-979, 2007.
3. B. Reggiani *et al., J. Biomech.*, 40(11):2552–2558, 2007.
4. E. Schileo *et al.*, *J. Biomech.*, 41(2):356–367, 2008.
5. G. R. Maharaj and R. D. Jamison, *Compos. Mater. Implant Appl. Hum. Body Charact. Test.*, 1993.
6. A. Dubory *et al.*, *J. Mech. Behav. Biomed. Mater.*,103: 103535, 2020.

Acknowledgements

COMBINED MULTIBODY AND FINITE ELEMENT ANALYSES FOR THE EVALUATION OF THE TAPER JUNCTION IN THA

Giovanni Putame (1), Federico A. Bologna (1), Mara Terzini (1), Alberto L. Audenino (1)

1. Polito^{BIO}Med Lab, Department of Mechanical and Aerospace Engineering, Politecnico di Torino, Italy

Introduction

Due to the rising of the average population longevity and the concurrent decrease of the age at which arthroplasty is performed, an important demand growth for orthopaedic implants is expected for the next few decades. Indeed, an increase of +137% in revision surgery for total hip arthroplasty (THA) has been estimated by the year 2030 [1]. In this framework, enhancement in prostheses design and manufacturing is necessary to postpone, or even avoid, secondary surgeries that involve stress and risks for patients, beside representing an important spending for National Health Cares. Wear, corrosion, or oxidation phenomena represent the main causes of implants failure, and consequent revision [2]. These are induced, *in vivo*, by micro-movements at the taper junction level [3], which ultimately lead to a fretting-corrosion process generating cytotoxic metal debris and ions. In this study, micro-movements and contact pressures at the head-neck taper junction were assessed through a biomechanical analysis of a parametrized hip prosthesis, combining multibody (MB) and finite element (FE) simulations.

Methods

A MB model of a lower limb was created (Adams View, MSC Software, USA) including bony geometries (from pelvis to tibia), main muscles, and a parametrized hip prosthesis (Figure 1A). Muscle-driven dynamic simulations were performed after varying the femoral head diameter (*d*, 22-38 mm) and offset distance (*o*, 20-35 mm) of the parametrized prosthesis in order to identify the implant configuration responsible for the highest reaction forces/torques at the head-neck junction (Figure 1B-C). Derived loads were used as boundary conditions in a static FE model (Abaqus, Dassault Systèmes, France) of the head-neck taper junction (Figure 1D) to estimate contact pressure and relative micro-movements between the contacting parts. In particular, after the preparatory assembly of the head-neck junction (4 kN compression) loads derived from the MB analyses were applied in FE environment.

Results

The MB analyses showed a maximum resultant reaction force at the head-neck junction (3.6 times the body weight) when *o* = 20 mm and *d* = 38 mm. As opposed to the offset length, the head diameter variation did not considerably affect the reaction forces/torques. Preliminary results from the FE analysis showed a peak contact pressure of 50 MPa on the neck surface, where a micro-movement of about 10 µm was computed.
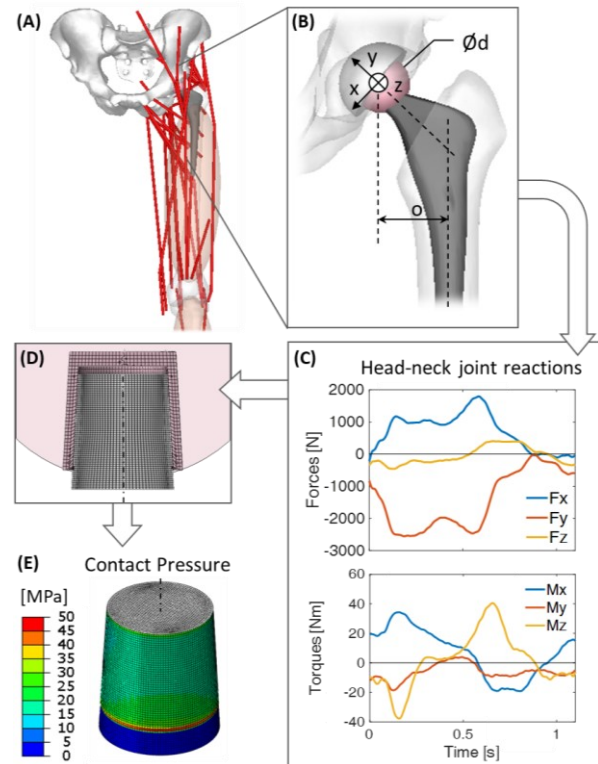
Figure 1: Workflow of the combined numerical analysis. (A) multibody model; (B) parametrized hip prosthesis with indicated femoral head diameter (Ød), offset length (o), and reference system for loads components (x,y,z); (C) explanatory reaction forces and torques; (D) finite element model of the taper junction; (E) explanatory result of the finite element analysis.

Discussion

The MB modelling has been revealed to be a fast and computationally low-cost approach for the investigation of THA configurations, able to provide realistic boundary conditions for detailed FE analyses. Overall, after its automatization, the described computational workflow might represent a powerful tool to improve implant design, thus reducing the risk of implant failures, and, in the long run, to support clinical decision-making processes.

References

1. Kurtz S. et al, J Bone Jt Surg Am, 89(4):780–785, 2007.
2. Ansari J. S. et al, J Orthop Trauma, 2017.
3. Falkenberg A. et al, J Biomech, 98, 2020.

Acknowledgements

ADVANCES IN FIXATION STRENGTH OF REORIENTING RECTANGULAR TRIPLE PELVIC INNOMINATE OSTEOTOMY

Jens Richter (1), Daniel Ciric (2), Klaus Kalchschmidt (3), Claudia D'Aurelio (1), Axel Pommer (1), Jan Dauwe (2)(4), Boyko Gueorguiev (2)

Center of Trauma and Orthopedic Surgery, Helios University Clinic Wuppertal, Germany; 2. AO Research Institute Davos, Switzerland 3. Orthopaedic Clinic Dortmund, Germany; 4. Orthopaedic Department of Orthopaedic Surgery, University Hospitals Leuven, Belgium

Introduction

Reorientating pelvic osteotomies are performed to improve femoral head coverage and prevent femoral-acetabular impingement or secondary degenerative arthritis, particularly in young patients. A rectangular triple pelvic innominate osteotomy (3PIO) is performed in symptomatic cases [1]. However, deciding the optimal screw fixation type to avoid migration, pseudarthrosis and loss of correction remains a concerning question. Therefore, this study aimed to investigate the biomechanical behavior of two different acetabular screw configurations used for rectangular 3PIO osteosynthesis. It was hypothesized that bi-directional screw orientation for acetabular fragment fixation would be biomechanically superior to a mono-axial screw fixation technique.

Materials and Methods

A rectangular 3PIO was performed in twelve right-side artificial Hemi-pelvises, randomly assigned to two study groups for fixation with different screw orientations (Figure 1A). Group 1 were treated with two axial and one transversal screw in a bi-directional orientation. In contrast, in Group 2, they were instrumented using three screws inserted in the axial direction through the iliac crest. Prior to osteosynthesis, a reorientation of the acetabular fragment was performed with 10.5° increased inclination in the coronal plane, and 10.0° increased anteversion in the axial plane. A polyethene acetabular cup prosthesis was implanted, and all specimens were biomechanically tested until failure under progressively increasing cyclic loading at 2 Hz, starting at 50 N peak compression force and increasing it at a rate of 0.05 N/cycle, using a setup from previous work [2] (Figure 1B). Initial stiffness was calculated from machine data. Acetabular fragment anteversion, inclination and medialization were evaluated from motion tracking data after 250, 500, 750, 1000, 1250, 1500, 1750, 2000, 2250 and 2500 cycles. Cycles to failure and failure load were evaluated based on a 5° change in anteversion failure criterium.

Results

Initial stiffness was higher in Group 1 (56.46 ± 19.45 N/mm) versus Group 2 (39.02 ± 10.93 N/mm); however, this difference was not significant, $p = 0.31$. Acetabular fragment anteversion, inclination and medialization increased significantly during cyclic loading in each group ($p \leq 0.02$) and remained non-significantly different between the groups ($p \geq 0.69$). Cycles to failure and failure load were not significantly different between Group 1 (4406 ± 882, 270.30 ± 44.10 N) and Group 2 (5059 ± 682, 302.95 ± 34.10 N), $p = 0.78$.

Discussion

Biomechanical studies have not considered rectangular geometry of the acetabular fragment in 3PIO osteosynthesis. From a biomechanical perspective, the present study demonstrates that a bi-directional screw orientation does not necessarily result in considerable advantages versus mono-axial alignment when the latter has all three screws evenly distributed over the osteotomy geometry. Moreover, the 3PIO fixation is susceptible to changes in anteversion, inclination and medialization of the acetabular fragment until the bone is healed. Therefore, a cautious rehabilitation program with partial weight-bearing is recommended.
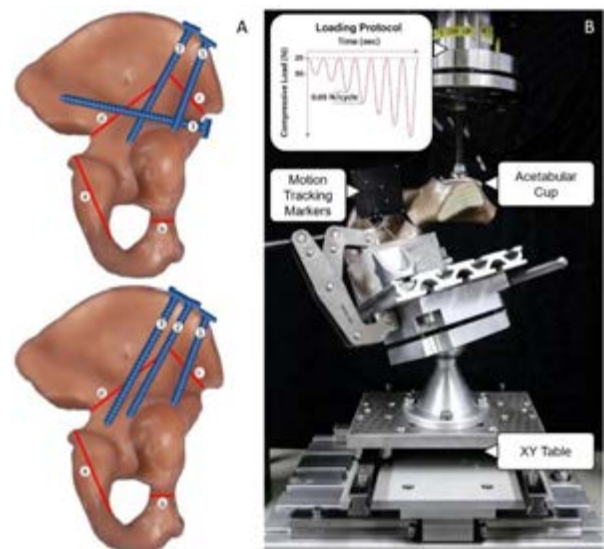
Figure 1: (A) Fixation techniques in Group 1 (top) with two axial (1, 2) and one transversal (3) screws, and Group 2 (bottom) with three screws in axial direction (1, 2, 3). Rectangular 3PIO osteotomy is performed along lines a-b-c-d. (B) Setup with a specimen mounted for biomechanical testing. Embedded picture visualizes loading regime.

References

1. Janssen D et al. Int Orthop 2009;33(6):1555–9.
2. Acklin YP et al., Injury 2016;47(7):1456–60.

DVC: A NEW DIAGNOSIS METHOD FOR MICROMOTION AND REMAINING ATTACHMENT LOOSENING OF HIP ARTHROPLASTY

**Mathieu Severyns (1,2), Kevin Aubert (1), Valéry Valle (1),
Tanguy Vendeuvre (1,3), Arnaud Germaneau (1)**

*1 Institut Pprime, UPR 3346 CNRS – University of Poitiers – ISAE-ENSMA, France
2 Department of Orthopaedic surgery and Traumatology, University Hospital, Martinique, France
3 Department of Orthopaedic Surgery and Traumatology, University Hospital, Poitiers, France.*

Introduction

The failure of primary or secondary Total Hip Arthroplasty (THA) osteointegration can be responsible of micromotions and pain with poor functional results [1]. Similarly, THA periprosthetic fractures classified Vancouver B1 require the evaluation of the remaining attachment to keep or not the femoral stem during the revision surgery [2]. The Digital Volume Correlation (DVC) [3] was initially developed to measure micromotions and deformity of bone structures with a µCT-scan device [4–6]. The aim of this work is to present a cases series of in vivo DVC results which would allow the measurement of mechanical displacement fields and the optimization of the surgical procedure.

Methods

This study relates the case of a THA periprosthetic fracture Vancouver B1. Two CT scans were acquired with and without mechanical stress (loading traction system of 100N) on the lower limb. Bone structures were segmented and image registration was applied on acetabular implant or femoral stem (Figures 1a and 2a-b-c). DVC was used to measure volume displacements of the femoral or the pelvic structures. The voxel size and the correlation subset were respectively of 0.816x0.816x1.19mm and 16x16x16voxels. The observation of motions along the tensile load axis was intended to identify the remaining attachment loosening.

Results

DVC method was used to determine the three components of displacement and its spatial variations within the adjacent bone structure (Figures 1b and 2d). The measured mean displacement was 2.5mm in the acetabulum and 3mm in the femur. The observation of micro-mobility between the two structures indicated a loss of prosthetic fixation. The displacement fields observed along the tensile load axis showed homogeneous displacements of the bone structure in relation to its femoral or acetabular prosthetic component.

Discussion

The purpose of micro-mobility measured by DVC method during the placement of a THA would be to measure the displacement fields of an implant presenting the characteristics of a primary osseointegration defect whose stress migration threshold remains to be defined with a view to an indication for prosthetic replacement.

The present study validates the in vivo use of DVC method on patient for two different tensile states in order to evaluate anchorage defects of implant. DVC method would allow particularly the optimization of surgical procedures such as periprosthetic. The evaluation the remaining attachment is currently not sufficient and probably causes of error regarding high rates of early aseptic loosening.
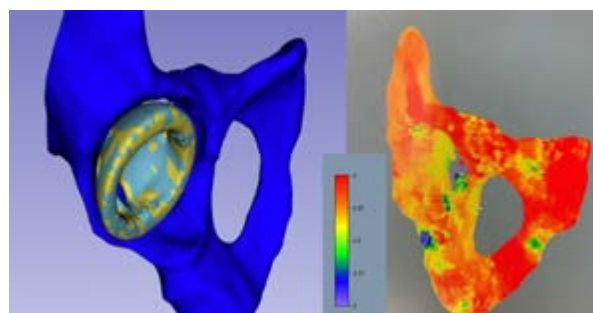
Figure 1. *Segmentation and image registration of the acetabular component (A) and visualization of the displacement fields along the tensile load axis (B)*

Figure 2. *Image registration of a femoral stem (A) and displacement fields Recalage d'images de segmentation de pièce fémorale et DVC appliquée à un masque de fémur proximal à la recherche d'une perte de fixation restante.*

References

1. Kärrholm J et al, J Bone Joint Surg Br, 76:912–7, 1994.
2. Andriamananaivo T et al, Orthop Traumatol Surg Res. 106:1413–7, 2020.
3. Valle V et al, Exp Mech. 59:1–15, 2019.
4. Bay BK et al, Experimental Mechanics. 39:217–26, 1999.
5. Buljac A et al, Experimental Mechanics. Society for Experimental Mechanics; 58:661–708, 2018.
6. Disney CM et al, Journal of Microscopy. 272:165–79, 2018.

INCIDENCE OF PELVIC BONE OVER THE STRESS STATE AT THE RESIDUAL LIMB/SOCKET INTERFACE OF TRANSFEMORAL AMPUTEES

Juan Atehortua (1) , Valentina Mejía Gallón (1), Juan Ramírez (1)
1. Department of Mechanical Engineering, Universidad Nacional de Colombia, Medellin Colombia

Introduction

For the transfemoral amputees (TA), the quality of life is related to the comfort. In turn this, should be associated with the pain. Doing an appropriate design socket, the stress distribution (SD) could be modified looking for reducing the pain in residual limb (RL). In bioengineering, Finite Element Analysis (FEA) was performed to evaluate the interaction between RL – Socket [1]–[3]. Some of those have been developed including only the residual femur bone [2], [4]. The aim of this study is to evaluate the incidence of include the Pelvic Bone (PB) and the change in boundary conditions over the stress state at the RL-Socket interface on TA.

Methods

Five unilateral TA participated in this study. Ten models were developed, five with PB (condition 1) and five without it (condition 2). The simulation process was carried out for donning and standing condition. (Figure 1).
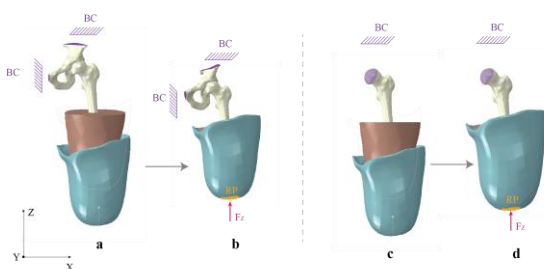
Figure 1: Simulation process. (a) Socket donning with PB; (b) Standing with PB; (c) Socket donning without PB; (b) Standing without PB.

Bone geometry was obtained from computerized axial tomographic; socket and soft tissue geometry were obtained in previous studies [1].

Results

Contact pressure (CPRESS), Circumferential (CSHEAR1) and Longitudinal (CSHEAR2) shear stress at soft tissues were evaluated. Figure 2 shows the results for the reference patient and how the SD changed between the two conditions in the donning and standing stage.

Tukey repeated measures analysis with 95% CI was performed. The results of the SD and the total contact area (TCA) for two conditions were compared. It was found that there is no statistically significant difference between the two conditions.
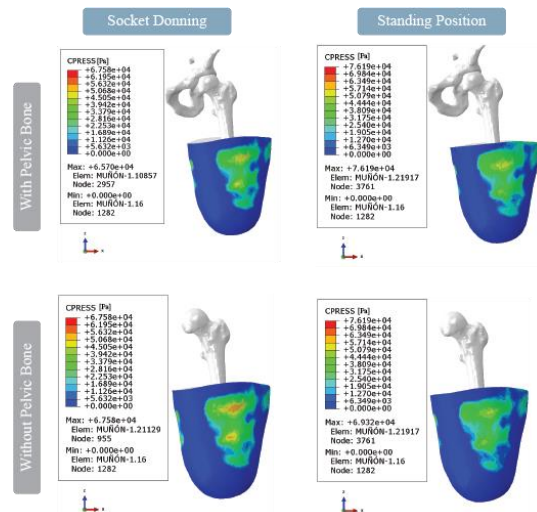
Figure 2: Patient 1 CPRESS distribution between the two conditions.

Discussion

As reported in [2]–[4], there are not many studies that include the pelvic bone in FEA of TA. The study proposed by [2] includes pelvic bone. Nonetheless, this study has improvements because it included accurately the donning process in the simulation and adequate socket and soft tissue reconstruction. To achieve a more realistic model, future work should include a dynamic simulation condition of human gait. This study demonstrates that include of the pelvic bone in the RL–Socket for TA models with these conditions no generate changes in the SD.

References

[1]   D. Lacroix and J. F. Ramírez Patiño, "Finite element analysis of donning procedure of a prosthetic transfemoral socket," *Ann. Biomed. Eng.*, vol. 39, no. 12, pp. 2972–2983, 2011, doi: 10.1007/s10439-011-0389-z.

[2]   A. van Heesewijk, A. Crocombe, S. Cirovic, M. Taylor, and W. Xu, "Evaluating the effect of changes in bone geometry on the trans-femoral socket-residual limb interface using finite element analysis," *IFMBE Proceedings*, vol. 68, no. 2. pp. 587–591, 2018, doi: 10.1007/978-981-10-9038-7_109.

[3]   S. C. Henao, C. Orozco, and J. Ramírez, "Influence of Gait Cycle Loads on Stress Distribution at The Residual Limb/Socket Interface of Transfemoral Amputees: A Finite Element Analysis," *Sci. Rep.*, vol. 10, no. 1, pp. 1–11, 2020, doi: 10.1038/s41598-020-61915-1.

[4]   A. S. Dickinson, J. W. Steer, and P. R. Worsley, "Finite element analysis of the amputated lower limb: A systematic review and recommendations," *Med. Eng. Phys.*, vol. 43, pp. 1–18, 2017, doi: 10.1016/j.medengphy.2017.02.008.

TRIPLY PERIODIC MINIMAL SURFACE FOR BIOINSPIRED DISSIMILAR MATERIAL INTERFACING

Mauricio C. Saldivar (1), Edwin Tay (1), Eugeni L. Doubrovski (2), Mohammad J. Mirzaali (1), Amir A. Zadpoor (1)

1. Department of Biomechanical Engineering, Faculty of Mechanical, Maritime, and Materials Engineering, Delft University of Technology (TU Delft), The Netherlands; 2. Faculty of Industrial Design Engineering (IDE), Delft University of Technology (TU Delft), The Netherlands

Introduction

The design of high-performing material interfaces with dissimilar mechanical properties (*i.e.,* hard-soft connections) has always been challenging due to the development of interfacial stress concentrations [1]. Conversely, natural architected interfaces (*e.g.,* the bone-ligament enthesis) that have originated from millennia of evolution present us with sophisticated strategies (*e.g.,* functional grading, mechanical interlocking) to improve the performance of synthetic interfaces [2]. Besides, the integration of these bioinspired features is widely available thanks to developments in voxel-based additive manufacturing (AM= 3D printing) [3]. This advanced AM technique enables the material deposition of 'hard' and 'soft' particles arbitrarily in a 3D space, providing unlimited freedom to create complex architected structures. Therefore, we used this AM technique to explore the interfacing performance of some of the most popular lattices in AM (*i.e.,* triply periodic minimal surfaces, or TPMS) and considered the best performing design to integrate different bioinspired modalities to yield optimal hard-soft connections.

Methods

In total, we considered four different geometries to work as graded topologies: three sheet-based TPMS (*i.e.,* Gyroid, Diamond, and Octo) and one made of randomly-distributed particles. We implemented these geometries into the narrow section of standard dumbbell-shaped tensile test specimens across two gradient widths (*i.e.,* short $W_G = 4mm$ and long $W_G = 12mm$) and included a gradientless control group ($W_G = 0mm$). Polyjet 3D printing techniques (Stratasys, USA) with voxel-level control allowed manufacturing these specimens. Then, we mechanically tested them under quasi-static tensile loading conditions while recording the displacements with digital image correlation (DIC) and generated finite element analyses (FEA) of each design. After post-processing, we selected two best-performing geometries (*i.e.,* Gyroid and Particles) and integrated them to generate a multi-scale hierarchical gradient, which we printed and tested to assess its performance.

Results and discussion

Amidst the tested designs, the short Gyroid gradients were the strongest, and the long Particles were the toughest. Besides, all the specimens of these group

failed at the soft region. The DIC and FEA strain maps showed that these designs released strains at the interface edges, preventing the propagation of cracks. Contrarily, the gradientless and the Octo designs presented high strain concentrations at the hard-soft interface. These phenomena explain the failure at the interface and the low performance of these designs.
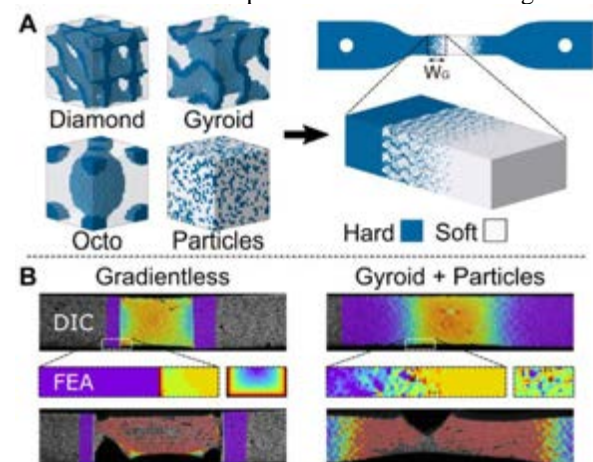
Figure 1: A) Unit-cells and tensile specimen designs used to create hard-soft functional gradients. B) DIC and FEA analyses of the gradientless design and the hierarchical functional gradient (Gyroid + Particles).

The strain concentrations were lower after integrating the Gyroid and Particle designs in a hierarchical arrangement. Besides, the regions that did show strain concentrations were ultimately constrained by hard material particles, preventing early failure. These effects resulted in optimal functional gradients that failed at the soft region and yielded the highest toughness value of all the tested designs. These findings prove that TPMS are great candidates to generate high-performing multi-material interfaces and indicate that their combination with voxel-based designs could result in the next generation of designer materials, with optimal interface properties required in many high-tech industries.

References

1. Martinsen, K. et al, CIRP Ann. 64: 679–699, 2015.
2. Kruize, C. et al, ACS Biomater. Sci. Eng., 2021.
3. Mirzaali M.J. et al, Adv. Eng. Mater. 22 1901142, 2020.

Acknowledgments

LONGITUDINAL FUNCTIONAL ASSESSMENT OF A TRANSFERMORAL AMPUTEE PATIENT TREATED WITH OSSEOINTEGRATION SURGERY

Stefano Di Paolo (1), Domenico Alesi (2), Agostino Igor Mirulla (1), Emanuele Gruppioni (3), Stefano Zaffagnini (2), Laura Bragonzoni (1)

1. University of Bologna, Italy; 2. IRCCS Rizzoli Orthopaedic Institute, Italy; 3 INAIL Prosthesis Center, Italy

Introduction

The socket-type prosthesis is the treatment of election for the lower-limb transfemoral amputation. However, patients often report skin abrasions, skin sweating, lack of balance, and walking difficulties [1-2]. The osseointegration technique is an alternative treatment for amputee patients that limits the socket-related problems and provides a more physiological mechanical loading [1].

After surgery, a critical functional recovery and dedicated rehabilitation phase is required. Little functional assessment of these patients has been reported in the literature. The purpose of the present study was to provide the functional assessment of a transfemoral amputee patient before osseointegration surgery and after rehabilitation by means of wearable sensors.

Methods

A transfemoral amputee patient (male, 47 years, time from amputation 18 years, Figure 1) scheduled for osseointegration surgery was enrolled. The patient was able to walk without aids and performed a gait test the day before surgery with his standard socket-type prosthesis, consisting in 10-meters walking in a hospital indoor hall, two at self-selected speed and two at the fastest speed possible. The test was repeated 3 months after surgery (after the clearance from the rehabilitation, 3M FU), and 6 months after surgery (6M FU).

Figure 1: Radiographs of transfemoral amputation (left) and osseointegration prosthesis (right).

A set of 15 wearable inertial sensors (Awinda, Xsens Technologies) was used to collect full body kinematics. Complete gait cycles were isolated and spatiotemporal and kinematical parameters were extracted. The differences between the amputee (AL) and the sound (SL) limb among the follow-ups were reported. One-way ANOVA with post-hoc comparisons was conducted in Spm1D ($p < 0.05$).

Results

Shorter step length and longer swing phase were found for the AL at pre-op, with greatest differences in the midstance. Also, hip abduction and rotation, pelvis forward tilt and obliquity, trunk forward tilt, and lateral bending on the AL were also noticed. At follow-ups, symmetry index progressively improved (1.14, 1.09, 1.06 at pre-op, 3M FU, and 6M FU, respectively). Asymmetries in hip abduction, hip rotation, and pelvis rotation decreased at follow-ups and no more trunk forward and lateral tilt were found.
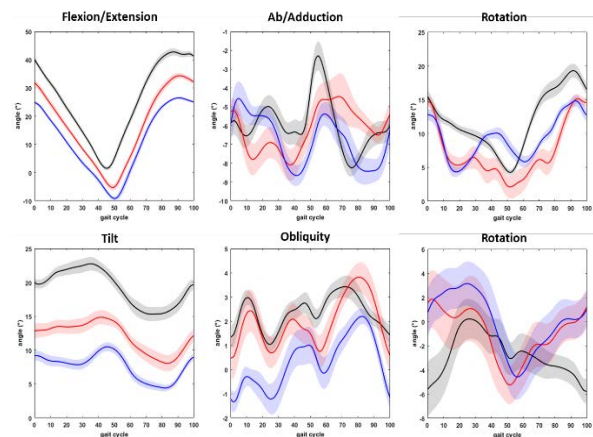
Figure 2: Kinematics differences among the pre-op (black), 3months follow-up (red), and 6months follow-up (blue) for hip (top line) and pelvis (bottom line).

Discussion

The altered spatiotemporal and kinematical parameters found preoperatively were in line with the current literature [1]. After rehabilitation, the patient showed higher time spend on the AL and lesser kinematical asymmetries. The osseointegration surgery showed to progressively restore a physiological kinematics in the transfemoral amputee patient.

References

1. Jamal M, et al., 2021 Clin Orth Rel Res doi: 10.1097/CORR.0000000000002074
2. Cutti AG, et al., J Neuro Eng Rehab, 2018 Sep 5;15(Suppl 1):61

Acknowledgements

THE INFLUENCE OF SCREW CONFIGURATIONS ON LCP UNDER THE TIME-DEPENDENT CALLUS HEALING PROCESS

Zeyang Li (1), Ziyun Ding(2), Shuai Zhu (1) Zhangming Wu (1)

1. School of Engineering, Cardiff University, UK 2. Department of Mechanical Engineering, University of Birmingham, UK

Introduction

The configuration of implants plays a key role to influence the bone healing effect of the internal fixation system of fractures. Up to now, some gold standards for the configuration of implants had been proposed in many studies to achieve high structural stability and low complication probability in the LCP osteosynthesis. However, most of the above studies only focused on the static analysis and ignored the influence of fixation property by bone self-healing effect, which is varying with time. Therefore, the fixation axial stiffness in these studies was often considered as a constant. However, due to the growth of callus tissue in the fracture, the fixation axial stiffness will significantly increase during the bone healing process, rather than remaining as a constant [1]. Up to now, the research on the implants (e.g., screws) configuration planning considering the bone healing effect is far from sufficient, and the interaction mechanism between fixation axial stiffness and the bone healing process is still not well understood.

To address the above issues, in this research work, a time-dependent fixation model with respect to different screw configurations was developed to study the fixation stiffness and bone healing efficiency during the whole fracture recovery period. As such, this study will overcome the limitations in the conventional studies that only consider the time period just after operation. Finally, this work established an accurate relationship for the fixation stability with callus healing behaviours to provide an exact evaluation for the screw configuration planning.

Methods

In this work, a 32-A3 femoral shaft fracture osteotomy model with a fracture gap of 2.1mm being fixed by LCP fixation is shown as the Fig.1. One bone segment was fixed on the distal section, while another one afforded a compressive loading. To simulate the bone recovery behavior, a callus part with the time-dependent Young's modulus was defined refer to [2]at the fracture site in the model. We assumed that the effective callus growth only occurs on the fracture section where the Interfragmentary strain (IFS, ε) is in the rage of 2-10 %. Therefore, the healing efficiency (δ) of the callus can be expressed as the δ =Ac/At. Ac is the area of the facture cross-section where IFS is in the range of 2-10% and At is the total area of the facture cross-section.

The whole bone recovery process was divided into four healing periods (i.e., 1–4 week, 4-8 week, 8-12week, 12-16 week). In a particular healing period (n), the Young's modulus of the callus E_n is estimated as following equation,

$$E_n = \delta_{n-1} \cdot E_{standard,n} + (1 - \delta_{n-1}) \cdot E_{n-1} \quad (1)$$

where the healing efficiency δ_{n-1} for the $(n-1)$ healing period is given by the results obtained from FEM model, $E_{standard,n}$ is the standard modulus value for the n period regarding $\delta = 100\%$ refer to [3]. The geometry of screw thread was omitted for reducing computational costs. The interface of bone-LCP, bone-screw were defined as completely bonding.
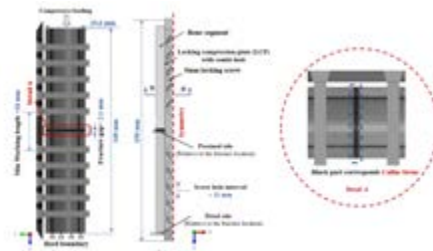
Figure 1: The fixation modelling with callus part.
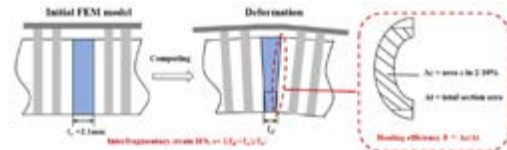
Figure 2: The illustration diagram of bone interfragmentary strain and healing efficiency

Results and Discussion

The different configurations are classified into three configuration parameters: working length, screws number, screws location. The predicted result proves that 'working length' is the most crucial configuration parameters influencing the fixation axial stiffness no matter in the post-operation period or the healing process as Fig.3. Furthermore, the configuration with high stiffness in this osteotomy case generally corresponds to a high healing efficiency.
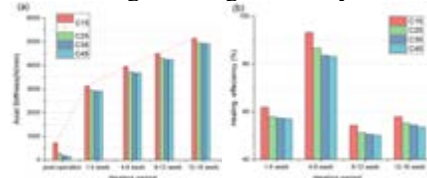
Figure 3: The a) axial stiffness and b) healing efficiency for configurations under different working length. C15, C25, C35, C45 corresponds values of 26,48,70,92 mm, respectively.

References

1. A. Macleod et al, Bone Jt. Res., 7:111-120, 2018.
2. H. J. Kim et al, Compos Struct, 93:2953-2962, 2011.
3. T. N. Gardner et al, Science, 33:415-425, 2000.

VALIDATED FINITE ELEMENT SIMULATION OF POROUS TITANIUM SAMPLES UNDER FATIGUE LOADING FOR DESIGN OPTIMIZATION

Antoine Vautrin (1), Jensen Aw (2), Ed Attenborough (2), Peter Varga (1)

1. AO Research Institute Davos, Switzerland; 2. Attenborough Dental, United Kingdom

Introduction

Porous titanium scaffolds exhibit elastic properties close to that of bone, and they can promote osseointegration. These features render their use as medical implants attractive. Dental implants represent one of the potential applications of this structure type [1]. Nevertheless, it must be ensured that the porous structure of these implants possess sufficient mechanical stability under fatigue loading occurring in cyclic masticatory loads. Adopting a trial-and-error design optimization strategy using experimental fatigue testing can become costly and time-intensive [2]. This study aims developing and experimentally validating a finite element (FE) simulation approach to predict the fatigue failure of different porous geometries to be used in design optimization.

Methods

Custom cylindrical samples featuring a hemispherical head and incorporating a porous scaffold section in the middle were designed for this study (Fig 1) using. Two porous designs utilizing the Schwarz primitive (SP) and the Schwarz W (SW) cell geometries were compared (Fig 2). Scaffold porosity of 60% and a strut thickness of 200 µm was used for both designs. The samples were additively manufactured (AM) by selective laser melting (SLM) of Ti6Al4V powder. Cyclic mechanical testing to fatigue failure was performed in a combined bending-compression loading mode at 30° angle following the ISO 14801 standard using a dedicated dental testing device (DYNA5dent, DYNA-MESS, Germany). The load level was set to 150 N for all samples. FE models of both designs were created in Abaqus and the durability analysis software fe-safe (SIMULIA, France), replicating the experimental fatigue test and evaluating different load levels. The material and surface properties were taken from a previous study on AM Ti6Al4V [3]. Surface roughness of the scaffold was assessed and considered in the simulations by means of a stress concentration factor [3]. Failure was determined as the number of cycles for which 0.5% of the scaffold's volume failed.

Results

In an ongoing analysis, testing of three samples with the SP design has been accomplished. Failure location predicted by the FE simulation (Fig 1d) corresponded well to the experimentally observed results (Fig 1b). The FE-based fatigue lifetime matched well the experimental results, with the latter showing good reproducibility (Fig 2). The SP design exhibited a

significantly higher fatigue resistance than the SW designs for all load levels of the FE analyses.
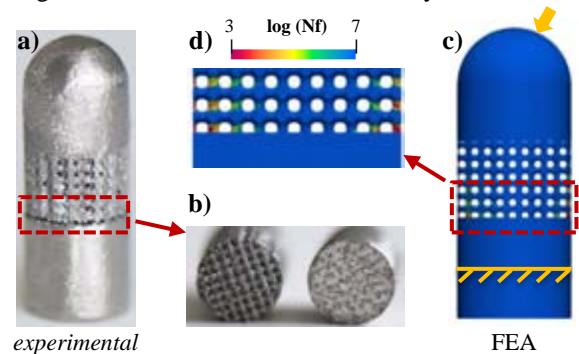
Figure 1: a) Fractured 3D-printed porous titanium sample with SP cell geometry; b) Failed sample; c) Corresponding FE model; d) contour plot of the number of cycles to failure (log (Nf)) for a 150 N fatigue load.
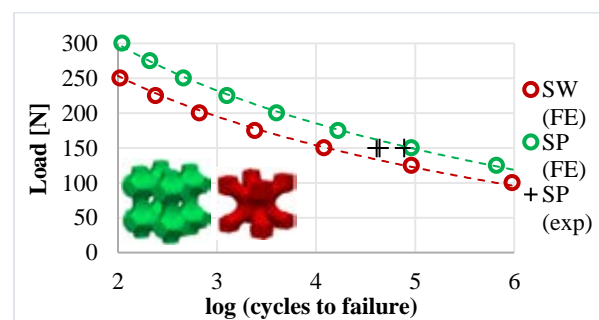
Figure 2: Number of cycles to failure versus the fatigue load level for both the Schwarz primitive (SP, green) and the Schwarz W (SW, red) cells geometry designs. Circles: simulations, crosses: experiments.

Discussion

These preliminary results demonstrate the potential of FE models in accurately predicting the fatigue failure of AM porous titanium scaffolds. Once fully validated, the in silico method presented here can be further utilized to investigate further scaffolds designs and customize their properties while ensuring stability.

References

1. Pałka and Pokrowiecki, Adv Eng Mater, 20:1700648, 2018
2. Zhang et al, Additive Manufacturing, 32:101015, 2020
3. Pegues et al, Mat Design & Proc Comms, 1:e36, 2019

Acknowledgements

THE ROLE OF THE SOCKET IN BMD LOSS IN TRANSFEMORAL AMPUTEES

Jose L Zavaleta Ruiz(1), Simone Dimartino(1), Lynn Hutton (2), Pankaj Pankaj (1),

1. Institute for Bioengineering, School of Engineering, The University of Edinburgh, UK
2. Astley Ainslie Hospital, NHS Lothian, Edinburgh

Introduction

A well-fitted socket aids an amputee to reclaim independence. A good fit aims to eliminate any discomfort or pain. The commonly used Ischial Containment Socket (ICS) for Above Knee Amputees (AKA), aims to capture the ischium else, it could induce pain through axial loading at the distal end of the femur [1].

The ischium, as the socket's primary support, allows users to increase activity levels unrestrained by pain. It is then important to consider highly active and young AKA (e.g. military personnel) evidencing Bone Mineral Density (BMD) losses similar to postmenopausal or bedridden patients [2]. Previous studies have shown the involvement of gait asymmetry, and disuse atrophy in bone resorption [3]. This study considers the hypothesis that the force isolation: distally by design, and proximally by effect, leaves the surviving bone in a state we term as a "floating femur", inside the ICS, depriving the hip joint of strains needed for a healthy femoral mechanostat. To test this hypothesis a finite element (FE) idealized prosthetic system is considered.

Methods

A FE model using idealized geometries representing femur, pelvic, soft tissue and ICS and articular cartilage were created in ABAQUS. Different materials included in the model were: cortical and trabecular bone, soft tissue, carbon fibre socket and articular cartilage. All materials were defined as linear elastic, homogenous and isotropic. The Young's modules and Poisson's ratio were taken from the literature. The model was tested in two scenarios (Fig. 1): (a) with socket aligned and in contact with the ischium; and (b) with socket aligned without contact with the ischium.

Simulating position of the skeletal system in upright standing, with a 5° flexion at the hip, ICS aligned to the ischium (with an intermediate layer of 0.5mm soft tissue), as set in regular static alignment, with the system fully restrained at spatial location of S1. Finally, a ground reaction force of 500N was applied at the socket, where prosthetic componentry would be attached.

Results

The idealized model with socket aligned and in contact with the ischium is shown in Fig. 1a. Stresses levels were examined in 4 regions as shown in Fig. 2b. Comparison of the contact and no contact models show similar levels of stress in the distal region D (Fig 2a), a comparable behavior in the medial regions B and C (Fig

2a). However, stresses in the No Contact model in the proximal region register significant higher levels of stress when compared to the distal end, while in the Ischial Contact model the respective regions share equivalent stress levels.
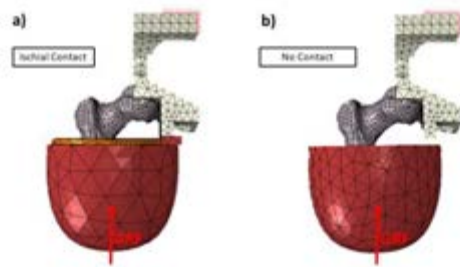
Figure 1: Simulation scenarios with idealized geometries, and force input in static alignment.
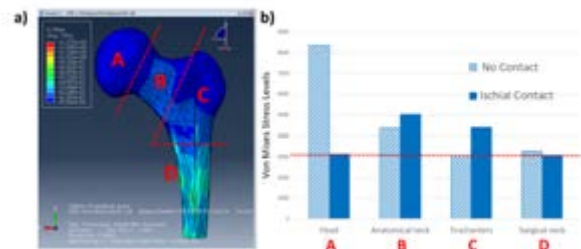
Figure 2: (a) Regions for comparison of stresses; (b) Stress levels in different regions of the femur for the two simulation scenarios.

Discussion

To our knowledge, this idealized prosthetic system analysis is the first to incorporate the acetabular interaction in combination with an ICS. The idealized model has shown the concentration of stress at the ischium and socket´s ischial pocket, consequently rendering the hip joint to a "floating femur" state through deprivation of strain at the proximal femur. Further research is required to define the role of the floating femur in BMD loss and its role in comparison to kinematic asymmetries and muscular disuse previously discussed in the literature.

References

1. Muller et al, AAOS, 46:542-544, 2016.
2. Sherk et al, J Bone Mine R, 23:1449-1457, 2008.
3. Flint et alm J Orthop Trauma, 28(4), 238-244, 2014.

A LUBRICIN-BINDING COATING FOR CARTILAGE RESURFACING IMPLANTS TO REDUCE FRICTION

Alicia H.A. Damen (1), Corrinus C. van Donkelaar (1), Prashant K. Sharma (2), Tannin A. Schmidt (3), Keita Ito (1)

1. Dept. Biomedical Engineering, Eindhoven University of Technology, the Netherlands
2. Dept. Biomedical Engineering, University Medical Center Groningen, the Netherlands
3. Dept. Biomedical Engineering, University of Connecticut Health Center, Farmington, CT, USA

Introduction

Frictional properties of cartilage resurfacing implants need to be sufficiently low to ensure that the opposing cartilage is not damaged during articulation. A polycaprolactone (PCL) implant currently under development still lacks such properties. To improve lubrication and wear resistance, surface modifications like coatings can be used. Ideally, lubricious molecules like lubricin, also known as proteoglycan 4 (PRG4), functionally adsorb from the synovial fluid to the implant surface [1][2]. Therefore, the present study determines if PRG4 can adsorb onto a layer-by-layer bioinspired coating composed of poly-l-lysine (PLL) and dopamine modified hyaluronic acid (HADN) and thereby reduce friction when PCL articulates against articular cartilage.

Methods

A custom ELISA was developed to quantify the amount of immobilized human recombinant (rh)PRG4 after exposure to a PLL-HADN coating. PCL disks (25 x 25 mm, n=12) were obtained by melting medical grade PCL granules. Half of the sample group (n=6) was coated with 8 layers of alternating PLL or HADN in phosphate buffered saline (PBS). The water contact angle and surface roughness of the PCL disks were measured prior and after the coating procedure and compared using a one-tailed paired t-test. Cartilage rings ($\phi_{out} = 20$ mm, $\phi_{in} = 12$ mm) were obtained from bovine patella (3-6 years-old). The coefficient of friction (CoF) between PCL and cartilage was measured using a DHR3 rheometer extended with a ring-on-disk accessory, using an intermittent loading protocol (normal pressure: 0 and 0.1 MPa and sliding velocity: 0 and 6 mm/s). PBS with 10 mg/ml bovine serum albumin, 3 mg/ml hyaluronic acid and 200 µg/ml rhPRG4 was used as lubricant in between the two contacting surfaces and kept at a constant temperature of 32˚ C.

Results

The ELISA showed that the PLL-HADN coating effectively immobilized rhPRG4. A visible difference between bare and coated PCL surfaces was shown using bright field microscopy (Fig. 1). The surface roughness was significantly higher, 54.9 ± 6.8 nm vs 83.0 ± 24.0 nm ($P=0.02$) and the water contact angle significantly lower $69.5 \pm 4.8˚$ vs $53.5 \pm 3.5˚$ ($P=0.001$) after application of the coating. The average CoF measured during the first minute of the friction measurement of

the bare PCL against cartilage exceeded twice the CoF of the PLL-HADN coated PCL against cartilage, 0.20 ± 0.07 and 0.10 ± 0.03 ($P=0.02$), respectively. After 60 minutes, the CoF reached equilibrium values which were still significantly higher for the bare PCL disks compared to the coated PCL disks ($P=0.047$, Fig. 2).
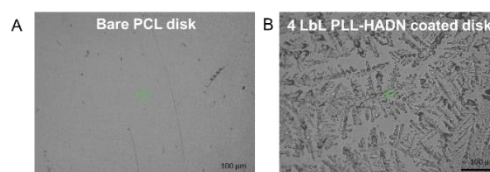
Figure 1: Bright field images of a (A) bare and (B) PLL-HADN coated PCL disk.
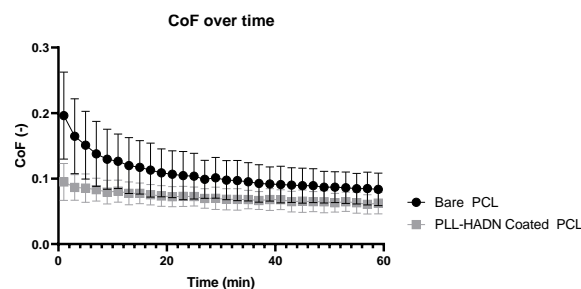
Figure 2: Coefficient of friction (CoF) over time for bare PCL (black) and PLL-HADN coated PCL (grey) against cartilage.

Discussion

The present study demonstrates that PCL can effectively be coated with PLL-HADN and that this coating significantly reduces the friction between PCL and cartilage when a synovial fluid-like lubricant is used. Presumably the coating is able to bind rhPRG4 from the lubricant thereby mimicking the lubricating surface of native cartilage. This makes PLL-HADN coating promising to improve the clinical success of PCL-based cartilage resurfacing implants.

References

1. Wan et al, Appl. Mater. Interfaces, 12: 23726-23736, 2020.
2. Damen et al, Osteoarthr. Cartil., 29,6:894-904, 2021

Acknowledgements

BIOMECHANICAL EVALUATION OF A NOVEL BIOMIMETIC ARTIFICIAL DISC PROSTHESIS IN CANINE CERVICAL CADAVERIC SPINES

C.A.M. Jacobs (1), R.J.P. Doodkorte (2), S.A. Kamali (3), A.M. (Abdelgawad (4), S. Ghazanfari (4), M.A. Tryfonidou (3), J.J. Arts (1,2), B.P. Meij (3), K. Ito (1)

1.Orthopedic Biomechanics, Dept. of Biomedical Engineering, Eindhoven University of Technology, the Netherlands 2. Dept. of Orthopedic Surgery, Research School CAPHRI, Maastricht University Medical Center, the Netherlands 3. Dept. of Clinical Sciences, Faculty of Veterinary Medicine, Utrecht University, the Netherlands 4. Aachen-Maastricht Institute for Biobased Materials, Dept. of Science and Engineering, Maastricht University, the Netherlands

Introduction

Cervical disc replacement aims to restore motion of the treated spinal level to reduce the risk of adjacent segment disease compared to fusion. First generation articulating disc replacements are unable to mimic the complex deformational kinematics of natural intervertebral discs [1]. Therefore, a biomimetic artificial intervertebral disc (bioAID) containing a hydrogel core replacing the nucleus pulposus, an ultra-high molecular weight polyethylene (UHWMPE) fiber jacket acting as annulus fibrosis, and titanium endplates with pins for mechanical fixation was developed (Fig. 1). An ex vivo biomechanical study in 6-degrees-of-freedom was performed to assess the initial biomechanical effect of the bioAID on the kinematic behavior of the spine.
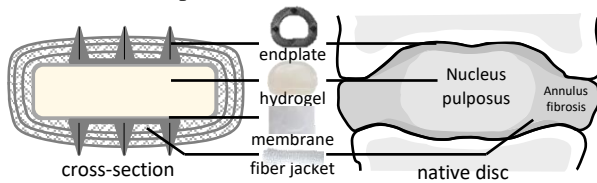
Figure 1: Schematic representation of bioAID design.

Methods

Six cadaveric canine specimens (C3-C6) were subjected to cyclic application (1°/sec) of flexion-extension (FE), lateral bending (LB), and axial rotation (AR) with a spine tester in the following three conditions: intact, with bioAID, and after fusion using an anchored cage (C4-C5). A hybrid protocol was used where the intact spines were first subjected to a pure moment of ±1 Nm whereafter the instrumented spines were subjected to the total range of motion (ROM) of the intact condition [2]. Three-dimensional segmental motions were measured using an optoelectronic system while recording the applied torsion. ROMs normalized to intact were calculated at peak torsion for comparison.

Results

The normalized ROMs at the treated level of the bioAID were similar to intact for FE. The motion at the two adjacent levels showed similar values for the intact compared to the bioAID for FE and AR (Fig. 2A). In contrast, levels adjacent to fused segments showed an increased motion in FE and LB, compensatory to the loss of motion at the treated level. The moment-rotation (Fig. 2B) graphs showed that the bioAID provides similar non-linear curves including a neutral zone (NZ) and elastic zone (EZ) at the treated level compared to intact for both LB and FE.
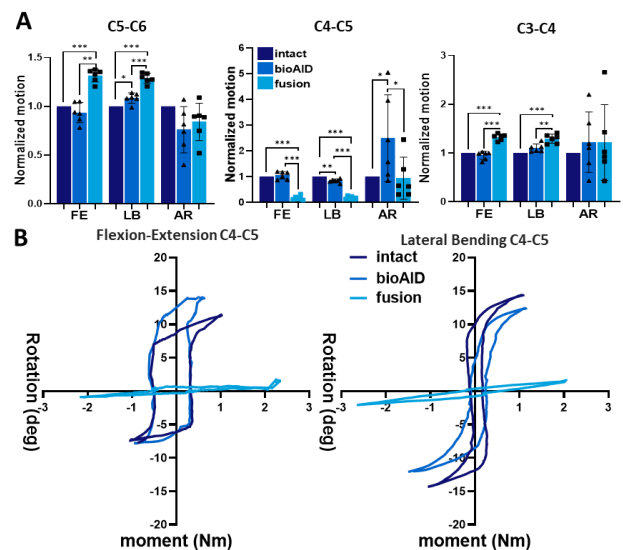
Figure 2: A: normalized segmental ROM (mean ± SD, (repeated ANOVA, Tukey Post-Hoc). B: representative moment-rotation curves.

Discussion

This study indicates that the bioAID device can better mimic the biomechanics of the intact intervertebral disc compared to fusion for the adjacent and treated levels. Unlike fusion, the bioAID can preserve the typical sigmoidal hysteresis shape of the moment-rotation curve, indicating its potential to preserve both the ROM and the quality of motion allowed by the spinal segments [3]. As a result, cervical disc replacement using the novel bioAID can be a promising alternative treatment for replacing severely degenerated intervertebral discs while preserving similar kinematics as a natural disc.

References

1. J. J. Costi., Spine (Phila. Pa. 1976).,33:1731–1738, 2008.
2. M. M. Panjabi, Clin. Biomech., 22: 257–265, 2007.
3. P. MM, J. Spinal Disord., 5:90–397, 1992.

Acknowledgements

HIGH-FIDELITY FINITE ELEMENT STENT-GRAFT MODELING

Anna Ramella (1), Francesco Migliavacca (1), Josè F. Rodriguez Matas (1),
Francesca Dedola (2), Michele Conti (2), Frederic Heim (3), Sara Allievi (4), Daniele Bissacco (4),
Maurizio Domanin (4), Santi Trimarchi (4), Giulia Luraghi (1)

1. Politecnico di Milano, Italy; 2. Università degli Studi di Pavia, Italy;
3. Universitè de Haute Alsace, France; 4. Università degli Studi di Milano, Italy.

Introduction

The Thoracic Endovascular Aortic Repair (TEVAR) is the preferred treatment option for thoracic aorta pathologies, such as aneurysms or dissections, and consists of inserting a self-expandable stent graft into the pathological region to restore the lumen [1]. Computational models help investigate the TEVAR procedure and play a significant role in pre-operative planning, therefore they must be reliable. For this reason, the verification and validation process (V&V) on the device and the *in-silico* procedure modeling is of foremost importance [2]. In this context, high-fidelity Finite Element (FE) simulations are here proposed to model a commercial device and reproduce the TEVAR procedure.

Methods

The commercial Valiant Captivia 24-24-150 thoracic stent-graft (Medtronic Inc, Santa Rosa, CA) model is realized using Solidworks (Dassault Systemes) and meshed with ANSA (BETA CAE System). The stent is discretized with beam elements and the graft with triangular membrane elements. Experimental crimp/release and bending tests are performed on the stent-grafts to calibrate – and then validate – the superelastic Nitinol (stent) and linear elastic fabric PET (graft) material parameters. The removal of the sutures between the stent and graft reveals that the sutured stent is not in its stress-free configuration, but it presents a 17.5% of pre-stress that must be considered in the simulation (*Fig.1a*). Then, explicit FE simulations are carried out with LS-Dyna (ANSYS) to reproduce the stent graft deployment into an aorta with physiological anatomy: the stent-graft is virtually crimped and morphed to match the vessel geometry, and then released.
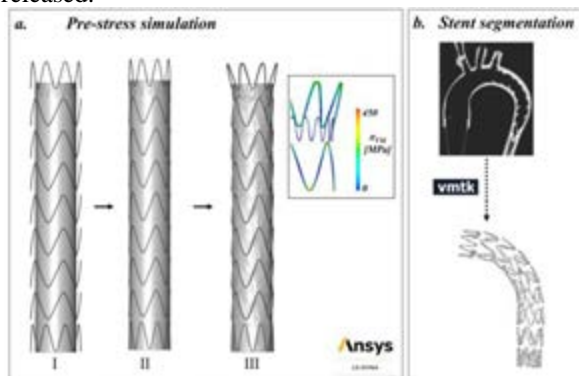
Figure1. (a) Stent-graft pre-stress simulation and von Mises stress distribution detail in the stent; (b) Stent segmentation from CT images using VMTK.

To validate the simulation results, the same stent-graft model is experimentally deployed into a 3D silicon aortic phantom and then subjected to CT scan: the stent is segmented using the software VMTK (*Fig.1b.*) and compared with the simulation results [3].

Results

The initial and final configurations of the deployment simulation are depicted in *Fig.2(a)*. The simulation validation results are depicted in *Fig.2(b)*. A qualitative comparison is managed by superimposing the stent configuration obtained after the simulation (red) and after the segmentation (grey). The local Opening Area (OA) for each ring is computed and the error (e_{OA}%) between the segmentation and simulation is below 4%.
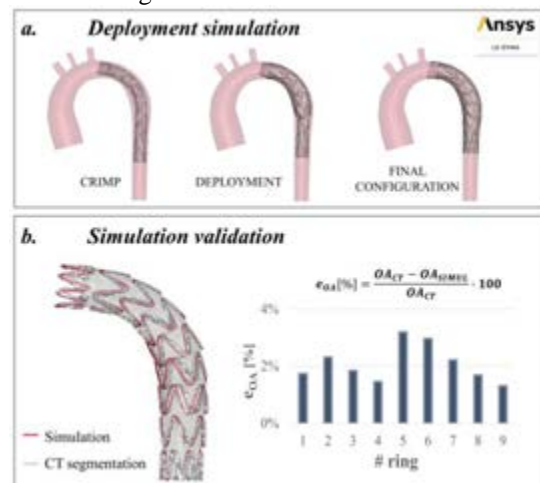
Figure2. (a) Steps of the deployment simulation; (b) Simulation validation results: qualitative comparison on the left and quantitative analysis on the right ('#ring' is the position of each ring from proximal to distal).

Discussion

The development of high-fidelity numerical simulations can be useful to improve the TEVAR procedure, to design and optimize new devices, and to help in clinical decisions and intervention planning. The presented FE tool is versatile and customizable for different commercial devices and future patient-specific *in-silico* analyses.

References

1. Daye et al, Cardio Diagn & Ther, 8:S138, 2018.
2. Viceconti et al., Methods, 185:120-127, 2021.
3. Perrin et al., J. Biomech, 48:1868-1875, 2015.

Acknowledgements

LOAD TRANSFER IN CUSTOM MADE IMPLANT FOR OSTEOCHONDRAL LESION, A FINITE ELEMENT STUDY

Mafalda Vieira (1), António Ramos (2)

1. TEMA-DEM, Biomechanics Group, University of Aveiro, Portugal, mafalda.vieira98@ua.pt , 2. TEMA-DEM, Biomechanics Group, University of Aveiro, Portugal, a.ramos@ua.pt

Introduction

The ankle joint sprain is frequent situation in the sports and 15-25% originates osteochondral lesion of the Talus (OLT), it can become extremely unstable causing pain, disability [1], and discomfort to the patient.

The treatment of this type of lesion depends on the extension and severity, current clinical guidelines favor autogenous [2] or allogenic osteochondral grafting procedures for lesions larger than 10 mm in diameter [3]. There is no optimal treatment for large lesions, but when the lesion presents a cutoff defect size of 150 mm^2 and poor clinical outcomes the (HemiCAP™, Arthrosurface Inc., Franklin, MA, USA) is one possible solution for these defects [4].

The present work intend study the effect of a custom-made prosthesis in surround tissues as solution in ankle joint osteocondral lesion.

Materials and methods

The geometric model of left ankle joint was obtained from the previous models [5]. Was considered the bone structures as tibia, fibula and talus, with a layer of cortical and cancellous bone. Was considered the cartilage in the tibia and in the talus and the ligament between fibula and tibia as presented in figure 1 The model presents an osteocondral lesion in the medial side with 10mm of diameter.
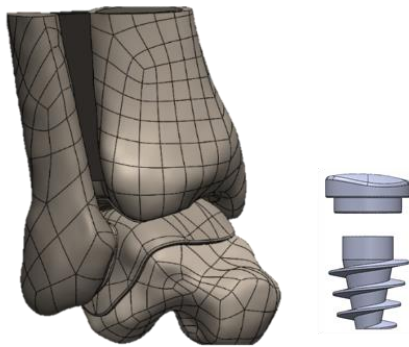
Figure 1: CAD model of ankle joint and structures considered for the implant.

A custom-made resurfacing implant was considered in the lesion, using the same concept as the HemiCAP™, using a custom-made upper surface to adapt the joint geometry with 10mm of diameter size. The implant presented two components the upper surface in CrCo material and the implanted surface talus with a screw in in Titanium alloy. The model was simulated using the finite element method, considering the linear elastic behavior of materials. In the table 1 are presented the mechanical properties of different tissues and implant.

Structure models	Youg Modulus (MPa)	Poisson ratio
Cortical bone	17 000	0,3
Cancellous bone	400	0,3
cartilage	20	0,45
Ligament	255,5	0,4
CrCo prosthesis	220 000	0,29
Ti prosthesis	110 000	0,34

Table 1: Material properties used in FE simulation.

Results

The results of the tree models, intact, with lesion and implanted point out the influence of lesioning in the contact stress observed at the cartilage as reported in previous study [5]. The implant offset in the articulation influences the stress in the tibia cartilage if the offset is positive. Relatively to the Von Mises stress in the cartilage around lesion, it presents an increase comparatively with same position in the intact situation (figure 2). The HemiCaP solution needs a very defined surgical position and in the preliminary results presented an increase of stress in cartilage.
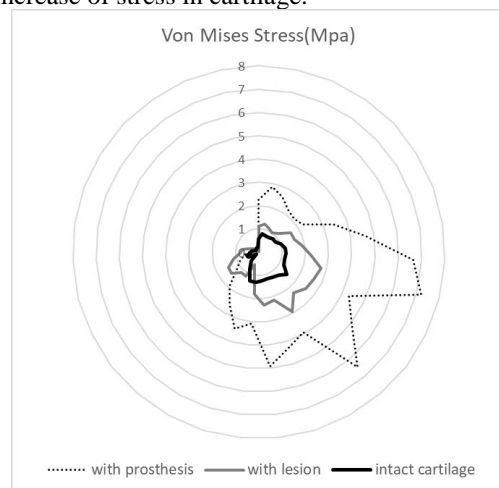
Figure 2: Von mises stress distribution around osteocondral damage.

References

1. K.J. Hunt, et al., Am. J. Sports Med., 40, 2012.
2. Heida K.A., Jr., Foot and Ankle International, 41,2020.
3. K.J. Hunt, Am. J. Sports Med., 40, 2012.
4. C. J. A. van Bergen, et al. Acta Orthop., 81, 2010.
5. Ramos et al, Medical Eng.& Physics, 2021, 98, pp. 73–82.

Acknowledgements

INTEGRATION OF MUSCULOSKELETAL AND MODEL ORDER REDUCED FE SIMULATION FOR PASSIVE ANKLE FOOT ORTHOSIS DESIGN

David Scherb, Patrick Steck, Sandro Wartzack, Jörg Miehling

Friedrich-Alexander-Universität Erlangen-Nürnberg (FAU), Engineering Design, Martensstraße 9, 91058 Erlangen, Germany

Introduction

Motor disorders are caused by nerve damages that affect the control of muscles resulting in paralysis or paresis [1]. A common example is the paralysis / paresis of the lower leg muscles (e.g. caused by stroke) leading to a pathologic gait, so called foot drop syndrome [2]. For the treatment of this disease, technical devices are increasingly used, like ankle foot orthoses (AFOs). There are two distinguishing types of AFOs. The first ones are active AFOs that are mainly driven by motors and actuation algorithms. However, there are issues with weight and power supply. The second type of AFOs, passive AFOs, on the other side have a low weight, are mobile and do not use external power supply, but lack to provide sufficient support in the stance phase of gait. New, innovative designs, however, prove to be able to address this problem [3]. Therefore, we decided to develop a new passive AFO design that is provided with fiber-reinforced composites (FRCs) [4] for simultaneously maximizing the stiffness of the stressed areas during load phases while keeping the design lightweight. In order to ensure a suitable support of the human gait behaviour, a model order reduced finite element model (MOR-FEA) [5] of the AFO is linked with a musculoskeletal human model (MHM) [6] (Fig.1)

Methods

To realize the new AFO, in the first step the basics for the further work had to be compiled. Thus, the conceptual design of the orthosis was developed using methods of engineering design. The main requirement was that the AFO is capable of supplying different support in different directions during gait. Furthermore, this required support in the gait phases had to be determined. For this purpose, healthy subjects are recorded in gait laboratory and their muscle activation is computed with MHMs. Afterwards, the muscles are weakened according to the condition in foot drop and a supportive torque is applied to the models. The torque was applied as a reserve actuator and adjusted in such way that the muscle activation shall remain the same as in healthy condition.

Results

A conceptual design is found that is able to detect different phases during gait. By triggering a coupling, movement of the ankle can either be blocked or allowed. Additionally, a ratchet clutch mechanism is controlled to load and unload the force-generating structures, which results in the supportive torques during the gait. In the stance phase of gait the most support from the AFO is required. The required quantitative supportive torque depends on the condition of the patient. Patients with less remaining force capability in the lower leg muscles require more support than patients with more remaining force capability. The resulting muscle activations can be decreased by applying more support torque until the muscle activations of the non-paralyzed muscles are similar to the corresponding ones of healthy subjects for all diseased conditions.

Discussion

The design concept is characterized by the possibility to support all phases during gait. The main criteria for a successful application is the design of the force generating structure. Together with the simulated supportive torques, which mainly match the previous expectations, the development of the method to link the MOR-FEA with MHMs can be approached in the next step to reach an agreement between supplied force and gait behaviour of the patients. In order to enable an evaluation of the simulated results and generated method, a validation with a manufactured prototype of the AFO is planned.
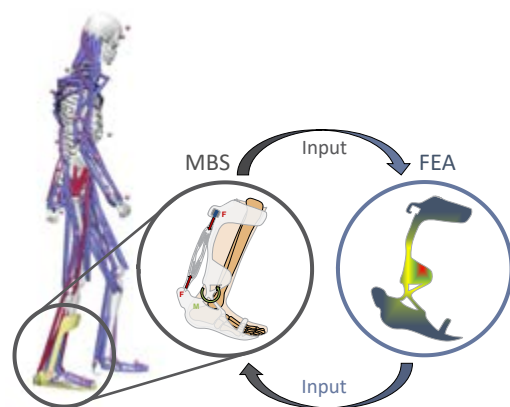
Figure 1: Conceptual approach to design the ankle-foot-orthosis based on the integration of model order reduced finite element analysis and musculoskeletal simulation

References

1. Younger, Lippincott Williams & Wilkins, 1999.
2. Stewart, Pract Neurol, 3: 158–169, 2008
3. Collins, et al., Nature, 7555: 212–215, 2015
4. Völkl, et al., Composite Structures: 359–367, 2018
5. Schilders, et al., Springer Berlin Heidelberg, 2008.
6. Miehling, et al., Biosystems & Biorobotics: 219–227, 2018.

Acknowledgements

HIP CONTACT FORCES IN PATIENTS WITH INCREASED FEMORAL ANTETORSION DO NOT DIFFER WITH DIFFERENT GAIT PATTERNS

Nathalie Alexander (1), Elke Viehweger (2,3), Johannes Cip (1), Reinald G. H. Brunner (2,3), Enrico De Pieri (2,3)

1. Children's Hospital of Eastern Switzerland, Switzerland; 2. University of Basel Children's Hospital, Switzerland; 3. University of Basel, Switzerland

Introduction

Kinematic and kinetic gait deviations due to increased femoral antetorsion have been described in the literature [1,2]. Passmore et al. compared joint loadings using a generic and subject-specific musculoskeletal model in patients with increased femoral antetorsion and increased tibial torsion [2]. However, no study to date compared joint loadings between patients and controls. Furthermore, it was previously shown that patients with increased femoral antetorsion can exhibit different kinematic gait patterns. Therefore, the aim of the current study was to analyze hip contact forces (HCFs) in patients with increased femoral antetorsion, while also building sub-groups based on their kinematic gait patterns, and controls using personalized musculoskeletal models based on individual morphological data.

Methods

Forty-two pediatric patients with isolated, CT-confirmed increased femoral antetorsion (26 females, mean age = 12.8 years, mean antetorsion = 39.4°) [1] and 9 healthy controls with MRI-confirmed normal torsion (5 females, mean age =12 years, mean antetorsion =21°) were included in this retrospective study. Patients were referred to gait analysis because of gait abnormalities going along with an increased femoral antetorsion ≥30°. Kinematic and kinetic data were recorded during 3D gait analysis using the Plug-In Gait model. HCFs were evaluated with inverse dynamics (AnyBody Technology, Denmark) and reported in a pelvis-based reference frame. Subject-specific models were created from a generic lower-limb model [3], which was scaled according to marker data from a static trial. The modelled femurs were morphed (Figure 1a) to match each subject's femoral antetorsion measurements. Differences in HCF 3D components between patients and controls were evaluated over stance phase through statistical parametric mapping (SPM) with Hotelling T2 and post-hoc t-tests (α = 0.05/3). Subsequently, patients were divided into two groups for each of the three different kinematic gait deviation scenarios: hip rotation, foot progression angles and knee extension (defined by the mean in terminals stance whether it is exceeding the control's mean $\pm$ 1 standard deviation). A SPM ANOVA with post-hoc t-tests was used to assess statistical differences between groups.

Results

Statistically significant differences in HCF components were observed between the two groups in various phases of the stance phase (Figure 1). The resulting HCFs were less proximal, less medially and less posteriorly oriented in patients with increased femoral antetorsion, even though they also presented an overall lower HCF magnitude. No significant differences in HCFs were found for the different sub-group scenarios.
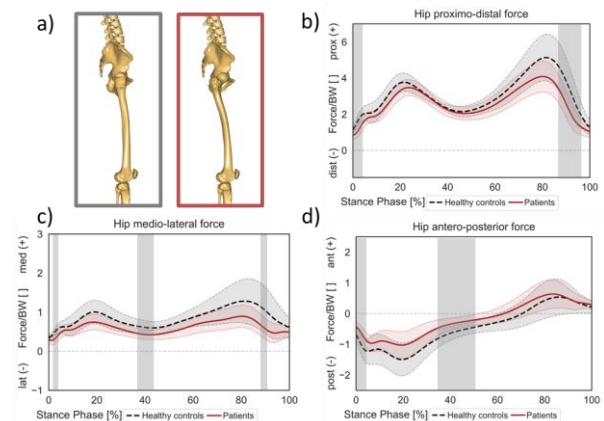
Figure 1: Predicted HCF 3D components in patients with increased femoral antetorsion (red) and controls (grey). Significant difference are indicated by grey bars.

Discussion

The differences in HCF orientation found might be of interest with regards to acetabular cartilage damage that could arise during adulthood in concomitance with other morphological alterations, such as femoroacetabular impingement syndrome [4]. Nevertheless, the magnitude of the HCFs was lower in patients compared to controls. Furthermore, no HCF differences were found whether patients showed increased in-toeing, increased hip internal rotation or increased knee flexion in terminal stance. Therefore, it can be assumed that different kinematic gait patterns do not aim in reducing the hip joint loading, but might due to functional reasons.

References

1. Alexander et al, J Biomech, 86:167-174, 2019
2. Passmore et al, Gait Posture, 63:228-235, 2018.
3. De Pieri et al, PLoS ONE, 13(9), 2018.
4. Pascual-Garrido et al, Clin Orthop Relat Res, 477(5): 1021-1033, 2019.

DIFFERENCES IN IMPINGEMENT PATTERNS IN CAM-TYPE HIPS WITH SUPERIOR AND ANTERIOR ASPHERICITY OF THE FEMUR

Alison Jones (1), Todd Stewart (1), Niall Maher (2), Colin Holton (2)

1. Institute of Medical and Biological Engineering, University of Leeds, UK; 2. Leeds Teaching Hospitals, Leeds National Health Service Trust, UK

Introduction

In cam-type hips additional bone at the femoral head-neck junction can cause impingement in the joint, leading to tissue damage, joint pain, and an increased risk of osteoarthritis. There is currently a lack of understanding of which patient factors lead to damage, making the patient selection for surgery, and optimisation of surgery, challenging. Some correlation has been shown between volumetric CT measures and surgically observed damage [1]. To establish which parts of the bone are involved in impingement, it is necessary to take into consideration an envelope of motions the hip is likely to undergo. This requires efficient modelling methods to combine joint shape features with movement data.

Methods

A parameterised hip shape model capable of predicting impingement incidence, location and depth was developed in Matlab (Mathworks Inc). Point sets described the acetabular rim and parts of the femur head and neck which are outside the radius of the spherical part of the head. Using geometric descriptions from the literature, two hip shape models were generated with large cam-type features; one located superiorly, and one anteriorly (Figure 1). The hip joint angles from an envelope of hip activities were applied (14 activities and nine subjects, totaling 126 motion cases) and the difference in impingement incidence, location and depth were compared between the two hips. Typical neutral hip orientation was established from population studies in the literature and used as a baseline case. The femoral neck shaft angle, femoral version angle and pelvic tilt angle were each varied by 10° and the sensitivity of the impingement incidence and depth were assessed.
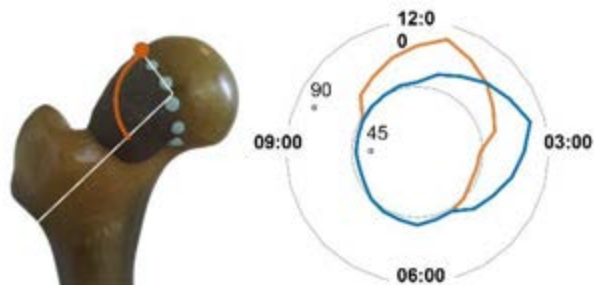
Figure 1: The angular location of points on the edge of the cam and femoral neck for a superiorly (orange) and anteriorly (blue) location cam-type bone feature. Points were recorded by the angle between the femoral neck axis and the line from head center to the point. (A similar method was used for the acetabular rim shape.)

Results

Qualitatively, the predicted impingement was focused in the superior-posterior acetabulum for the superior cam hip and superior-anterior for the anterior case (Figure 1). The high impingement incidence for the anterior cam (71/126 motion cases) compared to the superior cam (17/126) was influenced by the inclusion of several high flexion activities. The mean (and standard deviation) of impingement depth over the motion cases, were similar in the superior cam (7.9°±5.8°) and anterior cam (6.8°±5.4°) cases. For the anterior cam, reduction in femoral version had the greatest effect, while for the superior cam, reducing the neck-shaft angle made the greatest difference (Table 1).
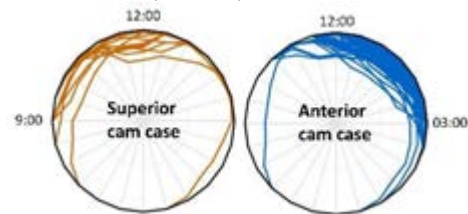
Figure 1: Clockface plots of the acetabulum (3o'clock anterior). Each line shows the impingement depth reached throughout a motion case.

	Incidence - out of 126 motion cases	Depth, mean±stdev (°)
Superior cam		
baseline	17	7.9 ± 5.8
+10° pelvic tilt	21	5.6 ± 5.0
-10° neck shaft angle	46	6.1 ± 7.5
-10 femoral version	26	5.6 ± 5.6
Anterior cam		
baseline	71	6.8 ± 5.4
+10° pelvic tilt	77	8.6 ± 5.8
-10° neck shaft angle	79	7.8 ± 5.7
-10 femoral version	84	11.7 ± 6.8

Table 1: The effect of changes to the neutral joint orientation on predicted impingement incidence and depth.

Discussion

This shape-motion model can be applied to patient-specific 3D imaging data, with the potential to enhance predictive ability above shape features alone. Data presented here shows that impingement predictions distinguish hips with different cam locations.

References

1. Dessouky et al, Euro. Radiol. 29:3431-40, 2019

Acknowledgements

VALIDATION OF AN ELECTROMYOGRAPHY-DRIVEN MUSCULOSKELETAL MODEL FOR TRUNK MECHANICAL ANALYSIS

Alejandro Moya-Esteban (1), Herman van der Kooij (1,2), Massimo Sartori (3)

1. Department of Biomechanical Engineering, University of Twente, The Netherlands
2. Department of Biomechanical Engineering, Delft University of Technology, The Netherlands

Introduction

Active back-support exoskeletons have the potential to alleviate the load on lumbar joints and musculature, therefore, minimizing the incidence of low back pain. Currently, there is no consensus on the optimal control strategy for these devices. In this abstract, we present the validation of an electromyography (EMG)-driven musculoskeletal model, capable of estimating of lumbo-sacral (L5/S1) joint moments and compression forces, during symmetric and asymmetric box-lifting tasks. Our ultimate goal is to develop an exoskeleton controller capable of modulating lumbar compression forces, estimated via our musculoskeletal model.

Methods

Ten participants (28±2 years old; body mass: 72±8 kg; height: 177±9 cm) lifted 5 and 15 kg boxes, using two symmetric (squat and stoop) and two asymmetric lifting techniques. For asymmetric liftings, two tables were placed on each side of the participant, with an angle of 60 degrees with respect the sagittal plane. Twist-transfer consisted of transferring a box from the left to the right table, while, in lift-transfer subjects lifted a box from the ground and placed it on the right table.

Our previously described EMG-driven model [1] used bipolar EMG and joint kinematics to compute trunk muscle forces, which were later used to compute L5/S1 joint moments and compression forces. L5/S1 joint moments were also calculated via inverse dynamics and were used as reference for validation purposes.

Additionally, we compared EMG peaks (normalized to maximum voluntary contraction) at lifting and lowering stages, altogether, with the corresponding muscle-tendon force for the longissimus lumborum pars lumborum (LLpL) muscle. This preliminary analysis was only performed for stoop 15 kg condition.

Results

For all experimental conditions and participants, mean R^2 and $RMSE_{BW}$ (root mean squared error normalized to body weight) between model-based and reference inverse dynamics moments, were 0.91 and 0.27 Nm/kg respectively. Maximum lumbo-sacral compression forces were maximum during squat 15 kg condition, and reached 7.83 times of body weight.

Across all participants, box-lowering EMG peaks were found to decrease on average $17.9 \pm 11.9\%$, with respect box-lifting EMG peaks. Nonetheless, LLpL lowering forces displayed an increase of magnitude of $0.3 \pm 8.7\%$, with respect to lifting (see Fig. 1).
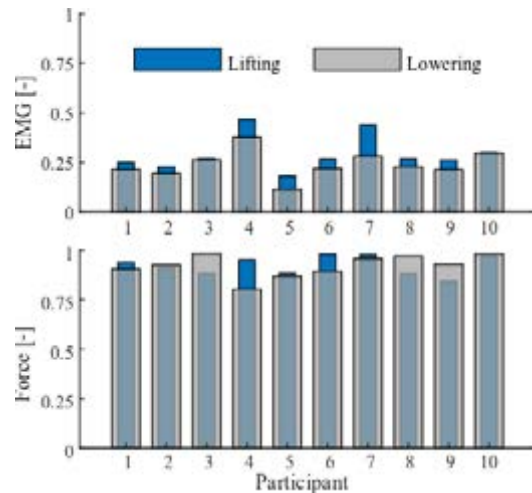
Figure 1: Mean normalized EMG peaks at box-lifting and box-lowering stages, and corresponding model-derived muscle-tendon forces (normalized to maximum force across all conditions), for the longissimus lumborum pars lumborum (stoop 15 kg condition).

Discussion

R^2 and $RMSE_{BW}$ values between model-derived and reference lumbo-sacral moments suggest that our EMG-driven model is capable of deriving valid lumbo-sacral moments across participants, weight, symmetric and asymmetric lifting conditions. We did not perform a direct validation of our L5/S1 joint compression force estimates, due to the current invasive methodologies. However, the magnitude of our estimates is in line with previous studies [2].

Despite the EMG decrease found during box-lowering, LLpL muscle-tendon forces did not experience an analogous reduction. Actually, on average, muscle forces were found to be higher during box-lowering. Such behavior may be explained by the fact that during lowering muscles worked eccentrically (lengthening), therefore, experiencing muscle force enhancement due to the force-velocity relationship. The ability to detect such neuromechanical mechanisms is essential for the development of robust back-support exoskeleton controllers.

References

1. Moya-Esteban et al., 8th IEEE RAS/EMBS Conference BioRob, 1109-1114, 2020.
2. Koopman et al., J. Biomechanics, 105:109795, 2020.

Acknowledgements

COMPARATIVE EFFECTS OF SURGICAL AND NON-SURGICAL THERAPY ON HIP CONTACT FORCE FOR FEMOROACETABULAR IMPINGEMENT SYNDROME

Azadeh Nasseri (1), Laura Diamond (1), Trevor Savage (1), Tamara Grant (1), Michelle Hall (2), Kim Bennell (2), Jillian Eyles (3), Libby Spiers (2), David Hunter (3), David Lloyd (1), David Saxby (1)

1. Griffith University, Australia; 2. The University of Melbourne, Australia; 3. The University of Sydney, Australia

Introduction

Femoroacetabular impingement (FAI) syndrome is a motion-related clinical disorder of the hip common in young active adults, whereby abnormal morphology of the femur and/or acetabulum can cause hip and groin pain, and physical dysfunction [1]. Both arthroscopy and non-operative physiotherapist-led care approaches are used for management of FAI syndrome. Results of randomized-controlled-trials, systematic-reviews, and meta-analyses indicate arthroscopy is marginally more effective than physiotherapy for improving hip-related quality of life during short-term follow-up [2], which is consistent with recent findings from the Australian FASHION trial [3]. However, the effects of arthroscopy and physiotherapist-led treatment for FAI syndrome on hip joint loading, relevant to joint health, have not been examined. The current study compared effects of arthroscopy versus physiotherapist-led personalised hip therapy (PHT) on hip contact forces (HCF) during walking across 12-months.

Methods

A subset of the Australian FASHIoN trial, consisting of 38 individuals with FAI syndrome, attended a biomechanical testing session before they were randomised to receive either arthroscopy (n=17) or physiotherapist-led care (n=21). All participants attended second testing session following treatment, 12 months after the first session. During both testing sessions, participants walked at a self-selected speed while three-dimensional whole-body motion, ground reaction forces, and surface electromyography were acquired. These data were then used in a neuromusculoskeletal modelling framework to estimate external biomechanics, lower limb muscle forces, and HCF (Newton/bodyweight, N/BW). Statistical analysis was performed using a two-way repeated measures analysis of variance applied through Statistical Parametric Mapping (SPM) to compare the 12-month main effects of, and interactions between, treatment and time on HCF during the gait cycle. Statistically significant results were indicated by $P<0.05$.

Results

There were no significant differences in HCF between the two treatment groups at follow-up. Both treatments resulted in an increase in HCF magnitude from baseline to 12-month follow-up (Figure 1), and these increases were statistically significant across most of the gait cycle. No interaction effects were found.
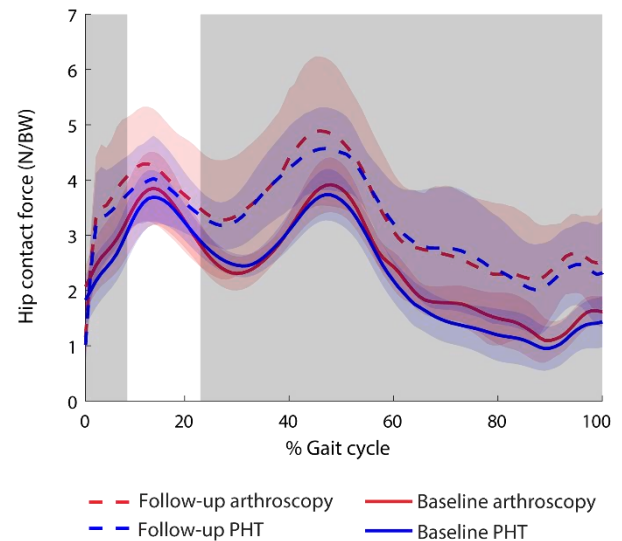
Figure 1: Ensemble average (±1 standard deviation) hip contact force over the gait cycle at baseline (solid) and 12-months follow-up (broken) for arthroscopy (red) and Personalised Hip Therapy, PHT (blue). Grey shading represents significant main effect of time (baseline versus follow-up).

Discussion

This is the first study to examine effects of arthroscopy and PHT to treat FAI syndrome on HCF generated during walking. We found no differences between treatment groups at follow-up, meaning both treatments similarly increased HCF. Following arthroscopy and PHT, the average increase in HCF was ~0.87 and 0.91 BW, respectively. Due to lack of untreated control group in this study, it is unclear whether the increased HCF seen in both groups was an effect of treatment or due to natural progression. However, HCF in both treatment groups at follow-up were of comparable magnitudes to those previously reported in healthy controls [4] and we speculate the observed increase in HCF could be an effect of treatment. In future, comparing muscle contributions to HCF between the two treatment groups might clarify the mechanism by which the treatments increase HCF during gait, and inform clinical decision making in treating FAI syndrome.

References

1. Griffin et al, Br J Sports Med, 50(19):1169-1176, 2016.
2. Ishøi et al, Br J Sports Med, 55:1301-1310, 2021.
3. Hunter et al, BMC Musculoskelet Disord, 22(1):697, 2021.
4. Savage et al, Med Sci Sport Exe, under-review, 2021.

SINERGY-BASED MULTIBODY KINEMATICS OPTIMIZATION TO TRACK ALL THE FOOT BONES WITH A STANDARD GAIT PROTOCOL

Alessandro Pompili (1), Michele Conconi (1), Nicola Sancisi (1), Alberto Leardini (2), Stefano Durante (3), Claudio Belvedere (2)

1. Dept. of Industrial Engineering, University of Bologna, Italy; 2. Istituto Ortopedico Rizzoli, Bologna, Italy; 3 IRCCS S. Orsola Malpighi Hospital, Bologna, Italy

Introduction

The measurement of foot kinematics in gait analysis is generally performed through stereophotogrammetric optoelectronic systems and skin markers, clusters of skin markers and multi-segment protocols [1]. However, motion track is impossible for several bones because of the limited access, such as the talus. In addition, measurements are affected by soft tissue artifact (STA). As a result, bone tracking may result in a foot posture not consistent the patient anatomy. Multibody kinematics optimization (MKO) may improve gait analysis results by introducing kinematic models that reproduce the natural human movement. These models are fitted on marker motion during the inverse kinematics computation, obtaining estimates of position and orientation of relevant bones [2].

The aim of this preliminary study is to use the foot synergies [3] to perform the MKO on the foot of a patient. We hypothesized that the method should reduce the STA impact, obtaining at the same time the kinematics of all the bones of the foot.

Methods

In a previous cadaveric study [3] we defined four significant foot synergies explaining more that 95% of the motion of the foot and ankle complex. Mean bone and synergies were computed and skin markers were simulated on average bones. Gait data were collected for one subject following the Rizzoli protocol [4]. Three MKO strategies were tested and compared: the whole foot was considered as a single its and tibia poses were rigidly tracked using all the markers at once; the foot was decomposed in three rigid segments [4] tracking the rigid motion of each of them by subset of markers; the foot and ankle complex was considered as a 4 degrees of freedom system, whose posture was computed minimizing the residual error on the marker position. Results were compared in terms of anatomical consistency of the resulting foot posture and ground copenetration.

Results

Rigid body model of the foot is uncapable to map variation in its posture and result in a physically impossible interaction with the ground (figure 1, first row). Although multi-segment MKO may result in the minimum residual error, the associated foot posture are inconsistent with the foot anatomy, resulting in an excessive flexion of the calcaneus and in a general flattening of the foot (figure 1, second row). Sinergy-based approach preserves anatomical consistency,

capture the foot flexion during the step, and result in a natural interaction with the ground (figure 1, third row).
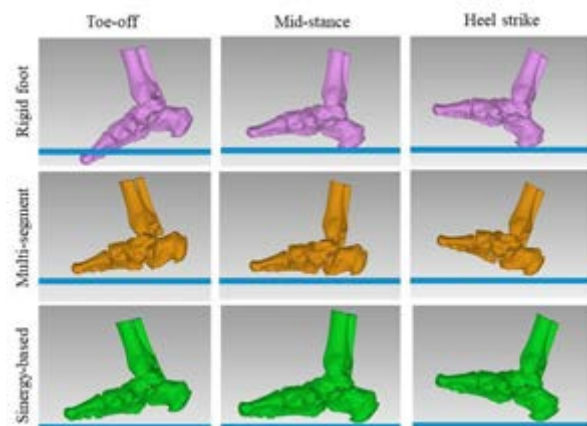
Figure 1: Comparison of single rigid body (first row), multi-segment bone clusters (second row), and synergy-based MKO at heel strike, mid-stance, and toe-off. Ground is depicted in blue.
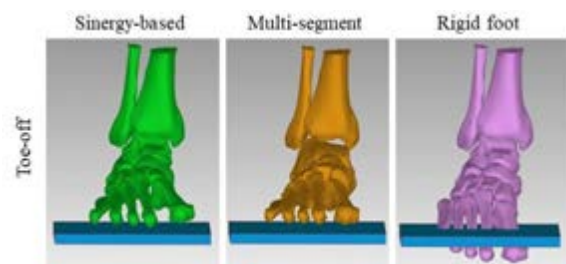
Figure 2: Comparison of single rigid body, multi-segment bone clusters, and synergy-based MKO at toe-off (frontal view).

Discussion

This preliminary study shows the potentiality of synergies-based MKO in tracking the motion of all bones in the foot. In comparison with classical approaches, the one here proposed has several advantages: it is capable to map the foot deformation; it maintains the anatomical consistency; it produce plausible interaction with the ground; finally, it allows the indirect tracking of the talar motion. Future development may lead to the definition of experimental protocol that exploit synergy-based MKO to minimizing the number of required marker to track the foot motion. Future work will extend the number of subjects and implement a bone-to-bone distance mapping to further compare the performances of the three methods.

References

1. Leardini et al., 2005. *Gait&Posture.* **21**:212-225.
2. Leardini et al., 2017. *J. of Biomech.* **62**: 77-86.
3. Conconi et al., 2021. *Proc. XXVIII ISB Congress.*
4. Leardini et al., 2007, *Gait&Posture,* **25**: 453-462.

REFINING THE OXFORD FOOT MODEL TO DESCRIBE THE KINEMATICS OF THE MEDIAL LONGITUDINAL ARCH

Jerneja Uhan (1,2), Alpesh Kothari (1,2), Amy Zavatsky (1), Julie Stebbins (1,2)

1. University of Oxford, United Kingdom; 2. Oxford Gait Laboratory, United Kingdom

Introduction

During clinical assessment of the foot, appropriate evaluation of the medial longitudinal arch (MLA) is arguably the most important aspect for characterising foot morphology. In clinical gait analysis, multi-segment foot models (MSFMs) are often used for diagnosing and planning the treatment of a wide range of musculoskeletal disorders of the lower limb. Despite the importance of the MLA, there is limited representation of it in many MSFMs. The Oxford Foot Model (OFM) [1] is one of the most widely utilised MSFMs; however, it only tracks the forefoot and hindfoot, providing only indirect information on midfoot function. Therefore, this study aimed to assess various novel methods for representing the MLA in the OFM, to make it a more comprehensive and versatile tool. The criteria for evaluating each MLA measurement method were that it would a) detect kinematic differences between different foot morphologies (typically developed feet (TDF)) and flexible flat feet (FFF)), and b) be strongly correlated with clinical assessment measures of arch height index (AHI).

Methods

Eight potential definitions of MLA angle were developed, based on a similar study by Caravaggi et al. [2], using various combinations of skin markers located on the calcaneus (HEE), sustentaculum tali (STL), talo-navicular tuberosity (NAV), base of the 1st metatarsal (P1M), and head of the 1st metatarsal (D1M), and virtual markers (projected to the floor during standing) (Figure 1). The MLA definitions were chosen to reflect standard clinical and x-ray assessment of the MLA. 42 children (84 feet) were assessed (mean age of 11 years, 50 TDF and 34 FFF). AHI is a ratio between the height of the dorsum at 50% of the foot length and the truncated foot length. Clinical measurement of AHI required the use of calibrated callipers and a standardised protocol [3]. Marker positions were tracked with the feet loaded (standing) and unloaded (sitting) using a 12 or 16 infra-red camera system (Vicon MX/T40, Vicon, Oxford UK, 100 Hz sample rate). Data was processed in the Vicon Nexus (v2.12, Vicon, Oxford, UK) software environment. Differences between positions (standing and sitting) and foot morphologies (TDF and FFF) were determined using One-Way ANOVA tests (mean angle, Greenhouse-Geisser correction and mean difference). In addition, the correlation of each MLA angle definition with the clinical AHI calculation was explored using the Pearson correlation coefficient.

Results

Significant differences ($p<0.05$) in MLA angles were observed across most of MLA definitions (1,3,5,6,7,8) when comparing TDF and FFF and across all the MLA definitions when comparing sitting and standing positions. The mean standing angles were greater than the mean sitting angles across all the MLA definitions, with the mean differences ranging from 2.0 to 13.6 degrees. Most MLA definitions (1,3,6,7,8), when utilised in the standing position, elicited significant inverse correlations ($p<0.05$) with clinically assessed AHI. Overall, the biggest difference in MLA angle between TDF and FFF was observed upon using the non-projected MLA angle definition of HEE, NAV and D1M. This was also the MLA definition that demonstrated the strongest inverse correlation ($r=-0.607$; $p<0.001$) with the clinical AHI calculation.
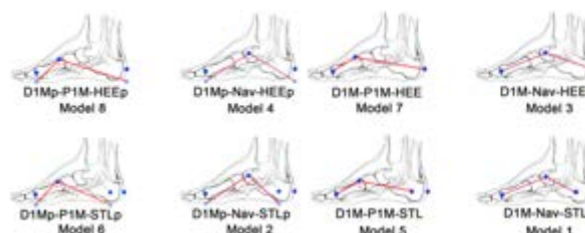
Figure 1: Eight potential definitions of MLA angle

Discussion

These results suggest the choice of markers to use to detect changes in MLA shape both between loaded and unloaded foot conditions, and between groups of individuals with different foot types (TDF and FFF) is HEE, NAV and D1M. While Caravaggi et al. [1] recommended the use of projected markers to improve repeatability of measurements, the results of this study suggest that this may reduce the ability to observe fine differences across varying foot morphologies, and therefore actual rather than virtual markers may be preferred.

References

1. Stebbins et al, Gait & posture, 4:401-410,2006
2. Caravaggi et al, Journal of Biomechanics, 88:180-185, 2019
3. Cutler et al, Journal of the American Podiatric Medical Association, 98:102-106

CALIBRATION OF A NEUROMUSCULOSKELETAL MODEL AT THE JOINT TORQUE AND JOINT STIFFNESS LEVELS SIMULTANEOUSLY

Christopher P. Cop (1), Alfred C. Schouten (1, 2), Bart Koopman (1), and Massimo Sartori (1)

1. University of Twente, The Netherlands; 2. Delft University of Technology, The Netherlands

Introduction

Neuromusculoskeletal (NMS) models informed by electromyograms (EMGs) are valuable tools to estimate muscle forces and joint torques using EMGs and joint kinematics as input. NMS models are defined by a set of parameters that are typically calibrated by minimizing the difference between reference and estimated joint torques [1]. In this way, EMG-driven NMS models have been able to successfully estimate joint torques in a variety of tasks. However, their ability to predict joint stiffness, i.e., a neuromechanical property that characterizes our joint's compliance, is limited. Joint stiffness is crucial for stable interaction with our environment.

In this work we present an EMG-driven NMS model that was calibrated by tracking reference joint torque and stiffness profiles simultaneously, and we compared performance against a model that was calibrated by only tracking reference joint torque.

Methods

A healthy individual was instructed to follow a sinusoidal angle trajectory (amplitude: 0.15 rad, frequency: 0.6 Hz) by plantar- and dorsiflexing his ankle using a dynamometer. Surface EMGs of the main lower leg muscles were acquired. Ankle angle and torque were measured while position perturbations (amplitude: 0.03 rad, switching time: 0.15 s) were applied to obtain reference joint stiffness values using a multi-segment time-varying system identification method [2].

An EMG-driven NMS model was calibrated by minimizing using the following objective function $F_{obj} = (\tau_{ref} - \tau_{mod})^2 + \gamma \cdot (K_{ref} - K_{mod})^2$, where τ_{ref} and τ_{mod} are the reference and modelled torques, respectively, K_{ref} and K_{mod} are the reference and modelled joint stiffness, respectively, and γ is a positive scalar weighting factor. Two calibrations were performed: the traditional calibration tracking only joint torque (i.e., $\gamma = 0$) and our novel calibration that simultaneously takes joint torque and joint stiffness into account (i.e., $\gamma = 0.2$).

The two calibrated models were used to predict joint torque and joint stiffness using a novel dataset, i.e., data not used for calibration. For both models, reference and modelled torque and stiffness were validated against reference values using the root mean squared error (RMSE) and the coefficient of determination (R^2).

Results

Figure 1 and Table 1 summarize the preliminary results.
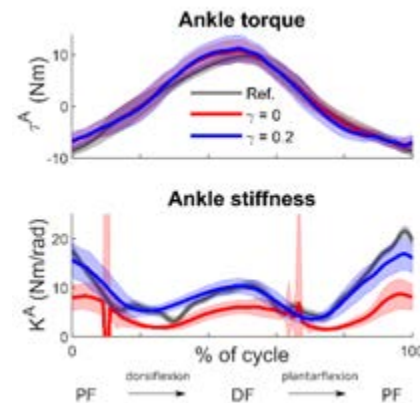
Figure 1: Ankle torque (top) and stiffness (bottom) profiles. Reference in black; traditional calibration only tracking torque in red; new calibration tracking torque and stiffness in blue. Results shown as mean (solid lines) ± standard deviation (shaded area).

Calibration type	RMSE τ_{mod} (Nm)	RMSE K_{mod} (Nm/rad)	R^2 τ_{mod}	R^2 K_{mod}
$\gamma = 0$	1.5 (0.4)	8 (12)	0.95 (0.02)	0.5 (0.3)
$\gamma = 0.2$	1.9 (0.4)	2.6 (0.8)	0.93 (0.03)	0.7 (0.2)

Table 1: RMSE and R^2 values of the modelled joint torques and stiffness using each calibrated model. Results expressed as mean value (standard deviation).

Discussion

We present, for the first time, an EMG-driven NMS model that was calibrated to simultaneously predict joint torque and joint stiffness. Including joint stiffness in the calibration's optimization routine resulted in a set of model parameters that was able to closely track the reference joint stiffness profile (in contrast to the model calibrated only at the torque level, that presented discontinuities due to model parameters resulting in tendons operating at lengths shorter than their slack length), without compromising joint torque estimation capabilities (Figure 1, Table 1). Our preliminary results may suggest that we narrowed down the model's solution space resulting in parameters that are dynamically consistent at the torque and stiffness levels.

References

1. C. Pizzolato et al., J. Biomech., 48:3929–3936, 2015.
2. A. M. Esteban et al, Proc. Annu. Int. Conf. IEEE Eng. Med. Biol. Soc. EMBS, 2119–2122, 2019.

Acknowledgements

ESTIMATING A SINGLE MAXIMUM MUSCLE-TENDON LENGTH FROM DISCRETISED MUSCLES

Claude Hayford (1,3), Erica Montefiori (1), Emma Pratt (2), Claudia Mazzà (1)

1. Department of Mechanical Engineering & Insigneo Institute for in silico Medicine, University of Sheffield, UK; 2. Gait Analysis Laboratory, Sheffield Children's Hospital, UK; 3. Department of Biomedical Engineering, University of Ghana, Ghana

Introduction

Musculoskeletal models permit the estimation of clinical factors such as muscle-tendon lengths and forces not easily accessible by non-invasive means [1]. Muscles, particularly those with broad attachment points, are usually represented in these models by discretising them into multiple elements [2]. Downstream analysis of muscle action such as forces and loadings on the body segments have been shown to be sensitive to the level of discretisation [3]. Another challenge associated to this discretisation is the clinical interpretation of the output when a muscle needs to be reconsidered as a single unit. An example is the calculation of the muscle tendon lengths (MTLs), for which there is no consensus on selecting a representative estimate among the muscle elements. The aim of this study was to explore an appropriate and representative estimate of maximum MTLs for two different musculoskeletal models.

Methods

Data from 13 juvenile volunteers (11.5 ± 3.0 years; 44.4 ± 15.9 kg; 1.43 ± 0.17m) was retrospectively analysed. Gait analysis and magnetic resonance (MR) imaging data were used to build subject-specific models of the right limb of each participant in addition to a scaled generic model (SG, gait2392). All models were subsequently used to simulate gait in OpenSim 3.3 and estimate joint angles and MTLs. MTLs were normalised to standing length and the maximum lengths (MTL_{mx}) attained over the gait cycle were then extracted. Focus was on four muscles: adductor magnus - *aMg*, gluteus maximus - *gMx*, gluteus medius - *gMd,* and gluteus minimus - *gMn*. The average of MTL_{mx} (avg_MTL_{mx}) between the three elements representing each of these muscles was calculated. Concordance between the MTL_{mx} from MR and SG was established using a correlation analysis, while absolute difference expressed as a percentage of the MR value were used to investigate agreement between the two model types. To determine the consistency between the two choices, the avg_MTL_{mx} was compared to the MTL_{mx} from the middle element (mid_MTL_{mx}) using correlation and paired samples test.

Results

Absolute differences in MTL_{mx} between MR and SG were generally lower than 6% of the MR value for each element and avg_MTL_{mx} (Table 1). avg_MTL_{mx} and mid_MTL_{mx} were highly and significantly correlated for all four muscles ($r > 0.92$, $p < 0.001$) in both MR and SG, indicating consistency in the estimates from the two models.

Name	Correlation				Absolute difference (%)			
	1	2	3	Avg	1	2	3	Avg
aMg	.8	.8	.7	**.8**	3.3	2.5	1.4	**1.8**
gMx	.5	.7	.7	**.8**	4.3	5.3	5.6	**5.1**
gMd	.2	.08	.6	**.1**	2.8	2.3	3.3	**2.1**
gMn	.4	.1	.2	**.1**	3.3	2.7	2.4	**2.7**

Table 1: Average correlations and %differences in MTL_{mx} estimates between MR and SG for the 3 elements (1,2,3) and avg_MTL_{mx} (Avg) of each muscle.

Significant differences between the avg_MTL_{mx} and the mid_MTL_{mx} of the glutei maximus and medius were observed for the SG but not the MR (Figure 1).
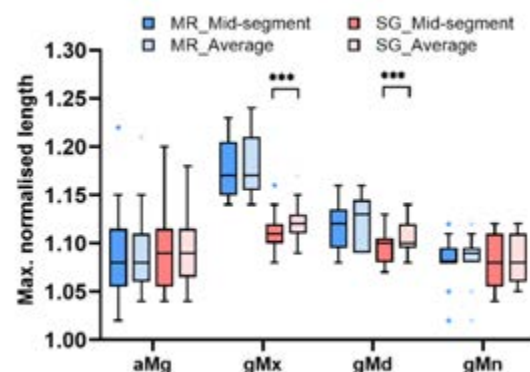
*Figure 1: Comparison of avg_MTL_{mx} and mid-MTL_{mx} for MR and SG models. ***p-value < 0.001*

Discussion

Although differences exist between MR and SG estimates of MTL_{mx} for discretised muscles, the inter-model agreement when using avg_MTL_{mx} was most similar to that from the middle element for all four muscles of focus. avg_MTL_{mx} also presented a representative estimate that did not change the interpretation for each muscle bar *gMx* and *gMd* in the generic model. It is recommended to report the avg_MTL_{mx} as a convenient and accessible summary value to the clinician as it had relatively lower differences between MR and SG than the mid_MTL_{mx}.

References

[1] Arnold et al, Gait & Posture 23(3): 273-81, 2006
[2] Delp et al, IEEE Trans Biomed Eng 37(8): 757-67, 1990
[3] Valente et al, J Eng Med 226(2): 161-169, 2012

TENDON COMPLIANCE INFLUENCES TIME-SERIES ENERGY EXPENDITURE ESTIMATIONS

Israel Luis (1), Maarten Afschrift (2), Friedl De Groote (3) and Elena M. Gutierrez-Farewik (1)

1. KTH MoveAbility Lab, Dept. Engineering Mechanics, KTH Royal Institute of Technology, Sweden
2. Faculty of Behavioural and Movement Sciences, Vrije Universiteit Amsterdam, Netherlands
3. Department of Movement Sciences, KU Leuven, Belgium

Introduction

Energy expenditure (EE) provides a quantitative assessment of metabolic demand of locomotion. In the absence of experimental measures, accurate model-based prediction may support rehabilitation programs and assistive device design. Instantaneous energy expenditure may be estimated by using metabolic cost models, which consist of a set of equations that relate muscle excitations, states, and state derivatives to metabolic energetics. Tendon compliance influences muscle mechanics and, consequently, it is important to evaluate its effect on muscle energetics. This study aims to examine the influence of tendon stiffness in the time-series EE estimation using musculoskeletal simulations.

Methods

Eight able-bodied adults were asked to walk at 55%, 70%, 85%, 100%, 115%, 130%, and 145% of their preferred walking speed (PWS), during which gait kinematics (Vicon V16, CGM2.4), ground reaction forces (AMTI), and electromyographic signals (EMGs) in one leg were recorded in biceps femoris long head, semitendinosus, vastus lateralis (VL), vastus medialis (VM), tibialis anterior (TA), gastrocnemius lateralis (GL), gastrocnemius medialis (GM) and soleus (SO), using bipolar surface wireless electrodes (Cometa). Vastus intermedius (VI) excitation was estimated as the average of VL and VM. A musculoskeletal model [1] was scaled to each subject's dimensions, and maximum isometric force was scaled according to muscle volume, estimated based on body weight and height [2]. Inverse kinematics and inverse dynamics were computed in all trials using OpenSim 4.1. A muscle-redundancy solver based on direct collocation [3] was used to estimate muscle excitations by minimizing muscle excitations squared and tracking errors between simulated muscle excitations and joint torques, and EMG and inverse dynamics torques, respectively. We either imposed normalized tendon stiffness (kT) (generic value of 35 [3]) (SIM-GEN) or allowed Achilles tendon (GM, GL, SOL) and patellar tendon (VM, VL, VI) stiffness to vary (SIM-OPT). EE was estimated using a metabolic cost model proposed by Uchida et al [4].

Results

Mean optimized Achilles and patellar tendon stiffness was 12.97 and 7.28, respectively. Simulated fiber lengths were in closer agreement with reported values [5][6][7] for optimized than for generic tendon stiffness

(Figure 1A). Estimated EE trajectories had two peaks – one in early stance and one near pre-swing (Figure 1B) in both cases. However, when allowing tendon stiffness to vary (SIM-OPT), the peaks were lower and earlier than when using generic stiffness. The lower first peak could be explained by more isometric contraction of the vasti. The lower second peak was due to increased energy storage in the Achilles tendon during mid- and terminal stance reducing EE of the plantarflexors. This was more pronounced at higher walking speeds.
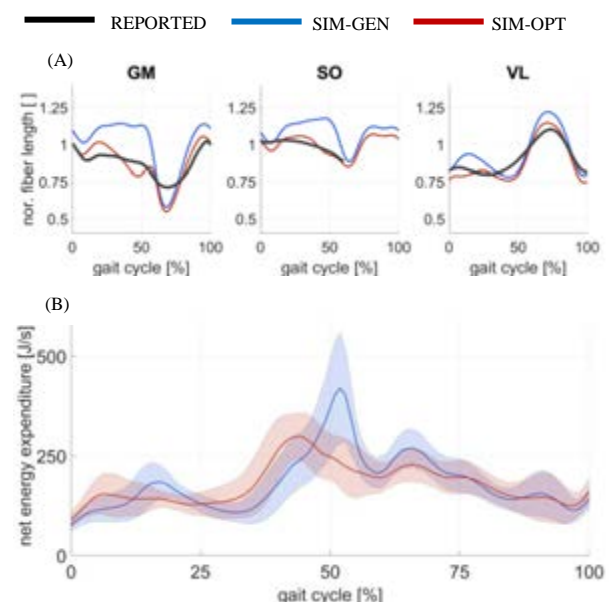
Figure 1: (A) Computed normalized fiber length over the gait cycle of VL, GM, and SO, and reported fiber lengths [5][6][7]. (B) Sum computed EE of all leg muscles at PWS.

Discussion

Tendon compliance has a large influence on muscle-tendon behavior and energetics. Simulations with estimated tendon stiffness values resulted in more realistic fiber lengths and should be considered for a better description of muscle-tendon behavior.

References

1. Rajagopal et al, IEEE Biomed, 63, 2068-2079, 2016
2. Handsfield et al. J. Biomech, 47, 631-638, 2014
3. De Groote et al, Ann. Biomed. Eng., 44, 2922–2936, 2016
4. Uchida et al, PLOS ONE, 11, e0150378, 2016
5. Farris et al, PNAS, 109, 977-982, 2012
6. Lai et al, J. Appl. Physiol., 118, 1266–1275, 2015
7. Chleboun et al, J Orthop Sports, 37, 372-379, 2007

SMART FLEXIBLE GARMENT AND RAPID NEUROMUSCULOSKELETAL MODELLING FOR FAST AND ACCURATE CLINICAL DECISION-MAKING

Donatella Simonetti (1), Bart Koopman(1) and Massimo Sartori (1)

1. University of Twente, The Netherlands

Introduction

Rapidity and reliability are not yet possible simultaneously during neuromusculoskeletal (NMS) assessment. While clinics need rapidity and low-cost methodologies [1], sports training or biomechanical lab can access costly and time-consuming technologies, such as electromyography (EMG), motion tracking systems and force plates, that can provide quantifiable estimates of an individual's NMS functionality. We aim to balance rapidity and NMS quantifiability by integrating (1) a flexible sensorized garment comprising 64 equally distributed monopolar EMG electrodes and inertial measurements units (IMUs), thus allowing to get over the lengthy setup; (2) a clustering algorithm for automatic localization of the muscles lying under the multi-channel (MC) EMG grid preventing non-systematic human error in manual muscle localization and electrodes' placement; and (3) a computationally efficient NMS model. We present preliminary results toward the realization of such technology with two experiments. The initial goals are (1) to automatically extract muscle-specific clusters from a few repetitions of a slow locomotion task and unknowingly located electrodes and (2) to assess whether the automatically identified muscle-specific activation profiles translate into consistent ankle torque profiles. With the second experiment, we analyze kinematics retrieved from IMUs instead of marker trajectories and how they affect the NMS modeling torque estimation.

Methods

Three healthy subjects were instrumented with a flexible lower leg garment sensorized with 64 equally distributed monopolar electrodes, and 33 reflective markers. The subjects were instructed to walk at three speeds (1, 3 and 5 km/h – FW1, FW3, FW5) on an instrumented split-belt treadmill. The 64-EMGs signals of the slowest speed were processed with non-negative matrix factorization (NNMF) [2]. It was interactively applied to extract 5 clusters specific for each of the main lower leg muscles including: Tibialis Anterior, Peroneus, Gastrocnemius Medialis and Lateralis, and Soleus. The muscle-specific clusters extracted from one walking trial were then used on all locomotion tasks to derive average muscle-specific activations. Those were employed to drive an offline NMS model and estimate ankle torques. The automatic activations were validated and compared with the activations of electrodes manually selected on top of each muscle belly also used to compute ankle torques.

A similar experimental protocol was applied on a healthy subject instrumented also with 8 inertial motion sensors (IMUs – on torso, pelvis, shanks, thighs and feet). Both marker trajectories and quaternions from the 8 IMUs as well just the 3 on the instrumented leg were processed to compute joint angles as well as reference ankle moments (T_{ref}) and muscle-tendon unit (MTU) kinematics. Both MTU kinematics and T_{ref} retrieved from markers or IMUs and automatically retrieved muscle-specific activations were input to an EMG-driven NMS model to estimate ankle torque.

Results

Figure 1 shows the results of the first experiment while Table 1 presents the results of the second study.
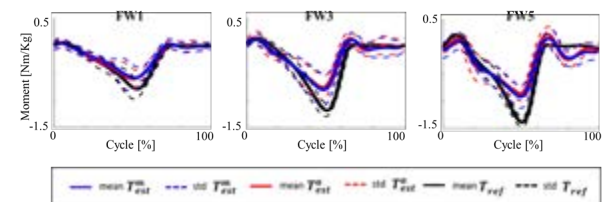
Ankle moments retrieved via inverse dynamics (T_{ref} -black lines) and estimated via offline EMG-driven modeling using automatic (T^u_{est} – red lines) and manual activations (T^m_{est} - blue lines). The plots report the mean (solid lines) and standard deviation (dashed lines) across all subjects for T^m_{est}, T^a_{est} and T_{ref} for walking at 1km/h (FW1), 3km/h (FW3) and (FW5).

	Markers	8 IMUs	3 IMUs
NRMSE	0.13 (0.19)	0.36 (0.21)	0.37 (0.23)
R^2	0.94 (0.75)	0.93 (0.77)	0.91 (0.80)

Table 1: NRMSE and R^2 of estimated ankle torques values for 1 km/h and 3 km/h (in brackets) walking speed using kinematics from markers or two different configurations of IMUs, 8 IMUs or 3 IMUs.

Discussions

The combination of fully wearable technologies with automatic EMG clustering and NMS modeling techniques can allow understanding individual muscle function and drastically change the way the musculoskeletal assessment is performed. Rapid and quantitative estimates on internal subject-specific NMS properties can be crucial in several domains such as clinical-decision making, rehabilitation, sports training and injury prevention.

References

1. J. Mehrholz et al., Arch. Phys. Med. Rehabil., 88-10/1314–1319,2007.
2. D. D. Lee and H. S. Seung, Nature, 1999.

QUANTITATIVE VALIDATION OF A DEEP LEARNING BASED MARKERLESS MOTION CAPTURE SYSTEM

Tylan Templin (1), Travis Eliason (1), David Chambers (1), Nathan Louis (1), Omar Medjaouri (1), Kase Saylor (1), and Daniel P. Nicolella (1)

1. Southwest Research Institute, USA

Introduction

The accurate quantification and analysis of human movement biomechanics has provided critical insight across a broad range of health, disease, and performance related applications. However, the accurate and reliable measurement of biomechanics requires a dedicated laboratory with advanced instrumentation operated by highly trained individuals, and is exceedingly time consuming, all of which significantly limit its use in routine clinical and operational assessments. The ability to quickly, easily, and reliably perform accurate, health and performance related, biomechanical measurements outside of the laboratory is an unmet need.

Methods

A custom deep convolutional neural network (dCNN) was trained to detect a set of virtual markers representing the joint centers and specific anatomical landmarks of the subject of interest. The network was trained with both publicly available hand-labeled pose datasets and a custom training dataset where video images were automatically labelled using Vicon and OpenSim processed data (1). To quantitatively evaluate the performance of the markerless motion capture system, synchronized video from 4 video cameras was captured along with Vicon marker-based data from 9 subjects who performed 8 movements (counter movement jump (CMJ), squat, left and right single leg jump, left and right single leg squat, and left and right lunge) each repeated 3 times. 2D virtual marker dCNN detections were used to generate 3D locations of each virtual marker using a robust probabilistic triangulation algorithm. Vicon data was processed using standard methods. Subject kinematic data was determined using a skeletal kinematics model (2) automatically scaled to each subject via inverse kinematics (OpenSim, v.4.1). Quantitative performance was evaluated using root mean square error (RMSE) between the markerless and marker-based motion capture derived kinematic data.

Results

Excellent qualitative agreement was seen between the two systems (Figure 1). The markerless systems demonstrated a high degree of agreement with the Vicon derived data with the average RMSE values of between 4.54 and 9.21 degrees for hip, knee, and ankle angles, respectively across all movements (Table 1).

Discussion

We have successfully demonstrated the accuracy and reliability of a markerless motion capture system that uses standard off the shelf video camera hardware compared to a traditional marker-based system. Further development and validation of markerless systems will lead to more ubiquitous, routine quantification of biomechanics in non-laboratory settings including clinical environments, rehabilitation settings, etc. without the need for sophisticated laboratory or body worn equipment.
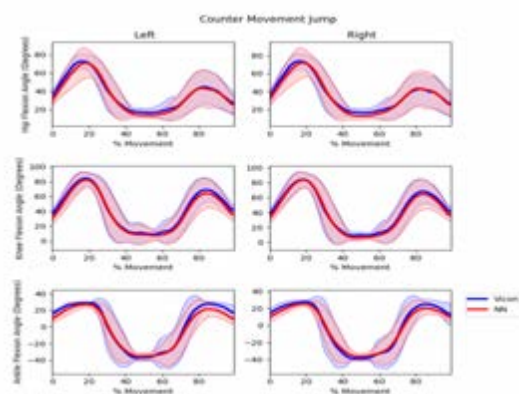
Figure 1: Comparison of markerless (red) and marker-based (blue) kinematics data for the CMJ for all nine subjects.

DOFs	Counter Movement Jump	Single Leg Jump L	Single Leg Jump R	Lunge R
Hip Flexion	7.46 (4.23)	8.67 (4.38)	8.14 (3.24)	8.2 (3.24)
Hip Adduction	4.93 (8.73)	7.2 (3.74)	6.56 (2.86)	9.21 (3.45)
Knee Flexion	4.93 (1.58)	5.14 (2.03)	4.54 (1.74)	5.02 (1.55)
Ankle Flexion	7.48 (2.31)	6.83 (2.47)	7.16 (3.7)	6.22 (2.94)

Table 1: Quantitative validation results – RMSE (SD).

References

1. Eliason et al., ISB Proceedings, 2019.
2. Rajagopal et al., IEEE Trans. Biomed., 2016.

Acknowledgements

A NEW GENERALIZED CONTINUUM APPROACH TO MODEL SPINAL GROWTH

Natalia M. Castoldi (1,2), Maria Antico (2), Madge Martin (1), Peter Pivonka (2), Vittorio Sansalone (1)

1. Univ Paris Est Creteil, Univ Gustave Eiffel, CNRS, UMR 8208, MSME, F-94010 Créteil, France
2. School of Mechanical, Medical and Process Engineering, Queensland University of Technology, Australia

Introduction

Living tissues can grow responding to both mechanical and biochemical effects [1]. Physiological spine growth gives rise to vertebral bodies with appropriate trabecular architecture and strength, healthy intervertebral discs and adequate spinal curvature to distribute loads throughout the spinal column. By contrast, abnormal spine growth may lead to pathologies such as scoliosis. Thus, understanding the mechanisms of spinal growth and being able to model this phenomenon can help to understand the adverse effects of certain pathologies, and provide insights into strategies to counter them. The current work outlines a bulk growth model set up in the framework of generalized continuum mechanics [2] that has been used to simulate the growth of a healthy spine.

Methods

Kinematics. The total deformation of a growing body element results from both growth and elasticity: $\nabla p = \mathbf{F}\mathbb{P}$, where ∇p is the deformation gradient, $\mathbb{P}$ is the growth tensor (describing the actual stress-free shape of a body element) and $\mathbf{F}$ is the elastic strain.

Growth law. By contrast with most existing growth models [1], our growth law is obtained by relying on generalized statements of the virtual power and dissipation principles [3] involving both mechanical and biochemical stimuli. Eventually, this leads to a thermodynamically compatible growth law, reading:

$$\dot{\mathbb{P}} = \alpha^{-1}\big(\mathbb{B} - \breve{\psi}\mathbf{I} + \mathbb{J}^{-1}\mathbf{F}^{\mathrm{T}}\mathbf{S}\mathbb{P}^{\mathrm{T}}\big)\mathbb{P} \qquad (1)$$

Where $\dot{\mathbb{P}}$ is the growth rate, $\breve{\psi}$ is the free-energy density (per unit stress-free volume), which depends only on $\mathbf{F}$, $\mathbb{J} = \det(\mathbb{P})$, $\mathbf{I}$ is the second-order unit tensor, $\mathbf{S}$ is the Piola stress tensor (on the reference configuration), $\mathbb{B}$ is a second-order tensor representing the mechanical feedback of the growth-related biological stimuli, and α is a positive scalar representing the resistance to growth.

Spine model. A simplified spine model was developed to study the physiological spine growth. The model involves the thoracolumbar vertebrae (described as linearly elastic, growing bodies, as per Eq. (1)) and intervertebral discs (described as hyperelastic bodies). The spine is clamped on the bottom (L5) and lateral displacements are constrained on the top (T1) to trigger the deformation in the sagittal plane. The *effective* growth stimulus $\alpha^{-1}\mathbb{B}$ was identified based on clinical data [4] and by neglecting the mechanical loads. Thus, $\alpha^{-1}\mathbb{B}$ embeds the effect of body weight in healthy physiological growth.

Results

The physiological growth of a spine from age 6 to 18 was simulated, see Figure 1. Panel (A) shows the time course of the growth rate and of the length of the spine, as well as the data of [4]. Panels (B) and (C) show the patterns of the growth and Piola stress, respectively (vertical components) in the final configuration. The initial shape of the spine is also depicted (light gray).
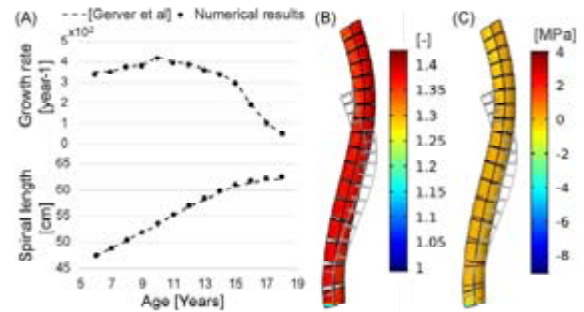
Figure 1: (A) Growth rate $\dot{\mathbb{P}}$ and length of entire spine; (B) Growth $\mathbb{P}$; (C) Piola stress $\mathbf{S}$. See text for details.

Discussion

Our numerical results are in excellent agreement with the literature data (Fig. 1-A), thus validating the identification of the effective growth stimulus $\alpha^{-1}\mathbb{B}$ in physiological conditions. Lacking more precise data, we applied the same stimulus to all vertebrae, which resulted in nearly uniform growth across the spine (Fig. 1-B). As neither mechanical loads nor kinematical constraints were applied along the spine, the stress pattern is nearly zero (Fig. 1-C). Non-uniform growth and stress appearing close to the clamped end are not physiological.

Next steps of our work include: *(i)* improving the geometry and material description of the spine, and *(ii)* investigating the effects of non-uniform growth stimuli and mechanical loads on abnormal spinal growth.

References

1. Kuhl, E., J Mech Behav Biomed Mater, 29, 529-543, 2014
2. Germain, P., SIAM J Appl Math, 25(3), 556-575, 1973.
3. DiCarlo, A., et Quiligotti, S., Mech Res Commun, 29(6), 449-456, 2002.
4. Gerver, W. J. M., & Bruin, R. Paediatric morphometrics: a reference manual, 2011.

Acknowledgements

HIGH TIBIAL OSTEOTOMY NORMALIZES KNEE AMBULATORY LOADS

Enrico De Pieri (1,2), Corina Nüesch (2,3,4,5), Geert Pagenstert (5,6), Elke Viehweger (1,2,7), Christian Egloff (2,3,5), Annegret Mündermann (2,3,4,5)

1. *Laboratory for Movement Analysis, University of Basel Children's Hospital, Switzerland; 2. Department of Biomedical Engineering, University of Basel, Switzerland; 3. Department of Orthopaedics and Traumatology, University Hospital Basel, Switzerland; 4. Department of Spine Surgery, University Hospital Basel, Switzerland; 5. Department of Clinical Research, University of Basel, Switzerland; 6. Clarahof Orthopaedics, Switzerland; 7. Department of Neuro-Orthopaedics, University of Basel Children's Hospital, Switzerland*

Introduction

High tibial osteotomy (HTO) is a well-accepted surgical procedure for patients with knee osteoarthritis (OA) and varus alignment aimed at re-establishing a more even distribution of ambulatory load between the affected medial and the lateral knee compartment. The aim of this study was to compare pre- and postoperative lower limb kinematics and kinetics, and knee intra-articular forces during gait estimated via musculoskeletal modelling between patients with knee OA undergoing HTO and matched controls, and to investigate relationships between HTO-induced changes in gait-related biomechanical measures and the Knee Osteoarthritis Outcome Score (KOOS).

Methods

Sixteen patients with isolated, symptomatic medial compartment knee OA completed pre- and postoperative gait analysis. Sixteen age- and sex-matched asymptomatic volunteers participated as controls. The collected motion capture data was used as input for an inverse dynamics analysis (AnyBody Technology, Denmark) to evaluate external knee moments and knee contact forces. Knee varus/valgus alignment was estimated from a static reference trial and implemented as a fixed change in orientation of the knee joint axis. The distribution of the compressive knee force across the medial and lateral compartments was evaluated [1]. Statistical parametric mapping (SPM) was used to identify difference between groups (t-tests) and correlations with KOOS scores (linear regressions).

Results

KOOS scores increased after HTO but stayed below values of controls. The influence of HTO on sagittal plane kinematics and kinetics were limited to narrow phases of the gait cycle. The ankle dorsiflexion moment at push off – preoperatively lower than in controls – increased to normal values postoperatively, while the concomitant deficiency in the hip extension moment was not restored after surgery. HTO elicited changes in the load distribution at the knee level, with a lower postoperative compressive load on the medial compartment during midstance and a higher postoperative compressive load on the lateral compartment during early and late stance that were comparable to those of the control group (Figure 1). The lateral shear force in midstance was significantly

reduced after surgery. Changes in the external knee adduction moment (KAM) did not always coincide with reductions in the knee compressive force in the medial compartment, and these changes did not correlate with improvements in KOOS scores.
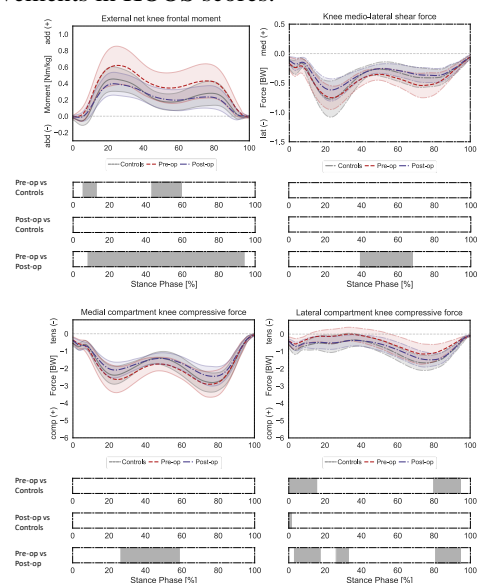
Figure 1: Mean ± 1SD KAM, medio-lateral shear force, and medial and lateral compartment compressive forces (dashed red lines—patients preoperatively; blue dashed-dotted lines—patients postoperatively; solid grey lines—controls). Grey bars below each subplot—periods with a statistically significant SPM t-tests.

Conclusions

HTO effectively unloads the medial compartment by redistributing part of the overall compressive force to the lateral compartment during gait without affecting gait functionality. The KAM may not adequately describe ambulatory load or changes induced by interventions at the compartment level. HTO elicited a rapid change in joint mechanics by a sudden change in limb alignment. Symptoms and pain might continue to improve beyond the postoperative follow-up time reported here possibly explaining the lack of correlations between changes in load and KOOS.

References

1. Stoltze JS et al. (2018), *Int Biomech*, **5(1)**, 63-74.

Acknowledgements

EXPERIMENTAL INVESTIGATION OF THE FRACTURE MECHANICS OF FEMURS OF ZUCKER DIABETIC FATTY (ZDF) RATS

Genna E. Monahan, Jessica Schiavi-Tritz, Ted J. Vaughan

Biomechanics Research Centre (BioMEC), National University of Ireland, Galway, Ireland.

Introduction

An increased risk of fracture is becoming a growing concern in patients with type-2 diabetes (T2Ds). Research has found that T2 diabetic patients can have up to a 3-fold increased risk of bone fracture, where individuals with long-term diabetes have a higher incidence of fracture than short-term [1]. Interestingly, a reduction in bone mineral density (BMD) is not the explanation for this increased fracture risk. T2 diabetic patients often present with normal-healthy BMD. However, it is possible the cortical and trabecular bone microarchitecture is altered, essentially reducing the quality of the bone. It is hypothesized that T2 diabetic subjects may have a reduced bone toughness, inhibiting the bones ability to resist fracture [3]. This study aims to assess the fracture mechanics of T2 diabetic femoral bone using innovative tests, whilst also examining the cortical and trabecular bone microarchitecture as the disease progresses.

Methods

Male [Zucker Diabetic Fatty (ZDF: fa/fa) (T2D) and Zucker Lean (ZL: fa/+) (Control)] rats were euthanized at 12-weeks of age (n = 4, per age, per condition), thereafter, right femora were dissected. Bone length and diameters were measured. Femurs were notched on the posterior side of the midshaft using a using a low-speed saw with a diamond-embedded blade. A micro-notch was placed at the top of the initial notch. Micro-computed tomography (CT) was used pre- and post-mechanical testing to scan the proximal femur (33.4% of total femur length), notched and unnotched femoral midshaft. Femurs were tested until failure in a three-point bend configuration, loading the anterior side (Zwick 2.5 kN load cell, 0.1 N pre-load, 0.06 mm/min crosshead speed) to measure the stress intensity factor (K_{ic}). Immediately after, proximal femurs were set into a quick-drying polyurethane resin (Xencast P2 Fast Cast Polyurethane Resin, Easy Composites) up to 40% of the total proximal height. A sideways fall test was simulated using a custom-built rig. Femoral heads were compressed until failure (Zwick 2.5 kN load cell, 5 N pre-load, 2 mm/min crosshead speed).

Results

	K_{ic} ($MPa\sqrt{m}$)	Sideways Fall		
		Stiffness (N/mm)	Energy-to-failure(mJ)	Max load (N)
D	15.7±2.36	45.2±9.85	28.8±3.14	49.5±6.99
C	14.2±0.83	55.5±16.7	27.0±8.71	53.0±13.2

Table 1: Mechanical properties from fracture toughness (K_{ic}) and sideways fall tests (D=diabetic, C=controls).

No significant differences were found for any of the mechanical properties between T2D and controls, although T2D bones had more ductile characteristics.
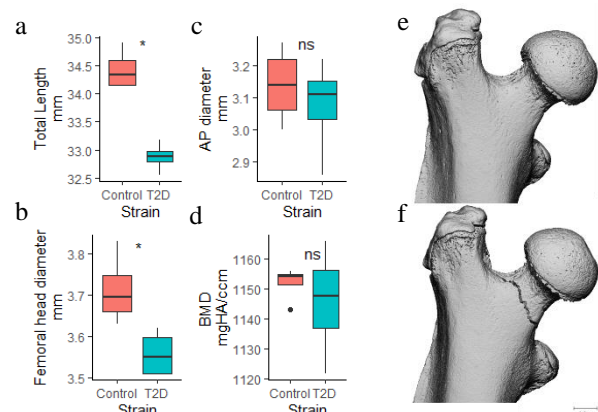
Figure 1: (a-c) Geometrical properties (AP=Anterior-posterior), (d) BMD of cortical bone from midshaft, CT scan (e) pre- and (f) post-fracture of proximal femur.

Although T2D rats had shorter bones and smaller femoral heads, the AP midshaft and femoral neck diameter was not statistically different to controls. BMD was also not statistically different.

Discussion

At 12-weeks of age, rats are experiencing early-stage T2Ds and the disease impact is currently not very clear. T2D rats had significantly smaller bone length and femoral head diameters. Yet, there was no difference between the AP diameter in the midshaft and femoral neck, which may explain no significant difference in stiffness and maximum load of the femoral neck between strains. Although not significant, results show that diabetic rats at 12-weeks exhibit a more ductile behavior, since the mean energy-to-failure of the femoral neck and stress intensity factor (K_{ic}) is higher for rats with T2Ds. Control rats often experienced a transcervical neck fracture, whereas, T2D rats presented with intertrochanteric fractures.

References

1. Janghorbhani et al, Diabetes Care, 29:1573-1578, 2006
2. Dragomir-Daescu et al, Annals of Biomedical Engineering, 39:742-755, 2011
3. Tang et al, Bone, 40:1144-1151, 2007

Acknowledgements

CHARACTERISING THE RELATIONSHIP BETWEEN KNEE BONE GEOMETRY AND PASSIVE KINEMATICS

Dermot O'Rourke (1), Francesca Bucci (1), William Burton (2), Rami Al-Dirini (1), Mark Taylor (1), Saulo Martelli (3)

1. Flinders University, Australia; 2. University of Denver, USA; 3. Queensland University of Technology, Australia

Introduction

Knee mechanics depends on the knee passive motion characteristics which are determined by the bone and ligament constraints [1]. Understanding the influence of bone geometry on passive motion can provide insight into knee function and the mechanisms of injury. However, the complexity of the geometric constraints has made quantifying this relationship challenging. Statistical shape and appearance models (SSAMs) have investigated variation in knee bone geometry and kinematics during dynamic loading activities [2]. However, establishing the principal geometric determinants of passive motion with SSAMs has remained difficult. Partial least square regression (PLSR) determines a set of modes of geometry variation that maximize the variance of the motion in a multiple regression model [3]. Therefore, the aim of the study was to determine the knee bone geometries that explain the variation in passive knee motion using PLSR.

Methods

MRI images were obtained of 29 cadaveric knee specimens (10F/19M, 43-82 years) with no reported history of pathology. Femur and tibia bone geometries were extracted from the MRI by semi-supervised 3D CNNs automatic segmentation [4] and reconstructed with a surface mesh. Template meshes were morphed over each bone shape with a non-rigid iterative closest point (ICP) registration to characterise the bone geometries with mesh correspondence. Passive kinematics were determined by performing five flexion-extension cycles on the knees with a minimal medial force (~6 N). Trajectories of reflective markers placed on 3-D printed potting cups fitted to the bones were recorded using a stereo-photogrammetric system (VICON, UK). A CT image of the specimen and potting cup assembly was obtained, and the bone geometries were segmented. Local femur and tibia coordinate systems were defined for each specimen [5]. The kinematics for the six axes of motion were estimated by calculating the relative pose of the local femur coordinate system with respect to the tibia throughout the flexion cycle. PLSR was applied on the bone geometry (predictor variables) and passive kinematics (response variables).

Results

The first 13 PLS modes accounted for 90% of kinematics variance and 89% of the geometry variance. The first PLS mode accounted for 5% of the geometry variation but 15% of the kinematics variation. It was primarily characterised by changes to the medial tibial condyle (Fig. 1) and explained a combination of variation in flexion-extension and anterior-posterior translation (Fig. 2). The fourth PLS mode accounted for the greatest portion of the geometric variation (50 %) and was a pure size change. However, it explained just 10% of the kinematics, primarily the variation in abduction-adduction.
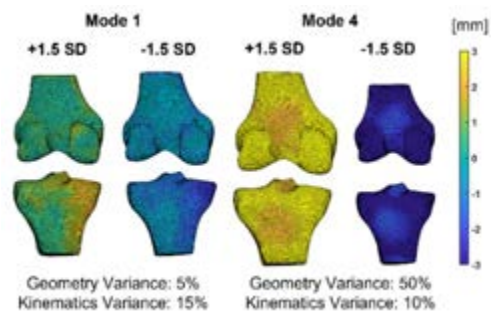
Fig. 1. Geometry for the first and fourth PLS modes of geometry variation at ± 1.5 standard deviations (SD).
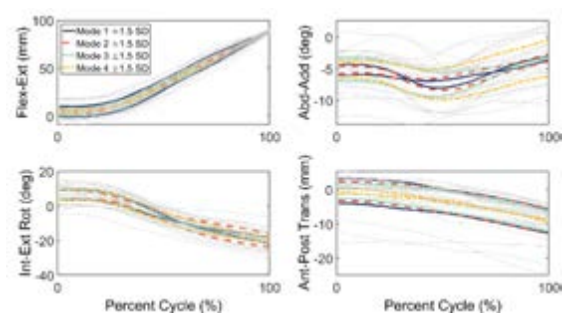
Fig 2. Kinematics for the first four PLS modes of variation at ± 1.5 SD.

Discussion

Changes to the tibial condyle geometry explained the greatest amount of the passive kinematic variation. Scaling accounted for greatest amount of variation in bone geometry, although it explained a small proportion of the variation in kinematics. This work significantly reduces the error in current linear models relating knee geometry and motion. Accounting for their complex non-linear relationship may improve the model further.

References

1. Blankevoort et al, J Biomech, 21(9): 705-720, 1988.
2. Smoger et al, J Orthop Res, 33: 1620-1630, 2015.
3. Wold et al, Chemometr Intell Lab Syst 58: 131-150, 2001.
4. Burton et al, Comput Methods Programs Biomed, 2020
5. Gray et al, J Orthop Res, 37: 615–630, 2019.

INFLUENCE OF LIMB ALIGNMENT AND KNEE JOINT LOADING ON CONDYLAR KINEMATICS USING DYNAMIC VIDEOFLUOROSCOPY

Barbara Postolka (1), Oliver Ulrich (1), William R. Taylor (1), Renate List (1,2), Pascal Schütz (1)

1. Laboratory for Movement Biomechanics, Institute for Biomechanics, ETH Zürich, Switzerland
2. Human Performance Lab, Schulthess Clinic, Switzerland

Introduction

Knowledge of factors modulating knee joint kinematics is important for personalising clinical interventions. Limb alignment has been shown to only play a minor role in governing tibio-femoral kinematics [1] but critically influencing tibio-femoral joint loading [2]. To understand the interaction of knee joint loading and the resulting motion, an evaluation of both, kinematics and joint moments in the same cohort is critical. Therefore, the aim of this study was to investigate the relationship between transverse knee joint kinematics and frontal plane knee joint loading during gait activities.

Methods

5 subjects with valgus (-5.6±1.5°, 37±20 years), 12 with neutral (0.5±1.6°, 24±4 years), and 10 with varus (5.7±1.8°, 26±7 years) limb alignment were assessed during 3-6 complete gait cycles of level walking, downhill walking, and stair descent using a dynamic videofluoroscope and synchronised ground reaction force plates [1, 3]. Following 2D/3D registration of the fluoroscopic images [4], medial and lateral condylar antero-posterior (A-P) translations, the location of the centre of rotation (CoR) [5], and the peak knee adduction moment (PKAM) were determined.

Results

Across all gait activities, the limb alignment groups showed comparable ranges of condylar A-P translation (medial: 5.6-7.7mm, lateral: 6.8-8.3mm) and a tendency towards a medial CoR. Significant differences between the groups were found for the PKAM, especially between the varus and valgus subjects (Table 1). Furthermore, while the PKAM showed a significant correlation with a medial CoR during downhill walking, no correlations were found for level walking and stair descent (Figure 1).

peak knee adduction moment [%BW · height]		
level walking	valgus -1.68±0.63	
	neutral -2.59±0.61	*
	varus -3.58±0.65	
downhill walking	valgus -1.90±1.15	
	neutral -2.58±0.71	*
	varus -3.63±0.42	
stair descent	valgus -1.81±0.80	
	neutral -2.32±0.69	*
	varus -3.70±0.76	*

*significant on an adjusted level of significance of α = 0.0056

Table 1: Peak knee adduction moment during level walking, downhill walking, and stair descent.
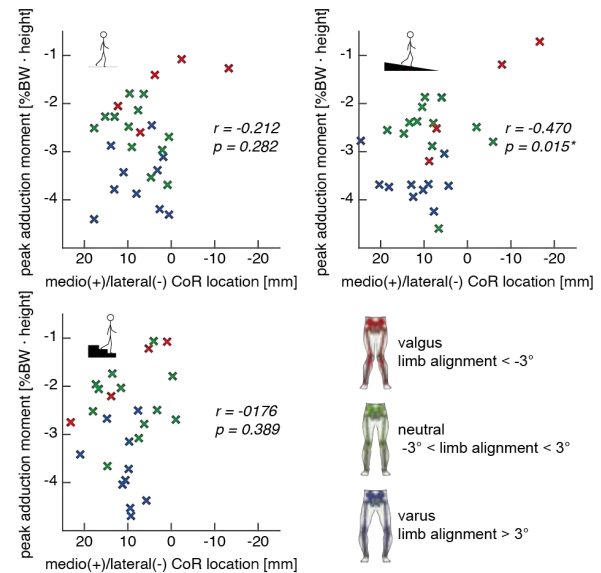
Figure 1: Relationship of the mean CoR and the mean peak knee adduction moment for each subject during level walking, downhill walking, and stair descent.

Discussion

While limb alignment is not reflected in the condylar kinematics, the PKAM was significantly reduced from varus to neutral to valgus subjects within the same cohort. With only a minor correlation during downhill walking, the frontal knee moment is not assumed to be a main modulator of condylar kinematics. The presented results are in line with recent findings in instrumented knee implants, where the load distribution did not necessarily correlate with the pivoting location [6]. Consequently, muscle activation strategies, ligament properties or bone morphology could be more important in governing individual knee motion then limb alignment or knee joint loading. Together with further musculoskeletal modelling, this data can help to inform decision-making regarding limb alignment when aiming to restore physiological knee joint function.

References

1. Postolka et al., submitted.
2. Schipplein & Andriacchi, J Orthop Res, 9:113 – 119, 1991.
3. List et al., PloS One, 12:e0185952, 2017.
4. Postolka et al., Med Eng Phys, 77:107-113, 2020.
5. Ehrig et al., J Biomech, 39:2798-2809, 2006.
6. Trepczynski et al. Sci Rep, 9:182, 2019.

Acknowledgements

VARIATION IN KNEE CONTACT MECHANICS DUE TO ANATOMY

Jiacheng Yao, Gavin Day, Nagitha Wijayathunga, Alison Jones, Ruth Wilcox, Marlène Mengoni
Institute of Medical and Biological Engineering, School of Mechanical Engineering, University of Leeds, UK

Introduction

The knee anatomy is an important factor in the knee biomechanics but the role of the anatomy alone is difficult to assess in patients as they present with variable confounding factors such as variability in BMI and joint health. Investigation of the knee contact mechanics by finite element (FE) modelling of a range of donors can aid in understanding the trends and variations in the knee biomechanics due to variation in anatomy. The aim of this study was to investigate the effect of anatomy alone on the contact biomechanics of the tibial compartments in knees from different donors.

Methods

A total number of six cadaveric knees were used to develop computational models following ethical approval (East Midlands—Leicester South REC, UK, 18/EM/0224.). The donors were 71.5±14.4 years old. Most knees had an extruded meniscus in at least on one compartment. Micro computed tomography images (82-micron isotropic resolution) were obtained for segmentation of bones and cartilage using Simpleware ScanIP O-2018.12-SP2 (Synopsys, CA, USA). Magnetic resonance imaging was used for segmentation of menisci (double echo sequence, 0.36 mm in plane, 0.7 mm in medial-lateral direction). Tetrahedral elements were used for development of the knee FE models[1] with Abaqus. An axial load of 500 N was applied through the femur centre of rotation at neutral alignment of the knee under intact and meniscectomy cases. The femur was free to move in adduction-abduction and superior-inferior displacement only, with the tibia fixed in all degrees of freedom in both cases. Material models and parameters were maintained constant for all six knees, following a validation study for contact mechanics on three knees where comparisons were made to the models' experimental counterparts. The mean contact pressure was calculated on each tibial compartment. The total contact area was recorded on the whole tibial cartilage. The distribution of contact pressure was investigated by fitting a 3x3 grid on each compartment, adapted from clinical evaluation guidelines[2].

Results

Mean contact pressures were 0.62±0.11 MPa and 0.58±0.10 MPa for medial and lateral tibial cartilages under intact cases, which increased to 0.72±0.12 MPa and 0.90±0.12 MPa respectively without the menisci. The total contact area decreased from 807±119 mm^2 to 619±90 mm^2 due to the loss of menisci. The knee-specific increase in contact pressure following meniscectomy varied from 1 to 53 % medially and from 53 to 63% laterally. In the intact cases, the contact pressure was concentrated in the posterior medial and posterior lateral areas (Figure 1). It shifted to central medial and central lateral areas in the meniscectomy cases.
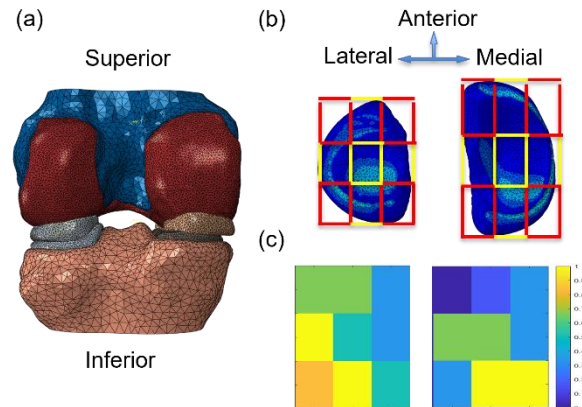
Figure 1: (a) example of one FE knee mesh, (b) tibial cartilage contact pressure for one knee with overlapping 3x3 grid, (c) summary of contact location for six knees (blue = no knees in contact within the corresponding grid cell, yellow = all knees in contact within the grid cell) - right knees were mirrored to show medial on the right of the image.

Discussion

This study showed a contact pattern on the tibial plateau under intact cases similar to a previous study under simulated gait[3], with a slight medial concentration. The contact pattern demonstrated that more of the load was transferred through the menisci than directly from cartilage to cartilage. Meniscectomy cases showed a systematic large increase in contact pressure on the lateral side of the tibial cartilage while the increase was much more variable on the medial side. This variability would affect how each knee reacts to a loss of meniscus integrity. The coefficient of variation for contact area due to variation in anatomy alone was 15% in both intact and meniscectomy cases.

Conclusion

This work demonstrated a high variability in contact biomechanics between different donors, when only the anatomy variation is considered. The variance across the group of donors was similar with or without meniscus present, but the variability in the medial compartment was larger than in the lateral compartment.

References

1. Cooper et al, J Mech Behav Biomed, 109:1-9, 2020.
2. ICRS Cartilage Injury Evaluation Package, 2000.
3. Wang et al, J Biomech, 47:568-574, 2014.

Acknowledgements

A REPRESENTATIVE VOLUME ELEMENT FOR BONE EXTRACELLULAR MATRIX

Elham Alizadeh (1), Daniele Casari (2), Johann Michler (3), Jakob Schwiedrzik (4) & Philippe Zysset (5)

1 & 5 ARTORG Centre for Biomedical Engineering Research, University of Bern, Switzerland
2,3 & 4 EMPA, Laboratory for Mechanics of Materials and Nanostructures, Thun, Switzerland

Introduction

Bone stiffness plays a key role musculoskeletal function, while bone strength and its ability to dissipate energy protects vital organs. Recent experimental studies in our laboratories consisted in quantifying micromechanical properties to investigate the stress transfer and damage accumulation at the extracellular matrix (ECM) scale. The aim of this work is to propose the simplest representative volume element (RVE) of the bone ECM indicating a consistent anisotropic elasticity with recent results.

Methods

Both cylindrical micropillar [1] and micro-tensile [2] bone samples were manufactured in osteons from ovine tibiae. Monotonic and cyclic tests were conducted both along and across the mineralised collagen fibrils. Representative volume element of a mineralised collagen fibril array (FAY) was designed including a cylindrical mineralised collagen fibril (MCF) embedded in an extrafibrillar matrix (EFM). The MCF is composed of hydroxyapatite mineral platelets (HA) embedded in a collagen matrix, while the EFM is made of mineral particles embedded in non-collagenous proteins (NCP).
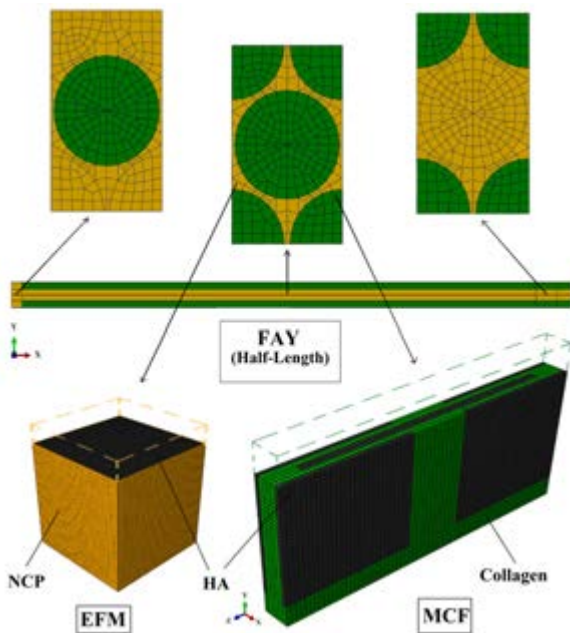
Figure 1: Unit-cell finite element models of bone ECM.

Two periodic, unit cell finite element (FE) models were created to compute the apparent elastic properties of MCF and EFM combined into a third unit cell model to estimate the anisotropic elastic constant of the FAY (Fig. 1) [3]. Tensile strength of the calibrated FAY was computed by inserting cohesive layers between MCF and EFM and in a transverse plane in the central part of the MCF.

Results

Micropillar compression revealed a ductile behaviour of the FAY with mean axial and transverse elastic moduli of 31.1 and 16.5 GPa, respectively [1]. Microtensile tests showed a highly brittle behaviour of the FAY with consistent mean axial and transverse elastic moduli of 28.9 and 13.6 GPa, respectively [2]. The mean axial and transverse tensile strength were 0.35 and 0.13 GPa respectively. The MCF and EFM models provided elastic properties with orthotropic and cubic material symmetry respectively and the combination delivered an orthotropic FAY with axial and averaged transverse elastic moduli within 1.5% of the above experimental means [3]. The cohesive FE model of FAY delivered tensile strength within 8% of the above experimental means.

Discussion

Elastic properties of bone FAY were obtained for both axial and transverse directions and were similar in tension and compression. A simple RVE is proposed extending the classical 1D shear lag model into a 3D building block of FAY, which elastic anisotropy is highly consistent with the experimental data.
The RVE will be exploited in future work to investigate damage mechanisms in compression.

References

1. Schwiedrzik et al., Nature Materials 13(7):740-747, 2014.
2. Casari et al., Acta Biomater 120:135-145, 2021.
3. Alizadeh et al., Biomech Model Mechanobiol 19:2127-2147, 2020

Acknowledgements

ALTERED MECHANICAL LOADING IN AMPUTEES RESULTS IN MILD SIGNS OF KNEE DEGENERATION 8 YEARS POST TRAUMA

Fearghal P. Behan (1), Alexander N. Bennett (2), Anthony M.J. Bull (1)

1. Imperial College London, UK; 2. Academic Department of Military Rehabilitation, Defence Medical Rehabilitation Centre, UK

Introduction

Studies in older amputees have shown an increased risk of medial knee osteoarthritis (OA) in the intact limb over 25 years from amputation [1, 2]. Increased medial knee joint contact forces on the intact limb have been shown in unilateral amputees [3], suggesting that this increased degeneration is biomechanical in nature. How quickly this altered loading can result in articular or functional changes in amputees is currently unknown. The Armed Services Trauma Rehabilitation Outcome (ADVANCE) Study investigates the long-term outcomes of battlefield casualties from the Afghanistan (over 500 injured participants and 500 controls) and is the first prospective cohort study in this area [4]. The current study aims to investigate the differences in radiographic and clinical outcomes of knee OA between injured (amputees and non-amputees) and uninjured UK service personnel in the ADVANCE cohort.

Methods

Knee radiographs and the knee injury and osteoarthritis outcome scores (KOOS) were obtained in 522 uninjured participants and 428 injured participants (374 non-amputees, 54 amputees). Participants had a mean age of 34 years, and the injured participants were on average, 8 years post injury. Using semi-automated methods [5], imaging measures of OA were obtained: Kellgren and Lawrence (KL), joint space narrowing (JSN), sclerosis and osteophyte scales. *T*-tests (injured vs uninjured) and one-way ANOVAs (uninjured vs injured non-amputees vs injured amputees) were used to compare between groups.

Results

There was a significant difference between injured and uninjured participants in all imaging measures (KL, JSN, sclerosis, and osteophytes, $p < 0.05$) and in all KOOS scales (pain, symptoms, activities of daily living, sport/ recreation, quality of life (QOL), $p < 0.05$). However, the mean imaging values in the injured group remained below levels that would even be described as doubtful OA [6] and above patient acceptable symptom state (PASS) levels for KOOS [7].

Amputees demonstrated higher levels of KL and osteophytes compared to uninjured participants only, higher levels of sclerosis compared to uninjured and injured non-amputees, but no differences between any group for JSN (Table 1). No differences were found between amputees, injured non-amputees and uninjured participants in three out of five KOOS variables (Table 1), with amputees reporting better symptoms and QOL than injured non-amputees.

	Uninjured	Injured non-amputees	Amputees
Imaging			
KL	0.16±0.44	0.27±0.51$^\$$	0.42±0.69$^\$$
JSN	0.26±0.40	0.31±0.43	0.34±0.50
Osteophytes	0.11±0.34	0.20±0.43$^\$$	0.33±0.62$^\$$
Sclerosis	0.05±0.19	0.07±0.22	0.17±0.42*
KOOS			
Pain	91.7±11.5	87.5±15.6$^\$$	90.5±11.7
Symptoms	60.9±12.0	58.1±11.9$^\$$	64.3±14.1$^\#$
ADL	93.9±9.8	89.2±14.7$^\$$	91.6±12.3
Sports	82.7±17.9	74.3±23.4$^\$$	80.9±22.2
QOL	81.1±19.1	74.2±22.5$^\$$	82.1±18.2$^\#$

*Table 1: Knee imaging results and KOOS scores for the three groups. $^\$$Different to uninjured only; $^\#$different to injured non-amputees only; *different to both groups*

Discussion

Injured participants had increased signs of radiographic and clinical signs of knee degeneration compared to controls, even only 8 years post injury in a young cohort. However, these differences do not appear clinically relevant at present. The amputees displayed no functional signs of knee degeneration compared to the other two groups. However, the amputees displayed some mild, early signs of the articular consequences of altered biomechanical loading within 8 years post trauma.

References

1. Norvell et al. Arch Phys Med Rehab, 86:487-93, 2005.
2. Lemaire, Fisher. Arch Phys Med Rehab, 75:1094-9, 1994.
3. Ding et al. J Orthop Res, 39:850-60, 2021.
4. Bennett et al. BMJ Open, 10:e037850, 2020.
5. Nehrer et al. Cartilage, 13:957S-965S, 2021.
6. Kellgren, Lawrence. Ann Rheum Dis. 16: 494-502, 1957.
7. Boffa et al. Orthop J Sports Med, 9:1-8, 2021.

Acknowledgements

TOWARDS AN *IN SILICO* BIOREGULATORY MODEL OF OSTEOGENESIS AND SPROUTING ANGIOGENESIS IN 3D

Laura Lafuente-Gracia (1,2), Mojtaba Barzegari (1), Liesbet Geris (1,2,3)

1. Biomechanics section, Department of Mechanical engineering, KU Leuven, Belgium; 2. Prometheus: Division of Skeletal Tissue Engineering, KU Leuven, Belgium; 3. Biomechanics research unit, GIGA in silico medicine, University of Liège, Belgium

Introduction

The process of bone regeneration involves the action and interaction of a myriad of cells, regulated by biochemical and mechanical factors. After fracture, the bone healing process is strongly linked to the development of a new blood vessel network in the callus. To date, there exist many *in silico* models investigating the healing progress of bone fractures. This work builds on our previous modeling work where bone regeneration (including angiogenesis) was studied in 2D. In this work, we developed an oxygen-driven multiscale *in silico* model to simulate osteogenesis and sprouting angiogenesis in 3D. This upgraded model allows us to understand biological events happening within the fracture region and to investigate potential treatments for skeletal disorders, such as congenital pseudarthrosis or other cases of non-union occurrence.

Methods

Overview. The model was developed in FreeFEM [1] following an existing multiscale bioregulatory 2D model of bone fracture healing [2] implemented in MATLAB. The model captures biological processes across different time and space scales. At tissue/cellular level, the spatiotemporal evolution of different biochemical factors, cells and extracellular matrices is described using a non-linear system of ten taxis-diffusion-reaction partial differential equations (PDE). At (intra)cellular level, the developing vasculature is represented with discrete endothelial cells, each of them regulated individually by one ordinary differential equation (ODE) representing its intracellular module.

Implementation details. Suitable initial and boundary conditions were set to ensure the existence, uniqueness and non-negativity of the solution of the PDE system.
The PDE system was implemented in its variational formulation in FreeFEM, following the Petrov-Galerkin method. The Newton-Raphson method was used to treat the non-linearities of the PDE system, which was solved using the finite element (FE) method for spatial terms and the finite difference method for temporal terms.

Domain. The geometrical domain (Fig.1A) was deduced from a 4 mm murine callus geometry [2] to simulate bone healing in a large skeletal defect. Initially, a 2D c-shaped domain (Fig.1B) was adapted to replicate the results of the previous MATLAB model [2], which was later altered (Fig.1C) to describe a more realistic fracture callus geometry. Finally, the model was upgraded to 3D (Fig.1E-F).

Results

Upgrading the *in silico* model to 3D highly increased the computational cost of the simulation, but also provided results which resembled the reality better. Both 2D and 3D FreeFEM-based models provided accurate predictions of the bone regeneration outcome and its corresponding biological processes. For instance, Fig.1B-C-E-F illustrate the migration of skeletal progenitor cells from the periosteum and bone ends into the fracture zone, with subsequent proliferation and differentiation into other types of cells. As showed by the figures, both models showed good agreement in their results. Additionally, Fig.1D presents the developing vasculature in the fracture area, which provides the necessary nutrients in the model.
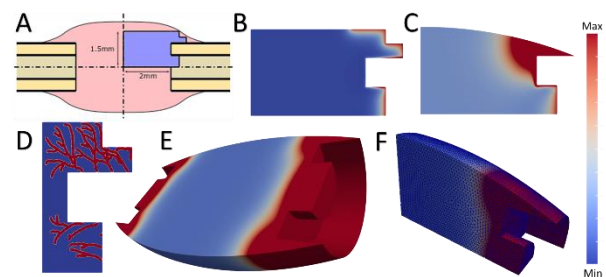
Figure 1: (A) Schematic representation of the geometrical domain. Due to symmetry, only one-fourth of the domain (blue region) was simulated. (B) Initial 2D c-shaped domain. (C) Altered 2D c-shaped domain: top border was smoothened to describe the fracture callus geometry more accurately. (D) Blood vessels network predicted by the model. (E) 3D representation of (A). (F) Detail of the FE mesh of the simulated 3D domain.

Discussion

We developed a 3D *in silico* model of bone regeneration including angiogenesis using the FreeFEM software. This 3D model has several potential biomedical applications, as it captures the reality more accurately, hence providing results which resemble the biological situation better.

References

1. Hecht, *J Numerical Mathematics* 20(3-4):251-266, 2012.
2. Carlier et al., *Biofabrication* 8(2):025009, 2016.

Acknowledgements

FATIGUE ANALYSIS USING ELECTROMYOGRAPHY DRIVEN MUSCULOSKELETAL TRUNK MODELS

Mohamed Irfan Mohamed Refai*, Huawei Wang, Alejandro Moya-Esteban and Massimo Sartori
* *m.i.mohamedrefai@utwente.nl*
Biomechanical Engineering, University of Twente, The Netherlands

Abstract

Muscle fatigue progression is commonly studied using Electromyography (EMG). Although muscle forces can be obtained using EMG-driven neuromusculoskeletal models (EDMM), these do not reflect changes in force generation due to fatigue. Here, we studied trunk muscle forces in 3 participants using EDMM during a fatigue task. We discuss results and model updates needed to obtain realistic muscle forces during fatiguing tasks.

Introduction

Factory workers are prone to musculoskeletal disorders as a result of increasing likelihood of injury and fatigue progression [1]. Tracking fatigue progression helps understand likelihood of risk in factory workers. Muscle fatigue is a progressive decline in maximal force or power capacity of the muscle [2]. Temporal and frequency analysis methods of EMG were used to study fatigue [3].

EDMM were used to estimate muscle forces during different motor tasks [4]. However, these models did not include fatigue dynamics and therefore, cannot reflect resulting changes in muscle force generating capacity. Realistic muscle force estimation is needed to design bio-protective active exosuits that assist factory workers by preventing excessive loads on the musculoskeletal system. In this study, we analyze a trunk EDMM within the context of a fatiguing task, and study whether the estimated muscle forces were influenced by fatigue.

Methods

Three participants (Mean (SD) Age: 27.7 (2) years, height: 1.8 (0.05) m, weight: 72 (3) kg) performed an endurance task at $30 \pm 5^{\circ}$ lumbar flexion until exhaustion while the pelvis was fixed. Motion data was captured using Qualisys (Qualisys Medical AB, Sweden). High Density EMG (HDEMG) was measured using the Refa system (TMSi, The Netherlands). Four 8x8 grids were placed on the right back, each consisting of evenly spaced 64 electrodes 8.5 mm from each other [5]. Kinematic, kinetic, and HDEMG data were synchronized by Qualisys Track Manager software.

Bipolar EMG data for the iliocostalis lumborum (6 cm lateral to L2), longissimus thoracis pars lumborum (3 cm lateral to L1) and pars thoracis (4 cm lateral to T10) muscles on the right were extracted from HDEMG data by differentiating adjacent channels along the muscle line of action. The EDMM was applied to the Lifting Full-Body model within OpenSim 4.3 to extract muscle lengths and force [6].

The Root Mean Square of the amplitude (RMS) was estimated using a moving window (size 60 s with an overlap 30 s) and compared between the EMG and muscle force.

Results

Change in the RMS from the initial value was identified at two instances (halfway (M) endurance task and at exhaustion (E)) as percent difference (%Δ). The changes per participant are shown in Table 1.

% Δ		Sub 1		Sub 2		Sub 3	
		M	E	M	E	M	E
IL	EMG	-1.5	3.6	0.6	1.5	37	46
	Force	0.9	5.2	27	33	68	34
LL	EMG	-7.9	-11.7	4.5	-2	16	34
	Force	-7.5	-11.5	5	-0.5	21	33
LT	EMG	-4.1	3.8	-2	17	11	27
	Force	-2.1	4.6	1.5	19	15	27

Table 1: Iliocostalis Lumborum (IL), Longissimus thoracis pars lumborum (LL) and pars thoracis (LT) measured halfway endurance task (M) and at exhaustion (E).

Discussion

We observed that changes in muscle force RMS follows that of EMG (R2>0.9). Although the participants were exhausted at the end of their trials, not all muscles seemed to have fatigued (shown by an increase in EMG RMS) as they performed sub-maximal contraction [7]. In most cases, EDMM based muscle forces increase for subjects due to increase in EMG amplitude and lack of fatigue modelling within the EDMM. Therefore, individualized fatigue models that modulate muscle forces based on the amplitude and duration of contraction during motor tasks must be included in EDMMs.

References

1. Ma et al, *Int. J Ind. Ergon*, 39:211-220, 2009
2. Enoka et al, *J Physiol*, 5861:11-23, 2008
3. Dimitrova et al, *J. Electromyogr. Kinesiol.*, 13:13–36, 2003
4. Sartori et al, *IEEE Trans. Biomed. Eng.*, 63:879–893, 2016
5. Moya-Esteban et al, *Proc. IEEE RAS EMBS Int. Conf. Biomed. Robot. Biomechatronics*, 2020
6. Beaucage-Gauvreau et al, Comput. Methods Biomech. Biomed. Engin., 22:451-64, 2019
7. Farina et al, *J. Electromyogr. Kinesiol.*, 13:319–32, 2003

Acknowledgements

TEMPORAL CHANGES IN THE BONE MICROENVIRONMENT PRIOR TO AND FOLLOWING OVERT BREAST-CANCER OSETOLYSIS

Anneke S.K. Verbruggen, Roisin M. Dwyer, Elan C. McCarthy, Laoise M. McNamara

National University of Ireland, Galway

Introduction

Breast cancer cells favour metastasis to bone tissue and it has been proposed that bone tissue properties facilitate tumour invasion resulting in bone resorption and osteolytic lesions, but may also result in osteoblastic formations. Bone volume and tissue stiffness have been shown to decrease after overt metastatic osteolysis [1,2]. Such changes may alter the mechanical environment of both the bone and tumour cells, and thereby play a role in perpetuating the cancer vicious cycle during breast cancer metastasis. Computational analyses of simulated metastatic bone report increased stress about osteolytic bone, but lesions have been introduced synthetically [3,4]. Thus, it is not yet known how specific *in vivo* bone tissue mechanical strain distribution is associated with tumour invasion over time. The objective of this study is to characterise temporal changes in the bone mechanical environment during breast cancer metastasis via finite element analysis (FEA) derived from high resolution micro-CT images of metastatic mouse bone.

Methods

Female immune-competent BALB/c mice (6 wo) were inoculated with 4T1 breast cancer cells in the mammary pad to induce primary tumours. Femurs were dissected from tumour-inoculated (MET, n = 5) and healthy cohorts (CTRL, n =5) euthanised at either 3 weeks or 6 weeks post-inoculation. High resolution micro-computed tomography (μCT) scans (μCT100, 5μm, 70keV, 57μA) were segmented (MIMICS) and imported to ABAQUS for mesh generation (4-node linear tetrahedral). Voxel-specific material properties (Young's modulus, E) were assigned according to μCT data (HU, ρ_{CT}) from DICOM (Fig1A, B) by the following equations (Eq. 1-3) [5,6].

$$\rho_{CT} = -0.01152 + 0.0006991 \text{ HU} \qquad (1)$$
$$\rho_{ash} = -0.079 + 0.8772 \ \rho_{CT} \qquad (2)$$
$$E = 1710 \ (\rho_{CT}^{\ 1.797}) \qquad (3)$$

Boundary conditions and a load (0.21N) were applied to femoral heads to mimic weight bearing [7] (Fig1C). Tumour-adjacent femoral head regions were analysed to determine Von Mises stress. Strain-energy density (SED) was analysed and thresholds were defined to categorize likelihood of: Resorption (<4.5 J/m^3), Apposition (bone formation, >5.25 J/m^3) and homeostasis (4.5–5.25 J/m^3), based on a prior study [7]. Bone volume % within these thresholds were compared. Statistical analysis used paired 2-sample T-tests.

Results

3 weeks: Although overt osteolysis was not detected, there was evidence of trabecular thinning. Von Mises stress distributions were altered in MET femoral necks compared to CTRL counterparts (Fig1E). The % bone volume within the different thresholds for resorption or formation did not differ between samples (Fig1.D).
6 weeks: Osteolysis was detected in all MET femora

(Fig1A). Von Mises stresses were elevated in MET trabeculae and femoral neck cortical tissue compared to CTRL (Fig1E). For the MET femoral head regions there was a lower % bone volume in the resorption range compared to CTRL (44.7% $\pm$ 4.8 % vs. 62.1 % $\pm$ 5.7 %, p<0.01) whereas a higher % bone volume was above the apposition threshold values in MET compared to CTRL (51.3% $\pm$ 5% vs. 33.9% $\pm$ 5.1% J/m^3, p<0.01).
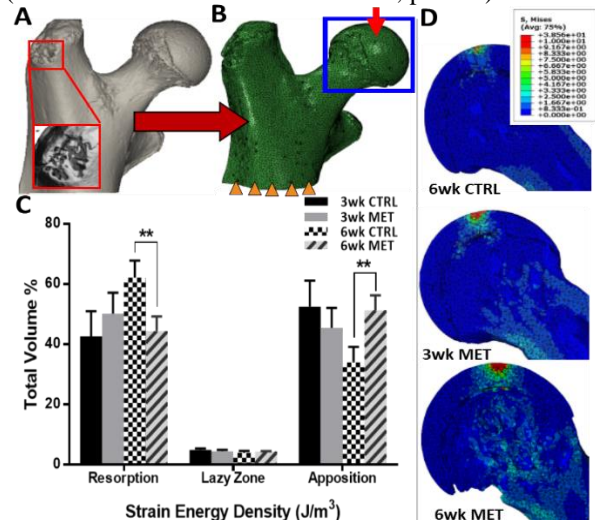
Figure 1: (A) 3D reconstructed μ-CT scan of metastatic femur with osteolysis by 6 weeks, (B) Finite element model derived from μ-CT images depicting the femoral head region (blue box). (C) Mean model % volumes within defined thresholds (D)Von Mises stress contour plots of femoral head regions 3- and 6-weeks post-inoculation (**p<0.01).

Discussion

This study analysed the evolving mechanical environment within bone tissue during breast cancer metastases, prior to and following overt osteolytic destruction. At 3 weeks post-inoculation there was a trend toward bone resorption in the metastatic group compared to healthy controls, which is consistent with the expected osteoclast activation and osteolytic nature during breast cancer metastasis. However, by 6 weeks, the % of bone volume which experienced strains within the bone formation range is significantly increased in the metastatic group, which might indicate a later osteoblastic response. These findings reveal temporal changes in the bone mechanical environment following metastasis, and may indicate a role for mechanobiology in facilitating metastatic invasion. Ongoing studies are assessing the sensitivity of predictions to the applied thresholds and implementing a bone remodelling algorithm to predict the evolution in bone tissue due to the evolving mechanical environment.

References

[1] Chiou et al, 7(12), Sci Adv, 2021 [2] Sekita et al, J Struct Biol, 197:260-70, 2017 [3] Rennick et al, J Biomech, 46:2701-9, 2013 [4] Spruijt et al, Acta Orthop, 77:474-81 [5] Morgan et al, J Biomech, 36:897-904, 2003 [6] Schileo et al, J Biomech, 40:2982-9, 2007 [7] Cheong et al, Biomech Model Mechobiol,19:985 1001, 2019.

SHOULDER POSITIONING DURING SUPERIOR CAPSULAR RECONSTRUCTION: A COMPUTATIONAL ANALYSIS

Madalena Antunes (1), Carlos Quental (1), João Folgado (1), Clara de Campos Azevedo (2,3) and Ana Catarina Ângelo (2,3)

1. IDMEC, Instituto Superior Técnico, Universidade de Lisboa, Portugal; 2. Hospital dos SAMS de Lisboa, Portugal; 3. Hospital CUF Tejo, Portugal

Introduction

Arthroscopic superior capsular reconstruction (ASCR), for the treatment of irreparable rotator cuff tears (RCTs), aims to restore the stability and physiological kinematics of the shoulder [1]. ASCR has been shown to produce excellent clinical outcomes; however, graft tear rates can range from 4.2% up to 75% [2]. A key factor that may affect the outcome of ASCR is the position of the shoulder during graft fixation. The role of this positioning has been recently evaluated for a full-thickness tear of the supraspinatus tendon (SSP) [3], but no data exist for more extensive RCTs. The aim of this study was to evaluate the influence of the positioning of the graft in ASCR on shoulder stability and graft tear risk considering different RCTs.

Methods

A 3-D musculoskeletal model of the upper limb was modified to account for the fixation of the graft in ASCR for 4 types of RCTs [4]. Full-thickness tears of the following rotator cuff tendons were assumed: (1) SSP, (2) SSP and Infraspinatus (ISP), (3) SSP and Subscapularis (SC), and (4) SSP, ISP and SC. The single-piece graft was modelled as a set of four parallel segments, as illustrated in Figure 1. The material properties of the graft were defined based on previous experimental data of fascia lata graft constructs [5].
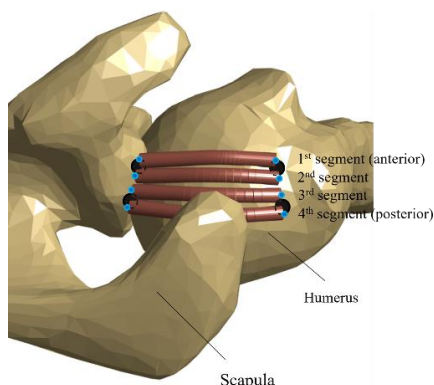
Figure 1: Graft path for each segment of the graft (superior view). The black circles denote the anchor's site, and blue circles denote the origin and insertion sites for each segment.

Two biomechanical parameters were used to evaluate the integrity of the graft and shoulder stability: the graft strain and the glenohumeral joint reaction force (GH JRF), respectively. Muscle and joint reaction forces were estimated through inverse dynamic analyses considering experimental data collected at the Laboratory of Biomechanics of Lisbon for 18 healthy subjects.

Results

For abduction angles above 15° during fixation, the graft had a high risk of tearing when the arm returned to the resting position (at the side of the trunk), as illustrated in Figure 2. For abduction angles below 15°, the mean shoulder stability after graft fixation improved significantly, ranging between 6% and 20% ($p < 0.001$), compared with the preoperative condition, in a RCT of type (1).
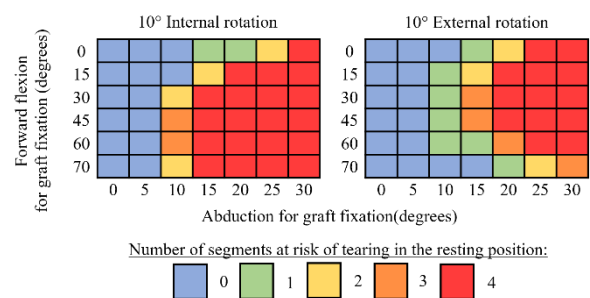
Figure 2: Number of segments of the graft at risk of failure when the arm rested at the side of the trunk.

Discussion

Preliminary findings of this study showed that the position of the shoulder, during graft fixation, affected both graft tear risk and shoulder stability, regardless of RCT type. ASCR also improved shoulder stability, compared to the preoperative condition, regardless of the shoulder position. This study provides important insight regarding the role of position of the shoulder during graft fixation for different types of RCTs.

References

1. Altintas, B. et al, Am. J. Sports Med 2020, 48, 3365–3375.
2. de Campos Azevedo, C.I. et al, Am. J. Sports Med. 2020, 48, 2115–2128.
3. Antunes, M. et al, Biology 2021, 10, 1263.
4. Mihata, T. et al, J. Arthrosc. Relat. Surg. 2013, 29, 459–470.
5. de Campos Azevedo, C.I. et al, JSES Int. 2021, 5, 439–446.

Acknowledgements

GLENOHUMERAL JOINT FORCE PREDICTION WITH MACHINE LEARNING

Pezhman Eghbali (1), Fabio Becce (2), Patrick Goetti (2), Philippe Büchler (3), Dominique Pioletti (1), AlexandreTerrier (1,2)
1) Ecole Polytechnique Fédérale de Lausanne, Switzerland, 2) Lausanne University Hospital (CHUV), Switzerland, 3) ARTORG Center for Biomedical Engineering Research, Switzerland

Introduction

Supervised machine learning (ML) can replace computationally expensive optimizations with a fast solution learned under supervision [1]. Therefore, these techniques can speed up musculoskeletal models (MSM) as these models perform a complex optimization process to predict forces. Studies that apply ML for MSM are not frequent in the literature. Smirnov et al. approximated the posture-dependent moment arm and muscle length relationships of the human arm and hand muscles with two ML algorithms (gradient boosting and multi-layer perceptron (MLP)) [2]. They reported similar errors for both models: 0.08-0.18 for muscle length and 0.13-0.53 for moment arms. After training, the ML models are fast and light (memory). Therefore, the purpose of this study was to predict the glenohumeral (GH) joint forces after total shoulder arthroplasty (TSA) with ML to speed up the force calculation with a much lighter model, which alleviates further patient-specific models.

Methods

With Monte Carlo simulations, we generated 1000 virtual patient-specific inputs (patient parameters) and outputs (joint force) using an upper-limb MSM [3]. We set a reasonable range for the patient parameters of the MSM (Table 1). The patient gender, height and weight were considered, as well as the glenoid version and inclination, and the cross-sectional area (CSA) of each of the four rotator cuff muscles: supraspinatus (SSp), infraspinatus (IS), subscapularis (SSc), teres minor (TM). The MSM replicated both the anatomical and reversed shoulder arthroplasty. Three activities were simulated by the MSM: abduction in the coronal plane with 2 kg in the hand, abduction in the scapular plane with 2 kg in the hand, slow abduction in the scapular plane.

We built two ML models based on gradient boosting (GB) and MLP algorithms for force magnitude prediction and a multi-output GB for force magnitude and direction prediction with Scikit-Learn library (scikit-learn.org) in Python. The ML input-output were the same as for the 1000 MSM. We optimized these models with grid search to maximize their predictions' coefficient of determination (R^2). The correlation (r) of GH force magnitude between MSM and ML was also assessed.

Results

R^2 was 0.93 for the GB, 0.92 for MLP in force magnitude prediction, and 0.91 for multi-output GB in force magnitude and direction prediction. There was a very strong correlation (r = 0.96) of the prediction of glenohumeral joint force between MSM and ML models with a root mean squared error of 35.20 for ML predictions (Fig. 1 (only for GB)).

Discussion

Using machine learning, we predicted the GH joint force calculated by an upper-limb MSM with reliable accuracy ($R^2 \geq 0.9$). A detailed comparison of our results with previous studies was not possible because we predicted GH joint force from a different MSM model than others. However, the correlation coefficient (r) between our predictions and MSM was in the same range as in [4], in which a recurrent deep neural network was developed for estimation of skeletal muscle force from kinematics data with r = 0.95-0.99 between data and predicted muscle forces. This ML prediction took less than a second on a standard computer compared to several minutes for MSM and required much less memory (code and running). This ML model could thus be used to quickly obtain boundary conditions of a series of patient-specific finite element models.

Parameter	Range
Height (cm)	(145, 190)
Weight (kg)	(45, 130)
Glenoid version (°)	(-20, 10)
Glenoid inclination (°)	(-10, 20)
CSA SSp (cm^2)	(16.5, 33.0)
CSA IS (cm^2)	(10.5, 21)
CSA SSc (cm^2)	(18.0, 36)
CSA TM (cm^2)	(3.4, 6.8)

Table 1: Patient-specific parameter ranges.
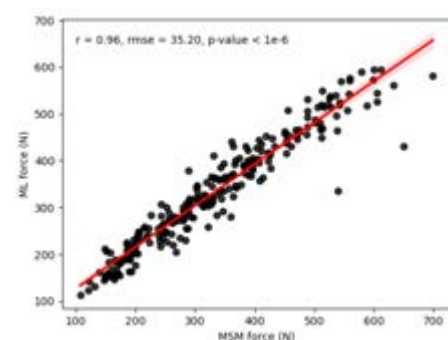

Figure 1: ML (GB) vs. MSM glenohumeral joint forces.

References

[1] L. Rane, Z. Ding, A.H. McGregor, A.M.J. Bull, Ann Biomed Eng. 47 (2019) 778–789.
[2] Y. Smirnov, D. Smirnov, A. Popov, S. PeerJ Comput Sci. 7 (2021) e663.
[3] E. Sarshari, Y. Boulanaache, A. Terrier, A. Farron, P. Mullhaupt, D. Pioletti, Sci Rep. 11 (2021) 20806.
[4] T.T. Dao, Med Biol Eng Comput. 57 (2019) 1049–1058.

THE POSITION OF THE SCAPULA INFLUENCES THE DISTANCE BETWEEN LIGAMENTOUS INSERTION OF THE AC AND CC LIGAMENTS

J. Christoph Katthagen (1), Julia Sußiek (1), Michael J. Raschke (1), Elmar Herbst (1), Felix Dyrna (2), Oliver Riesenbeck (1), Sebastian Oenning (1), Jens Wermers (1)

1. Department of Trauma-, Hand- and Reconstructive Surgery, University Hospital Muenster, Muenster, Germany; 2. Gelenkzentrum Rose, Leipzig, Germany

Introduction

The anatomy and length of the acromioclavicular (AC) and coracoclavicular (CC) ligaments have been regularly object of investigation. Until today, the characteristics and lengths were mostly analyzed in a stable position of the scapula but not yet in relation to the position of the scapular body.

This may be of important clinical relevance, as loss of reduction is a frequent complication in AC joint stabilization [1]. As overreduction could improve the stabilization quality [2], it was assumed that it may be beneficial, that the ligamentous insertions are as close as possible together during the surgical procedure.

It was hypothesized that overreduction can be achieved when the inferior angle of the scapula points in anterior direction, which corresponds to operating the patient on a shoulder table with dorsal support in contrast to a free floating shoulder in the beach chair position.

Methods

24 fresh frozen scapulae were analyzed. All soft tissue superficial to the CC ligaments was removed and the ligamentous insertions were exposed.

In the first step, the clavicle and scapula were statically fixed. In this position, the anatomical ligament attachments and four reference points on the scapula were recorded with a 3D-measuring arm. The reference points were used to define a rigid body system for the scapula. In the next step, the scapula was moved into maximum deflections. By measuring the reference marks, the positions of the ligament attachments and their distances could finally be calculated based on the rigid body system.

To analyze the distance between the ligamentous insertions under dynamic conditions the inferior angle of the scapula was manually pulled in maximum anterior, posterior, medial and lateral direction (Figure 1). Thereby a patient lying on a shoulder table with dorsal support was simulated when the inferior angle pointed in anterior direction. Each movement was repeated six times.

For the statistical evaluation the distance in anterior deflection was set to 100 % and the other distances were assessed accordingly. A repeated measures one-way ANOVA followed by a Tukey's test with correction for multiple comparison was used.

Results

The distance between the ligamentous insertions was significantly affected by the scapular deflection. Regarding the conoid ligament the mean distance was almost twice as long in posterior deflection compared to anterior deflection of the inferior angle (195.3 % vs. 100%, p = 0.028). In addition, when the inferior angle pointed medial the distance of the ligamentous insertions was significantly shorter (medial 118.5 % vs. lateral 151.5%, p = 0.001).

For the trapezoid ligament the distance was shorter with the inferior angle in anterior compared to posterior deflection but the difference was not significant (anterior 100 % vs. posterior 117.0 %, p = 0.174).

In line with the CC ligaments the distance between the insertion of the AC capsule was significantly shorter in anterior deflection, simulating a shoulder with dorsal support (posterior 116.1 % vs. anterior 100 %, p = 0.008).

Discussion

The distance between the ligamentous insertions of the acromioclavicular and coracoclavicular ligaments can be significantly influenced based on scapular positioning.

To reduce loss of reduction in AC and CC joint stabilization dorsal support of the scapula may be advantageous as the distance between the ligamentous insertions is reduced.

Figure 1: Deflection of the inferior angle into maximum anterior position (SB–scapular body, C–clavicle, R–3D-measuring device)

References

1. Clavert et al., Orthop Traumatol Surg Res, 101:S313-316, 2015
2. Maziak et al, Am J Sports Med, 47:2670-2677, 2019.

EFFECT OF SHAPE AND SIZE OF SUPRASPINATUS TEARS IN ROTATOR CUFF STRAIN DISTRIBUTION: AN IN-VITRO STUDY

Inês Santos (1), Lieselotte Pichler (1), Christoph Thorwächter (1), Maximilian Saller (1), Hannes Traxler (2), Peter E. Müller (1)

1. Department of Orthopaedics and Trauma Surgery, Musculoskeletal University Center Munich (MUM), University Hospital, LMU Munich, Germany; 2. Center for Anatomy and Cell Biology, Medical University of Vienna, Austria

Introduction

Despite the high incidence of rotator cuff (RC) tears, a clear guide for therapeutic decision-making based on their shape has not been established. Tear size has been indicated as the most critical factor in predicting the likelihood of tear progression, but previous studies have shown that other parameters, such as tissue strain, more directly reflect the complex RC loading environment [1,2]. Thus, understanding the relationship between tear size and shape, tendon loading, and strain adjacent to a tear would provide important insight into identifying tears that are more likely to propagate. The objective of this study was to evaluate the effect of two common types of supraspinatus (SSP) tears (crescent-shaped and reverse-L-shaped) in the RC strain distribution during active abduction in the scapular plane by generating a 50% and 100% wide tendon tear.

Methods

The distal tendinous insertions of the SSP, subscapularis (SCP), infraspinatus (ISP) and teres minor (TM) muscles of 12 healthy, fresh-frozen cadaveric shoulders were sutured using a baseball stitch to allow application of loads. The bursal side of both SSP and ISP was air-brushed with black and white paint to create a fine speckled pattern for subsequent digital image correlation analysis. An intramedullary rod was cemented into the humeral shaft and attached with masses to simulate the weight and center of mass of the arm (Figure 1). Optical tracking markers (GOM GmbH, Braunschweig, Germany) were fixed to the humerus and scapula, and anatomical landmarks were digitized in order to create bone fixed local coordinate systems following the International Society of Biomechanics recommendations [3]. Glenohumeral abduction to a maximum of 30° was simulated in the scapular plane by loading the SSP at 2 mm/s (EletroPuls E10000, Instron, MA, USA), while a constant load was applied to the remaining RC (SCP=15N, ISP/TM=15N). The loading protocol was first applied to the intact SSP tendon, then repeated after a 50% wide full-thickness tear was surgically created from the bursal side of the SSP, and again after the tear was further extended to 100% of the width of the tendon. The first group (n=6) was tested with a crescent-shaped (CS) tear and the second group (n=6) with a reverse L-shaped (rLS) tear. Statistical analysis was performed using the random intercept model in SPSS Statistics (IBM, USA).

Results

Both tear shapes led to an increase in internal rotation, SSP loading force (except for the "100% wide rLS" group) and superior translation of the humeral center of rotation (except for the "50% wide CS" group). An anterior translation was observed in the CS group after creation of a 100% wide tear, while for the rLS group this translation occurred mainly in the posterior direction. The ISP strain was higher than the SSP strain until approximately 25° of abduction in both groups of shape and size. An analysis of the anterior and posterior borders of each tear showed that the strain peaks location remained constant throughout abduction for the CS group (50% and 100% tear width).
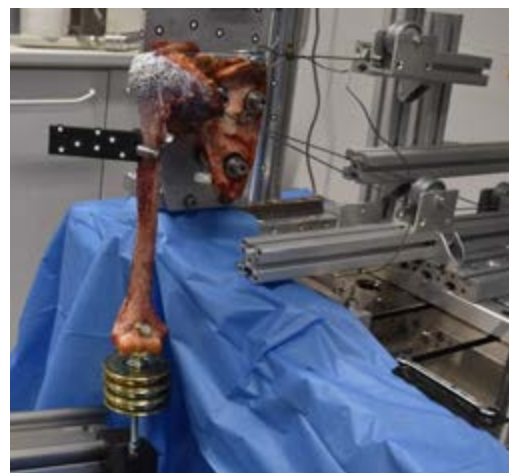
Figure 1: Experimental setup.

Discussion

The influence of tear shape in anterior-posterior translation was evident in both groups. The strain analysis showed a stress-shielding effect of the ISP in the early stages of abduction, which corroborates the importance of ISP reconstruction, as shown in previous studies [4]. The constant location of strain peaks observed in the CS group may lead to an earlier tear progression in contrast with the rLS tear.

References

1. Bey et al, J Shoulder Elbow Surg,11(6):562–9, 2002.
2. Andarawis-Puri et al, J Biomech, 42(2):158–163, 2009.
3. Wu et al, J Biomech, 38(5):981-992, 2005.
4. Andarawis-Puri et al, Am J Sports Med, 37(9):1831–1839 2009.

PERSONALISED APPROACH TO RESTORATION OF ARM FUNCTION IN PEOPLE WITH TETRAPLEGIA: IDENTIFYING MUSCLE WEAKNESS

M. Seyres (1), D. Blana (2), N. Postans (3), R.J. O'Connor (4), S. Pickard (3), E.K. Chadwick (1)

1. Aberdeen University, School of Engineering, UK; 2. Aberdeen University, School of Medicine, Medical Sciences and Nutrition, UK; 3. ORLAU, Robert Jones and Agnes Hunt Orthopaedic and District Hospital NHS Trust, Oswestry, UK; 4. Leeds University, Faculty of Medicine & Health, UK

Introduction

Spinal cord injury (SCI) results in a loss of signal from the brain to the muscles and leads to reduced upper limb function. Functional Electrical Stimulation (FES) can be used to activate the muscles and restore movement. Our aim is to use a personalised musculoskeletal model to determine suitable activation patterns. Here we present an efficient method to identify individual muscle weakness from functional measurements using parameter optimisation. We adjust muscle parameters to reflect the unique limitations of a patient's muscular system, which allows efficient design of FES system and control. The optimised parameters include reduced excitation of the muscle due to nerve damage and reduced muscle force due to atrophy.

Methods
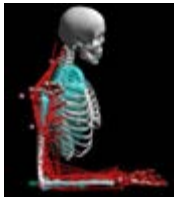
A minimal set of measurements of bony landmarks [1] is used to scale the model [2] in terms of geometry and strength. One individual with C5 SCI participated in the measurements. The study was approved by IRAS 241121.

Figure 1: Scaled individualised musculoskeletal model in testing position of elbow flexion

Subsequently, measures of maximum moments generated about the elbow are made under two conditions: (i) maximum voluntary contraction and (ii) electrical stimulation of specific muscle(s). Their difference is used to estimate individual muscle weakness. Optimisation is then used to distribute the muscle weakness across the muscles. The force output for each muscle, k, is scaled by the excitation reduction (SE) and by the atrophy (SM). Voluntary maximum isometric moment is given by:

$$\text{Mvol} = \sum_{k=0}^{n} \big((SE * \alpha) * (SM * \text{maxForce}_k) * r_k \big)$$

with α = max_activation = 1, and r moment arm.
We assume that SE and SM are the same (S), since a lack of excitation of the muscle will lead to atrophy over the longer term. Hence:

$$\text{Mvol} = \sum_{k=0}^{n} \big(S_k{}^2 * \text{maxForce}_k * r_k \big)$$

The joint moment recorded under electrical stimulation is given by the sum of the stimulated muscles assuming 50% activation [3]:

$$\text{Mstim} = \sum_{j=0}^{m} \big(0.5 * (S_j * \text{maxForce}_j) * r_j \big)$$

This allows us to compute the scaling factor for the stimulated muscles and therefore also their contribution under maximal voluntary contraction (VCT). The load across the other muscles during maximal voluntary contraction is given by the following optimisation:

$$\min f(S) = \sum \frac{1}{S^2} \qquad (0 \le S \le 1)$$

$$VCT + \sum_{k=0}^{n} \big(S_k{}^2 * \text{maxForce}_k * r_k \big) = Mvol$$

implemented using SciPy Optimize. In this nonlinear equality constraint, maximum voluntary contribution of tested muscles (VCT) was calculated from the stimulation measurement (Mstim). The second part of the equation is the moment generated by the other muscles for which we are optimizing the scaling factor.

Results

Muscle	Scaling factor (S)	Fmax (N)
Biceps	0.381	343.12
Brachialis	0.1888	242.73
Brachioradialis	0.199	42.45

Table 1: Optimization output S is the scaling factor for muscle force and excitation. S^2 is muscle weakness.

Discussion

Preliminary results of static optimization show well distributed loads with physiologically plausible scaling factors for both the reduced innervation and muscle atrophy. Our chosen cost function keeps the muscle weakness scale factors as high as possible, and as similar to each other as possible; further work will explore the validity of these estimated muscle weaknesses. These results allow personalisation of the musculoskeletal model for subsequent use in FES system and control design.

References

1 R. Readioff et al,. doi: 10.1016/j.gaitpost.2020.08.043
2 E. Chadwick et al,. IEEE Trans Biomed Eng. 2009 Apr;56(4):941-8 doi: 10.1109/TBME.2008.2005946
3 J.Hincapie et al, IEEE doi:10.1109/TNSRE.2008.922681

Acknowledgements

FUNCTIONAL SIMPLIFICATION OF MOTOR CONTROL OF ANTAGONIST MUSCLES AFTER STROKE.

Célia Delcamp (1), Camille Cormier (1), Alexandre Chalard (2), David Gasq (1), David Amarantini (1)

1. ToNIC, Toulouse NeuroImaging Center, Université de Toulouse, Inserm, UPS, France; 2. Department of Neurology, University of California, Los Angeles, California.

Introduction

In stroke patients, muscular coactivation is altered when compared to healthy subjects, leading to an exaggerated antagonist co-contraction that can contribute to the limitation of the active range of motion[1]. The mechanisms underlying such impairments are yet to be understood. To fill this gap, the analysis of the oscillatory link between the electromyographic activity (EMG) of antagonist muscles can provide information on the motor control mechanisms[2] involved in the alteration of motor function. Through this measure, called intermuscular coherence (IMC), the objective of this work is to better understand the changes in motor control of antagonistic muscles in stroke patients and their implication in the alteration of upper limb function.

Methods

25 chronic stroke subjects and 24 healthy subjects were included. Patients performed 20 active elbow extensions with their paretic limb while control performed them with their non-dominant limb. Kinematic data and EMG of biceps brachii (BB) and brachioradialis (BR) were simultaneously recorded. IMC of the BB-BR muscle pair was calculated in the beta frequency band (13-31 Hz) in a time window of interest of 200 ms before the velocity peak (Fig. 1). Concomitantly, antagonist co-contraction was calculated during elbow extension. Mann-Whitney test was performed between IMC of stroke patients and control subjects. Spearman correlation was done between the IMC of BB-BR muscle-pair and antagonist co-contraction.
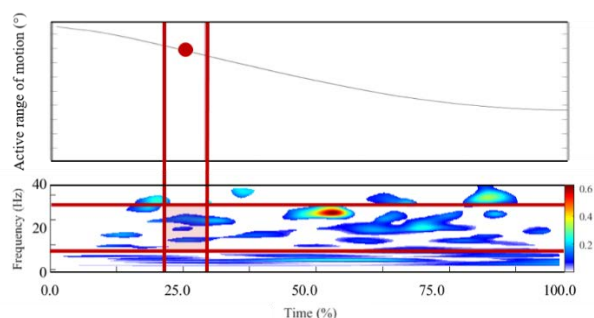
Figure 1: Typical time-frequency map of IMC for stroke patients during active elbow extension. The red surface represents the region where IMC was quantified.

Results

Intermuscular coherence was higher in stroke patients compared to healthy subjects (p=0.03, ES=-0.36[-0.60:-0.05]) (Fig. 2). IMC of the BB-BR muscle pair presented a significant negative link with antagonist co-contraction for stroke patients only (p=0.03, Rho=-0.44[-0.71:-0.6]).
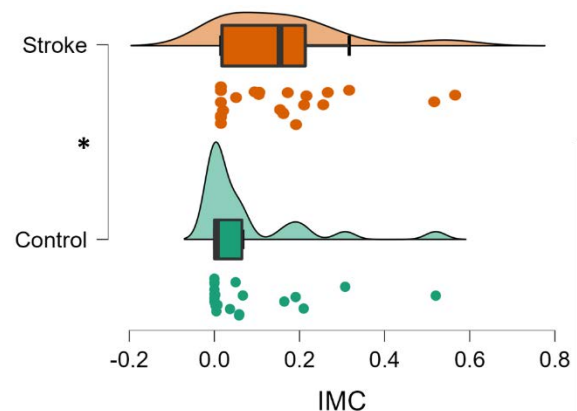
Figure 2: Raincloud plot of IMC of stroke patients and control subjects.

Discussion

In accordance with the common drive theory[3], higher IMC in stroke patients could reflect higher share of the common drive to the antagonist muscles. This finding can be viewed as a simplification of motor network interaction after stroke, the muscles with the same functional role being driven together[4]. The negative correlation between BB-BR IMC and antagonist co-contraction highlights for the first time the involvement of intermuscular connectivity in motor function of stroke patients. One can suggest that the observed changes in IMC would not reflect a maladaptive simplification but rather a functional simplification necessary to allow movement realization after stroke.

References

1. Chalard A, Amarantini D, Tisseyre J, Marque P, Tallet J, Gasq D. Spastic co-contraction, rather that spasticity, is associated with impaired active function in adults with acquired brain injury: A pilot study. *J Rehabil Med*. 2019;51(4):307-311.
2. Boonstra TW. The potential of corticomuscular and intermuscular coherence for research on human motor control. *Front Hum Neurosci*. 2013;7.
3. De Luca CJ, Erim Z. Common drive in motor units of a synergistic muscle pair. *J Neurophysiol*. 2002;87(4):2200-2204.
4. Houston M, Li R, Roh J, Zhang Y. Altered Muscle Networks in Post-Stroke Survivors. In: *2020 42nd Annual International Conference of the IEEE Engineering in Medicine & Biology Society (EMBC)*. IEEE; 2020:3771-3774.

ALTERATIONS IN UPPER EXTREMITY MUSCLE COORDINATION RESULTING FROM MUSCLE DYSTROPHY AND GRAVITY COMPENSATION

Johannes Essers (1), Kenneth Meijer (1), Anneliek Peters (2), and Alessio Murgia (2)

1. Maastricht University Medical Centre + (MUMC+), The Netherlands;
2. University Medical Center Groningen (UMCG), The Netherlands

Introduction

Facioscapulohumeral Dystrophy (FSHD) is a neuromuscular disorder characterized by muscles strength loss in the upper extremity and compensatory muscle activations [1]. Dynamic arm supports compensate for gravity thus reducing muscle efforts and enhancing task performance. It is postulated that the use of an arm support in persons with FSHD leads to larger individual-specific alterations of muscle coordination than in healthy controls. To clarify this effect, we investigate the effect of muscular weakness and support on muscle coordination in persons with FSHD, when performing functional tasks. We hypothesize firstly, that the FSHD population presents less consistent muscle coordination than healthy controls and secondly, that the support greatly improves consistency of muscle coordination within the FSHD population.

Methods

Electromyograms of eight upper extremity muscles were recorded for twelve FSHD (56.0±14.5yrs, 1.76±0.10m, 75±20kg) and twelve age-matched healthy control participants (55.5±13.4yrs, 1.76±0.08m, 72±14kg) while they performed ipsi-/contralateral reaching, eating/drinking, and a push/pull task with/without support. Muscle synergies were extracted by non-negative matrix factorization [2] and clustered based on the Pearson's correlation coefficients (r) between the participants' synergy weights, respectively for population, w/o support, and task. The r-values within (consistency) and between clusters (similarity) were investigated to quantify the effect of FSHD and support. Synergies' internal consistencies were tested with a non-parametric analysis of variance ($\alpha=0.05$ and post-hoc: $\alpha=0.01$) [3]. Synergies' between-group similarities were interpreted as low ($r<0.3$), medium (r: 0.3-0.5), high (r: 0.5-0.8), or very high ($r>0.8$).

Results

Post-hoc analysis revealed that muscle synergies in FSHDs were less consistent than in controls (first synergy's task averaged r: -0.63) (figure 1) and were not affected by support, while for controls the consistency increased significantly (first synergy's averaged r: +0.28) when using support. Furthermore, synergy similarity between FSHDs and controls was higher when FSHDs used the support and controls did not (first synergy's averaged r: +0.52) (figure 2). Similarity between the two groups also increased (first synergy's averaged r: +0.61) when both groups used the support.
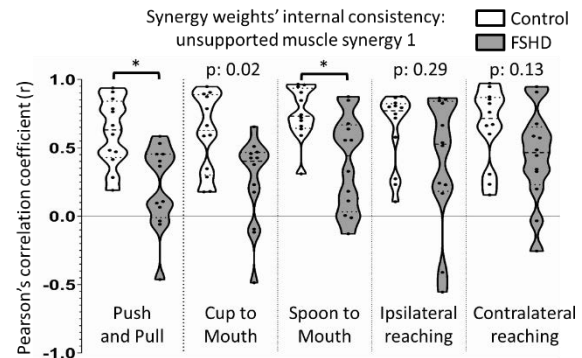
Figure 1: Synergy weights' consistency as Pearson's correlation coefficient (r) of the first muscle synergy for controls (white) and FSHD (gray) as violin plots. Asterisks indicate significant group difference (p<0.01).
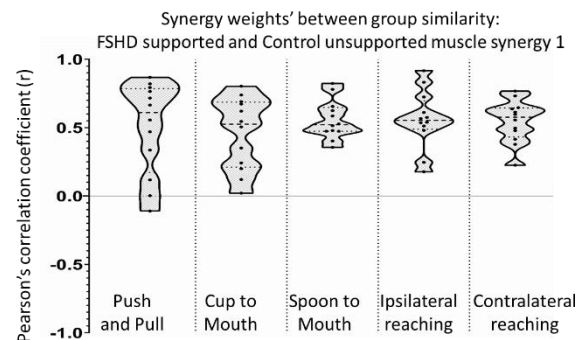
Figure 2: Synergy weights' similarities between controls and FSHDs as Pearson's correlation coefficient (r) of the first muscle synergy as violin plots.

Discussion

These findings support our first but not our second hypothesis and indicate that muscle coordination in FSHDs is heterogeneous, i.e. it is not affected by the arm support to similar levels as in controls. However, the support does increase the similarity between populations, which seems a generalizable effect in FSHDs leading towards a muscle coordination that resembles that of healthy controls. The alterations in muscle coordination in FHSD are likely the result of the individual-specific deficits of muscle weakness and compensatory strategies when using the support.

References

1. Bergsma et al., Archives of Physical Medicine and Rehabilitation, 95:1731-1741, 2014
2. Ting and Chvatal, Motor Control: Theories, Experiments, and Applications, Oxford University Press, chapter 5, 2010
3. Noguchi et al. Journal of Statistical Software, 50:1-23, 2012

SHARED SYNERGIES BETWEEN COMPLEX MOVEMENTS

Paul Kaufmann (1), Lorenz Zweier (1), Arnold Baca (1), Hans Kainz (1)

1. Centre for Sport Science and University Sports, University of Vienna, Vienna, Austria

Introduction

Muscle synergy can be used to model how the central nervous system solves the redundancy problem of the musculoskeletal system [1]. It is assumed that each synergy vector W controls several muscles with a single activation command (= activation coefficient C). Previous studies found shared synergies across different movements, e.g., normal walking and: slipping [2]; standing reactive balance [3]; nordic-walking [4]. So far, no studies, evaluated if more complex movements also share the same synergies. This study aims to close this research gap, and therefore analyzes three different skateboard tricks, which are very complex, from a motor control perspective: Ollie, Kickflip (KF) and 360°-flip (Treflip). The twofold aim of the study was to (i) identify inter-subject variability and (ii) analyze number and behavior of shared synergies between tricks.

Methods

Surface electromyography (sEMG) data (Cometa, Milan, Italy) of 16 lower limp muscles (8 per leg) were collected of 7 healthy experienced skateboarders. Six successful trials per trick (Ollie, KF, Treflip, fig.1) were further analyzed. Raw sEMG data were band-pass filtered, demeaned, rectified, low-pass filtered, time-normalized for an interval between the lowest and highest point of a sacrum cluster marker (Vicon, Oxford, UK), concatenated and amplitude normalized. Muscle synergies were extracted by non-negative matrix factorization (NNMF) [5]. The individual number of needed synergies (NoS) was defined as the lowest number which fulfills our criterions for calculated total Variance accounted for (tVAF>90%, adding an additional synergy tVAF must not increase >1%). NoSoA was defined as the lowest number which fulfils the tVAF criterion for all conditions. Synergies were ordered across participants according to their cosine similarity (CS) of W [2]. Across participants, W was considered as similar if averaged Pearson's correlation coefficient r>0.623 [3], and/or CS>0.8 [4] for all possible pairs of participants. Additionally, C of each participant were reconstructed [4, 5] by W of all other participants and with random inputs W_{rand}. Reconstructed $tVAF_{rec}$ and $tVAF_{rand}$ was compared with original tVAF with repeated-measures ANOVA (p<0.05). Shared synergies between tricks (r>0.623) were determined per participant, firstly for NoSoA and further for NoS. Thus, r was calculated for all possible synergy pairs of W for two compared tricks. C_{rec} was calculated, with W of the other tricks and with W_{rand}. Then tVAF, $tVAF_{rec}$ and $tVAF_{rand}$ were compared as mentioned previously.

Results

NoS ranged from 4 to 5, 3 to 5 and 2 to 5 for Ollie, KF and Treflip, respectively. As a result, NoSoA was 5. Only the second synergy vector W of Ollie was similar (r = 0.63±0.15) across participants, consequently the inter-subject variability was rather high. For inter-subject variability the tVAF was significantly higher than $tVAF_{rec}$ and $tVAF_{rand}$. Also, $tVAF_{rec}$ was significantly higher than $tVAF_{rand}$. Number of shared synergies of NoSoA ($n_{sharedOA}$) was on the one hand different between participants per trick comparisons, and on the other hand different between comparisons for each participant (fig. 1). A similar result was obtained with NoS. In both methods it was notable, that at least one motor module was shared across all comparisons (Ollie = KF = Treflip). Reconstructions between tricks led to significantly higher tVAF values than $tVAF_{rec}$ and $tVAF_{rand}$. Again, $tVAF_{rec}$ was significantly higher than $tVAF_{rand}$.
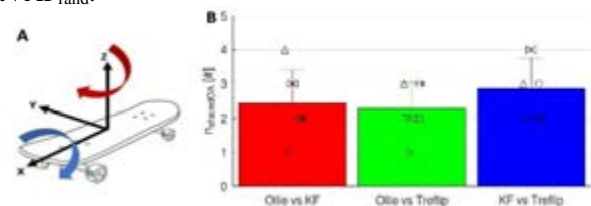
Figure 1 A: Tricks: Ollie= without any rotation; KF= with a 360° rotation around the x-axis; Treflip= with a 360° rotation around the x- and z-axis. B: $n_{sharedOA}$ for trick comparisons. Bars/errorbars = mean/standard deviation, markers indicate each participant.

Discussion

Unlike previous studies, which investigated inter-subject variability in complex movements [6], we found barely any similarity of W. As no previous studies had evaluated shared synergies among complex movements, our findings suggest, that at least one synergy is shared between different tricks, but the number of shared synergies does not follow certain rules between tricks and participants. Therefore, we conclude, that strategies to perform complex movements are very different across tricks and participants and require the development of trick-specific synergies. Moreover, the lower $tVAF_{rec}$, again points out the difference in motor modules between participants.

References

1. Ting et al, J Neurophysiol, 93: 609-13, 2005.
2. Nazifi et al, Front Hum Neurosci, 11: 26-40, 2017.
3. Allen et al, Gait & Posture, 82: 242–247, 2020.
4. Boccia et al, Scand J Med Sci Sports, 28: 905–918, 2018.
5. Lee at al, Adv. Neural Inform. Process. Syst., 13, 2001.
6. Frère et al, Front Comp. Neuroscience, 6 (99), 2012.

A NOVEL NEUROMECHANICAL MODEL FOR PREDICTING MUSCLE FORCE FROM MOTONEURON SPIKE TRAINS

Luca Modenese (1,2), Arnault Caillet (1), Andrew TM Phillips (1), Dario Farina (3)

1. Dept of Civil and Environmental Engineering, Imperial College London, UK; 2. Graduate School of Biomedical Engineering, University of New South Wales, Australia; 3. Dept of Bioengineering, Imperial College London, UK

Introduction

The current state-of-the-art neuromechanical muscle models take as neural input a processed surface electromyographic signal (sEMG) to estimate muscle force through a Hill-type musculotendon model with parameters calibrated to match the measured mechanical output [1]. This approach has the merit of implementing personalised neural control in musculoskeletal modelling, but some shortcomings are also evident. The neural model, for example, is limited by the nature of the sEMG measurement, which only offers a partial window on the underlying muscle activity and provides a single neural control to the muscle model. The latter, on the other hand, is designed as a single scaled muscle fibre, so confining its range of applicability to whole-muscle analyses.

In this work we propose a novel neuromechanical muscle model that, using as input decomposed high-density sEMG (HDEMG) signals, can represent the recruitment of individual motor units (MU) and accurately simulate their force generation dynamics. The model is applied to HDEMG recordings obtained at the tibialis anterior (TA) muscle during a trapezoidal contraction at 35% of maximum voluntary contraction [2] and validated against synchronous external joint torque measurements.

Methods

The proposed model includes a novel neural element and an improved excitation-to-activation dynamics. The neural element takes as input an experimental estimation of the synaptic current and consists of a pool of leaky-and-fire motoneuron (MN) models. The parameters of the MN pools are tuned using the MN firing behaviour identified from HDEMG decomposition and the relationships among MN electrophysiological properties and size recently proposed in [3]. Each of the MN spike trains simulated by the neural element drives a Hill-type muscle model that represents a muscle unit and produces its contractile force. In each MU, the action potential propagation is modelled in the neuron and in the muscle with an excitation dynamics updated from [4], followed by a model of calcium transient in the sarcoplasm, a model of cross-bridge cycling mechanism [5] and a standard contraction dynamics.

In the simulations, the TA moment arm and maximum isometric force were estimated at the same joint angles of the experiments [2] using a musculoskeletal model [6]. The maximum contractile force of each MU was assigned using a non-linear force distribution. The TA neural command was reconstructed from 21 experimental MN spike trains as the firing behaviour of 400 MN models (Figure 1-A), and the total muscle force estimated as the linear summation of the MU forces. The ankle joint torque was finally calculated using the same moment arm for all MUs. To evaluate the model predictions, the normalized root-mean-squared error (NRMSE) and coefficient of determination (r^2) were computed.

Results

The ankle joint torque computed by the neuromechanical muscle model was in remarkably good agreement (r^2=0.91, NRMSE=16%) with the experimental measurements (Figure 1-B).
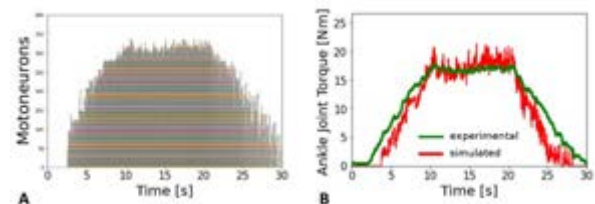
Figure 1: A) simulated neural spike trains for the TA reconstructed MN pool (400 motoneurons); B) comparison of experimental [2] and simulated joint angle torque produced by the TA force.

Discussion

This model demonstrated how, with an improved neural element and a coupled discretised muscle model, neuromechanical models can be used to simulate and investigate muscle contractions at the MU level, opening new research possibilities in the biomechanics and motor control fields. At this development stage, the musculotendon parameters are not personalised or calibrated, which could further improve the accuracy of the model.

References

1. Lloyd and Besier (2003). J Biomech,36:765-776
2. Hug et al. (2021). J Elec Kin, 58:102548
3. Caillet et al. (2021). BioRxiv, doi: https://doi.org/10.1101/2021.08.05.455188
4. Hatze (1978). Biol Cyber, 28:143-157
5. Zot and Hasbun (2016). Front Physiol 7:406
6. Rajagopal et al. (2016). IEEE Trans Biom Eng, 63:2068-79

Acknowledgments

A THEORETICAL MODEL OF AQUEOUS HUMOUR PRODUCTION

Mariia Dvoriashyna(1), Alexander J. E. Foss(2), Eamonn Gaffney(3), Rodolfo Repetto(4)

1. Department of Applied Mathematics and Theoretical Physics, University of Cambridge, UK;
2. Department of Ophthalmology, Nottingham University Hospitals NHS Trust, UK;
3. Wolfson Centre for Mathematical Biology, Mathematical Institute, University of Oxford, UK;
4. Department of Civil, Chemical and Environmental Engineering, University of Genoa, Italy

Introduction

Aqueous humour (AH) is a transparent water-like fluid that fills the anterior segment of the eye. It is produced by a tissue called ciliary body, located behind the iris, where it is secreted by the ciliary epithelium (CE). It then flows through the posterior chamber of the eye (i.e. the region between the iris and the lens) and exits via the pupil into the anterior chamber (i.e. the region between the cornea and the iris), where it is drained into the trabecular meshwork. This flow is very important physiologically, as the balance between the rate of AH production and resistance to its drainage governs the intraocular pressure (IOP). Elevated IOP is correlated with the occurrence of glaucoma. Lowering AH production rate may assist in prevention or treatment of glaucoma. Therefore, understanding of underlying physical mechanisms that govern the production of AH is of great clinical relevance.

Mathematical model

In this work we propose a mathematical model of fluid and solute transport across the CE, with the aim to study mechanisms of AH production, determine how the AH production rate depends on the controlling parameters and how it can be manipulated.

We employ a compartmental transport model that consists of stroma, CE and the posterior chamber (see Figure 1), filled with the fluid and 7 solute species (Na^+, K^+, Cl^-, HCO_3^-, H^+, CO_2 and H_2CO_3). We impose conservation of mass in the CE and the posterior chamber for water and for each considered solutes. We account for the presence of ion channels, co-transporters and exchangers, located on the cell membranes (see Figure 1) and for the following reactions
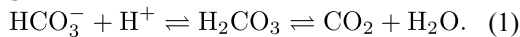
$$HCO_3^- + H^+ \rightleftharpoons H_2CO_3 \rightleftharpoons CO_2 + H_2O. \quad (1)$$

The second reaction is normally slow, but can be catalysed up to six orders of magnitude in speed by carbonic anhydrase (CA).

We impose the concentration of all species on the stromal side and compute water flux produced by osmosis, the solute concentrations in the aqueous humour and the transepithelial potential difference.

Results

With a feasible set of parameters the model predictions of water flux from the stroma to the posterior chamber and of the solute concentrations in the aqueous humour are in good agreement with measurements [1].

Using global sensitivity analysis we identify the key parameters that impact the aqueous production rate. A relevant role is predicted to be played by cell membrane permeability to K^+ and Cl^-, by the NHE channel and by CA. CA inhibitors are effective drugs used to reduce AH production rate. We studied with the model the effect of inhibiting CA and found that this leads to a significant decrease in AH production, in agreement with clinical and experimental observations [2].

Conclusions

The model provides insight into the physical processes underlying the functioning of drugs that are adopted to regulate AH production. It also suggests ion channels and cell membrane properties that may be targeted to manipulate aqueous production.
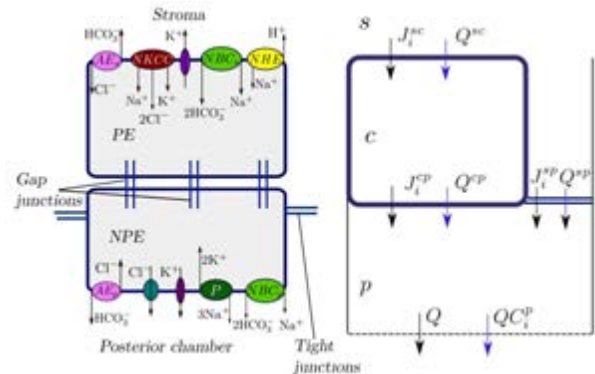
Figure 1: Left. Ion channels in the CE. PE basolateral membrane: NKCC: co-transporter of $Na^+/K^+/2Cl^-$; AE_s: Cl^--HCO_3^- exchanger; NHE: Na^+-H^+ exchanger; N BC s : Na^+- HCO_3^- cotransporter; K^+ channels. NPE basolateral membrane: P: Na^+-K^+ ATPase; AE_p: HCO_3^--Cl^- exchanger; NBC_p: Na-HCO_3^- cotransporter; K^+ and Cl^- channels. Right. Sketch of the compartmental model with water and ion fluxes. The symbols s, c and p denote stroma, intracellular space and posterior chamber, respectively. J_i^{mk} denotes flux of solute i and Q^{mk} the water flux, from region m to region k.

References

1 Brubaker, Inves. Ophthalmol. Vis. Sci., **32**(13):3145-3166, 1991.
2 To et al., Am. J. Physiol. - Cell Physiol., **280**(6):C1521-C1530, 2001.

DOES CORNEAL STIFFNESS PLAY A ROLE IN POST-SURGICAL CORNEAL ECTASIA?

Benedetta Fantaci (1), Begoña Calvo (1,3), Jorge Grasa (1,3), Miguel Ángel Ariza-Gracia (2)

1 Aragón Institute of Engineering Research (i3A), University of Zaragoza, Spain; 2 ARTORG, University of Bern, Switzerland; 3 Bioengineering, Biomaterials and Nanomedicine Networking Biomedical Research Centre (CIBER-BBN), Zaragoza, Spain.

Introduction

Lasers have been widely adopted in Ophthalmology for correcting vision by reshaping the shape of the cornea. Among post-surgical setbacks, corneal ectasia is a vision-impairing complication in which the cornea bulges out as it cannot withstand physiological loads such as intraocular pressure (IOP) [1]. Currently, factors that can drive ectasia's development imply, indirectly, that corneal mechanics does play a role.

This preliminary study aims to start discerning whether corneal stiffness might be involved in this phenomenon. The ratio between the anterior and posterior corneal stiffness is controlled in a parametric study to those factors that may drive the ectatic opto-mechanical response.

Materials and Methods

A 2D axisymmetric finite element (FE) model of the cornea is built using average parameters (R=7.77 mm, CCT=490 μm). A non-linear isotropic Neo-Hookean constitutive model was used to mimic the behavior of corneal tissue and a pre-stretch iterative algorithm was used to introduced stromal stresses related to intraocular pressure (15 mmHg).

To study the impact of corneal stiffness on the possibility of developing an ectasia, a heterogeneous distribution of corneal material properties has been defined along the thickness of the cornea by linearly scaling the material constants (ratios: 1/2, 1/5, 1/10).

A PRK laser surgery was simulated by removing corneal tissue in the anterior surface. The ablation depth was calculated using Munnerlyn's formula [2], aiming at correcting the maximum diopters allowed with this technique. All mechanical simulations were calculated using ABAQUS. Corneal optics was calculated using an in-house raytracing algorithm.

Geometrical parameters such as corneal central thickness (CCT), residual stromal bed (RSB), change in average corneal central curvature ΔK_{mean}, the spherical equivalent (SE), the axial length (AL), stress and strains were analyzed to find indications of corneal ectasia.

Results

The extreme case (ratio: 1/10) showed indications of corneal ectasia as its change in curvature (ΔK_{mean}) and axial length (ΔAL) were positive (see, *Figure 1*), while they should usually decrease after performing laser surgery. Mechanically, there is a threshold in the increment of corneal stretch around 2.5% that clusters those positive changes and lower residual stromal beds. Those cases were not able to correct target pre-surgical vision correction but even regressed to a higher post-surgical refractive error (+1D).

Discussion

This preliminary analysis suggests that stiffness heterogeneity ratios (from 1/5 onwards) and thin RBS cannot withstand loading without presenting high deformation levels that could be associated to a development of corneal ectasia. Currently, we are extending our simulations to both patient-specific geometries and anisotropic material properties. This methodology could become a useful tool for the clinicians to guarantee a successful surgery outcome in time.

References

[1]. Randleman et al., *Ophthalmology*, *115*(1), 2008.
[2]. Munnerlyn et al., *Journal of Cataract and Refractive Surgery*, *14*(1), 46–52, 1998.

Acknowledgements

Figure 1. *ΔRadial Stretch vs ΔKmean (left), RSB vs ΔKmean (center) and ΔAL vs ΔKmean (right)*

27th Congress of the European Society of Biomechanics, June 26-29, 2022, Porto, Portugal
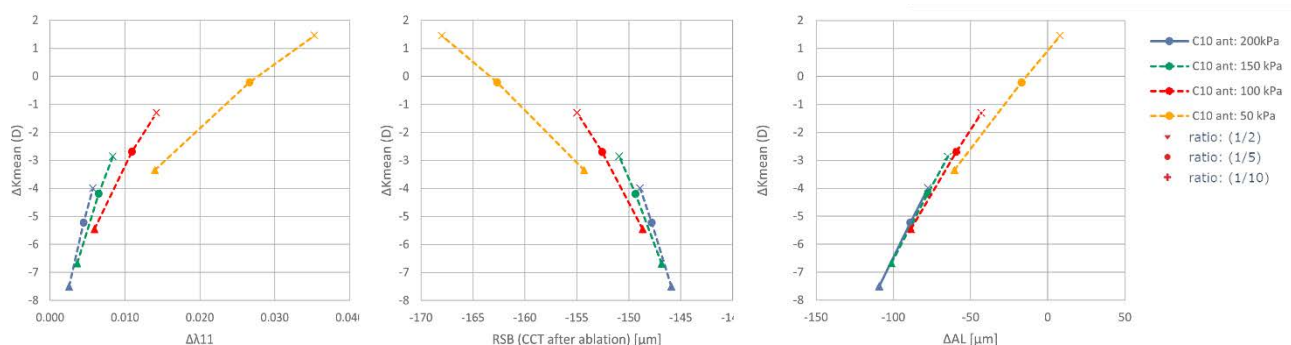
MECHANICAL MODELING OF LOCALIZED CROSS-LINKING PATTERN IN HUMAN AND PORCINE CORNEAS

Matteo Frigelli (1), Philippe Büchler (1), Sabine Kling (1,2)

1. ARTORG Center for Biomedical Engineering Research, University of Bern, Switzerland; 2. Computer Vision Laboratory, ITET department, ETH Zürich, Switzerland

Introduction

Corneal cross-linking (CXL) can be exploited both, to interrupt the progression of keratoconus, and to correct mild to moderate refractive errors in healthy persons. From a biomechanical perspective, localized thickness and curvature changes affecting the cornea can be explained by inhomogeneous distribution of the biomechanical property [1]. Thus, it has been suggested that strengthening the entire tissue could be unnecessary, since even more tailored results could be achieved applying CXL only on the weak parts of the cornea. Moreover, locally increasing corneal stiffness has the potential to induce predictable refractive changes. The aim of the present work is to develop a finite element model (FEM) to simulate the patterned localized CXL procedure.

Methods

An inverse FEM optimization algorithm was developed to quantify the changes in mechanical properties induced by CXL, by combining Python scripting and finite element simulations (Abaqus/Standard (SIMULIA, Dassault Systémes, USA). Experimental data from previous literature showing uniaxial tensile tests, performed on both untreated and cross-linked porcine and human strips, were used as reference [2]. HGO material properties [3] were assigned to the models with a circular fibers distribution for porcine and an orthogonal distribution for human models. The combined optimization was performed under the following hypotheses: i) CXL affects proportionally the fiber components (k_1 and k_2) of the HGO model and ii) the relative mechanical stiffening induced by CXL is identical in porcine and human tissues. Different patterns of CXL were simulated and subjected to a physiological pressure change of 2mmHg on a pre-stressed (p0=14 mmHg) 3D model of the cornea. Axial strain (i.e. strain along optical axis direction) and anterior corneal curvature were calculated with an in-house script.
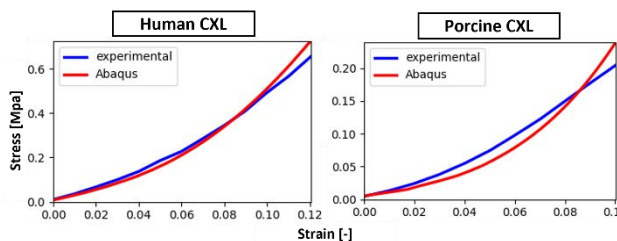
Figure 1: Experimental and model stress-strain relationship derived from the optimization algorithm

Results

The CXL procedure yielded to a stiffening factor of 15 for k_1 and 17 for k_2 parameters of the HGO model (Figure 1). Differences in axial strain and anterior corneal refractive power after inflation w.r.t. untreated condition are presented for porcine cornea (Figure 2). The regions treated by CXL (colored red) showed a lower axial strain amplitude (i.e. a more positive strain by 3×10^{-3}[-]) and lower corneal refractive power (reduction of 1-3 diopters) than the untreated condition.
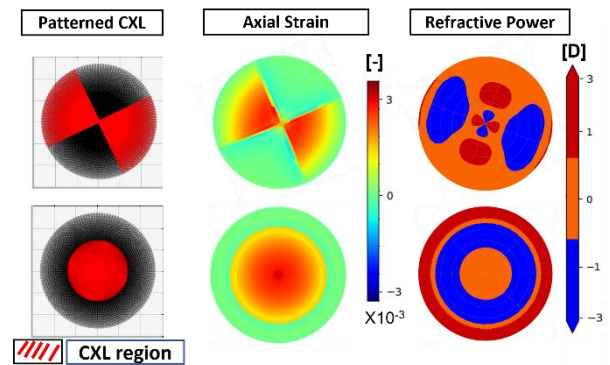
Figure 2: variations in axial strain and curvature after inflation computed with respect to the untreated condition.

Discussion

We report the modeling of changes in mechanical properties induced by CXL. After inflation with a physiological pressure, a decrease in refractive power and amplitude of the mechanical strain was observed in the regions treated with CXL (Figure 2). These numerical results, despite important assumptions, match well with experimental data from OCT elastography [4] (shift toward positive axial strain in CXL region) and with clinical outcomes (CXL induced decrease in refractive power). Such a model can be exploited to predict the optimal locations and extent of corneal stiffening to achieve patient-specific refractive changes.

References

1. Roberts C. et al, J Cataract Refract Surg, 40:991–998, 2014.
2. Wollensak et al, J Cataract Refract Surg, 29:1780-85, 2003.
3. Holzapfel et al, J. Elast., 61:1-48, 2000.
4. Kling S., J. R. Soc. Interface, 17:20190786, 2020.

Acknowledgements

TISSUE BIOMECHANICS AND PARAMETER IDENTIFICATION OF *EX VIVO* PORCINE CORNEAL TISSUE

Malavika Nambiar (1), Layko Liechti (1), Fabian Müller (2), Werner Bernau (2),
Theo G. Seiler (3,4,5), Philippe Büchler (1)

1. University of Bern, Switzerland; 2. Ziemer Ophthalmic Systems, Switzerland; 3. IROC, Switzerland; 4. University Hospital Bern, Switzerland; 5. Universitätsklinikum Düsseldorf, Germany

Introduction

The porcine cornea is the most commonly used animal model in ophthalmic research, making its biomechanical modelling important for many applications. A major drawback of currently available biomechanical models is the limitations of experimental techniques and its accurate replication by numerical models. While several studies have been performed on the entire cornea[1], there is only one publication on the depth dependence of porcine corneal biomechanics[2]. However, this study suffers from limitations. For example, this study combines the mechanical response of the stroma and Descemet's membrane into a single measurement. In addition, the conclusions of this study are inconsistent with tests performed on the entire cornea. With an improved uniaxial testing protocol and clear thickness profile, our study aims to accurately describe porcine biomechanics and to provide a numerical model that could reduce dependency on animal experimental methods.

Methods

Experimental: Freshly enucleated porcine corneas were obtained in less than 24 hours after slaughter. A femtosecond laser was used to cut the corneas into 150μm thick strips in the nasal-temporal, superior-inferior, and diagonal directions. Samples were taken at depths of 100 μm, 350 μm, and 600 μm and tested in uniaxial extension (CellScale, UStretch & Biorakes). The tissue was pre-stretched with a force of 20 mN and pre-conditioned with 6 cycles of 13 % strain. The last cycle of force displacement data was recorded for analysis.

Numerical: The geometry of the corneal strip and the experimental loading were replicated using the finite element software ABAQUS. The strips were modelled with collagen fibers running in a circular orientation. The material behaviour was described using the anisotropic models proposed 1) by Gasser, Holzapfel, and Ogden (HGO)[3] and 2) by Markert et al[5]. A Bayesian optimization process was used to identify the material parameters that best fit the experimental data.

Results

The mechanical properties of the cornea appear to remain constant and independent of the orientation, up to the center of the cornea (depth D1 & D2). However, experimental results indicate a difference in material properties in the 600 μm depth group (D3): this layer is softer than the other two, and at this depth the superior-inferior direction was found to be stiffer than the other two orientations (Fig.1). The HGO and Markert material models, both fitted on four parameters, agreed well with the experimental results (Fig. 2).
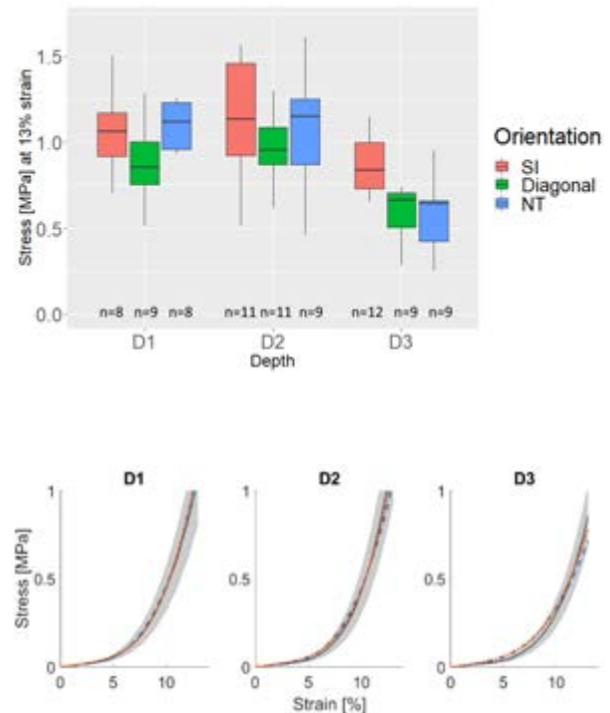
Figure 2: Result of the optimization in SI-direction for the HGO (blue) and Markert (red) models compared to the experimental data (black).

Discussion

The experimental technique used in this study produces strips of uniform thickness and dimension, making this data very valuable and reproducible. While our measurements confirmed a strong dependence of material properties on depth, the mechanical response of porcine cornea was only slightly affected by sample orientation, consistent with a circular arrangement of the collagen network in porcine. Therefore, our numerical models assume a circular collagen alignment in which a portion of the fibers are randomly aligned based on X-ray diffraction data[5]. The quality fit we obtained based on this assumption is high (R2 = 0.98), supporting our hypothesis. To the best of our knowledge, this is the first numerical study modeling the porcine cornea with a circumferential collagen fiber orientation.

References

1. Elsheikh et al. J Exp Eye Res, 2009 2.Du et al, J Soft Mater. 2017 3. Holzapfel et al, 2000: 4. Markert et al. Proc. App. Math. and Mech. 2005 5. Hayes et al. J. Anat Rec. 2007

A MECHANICAL MODEL OF EXUDATIVE MACULAR OEDEMA

Alessia Ruffini (1), Mariia Dvoriashyna (2), Rodolfo Repetto (1)

1. Department of Civil, Chemical and Environmental Engineering, University of Genoa, Italy
2. Department of Applied Mathematics and Theoretical Physics, University of Cambridge, UK

Purpose

Age-related macular degeneration (AMD) and glaucoma are the leading causes of blindness in developed countries. Macular oedema, which consists of intra- or sub-retinal fluid accumulation in the macular region, is closely associated with AMD. In this work we develop a mathematical model to study the formation of macular oedema. In the first part of the work we estimate retinal permeability to water, based on the use of homogenisation theory. We then propose a model of fluid and solute transport in the retina. Clinical observations show that fluid accumulation typically takes place in the fovea, although there are no blood vessels there. The model seeks an explanation for this observation.

Methods

The retina is bounded on the vitreous side by the Internal Limiting Membrane (ILM) and on the choroidal side by the Retinal Pigmented Epithelium (RPE), as shown in Figure 1. We assume that Müller cells, which span the retina for almost its entire thickness, play a major role in determining the value of the permeability of the retinal tissue, owing to their high density. The model considers that Müller cell density varies within the macula, being very low in the fovea and fifty times larger in the parafovea, which is the pink area shown in Figure 1. Moreover, these cells are orthogonal to the retinal surface at their extremities and inclined in the middle layer. Inclined cells are packed more closely, reducing tissue permeability. This is confirmed by our calculation of tissue permeability, according to which the middle layer is approximately 10 times less permeable. Thus, we treat the retina as effectively consisting of three superposed layers, characterised by different permeabilities, as shown in Figure 1.

We solve the problem for fluid flow and albumin transport in the tissue, treating it as a porous medium. We assume that proteins and fluid leak from blood vessels in a specific region of the innermost layer in the parafovea, owing to impairment of the blood-retinal barrier. We consider both fluxes induced by mechanical pressure gradients and also osmotic fluxes across the RPE and ILM. Water flux is permitted both through the RPE and ILM, while proteins cannot cross the RPE and can only escape the retina being transported into the vitreous through the ILM.

The equations are simplified using lubrication theory, taking advantage of the slenderness of the domains.
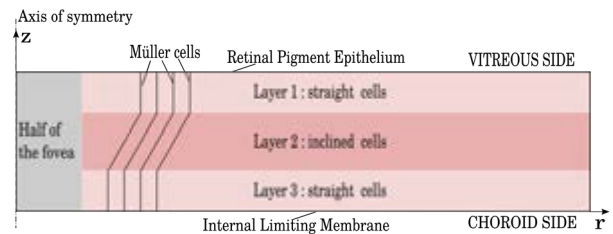
Figure 1: Sketch of the geometry of the model.

Results

The overall hydraulic conductivity of the retinal tissue in the z-direction predicted by our model is 1.2×10^{-11} m^2/s/Pa and it is in good agreement with the value measured by Fatt et al [1], which is 9.4×10^{-12} m^2/s/Pa. However, Anticliff et al. [2] measured a hydraulic conductivity of the retina of 8.1×10^{-14} m^2/s/Pa, which is almost two orders of magnitude smaller than our prediction and Fatt et al.'s experimental results.

Concerning the fluid circulation in the retina, the pressure peaks in the region where fluid exudates from blood vessels. Since the middle layer is much less permeable than the other two, fluid moves to a large extent along the retina before crossing it. The maximum albumin concentration occurs in the bottom region, due to the advective transport: since water flows mostly out of the bottom surface it transports proteins towards that region.

Discussion

The difference between the results obtained with our model and the measurements of Anticliff et al. [2] can be attributed to the fact that we neglect the presence of other structures (such as photoreceptors) that would decrease the permeability of the retina. However, the model clearly shows that the permeability of the middle retina is much smaller than close to the ILM and RPE. This affects the circulation of fluid in the retina and facilitates fluid accumulation in the foveal region.

References

1. Fatt, I., & K. Shantinath. *Experimental Eye Research* 12(2): 218-226. 1971.
2. Antcliff, Richard J., Ali A. Hussain, & John Marshall. *Archives of Ophthalmology* 119(4): 539-544. 2001.

A NOVEL TECHNIQUE FOR RETINA BIOMECHANICAL CHARACTERIZATION

Beatrice Belgio (1), Francesca Berti (1), Sara Mantero (1), Federica Boschetti (1)

1. Dept. of Chemistry, Materials, and Chemical Engineering "Giulio Natta", Politecnico di Milano, Italy

Introduction

Retinal diseases are a leading cause of blindness worldwide. Mechanical factors are believed to play a key role in the pathogenesis of these diseases [1]. Hence, understanding retinal biomechanics is crucial to build suitable *in vitro*/*in silico* models and to develop new therapies, such as implantable tissue engineered constructs. Currently, the knowledge of retina mechanical properties is still limited and mainly based on uniaxial tensile tests [2]. Despite its extensive use, this test does not replicate retina *in vivo* conditions. Multiaxial tests seem more representative of the *in vivo* loadings. Here, we present a novel method to evaluate retina response to multiaxial stresses. We developed an innovative setup to measure the load-displacement response and we investigated tissue elastic properties by using numerical simulations.

Methods

Nine-month-old pig eyes (n=10) were obtained from a local abattoir within 1-hour postmortem. After careful detachment from the posterior wall of the eye, retina was preserved in PBS solution at 4 °C until testing. For mechanical tests, retinal specimens were clamped between two 3D printed discs mounted on an electromechanical testing machine (Bose EnduraTEC ELF 3200) (Figure 1a). The discs had a circular hole of 5 mm in diameter at their center. A hemispherical stainless-steel head punch is pushed through the sample at a displacement rate of 0.1 mm/s (Figure 1b).

The load applied to the specimen was measured with a load cell, whereas the displacement was recorded with the machine LVDT transducer.

Numerical simulations were performed in Abaqus/Standard 2020 mimicking the experimental setup. A linear elastic material (E=220 GPa, ν=0.3) was assigned to the punch, while elastic-plastic properties were assumed for the retina. To identify the actual values, retinal elastic (E) and plastic (σ_y) parameters were varied starting from our previous results of uniaxial tensile tests [3].

The thickness of retina samples was determined using optical coherence tomography (DRI OCT Triton Plus, Topcon) in order to account for variability in the model geometrical features.

Results

The average retina thickness was 0.35 mm ± 0.04 mm. The load-displacement curve obtained from experimental results shows an initial lower load area followed by a region of increased mechanical response to the applied stresses. The computational data well fitted the average experimental behavior with E=7 kPa and σ_y=3.5 kPa (Figure 1c).
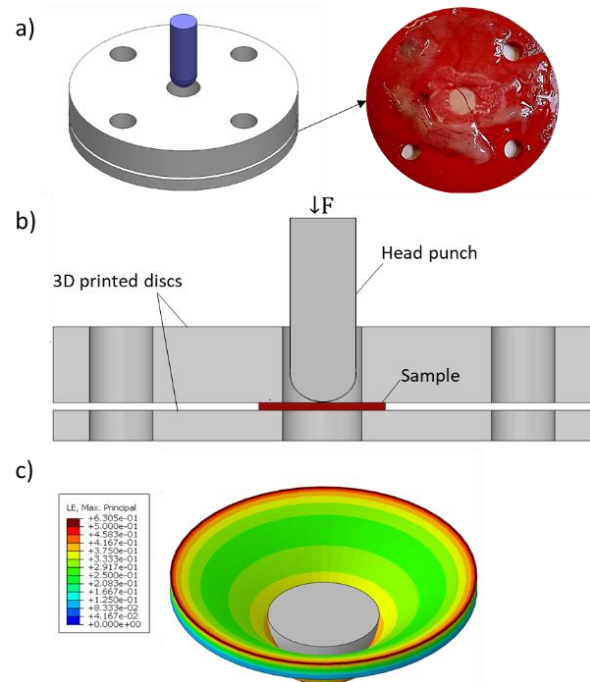
Figure 1: a) Top view of the two 3D printed discs and picture of a retinal sample placed on the lower disc; b) Scheme of the setup developed for multiaxial tests; c) Contour plot of max principal strain in the numerical simulations of retina sample.

Discussion

We developed a novel simple experimental technique for determining retina biomechanical properties when subjected to multiaxial stresses as *in vivo*. The association of this method with numerical simulations allows the determination of retina elastic modulus and plastic properties. This value could be set as a reference property which scaffolds, meant for retina tissue engineering, and *in vitro*/*in silico* models must approximate in order to well reproduce retinal tissue.

References

1. I. C. Campbell et al., J. Biomech Eng., 136(2): 021005-021024, 2014.
2. M. Ferrara et al., Eye, 35:1818-1832, 2021.
3. B. Belgio et al., Bioengineering, 8(2): 18-30, 2021.

Acknowledgements

COMPUTATIONAL STUDY OF RETINAL BLOOD FLOW COUPLED TO A GLOBAL CIRCULATION MODEL

Alessia Casalucci (1), Lucas Müller (2), Annunziato Siviglia (3), Eleuterio Toro (3), Rodolfo Repetto (1)

1. Department of Civil, Chemical and Environmental Engineering, University of Genoa, Italy; 2. Department of Mathematics, University of Trento, Italy; 3. Laboratory of Applied Mathematics, DICAM, University of Trento, Italy

Introduction

The optic nerve transmits visual information from the retina to the brain. Anatomically, it is composed of pia mater, arachnoid mater, and dura mater. The space between these sheaths is filled with cerebrospinal fluid (CSF) that is continuous with the entire CSF system. Therefore, the interactive dynamics of all fluid compartments within the craniospinal space will have a direct effect on CSF pressure and volume in the optic nerve sheath. Moreover, the dura sheath of the optic nerve is pierced by the central retinal artery and central retinal vein. The flow in these vessels is directly affected by the CSF pressure which acts as external pressure. Blood vessels inside the eye are affected by the intraocular pressure (IOP), which in turn is governed by aqueous humour production and drainage.

Methods

We present a detailed geometric multiscale model for the retinal circulation, involving arteries, veins and microvasculature. The topology of arterial and venous networks is extracted using the Automated Retinal Image Analyzer (ARIA) [1] from medical images included in the Digital Retinal Images for Vessel Extraction (DRIVE) [2] (Fig. 1). Terminal points of large/medium arteries are coupled to the venous network via lumped parameter models representing the microcirculation.
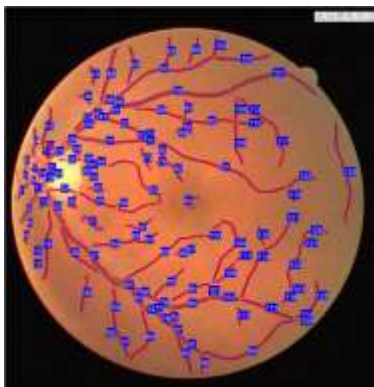
Figure 1: Segmentation of major retinal vessels with ARIA [1].

The constructed model is coupled to an existing global multiscale human circulation model [3,4]. This model is closed-loop and it comprises a one-dimensional representation of major arteries and veins, lumped-parameters models of the microcirculation, heart, pulmonary circulation, cerebrospinal fluid, Starling resistors and venous valves (Fig. 2). Simplified intraocular ocular pressure (IOP) and optic nerve pressure (ONP) models are coupled to the existing intracranial pressure (ICP) model.

Results and Discussion

Our model reproduces blood flow and pressure wave propagation in the retinal network. Moreover, it allows us to explore the interaction of vasculature with IOP and ONP. This model constitutes a first step towards the study of the relationship between IOP and ICP.

The present model represents a framework that can be used to study various pathological conditions that regard the interaction of the eye vasculature with other fluids (such as glaucoma).
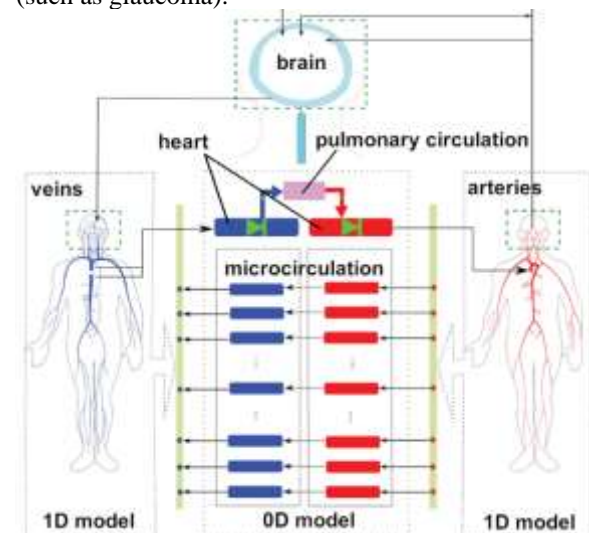
Figure 2: Representation of the global model for the full human blood and cerebrospinal circulation [4].

References

1. Bankhead et al. PLoS ONE 7(3): e32435, 2012.
2. J. Staal et al, in *IEEE Transactions on Medical Imaging*, vol. 23, no. 4, pp. 501-509, 2004.
3. Müller et al, Int J Numer Method Biomed Eng, 30(7):681–725, 2014.
4. Toro et al, Int J Numer Method Biomed Eng,: e3532, 2021.

A DETAILED METHODOLOGY TO MODEL THE NON-CONTACT TONOMETRY: A FLUID-STRUCTURE INTERACTION STUDY

E. Redaelli (1), J. Grasa Orús (1) , J. F. Rodriguez Matas (2), B. Calvo Calzada (1) , G. Luraghi (2)

1. Universidad de Zaragoza, Spain; 2. Politecnico di Milano, Italy

Introduction

Understanding corneal biomechanics is relevant for the study of corneal pathologies and the prediction of refractive surgery outcomes. Non-Contact Tonometry (NCT) is a non-invasive diagnostic tool intended to characterize corneal biomechanics *in vivo* by applying a high-velocity air jet to the tissue. The parameters extracted from this test can only be considered as indicators of biomechanical behaviour rather than intrinsic biomechanical properties. The identification of the corneal structural parameters using an NCT test relies on an inverse finite element method, which requires accurate and reliable modelling to translate the results of the test into clinical data. From a modelling perspective, the best numerical approach to reproduce the procedure is the Fluid-Structure Interaction (FSI) simulation [1]. This work presents an FSI analysis to virtually apply an air-jet to a 3D idealized eye model.

Methods

The 3D model of the eye (Fig. 1a), based on averaged anatomic measures, is meshed with hexahedral solid elements with full integration. The mesh density is chosen thanks to a mesh sensitivity analysis. The cornea and the limbus are modelled with an anisotropic quasi-incompressible hyperelastic material (Holzapfel Gasser Ogden model [2]). Firstly, the zero-pressure configuration of the eye is found through an iterative algorithm; then, the humours are pressurized at a homogeneous intraocular pressure of 15mmHg. Once the eye is pressurized, the air puff velocity is applied to the fluid domain to simulate the NCT. A turbulence model based on a variational multiscale approach is adopted. The simulations are carried out using 16 CPUs of an Intel i9-10940X CPU (3.30GHz) with the finite-element solver LS-DYNA (ANSYS). The structural part is solved through the implicit structural solver, while the air is modelled as an incompressible fluid (Fig. 1b) and solved through the implicit ICFD (ANSIS) software. Hence, Non-Contact Tonometry is simulated using a strongly coupled, 2-way and boundary fitted FSI approach.

Results

It is possible to appreciate the difference between the undeformed shape of the cornea's central section (Fig. 2a) and the configuration at the instant of highest concavity (Fig. 2b), when the air pressure and velocity are at their maximum value as shown in Fig. 2c/d. A maximum peak pressure of 130 mmHg is achieved at the center of the cornea corresponding to a vertical displacement of the tissue of 1 mm. These results could be extended and compared to a real clinical database (with patient-specific corneal geometry and IOP) for validation.
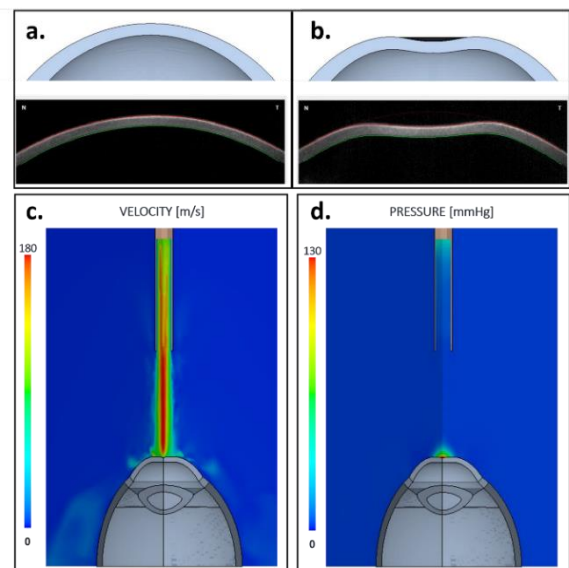
Figure 2: Undeformed (a) and deformed (b) cornea's central section. Air velocity (c) and pressure (d) at the instant of highest concavity.

Discussion and Conclusions

The development of a strong FSI tool amenable to model coupled structures and fluid can be useful to find the biomechanical properties of the corneal tissue *in vivo* comparing the deformation obtained with the numerical simulation and the clinical outcomes.

References

1. Ariza-G. et al., C Meth Ap Mech Eng, 340: 202-215, 2018.
2. Holzapfel et al. J. Elast., 61(1), 1-48, 2000.

Acknowledgements

Figure 1: (a) Section of the 3D eye model; (b) FSI domain simulating the surrounding air.

CT-BASED FEA AND COMPUTATIONAL FLUID DYNAMICS APPLIED TO SCAFFOLD-BASED RECONSTRUCTION OF A SHEEP MANDIBLE

Ben M. Ferguson (1), Will Lewin (2), Hala Zreiqat (3), Jonathan Clark (2), Qing Li (1)

1. School of Aerospace, Mechanical and Mechatronic Engineering and Australian Research Council Centre for Innovative BioEngineering, The University of Sydney, NSW 2006, Australia
2. Chris O'Brien Lifehouse and Sydney Medical School, Faculty of Medicine and Health, The University of Sydney, NSW 2006, Australia
3. School of Biomedical Engineering and Australian Research Council Centre for Innovative BioEngineering, The University of Sydney, NSW 2006, Australia

Introduction

Although recent clinical studies of scaffold-based mandibular reconstruction have produced promising results, there remains significant challenges in designing these implantable devices so that they meet all of the mechanical and biological criteria necessary for successful bone reconstruction. This research considers the variation with scaffold microstructure of the biomechanical and interstitial fluid flow conditions of a porous implant used to reconstruct a sheep's mandible.

Methods

The microstructure of the scaffold is expressed mathematically as:

$$f(X, Y, Z, k) = \cos X + \cos Y + \cos Z - k \qquad (1)$$

where $X = 2\pi x/a$, $Y = 2\pi y/a$ and $Z = 2\pi z/a$; (x, y, z) are the Cartesian coordinates at a given point on the scaffold surface, a denotes the spatial period of the unit cell, and k denotes the isovalue. Note that $1/a$ is equivalent to the wavenumber (or spatial frequency). Here, the microstructure of the scaffold is varied as a function of the spatial period, a, and isovalue, k. Consistent with other studies reported in the literature [1], the porosity of the scaffold varies from 50% to 90%. For instance, a porosity of 50% corresponds to $a = 1$ and $k = 0$.

Computer tomographic (CT)-based finite element (FE) modelling and computational fluid dynamics (CFD) techniques are used to visualize and quantify the variation with scaffold microstructure of the:

- mechanical stimulus conditions (for tissue regeneration within the scaffold),
- structural strength (so that the implant remains intact with a diminished risk of failure), and
- interstitial fluid flow conditions (for nutrient and oxygen transfer within the scaffold).

The implant biomaterial is selective-laser-sintered polyether ether ketone (PEEK) in which the linear elastic orthotropic mechanical properties are characterized by INSTRON testing.

Results

Figure 1 shows the results of the FE and CFD modelling. In Figure 1(a) high stress (in red) in the implant occurs in region of the hole where the neck of the screw is in contact with the implant, and on the struts of the scaffold. Figure 1(b) shows the velocity vectors as arrows (green denotes higher velocity and blue, lower velocity) with the fluid flowing principally from right to left. The struts of the scaffold are represented by white solid-filled circles.
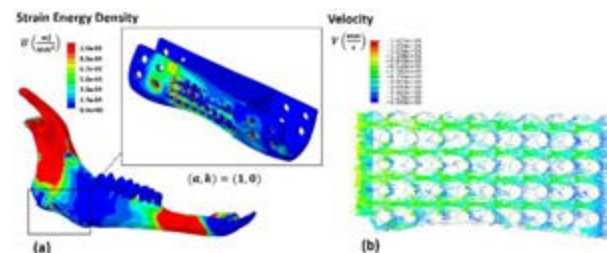
Figure 1(a) Strain energy density distribution of the reconstructed side of the mandible and (b) distribution of the velocity of interstitial fluid flow for a cross-sectional slice of the porous implant.

Conclusion

The scaffold microstructure of the implant is observed to have a significant effect on the biomechanical and interstitial fluid flow conditions under physiological load. This research can be readily extended to determine the optimal microstructure of the scaffold using multiobjective optimization techniques developed by Ferguson et al., (2021) [2].

References

1. Li, J.J., D.L. Kaplan, and H. Zreiqat, *Scaffold-based regeneration of skeletal tissues to meet clinical challenges.* 2014. **2**(42): p. 7272-7306.
2. Ferguson, B.M., et al., *Optimal placement of fixation system for scaffold-based mandibular reconstruction.* Journal of the Mechanical Behavior of Biomedical Materials, 2021: p. 104855.

ULTRASOUND-BASED FSI MODELING OF AORTIC ANEURYSMS: IMPACT OF THE AORTIC BIFURCATION AND INLET VELOCITY PROFILE

Judith Fonken (1,2), Eline van Engelen (1), Esther Maas (1,2), Arjet Nievergeld (1,2), Marc van Sambeek (1,2), Frans van de Vosse (1), Richard Lopata (1)

1. *Eindhoven University of Technology, Netherlands; 2. Catharina Hospital Eindhoven, Netherlands*

Introduction

Research on abdominal aortic aneurysm (AAA) development, growth and rupture risk requires a large, longitudinal study on mechanical properties of AAAs. Since both wall mechanics and hemodynamics are highly dependent on AAA geometry, a patient-specific risk assessment is required, based on fluid-structure interaction (FSI) models. Time-resolved 3-dimensional ultrasound (3D+t US) is the preferred image modality to extract the patient-specific geometry, since it is safe, fast and affordable. A previous study has shown the feasibility of 3D+t US-based FSI simulations and the importance of incorporating the pre-stress [1].

Due to the limited field-of-view of 3D+t US, the aorto-iliac bifurcation is often not included. The presence of this bifurcation does not significantly influence the wall mechanics in the AAA region [2]. However, the aorto-iliac bifurcation might influence the hemodynamics in the AAA. Furthermore, the hemodynamics may highly depend on the prescribed inlet velocity profile. This study aims to quantify the influence of excluding the bifurcation and altering the inlet velocity profile.

Methods

To quantify the impact of excluding the bifurcation, a patient-specific geometry including the bifurcation was segmented from CT. An additional geometry was created, in which the bifurcation was replaced by a single outlet. The influence of the prescribed velocity profile was examined by prescribing either a model or Doppler-derived velocity profile. The former was obtained from a 1D model, assuming Poiseuille flow, whereas for the latter, the velocity profile over time and vessel radius were extracted from pulsed-wave and color Doppler acquisitions (Fig.1). FSI simulations with and without bifurcation, and with the two different inlet velocity profiles were executed, resulting in a total of four simulations. In all simulations, the same patient-specific outlet pressure was prescribed and the pre-stresses in the wall were incorporated [1]. The results in the AAA region were compared to quantify the influence of the bifurcation and inlet velocity profile.

Results

Figure 2 visualizes the systolic wall stress, time-averaged wall shear stress (TAWSS) and oscillatory shear index (OSI) in the AAA region for all FSI simulations. Only slight differences in wall stress, TAWSS and OSI were observed when the bifurcation was omitted. Employing a Doppler-derived inlet velocity profile resulted in increased TAWSS and OSI, whereas minor differences in wall stress were observed.
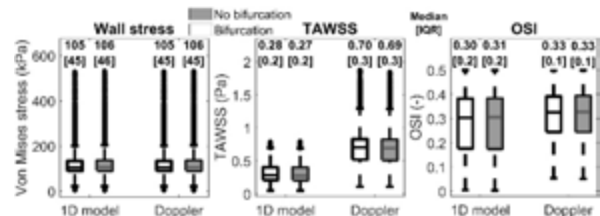
Figure 2: boxplots of the systolic wall stress, time-averaged wall shear stress (TAWSS) and oscillatory shear index (OSI) for the 4 different FSI simulations.

Discussion

In this study, the influence of excluding the bifurcation in FSI simulations was quantified. Furthermore, incorporating a Doppler-derived velocity profile was shown to be feasible. Preliminary results show only slight differences in the AAA region when the bifurcation was excluded. Furthermore, the velocity inlet profile significantly influences the hemodynamics, highlighting the importance of using a patient-specific profile. In future research, simulations for additional patients will be executed to further quantify the influence of the bifurcation. Additionally, the FSI framework will be further personalized by including the patient-specific inlet velocity profile, derived from US-Doppler data, and the patient-specific shear modulus. The personalized 3D+t US-based FSI framework paves the way for longitudinal studies on AAA mechanics.

References

1. Fonken et al., Front. Physiol., 1255, 2021.
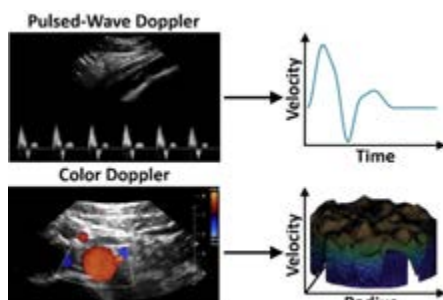2. Disseldorp et al., J. Biomech., 2405-2412, 2016.

Acknowledgements

Figure 1: pulsed-wave (top) and color (bottom) Doppler acquisitions used to extract the velocity profile over the time and radius, respectively.

EVALUATING THE EFFECT OF COMPUTATIONAL DOMAIN REDUCTION IN ASCENDING AORTA SIMULATIONS

Antonio Martinez (1,2), Leonardo Geronzi (1,2), Morgan Daniel (3), Pierre Escrig (3), Jaques Tomasi (3), Michel Rochette (2), Marco Evangelos Biancolini (1)

1. University of Rome "Tor Vergata", Rome, Italy; 2. Ansys Lyon, France; 3. CHU Rennes, France

Introduction

Novel diagnostic techniques and promising treatments are arising by enhancing medicine with the insight given by simulation. However, it is often difficult to adapt these advances into everyday clinical-routine as data needed to personalize the models is often missing, or incomplete. In the scope of developing personalized treatment for the ascending thoracic aortic aneurysm (ATAA), a model with reduced extents is proposed by eliminating the arch and descending sections in the computational domain. This allows for an effortless characterization of the geometry via Statistical Shape Models, enabling simple and fast personalization of reduced order models, which is key in clinical practice. In this work, the effect of this simplification is analyzed in terms of wall pressure and velocity field for four different patients.

Figure 1: Geometries of the four patients, highlighting the position of the cut.

Methods

The geometries of four ATAA were obtained from a dataset of CT scans with spatial resolution of 0.5–0.625 mm in the z-axis and 0.5 mm in the x- to y-axes. The patients were selected in order to provide maximum geometrical diversity. A semi-automated segmentation and centerline extraction was performed using *EndoSize*. The geometries obtained were processed in order to build a domain suitable for the present computational fluid dynamics (CFD) study: the valve opening was inserted using a projection of the shape used in [1], the outlets were appropriately prepared by extruding the domain a minimum of 5 hydraulic diameters and the surface was smoothed using a volume-aware procedure. Finally, the domain was cut at the ostium of the brachiocephalic trunk, perpendicular to the centerline (*Figure 1,* numbered from left to right). A steady state CFD analysis of the flow at systole was performed on both the full and reduced domain. A total mass flow of 0.53 kg/s was used, distributed amongst the different outlets proportionally to their cross-section area. At the valve, a pressure of 16 kPa was imposed. For the computation, a Transition SST turbulence and Newtonian fluid model for the blood was used, with density $\rho=1056$ kg/m^3 and viscosity $\mu=0.0035$ Pa·s. A mesh convergence study was performed, resulting in a cell size of 0.5mm.

Results and Discussion

To evaluate the domain reduction effect, velocity and pressure differences were analyzed. In *Table 1* the differences of maximum velocity at the cutting plane are summarized. Maximum discrepancy is observed in patient 2, where peak velocity is overestimated by 18.9%. However, the flow pattern is well captured as shown by the velocity contours and streamlines (*Figure 2)*. Maximum wall pressure differs by 1.6 Pa for patient 2 and by less than 0.12 Pa for the other patients, considering a systolic pressure of 16 kPa, these differences are negligible.

The comparison between the full and reduced domains shows a satisfactory agreement considering the significant reduction of the domain. Further analysis considering additional geometries and transient phenomena are required to better understand if this approach is feasible for patient specific simulations.
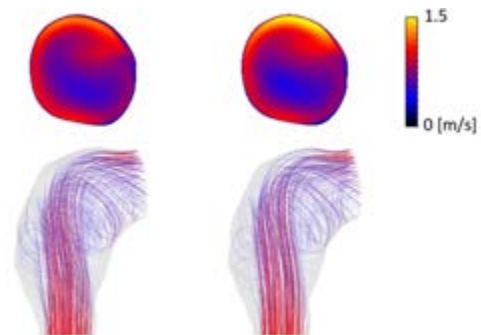
Figure 2: Velocity at the cutting plane and velocity streamlines for the full and reduced domain (left and right respectively) of patient 2.

Patient	Full [m/s]	Red. [m/s]	Error (%)
1	0.9947	1.0688	+7.45
2	1.2540	1.4905	+18.9
3	1.2489	1.4472	+15.9
4	0.9716	0.9640	−0.79

Table 1: Maximum velocity on the cutting plane.

References

1. Geronzi et al, J Computational Science, 51, 101327, 2021.

Acknowledgements

VALIDATION OF AN IMAGE-BASED APPROACH FOR PATIENT-SPECIFIC ARTERIAL MODELLING IN CORONARY STENTING SIMULATIONS

Gianluca Poletti (1), Luca Antonini (1), Panagiota Tsompou (2), Georgia S. Karanasiou (2), Dimitrios I. Fotiadis (2), Lorenza Petrini (3), Giancarlo Pennati (1)

1. LaBS – Dept. of Chemistry, Materials and Chemical Engineering, Politecnico di Milano, Milan, Italy;
2. Dept. of Biomedical Research, FORTH-IMBB, GR 45110 Ioannina, Greece;
3. Dept. of Civil and Environmental Engineering, Politecnico di Milano, Milan, Italy.

Introduction

In the context of coronary stent implantation, numerical simulations providing a virtual representation of the patient-specific case could represent a step toward improving individual treatments. Clinical images recorded during the surgical act can provide useful information for the reconstruction of the coronary artery geometry and partially address the great uncertainties involved in the mechanical modelling of the patient-specific vessel [1]. For a potential clinical use of such simulations, it becomes essential to have simple but at the same time effective and robust methods able to provide virtual insights on the treatment outcomes in a reasonable time according to clinical requirements. With such purpose, this work proposes a methodological approach for patient-specific artery modelling and validation through the numerical replication of clinical cases and comparison with *in vivo* post-treatment data.

Methods

On the basis of coronary OCT and X-Ray biplane angiographies, patient-specific arteries were 3D reconstructed and the distribution of the different plaque components was identified. Special care was taken to realistically model the media and adventitia layers. Indeed, the *in vivo* pressurization and axial pre-stretching of the arterial wall were considered in the assignment of the mechanical properties, without a time-consuming inverse analysis for the identification of the unloaded vessel geometry. A phenomenological description consistent with more complex constitutive models was therefore developed.

The effectiveness of the whole arterial modelling approach was evaluated by replicating the stenting treatment of the available clinical cases. Previously validated device models as well as a numerical methodology for coronary stent deployment developed and assessed in previous work by the authors [2] were used for an accurate reproduction of the clinical treatments.

Results

Figure 1a shows one of the reconstructed coronary arteries highlighting the identified plaque components and the media and adventitia layers. The comparison between numerical results and post-treatment OCT data reveals for this case a good correspondence of the lumen area values in stented artery region (Figure 1b).
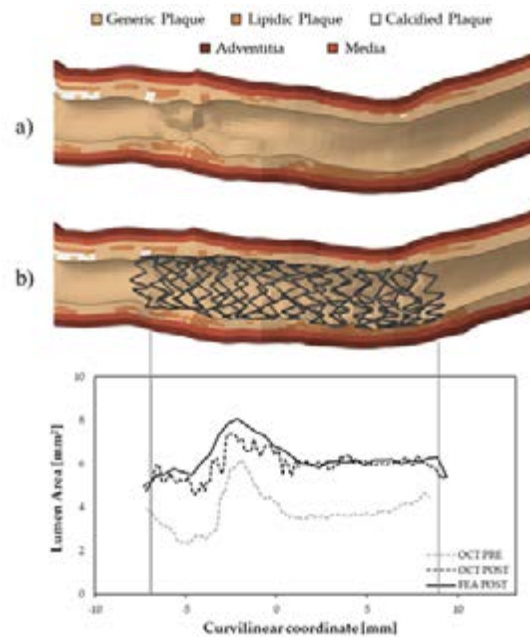
Figure 1: a) section of a reconstructed artery; b) post-treatment artery with associated lumen area plot for the comparison of the finite-element analysis (FEA) results with the OCT clinical measurements.

Discussion

Considering the uncertainties related to clinical images involved both in geometry reconstruction and post-treatment comparison with numerical results, a good effectiveness of the proposed method was found. An approach was developed to account for arterial strains associated with *in vivo* pressurization and axial pre-stretching without the need of an iterative process for the identification of the unloaded geometry. This proved to be a good approach for both reliability and time savings in generating patient-specific artery models.

References

1. Chiastra et al., J. Biomech., 49: 2102-2111, 2016.
2. Berti et al, Front. Med. Technol., 3:702656, 2021.

Acknowledgements

PATIENT-SPECIFIC PRE- AND POST-SURGICAL STOMACH MODELS

Ilaria Toniolo (1,2), Alice Berardo (2,3), Silvana Perretta (4), Giuseppe Quero (5), Claudio Fiorillo (5), Emanuele Luigi Carniel (1,2)

1. Department of Industrial Engineering of the University of Padova, Italy; 2. Centre for Mechanics of Biological Materials, University of Padova, Italy; 3. Department of Civil, Environmental and Architectural Engineering, University of Padova, Italy; 4. IHU Strasbourg, Strasbourg, France; 5. Digestive Surgery Unit, Fondazione Policlinico Universitario Agostino Gemelli IRCCS, Rome, Italy.

Introduction

Obesity is a major health concern, which affects people of all age groups adding risks for related comorbidities. To treat eligible people with morbid obesity, bariatric surgery is the best choice since it should entail both a loss of a large amount of weight and an improvement of patients' quality of life and clinical situation [1]. In recent years, laparoscopic sleeve gastrectomy (LSG) has gained space resulting in the most performed procedure worldwide, showing a continuous growth, even though some limitations remain, and late complications may arise (e.g., GERD). For these reasons, the development of computational patient-specific models represents a valuable solution to overcome the main limits and controversies.

Materials and Methods

From a single centre study reported by Quero et. al. [2], twenty-three adult patients affected by severe obesity who underwent LSG were considered. The MRI scans before and after bariatric surgery were processed, leading to the generation of forty-six virtual solid models characterized by a double-layered geometry in order to engender the submucosa-mucosa layer and muscolaris stratum. The mechanical behaviour of the stomach tissues was defined by means of a fibre-reinforced hyperelastic constitutive formulation, which included the tissue anisotropy and non-linear elasticity [3]. The finite element discretisation was performed with linear hexahedral elements. The simulation consisted in an inflation process by means of Abaqus Explicit 2018 (Dassault Systemes Simulia Corp., Providence, RI).
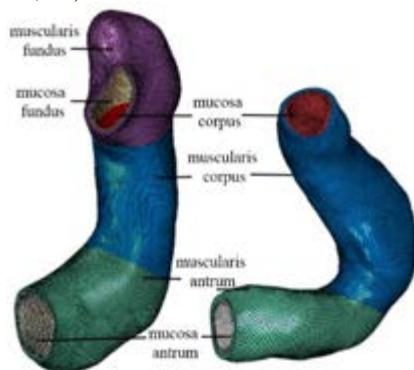
Figure 1: Pre- and post-surgical patient-specific finite element models of a stomach.

Results

The results showed a high inter-patient's variability which affected the biomechanical response both in pressure-volume relationships and in logarithmic elongation strain values (Fig. 2).
Statistical minor values of elongation strain in post-surgical models than pre-surgical ones were recorded at the same intragastric pressure.
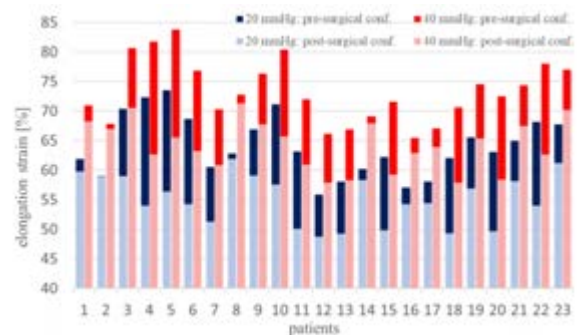
Figure 2: Average elongation strain (LE) for each pre- and post-surgical model obtained at different intragastric pressure levels (blue: 20 mmHg, red: 40 mmHg).

Conclusions

Results highlighted a significant difference between the mechanical behaviour of pre- and post-surgical stomachs subjected to the same internal gastric pressure, that can be correlated to a difference in the activation of mechanoreceptors, leading to a different satiety feeling. Patient-specific gastric mechanics appears to be an extremely promising field of biomechanics. Computational modelling can be a powerful tool to address the main limits and controversies which still affects bariatric surgery, without performing clinical trials and animal testing.

References

1. Buchwald et al, Obes. Surg., 23, 2013.
2. Quero et al, Obes. Surg., 30, 2020.
3. Toniolo et al, J Mech Behav Biomed Mater, 125, 2021.

Acknowledgements

ON THE USE OF DIGITAL TWIN TECHNOLOGY *ARIELLE* FOR THE DEVELOPMENT OF PERINATAL LIFE SUPPORT SYSTEMS

B. G. van Willigen(1,2), M. B. van der Hout-van der Jagt(1,2,3), W. Huberts(1,4), F. N. van de Vosse(1)

1. Cardiovascular Biomechanics, Biomedical Engineering, Eindhoven University of Technology, The Netherlands; 2. Obstetrics and Gynaecology, Máxima Medical Centre, Veldhoven, The Netherlands; 3. Signal Processing Systems, Electrical Engineering, Eindhoven University of Technology, The Netherlands; 4. Department of Biomedical Engineering, Cardiovascular Research Institute Maastricht, Maastricht University, Maastricht, The Netherlands

Introduction

To reduce the mortality and morbidity rate of extremely preterm infants (< 28 weeks of gestational age, GA), the Perinatal Life Support (PLS) consortium is developing a PLS system that serves as an incubator in which the preterm infant is kept in a liquid environment to allow for the lungs to further mature. The umbilical cord is connected to a extracorporeal oxygenator (artificial placenta).[1]. To develop such a complex device, knowledge from multidisciplinary fields must integrate into one single system. Mathematical models are used to support this integration by composing a digital twin, *Arielle,* of the PLS system and the preterm infant. In addition, these models are connected to a manikin to support clinical implementation. Since blood velocity profiles are important to estimate the well-being of the fetus in the clinic, the development of *Arielle* starts with the fetal cardiovascular system. In addition, fetal growth should be incorporated as the fetus growths twice it size from 24 to 28 weeks of GA [2]. This study presents a model of the fetal cardiovascular system allowing fetal growth.

Methods

To verify whether fetal growth is feasible with the means of scaling laws, the lumped parameter model of Yigit et al. 2015 is used [3], [4] as a basis. This model describes a full-term healthy fetal cardiovascular system. To simulate the underlying phenomena of cardiac contraction and allow for cardiac growth modeling, the time varying elastance model of the heart is replaced with a one-fiber model [5]. The left (LCO), right (RCO), and combined cardiac output (CCO) as function of gestational age (GA) are compared with literature [6]–[9] as initial verification of *Arielle*.

Results

Figure 1 shows the LCO, RCO, and CCO of *Arielle* (green) and regression lines based on empirical data of several studies (black) [6]–[9]. Compared with these empirical studies [6]–[9], *Arielle* shows a realistic cardiac output, while growing from 20 to 40 weeks of GA. Furthermore, *Arielle* shows a right ventricular dominance, which agrees with literature [10].

Discussion

A cardiovascular model of a healthy growing fetus is implemented and shows realistic cardiac output. A more thorough verification, which includes blood velocity waveforms at the valves and within important vessels, has to be performed. Furthermore, to support development of the PLS system and its clinical implementation, next steps include the addition of maternal-fetal gas exchange, baro- and chemoreceptor reflexes, and metabolism.
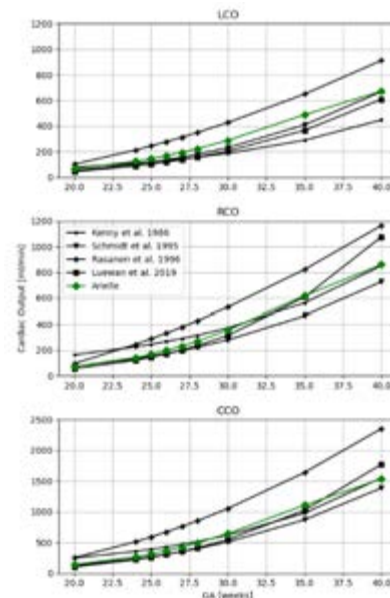
Figure 1: From top to bottom: left, right, and combined cardiac output over GA of Arielle (green) and regression lines (black) of several studies.

References

[1] M.B. van der Hout-van der Jagt et al, Front. Pediatr., 9, 2022

[2] G.R. Alexander et al, Obstet. Gynecol, 87:163–168, 1996

[3] M.B. Yigit et al., J. Biomech., 48:1662–1670, 2015

[4] M.B. Yigit et al., Matern. Health Neonatol. Perinatol., 5:5, 2019

[5] P.H.M. Bovendeerd et al, Ann. Biomed. Eng., 34:1833–1845

[6] J. F. Kenny et al., 74:1208–1216, 1986

[7] C.E. Schmidt et al, Proc. Natl. Acad. Sci. U. S. A., 94:8948–8953, 1997.

[8] J. Rasanen et al, Circulation, 94:1068–1073, 1996

[9] S. Luewan et al, J. Ultrasound Med., 39:515–527, 2020

[10] G. Mielke and N. Benda, *Circulation*, 103:1662–1668, 2001

INTRA-SUBJECT VARIABILITY OF FEMORAL GROWTH SIMULATIONS BASED ON PERSONALIZED FINITE ELEMENT MODELS

Willi Koller (1), Arnold Baca (1), Hans Kainz (1)

1. Centre for Sport Science and University Sports, University of Vienna, Vienna, Austria

Introduction

Mechanobiological bone growth predictions have a huge potential for improving clinical decision-making in children with bony deformities. A typical workflow to predict bone growth is based on a combination of musculoskeletal (MSK) and finite element (FE) simulations. The FE model usually requires hex elements aligned with the growth plate. Creating such a model is very time-consuming and therefore previous studies [1-3] only included small sample sizes (n<3), which limited the generalization of the research findings. The proposed mechanobiological model to predict bone growth is based on the osteogenic index (OI), which is determined by the octahedral shear stress and the hydrostatic stress. The twofold aim of the current study was i) to identify intrasubject variability of the OI and ii) to analyze how material properties and MSK loadings affect the OI.

Methods

We collected and analyzed three-dimensional motion capture data and magnetic resonance images (MRI) of eight typically developing children. MRI of each femur was segmented using 3D Slicer and used to calculate the subject-specific neck-shaft angle and anteversion angle. Two models were used for the MSK simulations:

1. we used the torsion tool [4] to create personalized models based on the measured angles from the MRI and subsequently scaled each model to the anthropometry of each participant [5].
2. the generic "gait2392" model was scaled by the identical scale setup file.

Joint kinematics, muscle and joint contact forces were calculated using OpenSim [6]. We developed a semi-automated workflow using Coreform Cubit, MeshLab, STAPLE toolbox and MATLAB to create FE models with subject-specific hex meshes from the segmented femurs. The FE models, including muscle forces and hip joint contact forces from the OpenSim simulations, were used to calculate the OI [1–3] in FEBio. Two FE models were used with Youngs' modulus of 1, 10, 10 and 0.1, 2, 5 GPa for growth plate, proximal and distal trabecular bone, respectively. The OI was then plotted as heatmaps and the shape and distribution of these images were compared within participants (left versus right femur) using OpenCV's template matching and histogram comparison. Additionally, the magnitude (mean and range) of the OI was compared between the left and right growth plate.

Results

The range of the magnitude of the OI between left and right side differed up to 0.074 while the mean OI values were quite similar with a maximum difference of 0.038 (Figure 1). Altering material properties of the FE model mainly changed the distribution of the OI (0.056±0.035 vs 0.089±0.06). Changes in MSK loading only had a minor effect on the OI (Figure 1, blue bars).
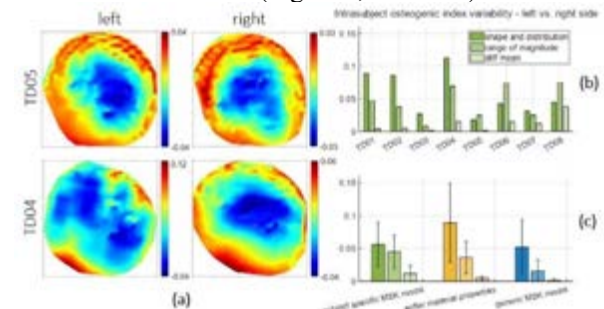
Figure 1: (a) heatmap plots of the OI of the left and right femur of 2 children; (b) intrasubject variability of OI; (c) OI variability for the baseline FE model and models with different material properties and MSK loadings.

Discussion

Previous research showed that a simplified growth plate leads to different OI magnitude and distribution when compared to a subject-specific growth plate [2]. Our work based on personalized FE models further highlights that the OI is similar between the left and right femur in most typically developing children.

Using a generic-scaled instead of a subject-specific MSK model mainly changed the magnitude and not the direction of the hip joint contact forces. Therefore, the general loading environment barely changed, leading to similar OI distributions between the generic-scaled and subject-specific MSK models.

Only half of the simulations converged when lowering the values of the Youngs' modulus in the FE model. Considering that little is known about the material properties of pediatric femurs, FE simulations based on subject-specific geometry and loading might help us to narrow down material properties to a realistic range.

In conclusion, we developed a workflow to create personalized FE models with a hex mesh based on MRI images in a rapid way and quantified the intra-subject variability of the OI. We hope our workflow and reference simulations will enable peers to conduct mechanobiological growth studies with larger sample sizes and enhance our understanding of femoral growth.

References

1. Carriero et al, Comp Meth Bio Bio Eng, 14:253–262, 2011.
2. Yadav et al, J Biomech, 49:1613–1619, 2016.
3. Kainz et al, PLOS ONE, 15:e0235966, 2020.
4. Veerkamp et al, J Biomech, 125:110589, 2021.
5. Kainz et al, J Appl Biomech, 1–21, 2017.
6. Delp et al, IEEE Trans Biomed Eng, 54:1940–1950, 2007.

SIGNATURE OF DISEASE PROGRESSION IN KNEE OSTEOARTHRITIS: INSIGHT FROM AN INTEGRATED MULTI-SCALE MODELING APPROACH

Ikram Mohout (1), Amir Esrafilian (2), Seyed Ali Elahi (1), Bryce Killen (1), Rami Korhonen (2), Sabine Verschueren (1), Frank Luyten (1), Ilse Jonkers (1)

1. KU Leuven, Belgium; 2. University of Eastern Finland, Finland

Introduction

Osteoarthritis (OA) is the most common joint disease, with the highest prevalence at the knee joint. Despite the huge burden the disease inflicts on society, no successful curative or preventive intervention has been identified yet, as the underlying mechano-biological processes that leads to OA onset and progression are still not fully understood [1]. However, it is known that cartilage degeneration is the hallmark of OA and mechanical loading plays a key role in the degenerative process of cartilage constituents. In this study, the aim is to identify key differences in mechanical parameters, important for cartilage degeneration, in the human knee joint during gait between a healthy and a fast progressing knee OA (KOA) patient based on a unique multi-scale patient-specific *in silico* approach.

Methods

A finite element (FE) model of the human knee joint was created that includes geometries of tibial & femoral cartilage and the menisci. A fibril reinforced poroviscoelastic (FRPVE) material model was assigned to the cartilage tissue [2, 3]. To define patient-specific loading for the FE models, motion capture data were used from a healthy and a progressing KOA patient ($\geq$ 1 increase on the Kellgren-Lawrence OA classification system after a two-year follow-up) at baseline and processed through a musculoskeletal (MS) workflow [4]. The secondary and primary kinematics (anterior-posterior translation, medial-lateral translation, internal-external rotation and knee flexion) as well as the varus-valgus moment and contact force in the superior-inferior direction of the knee joint were estimated by the MS workflow during the stance phase and used to drive the FE model. At peak knee flexion, the strains in the collagen fibril direction (SFD) and the maximum shear strains (MSS) of the tibial cartilage tissue were evaluated as they reflect collagen fibrils degeneration (threshold 10%) [5] and proteoglycans (PG) depletion (threshold 50%) [6] respectively.

Results and discussion

Table 1 shows that the maximum (mean of values >99th percentile) SFD and the MSS in the tibial cartilage of the KOA subject consistently exceeds the magnitude of the healthy control subject. For the control subject, the SFD and MSS thresholds are not exceeded, except for a minimally higher MSS in the medial compartment. In contrast, in the case of the progressing OA subject the thresholds are exceeded, except for a minimally lower SFD in the medial compartment. This suggests more

degeneration of collagen fibrils and PG depletion is present in the progressive KOA subject. **Figure 1** shows that in the KOA subject, elevated strains in the tibia cartilage are present and indicate more collagen fibril degeneration and PG depletion compared to the control subject. These results further elaborate on a previous study that reported higher contact pressures in the tibia cartilage of KOA subjects [7]. The developed patient-specific FE models in this study can be used within adaptive models [5, 6] to enhance our understanding of the personalized mechano-biological processes underlying the onset and progression of OA.

	Control		Progressive	
Maximum >99%	Lateral	Medial	Lateral	medial
SFD	8.4%	8.7%	10.3%	9.2%
MSS	43.3%	51.6%	56.6%	64.0%

Table 1: The maximum strains >99th percentile of SFD (reflecting collagen degradation, threshold=10%) and MSS (reflecting PG depletion, threshold=50%) in the lateral and medial tibial compartment for a healthy and progressive KOA subject.
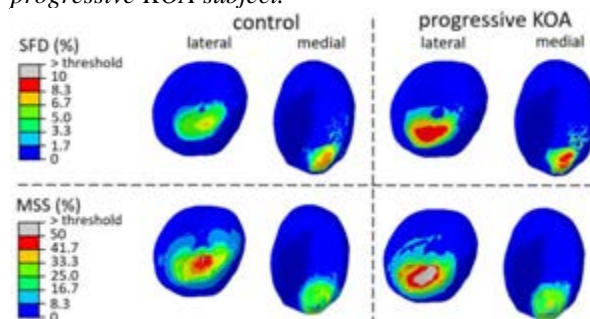
Figure 1: SFD (reflecting collagen degradation) (top) and MSS (reflecting PG depletion) (bottom) in medial and lateral tibial cartilage of a healthy (left) and progressive KOA (right) subject.

References

1. J. Martel-Pelletier et al, Nat. Rev. Dis. Prim, 2: 1-18, 2016.
2. P. Julkunen et al, J. Biomec, 40: 1862–1870, 2007.
3. W. Wilson et al, J. Biomec, 37: 357–366, 2004.
4. C. R. Smith, et al, J. Knee Surg, 29: 99–106, 2014.
5. S. A. Elahi et al, Front. Bioeng. Biotechnol: 9, 2021.
6. G.A. Orozco et al, Sci.Rep, 8:1-16, 2018.
7. B.A. Killen et al, ESB conference, 2021.

Acknowledgements

COMPARATIVE VALIDATION OF TWO PATIENT-SPECIFIC MODELLING PIPELINES FOR PREDICTIVE KNEE JOINT FORCES

Domitille Princelle[12], Giorgio Davico[12], and Marco Viceconti[12]

[1] Department of Industrial Engineering, Alma Mater Studiorum - University of Bologna (IT)
[2] Medical Technology Lab, IRCCS Istituto Ortopedico Rizzoli, Bologna (IT)

Introduction

Over the years, there has been a shift towards more personalized/patient-specific models. This is because there are several clinical problems where knowing the force being transmitted at the patient's joints would be paramount [1]. While such forces can only be measured invasively, they can be predicted using patient-specific models of musculoskeletal (MSK) dynamics, built off medical imaging data. Although associated with more accurate predictions, with existing pipelines that have been tested and validated (i.e., *INSIGNEO* [2] using NMSBuilder [3]), the model generation can still be time-consuming. As new toolboxes like *STAPLE* [4], which automates parts of the process, become available, it becomes important to use them. Compared to NMSBuilder, *STAPLE* fully automates the generation of the skeletal portion of the model and was already found as accurate as *INSIGNEO* in doing so [4]. From there, we developed a new pipeline combining *STAPLE* and steps in NMSBuilder. This work aims to compare and validate this new pipeline against the *INSIGNEO* one in terms of predictive accuracy, using the "Grand Challenge Competition to Predict In Vivo Knee Loads" [5] (henceforth KGC) data.

Methods

Experimental data (CT scans, motion capture and ground reaction forces during level-ground walking) from three subjects implanted with an instrumented knee replacement were obtained from the 4th, 5th and 6th editions of KGC. Overall, six patient-specific models were generated: three using *INSIGNEO* pipeline [2], and three using the newly proposed pipeline combining *STAPLE* (v. beta3) and NMSBuilder. Specifically, this new pipeline uses *STAPLE* to automatically create the skeletal model and NMSBuilder to define the geometry path of the muscle-tendon units from a generic atlas of 40 Hill-type musculotendon. Each generated MSK model had eight degrees of freedom. The hip joint was idealised with a ball-and-socket, while the knee, ankle flexion and subtalar, and toes joints were idealised as hinges. Last, a patellofemoral joint [6] was added. Biomechanical simulations of level ground walking were performed using OpenSim 4.1 and MATLAB (v2021b)®. As validation, the knee contact forces predicted by the models were compared to the experimental values. Specifically, the accuracy of each prediction against the correspondent *in-vivo* measurements was done using a Statistical Parametric Mapping (SPM) [7] two-tailed t-test analysis (significance level: α= 0.05) and each trial was treated as an individual patient.

Results

Only preliminary results from the 6th KGC editions are presented in this study (Figure 1). For both models, the computed joint contact forces were highly correlated to those measured experimentally. Specifically, each trial presented an R^2>0.6499 and RMSE<0.4760, for the INSIGNEO predictions, and an R^2>0.7219 with an RMSE<0.4303 for the {*STAPLE*+NMS}.
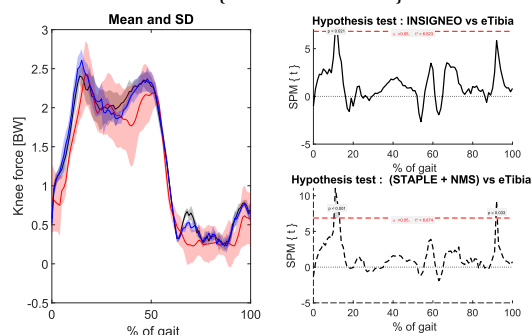
Figure 1: Mean (solid line) and range (shaded area) knee contact force expressed in body weight (BW) for the eTibia (red), the INSIGNEO (black) and the STAPLE (blue) models.

Discussion

This work presented a new pipeline for generating an MSK model and compared it against an existing pipeline by using the 6th KGC dataset. In both models, the predicted joint load at the knee presented a similar margin of error which add up to the previous validation of [4]. Moreover, the adopted models explicitly included a patellofemoral joint which was not integrated within the latest released version of *STAPLE*. The next step would be to complete the planned validation study, with data from the 4th and 5th KGC editions.

References

1. Viceconti et al, J Orthop Res, 37:1537–1545, 2019.
2. Modenese et al, J Biomech, 73, 108-118, 2018
3. Valente et al, PLoS ONE 9(11): e112625, 2014
4. Modenese and Renault, J Biomech, 116:110186, 2021
5. Fregly et al, J Orthop Res, 30:503–513, 2012
6. Sancisi et al, Meccanica, 46:207-220, 2011
7. Pataky et al, J Biomech, 46.2394–2401, 2013

Acknowledgements

SUBJECT SPECIFIC LOWER LIMB ANTHROPOMETRIC REGRESSION WITH LONG, SHORT AND NO COUNTERMOVEMENT PERFORMANCE

Carlos Rodrigues (1,2), Miguel Correia (1,2), João Abrantes (3)
Marco Benedetti (4), Jurandir Nadal (5)

1. FEUP, Portugal; 2. INESC TEC, Portugal; 3. MovLab - ULHT, Portugal
4. PPGEE - UFPE, Brazil; PEB - COPPE/UFRJ

Introduction

Countermovement presents as a natural form of strength increase on concentric action preceded by eccentric action associated to muscle stretch shortening cycle (SSC) [1]. At lower limb, countermovement can be observed on gait and run [2], with its higher expression and accessibility on standard maximum vertical jump (MVJ) with long and short countermovement (CM) and SSC on countermovement (CMJ) and drop jump (DJ) comparison to squat jump (SJ) and no CM [3]. Subject specific strength relation was postulated based on body size and body weight [1] with assessment of the relation of force development to body weight at different standard MVJ [4] and an open issue on long, short and no CM performance with subject specific lower limb anthropometric measurements.

Methods

A small sample of six voluntary heathy higher education sports students without specific train or sport modality was selected with ages (21.5 ± 1.4) years, mass (76.7 ± 9.3) kg and height (1.79 ± 0.06) m. Anthropometric measurements were performed for the distance between anterior superior iliac spines (ASIS), thigh length (T_l), midthigh circumference (MT_c), calf length (C_l), calf circumference (C_c), knee diameter (K_d), foot length (F_l), malleolus height (M_h) and width (M_w), and foot breadth (F_b). Best MVJ trial with higher flight time from AMTI BP2416-4000 CE force plate was selected for each subject from 3 SJ, CMJ and DJ repetitions. The relations between subject specific lower limb anthropometric measures with long, short and no CM performance vertical height from flight time (h_t) were assessed by the regression equations [5] for the thigh, calf, and foot mass (m_T, m_C, m_F) and the moments of inertia for the flexion-extension ($I^{Flex-Ext}$), abduction-adduction ($I^{Abd-Add}$), and internal-external ($I^{Int-Ext}$) axis. Additional relations with long, short and no CM performance vertical height from flight time (h_t) were also assessed with total body mass.

Results

Subjects mass and height presented for selected sample statistical significative correlation ($r=0.844$; $p<0.05$), but no statistical correlation ($p \geq 0.05$) of mass and height with MVJ vertical height from flight time (h_t) at SJ, CMJ and DJ, Table 1. Vertical jump height presented on CMJ and SJ statistical significative correlation ($r=0.917$; $p<0.05$) and no statistical significative correlation at SJ and CMJ with DJ.

Lower limb anthropometric measures presented no statistical significative correlation ($p \geq 0.05$) with MVJ vertical height from flight time (h_t) on SJ and CMJ, with significative correlation ($p<0.05$) of T_l and C_c at DJ. Significative correlations ($p<0.05$) were also detected solely on DJ (h_t) with mass segments m_T, m_C, m_F and moments of inertia, Table 1.

$r\,(\,p\,)$	SJ (h_t)	CMJ (h_t)	DJ (h_t)
Mass (kg)	0.488(0.326)	0.291(0.576)	0.105(0.843)
Height (m)	0.284(0.586)	0.292(0.575)	0.427(0.398)
ASIS (m)	0.386(0.449)	0.371(0.469)	0.122(0.818)
T_l (m)	0.458(0.361)	0.555(0.253)	**0.876**(0.022)
MT_c (m)	0.066(0.901)	0.385(0.451)	0.713(0.112)
C_l (m)	-0.529(0.281)	-0.278(0.594)	0.582(0.226)
C_c (m)	0.188(0.722)	0.357(0.488)	**0.825**(0.043)
K_d (m)	0.413(0.415)	0.396(0.437)	0.657(0.156)
F_l (m)	0.055(0.918)	0.124(0.814)	0.301(0.562)
M_h (m)	-0.138(0.795)	0.015(0.978)	-0.364(0.479)
M_w (m)	0.220(0.675)	0.491(0.323)	0.467(0.351)
F_b (m)	0.168(0.750)	0.306(0.556)	0.492(0.322)
m_T (kg)	0.231(0.660)	0.427(0.399)	**0.851**(0.032)
m_C (kg)	0.117(0.825)	0.311(0.548)	**0.856**(0.029)
m_C (kg)	0.244(0.641)	0.571(0.236)	**0.841**(0.036)
$I_T^{Flex-Ext}$	0.361(0.482)	0.522(0.288)	**0.923**(0.009)
$I_T^{Abd-Add}$	0.361(0.482)	0.522(0.288)	**0.923**(0.009)
$I_T^{Int-Ext}$	0.191(0.717)	0.441(0.382)	**0.828**(0.042)
$I_C^{Flex-Ext}$	-0.047(0.930)	0.184(0.727)	**0.868**(0.025)
$I_C^{Abd-Add}$	-0.045(0.933)	0.184(0.727)	**0.867**(0.025)
$I_C^{Int-Ext}$	0.257(0.624)	0.412(0.418)	**0.828**(0.042)
$I_F^{Flex-Ext}$	0.195(0.712)	0.454(0.365)	**0.993**($<10^{-3}$)
$I_F^{Abd-Add}$	0.232(0.659)	0.456(0.363)	**0.980**($<10^{-3}$)
$I_F^{Int-Ext}$	0.128(0.810)	0.386(0.450)	0.684(0.134)

Table 1: Linear correlation (r) and significance (p) of anthropometric values with SJ, CMJ and DJ (h_t).

Discussion

Statistical significative linear correlations of lower limb anthropometric measures, regression mass and moments inertia were detected only with MVJ performance at DJ.

References

1. Zatsiorsky, VM, Kraemer, WJ, "Science and Practice of Strength Training", Human Kinetics, Champaign, 2006.
2. Komi et al, Portuguese J Sport Sc., 11(2):31-34, 2011.
3. Asmussen, E, Acta Physiol. Scand., 91(3):385-392, 1974.
4. Rodrigues et al., "Assessment of the relation of force development with body weight at different standard maximum vertical jump", Proceedings of DCE2019.
5. Vaughan, CL, Davis, BL, O'Connor, JC "Dynamics of Human Gait", Kiboho Publishers, Cape Town, 1992.

SHOULD ROBOTIC-ASSISTED TKA RECONSTRUCT PREMORBID STAGE? THE EFFECTS OF OSTEOPHYTES ON KNEE FUNCTIONALITY

Periklis Tzanetis (1), Kevin de Souza (2), Seonaid Robertson (2), René Fluit (1), Bart Koopman (1), Nico Verdonschot (1,3)

1. Department of Biomechanical Engineering, University of Twente, Enschede, The Netherlands; 2. Stryker, Manchester, United Kingdom 3. Orthopedic Research Laboratory, Radboud Institute for Health Sciences, Radboud University Medical Center, Nijmegen, The Netherlands

Introduction

One of the challenges in total knee arthroplasty (TKA) is to restore function of the arthritic knee. Robotic-assisted surgery has been shown to be highly accurate in the postoperative alignment of prostheses [1], but the question becomes where the components should be positioned in order to achieve restoration of the premorbid joint state. Precise knowledge of premorbid kinematics and ligament loading is important for pre-planning an optimal alignment scheme, thereby reproducing a balanced knee motion comparable to healthy individuals. The aim of this study was to investigate differences in tibiofemoral kinematics and ligament loads between arthritic knees and their corresponding premorbid state, using a novel approach combining imaging-based statistical modeling and musculoskeletal simulation.

Methods

A template cadaver-specific musculoskeletal knee model was developed in the AnyBody Modeling System (AnyBody Technology A/S, Aalborg, Denmark) based on computed tomography (CT) and magnetic resonance (MR) images of a cadaveric lower extremity specimen. This is a force-dependent kinematics model, following a previously established methodology [2]. To scale the model to a patient-specific morphology, CT images of three individual patients with different severity of knee osteoarthritis were segmented with a custom developed research tool (Stryker, Manchester, UK), whereby a statistical model of shape and appearance identified the arthritic and premorbid femoral and tibial bone surfaces; a statistical shape model trained on MR data to estimate cartilage thickness from the bone surface segmented in CT. Disease severity was classified as mild, moderate, and severe based on the osteophyte volume around the distal end of the femur (Figure 1). Differences between arthritic and premorbid model predictions were quantified in terms of root mean square deviation (RMSD) during an unloaded extension simulation.

Results

Compared to the arthritic model, the premorbid model predicted tibiofemoral kinematics with an RMSD greater than 0.3 mm and 0.5 degrees over all patients. The largest RMSD in kinematics was found in tibial external rotation (2.7 degrees) and anterior tibial translation (1.5 mm) in the patient with severe knee osteophytes (Table 1). Both cruciate and collateral

ligament load predicted deviations were highly similar regardless of the osteophyte severity and lower than 64 N and 34 N, respectively, among patients.
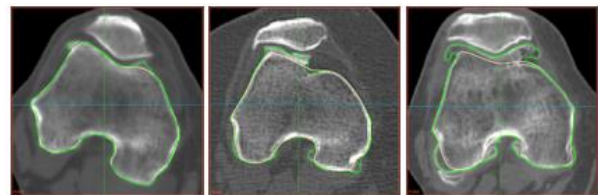
Figure 1: Axial view of CT scans identifying osteophyte formation around the distal femur (green line). From left to right: patient 1 (mild), patient 2 (moderate), and patient 3 (severe).

Patient ID	Disease severity	External rotation (deg)	Anterior translation (mm)
P1	mild	1.2	0.7
P2	moderate	1.7	0.9
P3	severe	2.7	1.5

Table 1: RMSD prediction of knee kinematics during an unloaded extension simulation from 90 to 0 degrees.

Discussion

Severe osteophyte formation substantially altered the kinematic predictions in the premorbid knee. The reported kinematic differences are larger than the accuracy attained by Mako total knee system [3]. Osteophytes slightly affected ligament function, but this warrants further investigation in relation to osteophyte location. The proposed methodology enables preoperative kinematic and ligament load analysis based on premorbid knee joint surface reconstruction and can assist orthopedic surgeons towards an optimally planned TKA, thereby maximizing the utilization of robotic-assisted surgery.

References

1. Agarwal et al, J Arthroplasty, 35:3393-3409, 2020.
2. Skipper et al, J Biomech Eng, 139:091001, 2017.
3. Sires et al, J Knee Surg, 34:745-748, 2021.

Acknowledgements

PATIENT SPECIFIC GROWTH MODEL FOR CRANIOSYNOSTOSIS

Maya Geoffroy (1,2,3), Meryem Abbad Andaloussi (1), Pierre-Marc François (2), Roman Hossein Khonsari (3), Sebastien Laporte (1)

1. Arts et Métiers Institute of Technology, Université Paris Nord, IBHGC – Institut de Biomécanique Humaine Georges Charpak, HESAM Université, France ; 2. BONE 3D, France ; 3. Service de Chirurgie Maxillofaciale et Chirurgie Plastique, Hôpital Necker – Enfants Malades, Assistance Publique – Hôpitaux de Paris; Faculté de Médecine, Université de Paris, France

Introduction

Non-Syndromic Craniosynostosis (NSCS) are rare conditions (1/2500) cases [1]) of unknown origin, caused by the premature fusion of one or more skull vault sutures. In theory, a compensatory growth occurs perpendicularly to the fused suture leading to the predictable deformations of the vault [2]. However, clinical observations often contradict classical theories and the role of many anatomical units is not well understood. Finite Element models can be used to study growth and analyse various factors [3,4]. The aim of the present study was to develop a validated patient-specific model to analyse the influence of anatomical variability on skull growth of NSCS.

Material and Methods

A generic model was developed as an ellipsoid defined by length, width and height, sectioned along the Frankfurt plane (Fig 1).
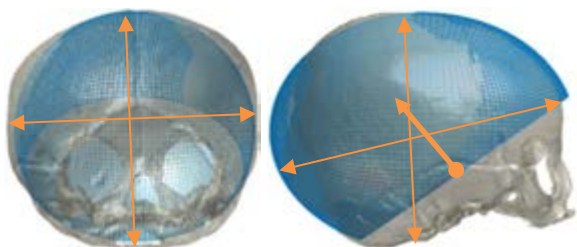
Figure 1: Skull of a 52 days old patient and its modelled geometry (blue) from the morphometry data (orange).

Bone thickness and material properties were provided by literature [5]. Growth was modelled from 0 to 2 years old, as an uniform pressure on the internal vault surface. A normal growth model was first developed and evaluated based on literature morphological data [6]. The NSCS model was developed by defining the affected suture as bone, as proposed in literature [7]. This model was evaluated using geometric data from three NSCS patients (Table 1) who had CT-scans at two different ages to validate the abnormal growth and skull deformation.

Table 1: Evaluation data for the NSCS growth model.

Reference	Sex	Initial age (days)	Final age (days)
Patient 1	F	160	338
Patient 2	M	3	289
Patient 3	M	137	263

The patient-specific growth model then enabled to conduct an influence study by modifying the suture width growth from birth, bone thickness and degree of fusion of the impacted suture (for NSCS models only) from values found in newborns to 2 year olds [8,9] (respectively 5 to <1mm, 1mm to 6mm, 0 to 30, 50 and 100%).

Results

Length, width, circumference, and overall shape of the normal skulls after growth were consistent with what was found in literature. Data from NSCS patients with repeated CT-scans available at 2 ages showed that the shape obtained could be improved. Material properties and bone thickness had a combined effect on the strain, with maximum values along the limits of the metopic suture. The influence study further showed how the increased degree of fusion, increased bone thicknesses and narrower sutures lead to more severe forms of NSCS.

Discussion

The proposed growth models of the cranial vault had a simplified geometry and shows the difficulties of correctly portraying the physiologically complex mechanisms. The strains obtained in the influence study were coherent with sutural growth mechanisms and sites. CT-scans cannot be repeated in children without clear clinical indications due to irradiation: limited pediatric geometrical data are available for model validation. Future work is necessary to include sutural growth to the model.

References

1. Cohen et al, AM J Med Genet, 47:581-616, 1993.
2. Panchal et al, Plast Reconstr Surg, 108 :1492-8, 2001.
3. Jin et al, J Korean Neurosurg Soc, 59 :192-6, 2001.
4. Weickenmeier et al, Phys Rev Lett, 118:1-5, 2017.
5. Coats et al, J Neurotrauma, 23 :1222-23, 2006.
6. Loyd et al, sae Tech Pap, 54 :167-96, 2010.
7. Margulies et al, J Biomech Eng, 122 :364-71, 2000.
8. Li et al, PLos ONE, 10, 2015.
9. Mitchell et al, Pediatrics, 32 :1801-5, 2011.

Acknowledgements

VERTEBRAL STRENGTH PREDICTION FROM SINGLE ENERGY BIPLANAR RADIOGRAPHS

Cecile Heidsieck (1), Laurent Gajny (1), Jean Yves Lazennec (2), Chistophe Travert (1, 2), Wafa Skalli (1)

1. Arts et Métiers Institute of Technology, Institut de Biomécanique Humaine Georges Charpak, Paris, France
2. Department of Orthopaedic and Traumatological Surgery, Pitié-Salpêtrière Hospital Group, Paris France

Introduction

Vertebral fractures associated with osteoporosis are a significant risk factor for the development of future fragility fractures [1]. Areal bone mineral density (aBMD) measurement by dual-energy x-ray absorptiometry (DXA) is the gold standard for assessing fracture risk, but has low sensitivity [2]. Personalized finite element models (FEM) have been investigated to improve fracture risk prediction. Quantitative computed tomography (qCT) based FEM can provide a validated estimation of vertebral intrinsic strength [3] but are performed in a supine position. Postural changes observed with age are not assessed by CT scan FEM but are a significant risk factor for the occurrence of fractures [4] and are associated with decreased strength [5]. Biplanar radiographs allow simultaneous head to feet lateral and frontal radiographs in the standing position and promising results were obtained with a dual energy X-rays based FEM [3]. However, the dual energy technology is not yet used in clinical routine. The purpose of this study is to evaluate strength estimation from a single energy biplanar X-rays based FEM, in comparison with a validated qCT-based FEM [3].

Materials and methods

Fourteen L3-L4 vertebrae from cadaveric specimens (mean age 60, standard deviation (SD) 7) were included in the study. CT scan (iCT256, Philips Healthcare, Netherlands) and low dose biplanar X-Rays (EOS, EOS imaging, France) images of the specimens were acquired alongside a calibration phantom (Electron density phantom, CIRS, USA), allowing the conversion to equivalent bone density. The single energy biplanar X-rays based FEM was built from 3D reconstruction performed on the EOS images [6]. Then, a generic distribution of volumetric densities was applied to the mesh and projected to generate a virtual lateral image. The real EOS lateral image was converted in equivalent bone densities. A scaling factor was computed from the comparison between the virtual and the real lateral images. This factor was then applied to adjust the densities of the model. For comparison, a CT scan-based FEM was built from semi-automatic segmentation and material properties were assigned from the volumetric BMD calibrated CT images [3]. Densities were then converted to mechanical properties for both models [7]. Vertebral strength in anterior compression was computed on each model.

Results

The mean failure load for the qCT-based FEM and the single energy biplanar X-rays based FEM were 4912N (SD 1352N) and 5043N (SD 1374N) respectively.

From linear regression analysis, the coefficient of determination (R²) and the root mean squared error (RMSE, %) of the single energy biplanar X-rays FEM strength against the qCT-based FEM strength were 0.84 (RMSE 11%). A similar analysis was performed on the specimens from [3] evaluating aBMD against qCT-based FEM strength giving the following results: 0.78 (RMSE 21%).

Bland and Altman analysis is plotted in figure 1.
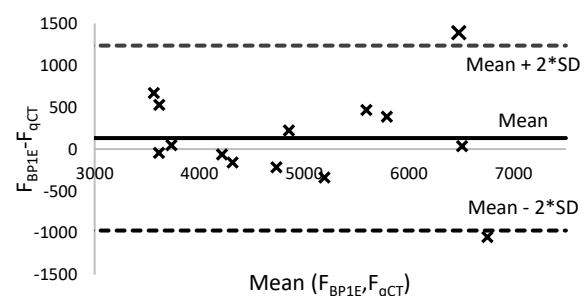
Figure 1: Bland and Altman plot between strength determined by qCT-based FEM strength (F_{qCT}) and by single energy biplanar X-rays FEM strength (F_{BP1E}).

Discussion - Conclusion

From the results, routine single energy biplanar X-rays based FEM appears to be a better predictor of simulated vertebral strength from qCT based FEM than aBMD from DXA, with the major advantage of acquisition in standing position. Although, results were not assessed against experimental data, the qCT-based FEM used for evaluation showed excellent estimation of experimental vertebral strength [3]. In addition, the number of specimens is low, but this preliminary in vitro assessment looks promising as a proof of concept. In vivo research is underway for a routine estimation considering both the intrinsic vertebral strength and the potential postural trouble.

References

1. Roux et al., Osteoporos Int, 18:1617-24, 2007.
2. Cosman et al., Osteoporos Int, 28:1857–1866, 2017
3. Choisne et al., J. Mech Behav Biomed, 87, 190–196, 2018.
4. Lin et al., Spine J. 21(8), 1362–1375, 2021.
5. Heidsieck et al, Osteoporos Int, 2021.
6. Humbert et al, Med Eng Phys, 31:681–687, 2009.
7. Kopperdahl et al., J Orthop Res., 20(4):801-5, 2002

Acknowledgements

LUMBAR INTERVERTEBRAL DISC 3D SEGMENTATION FOR BIOMECHANICAL SIMULATION

R. Matos (1), P. R. Fernandes (2), N. M. P. L. Matela (3), A. P. G. Castro (2, 4)

1. Faculdade de Ciências da Universidade de Lisboa, Portugal; 2. IDMEC, Instituto Superior Técnico, Universidade de Lisboa, Portugal; 3. Instituto de Biofísica e Engenharia Biomédica, Faculdade de Ciências da Universidade de Lisboa, Portugal; 4. Escola Superior de Tecnologia de Setúbal, Instituto Politécnico de Setúbal, Portugal

Introduction

Intervertebral disc (IVD) degeneration is one of the conditions associated with lower back pain. Image segmentation of IVD for clinical purposes is usually done manually from selected MRI sagittal slices; this is time and labor-intensive and provides limited information [1]. In 2016, Zhu et al. [2] developed a 2D IVD segmentation method for MRI based on Gabor filters. In this paper, we propose a 3D segmentation method based on Zhu et al.'s method, aiming for more accurate models for biomechanical simulation.

Methods

Gabor filters were used to extract vertical and horizontal features from sagittal slices of the spine. Data was retrieved from [3]. This allowed the semi-automatic detection of the spine curves, which were used to detect the regions containing the IVD. The 2D profiles of the IVD were segmented in the detected regions through grayscale thresholding. The annulus fibrosus (AF) and nucleus pulposus (NP) were segmented as separate structures, to allow for the accurate constitutive modeling of each tissue. 3D data was obtained by running the 2D method through an interval of slices and adjusting the spine curves accordingly.

The segmentation interval in each slice were given by statistical models generated from ground-truth manual segmentations of vertebral bodies. MRI images from 18 spines were used to generate the statistical models, and 3 other spines were used to test the method's accuracy. IVD intensity and proportion of NP/AF were compared to the average values in each spine to automatically attribute a binary healthy/degenerated classification. An IVD was considered degenerated if it could be visibly classified as grade III-V in the Pfirrmann scale [4]. The segmentation method's accuracy was evaluated through its Dice coefficient, sensitivity and specificity using manually segmented ground-truth data for comparison.

Results

The method showed average values of 87%, 82% and 98% for the Dice coefficient, sensitivity and specificity, respectively. This is within the range of existing 3D IVD segmentation methods in the literature (81-92%). In addition, this method correctly identified 65 of 68 (96%) IVDs as either visibly healthy or degenerated. The method took on average 6-7 secs to perform a full 3D segmentation, which is within the range of existing methods (2 secs – 19 min). [1] Figure 1 shows an example of a model obtained with this method.
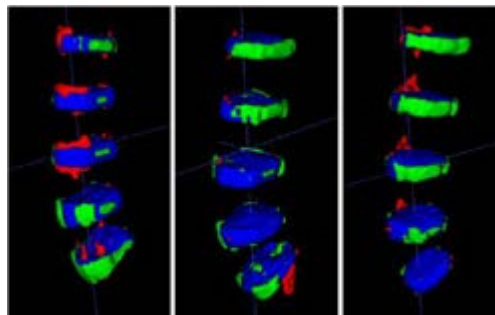
Figure 1: 3D segmentation results. Ground-truth in green, segmentation results in red, intersection in blue

Discussion

The relatively low sensitivity and high specificity of this method suggest that most of the segmentation error comes from under-segmentation, which in turn seems to be caused by the statistical model's excessive adjustments to the spine curves. However, the low sample size means the method would have to be tested with a wider database. The statistical models were generated from segmentation masks, which increases the possibility of cumulative error; new statistical models could be generated from vertebral CT data.

The method for identifying IVD degeneration successfully compared each IVD to all other IVD in the same spine, assuming the degenerated IVD are in lower number. Despite the method's 96% accuracy with the test data, it is still not able to distinguish specific grades of degeneration, leading to a certain ambiguity in borderline degeneration cases. These limitations will be addressed in future work, but it must be highlighted that this method can already generate enhanced 3D models for patient-specific biomechanical simulation.

References

1. Zheng et al, Medical Image Analysis, 35:327–344, 2017
2. Zhu et al, BioMedical Engineering OnLine, 15(1):32-47, 2016
3. Chu et al, PLOS ONE, 10(11):e0143327, 2015
4. Pfirrmann et al, Spine, 26(17):1873–1878, 2001

Acknowledgements

EFFECT OF INSTRUMENTATION INACCURACIES ON BIOMECHANCIAL AND COMPUTATIONAL FAILURE RISK OF FRACTURE FIXATIONS

Dominic Mischler (1), Lara Tenisch (1), Jana Felicitas Schader (1), Jan Dauwe (1,2), Boyko Gueorguiev (1), Markus Windolf (1), Peter Varga (1)

1. AO Research Institute Davos, Switzerland, 2. University Hospital Leuven, Belgium

Introduction

Despite existing advanced implant systems, complication rates of the fixation of complex fractures such as in the proximal humerus remain high [1,2]. These may be related to the sub-optimal quality of the surgical procedure, including fracture reduction and implant positioning, leading to a deviation from the planned state. Similarly, in computational validation studies, small deviations between experiments and models might be a confounding factor. Therefore, the aims of this study were to quantify the accuracy of a standardized and guided instrumentation process, its influence on the biomechanical outcome, and the related predictive power of computational simulations.

Material and Methods

Eight pairs of low-density proximal humerus samples from elderly female donors (age: 85.2 ± 5.4 years, range: 73–91 years) were scanned with high resolution peripheral quantitative computed tomography (HR-pQCT) scanner (XtremeCT). Preoperative planning, including osteotomizing to mimic an instable 3-part fracture and positioning of a locking plate with six proximal screws, was performed by an experienced surgeon on the scans via a custom-developed and semi-automated workflow in Amira. Finite element (FE) simulation of the planned instrumentation (FE-Plan) was performed in Abaqus to predict the failure risk of each sample using an established approach and the peri-screw bone strain being a validated measure for cut-out failure [3]. The bone samples were osteotomized and instrumented with specimen-specific 3D-printed guides with design based on the pre-OP planned configurations. Following, post-OP CT scans were acquired. Instrumentation accuracy in terms of screw lengths and orientations was determined by comparing the planned with the post-OP CT-based configurations. Another set of FE models was generated based on the post-OP CT scans to simulate the experimentally realized fixations (FE-Real). The bone-implant constructs were biomechanically tested under progressively increasing cyclic loading until cut-out failure of the head fragment [3]. The predictions of both FE-Plan and FE-Real were correlated with the experimental data to investigate predictive power.

Results

Slight deviations compared to the planned configuration were detected for screw trajectories in the proximal-distal ($0.3 \pm 1.3°$, range: -2.5–3.9°) and anterior-posterior directions ($-1.7 \pm 1.8°$, range: -5.5 – 4.7°), and

for screw tip to joint distances (-0.3 ± 1.1 mm, range: -3.1–2.2 mm); the latter was caused mainly by the 2 mm increments in commercially available screw lengths. Significantly higher peri-screw bone strains were registered for the FE-Real (514 ± 89 μmm/mm, range: 343–654 μmm/mm) compared to the FE-Plan models (414 ± 67 μmm/mm, range: 285–516 μmm/mm), $p < 0.01$ (n = 18). One sample had to be excluded experimentally. The number of cycles to failure did not correlate with FE-Plan results but demonstrated strong correlation with FE-Real predictions ($R^2 = 0.70$, n = 17).
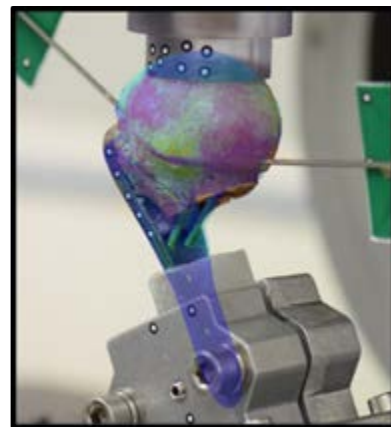
Conclusion

Using specimen-specific 3D-printed guides, the instrumentations could be performed with high accuracy. Nevertheless, even minor deviations significantly increased the predicted failure risk in the FE simulations. This underlines the importance of advanced intraoperative navigation technologies [4] to assist the surgeons in accurately achieving the pre-OP plans, that in turn are expected to help lowering complication rates. Moreover, these findings indicate the need for incorporating exact details into FE modeling to accurately predict experimental results, which is particularly important for validation studies.

References

1. Kralinger et al., J Bone Joint Surg Am, 96; 1026-32, 2014.
2. Panagiotopoulou et al, Injury, 50:2176-95, 2019.
3. Varga et al., J Mech Behav Biomed Mater, 75:68-74. 2017.
4. Windolf and Richards, J Med Device, 15:025002, 2021.

Acknowledgements

TOWARDS A REPOSITORY OF PATIENT-SPECIFIC INTERVERTEBRAL DISCS FINITE ELEMENT MODELS

Estefano Muñoz-Moya, Morteza Rasouligandomani, Carlos Ruiz Wills, Gemma Piella, Jérôme Noailly

BCN MedTech, Department of Information and Communication Technologies, Universitat Pompeu Fabra (UPF), Barcelona, Spain

Introduction

Numerical analysis methods, such as Finite Element Analysis (FEA), have been widely used to study the biomechanics of human tissues and organs. However, patient-specific (PS) model creation usually requires complex procedures that are difficult to automatize in some instances. For example, in spine computational studies, intervertebral disc (IVD) modeling requires structural meshing, as the synchronized mechanical behavior of specific tissue domains needs to be explored under large deformations [1]. Multiple studies related to IVD degeneration (DD) have been carried out using FEA, but a repository of IVD PS models has not yet been created to explore in-depth PS particularities, e.g., as hypothesized in [2]. A significant challenge is the ability to map different tissue regions, such as the Cartilage Endplate (CEP), Annulus Fibrosus (AF), Nucleus Pulposus (NP), and the Transition Zone (TZ) in PS IVD shapes. Such mapping can provide further information about the influence of the CEP on DD combined with the effects of different sets of diffusion distances from the peripheral vasculature to the NP [1]. This work aims to generate a repository of PS finite element meshes of IVD models with the same mesh connectivity and different geometries of the external surface and its internal components for systematic mass FEA.

Methods

Using T2-weighted magnetic resonance images, 176 PS IVD models were obtained through 3D segmentation, acquired during the European project My Spine (FP7-269909) [3]. Segmentations included the AF and NP. The Bayesian coherent point drift (BCPD) algorithm was used to non-rigidly align the meshes [4]. This code fits a point cloud of a source mesh (template) to a target mesh (segmentations). In this way, a pre-existing structural mesh of an IVD [1] was adapted to the PS models.

The external surfaces of the AF and NP were represented by point clouds, which were used as targets. The morphing process of the template was carried out in three stages. First, the AF and the NP surfaces were adapted. Then, the results were merged into a single point cloud, used as a target, for the final fitting of the complete volumetric mesh of the template. The CEPs, not visible in the images, were automatically recreated, with a thickness between 0.7 and 1 mm. The development of the second stage preserved the surface area initially covered in the IVD. Mesh quality of the morphed models and Euclidean distance between the morphed and the target were checked to ensure a good quality of the elements.

Results

A repository of 176 PS IVDs finite element meshes with the same connectivity was created following the abovementioned method (Figure 1). Regarding mesh quality, the average criteria limits of all morphed IVDs were: Min and Max angle on Quad Faces (<10 and >160) were less than 0.2 and 0.8 % of the total elements, respectively. The Hex elements that exceeded the Aspect Ratio criteria limit (>10) were less than 6% of the total elements. Quad elements were not impaired under these criteria.
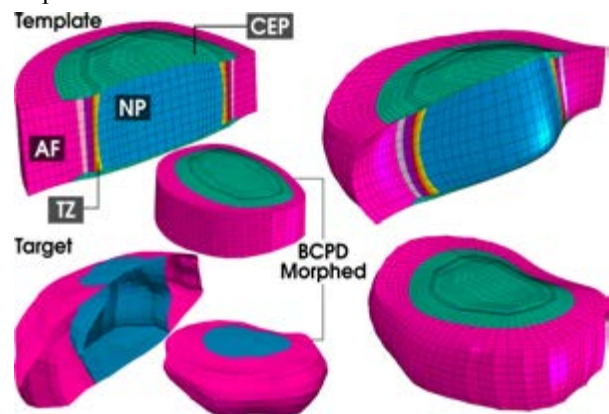
Figure 1: Target, Template, and Morphed disc using Bayesian coherent point drift. CEP, AF, NP, and TZ are represented.

Discussion

This repository is a unique set of model collections to explore the effect of multiple geometrical variations on the IVD multiphysics and mechanobiology, including the likely substantial impact of the CEP [2]. Although the template elements tend to deform and impair their mesh quality, they are not close to the CEP. The algorithm can generate PS FE models from any segmented surfaces third parties provide. The database will be used to train a metamodel of FEA outcomes.

References

1. Ruiz, C. et al. (2018). Theoretical Explorations Generate New Hypotheses About the Role of the Cartilage Endplate in Early Intervertebral Disk Degeneration. Frontiers in Physiology.
2. Malandrino, A. et al. (2015). On the Relative Relevance of Subject-Specific Geometries and Degeneration-Specific Mechanical Properties for the Study of Cell Death in Human Intervertebral Disk Models. Front. Bioeng. Biotechnol.
3. Castro-Mateos I et al. (2014). 3D segmentation of annulus fibrosus and nucleus pulposus from T2-weighted magnetic resonance images. Physics in Medicine & Biology.
4. O. Hirose. (2021) "A Bayesian Formulation of Coherent Point Drift," in IEEE Transactions on Pattern Analysis and Machine Intelligence.

Acknowledgements

MODELLING STRATEGIES FOR ORTHOGNATHIC SURGERY: MECHANICAL OPTIMIZATION OF PATIENT-SPECIFIC PLATES

Ilaria Rota (1), Andrea Giglio (1), Francesco Grecchi (2), Matteo Bonacina (3), Dario Gastaldi (1)

1. Politecnico di Milano, Department of Chemistry, Materials and Chemical Engineering, Italy;
2. IRCCS Orthopedic Institute Galeazzi, Italy; 3. Ars&Technology Srl, Italy

Introduction

Le Fort I osteotomy is a straightforward and flexible surgical procedure performed to correct specific maxillofacial deformities and malocclusions. During the surgery, titanium plates and screws are used to fix the correct position of the maxilla [1].

Modern additive manufacturing processes (i.e. LPBF or EBM) allow the creation of patient-specific devices with complex geometry in titanium alloy-medical grade. Their advantage is the possibility to develop innovative devices for maxillofacial surgeries with anatomic-based geometry and ad hoc surface features design [2].

This study exploits the numerical modelling of an orthognathic surgery case to support the design of plates. The aim of the work is to optimize the plate design through the prediction of stress distribution with a numerical FE model in static and cyclic loading conditions.

Methods

An orthognathic case, in which the patient undergone to a Le Fort I osteotomy surgical treatment, was investigated.

The model is reconstructed starting from the CT-images of the maxillofacial bone segments. The complete case includes two zygomatic implants and two plates (with fixation screws).

Material properties of the bone were set using Bonemat [3] which maps the elastic modulus over the 3D mesh (Figure 1), adopting the relationships between Young modulus and grey-values of the CTs throughout the bone density.

Mechanical properties of the LPBF-titanium adopted for implants and plates were characterized by uniaxial tests and indentation protocols. Homogeneous and isotropic material properties (E=107 GPa, ν=0.34, σ_y=1025 MPa) were assigned to plates and zygomatic implants.
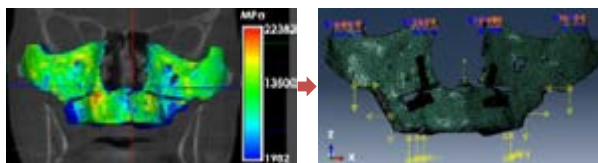
Figure 1: Elastic modulus distribution of bone and FEM with loading and boundary conditions.

Loading and boundary conditions were applied to replicate the physiological conditions of the occlusion. An occlusive load, muscular forces of masseters, lateral and medial pterygoids were imposed (Table 1), while the upper bone were fully constrained (Figure 1).

Different plate designs were simulated to identify the minimum thickness which satisfies the tradeoff between biomechanical compatibility and mechanical reliability under static and cyclic loading.

Direction	Occlusion (N)	Masseter (N)	Pterygoids (N)
X	0	±62	±193
Y	-108	126	71
Z	63	-265	-151

Table 1: Occlusive and muscular forces.

Results

Von Mises stress distribution of the preliminary plate design with a focus on the elements that exceed the yielding stress of the material is shown in Figure 2. As can be observed, there is a small yielding zone. This area was identified and properly thickened to ensure the stress values remain under the elastic limit which define the condition for the static reliability.

A prediction of the fatigue life has been obtained adopting the Matake fatigue criterion implemented with the results of the FE model.
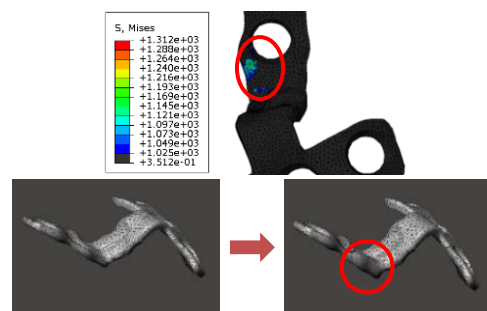
Figure 2: Von Mises stress of a plate and thickening of the yielding zone.

Discussion

Simulating the patient-specific biomechanical context of the surgical procedure, static and fatigue resistance prediction were obtained. The numerical modelling allowed the definition of a strategy for the optimization of the patient-specific plate design to achieve an appropriate mechanical reliability.

References

1. Grecchi et al, Journal of Cranio-Maxillofacial Surgery, 2021.
2. Seebach et al, Journal of Medical Devices, 15.2: 021004, 2021.
3. Taddei et al, Med Eng Phys, 29.9:973-9, 2007

USING CARBON FIBER CUSTOM DYNAMIC ORTHOSES TO PREVENT POST-TRAUMATIC ANKLE OSTEOARTHRITIS

Kirsten M. Anderson, Molly A. Corlett, Jason M. Wilken, Donald D. Anderson

University of Iowa, United States of America

Introduction

Post-traumatic osteoarthritis (PTOA) develops after a joint injury, affects millions worldwide, and results in billions of dollars in healthcare expenditures annually.[1] PTOA risk of after an ankle intra-articular fracture is correlated with chronic contact stress elevation.[2] Carbon fiber custom dynamic orthoses (CDOs) have reduced pain and improved mobility in individuals with traumatic lower limb injuries.[3] However, little is known about the effects of CDOs on muscle forces, joint reaction forces, and intra-articular contact stress. The purpose of this study was to combine weight bearing CT (WBCT), gait analysis, and computer modeling to determine the effects of CDOs in this context.

Methods

An Institutional Review Board approved this study, and informed consent was obtained prior to the study. A 40-year-old male (1.84m, 97.9kg) with an intra-articular fracture one year prior was enrolled for study. Three CDOs of different designs and stiffnesses were tested in a random order (Figure 1). CDOA: PhatBrace 1.0 (5.7Nm/°). CDOB: PhatBrace 2.0 (7.5Nm/°). CDOC: PhatBrace 2.0 (4.4Nm/°). WBCT images were acquired

Figure 1: The three study CDOs are shown here.

for use in computing ankle contact stress. A certified prosthetist orthotist cast and fit the subject for the CDOs. Gait analysis was performed under each condition using 12 infrared motion capture cameras (120Hz, Vicon Inc) and three force plates (1200Hz, AMTI Inc) embedded in the floor as the subject walked at a controlled speed. Kinematic and kinetic data were low-pass filtered in Visual 3D (C-Motion Inc) and scaled to subject height and mass. Gait was simulated in OpenSim v4.0 (SimTK.org) using the Gait2392 model, with 23 degrees of freedom and 92 musculotendon actuators. Virtual CDOs, representing those tested, were added to the model by applying a Coordinate Limit Force to the ankle acting about the flex-extension axis. OpenSim provided estimates of the muscle forces needed to replicate gait kinematics and kinetics and to compute the associated joint reaction forces. Discrete element analysis was then used to estimate tibio-talar contact stress during the stance phase of gait.[4]

Results

Peak soleus muscle force decreased with CDO use compared to walking with NoCDO (CDOA 30.47%, CDOB 34.18%, CDOC 44.79% – Figure 2). Joint reaction forces between the tibia and talus also decreased with CDO use (CDOA 16.77%, CDOB 30.13%, CDOC 25.58%). Ankle contact stress correspondingly decreased with CDO use (CDOA 16.18%, CDOB 23.41%, CDOC 19.36%).
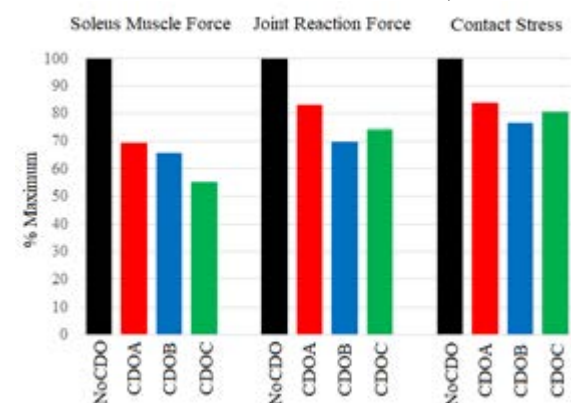
Figure 2: Reductions in soleus muscle force, joint reaction force, and contact stress relative to NoCDO.

Discussion

The data from this first test subject suggest that CDOs can successfully aid in reducing muscle forces and offloading the ankle joint during gait. The musculoskeletal modeling completed in this study demonstrates that CDO design and mechanical characteristics may influence the effects of CDOs on offloading capabilities. Muscle forces, joint reaction forces, and intra-articular contact stress may be meaningfully reduced with CDO use reaching a level consistent with preventing PTOA development.[2]

References

1. Brown et al., J Orthop Trauma 20, 739-44, 2006.
2. Anderson et al., J Orthop Res 29, 33-9, 2011.
3. Bedigrew et al., Clin Orthop Relat Res 472, 3017-25, 2014.
4. Anderson et al, J Appl Biomech 26, 215-23, 2010.

Acknowledgements

VALIDATION OF AN MRI-BASED PERSONALIZED MODEL OF THE SUBTALAR JOINT

Michele Conconi (1), Alessandro Pompili (1), Nicola Sancisi (1), Alberto Leardini (2), Claudio Belvedere (2)

1. Dept. of Industrial Engineering, University of Bologna, Italy; 2. Istituto Ortopedico Rizzoli, Bologna, Italy

Introduction

Personalization of biomechanical models is receiving increasing attention, in the attempt to increase their effectiveness and their clinical impact. Recently, we shown the impact of different personalization strategies of the ankle joint on musculoskeletal model outputs: the higher the personalization the more consistent the model will be to the patient anatomy [1]. In this work we want to validate a model that predict the individual motion of the subtalar joint from an MRI representation of the articular surface. The model, previously validated on the knee [2] and ankle [3], reconstructs the kinematics by optimizing the contact pressure distribution, evaluated by a measure of joint congruence [4].

Materials and Methods

We analyzed three feet from cadaver dissection, free from anatomical defects. First, the legs were casted with extended knee, leaving the foot and ankle free to move. The feet were then scanned via Cone Beam CT (fig. 1.c) in 15 positions, varying ankle dorsiflexion among [-30° -10° 0° 10° 20°] and foot supination among [-10° 0° 10°] through a set of wedges (fig. 1.b). The same scans were repeated by applying a vertical load equal to the subjects' half weight (35 kg). CBCT scans were segmented through a semi-automatic procedure (DICE > 95%), for a total of 30 scans. Anatomical reference systems were defined for the neutral foot [5] and registered automatically to those from the other scans (accuracy <0.5° and 0.1 mm). Bone position and orientation were expressed through a cardanic sequence defined for this study (z-y-x). 3T MRI of the feet were also acquired. The bone and cartilage of both talus and calcaneus were segmented and registered to CBCT bone models. Subtalar kinematics were reconstructed imposing congruence maximization through calcaneus inversion/eversion. Computed and experimental motion were compared by computing rotational and translational mean absolute errors (MAE).

Results

On an average range of 25° of inversion/eversion, the rotational and translational MAE for the three feet were 1.16° ± 1.02 and 1.63 mm ± 1.92, respectively.
Figure 1 shows the comparison between predicted and measured subtalar kinematics. Figure 2 shows corresponding envelope of instantaneous helical axes of rotation.
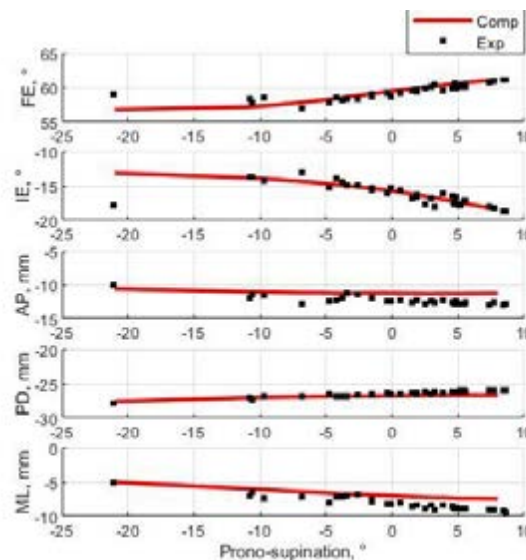
Figure 1: Computed (red line) vs experimental (black dots) subtalar kinematics. Calcaneus flexion/extension (FE), internal/external rotation (IE), anterior/posterior (AP), proximal/distal (PD), and medial/lateral (ML) translations are plotted versus the prono-supinations angle.
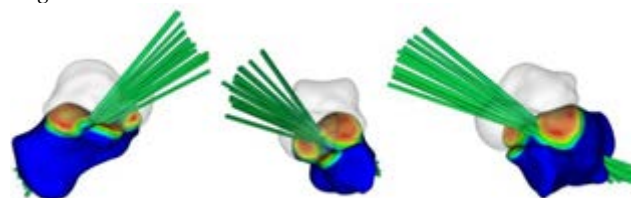
Figure 2: Envelope of instantaneous helical axes (in green) for the motion depicted in figure 1. Talus is shown in transparence while colors on the calcaneus are proportional to the distance from talus.

Discussion

The proposed model shows a remarkable agreement with experimental data. Personalization of articular model through joint congruence maximization appear to be a promising approach for musculoskeletal model of the whole lower limb.

References

1. Conconi et al., Applied Sciences11.18: 8348 , 2021.
2. Conconi et al., IEEE Trans Biomed Eng, 68.3: 1084-1092, 2020.
3. Conconi et al., J Biomech, 48.12: 2960-2967, 2015.
4. Conconi et al., Proc. Inst. Mech. Eng. H: J. Eng. Med., 228.9: 935-941, 2014.
5. Conconi et al., J. Foot Ankle Res, 14.1: 1-13, 2021

INVESTIGATION OF THE EFFECT OF FOOT SOFT TISSUE STIFFENING ON THE PLANTAR CONTACT PRESSURE

Zeinab Kamal*, Edsko E.G. Hekman, Bart G.J. Verkerke
*z.kamal@utwente.nl
University of Twente, 7500 AE Enschede, Netherlands

Introduction

Foot's soft tissue stiffening has been reported as a possible cause of ulceration development[1]. Knowledge of the effect of soft tissue compliance on the stress distribution of the plantar foot surface is essential for devising an appropriate individualized treatment strategy. The effect of different magnitudes of stiffness of the foot's soft tissue on the plantar stresses has not been investigated yet. In this work, it was hypothesized that increased stiffness of the plantar soft tissue can significantly increase the plantar contact pressure. For this purpose, a subject-specific 3D ankle-foot finite element model was constructed and validated against the same patient's data in the midstance phase. The results showed a significant correlation between the stiffness and contact pressure of the foot.

Keywords: Finite element analysis, Gait measurement.

Method

A foot model was created based on one individual's foot CT images (49yrs, height of 160cm, and weight of 67kg) in the neutral posture. The bones and ligaments were considered as rigid bodies [2-5] and linear elastic springs (E=260MPa), respectively[2]. Soft tissue was added, having an elastic modulus E=1.15MPa and Poisson's ratio=0.49)[2]. For the simulation of stiffened tissue, the E-modulus was increased by 50%. The upper surface of the soft tissue, Fibula and Tibia was fully constrained. The interaction between the foot plantar surface and the ground was defined with a frictional coefficient of 0.6[6]. The muscle forces and ground reaction forces (GRF) were estimated using OpenSim and gait measurement, respectively, and applied on the foot FE model as an alternative to the in-vivo loading condition [3].

Results

The force of Lateral gastrocnemius, Medial gastrocnemius, Soleus, Tibialis posterior, Tibialis anterior and Peroneus longus muscle in the midstance phase was found to be 132.2, 537.1, 733.6, 519.1, 71.6 and 8.2N, respectively. The vertical ground reaction force (GRF) was found to be 0.6kN. the horizontal GRF and ground reaction moment (GRM) about the centre of pressure were found to be zero at the midstance phase. A quasi-static analysis was performed on the FE model using Abaqus. Fig.1 shows the results of the contact pressure of the foot model with different stiffness.

Conclusion

A significant compatibility was found between the kinetic results of gait measurement of the patient and the FE model of the foot with normal stiffness. The results of this study predicted a linear association between increasing the contact pressure at the plantar tissue, i.e.
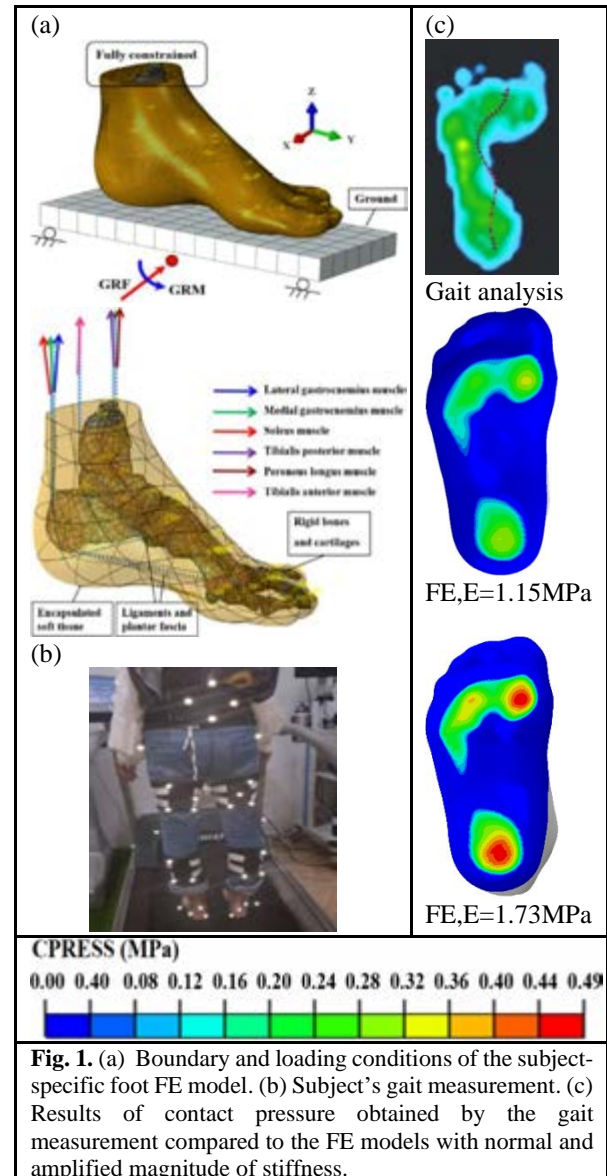
Fig. 1. (a) Boundary and loading conditions of the subject-specific foot FE model. (b) Subject's gait measurement. (c) Results of contact pressure obtained by the gait measurement compared to the FE models with normal and amplified magnitude of stiffness.

47%, and soft tissue stiffening, i.e. 50%, that were formerly reported as symptoms of a diabetic foot with an ulceration [1]. The results suggest that considering changes in soft tissue stiffness seem crucial when diabetes is considered in FE modeling and preventive strategies in the diabetic feet are designed.

References

[1] Naemi et al. J. Diabetes Complicat (2016) 30(7): 1293-1299. [2] Kamal and Rouhi. J Biomech (2020) 111:109997. [3] Kamal and Rouhi. Med Eng Phys (2019) 71:51-63. [4] Kamal et al. Med Eng Phys (2019) 64:46-55. [5] Kamal and Rouhi. J Mech in Med and Biol (2015). 16(2):1-15. [6] Akrami et al. Biomech Model Mechanobiol (2018) 17:559–576.

A COMPARISON OF FOOT MECHANICS BETWEEN AUTOMATICALLY GENERATED PERSONALISED AND SCALED GENERIC SKELETAL MODELS

Erik A Meilak (1, 2), Luca Modenese (3, 4), Caroline Stewart (1, 2)

1. School of Pharmacy and Bioengineering, Keele University UK, 2. ORLAU RJAH Orthopaedic hospital, UK
3. Dept of Civil and Environmental Engineering, Imperial College London, UK, 4. Graduate School of Biomedical Engineering, University of New South Wales, Australia

Introduction

Scaled generic models are widely used to create skeletal models. The alternative of manual characterisation has previously been too arduous to be practical [1,2]. The Shared Tools for Automatic Personalised Lower Extremity (STAPLE) [3] modelling pipeline offers an efficient, automatic alternative to the process of manually characterising personalised skeletal models [3]. The aim of this study was to compare ankle and subtalar joint (STJ) moments between a model automatically characterised from MRI scans using STAPLE and a scaled generic model.

Methods

Previously published segmented tibia, fibula, talus calcaneus and all foot bones geometries [4] were used to automatically generate a personalised skeletal model of the right lower limb with the STAPLE toolbox [3]. A second model was characterized by scaling a generic model available from OpenSim [1]. Idealised marker coordinates were created, compatible with the theoretical models, thus eliminating soft tissue artefact effects. These markers coordinates were derived from Inverse Kinematics (IK) on 6 gait trials using the automatically generated model. The resulting marker coordinates were then used as input to subsequent IK analyses performed using the scaled generic model. Inverse dynamics (ID) analyses were conducted on both models using the IK data and corresponding kinetics data (filtered with a low pass filter of 6 Hz) to assess ankle and STJ moments. Moments derived from both models were normalized over gait cycle and means and standard deviations compared to assess the impact of modelling alone in the absence of soft tissue effects.

Results

Mean peak net ankle joint moments for the automatically generated and generic models were -1.36±0.02 and -1.27±0.01 Nm kg^{-1} respectively, both acting in plantarflexion. However, mean peak net STJ moments between the two models were acting in opposite directions; with the automatically generated and scaled generic models displaying a net mean peak moment of 0.22±0.02 (inversion) and -0.23 ±0.02 Nm kg^{-1} (eversion) respectively (Figure 1).

Discussion

The peak STJ moment calculated with the automatically generated model acted in inversion, agreeing with findings published in the literature [2, 4]. However, for the generic model the peak moment acted in eversion with a 197% difference in value between the two models. Where the STJ axis of the generic model was aligned with the axis of the tibia, the axis in the automatically generated model was characterized with a 40° inclination and 19° deviation medially, explaining the difference in values (Figure 2). Peak ankle joint moments calculated with the automatically generated model were 9% larger in magnitude than those calculated using the generic model, both acting in plantarflexion. For biomechanical analyses of patients with pathologies such as cerebral palsy in which the STJ may be abnormal and its accurate definition essential, the STAPLE pipeline offers an alternative to manually generated personalised and scaled generic models, assuming the segmented bone geometries are available.
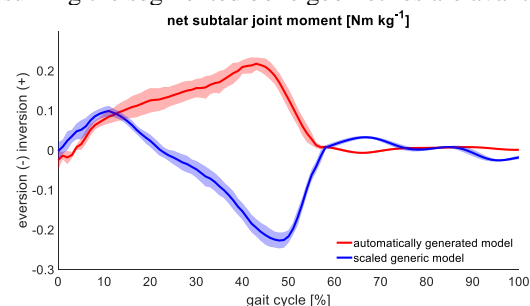
Figure 1: time normalized mean net subtalar joint moments of six gait cycles calculated with automatically generated (red) and scaled generic (blue) models with shadow regions representing ± 1 standard deviation.
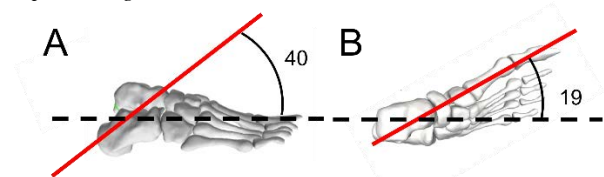
Figure 2: Sagittal view (A) and transverse view (B) of the subtalar axis (red line) on the right foot bones of the STAPLE model. Dotted line represents anterior/posterior axis perpendicular to talocrural axis.

References

1. Delp et al, IEEE Trans Biomed Eng, 54, 1940-1950, 2007
2. Maharaj et al, J Biomech, 92, 29-34, 2019
3. Modenese et al., J biomech, 116, 110186, 2021
4. Montefiori et al, Ann Biomed Eng, 47, 2155-2167, 2019.

Acknowledgements

GENERATING PATIENT GAIT SPECIFIC FINITE ELEMENT MODELS OF THE HAEMOPHILIC ANKLE

Harriet Talbott (1), Richard Wilkins (2,3), Anthony Redmond (2), Claire Brockett (1,2), Marlene Mengoni (1)

1. Institute of Medical and Biological Engineering, University of Leeds, United Kingdom; 2. Leeds Institute of Rheumatology & Musculoskeletal Medicine, United Kingdom; 3. Leeds Haemophilia Comprehensive Care Centre, United Kingdom

Introduction

Altered gait is seen as a consequence of haemarthropathy in the ankle [1,2]. Haemarthropathy presents in around 90% of hemophilic patients who suffer recurrent musculoskeletal bleeds [3]. Structural and functional changes are seen to occur most commonly in the ankle [4]; with significant reduction in joint range of motion (ROM) reported [1,2]. In order to understand the influence of this adapted gait, a method for simulating the hemophilic ankle through patient specific stand phase of gait using finite element models was generated.

Methods

Four hemophilic ankle models were built in Simpleware-ScanIP (Synopsis, 2019) from clinical MRI data (Local Ethical Approval: MEEC 18-022), and a quasi-dynamic simulation run through patient specific heel strike, mid stance and toe off (Abaqus 2017, Dassault Systèmes). The joint angles (JA) and ground reaction forces (GRF) were taken directly from biomechanical analysis of each patient (Local Ethical Approval: MEEC 20-008). The biomechanical analysis was carried out in shoe due to the nature of the disease where barefoot walking is not encouraged. Biomechanical analysis was also carried out on a non-diseased control group, in order to have control JA and GRF to contrast each hemophilic ankle with.

The outputs of interest in the finite element analysis were contact pressure and area in contact for both the tibial and talar cartilage components. Peak and mean values were reported to understand how these changed with each patient's adapted gait.

Results

Biomechanical analysis showed that each ankle had a differing degree of altered gait, with a tendency to plantarflexion (Table 1).

		Non-diseased	A1	A2	A3	A4
HS	JA (deg)	-8.23	-4.92	-8.35	-5.47	-12.60
	GRF (N/kg)	0.922	0.874	1.071	0.847	0.895
MS	JA (deg)	3.44	4.79	5.69	5.60	1.43
	GRF (N/kg)	0.694	0.803	0.657	0.659	0.626
TO	JA (deg)	8.97	10.55	10.00	8.96	8.58
	GRF (N/kg)	1.139	1.026	1.048	1.151	1.275

Table 1: Joint angle (plantar/dorsi-flexion) and GRF at heel strike (HS), mid stance (MS), and toe off (TO).

The finite element outputs of the patient specific gait models, and non-diseased models (Figure 1) indicated that JA influenced area in contact, and contact pressure.
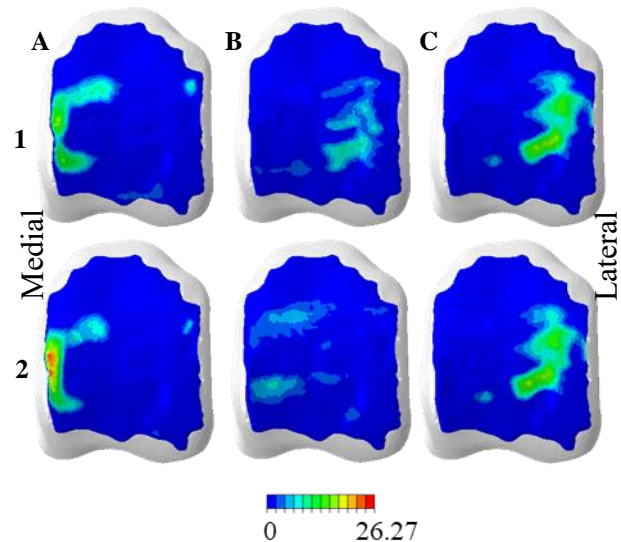
Figure 1: Joint contact pressure (MPa) distribution in the talar cartilage at A) heel strike, B) mid stance and C) toe off, for A4 with 1) non-diseased, and 2) patient specific gait.

Discussion

In this small patient cohort there were varying changes to joint mechanics; the tendency to plantarflexion that is observed clinically was seen in both mid stance and toe-off. Each ankle is at a different stage of joint disease, including A3 and A4 which are bilaterally presenting ankles from one patient.

The adapted gait influenced both the distribution and magnitude of contact pressures. The results indicated a reduction in ROM decreases contact pressures; in turn reducing joint pain and risk of initiating a joint bleed [5].

References

1. Lobet et al., Haemophilia, 16:813-21, 2010.
2. Soucie et al., Blood, 103:2467-2473, 2004.
3. Rodriguez-Merchan, HSS Journal, 6:37-42, 2010.
4. Stephensen et al., Haemophilia, 15:1210-1214, 2009.
5. Buckwalter and Saltzman, Instructional Course Lectures, 48:233-41, 1999.

Acknowledgements

MECHANICAL CHARACTERIZATION OF THE FETAL MEMBRANE AS A BILAYER STRUCTURE

Daniel Fidalgo (1), Dulce Oliveira (1), Kristin Myers (2), Ewelina Malanowska (3), Marco Parente (1), Renato Natal (1)

1. LAETA/INEGI - FEUP, Portugal; 2. Columbia University, United States; 3. Pomeranian Medical University, Poland

Introduction

The fetal membrane has a bilayer structure, comprising two layers: a thick and cellular layer called the chorion, and an interior thin layer named amnion [1]. The chorion acts as an immunological barrier, preventing degradation of the amnion, which dominates the mechanical response of the fetal membrane [1]. The integrity of the fetal membrane is important to avoid preterm delivery [2]. The main goal of this work is to characterize from a mechanical point of view the fetal membrane as a bilayer structure, using computational models. It is also intended to analyze how each layer mechanically responds over the gestational age.

Methods

A finite element setup of an inflation mechanical test was developed in ABAQUS®, following the Skala Lab institution protocol. The membrane comprised three layers: the amnion, the chorion, and part of the decidua. The amnion was characterized by a compressible version of Mazza's constitutive model [2], after performing some adjustments. The chorion and the decidua were characterized by elastic linear properties. Figure 1 represents the finite element setup, which was calibrated by resorting to the Skala Lab data set. After the calibration, the maximum principal stress values were analyzed for the amnion and the chorion layers over the pregnancy gestational weeks, applying the intrauterine pressures listed in Table 1.

Gestational Week	Pressure [KPa]
> 30	1
35	2
40	6,7
Finite Element Analysis (FEA)	10

Table 1: Pressure evolution over the gestational weeks [1].

Results

Figure 2 illustrates the maximum principal stress evolution in the amnion and chorion layers throughout the gestational weeks. The amnion layer exhibits greater maximum principal stress values than the chorion after the 35th gestational week. That discrepancy tends to get more evident as we reach the 40th gestational week when labor is about to occur.
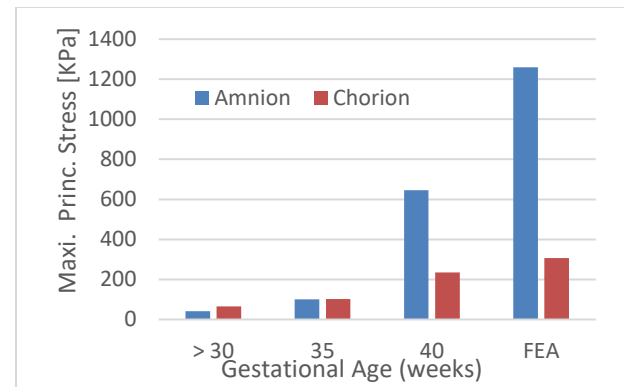
Figure 2: maximum principal stress evolution in the amnion and chorion layers throughout the gestational weeks.

Discussion

The results reported by our study highlight the mechanical dominance of the amnion over the chorion layer [1]. The development of a numerical model able to represent the fetal membrane as a bilayer structure is essential to study a range of questions, such as premature rupture of the fetal membrane, which is often associated with the mechanical contact between the amnion and the chorion.

References

1. Verbruggen et al, PloS ONE, 12(3): e0171588, 2017.
2. Mazza et al, Interface Focus, 9:20190010, 2019.
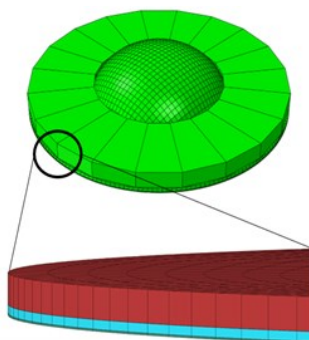
Acknowledgments

Figure 1: Finite element setup of the inflation test; the red layer represents the decidua, the blue one is the chorion, and the thin layer below represents the amnion.

DEVELOPMENT OF A FINITE ELEMENT MODEL TO SIMULATE CHILDBIRTH-RELATED INJURIES

Rita Moura (1), Dulce Oliveira (1), Marco Parente (1), Teresa Mascarenhas (2), Renato Natal Jorge (1)

1. INEGI-LAETA, FEUP, Portugal; 2. CHUSJ, FMUP, Portugal

Introduction

The second stage of labor is widely associated with childbirth trauma. Severe degrees of perineal tears and levator ani muscle (LAM) avulsions can lead to long-term consequences such as incontinence and pelvic organ prolapse [1]. Computational models are reliable resources to quantitatively analyze the physiology of labor [2]. Most reported childbirth computational models focus mainly on the LAM. Literature refers that the superficial perineal structures play a critical role in female birth injuries and must be considered in computational simulations of vaginal delivery [3, 4]. The main goal of this work is to develop a finite element model of the fetal head and female pelvic floor, including the superficial perineal structures and the anal sphincter complex, to simulate the main lesions suffered during childbirth.

Methods

A geometrical model of the fetal head was developed. The cranium was built from a CT scan, and the sutures and fontanelles were design according to the literature and anatomical dimensions. The fetal skin was adapted from the one developed by Parente et al. (2008) [5]. The finite element mesh was created in Abaqus® software (Figure 1). The bones were discretized into S4 shell elements, and the sutures and fontanelles into membrane elements of type M3D4. The fetal skin was meshed with solid elements (C3D4).
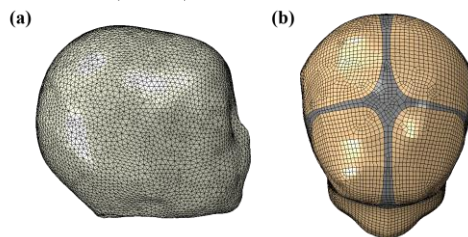
Figure 1 – Finite element model of the fetal head. (a) Lateral view of the fetal head skin. (b) Top view of the skull with sutures and fontanelles.

The geometrical model of the pelvic floor muscles (levator ani and coccygeus muscles) was based on magnetic resonance images (MRI). The geometries were created in Rhinoceros® software and exported to Abaqus®. Posteriorly, and since the superficial perineal structures are very difficult to distinguish in MRI, these were design according to anatomical descriptions and information provided by obstetricians. All the structures were discretized into hexahedral solid elements (C3D8). To validate the finite element model of the fetal head, the compression tests performed by Loyd [6] were replicated in both the anterior–posterior (AP) and right–left (RL) directions. The setup of the simulations was replicated according to the experimental tests. The head was placed between two rigid plates and a displacement of 5.0 mm was applied in the RL compression and 3.2 mm in the AP compression.

Results

The force-deflection curves obtained in the AP and RL compression tests are presented in Figure 2.
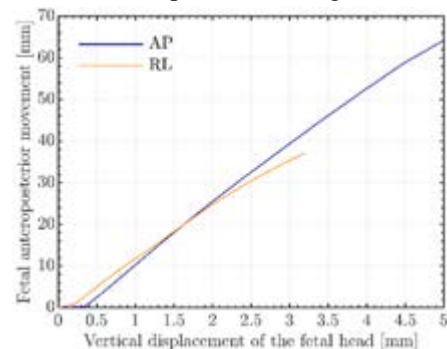
Figure 2 – Force–deflection curve obtained with the AP and RL compression tests of the fetal head model.

In the force-deflection curve of a 1-day-old RL compression test performed by Loyd, a maximum force of approximately 33 N were obtained for a displacement of 3.2 mm. Furthermore, for the AP test of the same sample, a displacement of 5 mm corresponds to a maximum force of approximately 62 N. These results corroborate the ones obtained in the present study.

Discussion

Despite being a widely discussed subject, childbirth trauma remains mainly unpredictable. Although there is already considerable work regarding childbirth simulations, a set of sophisticated computational models is a need. A thorough anatomical representation is essential mainly to assess the origin of specific injuries, determine which risk factors are responsible for these lesions and their severity, and investigate if superficial lesions may be indicative of deeper and non-visible ones. The answer to these questions is crucial to support clinical decisions. Future work consists of performing childbirth simulations with the developed models to analyze the distinct types of injuries.

References

1. Doumouchtsis, Springer, 2016.
2. Hoyte and Damaser, Academic Press, 2016.
3. Routzong et al, Interface Focus, vol. 9, Aug. 2019.
4. Chen and Grimm, J. Biomech. Eng., vol. 143, May 2021.
5. Parente et al, Int Urogynecol J, 19(1):65–71, 2008.
6. Loyd AM. PhD thesis. Durham: Duke University. 2011.

SIMULATION OF FLUID-STRUCTURE INTERACTION OF FLOW IN COLLAPSIBLE TUBES: A SIMPLIFIED MODEL FOR OBSTRUCTIVE SLEEP APNEA

Batool Akbar (1), Sverre Gullikstad Johnsen (2), Paul Roger Leinan (2), Bernhard Müller (1)

1. NTNU, Dept. Energy and Process Engineering, Norway; 2. SINTEF Industry, Norway

Introduction

Obstructive Sleep Apnea (OSA) is a common sleeping disorder which momentarily blocks the airflow in the upper airways, causing breathing to stop during sleep. OSA can lead to significant reduction of sleep quality, as well as more serious health issues [1]. One way of mitigating events of OSA is the use of a continuous positive airway pressure (CPAP) device during the night. Surgical intervention is another mitigation technique. However, medical doctors and surgeons, will in most cases not know if surgery will lead to improving, no change or worsening of the patients' sleep apnea. Researchers have therefore tried to numerically simulate processes in the upper airways as an attempt to get a better understanding of what happens in the airways during sleep apnea, in order to eventually more accurately predict the outcome of surgery.

It is believed that the Venturi effect occurring in the narrow passages in the upper airways is responsible for the onset of OSA. The logic behind this statement is that some parts of the upper airways consist of soft, collapsible tissue and when air flows through these parts, the pressure difference between the inside and outside of the airway can lead to deformation of the soft tissue, making the airway even narrower, eventually leading to collapse. Because there is a strong dependency between the behavior of the tissue and the air flowing through, fluid-structure interaction (FSI) is necessary to be considered when simulating such events numerically. In the current work, two-way FSI simulations have been conducted for a simplified geometry of the upper airways using commercial software.

Method

Two-way FSI simulations of collapse of a flexible tube have been created using ANSYS Workbench 2021 R1. ANSYS Fluent and ANSYS Mechanical are used to solve the governing equations of the fluid and solid, respectively. ANSYS System Coupling is used to transfer data between the fluid and solid domains, creating the partitioned fluid-structure interaction.

The solid was modelled as a hyperelastic material using the Arruda-Boyce model [2]. Initial validation of the solid model was performed excluding the fluid domain. Two airflow scenarios were investigated: 1) initially stagnant flow being displaced by the solid deformation; and 2) constant predefined air flow.

Results and Discussion

The structural model has been compared with experimental and numerical results by Zarandi et al. [3], displaying good agreement. Figure 1 shows the deformation of the solid and fluid after the tube has been exposed to external pressure, when the fluid is initially stagnant (scenario 1). Reasonable qualitative results, in accordance with results by Scroggs [4], have also been obtained when the fluid was given an inlet velocity.

Results to be obtained from these models will give insight into what happens with both the fluid flow and the material in collapsible tubes. Due to the similarity with the upper airways, it is reasonable to believe that trends and results from this model can be translated to the upper airways. Furthermore, once the model has been validated, it will be possible to change the model for it to be more realistic in terms of representing the behavior of the upper airways during OSA. This work forms a basis for ongoing studies on how to use commercial simulation software in the development of computer-aided decision support-tools for patient specific OSA treatment. In the future, we foresee that such tools can be used to evaluate patient specific treatment options. The ultimate goal is to reduce risk and inconvenience for patients and societal costs by providing the optimal treatment.

References

1. Tarek Gharibeh and Reena Mehra. Nature and Science of Sleep, 2:233, 2010.
2. Ellen M Arruda and Mary C Boyce. Journal of the Mechanics and Physics of Solids, 41(2):389–412, 1993.
3. M Amin F Zarandi et al. Computers in Biology and Medicine, 136, 2021.
4. Richard A Scroggs. PhD thesis, University of Sheffield, 2002.
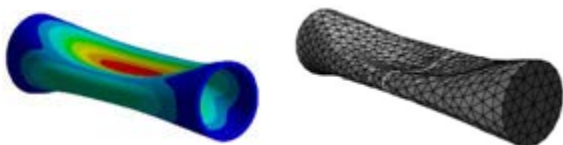
Acknowledgements

Figure 1 Deformed solid (left) and fluid domain (right).

HOW LUNG LESIONS LOCATION IN ARDS MODIFIES RESPIRATORY BIOMECHANICS? A COMPUTATIONAL FRAMEWORK

Claire Bruna-Rosso (1), Salah Boussen (1,2)

1. Laboratoire de Biomécanique Appliquée, Aix-Marseille Univ., Gustave Eiffel Univ., Marseille, France ;
2. Department of Anaesthesiology and Critical Care Medicine, University Hospital Timone, AP-HM, Aix-Marseille Univ., Marseille, France

Introduction

Acute Respiratory Distress Syndrome (ARDS) is a critical condition with a death rate in hospital as high as 40%. Various etiologies exist for this disease such as uptake of toxic substances, or infections such as COVID19. Mechanical Ventilation (MV) must be used to ensure a correct oxygenation of the ARDS patients. This pathology, being highly patient-specific, suffers from a lack of standard in terms of management. Moreover, two patients beneficiating from the same treatment might have very different outcomes. One hypothesis to explain this is that the location of the damaged tissue within the lung significantly influences its global biomechanics and consequently the capacity of a patient to respond to intensive care procedures. To test this hypothesis, a computational model of the lung was developed.

Methods

The approach adopted to conceive a simplified model of the lung is illustrated in figure 1.
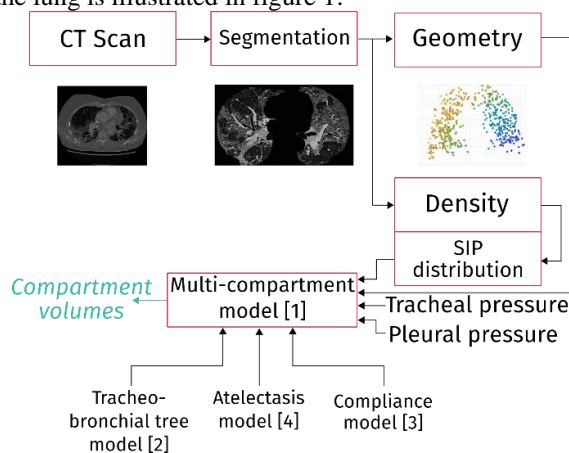
Figure 1: Methodological pipeline

In brief, this model, so-called "exit compartment model", [1] represents the lungs as several "balloons". The input data is a tracheal pressure P_{tr} representing the MV, characterized by an end-expiratory pressure (P_{eep}) and a plateau pressure (P_{plat}), and a superimposed pressure (SIP) that embodies the weight of the overlying lung. The balloons coordinates and SIP are retrieved from the patient CT scans by a dedicated procedure. The equation solved by the model is the following [1]:

$$\mathbf{R}\dot{V}(t) + \mathbf{E}(V, x).V(t) = P_{tr}(t) − P_{pl}(x) − SIP(x) \quad (1)$$

Where $\mathbf{R}$ is a matrix representing the resistance of the tracheobronchial tree. $\mathbf{E}$ is a diagonal matrix filled with the volume- and position-dependent balloon elastances and P_{pl} is the pleural pressure which depends on the antero-posterior coordinate since patients are assumed

to be lying down. The lung is assumed to be hyperelastic with a strain-energy density: $W = \frac{\xi}{2}\exp(aJ_1^2 + bJ_2)$ [3], where a, b, and ξ are material constants without physical meaning and J_1 and J_2 are the first and second invariants of the Green-Lagrange finite strain tensor, respectively. An expression for the volume dependent elastance can be retrieved from this formula (see [3]). Finally, a feature was implemented to represent alveoli opening and closure, as described in [4]. To test the model ability to simulate ARDS lung biomechanics, two simulation at 0 and 5 cmH2O levels of P_{eep} were performed.

Results and discussion

Examples of simulation results are given in figure 2.
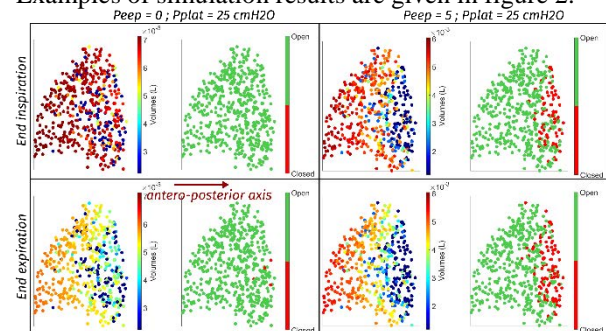
Figure 2: Volume and alveoli state computed at end expiration and inspiration

The model behaves as expected concerning the volume gradient along the antero-posterior axis due to gravity. Moreover, the role of the P_{eep} in alveoli recruitment is clearly visible. The model also puts into evidence the variation of aeration with respect to the location of the damaged tissue within the lungs as hypothesized. This suggests that this parameter should be considered in the therapies used to take care of ARDS patients.

Conclusion

An original computational framework was developed and implemented. The preliminary results obtained showed that while such a simplified model does not allow to compute quantitative data, it offers a good insight in the biomechanics of the mechanically ventilated ARDS lung, which is of high interested toward a better management of this pathology.

References

1. Pozin et al. Int J Numer Meth Biomed Engng, 33:e2873, 2017.
2. Maury, ESAIM: Proc, 47:75-96, 2014.
3. Swan et al. J Theo Biol, 222-231, 2021.
4. Bates & Irving. J Appl Physiol, 705-713, 2002.

SPHERICAL, TRANSPARENT AND STREATCHABLE MEMBRANES FOR REPLICATING THE ALVEOLAR INTERFACE IN-VITRO

Ludovica Cacopardo (1), Nicole Guazzelli (1, 2), Paolo Signorello (2), Arti Ahluwalia (1,2,3)

1. Research Center 'E. Piaggio', University of Pisa, Italy Country; 2. Department of Information Engineering, University of Pisa, Italy. 3 Centro 3R, Italy.

Introduction

Lung in-vitro models are commonly based on flat, 2D semipermeable membranes at the air-liquid interface. Only recently have some studies attempted to replicate the spherical alveolar geometry. For instance, curved polycarbonate membranes were fabricated via microthermoforming achieving the formation of confluent lung epithelial layers in the microwells [1-2]. However, they still lack relevant lung properties such as stretchability.

Here we describe transparent spherical membranes which replicate the alveolar architecture in a more accurate manner, and which can be used in dynamic breathing conditions.

Methods

The membranes were fabricated by casting 1% w/v agarose in custom moulds obtained by stereolithographic 3D printing (Fig.1). After agarose crosslinking (1h at 4°C), the samples were dried overnight at 37°C. Membrane water content was calculated as the difference between the mass in hydrated and dry conditions, normalised with respect to the hydrated mass.
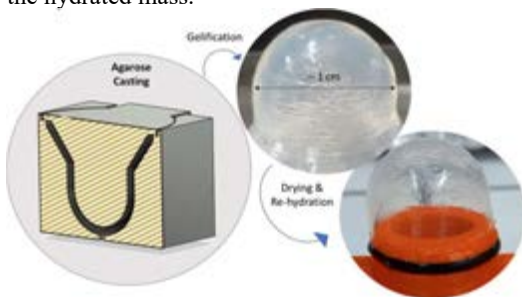
Figure 1: Workflow for membrane fabrication

Mechanical tensile tests at break were performed at a constant strain rate (0.2 s^{-1}) on flat membranes, which were prepared by agarose casting in petri dishes and kept in incubator in wet conditions for 7 days [3]. Cyclic tests at 5% strain, typical of physiological breathing, were also performed. Membrane thickness was measured using a micrometer. Dry and hydrated weight was also acquired with a microbalance (Radwag AS220) to calculate water content.

Permeability tests were then performed using transwell supports, filling the apical compartment with 30 μg/mL methylene blue. Samples were collected from the basal compartment at different time points and absorbance was measured at a wavelength of 664 nm with a spectrofluorometer (PerkinElmer).

Results

Fig.2A-B show the flat membranes used for the characterization; they are transparent. In hydrated conditions, the membranes have a thickness of 33.2 ± 1.8 μm and a water content of 89.4 ± 0.6 %. Moreover, the permeability of the membranes to methylene blue is similar to that of transwell membranes (Fig 2C).

They are also highly elastic (Fig. 2D) in the range of physiological strains. The apparent elastic modulus (Fig.2E) was stable over typical cell culture times. Cyclic tensile testing also demonstrated a good fatigue behaviour with a low residual strain (under 1%).
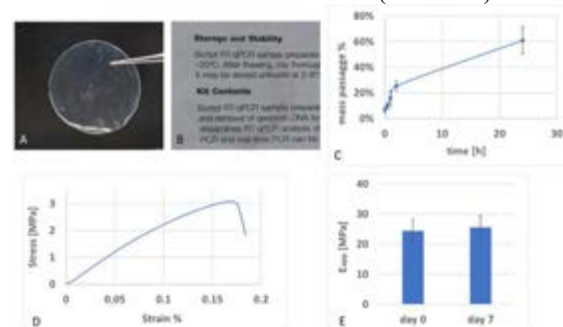
Figure 2: Flat membrane on dark (A) and text (B) background; C) Methylene blue passage percentage in the basal compartment with respect to the initial apical mass; D) typical stress strain curve; E) Apparent elastic moduli (E_{app}) measured immediately after hydration and after 7 days in the incubator.

Discussion

Spherical agarose membranes were fabricated and characterised demonstrating their suitability for in-vitro applications. In addition to the geometrical factor, the main advantages are their transparency and their elastic behaviour over physiological strains observed in the lung (≈5 to 15%).

Further developments include the optimisation of cell seeding protocols on the spherical membranes and their integration with a fluidic model including the alveolar and capillary compartment.

In summary, these membranes provide an innovative solution for alveolar models, and pave the way for more reliable and physiologically relevant inhalation tests.

References

1. Nossa et al, J Tissue Eng, 12:1-28, 2021.
2. Baptisa et al, Biomat, 266: 120436, 2021.
3. Seow et al, ACS Biomat & Eng, 5:4067-4076, 2019.

THE EFFECT OF PRONE AND SUPINE POSITION VENTILATION ON ALVEOLAR OVERDISTENSION AND COLLAPSE

Sjeng Quicken (1), Ulrich Strauch (2), Eline van Engelen (1), Milou van Mil (1) Frans van de Vosse (1)

1.Department of Biomedical Engineering, Eindhoven University of Technology, the Netherlands;
2. Department of Intensive Care, Maastricht University Medical Center+, the Netherlands

Introduction

Intensive care patients often require mechanical ventilation (MV). During MV an external ventilator applies a pulsatile pressure to the trachea to ventilate the patient. While MV is crucial for patient survival, it typically induces ventilator-induced lung injury (VILI) which can potentially be life-threatening. VILI is primarily caused by regional alveolar collapse or overdistension due to pressure inhomogeneities in the ventilated lung.

During the COVID-19 pandemic a surge in patients requiring MV was observed, resulting in an increased incidence of VILI. Hence, there is a clear need for strategies that minimize VILI. A widely adopted approach to improve patient oxygenation during the COVID pandemic is prone position ventilation as opposed to supine position ventilation. Prone position ventilation has however also been suggested to prevent VILI. The mechanisms responsible for the benefit of prone ventilation with respect to VILI development are however largely unknown. In this research we investigate how prone position ventilation may prevent VILI by assessing its impact on alveolar mechanics.

Methods

A realistic lung geometry was generated using a single CT scan from the LIDC-IDRI dataset (*1*). First, lung lobes and large airways were segmented from CT data, after which smaller airways were automatically generated using a modified implementation of the lobe-filling algorithm proposed in (*2*). Artificial airways were truncated at airway generation 10 to reduce simulation time. Individual airways were modelled using a non-linear resistor. Terminal airways were truncated using a lumped-parameter acinar model (*3*). A representative MV pressure curve was prescribed at the trachea. Intrapleural pressure was prescribed at the acinar elements. Supine and prone intrapleural pressure distributions were based on the esophageal pressure measurements and theoretical intrapleural pressure gradients reported in (*4*) and (*5*), respectively. Alveolar overdistension and collapse were quantified using alveolar volumetric strain: $(V - V_{ref})/V_{ref}$, where, V_{ref} was computed at functional residual capacity.

Results

During exhalation in the supine position simulation, more than half of the acini experienced very low strains ($<$-0.5), which may be indicative of alveolar collapse. Only during peak inhalation in supine position more

than half of the acini experienced strains larger than 0.0. On average, alveolar strains in the prone position simulation were higher than those observed in the supine position ventilation and none of the acini experienced strains lower than -0.5. Furthermore, during inhalation in prone position all acini experienced alveolar strains larger than 0.0, up to a maximum of 0.6. Finally, strain heterogeneity was considerably higher for the supine- than for the prone position simulation (Fig. 1).
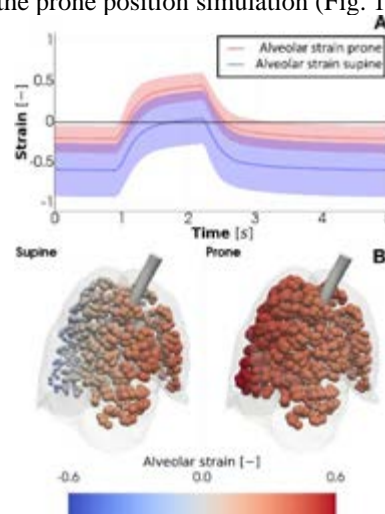
Figure 1 A: Range of the alveolar strain over time. The solid lines represent median strain B: End-inspiratory strain during supine (left) and prone (right) positioning of the patient.

Discussion

Our results suggest that alveoli in prone position ventilated patients are less susceptible to collapse than those in supine position ventilated patients. Furthermore, during inhalation in prone position, alveoli stay far below the safe strain threshold of 1.5-2.0 reported in (*6*). Therefore, the risk of lung damage due to alveolar overdistension seems to be low. Hence, our results present a potential mechanism for the benefit of prone ventilation to combat VILI. Nonetheless, future research to verify these findings using multiple lung geometries and ventilation settings is required.

References

1. Armato et al., Med Phys, 38:915–931, 2011
2. Tawhai et al., Ann Biomed Eng, 28:793–802, 2000
3. Ismail et al., Int J Numer Method Biomed Eng, 29:1285–1305, 2013
4. Kumaresan et al., Anesthesiology. 128:1187–1192, 2018
5. Tawhai et al., J Appl Physiol, 107:912–920, 2009
6. Protti et al., Am J Respir Crit Care Med, 183:1354–1362, 2011

ASTHMA SEVERITY LEVELS MONITORING BASED ON EEG SIGNALS USING NOVEL CLASSIFICATION ALGORITHMS

Anat Ratnovsky (1), Rotem Haba (2), Gonen Singer (2), Mordechai Reuven Kramer (3), Sara Naftali (1)

1. School of Medical Engineering, Afeka Academic College of Engineering, Israel; 2. Faculty of Engineering, Bar Ilan University, Israel; 3. Rabin Medical Center, Beilinson Campus, Israel

Introduction

Asthma is a complex respiratory disorder in which structural changes in the conducting airway cause variable airflow limitation. It is important to monitor the progression of the disease and to gather continuously data as an objective marker of morbidity and in order to support therapy. Currently, patients with asthma are being examined only a few times a year. This prevents a continuous monitoring and any advance in precision medicine. Remote non-invasive monitoring tools will enable the collection of data with minimal effort from patients, which is especially important in the case of children. Currently, asthma is being diagnosed and monitored by an active test that strongly depends on the patient's effort. Therefore, there is a need for innovative methods that do not depend on the patient's effort for both accurate identification of asthma at an early stage and to monitor the disease progression. Inspiratory occlusion is a mechanical load that resulted in the observation respiratory-related, evoked potential. Recently, our novel, non-invasive procedure for identification of tracheal obstruction was suggested based on electroencephalogram (EEG) signals [1] yielded promising results compared to other common classification algorithms. Thus, EEG has the potential to become a non-invasive tool to passively and continuously provide an indirect estimation of airflow obstruction for asthma patients.

Methods

EEG signals and breathing motion signals (using abdominal belt) were acquired continuously and noninvasively throughout methacholine challenge tests, which is used to evaluate the sensitivity of patients with suspected asthma to an agent triggering bronchoconstriction. The patients' data were classified into 3 levels of asthma severity based on the decrease in the forced expiratory volume in 1 second (FEV_1) percentage. Each raw EEG signal included all breathing repetitions that were measured after each dose inhalation and was segmented according to full breathing cycle (Figure 1). The EEG segments were then transformed to the frequency domain by computing the short time Fourier transform (STFT). These feature extraction outputs were used as inputs to ordinal classification algorithms, which take into consideration the ranking relationship among class attribute (i.e., the severity level of asthma disease).
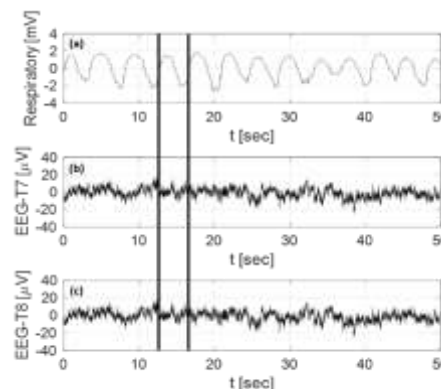
Figure 1: An example of the respiration motion (a) and the corresponding EEG signals from channel T7 (b) and channel T8 (c). Solid horizontal lines indicate one breathing cycle and its corresponding EEG signal.

Results

The AUC per subject ranges between 73% and 91%. Figure 2 illustrates the AUC values of the best model obtained for each severity level of Asthma for each subject.
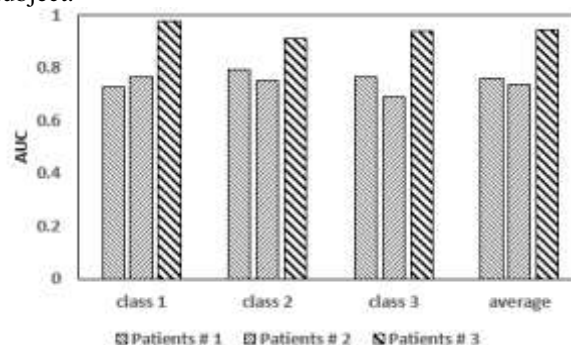
Figure 2: Best AUC results obtained for each of the three patients.

Discussion

The proposed method of using EEG signals to identify the degree of respiratory obstruction for each patient shows promise results. The performance needs to be investigated on a large clinical population. Classification of obstruction rate of a new subject based on the data of other subjects should be further explored.

References

1. Singer, G., Ratnovsky, A., and Naftali, S. (2021). Classification of severity of trachea stenosis from EEG signals using ordinal decision-tree based algorithms and ensemble-based ordinal and non-ordinal algorithms. Expert Systems with Applications, 173, 114707.

INTERFACING NEUROMUSCULOSKELETAL MODELS WITH EXOSKELETONS FOR CONTROLLING NEURO-MUSCULOTENDON PARAMETERS IN VIVO

Guillaume Durandau (1), Herman van der Kooij (1), Massimo Sartori (1)

1. Department of Biomechanical Engineering, University of Twente, The Netherlands

Introduction

One of the current paradigm in exoskeleton research focuses on the reduction of metabolic cost but exoskeleton could provide further benefit by controlling internal body variables such as muscle excitation, stiffness or muscle-tendon load [1]. Unfortunately, this is rather difficult using current imaging technics such as ultrasound or experimental recording devices such as force sensor for recording variables like muscle force, stiffness or tendon loading. A way to compute these variables without experimentally recording them is to use *in silico* human models such as neuromusculoskeletal (NMS) model working in real-time. These models would give access to the variables of interest and by interfacing them with an exoskeleton and closing the loop on them, we could influence them *in vivo*. In this overview, we present our latest works going toward the fine control of NMS variables by an exoskeleton, notably of the electromyograms (EMG) level.

Methods

The first part to achieve this goal was the development of a real-time NMS framework achieving computation of NMS variables under the muscle electromechanical delay. We then interfaced this new framework with an ankle exoskeleton. The control command of the exoskeleton was the joint torque multiplied by a gain to be able to change the intensity of the received assistance. First experiments were done on paretic patients and the main question was to see if a modulated assistance resulted in modulated muscle excitation during a position tracking task. The second experiment was done on healthy subjects and we looked at if the provided assistance was able to reduce muscle excitation when compared to a non-assistance condition over different walking tasks (speed and elevation) on a treadmill.

Results

Results showed the possibility to compute joint torque under the electromechanical delay (<50 ms) [2].
We also showed the possibility to modulate EMG level in patients (stroke and spinal cord injury (SCI)) with a reduction from 0.69 to 0.36 (unitless) (stroke) and from 0.90 to 0.89 (SCI) and EMG variation reduction from 26 to 21 (unitless) (stroke) and from 6 to 4.2 (SCI) [3].
Results for the second experiment showed the possibility to reduce EMG level for all tested walking tasks while having the total ankle joint torque almost invariant between conditions (Fig. 1) [4].
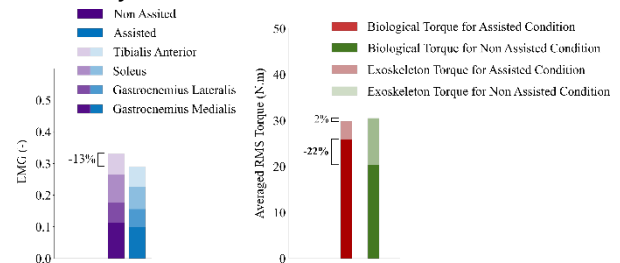
Figure 1: Change in electromyograms (EMG) and joint torque for tested walking tasks for the two tested conditions. Results for 5 subjects (assisted and zero torque) (see [1] for more results and information).

Discussion

We showed the possibility of controlling muscles' EMG during different walking tasks without impeding the user (no change in total torque) and also results on patients. Those results could pave the way for the use of exoskeleton mediated neurorehabilitation.
The NMS model offers the computation of other biomechanics variables in real-time offerings the possibility to control other variables. Our current work is looking into bounding some of these variables to offer a bio-protective aspect with an exoskeleton. Such as limited overloading of tendon or muscle to impede the development of musculotendon disease or injury.
Numerous challenge remains to make this methods mainstream such as the difficulty to personalize NMS model to patient, validation of internal NMS variables while wearing an exoskeleton.

References

[1] M. Sartori, *et al*, "Closing the loop between wearable technology and human biology: A new paradigm for steering neuromuscular form and function," *Prog. Biomed. Eng.*, vol. 3, no. 2, 2021.

[2] G. Durandau, *et al*, "Robust Real-Time Musculoskeletal Modeling driven by Electromyograms," *IEEE Trans. Biomed. Eng.*, 2017.

[3] G. Durandau *et al.*, "Voluntary control of wearable robotic exoskeletons by patients with paresis via neuromechanical modeling," *J. Neuroeng. Rehabil.*, vol. 16, no. 1, p. 91, 2019.

[4] G. Durandau, *et al*, "Neuromechanical model-based control of bi-lateral ankle exoskeletons: biological joint torque and electromyogram reduction across walking conditions," *arXiv2108.00980*, 2021.

Acknowledgment

CONTROL SYSTEM OF A MUSCULAR CONTROLLED, EXPERIMENTAL GLENOHUMERAL SIMULATOR

Jeremy Genter (1, 2), Georg Rauter (3), Markus Rohner (1), Andreas M. Müller (4), Annegret Mündermann (2, 4), Daniel Baumgartner (1)

1.IMES Institute for Mechanical Systems, ZHAW School of Engineering, Switzerland; 2. Functional Biomechanics Laboratory, 3. BIROMED-Lab, Department of Biomedical Engineering, University of Basel, Switzerland; 4. Department of Orthopaedics and Traumatology, University Hospital Basel, Switzerland

Introduction

Shoulder joint and muscle forces cannot be easily and accurately measured directly in-vivo. An ex-vivo approach is often chosen to conduct biomechanical studies of the shoulder, especially when investigating the active and passive contribution of individual muscles, and various glenohumeral simulators have been developed [1]. However, currently only few simulators can simulate dynamic glenohumeral motion induced by active muscle forces, and a standard for such an experimental set-up and its control system is lacking. In this work, we present a control system for a shoulder simulator with the goal of mimicking physiological glenohumeral motion while tackling the challenge of over actuation.

Methods

The current simulator is a further development of an existing unconstraint glenohumeral simulator [2] designed for ex-vivo experiments with different rotator cuff injuries and hand-held weight conditions (0kg, 2kg, 4kg; Figure 1). The simulator consists of eight active muscle units, three segments each of the rotator cuff and the deltoid muscles, pectoralis major and latissimus dorsi muscles and a simulated arm with appropriate weight. A cascade feedback control system was developed to activate the eight muscle units to control six degrees of freedom in the glenohumeral joint (Figure 2). The outer cascade controls the position of the humerus and yields the net torques $\tau_{corrected}$ which is used as input to an optimization scheme. The optimizer provides $F_{desired}$ to actuate the glenohumeral joint. The optimization minimizes the loss function

$$L = \alpha \cdot F_{desired}^{T} \cdot F_{desired} + \beta \cdot F_{estimated}^{T} \cdot F_{estimated} \quad (1)$$
$$\text{s.t} \quad MA \cdot F = \tau_{corrected}$$

where α and β are weighting parameters, $F_{estimated}$ is a model-based estimation of the muscle forces and MA a matrix stored with the current moment arm of the muscles. The inner cascade is implemented to ensure that the $F_{desired}$ is reached.

Results

The repeatability of the simulator was tested by running the same abduction motion multiple times. The mean (standard deviation) of the motion at its peak abduction angle was -35° (3.6°).

Discussion

The experimental setup reproduces the given motion profile well. The optimization scheme actuates the humerus in a physiological manner. The limitations of this experimental setup include the approximation of the line of action of the muscles. The activation level of each muscle group can only be estimated, and hence does not necessarily reproduce the in-vivo situation [3]. These limitations are inherent to all glenohumeral simulators [1]. These limitations are addressed with adjustable insertion points of the muscles and the optimization scheme presented here. This simulator shows promising potential to simulate and track the complete kinematics of the glenohumeral joint and further improve its repeatability.

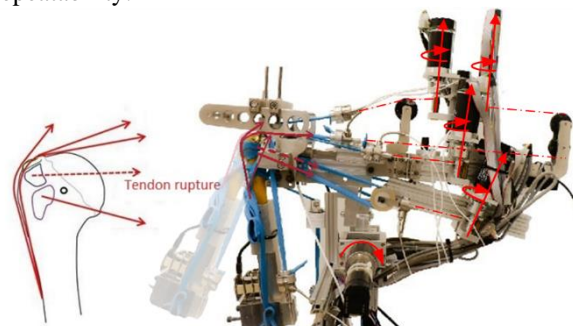*Figure 1: Illustration and photograph of the simulator and the muscles included. The muscles are actuated with EC-Motors and wound onto a rope winch.*
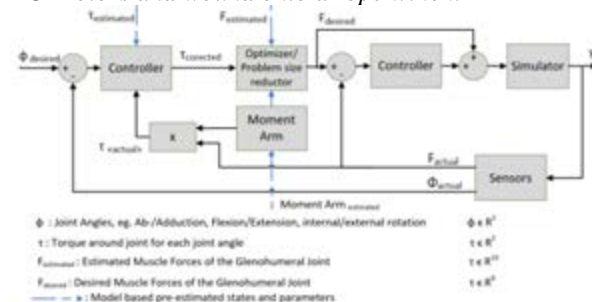

Figure 2: Control scheme of the shoulder simulator.

References

1. Williamson P et al, J Biomech Eng, 82:280-290, 2019.
2. Baumgartner D et al, Med Biol Eng Comput, 52(3):293-9, 2014
3. Prilutsky BI et al, Exerc Sport Sci Rev. 30(1):32-38, 2002.

Acknowledgements

FORM AND FUNCTION IN THE TAIL FEATHERS OF CLIMBING BIRDS

Michael C. Granatosky (1, 2), Melody W. Young (1), Nicholas D. Flaim (1), David Deleon (1), Bettina Zou (1), Burcak Bas (1), Lindsey L. Reader (3), Edwin Dickinson (1)

1. *New York Institute of Technology College of Osteopathic Medicine, United States of America; 2. Center for Biomedical Innovation, United States of America; 3. University of Utah, United States of America*

Introduction

Climbing birds balance counteracting torques by using the hindlimbs, and beaks in the case of parrots, to provide superior tensile forces, while the tail serves as an inferiorly positioned compressive strut [1, 2]. Numerous studies have claimed that the tails of climbing birds are "well-adapted" to this biomechanical function. Specifically, a tail feather adapted to climbing should be sufficiently stiff to resist compressive loading and relatively long to reduce muscular effort from the limbs [3]. Despite these inferences, few morphological studies that has directly compared tail feather anatomy of climbing birds relative to more generalized non-climbing species, nor has any work quantified substrate reaction forces acting on the tail during climbing.

Methods

We collected morphometric data on the tail feather shafts from a broad phylogenetic sample of birds. Using phylogenetic generalized least squares, we assess the influence of locomotor mode on shaft morphology. The material properties of the rachis at the calamus were determined by subjecting a subsample of the feathers to quasi-static three-point bending in the dorsoventral plane. The resulting force displacement curves were used to calculate the maximum bending moment (M_{max}, N m) and Young's modulus (E_{bend}, GPa) [4]. To understand the natural loading environment during climbing, we collect kinetic tail loading data from rosy-faced lovebirds (*Agapornis roseicollis*) and hairy woodpeckers (*Leuconotopicus villosus*) during vertical climbing. From these data, we calculate the peak fore-aft and tangential force and average power (W kg^{-1}).

Results

Rachis diameters correlated positively with body mass across all species. However, scansorial species have longer feathers, larger rachis diameters both at the base and the tip, and greater mean cortical thickness for a given body mass than non-climbing species. No differences in material properties at the calamus were attributable to locomotor mode. *In vivo* experiments of parrot climbing reveal that movement of the tail is complex, and not only rotates inward, but also wraps around the support. The tail feathers of parrots and woodpeckers experience both bracing and compressive loading ~10-50% of body weight and contributes negative mechanical work.

Discussion

The tail of climbing birds serves to counteract backward pitching during vertical ascent and supports a significant proportion of body weight. Further, because of the inward wrapping motion, the tail of climbing birds theoretically possess some "gripping" abilities. The tail feathers of climbing birds tend to be relatively long for their body weight. Stiffness of the calamus is achieved through structural, rather than material, modifications to both the proximal and distal morphology of the rachis. Loads supported by the feet require metabolic energy, whereas loads supported by the tail, and aligned along its long axis, theoretically do not. As such, by lengthening and buttressing the tail, scansorial birds circumvent Euler buckling at the single-feather and whole-tail scales while likely reducing the metabolic cost of pitch resistance. Future work will use these data to develop a bioinspired tail meant to replicate the movements and performance observed during climbing in birds to aid in the development of a (Figure 1).
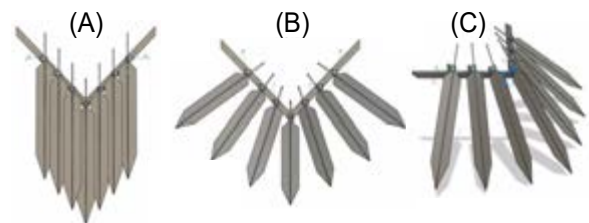
Figure 1: Model demonstrating movements of the tail of climbing birds (A). During climbing, the tail provides a means of compressive stabilization. In vivo experiments reveal that during climbing the tail fans out (B) and rotates inward (C). Movement in this manner may allow the tail of climbing birds possess some "gripping" abilities. Biarticualar joints at the tail base can be used in bioinspired designs to mimic such movement.

References

1. J. B. Hanna, M. C. Granatosky, P. Rana, D. Schmitt, Journal of Experimental Biology. 220, 3039–3052 (2017).
2. L. L. Reader et al., Journal of Experimental Biology, in press, doi:10.1242/jeb.242305.
3. R. Å. Norberg, Ornis Scandinavica (Scandinavian Journal of Ornithology). 17, 191–209 (1986).
4. J. Lees, T. Garner, G. Cooper, R. Nudds, Royal Society open science. 4, 160927 (2017).

COMBINED MEASUREMENT OF FRICTION AND THROUGH-THICKNESS DEFORMATION ON EX VIVO SKIN SAMPLES

Bastien Eydan (1), Baptiste Pierrat (1), Nicolas Curt (1), Hassan Zahouani (2), Jérôme Molimard (1)

1. Mines Saint-Etienne, Univ Lyon, Univ Jean Monnet, INSERM, U 1059 Sainbiose, Centre CIS, Saint-Étienne, France; 2. Laboratoire de Tribologie et Dynamique des Systèmes, UMR 5513, CNRS, ECL, ENISE, Saint Etienne, France

Introduction

The working principle of many medical devices (e.g. lumbar belts, stocking) is based on their mechanical action on the body, therefore they are in contact with the skin. Unfortunately, skin irritation is a common phenomenon that becomes a concern, as many patients cannot withstand their medical devices, leading to poor therapeutic compliance. Exposure to a chemical agent or an allergic reaction is unlikely here, as these medical devices are designed to be hypoallergenic. We therefore hypothesised that these skin irritations are caused by the mechanical interaction of the skin with the objects. Even though skin damage can be related to a prolonged pressure [1], shear has been shown to accelerate and aggravate skin damage [2]. In addition several researches have demonstrated how friction is involved in the process of skin abrasion [3]. Despite the complexity of the skin mechanical behavior, most of the current literature on skin tribology is based on surface measurements. An analysis of the deformations undergone by the skin in its thickness during contact could provide new insights into the phenomenon of mechanical irritation. This is particularly true considering the variety of mechanical phenomena that can cause skin irritation, and the fact that they involve mechanoreceptors within the different skin layers. The aim of this work was to develop a new device to study the strain in the layers of ex vivo skin samples under friction with objects.

Materials and methods

The bench test was designed in the purpose of measuring full-field through-thickness deformation along with frictional properties of ex-vivo skin strips in contact with a cylindrical probe (Figure 1A). Pictures of the sample section were acquired during the interaction with the probe using a camera. In this configuration, the pixel size in the object plane was approximately 6µm, giving a total field of view of 7.56mm × 5.88mm. A LED light source was located on the other side and allowed the sample to be back lit. Deformations were later computed using Digital Image Correlation.

The skin sample was prepared in an eosine/hemalun solution to enhance optical texture. Then it was put in a holder pre-stretching its two sides, the bottom surface resting on the device. This holder was mounted on a motorized displacement table in order to control sliding of the sample against the cylindrical probe that was loaded using a dead weight. The probe was directly screwed on a 6-axis force sensor. All elements were controlled by a dedicated LabView program.
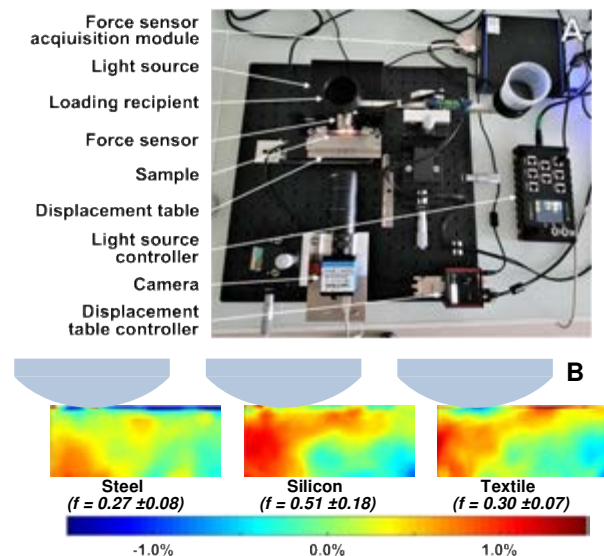
Figure 1: experimental bench test (A) and shear strain on a cleaned skin sample after 1mm sliding (B).

Results

As a first application, pig samples were subjected to cyclic friction experiments with a 50g normal load and 3mm sliding stroke (v = 0.2mm.s^{-1}). Experiments were repeated with three different materials of contact: steel from the raw probe, silicone and textile from a compression stocking. The results presented figure 1B shows how surface friction monitors shear strain distribution. In particular, dermo-epidermal junction is a place rich in nerve terminations; results show a high shear strain in this region with silicone, when the maximum shear locuus is deaper with steel.

Conclusions

A novel experimental set-up was successfully designed and validated. It is the first step for original studies on skin behavior under friction. Further works will investigate the effect of different tribological conditions representative of medical devices-skin interactions.

References

1. U. Wollina. Mechanical skin irritations due to textiles. In Handbook of Medical Textiles, pages 248–268e, 2011.
2. B. Goldstein et al.. Arch Phys Med Rehab, 79(3):265–272, 1998.
3. C. Thieulin et al. Wear, 376:259–265, 2017.

TENSILE TESTING OF CELL SHEETS: AN EXPERIMENTAL APPROACH

M. G. Fernandes (1,2), M. D. Malta (1,2), A. Andre (3), P. Martins (3,4), A. P. Marques (1,2)

1. 3B's Research Group, I3Bs – Research Institute on Biomaterials, Biodegradables and Biomimetics, University of Minho, Headquarters of the European Institute of Excellence on Tissue Engineering and Regenerative Medicine AvePark, Zona Industrial da Gandra, 4805-017 Barco, Guimarães, Portugal; 2. ICVS/3B's–PT Government Associate Laboratory, Braga/Guimarães, Portugal; 3. INEGI, Porto, Portugal; 4. ARAID, i3A, Universidad de Zaragoza, Spain

Introduction & Objectives

The extracellular matrix (ECM) is one of the most important regulators of tissue homeostasis and one of the key elements in bioengineering human tissue models for studying the tissue's environmental milieu. Cell sheet engineering is a technology that relies on cells as the only producers of ECM faithfully recreating their native 3D microenvironment [1]. However, Cell sheet (bio)-mechanics characterization remains poorly explored. Tensile testing is the most common approach to estimate the bulk mechanical properties, but it requires a firm attachment of the sample edges, which is a problem due to the fragility of the cell sheets. Moreover, a compromise between appropriate grips and clamping force is required to keep the sample's edges integrity and reduce slippage. Thus, this work proposes the development of an experimental setup comprising a mechanical testing prototype relying on customized 3D printed grips and racks, and the validation of its efficacy using human fibroblast cell sheets.

Materials & Methods

The prototype consisted of two arms, connecting two actuators that can be programmed to move independently under displacement control. Poly lactic acid (PLA) grips and racks were designed with suitable geometry and roughness to avoid cell sheet structural damage caused by clamping or sample slippage during stretching and printed in a FDM-based 3D printer Figure 1 A). To validate the system, primary human dermal fibroblasts cell sheets were used. The cells were seeded at a density of $50x10^3$cells/cm^2 and cultured for 14 days in XX medium supplemented with 50μg/mL ascorbic acid, to promote maximum ECM deposition. After this period, the cells were embedded in a 15% gelatin solution, let to solidify and punched using a dog-bone shape cutting form of standardized dimensions (12x3.6mm). Gelatin dog-bone samples were used as control. For the tensile tests, cell sheets (n=13 for each condition) were fixed to the actuators by grips and stretched along the longitudinal axis at a constant elongation rate of 2 mm/min until failure. A PBS bath at room temperature was used to maintain hydration. The load was measured using a 2.5 N load cell throughout the testing period. Fractured surface and surrounding regions were investigated using scanning electron microscopy (SEM).

Results

Stress-strain data showed that the proposed apparatus measurements are reproducible and accurate. All samples fractured in the gage region and no slippage was observed during the test (Figure 1B). The mean ultimate tensile strength (UTS), Young's modulus (E) and failure strain (ε_f) were found to be 0.013MPa, 0.024MPa and 0.489 respectively for the cell sheet and 0.008MPa, 0.027MPa and 0.246 for the control (Figure 1C). SEM image of the fractured region confirmed the rupture and the alignment of matrix components in the direction of applied force (Figure 1B).
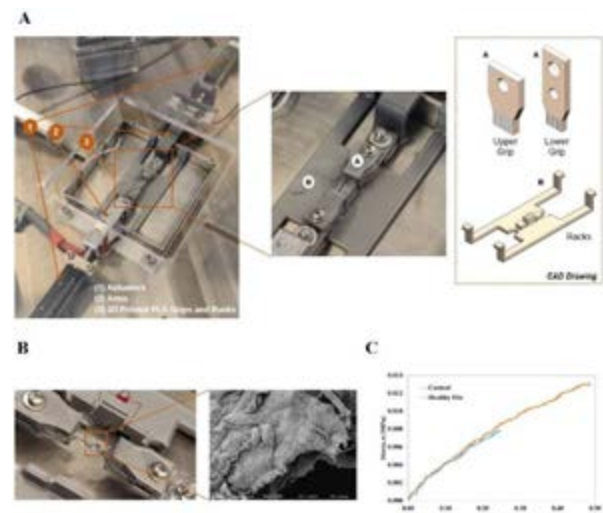
Figure 1: (A) Diagram of the experimental setup, including planar mechanical testing prototype and 3D Printed PLA Grips and Racks. (B) Representative SEM image of fractured region. (C) Stress-strain curves of cell sheet and control.

Discussion

The proposed experimental setup proved to be suitable to measure the tensile proprieties of cell sheets, overcoming the limitations of current devices and opening new perspectives in the mechanical characterization of soft tissue engineered models.

References

1. M.T. Cerqueira, et al. Acta Biomater. 10 (2014) 3145–3155

Acknowledgements

CHARACTERISING THE MECHANICAL PROPERTIES OF SKIN WOUNDS

Sara Medina-Lombardero (1), Jenna Cash (2), Bob Reuben (1), Michael Crichton (1)

1. Institute of Mechanical, Process and Energy Engineering, School of Engineering and Physical Sciences, Heriot-Watt University, Edinburgh, UK; 2. MRC Centre for Inflammation Research, University of Edinburgh.

Introduction

Chronic wounds are a global socio-economic burden. Mechanical biomarkers show promise for the early diagnosis of chronicity, but their clinical application has been hindered by a lack of standardisation and accuracy in their measurements. In this work, a non-contact modality (Digital Image Correlation, DIC) has been combined with traditional mechanical testing techniques (such as tensile testing), to measure both global and local properties of wounded mice skin. Stress-strain values have been measured at different healing stages, obtaining elasticity parameters at very small tensions. Such low tensions are comparable to the forces that are experienced by skin on a daily basis, thus ensuring no further damage is caused to the tissue in the tests. The data obtained in these experiments, together with histological analysis, will be used to understand how different microstructural skin features affect the overall mechanical behaviour during the healing process.

Methods

Twenty male mice (C57BL/6J) were anesthetised and wounded *in vivo* by using a biopsy punch (4 mm) on their dorsal area, and were left to heal unaided (Fig.1). The wounding process and posterior animal care were in accordance with UK Home Office regulations.
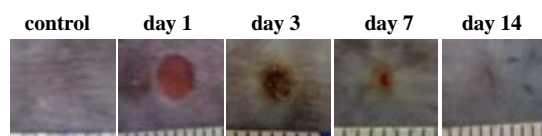
Figure 1. Wound progression of biopsied skin.

For tissue harvesting, some mice were sacrificed unwounded (control group) and others at days 1, 3, 7 and 14 post-wounding. Two samples of 40×10 mm were obtained from each mouse. The skin was stretched at low loads up to 0.5 N, at 0.05 s^{-1}, using an ElectroForce TestBench (TA instruments). A dual camera system (Canon EOS 2000D) was used to record top and lateral views during loading. The post-processing of the videos was performed using the free MATLAB application Ncorr [1]. Global tensile test data was fitted with a hyper-elastic Ogden model of 1st order (Eq. 1) [2]:

$$\sigma(\lambda) = \frac{2\mu}{\alpha}\left(\lambda^{\alpha} - \lambda^{-\frac{\alpha}{2}}\right) \tag{1}$$

where μ is the shear modulus, α the strain hardening, λ the stretch ratio and σ is the Cauchy stress.

Results

Global parameters of (hyper-) elasticity did not present significant differences (measured with ANOVA) across the different time points (Fig.2), despite the apparent small upwards trend of the strain hardening component.
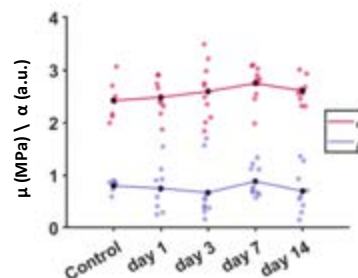
Figure 2: Elasticity measures of skin at different time points

On the other hand, the DIC data from the same tensile tests (Fig. 3) did show a mean increase in deformation at the wound centre on day 1, which gradually decreased throughout the healing process. By day 14, the strain looked similar to that of unwounded skin.
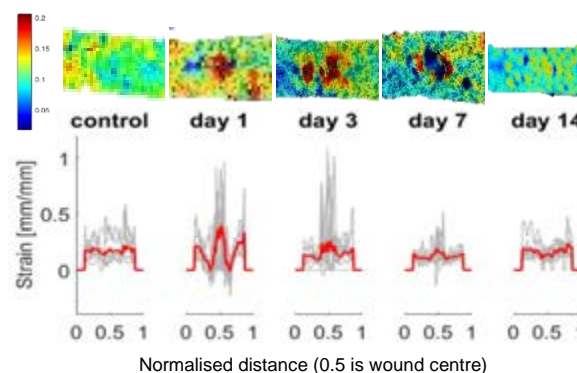
Figure 3: Top, DIC data. Bottom: grey are raw strains obtained from DIC maps (across wound); red is their average.

Discussion

The apparent recovery in the local deformation properties over time (Fig. 3) clearly indicates a measurable healing progression, despite global data not showing significant changes at such low strains. All data is being analysed against the structural composition of the tissues, which will help identify key areas for monitoring wound progression with non-invasive mechanical approaches.

References

1. Blaber et al, Experimental Mechanics, 55:1105–1122, 2015
2. Wang et al, PLoS ONE 10(3): e0120897, 2015

Acknowledgements

FRACTURE TOUGHNESS DETERMINATION OF MUSCLE TISSUE BASED ON AQLV MODEL DERIVED VISCOUS DISSIPATED ENERGY

Othniel J. Aryeetey (1,2), Martin Frank (2), Andrea Lorenz (3), Dieter H. Pahr (1,2)

1. *Division Biomechanics, Karl Landsteiner University of Health Sciences, Krems, Austria.*
2. *Institute of Lightweight Design and Structural Biomechanics, TU-Wien, Vienna, Austria.*
3. *Austrian Center for Medical Innovation and Technology (ACMIT), Wiener Neustadt, Austria*

Introduction

An understanding of failure mechanisms in soft biological tissue is vital in medical issues such as rupture of foetal membranes and injuries to skin, muscle, and tendon during sporting activities. Fracture toughness determination in soft collagenous tissues (SCT) is often modelled as an interchange between the work done to overcome internal strain energy of the tissue (viscous energy) and the irreversible work done to propagate a defect (fracture energy). Conventionally, the viscous energy is determined on unnotched samples experimentally and after notching the fracture toughness can be calculated, based on the increase in dissipated energy. We hypothesized that the adaptive quasi-linear viscoelastic (AQLV) model [1] is able to predict the viscous energy of unnotched samples properly and hence, enable reasonable fracture toughness determination by modeling.

Methods

Notched and unnotched (8 each) porcine muscle tissue samples were tested under triangular wave excitation and hysteresis energy was determined with and without crack propagation. First, the AQLV model was extended to describe the load-unload hysteresis. Next, material parameters were obtained for porcine muscle tissue from a previous study on ramp-hold tests [2] and applied to unnotched strain data to determine dissipated energy ratio (U_D). Fracture toughness was determined by subtracting viscous dissipated energy based on experimental and AQLV model approaches (Fig. 1) from total dissipated energies in notched samples.
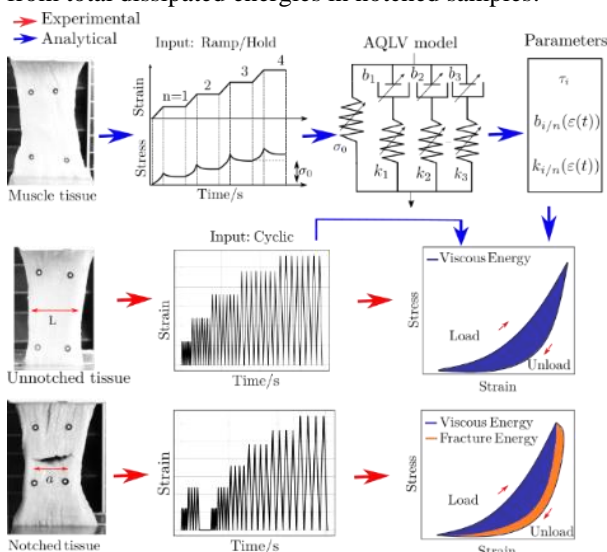
Figure 1: Study design showing the workflow of experimental and AQLV model approaches in the study.

Results

The distribution of U_D for an unnotched and notched sample per cycle are shown in Fig. 2A and 2C respectively. The mean dissipated energy ratio obtained from experimental stress strain curves was 0.24 ±0.04, compared to 0.28 ± 0.03 for the AQLV model (Fig. 2B) for unnotched samples. The mean fracture toughness obtained from experimental approach was 0.84 ± 0.80 kJ/m^{-2} and 0.71 ± 0.76 kJ/m^{-2} for the AQLV model approach (Fig. 2D) which were not significantly different (p=0.87).
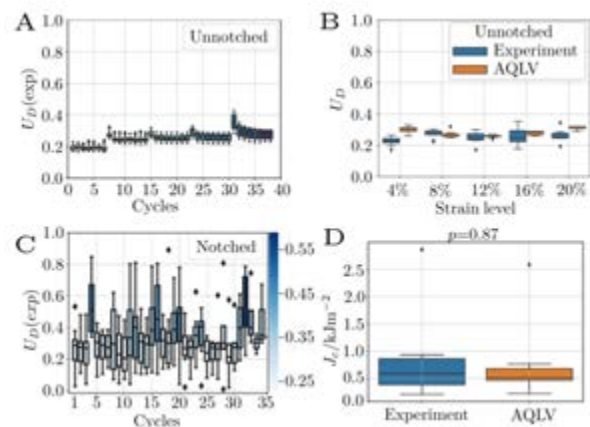
Figure 2: Plots showing the distribution of U_D per cycle for A) unnotched samples and C) notched samples (boxes colour coded for median). Further plots show the B) U_D and D) fracture toughness from experiment and AQLV model.

Discussion

It was observed that the viscous dissipated energy remains relatively constant with increasing strain levels (Fig. 2A) and hence could be viewed as a material constant. The viscous dissipated energy could be reasonably described with the AQLV model (Fig. 2B). Further, fracture toughness values computed via experimental or AQLV were not significantly different. These results enable the isolation of fracture terms and will aid in describing complex fracture behaviour which is relevant for medical applications, such as rupture of tissue in injuries or surgical procedures.

References

1. Nekouzadeh et al., J Biomechanics 40;3070-8,2007
2. Aryeetey et al., J Mechanical Behavior of Biomedical Materials,126,104999,2022

Acknowledgements

MECHANO-STRUCTURAL MATURATION OF THE BONE CALLUS TISSUE UNDER DISTRACTION

Pablo Blázquez-Carmona (1), José A. Sanz-Herrera (1), Juan Mora-Macías (2), Juan J. Toscano (1), Juan Morgaz (3), Jaime Domínguez (1), Esther Reina-Romo (1)

1. Escuela Técnica Superior de Ingeniería, Universidad de Sevilla, Spain; 2. Escuela Técnica Superior de Ingeniería, Universidad de Huelva, Spain; 3. Hospital Clínico Veterinario, Universidad de Córdoba, Spain.

Introduction

Distraction osteogenesis is a widespread bone regeneration process based on the gradual separation of osteotomized bone fragments after a latency period until a clinically fixed length [1]. The success of the process depends on multiple biomechanical factors (i.e., fixator stiffness, rate, and frequency of distraction) that define the mechanical environment of the callus.

Despite the multitude of histopathological analyses [2], the real mechanism of mineralization is still unknown. Improvements to promote the mineralization process relies on the understanding of its relationship with the mechanobiological accommodation of the distraction callus tissue for a satisfactory apatite deposition. This work aims to combine imaging techniques and mathematical modeling to unravel the mechano-structural changes suffered by the bone callus micro-organization in the early distraction stage.

Materials and Methods

Distraction experiments were performed on six ovine right-back metatarsus (reference 2021PI/21). Non-mineralized tissues were extracted from different callus interzones at several time-points of the regeneration process: days 0, 3, 5, 10, 15, and 22 after seven latency days. Samples were fixed, cut into 100 µm section, and structurally characterized using confocal microscopy Zeiss LSM7 DUO® and SEM Zeiss EVO® (Carl Zeiss AG, Oberkochen, Germany). Sections for confocal imaging were previously stained with Picrosirius red to identify collagen fibers as the predominant elastic component in the extracellular matrix. The images were processed using the package Fiji/ImageJ, quantifying the fiber orientation and density.

A mathematical model based on the imaging data for the callus stiffening was defined by considering three players: the orientation of the fibers, their densification, and their crosslinkage/packaging. While the orientation contribution was defined through probability distributions integrated over the unit sphere [3], the density influence was modeled by dimensional correlation in natural-based lattice structures [4]. The packaging was described using analytical maturation models [5]. This model was validated with axial stiffness data previously measured *in vivo* [1].

Results

According to the confocal data, collagen fibers increase in density up to about 85% and approximately halve the standard deviations of the orientation distributions during the analyzed regeneration time. Similarly, SEM images allow visualizing the continuous maturation process through the formation of bundles (Fig 1). Meanwhile, the mathematical model significantly predicts the exponential callus stiffening measured in the *in vivo* experiments up to around 50 N/mm at the end of the distraction phase (R-square 0.9795, p-value < 0.01).
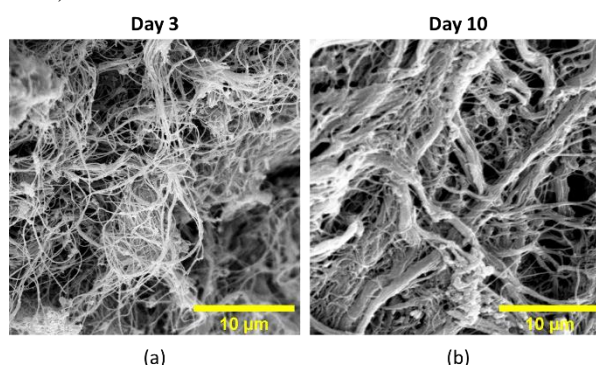
Figure 1: SEM images of the distraction bone callus collagen fibers at different time-points: (a) day 3; (b) day 10 after latency.

Discussion

The distraction process leads to notable fiber arrangement and concentration changes, probably due to the applied traction forces and the induced mechanical stimulus [1]. According to the mathematical model, the considered agents of reorientation, densification, and packaging seem to govern the mechanical maturation problem prior to the beginning of mineralization. The tissue organization tends to form a previously reported central fibrous matrix between the ossification focuses near the bone fragments [6]. Future studies could explore this relationship between the tissue mechano-structural environment and mineralization through different distraction protocols.

References

1. Blázquez-Carmona et al, Ann Bio Eng, 49:642-652, 2020.
2. López-Pliego et al., Injury, 47:7-14, 2016.
3. Mirkhalaf et al, Composites Part B, 202:108388, 2020.
4. Gibson, J Biomech, 38:377-399, 2005.
5. Komarova et al, Front Cell Dev Biol, 3:51, 2015.
6. Ai-Aql et al., J Dental Res, 87:107-118, 2008.

Acknowledgements

THE IN-VITRO TEST CONDITIONS INFLUENCE THE BIOMECHANICAL PROPERTIES OF DEGENERATED LATERAL MENISCI

L. de Roy(1), O. Piquet(1), G. Teixeira(1), M. F. Weiske(2), H.O. Mayr(2), M. Seidenstuecker(2), A.M. Seitz(1)

1. *Institute of Orthopaedic Research and Biomechanics, Ulm University Medical Center, Germany*
2. *G.E.R.N. Tissue Replacement, Regeneration & Neogenesis, Faculty of Medicine, Albert-Ludwigs-University of Freiburg, Germany*

Introduction

The biomechanical properties of degenerated meniscal tissue are of increasing interest in the context of osteoarthritis research [1,2]. Spatial indentation testing using a multiaxial testing machine (Mach-I, Biomomentum Inc.) allow for non-destructive characterization of the viscoelastic material properties of the wedge-shaped menisci [3]. However, when testing biological tissue, the in-vitro test conditions are very likely to affect the outcome measures [2,4]. Therefore, the aim of this round robin study was to investigate the influence of different fixation methods and related laboratory environments on the determination of the viscoelastic properties of degenerated lateral menisci using normal indentation.

Methods

Spatial normal indentation tests of nine degenerated lateral human menisci (IRB 305/10 Freiburg University Medical Center; KL-score: 2-3; 70 ± 9 years) were performed in two laboratories (Lab A: Freiburg, Lab B: Ulm), using a multiaxial testing machine with different meniscus conditions and fixation methods (Fig. 1).

Fig. 1: Summary of the test conditions and fixation methods used in the two Laboratorys of this round robin study.

To ensure repeatability of the spatial mappings in both laboratories, the measurement points coordinates were exported at Lab A and imported at the testing machine at Lab B. Additionally, the points were marked at the tissue using special marker. The indentation parameters for both test runs were as follows: indenter diameter =1mm, indentation depth = 0.2mm, indentation velocity = 0.2mm/s, relaxation time=10s. The maximum applied force (P_{max}), the instantaneous modulus (IM, initial elastic response) and the relaxation modulus (E_{t10}, initial viscous response) were determined. The meniscus surface was divided into the anterior horn (AH), pars intermedia (PI) and posterior horn (PH), with a further subdivision in an inner, middle and outer part (Fig. 2 C). Differences in P_{max}, IM and E_{t10} between Lab A and Lab B were analysed for all regions using non-parametric tests, $p \leq 0.05$ was considered statistically significant.

Results

Significant lower ($p<0.05$) IM values were found in the inner and middle PI region and inner PH region in Lab B (Fig. 2 A). In the outer PI and PH region the IM was statistically higher in Lab B. Statistically lower values for the viscoelastic E_{t10} were assessed in Lab B in the inner and middle regions of the AH, PI and PH ($p<0.05$; Fig. 2 B). Statistically higher values for P_{max} were assessed in Lab A at the inner and middle meniscus region ($p<0.05$), except for the AH middle region (Fig. 2 D).
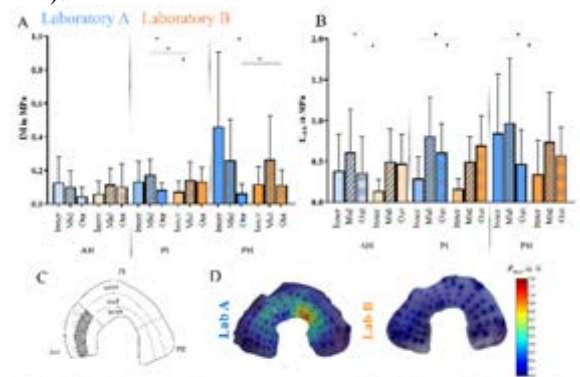
Fig. 2: Results for (A) the instantaneous modulus (IM) in MPa, and (B) the relaxation modulus (E_{t10}) in MPa. (C) Subdivision of the meniscus surface. (D) Exemplary mappings of the maximum applied force during indentation. n= 9, non parametric statistical testing. * p<0.05

Discussion

This round robin study indicated, that different *in-vitro* testing conditions (fixation methods, environmental conditions, freeze-thaw cycles) influence both the initial elastic and viscoelastic properties of degenerated human meniscal tissue. The defined indentation depth resulted in unphysiological strains, especially at the very thin inner meniscus regions. Therefore, strain-controlled indentation testing would be superior for spatial indentation testing compared to distance-controlled testing. Each meniscus underwent a freeze-thaw cycle and was tested twice, which is known to decrease the intrinsic compressive resistance of meniscal tissue [4]. The results of this study add emphasis to earlier studies stating that care should be taken when comparing own biomechanical measures with those published in literature.

References

1. Pordzik, J. et al. (2020) Appl. Sci.
2. Seitz, AM et al. (2021) Front. Bioeng. Biotechnol.
3. Sim, S. et al. (2017) J Orthop Res.
4. Lewis P.B et al. (2007) Wiley InterScience;

ADVANTAGES OF ESTIMATING BIOMECHANICAL PROPERTIES OF THE CORNEA USING TORSIONAL WAVE ELASTOGRAPHY

Inas H Faris(1,2), Jorge Torres (1,2), Antonio Callejas (1,2), Guillermo Rus (1,2,3)

1. Ultrasonics Lab, Dept. Structural Mechanics, University of Granada, Spain; 2. Instituto de Investigación Biosanitaria, ibs.GRANADA, 18012 Granada, Spain; 3. Excellence Research Unit "Modelling Nature" (MNat) University of Granada, Granada, Spain

Introduction

The interweaving of lamellae and the fibres have been pointed as mechanisms that oppose shear and tensile forces. Substantial changes in the organisation of this layer lead to corneal disorders, including progressive and generalised deterioration of the cornea, corneal opacity and subsequent vision loss[1]. Among that chemical eye burns, keratoconus and other ectatic diseases arise as a priority because of their incidence, severity, and impact on the patient's quality of life.

In this paper, an elastography technique based on torsional waves (TWE) was used [2], where the sensor is adapted to the specificities of the cornea. The effect of guided waves in plate-like media is verified negligible since, via TWE, the propagation plane's displacements measurements are perpendicular to the emitter's axis[3] As far as the authors know, no other investigations have studied this mechanical plane under low strain ratios, typical of dynamic elastography in corneal tissue. Ex vivo experiments were carried out on porcine corneal samples considering; (1) control group and (2) alkali burn treatment (NH4OH) group. After TWE scans, corneas were removed for a tensile test to compare the results' trends since both procedures provided responses in the same mechanical plane. The phase speed was retrieved as a function of intraocular pressure (IOP), and to estimate the viscoelastic parameters, a Kelvin-Voigt rheological model was fitted to the dispersion curve[4].

Methods

Porcine corneal samples were obtained from a local abattoir and enucleated immediately post-mortem. Measurements were performed at physiologically relevant controlled pressures of 5, 10, 15, 20, 25, and 30 mmHg and a range of frequency from 500 to 1000Hz.. The excitation generated torsional waves in the specimen by direct contact. These were shear waves that propagate axisymmetrically within the cornea's surface, transmitting an oscillatory rotation through a cone-shaped disk (4 mm base) that was driven by an electromechanical actuator. The dimensions and geometry of the contacting receiving ring were selected to match the samples. The external and internal diameters were 13 mm and 9.6 mm, respectively, with an internal curvature that covered the corneal shape completely. Uniaxial tensile tests were conducted to obtain the shear wave speed of porcine corneas in the two studied groups. The device used was ElectroForce 3200 Series. The lower clamp was attached to a load cell whose maximum capacity was 22 N, with a resolution of 0.001 N.

Results

Both shear elasticity and viscosity correlated positively with IOP, being higher and lower for the control group (Figure 2).
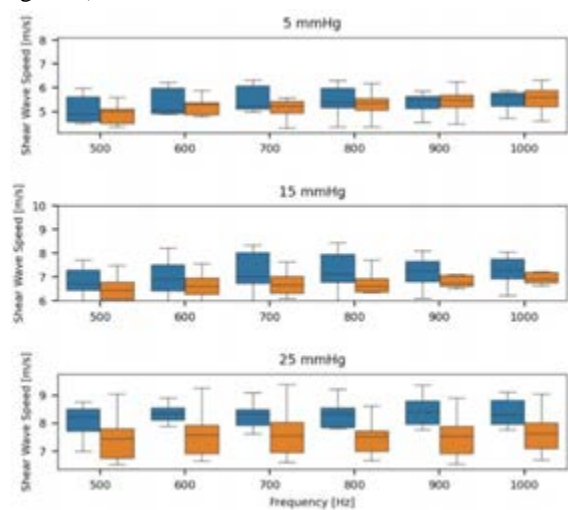
Figure 2: TWE dispersion curves differentiating each group. Two increasing trends are observed, the first with increasing frequency, and the second with increasing intraocular pressure (IOP).

Discussion

The experimental results showed that TWE could discern different mechanical states and paved the way for supporting current in vivo techniques, given its methodological simplicity and fast parameter reconstruction.

References

1. Blackburn, B. et al Front Bioeng Biotechnol 2019 Mar 29;7:66.
2. Callejas, A. et al.. Sensors 17, 2078, (2017).
3. Tanter, M., et al. IEEE Trans. Med. Imaging 28, 1881–1893 (2009).
4. Rus, G., Faris, I. H., et al Sensors 20, 2379 (2020).

Acknowledgements

MECHANICAL MEASUREMENTS FOR CLINICAL ASSESSMENT OF COMPARTMENT SYNDROME

Carolina Tacchella (1), Eddie Clutton (2), Yuhang Chen (1), Michael Crichton (1)

1. *School of Engineering and Physical Sciences, Heriot-Watt University, Edinburgh, United Kingdom*
2. *LARIF Critical Care Unit, University of Edinburgh, United Kingdom*

Introduction

Acute compartment syndrome (ACS) is a serious condition that occurs when the pressure within a muscle compartment increases, restricting the blood flow to the area and damaging the muscles and nearby nerves [1] (Figure 1). Early diagnosis of ACS is vital to avoid muscle necrosis as well as an irreversible disability [2]. Unfortunately, ACS symptoms are subtle in the early stages.
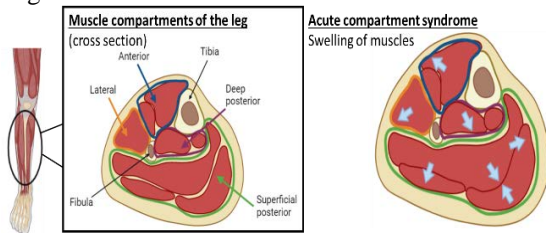
Figure 1: Muscle compartments of the leg and ACS.

Every day, doctors use mechanical methods to check the health of their patients by poking different parts of the body. However, these tactile assessments are qualitative and require the presence of a highly skilled clinician. In this work, we propose a new quantitative way of evaluating ACS by mechanical assessment of soft tissue changes.

Our study comprises of two components. First, we have developed an animal model of ACS to replicate the physiological changes during the condition. Secondly, we have developed a mechanical assessment tool for quantitative pre-clinical assessment of ACS. Our in-situ model of ACS uses blood injected to the muscle under pressure via the bone during which time our hand-held indentation device provides us with a correlation of internal pressure changes to the surface tissue (i.e., skin) mechanical properties.

Methods

Our compartment syndrome model was developed on the cranial tibial and the peroneus tertius muscles of a pig's leg (*postmortem*). The compartment syndrome pressure values were obtained by injecting blood from the bone through and around the muscle (Figure 2). By applying a pressure of 270 mmHg from the bone, the muscle reached a pressure between 40 mmHg and 60 mmHg. Two pressure transducers were used to measure the pressure injected in the bone and the one inside the muscle compartment.

To enable ACS assessment by a hand-held indentation device we combined three main components: a load cell, which measured the indentation force, a linear actuator, and a 3-axis accelerometer, which measured the indentation depth. To validate our equipment, we used a silicone model of a leg, where various pressures were applied inside, and indentation tests were performed.
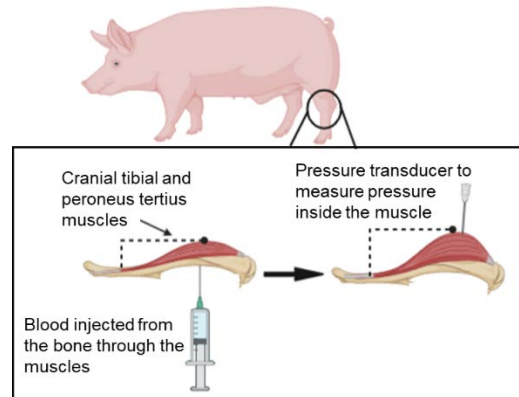
Figure 2: Compartment syndrome model on a pig's leg.

Results

From the indentation tests on the silicone model, we obtained that, when a pressure is applied internally, the measured peak force gets higher.
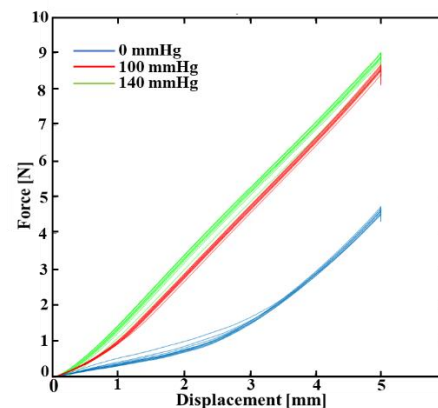
Figure 3: Force-displacement curve, comparing pressures applied inside the silicone model of a leg.

In our animal model, local muscle pressures reached values between 40 mmHg and 60 mmHg, which correlate with observed human physiology in ACS [3]. In our presentation we will share our static and dynamic indentation results on this model to demonstrate the sensitivity of our measurement techniques.

Discussion

Compartment syndrome is recognised as needing improved clinical management tools [4]. Our approach provides both a model that reflects physiological behaviour of ACS, and a method for in-situ non-invasive assessment and monitoring.

References

1. Oyster N. et al., Muscle and Nerve, Vol. 51., 2015
2. Uliasz A. et al., The American journal of emergency medicine, Vol. 21, pp. 143-145., 2003
3. Torlincasi A. M. et al., Extremity. StatPearls. 2021
4. Coe M. et al., Journal of the American Academy of Orthopaedic Surgeons., 2020

TISSUE INTERNAL STRAINS COMPUTED BY A FINITE ELEMENT MODEL OF THE HUMAN HEEL AND MEASURED FROM MR IMAGES

Alessio Trebbi [1], Mathieu Bailet [2], Antoine Perrier [1,2,3], Yohan Payan [1]

1. Univ. Grenoble Alpes, CNRS, UMR 5525, VetAgro Sup, Grenoble INP, TIMC, 38000 Grenoble, France; 2. TwInsight, France; 3. Groupe hospitalier Diaconesses Croix Saint-Simon, France

Introduction

Pressure ulcers are a severe disease mostly prevalent in patients that are bedridden or on wheelchair bound. These wounds can start developing in the deep layers of the skin of specific parts of the body, mostly on heels or sacrum, making them hard to detect in their early stages. It is recognized that prevention could be possible with the implementation of patient-specific Finite Element (FE) models to calculate dangerous levels of strains in the deep tissues that could trigger a pressure ulcer [1]. Validation of such FE models is a complex task. The current implemented techniques are limited as they consider only external displacements and pressures, or cadaveric samples [2]. In this work, we propose an *in vivo* technique for evaluating the simulations provided by an FE model of the human heel. This solution is based on the 3D non-rigid registration between two Magnetic Resonance (MR) images (one with heel at rest and the other one after applying a surface load below the heel) that is used to estimate tissue *in vivo* internal strains.

Methods

A Magnetic Resonance-compatible device has been designed to apply external loads on the heel while acquiring 3D MR images [3] (Figure 1). Using non-rigid registration techniques, the deformation field between the undeformed and deformed configuration is computed. From the obtained deformation map the Green-Lagrange strain filed is subsequently calculated. On the other hand, the segmentation from the unloaded MR image allowed to generate an ANSYS FE model of the heel. The MR load experiment was then simulated to compare the shear strain results between the FE method and the image registration (Figure 2).

Results

The MR-compatible device permitted to obtain good quality images allowing for a reliable image registration. The strain distribution, calculated respectively with 3D image registration and FE, resemble the expected results showing the highest strains around the bony prominence of the calcaneus (Figure 2).
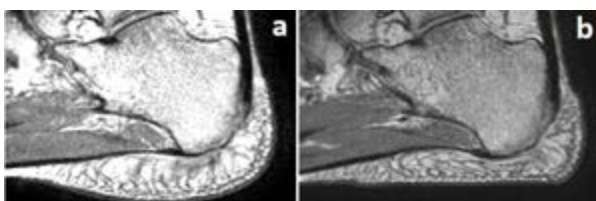
Figure 1: (a) MR image of the heel at rest. (b) MR image of the loaded heel.
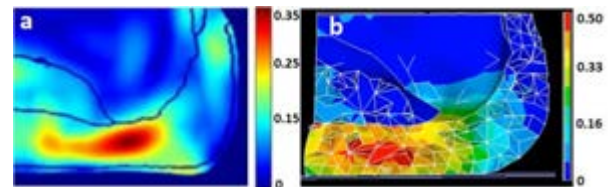
Figure 2: Comparison of tissue shear strains. (a) Green Lagrange strains map estimated from the displacement field computed in the image registration [2]. (b) Hencky shear strains computed by ANSYS.

Discussion

The implemented technique adds a useful tool for better understanding the propagation of strains in heel deep tissues that could generate pressure ulcers. Strain estimations through 3D image registration offers a promising technique for evaluating FE models for biomechanical applications. Further investigation is required towards identifying optimal material parameters to be implemented in the FE model. This would allow to find a stronger match in terms of magnitude and location of computed strains with both techniques.

References

[1]   K. K. Ceelen, A. Stekelenburg, S. Loerakker, G.J. Strijkers, D.L. Bader, K. Nicolay, F.P.T.Baaijens & C.W.J. Oomens (2008). Compression-induced damage and internal tissue strains are related, *J. Biomech.*, vol. 41, no. 16, pp. 3399–3404.

[2]   B. E. Keenan, S. L. Evans, and C. W. J. Oomens, "A review of foot finite element modelling for pressure ulcer prevention in bedrest: Current perspectives and future recommendations," *J. Tissue Viability*, Jun. 2021, doi: 10.1016/J.JTV.2021.06.004.

[3]   A. Trebbi, A. Perrier, M. Bailet, and Y. Payan, "MR-compatible loading device for assessment of heel pad internal tissue displacements under shearing load.," *Med. Eng. Phys.*, vol. 98, pp. 125–132, Dec. 2021, doi: 10.1016/J.MEDENGPHY.2021.11.006.

Acknowledgements

A BAYESIAN CONSTITUTIVE MODEL SELECTION FRAMEWORK FOR BIAXIAL MECHANICAL TESTING OF PLANAR SOFT TISSUES

The author list goes here ("Authors" style)
Ankush Aggarwal (1), Luke T. Hudson (2), Devin W. Laurence (2), Chung-Hao Lee (2), Sanjay Pant (3)

1. University of Glasgow, UK; 2. The University of Oklahoma, USA; 3. Swansea University, UK

Introduction

A variety of constitutive models have been developed for soft tissue mechanics, however there is no established criterion to select a suitable model for a specific application. Although the model that best fits the experimental data can be regarded as the most suitable model, this often can be insufficient given the inter-sample variability of experimental observations. Herein we present a Bayesian approach to calculate the relative probabilities of constitutive models based on biaxial mechanical testing of tissue samples.

Methods

46 samples of porcine aortic valve tissue were tested using a biaxial stretching setup. For each sample, seven ratios of stresses along and perpendicular to the fiber direction were applied. Each resulting curve was regressed to smooth and interpolate the data using a one-dimensional function. Principal component analysis was used to calculate the dominant modes in the experimental data and thereby construct a statistical model of the data. Prior probabilities of the models were considered equal, and the those of the model parameters were considered uniformly distributed around the classical best fit. Finally, the probability of eight constitutive models were calculated given the experimental data using Bayes' rule via Monte Carlo integration.
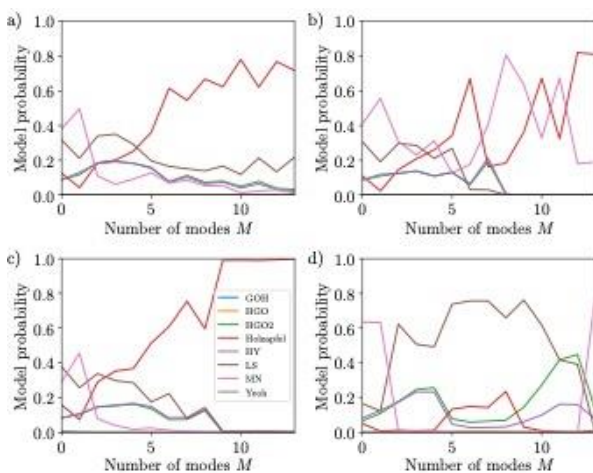
Figure 1: The probabilities of models using the second prior choice versus number of modes M for (a) all, (b) LCC, (c) RCC, and (d) NCC.

Results

The interpolation and smoothing gave a robust statistical model with ten dominant modes. Monte-Carlo integrations converged for all the simulations. The calculated probabilities showed the Holzapfel model [1] originally developed for arteries was the most probable model for the aortic valve data, closely followed by the Lee-Sacks model [2] (Fig. 1a). When the samples were grouped into different cusp types, Holzapfel model remained the most probable for the left- and right-coronary cusps (Fig. 1b,c). However, the Lee--Sacks model had the highest probability for the non-coronary cusps (Fig. 1d). The difference in the cusps was found to be associated with the second PCA mode; the second mode amplitudes of non-coronary and right-coronary cusps were found to be significantly different (Fig. 2).
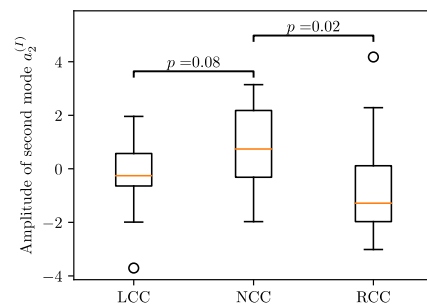
Figure 2: Statistical tests between the second PCA mode amplitudes of different cusp types showed a significant difference in the second principal mode between NCC and RCC

Discussion

The results show that the PCA-based statistical model can capture a significant variation in the mechanical properties of soft tissues. The presented framework is objective, applicable to any tissue type, and has the potential to provide a rational way of making simulations population-based.

References

1. Holzapfel et al, American Journal of Physiology-Heart and Circulatory Physiology, 289(5), H2048-H2058, 2005
2. Lee et al, J Biomechanics 47(9): 2055-2063, 2014.

Acknowledgements

OPTIMIZATION OF SINGLE-SIDED NMR AND INDENTATION PROTOCOLS IN EVALUATING CARTILAGE STRUCTURE AND MECHANICS

Matteo Berni (1), Carlo Golini (2), Claudia Testa (2), Nicola Francesco Lopomo (3), Leonardo Brizi (2), Massimiliano Baleani (1)

1. IRCCS Istituto Ortopedico Rizzoli, Medical Technology Laboratory, Italy; 2. University of Bologna, Department of Physics and Astronomy, Italy; 3. University of Brescia, Department of Information Engineering, Italy

Introduction

Articular cartilage is a highly specialized tissue, whose degradation plays a crucial role in the development of joint diseases. Detecting structural alterations, and accurately assessing the corresponding changes in mechanical behavior, would aid to better understand the subtle pathological processes occurring in the early stage of osteoarthritis (OA), then leading to macroscopic alteration of tissue morphology in late OA [1]. Mobile single-sided Nuclear Magnetic Resonance (NMR) instruments were reported to allow accurate assessment of parameters related to the cartilage microstructure [2]. The experimental approach to carry out NMR evaluation on cartilage has not yet been defined, considering possible tissue degradation during measurement. Furter, from the mechanical perspective, the effect of indentation parameters on the cartilage response has not yet been investigated [3]. The aim of this study is twofold: i) to optimize a single-sided NMR approach capable of quantitatively evaluate cartilage structure; ii) to implement reliable methods able to mitigate inaccuracies during indentation of cartilage tissue.

Methods

Osteochondral specimens were extracted from bovine knees articular surface. Twenty cores ($\emptyset$ = 10mm, h = 10mm) were analyzed by NMR single-sided device (MOUSE PM10, Magritek) to monitor T_1, T_2, M_0 and D while maintaining cartilage tissue at room temperature for 10 hours. CPMG, Saturation Recovery and Stimulated Spin-Echo were performed on 3 setups (S1, S2, S3). Sample in glass tube + sponge imbibed in PBS solution (S1); + a layer of PTFE for sealing (S2); for S3 the core was immersed in PBS. Once evaluated the best setup, an automatized procedure (AP) to determine NMR parameters of cartilage layers (superficial, middle, deep) was established minimizing the acquisition time. Six rectangular samples (about 30mm x 22mm x 10mm) were indented aiming to determine cartilage instantaneous elastic response (E_0). Since cartilage response is strain and strain-rate dependent, specimens were indented by reproducing in vivo conditions, i.e. 15% nominal deformation, $0.15s^{-1}$ strain rate. This approach requires a priori the measurement of cartilage thickness, estimated by evaluating nearby locations. Tests were performed by spherical indenters of different size, up to 8mm diameter. Aiming to determine the estimates accuracy, cartilage thickness was accurately measured after indentation testing.

Results and discussion

A decrease of all the NMR parameters was observed during degradation. The highest was for S1 (Fig. 1 for M_0 and T_2). S2 and S3 had the best performance for preserving the parameters with S3 ahead. Considering absolute values of D, S3 showed an increase of ~26% vs. S1 and S2. S3 minimized the dehydration of the core but significantly influenced D values due to interactions of PBS with the NMR signal. The results allowed to optimize the AP by choosing S2 and the total duration (< 4 h). Preliminary analyses with AP indicated significant differences (p<0.05) of all the NMR parameters among different layers. Estimating a priori the cartilage thickness through the proposed method allowed to obtain measures close to the real values (median of the estimate error 0.6%, 25th percentile -5.1%, 75th percentile 7.0%). Keeping constant nominal strain and strain-rate, cartilage E_0 seems to depend on indenter diameter, at least up to 5 mm.
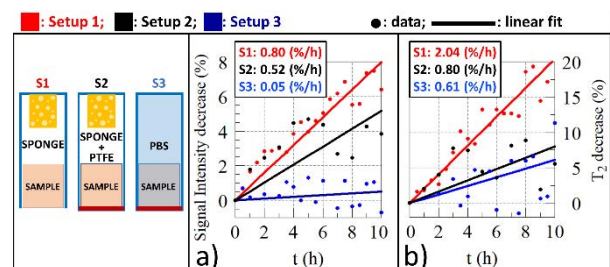
*Fig. 1: Percentage decrease of **a**) Signal Intensity (M_0) and **b**) T_2 parameter for the 3 Setups (CPMG). Computed linear decrease rates are reported in insets.*

Conclusions

This work lays solid foundations in determining NMR and mechanical peculiarities related to cartilage chemical-physical and structural features. Future developments will concern the assessment of correlations between NMR parameters and tissue mechanics, thus to apply such integrated framework in evaluating cartilage changes throughout OA.

References

1. Hatcher et al, J Biomech, 55:18-26, 2017.
2. Casanova et al, Springer Nature 2011.
3. Patel et al, Tissue Eng Part C Methods, 25(10):593-608.

Acknowledgements

UNIAXIAL TENSILE TESTS ON HUMAN FASCIA LATA: STRESS RELAXATION AND FAILURE PHENOMENA FROM FROZEN CADAVERS

Lorenza Bonaldi (1), Chiara Giulia Fontanella (2), Carla Stecco (3), Alice Berardo (1, 4)

1. Department of Civil, Environmental and Architectural Engineering, Via F. Marzolo 9, 35131 - Padova, Italy; 2. Department of Industrial Engineering, Via Venezia 1, 35121 - Padova, Italy; 3. Department of Neuroscience, Via A. Gabelli 65, 35121 - Padova, Italy; 4. Department of Biomedical Sciences, Via U. Bassi 58/B, 35131 - Padova, Italy.

Introduction

Human Fascia Lata is a connective tissue also known as aponeurotic fascia. The biomechanics is influenced by its arrangement in several layers (usually 2÷3) separated by loose connective tissue. In each layer, most of collagen fibers run parallel in a distinct direction (inter-layers angle: 75°÷80°), mirroring the fascia's ability to adapt and withstand specific tensile loads [1]. Despite the structural importance of Fascia Lata as key connective tissue in both musculoskeletal dysfunctions and tissue engineering, an experimental protocol free from biases (that alter tissue properties, misleading results interpretation) is still a challenge. For this reason we investigate this open theme as the main purpose of this research work.

Methods

Fascia Lata was harvested and stored (-80°C) from four fresh-frozen donors, according to *Body Donation Program* of the Institute of Anatomy of the University of Padua [2]. After thawing, samples were cut into strips and mounted on Mechanical Tester (Model Mach-1, ©Biomomentum Inc.). Specimen's cross-sectional area was calculated on the average thickness value acquired with a manual caliper, meanwhile inter-layers angles with image processing. Multiple samples were cut, oriented and loaded during testing according to the directions of the collagen fibers for each individual layer (principal and transverse). The sample size for each configuration was defined based on the availability of native tissue (for each subject). Samples were kept moist during testing, pipetting them with phosphate buffered saline solution, and their temperature was monitored with an infrared scan prior to testing. Ten preconditioning cycles were performed before stress relaxation and failure protocols. Results have been analyzed with MATLAB [3]. Statistical analyses were performed for the different groups of specimens (subjects/layers/directions), also correlating the results with inter-layers angles.

Results

Experimental outcomes show a time-dependent (e.g. Figure 1a, b) and anisotropic behavior (e.g. Figure 1c).

Discussion

The proof of specific tissue anisotropy (between subjects/layers/directions), in term of ultimate strength/ Young's Modulus and viscoelastic behavior, is a key information for a wide range of clinical applications. It could help in guiding surgeons during graft preparation and positioning; clinicians in risk assessment after surgery; physiotherapists during musculoskeletal rehabilitation (manual therapy); engineers in modeling in-silico tests towards a personalized medicine.
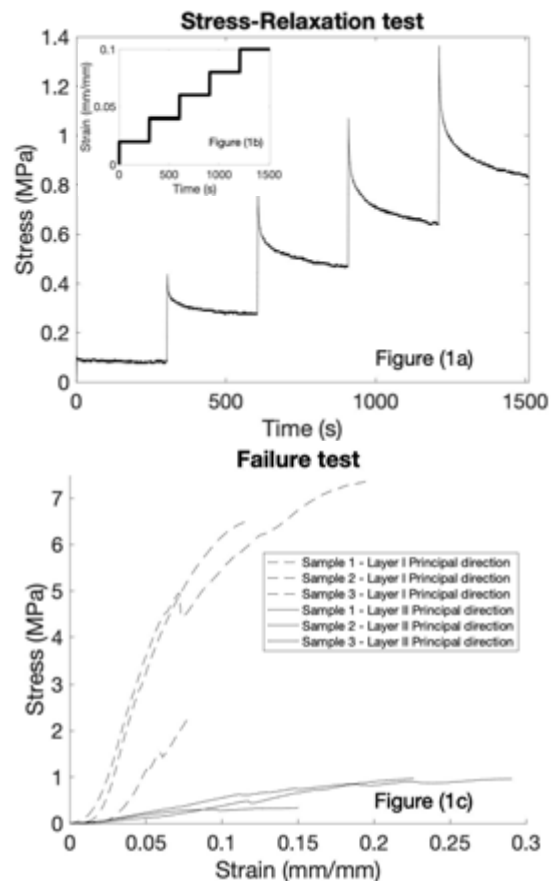
Figure 1: Stress-Relaxation (a) obtained as response of applied Strain-time history (b); Failure curves (c).

References

1. Stecco C., Functional Atlas of the human fascial system, Churchill Livingstone, Elsevier Ltd, 2015.
2. Porzionato A, et al., Quality management of Body Donation Program at the University of Padova. Anat Sci Educ. 2012 Sep-Oct; 5(5):264-72.
3. MATLAB and Statistics Toolbox Release 2021b, The MathWorks, Inc., Natick, Massachusetts, United States.

Acknowledgements

INTER-DONOR VARIABILITY IN THE TENSILE AND COMPRESSIVE BEHAVIOUR OF IN VITRO HUMAN THROMBI

Rachel M.E. Cahalane (1), Judith J. de Vries (2), Moniek P.M. de Maat (2), Kim van Gaalen (1), Heleen M. van Beusekom (3), Aad van der Lugt (4), Ali C. Akyildiz (1,5) and Frank J.H. Gijsen (1,5)

1. Department of Biomedical Engineering, Erasmus Medical Centre, Rotterdam, the Netherlands. 2. Department of Hematology, Erasmus Medical Centre, Rotterdam, the Netherlands. 3. Experimental Cardiology, Erasmus Medical Center, Rotterdam, the Netherlands. 4. Department of Radiology and Nuclear Medicine, Erasmus Medical Centre, Rotterdam, the Netherlands. 5. Department of Biomechanical Engineering, Delft University of Technology, Delft, the Netherlands.

Introduction

Adequate reperfusion is still not achieved in 41% of endovascular thrombectomy (EVT) procedures [1]. These procedures are significantly influenced by the behaviour of the occluding thrombus [2], which is exposed to multi-axial loading during retrieval [2]. Unconfined compression is commonly used to determine thrombus stiffness. However, difficulties in specimen handling have led to a shortage of data on thrombi in tension. Composition alone cannot explain the observed compressive stiffness variation for retrieved thrombi [3]. Data suggests that a mechanical variation exists between comparable thrombi from different donors [4]. Here, we report on the tensile and compressive properties of comparable thrombus analogues produced from the blood of human donors.

Methods

Thrombus analogues were prepared from the blood of 6 healthy human donors (3 males). Platelet-rich plasma (PRP), platelet-poor plasma (PPP), whole blood (WB) clots and clots with a range of red blood cell (RBC) volumes (0%, 5%, 10%, 20%, 40%, 60% and 80%) were produced. Uniaxial tensile stretching was conducted until failure. Compression was conducted until 80% strain. A high-strain stiffness value was acquired by applying a linear fit to the final 10% of the stress-strain data. Scanning Electron Microscopy (SEM) was performed to examine the thrombi microstructure.

Results

A marked strain-stiffening compressive response is observed for all compositions, in contrast to the approximately linear nominal stress-strain profiles under tension (Fig.A). There are overlapping behaviours for thrombi of different compositions from different donors (Fig.B). Thrombus tensile stiffness values generally decrease for each increasing RBC volume (Fig.C). In contrast, compressive stiffness increases from 0% to 10% RBC volume, followed by a decrease in stiffness with subsequent RBC volumes (Fig.D). SEM analysis reveals network pores within the PRP fibrin network (Fig.E). RBCs are tightly packed within the 5% RBC network (Fig.F). The network becomes looser again for a 60% RBC sample (Fig.G). High-strain tensile and compressive stiffness values exhibited 49% and 30% variance, respectively.
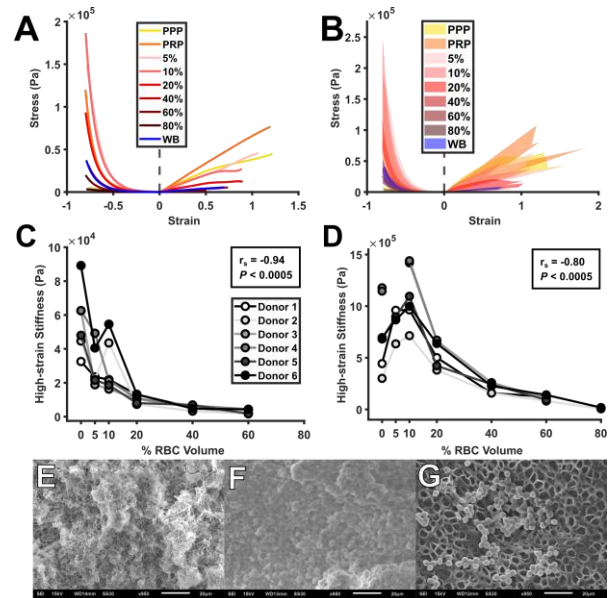
Figure 1: Nominal stress-strain (A) midlines and (B) range per composition. (C) Tensile and (D) compressive high-strain stiffness values per RBC volume. SEM of (E) PRP, (F) 5% and (G) 60% RBC volume clots.

Discussion

This is the first investigation of the stiffness properties of thrombus analogues made from the blood of healthy human donors in a range of compositions under both tensile and compressive loading. There is a pronounced asymmetry in the tension-compression nominal stress-strain profiles of in vitro healthy human thrombi. Accordingly, different material models are required to adequately capture the thrombus response to EVT. There is significant variation present in the stiffness of whole blood clots derived from different healthy human donors. Future studies should assess the utility of this mechanical variation in the prediction of EVT success in patients undergoing AIS treatment.

References

1. Jansen et al, BMJ, 360: k949, 2018.
2. Yuki et al, Am J Neuroradiol, 33:643–648, 2012.
3. Boodt et al, Stroke, 52:2510-2517, 2021.
4. Malone et al, Cardiovasc Eng Technol, 9:489–502, 2018.
5. Cahalane et al, J Biomech, 129:110816, 2021.
6. Johnson et al, J Neurointerv Surg, 12:853-857, 2019.

VISCOELASTIC PROPERTIES OF TUMOUR TISSUE: RELATION WITH STRUCTURE AND COMPOSITION

A. Levillain (1,2), C.B. Confavreux (1,3,4), M. Decaussin-Petrucci (3,5,6), E. Durieux (3,7), P. Paparel (3), K. Le-Bail Carval (3), L. Maillard (3), F. Bermond (2), D. Mitton (2), H. Follet (1)

1. Univ Lyon, UCBL, INSERM, LYOS UMR 1033, Lyon, France; 2. Univ Lyon, Univ Gustave Eiffel, UCBL, LBMC UMR_T9406, Lyon, France; 3. Hospices Civils de Lyon, Centre hospitalier Lyon Sud, Pierre Bénite, France; 4. CEMOS, Service de Rhumatologie, Institut de Cancérologie, Lyon, France; 5. Department of Pathology, France; 6. UCBL, EA 3738 CICLY, Oullins, France; 7. Centre de Pathologie et de Neuropathologie Est, Lyon, France

Introduction

Mechanical properties of the extracellular matrix (ECM) play a significant role in regulating cancer cell activities [1]. In breast cancer, ECM stiffening promotes tumour progression and metastasis formation, including bone metastasis. In thyroid cancer, an increase or a decrease in the elastic properties was found depending on the histological type [2], suggesting that different cancer cell types likely respond differently depending on their microenvironment. Atomic force microscopy (AFM) has the potential to elucidate the mechanical signature of breast cancerous tissue at the tissue scale [3]. The aim of this study was to characterise the viscoelastic properties of different types of human tumour tissue that frequently metastasize to the bone using AFM and to correlate them with tissue composition.

Material and methods

Human breast (n=6), kidney (n=5), and thyroid (n=4) specimens containing normal and tumour tissue were collected post-surgery. From each specimen, one sample was used for histology (hematoxylin phloxine saffron staining) and one sample was used for AFM testing. Fresh frozen samples were immersed in PBS and AFM tests were performed using a Nanowizard3 AFM (JPK Instruments AG) equipped with an MLCT cantilever (Bruker) and a pyramidal tip. First, tapping mode topography was used to identify a region of interest with minimal slope. Second, 25 force-displacement curves were recorded over the region of interest, following a trapezoidal loading profile. Elastic modulus was identified from the force-indention curve using the Hertz-Sneddon model [4]. Elastic fraction, defined as the ratio between the equilibrium and instantaneous moduli, was identified from the indentation-time curve using the standard linear solid model [5]. It varies between 0 (viscous) and 1 (elastic).

Results and discussion

The change in the mechanical properties of tumour tissue was highly dependent on the composition and structure of the tissue. Breast tumour samples, which were composed of dense fibrous tissue, displayed an increased elastic modulus compared to their normal counterpart. The elastic properties of kidney tumour samples were differently affected depending on their histological type (Fig 1). Clear cell renal cell carcinomas (RCC) displayed a high cellular density, which was associated with a decreased elastic modulus (Fig 1A, B). Papillary RCC displayed dense fibrous tissue, which was associated with an increased elastic modulus (Fig 1A, C). One specimen was composed of densely cellular (clear cell RCC) and fibrous (sarcomatoid) regions, resulting in heterogeneous elastic properties (Fig 1A, D). Similarly, the elastic properties of thyroid tumour samples were differently affected depending on their histological type. Moreover, thyroid tumour samples showed a decreased elastic fraction, while no difference was observed for kidney and breast tissue.
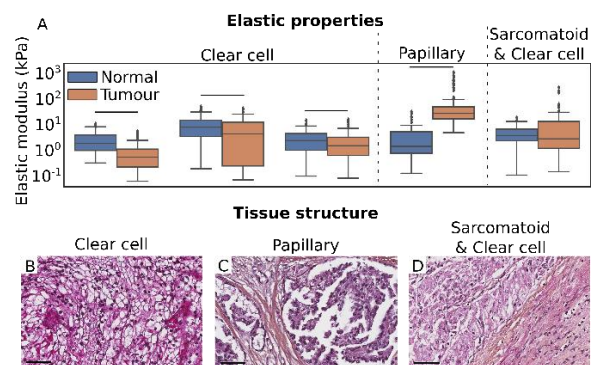
Figure 1: Elastic modulus (A) and histological sections (B, C, D) of kidney tumour specimens of different types. Bars show significant differences between normal and tumour samples (p<0.05). Scale bars: 60 µm.

Results demonstrate that the mechanical properties of tumour tissues are differently affected depending on their type, suggesting a link between the mechanical properties and aggressiveness of the cancer. Future work will assess the relationship between the mechanical properties of tumour tissue and its metastatic potential.

References

1. Northcote et al, Front. Cell Dev. Biol., 6:17, 2018.
2. Lyshchik et al, Ultrason. Imaging, 27:101-110, 2005.
3. Plodinec et al, Nat Nanotechnol, 7(11):757–765, 2012.
4. Rico et al, Phys. Rev. E, 72 (2): 021914, 2005.
5. Oyen et al, J. Mater. Res., 20(8):2094–2100, 2005.

Acknowledgements

MECHANICAL PROPERTIES OF PLANTAR TISSUES: A COUPLED EXPERIMENTAL AND NUMERICAL APPROACH

Sofia Pettenuzzo (1), Alice Berardo (1,2), Elisa Belluzzi (3), Assunta Pozzuoli (3), Pietro Ruggieri (3), Rafael Boscolo Berto (4), Raffaele De Caro (4), Emanuele Luigi Carniel (5), Chiara Giulia Fontanella (5)

1. Department of Civil, Environmental and Architectural Engineering, University of Padova, Italy; 2. Department of Biomedical Sciences, University of Padova, Italy; 3. Orthopedics and Orthopedic Oncology, DiSCOG, University of Padova, Italy; 4. Department of Neuroscience, Institute of Human Anatomy, University of Padova, Italy; 5. Department of Industrial Engineering, University of Padova, Italy

Introduction

Plantar tissue is the first part of the body that interacts with the ground during locomotion (Fig. 1a) [1]. It is a soft connective tissue composed by adipose tissue and skin. These tissues play a key role in distributing body weight and in adsorbing shock e.g. during static standing and gait cycle. Different factors, such as age, sex, body max index (BMI) or disease can affect plantar tissues configurations and their mechanical properties. One of such disease is diabetes, a systemic disorder that affects thousands of people worldwide and that can lead to severe complications [2]. In this context, the mechanical properties of plantar adipose tissues were investigated by means of a combined experimental and computational approach, accounting for the non-homogeneous distribution.

Materials and Methods

Foot plantar tissues were collected from seven human donors, according to *Body Donation Program* of the Institute of Anatomy, Padova (M: 4, F: 3; mean age 64±23 years) (Fig. 1a). Confined compression tests and unconfined compression tests were carried out using a multi-step procedure (Fig. 1b). After preconditioning, each step was composed of 15% strain at 3000%/s strain rate, and subsequent 300 s of resting to allow the almost complete development of relaxation phenomena.

A three-dimensional finite element model of the foot, including bones, adipose tissues, skin, cartilage and ligaments (Fig. 1c), was realized with the finite element pre-processor Abaqus CAE 2019 (Dassault System). The plantar adipose tissues were described with a visco-hyperelastic constitutive model [3] and the model parameters were identified considering the experimental data from the developed tests [4]. Static standing condition was simulated in order to identify the stress-strain distribution on tissues.

Results

Experimental results showed differences in the mechanical behaviour between adipose samples taken from different plantar regions, e.g. higher stiffness in the metatarsal and lateral regions than in the anterior or posterior ones (Fig. 1d). Results also highlighted the non-linear stress-strain relationship and time depend effects that are typical of the visco-hyperelastic soft tissues behaviour (Fig.1e). Furthermore, computational results allowed to observe the stress and strain distribution, as well as the pressure field.
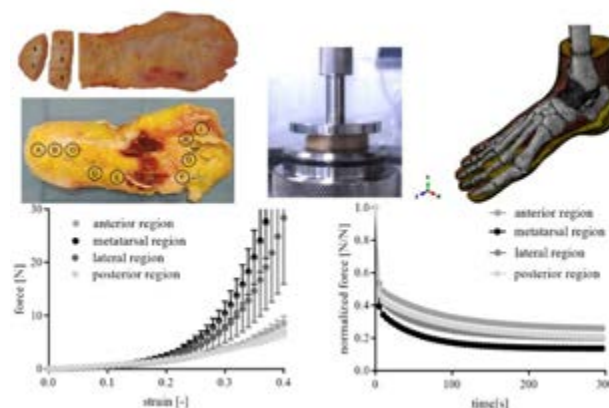
Figure 1: (a) plantar tissues samples; (b) confined compression test (c) numerical model of foot; (d) equilibrium force-strain data (d) and normalized force-time (e).

Discussions

While experimental tests have been useful to assess the mechanical properties of adipose tissues from different foot regions, the computational model provided information on mechanical behaviour of plantar tissues during functional loading conditions. Numerical model could also be a valuable tool to simulate different foot configurations, such as the interaction between foot and footwear or the comparison between the mechanical response of tissues in healthy and pathologic conditions. These insights could help in the design of specific insoles for diabetic patients to minimize pain caused by plantar ulcers.

References

1. Ledoux et al, J Biomech, 40: 2975-2981, 2007
2. Brady et al, J Biomech, 129:1-8, 2021.
3. Fontanella et al, Annals of Anat, 221:108-114, 2019.
4. Ou et al, Biomech Model Mechanobiol, 17: 1373-1388, 2018.

Acknowledgements

STRUCTURAL MECHANISMS IN SOFT FIBROUS TISSUES: LESSONS FROM BIOMIMETICS

Mirit Sharabi

Department of Mechanical engineering and Mechatronics, Ariel University, Ariel 407000, Israel

Introduction

Through years of evolution, biological soft fibrous tissues have developed remarkable functional properties, unique hierarchical architectures, and -most notably, an unparalleled and extremely efficient mechanical behavior. From a mechanical and material point of view, soft tissues are composite materials that are made from simple repeated building blocks (e.g., collagen, proteoglycans, and elastin) with diverse structural motifs. Although these structures have entirely different functions, they share a similar regime of large deformations and strain stiffening [1].

The unique properties of soft fibrous tissues stem from their structural complexity, which, unfortunately, also hinders our ability to generate adequate synthetic analogs, such that autografts remain the "gold standard" materials for soft-tissue repair and replacement.

Whereas the structure-function relationship is well-studied in natural hard materials, soft materials are not getting similar attention, despite their high prevalence in nature. Thus, reverse biomimetics of these materials and structural motifs in soft composites holds valuable insights that could be exploited to generate the next generation of biomaterials for soft tissue repair and replacement.

Soft tissue biomimetics- Methodology and results

Our research is focused on combined material fabrication, mechanical and structural characterization, and computational simulations to get a better understanding of the structure-function relationship in soft fibrous tissues by using biomimetic fiber-reinforced composites.

We have recently developed new biomimetic material systems based on silk fibroin and collagen fibers reinforced hydrogels. These materials can be tailor-designed to different soft tissue behaviors using biomimetic structural motifs such as weak interfaces, fiber crimping, and various fiber fractions and orientations.

As in native tissues, our composites demonstrated hyperelastic, anisotropic, and asymmetric mechanical behavior, with toe, heel, and linear regions. These soft composites demonstrated similar large-deformation behavior to different tissue structures such as the annulus fibrosus in the intervertebral disc [2,3], small-diameter blood vessels [4], and the knee meniscus [5].

Moreover, dedicated 3D hyperelastic and heterogeneous finite-element models were constructed to model the mechanical behavior of the composite laminates under physiological conditions, and the composites' mechanical compatibility with the native tissues was investigated. These models will be further used to tailor-design the mechanical behavior of the composites to the physiological loading modes.

Conclusions

Mimicking the native structural mechanisms in simpler material systems can provide a better understanding of the soft-tissues structure-function relationship in very complex tissues. For example, the cumulative influence of controlled fiber crimping, orientation and fraction on the large deformation behavior. This would lead to the design of the next-generation materials with custom-made mechanical behavior. These materials will revolutionize future soft-tissue repair and replacement applications by creating mechanically biocompatible native tissue behaviors.

References

1. Sharabi M. Structural Mechanisms in Soft Fibrous Tissues: A Review. (2022) Front. Mater. 8:793647. doi: 10.3389/fmats.2021.793647.
2. Sharabi, M., Wertheimer, S., Wade, K. R., Galbusera, F., Benayahu, D., Wilke, H. J., & Haj-Ali, R. Towards intervertebral disc engineering: bio-mimetics of form and function of the annulus fibrosus lamellae. JMBBM. (2019). 94, 298-307.
3. Mordechai HS, Ben-Yehuda A, Bonshtein I, Sivan SS, Sharabi M. Towards intervertebral disc engineering: simultaneous biomimetics of the annulus fibrosus and nucleus pulposus. In Preparation.
4. Sharabi M.*, Wertheimer S.*, Shelah O., Lesman A., & Haj-Ali R.. Bio-Composites Reinforced with Unique Coral Collagen Fibers: Towards Biomimetic-Based Small Diameter Vascular Grafts. JMBBM, (2021) 104526
5. Ben-Yehuda A, Mordechai HS, Sharabi M. Silk fibroin reinforced hydrogel biocomposites for soft tissue biomimetics. In Preparation.

CHARACTERIZATION OF MECHANICAL DAMAGE ON THE ESOPHAGEAL WALL OF CHRONIC-HYPOXIC LAMBS

Alejandro Bezmalinovic (1), Eugenio Rivera (1), Claudio García-Herrera (1), Diego Celentano (2), Alejandro González-Candia (3), Emilio A. Herrera (3)

1. Departamento de Ingeniería Mecánica, Universidad de Santiago de Chile, Chile; 2. Departamento de Ingeniería Mecánica y Metalúrgica, Pontificia Universidad Católica de Chile, Chile; 3. Laboratorio de Función y Reactividad Vascular, Programa de Fisiopatologia, ICBM, Facultad de Medicina, Universidad de Chile, Chile.

Introduction

The esophagus is an organ present on most vertebrates, whose primary function is the peristaltic transportation of previously chewed food-mass (bolus) from the pharynx into the stomach.

At high altitudes – above 2500 masl – animals are exposed to a low oxygen-pressure environment-induced condition, known as "hypobaric hypoxia". Chronic hypoxia during development impairs the function and structure of several organs [1]. These effects are in part mediated by oxidative stress, hence it has been proposed that an antioxidant treatment may prevent them [2]. However, few is known about the effects of high-altitude hypoxia on the esophagus biomechanical characteristics. Therefore, the objective of this work is to characterise the mechanical damage of esophageal tissue, particularly exploring the effects of its exposure to chronic hypobaric hypoxia and an antioxidant treatment with melatonin, on its passive mechanical properties. Thus, the final goal is to provide the biomedical area with reliable constitutive models aimed at improving the understanding of its mechanical response.

Methods

All procedures were approved by the Bioethics Committee of the Faculty of Medicine, University of Chile (CBA 0761 FMUCH). Eight lambs – conceived, gestated, born and raised at Putre Research Station, INCAS (3600 masl) – were studied. Neonates were randomly separated into two groups: 4 melatonin-treated (1.0 mg kg-1d-1 of melatonin; vehicle: 0.5 ml kg-1d-1 of ethanol 1.4%) and 4 controls (vehicle: 0.5 ml kg-1d-1 of ethanol 1.4%). Once euthanized, two rectangular samples were cut from the full esophageal wall (i.e. comprising the mucosa, submucosa and muscularis tunicae) of each subject, one with its main axis oriented along the circumferential (θ) direction of the organ and the other oriented along the longitudinal (z) direction (Fig. 1). Samples were assessed for in-vitro displacement-controlled uniaxial tensile tests, in order to evaluate the passive mechanical properties of esophageal tissue.

Constitutive modelling

The mechanical characterization of the esophagus is based upon uniaxial tensile-test results (Fig. 1). A damage model [3] is associated to the isochoric strain-energy component of an anisotropic hyperelastic model [4], assuming material incompressibility and isothermal conditions.
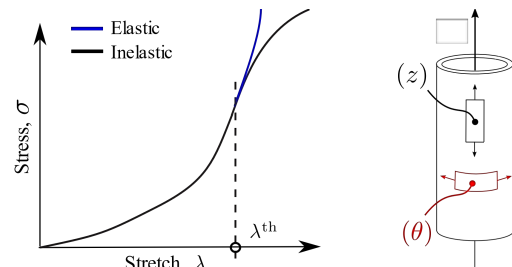
Figure 1: (Left) Typical uniaxial-tensile test stress-stretch elastic and inelastic curves.
(Right) Esophagus scheme with longitudinal (z) and circumferential (θ) sample orientations.

Results

The passive inelastic mechanical behaviour of the esophageal wall was group-wise characterised. The analysis of stress-stretch curves allowed us to evaluate differences between groups of lambs and possible effects of the pharmacological treatment. Although it is observed that melatonin reduces the esophageal-wall stiffness, no statistically-significant differences – on the uniaxial-stress median between groups – are found. Results further show a delay in the circumferential damage onset; an expected mechanical-resistance hierarchy due to the in-vivo physiological function of the organ.

Conclusion

The damage-based characterization proposed is adequate to describe the passive mechanical response of chronic-hypoxic lamb esophageal tissue, providing reliable parameters for its numerical simulation.

References

1. Ducsay CA et al, Physiol Rev, 98(3):1241-1334, 2018.
2. González-Candia A et al, J Pineal Res, 68(1):e12613, 2020.
3. Peña E. et al, Int J Numer Meth Eng, 74:1198-1218, 2008.
4. Gasser T. et al, J R Soc Interface, 3:15-35, 2006.

Acknowledgements

PORCINE KNEE CARTILAGE MAPS DETERMINED WITH AUTOMATED INDENTATION AND CHARACTERIZED BY MACHINE LEARNING

Erfan Hamsayeh Abbasi Niasar,   LePing Li

Department of Mechanical and Manufacturing Engineering, University of Calgary, Canada

Introduction

The zonal differences of articular cartilage, i.e., the tissue property variation with the tissue depth, are well established [1]. Cartilage in the knee joint exhibits site-specific gene expressions, or regional differences, in response to mechanical loadings [2], which cannot be explained by the zonal differences. Site-specific mechanical properties of the whole cartilage must be determined for this purpose. The site-specific properties are also required in the subject-specific finite element models [3], to better understand the contact mechanics, a necessary step to the knowledge of pathomechanics of the joint. The objective of the present study was to determine the regional differences in the mechanical properties of porcine knee cartilage using indentation maps and finite element modelling.

Methods

Fresh porcine cartilages from each knee joint were dissected into 4 cartilage-bone blocks to facilitate indentation tests on the Mach-1 tester (Biomomentum Inc): lateral and medial femoral specimens, and lateral and medial tibial specimens. Six complete sets, or 24 specimens from 6 porcine stifle joints, were so far collected from which 22 specimens were successfully tested (more tests are being performed). A 2-mm spherical indenter was used to map the tissue response of each specimen with ~30 indentation sites. A relaxation testing of 100 seconds was measured at each site with 0.2mm-compression applied at 0.2 or 0.4 mm/s. Cartilage thickness was then mapped with needle probing. K-means clustering algorithm in coupling with differential evolution was used to optimize the number of regions or clusters required to quantify the site-specific tissue properties for each specimen, which was determined from the indentation data with the Elbow method after testing 2-8 clusters (Fig. 1).

The average load response from the data points in each region was then curve-fit (Fig. 1) to extract the mechanical properties of cartilage using a finite element model of indentation in ABAQUS. A previously developed fibril-reinforced constitutive model was used for the simulation of the load response at the rather high compressive rates used in the tests. Mechanical properties of cartilage include the elastic modulus, E_{m}, and Poisson's ratio of the proteoglycan matrix, the nonlinear modulus of the collagen fibrillar matrix, $E_{\mathrm{f}} = E_0 + E_\varepsilon \varepsilon$, and tissue permeability k. Cartilage was modelled as orthotropic with x to be the primary fibre direction.

Results

Based on the results obtained so far, 4 distinct regions would best represent the site-specific tissue properties for the medial tibial cartilage, while 3 regions would be sufficient for the lateral tibial cartilage, lateral or medial femoral cartilage (Fig. 1). Therefore, 13 distinct regions in total are needed to fairly describe the variation of cartilage properties for the tibiofemoral joint.

There was a good agreement between the relaxation data and the finite element results with an error < 10%. A variation in the range of 25-40% was seen when comparing the material properties extracted for different regions. For instance, the mechanical properties for lateral tibial cartilages were in the following range: E_{m} = 0.06-0.33 MPa; E_{0x} = 1.3-4.0 MPa; $E_{\varepsilon x}$ = 825-4200 MPa; k_x = 1.0-3.0×10^{-3} mm^4/Ns.
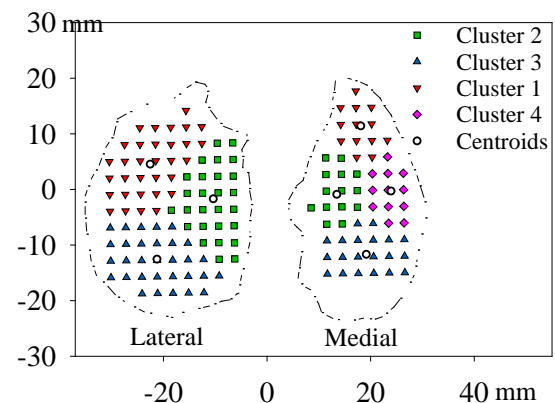
Figure 1: K-means clustering results for tibial cartilages

Discussion

The methodology developed in this study can be used to characterize the site-specific cartilage properties of human knee cartilages. Characterizing cartilages in the joint into several regions, rather than using continuous domains to define the differences in the tissue properties, will simplify lab tests and implementation of material properties in a finite element model of the joint. Only 13 sites need to be tested instead of over 100 testing sites according to our preliminary analysis. The study may pave the way, e.g., for understanding site-specific cartilage gene expressions and degenerations under *in-vivo* joint loadings [2].

References

1. Schinagl et al, J Orthop Res, 15(4): 499-506, 1997.
2. Otoo et al, J Biomech Eng, 144(2): 024502, 2022.
3. Dabiri & Li, Med Eng Phy, 35(11): 1591-1598, 2013.

NON-LINEAR HOMOGENIZATION OF SOFT TISSUES: APPLICATION TO TENDONS AND ARTERIES

Claire Morin (1), Christian Hellmich (2), Stéphane Avril (1,2)

1. *Mines Saint-Etienne, Univ Lyon, Univ Jean Monnet, Etablissement Français du Sang, INSERM, U 1059 Sainbiose, F - 42023 Saint-Etienne, France;*

2. *Institute for Mechanics of Materials and Structures, TU Wien, Vienna, Austria*

Introduction

The nonlinear macroscopic mechanical properties of soft tissues such as tendons or arteries originate in physical mechanisms (such as fiber straightening, reorientation and elasticity) and mechanobiological effects (such as cell mechanosensing mediating tissue remodeling), which occur within the microstructure. The traditional hyperelastic approach, tracing back the tissue behavior to some initial configurations, cannot always reproduce the actual experimental observations [1]. All this motivates us to to develop detailed multiscale models of soft tissues within a continuum micromechanics framework [2].

Methods

We represent the crimped collagen fibers through a number of straight fiber phases (labelled with f) with different orientations, being embedded into a matrix phase (labelled with m). The corresponding representative volume element (RVE) hosting these phases is subjected to "macroscopic" strain rates, which are downscaled to fiber and matrix strain rates on the one hand, and to fiber spins on the other hand. This gives quantitative access to the fiber decrimping (or straightening) phenomenon under non-affine conditions [2]. The microscopic stresses stem from a hypoelastic constitutive relation. Finally, the macroscopic stress is obtained as the volume average of the microscopic stresses. This framework is applied to the mechanical behavior of tendon and arterial tissues.

Within both the tendon and the adventitial tissues (see **Erreur ! Source du renvoi introuvable.**), two scales are modeled so as to account for both the fiber decrimping (through the progressive fiber reorientation at the lowest scale) and bundle realignment (at the macroscopic scale); although tendinous bundles are parallel to the load direction in the initial state.

Results

We validated our models against different sets of experimental data, stemming from different tendon organs, porcine and human arterial tissues, by comparing their uniaxial tensile responses in different directions, see Figure 2.

Discussion

This modelling framework allows to capture different features of arterial mechanics such as the role of elastin in healthy and aged samples. Besides, our model reveals the mechanical cooperation of the tissue's key microstructural components: while the fibers carry tensile forces, the matrices undergo hydrostatic pressure. Oscillating hydrostatic pressure has been shown to play a vital role in the mechanobiology of bone [3,4], and accordingly, our results on similar stress states in soft tissue matrices offer a totally new perspective on soft tissue remodeling.
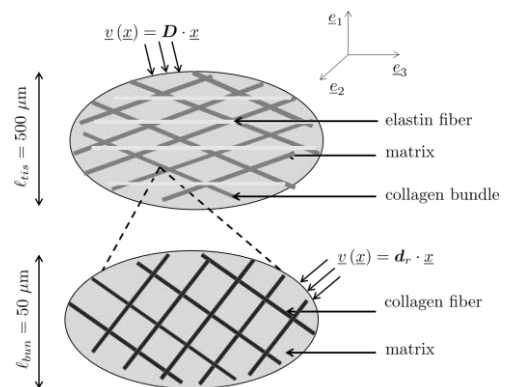
Figure 1: micromechanical representation of tendinous and adventitial tissues.
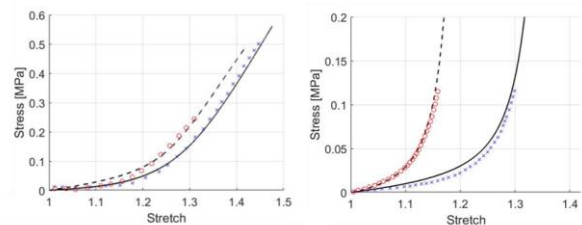
Figure 2: Comparisons between model predictions (lines) and experimental observations (markers) for uniaxial stress-stretch response in the longitudinal (red) and circumferential (blue) directions for porcine adventitia (left), and aged human adventitia.(right).

References

1. Skacel,, Bursa, J. Mech. Behav. Biomed. Mater. 90, 538-546, 2019.
2. Morin et al., Front. Bioeng.Biotech. 9, 725047, 2021.
3. Pastrama, et al., Bone 107, 208-271, 2018.
4. Scheiner, et al., Biomech. Model. Mechanobiol. 15, 9-28, 2016.

Acknowledgements

MESH ANCHORING TECHNIQUE IN UTERINE PROLAPSE REPAIR SURGERY: A FINITE ELEMENT ANALYSIS

Elisabete Silva (1), Rita Rynkevic (1), Sofia Brandão (2), Teresa Mascrenhas (3), António Augusto Fernandes (1)

1. LAETA, INEGI, Faculty of Engineering, University of Porto, Porto, Portugal; 2. Dep. of Radiology, CHSJ-EPE / Faculty of Medicine, University of Porto; 3. Dep. of Obstetrics and Gynecology, CHSJ-EPE / Faculty of Medicine, University of Porto.

Introduction

Pelvic organ prolapse (POP) is a complex urogenital condition resulting from defects of the structures supporting the pelvic organs, such as fascia and ligaments [1]. POP is most common after pelvic surgery, in elderly women with associated obesity or constipation, where increased intra-abdominal pressure (IAP) is frequent. POP affects 41-50% of women over the age of 40 [2] and it is estimated that from 2010 to 2050, the total number of women undergoing surgery for POP will increase by 48.2%, with a re-operation rate of 30%. In women with severe POP, surgical therapy is adopted using vaginal meshes or native tissue. However, in 2019, FDA ordered all manufacturers of surgical mesh used in transvaginal repair of anterior compartment prolapse to stop selling and distributing their products. Complications of transvaginal implant surgeries were associated with surgical technique itself, surgeon's experience and the quality of the mesh. The recurrence of POP is common after implantation of a vaginal mesh implantation and may be related to a strong attachment point for mesh anchorage. On average, failure of mesh anchoring was observed in 38% of patients 1.8 years after mesh placement [3].

This study aims to simulate reconstructive surgery to mimic the cardinal ligaments (CLs) and the suturing technique. For this purpose, the suturing technique with two different anchoring points (simple stitch - a set of four nodes and continuous stitch - a line of nodes) was simulated.

Materials and Methods

A computational model of the pelvic cavity was used (Figure 1 a)). Additionally, the model of the implant was built and included (based on literature specifications) to mimic the CLs (Figure 1b)) after their total rupture (100% impairment) and with 90% and 50% of impairment. Its mechanical properties were obtained through uniaxial tensile tests performed on a synthetic surgical implant (used for transvaginal POP repair). Also, different anchoring points (simple stitch and continuous stitch) were applied.

Result

The simple stitch causes a higher supero-inferior displacement of the vagina than the continuous suture for 50%, 90% impairment and complete rupture (Table 1). The simple suture allows more freedom movement of the implant since it is only fixed in a set a loose point

rather than a continuous suture. Figure 2 shows that the incorporation of the mesh implants allowed an approximation to the values for magnitude displacement of the healthy model.

a)   b)
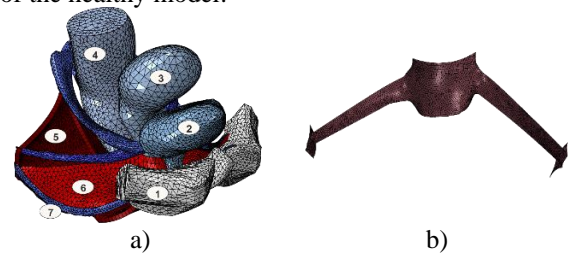
Figure 1. a) 3D computational model. (1) symphysis pubis, (2) bladder, (3) uterus, (4) rectum, (5) levator ani muscle, (6) pelvic fascia, (7) arcus tendineous fasciae pelvis. b) CLs implant.

Variable	Supero-inferior displacement of the vagina (mm) - CLs Implant		
	Simple	Continuous	Variation (%)
50% Impairment	6.74	6.21	8%
90% Impairment	7.73	7.05	9%
Total rupture	8.49	7.78	8%

Table 1. *Supero-inferior displacement of the vagina, during Valsalva maneuver, after implantation with different anchoring points (simple and continuous suture).*
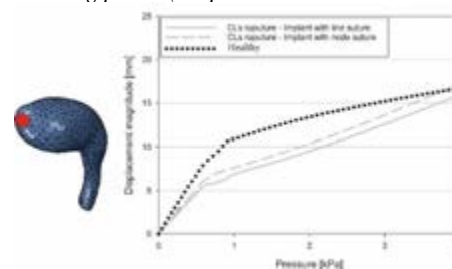
Figure 2. Maximum displacement magnitude of the uterus for healthy model and after incorporation CLs implant with different anchoring points.

Discussion

Different anchoring points caused a variation of approximately 10% between simple stich and a continuous stich. The simple suture leads to a higher supero-inferior displacement of the vagina than the continuous suture.

References

1. Grob ATM et al., *Int Urogynecol J* 2019; 30: 1939–1944.
2. Abhyankar P et al., *BMC Womens Health* 2019; 1–12.
3. Shek KL et al., *Ultrasound Obstet Gynecol* 2013; 42: 699–704.

Acknowledgements

MECHANICAL LOADING PROMOTES ANGIOGENESIS: A COMPUTATIONAL APPROACH

Ana Guerra (1), Jorge Belinha (2), Renato Natal Jorge (3,4)

1. Institute of Science and Innovation in Mechanical and Industrial Engineering (INEGI), Portugal; 2. School of Engineering, Polytechnic of Porto (ISEP), Portugal; 3. Associated Laboratory in Energy, Transport and Aeronautics (LAETA – INEGI), Portugal; 4. Faculty of Engineering of the University of Porto (FEUP), Portugal.

Introduction

A functional vasculature is essential to supply the cells with nutrients and oxygen. Angiogenesis is the primary process responsible for new blood vessels formation from pre-exist ones. This process is regulated by growth factor gradients, oxygen levels and mechanical forces. The modulation of angiogenesis due to growth factor gradients, namely by the vascular endothelial growth factor (VEGF), has already been extensively described [1]. However, blood vessels live in mechanically active environments, being exposed to stress and strain fields. Thus, to improve angiogenesis it is necessary to understand how the vasculature respond to mechanical stimulus. However, there are still scarce computational models capable to analyze the effect of mechanics in angiogenesis. Accordingly, in this work, the effect of compressive loading in angiogenesis was addressed, using a computational model.

Methods

In this work, the Radial Point Interpolation Method was combined with an elasticity formulation and with a capillary growth algorithm to simulate angiogenesis. The VEGF gradient regulates the endothelial cell migration, and the compressive loading affects the branching occurrence. With this approach, the effect of unloaded, 5%, 10% and 30% strain in angiogenesis were analyzed using different domains. The angiogenic response was evaluated by counting the number of branches and the total vessel length. Moreover, the numerical results were compared with experimental data available in the literature [2].

Results

In all the performed simulations, it was demonstrated that the endothelial cells migrate from the parent vessel to the VEGF release region, following the VEGF gradient. Moreover, the density of capillaries increased in the simulations under 5%, 10% and 30% strain (Figure 1). Therefore, despite the different tested domains it was verified that, approximately, 5%, 10% and 30% strain increased the number of branches by 68%, by 41% and by 56%, respectively. It was also verified that, approximately, 5%, 10% and 30% strain increased the total vessel length by 33%, by 23% and by 29%, respectively. Additionally, the capillary network structure and morphology obtained in simulations resembles the one presented in experimental assays and the numerical results agree with the experimental ones, mainly the ones obtained for the number of branches.
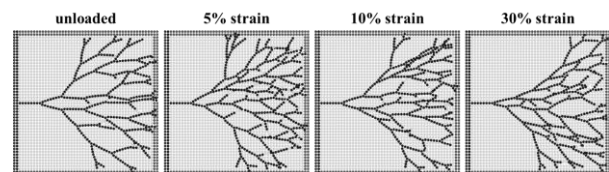
Figure 1: Final simulation results obtained for unloaded and under 5%, 10% and 30% strain loading, using a regular nodal discretization mesh. Images sized: 5 × 5 mm².

Discussion

In this study, it was demonstrated that computational models can be used to simulate the effect of compressive loading in angiogenesis. All the tested strain magnitudes promoted angiogenesis, being the 5% strain the most effective one. The capillary network obtained resembles the one presented in experimental assays and the obtained numerical results were identical to the experimental ones. Nevertheless, this study possesses some limitations since the viscoelastic properties of the tissue, the dynamic loading effect and the effect of the time variable were not considered. In the future, the development of more complex computational models and closer to reality as possible will be very useful to understand and to define the role of mechanics in angiogenesis, allowing to improve tissue vascularization.

References

1. Selvaprithviraj et al, Curr Med Chem, 24:3413-3432, 2017.
2. Ruehle et al, Sci Adv, 6(34):eabb6351, 2020.

Acknowledgements

IN VIVO UNLOADING OF RAT ACHILLES TENDONS LEADS TO A DELAYED COLLAGEN STRUCTURAL RESPONSE TO *IN SITU* LOADING

Isabella Silva Barreto (1), Maria Pierantoni (1), Malin Hammerman (1,2), Ana Diaz (3), Jonas Engqvist (1), Pernilla Eliasson (2), Hanna Isaksson (1)

1. Lund University, Sweden; 2. Linköping University, Sweden; 3. Paul Scherrer Institut, Switzerland

Introduction

Achilles tendons actively adapt to their *in vivo* loading environment. Their mechanical properties depend on a complex hierarchical design, with collagen being the smallest load-bearing unit. At the nanoscale, collagen molecules are organized into fibrils in a regular arrangement similar to crystalline materials and can thus be probed using diffraction techniques such as small-angle X-ray scattering (SAXS). On the tissue scale, *in vivo* unloading result in a more disorganized structure, resulting in a less viscoelastic tendon [1]. However, it is not known how *in vivo* unloading affects the local collagen structural response to *in situ* loading. This study aims to characterize this effect in rat Achilles tendons.

Methods

Achilles tendons from female Sprague-Dawley rats (10-12 weeks) were subjected to two different loading scenarios *in vivo* for 4 weeks [2]; 1) full loading by free cage activity (FL) and 2) unloading by Botox injections combined with cast immobilization (UL). The experiment was approved by the Regional Ethics Committee for animal experiments (Jordbruksverket, ID1424). SAXS experiments were performed at cSAXS beamline (Swiss Light Source, PSI. Energy: 12.4keV, beam size: 150μm, exposure time: 50ms). The tendons were loaded *in situ* (5 mm/min) in ramp to failure (4 FL and 4 UL) or stress relaxation (6 FL and 4 UL) using a custom-made uniaxial tensile device [3] simultaneously as acquiring scattering patterns ($q=0.05$-1.45nm^{-1}) from the centre of the tendon (Fig. 1.A). From the integrated intensity, collagen fibril strain and other collagen fibril structural parameters were extracted [1,4].

Results

UL tendons displaced more than FL tendons and carried less force at certain displacements (Fig 1.B). Additionally, the fibrils in ULs did not strain as much as fibrils in FLs (Fig 1.C). During the second step of stress relaxation, the fibril strains within the ULs remained lower than those of the FLs, despite that the force had reached similar magnitudes. With increasing forces, the fibrils within ULs became gradually more ordered. Additionally, two types of fibril organizations were found (Fig. 1.D); i) a single population of fibrils and ii) two subpopulations of fibrils with clearly distinct and separated orientations. In the second case, one of the fibril populations always stretched more than the other. The second fibril organization was observed in 4/8 ULs, but only in 1/10 FLs.

Discussion

In vivo unloading resulted in a delayed mechanical response at the collagen level. This delayed response seems to be attributed to a longer toe region as the tissue displaces more before it starts carrying load and enters the linear region. Unloading also altered the orientational organization of the fibrils. The two orientational populations together with the larger increase in intrafibrillar order suggests that the disorganization is present at larger length scales. Further, *in vivo* unloading altered the collagen fibril response, possibly by making them weaker or by altering the strain partitioning between hierarchical levels, ultimately resulting in the fibrils carrying less load.

References

1. Khayyeri et al., Sci Rep, 2017.
2. Hammerman et al., PLoS One, 2018.
3. Gustafsson et al., Acta Biomat, 2018.
4. Fessel et al., PLoS One, 2014

Acknowledgements
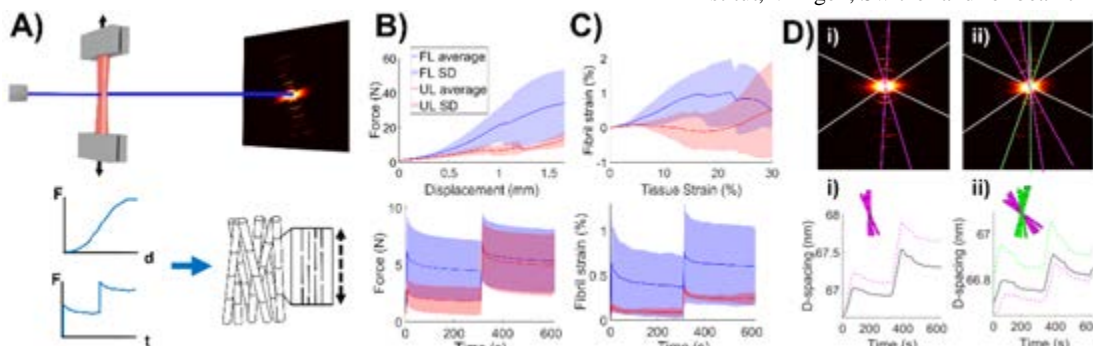
Figure 1. A) Schematic of experiment. B) Tissue and C) fibril mechanical response. D) Fibril sub-populations.

THE INFLUENCE OF LOADING CONDITIONS ON THE PRINCIPAL AND NON-PRINCIPAL STIFFNESS OF CERVICAL DISC PROSTHESIS

Hossein Ansaripour[1,2], Stephen J. Ferguson[2], Markus Flohr[1]

1. CeramTec GmbH, Germany; 2. Institute for Biomechanics, ETH Zurich, Switzerland.

Introduction

Biomechanical in-vitro testing is critical for the evaluation of cervical disc replacement implants. In previous studies, tests were performed on cadaveric models to evaluate motion preservation after disc replacement [1]. However, variations in cadaveric models, test protocols, and surgical techniques for disc replacement produce inconsistent predictions of disc prosthesis performance. To the best of our knowledge, no study reported the intrinsic kinetic properties of a disc prosthesis, although it is essential to understand design-specific behavior, independent of the contribution of the surrounding residual tissue structures. This study aimed to perform a kinematic test on disc prostheses to investigate the influence of load conditions on principal and non-principal stiffnesses.

Methods

Five generic zirconia-toughened alumina (ZTA) ball and socket samples were tested in a 6 DOF spine simulator (MTS-370.02 MN U.S.A). Forces and moments were recorded with a 6-component load cell (FT 15954, mini-45/SI-580-20). The samples were tested under displacement control at a rotation rate of 1.2°/s in two sinusoidal motion modes: 1) flexion-extension (FE) of 0-7.5°, 2) lateral bending (LB) of 0-6°, synchronized with a dynamic compressive load (Fig. 1a) in two conditions: 1) load range (-100, -50) N, 2) load range (-150, -50) N. Four cycles were considered as pre-conditioning and the fifth cycle was used for analysis. The combination of rotation and eccentric axial load (Fig. 1b) induces an antero-posterior (AP) load and a medio-lateral (ML) load in FE and LB, respectively. Two stiffness values were calculated, utilizing a linear least squares method: 1) the principal stiffness (Nm/°) which is identified in the moment-rotation curve and 2) the non-principal stiffness (N/°) which is derived from the AP and ML loads induced during FE and LB, respectively. The resultant values for stiffnesses were compared between loading conditions with a Wilcoxon signed-rank test, with a defined significance value ($p \leq 0.05$).
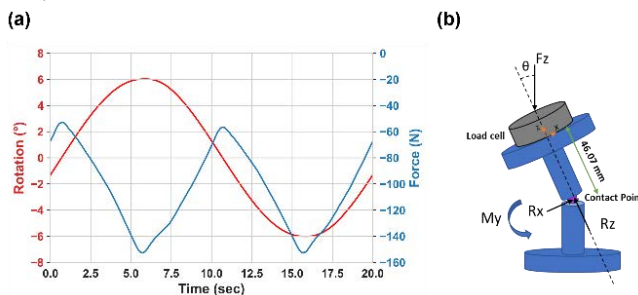
Figure 1: a) Load (blue) and rotation (red) profiles defined for testing. Maximum load applied when the samples were fully flexed or extended. b) During rotation, eccentric axial load induced moments and shear loads.

Results

An increase in the range of dynamic load led to an increase in the nonlinear behavior, i.e., the hysteresis curve (Fig. 2a). Moreover, the principal and non-principal stiffnesses obtained in the test with a dynamic load range of (-150, -50) N were higher than those obtained in the test with a dynamic load range of (-100, -50) N (Fig. 2b).
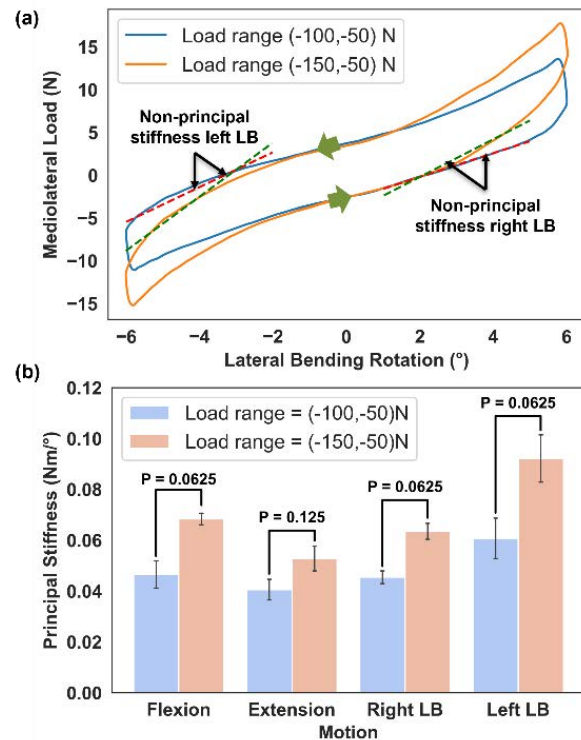
Figure 2: a) Non-linear load-rotation curves in the load range of (-100, -50) N and (-150, -50) N. b) Comparison of the principal stiffness (Nm/°) for flexion, extension, right LB, and left LB between two different dynamic load conditions.

Discussion

The obtained stiffnesses for both conditions in the study were lower than those reported in the literature [2] due to the lack of ligaments and facet joints in our model. According to the study, it is recommended to consider the stiffness and loading conditions to evaluate the performance of disc prosthesis.

References

1. Cédric et al, Eur. Spine J., 21 : 432-442, 2012.

2. Daniels et al, J Spine Surgery, 6 :190-194, 2012.

Acknowledgements

DESIGN AND CHARACTERISATION OF A NOVEL TI-PVA/PAAM ARTIFICIAL INTERVERTEBRAL DISC

Xiaoyu Du, Lucia Kölle, Delia Schümperlin, Stephen J. Ferguson

Institute for Biomechanics, ETH Zurich, Zurich, Switzerland;

Introduction

Spinal disorders have become a global healthcare concern. Spinal fusion is a successful treatment that aims to fuse adjacent vertebrae together through osseointegration to eliminate pain. However, the compromise is that the mobility of the treated spinal segments is reduced [1]. To overcome this, disc arthroplasty has been explored as a motion-preserving treatment. We present here a novel artificial disc system for clinical disc replacement. This artificial disc consists of a flexible hydrogel-based segment sandwiched between two titanium endplates for bone fixation, with a mechanical response similar to that of a natural intervertebral disc.

Methods

An artificial intervertebral disc was designed and fabricated, consisting of a stiff and tough hydrogel that is attached to a titanium endplate via chemical anchors. The tough hydrogel was a polyvinyl alcohol/polyacrylamide (PVA/PAAm) dual network hydrogel system. The titanium endplates were functionalized by grafting silane 3-(Trimethoxysilyl)propyl methacrylate (TMSPMA) to the surface. The grafted TMSPMA has methacrylate terminal groups that can copolymerize with acrylate groups in AAm under a free radical polymerization process, generating chemically anchored long-chain polymer networks onto the solid surfaces [2]. The mechanical properties of the disc were comprehensively evaluated, including compressive, tensile tests and torsion tests.

Results

The artificial intervertebral discs could be successfully fabricated by the method we proposed. The PVA/PAAm composite gel core was observed to form a tough and stiff dual cross-linked network. The connection between the titanium plate and the PVA/PAAm gel was strong. The implant with a diameter of 30 mm and a height of 10 mm could withstand over 100 N of compressive and tensile load. We observed a large hysteresis loop in the first cycle because of the water contained inside the implant, but the force-displacement curves were similar in the following cycles. For the axial torsional loading, the artificial disc could withstand a torque of ~0.5 Nm with a magnitude of torsion up to 6 degrees.

Discussion

Natural intervertebral disc has six degrees of freedom. The results showed that the artificial intervertebral discs

in our study have the potential to restore a dynamic physiological motion due to the hydrogel-based movable segments. However, the stiffness of the artificial disc was around 150 N/mm, which is still lower than that of human cervical spinal segments (492 ± 472 N/mm [3]) and lumbar segments (847 ± 39 N/mm [4]). Moving forward, we aim to improve the mechanical properties of the artificial intervertebral disc by tailoring the cross-linking parameters of the tough and stiff gel and adding reinforcing structures. Overall, the combination of titanium endplates and tough and stiff hydrogels, along with an easy method of fabrication, enables the further development of novel and advanced materials for intervertebral disc replacement applications.
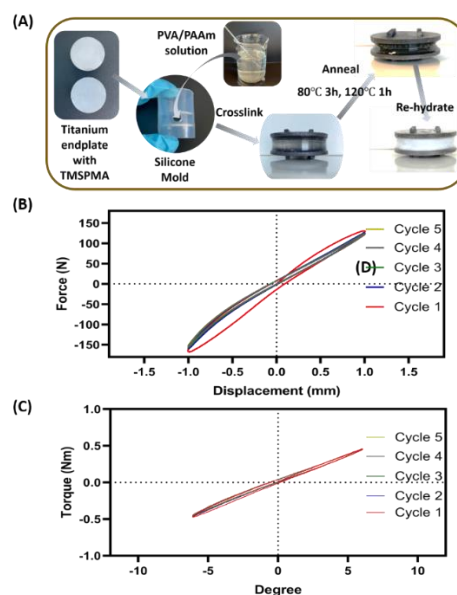
Figure 1: (A) Fabrication of the artificial disc implant; (B) Force-displacement curve under compression-tension for 5 cycles (0.1 Hz); (C) Torque-angle curve under axial torsion for 5 cycles (0.1 Hz).

Acknowledgements

References

[1] Schleicher et al., Eur Spine J 17(12) (2008) 1757-1765.
[2] Yuk et al., Nat Mater 15(2) (2016) 190-196.
[3] Moroney et al., J Biomech 21(9) (1988) 769-779
[4] Asano et al., Spine 17(11) (1992) 1343-1352

DEVELOPMENT OF IMAGE-BASED MULTIPHASIC MODELS OF THE INTERVERTEBRAL DISC

Ingmar Fleps (1), Elise F. Morgan (1)

1. Boston University, USA

Introduction

State-of-the-art modelling of the intervertebral disc (IVD) considers the poroelastic nature of IVD tissues and the pre-stresses within them [1]. However, these current multiphasic models have been limited to average IVD geometries. In addition to anatomical variation among healthy IVDs, disc degeneration is associated with systematic changes in geometry, including reduction in disc height, endplate flattening, and irregular IVD thickness, suggesting a need for image-based methods of extracting geometry for the purpose of estimating patient-specific IVD mechanics.

The goal of this study is two-fold: a) Develop an image-based finite element (FE) approach for multiphasic modelling of the IVD across degeneration grades; b) Investigate the effect of geometry on the IVD deflection and pressure distributions during axial compression.

Methods

Image-based geometries of 17 IVDs were extracted from CT scans (resolution 0.39x0.39x0.675 mm) and discretized with hexahedral elements using an automated meshing approach (Figure 1) and applied to an established IVD FE model, which includes tissue properties for mild degeneration of Pfirrmann grade 2 (PF2) [1,2]. IVD degeneration was evaluated from MRI according to the Pfirrmann grade (PF) classifying 5,4,4,1, and 3 IVDs into PF1-5, respectively. A mesh convergence study was conducted on 3 IVD geometries with PF grades of 1, 3, and 5. The IVD height (h_{IVD}) was calculate as the median thickness across all nodes on the IVD interfaces. FeBio3.4 was used to solve the FE models. Force-displacement curves for models with PF 2-3 subjected to axial compression were compared to experimental data [5]. The influence of the h_{IVD} on the maximal axial displacement (d_{max}) was evaluated based on the coeffect of determination.
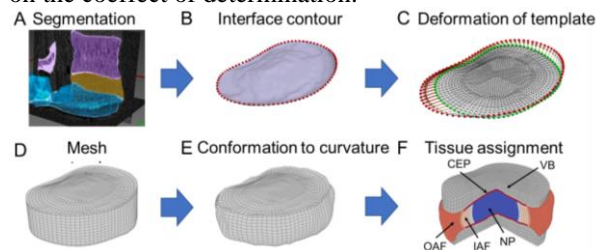
Figure 1: Schematic of the procedures for extracting and discretizing the IVD geometry from CT scans

Results

The mesh convergence analysis resulted in a difference of $< 2\%$ for d_{max} and the maximum axial pressure for a mesh with 1.5mm element size in the axial plane vs. 1.0mm element size, as well as a mesh with 8 layers thorough the IVD thickness compared to 10 layers. All results are reported for IVDs meshed with an element size of 1 mm and with 10 layers through the IVD.

The force-displacement curves in axial compression for simulations of IVDs with PF2-3 (Figure 2A) were within the experimental corridor except for one model. d_{max} was strongly correlate to h_{IVD} (R^2=0.95) (Figure 2B). The axial pressure through the IVD was comparatively homogeneous for IVDs with PF1-4, whereas for IVDs with PF5, high pressures were found in areas with low thickness (Figure3).
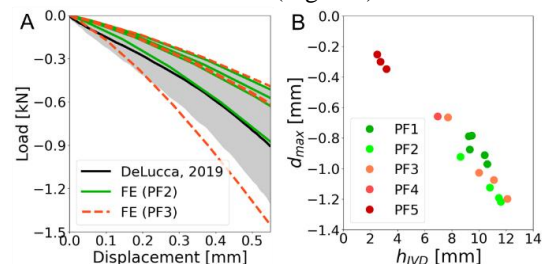
Figure 2: A) axial compression response (PF 2-3) comparing FE to ex vivo B) d_{max} vs. h_{IVD}.
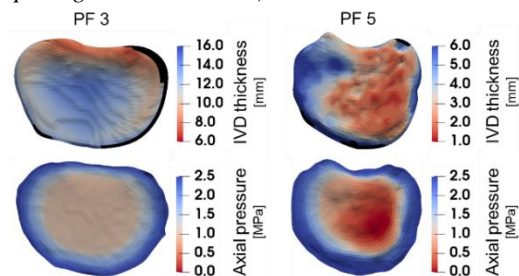
Figure 3: IVD thickness (top) and axial pressure (bottom) for an IVD with PF3 (left) and PF5 (right).

Conclusions

The image-based FE models of moderately degenerated IVDs (PF2-3) displayed axial compressive responses consistent with experimental data. Across all grades, d_{max} was highly correlated with h_{IVD}, suggesting that IVD stiffness is relatively insensitive to the image-based geometry. However, the local thickness distribution for thin IVDs appeared to drive pressure distribution, indicating a need for accurate geometric representation when studying the effects of local, intra-IVD stresses on cellular responses, tissue degeneration, and vertebral loading. Future comparisons against ex vivo data spanning PF1-5 are needed for further validation.

References

1. Newman et al, JOR Spine, e1145, 2021.
2. Jacobs et al, J Biomech, 47:2540–2546. 2014.
3. DeLucca et al, JOR Spine, e1047, 2019.

Acknowledgements

USE OF DISPLACEMENTS FIELD TO VALIDATE SUBJECT-SPECIFIC FINITE ELEMENT MODELS OF SPINE SEGMENTS WITH METASTASIS

Chiara Garavelli (1,2), Cristina Curreli (1,2), Alessandra Aldieri (1,2), Elda Paoli (2), Marco Palanca (1), Luca Cristofolini (1), and Marco Viceconti (1,2)

1. Department of Industrial Engineering, Alma Mater Studiorum - University of Bologna, Italy;
2. Medical Technology Lab, IRCCS Istituto Ortopedico Rizzoli, Bologna, Italy

Introduction

Recent achievements in the oncological field have increased life expectancy. Consequently, the incidence of bone metastases has incremented as well. The spine is the most frequent site of bone metastasis. The evaluation of the residual bone competence in metastatic patients is still an open challenge, often leading to unnecessary surgery on subjects already debilitated by the treatment of primary tumour. Finite element (FE) models generated from diagnostic images of the patient could help clinicians to make the most suitable decision [1]. However, these tools need to be validated against experimental data. The aim of this work is the validation of a recently developed FE framework through the comparison between full-field numerical displacements on the vertebral surface and experimental displacements measured using Digital Image Correlation (DIC) [2] on multiple specimens with metastasis.

Materials and Methods

Two thoracolumbar four-vertebrae human spine segments with mixed metastasis (metastatic, control and two adjacent vertebrae) were obtained from an ethically approved donation program. Quantitative computed tomography (qCT) images were acquired (voxel 0.24 x 0.24 x 1 mm^3). Compression-flexion tests were performed loading each segment in elastic regime. A 4-camera state-of-art DIC (GOM Aramis 12M) was used to measure the displacement field on the vertebral body surfaces [3]. To track the displacement of the specimen extremities, markers were glued on the two pots used to constrain the specimen. FE models were generated from qCT images and using a 10-node tetrahedral mesh. Material properties of the bone were mapped on each element (Bonemat, Istituto Ortopedico Rizzoli) using a density-elasticity equation [4]. Intervertebral discs (IVDs) were modelled with Poisson's ratio of 0.1 and elasticity modulus calibrated for the specified loading condition so that the global stiffness of the spine FE model matched the experimentally measured one. The boundary conditions replicated the experimental test: the lower vertebra was fixed, while the rigid-body motion of the superior pot was transferred at the upper vertebra using a remote displacement approach. Rigid registrations were performed using a feature-based registration algorithm (Mimics, Materialise NV) to align the DIC data to the FE models. The models were solved (APDL, Ansys) and the FE-predicted displacements of the vertebral surface were compared to the full-field DIC-measured experimental displacements for the metastatic and control vertebral bodies of each specimen.

Results

The elastic moduli of the discs were in the range 1.9-6.2 MPa. The average registration error was less than 0.5 mm. FE-predicted displacements showed good agreement compared to DIC results in elastic regime (Fig. 1), with RMSE=0.03-0.12 mm (%RMSE <8%).
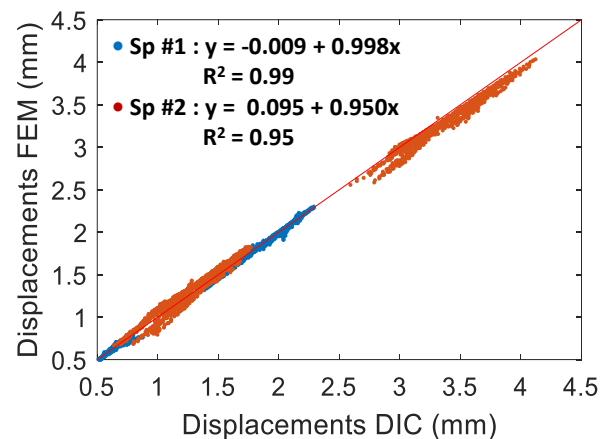
Fig.1: Local comparison between DIC-measured and FE-predicted displacements for 2 specimens.

Discussion

The results obtained demonstrated the possibility to apply the recently developed validation framework to different specimens. Compared to other similar validation studies [5], the presence of the IVDs was considered to better simulate the bone mechanical response in vivo. These promising achievements encourage the use of the proposed modelling approach in future works to assess strain-based prediction errors, of fundamental importance in clinical applications.

References

1) Standelmann et al, Bone 141: 115598, 2020.
2) Garavelli et al, EUROSPINE, 2020.
3) Palanca et al, Bone 151: 116028, 2021.
4) Morgan et al, J Biomech, 36: 897–904, 2003.
5) Gustafson et al, J Mech Behav Biomed Mater, 65:801–807, 2017.

Acknowledgements

IN VITRO TESTING OF HYDROGELS FOR THE IVD THERAPY USING A NOVEL ORGAN CULTURE APPROACH: CHONDROITINASE OR PAPAIN?

Jan Ulrich Jansen (1), Graciosa Q. Teixeira (1), Andrea Vernengo (2), Sibylle Grad (2), Karin Benz (3), Cornelia Neidlinger-Wilke (1), Hans-Joachim Wilke (1)

1. *Institute of Orthopaedic Research and Biomechanics Ulm, Germany; 2. AO Research Institute Davos, Switzerland; 3. TETEC Tissue Engineering Technologies AG, Germany*

Introduction

Hydrogels are playing an increasingly important role in the development of regenerative approaches for the intervertebral disc (IVD) [1,2]. Since there is limited availability of native human discs for research and often animal models do not mimic human disc degeneration, testing the biomechanical performance of a hydrogel after implantation remains difficult. The objective of the present study was to adapt and optimize an in vitro organ culture model of bovine tail discs for biomechanical testing. Discs were artificially degenerated with different enzymes. The distribution and biomechanical effects of a hydrogel after injection were investigated.

Methods

In total, three groups of motion segments (CY3/4, n=6/group) were prepared from 18 fresh bovine tails and embedded in PMMA. Each group was injected with 5 U/ml chondroitinase ABC (ChABC), 65 U/ml papain or PBS (sham control), and cultured for 7 days (6% O_2, 37°C). After culture, complex loading was applied to diminish the swelling of the discs. Then, as much as possible of a radiopaque albumin/hyaluronan hydrogel (Albugel) was injected and the injected volume documented. After injection, specimens were either analyzed by μCT or transversally dissected for macroscopic views and histology. Before and after enzyme treatment, after complex loading, and after injection, the range of motion (ROM) and disc height were determined. Statistics: Mann-Whitney-U, Friedman, two-stage step-up [3] (p≤0.05).

Results

At day 7, all specimens digested with papain developed a cavity in the nucleus, whereas the specimens from all other groups seemed macroscopically intact. After incubation and subsequent loading, the disc height significantly decreased in all groups. The strongest decrease was observed for the papain, followed by ChABC (p≤0.009, Fig. 1A). After loading, the ROM increased for all groups, reaching for ChABC and papain up to 78% (p≤0.026). Significantly more hydrogel could be injected into ChABC- and papain-digested discs than into controls with no enzymatic treatment (p=0.002). μCT reconstructions and dissections of the IVDs showed one large sphere for papain and a more inhomogeneous fluffy-cloud-like distribution of the Albugel in ChABC-digested specimens (Fig. 1 B/C). The injection of Albugel restored the initial disc height in all digested groups, and

also increased the height of non-treated discs (p≤0.015). For ChABC and papain, the ROM decreased to the intact state (90% and 101%, respectively, p≤0.037) and for the non-treated group to 65% (p=0.004).
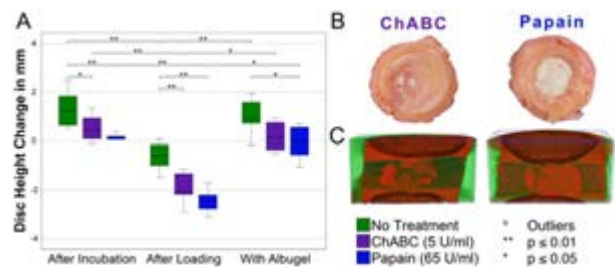
Figure 1: A) Disc height change normalized to the intact condition B) Exemplary discs at day 7 after Albugel injection for ChABC and papain group. C) Micro-CTs depicting Albugel distribution after injection into digested IVDs (examples either with ChABC or papain).

Discussions

The ROM increase and loss of disc height, as well as cavity formation in the papain-treated group indicate a similar behavior as described for human discs with cavities, e.g., due to disc herniation or nucleotomy [4] This allows the targeted simulation of such pathologies. ChABC more closely mimics human degeneration occurring without cavities. But the used ChABC concentration leads to similar changes of ROM and disc height as papain, indicating that ChABC digestion is also suitable to simulate progressed degeneration. Both ChABC and papain allow standardized hydrogel injections and testing. But differences in the hydrogel distribution could also be noticed. We hypothesize that the specific digestion of glycosaminoglycans by ChABC may lead to different structural defects than papain. These results have improved our overall understanding of the biomechanical effects of IVD tissue digestion with ChABC and papain, and indicate that hydrogels can be investigated with both models depending on the research question.

References

1. Teixeira et al, Tissue Eng Part C Methods, 22:8-19, 2016.
2. Zheng et al, J Tissue Eng Regen Med, 15:299-321, 2021.
3. Benjamini et al, Biometrika, 93:491-507, 2006.
4. Wilke et al, Spine (Phila Pa 1976), 38:E587-93, 2013.

Acknowledgements

BIOMECHANICAL COMPARISON BETWEEN POLY AXIAL AND OAK SCREWS FOR THORACOLUMBAR FRACTURE REDUCTION

Abdollah Yassine Moufid (1), François Zot (2), Anneli Duits (3), Mathieu Severyns (2,4), Arnaud Germaneau (2), Tanguy Vendeuvre (1,2)

1 Department of Orthopaedic Surgery and Traumatology, University Hospital, Poitiers, France.
2 Institut Pprime, UPR 3346 CNRS – Université de Poitiers – ISAE-ENSMA, France
3 UMC Utrecht, The Netherlands
4 Department of Orthopaedic surgery and Traumatology, University Hospital, Martinique, France

Introduction

Spine trauma of the thoracolumbar junction represent 60-65% of thoracolumbar spine fractures [1]. A great restoration of the angulations according to the operated location makes it possible to limit many complications [2]. For each spinal fracture needing posterior reduction and fixation, the question of instrumentation arises (choice of screw type, rod materiel and rod angulation). In the last decade, we assisted at an increase of number and type of implants available. Moreover, the importance of restoring spinal sagittal balance (inter vertebral angulation) after spinal fracture was demonstrated. In spite of numerous stabilization solutions, the effect of posterior instrumentation on the inter vertebral angulation remains to be defined. The factors influencing the link between rod angulation and inter vertebral angulation has been studied on lateral view X-rays: it has been demonstrated that some factors are due to screw positioning and some depends on the specificity of the implant used without specifying [3]. The objective of this work was to study the effects of rod angulation and of the use poly axial or Oak screws (Safe Orthopaedics®, France) on intervertebral angulation during fracture reduction. Oak screw offers the advantage to be poly axial with its head which becomes orthogonal to the thread during the locking of the rod.

Methods

Experiments were performed on 9 fresh anatomic spine segments centered on L1 (T11-L3, from the anatomical laboratory of University of Poitiers). A compressive fracture was produced on L1 using a dynamic loading system to obtain a kyphotic reducible traumatic deformation [4]. Five specimens were instrumented on T12 and L2 with mono axial screws; four with Oak screws. The screw positioning was verified on CT, then the rods were inserted first straight, then bended with 25 degrees of lordosis. Kinematical fields of each structure (bone and instrumentation) were measured during reduction procedure (insertion and fixation of the rods) by 3D mark tracking technique [5].

Results

Figure 1 shows evolution of reduction angle according to the type of implant for bended rods. In the latter case, the use of Oak screws allowed a mean reduction of 10° [5°- 16°] whereas the use of poly axial screws only permitted a mean reduction of 3° [0°- 6°]. Those last results with poly axial screws and bended rod were similar to the result of the group with Oak screws and straight rods with 3° of reduction [1°- 6°]. At last the group with poly axial screw and straight rod had the worst capacity of reduction with a mean of 2° of reduction [1°- 4°]. The CT analysis allowed observation of the screws positioning and the analysis of the uniformity of penetration and the parallelism to the endplates explained the difference between the rod angulation and the inter vertebral angulation.
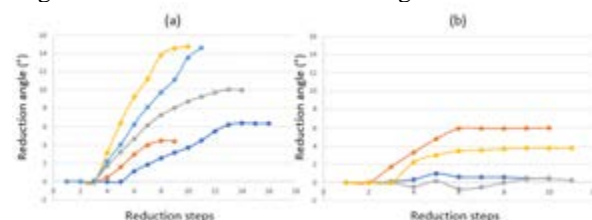
Figure 1: Evolution of reduction angle of the fractured vertebra for (a) Oak screws and (b) poly axial screws.

Discussion

This biomechanical study using mark tracking analysis highlights the effectiveness of Oak screws compared to poly axial screws on fracture reduction regardless of the rod angulation. It also reinforces the importance of the screw positioning to manage a good match between the planned and the effective post-operative inter vertebral angulations. Indeed, positioning the screw parallel to the vertebral plate and evenly penetrated with the use of Oak screw would lead to perfect match. Further experiments by imposing physiological loadings on spine segments have to be performed to evaluate stabilization provided by each solution.

This study has provided some insight into the effects of some specificities of therapeutic possibilities offered to the surgeon to envisage optimal planning and management.

References

1. Bensch et al. Emerg Radiol, 12:124-129, 2006.
2. Le Huec et al. Eur Spine J, 28:1889-1905, 2019.
3. Sardi et al. Global Spine J, 25, 2021.
4. Germaneau el al. Clin Biomech, 49:139-144, 2017.
5. Germaneau et al. JMBBM, 59:291-303, 2016.

Acknowledgements

COMPARATIVE STUDY OF PEDICLE SCREW STABILIZATIONS FOR METASTASIS TREATMENT ON A BIOMIMETIC LUMBAR CONSTRUCT

Simone Borrelli (1,2), Giovanni Putame (1,2), Mara Terzini (1,2), Andrea Ferro (3), Stefano Marone (3), Alberto L. Audenino (1,2)

1. Polito^BIO Med Lab, Politecnico di Torino, Turin, Italy; 2. Department of Mechanical and Aerospace Engineering, Politecnico di Torino, Turin, Italy; 3. Oncologic Orthopaedic Surgery Division, CTO Hospital - Città della Salute e della Scienza di Torino, Turin, Italy.

Introduction

Spinal stability plays a crucial role in the success of the surgical treatment of lumbar vertebral metastasis. The recent introduction of carbon radiotransparent material has opened debates about new stabilization strategies [1]: the present study intends to compare experimentally the efficacy of long *vs* short posterior pedicle screw fixations by analysing the stiffness of the lumbar segment under small displacements.

Methods

This experimental study was conducted on a Sawbones biomimetic lumbar construct including T12 and S1 (SKU340). Experimental loading protocol consisted of anterior, posterior, and lateral bending [2] as well as clockwise and anti-clockwise torque (rotation-control at 0.5°/s up to 3°). Vertebral displacements were measured through multi-camera marker tracking system (Figure 1). Orthopaedic surgeons replicated five stabilization configurations using carbon rods and pedicle screws from CarboFix Orthopedics Ltd: a long stabilization (LS) involving two spinal levels above and below the lesion level, a short stabilization without (SS) and with (SS-T) a transversal connector, SS and SS-T with the mobilization of one L2 pedicle screw (SSm, SS-Tm).
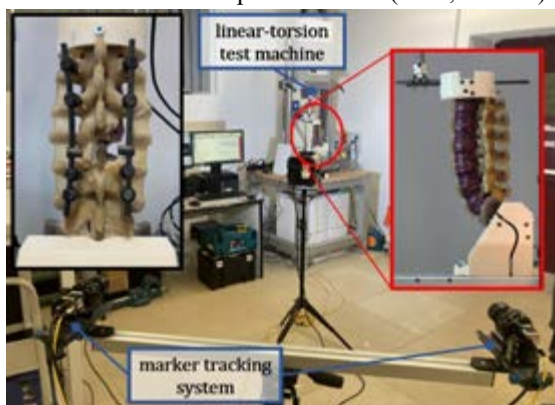
Figure 1: Experimental set up. On the left, the LS with the osteolytic lesion and the posterior decompression.

The evaluation of the stiffness in antero-posterior, lateral bendings, and torsion, recurred respectively to the lordosis angle, α, to the angle L1-L5 on the coronal plane, ϑ, and to the axial rotation of the most cranial vertebra. Measures refer to the initial spine stance.

Results

Figure 1 shows how each stabilization makes the angular motion differ compared to the intact construct for each kind of bending. Given a load of 3 Nm, the maximum reduction of angular motion reaches the 73 % with LS against the 43 % with SS-T. As concerns the transversal connector, its introduction slightly deviates the SS response; however, its presence limits the loose of rigidity in case of mobilisation (i.e., from the 21 % (SS) to the 8 % (SS-T) in lateral bending).
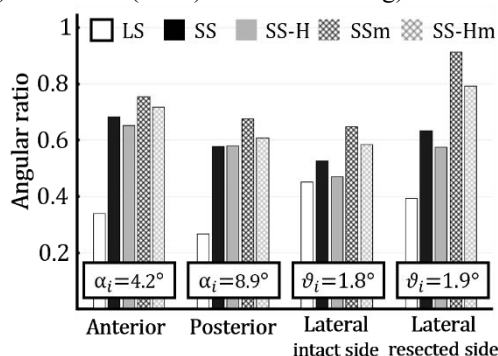
Figure 2: Ratio of α and ϑ of each stabilization with the analogous intact construct values, α_i and ϑ_i, at 3 Nm.

Torsional stiffness at 1.5 Nm is reported in Table 1. As shown, only LS and SS-T deviate less than the 10% from the intact configuration on both sides. Finally, the one-way ANOVA on torsional stiffness suggests a non-significant difference between SS-Tm and SS.

Torsion	Intact Nm/°	LS	SS	SS-T	SSm	SS-Tm
			Percentage change			
Resected side	2.24 (a)	+7.9% (b)	-9.9% (c)	+0.7% (a)	-17.5% (d)	-10.4% (c)
Intact side	2.23 (A)	+0.7% (A)	-14.3% (B)	-4.4% (C)	-25.0% (D)	-14.2% (B)

Table 1: Stiffness of each stabilization with respect to the intact lumbar construct, at 1.5 Nm. Labels indicate statistical significance among the resulting stiffnesses.

Discussion

The kinetic response in the range of neutral posture is correlated to spinal stability [3]. Within the limits of this study (so far only one replica has been processed for bending results), the findings confirm LS as the stiffest configuration, while SSs as an intermediate possible strategy. The transversal connector in short stabilization is shown to be a conservative surgical solution reducing the stability loss in case of mobilization, which is a central issue in metastatic postoperative complications.

References

1. Tedesco G. et al, J Spine Surg., 4(1), 2017.
2. Borrelli S. et al, Int. J Comp. Meth. and Exp. Meas, 9, 2021.
3. Di Pauli von Treuheim T. et al, JOR Spine, 3(2), 2020.

MICRO-FE MODELS CAN PREDICT THE DISPLACEMENT FIELD IN HUMAN VERTEBRAE WITH LYTIC AND BLASTIC METASTASES

Marco Palanca (1), Giulia Cavazzoni (1), Luca Cristofolini (1), Enrico Dall'Ara (2)

1. *Dept of Industrial Engineering, Alma Mater Studiorum- University of Bologna, IT*
2. *Dept of Oncology and Metabolism, INSIGNEO Institute for in silico medicine, University of Sheffield, UK*

Introduction

Spine bone metastases alter the microstructure of bone tissue introducing denser (blastic metastasis) and/or soft (lytic) tissue, affecting the load bearing capacity of the bone. The complex mechanical behavior of metastatic vertebrae has been explored experimentally, evaluating the strain field [1], and with finite element (FE) models evaluating the stiffness and failure load [2].

Micro-FE models can provide a detailed biomechanical characterization of the trabeculae, within and around the metastatic tissue [3], highlighting weaker regions and the redistribution of strains. However, it is unknow how accurately micro-FE models can predict the deformation of the human vertebral metastatic tissue.

Our aim was to validate the displacement field predicted by micro-FE models against Digital Volume Correlation (DVC) measurements in human metastatic vertebrae.

Material and methods

Five spine segments, each including a metastatic and a radiologically healthy (control) vertebra in the middle, were tested. The specimens were prepared removing the posterior arches and embedding the two adjacent vertebrae in bone cement to fit a custom loading jig equipped with a 10kN load cell. Each spine segment was scanned in a micro-computed tomography (VivaCT80, isotropic voxel size = 39μm) unloaded and after applying a compressive load within the elastic regime [1]. A global DVC approach (BoneDVC) was used to evaluate the displacement field inside the vertebral body with a measurement spatial resolution of 1.95mm. This is expected to yield an uncertainty on the measured displacements of 1.2-8.3 μm, in all directions [3].

Linear elastic hexahedral micro-FE models of the metastatic and control vertebrae were generated from the unloaded scans after image binarization [4]. Elastic modulus of 12GPa and Poisson Ratio of 0.3 were assigned to the bone elements, regardless the tissue type (metastatic/control). Displacement boundary conditions were applied on the top and bottom nodes of the vertebrae interpolating those measured by the DVC. The micro-FE displacements were calculated (ANSYS, APDL) at the location of the DVC nodes in the 75% central portions of the vertebra, and compared to the DVC values.

Results

Displacements measured by the DVC ranged from 15 to 550 μm. In particular, the displacements measured in the metastatic vertebrae were larger than those in the control vertebrae.

Correlation between measured (DVC) and predicted (microFE) displacements showed a fair-to-excellent agreement (Table 1), both for metastatic ($0.74 < R^2 < 0.88$, fig. 1) and control vertebrae ($0.51 < R^2 < 0.90$). Significantly different correlations were observed between the metastatic and the control vertebrae (z test, $p < 0.001$).

Type of Vertebra	Direction	Displ range [μm]	R^2	RMSE [μm]
Metastatic	AP	191	0.84	5.85
	RL	133	0.74	6.05
	CC	252	0.88	5.79
Control	AP	80	0.60	15.87
	RL	49	0.51	9.65
	CC	109	0.90	6.99

Table 1: Correlation coefficients for metastatic and control vertebrae in the antero-posterior (AP), right-left (RL), and cranio-caudal (CC) directions.

Discussion

The linear micro-FE models predicted well the experimental displacements in the control as well as in the metastatic vertebrae, despite the presence of blastic and lytic lesions (Fig. 1). Better correlations were observed when the vertebrae were subjected to larger displacements, which typically occurred in the vertebrae with lesions. More investigations will be done to understand the optimal material properties to assign to the healthy and metastatic bone tissue in the models.
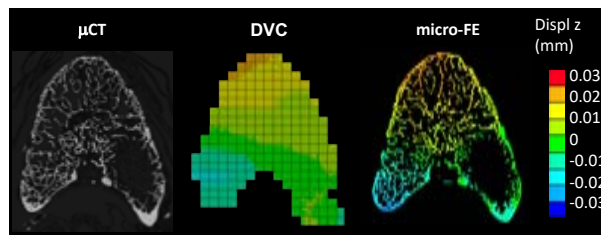
Fig. 1: Cross section of a metastatic (lytic vertebra), displacements, in CC direction, measured by DVC and predicted by micro-FE.

References

1. Palanca et al., 2021, Bone, 151: 116028
2. Stadelmann et al., 2020, Bone, 141: 115598
3. Palanca et al., 2022, JMBBM, 125: 104872
4. Costa et al., 2017, PlosOne, 12(7): e0180151

Acknowledgements

HARDWARE DENSITY REDUCTION AVOIDS T3 PROXIMAL JUNCTION FAILURE IN ADULT SPINE SURGERY: FE SIMULATION

Morteza Rasouligandomani (1), Alex del Arco (3), Ferran Pellisé (4), Miguel González Ballester (1,2), Fabio Galbusera (5), Jérôme Noailly (1)

1. BCN MedTech, DTIC, Univ. Pompeu Fabra, Spain; 2. ICREA, Spain; 3. Hospital del Mar, Spain; 4. Univ. Hospital Vall d'Hebron, Spain; 5. Lab. of Biological Struct. Mech., IRCCS Istituto Ortopedico Galeazzi, Italy

Introduction

Proximal Junctional Failure (PJF) is post-operative mechanical complication observed in at least 8.7% of sagittal imbalance surgery [1]. Since lumbar osteotomy induces 34.8% [2] of post-op complications in elderly patients, it's not optimal to recorrect lumbar curvature for the patients who suffers PJF at T10. Hence, a suboptimal decision is to extend the hardware from T10 to T3, even with a severe Global Alignment and Proportion (GAP) score [3]. High GAP score may conduct PJF, but hardware density (HD) may help to stabilize the biomechanical loads at adjacent Upper Instrumented Vertebra (UIV). Hence, the aim of this study is to explore effect of HD to avoid T3 PJF with severe GAP score. A patient-specific finite element (FE) model with iliac/T3 fixations was generated thanks to Statistical Shape Modelling (SSM) and mesh morphing techniques. We analysed the intervertebral disc (IVD) fibre strains at UIV+1, for different HD. Trade-off between fibre strain and screw pull-out force indicated possible best configurations to avoid PJF at T3.

Methods

In this study, 42 pre-operated patients were selected. Inclusion criteria: age 50-75, Pelvic inclination $> 20°$, SVA > 5cm, PJF post-op complications [4]. Pipeline of modelling and FE steps are introduced in Fig.1.
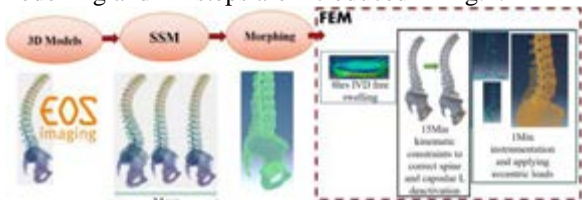
Fig.1. Geometrical and FE Modelling pipeline

3D thoracolumbar surfaces were obtained using sterEOS software. Then, to train SSM, Principal Component Analysis allowed to learn the main modes of shape variation. A patient (76 y.o.) with T10 PJF and further hardware extension to T3 with GAP11, was selected (Fig.2).

Fig.2. T3PJF patient (76 y.o.)

A 3D geometry model of this patient was recreated by activating different modes of the SSM. Structured FE meshes, including the ligaments, were morphed to the mesh of the recreated geometry (Thin Plate Splines for vertebras, and Coherent Point Drift for IVD [5]). Tissue

models and boundary conditions are summarised in Table1.

Material properties	Intervertebral disc	Vertebras	Ligaments
	Anisotropic hyperelastic model [6]	Linear elastic [7]	**Hypoelastic model [8]**
Boundary Conditions	Eccentric load in vertebra center; Sacrum is fixed		

Table1: Material properties and boundary conditions

Fibre strain in the UIV/UIV+1 IVD was calculated in different HD scenarios, and optimal trade-offs between fibre strain and screw pull-out force were analysed.

Results and discussion

Fibre strain values at UIV/UIV+1 were compared to control values [9]. Results showed that HD reduction from 5 to 4, 3 and 2 vertebrae led respectively to 41%, 58%, 70% fibre strain reductions (Fig.3).
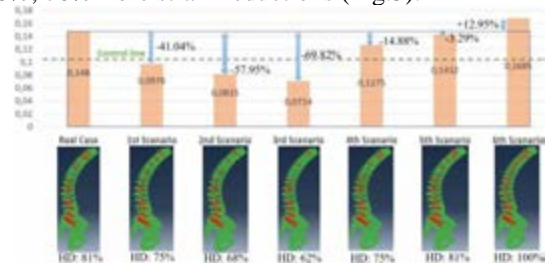
Fig.3. Maximum principal fibre strain at T3/T2 for 7 scenarios

However, HD reduction increased the screw pull-out forces at the UIV (e.g., +34% for the 3rd scenario). While the forces appear to be well below the threshold force of healthy bone, the 2nd and 3rd scenarios seemed at risk in presence of osteoporotic bone. In such a case, only the HD reduction of the 1st scenario could be acceptable.
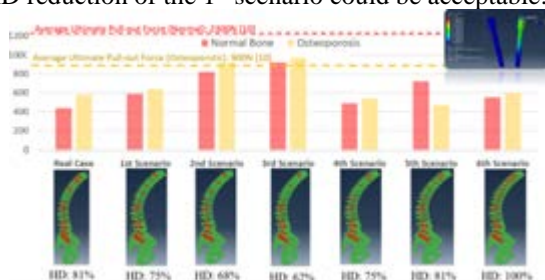
Fig.4. Pull-out Force (N) on UIV screw for 7 scenarios

This study showed that HD reduction reduces the chronic load of upper IVD and might help to decrease the risk of PJK in case of suboptimal surgical decision. Bone quality must be considered, though, and muscle effects should be investigated in the future.

References

1.Acaroglu, E, et al., Acta Orth., 51.3, 2017
2.Berjano, P, et al., Euro. Spine J 24.1, 2015
3.Yilgor C, et al., The Spine J, 17(10), 2017
4.Hart, R., et al., Neurosurgery Clinics, 2013
5.Rasouli, M, et al., 26th ESB congress, 2021
6.Malandrino, A., et al., Front. Bioeng., 2015
7.Galbusera, F., et al., Med. Eng., 2011
8.Noailly, J., et al., Eur. Spine J., 2012
9. Rasouli, M, et al., ESB Cap.Esp, 2021
10.Jendoubi, K., et al., Applied Biomech., 2018

Acknowledgements

LOWER LIMB COMPENSATION DURING SIT-TO-STAND-TO-SIT AFTER MULTI-LEVEL FUSION SURGERY IN ADULT SPINAL DEFORMITY

Pieter Severijns (1,2), Thomas Overbergh (1), Erica Beaucage-Gauvreau (1), Thijs Ackermans (1), Lieven Moke (1), Lennart Scheys (1)

1. Institute for Orthopaedic Research and Training (IORT), Faculty of Medicine, KU Leuven, Leuven, Belgium; 2. Faculty of Rehabilitation Sciences, KU Leuven, Leuven, Belgium

Introduction

Despite improvements in alignment and pain, the invasiveness and inherently spine-immobilizing character of spinal fusion surgery for progressive adult spinal deformity (ASD) have a large impact on post-operative functional abilities [1]. Moreover, quality of life in post-surgical patients with ASD showed to be lower compared to other chronic disorders such as heart failure or diabetes [1]. Although decreased spinal mobility is obvious after spinal fusion, little is known on the changes in lower limb kinematics during activities of daily life. Therefore, in this study we investigated the impact of multi-level fusion on lower limb kinematics during sit-to-stand-to-sit.

Methods

Spinal and lower limb kinematics during sit-to-stand and stand-to-sit were measured on 10 patients with ASD (Age: 63.0y ± 6.7; BMI: 24.4kg/m^2 ± 4.7; Gender: 7F/3M) in the motion lab pre- and 6 months post-operatively. Surgery consisted of multi-level

Figure 1. a. marker position (red) correction towards anatomical position. (green). b. Angle definitions for thoracic kyphosis and lumbar lordosis.

spinal fusion (> 4 levels) with iliac fixation. To measure lumbar lordosis and thoracic kyphosis, a novel method (Fig. 1) was used, able to measure dynamic spinal alignment using spinal skin markers with the possibility to correct marker positions to the true anatomical vertebral body positions [2]. Three-dimensional coordinates for these corrections were obtained from standing x-rays after biplanar imaging with the markers attached to the spine (Fig. 1a). Lower limb kinematics of pelvis, hip, knee and ankle were obtained using the plug-in-gait marker model. Patients were instructed to stand up from a chair and after three seconds return to sitting without hand support. A Wilcoxon signed-rank test was used to compare pre- and post-operative range of motion (ROM).

Results

Post-operatively, ROM decreased for lumbar lordosis and increased for the knee angle during sit-to-stand. During stand-to-sit, both thoracic kyphosis and lumbar lordosis ROM decreased, while knee and ankle ROM increased after fusion surgery. Exact values can be found in table 1. Figure 2 provides kinematic curves for sagittal knee and ankle angles pre- and post-operatively.

Discussion

As expected, spinal ROM in terms of thoracic kyphosis and lumbar lordosis during sit-to-stand and stand-to-sit decreased after multi-level spinal fusion surgery. This decrease in spinal mobility was compensated by increased lower limb range of motion, mainly at knee and ankle levels. Increased lower limb ROM can be partially explained by increased knee extension and ankle dorsiflexion during stance. However, also during the middle third of the motion, knee and ankle angles were systematically larger in the post-operative group (red curves in Fig. 2). Although these post-operative changes in movement strategy are essential to complete the task and consequently preserve functionality, they might have important clinical implications. Firstly, increased knee flexion, which has been associated with increased knee loading [3], potentially results in secondary lower limb pathology in the longer term. Secondly, decreased spinal ROM possibly limits the necessary forward propulsion needed to stand up, as well as decreases body stability during sitting down by limiting the ability to bring the mass of the trunk over the knees [4]. Therefore, post-operative rehabilitation including lower limb strengthening seems warranted to optimize post-operative functionality and consequently requires further research.

References

1. Pellisé, F. et al. Eur. Spine J. 24, 3–11 (2014)
2. Severijns, P. et al. Spine J. 20, 934–946 (2020)
3. Van Rossom, S. et al. J. Orthop. Sports Phys. Ther. 48, 162–173 (2018)
4. Shia, V. et al. J. Biomech. 72, 37–45 (2018)

Sagittal ROM	Sit-to-stand			Stand-to-sit		
	Pre-op	Post-op	p	Pre-op	Post-op	p
TK (°)	5.4 (6.0)	4.5 (6.0)	N.S.	6.4 (10.7)	3.2 (2.6)	0.017
LL (°)	19.0 (15.3)	8.7 (5.6)	0.015	20.6 (9.5)	7.1 (8.8)	0.017
Pelvis (°)	38.8 (20.4)	36.1 (13.0)	N.S.	39.0 (12.1)	37.6 (7.0)	N.S.
Hip (°)	88.8 (19.2)	88.3 (10.1)	N.S.	92.2 (17.9)	89.6 (11.4)	N.S.
Knee (°)	80.0 (9.5)	86.2 (7.8)	0.036	79.2 (13.6)	84.1 (7.9)	0.017
Ankle (°)	12.8 (7.2)	16.0 (4.4)	N.S.	9.9 (5.8)	13.2 (4.9)	0.012

Medians and interquartile ranges are reported. TK: Thoracic kyphosis. LL: Lumbar lordosis. N.S.: Non-significant. **Significance level: α = 0.05**

Table 1. Sagittal range of motion during sit-to-stand and stand-to-sit before and after spinal fusion surgery.

Figure 2. Curves for knee and ankle angle over time. Full lines indicate sit-to-stand and dashed lines stand-to-sit. **Black: pre-op; Red: Post-op.**

EVALUATION OF METHODS FOR SCREW-VERTERBA FIXATION USING FINITE ELEMENT MODELLING

Samuel Vallejo Pareja (1), Carlos Ruiz Wills (2), Juan Ramirez (1)

1. Department of Mechanical Engineering, Universidad Nacional de Colombia campus Medellín, Colombia;
2. BCN MedTech, Universitat Pompeu Fabra, Spain

Introduction

Lumbar spine diseases treatments selection still a process without consensus that requires understanding the biomechanical behavior of vertebrae in interaction with fixation techniques [1]. Employing Finite Element Method (FEM) as modeling and analysis source is a way for this purpose of development of knowledge to make decisions. Nevertheless, FEM is well known by its dependence on mesh and geometry, and suppose defining the approach for optimal results (Avoid overestimated values) considering available resources, whether simplifying the geometry or constraint method [2]. The aim of this study is to evaluate two constraint approaches for screw fixation in lumbar spine by FEM.

Methods

A L5 vertebral body (VB) fixed with screws model was used for two constraint conditions: a) VB perforated and screws tie to the inner hole surface (Model A), and b) full/intact VB and screw embedded in the vertebra (Model B). The L5 VB 3D models for each condition was obtained as full shape, using Scalismo Lab (by University of Basel), and perforated using the screws shape as boolean tools in Solidworks (Dassault Systèmes). The screws were 3D as simplified cylinder with length of 50 mm, and 5 mm of diameter with 40° between shafts (see Figure 1). VB and screw were modelled as linear elastic, isotropic cortical bone and TI-6Al-4V with 0.3 Poisson's Ratio, 12 GPa and 110 GPa Young's modulus, respectively [3,4]. 3-Matic software (Materialise Research license) was used for both L5 VB for both models were meshed with tetrahedral elements (C3D10) and the screws with hexahedral elements (C3D8R). For model A, Tie constraint was defined between inner hole surface of VB and the external surface of the screw. The simulation consisted in the application of a compression of 1.1 MPa at the bottom of the VB and the upper surface of the VB and the screw heads were fixed. The stresses fields were evaluated at the screws using software Abaqus 6.12.
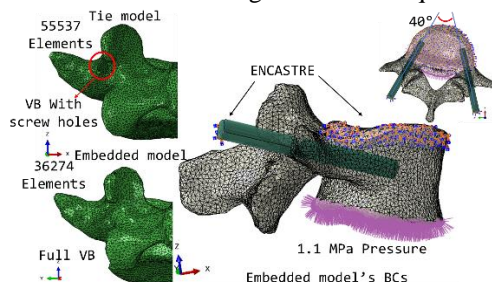
Figure 1: Geometry and Boundary conditions for both tie and Embedded region models.

Results

The Von Mises stress field of a probe screw were obtained for both Model A and B, and are presented in figure 2. Model A converge at 0.05 mm element size with 2.57x10^6 elements (3,67% Rel. error) reporting 0,51124 MPa at the center of the left screw tip. Separately, Model B converge at 0,12 mm with 4,81x10^5 elements (0,306% Rel. error) reporting 4,54697 MPa. Model A takes 6 times the B (CPU time).
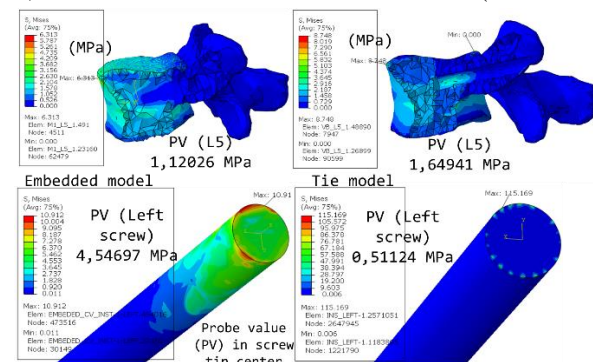
Figure 2: Von Mises Stress distribution at convergence for left screw in Tie and ER cases.

Discussion

At convergence state with finer screw element sizes, tie approach provides results over the screws with a lower order of magnitude (10^-1MPa) than embedded constraint that converge at coarser sizes. It seems through the stress field obtained in screws-vertebra fixation zone that both methods provide similar global results for the vertebra, but different local results for screws. Tie approach includes the local effect over the vertebra but not over the entire screw surface, probably due to inherent dissimilar orphan meshes interaction. This work provides a recommendation to model screw-vertebra fixation considering the importance of avoid overestimated values through tie and embedded methods, due to the surface conditions of each method, meshing implications and CPU time issues to consider.

References

1. Wang et al., Med. Biol. Eng. Comput., 54, 4: 619–628, 2016.
2. Sensale et al, Front. Bioeng. Biotechnol., 9:643154, 2021.
3. Kurutz et al, IntechOpen, 2010.
4. Qu et al., Biomed Res. Int., 2018, 2018.

Acknowledgements

RECOVERY OF TRUNK MOTION DURING GAIT AT 1-WEEK AND 3-MONTHS AFTER SPINAL FUSION SURGERY IN AIS PATIENTS

Thijs Ackermans (1), Sebastiaan Schelfaut (2), Pieter Severijns (1), Pierre Moens (2), Lieven Moke (1, 2), Lennart Scheys (1, 2)

1. Institute for Orthopaedic Research and Training (IORT), Faculty of Medicine, KU Leuven, Leuven, Belgium; 2. Division of Orthopaedics, University Hospitals Leuven, Leuven, Belgium

Introduction

Adolescent Idiopathic Scoliosis (AIS) is a growth defect of the spine that primarily occurs in pre-pubertal children and is surgically treated when a curve exceeds 50°. Presently, surgical outcomes are evaluated through 2D static radiographs, clinical examination and questionnaires. Although, the functional outcome (e.g. the gait performance) plays an important role in the patient's evaluation of treatment success, no accurate, evidence-based predictions regarding the early recovery of this functional outcome can be provided by the surgeon. Indeed, postoperative gait analysis of AIS patients has thus far only been documented 1-2 year postoperative at the earliest [1, 2]. Consequently, no information on the preceding recovery of gait in AIS patients exist, which prevents the understanding of early recovery or compensation mechanisms, e.g. in terms of trunk and shoulder motion, as well as its possible implications for enhanced rehabilitation. Therefore, the present study aimed to investigate the early gait recovery in terms of shoulder and pelvis motion after spinal fusion surgery in AIS patients.

Methods

Nineteen AIS patients (Age: 17.3 ± 4.0; Gender: 15 Female and 4 Male) scheduled for spinal fusion surgery underwent an instrumented gait analysis protocol using a validated spinal deformity-specific marker protocol [3], both preoperatively (Pre-op) and postoperatively (Post-1Week and Post-3Months). At all timepoints, patients walked on an instrumented, split-belt treadmill (Motek, Amsterdam, NL) at 0.75m/s and 1.25m/s walking speeds (not possible at Post-1Week) recorded using a 10-camera motion capture system (VICON Motion systems, Oxford, UK). Based hereon, range of motion (RoM) of the shoulder and pelvis angle in the frontal and transverse plane was determined. A one-way ANOVA, followed by Bonferroni post-hoc testing ($p < 0.05$), was performed to identify differences between timepoints.

Results

When walking at 0.75m/s, the RoM of both the shoulder and pelvis angles in the transverse plane significantly ($p < 0.05$) decreased at Post-1W compared to Pre-op and significantly ($p < 0.05$) increased back to preoperative levels at Post-3M (Table 1). When walking at 1.25m/s, the significant ($p < 0.05$) reduction in shoulder angle RoM persisted at Post-3M in both the transverse and frontal plane (Table 1).

RoM	Pre-Op	Post-1W	Post-3M
Speed: 0.75 m/s			
Frontal plane			
Shoulder [°]	4.9±1.4	4.7 ± 1.2	4.3 ± 1.0
Pelvis [°]	7.8±1.8	6.7 ± 2.0	7.6 ± 2.1
Transverse plane			
Shoulder [°] *	13.3±3.6 [a]	10.1 ± 3.1 [b]	12.9 ± 2.7
Pelvis [°] *	11.9±3.0	9.6 ± 3.0	11.8 ± 2.5
Speed: 1.25 m/s			
Frontal plane			
Shoulder [°] *	5.7 ± 1.9		4.4 ± 0.8
Pelvis [°]	10.0 ± 2.4		9.6 ± 2.0
Transverse plane			
Shoulder [°] *	15.0 ± 3.4		12.2 ± 2.9
Pelvis [°]	12.7 ± 3.1		12.1 ± 2.6

Table 1. Overview of the range of motion (ROM) of the pelvis and shoulder angle in the transverse and frontal plane when walking (at 0.75m/s and 1.25m/s) at the different timepoints.
* Statistically significant (p<0.05) Timepoint effect
[a] Different (p<0.05) compared to Post-1Week
[b] Different (p<0.05) compared to Post-3M

Discussion

The present study is the first study to investigate the early gait recovery in terms of shoulder and pelvis motion after spinal fusion surgery in AIS patients. At 1 week postoperative, AIS patients walked with a reduced RoM of the shoulder and pelvis, which increased back to preoperative levels at 3 months after surgery. However, this recovery in shoulder angle was not present at 3 months postoperatively when higher walking speeds were imposed. This is assumed to be due to increased motor task demands. These findings suggest that early postoperative dynamic assessments could provide new insights in patient-specific and task-dependent recovery. This novel information could serve as a basis for patient-specific early rehabilitation protocols.

References

1. Mahaudens et al, Gait & Posture, 61:141-148, 2018.
2. Lenke et al, Spine, 26:330-337, 2001.
3. Severijns et al, Spine J, 20:934-946, 2020.

MULTISCALE MECHANICS OF COLLAGEN-HYALURONAN INTERFACES IN ANNULUS FIBROSUS

Shambo Bhattacharya (1), Devendra K. Dubey (1)

1. Department of Mechanical Engineering, Indian Institute of Technology Delhi, New Delhi, India

Introduction

Synchronous and multiaxial deformation exhibited by Annulus fibrosus (AF) is contributed by its hierarchical and specialized fibre-reinforced laminated structure – consisting of collagen fibers embedded in a proteoglycan (Aggrecan and Hyaluronan) matrix. Biochemically, AF fibrillar collagen comprises type I and type II collagen molecules following a radial interchanging distribution. In addition, the non-fibrillar proteoglycan component consists of primarily hyaluronan and aggrecan [1,2]

This work presents a molecular dynamics-finite element (MD-FEM) based multiscale analysis to understand how molecular-scale mechanical response of collagen (type I and type II), hyaluronan and collagen-hyaluronan chemo-mechanical interplay governs the tissue-scale mechanical response of AF.

Methodology and Framework

In this work, multiscale analysis of collagen-hyaluronan interfaces in AF is performed by developing the atomistic models of collagen-hyaluronan interface system from collagen and hyaluronan molecules for four regions in AF – Outer Lamellae (OL), Outer Middle Lamellae (OM), Inner Middle Lamellae (IM) and Inner Lamellae (IL). The details of collagen type II and water content for four regions are shown in Table 1.

Table 1: Regions of AF simulated

Location	Type II %	Water %
Outer (OL)	0	65
Outer Mid (OM)	25	68.3
Inner Mid (IM)	50	71.6
Inner (IL)	75	75
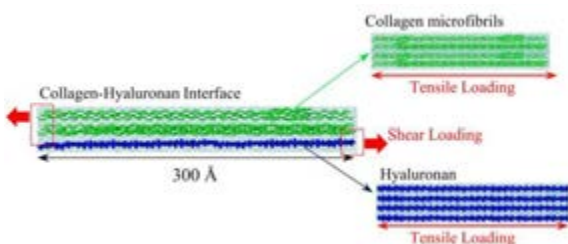
Figure 1: Atomistic Model of collagen-hyaluronan interface with the atomistic model of collagen and hyaluronan components.

Development of atomistic models of collagen molecular segments, collagen microfibril and hyaluronan is presented in author's previous works [3–5]. Atomistic models of collagen-hyaluronan interfaces are developed using the atomistic models of collagen microfibrils and hyaluronan molecule (Figure 1). Tensile tests on atomistic models of collagen molecules, collagen microfibrils and hyaluronan, and shear tests on atomistic models of the collagen-hyaluronan interface are conducted using the quasistatic methodology developed in previous works [3–5] to derive their molecular mechanical behaviour.

Results and Analyses

Results show that intramolecular hydrophobic and attractive forces lead to type I collagen molecular segments exhibiting stiffer tensile chararacteristics compared to type II [4]. Thus, presence of softer type II collagen softens the collagen microfibrils moving from OL to IL (Figure 2) but softening of microfibrils is largely contributed by increase in water concentration. In-silico MD Analysis of Axial Shear show that moving from OA to OM, results in weakening of the interface. This is due to weakening of electrostatic interactions and weaker water bridges formed between type II component of collagen and hyaluronan (Figure 2).
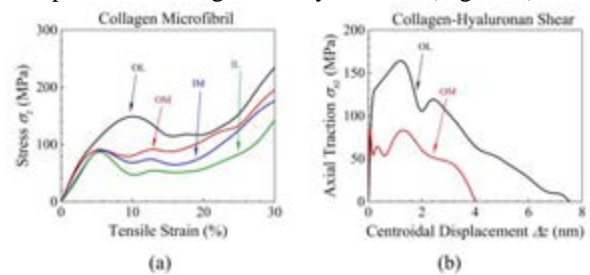
Figure 2: Molecular Mechanical Response of (a) collagen microfibrils in axial tension, and (b) collagen-hyaluronan interface in Axial Shear.

Discussion and Conclusions

The outer AF primarily controls the spinal range of motion. Hence, presence of type I collagen and stiffer interface formed between type I collagen and hyaluronan imparts the necessary stiffness for maintaining spinal range of motion within physiological limits.

References

[1] D.R. Eyre et al, Biochem. J. 157:267–270, 1976
[2] J.E. Scott et al, Biosci. Rep. 6:879–888, 1986.
[3] S. Bhattacharya et al, J. Mech. Behav. Biomed. Mater. 107: 103752. 2020
[4] S. Bhattacharya et al, J. Mater. Res. 2021. 36:3407–3425,2021
[5] S. Bhattacharya et al, J. Biomech. Eng. 144(4):041004, 2022.

Acknowledgements

DETERMINATION OF A LUMPED-PARAMETER MODEL OF THE INTERVERTEBRAL JOINT FROM AN EXPERIMENTAL DATASET

Samuele Gould (1, 2), Giorgio Davico (1, 2), Marco Palanca (1, 3),
Luca Cristofolini (1), Marco Viceconti (1, 2)

1. Alma Mater Studiorum - University of Bologna, Italy; 2. IRCCS Istituto Ortopedico Rizzoli, Italy;
3. INSIGNEO Institute for In Silico Medicine, UK

Introduction

The intervertebral joint (IVJ) stiffness plays a crucial role in spinal multibody models (MBM) [1]. MBM have often simplified the joint (formed of multiple soft tissues) to lumped-parameter models [1, 2], where IVJ stiffness values are often tuned solely so predicted motions fall within reported ranges [1, 3]. While specimen specific MBMs tuned to specific *ex vivo* experiments exist [2], they are less common. In either case, lumped parameters need to be specific to the loading scenario due to their high non-linearity and motion dependency [2]. Therefore, this study aimed to establish a method to determine specimen specific linearized lumped parameters for the IVJ.

Methods

A specimen specific MBM was built off CT data using Slicer3D, NMSBuilder 2.0, and OpenSim 4.2 (Figure 1), and used to simulate an *ex vivo* experiment on a L1-L4 human cadaver spine segment [4]. *Ex vivo*, flexion-compression was induced by applying a force with a ball joint anteriorly offset from the specimen. A 4-camera digital-image correlation system (Aramis, GOM) tracked the surface motion throughout the load cycle [4].
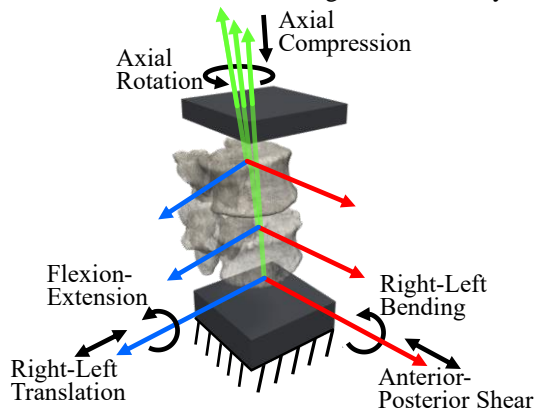
Figure 1: OpenSim model of the inferior pot, L3, L2 and superior pot with the IVJ axes and the enabled DoFs.

The model IVJ poses were based on the ISB recommendations [5]. Transformation matrices were applied to the joints and vertebrae to correct for changes of the relative pose of the vertebrae between the CT scan and the testing machine. The IVJs were assigned six degrees of freedom (DoF). A linear spring-damper element was implemented in each DoF. The inferior pot (and embedded L4) was completely constrained, the experimental load was applied to the superior pot (and embedded L1) at the actuator location. A quasi-static, forward dynamics simulation was run with the OpenSim API to predict the kinematics of the vertebrae. An interior-point optimization algorithm (Matlab 2020b) minimized the difference between experimental and predicted vertebral motion by tuning the flexion, axial, and posterior-anterior (PA) stiffnesses.

Results

The tuned stiffness, and experimental and predicted motions are reported (Table 1). Employing specimen specific tuned stiffnesses, the mean percentage error of the predicted motion was 10% in flexion, 32% in axial compression, and 13% in PA shear.

DoF		Experimental Motion	Predicted Motion	Tuned Stiffness
Flexion	L2	1.46°	1.63°	18Nm/ rad
	L3	2.25°	2.05°	
Axial Comp.	L2	0.22mm	0.31mm	210N/ mm
	L3	0.40mm	0.31mm	
PA shear	L2	0.29mm	0.25mm	25N/mm

Table 1: The tuned stiffness and the difference between experimental and predicted motion in flexion, axial compression, and posterior-anterior shear.

Discussion

We proposed a method to define a specimen specific lumped-parameter IVJ stiffness combining *ex vivo* experimental data and *in silico* simulations. Discrepancies between the experiment and model were of the same order of magnitude as the measurement uncertainty. The methodology requires a specimen specific geometry, sufficient data to determine the three-dimensional (3D) experimental vertebra poses, the 3D loading point position relative to a vertebra, and their motion throughout the load cycle. To tune properties in a DoF the cost function must be sensitive to that DoF; hence tuning properties in all six DoF would require multiple loading conditions. The proposed method may improve the definition of IVJ stiffness values in MBMs. Future research will apply this method to longer spine segments and multiple loading conditions. Further development should consider damping properties, spinal level dependency, and IVJ non-linearity.

References

1. Senteler et al, CMBBE, 19:5, 538-548, 2016.
2. Silvestros et al, PLoS ONE 14:5, e0216663, 2019.
3. Wang et al, J Biomech, 98, 109437, 2020.
4. Palanca et al, Bone, 151, 116028, 2021.
5. Wu et al, J Biomech, 35:4, 543-548, 2002.

THE EFFECT OF INTERVERTEBRAL DISC DEGENERATION ON THE FLEXIBILITY OF THE THORACIC SPINE: AN IN VITRO STUDY

Christian Liebsch (1), Hans-Joachim Wilke (1)

1. Institute of Orthopaedic Research and Biomechanics, Ulm University, Germany

Introduction

Intervertebral disc degeneration usually represents the result of natural ageing processes in the human body, affecting both the morphological and biomechanical properties of the spine. The effect of degenerative changes of the intervertebral disc on the range of motion was predominantly investigated for the lumbar spine in the past, generally exhibiting a reduction in flexibility in flexion/extension and lateral bending as well as a slight increase in axial rotation with increasing degeneration grade [1]. In the thoracic spine, however, solely an influence of disc degeneration on the kinematics was shown so far [2]. The purpose of this study therefore was to investigate the effect of different degeneration grades on the range of motion of the thoracic spine.

Methods

95 human thoracic spinal motion segments (min. n = 4 per level from T1-T2 to T11-T12) from 33 donors (15 female / 18 male, mean age 56 years, age range 37-80 years) were loaded with pure moments of 5 Nm in flexion/extension, lateral bending, and axial rotation in order to determine the range of motion and the neutral zone. Degeneration grades of all single intervertebral discs were assessed using a recently developed and validated grading scheme for the radiographic determination of thoracic intervertebral disc degeneration [3] (0 = no, 1 = mild, 2 = moderate, 3 = severe degeneration). Statistically significant differences were evaluated using the Kruskal-Wallis test with Dunn-Bonferroni post-hoc correction together with the Mann-Whitney-U test, each with a significance level of 0.05.

Results

The investigated specimens exhibited degeneration grades between 0 and 2 (Fig. 1). In all six motion directions, the range of motion significantly decreased for grade 1 as well as grade 2 compared with grade 0, respectively. The strongest decrease was found in extension comparing grade 2 with grade 0 (-42%, Fig. 2). No significant differences were detected between grades 1 and 2 in all motion directions. Neutral zone was significantly reduced for grade 1 compared with grade 0 in flexion, extension, and lateral bending, as well as for grade 2 in extension, where the strongest decrease of the neutral zone was found (-47%). Donor age did not significantly affect the range of motion (p > 0.05), whereas the range of motion was significantly reduced in specimens from male donors (p < 0.05), since the mean degeneration grade was significantly increased in male donors compared with the female ones (p < 0.05).

Figure 1: Exemplary lateral radiographs of different thoracic intervertebral disc degeneration grades.
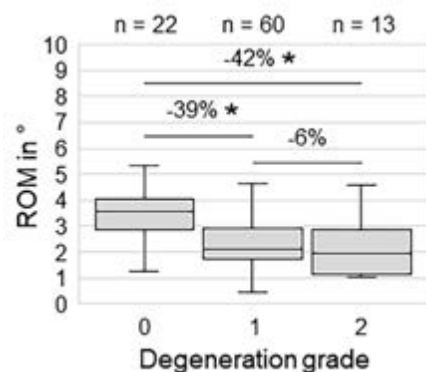
Box-and-whisker plots illustrating the effect of degeneration grade on Range of Motion (ROM) of the thoracic spine in extension direction. Statistically significant differences (p < 0.05) are depicted by asterisks.

Discussion

The results of this study revealed that already mild intervertebral disc degeneration reduces the range of motion of the thoracic spine, whereas progressing degeneration does not further affect its flexibility. The effect of grade 3 could not be evaluated in this study due to the lack of appropriate specimens, while a further, strong decrease of the range of motion can be assumed, since severely degenerated discs do usually not exhibit flexible structures. Differences regarding the effect of disc degeneration compared with the lumbar spine, especially in axial rotation, might be explained by morphological differences between thoracic and lumbar intervertebral discs or the additional stabilizing effect of the rib cage.

References

1. Kettler et al., Eur Spine J 20(4):578-584, 2011.
2. Liebsch et al., Spine J 20(3):488-498, 2020.
3. Liebsch et al., Eur Spine J, 2021, doi: 10.1007/s00586-021-06970-6.

Acknowledgements

VERTEBRA AND DISC SLENDERNESS ARE NOT AN EARLY SIGN OF ADOLESCENT IDIOPATHIC SCOLIOSIS PROGRESSION

Claudio Vergari (1), Wafa Skalli (1), Kariman Abelin-Genevois (2), Jean Claude Bernard (2), Zongshan Hu (3), Jack Chun Yiu Cheng (3), Winnie Chiu Wing Chu (3), Ayman Assi (1,4), Mohammad Karam (4), Ismat Ghanem (4), Tito Bassani (5), Fabio Galbusera (5), Luca Maria Sconfienza (5), Marco Brayda-Bruno (5), Isabelle Courtois (6), Eric Ebermeyer (6), Raphael Vialle (7), Tristan Langlais (7), Jean Dubousset (1)

1. Arts et Métiers Institute of Technology, Institut de Biomécanique Humaine Georges Charpak, Paris, France; 2. Department of Orthopaedic Surgery and Children Conservative treatment, Centre Médico-Chirurgical et de Réadaptation des Massues, Lyon, France; 3. The Prince of Wales Hospital, The Chinese University of Hong Kong, Shatin, Hong Kong; 4. Faculty of Medicine, University of Saint-Joseph, Beirut, Lebanon; 5. IRCCS Istituto Ortopedico Galeazzi, Milan, Italy; 6. Unite Rachis, CHU - Hopital Bellevue, Saint-Etienne, France ; 7. Department of Pediatric Orthopaedics, Hôpital Armand Trousseau, Paris, France

Introduction

Adolescent idiopathic scoliosis (AIS) is a deformity of the spine which is characterized by a deviation of the spinal line in the patient's frontal plane and an axial rotation of the scoliotic curve. This deviation resembles a buckling of the spinal column. Spine slenderness represents the potential instability of the spine to buckling under compressive loads, and it was previously shown that AIS patients have more slender spines than non-scoliotic subjects [1-2]. However, it is not clear at what stage of the progression this difference appeared. We hypothesized that an early appearance of slenderness could signify a higher risk of progression, and therefore it could be an indication for early treatment. The aim of this study was to compare slenderness between stable and progressive patients, as well as with asymptomatic controls.

Methods

In total, 138 patients and 93 non-scoliotic subjects were included. Patients were included at their first exam for AIS (Cobb angle: [10- 25°]) and they were followed up until skeletal maturity without progression (stable patients) or until progression and prescription of brace (progressive patients). All subjects underwent standing biplanar radiography at inclusion and 3D reconstruction of the spine. Vertebral slenderness ratio was computed automatically from the 3D model of each vertebra as $r = H\sqrt{A/I}$, where H is the vertebra body height, A is the average area of the two endplates, and I is the average of the smallest second moment of area of each endplate. Disc slenderness ratio was computed from the endplates of the two adjacent vertebrae. Results are reported as median [1st, 3rd quartile].

Results

Vertebral slenderness ratio in AIS patients varied between 2.9 [2.7; 3.0] (T9) and 3.4 [3.2; 3.6] (T1), while disc slenderness ranged from 0.6 [0.6; 0.7] at T6-T7 to 1.2 [1.1; 1.3] at L4-L5. Slenderness ratio increased with age at all vertebral levels (Figure 1, p < 0.001), while disc slenderness tended to decrease with age and Cobb

angle, but only in a few vertebral levels. Slenderness was similar between progressive and stable patients at all levels (p > 0.05), and also between patients and non-scoliotic subjects (p > 0.05).
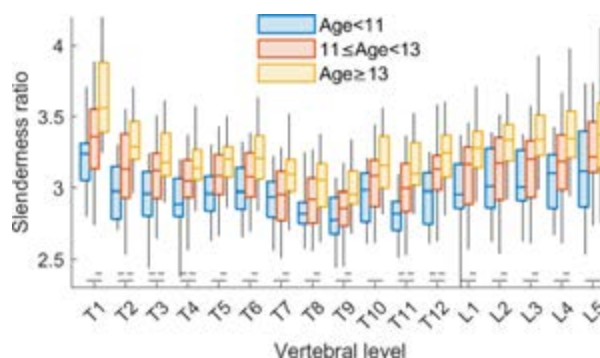
Figure 1: Slenderness ratio at vertebral levels by age.

Discussion

The main hypothesis of this study was not corroborated by the results, which suggest that slenderness is not an early sign of progression. Nevertheless, this observation gives an insight into the development of the pathology: while slenderness does not initiate the scoliotic deformity, it still increases during the later progression. To our knowledge, this is the first study to analyze spine slenderness in mild AIS, in standing position, and to relate it to the natural history of the patient. Further studies should analyze the relationship between the progression of the deformity and that of slenderness, but also if slenderness is related to the axial plane of the deformity, and in particular on the vertebral axial rotation and the torque [3].

References

1. Vergari et al, Europ Spine J, 29:726–736, 2020.
2. Chen et al, Sci Rep 7:46448, 2017.
3. Thenard et al., Spine Def, 7 :525-532, 2019

Acknowledgements

The reliability of a novel 3D motion capture protocol for the analysis of instep soccer kick kinematics

Dalia Al Otti[1], Stijn Ghijselings[1], Filip Staes[2], Lennart Scheys[1]

[1]*Institute for Orthopaedic Research and Training, Department of Development and Regeneration, KU Leuven/University Hospitals Leuven, Leuven, Belgium;* [2]*Research Group for Musculoskeletal Rehabilitation, Department of Rehabilitation Sciences, KU Leuven, Belgium.*

Corresponding author: **Dalia.alotti@kuleuven.be**

Introduction

Ball kick in Soccer is an essential, common, and distinctive part of a soccer player's performance. An analysis of injury risk while playing soccer indicated that kicking accounted for 51% of potential actions that could lead to injury. [1] Therefore it is highly important to develop methodological techniques that allow researchers to investigate the kinematics and of soccer kicks adequately.

When compared to other highly dynamic tasks, there is a notable scarcity in full utilization of 3D motion capture systems to analyse soccer kicks. This can be attributed to the difficulty in stimulating a football kick realistically inside a laboratory setting, while having cameras safely yet accurately cover all angles. Therefore in this study we aimed to investigate the inter-session and inter-observer reliability of a novel protocol that utilized an indoor stationary kick tool.

Methods

5 Subjects were recruited, all with a background of playing football at least twice a month. (Age = 25.1 ± 2.8 years, height = 178.6 ± 2.30 cm, weight = 72.0 ± 3.94 kg, BMI = 22.6 ± 0.73 kg/m²)). The motion analysis session was captured at 240hz capture frame rate using a 12–infrared camera system (Vicon MX-13). This was combined with a commercial training tool (kick it, USA) that has been additionally customized in order to be stable during powerful kick action. A previously validated reflective marker protocol for the lower limb was used.[2]
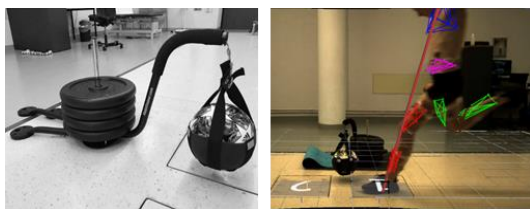
Fig. 1: Image (a) shows the customized kick it indoor kicking tool. Image (b) A subject in the cocking phase of the kick mid-trial.

The marker placement protocol was conducted by a total of three observers, one principal observer (PO) and two other observers (SO). Each subject performed three measurement trials on the same day: one conducted by the PO and one undertaken by each SO. In each trial the subjects were asked to perform an 5 instep kick with their dominant kicking leg. Resulting data was exported to Visual3D software (C-motion, USA) for analysis of total range of motion(ROM) and peak joint angles of pelvis and hip in all movement planes.

Inter-observer and inter-trial analysis was assessed by interclass correlation coefficients (ICC) calculated using a two-way mixed effect model with absolute agreement. Standard error of measurement (SEM) and minimal detectable change (MDC) were also calculated for all parameters.
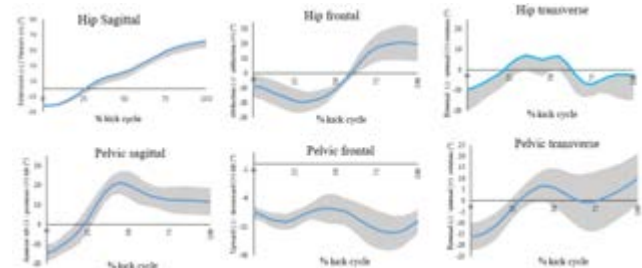
Fig. 2: the top three graphs represent the total ROM of the hip during one kick cycle , while the below three graphs represent it for the pelvic ROM.

Results and Discussion

The protocol revealed excellent inter-observer reliability for both hip and pelvic total ROM data (ICC = 0.92 - 0.98, SEM = 2.04 - 8.01, MDC_{90} = 6.30 - 16.70), except for total sagittal and transverse hip ROM. Total transverse hip ROM demonstrated good inter-observer reliability (ICC = 0.78, SEM = 6.43, MDC_{90} = 6.39), while inter-observer reliability of total sagittal hip ROM was poor (ICC = 0.32, SEM = 14.26, MDC_{90} = 8.07). Furthermore, hip angular displacement data revealed excellent inter-trial reliability for peak hip flexion (ICC = 0.96, SEM = 4.06, MDC_{90} = 9.47), adduction (ICC = 0.97, SEM = 6.58, MDC_{90} = 17.73) and external rotation (ICC = 0.98, SEM = 6.28, MDC_{90} = 20.72). For the remaining peak values of the hip, the motion capture protocol demonstrated good intertrial reliability (ICC = 0.84 - 0.87, SEM = 5.76 - 14.84, MDC_{90} = 7.19 - 17.31). In addition, excellent intertrial reliability was found for peak anterior pelvic tilt (ICC = 0.97, SEM = 3.31, MDC_{90} = 8.91) and peak internal pelvic rotation (ICC = 0.97, SEM = 7.24, MDC_{90} = 19.50), while good intertrial reliability was found for the remaining peak angular displacement values of the pelvis (ICC = 0.80 - 0.89, SEM = 5.24 - 8.72, MDC_{90} = 5.93 - 9.10).

Conclusion

The results for both the inter-trial and inter-observer measures are encouraging for the use of such set up in indoor 3D motion analysis of highly dynamic soccer kicks. However the incorporation of a target-component could further improve reliability measures for hip sagittal ROM.

References

1. Rahnama N et al.,(2002) *Br. J. Sports Med.*, ;36:354-359
2. Vanrenterghem et al.,(2012) *Journal of Biomechanics* ;45:2444-2449

HIGHER JOINT LOADING DUE TO INCREASED JOINT ANGLES IN PROFESSIONAL COMPARED TO NOVICE LATIN DANCERS

Clara Egner (1,2), Heinz-Bodo Schmiedmayer (1), Hans Kainz (2)

1. Institute of Mechanics and Mechatronics, Technical University of Vienna, Vienna, Austria
2. Centre for Sport Science and University Sports, University of Vienna, Vienna, Austria

Introduction

Dancing is an increasingly popular competitive and recreational sport with high injury potential: In a study among dancers competing at international level, 69 % reported injuries within 12 months [1]. The most common sites of injuries and pain are the neck, lower back and lower extremities [1,2]. The majority of dancers do not include any supplementary training apart of dancing [2]. Latin American Dancing is usually practiced in high-heeled shoes and with a specific technique. In order to gain insights for injury prevention, the influence of two important factors - footwear and level of proficiency - on joint kinematics and loading in the lower extremities was investigated on the example of basic Rumba dance steps. We hypothesized to find higher joint loadings in the lower extremities with higher level of proficiency.

Materials and Methods

Participants were female dancers from Viennese competitive dancing clubs of either the lowest (D-class, N=8) or one of the two highest (A/S-class, N=6) performance classes of the Austrian competition system. A 3D motion capture system (Vicon, Oxford, UK) was used to collect marker trajectories of the lower extremities, ground reaction forces and electromyography data. Basic Rumba dance steps were collected barefoot (BF) and with two different dance shoes (latin shoes (LS), with approx. 6.5 cm, and training shoes (TS) with approx. 4 cm heel height). Based on the experimentally collected data, musculoskeletal simulations were performed in OpenSim to calculate joint angles and joint contact forces (JCF) in hip, knee and ankle joints. The range of motion (ROM), mean joint angles and peak resultant JCF during the stance phase of the movement were then compared using mixed factorial analysis of variance (ANOVA) and Bonferroni-adjusted post-hoc analysis.

Results

ANOVA revealed several significant main effects of both shoe height and performance class on joint angles and JCF. One of the most interesting results were the effects of performance class in the movement of a checked forward walk and will therefore be discussed in detail in this abstract.
Mean joint angles over the stance phase were significantly higher in pelvis list (p = .004, MDiff = 8.347°, 95%-CI [3.341, 13.354]) and outward hip rotation (p = .003, MDiff = 17.768°, 95%-CI [7.818,

27.718]) for A/S-class compared to D-class when dancing with LS (Figure 1). Furthermore, dancers of A/S-class experienced higher peak hip JCF compared to D-class when wearing LS (p = .002, MDiff = 5.927 [xBW], 95%-CI [2.714, 9.14]).
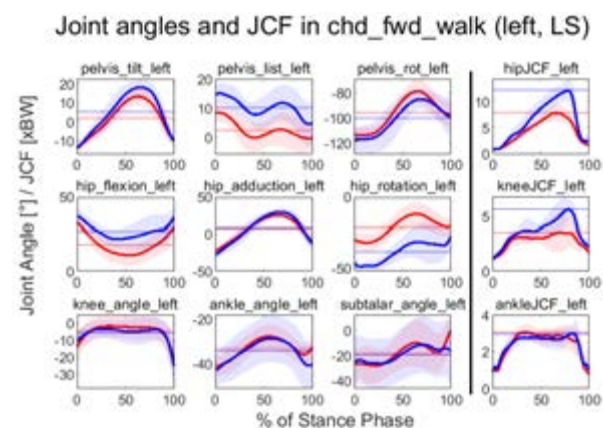
Figure 1: Joint angles (left) and JCF (right) in the left leg over % of stance phase, mean (solid line) ± one standard deviation (shadowed) for A/S-class (blue) and D-class (red) in LS, horizontal lines denote means over the stance phase for joint angles and maxima for JCF

Discussion

In agreement with our hypothesis, we found increased JCF in dancers with a higher level of proficiency compared to novice dancers. The higher peak JCF were likely caused by the increased mean joint angles used by professional dancers. This more-pronounced movement pattern might be used by referees to judge the esthetics of the dance movements.
The JCF from our dance simulations were higher compared to JCF experienced during normal walking [3,4]. Considering that professional dancers train several hours per day, the increased JCF and musculoskeletal loading in general might be the reason for dance-related injuries.
In conclusion, we quantified joint kinematics and joint loading during dancing. Our findings can be used to design dance-specific supplementary training programs or dance shoes with the aim to prevent injuries in the long run.

References

1. Premelc et al, Int. J. Env. Res. Pub. H. 16, p. 4164, 2019
2. Miletic et al, Int. J. Athl. Ther.Tr., 20.1, pp. 57–62, 2015
3. Kainz et al, PLOS ONE 15.7, pp. 1–18, 2020
4. Palmowski et al, Sci Rep 11, p. 10073, 2021

V-SPINE ANGLE AND GROUND REACTION FORCES IN FAST BOWLING IN CRICKET

René E.D. Ferdinands [1], Utkarsh Singh [2]
1. *Faculty Medicine and Health, University of Sydney, Australia; 2. Sports Dynamix Private Limited, Universidad de Los*

Background

Fast bowlers in cricket are required to generate high ball release speeds, reaching up to 45 m s^{-1}, to minimize the available response time of the batsman. To generate such ball speeds, fast bowlers must coordinate the body segments in an approximate proximal to distal sequence to achieve certain body postures at critical points in time [1]. One such critical time is when maximum braking ground reaction forces are applied at the centre of pressure of the front foot. Coaches generally recommend a fully extended front leg at this instant in order to maximize the use of the ground reaction braking forces [2], which propel the upper body segments as they rotate about the front hip joint [3]. However, in this study we posit that the V-spine angle is a functional variable that quantifies one of the key postural configurations in fast bowling that is more strongly linked to the ground reaction braking forces. The V-spine angle is calculated about the flexion-extension axis of the joint coordinate system. (Figure 1). We hypothesise that the more obtuse V-spine angles are correlated with the braking component of ground reaction forces to enhance the transfer of momentum from the run-up to the upper body segments.

Methods

Fifteen young fast bowlers (17.1 ± 1.4 years) were recruited from Cricket NSW. A Cortex Motion Analysis System (Version 1.0, Motion Analysis Corporation Ltd., USA) was used to capture the three-dimensional (3D) motion (200Hz) and force plate (1000 Hz) data from 6 bowling trials. Each bowler was instructed to bowl at maximum effort and pitch the ball within a 'good length' area demarcated by two white lines, 13 m and 19 m from the stumps at the bowler's end. The kinematic data were smoothed at a cut-off frequency of 15 Hz using a fourth-order Butterworth filter before being used as input to a 3-D full body model of the human body using Visual3D software (Version 6, C-Motion, Germantown, MD). An X-Y-Z Cardan sequence of rotation was used to express the V-spine angle (lumbar spine segment relative to front shank) in relation to the flexion-extension joint coordinate axes. Other variables calculated were the front shank angle with respect to global sagittal plane (front shank angle GL), front knee flexion-extension angle, the ratio of braking to vertical ground forces (GRF ratio), and the ball speed. IBM SPSS (Version 26.0) was used to calculate Pearson product-moment correlations between V-spine flexion angle and front shank angle, knee extension angle and GRF ratio, and front shank angle and GRF ratio – all calculated at the instant of maximum braking ground reaction force on the front foot.

Results

A strong significant relationship was shown between the V-spine and the GRF ratio (r = 0.631, p < 0.001), whereas the correlation between front knee extension angle and GRF ratio was not significant (p = 0.184). V-spine angle was strongly correlated with the front shank angle GL (r = 0.800, p < 0.001). In turn, the front shank angle was strongly correlated with the GRF ratio (r = 0.722, p < 0.005). V-spine angle was not significantly correlated with ball speed.

Figure 1: A V-spine flexion angle is calculated between lumbar spine and front shank about the flexion-extension axis of the joint coordinate system.

Discussion

The preliminary data suggests that the V-spine angle is a good predictor of ground reaction braking forces in bowling. Coaches who subscribe to the method of increasing braking forces during delivery stride may observe the obtuseness of the V-spine angle in bowlers at the time of maximum GRF. However, it is premature at this stage to advocate this as a universal coaching measure. Ball speed was not significantly correlated with V-spine angle, but the small size of the sample, and the variance in ball speeds may have reduced the power of this statistic. More research on the V-spine angle using larger samples is strongly recommended.

References

1. Ferdinands et al, Sports Technology, 6 (1): 10-21, 2013
2. Portus et al, Sports Biomechanics, 3: 263–284., 2004.
3. Hinchliffe D, PitchVision Sports Technology, 2008.. Retrieved from https://www.pitchvision.com/technical-jargon-busting-brace-the-front-leg

HIP CONTACT FORCES DURING SPRINTING IN FEMOROACETABULAR IMPINGEMENT SYNDROME

Basilio AM Goncalves (1), Evy Meinders (1), David J Saxby (1), Rod S Barrett (1), Laura E Diamond (1)

1Griffith Centre of Biomedical and Rehabilitation Engineering, Griffith University, Gold Coast, Australia

Introduction

Asphericity of the femoral head/neck junction, i.e. cam morphology, is a common imaging finding in active individuals [1]. During activities involving repetitive hip flexion and high impact loading, like sprinting, cam morphology can lead to hip pain and femoroacetabular impingement syndrome (FAIS) [1]. However, it is unclear why many athletes with cam morphology remain asymptomatic despite frequent participation in high impact activities [2]. This study aimed to compare the magnitude of hip contact force (HCF) during sprinting between individuals with FAIS, asymptomatic cam morphology (CAM), and healthy controls without symptoms or cam morphology (control). Since the anterior region of the acetabular cartilage is most often damaged in individuals with FAIS [5], a secondary aim of this study was to determine the phase of the gait cycle with the largest anteriorly directed HCF.

Methods

Participants (n=47) were divided into three groups (FAIS, n=14; CAM, n=15; control, n=17) based on hip symptoms, clinical presentation, and alpha angle (FAIS and CAM groups >55º; control group <55º). Three-dimensional motion capture, ground reaction forces, and electromyograms (EMG) from 12 lower limb muscles were recorded during two 10-metre overground sprints. Hip angles, hip moments, and moment arms from 40 muscle-tendon units (MTU) were estimated using linearly scaled musculoskeletal models in OpenSim [3]. A calibrated EMG-assisted neuromusculoskeletal model [4] was used to simulate musculotendon dynamics and estimate individual MTU forces which were used to calculate HCF in OpenSim. The resultant and component HCF magnitudes (normalised to body weight, BW) were compared between groups using statistical parametric mapping. Time-variant HCF were compared between groups using a independent sample t-tests via statistical parametric mapping (p<0.05).

Results

There were no between-group differences in running speed (5.6-5.8 m/s). No significant differences in resultant and component (inferior-superior, anterior-posterior, and medio-lateral) HCF were observed between FAIS and CAM (mean difference [95% CI] = 0.55BW [-0.71 to 1.82]) or FAIS and control (0.05BW [-1.10 to 1.19]) groups at any phase of the gait cycle (Figure 1). The largest anteriorly directed HCF were

observed during early swing (mean [95% CI]; FAIS=10.8 BW [10.1 to 11.6]; CAM = 11.5 BW [8.9 to 14.2]; control = 10.0 BW [8.5 to 11.5]).
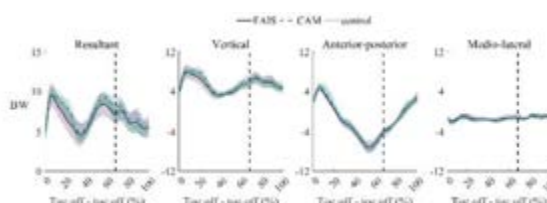
Figure 1: Ensemble averages (±95% confidence intervals) of hip contact force components during a 10-metre sprint for individuals with femoroacetabular impingement syndrome (FAIS, solid), asymptomatic cam morphology (CAM, dashed), and asymptomatic individuals without cam morphology (control, dotted). Vertical dotted line represents foot contact.

Discussion

Individuals with FAIS sprint with similar HCF compared to asymptomatic individuals with and without cam morphology. The largest magnitude of anteriorly directed HCF during sprinting occurs during early swing which could represent a potential mechanism for the development cartilage damage in individuals with FAIS. These results may help explain why sprinting is more often reported as painful compared with submaximal running, a task where peak HCF are posteriorly oriented [6]

References

1. Frank Arthroscopy, 31, 1199-1204, 2015
2. van Klij Scand J Med Sci Sports, 30, 1221-31, 2020
3. Rajagopal IEEE Trans Biomed Eng 63,2068-79,2016
4. Pizzolato J Biomech 48, 3929-36, 2015
5. Ng, Clin Orthop Relat Res 477, 1053-63, 2019.
6. Giarmatzis. J Bone Miner Res.;30,:1431–40 2015.

Acknowledgements

A POSTURAL STRATEGY AT STRING RELEASE IN ELITE ARCHERS

Andrian KUCH (1,2), Romain TISSERAND (2), François DURAND (3), Tony MONNET (2)

1. CRITT Sport Loisirs, France ; 2. Institut Pprime, CNRS/Université de Poitiers/ISAE-ENSMA, France ; 3. CREPS de Poitiers, France

Introduction

Limiting motion around the string release instant is decisive for performance in archery [1]. Indeed, the string release changes the {archer + bow} system dynamics maintained during the aiming phase, to propel the arrow towards the target. Not taking these dynamics into account may compromise the archer's postural stability and consecutively reduce his/her performance. For efficient upright balance control associated with voluntarily initiated movements, humans integrate the consequences of the forces they will create into the motor command to ensure postural stability [2]. When the movement initiation instant is predictable, humans can time coordinated motor sequences, called Anticipatory Postural Adjustments (APA), to limit the mechanical consequences of the forthcoming movement on balance [3]. Particularly, the mechanical consequences of these muscles contractions can be observed through the displacement of the center of pressure (COP) that occurs *before* movement onset.

Elite archers are likely to have mastered the mechanical perturbation consecutive to string release. Hence, we hypothesized that their APA would be finely coordinated with string release, to limit detrimental effects on postural stability and maximize performance.

Material and Methods

Standing on two force plates (Kistler) sampled at 1000 Hz, 6 French international level archers (3M, 3F) shot 18 arrows, at the 70m Olympic distance in an indoor range. The score of each arrow was collected.

A high-speed camera (Photron), synchronized with the force plates, captured each shot at 1000 fps, and was used to identify two instants: the clicker falling time (CFT) and the clicker reaction time (CRT). The CRT is the onset of the string release. The archers' reaction time was the duration between CFT and CRT.

Postural stability was characterized using the COP trajectory in the mediolateral (ML), i.e. the shooting, direction. On each trial, we observed a backward COP movement, starting after CFT (Fig. 1). The onset of the COP backward movement ($t0$), its maximal backward amplitude (COP_A) and peak velocity (COP_v) were computed. If $t0$ preceded CRT, an *early* postural strategy was identified, whereas if it occurred after CRT, a *late* postural strategy was identified. For comparison, COP trajectories were normalized by the archers' reaction time. Scores, COP_A and COP_v were compared between *early* and *late* strategies using a Welch's t-test, with $p < 0.05$ for significance.

Results and Discussion

The mean reaction time was 146 ± 11 ms after CFT, which is consistent with previous studies [4].

All archers used both strategies, but they mainly used the *early* one ($73 \pm 8\%$ of their shots). The average $t0$ for the *early* strategy was 16 ± 23 ms after CFT, while it was 11 ± 14 ms after CRT for the *late* strategy. Such short duration between $t0$ and CFT or CRT, alongside their low variability, suggest that elite level archers anticipate the forthcoming perturbation and are able to finely coordinate the display of their APA with these two specific instants during a shot.
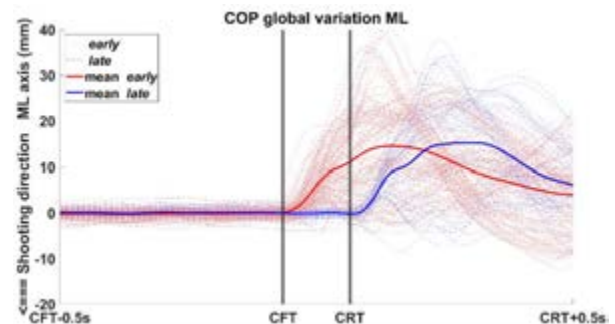
Figure 1: COP in the ML axis.

No statistical differences were found between the two strategies for COP_A and COP_v (Tab. 1). These results indicate that both strategies were identical from a biomechanical standpoint, but only displayed at two different moments in time. Additionally, despite slightly higher scores for the *early* shots, no performance difference was found between the two strategies. Thus, having a later APA does not seem to negatively affect scores in elite level archers.

	early	*late*	*p*
scores	9,2 ± 0,8	9,0 ± 0,9	0,17
COP_A (mm)	21 ± 7	20 ± 9	0,54
COP_v (mm/s)	205 ± 85	209 ± 92	0,60

Table 1: Compared indicators between strategies

Conclusion

Our findings suggest that elite level archers have automatized the perturbation caused by the string release and minimize its consequences on postural stability using a postural strategy finely coordinated with either the clicker falling time or the string release, with no differences in performance.

References

1. Keast et al, Journal of Sports Sciences, 8:3, 203-213, 1990
2. Massion, Progress in Neurobiology, 38, 35-56, 1992
3. Bouisset et al, J. Biomech, 20:8, 735-742, 1987
4. Tinazci et al, Procedia Engineering, 13:290-293, 2011.

Acknowledgements

MUSCLE CONTRIBUTIONS TO KNEE BONE-ON-BONE FORCES DURING AN HORIZONTAL DECELERATION TASK IN ELITE ATHLETES

Rodrigo B. Mateus (1), Ventura Ferrer-Roca (2), Filipa João (1), António P. Veloso (1)
1. CIPER, Faculty of Human Kinetics, University of Lisbon, Cruz Quebrada, Portugal

2. High Performance Center (CAR), Sant Cugat del Valles, Spain

Introduction

Improving joint stabilization during high-impact tasks plays a key factor to be accounted for in training programs that increase muscle coordination and strength. In addition to this, knowledge about how joint kinematics and muscle forces affect knee joint loading, whilst performing ballistic tasks remains scarce. The use of computational modeling allied with non-invasive experimental techniques to study injury mechanisms is an advantageous approach. To this end, the main purpose of this study is the identification of the main muscle contributors to the bone-on-bone forces exerted at the knee joint whilst performing a maximal forward braking and backward acceleration in elite athletes.

Methods

Fourteen elite male team-sports injury-free athletes participated in this study (age: 22 ± 4 years, height: 185 ± 4 cm, weight: 77 ± 11 kg). Kinematic and kinetic data were collected using 8 infrared cameras (Qualisys) working at a frequency of 300Hz and 2 force plates (Kistler). Muscle and joint contact forces were attained through OpenSim [1]. The musculoskeletal model was manually scaled to match each subject's anthropometry. A residual reduction algorithm (RRA) step was used to minimize errors related to kinematic inconsistencies and modelling assumptions. Muscle forces were estimated using a Computed Muscle Control (CMC) optimization technique. The forces obtained from CMC and the adjusted kinematics from RRA were used for this analysis. Muscle contributions to the bone-on-bone forces were estimated based on [2].

Results

The main muscle contributions in relation to the knee bone-on-bone forces are given in Figure 1. Results for this task contain the contact phase and can be divided into two distinct stages: a braking stage, where the body decelerates by dissipating energy, and a backward acceleration phase, where a change in direction occurs.
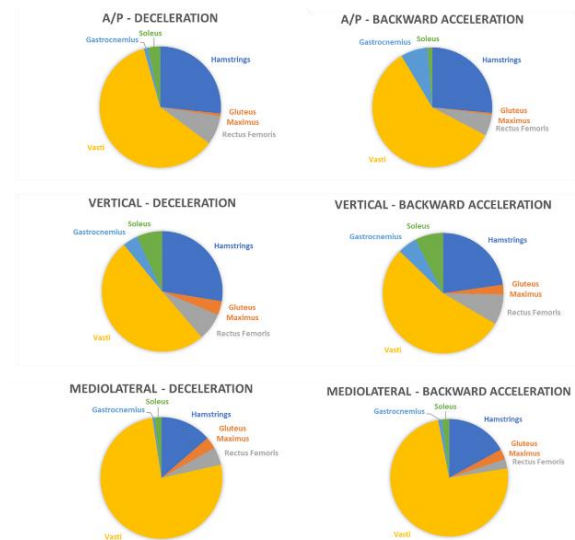
Figure 1: Main muscle contributions to knee bone-on-bone forces along all three direction, during both the deceleration and backward acceleration phases of this task.

Discussion

As expected from this task, the joint reaction forces at the knee are the highest along the A/P direction, being applied anteriorly on the tibia. These forces along the fore – aft direction recorded at the knee, are related to the fact that the muscles that exerted the most force in this task, *vasti*, are inserted in this joint. In addition to this, the hamstrings act as a minor contributor to the anterior bone-on-bone forces. Compressive forces along the vertical directions are applied at the knee joint. Once again, compressive force contributions by the *vasti* are also predominant. Slight contributions by the *soleus* are also of note. Along the mediolateral direction, at the knee joint, the medial bone – on – bone forces are key to the realization of the task, as they help maintaining the knee in a neutral position. Along this direction, the *vasti* are the main contributors. The results of this work present a preventive approach to understand the injury mechanisms of knee injuries during deceleration tasks.

References

1. S. L. Delp et al.(2007), IEEE Trans. Biomed. Eng.,54: 1940–1950.
2. Sasaki, K. and Neptune, R.R.(2010), *Journal of biomechanics*, 43**:** 2780–278

Acknowledgements

CONTRIBUTIONS TO THE SHAPE OF THE FORCE-VELOCITY RELATIONSHIP IN SIMULATIONS OF LOADED SQUAT JUMPS

Sam Allen (1)

1.   *School of Sport, Exercise, and Health Sciences, Loughborough University, UK*

Introduction

In multi-segment movements the relationship between the external applied force and the velocity of the whole body or limbs (F-v) has often been shown to be quasi-linear [1]. Bobbert [2] attributed the quasi-linearity of the observed F-v relationship between applied force and instantaneous endpoint velocity at a fixed point (80% of leg length) in a simulated leg press task to the effects of segmental dynamics since the underlying torque-velocity (T-v) relationship remained convex. In other tasks where linearity of the F-v relationship has been observed, such as loaded squat jumps [3] the force used to establish the F-v relationship was not the load carried by the athlete, but the normal reaction force at the feet, which represents the force necessary to match the applied load, *plus* the force required to overcome the system inertia. Furthermore, the calculated force and velocity values were not measured at a particular instant but time-averaged over the push-off phase. Hence, the aim of this study was to simulate loaded squat jumps with a two-segment torque-driven computer model, sequentially adding torque-angle (T_{AV}), and activation rate (Act) components to the torque-angular velocity (T_{AV}) component of the torque generators to establish how each of these factors affect the shape of the time-averaged F-v relationship.

Methods

A two-segment rigid body planar computer model was constructed in Simscape Multibody (R2021a, Mathworks, MA, USA) to simulate a weighted squat jump. The two segments represented the shanks, and the thighs, with the mass of the combined head, arms, and trunk (HAT) plus additional mass representing a weighted barbell added as a point mass at the hip. The hip joint was constrained to move vertically, directly above a fixed ankle joint, resulting in only one degree of freedom in the model, the knee joint angle. The model was actuated by a torque generator at the knee joint representing the knee joint musculature. Model parameters were taken from Allen et al. [4]. Three versions of the torque generator were used: the first (Model 1) had only a T_{AV} component; the second (Model 2) had T_{AV} and T_A; and the third (Model 3) had T_{AV}, T_A, and Act. Simulations began with an initial knee angle of 90° and ended when the ground reaction force (GRF) decayed to zero. Initial activation levels in Model 3 were chosen to ensure a static starting position. Simulations were run with additional masses ranging from 0 kg to 160 kg (the maximum mass at which all models were able to complete the movement) at 10 kg intervals. The vertical velocity of the system centre of

mass (CoM) and the vertical GRF were time-averaged over the simulation and least squares 2nd order polynomial regression lines were fit to the data to obtain force-velocity (F-v) relationships.

Results

The F-v relationship was convex when the torque generator contained only a T_{AV} component, the addition of a T_A component resulted in a less convex F-v relationship, and the addition of the Act component resulted in a slightly concave F-v relationship (Figure 1).
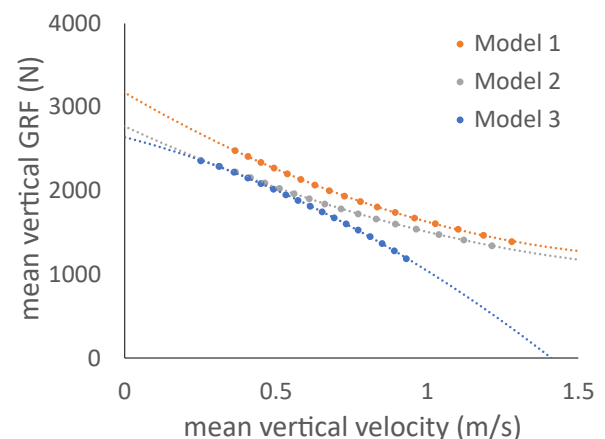
Figure 1: Force-velocity relationships for the three models with associated regression lines.

Discussion

The F-v relationship observed when the torque generator contained only a T_{AV} component was convex but less so than the underlying T-v relationship, because of the dynamics of the system [2]. The addition of a T_A component resulted in a less convex relationship due to a reduction in convexity in the T-v relationship. Lastly, the addition of Act component resulted in a slightly concave F-v relationship due to the resulting quasi-linearity of the underlying T-v relationship. It can be concluded that, in addition to the system dynamics, the torque-angle relationship and activation rate contributed to a reduction in the convexity of the T-v relationship and therefore are likely to contribute to the quasi-linearity of the F-v relationship observed in loaded squat jumps in vivo [3].

References

1. Jaric, Int J Sports Med, 36(9):699-704, 2015.
2. Bobbert, J Appl Physiol, 112:1975–1983, 2012.
3. Samozino et al, Int J Sports Med, 35(6), 2013.
4. Allen et al, J Biomech, 43(16): 3156-3161, 2010.

DO FATIGUE-INDUCED CHANGES IN COGNITIVE PERFORMANCE RELATE TO CHANGES IN KNEE MECHANICS?

Filippo Bertozzi (1,2), Patrick D. Fischer (3), Fatemeh Aflatounian (3), Keith A. Hutchison (3), Manuela Galli (2), Marco Tarabini (2), Chiarella Sforza (1), Scott M. Monfort (3)

1. Università degli Studi di Milano, Italy; 2. Politecnico di Milano, Italy; 3. Montana State University, USA

Introduction

Many non-contact ACL injuries occur during sports movements in response to an external, unanticipated stimulus [1]. Physical fatigue may also affect lower limb mechanics related to non-contact ACL injuries [2]. Additionally, lower cognitive ability has been demonstrated to be a risk factor for ACL injury during unanticipated movements [3]. However, no study has been conducted to understand the potential relationship between fatigue-induced changes in knee mechanics and cognitive function. Therefore, this study aimed to analyze how the changes between baseline and post-fatigue cognitive performance relate to fatigue-induced knee mechanics during unanticipated landing.

Methods

Twenty-two athletes (22 ± 3 years; 69 ± 12 kg; 176 ± 11 cm; 8F/14M) completed four computer-based cognitive tests in a randomized order, targeting reaction time (RT) and attentional control (AC). After performing maximal vertical jumps (MVJ) taken as reference, they performed a jump-land-jump task from a 30-cm box, recorded with a marker-based motion capture system [4]. After contacting force plates, participants jumped in a secondary direction (straight-up, 45° to dominant or non-dominant side) based on unanticipated visual cues. Then, participants completed rounds of a fatigue protocol including countermovement jumps (CMJ), step-ups, squats, and a 5-10-5 agility drill, until CMJ height decreased below 85% of MVJ height [5]. Afterward, they repeated the jump-land-jump task and the four cognitive tests. Only straight-up trials were included in this analysis. Peak knee flexion (pKFA) and abduction (pKAbA) angles and peak external knee abduction moment (pKAbM) were computed for the dominant limb within 50 ms after initial contact and are all presented as positive. pKAbM was normalized to participant height and weight, and then transformed using natural logarithms, ln(pKAbM). Averaged RT and AC test performance scores provided baseline and post-fatigue composite scores for each domain. Paired t-tests tested for differences between baseline and post-fatigue values for RT and AC. Change scores (Δ) were computed for the biomechanical and cognitive variables as the difference between the post-fatigue and the baseline values. ΔAC and ΔRT were entered as candidate continuous predictors for ΔpKFA, ΔpKAbA, and Δln(pKAbM) in three stepwise regression models, and standardized regression coefficients (β_{std}) were computed. Significance was set to $\alpha=0.05$ for all statistical tests.

Results

Post-fatigue RT scores increased ($p<0.001$, 323 ms vs. 339 ms) and AC decreased ($p<0.001$, 96.4% vs. 93.2%) compared to baseline values. Stepwise regression for ΔpKAbA revealed a significant relationship with ΔAC ($p=0.037$, $\beta_{std}=0.826$; Figure 1). Standardized model residuals identified an influential point for ΔpKAbA (>4°), and regression analysis was repeated with omitting this point. The follow-up analysis confirmed the relationship with ΔAC ($p=0.003$, $\beta_{std}=1.015$) and suggested an association with ΔRT ($p=0.038$, $\beta_{std}=0.658$). ΔpKFA and Δln(pKAbM) yielded no significant interactions with cognitive change scores.
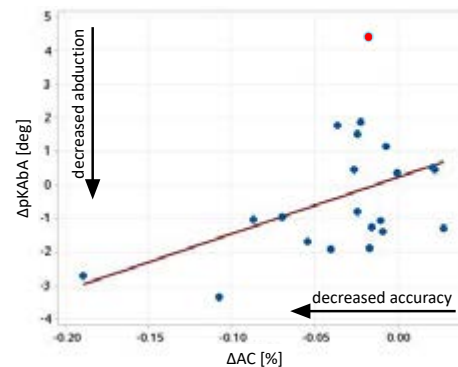
Figure 1: regression analysis between ΔpKAbA and ΔAC. The influential point is highlighted in red.

Discussion

The cognitive performance declined for RT and AC after the fatigue protocol, supporting a plausible effect of physical fatigue on cognitive function. ΔpKAbA significantly correlated with ΔAC, with a worsened post-fatigue AC corresponding to smaller fatigue-induced knee abduction angles. Individuals who maintained a similar AC performance after the fatigue protocol also showed riskier knee mechanics when fatigued. Additionally, after removing the influential point, ΔRT revealed a relationship: a worse cognitive performance (higher reaction time increases) resulted in increased knee abduction angles after the fatigue protocol. The present results demonstrate that cognitive function may mediate fatigue-related changes in established biomechanical risk factors for ACL injury.

References

1. Whyte et al, J Sports Sci, 36:889-900, 2018.
2. Benjaminse et al, Sport Med, 49:565-586, 2019.
3. Avedesian et al, Am J Sports Med, ahead-of-print, 2021.
4. Fischer et al, J Appl Biomech, 37:388-395, 2021.
5. Cortes et al, J Athl Train, 48:306-313, 2013.

FINGERBOARD HANGING LOCK-OFFS: REFINING PRACTICE GUIDELINES FOR CLIMBERS

Juliana Exel, Olivia Froschauer, David Deimel, Arnold Baca, Hans Kainz

Department of Biomechanics, Kinesiology and Computer Science in Sport, University of Vienna, Austria

Introduction

Sustained isometric strength of the forearm muscles is determinant of success in climbing [1], therefore, training protocols involving arm lock-off in hangings are frequently practiced to enhance this capacity [2, 3]. Finger tendons kinetics have been previously estimated, however, the transmission of moments and forces across the arm is still unknown. Considering that 14% and 30% of climbers have already been affected by elbow injuries, depending on the climbing modality and level of experience/performance [4], understanding the biomechanics of specific exercises applied in climbing training programs could contribute to improve the quality of protocols and mitigate sources of injuries. Thus, the present study aimed to describe upper limb joint moments and muscle activations involved in isometric finger hangs with 3 different elbow flexion angles.

Methods

Four experienced climbers were recruited (28±4.6 years; 175±10.6 cm height; 71±10.6 kg weight, 16.5±4 IRCRA scale) to perform 5 seconds –finger hang in 20 mm-depth hold, open crimp, in 3 different conditions: elbows flexed at 90°, 135° and 180° (fully extended). Electromyography (EMG) of the superficial finger flexor muscles were recorded with a wireless EMG system (Cometa, Milan, Italy). Additionally, upper body kinematics were captured with a 3D motion system (Vicon, Oxford, UK). We scaled the ARMS model [5], which is an upper limb musculoskeletal model, to the anthropometry of each participant based on the surface markers. Afterwards, we calculated joint kinematics and joint moments using OpenSim [6]. EMG data was band-pass filtered, demeaned, rectified, low-pass filtered and amplitude-normalized to maximum voluntary contraction trials. Peak elbow and shoulder joint moments, and peak EMG signals were compared between the three conditions.

Results

The joint moments (mean± std, Nm/kg) in the elbow and in the shoulder were higher when climbers perform finger hangs with the elbow flexed at 90º (2.3±0.6 for elbow flexion, 1.1±0.7 for shoulder elevation, 1.1±1.6 for shoulder rotation) and 135º (1.4±1, -0.1±0.7, 0.5±1.1), respectively, compared to its full (180º) extension (-0.1±1.3, 0.2±1.2, 0.4±0.5). Muscle activations (%MVC) of the finger flexors did not differ between the three different conditions (1±0.6, 1.1±0.8, 1.1±0.6 for 90º, 135º and 180º, respectively).

Discussion

Our study showed that increasing elbow flexion in the performance of finger isometric hangs does not increase the muscle activation of the finger flexors. Additionally, flexed elbow positions during fingers hangings increased the joint moments at the elbow and shoulder joints, which, at long term, can be a source of pain and/or injury for climbers. Our results add information on previous reports about particularities of developing finger force capacity for climbers [7], which have described that finger force capacities decrease when elicited during more complex upper body movements.
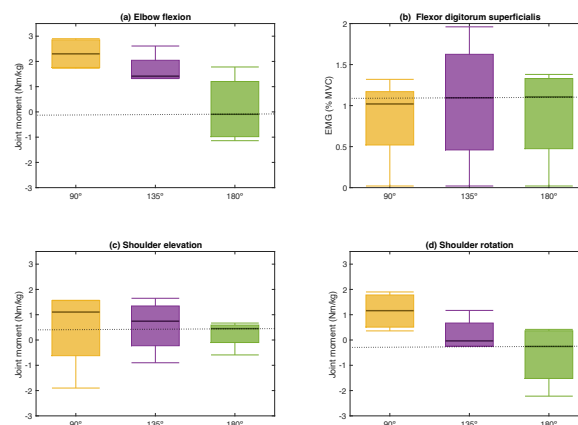
Figure 1: Elbow (a), shoulder (c and d) joint moments (Nm/kg), and EMG (% of MVC) of the fingers flexor during isometric open crimp finger hangings with elbows at 3 positions: flexed at 90º, 135º and fully extended (180º).

Although the present results are initial, therefore, exploratory, they indicate important and applicable information for training guidelines. Isometric finger hangings with straight arms are efficient for training finger flexor force capacities and concomitantly less stressful for the elbow and shoulder joints.

References

1. Saul et al, J Exerc Sci Fit, 17(3): 91–100, 2019.
2. Desnivel, 2001. https://tinyurl.com/3du9f2c8 Jan/2022.
3. Saeterbakken et al, Plos One, 13(10): e0203766, 2018.
4. Grønhaug, BMJ O Sport Exerc Med, 4(1): e000406, 2018.
5. Delp et al, IEEE T Biom Engin, 54(11): 1940-1950, 2007.
6. Saul et al, Comput Methods Biomech Biomed Engin, 18:13, 1445-1458, 2015.
7. Vigouroux et al, J Spo Sci, 37:8, 886-894, 2019.

ACCURACY OF A NEW LOCAL POSITIONING SYSTEM IN OBTAINING SPEED AND ACCELERATION DURING GAME SPORTS MOVEMENTS

Philip X. Fuchs (1,2), Yi-Cheng Chou (1), Wei-Han Chen (1,3), Nicholas J. Fiolo (1), Tzyy-Yuang Shiang (1)

1. National Taiwan Normal University, Taiwan; 2. University of Salzburg, Austria; 3. University of Taipei, Taiwan

Tracking player positions has increasingly become popular in game sports for tactical analyses and training load regulations. Although local positioning systems (LPS) were reported to be superior to GPS and video-based systems [1], data differentiated in the time-domain (i.e., speed and acceleration) were reviewed critically [2]. The objective was to assess the accuracy of a new LPS for speed and acceleration in dynamic movements, common to game sports.

Time-series and peak speed, acceleration, and deceleration were compared between concurrently collected data via LPS (50 Hz) and Vicon (100 Hz) data during 10 repetitions of linear, curved, triangle, and shuttle running in low and high intensity (n=80). Data processing followed the developer guidelines, filtering after residual analyses, and synchronization via time-shift until the minimum error was reached [3]. Concordance correlation coefficients (CCC), percentage root mean square errors (RMSE), Bland-Altman plots, and analyses of variances were provided.

CCC were 0.893 (time-series speed), 0.816 (time-series acceleration), 0.923 (peak speed), 0.486 (peak acceleration), and 0.731 (peak deceleration). RMSE were larger in time-series acceleration (14.4±3.8%) than speed (12.0±5.8%) (η^2=0.472, p<0.001) and larger in peak acceleration (28.0±14.3%) and deceleration (25.1±14.9%) than in speed (7.3±6.1%) (η^2=0.091, p<0.01). RMSE were also larger in high intensity compared with low intensity for time-series speed and acceleration as well as peak acceleration and deceleration (0.064≤η^2≤0.475, p<0.05), but not significantly for peak speed (η^2=0.029, p=0.149). Bland-Altman plots including 95% limits of agreement and Spearman correlation results for trendlines were depicted in Figure 1.

Strong concordance and smaller errors in time-series speed and acceleration as well as peak speed suggested that the tested LPS can be used for applications when entire time-series data are required (e.g., for energy expenditure estimation via acceleration) [4] and when peak speed serves as a performance identifier (e.g., for determination of intensity zones) [5]. In consideration of previous studies [2], the current accuracy of both time-differentiated time-series was very promising. However, serious deficits were found in peak acceleration and deceleration, comparable with previous findings [6]. The data suggested a lacking ability of the LPS to detect these peaks accurately with increasing magnitude of the true values. Acceleration data should be used with caution if peak values play a crucial role in the intended analyses (e.g., determining performance via peak values). Corroborated by others [7], this should be considered especially for very dynamic movements as errors increased in high intensity.

Figure and Tables
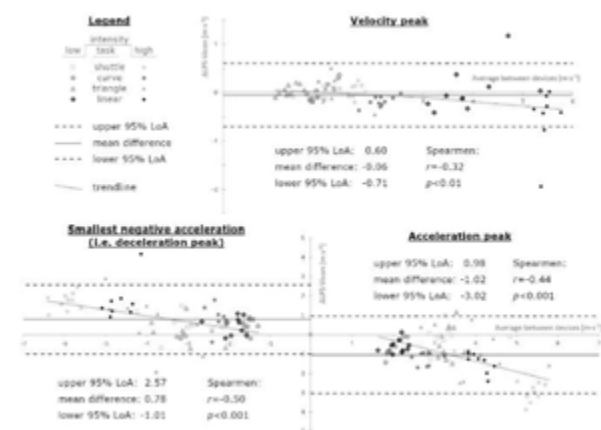
Figure 1: Bland-Altman plots of differences in peak speed, acceleration, and deceleration between LPS and Vicon including 95% limits of agreement (95% LoA) and Spearman correlation (r) for trendlines; derived from [8].

References

1. Pino-Ortega et al, P I Mech Eng P-P Spo, 0(0):1-10, 2021. Doi: 10.1177/1754337120988236
2. Rico-González et al, Appl Sci, 10(17):5994, 2020. Doi: 10.3390/app10175994
3. Blauberger et al, Sensors, 21:1465, 2021. Doi: 10.3390/s21041465
4. Osgnach et al, Med Sci Sport Exer, 42(1):170-178, 2010. Doi: 10.1249/MSS.0b013e3181ae5cfd
5. Wisbey et al, J Sci Med Sport, 13(5):531-536, 2010. Doi: 10.1016/j.jsams.2009.09.002
6. Buchheit et al, Int J Sport Physiol Perf, 9(3):442-445, 2014. Doi: 10.1080/02640414.2014.942687
7. Luteberget et al, Front Physiol, 9:115, 2018. Doi: 10.3389/fphys.2018.00115
8. Fuchs et al, Eur J Sport Sci, in submission.

A KINEMATIC ANALYSIS OF THE 10-BALL BREAK IN PROFESSIONAL POOL BILLARDS

Philipp Kornfeind (1), Thomas Boindl (1), Arnold Baca (1)

1. Centre for Sport Science and University Sports, University of Vienna, Austria

Introduction

In 10-ball billiards [1], the break is the first stroke, which is usually executed very powerfully with the aim of sinking a ball, as this allows to continue playing by executing the following shot also. Like any other stroke, it can be divided in time by the timing of the back reversal, the impact and the front reversal. We hypothesized that with hard breaks there is a tendency towards a sequence of movements characterized by a kinematic chain of joints involved.

Methods

22 elite players played series of two different breaks (one from the middle, one from the left wing using two different cues (breaker) and house cue) targeting at maximum velocity [2]. 3D-kinematics were obtained using a Vicon motion analysis system comprising 8 cameras (6pc. MX13, 2pc. MX40) operating at 250 Hz. 24 markers were attached to each player applying an adapted upper body model (modified golem) in order to reconstruct angular motions in shoulder, elbow and wrist joints (cf. Figure 1) and to determine stroke parameters velocity of the cue at impact, cue elevation angle and height of impact point. An uniaxial accelerometer (8772A10, Kistler) was mounted on the cap of the cue in order to capture longitudinal acceleration at 5kHz. In particular, time courses of angular velocities were determined. From the local maximum values of the angular velocities and the respective timing typical motion patterns were identified and contrasted with the cue velocities at impact.
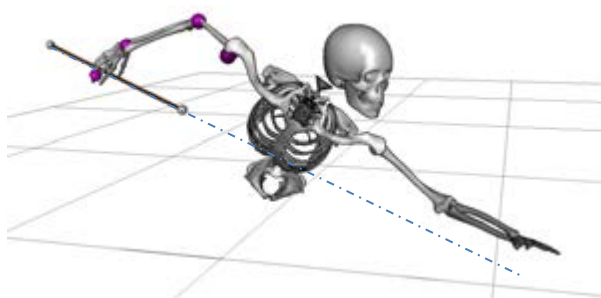
Figure 1: Shoulder, elbow and wrist joint at instant of back reversal.

Results

No significant differences were found for cue impact velocity or acceleration (Table 1) with regard to cue type and position.
At all trials, the instant of maximum cue velocity coincided with the impact event. Moreover, positive acceleration of the cues until the impact could be observed (Table 1).

		B_M	B_L	H_M	H_L
v	mean	6,275	6,165	6,063	6,177
	std.dev.	0,359	0,423	0,307	0,323
a	mean	4,141	3,955	3,656	3,918
	std.dev.	2,119	2,147	1,853	2,309

Table 1: Cue velocity v [m/s] and acceleration a [m/s^2] at impact for shots with breaker (B) and house cue (H) from the middle (M) and left wing (L) position.

Time course analysis of the angular velocities in the investigated joints (cf. Table 2 for selected values) revealed a variety of individual shot techniques including features for the identification and classification of movement patterns (i.e. timing sequence of local maxima/minima, joint contribution, backswing characteristics).

	Wrist abduction	Elbow flexion	Shoulder flexion
mean	50,843	34,890	431,431
std.dev.	77,683	180,617	183,092

Table 2: Angular velocities[°/s] at impact for shots with breaker cue (B) from the middle.

Shots with highest velocities showed one local maximum of the angular velocity in the elbow joint just before and one after the impact, maximum angular abduction velocity in the wrist joint just before, at or immediately after impact and highest angular flexion velocity in the shoulder joint just before or at impact.

Discussion

Even at elite level there seems to be a high degree of individualization of the movement patterns for performing the break. This confirms observations made in the analysis of other elementary shot techniques [2-4]. Particular movement patterns, which can be categorized by making use of certain kinematic features, may result in high cue velocities at impact. Successful shooting strategies might thereby be identified, even though individual differences need to be considered.

References

1. Alciatore, The Illustrated Principles of Pool and Billards. Stirling New York, 2004.
2. Kornfeind et al, Procedia Engineering 112:540-545, 2015.
3. Kornfeind et al, Book of Abstracts 19th Annual Congress of the European College of Sport science: 81, 2014.
4. Cheng et al, Proc Asian Pacific Conference on Biomechanics: S 242, 2007.

FINITE ELEMENT MODELLING OF SPORTS FOOTWEAR GRIP PERFORMANCE ON WET HARD SURFACES

Lise Sissler (1), Joanna Gringet-Charre (2), Kurt Beschorner (3), Tristan Tarrade (2)

1. DAES SA, Switzerland; 2. SALOMON SA, Footwear Department, France; 3. University of Pittsburgh, Department of Bioengineering, United States

Introduction

While friction performance has been of main interest in the safety footwear industry for a long time, the recent emergence of trail running has required sports footwear manufacturers to design shoes with adapted grip performance.

Physics-based computational models of shoe-floor friction have already been developed [1], however, very few have addressed trail shoe friction in wet conditions. The objective of this study was to develop a tool which could predict friction performance of trail running shoes on wet hard surfaces.

Methods

As previously correlated to user field tests in an internal study, the standardized SATRA test [2] on a wet quarry tile was used to obtain experimental measurements of the coefficient of friction (COF) of the shoes. Four lug configurations were tested with two different rubbers (Figure 1).
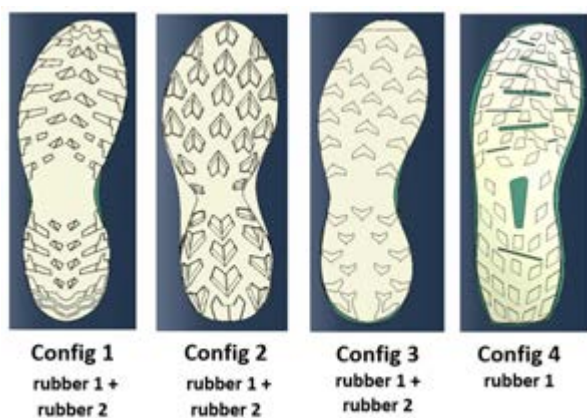
Figure 1: Different lug and rubber configurations tested both experimentally and with simulation

The roughness profiles and material properties of the two rubbers and quarry tile surface were used to create a microscopic-scale finite element (FE) model. The output of this model was the COF as a function of pressure for each of the two rubbers, which was then used to define a contact friction in a macroscopic-scale FE model. This macroscopic model simulated the experimental conditions of the SATRA test. Seven simulations were run, and the results were then compared to the experimental SATRA COF values.

Results

The simulated COF values were compared to the experimental SATRA COF values to evaluate the validity of the model. As shown in Figure 2, the simulated and experimental COF values were significantly linearly correlated ($p < 0.05$, $R^2 = 0.792$).
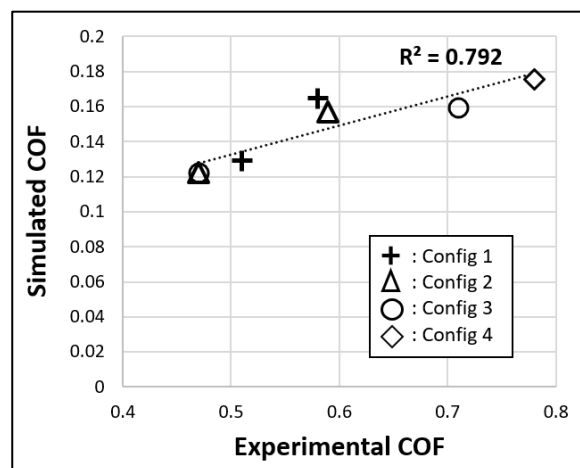
Figure 2: Simulated COF vs. experimental COF

Discussions

Similarly to Moghaddam et al.'s multiscale model for safety footwear [1], a multiscale FE model of grip performance of trail shoes was developed for wet conditions. The significant correlation between simulated and experimental data showed that the model can be used to predict the effect of lug configuration and material properties on grip performance.

The effects of adhesion and hydrodynamic pressures were considered as negligible in this model. Modelling water interaction with the outsole could allow for enhanced predictions. Additionally, pressure paper was used to compare the experimental contact area with the simulated contact area of each shoe, and a few discrepancies were observed. A minimization of the differences between real sole prototypes and idealized CAD sole shapes might improve the correlation further.

References

1. Moghaddam et al, Journal of Biomechanics, 66:145-152, 2018.
2. SATRA TM 144/ISO 13287

Acknowledgements

EFFECT OF DIFFERENT PLAYERS' MOTION MODELS ON LINEAR AND NON-LINEAR MEASURES OF SPACE CONTROL IN FUTSAL

Jonas Bischofberger (1), Juliana Exel (1), Bruno Travassos (2), Jaime Sampaio (3), Arnold Baca (1)

1. Department of Sport Science, Biomechanics, Kinesiology and Computer Science in Sport, University of Vienna, Austria; 2. CIDESD, University of Beira Interior, Portugal; 3. CIDESD, University of Trás-os-Montes and Alto Douro, Portugal

Introduction

The collective tactical behavior in futsal can be successfully captured by metrics based on positional data, one of which is the space control of each player [1]. The classic approach to space control involves the computation of Voronoi diagrams. It can be viewed as assigning dominance over a given location on the pitch to the player who could reach that location first. The assumptions in players' movement models should carefully consider the dynamical characteristics of players (human) displacement during their performance in a match. Previous studies have proposed and reported approaches to determine dominant regions in team sports [2], as well as the dynamics in the interaction of such areas, in particular phases of a game [3]. However, there is still a gap in the understanding of how these models of players' motion affect the analysis of variables related to space control. The present work aims to verify how a linear and non-linear measure of space control are affected by four different players' motion models.

Methods

Position and acceleration data of players during one official futsal match was obtained using the WIMU® system (RealTrackSystems, Almería, Spain), at 30 and 100 Hz, respectively. The raw position data was re-sampled and smoothed using the LOESS method, while the acceleration was filtered using a 4th order Butterworth low-pass with a cut-off frequency of 6 Hz. These procedures were defined by spectral and residual analysis. Four motion models for the calculation of space control were tested, assuming: (a) constant and equal velocity between players, set as the mean velocity mathematically derived from players position in the match, referring to classic Voronoi diagrams; (b) constant and equal mean team acceleration; (c) constant acceleration, but determined as the maximal individual value found for each player during the match; and (d) constant acceleration, but determined as the mean individual value for each player during the match. These models were calculated using dedicated codes developed in Python, solving the respective equations of motion and numerically computing the controlled space as area integrals. The mean space control and the Approximate Entropy (ApEn) were then computed for every player and compared across the four models using boxplots.

Results

When controlled space (m²) is averaged per player over the duration of the game, there is no significant difference between the four motion models (median [C.I.] = 73.54m² [70.08 – 77.00] for (a), 74.83 [72.18 – 77.48] for (b), 72.71 [68.70 – 76.73] for (c), and 74.04 [69.96 – 78.11] for (d), respectively). The estimated medians for the ApEn are (a) 0.027 [0.024 - 0.031], (b) 0.039 [0.036 – 0.043], (c) 0.036 [0.033 – 0.039] and (d) 0.047 [0.042 – 0.052], and they differ across models, as shown in Figure 1.
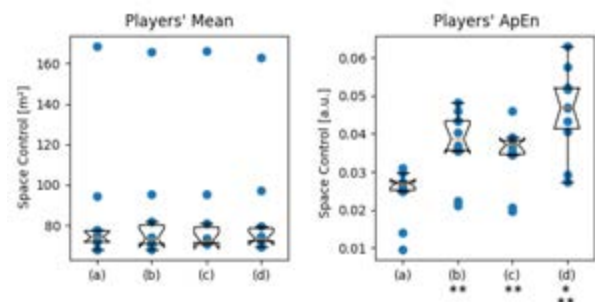
Figure 1: Comparison of players' individual mean and Approximate Entropy (ApEn) of the space control over the duration of the game, across the four underlying models of motion (a) to (d). (*) significantly different from (c). (**) significantly different from (a).

Discussion

When the amount of space control is averaged, the mean and its variability are the same, independent on the model of player motion applied.

In contrast, ApEn, as a measure of variability of the pattern underlying space control over time, showed to be sensitive to the different assumptions in the motion model, thus, picking up situational effects. Compared to the classic Voronoi approach, the use of proper acceleration data yields higher values of ApEn. Also, ApEn seems to be influenced by how acceleration is used to model players' motion, as the model with individualized values showed a different distribution compared to the others. This indicates the impacts of the methods for obtaining players' kinematics on the estimation of collective behavior parameters. Thus, further studies can rely on the present results to guide future analysis.

References

1. Rico-González M. et al, Biol Sport, 38(1):23-36, 2021.
2. Caetano, F. G. et al, Sci Rep, 11(1):18209, 2021.
3. Fonseca, S. et al, Hum Mov Sci, 31:1652-1659, 2012.

THE INFLUENCE OF SEX, AGE AND PEAK KNEE ISOKINETIC TORQUE ON SINGLE LEG HOP DISTANCE

Simon Herger (1,2)*, Linda Bühl (1,2), Corina Nüesch (1,2), Sebastian Müller (1,2), Christian Egloff (1,2), Annegret Mündermann (1,2)

1. University Hospital Basel, Switzerland; 2. University of Basel, Switzerland
*simon.herger@unibas.ch

Introduction

Single leg hop (SLH) for distance as part of performance test batteries in athletes are relevant for knee injury risk [1] and used to assess return to sports readiness after injury and/or surgery [2] where a limb symmetry index (=SLH distance injured/uninjured*100) higher than 90% has been recommended [2]. However, factors influencing SLH distance in healthy recreational athletes of various ages are unknown. We assessed whether maximal SLH distance can be predicted by sex, age and isokinetic peak torque, in recreational athlete participants.

Methods

36 female (age, 36.6 ± 12.0 years; age range, 19-59 years, body mass index (BMI), 22.7 ± 3.3 kg/m^2) and 29 male (age, 33.7 ± 8.9 years; age range, 21-53 years; BMI 23.9 ± 3.5 kg/m^2) healthy volunteers without previous lower extremity and back injuries were included (Figure 1). All participants had a maximum of 6 trials per side to reach their best SLH distance. Trials were excluded if the participant lost balance or had to readjust their foot after landing. Isokinetic knee extensor and flexor muscle strength was tested at 60°/s using a dynamometer (Biodex System 4 Pro: Biodex Medical Systems, Shirley, NY, USA) in two series of 4 extension-flexion repetitions. For the left side the maximal SLH distance and the predictor variables sex, age and the maximal peak torque in extension or flexion normalized to body mass were included in a multiple linear regression model in RStudio (R Core Team (2020); $p<0.05$).

Results

Knee extension and flexion peak torque decreased for every year of age by 0.013 Nm/kg and 0.007 Nm/kg, respectively ($p=0.005$ and $p=0.048$). Peak torque was 0.49 Nm/kg ($p<0.001$) and 0.31 Nm/kg ($p<0.001$) lower in females than in males for extension and flexion, respectively. Higher relative extension peak torque increased maximal SLH distance by 23.5 cm per 1Nm/kg ($p<0.001$, Figure 2), and every year of age reduced SLH distance by 1.0 cm ($p<0.001$) and being female by 21.0 cm ($p=0.001$; adjusted R^2: 0.578). Higher relative flexion peak torque increased maximal SLH distance by 29.4 cm per 1 Nm/kg ($p<0.001$), and every year of age reduced SLH distance by 1.1 cm ($p<0.001$) and being female by 23.6 cm ($p<0.001$; adjusted R^2: 0.577). All results were confirmed when calculated for the right side.
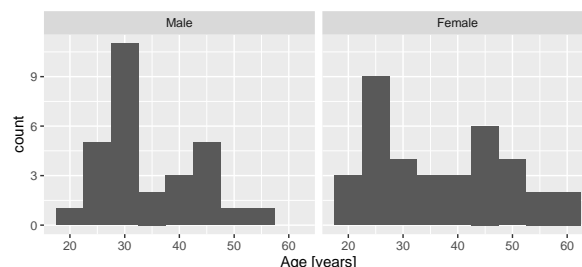
Figure 1: Histogram of age distribution for male and female participants.
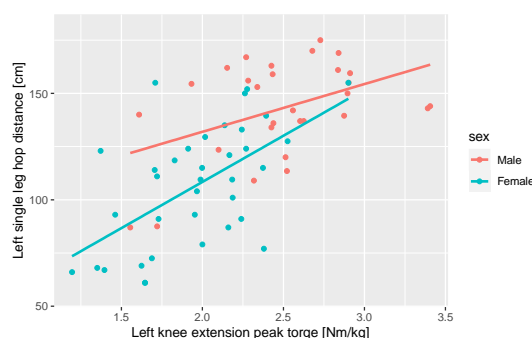
Figure 2: Dot plot with regression line $\pm$ SD (grey area) of single leg hop distance and knee extension peak torque for male (red) and female (blue) participants.

Discussion

These results confirmed our hypothesis that sex, age and isokinetic peak torque were predictors of SLH distance in recreational athletes aged 20 to 55 years. By adding peak extension or flexion torque to the regression analysis, the amount of explained variability of SLH distance increased to 57%. Interestingly not only extension but also flexion torque was a predictor of SLH distance confirming previous reports of a greater positive correlation between hamstring than quadriceps isokinetic strength [3]. Other factors not considered here, such as balance, muscle fiber content or flexibility, may explain the remaining variability in SLH distance. Our findings highlight the importance of a high relative muscle strength to maintain or regain function with aging or after knee injury.

References

1. Guild et al, J. Sport Rehabil., 30:320-326, 2021.
2. Sueyoshi et al, Orthop. J. Sports Med., 2017.
3. Pincivero et al, Clin J Sport Med, 7:11-16, 1997.

Acknowledgements

BALL-FINGER POSITIONING FOR ACCURATE BASEBALL PITCHING

Ayane Kusafuka (1), Kohei Nishikawa (1), Naoki Tsukamoto (1) , Kazutoshi Kudo (1)

1. The University of Tokyo, Japan

Introduction

In various motor skills in sports, such as throwing, kicking, and hitting, accurately controlling a ball to a target position is one of the important skills. The final arrival position of the ball is approximately determined by its physical state at the release or impact. In high-speed baseball pitching, reducing the variability of the ball's release angle is particularly necessary to reduce the variability of pitch location (Kusafuka et al., 2021). While previous studies have suggested hand and finger movements are important for accurate throwing (e.g., Hore et al., 1995), the body movements should be performed to achieve this are still unknown. Therefore, we focused on the positional relationship between the ball and the fingers, which is considered to be closely related to the ball movement and analyzed the process of determining release angle to clarify the characteristics of the body movements for the accurate pitching.

Methods

Two high-speed cameras (960 fps) were used to capture the pitching motions of 14 skilled pitchers (sex: male; age: 20.7 ± 1.9 years; height: 177.0 ± 5.6 cm; weight: 76.5 ± 7.7 kg; 13 right-handed and 1 left-handed), and the 3D positions of the joints of wrist, index finger, middle finger, and the ball during each pitching of 30 fast balls were obtained using an automatic image recognition technique based on deep learning (DeepLabCut). Therefore, no markers were placed on the body. Pitchers were instructed to aim at the catcher's mitt and throw as fast and accurately as possible.

Speed was defined as the magnitude of velocity vector at the ball release. The release angle was given by the elevation angle $\theta 1$ ($-90°$ to $90°$) and the azimuth angle $\theta 2$ ($-90°$ to $90°$) of velocity in polar coordinates.

Results

The time series changes in fingertip positions of index finger and middle finger relative to the ball were compared among the pitchers. The results showed that the pitchers whose fingertips of middle fingers were in contact with the lower part of the ball about 20-30ms before the release showed less SD of release angle. Figure 1 shows the time series of average fingertip positions of the index (blue) and middle (red) finger relative to the ball in a coronal plane for typical pitchers, and Figure 2a shows the correlation coefficients between average vertical position of middle finger at each time and SD of $\theta 1$, and their p-values. This trend was also true for SD of $\theta 2$ (Figure 2b). On the other hand, there were correlations between SD of vertical position of middle finger at the earlier and shorter time periods and SD of $\theta 1$ or $\theta 2$.
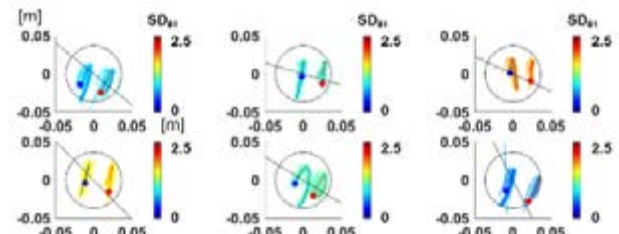
Figure 1: The time series of fingertip positions of the index and middle finger relative to the ball.
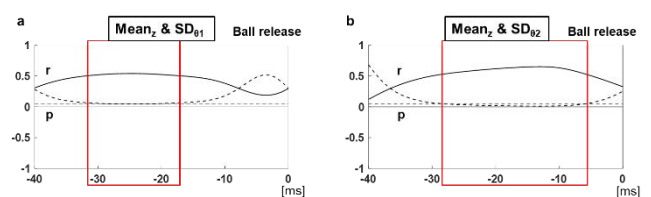
Figure 2: The correlation between average vertical position of middle finger and SD of release angle.

Discussion

It is suggested that the pitching style in which the fingertips were in contact with the bottom of the ball was able to control the release angle better because the force required to rotation of the ball, which doesn't have much relation on the release angle, was smaller. A previous research has shown that some of the best performing pitchers in throwing had highly robust hand trajectories that compensated for variability in release timing (Nasu et al., 2014). The result of this study indicates that the skilled person can achieve a robust movement against spatial as well as temporal variability.

References

1. Hore, J., Watts, S., Martin, J., & Miller, B. (1995). Timing of finger opening and ball release in fast and accurate overarm throws. Experimental Brain Research, 103(2), 277–286.
2. Kusafuka, A., Kudo, K., & Nakazawa, K. (2021). Control of Accuracy during Movements of High Speed: Implications from Baseball Pitching. Journal of Motor Behavior,
   https://doi.org/10.1080/00222895.2021.1960789.
3. Nasu, D., Matsuo, T., & Kadota, K. (2014). Two Types of Motor Strategy for Accurate Dart Throwing. PLOS ONE, 9(2), e88536.

Acknowledgements

GROUND REACTION FORCE PREDICTION DURING RUNNING USING A FULL-BODY MULTIBODY MODEL

Gonçalo Marta (1), João Folgado (1), Carlos Quental (1), Francisco Guerra Pinto (2)

1. IDMEC, Instituto Superior Técnico, Universidade de Lisboa, Lisboa, Portugal; 2. FEBOT, NOVA Medical School, Lisbon NOVA University, Lisboa, Portugal;

Introduction

Research regarding running biomechanics is growing, but some limitations on data acquisition have been slowing down the development of new computational models and their applications. Stereography has been the main technique to collect human body kinematics, with alternatives such as marker-less methodologies being equally valid. The same does not apply to ground reaction forces (GRF) measurements. The gold standard techniques for this field include the use of force platforms and both instrumented walkways and treadmills. These approaches are not portable, and are usually expensive and restricted to the laboratorial setting [1]. Accordingly, research has been done to search for alternatives. Considering a biomechanical model of the human body, computational studies have estimated GRF from running using only kinematic data, but the foot has been mainly limited to a single rigid body [2]. The influence of the addition of degrees of freedom to the foot in the study of GRF in running has still to be investigated. This work proposes an upgrade to the existing computational procedure used to estimate GRFs, joint reaction forces and muscular activations during running, while considering a 3-rigid body foot structure.

Methods

A full-body musculoskeletal model composed of 17 rigid bodies was developed for analyzing the biomechanics of running. The arms, forearms, head and trunk, pelvis, femora, tibiae, tali, calcanea, and toes were constrained by spherical and revolute joints, totaling 25 dof. The muscle system included 80 muscle-tendon units with their contraction dynamics represented by a Hill-type muscle model [3]. Kinematic data, required for the application of the developed biomechanical model in inverse dynamics, were acquired at the Laboratory of Biomechanics of Lisbon using 14 infrared cameras working at 200 Hz. One male subject, with no history of musculoskeletal disorders, ran at a self-selected speed over floor mounted force platforms. Markers were placed according to the ISB recommendations [4] and were used to drive the musculoskeletal model.

To estimate GRFs and the internal forces of the biomechanical system, an optimization routine was developed. The GRFs, their application points, and joint reaction forces were design variables. The optimization problem was formulated as the minimization of the residual forces and moments that drive the biomechanical model (applied at the pelvis), subjected to the fulfilment of the equations of motion, and of

bound constraints that limited the magnitude and timings of application of the GRFs and the position of the center of pressure. As a first approach, contact detection to time the application of the GRFs was done by evaluating the distance from the calcanea and toes' center of mass to the ground. To validate the proposed methodology, the estimated GRFs were compared with the measured force plate data.

Results

Preliminary results, depicted in Figure 1, show that the proposed methodology was able to estimate GRFs that were consistent with the data from the force plates. The joint reaction forces and joint torques estimated through inverse dynamics were also consistent with the literature.
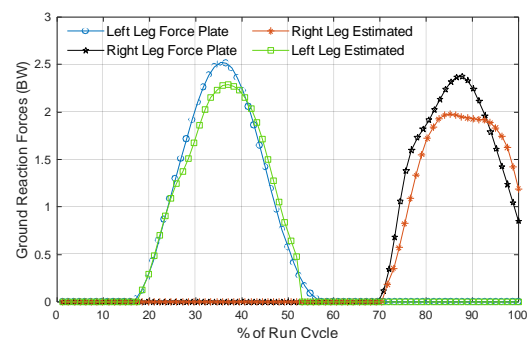
Figure 1: Vertical ground reaction forces in multiples of bodyweight for one running cycle measured by the force plates and estimated by the optimization process.

Discussion

The proposed method is expected to be a valid alternative to the use of force plates in laboratorial settings, allowing for a higher flexibility of GRFs acquisition while still maintaining high accuracy. This implementation is not without limitations, namely the algorithm of contact detection, which considers contact only after a certain user-defined threshold.

References

1. Oh et al. J Biomech. 2013;2372–80.
2. Skals et al. Multibody Syst Dyn. 2017;175–95.
3. Rajagopal et al IEEE Trans Biomed Eng. 2016;2068–79.
4. Wu G et al. J Biomech. 2005;981–92.

Acknowledgements

APPLYING PRINCIPAL COMPONENT ANALYSIS TO CHARACTERIZE THE BALANCING ABILITY OF ELITE SYNCHRONIZED ICE SKATERS

Zsofia Palya, Bálint Petró, Rita M Kiss

Department of Mechatronics, Optics and Mechanical Engineering Informatics, Faculty of Mechanical Engineering, Budapest University of Technology and Economics, Budapest, Hungary

Introduction

The balancing ability allows us to keep our body in a static position or maintain during locomotion. Synchronized skaters' performance emphasizes maintaining the group's precise formation and timing and includes artistic components such as long-lasting spins and lifting elements. It requires exceptional balance training and advanced balancing skills [1].

Principal component analysis (PCA) is a well-established method of studying coordination in clinical biomechanics [2]. In biomechanical interpretation, the most important principal components (PCs) can be regarded as the dominant synergies of the complex motion. Applied on joint angular time series, this provides a means to analyze the importance of individual joints to the whole of motion [3].

The main goal of the present study was to examine the balancing strategy of synchronized skaters compared to an age-matched control group under dynamic circumstances with the help of PCA.

Methods

Twelve female members of the Hungarian Synchronized Ice Skating Team (59.2±5.9 kg, 166.3±4.4 cm) and twelve healthy female age-matched non-skaters as control (61.1±5.5 kg, 171.3±3.5 cm) participated in the study. Balancing ability was examined with dynamic balancing test when subjects are imposed some external perturbations in mediolateral plane. An optical-based motion capture system (OptiTrack, NaturalPoint, Corvallis, OR, USA) was used to record the subject's movements (f_s=100 Hz). Three sets of sudden provocation tests were carried out in bipedal stance, then in single-leg stances for both legs. A rotational fatigue session was inserted between the perturbation tests using a so-called spin-trainer device (EDEA, Milan, Italy). Participants had to perform ten complete rotations in quick succession, standing with their preferred leg on the spin-trainer. Immediately after the spins, the perturbation tests were repeated. PCA was applied to the 3D marker coordinates of the anatomical landmarks (n=39 markers). Our goal with the analysis was to identify the first dominant principal movement and the less significant (compensatory) principal movements during the balancing test. The PCA was performed with the *PMAnalyzer* software in Matlab [4].

Results and Discussion

As a result of the PCA of the single-leg stances, at least 85% of the total variance was explained by the first five PCs. The first PC was the same for both groups and both stances (rotation of the whole body around the standing leg's hip joint). The relative variance of PC1 was examined with Wilcoxon's signed-rank test to compare the relative variances of the pre-tests with post-test trials ($\alpha = 0.05$). In the case of the control group, PC1's relative variance increased (Fig. 1) after the fatigue sessions significantly (p = 0.0137). Regarding the compensatory principal movements (PC2-PC5), the skater group often used the upper body and arms to fulfill the balancing test. On the other hand, the control group applied movements with larger amplitudes with their torso and the elevated legs instead of compensating with the arms.
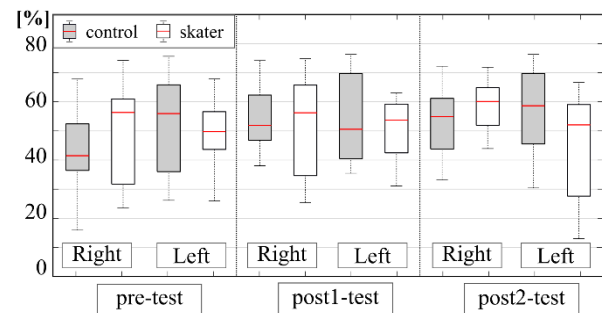
Figure 1: The relative variance of PC1 broken down into the three test sessions.

Considering the success rate of the perturbation tests, skaters were more successful in most of the cases (avg skater: 94%; avg control: 91%). Together with the PCA results, skaters' strategies that require more compensatory movement have proven to be more effective. In general, there are only a few periodic movements among the principal movements (PM1 is seemingly periodic), and there might be some simpler two-phase movements. As a further perspective of the presented method would be a detailed investigation of the PCs' time trial.

References

1. Alpini, D. et al, J Sport Sci for Health, 3(1): 11-17, 2008.
2. Brandon, S. C. E. et al, Journal of Electromyography and Kinesiology, 23(6):1304-1310, 2013.
3. Federolf, P., J of Biom, 49(3): 364-370, 2016.
4. Haid, T. H. et al, Frontiers in Neuroinformatics, 13:24, 2019.

Acknowledgements

COMPOSITE METHACRYLOYL GELATIN-BASED HYDROGELS FOR BONE TISSUE ENGINEERING APPLICATIONS

Gianluca Ciardelli (1), Rossella Laurano (1), Roberta Pappalardo (1),
Valeria Chiono (1), Monica Boffito (1)

1. *Politecnico di Torino, Department of Mechanical and Aerospace Engineering, Turin, Italy*

Introduction

Bone tissue engineering (BTE) aims at developing innovative approaches able to induce and drive the repair and regeneration of damaged bone tissue. In this context, the design of composite hydrogels resembling the composition of the native bone could represent a promising alternative [1]. Moreover, providing these hydrogels with the capability to cross-link at different levels of organization (e.g., physical and chemical cross-linking potential) can allow the formulations to be initially processed in mild conditions and then further stabilized through additional chemical cross-linking. Moving from these premises, in this contribution we report the design of new thermo-sensitive and photo-curable hydrogels based on methacryloyl gelatin (GelMA). Moreover, mimicking the composite nature of the native bone tissue, rod-like nanohydroxyapatite (nHA) was also added to the formulations as bone mineral counterpart. Finally, formulation potentialities as bioinks in the BTE field were assessed through the 3D-bioprinting of multi-layered structures.

Methods

GelMAs were synthesized by reacting gelatin (type A from porcine skin) with methacrylic anhydride (MA, 0.1-1 ml/$g_{gelatin}$) [2]. GelMAs were characterized by infrared (IR) and proton nuclear magnetic resonance (^{1}H NMR) spectroscopies, and the Ninhydrin assay. Thermo- and photo-sensitive hydrogels were designed by solubilizing GelMA (5-15% w/V) in Dulbecco's Phosphate Buffered Saline containing the photoinitiator phenyl-2,4,6-trimethylbenzoylphosphinate (LAP, 0.05-0.5% w/V). nHA was added to GelMA solutions to design composite formulations. Rheological and photo-rheological (365 nm, 10 mW/cm^2) analyses were performed to assess the contribution of GelMA DoM and the concentration of hydrogel constituents to the overall mechanical properties. Cytocompatibility was assessed according to the ISO 10993-5, meanwhile hydrogel potential as cell carriers was preliminary tested with NIH-3T3 murine fibroblasts. Lastly, hydrogel suitability for 3D bioprinting was assessed by extruding differently-shaped structures.

Results

GelMAs with DoM within the range 50-100% were successfully synthesized by tuning the amount of added MA. GelMAs retained the typical upper critical solution temperature (UCST) behavior of gelatin, with slight changes (around 2-3°C) in the gel-to-sol transition temperatures of their aqueous solutions. GelMA DoM and content within the hydrogel, and LAP concentration were demonstrated to allow the tuning of formulation mechanical properties. In detail, with increasing LAP content, the rate of storage modulus (G') increase during light irradiation as well as the measured G' at the end of the photo-curing (G'$_{final}$). With increasing GelMA concentration, G'$_{final}$ increased: a G'$_{final}$ three-fold increase was observed with increasing GelMA from 10 to 15% w/V concentration (from 15-20 to 50-60 kPa). Finally, higher G'$_{final}$ were achieved with increasing GelMA DoM: at 5% w/V concentration, a G'$_{final}$ growth from 1.4 to 3 kPa was registered with increasing DoM from 60 to 100%. nHA addition did not alter hydrogel thermo-responsiveness with similar gelation onset temperatures and kinetics. Differently, nHA effectively worked as a network reinforcement phase, resulting in improved mechanical properties in GelMA/nHA formulations compared to GelMA as such. The formulations were cytocompatible according to the ISO 10993-5 and exhibited proper rheological properties to avoid cell sedimentation. Moreover, the photo-curing process did not induce any cell death and the resulting gel network provided a suitable environment for cell spreading and proliferation up to 7 days. Lastly, the hydrogels showed good printability and were successfully bioprinted into multi-layered structures.

Discussion

Thermo- and photo-sensitive hydrogels hold a great promise in the biomedical field. Such formulations can be initially handled and processed under mild conditions by exploiting their physical nature and then further stabilized through light irradiation. GelMA can be exploited as constituent of hydrogels with many degrees of versatility. Moreover, nHA addition provides an additional tuning of hydrogel properties and allows a better mimesis of the native bone composition. Overall, the designed formulations exhibit promising features for application in the BTE field, as constituents of both bone tissue substitutes and *in vitro* models.

References

1. Yue S. et al, Nanomaterials, 10:1511, 2020.
2. Sun M. et al, Polymers, 10:1290, 2018.

Acknowledgements

TOWARDS CONTROLLED FORMATION AND RESORPTION IN A 3D HUMAN *IN VITRO* BONE REMODELING MODEL.

Bregje W.M. de Wildt (1), Lizzy A.B. Cuypers (1, 2), Keita Ito (1), Sandra Hofmann (1)

1. *Orthopaedic Biomechanics, Department of Biomedical Engineering and Institute for Complex Molecular Systems (ICMS), Eindhoven University of Technology, Eindhoven, The Netherlands. 2. Dept of Regenerative Biomaterials, Radboud University Medical Center, Nijmegen, The Netherlands.*

Introduction

In vitro bone models could facilitate the investigation of human bone remodeling, potentially reducing animal experiments. Physiological bone remodeling involves balanced formation and resorption. A shift in this balance is often a hallmark for bone pathologies like osteoporosis [1]. Osteoblast-osteoclast co-cultures are mostly used to mimic this process *in vitro*. However, culture conditions used for these co-cultures vary between studies and are often optimized for only one cell-type [2]. This could lead to unequal stimulation of osteoblasts and osteoclasts which might cause an unhealthy formation-resorption balance. Therefore, we aimed at screening the influence of commonly used culture conditions on formation and resorption in an *in vitro* bone remodeling model, using a design of experiments approach.

Methods

A resolution III fractional factorial design was created for investigating the main effects of the factors on *in vitro* remodeling. The factors were base medium, mesenchymal stromal cell (MSC):monocyte (MC) seeding ratio, mechanical stimulation, human platelet lysate (hPL) concentration, osteogenic supplements, osteoclast supplements, and Vitamin D3. Each factor had 2 levels: low or high stimulation, resulting in a total of 8 runs (R, Table 1). A negative control was added, in which there was low stimulation for each factor (R9), a positive control with high stimulation for all factors was part of the design (R7). Experiments were performed using mineralized silk fibroin scaffolds on which human MSCs and MCs were seeded and cultured for 28 days in the conditions according to the experimental design (N=4). To track remodeling, μCT scans were acquired on day 2 (baseline), 7, 14, 21, and 28 and registered to baseline scans. Resorbed and newly formed mineralized volumes were quantified and used to determine the main effect of each factor on these outcomes.

Factor	Low	High
Medium	Alpha-MEM	lg-DMEM
MSC:MC	1:2	1:5
Loading	0 RPM	300 RPM
hPL	5%	10%
Osteogenic supplements	10 nM Dex	100 nM Dex
		10 mM β-GP
Osteoclast supplements		50 ng/ml RANKL
		50 ng/ml M-CSF
Vitamin D3		10 nM

Table 1: *Investigated factors and their 2 levels.*

Results and Discussion

Initial results showed that in constructs cultured with high stimulation for all factors (R7), most mineralization but least resorption was present (Figure 1A+B). The main effect plots revealed that a low hPL concentration of 5%, a low concentration of osteogenic supplements, and no vitamin D3 tended to support resorption, while mechanical loading seemed to improve mineralization without influencing resorption (Figure 1C). Histological analysis is needed to study cell differentiation and tissue maturation in the co-culture models.
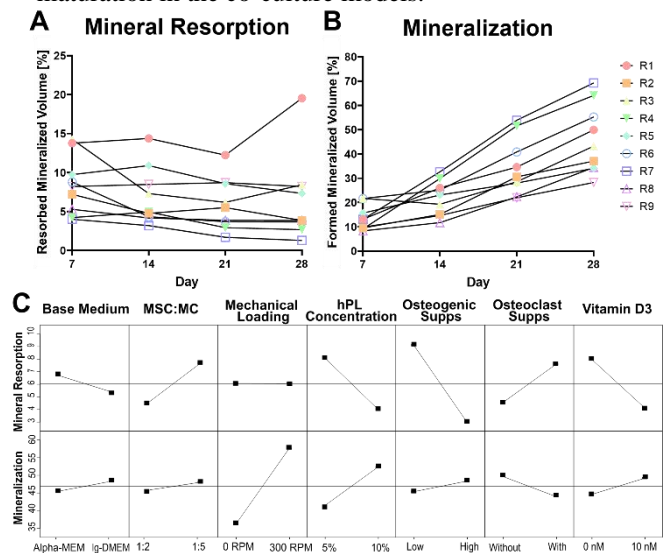
Figure 1: *Cumulative resorbed mineralized volume (A) and formed mineralized volume (B) since day 2 obtained by μCT scan registration. Data of day 28 were used for the main effect plots (C).*

Conclusion

Here, we screened for the influence of commonly used culture conditions on formation and resorption in an *in vitro* bone remodeling model. Thus far, R1 seems to be most beneficial for balanced resorption and formation. These results could help to improve culture conditions of *in vitro* bone remodeling models, towards a more physiological and controlled balance between formation and resorption.

References

1. R. Owen *et al*., *Front. Bioeng. Biotechnol*, 6:134, 2018.
2. S.J.A. Remmers *et al*., *PLoS ONE,* 16(11): e0257724, 2021

Acknowledgements

AUTOMATED PARALLEL BIOREACTOR PLATFORM COMBINING PERFUSION AND PEMF STIMULATION

Stefano Gabetti (1,2), Farah Daou (3), Beatrice Masante (1,2), Giovanni Putame (1,2), Alessandro Sanginario (4), Eleonora Zenobi (5), Federico Mochi (5), Costantino Del Gaudio (5), Cristina Bignardi (1,2), Lia Rimondini (3), Andrea Cochis (3), Diana Massai (1,2)

1. PolitoBIOMed Lab, Dept. of Mechanical and Aerospace Engineering, Politecnico di Torino, Italy; 2. Interuniversity Center for the Promotion of the 3Rs Principles in Teaching and Research, Italy; 3. Dept. of Health Sciences, CAAD, University of Piemonte Orientale, Novara, Italy; 4. Dept. of Electronics and Telecommunications, Politecnico di Torino, Torino, Italy; 5. Hypatia Research Consortium, Rome, Italy

Introduction

In bone tissue engineering research, physical stimuli, such as fluid flow-induced shear stress or electromagnetic field, have been shown to be crucial *in vitro* for stimulating proliferation and differentiation of osteoblasts and for promoting bone mineralization [1,2]. However, many mechanotransduction pathways remain unknown leading to empirical treatments, as it is for pulsed electromagnetic field (PEMF) stimulation applied in clinical practice for boosting bone healing [3]. For unravelling the genetic pathways driving bone healing *in vivo*, the *in vitro* modelling and analysis of 3D bone tissue models exposed to controlled physical stimuli would be essential. Inspired by this scenario, we developed an automated parallel bioreactor platform that allows combining uni/bi-directional perfusion and PEMF stimulation for investigating the biological response of 3D bone tissue models to defined physical stimuli.

Methods

The automated parallel bioreactor platform, to be incubated, is composed of: 1) three culture chambers (CC, Fig. 1A); 2) a controlled perfusion unit; 3) a PEMF stimulator. Each 3D-printed CC (priming volume = 2.5 ml, Dental SG resin, FormLabs) consists of two screwable cylindrical parts and allows housing scaffolds press-fit in tailored silicone holders for direct perfusion. Each CC is part of a closed-loop perfusion circuit, based on a multichannel peristaltic pump controlled by an Arduino-equipped control box, which enables setting uni/bi-directional flow (0.006-24 ml/min). A commercial device provides PEMF stimulation (1.5 mT, 75 Hz). The optimization of the CC design was supported by fluid dynamics and electromagnetic field simulations (COMSOL Multiphysics). As preliminary biological tests, human mesenchymal stem cells were seeded into commercial porous scaffolds (BioOSS, Geistlich Biomaterials) and, after 48 h of static culture, the constructs were transferred into the CCs and exposed to uni- or bi-directional flow (0.3 ml/min) without PEMF stimulation for additional 3 or 6 days (Fig. 1B). Control constructs were statically cultured. The release of the early osteogenic marker alkaline phosphatase (ALP) was assessed at day 3 and 6, and the extracellular matrix deposition was verified by histology at day 6.

Results

Computational simulations demonstrated that the CC design promotes the development of a symmetric flow profile while minimizing recirculation/stagnation zones; moreover, the construct is exposed to a uniform magnetic field (1.5 mT, Fig. 1C). Preliminary biological tests demonstrated that uni- and bi-directional perfusion modes boosted ALP release (+20%) and cell infiltration with respect to static control. Bi-directional perfusion even increased matrix protein deposition.
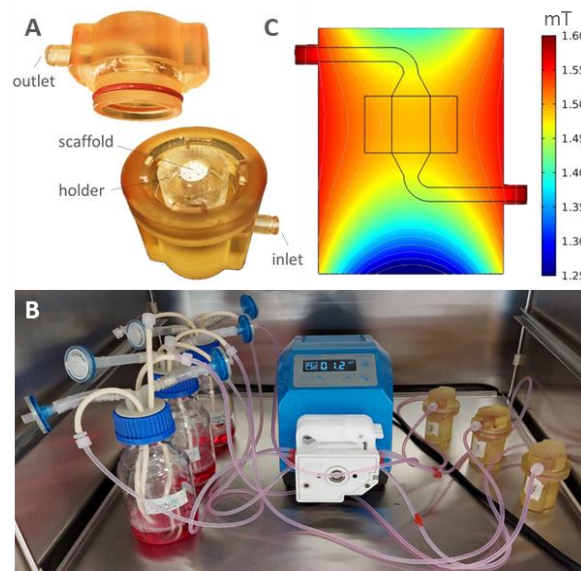
Figure 1: A) Bioreactor CC; B) Parallel bioreactor platform setup; C) Contour plot of the magnetic field.

Discussion

The proposed bioreactor platform allows parallelizing the culture, providing uni/bi-directional perfusion without user intervention, and combining perfusion and PEMF stimulation, representing a powerful tool for investigating *in vitro* the biological response of 3D bone tissue models to defined physical stimuli. Biological tests adopting 3D-printed biomimetic scaffolds resembling the microarchitecture of trabecular bone and imposing perfusion and PEMF stimulation are ongoing.

References

1. Wittkowske et al, *Front. Bioeng. Biotechnol.* 4:87, 2016
2. Hu et al, *Biomed. Pharmacother,* 131, 110767, 2020
3. Varani et al., *Int J Mol Sci*, 22:809, 2021

PATIENT SPECIFIC OSTEOGENESIS IMPERFECTA BONE ORGANOIDS DEMONSTRATE INCREASED TISSUE MINERALIZATION

Julia K. Griesbach (1), Anke de Leeuw (1), Tanja Minacci (1), Pei Jin Lim (2), Matthias Rüger (3), Marianne Rohrbach (2), Cecilia Giunta (2) and Ralph Müller (1)

1.Institute for Biomechanics, ETH Zurich, Switzerland; 2. Connective Tissue Unit, University Children's Hospital Zurich, Switzerland; 3. Department of Pediatric Orthopaedics and Traumatology, University Children's Hospital Zurich, Switzerland

Introduction

Osteogenesis imperfecta (OI) is a rare heterogeneous genetic disease characterized by bone fragility. Due to a wide spectrum of symptoms and severity, the availability of suitable treatments and understanding of disease pathomechanisms are limited. A cure for OI that specifically targets the individual's bone phenotype reducing the risk of bone fractures does not yet exist. To facilitate research into rare disease mechanisms and personalized treatments, bone organoids using patient-derived cells are an emerging new technology. Previous studies showed tissue mineral density as an indicator for the stiffness of organoids. In this study, we analyzed global and regional mineralization of patient derived OI bone organoids to gain new insights into the disease.

Methods

Osteoblasts were isolated from a healthy 15-year-old male and a 3-year-old OI female homozygous for an FKBP10 pathogenic variant. 3D-bioprinted graphene oxide-incorporated cell-laden scaffolds were cultured over 56 days in compression bioreactors [1], monitored using weekly micro-CT and subjected to uniaxial cyclic compressive loading (5x/week, 5 min, 1% strain, 5Hz). Samples were then tested for compressive stiffness.

Micro-CT images were gauss-filtered and divided into 27 (3x3x3) subsets for regional analysis. Multiple thresholds (84, 100, 125, 150 mg/cm^3) were applied to whole images and subsets, and tissue mineral density (TMD) and mineral volume fraction (MV/TV) were calculated. Density histograms of each subset were fit with two gaussian curves to differentiate between background and tissue [1].

Results

The global analysis revealed significantly higher TMDs for multiple thresholds for OI organoids (Fig. 1 A). OI samples also showed higher percentage of highly mineralized tissue (Fig. 1 B). However, stiffness of the OI samples was not significantly higher compared to healthy organoids (Fig. 1 D). Visual inspection of micro-CT images (Fig. 1 C) indicated different regional mineralization. Regional analysis using gauss fitting revealed significantly higher mineral heterogeneity for OI organoids in top (healthy: σ=44.4; OI: σ=58.59), middle (healthy: σ=53.7; OI: σ=60.23) and bottom (healthy: σ=65.2; OI: σ=81.7) third. Multilevel-thresholding mostly confirmed higher TMD for the OI organoids. However, the top center subset showed lower MV/TV and similar TMD, while middle center subsets showed lower TMD, although not significant (Table 1).
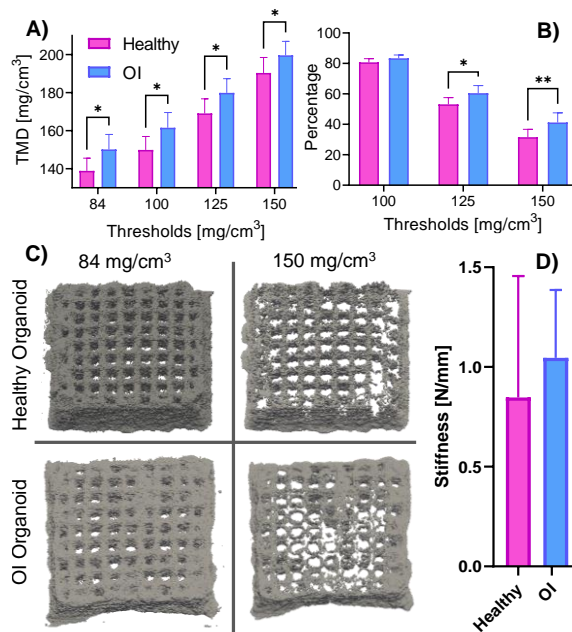
Fig. 1: A) TMD for multiple thresholds; B) Percentage of high-density tissue; C) OI and healthy organoid with different thresholds; D) Compressive stiffness

		Healthy		OI	
		mean	stdev	mean	stdev
center top	MV/TV	0.33	0.10	0.28	0.10
	TMD	122.25	7.98	123.43	20.24
center middle	MV/TV	0.45	0.15	0.43	0.12
	TMD	149.01	24.18	132.84	18.46

Table 1: Mineral volume fraction (MV/TV) and TMD (threshold 84mg/cm^3) for top and middle center subsets

Discussion & Conclusion

We found significantly higher TMD in patient-derived OI bone organoids compared to healthy controls. However, the stiffness was not significantly increased. This could be due to greater mineral heterogeneity [2] as well as weaker structures in the organoid center in OI. These results reveal new insights into the mechanisms of OI and specifically the FKBP10 genetic form. Future steps include finite element analysis and in-depth analysis of the mineral structure.

References

1. Zhang et al. Acta Biomater. 637-652, 2020
2. Tamminen et al. JBMR, 29 (5), 1110–1117, 2014

WALL SHEAR STRESS ANALYSIS TOWARDS THE OPTIMAL DESIGN IN TPMS TISSUE ENGINEERING SCAFFOLDS

T. Pires (1), A. P. G. Castro (1, 2), P. R. Fernandes (1)

1. IDMEC, Instituto Superior Técnico, Universidade de Lisboa, Portugal; 2. Escola Superior de Tecnologia de Setúbal, Instituto Politécnico de Setúbal, Portugal

Introduction

When designing scaffolds for Bone Tissue Engineering (BTE) a fundamental aspect to consider is the Wall Shear Stress (WSS) that will affect the cells inside the scaffold, as different levels of WSS lead to different mechanical signals for the cells. This will cause differences to the cellular differentiation process [1]. WSS is affected by various factors, with the major ones being the scaffold geometry and the topology of the scaffold surfaces. Accordingly, this study is focused on analyzing the difference in average WSS, in various Triply Periodic Minimum Surfaces (TPMS) scaffolds, with either smoothed or non-smoothed wall surfaces. Additionally, this study also investigates the implementation of a simulated annealing optimization method to aid in the design of the scaffolds with a specific average WSS (between 0.1 and 10 mPa [2]).

Methods

For this study two different TPMS structures were used (Schwartz D (SD), Gyroid (SG)), each one with three different levels of porosity (60%, 70% and 80%), resulting in a total of six different scaffold geometries. For each original geometry, a hexahedral mesh of a single cubic unit was created, alongside an empty chamber before and after the scaffold to allow the fluid flow to stabilize (Fig. 1) [3]. Afterwards, a Laplacian smoothing step was applied to the inner surface of the scaffolds to obtain the smoothed scaffold geometries in an analogous tetrahedral mesh (Fig. 2). Both the original and smoothed designed were then studied using FLUENT® ANSYS® (Ansys Inc., Canonsburg, Pennsylvania, USA) to perform a Computational Fluid Dynamic (CFD) analysis to determine their average WSS. For the optimization component of this study, a simulated annealing optimization method was combined with the CFD analysis implemented on both the SD and SG geometries (by changing their size and porosity) in order to obtain the target average WSS of 5 mPa [3].
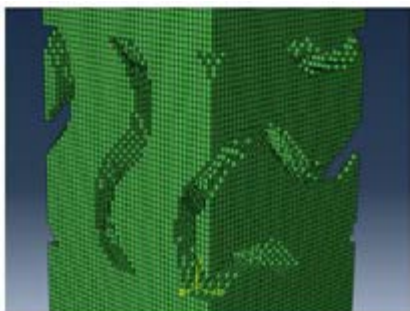
Figure 1. SG70 scaffold without smoothing (original).
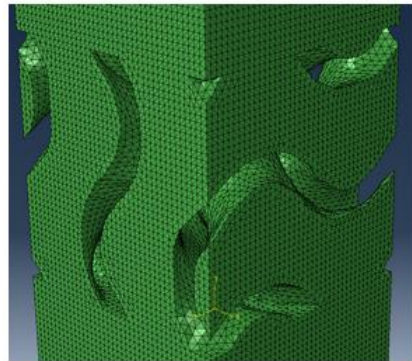
Figure 2. SG70 scaffold with Laplacian smoothing of the inner surfaces (tetrahedral mesh).

Results

Comparing the average WSS of the original scaffold surface with the analogous smoothed surface, the smoothed scaffolds had an average WSS increase of 26%, considering a minimum of 24.7% for the SG60 scaffold and a maximum of 27.2% for SG80. The optimization algorithm was successfully able to generate a scaffold with the desired average WSS within the maximum allowed number of 100 iterations.

Discussion

The WSS outputs showed a significant difference between the original and the smoothed TPMS scaffolds, with the smoothed surfaces allowing for higher WSS as theoretically expected. This difference highlights how the original jagged surfaces are not the best option to computationally analyze the average WSS of scaffolds, seeing as the increase in surface area compared to the smooth scaffold results in a much lower WSS. Regarding the optimization method, the fact that the program was able to quickly reach the desired average WSS (5 mPa) highlights how optimization methods could be a valuable tool in scaffold design by allowing scaffolds to be designed with a specific fluidic property, such as its WSS and/or permeability. Future work will extend the use of optimization methods in other design aspects of scaffolds for BTE.

References

1. McCoy et al., Tissue Eng Part B Rev, 587-601, 2010.
2. Zhao et al., Biomech Model Mechanobiol, 231-243, 2015.
3. Pires et al., J Biomech, 110263, 2021.

Acknowledgements

3D ELECTROSPUN ARCADE-LIKE SCAFFOLDS FOR ARTICULAR CARTILAGE

Ângela Semitela (1), Cátia Sousa (2), Alexandrina Mendes (2), Paula A.A.P. Marques (1) and António Completo (1)

1. *TEMA, University of Aveiro, Portugal; 2. CNC, University of Coimbra, Portugal*

Introduction

Articular cartilage is able to withstand the complex mechanical loading in joints due to its collagen fibers' arrangement in the shape of arcades, known as Benninghoff's arcades [1]. So, it is considered that this sophisticated fibrous architecture should be reproduced to some extent in engineered cartilage, using, in this instance, electrospinning. Despite the substantial progress made through the development of multi-layered three-dimensional (3D) fibrous scaffolds with depth-dependent fiber alignments, these mainly result from the stacking of fibrous meshes with specific fiber alignments, raising concerns regarding the design reproducibility [2,3]. Recently, a novel 3D electrospinning platform was developed that allows the fabrication of reproducible 3D aligned matrices with certain patterns of fiber alignments in a continuous mode [4,5]. Additionally, this platform enables precise cell placement inside matrix layers, resulting in a uniform cell distribution across the 3D design [5]. In this regard, in this work, 3D electrospinning was performed using this platform to recreate the Benninghoff's arcades in 3D fiber matrices laden with chondrocytes.

Methods

All experiments were performed in a patented electromechanically 3D electrospinning platform [4,5], where the fibers were produced and placed in a collector according to a programmed fiber alignment (Figure 1c). A polymeric blend of polycaprolactone (PCL) and Gelatin (GEL) in 2,2,2-trifluoroethanol mixed in a proportion of 6:4 was used to produce the scaffolds. An immortalized human chondrocyte cell line C28/I2 was incorporated within the fibrous layers of the 3D scaffolds using three approaches: pipetting or electrospraying the chondrocyte suspension or extruding a chondrocyte-laden agarose hydrogel. The resulting scaffolds were structural and biologically characterized after 21 days of culture.

Results

3D electrospun scaffolds were successfully fabricated in the automated platform, with an arcade-like pattern similar to the Benninghoff's arcades, as depicted in the scanning electron microscopy (SEM) images (Figure 1a) and the micro-computed tomography (μCT) reconstruction (Figure 1b).
The *in vitro* studies revealed that a higher percentage of chondrocytes survived when they were embedded in an agarose hydrogel, where they retained a round morphology. The production of extracellular matrix elements was also significantly higher when agarose was used as a carrier.
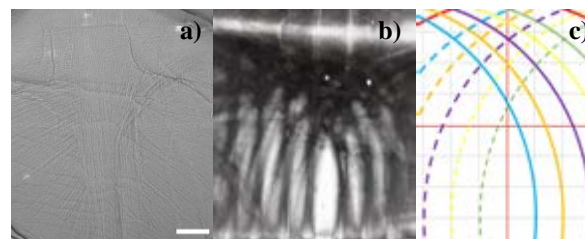
Figure 1: Resulting 3D scaffolds: SEM images (a), μCT reconstruction (b) and the programmed alignment (c). Scale bar: 500 μm.

Discussion

3D arcade-like fibrous scaffolds were successfully created using the 3D electrospinning platform in a reproducible way. Agarose-laden 3D scaffolds displayed the best *in vitro* results, with improved metabolic activity and extracellular matrix synthesis, which could be attributed to the 3D culture environment provided by this hydrogel, which mimics the physiological conditions found in native articular cartilage.

References

1. Y. Xia et al, in: Biophys. Biochem. Cartil. by NMR MRI, 1-43, 2016.
2. A. Semitela et al, J. Mech. Behav. Biomed. Mater., 117: 104373, 2021.
3. A.F. Girão et al, J. Mater. Sci. Mater. Med., 31: 69, 2020.
4. E. Silva et al, J. Comput. Artif. Intell. Mech. Biomech., 1: 81-91, 2021.
5. A. Semitela et al, in: Adv. Curr. Trends Biomech, 187-190, 2022.

Acknowledgements

TISSUE REMODELING AT THE INTERFACE BETWEEN PYROCARBON INTERPOSITION IMPLANTS AND HUMAN HUMERAL BONE

Rémy Gauthier (1), Ghassen Ouenzerfi (2), Imbert de Gaudemaris (3), Nina Attik (4), Michel Hassler (2), Ana-Maria Trunfio-Sfarghiu (3),

1. Univ Lyon, CNRS, INSA Lyon, UCBL, MatéIS, France; 2. Wright Medical, Grenoble, France 3. Univ Lyon, CNRS, INSA Lyon, LaMCoS, France; 4. Univ Lyon, CNRS, UCBL, LMI, France;

Introduction

While future clinical practices recommend to preserve native tissues in the course of surgical management, total shoulder arthroplasty currently remains the gold standard method [1]. Furthermore, the increasing number of young patients emphasizes the need for durable implants promoting a good mobility.

In that context, pyrocarbon interposition implant arthroplasty (PISA) appears as an interesting solution.

Figure 1: Shoulder PISA radiography

Pyrocarbon has been shown to promote chondrocytes expression of cartilage-like tissues markers [2]. In addition, the spherical shape of such interposition implants (Figure 1) is known to be associated with high mobility at other anatomical locations [3]. When applied to shoulder, PISA shows controversial clinical results [4].

However, such procedure is quite new in the framework of shoulder surgery, and efforts have to be made in understanding the interactions between the native humeral bone tissues and the implant.

Interestingly, some clinical observations have shown the formation of a new tissue between the implant and the humeral bone after a revision surgery. It is hypothesized that the biomechanical interactions between the humeral bone and the implant are at the origin of the formation of this new tissue through mechanotransduction [5].

Clinical cases and neo-tissue analysis

Cases	1	2	3	4	5	6
Months of implantation	5	6	6	20	25	60
Reason for revision	F	S	S	F	F	/
Bone binding	++	--	+	+	-	++

Table 1: 6 cases clinical data. --/-/+/++: not/loosely/slightly/firmly attached to humeral bone, respectively. F: Functional. S: Spacer. /: unknown.

Six patients implanted through PISA and who underwent surgery revision in Lyon, Nice, and Marseille (France) were considered after obtaining their informed consent. The time between initial implantation and revision surgery, and the reason for revision surgery are given in Table 1. Functional reason for revision means that the patient felt pain and/or decreased mobility, whereas a spacer is a temporary implant used to reduce the joint infection before a more sustainable surgery. After the removal of the interposition implants, the surgeons have harvested the neo-formed tissues with more or less difficulty because of different binding degree with the humeral bone, as provided in Table 1. The neo-tissue samples were fixed, embedded in paraffin, and cut in sections. Sections were stained with Hematoxyline-Eosine-Safran (HES), Safranin O, or immunolabelled for collagen I and II, and aggrecans.

Results and discussion

The neo-formed tissue not bonded to bone (--) appeared as a fibrocellular tissue, with low presence of collagen II and aggrecan markers. Those loosely (-) and slightly (+) bonded to bone presented some characteristics markers of cartilage, such as the presence of glycosaminoglycans. Finally, firmly bonded neo-formed tissues (++) presented cartilage-like
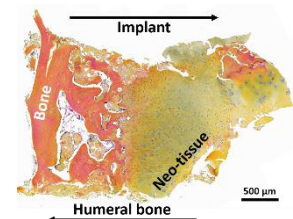
Figure 2: Neo-tissue histological section of the in clinical case 1 stained with HES.

characteristics, with a strong presence of collagen II and aggrecans. The interlock with bone can be seen in Figure 2. It is worth noticed that the neo-tissue never adheres to the pyrocarbon surface, allowing for a gliding motion of the implant on the humeral bone cavity.

Load transmission from the implant to the humeral bone differs depending on the binding degree of this neo-tissue on bone. According to these observations and to bone mechanosensitivity, this strongly suggests that the way bone is mechanically loaded influences its further remodeling promoting the formation of this neo-tissue. The challenge is hence to understand how and why the bonds between bone and the tissue appear during the loading. As a perspective, investigations on the mechanotransduction of human chondrocytes cultured on pyrocarbon surfaces will be performed [5,6].

References

1. Palsis et al. Orthopedics 41, 2018
2. Hannoun et al., Eur Cell Mater, 37:1–15, 2019
3. Bengezi et al., Plast Surg, 22:79, 2014
4. Barret et al., J Shoulder Elb Surg, 29:e1–10, 2020
5. Hannoun et al., Biotribo, 100158, 2021
6. Impergre et al., Biotribo, 100091, 2019

Acknowledgements

IN-VITRO/IN-SILICO MODELLING OF CORE-SHELL STRUCTURES AS ADVANCED BARRIER MODELS

Nicole Guazzelli (1,2), Ludovica Cacopardo (2), Antony Ieva (3), Alessandro Corti (3), Arti Ahluwalia (1,2)

1. Department of Information Engineering, University of Pisa, Italy, 2. Research Center 'E. Piaggio', Pisa, Italy, 3. Department of Translational research and new technologies in medicine and surgery, Pisa, Italy

Introduction

Although it is well known that the 3D architecture of the physiological environment profoundly influences cell behaviour, to date, in-vitro models of the biological barriers are mainly based on flat, 2D systems [1, 2]. Self-assembled spheroids and organoids are now emerging as powerful tools to replicate three-dimensional structures. However, the spontaneous formation of an internal lumen can be challenging and time-consuming.

Here, we present an in-vitro/in-silico strategy (Fig. 1) to obtain cell-laden core-shell structures with predictable and controlled geometry.
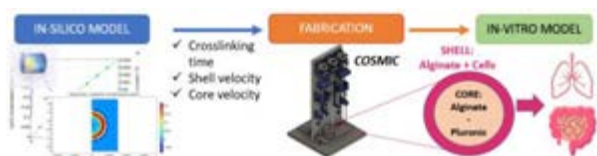
Figure 1: Workflow for generating in-silico/in-vitro models of biological barriers.

Methods

A COre-Shell Microbead Creator (COSMIC) was designed and fabricated using a commercial coaxial needle (16-26 Gauge) connected with two syringes, with pistons actuated by two stepper motors. The shell was composed of 2% w/v alginate and rat tail collagen (1 mg/mL) in Fetal Bovine Serum. The core was made of 1% w/v Pluorinc-127 and 1:100 w/w FITC-alginate (Creative PEGWorks). A 0.1 M calcium chloride ($CaCl_2$) solution was placed under the needle to allow alginate crosslinking.

An in-silico model of core-shell spheroid formation was implemented in Comsol Multiphysics 5.3a, solving the equations of the diluted species transport through porous media. $CaCl_2$ ion diffusion is hindered by the forming crosslinked alginate structure, therefore an apparent diffusion coefficient was considered [3]. This enabled the quantification of crosslinked alginate thickness as a function of the extruded material and of the crosslinking time.

Caco-2 cells were finally encapsulated in the shell (1.5 million/mL). Cell viability and permeability tests were performed using the Alamar Blue assay and quantifying the passage of FITC-dextran through the shell. All reagents were purchased from Sigma-Aldrich, unless otherwise specified.

Results

The in-silico model was able to simulate shell formation as a function of different crosslinking times (Fig. 2A): the best results were obtained in a range of 5 and 15 min. The predicted shell thickness was 0.3±0.2 mm (Fig. 2B, C), which also confirmed by the experimental results.
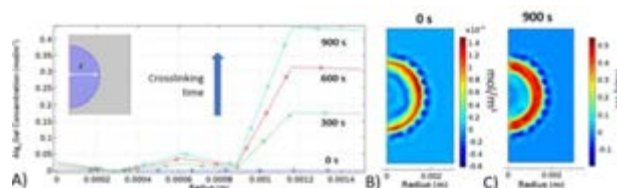
Figure 2: A) Crosslinked alginate concentration along the z=0 line, as a function of different crosslinking times. Shell formation after B) 0 and C) 900 s.

On the base of the in-silico results, the fabrication parameters were set as follows: core extrusion speed 10 µL/s, shell extrusion speed 20 µL/s, and crosslinking time 5 min (Fig. 3A).

Cell testing confirmed the cytocompatibility of the encapsulation procedure (Fig 3D). After 14 days of culture, dextran diffusion through the shell was reduced by 43% thanks to the presence of the cells (Fig. 3 B, C).
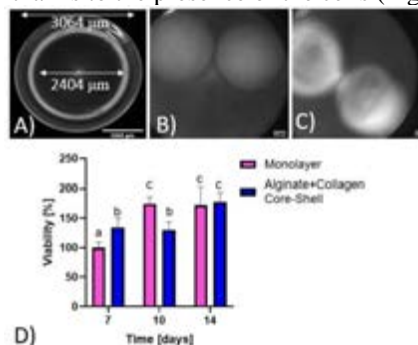
Figure 3: A) c10s20 core-shell bead; FITC-Dextran diffusion after 14 days of cell culture (B) compared to the alginate beads without cells (C) - 1.25X; D) Cell viability (different letters indicate significant differences, $p < 0.05$).

Discussion

The in-vitro/in-silico approach presented in this work represents a promising strategy for the fabrication of core-shell spheroids with defined geometry. In particular, the in-silico tool can be used to predict the effects of different core-shell material combinations, reducing experimental time and costs. Further improvements, which are currently on-going, include a multiphysics computational study to better model the core-shell interface during $CaCl_2$ diffusion. Moreover, a more complex cell model with Caco-2 cells and intestinal fibroblasts will be implemented to improve the physiological relevance of the intestinal barrier model.

References

1. S. Callens et al., Biomat. 119739, 2020
2. N. Arumugasaamy et al., *Ann. Biomed. Eng.* 1–21, 2019
3. A. Hajikhani et al., J. Mech. Phys. Solids 104476, 2021

ELECTROSPUN POLYMER GRAFT AS AN OPTION FOR TISSUE REPLACEMENT IN SEVERE SPRING LIGAMENT INJURIES

Sebastian Nieto (1), Christian Cifuentes (2), Juan Cruz (3), Jorge Hinojosa (4)

1,4 Teaching assistant, Colombia; 2. Assistant Professor, Colombia; 3. Associate Professor, Colombia

Introduction

Spring ligament (SL) is a cartilaginous connective tissue located between the space of the calcaneus and the navicular bone, this arrangement makes its mainly function be a critical support of the medial arch of the foot and, simultaneously, a stabilizer of the ankle along with other ligaments. [1] Compromising this structure to severe injury has consequences such as plantar pronation and acquired flat foot deformity. [2] The most used resource for the repair of this type of tissue are surgical procedures such as autografts, allografts, and arthrodesis, however, it has been shown that post-surgery results do not correct all the desired post-surgical movements and factors such as forefoot abduction [3,1,4] All these deficiencies have aroused interest in exploring the area focused on tissue engineering as an alternative solution, providing a complete regeneration or replacement of tissue, recovering its properties and natural architecture. [5,6]

Methods

Two solutions were prepared, 50:50 PCL-type II collagen at 20% w/v and 65:35 PCL-gelatin at 20%w/v, both solutions were dissolved in acetic acid and electrospun separated at 10kV, using a double disk collector, and a flow rate of 2.5mL/h. Both materials were characterized by uniaxial tensile test. PCL-gelatin was crosslinked using glutaraldehyde and analyzed by FTIR and SEM images. Mechanical properties of the PCL-type II collagen specimen were attached to foot computational model, replacing native spring ligament mechanical properties, to evaluate effects in mechanical response in the fascia plantar, long plantar ligament and short plantar ligament.

Results

Specimen	UTS [MPa]	E [MPa]	ν
PCL-T II collagen	1.375	7.767	0.1
PCL-gelatin	0.225	6.967	0.28
PCL-gelatin+GA	0.35	8.902	0.26

Table 1: Mechanical properties for 3 specimens. Where E is Young Modulus, ν is Poisson's Ratio and UTS is Ultimate Tensile Strength.

FTIR spectroscopy for gelatin before and after GA application showed all the characteristics bands (gelatin protein amides, carbonyl stretching, among others).

SEM images showed that fibers are displayed in a random order, morphology had a change in the GA-treated, causing the fibers to melt and increase in size due to GA concentration, resulting in average diameters of PCL-gelatin=0.3μm and PCL-gelatin+GA= 0.38μm.
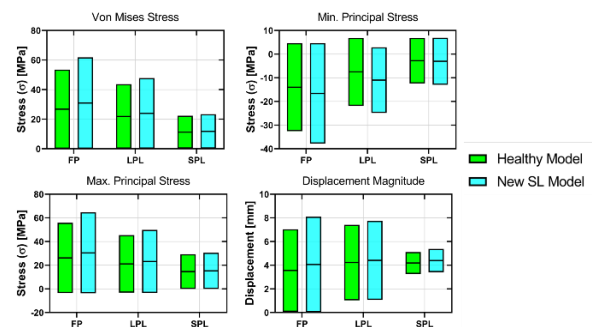
Figure 1: Simulation results of the Healthy model and new SL model, for the 3 tissues that contribute the most to plantar arch performance. Three plots are presented for three stress criteria: Von Mises, Max. Principal and Min. Principal; and a single plot for the structure's displacement magnitude.

Discussion

High concentration of gelatin can lead to excessive mechanical weakness in electrospun graft. GA can not only help in keeping gelatin structure, but also increase mechanical fiber strength properties. PCL-collagen had interesting mechanical properties and better than PCL-gelatin ones, for the moment, it has highly elastic properties, so it does not present greater resistance to the loads carried out in a foot monopodal support, this has a serious impact on the fall of the arc foot. It is necessary to explore novel techniques such as knitted fibers electrospinning manufacture to increase mechanical performance in the foot computational model.

References

1. Acevedo, J., et al. *Foot & Ankle Specialist*, 6(6), 441–445, 2013.
2. Cifuentes-De la Portilla, et al. *Clinical Biomechanics*, 76, 105018, 2020.
3. Williams, B. R., et al. *Foot & Ankle International*, 31(7), 567–577, 2010.
4. Kuo, C. K., et al. *BMC Sports Science, Medicine and Rehabilitation*, 2(1), 2010.
5. Heyes, G., et al. *Foot & Ankle International*, 41(7), 803–810, 2020.
Silva, M., et al. *Journal of Nanobiotechnology*, 18(1), 2020.

FABRICATION OF MAGNESIUM AND STRONTIUM SUBSTITUTED HYDROXYAPATITE-POLYCAPROLACTONE COMPOSITES VIA 3D PRINTING FOR THE USAGE AS BONE FILLER

Denata Syla[1], Laura Grillini[2], Lucia Forte[2], Frederik Claeyssens[3], Gwendolen Reilly[1]

1. University of Sheffield, INSIGNEO Institute for In Silico Medicine, England; 2. Fin-ceramica Faenza SPA, Italy; 3. University of Sheffield, Kroto Research Institute, England

Introduction

The current gold standard treatment for nonunion fractures is an autologous iliac crest transplant, which involves risks such as post-operative infections and donor site morbidity [1]. The replacement of these autologous transplants with a precise, custom-made synthetic mesh material could improve bone fusion and reduce post-surgical risks.

Synthetic hydroxyapatite is therapeutically used as bone graft substitute, bone filler, or as coatings to support attachment of bone to metal implants. However, the slow degradation rate of hydroxyapatite compromises its osteogenic activities and use as bone filler. In this project we aim to create a multisubstituted HAP (sHAP) to increase its solubility, osteogenic integrity and bioactivity. Furthermore, we incorporate sHAP into a polymer matrix based on polycaprolactone (PCL) to create a composite bone graft substitute which can be fabricated into a 3D mesh. PCL has strong mechanical properties and has been approved for the usage as bone graft substitute.

Methods

HAP was synthesized by a wet, continuous method in a mixing column. Different substitution degrees were synthetized (**Error! Reference source not found.**). The synthesis of substituted HAP (sHAP) was characterized via Fourier-transform infrared spectroscopy (FTIR) and inductively coupled plasma optical emission spectrometry (ICP-OES). Crystallinity was analysed via X-ray diffraction (XRD).

The first round of cytotoxicity was performed on Sr and Mg substituted HAP powders using Y201 mesenchymal stem cells (MSCs) [2] via a resazurin metabolic assay in a transwell system using 1000 µg powder/ml.

sHAP (10%, 20%, 30%) was incorporated into a 4-arm methacrylated polycaprolactone (PCL) matrix to create a bioink. Printability of the bioink was modified by increasing its shear-thinning character via the addition of hydrophobic silica (1-2%). Scaffolds were printed via an extrusion bioprinter and cured using UV light.

All cell culture experiments were performed using serum and xeno free medium (StemMACS™ MSC Expansion Media Kit XF, human (Miltenyi Biotec)).

Composition [mol%]	1	2	3	4	5	6	7
Ca	60	75	75	90	85	85	70
Mg	20	5	20	5	5	10	10
Sr	20	20	5	5	10	5	10

Table 1: Different compositions of Ca, Mg and Sr

Results

High amounts of Mg and Sr could be incorporated into the HAP structure but increasing substitution decreased the overall incorporation of Mg and Sr into the lattice structure. Results showed that MgSrHAP had no cytotoxicity on Y201 cells *in vitro*.

sHAP-PCL mesh composites could be successfully fabricated through 3D printing (Figure 3).
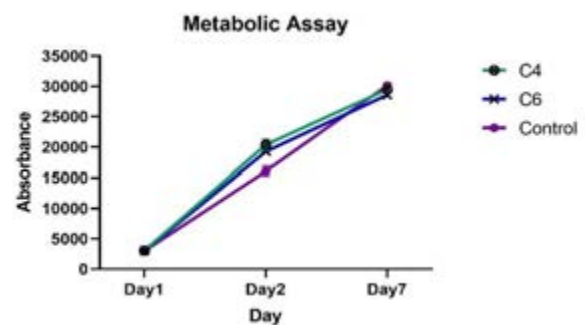
Figure 2: Resazurin metabolic assay: MSCs with MgSrHAP composition 4/6 and cell only control. Metabolic activity on day 1, 4 & 7.

Figure 3: Printing of 2-layer sHAP-PCL composite scaffold. Dimensions of scaffold: 5mm x 5mm x 2mm.

Discussion

Substituted HAP has no cytotoxic effects either in powder format or when incorporated into a PCL matrix. The sHAP/PCL composite has promise for applications as a bone graft substitute

References

[1] Sen MK, Miclau T. Autologous iliac crest bone graft: should it still be the gold standard for treating nonunions? Injury. 2007 Mar;38 Suppl 1:S75-80. doi: 10.1016/j.injury.2007.02.012. PMID: 17383488
[2] S. James, et al., Stem Cell Reports 4(6) (2015)1004 1015.

Acknowledgements

TISSUE-ENGINEERED COLLAGENOUS FIBROUS CAP MODELS TO EXPLORE ATHEROSCLEROTIC PLAQUE RUPTURE

Tamar B. Wissing (1,2), Kim van der Heiden (1,2), Sheila Serra (1), Anthal Smits (2), Carlijn Bouten (2), and Frank Gijsen (1,3)

1. Erasmus Medical Center, The Netherlands; 2. Eindhoven University of Technology, The Netherlands; 3. Delft University of Technology, The Netherlands

Introduction

Rupture-prone atherosclerotic plaques are characterized by a soft lipid core embedded in a collagenous matrix, separated from the bloodstream by a fibrous cap[1]. The stability of a plaque depends on the integrity of this fibrous cap strength. The cap strength values reported in literature vary widely, reflecting the different cap failure mechanisms. Several failure mechanisms have been proposed[2]. However, due to the paucity of experimental data, which cap rupture mechanism is dominant is unknown. We take the first step in developing a human disease model for atherosclerotic plaques to study cap rupture in vitro.

Methods

Plaque analogs were created by seeding human vena saphena cells. The samples were statically cultured for 7 days, whereafter a 2 mm Ø soft inclusion (SI) was created by punching a core in the center of each analog and filling this core with fibrin (Fig 1A). This fibrin inclusion mimics the soft lipid core of atherosclerotic plaques. The analogs were statically cultured for 7 more days, after which they were exposed to 7 days of dynamic culturing using the Flexcell FX-4000T Three different loading protocols were applied (Fig 1B), static, intermittent strain (I-strain) and continuous strain (C-strain) with n=5 for each group[3].

The samples were exposed to multiphoton microscopy (Leica TCS SP8X) with second harmonic generation to visualize the collagen architecture. The samples were incubated with CNA35 probe to visualize the collagen. After imaging, the samples were uniaxially strained until failure at a speed of 100%/min. The nominal engineering stress-strain curves were derived from the force and displacement measurements and the stiffness values were computed as the linear slopes at 2%, 5% and 10% strain based on local strain analyses[3].
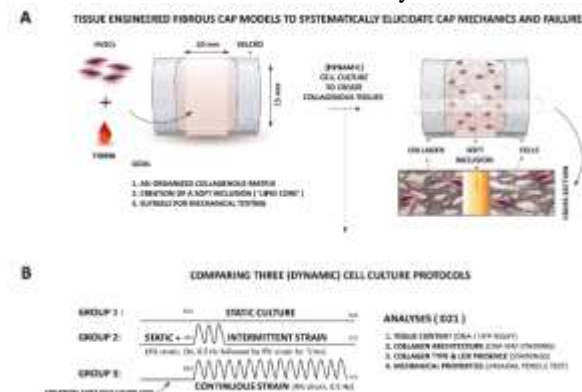
Figure 1: protocol to develop fibrous cap analogs.

Results

Fig. 2 demonstrates collagenous tissues for the I-strain sample. All top regions analyzed exhibited isotropic collagen organizations irrespective of the culture protocol applied. Moving towards the shoulder and mid cap regions, the fibers appear more anisotropic in the direction of the constraints for the dynamically loaded samples. The static control demonstrated a more isotropic collagen fiber distribution.
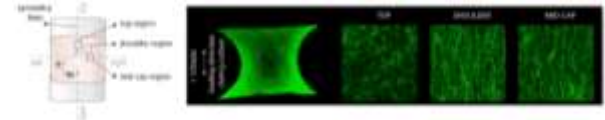
Figure 2: collagen fibre orientation.

All samples demonstrated physiological strain stiffening responses (Fig.3A) The stiffness values were 0.3 ± 0.2 (static), 0.3 ± 0.1 (I-strain) and 0.4 ± 0.2 (C-strain) MPa at 2% strain, 1.1 ± 0.5 (static) 1.1 ± 0.5 (I-strain) and 1.2 ± 0.4 (C-strain) MPa at 5% strain, and 2.3 ± 0.9 (static), 1.6 ± 0.3 (I-strain) and 2.2 ± 0.9 (C-strain) MPa at 10% strain (Fig.3B).
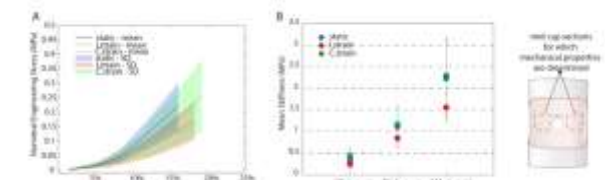
Figure 3: mechanical assessment of cap analogs.

Discussion and conclusion

Anisotropic collagen configurations in the direction of loading, similar to human caps, were observed. These responses are known to be a direct consequence of cellular orientations due to tissue constraints, contact guidance and the applied load[3].The histological analyses (not shown) indicate that the structural organization of the collagen mimics human cap composition.

All engineered tissues analyzed demonstrated physiological strain stiffening behavior and calculated stiffness values fell within the range reported for human carotid fibrous caps (i.e. 0.5-5 MPa).

We can conclude that not only the structural aspects of fibrous caps can be captured with this model, but we also generated a mechanical cap equivalent

References

1. Libby et al., Nat Rev Dis Prim, 2019, 5(1)
2. Cardoso et al, Journal of Bioemechanics 2014, 47(4)
3. Wissing et al., *BioRxiv*. Preprint. 2021

OACTIVE: VR-BASED GAIT RETRAINING TO ADDRESS KNEE OSTEOARTHRITIS

Georgios Giarmatzis (1), Socrates Zouras (2), Michail Pavlou (2), Konstantinos Moustakas ()

1. Physical Education and Sport Science Department, Democritus University of Thrace, Greece; 2. Electrical and Computer Engineering Department, University of Patras, Greece

Introduction

To address knee osteoarthritis (OA), gait retraining is proving to be an effective treatment for correcting gait alterations. Current gait retraining methods for knee OA rely on the use of simple biomechanical models for calculating the external knee adduction moment (KAM) as a target variable to control during the gait retraining interventions. Retrained gaits with minimal in vivo tibiofemoral contact forces may be more effective than gaits with minimal KAM peaks to the treatment of OA condition. The availability of musculoskeletal models that can predict accurate estimates of tibiofemoral forces in real time will offer the possibility of performing joint contact force-based gait retraining to any subject through VR games. Thus, the aim of this study was to present a gait retraining system that aims to reduce the loading of the knee and reduce pain.

Methods

The gait retraining system was implemented using the Unity game engine and includes a patient- and clinician front end. Exchange of data with the simulation back-end that calculates knee joint forces [1] was established through shared memory to improve efficiency and reduce latency. The system can utilize augmented or virtual reality output devices which would allow the implementation of interactive scenarios that could engage the user and make the training more fun and effective.

Results

Figure 1 presents the clinician's front-end main window and Figure 2 the patient's front-end, during a jumping exercise. The former contains the musculoskeletal visualizer, real-time plotting and footprint visualization, whereas the latter shows the gamification elements used to engage the user during a training session. Within the application, the operator can monitor the progress of the logged users, replay sessions, analyze events, create new objectives and scenarios. The clinician can define the objectives of a session based on values that are obtained from the back-end such as foot progression angle, vertical reaction forces on the knee amongst others. Once the range and desired values are defined one can use intuitive visualization primitives such as bar, gauge, or text indicators to provide real-time feedback to the user.
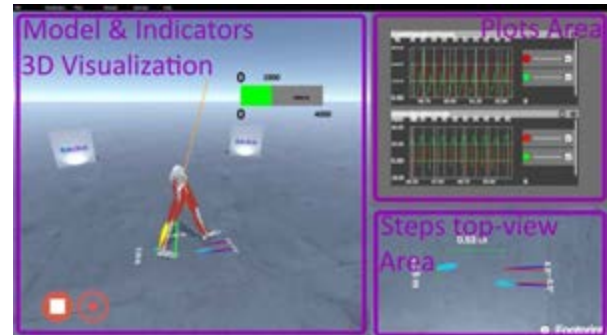
Figure 1
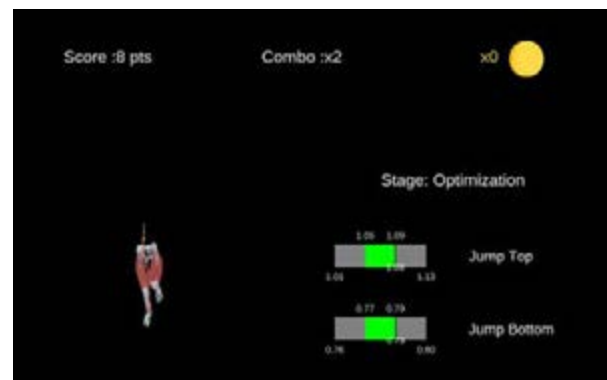
Figure 2

Discussion

For the first time, a gait retraining system was developed that utilizes real time knee joint forces to guide the patients to offload their knee structure. Such a system can find application in rehabilitation by providing biofeedback to the users during the training sessions. This technological leap will unveil new research directions that could target not only applications related to healthcare and human well-being but also translate to other fields as well.

References

1   Stanev, D. *et al. Sensors 2021, Vol. 21, Page 1804*, 2021, 21 (5).

Acknowledgements

A VIRTUAL REALITY ENVIRONMENT TO STUDY GAIT DERANGEMENTS IN PARKINSON'S DISEASE

Chiara Palmisano (1), Ibrahem Hanafi (1,2), Ioannis Ugo Isaias (1,2)

1. Department of Neurology, University Hospital Würzburg, Würzburg, Germany; 2. Julius Maximilian University, Würzburg, Germany

Introduction

Freezing of gait (FoG) is a dramatic gait symptom for patients with Parkinson's disease (PD), characterized by a sudden and transient inability to take a step, and causing high risk of falls, poor quality of life and increased morbidity and mortality. The neural derangements underlying FoG are still largely unknown, preventing the development of effective therapeutic strategies [1]. The elusiveness of FoG is based on its episodic nature, as it is difficult to evoke on demand in a standardised and controlled environment. Adjustments in speed or direction of gait in response to environmental challenges are known to trigger FoG episodes. We developed a virtual reality (VR) setup specifically designed to induce gait modulation in a highly immersive, realistic, controlled and standardized environment.

Methods

We programmed the VR environment (Fig. 1) with Unity (Unity Technologies, USA) and displayed it to the subjects via a wireless head mounted visor (Vive Pro, HTC, USA) connected to a PC (Intel Core i9- 181 10900X 10 cores, NVIDIA GEFORCE 11 GB RTX 2080, 32 GB RAM). The virtual environment was designed to closely resemble the gait laboratory and included a black carpet corresponding to the physical walkway on which the subjects walked (Fig. 1). Gait modulation was induced by means of a virtual agent (VA) which was programmed to cross the participants' pathway in a standardized fashion. Specifically, in each trial the VA stood next to the walkway 5 m in front and 1.5 m to the side (left and right alternately) of the subject's starting position and began walking towards the subject's path when the subject-agent distance reached 3 m, with a constant speed equal to 1.5 times the subject's speed recorded at the time of the VA's start. Subjects were instructed to modulate their gait in order to avoid a collision. We recruited 12 young participants and five patients with PD. All subjects underwent three sessions of 20 trials each: i) gait in the real world (RW), ii) gait in the VR environment without the VA (VR/A-), iii) gait in the VR environment with the VA (VR/A+). The VR/A+ session was repeated two times. Patients underwent the protocol after overnight suspension of all dopaminergic drugs. Kinematics was assessed thanks to an optoelectronic system with six cameras (sampling rate 100 Hz, SMART DX-400, BTS Bioengineering, Italy) and a full-body protocol of 29 markers. Dynamics was evaluated by means of four dynamometric force plates (P-6000, BTS Bioengineering, Italy). For the RW and VR/A- sessions, we considered only the strides performed at steady-state velocity. For the VR/A+ sessions, we considered a modulation window defined as the interval from the start of the VA to the return of the subject to steady-state velocity, as defined in the VR/A- sessions. We considered three strides in the modulation window (i.e., modulators) for the kinematic and dynamic evaluation. Specifically, stride length, duration, velocity and width, as well as braking and propulsive impulses and force peaks, were computed for each condition. We also computed trunk inclination, walking direction and medio-lateral oscillation, to assess medio-lateral strategies and perturbations induced by the interaction with the VA.

Results

The lack of differences in the kinematic and dynamic parameters between the RW and VR/A- conditions suggest that our VR environment may not influence per se the locomotor pattern. All HC reduced stride length and velocity and increased stride duration during the first modulator. Kinematic parameters were gradually restored to baseline values during the second and third modulators. A similar pattern was observed in patients. In the VR/A+ sessions, HC consistently showed increased trunk inclination, mediolateral trajectory deviation and oscillations than in the unperturbed conditions, while it was not possible to identify a common medio-lateral strategy in the patient cohort. In HC, braking impulse and force peak showed higher values during the first modulator than the unperturbed conditions and the other modulators. Conversely, the second and third modulators showed increased propulsive impulse and force peak. This pattern was also observed in all but one PD patient. One patient showed several FoG episodes exclusively during the VR/A+ sessions.

Discussion

Our VR paradigm effectively induced gait modulation in a controlled, immersive, and ecologic scenario. Also, it effectively evoked FoG in one PD patient. Our protocol could be a powerful research tool to study gait modulation and its derangements in patients with PD.

Figure 1: The VR environment in the VR/A+ condition. Green tiles indicated the starting and ending point of each walking trial.

References

1. Pozzi et al, Brain, Brain, 142, 2037–2050

BALANCE REACTION & MOTOR CONTROL DURING SIMULATED FEAR OF HEIGHT IN CHILDREN WITH CEREBRAL PALSY – A PILOT STUDY

Rebecca Winter (1), Regine Lohss (2,3), Navrag B. Singh (4), William R. Taylor (4), Norbert Zentai (2), Rosa M.S. Visscher (2,4) Elke Viehweger (2,3)

1. Bern University of Applied Sciences, Switzerland; 2. Department of Biomedical Engineering, University of Basel, Switzerland; 3. Neuro-Orthopaedic Unit, University of Basel Children's Hospital Basel, Switzerland; 4. Institute for Biomechanics, ETH Zurich, Switzerland

Introduction

Cerebral palsy (CP) is associated with postural instability and a high propensity for falling, which can lead to significant physical or psychological consequences, such as an increased fear-of-falling (FoF) [1,2]. Feeling unsafe can influence the control of upright stance [3]. Previous work has shown that anxiety related changes in postural stability are accompanied by changes in spinal reflex activity in healthy adults [4]. The aim of this study was to establish whether virtual reality (VR) protocols are able to elicit FoF, and hence recreate the same real-world anxiety related changes in postural stability in controlled laboratory environments in children with CP. Moreover, for the first time, we investigated if the response was driven by musculoskeletal co-contraction or adaptation of cortical control through measuring spinal reflex activity.

Methods

This pilot investigation included 5 participants with CP in a prospective study design. Main inclusion-criteria: 7-18 years, spastic CP, gross motor function classification level 1 or 2. Main exclusion-criteria: orthopaedic surgeries in the lower extremities (<1yr), botulinum toxin A (<6mths). In addition to the standard clinical gait analysis, our study protocol included measurements of standing still for 2x40s per condition on two force plates (FP) with one leg per FP, while experiencing two different virtual heights (0m, 10m) applied in a randomized order to elicit FoF (Figure 1).

Figure 1: VR environment & measurement set up

To quantify the spinal reflex activity with the 1a afferents, the soleus H-reflex was measured, randomized on the affected and non-affected limb. Muscle activity of the soleus was measured through surface EMG (Noraxon), placed according to the SENIAM guidelines. Before performing the standing trials, the tibial nerve was identified and the stimulation electrode placed while the participant lay in a prone position. Afterwards a recruitment curve was determined to identify 80%H-reflex intensity, which was used to elicit the H-reflex (H/M Ratio) during the standing trials. FOF was recorded using a numeric rating scale (NRS, 0-10). Standing balance was assessed with overall path-length as well as velocity and displacement of the centre of pressure (COP) in the anteroposterior (ap) and mediolateral (ml) directions [2].

Results

All participants showed increased FoF at 10m height compared to the 0m condition (Table 1). Three children with CP showed an increased COP path-length, velocity, and displacement, while two children exhibited postural stiffness with reduced COP displacement in the 10m environment. H-reflex was possible to elicit in all children below their pain threshold in either the affected and non-affected limbs. The change in spinal reflex activity due to increased FoF was highly individual.

Table 1: Results, median(1st Qu.,3rd Qu)

	FoF (NRS)	H/M Ratio (%)	CoP path-length (mm)
0m	*0(0/0)*	*11.6(7.7/15.0)*	*4.26(1.86/7.93)*
10m	*3(0/6)*	*10.4(7.6/14.0)*	*4.33(3.11/4.95)*

Discussion

The results show that the VR environment applied in our study is able to elicit a FoF response in CP children without inducing side effects, which is consistent with previous work in healthy subjects [5]. To our knowledge, this is the first study showing H-reflex could be elicited in both affected and non-affected limbs in CP. This work presents a critical development in establishing reliable protocols for eliciting fear responses, and therefore lays the foundations for understanding real-world neuromotor-adaptation in safe laboratory environments.

References

1. Morgan P et al, Handb Clin Neurol, 159, 323–336, 2018.
2. Tracy JB et al, Gait Posture, 72, 182–187, 2019.
3. Adkin AL et al, Front Neurol, 9, 789, 2018.
4. Sibley KM et al, Hum Mov Sci, 26(1), 103–112, 2007.
5. Cleworth TW et al, Gait Posture, 36(2), 172–176, 2012.

Acknowledgements

MOTION ANALYSIS FOR VIRTUAL REALITY AIDED TRAINING AND REHABILITATION

Magdalena Żuk (1), Michał Popek (1), Katarzyna Bulińska (2), Magdalena Wojtków (1), Marcin Łopusiewicz (1)

Enter the affiliation information here ("Affiliation" style)
1. Faculty of Mechanical Engineering, Wroclaw University of Science and Technology, Wroclaw, Poland
2. Department of Physiotherapy, Wroclaw University of Health and Sport Sciences, Poland

Introduction

The purpose of the show study was to present selected applications of motion analysis for virtual reality aided training and rehabilitation using developed methods and software tools. This paper is part of a wider project called eMotion, which aims to develop a system for computer-aided training and rehabilitation using virtual reality and motion capture technology.

Method

One subject without dysfunction within the musculoskeletal system was analysed. HTC Vive Pro Full kit with seven HTC Vive Trackers (HTC, Taiwan). The tracking devices were placed on both legs and pelvis according to the Simplified 6DOF protocol proposed in previous paper [1]. Three activities in custom-made eMotion Game were designed using eMotion Scenario Editor. During the game the user had to avoid incoming objects entailing lowering phase of squats and alternately hit other objects entailing standing phase. An arrangement of virtual objects is presented in fig. 1 Virtual objects reached user every second with speed of 2 m/s. Kinematics data was collected during: 1. avoiding VR1 objects at eye level, 2. avoiding VR2 objects 15 cm below eye level, 3. avoiding VR3 objects 30 cm below eye level, 4. Squats without VR. Joint kinematics was calculated using eMotion Analysis Tool.

Result

In Fig. 2 joint kinematics in the sagittal plane has been presented. Range of motion (ROM) has been shown in table 1. Alternating combination of virtual objects for hitting and avoiding entailed joint kinematics similar to squat with high symmetry and temporal repeatability. The high adjustment of virtual objects has influenced squat depth, especially by increasing knee flexion and ankle dorsiflexion.
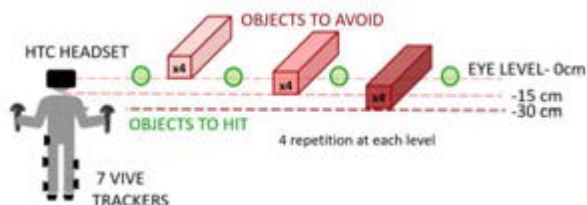
Figure 1: Experimental setup and a placement of virtual objects during gameplay

Summary

The developed method and software tools enable planning virtual reality gameplay together with simultaneous quantitative, three-dimensional motion analysis using a low-budget motion capture system (Vive Trackers).
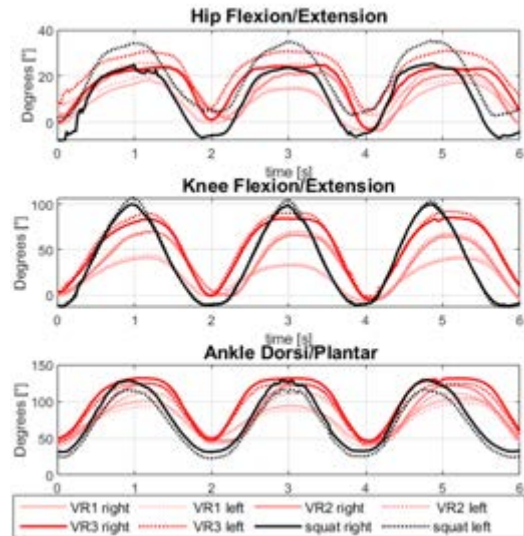
Figure 2: Comparison of joint kinematics for squats and activity in VR game for left and right side

	VR1	VR2	VR 3	squat
Hip	23°	28°	29°	33°
Knee	55°	83°	100°	112°
Ankle	73°	92°	102°	98°

Table 1: Range of movement (ROM) for different VR gameplay and squat

Kinematic analysis will allow for better diagnosis, evaluation of patient's/ user progress or generating reports for remote training and rehabilitation. In addition, developed tools may provide support for game scenario design. Enforcing precise movement patterns (joint kinematics and temporal parameters) can enable safe rehabilitation (also remote) and effective workout.

References

1. Żuk et al, Measurement, 188, 2022.

Acknowledgements

3D-PRINTER ENABLING CUSTOMIZED ANATOMIC MODELS

Laszlo Jaksa (1), Andrea Lorenz (1)
1. Austrian Center for Medical Innovation and Technology (ACMIT Gmbh), Wiener Neustadt, Austria

Introduction

Additive manufacturing is becoming an increasingly influential group of manufacturing methods in the field of medical technology. A frequently reported medically relevant application of additive manufacturing is the production of anatomical models that are more realistic than mass-produced ones from the standpoint of geometry, colour, mechanical or imaging properties. One emerging technology in this regard is extrusion-based silicone rubber 3D-printing, which allows the customization of mechanical properties of printed objects.

Methods

In this study, the abilities of a custom-built 3D-printer [1] (Figure 1) were investigated. The printer features three printheads, two of which can print with fluid materials and one with thermoplastic filaments, all in the same printjob. Various test objects were proposed to evaluate the geometric freedom allowed by the fluid printheads printing with single-component liquid silicone rubbers. Three such silicones rubbers were tested and compared in a quantitative manner, focusing on the sagging of unsupported overhangs and bridges as a function of printing material viscosity. Furthermore, the tuning of both mechanical and radiological properties through infill structuring is demonstrated through printing rectangular blocks of various infill densities with the gyroid infill pattern using the most viscous silicone rubber material. After crosslinking, the Shore A hardness of these blocks was measured.
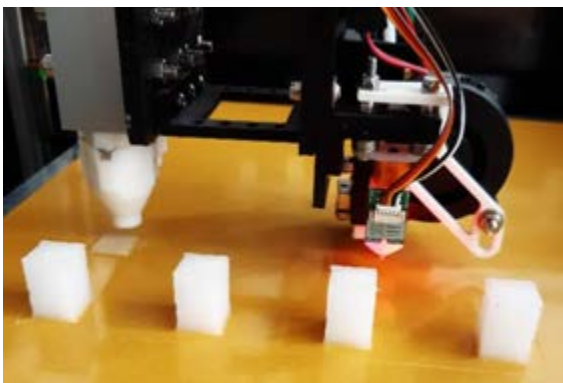
Figure 1: the 3D-printer printing rectangular blocks with gyroid infill structure out of silicone rubber

Results

To investigate the geometric limits concerning unstable features, parallelogram blocks featuring a 45° overhang angle and bridge structures featuring a 4 mm bridge distance were printed 6 times per material, then measured with a profile projector. The average sagging of the overhangs and bridges for each material is visible in Table 1.

Viscosity [Pas]	4 mm bridge sagging [mm]	45° overhang sagging [mm]
410	0.96 ± 0.17	1.56 ± 0.59
535	0.86 ± 0.18	1.78 ± 0.71
1080	1.02 ± 0.42	1.79 ± 0.59

Table 1: Sagging of bridges and overhangs printed with three materials of various dynamic viscosity

Concerning the rectangular blocks with various gyroid infill densities (ranging from 30% to 100% silicone volume fraction), the Shore A hardness values were heavily influenced by the infill percentage, as shown in Figure 2.
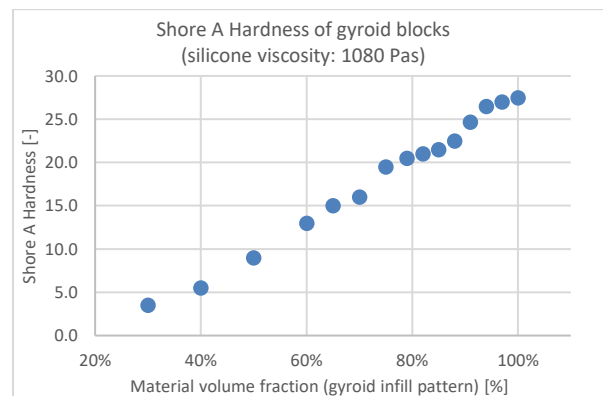
Figure 2: Shore A hardness values of rectangular blocks with gyroid infill

Discussion

It was observed that the liquid silicone rubber with the highest viscosity had the highest average sagging both in the overhang and the bridge specimens. The sagging values also showed a considerably higher variability in the overhang specimens with this material relative to the other two. These results suggest that a lower viscosity material may offer more geometric freedom and accuracy in case of printing anatomic models. It was also demonstrated that changing the infill percentage of printed silicone objects influences the mechanical properties of the object in the macroscopic sense, making this method potentially useful in making more realistic 3D-printed anatomic models for medical education, research, and preoperative planning.

References

1. Jaksa L, Pahr D, Kronreif G, Lorenz A, 2021, Development of a Multi-Material 3D Printer for Functional Anatomic Models. Int J Bioprint, 7(4):420. DOI: 10.18063/ijb.v7i4.420

Acknowledgements

DEVELOPMENT AND CHARACTERIZATION OF 3D PRINTED BONE SUBSTITUTES MIMICKING TRABECULAR BONE ARCHITECTURE

Fanny Leborgne (1), Laëtitia Caillé (1), Christophe Tromas (1), Donatien Campion (2), Mathieu Séveryns (1,3), Tanguy Vendeuvre (1,4), Arnaud Germaneau (1), Valéry Valle (1)

1. Institut Pprime UPR 3346, CNRS - Université de Poitiers - ISAE-ENSMA, France; 2. 3D Medlab – Marle Group, France; 3. Orthopaedic Surgery and Traumatology department, Martinique University Hospital, France; 4. Orthopaedic Surgery and Traumatology department, Poitiers University Hospital, France

Introduction

Valgus tibial osteotomy (VTO) is a surgical procedure aiming to correct the lower limb mechanical axis in case of femoro-tibial osteoarthritis of the medial compartment of the knee. During open wedge proximal tibial osteotomy, the surgeon inserts a filling material inside the bone gap to promote osteogenesis and to allow the patient to recover full weight bearing. Autologous grafts and allografts are the reference techniques used up to now. They encourage bone ingrowth and give superior osseointegration clinical results [1]. However, they are not able to fill large bone defects subject to high mechanical loads [2] and can lead to clinical complications (morbidity, infections) [1,3]. To address these limitations, synthetic bone substitutes are being developed. Current filling devices are produced by conventional manufacturing methods which do not allow to control rigorously the geometry and the porosity (pore size, interconnectivity) required for the mechanical strength, bone regeneration and tissue revascularization [3]. The growing development of additive manufacturing techniques can overcome these technological issues. In this study, we investigate the feasibility of producing and characterizing Ti-6Al-4V bone substitutes mimicking human trabecular bone architecture by laser powder bed fusion (L-PBF).

Methods

A cubic centimeter trabecular bone sample was harvested from the proximal epiphysis of a human tibia and scanned (Figure 1a) with a microCT scan (Ultratom RX Solutions, Institut Pprime). The images were then segmented (Figure 1b) by a thresholding method (Simpleware Scan IP v2018.03 Synopsys, 3D Medlab) in order to reconstruct and prepare (Netfabb, v2021.2 Autodesk, 3D Medlab) a numerical model of the bone segment compatible with the 3D printing technique resolution [4] (M290 EOS, 3D Medlab).

The printing accuracy was assessed by scanning two samples printed at 1:0 and 2:0 scales (Figure 1c). A morphological analysis was performed using BoneJ plugin (version 7.0.11) from Fiji (version 1.53f51), to assess the bone volume fraction (BV/TV), the degree of anisotropy (DA) as well as the mean trabecular thickness (Tb.Th) and spacing (Tb.Sp).

Results

The apparent bone density (BV/TV) measured on the digital model was 9.27% and the degree of anisotropy (DA) was equal to 0.2 corresponding to a very porous and rather isotropic structure. The mean trabecular thickness (Tb.Th) and spacing (Tb.Sp) were 171.9 µm and 1628.8 µm respectively whereas the minimal printable strut thickness was 300 µm. Printing scale comparison confirmed that scale 2:0 printed sample was more faithful to the digital model than the scale 1:0 specimen.

(a)   *(b)*   *(c)*
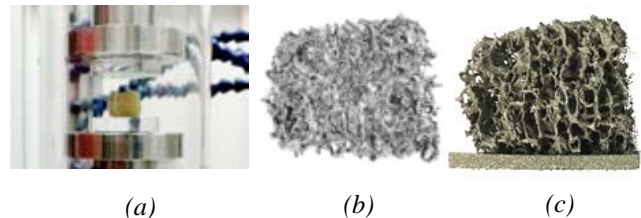
Figure 1: MicroCT scan acquisition and digital chain for additive manufacturing. (a) MicroCT scan setting of a human trabecular bone; (b) Segmented bone model; (c) Ti-6Al-4V 3D printed bone substitute.

Discussion

This study presents a methodology to develop and manufacture 3D bone substitutes by L-PBF process. It demonstrates that additive manufacturing is a valuable and promising tool to produce bone substitutes with an interconnected pores network. Further studies related to ongoing *in situ* microCT compression tests and digital volume correlation (DVC) analysis [5] (XDV-Correl, Pprime Institute) will be performed on the printed samples to quantify the 3D strain fields under compression.

References

1. Lash et al, Arthroscopy: The Journal of Arthroscopic & Related Surgery, 31, 2015.
2. Wagoner Johnson et al, Acta Biomaterialia, 7:16-30, 2011
3. Yang et al, Int J Bioprint, 5, 2018
4. McGregor et al, Additive Manufacturing, 47: 102273, 2021
5. Bokam et al, Comput Methods Biomech Biomed Engin, 22:S42-S44, 2019

Acknowledgements

SIMUALTION OF CELLULAR PROLIFERATION USING THE RPIM MESHLESS METHOD

Maria Inês Barbosa (1), Jorge Belinha (2), Renato Natal Jorge (3), Ana Xavier (4)

1. Institute of Mechanical Engineering and Industrial Management (INEGI), Portugal; 2. School of Engineering Polytechnic of Porto, Portugal; 3. Faculty of Engineering, University of Porto, Portugal; 4. Institute for Research and Innovation in Health (I3S), Portugal

Introduction

Cell proliferation is an extremely regulated and complex process [1, 2], which is made up of a chain of reactions that promote the growth and division of cells [3, 4] and allow for the balance between cell generation and cell death to be maintained [1, 3]. In order to ensure its proper functioning, this process is dependent on growth factors and the presence of nutrients, such as oxygen and glucose. So, an adequate concentration of these parameters is necessary [3, 5]. Computational models are usually used to study and comprehend biological phenomena, such as cell proliferation, since they allow to explore several hypotheses while saving time and financial resources [6, 7]. In the present work, a new computational model solved by the Radial Point Interpolation Method (RPIM) was proposed to simulate cell proliferation. In this, an iterative discrete model was used to establish the system of equations from the reaction-diffusion integro-differential equations, based on a new cell growth phenomenological law. Moreover, since the efficiency of the model depends on the efficiency of the RPIM, the optimal numbers of integration points per integration cell and of nodes for each influence-domain were analyzed.

Methods

The RPIM was used to solve the proposed algorithm. Its first step is to define the geometry of the problem, the solid domain, its limits, and its boundary conditions. After that, the domain is discretized using a nodal set, the nodal connectivity is imposed by overlapping influence-domains, and the shape functions are created by combining radial basis functions and polynomial basis functions [8]. Regarding the algorithm, specific input data is defined, and the growth law is established to initiate the process of cell growth. The growth continues until the cell doubles its initial volume, if the concentration of oxygen and glucose are higher than zero. During this period, oxygen and glucose are consumed. After doubling the volume of the cell, the growth stops and the cell divides into two new cells.

Results

The optimal number of integration points per integration cell and the optimal number of nodes for each influence-domain were explored in order to optimize the efficiency of the algorithm. Thus, several integration schemes and diverse influence-domain sizes were analysed, and their influence in several features was measured, such as: the evolution of the growth of the

volume of the cell until the process of division occurred; the computing time; the average error and; the error/computing time relation. In general, for both parameters, the usage of a higher number of points led to more accurate analyses, although more time-consuming.

Discussion

The objective of this work was to optimize the number of nodes inside each influence domain and the best integration scheme of the RPIM formulation to enhance the algorithm performance. Considering the results, lower numbers of integration points per integration cell and of nodes for each influence-domain lead to faster analyses but lower accuracy, while higher numbers lead to more accurate results but also more time-consuming analyses. Thus, an integration scheme of 6×6 per integration cell and seven nodes inside the influence domain was found to be the best solution to optimize the process, with a good balance between the relative error and the computing cost. Therefore, the algorithm was calibrated for further analyses using these two values.

References

1. Sandal, T., Molecular aspects of the mammalian cell cycle and cancer. The oncologist, 2002. 7(1): p. 73-81.
2. Nurse, P., Y. Masui, and L. Hartwell, Understanding the cell cycle. Nature medicine, 1998. 4(10): p. 1103.
3. Tortora, G.J. and B.H. Derrickson, Introduction to the human body. 2017: John Wiley & Sons, Incorporated.
4. Standring, S., Gray's anatomy e-book: the anatomical basis of clinical practice. 2015: Elsevier Health Sciences.
5. Saucedo, L.J. and B.A. Edgar, Why size matters: altering cell size. Current opinion in genetics & development, 2002. 12(5): p. 565-571.
6. Alfieri, R., et al., Modeling the cell cycle: From deterministic models to hybrid systems. Biosystems, 2011. 105(1): p. 34-40.
7. Youssef, B.B. Visualization of spatial patterns of cells using a 3-D simulation model for multicellular tissue growth. in 2014 International Conference on Multimedia Computing and Systems (ICMCS). 2014. IEEE.
8. Belinha, J. (2014). Meshless Methods in Biomechanics. Lecture Notes in Computational Vision and Biomechanics (1. ed.), Springer.

Acknowledgements

NUMERICAL MODELLING OF THE BREAST RECONSTRUCTION USING SILICONE GEL-FILLED IMPLANTS

Bruno Areias (1), António André (1), Ana Margarida Teixeira (1), Sofia Brandão (2), Pedro Martins (1,3)

1. INEGI, Portugal; 2. CESPU, Portugal; 3. ARAID, Spain

Introduction

In the last two decades, the number of women undergoing breast implant procedures, used in aesthetic, oncologic and risk reducing surgery has exponentially increased [1].

Breast reconstruction allows to reestablish breast shape and volume, restoring the patient's body image, the sense of femininity as well as improving the overall quality of life [2]. These artificial devices can be implanted under the breast tissue (subglandular) or the chest muscle (retropectoral) [3].

The breast implant procedure continues to improve, over time, but changes in breast behavior after augmentation have not been fully investigated, mainly by using of finite element methods. In this study, the authors pretend to apply the finite element method to investigate the static and dynamic behavior of the breast with and without implant, therefore it is possible to select materials which can lead to a more natural breast.

Methods

The numerical work of the human breast incorporates the ribs, pectoral muscles, adipose and fibroglandular tissues and skin (see Figure 1). The breast implant (silicone implant) was also included in the finite element model to investigate the effects of the breast augmentation surgery. In total, the mesh is composed by 565 576 nodes and 525 036 elements, from which 224 272 element of the type C3D8H (linear fully integrated hybrid element) type and 300 764 elements of type C3D8 (linear fully integrated element). The geometry of the breast model was obtained through a set of MRI images (from 1 patient). The images were segmented using the Mimics software (v19.0.0.347, Materialise) in order to obtain the geometry. The Software Abaqus Standard [4] was used in order to conduct all numerical analysis. The boundary condition applied to the model was the fixation of the rib, being then extracted the natural frequencies and the corresponding vibration modes. The mechanical properties of the tissues and implant were based on the literature.

Discussion

Natural breast augmentation is a surgical procedure that utilizes fat stored in the body to increase the breasts size through fat transfer surgery. They have advantages in comparison with the silicone or saline implants in relation to the biocompatibility and cost-effective [5]. However, this procedure has the disadvantage that can lead to radiological images which can be confused with breast cancer and are less permanent as fat can be absorbed. The use of non-natural implants (silicone and saline implants) lead to a change of the tissue behavior which is a disadvantage of the procedure. With this numerical study, the authors intend to investigate new materials and configurations to improve the natural feel and reduce the tendency to ripple in the silicone implant.
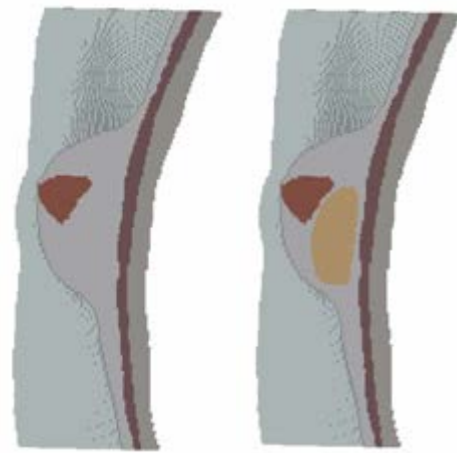
Figure 1: Cross section view of the finite element model - human breast with (right) and without silicone implant (left).

References

1. Marra, Antonio et al., Cancer Treatment Reviews, 84: 101963, 2020.
2. Cooper, D. et al., Plast Reconstr Surg Glob Open, 9:e3614, 2021.
3. Amisha and Bijal, Indian J Radiol Imaging, 26:216–225, 2016.
4. Dassault Systemes, ABAQUS analysis user's guide, 2016.
5. Yalcin Bayram et al., Arch Plast Surg., 46:498–510, 2019.

Acknowledgements

OPTIMIZATION METHODOLOGY FOR THE CORRECTION OF THORACIC SCOLIOSIS THROUGH THE USE OF ORTHOSES

David Felipe Landinez Leon

Universidad de los Andes, Colombia

Abstract

Scoliosis is a condition of angular deviation of the spine that occurs mainly in the lumbar region. Scoliosis is diagnosed when the angle formed between the upper and lower end plates, medically known as the Cobb angle, is greater than 10 degrees [1]. The severity and treatment vary according to the mentioned angle, the affected area and the cause, where the latter is usually unknown in babies and due to degenerative diseases in adults. This project seeks to design an optimization methodology for the correction of thoracic scoliosis through the use of orthoses [2]. The most common treatment is related to the use of orthoses. However, adherence to treatment decreases with time of use due to discomfort. Scoliosis braces have been shown to decrease vital capacity and can lead to ulcers [3][4]. In this project, the Rigo classification will be used in addition to computational tools to design a methodology to optimize the relationship between efficiency and comfort of an orthosis in the corrective process of thoracic scoliosis. For this, a computed tomography is used, which is processed by a computer vision algorithm to characterize the scoliotic curve. Likewise, the condition of scoliosis is modeled through a simplified Fusion 360 design of the spine, rib cage and pelvis and a buckling effect, which is caused by an axial load of 50% of the body weight on the cervical area and a modeling of intervertebral disc degeneration. Degeneration depends on two variables, precisely two percentages of degeneration in three areas of the spine. Among the most inclined vertebrae, the discs degenerate with one variable, and the other areas with another. Based on the above, 36 simulations are carried out, varying the percentages of degeneracy from 0 to 100%, with which a function was obtained through a two-dimensional polynomial interpolation. Finally, to model the orthosis, the initial configuration depends on the Rigo classification, where the device can have 3, 4 or 5 pressure zones, called pads. Then, a simulation is performed leaving only one pad with variable force, precisely the pad located at the apex, and the rest behave as fixed supports. It iterates until the maximum correction is reached, minimizing the risk of ulceration. With this, a generative design is obtained to determine the areas free of material to maximize the vital capacity. Finally, the orthosis straps are standardized, indicating how much force they exert based on the adjustment distance, so that the patient can adjust the forces obtained through the simulation. With that, one month later, the patient must take a new tomography, with which the Cobb angle is calculated again and the change with respect to the previous step is determined, if the change is less than a tolerance, the forces are restarted.

and the new angle is taken as the initial one, which is modeled by disc degeneration. If it is not less than tolerance, the patient must wait another month. This process is iterated until 90% correctness is reached. Regarding the results, it was possible to reach 90% for the case of an orthosis with 5 pads using 7 iterations. Although the algorithm is unable to determine the time of use, according to the literature, the patient must use it for more than 18 hours a day for at least 1 year and a half. Pressures never exceeded the threshold for ulcer risk, which was taken as 150 mmHg. As additional results, it was possible to determine the areas of the vertebrae and discs that suffered the most, where bone-to-bone contact and prolapse of the fibrous rings were found.

Results

Iteración		0	1	2	3
Rigo		A1	C1	C1	C1
Cobb [°]		34.9	15.3	6.8	2.6
Degeneración [%]	β_1	79	42	30	10
	β_2	75	40	24	6
Presiones pads [mmHg]	Torácico	20	16	14	
	Axilar	23	25	26	
	Cresta	30	28	23	
	Cadera	15	-	-	
Ajuste [mm]	Superior	29	27	24	
	Inferior	16	14	11	
Corrección [%]			56	81	92

References

[1] H. Schmidt, A. Kettler, A. Rohlmann, L. Claes y H.-J. Wilke, «The risk of disc prolapses with complex loading in different degrees The risk of disc prolapses with complex loading in different degrees,» 12 Abril 2007.

[2] J. Duncan, «All About Degenerative Scoliosis,» 2017.

[3] H. Kirkland, O. Teleten, M. Wilson, B. Raingruber. Pressure Mapping Comparison of Four OR Surfaces. July 2015.

[4] J. Kennedy, C. Robertson, I. Hudson, P. Phelan. Effect of Bracing on Respiratory Mechanics in Mild Idiopathic Scoliosis. 1989.

[5] C. Chung. Scoliosis Analog Model for the Evaluation of Bracing Technology. 2015.

[6] M. Rigo, M. Villagrasa, D. Gallo. A Specific Scoliosis Classification Correlating with Brace Treatment: Description and Reliability. 2010.

A VORONOI-BASED HOMOGENIZATION METHOD FOR TRABECULAR MICROACHITECTURE BASED ON PATIENT-SPECIFIC MICRO-CT

Zeyang Li (1), Shuai Zhu (1) Zhangming Wu (1)

1. School of Engineering, Cardiff University, UK

Introduction

The hierarchical structure for bone tissues have been extensively studied from a microscale to macroscale. Among these hierarchical structural components of bone tissues, the trabecular bone is particularly concerned by many researchers due to its complicacy in structural forms and anisotropic properties. Up to now, several kinds of representative volume element (RVE) for trabecular bone have been developed and applied into build the multiscale modeling for the analysis of mechanical behavior of bones. However, most of current RVE models are based on either homogenized solid elements [1] or a classical hexagon rod structure [2]. These methods are often based on an oversimplification of the geometry features of trabecular structure, which may not be suitable and accurate for the nonlinear analysis of bone structures.

To address the above issues, a new RVE modelling method for the trabecular bone based on Voronoi-based scaffold and homogenized anisotropic elasticity is proposed and developed in this work. The method is based on micro-CT trabecular images and aiming to provide both low computational costs and accurate basic units for establishing bone multiscale modeling. The specific rod structure of Voronoi-generated construction provides extensive flexibility for the bone modelling with complicated mechanical behaviors, such as trabecular buckling effect, etc. In addition, this Voronoi-based RVE has a natural advantage for industrialization, as it can be directly applied for graft manufacturing [3]. Voronoi polygon is one of the most popular geometries applied in the design of artificial implants due to its excellent biocompatibility. Furthermore, as the Voronoi -based RVE developed in this work considers the patient-specific information, this model has great potentials for applying in clinical automatic diagnosis field to build a precise customized multiscale model .

Methods

In this work, a 2D micro-CT image of trabecular tissue by [1] was utilized as the model sample. To capture the latent geometric features, we used the location and area of marrow cavities picked from the image as the basic parameters to build the Voronoi-based rod construction. The detailed modelling steps are given as follows: (1) Selecting the centroid of each cavity as a distinct Voronoi seed; (2) Drawing basic Voronoi scaffolds based on Voronoi seeds; (3) Calculating the BV/TV from micro-CT images; (4) Scaling the polygon by a weight ratio refer to BV/TV to transfer polygon edges into rods and establish the final RVE model. The final RVE model consists of rods with a certain width, whose value is decided upon a coupling effect of both cavity location and BV/TV. The specific pattern of rod construction in the RVE mode gives rise to the anisotropic elastic modulus of trabecular bone.
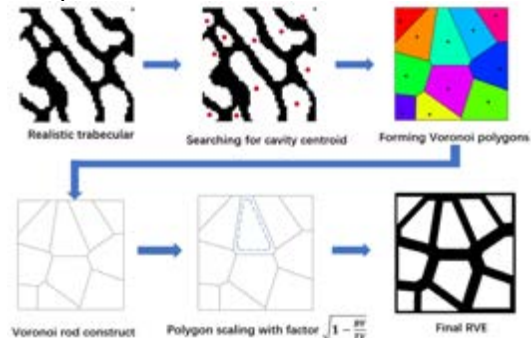
Figure 1: The flowchart of RVE modelling. Black pixel corresponds to the bone tissue; white area corresponds to marrow cavities.

Results and Discussion

The developed Voronoi-based RVE in this work had been examined by the fabric tensor method to validate its anisotropic material property. The polar diagram result suggested a fitted ellipse with orthogonal axis direction of approximate 107° and 17° as shown in Fig. 2. These values agree well with the numerical values of 116° and 26° for realistic trabecular sample given by [1]. The corresponding values of index 'axial/transverse modulus ratio' of this work are identical with the results presented in [1], which are of 2.10 and 2.28, respectively.
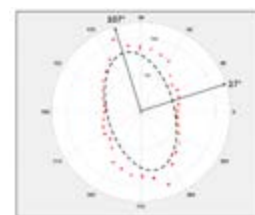
Figure 2: The polar diagram of test result by fabric tensor method. The fitted ellipse proves the RVE is of anisotropic material property.

The fabric tensor results obtained by this method show a decreased accuracy in RVE modulus direction for the trabecular samples that have more concave cavities structure, which may occur in the osteoporosis bones. Therefore, optimization methods for the present Voronoi-RVE models will be applied to further improve its accuracy and applicability. An investigation for the effective stress and yielding response for this RVE will also be carried out in our future work.

References

1. M. Marques et al, Eng Anal Bound Elem, 100:211-224, 2019.
2. L. J. Gibson, J Biomech, 18:317-328, 1985.
3. B. Grigoryan et al, Science, 364:458-464, 2019.

BIOMECHANICAL FINITE ELEMENT METHOD MODEL OF THE PROXIMAL CARPAL ROW AND EXPERIMENTAL CHARACTERIZATION OF THE INTEROSSEOUS

R.Marqués(1,2),J.Melcho(2,4,5),G. Rus (3,4,5),P. Hernández (6),O. Roda (7),I. Sánchez-Montesinos (7)

1 Instituto de Nanociencia y Materiales de Aragón (INMA), Universidad de Zaragoza, España; 2 Departamento de Estadística e Investigación Operativa, Universidad de Granada, España; 3 Departamento de Mecánica de Estructuras e Ingeniería Hidraúlica, Universidad de Granada, España; 4 Instituto de Investigación Biosanitaria, ibs.GRANADA, España; 5 Unidad de Excelencia Investigadora "Modeling Nature" (MNat), Universidad de Granada, España; 6 Departamento de Cirugía, Universidad de Granada, España; 7 Departamento de Anatomía y Embriología Humana, Universidad de Granada, España

1. Introduction

Scapholunate dissociation is the most frequent pattern (57% of wrist injuries) of carpal instability and is related to a lesion that affects the scapholunate interosseous ligament (SLIL). Hence, the scapholunate ligament is considered the primary stabilizer of the scapholunate joint. When there is an injury of the scapho-lunate ligament, the junction between scaphoid and lunate becomes unstable. The secondary stabilizers become progressively incompetent due to fatigue. The dramatic evolution of the lesion exposed and the absence of an effective treatment have promoted the experimental studies of kinetics and kinematics of the carpus (Rainbow, 2016). The objective of this investigation is to recreate a functional wrist model, in order to evaluate the instabilities detailed. Furthermore, both intact (SLIL) and non-functional (SLIL deleted) models will be made. Mechanical and kinetical properties are extracted from the bibliography [1,2,3,4,5].

Finally, an experimental test is performed to assess the ligaments' stiffness implemented in the model compared with the literature values.

2. Materials and methods

The geometrical representation of the model was obtained by computed tomography from DICOM images provided by the Hospital Clínico San Cecilio (HUSC), using open source software (Invesalius v3.1.1). With these 3D models of the bones, and using Boolean operations, the cartilage models were extracted.

The meshing process is implemented through the defined geometry, using the software Meshmixer (2D mesh) and Febio2.0 (conversion to 3D mesh).

Considering the modeling of materials (bone and cartilage), a simplified study was developed that presents the influence of trabecular bone on stress distribution. The bones were then modeled as fully cortical, linear elastic isotropes with a Young's modulus of 18 GPa and a Poisson's modulus of 0.2. On the other hand, a hyperelastic formulation (Mooney-Rivlin) is used to model cartilage and SLIL.

Six samples were evaluated with an axial test with a press designed for this purpose. The samples were scapholunate ligaments attached to the scaphoid and lunate.

3. Results

Four characteristic motions of the wrist were analyzed evaluating the stresses on the SLIL (Table 1).
Attending to the experimental validation, we can find that the values for the linear strength of the SLIL get so much closer to the ones we can see in the literature [1].

	Extension	Flexion	R. Deviation	U. Deviation
Max Compresion [Pa]	500	1000	200	200
Max Traction [Pa]	300	600	200	200

Table 1: Maximum pressure values in the Scapholunate ligament faced with the main wrist motions. Summary table.

4. Conclusions

As we see in the flexion and radial deviation, the scaphoid tends to flex, resting on the cartilage of the radius and forcing the lunate to move with it. In the case of radial deflection we have to add the interaction with the appropriate radial deflection motion, which causes a large compressed area on the lunate surface [4].
Faced with the extension movement and ulnar deviation, the lunate tends to extend in the complex due to its union with the pyramidal-hamate complex [5]. Our results can validate this hypothesis, since we can observe that, in the extension movement, the lunate face of the scapholunate ligament is compressed in the volar area. On the other hand, when we have an ulnar deviation movement, and in contrast to the radial deviation, compressions appear in the lunate facet.
Computational models are now indispensable in understanding the kinematics of an intact and pathological state of the carpus.

5. References

1. 1. BAJURI, M. N., et al. Medical engineering & physics, 2012, vol. 34, no 9, p. 1294-1302.
2. CARRIGAN, Shawn D., et al. Annals of biomedical engineering, 2003, vol. 31, no 6, p. 718-725.
3. GÍSLASON, Magnús Kjartan; NASH, D. K. InTech, Croatia, 2012, p. 77-98.
4. STOESSER, Helen L. A Biomechanical Investigation of Scaphoid and Lunate Kinematics During Wrist Motion. 2016.
5. QUIGLEY, Ryan. 2014. Tesis Doctoral. UC Irvine.

A NUMERICAL APPROACH TO THE CALLUS FORMATION IN BONE FRACTURE HEALING

J. M. Naveiro, L. Gracia, J. Rosell, S. Puértolas

Department of Mechanical Engineering, University of Zaragoza, Zaragoza, Spain

1. Introduction

The prevalence of bone fracture has become an increasing public health problem on a worldwide scale [1]. Since 2010, more than 250000 bone fractures per year have been recorded in the European Union due to accidents at work [2]. Within this number, the fractures were associated with morbidity and mortality, and increasing social costs [3].

In the past two decades, there has been an increase in the use of computational tools to analyze the bone fracture problem.

The most common approach in the majority of the works [4] focuses on tissular differentiation and bone remodeling, considering a predefined callus form (pre-meshed domain), changing or updating the type of material of the elements according to the evolution of strains, stresses and fluid pressure.

2. Methods

The structure of the problem-solving method is based in three phases: the diffusion problem, the callus growth trigger and the callus growth algorithm.

The diffusion problem phase consists in the solving of the diffusion problem through the finite element method with the initial conditions and the boundary conditions resulting from the previous time step.

The growth velocity and the total growth volume are controlled by the callus trigger phase. This phase controls what will happen in the growth phase with a sigmoid function adapted to various biological magnitudes. As main magnitudes, Mesenchymal Stem Cells (MSCs) and chondrocytes were chosen. And for the chemical velocity regulation factors, Tumor Necrosis Factor α (TNF- α) and Bone Morphogenetic Proteins (BMPs) were chosen.

Finally, the callus growth algorithm creates new elements. Some restrictions are considered in the growing algorithm. It works as shown in Figure 1.
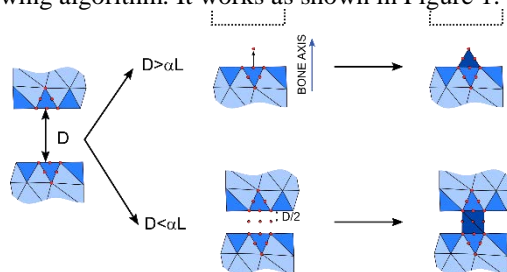
Figure 1: How the callus growth algorithm works.

3. Results

This work was applied to various fractures. The algorithm is capable to adapt to different fracture shapes. In the Figure 2 a comminuted fracture with an intermediate bone fragment with 2.0 mm for the upper gap (angle of 22 °) and 4.0 mm for the lower gap is shown.
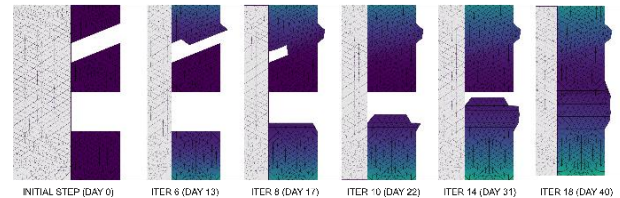
Figure 2: Comminuted fracture

4. Discussion

The approach combines a diffusion model with a mesh growing algorithm that allows free growth for the callus depending on previously established conditions, without a pre-meshed domain. Previous works on FE simulation in this field [4] have mainly focused on tissular differentiation and bone remodeling, considering a predefined callus form. They use a pre-meshed domain updating the type of material of the elements according to different mechanical and biological factors, but without considering the callus growth itself.

5. References

1. SE Roberts et al, BMJ 327 (7418): 771–775, 2003.
2. Eurostat, Accidents at Work By Type of Injury and Severity, 2021.
3. D Prieto-Alhambra et al, Arch. Osteoporos 14: I, 2019.
4. M Wang et al, Med. Biol. Eng. Comput. 55 (11): 1895–1914, 2017.

6. Acknowledgements

A VIRTUAL LABORATORY FOR THE DETERMINATION OF MINIMAL FUSION AREAS IN TIBIA PSEUDARTHROSIS

Michael Roland (1), Stefan Diebels (1), Kerstin Wickert (1), Annchristin Andres (1), Bertil Bouillon (2) and Thorsten Tjardes (2)

1. Saarland University – Chair of Applied Mechanics, Germany
2. Cologne Merheim Medical Center, Department of Trauma and Orthopedic Surgery, Germany

Introduction

Delayed union and non-union of fractures remain a challenging problem. Surgical resection of the non-union and transplantation of autologous bone are the mainstay of therapy often resulting in bone defects of variable size. However, mechanical stability, i.e. the patient being mobilized with full weight bearing is the attempted endpoint of non-union therapy. We hypothesize that it is possible to achieve the endpoint of mechanical stability with less than full circumferential cancellous bone transplantation and demonstrate this using a new simulation-based virtual laboratory.

Methods

The goal of this proof-of-concept study is the establishment of a virtual lab for the determination of the minimal fusion area of tibia pseudarthrosis to achieve mechanical stability. The basic component of our virtual lab is the generic generation of bone models based on computed tomography scans of human cadaveric specimens via segmentation, anatomical landmarks combined with a Procrustes analysis and a principal component analysis (PCA). These models represent also different anthropometric factors and in a second step are fitted with varying fracture morphologies based on the AO/OTA fracture classification using fracture models generated with a free-form software. In a computer-aided design step, the models of the fractured bones are provided with appropriate implants and passed to a finite element (FE) based optimization algorithm for the detection of the minimal amount of fracture union necessary to allow physiological loading. In contrast to previous approaches, cf. [1,2], this new virtual lab allows a significantly extended analysis of the mechanical stability including multiple loading scenarios from the patient's daily life combined with surgically relevant cancellous bone transplantation sizes and different healing stages reflected by appropriate material parameters. As a second major extension, the local micromechanics in the fracture gap and their medically reasonable constraints are considered in the optimization in addition to the implant stress.

Results

The virtual laboratory presented here allows the detection of the minimal area of a tibia pseudarthrosis that needs to be filled for a mechanically valid fusion under various loading scenarios representing different weight bearing regimes. The consideration of the healing window in the fracture gap as a second parameter in addition to the implant stress leads to improved results compared to simulations that consider only one optimization criterion. Nevertheless, minimal fusion areas can be less than 80% of the full circumferential area depending on individual fracture morphology, treatment and weight bearing regime.
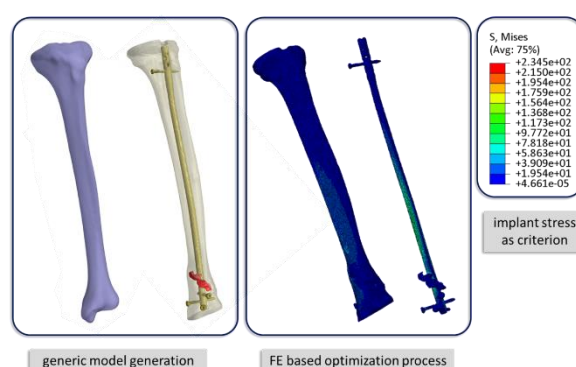
Figure 1: This figure illustrates individual steps from the virtual process from a generic tibia model to a von Mises stress analysis of the implant.
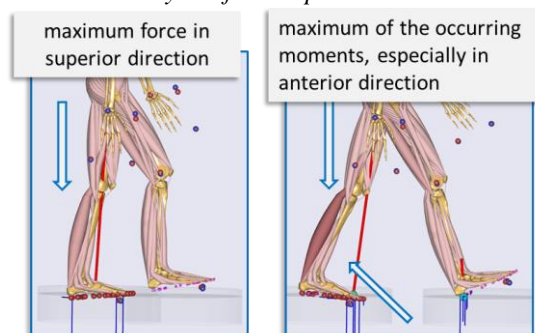
Figure 2: Computation of individual loading conditions from underlying musculoskeletal simulations.

Discussion

Generic model generation eliminates the time-consuming step of segmenting a fractured and treated tibia from the clinical imaging, while the differences between generic and patient-specific models in the simulation results remain acceptable. This new virtual lab show that minimal fusion areas can be determined also considering patient-specific aspects where an extension to other bones is possible.

References

1. Roland M et al. J Biomech. 48: 1119-1124, 2015.
2. Roland M et al. Biomedical Technology. Springer, Cham, 313-331, 2018.

INTRACRANIAL ANEURYSM PREDICTIONS WITH THE USE OF MORPHOMETRIC FEATURES IN A MACHINE LEARNING APPROACH

Nicolas Aristokleous (1,2), Kleo G. Achilleos (1), Myrianthi Hadjicharalambous, (1), Andreas S. Anayiotos (2), Costas S. Pattichis (1) and Vasileios Vavourakis (1,3)

1. University of Cyprus, Cyprus; 2. Cyprus University of Technology; 3. University College London, UK

Introduction

Intracranial aneurysm (IA) is a cerebrovascular disorder in which the wall of a cerebral blood vessel weakens and swells, thus, causing a localized dilation or ballooning of the artery. Although such aneurysms are mostly asymptomatic, a considerable number of IA patients remain on high risk of aneurysm rupture, a serious life-threatening condition. The rupture of IA and the consequent subarachnoid haemorrhage are associated with high rates of morbidity and mortality [1][2].

Recently, machine learning algorithms have been developed and applied to facilitate risk prediction of IA rupture [3,4]. Thus, this study builds upon previous efforts and it explores further the utility of a decision tree (DT) algorithm to extract rules and predict the likelihood of rupture in patients with IA.

Methods

Morphological data were acquired from a cohort of n=98 IAs from the Aneurisk dataset repository [5]. The following aneurysm features were considered: aneurysm location, index of multiple aneurysms existence, surface area, volume, shape factor and size ratio. The KNIME analytics platform was used to compute the DT [5,6] and extract the rules.

Results

Ten different training sets of 70 records (30 ruptures (R), 40 unruptured (U)) and test sets of 28 records (14 R, 14 U) were drawn at random from the database. The average percentage of correct classifications score achieved on the test set was 69%. The rules of a model that achieved a 75% are presented in Table 1.

Rule	Model Accuracy
Size Ratio <= 1.61 AND Volume <= 97 AND Location = "ICA" => "U"	
Size Ratio > 1.61 AND Volume <= 97 AND Location = "ICA" => "R"	
Volume > 97 AND Location = "ICA" => "U"	75%
Shape Factor > 0.7 AND Location= "MCA" => "R"	
Shape Factor <= 0.7 AND Location = "MCA" => "U"	

Table 1: Rules extracted from a DT algorithm to predict U vs R in an intracranial aneurysm dataset.

Discussion

In this study, we applied a DT algorithm on a dataset of 98 IA cases and 13 demographic and morphometric features. Our preliminary results show a good prediction score (75%). Ongoing research efforts focus on including a larger cohort dataset, and investigating more IA-relevant features, specifically hemodynamic metrics.

References

1. Cebral JR, *et al.,* Am J Neuroradiol. 2005;26:2550–9.
2. Berg P, *et al.,* J Biomech Eng. 2015;137.
3. Heo J, *et al.,* Sci Rep [Internet]. Nature Publishing Group UK; 2020;10:6921.
4. Weng SF, *et al.,* PLoS One; 2017;12:e0174944–e0174944.
5. Aneurisk-Team. Aneurisk-Team. Emory University Department of Math & CS. AneuriskWeb project website. Emory University, Department of Math & CS, 2012. Available: http://ecm2.mathcs.emory.edu/aneuriskweb.
6. Berthold MR, *et al.,* {KNIME}: The {K}onstanz {I}nformation {M}iner. Stud Classif Data Anal Knowl Organ (GfKL 2007). Springer; 2007.
7. Achilleos KG, *et al.,* 2020 IEEE 20th Int Conf Bioinforma Bioeng. 2020. p. 1036–41.

Acknowledgements

SALBUTAMOL TRANSPORT AND DEPOSITION IN THE CAT AIRWAYS UNDER DIFFERENT BREATHING CONDITIONS AND PARTICLE SIZES

Rocio Fernández-Parra (1), Carol Reinero (2), Pascaline Pey (3), Mauro Malvè (4)

1. Department of Small Animal Medicine and Surgery, Faculty of Veterinary Medicine Catholic University of Valencia "San Vicente Mártir", Spain; 2. Department of Veterinary Medicine and Surgery, University of Missouri, USA; 3. Antech Imaging Services, USA; 4. Public University of Navarre (UPNA), Spain

Introduction

Bronchodilators like salbutamol are commonly used for treatment of feline inflammatory lower airway disease. A pressurized metered dose inhaler (pMDI) with a specific cat spacer and a spherical mask is prescribed for use by owners at home. Different breathing rates and the non-cooperative character of cats may negatively influence efficacy of salbutamol inhalation therapy. During the treatments, a substantial amount of drug might be wasted upstream of their target, resulting in an inefficient practice and non-useful local overdoses. In a previous study [1], we evaluated salbutamol transport and deposition within cat airways using different devices and masks. The aim of this study was to analyze the influence of breathing conditions and salbutamol particle size on overall drug transport and deposition using specific spherical mask and spacer.

Methods

A computational model based on a healthy adult client-owned cat was developed using Mimics (Materialise Software) starting from computerized tomographic images of the cat airway. A three-dimensional airway cat geometry was created (Figure 1) and used for the computational fluid dynamics analysis. A commercialized spherical mask and a 10cm spacer completed the model. Three flow rates were tested: normal breathing conditions [2], hyperventilation [3] and under general anaesthesia. Droplet spray transport and deposition were simulated with different particle sizes (1, 5, 10 and 15μm) using Ansys CFX (Ansys Inc.). Simulations were performed using 7 respiratory cycles (Inspiratory:Expiratory ratio 1:2, inspiratory time 1s) to simulate a common treatment period technique.

Results

Figure 1: Particle deposition within the cat airways and devices under normal breathing conditions.

The results showed that small particles tend to deposit in the devices, muzzle and/or upper airways. For increasing particle size, the situation improves moderately. However, the amount of inhaled particles reaching the lung was very low in all scenarios. The particles distribution at normal peak inspiratory flow is represented (in %) in Figure 2.

Discussion

Contrarily to what described in the human literature, particles of the largest size reached the bronchial area more easily and/or remined in suspension for a larger time than smaller ones. In our model, smaller particles deposited on the muzzle and upper airways and thus were not capable of reaching the lower airways (target of drug action). We believe this may be due to the cats' upper airways anatomy, which is comparatively complex and narrowed. In humans, the inhalation is obtained though the oral tract and synchronized with the pMDI actuation. In contrast, in cats, the inhalation takes place through the nasal tract. Also, different flow rates may modify smaller particles trajectory enhancing the possibility of the particle to deposit.
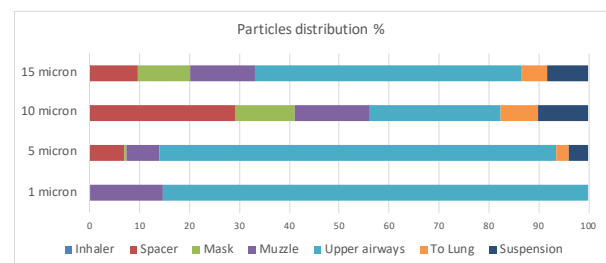
Figure 2: Percentage of particle distribution after 7 respiratory cycles under normal breathing conditions.

References

1. R. Fernández et al, Salbutamol Transport and Deposition in the Upper and Lower Airway with Different Devices in Cats: A Computational Fluid Dynamics Approach, Animals, 11:2431, 2021.
2. McKiernan et al, Tidal breathing flow-volume loops in healthy and bronchitic cats. J Vet Intern Med, 7(6):388-393, 1993.
3. García-Guasch et al, Evaluation of pulmonary function variables by using plethysmography in cats with respiratory disease associated to Dirofilaria immitis. Vet Parasitol, 187(1-2):254-258, 2012.

Acknowledgements

ON THE HINDLIMB BIOMECHANICS OF THE AVIAN TAKE-OFF LEAP

Erik A Meilak (1,2), Pauline Provini (3), Colin Palmer (2), Neil J Gostling (2), Markus O Heller (1,4,5)

1. Bioengineering Research Group, University of Southampton (UoS), UK; 2. School of Biological Sciences, Faculty of Environmental and Life Sciences, UoS, UK; 3. Université de Paris, INSERM U1284, Center for Research and Interdisciplinarity (CRI), F-75006 Paris, France; 4. Centre for Sport, Exercise and Osteoarthritis Research Versus Arthritis, Southampton, UK; 5. Institute for Life Sciences, UoS, UK

Introduction

Although extant land birds take to the air by leaping, generating the initial take-off velocity primarily from the hindlimbs, the detailed musculoskeletal mechanics of the leap remain largely unknown. Understanding how living birds navigate the interface between terrestrial and aerial locomotion not only provides insight into adaptations of modern birds to their environment but may also help to shed light on the evolution of flight. The current study thus simulated the take-off leap of the zebra finch (ZF), *Taeniopygia guttata*, a model species of passerine, a class of bird which includes over half of all extant bird species. To determine the mechanical requirements birds need to meet to take-off this study compared external net joint moments to the muscles' ability to balance across the hip, knee and ankle joints.

Methods

The skeletal model was derived from CT scans (isotropic resolution 0.04mm) of a ZF specimen [2] (15.4 g), whilst muscle attachment sites and via points were mapped from a previously established model of the magpie [3] by non-rigid iterative closest point registration of the hindlimb bones. Detailed 3D kinematics were derived from previously published X-ray reconstruction of moving morphology (XROMM) data of the left hindlimb throughout two autonomous take-off leaps [2]. Previously reported ground reaction forces (recorded at 400 Hz from Squirrel force plate, Kistler France, Les Ulis, France; resolution ±0.01N) of nine take-off leaps of the ZF [1] were used as inputs to the study. Each of the nine ZF kinetics trials were paired with the two sets of kinematics trials enabling analysis of 18 distinct take-off conditions. Using inverse dynamics, the external moments at the ankle, knee, and hip joints were calculated and contrasted to the cumulative muscle capability to balance these moments.

Results

Mean peak external flexion moments at the hip & ankle were 0.55 bodyweight times leg length (BWL) each whilst peak knee extension moments were half that value (0.29 BWL) (Figure 1). Muscles had the capacity to generate 146% (hip), 230% (knee), and 212 % (ankle) of the mean peak external moments at the joints.

Discussion

This first study to establish the detailed biomechanical requirements of the hindlimb of a passerine bird, a flying bird that leaps to take to the air. The take-off leap is characterised by substantial external moments at the hip

and ankle joints, reaching magnitudes of about two times of the values during running of a flightless bird [4]. These large external moments speak to the mechanical demands associated to the leap, a task the muscles appear to be well equipped to accomplish though, with ZF muscles able to produce over double the mechanical requirements at the ankle and knee and about 20% more than the extension requirements at the hip. Such substantial capacity provides further impetus for similar analyses in extinct birds to explore the possibility to take to the air by using the hind limbs.
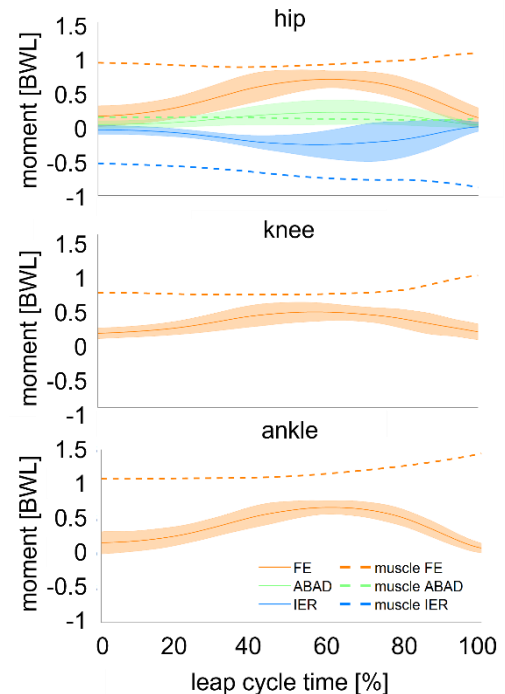
Figure 1: External joint moments at the hip, knee and ankle together with the total moment generating capacity of the muscles, plotted over normalised leap cycle time. Solid lines depict the mean external joint moments (requirements), bands depict ±2.5 standard deviations. Dashed lines depict the total moment generating capacity of the muscles (capacity).

References

1. Provini et al, J Exp Biol, 217 (15): 2659–2666, 2014.
2. Provini et al, Sci Nat, 105:12, 2018.
3. Meilak et al, Front Bioeng Biotechnol, 9, 2021.
4. Rankin et al, J R Soc Interface 1320160035, 2016.

Acknowledgements

OVERCOMING A "FORBIDDEN PHENOTYPE": THE PARROT'S HEAD SUPPORTS, PROPELS, AND POWERS TRIPEDAL LOCOMOTION

Melody W. Young (1), Edwin Dickinson (1), Nicholas D. Flaim (1), Michael C. Granatosky (1,2)

1. New York Institute of Technology College of Osteopathic Medicine, USA; 2. Center for Biomedical Innovation, USA

Introduction

There is no odd-legged vertebrate alive today, nor is there any evidence of such a creature ever existing in the fossil record [1]. One well-known, but anecdotal example of tripedal locomotion is the climbing behaviors of parrots (Order: Psittaciformes) [1,2]. Unable to use their wings as grasping forelimbs, parrots have evolved to be resourceful climbers by co-opting their feeding apparatus as an additional "limb". However, it is unclear if parrots use their beaks to simply hook into the substrate (serving a stabilizing function), or whether the head function is a true evolutionary novelty, exapting the head as a functional limb to propel and power the body in a cyclical manner. Here we present kinetic data to quantitatively assess the functional role of the head during the tripedal climbing gaits of parrots.

Methods

We collect frequency of beak, tail, and wing use on substrates at 0º, 22.5º, 45º, 67.5º, and 90º. To assess the limb-like nature of the parrot's beak, hindlimbs, and tail, we collect kinetic loading data from rosy-faced lovebirds (*Agapornis roseicollis*) during vertical climbing. From these data, we calculate the peak fore-aft and tangential force and average power (W kg^{-1}).

Results

When climbing, parrots effectively utilize the beak as a third limb. The beak generated a propulsive force no different than the hindlimb(s) ($p=0.357$; Figure 1). The beak also experiences tangential forces similar in magnitude to the hindlimb(s) ($p=0.593$). The beak generated a substantial magnitude of positive mechanical work, almost matching that of the hindlimbs ($p \leq 0.001$). These parrots are thus reliant on the combined contribution of positive power from the hindlimbs and beak to ascend vertical surfaces.

Discussion

Despite the absence of odd-limbed tetrapods, tripedal and/or pentapedal gaits have evolved in avian and mammalian lineages. We demonstrate that, when climbing, these birds utilize cyclical tripedal gaits in which the beak functions as an effective third limb, generating comparable tangential and propulsive forces and power to the hindlimbs. We conclude that the feeding apparatus and neck musculature of parrots has been co-opted to function as a third limb during vertical climbing. Utilizing the head as a limb represents an evolutionary novelty to Psittaciformes and may be facilitated by the neuromuscular modifications to limb CPGs and/or existing coupling between head and limb movements in birds.

Figures
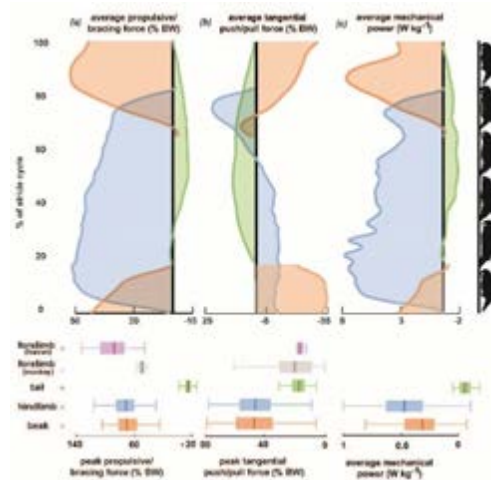
Figure 1. Force and power generation by beak, hindlimb (left), and tail during vertical climbing in rosy-faced lovebirds (Agapornis roseicollis). (a) Average (top) and peak (bottom) propulsive/braking substrate reaction force (SRF). (b) Average Tangential SRF (top) and Peak tangential forces (bottom). (c) Average single limb mechanical.
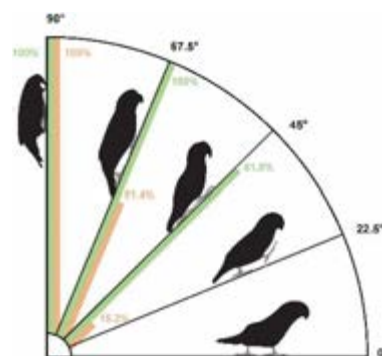
Figure 2: Frequency beak, tail, wing use on various degrees of substrate angles.

References

1. T. J. Thomson, BioEssays. 41, 1900061 (2019).
2. L. L. Reader et al., Journal of Experimental Biology, in "press, doi:10.1242/jeb.242305.

CORROSION RESISTANCE OF THE GRADE 2 TITANIUM AFTER THERMOPLASTIC DEFORMATION

Jakub Bańczerowski (1), Marek Pawlikowski (1), Tomasz Płociński (2), Marcin Grobelny (3),

1. *Warsaw University of Technology, Faculty of Mechanical and Industrial Engineering, Narbutta 85, 02-524 Warsaw, Poland;*
2. *Warsaw University of Technology, Faculty of Materials Science and Engineering, Poland;*
3. *Motor Transport Institute, Poland;*

Introduction

The leading material in the production of the medical implants is titanium and its alloys. Currently commonly used alloy is Ti6Al4V. However, due to harmful effects of aluminum and vanadium on the human tissue [1] it is advised to use pure titanium. Unfortunately, this material does not possess sufficient strength, therefore it must be processed by thermoplastic deformation method. However, changes in the grain size may influence the material corrosion resistance, which is a key parameter for bio prostheses [2,3]. Therefore, an investigation of the corrosion resistance along with the microstructure observations must be conducted.

Methods

The cylindrical Gr2 Ti samples (∅10 mm x 12 mm) were compressed at various temperatures (400-800 °C) and under different strain rates (0.01/s – 10/s). In order to assess grain fragmentation, scanning electron microscope (SEM) observations were made alongside with electron backscatter diffraction (EBSD) analysis. The corrosion resistance was measured using voltammetric methods. Polarization curves were registered at a potential change rate of 1mV/s in an electrolyte environment consisting of 0.5M NaCl.

Results

Thermoplastic deformation resulted in a grain fragmentation. The EBSD analysis confirmed average grain size reduction from 2-8 μm to values below 2 μm.
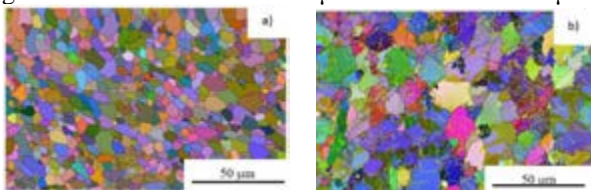
Figure 1: Ti microstructure a) before deformation, b) after deformation in . 600°C and strain rate 10/s

The change in the temperature had a slight influence on the rates of corrosion processes. However, influence of the temperature on corrosion resistance is noticeable. Higher temperature leads to an increase of corrosion resistance. The highest value of corrosion potential was recorded at 600°C
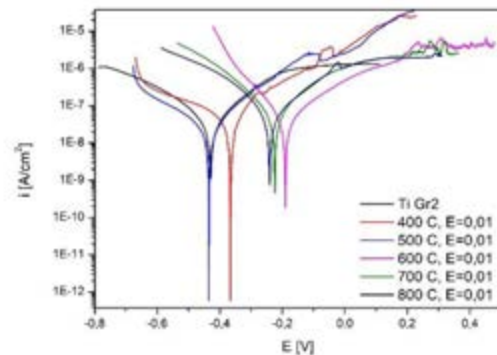
Figure 2: Voltammertric curves for Ti Gr2 in 0,5M NaCl after compression in 400 – 800 ºC.

In the case of the strain rates, increase in the corrosion resistance was also noted. The greatest difference of potential (and therefore in corrosion resistance) was recorded for the strain rate of 1/s.
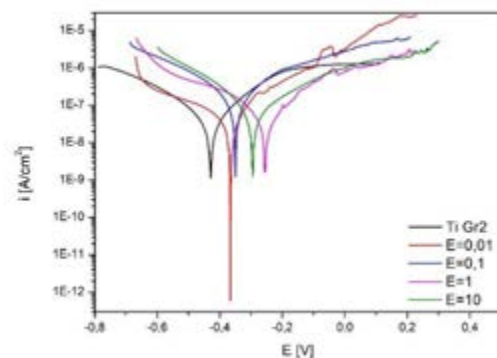
Figure 3: Voltammertric curves for Ti Gr2 in 0,5M NaCl after compression in 400°C with different strain rates.

Discussion

The corrosion resistance research of biomaterials used in prostheses is a vital task. In this case it seems that thermoplastic deformation influenced this parameter in a positive way. However further research would be beneficial. The corrosion resistance tests will be also conducted with the addition of fluoride ions.

References

1. Ansarian, I., et al.: J. Alloy Compd. **776**, 83–95 (2019)
2. Hoseini, M., et al.: Corr Sci. 51, 3064-3067 (2009)
3. Mazur M., et al.: Surf Coat Tech 307, 596-602 (2016)

EFFECT OF CONDUCTION GAPS AND INCREASED COLLECTOR ROTATION SPEED ON ELECTROSPUN PCL MATRICES

Elisa Bissacco* (1), Alessio Amicone* (1), Matthias X. T. Santschi (1), Stephen J. Ferguson (1)

1.   ETH Zurich, Institute for Biomechanics, Zurich, Switzerland

Introduction

Electrospinning is a technique that can produce fibers in the nanoscale range. The slow degradation of PCL provides suitable mechanical stability that allows an implant to withstand physiological levels of strain [1]. Several studies have revealed a correlation between the mandrel rotation speed, fiber alignment, and tensile moduli [1]. Studies have also shown conduction gaps affect alignment, but the interaction of the two has not yet been studied [1].

The aim of this study is to examine how the conduction gaps on the collector and its combination with higher rotation speed affect the mechanical and physical properties and the fiber morphology of the resulted PCL electrospun matrices [2].

Methods

Sample preparation. Two different electrospinning conditions were used.

In both conditions, an SES device was used to fabricate PCL electrospun matrices. PCL (Mw 80.000) polymer pellets were dissolved in CH3OH:CHCl3 + 0.04 % NaCl overnight at room temperature to create 11 % w/v concentration solution. The electrospinning was set to a flow rate of 1.62 ml/h, 20 cm working distance. A 10 ml glass syringe with 20G needle was used to spin the solution onto the rotating collector. Temperature and humidity around the device were controlled at 25 °C and 40 % respectively.

In the fully conductive collector condition (FC), a mandrel rotation of 200 RPM was used; in the conduction gapped collector condition (CG), electrical tape was placed across the mandrel to create gap in conduction and a mandrel speed of 800 RPM was used. Two samples were created for each condition resulting in a total of 4 samples.

Fiber physical characterization. The porosity (P) of FC and CG matrices was measured using the apparent density of each sample and the density of PCL (1.145 g/cm3) [3].

Mechanical properties. The scaffolds were cut to rectangular shapes (4.5 cm x 1.5 cm) for testing, and a uniaxial tensile test was performed under quasi-static conditions (0.1mm/s) until a strain of 150% was reached.

Results

Matrices consisting of nanofibers between 350 nm and 850 nm in diameter were fabricated. There was no noticeable difference in fiber diameter obtained from the two collector conditions (p>0.05). The fibers from CG showed higher directionality than the fibers from FC (Fig 1).
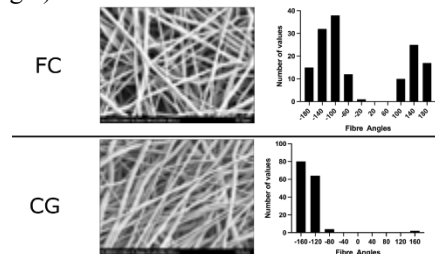
Figure 1: Fiber morphologies (Left). Distribution of fiber angles distribution (Right).

CG samples had higher (92.3%) porosity than FC samples (91.0%), however they were not statistically different (p > 0.05).

The CG samples showed a higher tensile E-Modulus (3.74 Mpa) than FC samples (3.07 MPa).
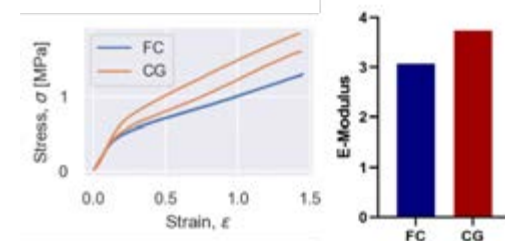
Figure 2: Left: Stress-strain curves of FC and CG samples. Right: Elastic modulus of FC and CG samples.

Discussion

CG fibers were much more aligned than FC. This is reflected in the lower variance observed in fiber orientations (Fig 1). This is likely why a higher modulus was observed in CG compared to FC and therefore may be advantageous for implanted conditions. At the same time, the porosities, and hence density and mass, remained similar between the two conditions.

To conclude, by introducing conduction gaps on the collector, we were able to positively affect the properties of the resulting electrospun scaffolds.

References

1. Alexeev D., Ferguson S. et al. (2020) Materials Today Communications, 24, 101211
2. Anindyajati A. et al. (2015) MATEC Web of Conferences 27, 02002
3. Ferreira J. L., S. Gomes, Henriques C. et al. (2014) Journal of Applied Polymer Science, vol. 131, n. 22

Acknowledgement

EFFECTS OF POLOXAMER ADDITIVES ON STRENGTH, INJECTABILITY OF BETA-TRICALCIUM PHOSPHATE CEMENT

Yeeun Kim, Kenichi Hamada

Dept. Biomaterials and Bioengineering, Institute of Health Biosciences, Tokushima University Graduate School of Biomedical Sciences, Japan

Introduction

The authors have developed a β-tricalcium phosphate (β-TCP) powder modified mechano-chemically through the application of a ball-milling (mβ-TCP). The calcium phosphate cement (CPC) paste using the modified powder can be injected easily into bone defects, however, there are two risks of leakage and migration after implantation. A good solution is the combination of CPCs with gelling agents. A gelling agent, poloxamer 407 shows an inverse thermoresponsive properties; it forms a sol at lower temperature and transforms into a gel form at higher temperature. Thus, the CPC paste containing it will maintain a good injectability at lower temperature and inhibit the two risks at body temperature. The objective of this study is to evaluate the effects of poloxamer addition on the strength and injectability of CPC paste using modified β-TCP powder.

Methods

The β-TCP powder was modified through ball-milling process for 24 h using planetary ball-mill and zirconia balls (mβ-TCP). Poloxamer 407 was mixed with distilled water at concentrations of 0.03, 0.05, and 0.1 g/ml. Then NaH_2PO_4 powder was mixed with the mixtures to prepare 0.75M NaH_2PO_4 solutions. The mβ-TCP powder was mixed with 1.25M $CaCl_2$ solution, and then with the NaH_2PO_4 solutions at a powder-to-liquid (P/L) ratio of 5:1:1 (g/ml/ml). Hereafter specimens without poloxamer, and with poloxamer using 0.03, 0.05, and 0.1 g/ml mixture are called mβ-TCP, pol-3, pol-5, and pol-10, respectively.

Approximately 2.8 g of the CPC paste was filled into a syringe immediately after mixing and then stored in a refrigerator (7°C) for 1 hour. The syringes were moved to an incubator (37°C) and stored for 1, 5, 15, 30, and 60 mins, respectively. Immediately after the storage, the injectability was evaluated through a mechanical loading at a cross-head speed of 20 mm/min and a maximum force of 300 N.

Results

The calculated injectability of the CPC paste containing poloxamer 407 reduced gradually with increasing storage time until 15 min, then it exhibited drastic decrease to 30 min. While the injectability of paste without poloxamer reduced gradually until 30 min. Note that, all the cement paste containing poloxamer lost injectability after 30 min storage at 37°C. Further, the addition of poloxamer 407 did not reduce the
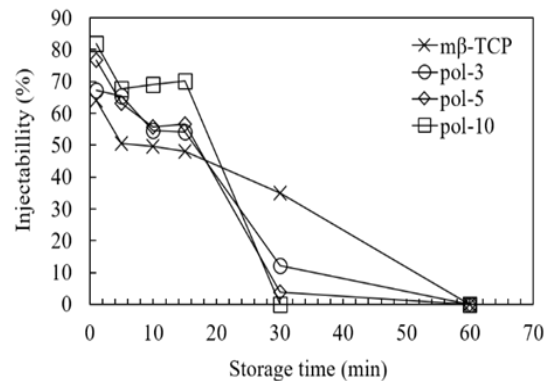
Figure 1: Effect of storage time at 37°C on the injectability of mβ-TCP, pol-3, pol-5 and pol-10 CPC paste under a maximum force of 300 N.

compression strength of the cement compacts from that of the mβ-TCP cement compacts.

Equations

The injectability was calculated according to the following equation: where W_{ext} is the mass of the paste extruded from the syringe during the loading, and W is the initial mass of the paste in the syringe before injection.

$$\text{Injectability (\%)} = \frac{W_{ext}}{W} \times 100 \qquad (1)$$

Discussion

Self-setting calcium phosphate cement pastes using modified β-TCP powder and containing poloxamer 407 exhibited sufficient injectability at lower temperature, and reduced fluidity until 30 min at 37°C, suggesting that the paste lost the fluidity and the risk of leakage 30 min after the injection into bone defects. Besides it also exhibited sufficient strength at body temperature. In conclusion, the combination of the modified β-TCP and poloxamer 407 is appropriate for minimally invasive treatment of bone defect filling.

References

1. Yassine Maazouz et al, Acta Biomaterialia, 49:563-574, 2017.
2. Yeeun Kim et al, Ceramics International, 47:1882-1890, 2021.
3. Jiyoung Bae et al, J Mech Behav Biomed, 47:77-86, 2015.

TEMPORAL DESIGN FOR ADDITIVE MANUFACTURING AND ITS POTENTIAL FOR TUNING THE SURFACE ROUGHNESS

Nasim Mahmoodi (1)[†], Barnaby Hawthorn (1)[†], Farhan Khan (2), Andrew Triantaphyllou (2), Rosemary Dyson (3), Lauren E. J. Thomas-Seale (1)

1. School of Engineering, University of Birmingham, UK; 2. The Manufacturing Technology Centre Ltd, UK; 3. School of Mathematics, University of Birmingham, UK.
† These authors contributed equally

Introduction

The impacts of additive manufacturing (AM) in manufacturing industries offer revolutionary benefits from aerospace to biomedical engineering [1].

The importance of surface roughness in biomedical engineering related context such as prosthetics has been widely investigated and shown that the surface roughness has a direct influence on biofilm formation and mammalian cell adhesion [2,3]. Moreover, it has an effect on the rate at which a biodegradable material resorbs into the body [4].

Advancement in the design for additive manufacturing (DfAM) creates more freedom in AM. Temporal DfAM introduces a new design dimension where the process parameters can be varied dynamically during manufacture and gives the designer more control over material properties [5].

The aim of this research is to develop a method to implement the temporal design in AM and study the effect of manufacturing parameters (print speed and nozzle temperature) on surface roughness.

Method

Autodesk Inventor was used to design $20 \times 20 \times 20$ mm^3 cube geometry. Following that, the designed geometry was sliced into G-Code using Ultimaker's Cura where the G-code was then post-processed by a temporal MATLAB code. Ultimaker S5 FDM printer with 3D4Makers White PLA was used to manufacture the cubes.

The effect of print speed (30-70 mm/s) and nozzle temperature (180-220 °C) on the roughness of the printed samples were systematically investigated. The other process parameters were kept constant across all samples with infill density, number of walls, top layer, bottom layer, nozzle diameter, layer height, infill pattern and bed temperature of 15%, 3, 4, 4, 0.4 mm, 0.15 mm, triangle and 60 °C, respectively. For each printing condition, the surface roughness of 3D-printed cubes' top layer over an area of 0.85×0.85 mm^2 has been measured by the MicroXAM100 optical interferometer and averaged along three samples with three random selected area for individual ones.

Results

The surface roughness S_A of 3D-printed cubes' top layer was measured as a function of printing speed and nozzle temperature and plotted in Figure 1. The results indicate that the surface roughness increases as the nozzle temperature increases from 180 °C to 220 °C and is almost independent of the printing speed. Melting of the PLA material is greatly influenced by the nozzle temperature and for the surface with lower roughness can be achieved at 180 °C.
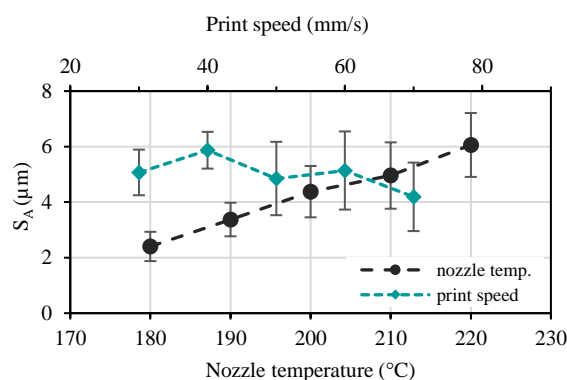
Figure 1: Effect of the nozzle temperature and print speed on the surface roughness of 3D-printed PLA cube

Discussion

This study highlights the possibility of tuning the surface roughness of a 3D-printed shape by controlling the process parameters, during the additive build. Considering the importance of surface roughness in biomedical implants, having the ability to tune the surface roughness could be very beneficial and bring a higher level of flexibility in the design process. The developed MATLAB code gives the designer the ability to temporally vary the process parameters and tune the material properties for the designed geometry.

References

1. Tofail SA et al, J Material Today 21(1):22-37, 2018.
2. Hacking SA et al, J Neuroscience Methods, 211(2):237-244, 2012.
3. Cox SC et al, ACS Biomater Sci Eng, 3:1616-1626, 2017
4. Gawlik MM et al, Materials, 11(12):2561, 2018.
5. Thomas-Seale L et al, Cogent Engineering, 6(1):1662631, 2019

Acknowledgements

LOW-COST METHODOLOGY FOR PVA PHANTOM MANUFACTURING AS SOFT TISSUE SIMULANT

Beatriz Miguélez (1), Luis Elvira (2), Javier Pascau (3), Miguel Marco (1)

1. Dept. of Mechanical Engineering, University Carlos III of Madrid, Spain; 2. ITEFI-CSIC, Spain;
3. Dept. of Bioengineering and Aerospace Engineering, University Carlos III of Madrid, Spain.

Introduction

Polyvinyl alcohol cryogel (PVA-C) is a widespread material used as a soft tissue-mimicking material (phantom) for surgical training noninvasive clinical imaging [1,2]. An autoclave is commonly used to control the optimal temperature and pressure required during the PVA-C phantoms manufacturing [1,3]. However, access to the autoclave may be difficult or economically unaffordable in some situations, e.g. developing countries. In this work, we propose an out-of-autoclave alternative procedure using a commercial express pot. Equivalent PVA-C samples have been manufactured and their features are analyzed in this work.

PVA-C samples manufacturing

An autoclave is used in the first step of the PVA-C manufacturing process to get its total dissolution in deionized water [1,3]. This step has been adapted to the express pot procedure by 30 minutes of cooking time at 121 °C approx. A water bath is applied inside the pot using a steaming rack to ensure most similar heat conditions as in the autoclave. Finally, cooling and freeze-thaw cycles are necessary to obtain the PVA-C samples.

Validation of the methodology

To check the viability of obtained samples, the sound speed was measured at 25ºC using an ultrasonic spectrometer for liquids inspection [4]. The sound speed propagation is measured at different PVA-C % weight/weight concentrations (5.0, 7.5, and 10.0%). At least, 8 samples/% are considered. As expected, the velocity increases with the % of the samples (Table 1).

PVA-C [%]	Sound speed [m/s]
5.0	1518.25 ± 1.02
7.5	1530.29 ± 2.17
10.0	1537.23 ± 3.15

Table 1. Sound speed at different PVA concentrations.

The results showed low scattering with the manufacturing procedure. Values for 10% concentration agree with those observed in [1] using the autoclave process (relative error about 0.2%), thus validating the procedure. In the literature, breast tissue shows sound speed in the range of 7.5% PVA-C [5].

Compression tests

Out-of-autoclave cylindrical specimens (26 mm diameter, 40 mm length) were tested at 4 mm/min

velocity in a universal testing machine (INSTRON, mod 3366). Representative stress-strain curves for different PVA-C concentrations are shown in Figure 1, while Young's modulus (*E*) is in Table 2. The values
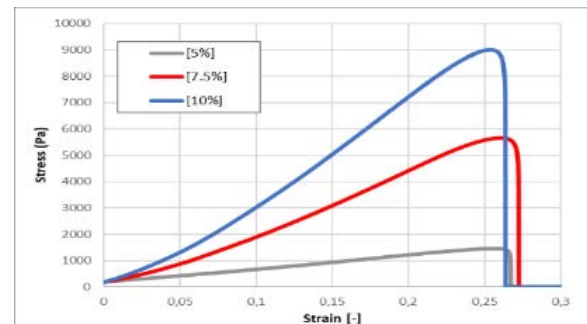
Figure 1. Stress-strain compression curves at 4 mm/min.

for each concentration are representative of different breast tissues, even tumors [6].

PVA-C [%]	E [kPa]	Similar breast tissue properties
5.0	5.16 ± 0.27	Fat, glandular, DCI tumour
7.5	22.85 ± 1.71	Fat, glandular, tumour
10.0	39.89 ± 1.53	Glandular, tumour

Table 2. Mechanical properties of PVA samples

Conclusions

This work presents an out-of-autoclave PVA-C sample procedure using an express pressure pot. The procedure is validated by comparing the sound speed velocity at different PVA concentrations with those obtained by the original procedure. Mechanical properties in compression tests are obtained, showing a stiffness increment for higher concentrations.

References

1. K.J.M. Surry et al, Phys. Med. Biol. 49 5529, 2004.
2. E. Villa et al, Sci Rep 10, 20401, 2020.
3. L. Elvira et al, J. Ultrasmedbio, 45, 2019.
4. M. Tiago et al, IEEE Trans. Ultrason. Ferroelectr. Freq. Control, 66:109-118, 2019.
5. K. Zell et al, Phys. Med. Biol. 52 (20), 2007.
6. N. G. Ramião et al, Biomechan. and Mod. in Mechanobiol, 15(5), 1307-1323, 2016.

Acknowledgements

DEVELOPMENT AND MODELLING OF FUNCTIONALLY GRADED BIOINSPIRED HIP IMPLANT IN REDUCING STRESS SHIELDING

Seyed Ataollah Naghavi (1). Jia Hua (1,2). Mehran Moazen (3). Steve Taylor (1). Chaozong Liu (1)*

1. Institute of Orthopaedics & Musculoskeletal Science, University College London, Royal National Orthopaedic Hospital Stanmore, London, HA7 4LP, UK

2. School of Science and Technology, Middlesex University, London, NW4 4BT, UK

3. Department of Mechanical Engineering, University College London, London, WC1E 6BT, UK

Introduction

Currently, total hip replacement surgery is an effective treatment for osteoarthritis, where the damaged hip joint is replaced with an artificial joint [1]. Stress shielding is a mechanical phenomenon that refers to the reduction of bone density as a result of reduced force distribution acting on the surrounding cortical bone. At present, solid hip implants undergo too much bone resorption secondary to stress shielding. This is due to their solid metallic nature, which are much stiffer than the surrounding bone. With the advance of 3D printing technology such as selective laser melting (SLM), we are now capable of producing graded lattice structures. Microstructures allow a better force distribution to the host bone which can mimic the surrounding bone tissue properties and reduce the stress shielding effect [2].

Methods

Bioinspired lattice structures such as Gyroid and Schwarz Diamond triply periodic minimal surface (TPMS) structures have high mechanical strength and osseointegration properties. Hence, these TPMS structures have a very high potential to be used for developing fully porous hip implant [3]. In a study by Kladovasilakis [4], several porous hip implants with different lattice structures (Gyroid, Voronoi and Schwarz Diamond) were developed and optimized via altering the strut thickness and relative density (50-65%) according to the initial the stress distribution on the struts with uniform distribution [4].

Results

In a study by Kladovasilakis, a load of 5,300 N was applied to different micro-structured hip implants and was shown that Scharwarz Diamond structure had the lowest peak compressive stress (529 MPa) when compared to Gyroid (615 MPa) and Voronoi (1088 MPa) structures. Factor of safety of Scharwarz Diamond, Gyroid and Voronoi were also calculated to be 2.08, 1.79 and 1.01 respectively. Based on these results, it is shown that the functionally graded TPMS Scharwarz Diamond could withstand almost twice the maximum static load that the hip implant receives [4].
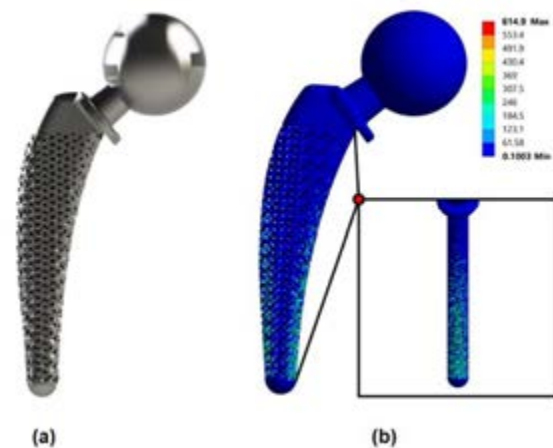
Figure 1: Topology optimization with functionally graded Gyroid structure (a) design and (b) FEA. [4]

Conclusion

In essence, functionally graded density implants have a reduced stress shielding compared to current solid hip implants. This is evidenced by higher amount of stress distribution on the surface of the cortical bone when comparing the porous implant with fully solid implant which transfers lower stress to the surrounding hot bone. The architected hip implants presented in recent studies shows clinical promise in reducing bone loss while preventing implant micromotion, periprosthetic fracture and the probability of revision surgery. [2].

Acknowledgements

References

1. Y. Wang, S. Arabnejad, M. Tanzer, D. Pasini (2018). Hip implant design with three-dimensional porous architecture of optimized graded density, Journal of Mechanical Design 140 (11).

2. He Y, Burkhalter D, Durocher D, Gilbert JM (2018). Solid-Lattice Hip Prosthesis Design: Applying Topology and Lattice Optimization to Reduce Stress Shielding From Hip Implants. ASME. Frontiers in Biomedical Devices.

3. Mansour, M.T.; Tsongas, K.; Tzetzis, D.; Antoniadis, A. The in-plane compression performance of hierarchical honeycomb additive manufactured structures. IOP Conf. Ser. Mater. Sci. Eng. 2019, 564, 012015.

4. Kladovasilakis N., Tsongas K., Tzetzis D. Finite Element Analysis of Orthopedic Hip Implant with Functionally Graded Bioinspired Lattice Structures. Biomimetics. 2020;5:44. doi: 10.3390/biomimetics5030044.

GELATIN/ CELLULOSE NANOFIBRIL COMPOSITE: A PROMISING FORMULATION FOR INJECTION AND BIOPRINTING PURPOSES

Sara Nejati, Luc Mongeau

Mechanical Engineering Department, McGill University, Canada

Introduction

Gelatin is a promising material for tissue engineering and regenerative medicine applications due to its biocompatibility, biodegradability, and abundance. Despite the advantages of gelatin, its fast gelation at room temperature and poor mechanical properties limits its applications in tissue engineering, particularly for injection and bioprinting purposes [1]. To overcome this important hindrance, we introduced cellulose nanofibrils (CNFs) into gelatin-based hydrogels. Nanocellulose has been widely explored for tissue engineering applications and shown to be a promising reinforcement for improving mechanical and rheological properties of biomaterials [2].

Methods

Firstly, methacrylated gelatin (GelMA) was synthesized as described elsewhere and Fourier transform infrared (FTIR) spectroscopy was used to confirm its proper methacrylation. Then, 10 %w/w GelMA solutions with different CNF filling content (0.25%, 0.5%, 0.75%, and 1%) were prepared and GelMA/CNF composite hydrogels were prepared by getting samples exposed to UV light. Prepared composites where finally characterized in terms of morphology, swelling ratio, gelation time, and rheological properties.

Results

The FTIR results confirmed the proper methacrylation of gelatin (Figure 1, a). The morphology of the CNF was studied using TEM and the diameter and length of the nanofibrils, measured using ImageJ, were around 26.3 ± 1.8 nm and 4.8 ± 0.22 µm, respectively (Figure 1, b). The swelling ratio of the samples were evaluated by immersing them in PBS at 37 °C. The rheological properties of the samples were characterized using a photorheometer and hydrogels' gelation time at room temperature, both without UV and under UV light, were measured (Figure 1, c. and Table 1).

Samples	Swelling ratio (%)	Gelation time without UV	Gelation time with UV (s)
GelMA	24.3	17 min	26
GelMA/0.25%CNF	26.55	1 h	32
GelMA/0.5%CNF	33.17	8 h	55
GelMA/0.75%CNF	38.21	5 d	78
GelMA/1%CNF	41.74	Never	105

Table 1
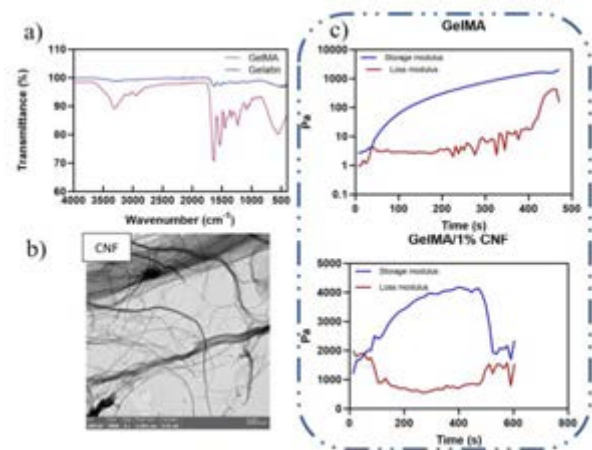
Figure 1: a) FTIR results of Gelatin and GelMA. b) TEM image of CNFs. C) Rheological properties of samples.

Discussion

It was observed that the swelling ratio of the samples increased as the CNF content increased. This occurred because the presence of CNF nanofibrils between GelMA chains inhibits some potential crosslinking, and the lower the crosslinking, the higher the swelling ratio. Moreover, incorporation of CNFs within GelMA-based hydrogels could significantly delay their gelation at room temperature. This is most likely because the physical association of gelatin chains, which is the main mechanism behind the gelation of gelatin at room temperature, can be highly limited by the CNF fibrils. This property is particularly favorable for injection and printing applications, where fast gelation would clog the needle and negatively affect the shape fidelity. Investigation of rheological properties under UV light displayed that although introducing CNFs delayed the gelation time from 26 s to 105 s, the gelation is still fast, meaning that the proposed composite is very promising for in situ forming applications.

References

1. Du, H., Liu, W., Zhang, M., Si, C., Zhang, X., & Li, B. (2019). Cellulose nanocrystals and cellulose nanofibrils based hydrogels for biomedical applications. *Carbohydrate Polymers*, *209*(January), 130–144.
2. Jiang, Y., Zhou, J., Shi, H., zhao, G., Zhang, Q., Feng, C., & Xv, X. (2020). Preparation of cellulose nanocrystal/oxidized dextran/gelatin (CNC/OD/GEL) hydrogels and fabrication of a CNC/OD/GEL scaffold by 3D printing. *Journal of Materials Science*, *55*(6), 2618–2635.

DEVELOPMENT OF SOL-GEL TiO$_2$/HYDROXYAPATITE COMPOSITE OSTEOINDUCTIVE COATINGS

José Rodrigues (1), Laura Grillini (2), Riccardo Bendoni (2), Lucia Forte (2), Gwendolen Reilly (1), Frederick Claeyssens (3)

1. University of Sheffield, INSIGNEO Institute for In Silico Medicine, United Kingdom; 2. Fin-ceramica Faenza SPA, Italy; 3. University of Sheffield, Kroto Research Institute, United Kingdom

Introduction

Coating an implant with an osteoinductive material is a common technique used to improve osteointegration of orthopaedic implants, including spinal implants. This is particularly important for implants based on Polyether Ether Ketone (PEEK), as its inert nature does not allow for proper integration, leading to implant failure. As the basis of bone mineral, hydroxyapatite (HAP) is a well-documented coating material. However, current coating techniques can alter HAP crystallinity, negatively affecting both mechanical and biological performance of the coating [1]. An alternative could be the development of a composite coating, where HAP is incorporated into a different material. A good candidate is TiO$_2$, as it naturally occurs on Ti-based implants, has good osteoinductive properties of its own, and can be sintered and crystallized at temperatures which do not affect HAP's own crystal structure. Moreover, TiO$_2$ can be synthesised through Sol-Gel chemistry, where organic liquid precursors are hydrolysed to form an inorganic gel. A substrate can then be dipped into the gel, forming an inorganic solid coating after dried and sintered [2]. This work aims to study the development of sol-gel TiO$_2$/HAP composite coatings on PEEK and Ti-based substrates. The goal is to find which conditions result in coatings with optimized mechanical and biologic performance.

Methods

TiO$_2$/HAP composite was synthesised by hydrolysis of titanium isopropoxide in absolute ethanol at 70 °C for 24 hours. Acetic acid glacial was used to control the reaction, and Mg-enriched HAP (Fin-ceramica) was added before starting hydrolysis with ultrapure water. The final volume was adjusted to 40 ml by adding absolute ethanol. The coatings were developed on glass, Ti-6Al-5V and PEEK substrates pre-treated with air plasma (Zepto, Diener). A TinkerKit Braccio Robot (Arduino) was used to dip coat the substrates, with each cycle involving: 1- Coating in TiO$_2$/HAP gel; 2- Drying at 70 °C; 3- Washing twice in ultrapure water; 4- Drying at 70 °C. The coated samples were sintered at 250 °C for 6 hours and washed in an ultrasonic bath for 15 minutes. A Definitive Screening Design (DSD) is being used to study the effect of coating conditions on overall performance. Table 1 summarised the factors in study. Samples from each run will be analysed by water contact angle (WCA), lap shear adhesion testing, and *in-vitro* biologic performance, measuring metabolic and ALP activity at day 14 on hTERT-MSCs Y201 [3].

Factor	Description	-	0	+
A	Substrate	Ti-6Al-4V	--	PEEK
B	TiO2/HAP (w/w)	1/0	1/0.75	1/1.5
C	Layers (number)	1	3	5
D	Dip time (min)	1	3	5
E	Robot timing (ms)	10	20	30
F	ΔT (°C/min)	4	12	20

Table 1 – DSD factor description.

Results

Preliminary results on glass substrates show changes on WCA between uncoated and coated substrates (table 2). Coating with non-sintered TiO$_2$ turns glass more hydrophobic, while sintered TiO$_2$ turns the sample more hydrophilic. The presence of HAP in sintered coatings drops WCA slightly lower. Similar results are also observable on Ti-6Al-4V samples.

Substrate	Condition	WCA
Glass	No Coating	42.82°
	TiO$_2$	86.55°
	TiO$_2$ sintered	27.41°
	TiO$_2$/HAP sintered	24.41°
Ti-6Al-4V	No Coating	52.46°
	TiO$_2$ sintered	18.70°
	TiO$_2$/HAP sintered	18.12°

Table 2 – Preliminary water contact angle results.

Figure 1 – Water contact angle on Ti-6Al-4V substrates: a) No coating; b) TiO$_2$ sintered; c) TiO$_2$/HAP sintered.

Discussion

Preliminary results show that it is possible to coat different materials with a sol-gel TiO$_2$/HAP composite. Sintering is also shown to affect the surface properties of the coating. The DSD results will allow to develop coatings with optimized mechanical and biologic performance.

References

1. R.I.M. Asri, *et al.*, J Mech Behav Biomed Mater 57 (2016) 95-108.
2. D. Kumar, *et al.*, Materials & Design 86 (2015) 855-862
3. S. James, *et al.*, Stem Cell Reports 4(6) (2015) 1004-1015

Acknowledgements

A BIOINSPIRED ORTHOPAEDIC BIOMATERIAL WITH TUNABLE MECHANICAL PROPERTIES BASED ON SINTERED TITANIUM FIBRES

Matthias Rüger (1,2), Andreas Seitz (3), Katja Nuss (4), Brigitte von Rechenberg (4), Daniel Seitz (5), Cris Kostmann (6), Peter Quadbeck (6), Olaf Andersen (6), Caitlyn J. Collins (1,7)

1. ETH Zurich, Switzerland, 2. University Children's Hospital, UZH, Switzerland, 3. UFB, Centre for Trauma Research, Ulm, Germany, 4. Vetsuisse Faculty, UZH, Switzerland, 5. BioMed Center Innovation gGmbH, Bayreuth, Germany, 6. Fraunhofer IFAM, Dresden, Germany, 7. Virginia Tech, USA

Introduction

Inadequate mechanical compliance of orthopaedic implants can result in excessive strain of the biologic interface and ultimately, aseptic loosening. To compound this issue, the elastic modulus of human trabecular bone within the proximal femur can vary by as much as 200% between the trochanteric region and femoral head [1]. With these significant interindividual variations in bone density and changes in remodelling capacity over time, a biomimetic orthopaedic material designed for load bearing bone should be (i) available in mechanical strengths and stiffnesses most suitable to the peri-implant bone tissue of a specific patient, (ii) allow for continuous remodelling processes within and around the implant to comply with biological changes at the host site and (iii) provide a large surface area for optional biofunctionalization or coatings [2]. We present a fibre-based biometal with adjustable anisotropic mechanical properties to facilitate remodelling and improve long-term implant survival.

Methods

A material comprised of strategically layered, sintered titanium fibres (TiFi) was developed. The matrix material is an unalloyed titanium with an oxygen content of 0.44±0.04 wt.-% in the sintered state. Parallel (//) and cross-ply topologies in a ratio of 1:1 and 2:1 (denoted X1:1 and X2:1) (Fig1A) at two different porosities (75% and 85%) were manufactured. Cubic and square beam specimens were tested under compression (in three orthogonal axes) and under 3-point bending and torsion until failure, respectively, to characterize anisotropy. Cylindrical, 70% porosity X2:1 TiFi samples were implanted in a sheep metaphyseal trepanation model for eight weeks, following institutional standard protocol and ethics approval (ZH 212/19). Osseointegration within the explants was investigated by micro-computed tomography (Scanco µCT 45, 10.4 µm voxel size) to confirm *in vivo* biocompatibility. For inferential statistics, we applied the Mann-Whitney U test for independent samples, when applicable.

Results

TiFi demonstrated compressive yield strengths of up to 50 MPa and anisotropy according to fibre layout (Table 1). Samples with 75% porosity were both stronger and stiffer than with 85% porosity (Fig 1B). The highest bending modulus was found in samples with parallel fibre orientation, while the highest shear modulus was found in cross-ply layouts. Implants demonstrated uncompromised circumferential osseointegration and bone invasion in vivo (Fig1B).

Porosity	Topology	X-Axis	Y-Axis	Z-Axis
	//	48.9±0.5	3.7±0.5	17.4±3.2
75%	X1:1	22.1±10	4.9±3.0	23.6±15
	X2:1	26.1±6.9	3.6±2.1	11.3±2.6
	//	14.3±0.8	1.2±0.8	4.0±0.3
85%	X1:1	12.3±2.1	2.8±2.5	10.9±2.5
	X2:1	8.7±1.6	1.0±0.3	8.8±8.1

Table 1: Compressive yield strength (MPa) at 0.2% offset (n=3 per topology (Top.) and per Axis for each porosity (Por.)).
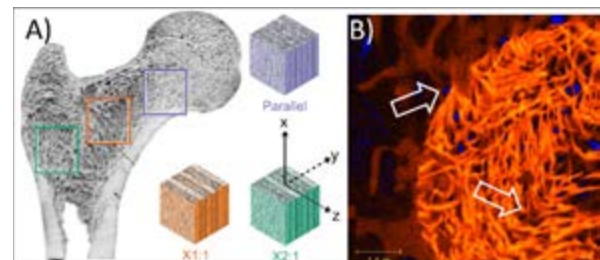
Figure 1: A) TiFi is based on multiple layers of interlaced titanium fibre mesh in parallel and cross-ply topologies. B) Osseointegration after 8 weeks (false colors for contrast: blue-low and orange-high density).

Discussion

Although mechanical testing relied on a low number of repetitions per modality, testing demonstrated small variance between trials and indicated TiFi mechanical properties were well within the range and anisotropy of human trabecular bone. Direct bone apposition and osseointegration was observed without obvious gaps or fibrous tissue on the implant surface, supporting the hypothesis that a lattice-like structure and tunable mechanical properties promote remodelling. Image-based quantification of osseous tissue ingrowth and histological analysis can confirm these initial findings. Ultimately, the biometal introduced in this study demonstrated anisotropic mechanical properties similar to natural bone, excellent osteoconductivity and consequently, feasibility as an orthopaedic implant material.

References

[1] Oftadeh et al, J Biomech Eng, 137:0108021-5, 2015
[2] Nagarajan et al., Engineering, 5:702-720, 2019

BIOLOGICAL AND MECHANICAL PROPERTIES OF AN EXPERMINTAL DENTAL ALGINATE MODIFIED FOR SELF DISINFECTION

Lamia Singer (1), Christiane Szekat (2), Gabriele Bierbaum (2), Christoph Bourauel (1)

1. Oral Technology, University Hospital Bonn, Germany;
2. Institute of Medical Microbiology, Immunology and Parasitology, University Hospital Bonn, Germany

Introduction

Dental impression is a potential cause of cross transmission of pathogens between the operator, patient and laboratory technician. However, disinfection of alginate impression material could compromise its dimensional accuracy and physical properties. Thus, this study aimed to incorporate natural and chemical antimicrobial agents to dental alginate for pre and post setting self-disinfection.

Methods

Conventional fast-set dental alginate impression material was used in this study. Colloidal silver solution (500 ppm), Colloidal copper (50 ppm) and an aqueous *Boswellia sacra* plant extract were prepared and used for preparation of different dental alginate groups. Antimicrobial activity was assessed using agar disc diffusion assay against *Candida albicans*, *Streptococcus mutans* and *Micrococcus luteus, Escherichia Coli, Staphylococcus Aureus* [1]. Dimensional accuracy was evaluated through taking alginate impressions of a metallic mold recommended by ISO 1563 standard [2], that were then poured with stone. Dimensional accuracy was determined from the mean of measurements taken between fixed points on the casts using stereomicroscope at magnification of 12X and was calculated using the following equation:

$$L = [(L2 - L1) / L1] \times 100$$

L1 is the distance between the lines on the matrix and L2 is the distance between the lines on the stone mode. Elastic recovery of alginate was assessed according to ISO 1563 using a circular split mold of 12.5 mm diameter and 20 mm height. Tear strength was evaluated using a Zwick testing machine until failure at a cross head speed of 500 mm/min [3].

Results

The two modified groups showed significantly higher inhibition zones against *E. coli, S. mutans and C. albicans* compared to the control that showed no antimicrobial activity at all. Nano metal ions (Ag+Cu) group showed higher antimicrobial activity against *M. luteus* compared to the other tested groups. There was insignificant difference between the groups against *S. aureus*. One-way analysis of variance (ANOVA) showed no statistically significant difference in the mean values of dimensional accuracy (%) and tear strength between all the tested groups.

Groups	Mean	SD
Control	0.82	0.3
Ag+Cu	0.79	0.7
B.sacra	0.77	0.2

Table 1: The mean (N/mm) and standard deviation (SD) values of tear strength for the three tested groups.

Elastic recovery of the *Boswellia sacra* extract and nano metal-ions modified groups were insignificantly different from the control group. All the tested groups showed elastic recovery greater than 95 %.
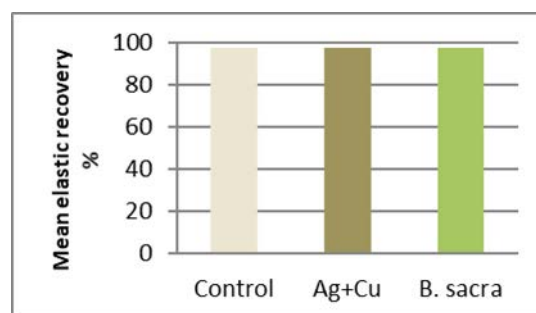
Figure 1: The mean and standard deviation (SD) values of elastic recovery in % for the three tested groups.

Discussion

Nano metal ion solutions and *Boswellia sacra* extract enhanced the antimicrobial activity of alginate without affecting its dimensional accuracy, tear strength and elastic recovery. Mixing alginate with plant extracts and nano metal ions could be a promising potential for preparation of a self-disinfecting alginate impression material without affecting its performance.

References

1. Wang J et al, Angle Orthod, 77:894-900, 2007.
2. ISO 1563 "Dental alginate impression material" Geneva Switzerland, 1990.
3. Sahin V et al, J. Prosthet. Dent, 124:69–74, 2020.

.

PRELIMINARY APPROACH OF AN ALTERNATIVE SOLUTION FOR THE BREAST IMPLANT SHELL

Ana Margarida Teixeira (1), António André (1), Bruno Areias (1), Pedro Martins (2,3)

1. INEGI/FEUP, Portugal; 2. INEGI/LAETA, Portugal; 3. ARAID, i3A, University of Zaragoza, Spain

Introduction

In 2020, breast augmentation was the most performed plastic surgical procedure worldwide [1]. Even though silicone implants are the gold standard, different factors might lead to implant failure, including mechanical loading. This was proved by our group, concluding that fatigue damage can be a potential cause of the in vivo failure [2]. Moreover, another major complication related to breast implants is capsular contracture, which might cause implant distortion, breast pain and poor aesthetic outcome [3]. To address this issue, most implants are manufactured with a textured surface, which is currently done by using calibrated salt grains [3] or through a negative-contact imprint of polyurethane foam [4]. As an alternative, in this work, a different texture is produced using an impression technique and its mechanical properties are investigated.

Methods

The textured surface was obtained through a PLA (polylactic acid) texture stamp and an alginate sheet. Firstly, a PLA stamp (Figure 1a) was printed using an Ultimaker 3 printer. Secondly, an alginate solution was poured over the mold and smoothed, being then crosslinked with 50 mM $CaCl_2 \cdot 2H_2O$ (Calcium chloride dihydrate) for ≈1h. The sheet of alginate was then used to stamp the PDMS (polydimethylsiloxane, SYLGARD™ 184), which was prepared in a ratio of 10:1 and initially cured at 75ºC for ≈5min. The alginate sheet was slowly placed on the top of the PDMS, with the textured surface facing down and slightly pressed. The PDMS was left at room temperature for the final curing during ≈24h. When cured, the alginate sheet was taken off and PDMS samples were cut in a dog-bone shape (Figure 1b). Using a uniaxial tensile machine, the PDMS samples were tested to failure at 20 mm/min with an initial preload of 0.20N. The force-displacement data was recorded, and the stress-strain data was calculated.
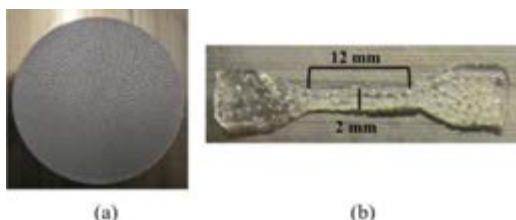
Figure 1: (a) PLA stamp; (b) PDMS sample

Results

For this study, 3 samples were tested, and the average results are presented. The final thickness was 1.05±0.16 mm, which is within the range found in literature [5]. In the final stress vs. strain curve (Figure 2), the stress was calculated at different strain percentages (33%, 66% and 133%) in order to compare with previous work [5].
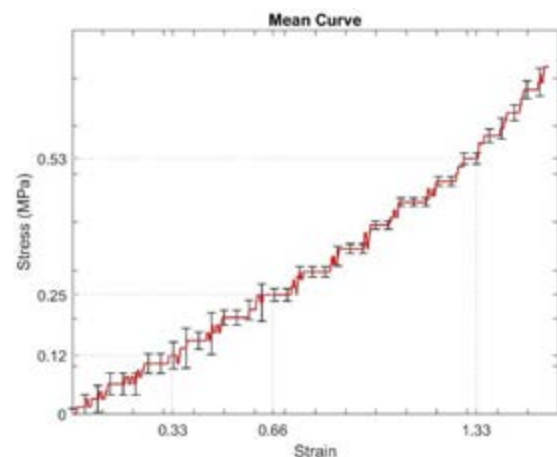
Figure 2: Mean curve for the new texture, indicating the stress at 33%, 66% and 133% strain.

Discussion

Comparing with literature [5], the stress values obtained in this work are significantly lower, a possible indicator that the proposed texture contributes to a weaker structure, leading to a quicker rupture. Comparing to PIP implants, this approach does not improve the mechanical properties. A design with smaller pores with a homogeneous distribution might provide better results regarding the mechanical properties. Therefore, for future work, the testing of alternative textures along with imaging analysis and cell interaction is required.

References

[1] "ISAPS International Survey on Aesthetic / Cosmetic Procedures Performed in 2020"
[2] Ramião et al, *J. Mech. Behav. Biomed. Mater,* 72:22–28, 2017.
[3] Garabédian et al, *Surf. Topogr. Metrol. Prop.*, 5(2):025004, 2017.
[4] Atlan et al, *J. Mech. Behav. Biomed. Mater.*, 88:377–385, 2018.
[5] Ramião et al, *Aesth Plast Surg*, 250–264, 2017.

Acknowledgements

HYBRID MEMBRANE AS INNOVATIVE MATERIALS FOR BIOMEDICAL APPLICATIONS

Martina Todesco (1)(2), Andrea Martella (3), Saima Imran (2)(4), Martina Casarin (2)(5), Gino Gerosa (2)(4), Chiara Giulia Fontanella (3), Andrea Bagno (2)(3)

1. Department of Civil, Environmental and Architectural Engineering, University of Padua, Italy
2. L.i.f.e.L.a.b. Program, Consorzio per la Ricerca Sanitaria (CORIS), Veneto Region, Italy
3. Department of Industrial Engineering, University of Padua, Italy;
4 Department of Cardiac, Thoracic Vascular Sciences and Public Health, University of Padova, Italy
5. Department of Surgery, Oncology and Gastroenterology, University of Padova, Italy

Introduction

Hybrid materials have been recently proposed to bypass the drawbacks of synthetic and biological grafts: they are obtained by coupling synthetic polymers with decellularized tissues to join the mechanical features of synthetic materials and the superior biocompatibility of biological tissues. In particular, when blood-contacting materials are requested, biological tissue are placed in contact with blood improving hemocompatibility [1].

In the present work, hybrid membranes (HYMEs) have been produced by assembling decellularized bovine pericardium and a polycarbonate urethane available in two formulations: Chronoflex AR (CF AR) and Chronoflex ARLT (CF ARLT) (AdvanSource Biomaterials, Wilmington, MA, USA). The second formulation differs from the first by the presence of 9% silica microparticles to reduce its tackiness [2].

Methods

Native bovine pericardium (NBP) was collected from a local slaughterhouse, isolated and decellularized following the TriCol procedure: alternate hypotonic and hypertonic solutions and two detergents, e.g. Tergitol and sodium cholate. Tissues were eventually treated with Benzonase^{TM} to degrade nucleic acids chains.

HYMEs were realized by solution casting: decellularized bovine pericardium (DBP) was placed into an aluminum frame and the polymer solution was gently poured over the fibrous side. The material was dried in a vacuum oven at 40°C for 30 hours.

Two HYMEs were made by coupling DBP with CF AR (DBP AR) and with CF ARLT (DBP ARLT): they were analyzed in terms of structure and composition, and from the biomechanical and cytotoxicity points of view. Mechanical characterization was carried out by uniaxial tensile tests evaluating HYMEs response to load until failure (strain rate of 1 mm/s). Fatigue tests were also performed to analyze the effect of repeated cycles on the material resistance. Test was conducted by imposing cycles up to 20% for 3600 seconds at a strain rate of 1.3 mm/s and, subsequently, the specimen was loaded to failure as previously described.

Tests were performed at room temperature and samples were immersed in saline solution (0.9% NaCl) to prevent dehydration.

In vitro tests were performed according to UNI EN ISO 10993-5 in order to check HYMEs cytotoxicity: human umbilical vein endothelial cells (HUVEC) were seeded over HYMEs. After 24 h and 7 days, cells vitality was analyzed and immunofluorescences were performed.

Results

HYMEs exhibited appealing features with regard to cytocompatibility: the absence of cytotoxic effects was ascertained, and after 7 days cell proliferation was improved. As to the mechanical tests, Young's modulus and ultimate tensile strength (UTS) values did not show significant differences comparing polymeric samples, and DBP AR and DBP CRLT. As shown in Figure 1, fatigue tests showed that cyclic loads affect material strength: failure strain (FS) decreased by 44.82% and 40.79% for DBP ARLT and DBP AR, respectively, UTS decreased by 64.8% and 30.62%, respectively.

Conclusions

Hybrid materials can usefully combine the mechanical resistance of synthetic polymers and the biocompatibility of biological tissues. These latter, once decellularized, are prone to in vivo recellularization.
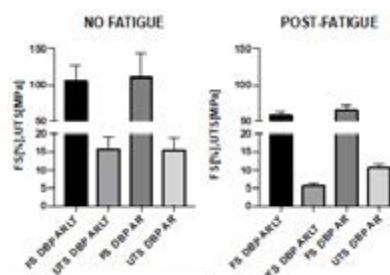

Figure 1: Failure Strain (FS) and Ultimate Tensile Strength (UTS) values before and after fatigue tests.

References

1. M. Todesco et al, J. Mater. Sci. Mater. Med., 32, 86, 2021.
2. M. Todesco et al, Biomater. Res. 25, 26, 2021.

Acknowledgements

COLOR-DOPPLER BASED HEMODYNAMICS OF AORTIC PHANTOMS

Maria Nicole Antonuccio (1,2), Francesco Bardi (1,2), Emanuele Vignali (1),
Emanuele Gasparotti (1,3), Alexandre This (4), Laurence Rouet (4), Stéphane Avril (2), Simona Celi (1)

1. BioCardioLab, Fondazione Toscana G. Monasterio, Italy; 2.MINES Saint-Étienne, Univ Lyon, Univ Jean Monnet, France; 3.Dept. of Information Engineering, University of Pisa, Italy; 4.Philips Research Paris, France.

Introduction

An effective assessment of patient-specific hemodynamics is fundamental for an early identification of risk factors related to vascular diseases. Flow patterns can be partially captured by 2D Color-Doppler ultrasound (US) imaging that provides a projection of the blood flow on the US beams. Biomechanics can augment the missing flow information to quantify hemodynamics patterns. This work presents an example of velocity vector fields reconstruction using Color-Doppler images and an aortic phantom.

Materials and Methods

A patient-specific model of thoracic aorta was 3D printed in Clear Resin (Formlabs). The phantom (Fig. 1a) was inserted in a mock-circulatory loop system that reproduces the blood flow inside the aorta. A steady flow was imposed at the inlet. The descending aorta (DAo) and supra-aortic branches were the outlets. The phantom was filled with a blood-mimicking fluid. Color-Doppler images were acquired in long and transversal views using an iE33 US scanner (Philips Healthcare) with a 5 MHz linear array. The velocity vector field was reconstructed by adapting to vessels the formulation introduced in [2]. The Color-Doppler velocity V_{US} is the input of the algorithm (Eq. 1) that minimizes a cost-function, $J[V_{Rec}]$, to retrieve the 2D velocity field V_{Rec} in the bi-dimensional domain of interest Ω_P:

$$J[V_{Rec}] = \lambda_{US} \int_{\Omega_P} (V_{Rec} \cdot r_i - V_{US})^2 +$$
$$\lambda_{Div} \int_{\Omega_P} (\nabla \cdot V_{Rec})^2 + \lambda_{BCs} \int_{\partial \Omega_P} \|V_{Rec} - V_{US}\|^2 + \lambda_{Neu} \int_{\partial \Omega_P^*} \|\nabla V_{Rec} \cdot n\|^2 +$$
$$\lambda_{Smooth} \int_{\Omega_P} \|\nabla V_{Rec}\|^2$$

(1)

The five terms of Eq. 1 are: 1) deviation of V_{Rec} from V_{US}; 2) divergence-free flow assumption, 3) Dirichlet conditions at boundary $\partial \Omega_P$; 4) Neumann conditions at inlet/outlet ($\partial \Omega_P^*$); 5) spatial smoothness constraint. A weighting factor (λ_i) is associated to each term.

Results

The results of the velocity reconstruction are reported in Figure 1b-1c. In the aortic arch, the reconstruction shows some zones with helical flow and recirculation. On the contrary, in the DAo, the flow regime appears to be laminar with no helical patterns. These results confirmed velocity trends observed both in-silico and in-vivo on the same aortic geometry [3].
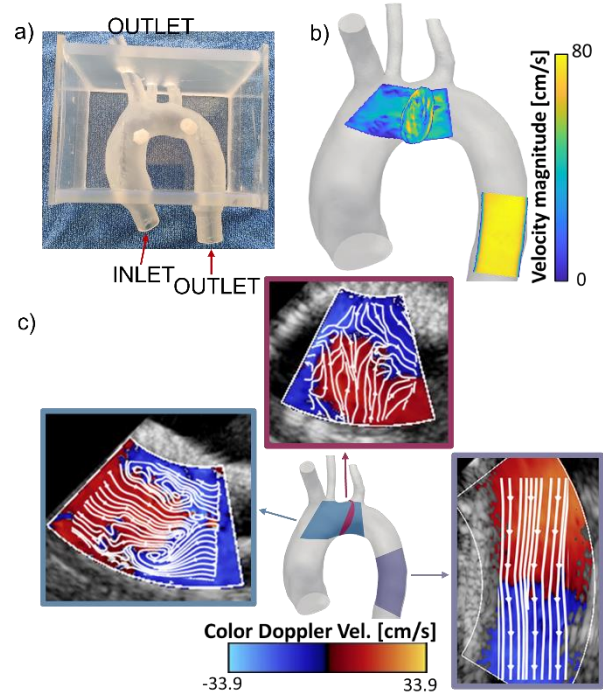
Figure 1: 3D printed phantom (a); Reconstructed velocity magnitude (b); 2D Color-Doppler acquisitions and reconstructed velocity streamlines (c).

Discussion

In the aortic arch, Color-Doppler images show swirling velocities that are preserved in the reconstructed velocity field. The reconstruction complements the missing flow information given by 2D Color-Doppler. The velocity reconstruction from Color-Doppler data is promising as it will also allow to compute other hemodynamic quantities such as wall shear stress/pressure and to complement vascular diseases diagnosis. Moreover, 3D printed models, inserted in a mock-circulatory loop, can be beneficially used to investigate a variety of geometries and flow conditions.

References

1. Gimbrone et al, Cardiovasc Pathol., 22(1):9-15, 2013
2. Assi et al, Phys. Med. Biol., 62:7131–7147, 2017.
3. Boccadifuoco et al, Cardiovasc Eng Tech 9:688–706, 2018.

Acknowledgements

RELIABILITY OF MAGNETIC RESONANCE IMAGING MEASUREMENTS OF FATTY INFILTRATION IN ADULTS WITH SPINAL DEFORMITIES

Erica Beaucage-Gauvreau (1), Pieter Severijns (1), Thomas Overbergh (1), Alexander Meyen (1), Thijs Ackermans (1), Niels Schepens (2), Lieven Moke (1, 2), Lennart Scheys (1,2)

1. Institute for Orthopaedic Research and Training (IORT), Faculty of Medicine, KU Leuven, Leuven, Belgium; 2. Division of Orthopaedics,, University Hospitals Leuven, Leuven, Belgium

Introduction

Adult spinal deformity (ASD) is a complex and heterogenous disorder of the spine [1], often impacting functional abilities of patients during activities of daily living (ADL) [2]. Despite the known degeneration of muscles in patients with ASD due to fatty infiltration [3], muscles are not routinely evaluated for clinical decision-making. Indeed, current surgical treatments for ASD are mainly based on two-dimensional radiographic parameters that measure upright global spinal alignment. However, adding objective measurements of muscle structure is imperative to understand how muscles impact functional abilities. These subject-specific measurements can be integrated into musculoskeletal model (MSKM) to determine if decreased muscle strength contribute to the observed impaired performance in ADL in patients with ASD [4]. A method [5] to quantify fatty infiltration in muscles has been developed and validated on a healthy population, but has not previously been assessed in the ASD population. The aim of the study was to evaluate the reliability of this magnetic resonance imaging (MRI)-based segmentation method in patients with ASD, due to their known muscle physiological changes.

Methods

Fatty infiltration of the erector spinae and psoas was quantified using the method by De Seze et al [5]. Briefly, manual segmentation (Mimics v.22, Materialise, Belgium) was performed bi-laterally at the L4 and T12 (erector spinae only) levels on T1-weighted MRI images. Six regions of interest of $1cm^2$ were manually selected on the segmented muscles (four at L4 and two at T12) to represent a region minimally infiltrated by fat (Fig. 1). The pixel intensities within these six regions were pooled to determine the mean muscle pixel intensity and the 95% confidence interval (CI) for each patient. Contractile element (non-fatty) was defined as the muscle area corresponding to the pixel values between the 5th and 95th percentiles, while the non-contractile (fatty infiltration) element was defined as the muscle area with pixel intensity values below the 5th and 95th percentile. Intra-rater reliability of this method was assessed with two sets of measurements performed by one rater on five patients with ASD, one month apart. Inter-rater reliability was assessed with three trained raters performing measurements on the same five patients. The agreement between the intra- and inter- rater measurements were calculated with the intra-class correlation coefficient (ICC) (SPSS v.25, Chicago). ICC values >0.91, between 0.71-0.91, between 0.51-0.70, and <0.51 correspond to excellent, good, moderate, and poor agreement, respectively.

Results

Based on five repeated measures, the intra-rater variability was excellent with an ICC value of 0.979, 95% CI [0.948-0.991] (p<0.05). The intra-rater reliability was also excellent with an ICC value of 0.963, 95% CI [0.926-0.982] (p<0.05).
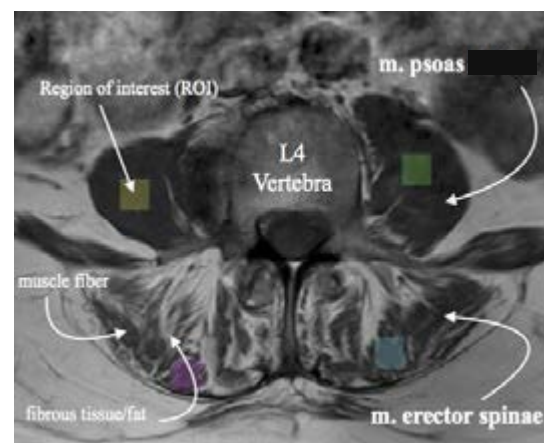
Figure 1: Axial view of MRI at L4. Four regions of interest (ROI) were placed bilaterally on the psoas and erector spinae to represent the regions with the least amount of fatty infiltration (black region), compared to region with fatty infiltration (white region) to differentiate these two regions in the muscles.

Discussion

The intra- and inter- rater reliability of this MRI-based segmentation method has been validated for patients with ASD, showing excellent results. This method allows to separate the contractile and non-contractile (fat and connective tissue) elements of the muscles in patients with ASD. The method can therefore be reliably used to integrate clinical parameters on muscle quality into subject-specific MSKM, to understand how fatty infiltration of the muscles in patients with ASD impact their movements and quality of life.

References

1. Smith et al, Neurosurg. Clin. N. Am, 24:143-56, 2013.
2. Pellise et al, Eur Spine J, 24:3-11, 2014.
3. Moal et al, Worl J Orthop, 6:727-737, 2015.
4. Severijns et al, Spine, 21:1059-1071, 2021.
5. De Seze et al, Surg Radiol Anat, 33:735-741, 2011.

IMAGE-BASED IN-VIVO ESTIMATION OF AORTIC LOCAL STIFFNESS AND HEMODYNAMICS

Katia Capellini (1), Emanuele Gasparotti (1), Emanuele Vignali (1), Benigno Marco Fanni (1), Martino Andrea Scarpolini (1), Filippo Cademartiri (2) and Simona Celi (1)

1. *BioCardioLab, Fondazione Toscana G. Monasterio, Italy; 2. Dipartimento Immagini, Fondazione Toscana G. Monasterio, Pisa, Italy.*

Introduction

Computational fluid dynamics (CFD) simulations and fluid structure interaction (FSI) simulations are effective instrument adopted in literature to investigate aortic hemodynamics. Nevertheless, these numerical approaches are characterized by some limitations such as the hypothesis of rigid wall for CFD and assumptions for material properties together with high computational times for FSI simulations. The knowledge of actual material properties of aortic tissues is crucial for the analysis of different pathologies. Currently the material stiffness is characterized through experimental tests requiring harvesting of ex-vivo tissues [1]. In order to in-vivo estimate wall stiffness and properly set FSI setup to improve simulation accuracy, a great effort was recently devoted on the development of new methods to evaluate wall stiffness. The integration of Radial Basis Functions (RBF) mesh morphing technique with numerical simulations turned out to be an effective tool to cope vessel deformation by modelling the shape of computational models starting from biomedical images and in a meshless way [2,3].

In this study an aortic hemodynamic evaluation overcoming the main limitations of standard simulations technique was performed together with the implementation of a new in-vivo method based on biomedical images and RBF mesh morphing technique to estimate aortic stiffness.

Methods

ECG-gated CT datasets were segmented with a specific UNET deep neural network to obtain thoracic aortic 3D models at each phase of cardiac cycle. Through a mesh morphing approach, the movement of aortic wall was replicated to follow the geometric changes of aorta during cardiac cycle in a meshless way. The wall movement was synchronized with patient pulsatile flow during a CFD simulation execution. Thanks to the aortic displacements reconstruction, a method to estimate aortic local stiffness was developed. The circumferential strains were calculated by considering the aorta centerline and the cross-section variation between the minimum volume phase and the phase at maximum deformation. Due to the meshless nature of the mesh morphing implemented technique, the identification of same nodes at different cardiac phases was achieved. The circumferential stresses were estimated according to the equilibrium of a pressurized elbow shell. Then the stiffness was computed by assuming a linear constitutive equation and by evaluating the Young's modulus (E).

Results

The mesh morphing approach resulted to be an accurate instrument that introduced a negligible mesh deterioration, and it was able to cope the aortic movements with high geometric accuracy. Differences in hemodynamic parameters estimated with the new simulation approach were found compared to the standard simulations strategies. In particular, a difference in terms of flow eccentricity and time averaged wall shear stress estimation. Regarding the aortic wall stiffness estimation, the Young's modulus values for each node of aortic surface are depicted in Figure 1.
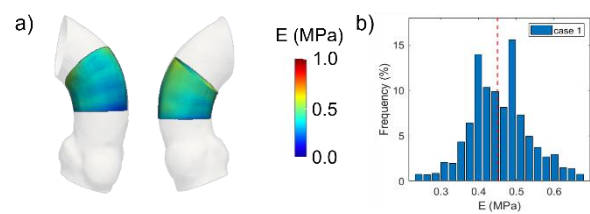
Figure 1: Young's modulus map on the ascending aorta (a) and the relative frequency of distributions for the mesh nodes (b).

Discussions

The integration of RBF mesh morphing technique, CT-gated images and CFD simulations was able to follow the aortic movements during cardiac cycle. In this way the consideration of actual geometric effects on the aortic hemodynamics was implemented with a relevant reduction in terms of computational costs compared to standard FSI approach. The estimation of aortic regional stiffness was successfully carried out and may represent an effective instrument for the in-vivo assessment of aortic material properties.

References

1. Vignali et al, Int. J. Robot. Res., 40(1): 224-235, 2020.
2. Capellini et al, J Biomech Eng, 140(11), 2018
3. Capellini et al, Med Eng Phys, 2020

Acknowledgments

IMPLEMENTATION OF A WAVELET-BASED PROCESSING METHOD ADAPTED TO DIFFRACTION ULTRASOUND COMPUTED TOMOGRAPHY OF BONE TISSUES

Elise Doveri, Mélanie Brie, Jeanne Baldisser, Laurent Sabatier, Vincent Long, Régine Guillermin, Philippe Lasaygues

Aix Marseille Univ, CNRS, Centrale Marseille, LMA UMR 7031, Marseille, France

Introduction

Current medical B-mode ultrasound does not readily allow imaging bone tissues and under subperiosteal cortical areas of bone. Many authors have discussed ultrasonic imaging of bones [1]. Our group has been focusing on the cross-sectional radial imaging process using diffraction-mode Ultrasonic Computed Tomography (USCT)[1],[2]. In the case of bone imaging difficulties are bound with the higher acoustical impedance difference, which strongly alters the propagation of the ultrasonic waves, and generally induces low Contrast-to-Noise Ratio (CNR) of the image. It is necessary to change the methods used for the processing of the ultrasonic signals. Our group developed a wavelet-based coded-excitation (WCE) method enabling to process all the information available in frequency and time [3]. The aim of this work is to investigate the feasibility of the WCE method as a mean of CNR enhancement of diffraction-mode USCT [4]. Experimental results on newborn arm phantom and on an ex vivo chicken drumstick, are presented and the usefulness of the WCE method discussed.

Material and Methods

USCT exploits the information resulting from the 2D-diffraction of the incident acoustic field by the bone and surrounding tissues, and the mutual information between transducers [2]. The USCT is based on the Radon transform and the FBP (filtered backprojections) algorithm [4]. A prototype has been developed, consisting of a crown (300 mm) of 8 1MHz-transducers distributed every 45°. A wavelet-based coded excitation method (WCE) has been adapted to this device [2] allowing to process the local wave packets propagating in the inter- or centro-diaphyseal areas, and thus reducing the low-pass filtering effect influencing the CNR of the image. The method can also be used as an inverse regularization filter in the FBP algorithm to reduce the effect of Radon's singularities [4].

Results

Experiments were conducted, using successively the pulse-mode (as reference method [4]) and the WCE-mode USCT, on a newborn arm phantom containing blood vessels, single and joined bones (Figure 1), and on a chicken drumstick with skin, different muscles, fat, tendons, nerves, tibia and fibula (Figure 2).
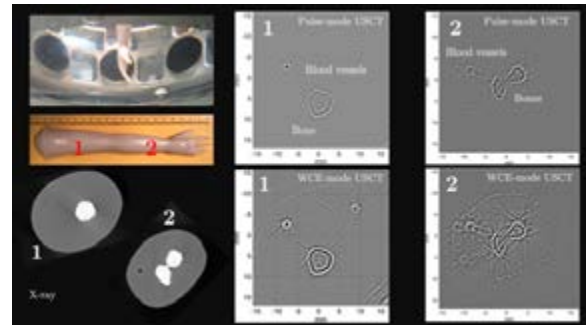
Figure 1: Newborn arm phantom (True Phantom Solution, Windsor, CA) at 6 mm (1) and 14 mm (2) from the elbow. (Left top) USCT circular antenna. (Left bottom) X-ray images obtained by µCT. (4 right images) 1-MHz pulse-mode (top) and WCE-mode (bottom) diffraction USCT.
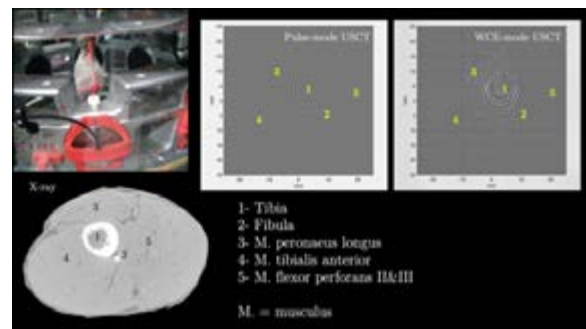
Figure 2: Chicken drumstick in the proximal area 25 mm from the upper tibio-fibular joint. (Left top) USCT circular antenna. (Left bottom) X-ray images obtained by µCT. (4 right images) 1-MHz pulse-mode (top) and WCE-mode (bottom) diffraction USCT.

The algorithm for CNR and gain calculation is detailed in [4]. The performance of the method is presented in the following table, showing a significant gain of CNR.

Target	CNR (Pulse-mode)	CNR (WCE)	Gain (%)
Arm 1	0.083 (0.076)	0.62 (0.54)	647
Arm 2	0.069 (0.058)	1.3 (1.1)	1784
Chicken	0.41 (0.31)	1.1 (1)	175

Table 1: Control-to-noise ratio (average and standard deviation) and gain (%) between pulse-mode and WCE-mode methods for USCT of the newborn arm phantom, and of the ex vivo chicken drumstick.

References.

[1]   P. Laugier et al, *Bone QUS*. Springer Science, 2011.
[2]   T. Hopp et al, *MUST*, KIT Scientific Publishing, 2018.
[3]   M. Loosvelt et al, *Ultrasonics*, 51: 325–339, 2011.
[4]   E. Doveri et al, *Appl. Sci.*, 11: 9368-98,2021.

IMAGE-BASED CHARACTERIZATION OF LARGE VESSELS INTEGRATING IN-VITRO AND IN-SILICO METHODS

Benigno Marco Fanni (1,2), Emanuele Gasparotti (1,2), Katia Capellini (1,2), Emanuele Vignali (1), Giuseppe Santoro (3), Simona Celi (1)

1. BioCardioLab, Heart Hospital, Fondazione Toscana "G. Monasterio", Massa, Italy; 2. Department of Information Engineering, University of Pisa, Pisa, Italy Country; 3. Pediatric Cardiology Unit, Heart Hospital, Fondazione Toscana "G. Monasterio", Massa, Italy

Introduction

Patient-specific vascular modeling represents a powerful tool for the enhancement of diagnosis and treatment of vessels pathologies. In particular, numerical models are nowadays used to simulate interventional procedures [1]. However, the implementation of reliable patient-specific material properties still represents a crucial uncertainty [2].

The availability of the patient-specific mechanical properties would significantly enhance the reliability of in-silico models, thus enforcing their predictive capabilities and favoring their integration with the clinical workflow. The aim of this study was to define an indirect and non-invasive methodology to infer the elastic modulus (E) of vessels from phase contrast magnetic resonance imaging (PC MRI), routinely acquired in patients undergoing cardiovascular interventions. The proposed image-based method was tested on either numerical or experimental models.

Methods

This work was based on a preliminary investigation [3] which included a crucial corrective factor, namely χ, to increase the effectiveness of a standard formulation able to estimate the local E value of vessels from cross-sectional area and flow-rate variations, information easily retrievable from PC MRI. While in the previous study the χ parameter was defined for a single vessel case, in this work we extended its applicability on a wider range of vascular structures. A massive numerical simulations campaign was run, implementing several fluid-structure interaction (FSI) models of different vessels, varying their caliber, maximum flow, and wall stiffness. The χ value was iteratively adjusted to make the formula output matching the E value assigned in the simulation. The corrected equation, including the χ factor, was tested on a series of in-silico vascular models, from which virtual image data were extracted, and in-vitro models, consisting in compliant 3D printed phantoms which were acquired in terms of PC MRI, while subjected to the cardiac-like pulsatile conditions simulated within an ad-hoc mock circulatory loop. The phantoms were fabricated using TangoPlus, a rubber-like material suitable for vascular applications [4].

Results

Flow and area variations were extracted from in-silico models (Figure 1) and phantoms PC MRI data at specific cross-sections. Results were computed in terms of percentage difference between the E value assigned to the models and the E value estimated from the χ-based equation and standard equation also. For the in-vitro cases, the reference E value was the Young's modulus obtained from the uniaxial tests conducted on TangoPlus specimens, equal to 0.5 MPa [4]. The results are summarized in Table 1.
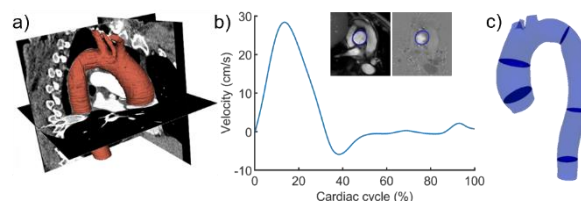
Figure 1: Example of in-silico model used for testing: geometry (a) and velocity extraction (b) from CT and PC MRI; indication of the analyzed cross-sections (c).

Models	χ-based equation	Standard equation
In-silico	9.3%	89.6%
In-vitro	41.2%	93.2%

Table 1: Percentage errors between target E values and estimated E values as obtained from χ-based and standard equations.

Discussion

In this work we presented an image-based method able to infer the local E value of vessel wall in a direct and non-invasive way. Results were promising, showing a huge reduction of the gap between target and estimated E value when using the equation including χ, with better outcomes with respect the standard formulation. However, a residual error is still present, and further investigation are necessary to increase the effectiveness of the presented methodology and enhance the reliability of patient-specific computational simulations.

References

1. S. Zhao et al, Sci Rep, 11, 16486, 95026-2, 2021.
2. J. H. Bracamonte, J Biomech Eng, 142(12): 121011, 2020.
3. B. M. Fanni et al, Cardiovasc Eng Tech, 11, 532–543, 2020.
4. S. Celi et al, Curr Pharm Des, 27(16), 2021.

Acknowledgements

INFANT GASTROCNEMIUS GROWTH IN THE FIRST TWO YEARS OF LIFE

Ricardo Florez (1), Hyun Kyung Kim (2), Matthew Bell (2), Sue Stott (2), Ali Mirjalili (2), Sian Williams (2), Thor Besier (1), Justin Fernandez (1)

1. *Auckland Bioengineering Institute, The University of Auckland, New Zealand;*
2. *Faculty of Medicine, The University of Auckland, New Zealand*

Summary

The medial and lateral gastrocnemius exhibits extraordinary growth in the first two years of life. Using 3D ultrasound, we have tracked the growth of the infant gastrocnemius from 3 to 24 months of age. A principal component analysis has revealed that the medial gastrocnemius starts to increase in volume, relative to the lateral side, about the time when infants show autonomous walking skills. This is consistent with changes in spatiotemporal parameters, joint kinematics and kinetics which start to approach adult characteristics by age 2 years. When age related muscle volume increases were removed from the analysis, principal component analysis revealed that muscle belly width was the primary shape change, with the medial side showing increased muscle belly width. Understanding typical infant muscle growth has implications for better identification of muscle pathology, including cerebral palsy.

Introduction

Infants experience rapid muscle changes during the first two years of life. During this time important biomechanical changes are observed. For instance, step width decreases, while step length and walking speed increases [1,2]. Kinematics and kinetics converge towards more adult like characteristics. Two of the most notable lower limb muscles for adequate gait function are the lateral gastrocnemius (LG) and medial gastrocnemius (MG) [3]. Most notably, the gastrocnemius muscles are involved in plantarflexion [4]. Little is known about form function relationships in infants less than 2 years of age. This is paramount because by 2 years of age mature features of gait and muscle function have already formed. In this study we evaluate infant muscle growth in the first 2 years of life. Understanding typical form function developments have important implications for clinical recommendations in pathologic gait.

Methods

Four OptiTrack cameras were integrated with a custom 3D ultrasound setup. 44 infants (3 to 24 months) were scanned using a single-sweep method for the MG and LG. Muscles were segmented from the femoral condyle to the distal musculotendinous junction [5] in the Stradwin/Stradview software suite. We used the software Gias2 to perform principal component analysis.
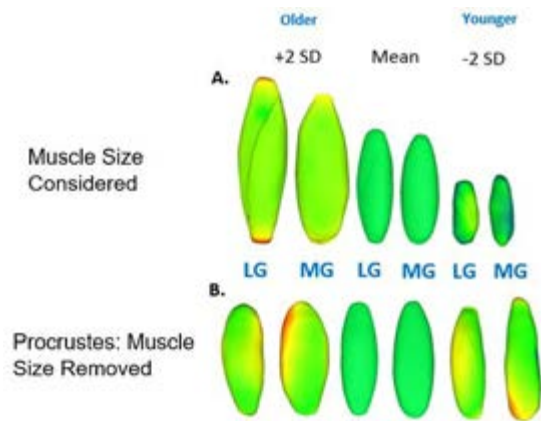
Figure: *Muscle shape changes across age (A) and with muscle volume removed (B). Mean and ± 2SD are shown with RED increase and BLUE decrease and GREEN the mean.*

Results

The gastrocnemius size increases across age and the LG and MG differentiate and become less symmetric (Figure A). Specifically, the LG appears more elongated while the MG shows a wider muscle belly. A secondary analysis (Figure B) involving a Procrustes analysis where muscle size is removed, revealed the primary shape change was in the muscle belly with the MG being wider than the LG.

Discussion

The changes in the muscle belly are consistent with what we observed in children, and adolescents through to adulthood [6]. There is an increase in the MG relative to the LG from the time independent walking occurs. This may in part be explained by the development in kinematics and kinetics.

References

1. Adolph et al, Child Dev, 74: 475-497, 2003.
2. Snapp-Childs & Corbetta, Infancy, 14: 101-116, 2009.
3. Honeine et al, PloS ONE, 8: 1-12, 2013.
4. Lichtwark et al, J. Exp. Biol, 216: 4388-4394, 2013.
5. Barber et al, J. of Anat, 234: 384-391, 2019.
6. Luke, Master Thesis, The University of Auckland, 2018.

Acknowledgements

CRANIAL BONE MICROARCHITECTURE IN A MOUSE MODEL FOR SYNDROMIC CRANIOSYNOSTOSIS

**Julia Hut (1), Sara Ajami (2), Erwin Pauws (2) , Dawn Savery (2), Alessandra Carriero (4),
Andrew J Bodey (5), Andrew Pitsillides (6), Noor Ul Owase Jeelani (3), Silvia Schievano (2),
Alessandro Borghi (2)**

1. Erasmus University Rotterdam; 2. University College London, UK; 3. Great Ormond Street Hospital, UK 4. The City College New York, USA, 5. Diamond Light Source, UK, 6. Royal Veterinary College, UK

Introduction

Crouzon syndrome is the most common craniosynostosis syndrome occurring in 1 in every 25,000 births worldwide (1). In these patients, mutation in fibroblast growth factor receptor 2 (FGFR2) is associated with premature fusion of coronal skull sutures leading to brachycephalic head shape (2). Treatment of craniosynostosis is predominantly surgical with the aim to allow normal brain growth and cognitive development and normalise the head shape. However, the timing of surgical intervention is controversial due to the limited understanding of cranial bone morphology leading to unpredictable changes in postoperative growth. The aim of this study was to investigate the effect of the FGFR mutation on the formation and homeostasis of cranial bones architecture at different stages of skull development using Crouzon mouse model (Fgfr2^{C342Y}). This is not currently known and will help in determining the best surgical procedure and optimal time for surgical intervention.

Methods

This research was carried out using WT (carrying two normal alleles) and HET (carrying one mutant allele) mice models to mimic the condition in human Crouzon patients. Crouzon mice (Fgfr2^{C342Y}) were re-derived through the European Mouse Mutant Archive (EMMA) at MRC Harwell. Litters were collected at postnatal day 7,14 and 21 (n=6 per genotype at each age group) and genotyped for heterozygous presence of the C342Y mutant allele by standard PCR protocols. All animal procedures were performed in accordance with the UK Animals (Scientific Procedures) Act 1986 (Project License number 70/7194). High-resolution 3D synchrotron X-ray microtomographic images were acquired at beamline I13-2 of Diamond Light Source using an effective pixel size of 1.625 μm (field of view 4.2 x 3.5 mm). Projections were recorded by a pco.edge 5.5 camera detector at equally-spaced angles over 180° of continuous rotation to magnify frontal and parietal bone sections separately. Datasets were reconstructed to produce 3D tomograms using the Savu software, processed and analysed using Simpleware ScanIP (Synopsis, USA) and CTAn (v. 1.14.4.1, Skyscan, Belgium). Morphometric measures of parietal and frontal bone such as Bone Volume (BV), Bone Volume Fraction (BV/TV), Bone Thickness (Th) and Bone Mineralization Density (BMD) and intracortical porosity including vascular canal number and density (NCa/TV. CaV/TV), osteocyte lacunar number and density (NLc/TV, LcV/TV) were examined.
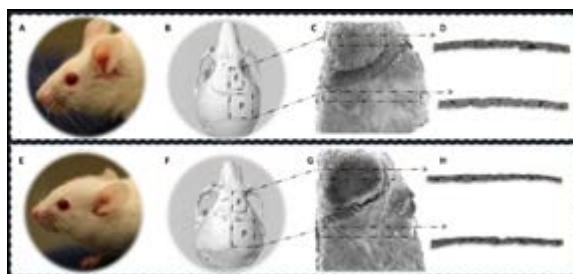
Figure 1: Different facial and calvarial phenotypes for WT (A) and HET mouse (E); (B, F) Visualisation of the regions of interest: frontal bone and parietal bone. (C, G) microCT of WT (C) and HET (G) mice showing difference in suture patency (D, H) High-resolution synchrotron scans of frontal and parietal bone for lacunar analysis. f, frontal bone; p, parietal bone.

Results

Preliminary morphological assessment of data for the frontal bone showed (n=3) (i) the number of lacunae (N.Lc/TV) tend to increase for both genotypes between P14 and P21, with HET having a marked increase. Lacunar volume density (LcV/TV) in the eldest HET group was higher than the WT counterpart; (ii) canals (N.Ca/TV) were more numerous in HET than WT at each time point. A marked decrease in canal volume density (Ca.V/TV) for the HET group from P14 to P21 shows that canals increase in number but decrease in size.

Discussion

Evaluation of postnatal cranial bone microarchitecture in various pathophysiological states will provide a better understanding of bone physical qualities such as strength and density at different stages of skull development. This would potentially provide useful information about bone healing capacity and would allow prediction of surgical outcomes of procedures such as spring assisted cranioplasty by means of numerical modelling (3). Future developments will address pharmacological treatment prior to surgery to improve bone morphology and quality.

References

1. Dunaway D et al. Plastic surgery (pp. 267-282). Elsevier.
2. Hersh D et al. Neurosurg. Clin. N. Am, 33(1), pp.105-112.
3. Borghi A et al, Med Eng Phys, 53: 58-65, 2018

Acknowledgment

ULTRASOUND IMAGING OF BONE CORTEX: BEAMFORMING OPTIMIZATION FOR OSTEOPOROTIC BONES

Amadou Sall Dia (1), Guillaume Renaud (1,2), Quentin Grimal (1)

1. Sorbonne Université, INSERM UMR-S 1146, CNRS UMR 7371, Laboratoire d'Imagerie Biomédicale, F-75006, Paris, France; 2. Department of Imaging Physics, Delft University of Technology, The Netherlands

Introduction

Ultrasound imaging of the cortex of long bones may enable a measurement of the cortical thickness and the wave-speed in cortical bone tissue [1]. These can help assess bone mechanical strength, and hence the risk of osteoporotic fracture [2]. Ultrasound imaging of the cortex is also the first step towards ultrasound measurement of intraosseous blood flow [3]. However, echographic signals from inside the bone cortex are weak due to scattering by the microstructure (vascular pores) and absorption in the viscoelastic matrix. This may prevent the identification of the inner cortical bone surface (endosteum) on the echographic image. The endosteal surface is more easily detectable for young healthy subjects than for the elderly or osteoporotic (Fig.1).
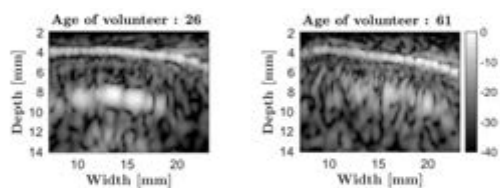
Figure 1: Typical in vivo ultrasound images of young and elderly volunteers. The echographic probe was placed on the tibia transversely to the bone axis. The bright line around 4 mm is the periosteum. Left: the bright region aroud 9 mm is the endosteum and is clearly visible for this young subject. Right: the endosteum is less visible for an older subject.

In this communication, we discuss the limitations of ultrasound imaging of cortical bone inner structure, with a focus on bones with altered microstructure as observed in the elderly and osteoporotic patients. We also introduce some candidate methods to improve imaging of the endosteum in these cases.

Method

The effects of increased porosity and pore size on ultrasound signals were quantified from simulated data obtained with a finite difference time domain elastic code [4]. We used 105 2D images of bone microstructure based on 3D synchrotron X-ray microcomputed tomography images (resolution 10 µm) from the femur diaphysis of 29 human donors. Porosity ranged from 2 to 24%. We implemented a synthetic aperture imaging sequence with an array transducer (central frequency 2.5 MHz). Image reconstruction was performed using delay-and-sum (DAS) beamforming with optimized receive f-number, correction of refraction at the soft tissue-bone interface and sample-specific wavespeed [1]. The same imaging protocol was used to image 5 femur bones ex vivo for which high resolution computed tomography images were available as reference images. Endosteum interface contrast (CEI) was calculated as the ratio of the average intensity of the endosteum over the average intensity of center of the cortex. For a given microstructure, a pore was considered "large" if its diameter is part of the last decile of the mean diameter distribution (typically larger than 250 µm).

Results

We found that as porosity increases, speckle intensity inside the bone cortex increases (Fig.2) whereas the intensity of the signal from the endosteum decreases leading to a 20 dB drop in CEI. On the other hand, for similar porosities, a microstructure containing "large pores" was associated to much lower endosteum visibility.
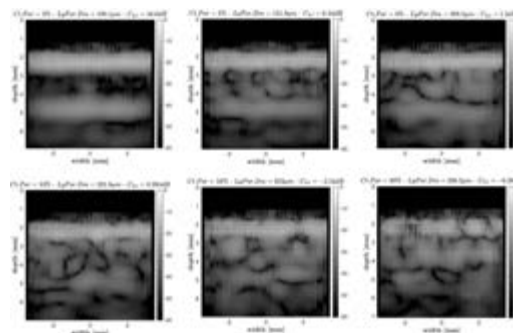
Figure 2: Reconstructed ultrasound images from simulated data for increasing porosity. The endosteum at 4.7 mm is hardly visible at high porosities.

Discussion

In altered microstructures, the endosteum is poorly visible on ultrasound images reconstructed with DAS. The improvement of image contrast with alternative beamforming approaches, enhancing specular reflection or filtering out some of the backscatter by the pores, will be presented and illustrated on simulated and ex vivo data.

References

1. Renaud et al, Phys. Med. Biol., 12;63(12):125010 2018
2. Grimal et al, IRBM, 40(1) 16-24 2018
3. Salles et al, JBMR Plus, 22;5(11):e10543 2021
4. https://www.simsonic.fr

A PRELIMINARY STUDY FOR THE ASSESSMENT OF A COMPLEMENTARY THERAPY IN PARKINSON'S DISEASE

Elena Pegolo (1), Alberto Cucca (2), Ester Berti (1), Daniele Volpe (2), Zimi Sawacha (1,3)

1. Department of Information Engineering, University of Padova, Italy; 2. Fresco Parkinson Center, Villa Margherita, S. Stefano, Vicenza, Italy; 3. Department of Medicine, University of Padova, Padova, Italy

Introduction

Parkinson's Disease (PD) is a neurodegenerative disorder that causes both non-motor and motor symptoms. The latter ones include general tremor, rigidity, and bradykinesia. These symptoms have been investigated in literature especially in the upper and lower limbs. However, they may also affect facial muscles causing hypomimia that is considered one of the clinical hallmarks of the disease. Patients experiencing hypomimia have a limited facial expression that often causes a reduction of their quality of life and social interaction difficulties. Despite the high prevalence of this feature in PD, hypomimia still remains under-investigated and no validated treatments are currently available [1]. The aim of the proposed preliminary study is to quantitatively assess the potential benefits of a complementary therapy based on experimental artistic interventions on hypomimia. A face tracking algorithm based on Facial Action Coding System (FACS) [2] is exploited and the pre- and post-treatment conditions are assessed.

Methods

Seven PD patients (mean(±SD) age: 70(±3.51) years) were considered in the present study. Data collection consisted in video acquisition of the participants. This session took place before (T0) and after (T1) four weeks of a complementary therapy. Videos were acquired by means of a commercial camera (GoPro Hero 8 camera, 30 fps) while they were comfortably sitting with a neutral background behind them. During the acquisition, subjects were asked to perform the six basic emotions (anger, disgust, fear, happiness, sadness, surprise) and the neutral expression as in [3]. Videos were segmented into four frames per each emotion and a set of 40 landmarks was tracked in the 2D-image space with TrackOnField (BBSoF S.r.l. [4]). Then, 40 Euclidean distances were computed from the coordinates of these points and averaged by frames (*n_dist*). A step of intra-subject normalization was performed dividing each distance to the corresponding one in the neutral expression (*ratio*). Finally, an index of face mobility (FMI) was computed as follows:

$$FMI_j = \frac{\sum_{i=1}^{n\_dist} |1 - ratio_j| \cdot 100\%}{n\_dist} \quad j = 1 \ldots 6$$

Results

Figure 1 reports the obtained results. Greater values of FMI indicate greater deviation from the neutral expression and consequent reduction of hypomimia. FMI per each emotion and subject is represented in a spider plot at T0 (Figure 1a) and T1 (Figure 1b).

Discussion

In this preliminary study, a quantitative evaluation of the treatment has been proposed and results seem encouraging. Pre- and post- treatment states per each subject and emotion are well depicted and differences are clearly visible. This approach could be employed to tailor and assess different rehabilitation treatments for hypomimia. Future developments will include the increase in the number of subjects considered in order to better assess the method proposed. Moreover, correlations between the new proposed metric and clinical scales could be included to further investigate patients' impairments.

References

1. Ricciardi L. et al, PLOS One, 12(1):e0169110, 2017
2. Ekman, P., Facial Action Coding System: Investigator's Guide; Consulting Psychologists Press, 1978
3. Wu P., et al., Comput Math Methods Med, 2014
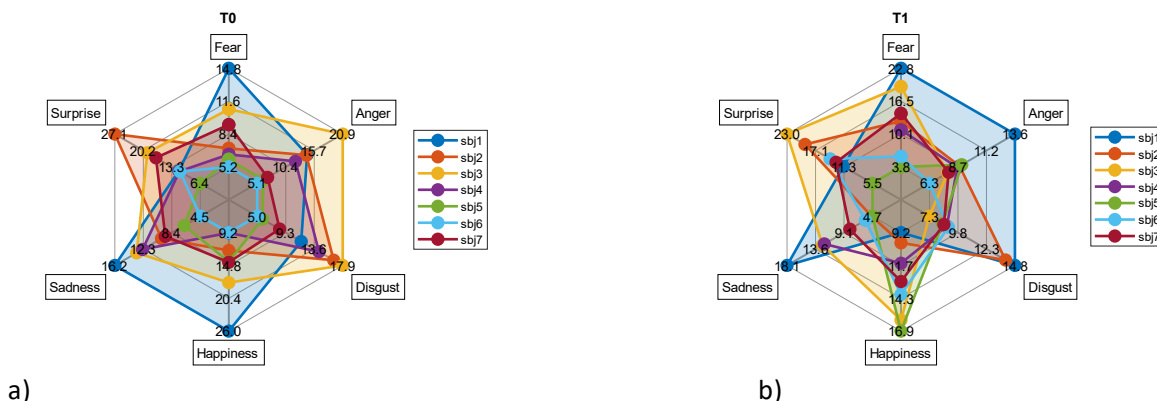4. Sawacha Z. et al, Sensors, 21(14):4746, 2021

Figure 1. Spider plot of FMI per each emotion and subject at T0 (Figure 1a) and T1 (Figure 1b).

WEIGHT-BEARING SYMMETRY IN HEALTHY AND ACTIVE WORKERS: AN OCCUPATIONAL STUDY WITH INSTRUMENTED INSOLES

Sónia A. Alves, Alison N. Agres, Georg N. Duda

Berlin Institute of Health at Charité Universitätsmedizin Berlin – Julius Wolff Institute, Berlin, Germany

Introduction

Monitoring weight-bearing symmetry (WBS) is of interest for tracking disease progression or rehabilitation progress [1]. Healthy individuals also exhibit a certain amount of WBS deficits [2, 3], which should be considered when investigating pathological cohorts. However, the investigations performed in healthy individuals are typically performed in laboratory settings, which may not be representative of real life situations. This study aimed to assess WBS of healthy individuals during a typical workday in an occupational setting, as a model system to analyze the naturally occurring WBS in everyday life. A further aim is to determine the relationship between an individual's relative activity level, as determined by step count, and WBS during a typical workday in an occupational setting. To achieve this, instrumented insoles measured weight-bearing during shift work in active hotel employees.

Methods

Twenty participants (14 females, 31.8±7.9 years, 24.9±4.2 kg/m^2) employed at five local hotels in housekeeping (n=8), reception (n=5), and service (n=7) departments were recruited. The local ethics committee approved protocols and participants gave written informed consent. Each participant received an iPod and a pair of instrumented insoles (loadsol, novel GmbH), then instructed on data collection. Participants wore insoles for a minimum of one work shift within two weeks. Insoles recorded the overall plantar force from each foot, transmitted via Bluetooth to the iPod for local storage. Upon equipment recovery, raw data was downloaded. A custom-step recognition script (RStudio Inc.) identified periods of static and dynamic loading. The absolute weighted Universal Symmetry Index (wUSI) [2] determined overall (input: left and right total impulse) and step (input: left and right step impulse) weight-bearing symmetries for each participant, where 0% indicates perfect symmetry and 100% indicates total asymmetry. After normality tests, one-way analyses of variance examined the effect of group on step count and wUSI values (α=0.05). A Pearson correlation examined the relationship between the mean number of steps per shift and overall wUSI and between the mean number of steps per shift and steps wUSI across all participants.

Results

In an average shift, reception workers took fewer steps (3358±2298, *p*<0.001) compared to housekeeping and service (14883±3785 and 14739±4599, respectively). The overall proportion of dynamic loading was 11% in the reception group, compared to 33% in housekeeping,

and 34% in service. A negative correlation was only found between overall wUSI and the mean number of steps taken per shift (Figure 1 A; *r*=-0.53; *p*=0.02). No association was found between steps wUSI and the mean number of steps taken per shift (Figure 1 B; *r*=-0.26; *p*=0.3).
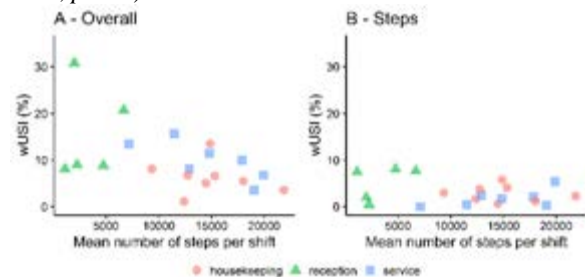
Figure 1: Absolute weighted universal symmetry index (wUSI) (A) and steps wUSI (B) versus mean steps per shift of housekeeping (pink circles) reception (green triangles) and service (blue squares) participants.

Discussion

Participants did not exhibit perfect WBS (wUSI≠0), supporting evidence from previous observations suggesting that healthy individuals do not exhibit perfect WBS profiles [2, 3]. Studies aiming to investigate return to WBS in pathological cohorts should consider the natural occurring WBS of healthy individuals. In particular, many participants exceeded wUSI when measured during gait in healthy participants in a gait laboratory [2]. These results further underline the disparity between laboratory measurements and real-life workplace settings. Hotel workers that took less steps during a work shift exhibited higher overall WBS deficits. Asymmetrical distribution of lower limb weight-bearing during daily work activities may accelerate musculoskeletal symptoms injuries [4, 5], which may be particularly exacerbated if constantly repeated during days, and eventually, years in the life of workers. These results imply that periods of dynamic movement can improve overall WBS, which can break up extended static periods. However, no association was found between the number of steps taken and WBS. This suggests that even though sectors have a different overall WBS profile, this effect might not be transferred to the WBS profile across all steps. Future work in expanded cohorts should aim to understand WBS and its relationship to musculoskeletal health.

References

1. Aqil et al., J. Arthroplasty 31: 2337-2341, 2016
2. Alves et al., Front Bioeng Biotechnol, 8: 57951, 2020
3. Sadeghi et al, Gait Posture, 12: 34-45, 2000
4. Coenen et al, Gait Posture, 58: 310-318, 2017
5. Block et al, Curr Opin Rheumatol, 22: 544-550, 2010

EFFECTS OF HANDLE-HEIGHT ON GAIT KINETICS IN OLDER ADULTS WHILE WALKING WITH A ROLLATOR

Marco A Avalos (1,2), Young-Hoo Kwon (2), Kirsten Tulchin-Francis (3), David Nichols (2), Jian Zhang (2), Noelle Tuttle (2).

1. Rosalind Franklin University of Medicine and Science, United States of America; 2. Texas Woman's University, United States of America; 3. Texas Scottish Rite Hospital for Children, United States of American.

Introduction

An increasing geriatric population has increased the demand for walking-aids among this population. Walking-aids are used to aid with neurodegenerative diseases or to aid in people with poor balance [1]. The use of walking-aids requires proper adjustment to maintain adequate shared weight-bearing while maintaining correct posture [2,3,4]. Current guidelines leave users with vague instructions not allowing for proper adjustment of these devices [1,5]. The purpose of this investigation was to determine the effects of handle-height adjustment on gait kinematics and kinetics in able-bodied older adults when walking with an all-terrain rollator.

Methods

Participants were tested while walking at 80 and 100% of their normal cadence. Thirty-three able-bodied older adults (16 females) were recruited from the Denton, TX, area. Every participant signed an IRB approved Informed Consent Form. Participants were asked to complete 5 successful trials for each of three different handle-height adjustments (i.e., 48% of the user's height [H48], 55% of the user's height [H55], and wrist crease height [HW]) on two cadences (i.e., normal cadence and slow cadence); the participant was also asked to walk without the rollator (NR) as a control condition for each walking cadence condition. Participants were instructed to walk barefoot and as naturally as possible while applying force over the rollator. Participants were asked to focus their sight at an eye-level target, to avoid foot targeting. Participants were asked to complete an exit survey about their perceptions of the handle adjustments. Kinetic variables measured included ground reaction forces and lower body resultant joint moment. Kinematic variables included postural back angles (Lordosis, kyphosis, L4/L5 flexion), elbow flexion, shoulder elevation (inter-shoulder girdle angle), and walking velocity which were extracted from the stance phase of gait on each limb in order to see the effects of the rollator.

Results

Only the H48 reduced the backward peak force. Even more, the most reduction of forces was achieved with the H48, while the least were with the H55. No significant difference was found between the three handle adjustments. The use of rollator significantly increased the L4/L5 flexor moment by 25%, and decreased the hip abductor, ankle plantar-flexor, and everter joint moments up to 16%. The hip flexor moment was significantly reduced only with the HW. At H55 there was significant decrease in kyphosis and lordosis with a 9 degrees shoulder elevation. The H48 and HW showed decreased lordosis with increased L4/L5 torso flexion and 6 degrees shoulder elevation.
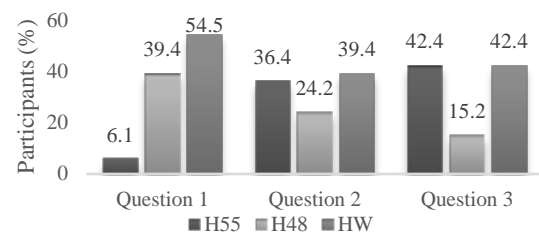
Figure 1. Participant perceptions. Q1. While walking with a rollator, which position felt that you unload better your weight? Q2. While walking with a rollator, which position felt more like your normal walk? Q3. While walking with a rollator, which position felt more comfortable to walk?

Discussion

The use of rollator improved spinal posture by reducing kyphosis and lordosis, but with increased shoulder elevation and torso flexion. The results of this study showed that all three adjustments allow shared weight-bearing. However, the body posture while using the device was not the same, generating a slight stooped posture at H48 and HW conditions, which can create lower back pain.

Overall, the adjustments that were more beneficial to the user were either the H48 or the HW conditions, but only the HW adjustment showed significant reduction in all joint moments. Even when 40% of the time the H48 was higher than the HW, the former is much easier to measure and adjust than the latter. However, this is only true if the purpose of using a rollator is to reduce the GRF and RJM; if the need for a rollator is as an assistant device for balance and stability while ambulating, the H55 condition showed to be preferred among the participants and they were able to maintain a more natural posture. With regards to walking velocity, the device did not limit step length, but velocity differences were seen due to changes in cadence.

References

1. Bradley et al, Am Fam Physician, 84(4):405-411, 2011.
2. Lacour et al, Clin Neurophysiol, 38(6):411-421, 2008.
3. Rosario et al, J Bodyw Mov Ther, 38(3):127-132, 2014.
4. Woollacott et al, Gait Posture, 16(1):1-14, 2002.
5. Van Hook et al, Am Fam Physician, 67(8):1717-1724, 2003.

EFFECT OF SENSOMOTORIC INSOLES ON POSTURAL STABILITY IN KIDS WITH CEREBRAL PALSY

Simona Bartošová (1,2), Vít Nováček (3)

1. NTIS, University of West Bohemia, Czech Republic; 2. Protetika Plzeň, Czech Republic;
3. NTC & Faculty of Health Care Studies, University of West Bohemia, Czech Republic

Introduction

There is a limited literature assessing the effects of sensomotoric insoles on postural stability of kids with cerebral palsy. Their positive effect on static and balance was previously demonstrated [1,2]. Sensomotoric insoles significantly improved gait velocity and cadence after three months of use but these positive changes were not maintained one month after withdrawal of the insoles [3]. The aim of this work was to assess the effect of sensomotoric insoles in five children with cerebral palsy on their static postural stability.

Methods

Five subjects with diagnosis of cerebral palsy were enrolled in the study (Table 1). Subjects 1–3 had spastic left hemiplegia, subject 4 spastic diplegia with moderate intellectual disability and subject 5 had spastic right hemiplegia.

Subject	Sex	Age (Years)	Days of Therapy
1	M	5	35
2	M	7	28
3	F	6	42
4	M	6	25
5	F	11	25

Table 1: Summary of subjects.

The effect of sensomotoric insoles therapy was assessed through center of pressure (COP) trajectory and its antero-posterior (AP) and medio-lateral (ML) sway measured by Kistler force plate 9286BA. Three repetitions were done for each instruction: upright plain stand with open eyes (AD), upright stand with feet together and open eyes (BE) and upright plain stand with closed eyes (CF). For each subject, the data was recorded in two separated sessions: before (ABC) and after (DEF) approximately one month of therapy. The data was recorded for 30s in each test and fragmented into six 5s intervals to remove outliers mainly due to failure to follow the instruction. Subject 4 was unable to execute upright plain stand with closed eyes.

Results

Boxplots of COP trajectory are shown in Figure 1 for illustration. Table 2 summarizes statistically significant improvements in measured variables for all subjects and instructions.

Discussion

Only subject 5 demonstrated improvements in all variables except for AP in upright stand with feet together. It also demonstrated less variance and lower values compared to the other subjects. This may be attributed to higher age and better control maturity. The proposed assessment seems strongly affected by maturity of the subjects and their particular condition. It will require further research and detailed stratification of population according to age and condition.
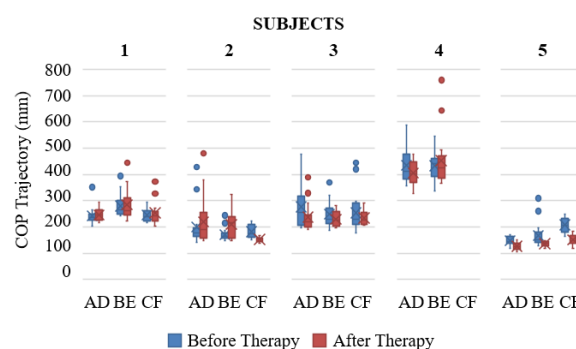
Figure 1: Boxplots of COP trajectory.

Subject		1	2	3	4	5
AD	COP	No	No	**Yes**	No	**Yes**
	AP	No	No	No	No	**Yes**
	ML	No	No	**Yes**	No	**Yes**
BE	COP	No	No	No	No	**Yes**
	AP	No	No	No	No	No
	ML	No	No	**Yes**	No	**Yes**
CF	COP	No	**Yes**	No	NA	**Yes**
	AP	No	No	No	NA	**Yes**
	ML	No	No	**Yes**	NA	**Yes**

Table 2: Statistically significant improvements. NA stands for Not Available.

References

1. Grecco et al, Braz J Phys Ther, 17(1):17-23, 2013.
2. Christovão et al, Braz J Phys Ther, 19(1):44-51, 2015.
3. Neto et al, J Bodyw Mov Ther, 21(4):890-895, 2017.

Acknowledgements

DESIGN, DEVELOPMENT, AND TESTING OF A NOVEL WEARABLE DEVICE FOR REHABILITATION AFTER ANKLE SPRAIN

Nitzan Breitman (1), Arielle Fischer (1)

1. Department of Biomedical Engineering, Technion, Israel Institute of Technology, Israel

Introduction

Ankle sprain is one of the most common injuries among athletes, combat soldiers, and active populations [1]. Lateral Ankle Sprains (LAS) often lead to Chronic Ankle Instability, Post-Traumatic Osteoarthritis, and chronic pain [1]. Following a LAS, pain is correlated to deficits in biomechanical parameters such as range of motion, peak torque, muscle activity, and step length [2,3]. We have developed a novel low-cost wearable device using vibration stimulus that implements gate control theory [4]. Using a single gyroscope placed on the shank and an adaptive algorithm, we detected gait events and engaged the somatosensory system to interrupt pain pathways from the ankle. The purpose of this study is to improve ankle range of motion and mobility by mitigating pain during gait of subacute LAS patients.

Methods

Using Arduino Nano 33 BLE Sense built-in inertial measurement unit, we developed an algorithm that records the change in angular velocity and provides stimulation synchronized to lower limb movement. The algorithm detects two distinct gait events i.e., Mid-Swing (MS) and Heel-Strike (HS), by calculating the local minima, maxima, and zero-crossing. We incorporated a patient specific gait pattern self-correcting adjustment of MS and HS thresholds.

Two small devices were strapped on the lower leg. Each device has its own vibration motor specifications depending on the placement. The first device causes stimulation of cutaneous mechanoreceptor afferents on the tibialis anterior peroneus longus, applied intermittently to achieve an analgesic effect from HS to Toe-Off (TO). The second device was placed on the Gastrocnemius muscle belly to provide stimulation of muscle spindle primary endings by mechanical vibration encouraging agonistic activation from Mid-Stance (MSt) to TO. All components were strategically organized in a custom designed enclosure 3D printed of polylactic acid (PLA) (figure 1).

Results

The design is based on low-cost off-the-shelf components. We validated our gait event detection algorithms by capturing a LED signal indicating HS using a slow-motion camera. Onboard algorithms calculated and triggered movement synced vibrational simulation from MSt to TO. The device was tested on six healthy subjects and successfully showed consistent gait event detection. Additionally, we developed an app that records and displays the data collected in real-time and sends it to the cloud. The app allows for subject specific adjustments of cutaneous stimulation parameters such as intensity, duration, and type of activity. Data were then analyzed offline using MATLAB. The real-time gait detection was designed to be an open-source algorithm. The effects of the device in healthy subjects are being collected and results will be presented at the conference.

Figure 1: Right, devices position on tibialis anterior peroneus longus and Gastrocnemius muscle. Left, gait event detection system components overview.

Discussion

This study provides an open-source gait phase detection algorithm and a low-cost off-the-shelf wearable device. The dual engagement of cutaneous afferents and muscle spindles of the somatosensory system has the potential to have an analgesic effect and encourage a "close to normal" gait in patients with ankle sprain injuries. Future studies will test the effect of the device on LAS patients. This device can potentially motivate patients and improve rehabilitation after an ankle sprain, by reducing the time of rehabilitation and progressively helping patients regain their muscle and gait function during daily walking and physical therapy.

References

1. Doherty C et al, Sport Med 44(1):123-140, 2014.
2. Punt IM et al, PM&R, 7(1):34-41, 2015.
3. Aiken AB et al, J Orthop Sports Phys Ther, 38(9):566-571, 2008.
4. Melzack R, Wall PD, Science, 150(3699):971-979, 1965.

QUANTIFICATION OF POST-OPERATIVE CORRECTION OF FOOT POSTURE THROUGH NEW ANATOMICAL REFERENCE SYSTEMS

Michele Conconi (1), Alessandro Pompili (1), Nicola Sancisi (1), Alberto Leardini (2), Stefano Durante (3), Claudio Belvedere (2)

1. Dept. of Industrial Engineering, University of Bologna, Italy; 2. Istituto Ortopedico Rizzoli, Bologna, Italy; 3 IRCCS S. Orsola Malpighi Hospital, Bologna, Italy

Introduction

The quantitative analysis of the three-dimensional foot posture is a topic of clinical and scientific interest [1], recently boosted by the diffusion of low dose Weight-Bearing CT scanner. This makes it possible to overcome the limit of the traditional 2D measurements made with X-Ray radiography [2]. However, to efficiently quantify the foot posture in 3D, the definition of anatomical reference systems (ARS) is needed to calculate the position and orientation of all the bones in the foot, still lacking in the literature [3].

The aim of the study is to test a new technique for the definition of ARS based on articular morphology [4]. In order to verify its clinical applicability, the technique is tested to measure the post-operative correction in flat feet after clinical intervention, comparing the surgery outcomes with healthy feet for a reference.

Methods

We investigated three flatfeet, scanned in Weight-Bearing CT both before and after the foot correction surgery. In addition, three healthy foot was also scanned with the same methodology. 3D bone models were generated using a semi-automatic segmentation procedure (DICE score>95%). ARS are defined according to a new procedure based on articular morphology which fit geometrical primitive on selection of joint surfaces [4]. To adapt the method to post-op feet, whose talus and calcaneus were surgically fused, pre-op bone model was registered to post-op talo-calcaneal complex through an ICP algorithm, in order to reconstruct the ARS poses. To measure the correction of the pathology, the traditional Djian-Annonier angle (DDA) was estimated as the differences in the flexion angle of the calcaneus and the first metatarsus. A one-way anova analysis followed by post-hoc t-test was performed to determine statistically significant differences among the three groups.

Results

The mean DAA for each group considered is shown in the table 1. Only flat feet differ significantly from healthy foot, both prior and after surgery. Although a in reduction in the DAA is observable, this is not statistically significant (p = 0.077).

Comparison among longitudinal arches (figure 1) shows that the intervention partially recovers the longitudinal arch, raising the talus and realigning the first ray of the foot.
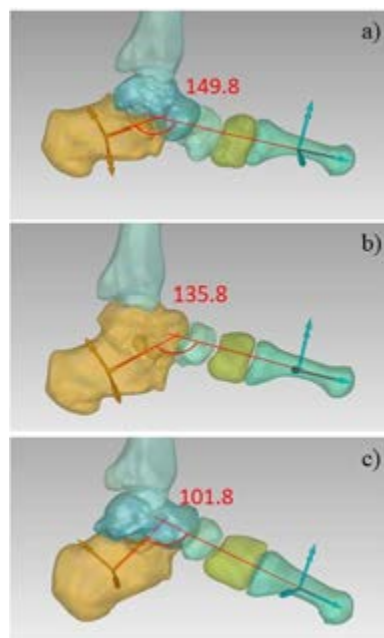
Figure 1: Representation of the Djian-Annonier angle (DDA) for one subject pre (a) and post (b) surgery, compared with and healthy one (c).

Group	DAA
Flat pre-op	$146.1° \pm 6.6$
Flat post-op	$133.8° \pm 6.2$
Healthy	$110.4° \pm 6.1$

Table 1: Mean value for the Djian-Annonier angle (DDA) in the three considered group.

Discussion

The proposed novel ARS allow a quantitative 3D description of foot bone orientations in healthy subjects and in subjects with pathology. This description makes it possible the objective evaluation of the efficacy of surgical treatments. Compared to 2D measurements, this approach is independent on the orientation of the CT scanning plane, this offering new insights in the assessment of pathologies and in the quantification of their severity and progression. Additional feet, both healthy and pathological, will be acquired and processed in the future to corroborate the present findings.

References

1. Gutekunst et al., J. of Foot&Ank Res., 6: 38, 2013.
2. Carrara et a., Foot&Ank Surg. 26: 509-517, 2020.
3. Lenz et al., J of Biomec, 110344, 2021.
4. Conconi et al., J. Foot Ankle Res, 14.1: 1-13, 2021

EVALUATION OF MARKER-BASED MOTION CAPTURING TO CHARACTERIZE BASIC HAND MOVEMENTS IN RHEUMATIC PATIENTS

Birte Coppers*(1, 2), Simon Heinrich(3), Uday Phutane(3), Dardan Berisha(3), Koray Tascilar(1, 2), Arnd Kleyer(1, 2), David Simon(1, 2), Johanna Bräunig(4), Johann Penner(3), Martin Vossiek(4), Verena Schönau(1, 2), Sara Bayat(1, 2), Georg Schett(1, 2), Sigrid Leyendecker(3), Anna-Maria Liphardt(1, 2)

1.Friedrich-Alexander-Universität Erlangen-Nürnberg and University Hospital Erlangen, Department of Internal Medicine 3- Rheumatology and Immunology, Germany, 2.Friedrich-Alexander-Universität Erlangen Nürnberg and University Hospital Erlangen, Deutsches Zentrum für Immuntherapie, Germany, 3.Friedrich-Alexander-Universität Erlangen-Nürnberg, Institute of Applied Dynamics, Germany, 4.Friedrich-Alexander-Universität Erlangen-Nürnberg, Institute of Microwaves and Photonics, Germany

Introduction

The analysis of hand movements is challenging due to the high complexity of the mechanical structure of the hand including more than 25 degrees of freedom [1]. Monitoring function in rheumatoid arthritis (RA) patients is essential for effective treatment [2] and functional impairment of the hand is characteristic [3] for this patient group. Hand movement patterns may provide new possibilities to quantitatively and qualitatively analyze the changes of hand function in relation to disease activity in patients with RA [4]. Anatomic and empirical studies of healthy individuals revealed that e.g. movement of the distal interphalangeal joint (DIP) and proximal interphalangeal joint (PIP) is related with an almost linear relationship [5]. The aim of this study is to analyse if (a) the DIP/PIP ratio extracted from a passive marker-based optoelectronic measurement system (OMS), applies to RA patients and (b) differences in the DIP/PIP ratio can discriminate between RA patients and healthy controls (HC).

Methods

RA patients (ACR/EULAR 2010 criteria [6]) recruited from the Internal Medicine 3 outpatient clinics, Erlangen, Germany and HC participated in this trial (Ethics #125_16B). Participants were asked to flex the DIP and PIP joints of both hands for three times, starting with an open hand posture. Hand segment movement was captured using an OMS (eight Oqus7+ cameras and one Oqus5+ camera, Qualisys AB, Sweden) at a frame rate of 100 Hz with a set of 29 retroreflective markers placed on the hand dorsum [1]. The ratio between the flexion angle of the DIP and PIP joint ($\frac{DIP}{PIP}$) was calculated for each finger using an approach previously described by Sancho-Bru et al. (2014) [1]. Additionally, the linear fit of the measurements was tested with the statistical measure R^2. We used linear mixed-effects models accounting for within-participant clustering of hands and adjusting for age and sex differences to compare RA with HC.

Results

Twenty-four patients with RA (sex: 17 f, 7 m; age: 62.3 ± 9.1 years; Disease Activity Score (DAS)-28: 2.5 ± 1.3) and 23 HC (sex: 12 f, 11 m; age: 50.2 ± 16.1 years +) participated in the study. The overall angle ratio for both groups was affected by sex, showing an 8% lower ratio for women (95% CI -15% to 1%). Measured angle ratios

(RA 0.60 ± 0.15; HC 0.68 ± 0 .17 ($\frac{DIP}{PIP}$)) and their linear fit (RA 0.96 ± 0.05; HC 0.97 ± 0.03 R^2) were similar for RA and controls (p>0.05).
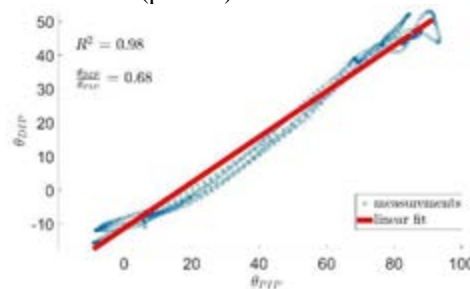
Figure 1: Linear relationship of the measured angle ratios ($\frac{DIP}{PIP}$) for the flexing movement and the linear fit (R^2) of the small finger of a RA patient.

Discussion

We found that the previously described linear relationship of angle ratios for the distal finger joints in healthy individuals [6] is also valid for RA patients in our cohort. Variation for the value of the ratio could only be explained by gender-specific differences and no significant group differences between RA und HC were identified. Gender differences are a common phenomenon in functional tests that need to be considered [4]. Also, this may reflect that DIP and PIP joints are less affected in RA compared to other inflammatory arthritic diseases, e.g. psoriasis arthritis [3]. In conclusion, OMS based kinematic analysis of hand function in RA patients with low to moderate disease activity (DAS28: 2.5 ± 1.3) was feasible.

References

1. Sancho-Bru et al, Proc Inst Mech Eng H, 228:182-9, 2014.
2. Günay et al, Reumatismo. 68:183-187, 2016.
3. Veale et al. RMD Open, 1:e000025, 2015.
4. Liphardt et al, ACR Open Rheumatol, 2:734-740, 2020.
5. Rijpkema et al, Computer Graphics, 25:339-347, 1991.
6. Aletaha et al, Arthritis Rheum, 62:2569-258, 2010.

Acknowledgements

Pre-operative Movement Analysis of Knee Osteoarthritic Patients

Abir Dutta (1), Rounak Bhattacharya (1), Deepak Gautam (2), Arun Swamy (2), Manish Gupta (2), Rajesh Malhotra (2), Anoop Chawla (1), Kaushik Mukherjee (1)

1. Department of Mechanical Engineering, Indian Institute of Technology Delhi, New Delhi, India;
2. Department of Orthopaedics, All India Institute of Medical Sciences, New Delhi, India

Introduction

Knee osteoarthritis (KOA) is a prevalent musculoskeletal disease which has influenced 28.7% of the total Indian population [1], whereas it has affected over 250 million adults worldwide, causing severe joint pain, decreased functional mobility along with altered gait cycle [2]. The terminal KOA requires total knee replacement (TKR) along with post-operative rehabilitation. Although there are multiple studies on knee biomechanics and design of knee implants, there is scarcity of studies comparing the gait of pre-operative KOA patients with those of the healthy population. Therefore, the objective of the present study is to compare the pre-operative gait of KOA patients with that of the healthy population in terms of various kinematic parameters (joint angles).

Methods

3D gait analysis was performed in 4 KOA patients (age 66 ± 10, height 161 ± 9 cm), before their bilateral knee replacement surgery, who walked at self-selected walking speed over the ground. A Helen Hayes marker protocol [3] using 18 reflective markers was used to capture the kinematic data using 12 BTS SMART DX-7000 cameras (BTS Bioengineering, Milan, Italy) operating at 200 Hz. Subject-specific musculoskeletal model was developed using OpenSim 4.2 [4]. The Gait 2392 musculoskeletal model consisting of 18 degrees-of-freedom and 92 musculotendon actuators was scaled based on the captured motion data. For healthy population, the gait2392 dataset was considered. Inverse kinematics (IK) was performed to estimate the subject-specific joint angles across a gait cycle.

Results

The kinematic waveforms for knee flexion-extension, hip Flexion-extension, and ankle plantar-dorsiflexion, obtained for all the KOA patients along with reference healthy model data (gait2392 dataset), were presented in Figure 1. The KOA group exhibited lower (~14%) values of knee flexion angles as compared to the healthy subject during the first half of the stance phase (0-30% of gait cycle), whereas a maximum decrease (~24%) in the values was observed during 25-30% of the gait cycle for all the patients. An increase in the knee flexion was observed in the swing phase, as compared to those of the healthy patient. Higher (~16%) hip extension was also observed during all phases of the gait cycle of the KOA group. Although the trend of the ankle plantar-dorsiflexion motion was similar among all the subjects, a subject-specific variation was observed during the second half of stance. The walking speed of the KOA patients was less than the healthy population.
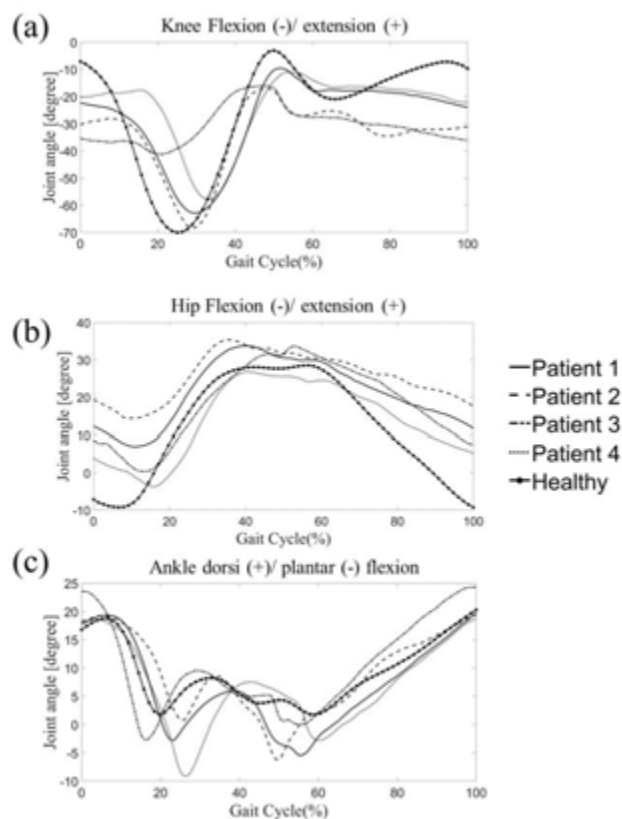
Figure 1: Comparison of (a) knee (b) hip (c) ankle joint kinematics for KOA subjects with healthy population

Discussion

The present study is the first-of-its-kind to evaluate and report pre-operative lower extremity kinematics of the terminal KOA patients undergoing bilateral TKR surgeries. Significant differences were observed in the kinematics for the hip (flexion-extension), knee (flexion-extension) and ankle (plantarflexion-dorsiflexion) between the KOA patients and a healthy subject [Figure 1]. Moreover, decreased walking speed was observed in the KOA patients compared with the healthy control [4]. The reduced knee range of motion resulted in an increase in hip extension in the TKA patients.

References

1. Kumar et al, J Clin Ortho trauma, s 125- 129, 2020;
2. Master et al, Osteoarthritis Cart, 28(12):1551-1558, 2020;
3. Richards et al, J Biomechanics, 43(13):2595-2600, 2010;
4. Delp et al, IEEE Trans Biomed Eng 54(11):1940-1950;

THE KINEMATICS OF THE FOOT DURING DROP JUMPS: A SIX-SEGMENT FOOD MODEL APPROACH

Lena Fennen (1), Rosemary Dubbeldam (1), Heiko Wagner (1,2)

1. Westfälische Wilhelms-Universität Münster, Germany; 2. Otto Creutzfeldt Center for Cognitive and Behavioral Neuroscience, Germany

Introduction

Understanding the foot's motion during different types of exercises is crucial when investigating balancing abilities and processes important for performance and particularly rehabilitation [1,2]. Many injuries occur during jumping and landing motions. A common tool to assess landing behavior is the drop jump (DJ). However, no previous research investigated the movement of multiple foot segments during DJ. In order to understand the role of foot segments in jumping and landing movements and the implementation of these findings in rehabilitation and treatment, a kinematic analysis of the foot segment's motion during drop jumps was performed.

Methods

Six subjects (N = 6, M_{age}=25 years, 33.33% female) performed four DJ captured using a 3D kinematic motion capture system from Qualisys AB (Göteborg, Denmark). The Ghent Foot Model with 21 markers was used, dividing the foot in six kinematic segments [1]. The drop jumps were performed according to a standardized protocol from 30 cm height and proceeded by training trials [3]. Kinematic data was analyzed for the full length of the DJ performance. Joint rotational angles on all three movement planes and cumulative range of motion (cum ROM) were determined for each jump defining the amount of motion over time using Visual 3D (C-Motion Inc., Germantown, USA).

The Ghent Foot Model divides the foot in the six joints: Rearfoot to tibia (RF_T), midfoot to rearfoot (MF_RF), medial forefoot to midfoot (MFF_MF), lateral forefoot to midfoot (LFF_MF), lateral forefoot to midfoot (LFF_MFF) and hallux to medial forefoot (H_MFF) (Figure 1). The mean CumROM on each anatomical plane was first calculated for each subject and then for each joint.

Results

The analysis of the motion of the foot segments over time of the execution of a drop jump in representation of the CumROM indicate high rotational movements within the sagittal plane of all segments. Furthermore, high values for the CumROM are present within the frontal plane of midfoot and both medial and lateral forefoot joints, indicating high inversion and eversion values (Figure 1, Table 1).

Figure and Tables
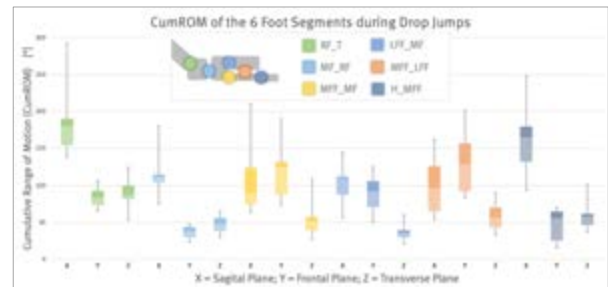
Figure 1: CumROM [°] (Mean ±SD) of DJ in the three anatomic planes for the Ghent Foot Model joints.

	Sagittal	Frontal	Transverse
RF_T	188 ±56	85 ±21	90 ±25
MF_RF	117 ±35	37 ±11	47 ±16
MFF_MF	110 ±57	120 ±50	56 ±30
LFF_MF	103 ±35	89 ±32	37 ±14
LFF_MFF	100 ±45	132 ±57	59 ±27
H_MFF	163 ±61	47 ±26	60 ±27

Table 1: CumROM [°] (Mean ±SD) plus standard deviation (SD) for the six joints of the Ghent Foot Model.

Discussion

The results indicate that during the drop jump anatomical structures represented as the midfoot and medial and lateral forefoot in the Ghent Foot Model have high flexion and extension as well as inversion and eversion CumROM values. Potentially indicating that these structures are of high importance during the execution of a DJ. The current findings indicate special importance of these areas of the feet within therapy concepts after foot and ankle injuries. Further research is needed to support this indication.

References

1. De Mits et al, J Orthop Res, 30 (4): 655-661, 2012.
2. Carson et al, J Biomech, 34: 1299-307, 2001.
3. Padua et al, J Athl Train, 50 (6): 589-595, 2015.

Acknowledgements

THE EFFECT OF THE OF RUNNING-INDUCED FATIGUE ON THE SYMMETRY OF KINEMATICS AND KINETIC VARIABLES OF KNEE JOINTS IN A COUNTERMOVEMENT JUMP.

Zixiang Gao[1,2], Yuqi He[1,2], Gusztáv Fekete[3], Yaodong Gu[2]

1. University of Pannonia, Hungary; 2. Ningbo University, China; 3. Eötvös Lorand University, Hungary;

Introduction:

Countermovement jumping (CMJ) is commonly used to assess leg strength under slow stretch shortened cycle (SSC) and low stretch load conditions. The CMJ is a key achievement claim in abounding sports (Maulder, 2005）. This study investigates the symmetry change in joint angle and joint moment of knee joints following a Running-Induced Fatigue during countermovement Jump.

Methods:

Twelve amateur runners were recruited for the study to perform the Countermovement Jump test. During the push-off and lending stage, joint angle and moment were recorded pre- and immediately posted fatigue. The prolonged-running protocol is enforced to induce fatigue(Gao, 2020). Symmetry function (SF) was used to assess the symmetry of the knee Angle and moment variation parameters over the entire push-off and lending phases based on time series. Paired sample T-test was used to examine changes in SF before and after acute fatigue.

In order to compare the symmetry of the entire push-off and lending stages of bilateral knee joints, symmetry function was applied to this study (Nigg, 2013).

$$\text{SF} = \int_{t=t_1}^{t_2} A|x_r(t) - x_l(t)|dt \qquad (1)$$

$$A = \frac{2}{\text{range}(x_r(t)) + \text{range}(x_l(t))} \qquad (2)$$

Where $x_r(t)$ was defined as the value of the parameter recorded for the right knee at the time t. $x_l(t)$ was defined as the value of the parameter recorded for the left knee at the time t SF is the symmetry function. In addition, t_1 and t_2 stand for the time at heel strike and time at take-off, respectively. Formula (1) is an integrand that is referred to as the SF. The time-dependent information of symmetry at 101-time points in the action stage is reflected in the SF. The closer SF is to 0, the more symmetric the bilateral variables are defined (Formula (2)). This study set a +/-5% symmetry threshold to discriminate asymmetry areas(Winiarski, 2021).

Results:

The Angle and moment of the knee are asymmetrical in all planes (SF>0.05), with SF ranging from 5% to 130% in angles and 5% to 110% at the moment. There is a significant increase in knee joint angle asymmetry in the horizontal plane during the push-off and lending stage

following the prolonged - Running Protocol implementation.
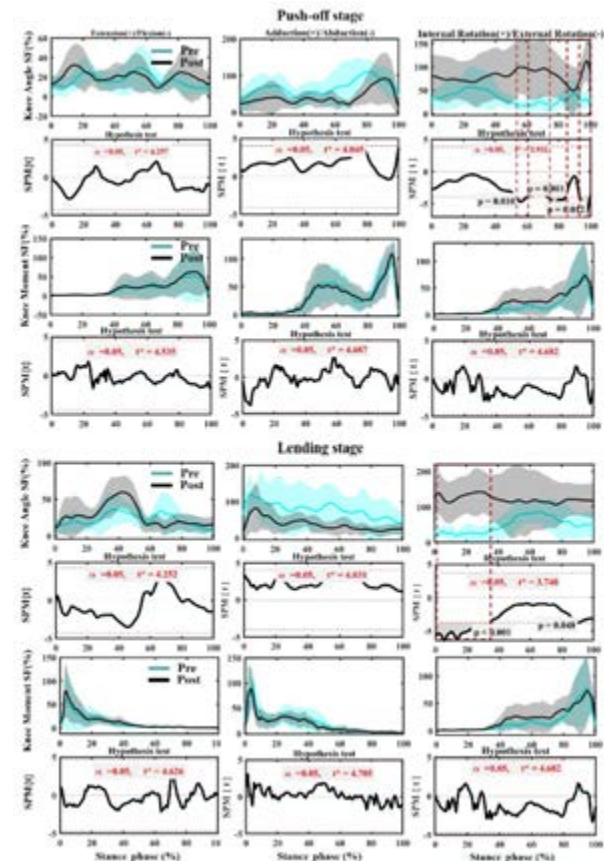
Figure 1. Comparing the mean values of SF of knee angle and moment from all participants between Pre-fatigue and Post-fatigue. Note: the dotted boxes indicate a statistically significant difference, p < 0.05. Pre means Pre-fatigue, and Post means post-fatigue.

Discussion:

This finding may provide evidence for a unilateral knee injury caused by running fatigue during jumping tasks. In performing related tasks, the risk of injury of the dominant knee joint should be concerned by coaches and shoe manufacturers.

References

1. Maulder et al, Phys ther Sport, 6: 74-82. 2005.
2. Gao eta al, Symmetry,12: 720-730, 2020.
3. Nigg et al, Gait & posture, 38:115-119, 2013.

EFFECTS OF BREATHING ON SPINE POSTURE AND STABILITY

Chaves P.(1), Ramirez J.(2), Noailly J.(1), Tassani S.(1)
1. BCN MedTech, DTIC, Univ. Pompeu Fabra, Barcelona, Spain
2. Universidad Nacional de Colombia, Medellín, Colombia

Introduction

Musculoskeletal disorders related to stress and bad posture are becoming common in the young population [1] and the current pandemic situation might have worsen the situation. Breathing affects motor control and postural stability and plays several roles in physiological and psychological regulation [2]. Furthermore, deep abdominal breathing is widely used as a method of relaxation [3], being therefore a good candidate to face the problem. However, previous studies have found that many young subjects seem unable to perform deep abdominal breathing [4]. Therefore, the purpose of this study was to investigate the relation between breathing, spine posture and posture stability to expand the knowledge of the effects of breathing on the body posture in young adults.

Materials and Methods

Twenty-two subjects were included for the stability analysis and seventeen in the spine analysis, 9 of the subjects being common to both analyses. All ages were between 18 and 23.

For the measurement of breathing and posture 8 infrared cameras were used, and eighty-nine markers were located on the trunk [5]. Subjects were asked to stand on a force plate for three minutes while breathing was recorded.

Subjects were classified as capable or not of abdominal breathing based on the volumes measured using the markers protocol. For the spine, the angles of flexo-extension between the sacrum and the thoracic-lumbar vertebrae were recorded and parameters extracted from the COP signal were used to analyze the stability [6]. All parameters were analyzed using a multifactorial ANOVA. The factors taken into consideration were gender for the posture analysis, and the two compartments of the chest used for breathing (Pulmonary or Abdomen) for both stability and posture. To correct the multiple testing error, the difference was deemed to be significant for $p < 0.005$ for the stability analysis and $p < 0.01$ for spine posture. Binary regression with forward selection of variables was used to discriminate between subjects able to breathe abdominally or not with the stability parameters.

Results

Out of the 30 subjects analyzed, only 6 were able to perform a deep abdominal breathing (60% abdominal volume, 40% pulmonary volume). In order to perform a preliminary analysis, the classification threshold was changed to 50% identifying an even distribution of 15 abdominal breathing and 15 pulmonary breathing.

The posture analysis did not show any significant results but the angles between the sacrum and the lower thoracic and upper lumbar region were close to the significance for the factor "gender" (respectively $p=0.03$ and $p=0.02$)).

In relation to stability, the factor "breathing" significantly affected the speed of the COP displacement ($p=0.002$) and inertial axis Y ($p=0.005$). Both with lower values in the subjects with abdominal breathing. The parameters equivalent area, equivalent radius and peak distance were close to significance (respectively $p=0.39$, 0.15, 0.17). The binary logistic regression in Figure 1 shows the classification of the two groups of volunteers breathing with the abdomen or with the pulmonary rib cage.
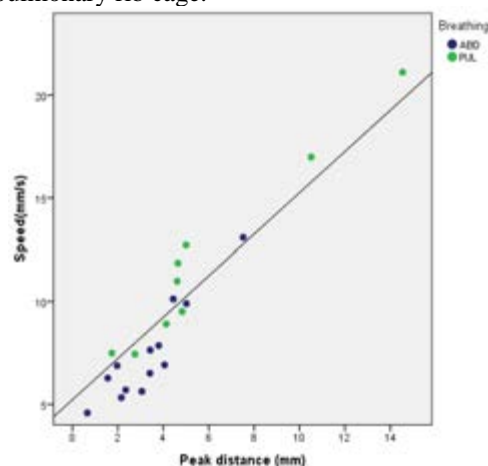
Figure 1: Binary logistic regression using the parameters of speed and peak distance

Discussion

The preliminary results reported hereby confirm the troubling fact that a consistent portion of the young population might not be able to properly control breathing. However, even a partial capability of deep breathing seems to improve the posture stability of the subjects allowing linear separability between the two groups. Breathing technique seems to have no effect over spine posture which might be slightly related to gender.

References

1. Diepenmaat, et al., Pediatrics, 117(2), 412–416, 2006.
2. Courtney, Osteopathic Med, 12(3), 78–85, 2009
3. Brown, et al., J. Altern Complement Med. 11(4), 711–717. 2005
4. Tassani, et al., Gait & Posture 68: 220–226, 2019
5. Aliverti, et al., Monaldi Arch Chest; 59: 1, 12-16, 2003
6. Mello et al, Int. Conf. of the IEEE Engineering in Med. and Biology Society, 31:1351-1354, 2009.

Acknowledgements

MECHANICAL BEHAVIORS OF THE SACROILIAC JOINT

Anna Jeon (1), Eunah Hong (1), Tae Soo Bae (2), Dai-Soon Kwak (1)

1. The Catholic University of Korea, South Korea, 2. Jungwon University, South Korea

Introduction

Dysfunctional sacroiliac joint (SIJ) was considered as a source of the lower back pain. Several researchers investigated anatomy and biomechanics of the SIJ to understand the relationship between the lower back pain and the SIJ. Many studies concluded the SIJ has little movement. However, some of the studies using spinopelvic parameters mentioned high pelvic incidence (PI) change. Moreover, with the development of imaging techniques such as EOS system and vertical CT / MR, interest in sacroiliac joint movement and sagittal balance is increasing. Therefore, in this study, the movement characteristics of the sacroiliac joint were investigated by constructing an environment that could be measured and controlled more precisely than in past experiments.

Methods

We used six fresh cadavers (male 1, female 5). The mean age was 85.25 (81~92) years and the mean height was 152.47 (142~161) cm. The pelvis was harvested by dissection. The hip bone, sacrum, coccyx, and ligaments between hip bone and sacrum were preserved. Patient-specific spacer blocks for fixation of the sacrum were designed by CT images and printed by a 3D printer. 3D printed patient-specific spacer blocks were fixated at the anterior and posterior surface of the sacrum, and the sacrum with the spacer blocks was fully fixated. The external load was applied in superior (+) and inferior (-) directions at pubic symphysis (Fig. 1). Hip bone tilt angle, the movement of the pubic symphysis, and posterior superior iliac spine were measured with applied load. For these measurements, 13 optical markers and 4 motion capture cameras were used.
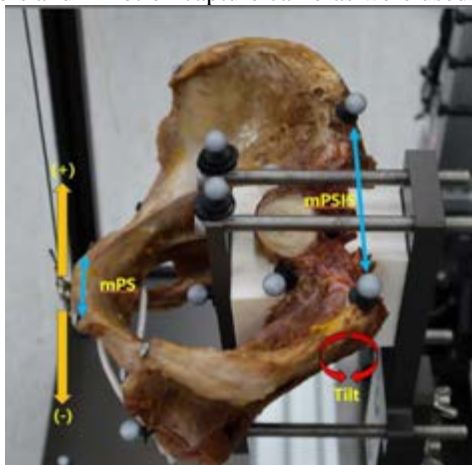
Figure 1: Sample configuration and measurement parameters

Results

We observed the remarkable SIJ movements in the female pelvis in 5 of 6 samples (Group B). However, only small movements were observed (-1.25 degrees and 1.90 degrees at +/- 200N, respectively, Group A) in one male samples. In the sample where the movement was observed (Group B), the hip bone tilt angle was $3.93 \pm 0.49°$ under +100N and $4.86 \pm 0.39°$ when applied with +200N. The tilt angle was $3.27 \pm 1.42°$ when -100N was applied and $5.76 \pm 1.63°$ applied with -200N (Fig. 2). The movement of the pubic symphysis was small (within 0.35 mm) in all cases, and the movement of the PSIS was 0.69 ± 0.52 mm, 0.70 ± 0.72 mm, 0.54 ± 0.02 mm, 0.79 ± 0.02 mm at +100N, +200N, -100N, and -200N respectively. Regardless of the loading direction, it showed an outward-opening behavior.
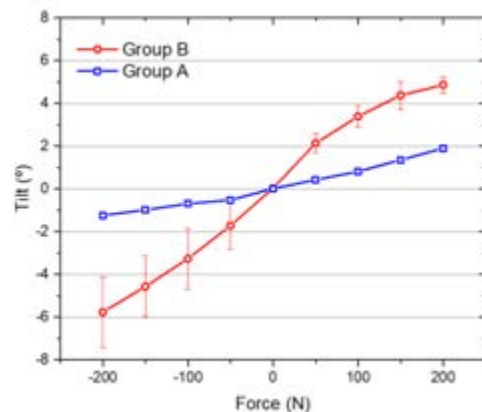
Figure 2: Hip bone tilt angle with various load

Discussion

In this study, we confirmed that the SIJ is a joint with movement. This is consistent with recently published clinical papers. In particular, significant movements were observed in females. Furthermore, when the SIJ were tilted with load, the spacing of the pubic symphysis had little change, and the PSIS moved in the widen direction according to the tilt motion of the hip bone.

References

1. Hammer et al, J Anat, 234(3): 346-358, 2019.
2. Lindsey et al, Med Devices (Auckl), 7:131-137, 2014.
3. Park et al, Arch Orthop Trauma Surg, 137(9):1223-1232, 2017
4. Endo et al, J Orthop Sci, 17(6): 682-686, 2012.

Acknowledgements

MIMU KINEMATICS FOR MONITORING RECOVERY FROM ANKLE FRACTURE

Olli-Pekka Mattila (1), Paavo Vartiainen (2,1), Toni Mujunen (1), Harri Piitulainen (1), Neil Cronin (1), Taina Rantanen (1), Timo Rantalainen (1)

1.Faculty of Sport and Health Science, University of Jyväskylä, Finland 2. Department of Applied Physics, Faculty of Science and Forestry, University of Eastern Finland

Introduction

Ankle fracture is a common trauma in sports with rapid changes in direction of movement, but also in falls of older people [1]. Surgical treatment of lower limb pathologies has been shown to benefit from 3D gait analysis [2]. Similarly, rehabilitation and follow-up of recovery from lower limb trauma could benefit from instrumented gait analysis [1,2]. Magneto-Inertial Measurement Units (MIMU), with accelerometer, gyroscope, and magnetometer, provide an attractive alternative to the traditional 3D optical marker-based gait analysis used in clinical gait labs. MIMUs are cheap and easy to deploy, permit freedom of movement, even outside the laboratory in natural environment, both indoors and outdoors, extend the capture volume and allow long data acquisitions [1]. Using MIMU motion tracking together with biomechanical model to produce lower limb kinetics and kinematics [1,3] can provide an additional source of information for clinical decision making and monitoring recovery. In this study, gait kinematics were computed from MIMU data to follow the recovery from ankle fractures. The changes in range of motion (ROM) for lower limb joints were monitored for two patients and compared to a normative set, derived with same method, from measurements of 30 healthy controls.

Methods

Two ankle fracture patients walked 400 m along a 20 m long straight path with speed attainable within the limits of pain and range of motion (ROM). The walking test was repeated 8 weeks, 6 months, and 12 months post-operation. The first post-operation measurement point was not available for one of the patients due to pain experienced during walking. The walking test was also done by 30 healthy control subjects to provide normative MIMU gait kinematics. Eight MIMUs were attached to the chest (representing the torso), lower back (representing the pelvis), thighs, legs, and feet to measure the angular speed and acceleration of the body segments, and the local magnetic field. MIMU data were processed to segmental rotations in a global reference frame with a sensor fusion algorithm from Madgwick et al. [4]. The single tuneable parameter in the algorithm was optimized with the sub-optimal parameter tuning method proposed by Caruso et al. [5]. The joint angular kinematics were derived from the resulting segment rotation data with OpenSense software, an extension of OpenSim [3,6]. The study was done in accordance with the principles of the Declaration of Helsinki.

Results

Figure 1 illustrates the increasing ROM in ankle dorsiflexion for two ankle fracture patients with two post-operation time points. For patient-1 the increase in the ankle dorsiflexion ROM (mean of 30 steps) between 6 months and 12 months post-operation was +5.6° and for patient-2, between 8 weeks and 6 months, +11°.
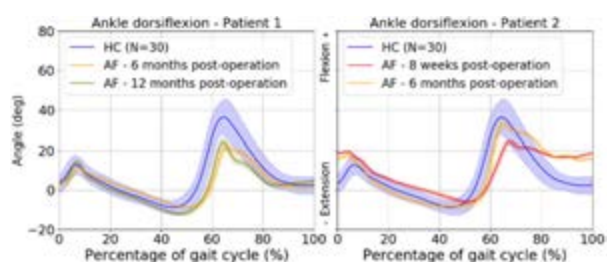
Figure 1: MIMU derived Mean and STD (30 steps) of ankle dorsiflexion during right step for healthy controls (HC) and for patients (1 and 2) with ankle fracture (AF).

Discussion

The results show that the recovery of ankle ROM of the injured side of an ankle fracture [7] can be confidently followed using low cost MIMU sensors and openly available algorithms and software [1,3,6] in a clinical setting. The data shows different compensation strategies and recovery patterns for the two patients. The normative dataset for healthy controls is also in line with those from optical motion capture [8]. Present literature estimates the accuracy of MIMU derived orientations, with sufficient optimization, to be from less than 3 degrees to 5 degrees [3,5]. The errors are comparable with optical motion capture traditionally used in clinical gait analysis [9], giving further confidence on applying MIMU derived kinematics in clinical decision making.

References

1. Mirando et al, Diagnostics, 12:1, 2022
2. Wren et al, Gait Posture, 80, 2020
3. Borno et al, bioRxiv, 2021.07.01.450788, 2021
4. Madwick et al, IEEE Int. Conf. Rehabil. Robot, 2011
5. Caruso et al, IEEE Sensors Journal, 21:3, 2021
6. Delp et al, IEEE. Trans. Biomed, 54:11, 2007
7. Gao et al, Appl. Sci., 9:21, 2019
8. Fukuchi et al, PeerJ 6:e4640, 2018
9. McGinley et al, Gait Posture, 29:3, 2009

Acknowledgements

MUSCULOSKELETAL SOFTWARE FOR TEACHING BIOMECHANICS AT UNDERGRADUATE AND MASTERS LEVEL

James Shippen, Barbara May

BoB Biomechanics Ltd., United Kingdom

Introduction

Whilst biomechanics is seen as fascinating by most researchers immersed in the field, many students being taught the subject do not share this level of interest. This situation can be partially attributed to the lack of teaching material which is informative, intuitive and engaging. BoB Biomechanics is addressing this deficiency by providing an environment in which the student is encouraged to experiment, enquire and gain a deep understanding of the principals employed in biomechanical analysis with a very short learning curve and minimal supervision.

Methods

BoB Biomechanics writes BoB/Research which is a musculoskeletal software package widely used for biomechanical analysis[1] with applications ranging from sports analysis[2] through clinical analysis[3] to ergonomic optimisation[4]. BoB/Research can import users' motion, force and EMG data to calculate many biomechanical metrics including joint range of motion, joint torques, muscle forces, joint contact forces etc.

BoB/Research was modified to embedded pre-recorded examples which illustrate biomechanical principles in a software package called BoB/Teaching. These examples range from simple single joint movements, through inverse dynamics illustration to motion captured trials. The trials include:

knee flexing, climbing stairs, ballet fouetté, basketball, manual handling, running, arm curl, single foot balance, jogging with EMG, wheelbarrowing, cycling with EMG, gait with EMG, baseball pitching, tennis serve and rowing.

BoB/Teaching inherits the sophisticated graphics of BoB/Research using the embedded interactive 3-dimensional viewer. BoB/Teaching also contains a template of student worksheets which can be edited to suit the preferences and style of individual instructors or used "straight from the box". There are also numerous on-line instructional videos to guide the student through the BoB/Teaching functions and features.

Results

BoB/Teaching has been beta tested by 12 instructors at teaching institutions in the UK, USA, Brazil and Germany who run biomechanics courses at undergraduate and Masters level.

The feedback from instructors on these courses indicated that the software package had a very short learning curve i.e. it was suitable for use in a single instructional session of 2 hours where the students had no prior biomechanical experimental experience.

Four instructors considered BoB/Teaching to be suitable as a substitution for experimental biomechanical laboratory exercises. In response to specific questioning, the instructors reported that the students found the examples of biomechanical activates to be engaging, informative and provoked independent learning.

Discussion

The utility and benefits of BoB/Teaching in the teaching of many biomechanical principles at undergraduate and Masters level has been demonstrated. The musculoskeletal software package has proven to be robust and practical to use in a teaching environment. Being interactive in a virtual environment, the students are receptive to the mode of operation of BoB/Teaching.

References

[1] Shippen J et al, HortTech, 27: 6, 746-753, 2017
[2] May B et al, J DanceSciMed, 14: 11-18, 2010
[3] Shippen J et al, Biosystems & Biorobotics, Springer: 917-921, 2018
[4] May B et al, Tech & Health Care, 26: (2018) 565–569, 2018

A NEW METHOD FOR DETERMINING THE KNEE AXIS OF ROTATION FOR MOTION CAPTURE

Eimear O'Regan[1], Dr Darren Dawson[1], Dr Keith Bryan[1]

1. *Munster Technological University, Cork, Ireland*

Introduction

The knee axis of rotation (AoR) is determined from motion analysis data and is used to determine knee joint kinematics. Currently, there are several predictive and functional methods used to determine the knee axis [1]. However, predictive methods require a static trial and are susceptible to errors caused by incorrect palpation and anthropometric measurements. Functional methods require a large range of motion (RoM) trial for accurate calculation of the joint axis, which can be difficult for participants with reduced mobility. This paper describes a new method for determining the knee AoR which overcomes the limitations of the existing predictive and functional methods.

Methods

The new method for determining the knee AoR is a functional method. The AoR can be calculated from a dynamic trial or three different positions of the leg. Therefore, no static or RoM trial is required and the markers can be placed anywhere on the thigh and leg segments.

In vitro validation of the method was carried out using a mechanical leg with a known hinge axis (see figure 1). Markers were placed randomly on the thigh and leg segments and the AoR was calculated using the new method and compared to the true AoR. The performance of the method was then compared to a widely used functional method, the Symmetrical Axis of Rotation Approach (SARA) [2].

Figure 1: Mechanical leg used for validation. The hinge axis is from KNE to KNEM.

Results

The AoR was calculated for varying joint RoMs. The new method was capable of calculating the AoR within 1.16° for a large range of motion (90°) and within 0.811° for a small RoM (5°) (see Table 1).

	New Method		**SARA**	
	Mean (°)	Standard Deviation (°)	Mean (°)	Standard Deviation (°)
90°	1.1618	0.3609	1.2567	0.0992
45°	1.0946	0.3393	0.8995	0.1612
30°	1.0412	0.4467	1.8477	0.1524
20°	0.7421	0.3546	2.0757	0.1700
10°	1.7674	0.2613	5.0358	0.0471
5°	0.8106	0.4132	10.121	0.0587

Table 1: Error in axis angle for varying RoMs.

The root mean square (RMS) error of the distance between the true axis and the functional axes were calculated. The RMS for the new method was less than 2.3mm for all RoMs. The new method had a lower RMS when compared to SARA for all RoMs (see figure 2).
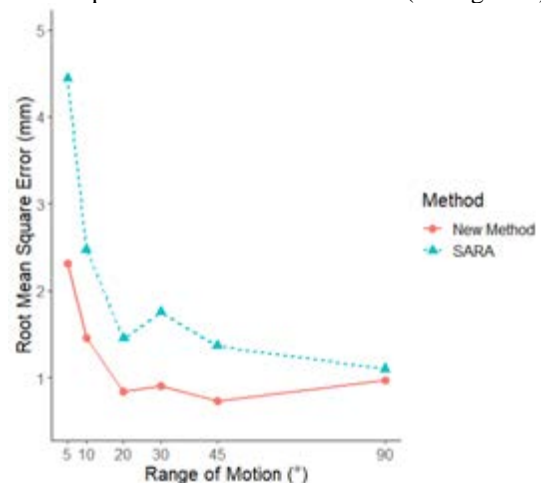
Figure 2: RMS error of the estimated AoR for the new method and the SARA method.

Discussion

The initial results using the new method suggest that the method is accurate, even during small ranges of motion and is independent of marker position. The new method appears to perform better than the SARA method as the RMS is less for all RoMs. In vivo validation of the new method will be carried out in a future study.

References

1. N. M. Fiorentino et al., Ann. Biomed. Eng., 44, 2168–2180, 2016.
2. R. M. Ehrig et al., J. Biomech., 40, 2150–2157, 2007.

Acknowledgements

CALIBRATION WAND DESIGN FOR MOTION ANALYSIS

Kristóf Rácz (1), Rita M. Kiss (2)

1. Budapest University of Technology and Economics, Faculty of Mechanical Engineering, Department of Mechatronics, Optics and Mechanical Engineering Informatics, Hungary

Introduction

Soft tissue artefacts are a well-known problem in marker-based gait analysis, but there is considerably less focus on the issue of anatomical landmark (AL) calibration accuracy, even though misplaced ALs can have significant impact on the results [1]. As a result, if AL locations are not consistent, the comparison of gait analysis results become very difficult. Experience shows that the inter-examiner distance of the placed AL positions is not negligible [2].

The goal of the present study is to establish how the design of a calibration wand used for locating ALs influence the precision of this calibration procedure in CAST [3] type motion analysis measurements.

Methods

Three experiments were performed to study the precision of 3 different calibration wand designs (Figure 1.), using an OptiTrack optical motion capture system.

Figure 1: Calibration wands. Wand A is an ad hoc design assembled with hot glue. Wands B and C are 3D printed with a tip machined on a lathe, with c being a slightly shorter design.

The calibration point of wand A was determined with 2 different methods: firstly, by placing a marker on the tip of the wand and setting the center of the tracked rigid body to that marker in the motion capture software (Wand A/I); secondly, by rotating the calibration wand with its calibration point fixed in a conical shaped hole and calculating the centerpoint of the rotation (Wand A/B). Wand B and C were only calibrated with the second method.

First, a single marker was placed on the ground, and the measure marker coordinates were recorded to establish the base precision of the system. Next, each calibration wand was placed 3 different points and orientations (all wands were placed in the same orientation in a given point) within the measurement volume, so that the long axis of the wand pointed approximately in the direction of one of the global coordinate-system's axes, and the position of the calibration point was measured for 1000 frames. Lastly, 3 distinct, well and exactly identifiably points were established in the measurement volume, and 4 examiners performed 31 calibrations with all wands at all 3 points.

The precision of each case is described with the RMS of the Euclidian distances of each data point from the center (average) of point belonging to the same case.

Results

The RMS of measuring a single marker with the motion capture system was 0.031 [mm]. Results of static and examiner measurements can be found in Table 1.

RMS [mm]	A/I	A/II	B	C
Static trial	0.115	0.122	0.087	0.289
Examiner A	1.190	3.541	1.570	3.738
Examiner B	2.030	3.761	1.741	8.376
Examiner C	2.742	2.413	2.51	5.495
Examiner D	1.789	2.432	1.53	8.758

Table 1: Average RMS across measurement locations of the static and examiner wand measurements

Discussion

Based on static trails, Wand B have a slight but noticeable increase in precision over wand A, wand C however is much worse. The smaller size of this design resulted in the motion capture system not being able to differentiate markers located close together.

Examiner trials further reinforce that wand C is not a good design. Between the two methods of calibration for wand A, counterintuitively the marker-based calibration makes for a more precise wand then the calculation-based calibration. This might be attributed to the fact that it was created with the marker-based calibration in mind, so the tip is less suitable for fixing in place with the conical helper hole.

Wand B shows a slight improvement on Wand A with ~0.2 [mm] better precision for 3 out of 4 examiners. The results show, that having a good, functional design for the AL calibration wand is important, as design mistakes can lead to considerably reduced precision.

References

1. Piazza et al, J Biomech 33:1029-1034, 2000
2. Rabuffetti et al, Hum Mov Sci, 21:439-455, 2002.
1. Cappozzo et al, Clin Biomech, 10:171-178, 1995.

Acknowledgements

HAND POSTURE AND FOREARM MUSCLE ACTIVITY DURING REACHING AND TRANSPORTATION TASKS: EFFECT OF PRODUCT WEIGHT AND TASK HEIGHT

A. Roda-Sales (1); N.J. Jarque-Bou (1); V. Bayarri-Porcar (1); J. L. Sancho-Bru (1); M. Vergara (1)
1. Departamento de Ingeniería Mecánica y Construcción, Universitat Jaume I. Spain.

Introduction

The ability to reach and manipulate objects involves complex dynamic relationships that are affected by many factors. This work aims to study the effect of object weight and task height on hand posture and forearm muscle activity.

Methods

Twenty-four right-handed healthy subjects (12 males, 12 females) participated in the experiment, approved by the university ethics committee. The participants wore a right-hand instrumented glove (Cyberglove Systems LLC) recording 18 degrees of freedom at 100 Hz, and surface EMG sensors (Biometrics Ltd) recording the muscle activity of seven specific spots of the right forearm [1] at 1000 Hz. They were asked to perform 6 transportation tasks using a cylindrical grasp: 3 bottles with same handle diameter (30 mm) and different weights (Figure 1, left), between 2 different heights (Figure 1, right): from H1 to H2, and from H2 to H3.

Figure 1: LEFT, bottles used: B1 (2 kg), B2 (3 kg) and B3 (4 kg). RIGHT, scenario with the different heights: H1 (1.5 m), H2 (0.95 m) and H3 (0.51 m).

Joint angles were obtained using a validated protocol [2], and filtered afterwards. EMG data was filtered and normalized using 7 MVC actions [3]. Data from each task were split into reaching and grasping phases using time stamps marked by the operator. Mean values were computed for each joint angle, subject, phase and task. A MANOVA (sig. ≤ 0.05) with Bonferroni post hoc was performed on the mean joint angles, with height, weight and their interaction as factors. Analogously, mean muscle activities were computed for each spot, subject, phase and task, and an analogous MANOVA was done.

Results

Figure 2 shows hand joints and muscle spots that showed significant differences. Significant differences are annotated with arrows, which in the case of the height indicate that the mean of the given parameter has been found higher (▲) / lower (▼) for the height H1-H2. In the case of weight, the arrow is accompanied with the affected bottle.

	Height		Weight	
Reach	CMC1_A▲, IP1_F▼, PIP2_F▼, MCP5_A▼, WR_A▼	Spots 1▲ 4▼ 6▼ 7▼	IP1_F (▲B1), MCP5_A (▲B1)	-
Grasp	CMC1_A▼, MCP1_F▼, IP1_F▼, MCP2_F▼, MCP4_F▲, MCP5_F▲, MCP5_A▼, PIP5_F▼, WR_A▼	Spots 1▲ 3▲ 6▲	IP1_F & MCP5_A (▲B1), MCP5_F (▼B1)	Spots 4 & 7 (▲B3)

Figure 2: Sig. differences. F for flexion, A for abduction; digits 1-5; Wrist (WR), Carpometacarpal (CMC), Metacarpophalangeal (MCP), Proximal Inter-phalangeal (PIP). Spot 1 (wrist flexors and ulnar deviators), spot 2 (wrist flexors and radial deviators), spot3 (finger flexors), spot 4 (thumb muscles), spot 5 (finger extensors), spot 6 (wrist extensors and ulnar deviators), spot 7 (wrist extensors and radial deviators).

Discussion

Task height and object weight affect hand posture and muscle activity. During grasping, height H1-H2 requires more flexed ring and little MCP joints, less flexed thumb joints and index MCP joint, and more muscle activity from finger flexors and wrist stabilizers (wrist ulnar deviators). This is attributable to the performance of the grasp at a less reachable position, which requires dynamic adjustments of the hand to fit the bottle handle diameter, observing that index and thumb do not fit completely. Bottle weight affects IP1_F and little finger as well as thumb muscles and wrist radial deviators (only for the bottle of 4 kg), which highlights the importance of thumb and wrist for a stable grasp during cylindrical grasping for heavier objects. Weight affects the muscles responsible for holding the object, while height affects the muscles responsible for wrist position during transport. During reaching, height H1-H2 requires more flexion from CMC1_A and more activity from wrist ulnar deviators. Object weight only affects hand posture, probably due to differences in the handle, or due to prior visual preparation for the task.

References

1. Jarque-Bou, NJ et al. J. NeuroEng. Rehabil. 15:1-11, 2018.
2. Gracia-Ibáñez, V. et al. Comput. Methods Biomech. Biomed. Eng. 20:587-597, 2017.
3. Jarque-Bou, NJ et al. Sci Data 6, 270, 2019.

Acknowledgements

MOTOR CONTROL IN A POPULATION OF YOUNG SUBJECTS WITH IDIOPATHIC SCOLIOSIS: THE MOTOR-CHILD STUDY

Rita Stagni (1), Giuseppina Maria Grazia Farella (2), Federico Vanzini (2), Roberto Tedeschi (2), Maria Grazia Benedetti (2), Maria Cristina Bisi (1)

1. Physical Medicine and Rehabilitation Unit, IRCCS-Istituto Ortopedico Rizzoli, Bologna, Italy; 2. Department of Electric, Electronic and Information Engineering "Guglielmo Marconi" – DEI, University of Bologna, Italy)

Introduction

Motor development is an adaptive process occurring within a self-organizing system and influenced by several factors. While evidence exists for motor control in severe pathologies (e.g. cerebral palsy), minor musculoskeletal conditions, such as scoliosis, have never been explored. Clinical-functional tests used for the analysis of motor control are time-consuming and significantly operator-dependent, hindering applicability to large populations. Inertial Measurement Units (IMUs) have paved the way to low-cost ambulatory quantitative assessment: allowing the estimation of temporal gait parameters [1], while nonlinear metrics such as multiscale entropy (MSE) [2] and recurrence quantification analysis (RQA) of trunk 3D acceleration, allowed to quantitatively assess motor development [3,4]. The aim of this work was to assess motor control alterations in children and adolescents affected by idiopathic scoliosis using clinical-functional tests and IMU-based metrics related to motor control.

Materials and Methods

Thirty-four children aged between 6 and 16 years with scoliosis (ATR $\geq 5\,°$ or Cobb $\geq 10°$) were included. They underwent MovementABC-2 for clinical assessment of motor competence.

Three tri-axial IMUs (MetamotionR, mbient-Lab, USA) were attached on the lower back and on the shanks of each child. 3D acceleration and angular velocity data were recorded at 200Hz while the participants walked at self-selected speed back and forth, two times in normal (NW) and once in tandem walking (TW) along a 15m path. Foot contacts and offs were identified from the angular velocity around the medio-lateral axis of the shank [5]; turns, and the first and last two strides of each walking section were removed from the signal [6]. Stride-, stance-, and double support- (DS) times were calculated from foot contact events. Temporal parameter variability *per* subject was calculated as standard deviation. MSE (τ=1 to 6), related to complexity and automaticity, and RQA, related to pattern regularity, were calculated on trunk acceleration data along the 3 directions (vertical, V, med-lat, ML, and ant-post, AP) [3,4]. Data were compared to those of healthy peers of corresponding age [3].

Results

As referred to Movement ABC-2 test, 12 patients received scores above the 50th percentile (35.3%) and 22 below (64.7%). No significant correlation was observed with the degree of scoliosis (Cobb angle) or the degrees of torsion (ATR).

As referred to temporal parameters, subjects resulted slower during NW, with larger dispersion of Stance and DS than healthy peers, while during TW, subjects above 12 years of age resulted slower, with longer stance and DS for increasing age as compared to their healthy peers. As referred to non-linear metrics, subjects showed larger MSE during NW for lower values of τ (1 to 3) in the ML and V direction and reduced RQA in AP direction for increasing age as compared to healthy peers; during TW, reduced MSE for lower values of τ (1 to 3) in the V and AP direction and increased RQA in AP direction.

Discussion

Children affected by idiopathic scoliosis showed alterations of motor control. In particular, temporal parameters highlighted a slower and less stable gait, more evident for increasing age as related to TW. Lower stability is also related to a less mature motor control with a delay in the development of the automaticity characterizing healthy peers, and a reduced development of the motor complexity required for more demanding locomotor tasks.

less mature motor control: in NW, increased MSE in the frontal plane highlights a delay in the development of the automaticity characterizing healthy peers, as well as reduced regularity (RQA) in the AP direction; in TW, reduced MSE in the sagittal plane and increased RQA in the AP direction are the manifestation of a reduced development of the motor complexity necessary for the management of the more demanding locomotor task.

These preliminary data suggest that idiopathic scoliosis affects motor control in the developing population. In addition, IMU-derived metrics demonstrated their effectiveness in complementing clinical assessment, allowing to characterize the type of motor alterations related to the specific clinical condition.

References

1. Clark et al., J. Sports Sci. 0:1-41, 2021.
2. Costa et al., Phys.Stat.Mech. Its Appl. 330:53–60, 2003.
3. Bisi et al. Gait&Posture. 68:232–237, 2019.
4. Bisi & R. Stagni, Gait&Posture. 47:37–42, 2016.
5. Salarian et al., IEEETransBiomedEng, 51:1434–43, 2004.
6. Tamburini et al., Gait&Posture, 59:248–252, 2017.

DYNAMIC ANALYSIS OF GAIT MOTION IN OSTEOARTHRITIC WOMEN

Torras J.(1), Espinoso A.(1), Tio L.(2), Castro-Domínguez F.(2,3), Monfort J.(2,3), Monllau JC.(2,4), Gonzalez-Ballester MA.(1,5), Noailly J.(1), Tassani S.(1)

1 BCN MedTech, DTIC, Universitat Pompeu Fabra, Barcelona, Spain; 2 IMIM, Barcelona, Spain; 3 Rheumatology Department, Hospital del Mar, Barcelona, Spain; 4 Orthopedic Surgery and Traumatology Department, Hospital del Mar, Barcelona, Spain; 5 ICREA, Barcelona, Spain;

Introduction

Over 300 million people around the world, mainly woman, suffers from Osteoarthritis (OA), a multifactorial disease affecting joints. It occurs most frequently in the hands, hips, and knees.

Nowadays, studies of human motion dynamics have been frequently applied with biomechanical and computational models that use kinematic and kinetic parameters. Some studies of gait analysis were also presented [1], however none of them consider OA subjects.

Nonlinear time series analysis forms a group of algorithms and measures used to extract dynamical features underlying measured signals. It allows one to describe dynamical systems where nonlinearities lead to complex time evolution. Unlike deterministic models that produce the same exact results for a particular set of inputs, stochastic models are the opposite; the model predicts outcomes that account for certain levels of unpredictability or randomness [2].

The main objective of this study is to analyse the human gait motion in women that suffer from OA to investigate the predictability of the underlying dynamics.

Material and Methods

We analyze data of 13 women who suffer from OA; 6 who planned Total Knee Replacement (TKR) and 7 who followed conservative treatment. Gait recordings were performed using 8 cameras BTS Smart-DX 700, 1.5 Mpixels 250 fps and 2 force plates BTS P-6000 500 Hz sampling (BTS S.p.A., Milan, Italy). Helen Hayes marker protocol with medial markers was used [1]. Each volunteer was asked to perform 5 valid gait sequences.

We apply the embedding theorem to obtain delay coordinates and obtain an estimation of how much this data is predictable. We applied a delay of $\tau = 45$. Pattern from the phase generated by the hip abduction adduction were studied and classified into deterministic or stochastic [1, 2].

Results

The embedding analysis shows the predictability from the patterns of the data studied from OA patients. The results of an exemplary TKR patient and one treated with conservative treatment are shown in Fig. 1 and Fig. 2, respectively.
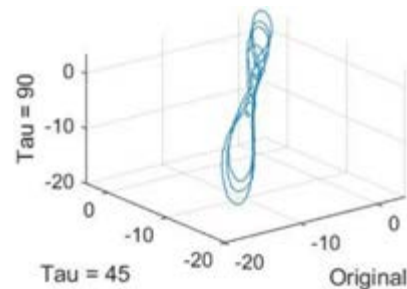
Figure 1: Embedding diagram of the right hip of an OA patient that has TKR.
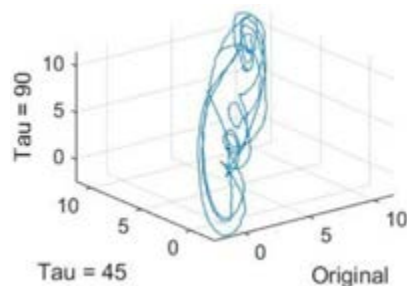
Figure 2: Embedding diagram of the right hip of an OA patient that was treated in a conservative way.

Discussion

Parallel lines presented in the embedding diagram identify region of the gait characterized by mainly deterministic behavior. When parallel trajectories are lost the behavior tends to be more stochastic. In general, in our results seem that patients with TKR are more resilient and maintain more coherence when embedding increases compared to conservative patients which seems to present a more stochastic behavior. However, this occurs in most cases but not in all patients. For future studies, analysis techniques are going to be used to study the variability of the dynamics underlying the human gait motion and possibly help the clinicians in the treatment decision.

References

1. Perc, M. (2005). Europ. J. of physics, 26(3), 525–534.
2. Andrzejak, R.G. (2011). Nonlinear Time Series Analysis in a Nutshell.
3. R. B. Davis et al. Hum. Mov. Sci., vol. 10, no. 5, pp. 575–587, 199

Acknowledgements

RECORDING WRIST CIRCUMDUCTION WITH DIFFERENT SENSORS FOR CLINICAL ASSESSMENT

Margarita Vergara, Raquel Lázaro Belenguer, Verónica Gracia-Ibáñez, Néstor Jarque-Bou, Joaquín L. Sancho-Bru

Mechanical Engineering and Construction Department, Universitat Jaume I. Spain, vergara@uji.es

Introduction

Wrist circumduction is increasingly used as a functional motion assessment for patients [1]. It is a better indicator of functionality in terms of activities of daily living performance [2] than the measurement of isolated flexion-extension (FE) and radial-ulnar deviation (RUD). Its measurement requires clear instructions, especially regarding the rotation sense and the fingers posture [3]. Goniometers have been traditionally used [2,4] and their accuracy is widely accepted, although differences can be found depending on the device used [1]. Less invasive or more affordable devices would be welcomed by practitioners to measure circumduction in clinical practice. In this work, two alternatives are analyzed: micro electromagnetic motion trackers (Micro Sensor 1.8 by Polhemus) and wifi IMUs sensors (MTAwinda from Xsens).

Methods

Wrist circumduction movement of 5 subjects (3 men, 2 women; 4 right-handed, 1 left-handed) were recorded in both hands with 3 different devices (Figure 1): electro-goniometers (EG), inertial measurement units (IMUs) and micro electromagnetic trackers (mEMT). With the forearm resting on the table, the hand cantilevered, and starting from a neutral posture, the subject completed six maximal circumduction laps in radial direction (counterclockwise right hand, clockwise left hand). The recording was repeated for mEMT and IMUs (2 sessions, twice each session) to assess reliability and repeatability. Only one measure was performed with EG. The envelope of the six circumduction laps was obtained (plot of angles of FE vs. RUD) and six values were considered for each record, the mean module of vectors with origin in 0.0º in each octant sector: UD, F-UD, F, F-RD, RD, E-RD, E, E-UD, being UD: ulnar deviation, F: flexion, RD: radial deviation and E-extension. Intra- and inter-session errors were computed. After averaging results of all the repetitions performed by each subject, measurements were compared by means of a repeated-measure ANOVA.

Results

Intra-session errors were smaller than 4.5º and 3º for IMUs and mEMT, respectively, and inter-session errors were smaller than 4.2º and 3.7º. Figure 2 shows mean circumduction records for each device, and significant differences marked. No significant differences were found between IMUs and mEMT except for E-RD direction in non-dominant hand. Significant differences appeared when comparing IMUs and mEMT with EG, EG showing higher values around UD and E-UD directions in dominant hand and around E in non-dominant hand (Figure 2).

Figure 1: Devices used: (a) Electrogoniometer, (b) IMUs and (c) Micro electromagnetic sensor.
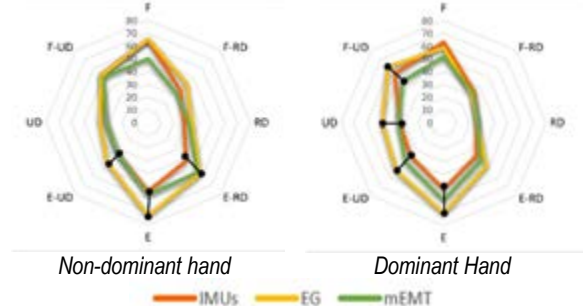
Figure 2: Mean values (degrees) in each octant with the three devices. Black lines: significant differences

Discussion

IMUs and mEMT are as reliable and repeatable as EG: intra- and inter-session errors are similar to EG errors (3º and 3.8º, respectively [5]). IMUs errors are a bit higher probably because they are more bulky and might hinder movement. When comparing with the EG, differences around extension and ulnar deviation directions appear. They can be due to the well-known crosstalk effect of EG [6]. The other devices do not present this effect as the forearm rotation is also computed: mean pronation angles recorded were 13º (IMUs) and 10º (mEMT), although subjects were advised to lay forearm on the table to avoid pronation. Other source of differences may come from the non-simultaneity of the recordings. IMUs and mEMT seem promising devices for clinical practice, being IMUs more affordable and mEMT smaller and less invasive.

References

1. Nadeem et al, J Hand Surg, doi:j.jhsa.2021.03.026, 2021.
2. Gracia-Ibañez et al, J Biomech, 110, 109975, 2020.
3. Gehrmann et al, J Hand Surg, 8, 1287-1292, 2008.
4. Dauncey et al. J- Hand Ther.3, 328-336, 2017.
5. Rawes et al, J Hand Surg. Br. Eur.,21, 600-603, 1996
6. Hansson et al, J Electromyogr Kinesiol, 14:355-67, 2004

Acknowledgements

DETECTING A NEW CATEGORY OF FLEXION CONTRACTURE PATIENTS IN TOTAL HIP ARTHROPLASTY

Claudio Vergari (1), Youngwoo Kim (2), Mitsuru Takemoto (2), Yu Shimizu (2), Chiaki Tanaka (3), Shunya Fukae (2), Shunsuke Fujibayashi (4), Shuichi Matsuda (4)

1. Arts et Métiers Institute of Technology, Institut de Biomécanique Humaine Georges Charpak, Paris, France, 2. Department of Orthopaedic Surgery, Kyoto City Hospital, Kyoto, Japan, 3. Department of Orthopaedic Surgery, Gakkentoshi Hospital, Kyoto, Japan, 4. Department of Orthopaedic Surgery, Kyoto University Graduate School of Medicine, Kyoto Japan

Introduction

Hip osteoarthritis is sometimes accompanied by flexion contracture of the hip, which is a partial flexion of the joint that cannot be straightened (Figure 1). It can can lead to pain, impaired locomotion and a decreased quality of life. Patients with flexion contracture must adapt their whole sagittal alignment to compensate this flexion while to keeping balance.

This condition is usually diagnosed with physical examination, but this method does not account for pelvic morphology and orientation, which play an important role in hip function.

In this work we propose a novel method to diagnose hip flexion contracture through radiological examination and analyse the biomechanical compensation mechanisms deployed by these patients.
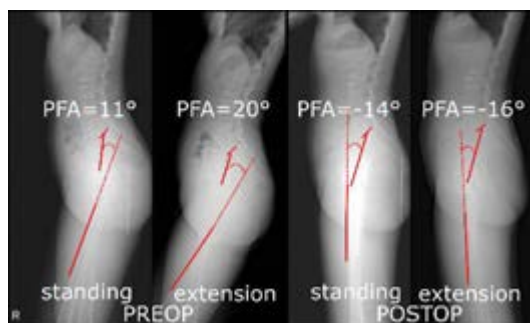

Figure 1: Example of hip flexion contracture which was solved postoperatively.

Methods

Patients with hip arthrosis and an indication for total hip arthroplasty (THA) were included in a prospective cohort. Full-body standing lateral radiographs were acquired in free standing position and in extension (Figure 1), both before and 6 months after THA. Standard spinopelvic parameters were measured: pelvic incidence (PI), pelvic tilt (PT), lumbar lordosis (LL), T1-pelvis angle.

Pelvic-femur angle (PFA) was measured as the angle between the femur and a line drawn from the middle of the sacrum endplate to the centre of the interacetabular hip axis [1]. Patients with low PI ($< 45°$) were included in the hip contracture group if their PFA was higher than $5°$, while the threshold was $-5°$ for patients with standard or high PI ($PI \geq 45°$). Patients were administered the Japanese Orthopaedic Association Hip Disease Assessment Questionnaire [2] to assess quality of life (QOL) before and after surgery. Results are reported as median [2nd quantile, 3rd quantile].

Results

129 patients were included, 105 women and 24 men, median age 70 [63; 76] year old. PFA was significantly correlated to PI (Spearman's rho=-0.4, p<0.001).

Thirty-seven patients (29%) were in the hip flexion contracture group, which by definitions showed higher PFA than non-contracture patients (p<0.001). Contracture patients also had lower PT and PI-LL mismatch, higher LL and lower T1-pelvis angle (p < 0.001). These differences tended to decrease postoperatively, but they remained significant. Both groups showed similar QOL before surgery (16 [11, 28]), but contracture patients showed higher postoperative improvement than non-contracture ones (67 [60, 76] versus 52 [39, 66]).

Discussion

This study showed that a new category of patients can be detected by measuring the pelvis-femoral angle in extension. This angle represents the extension capacity of the hip joint and, unlike the femoral tilt angle, it accounts for pelvic morphology. Indeed, the negative correlation between PFA and PI shows patients with higher PI can have higher hip mobility in flexion.

It is interesting to notice that this classification of patients based on PFA can highlight a population that shows a specific pattern of sagittal alignment at all levels of the sagittal chain of balance, from the hip to the head. The biomechanical strategies of these compensatory mechanisms and their clinical implications should be further studied.

References

1. McKnight et al, J Arthroplasty 34:S53–S56, 2019
2. Matsumoto et al, J Orthop Sci 17:25–38, 2012

Acknowledgements

TIGHTLY COUPLED INERTIAL AND RADIO-BASED FOOT-WORN SENSORS FOR AMBULATORY SPATIAL GAIT ANALYSIS

Frank Wouda (1), Ibrahim Bilal (1), Uthvag Sakthivelu (1)

1. Movella B.V., Pantheon 6A, 7521PR Enschede, The Netherlands

Introduction

Full-body ambulatory gait analysis is typically performed using inertial measurement units (IMUs), this analysis can be accurate by combining biomechanical constraints and boundary conditions (e.g., zero velocity updates) [1]. When the number of sensors in this setup is minimized, the position/orientational drift from IMU can result in inaccurate spatial outcomes due to sensor drift and magnetic distortions [2]. Previous works have combined IMUs on the feet with ultrasonic sensors to obtain drift-free feet positions [3]. However, ultrasonic sensors can only provide a one-dimensional distance measurement, and suffers from occlusions. To alleviate shortcomings of previous work, this study combines IMUs with ultra-wideband (UWB) sensors, which provide relative distance and angle of arrival (AoA) to obtain improved spatial gait parameters.

Methods

This work[†] fuses the data from Xsens DOT IMUs (Xsens B.V, Enschede, Netherlands) and the Decawave UWB PDOA (Decawave Inc. Dublin, Ireland) beta kit to obtain spatial gait parameters by use of an Error-State Extended Kalman Filter (ES-EKF). The EKF tracks the following states (for both feet): position, velocity, gyroscope bias, orientation error, and distance bias; and has the following measurements: acceleration, angular velocity, relative distance and AoA.

The performance of this method was evaluated by comparing the step length/width of four subjects (with height of 184 ± 6 cm). The proposed solution (shown in Figure 1) and lower-body Xsens MVN Awinda and HTC Vive (for accurate positioning) were used simultaneously for the measurements [4]. An ethical clearance was acquired from the University of Twente, Enschede, Netherlands for the experiments. Each trial begins with a standing pose calibration with a fixed distance between the feet, and then walking five metres in a straight line.

Figure 1: IMU and UWB sensors attached to the shoes of the subject.

Results

The distance between the feet is calculated from the position state of the filter. The estimate of the instantaneous distance between both feet during a walking trial is plotted against time in Figure 2. As a reference, a curve for the aforementioned ground truth is also plotted. Long trials were also conducted, and the root mean square error (RMSE) of the gait parameters is tabulated in Table 1.
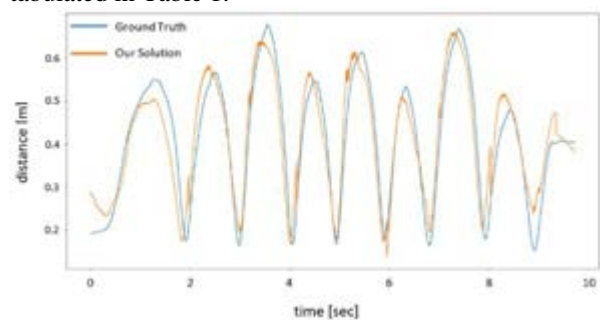
Figure 2: Estimated distance between feet from MVN+ Vive (Blue) and our solution (orange).

EKF input	step length	step width	overall
IMU only	5.6 ± 3.2	12.8 ± 13.6	10.6 ± 10.5
IMU+UWB	2.9 ± 2	2.9 ± 2.3	2.9 ± 2.2

Table 1: RMSE statistics of gait parameters (compared to MVN+Vive) as a percentage of subject's height.

Discussion

The results show considerable agreement between the ground truth and the minimal sensing gait analysis solution. The overall correlation between the relative feet distance was found to be around 0.89. The proposed solution has been tested over prolonged experiments (>10 min) with consistent results.

In future, the system will be tailored to provide real-time feedback to the user. A further improvement is to apply sophisticated antenna beamforming algorithms on the UWB node, that is equipped with multiple antennas. This provides better measurements of azimuth and elevation angles which can be exploited by the EKF.

This drift-free minimal sensing solution has potential in ambulatory analysis of gait, such as running, walking, remote rehabilitation in any environment.

References

1. D. Roetenberg, Xsens Technologies whitepaper, 2013.
2. H. Koyu, Front. Physiol., 10:1530, 2020.
3. D. Weenk et al, IEEE TNSRE 23.5: 817-826, 2014.
4. D. Niehorster, i-Perception, 2017.

† A provisional patent on the research has been applied at the USPTO.

PARROTS ACHIEVE GREATER MECHANICAL EFFICIENCY ON ARBOREAL SUBSTRATES

Melody W. Young (1), Edwin Dickinson (1), Nicholas D. Flaim (1), Aaron C. Bastian (1), Michael C. Granatosky (1, 2)

1. New York Institute of Technology College of Osteopathic Medicine, United States of America 2. Center for Biomedical Innovation, United States of America

Introduction

Arboreal locomotion is challenging because animals traverse thin, compliant substrates prone to oscillation. One strategy to achieve arboreal stability is to limit vertical oscillations of the center of mass (COM), thereby potentially negating further undesirable substrate oscillations(1, 2). The mechanical and energetic consequences of maintaining a steady, unchanging COM have scarcely been studied in the context of arboreal locomotion. We test these consequences in parrots, which are well-known for their arboreal prowess, but few studies have explored their locomotor behaviour. We present kinetic data to quantitatively assess how the parrot's COM varies between bipedal walking on flat substrate, to movement on a pole, and the energetic cost of arboreal locomotion.

Methods

To assess how COM shifts during bipedal walking and arboreal locomotion, we collect kinetic loading data as rosy-faced lovebirds (*Agapornis roseicollis*) walked on flat and a simulated arboreal substrate instrumented with an AMTI HE6X6 low load force plate. From these ground reaction forces, we use classic COM calculations to calculate phase, percent recovery, velocity, vertical displacement, energy expenditure, and power production.

Results

On all substrates, parrots adopt phase values consistent running gaits regardless of duty factor. On arboreal substrates, parrots adopt sidling gaits, in which forward motion is achieved with the frontal plane parallel, rather than perpendicular, to the line of travel. Sidling gaits are characterized by increased vertical displacements of the bird's COM and greater energy recovery. As such, parrots achieve greater percent recovery of energy (Figure 1a) on arboreal versus terrestrial substrates. Further, parrots' require overall lower power production per stride on the pole compared to flat substrate (Figure 1b).

Discussion

This study is the first to quantitively describe the sidling gait, which is likely a neuromuscular adaptation to achieve stability on arboreal substrates when ankle inversion potential is limited. This arboreal gait is associated with greater vertical displacements of the COM and increased energy recovery. Via this pendular mechanism of energy recovery, sidling birds produce a more mechanically efficient gait than when walking on a flat substrate, such that total power per stride is reduced by almost half. Our findings are the first to compare arboreal *vs.* terrestrial locomotor costs in a bird and demonstrate that adaptations for arboreal locomotion have mechanical consequences when moving terrestrially. Such data have evolutionary implications when considering the potential for invasion into terrestrial niches by arboreally-adapted species.

Figure and Tables
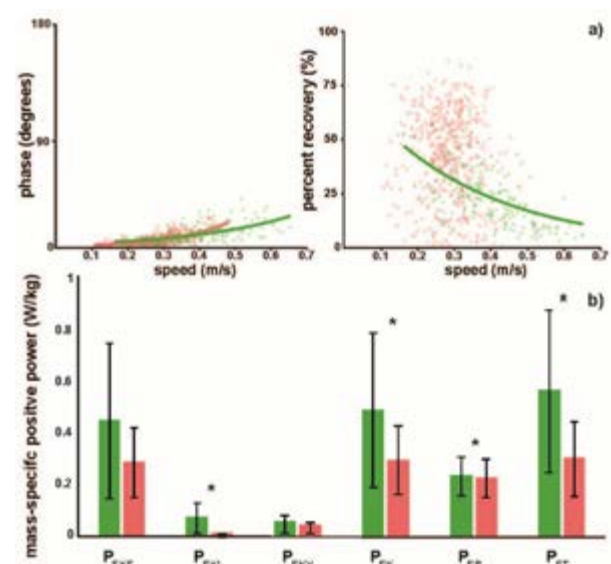
*Figure 1: Phase and percent recovery by speed (a) and mass-specific positive power across a stride (b) on flat (green) and pole (pink) substrates. In order: kinetic-fore-aft, kinetic-mediolateral, kinetic-vertical, kinetic, potential, total energy. * denotes significant difference between substrates after accounting for velocity.*

References

1. M. C. O'Neill, D. Schmitt, *J Exp Biol*. **215**, 1728-1739 (2012).
2. A. Schmidt, M. S. Fischer, *J Exp Biol*. **213**, 3615-2624 (2010).

EFFECT OF ACL RECONSTRUCTION ON THE MUSCLE ACTIVITY OF THE KNEE DURING SELECTED ACTIVITIES

Paulina Zalewska (1), Tomasz Guszczyn (2), Szczepan Piszczatowski (1)

1. Bialystok University of Technology, Poland; 2. The Medical University of Bialystok Children's Clinical Hospital, Poland

Introduction

A complex system of anatomical structures working together to prevent excessive bone movement is required to maintain the stability of the knee joint [1]. In this complex system all the muscles surrounding the knee, the hip muscles and the gastrocnemius muscle play an important role [2]. An anterior cruciate ligament (ACL) injury, the need to undergo reconstruction surgery and rehabilitation mean new working conditions for the muscles. So, the aim of the study is assessment of muscle activity of the knee in patients after ACL reconstruction during gait, jumping and one leg standing.

Methods

The studies involved 36 participants who underwent ACL reconstruction using one of the two methods – with use of the Internal Bracing method (12 patients), as well as an autologous graft (24 patients) and the rehabilitation process has been completed. Patients were qualified for the project on the basis of clinical assessment made by an orthopaedist. The research was approved by the bioethics committee. Seven actons were selected for the assessment of muscle activity: rectus femoris, vastus medialis, vastus lateralis, semitendinosus, biceps femoris, and the two heads of the gastrocnemius muscle (medial and lateral). The electrode was placed according to standardized procedures. Both the non-operated limb (ACL-NO) and the operated limb (ACL-O) were examined. The exercises consisted of: (1) gait, (2) jumping from an elevated platform, and then vertical jumping off the ground and (3) standing on one leg for 10 seconds after a simulated fall from a platform. Muscle activity was recorded until at least 5 good attempts were obtained. In order to normalize the results, the MVC (maximum voluntary contraction) procedure was performed. The obtained results were related to the duration of: (1) the gait cycle, (2) the contact with the ground (from the first contact of the toes, through the greatest knee flexion, until the toes off the ground), (3) for 10 seconds after first contact of toes with the ground.

Results

Figure 1 presents the example results for non-operated (ACL-NO) and operated limb (ACL-O).

Discussion

Analysing results presented in Figure 1 differences between the operated and the non-operated limb can be noticed. In the case of gait, higher activity of vastus medialis and semitendinosus were observed especially at the beginning of the gait cycle (approx. 0-30%), which suggests that these muscles work more in operated limb when stabilising the first knee flexion. This difference is even more pronounced in the case of jumping, where muscle activity of vastus medialis and semitendinosus for the operated limb was higher throughout. The differences reached even over a dozen percent.

Summarizing, there is a visible effect of muscle activity in persons after ACL reconstruction. The study is still continuing due to successive availability of people operated on by different methods. This will allow us to determine the effect of reconstruction type on muscle activity.

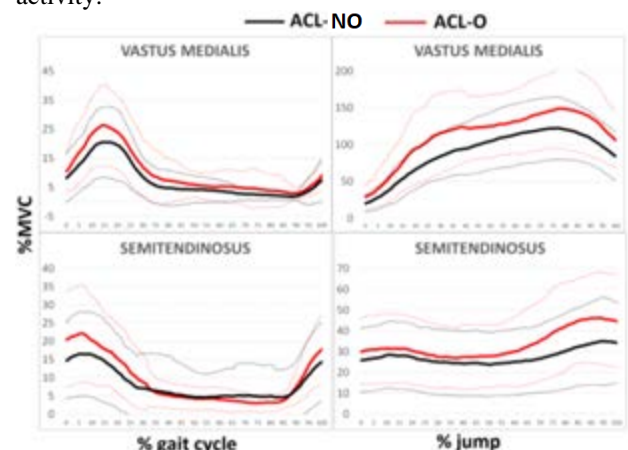*Figure 1: Muscle activity during gait and jumping as using vastus medialis and semitendinosus as an example (black line ACL-NO, red line ACL-O)*

References

1. Zlotnicki et al, Curr Rev Musculoskelet Med, 9:114-122, 2016.
2. Abulhasan et al, J Funct Morphol Kinesiol, 2(4), 34, 2017.

Acknowledgements

THE EFFECT OF STENT GRAFT CURVATURE ON MIGRATION RISK IN ABDOMINAL AORTIC ANEURYSM ENDOVASCULAR REPAIR

Moshe Brand (1), Bar Yoel (1), Moshe Halak (2), Chen Speter (2), Gil Marom (3)

1. Ariel University, Israel; 2. The Chaim Sheba Medical Center, Israel; 3. Tel Aviv University, Israel

Introduction

Abdominal aortic aneurysms (AAA) are usually repaired by endovascular treatment with a stent graft (SG) [1]. In some cases, there is a migration of the SG, which is caused by the hemodynamic drag force (DF) that acts on the walls of the graft [2]. The aim of this study is to determine the relationship between the curvature shape of the SG and the hemodynamic DF based on computational fluid dynamics (CFD) calculations for patient-specific anatomies.

Method

Here we suggest two methods to define and quantify the centreline curvedness (CLC) of the SG. The first is based on the local radius of curvature (CLC-R), and the second is based on the distances between the centrelines and similar idealized centrelines of straight branches (CLC-D) (Figure 1). Four 3D CFD models of specific patients were created from 3D CT scans. The geometries were reconstructed with SimVascular open-source software and then were smoothed with Autodesk Meshmixer. The finite volume model was solved in ANSYS Fluent. The DF was calculated throughout the cardiac cycle, and the maximum value was obtained at peak systole. The relationship between the CLC and the DFs was examined. In order to relate the values of the DF with the CLC, it is necessary to quantify the CLC values to a global value, and two methods were examined: average values and average variation along the centreline, for both CLC-R and CLC-D.
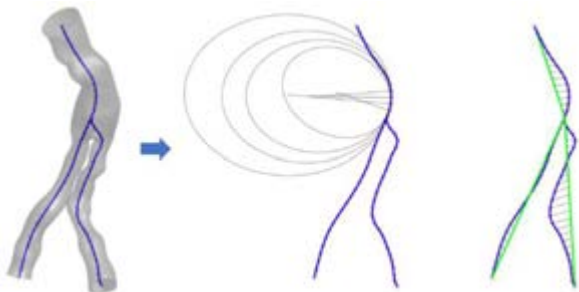
Figure 1: Centreline curvedness of the SG (CLC) (left), local radius of curvature (CLC-R) (middle), distances between the centrelines and similar idealized centrelines of straight branches (CLC-D) (right).

Results

Wall shear stress (WSS) distributions showed a match between high-stress regions and locations with high CLC (Figure 2). From the results obtained, it can be seen that curvature evaluation by the average variations gives an excellent prediction of the drag force value in both methods, with coefficients of determination of 0.9781 or 0.9379 (Figure 3).
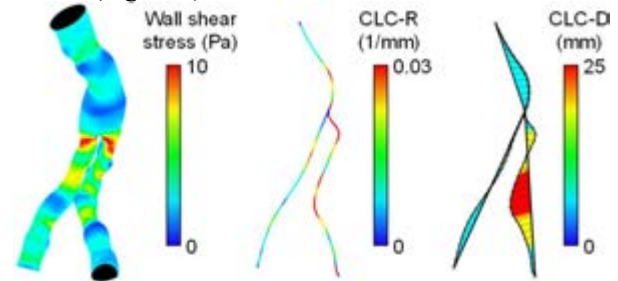
Figure 2: Comparison of WSS distribution (left), CLC-R (middle) and CLC-D (right) distributions along the centrelines.
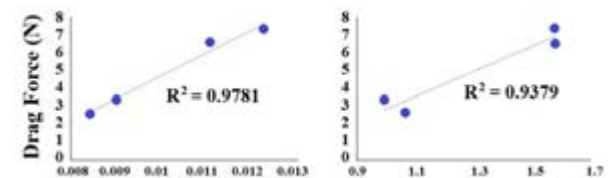
Figure 3: Average variation in curvature (1/mm) (left), Average variation in distance from line (mm) (right).

Conclusions

Our hypothesis, that curvature variability is a dominant factor that increases the shear stresses and drag forces, is supported by these results. These results will help surgeons diagnose possible migrations before or after the procedure and provide appropriate treatments.

References

1. Jones, SM., et al. "Computational fluid dynamic analysis of the effect of morphologic features on distraction forces in fenestrated stent grafts." *Journal of vascular surgery* 60.6 (2014): 1648-1656.
2. Altnji, H-E., B. Bou-Saïd, and H. Walter-Le Berre. "Morphological and stent design risk factors to prevent migration phenomena for a thoracic aneurysm: a numerical analysis." *Medical engineering & physics* 37.1 (2015): 23-33

NUMERICAL STUDY OF NON-NEWTONIAN EFFECTS ON THROMBUS FORMATION UNDER VENOUS FLOW CONDITIONS

Veronika Dušková, Alena Jonášová, Stanislav Plánička, Jan Vimmr

Dept. of Mechanics and NTIS, Faculty of Applied Sciences, University of West Bohemia, Czech Republic

Introduction

Although a necessary process, blood clot formation can in certain cases become life-threatening, especially in patients who underwent a vascular reconstruction procedure. To assess the risk of occlusive thrombotic events and to predict their future course, results of computer simulations can be used. Building on our previous study [1] on mathematical modelling of postsurgical thrombosis in portal vein reconstructions, where the formation and growth of blood clots were noted to be predominantly affected by the local haemodynamics and vessel geometry, the aim of the present study is to determine whether the blood viscosity affects the spatiotemporal formation of thrombi and their histological composition.

Methods

In accordance with the processes leading to intravascular blood clot formation, the mathematical model considered in the study accounts for the presence of two main thrombus components – bound platelets and fibrin polymers. In this context, the complex mechanism of blood clot formation can be divided into two stages: The initial one, governed by the continuum model proposed in [2], reflects the formation of a platelet plug at the injury site, while the final stage represents fibrin activation and polymerisation, described by a model loosely based on the Smoluchowski coagulation-fragmentation equation [3].

Modelling the growing thrombus as a porous medium with varying permeability, its complex interaction with the local blood flow is expressed by means of the modified Navier-Stokes equations and numerically solved using Ansys Fluent. To study the effect of blood viscosity, the blood is modelled both as a Newtonian and a non-Newtonian fluid of Carreau-Yasuda type.

Results and Discussion

For the purpose of the study, several models of portal vein reconstructions were acquired from available medical data in accordance with their geometrical predisposition to thrombotic events. An example of such a geometry is shown in Figure 1, where the injury site leaking the thrombosis trigger is assumed to be located at the upstream anastomosis (shown in blue).

The lower part of Figure 1 illustrates how the blood viscosity can affect the location and composition of the thrombi formed 11 minutes after initiating trigger release. Particularly notable in this regard is the significant difference in the distribution of both fibrin polymers (left) and bound platelets (right). The reason for these different developments can be found in the way the non-Newtonian rheology impairs the washout of coagulation factors in the low-velocity zones adjacent to the injury site, leading to accelerated formation of fibrin polymers. By contrast, the thrombus formed in the Newtonian blood flow is much smaller and comprises of a core of tightly packed platelets and an outer shell filled up with weakly bound platelets and fibrin polymers. Overall, our numerical results suggest that the blood viscosity is another important factor that should be taken into consideration when dealing with thrombosis, seeing as it plays a significant role in the formation and composition of the resulting thrombi.

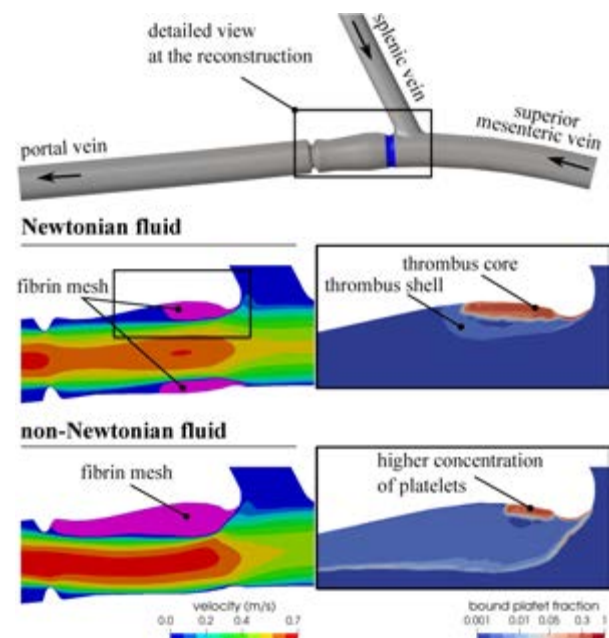*Figure 1: Selected vascular geometry and comparison of formed blood clots as computed for the Newtonian and non-Newtonian fluids – fibrin mesh (left) with corresponding distribution of bound platelets near the upper wall (right)*

References

1. Dušková V. et al, Proc ESB 2021.
2. Link K. et al, Multiscale Model Sim, 18:1489-1524, 2020.
3. Rukhlenko O.S. et al, PLOS One, 10:e0134028, 2015.

Acknowledgements

ANALYSIS OF THE INFLUENCE OF PLAQUES COMPOSITION AND GEOMETRY ON DRUG TRANSPORT FROM DRUG ELUTING STENTS

Javier Escuer (1), Estefanía Peña (1,2), Estela Pina (1), Miguel A. Martínez (1,2)

1. *Aragón Institute of Engineering Research (I3A), University of Zaragoza, Zaragoza, Spain; 2. Biomedical Research Networking Center in Bioengineering, Biomaterials and Nanomedicine (CIBER-BBN), Madrid, Spain.*

Introduction

Coronary artery disease (CAD) is one of the most relevant cardiovascular diseases. An important advance for the treatment of CAD has been the development of Drug Eluting Stents (DES). The drug eluted from the device allows to avoid the in-stent restenosis (ISR) caused by the device deployment and the damage caused in the wall. However, the transport of the drug through the vessel wall is affected by the type and the specific geometry of the atheroma plaque. Computational models can aide to better understand these dependences, but they usually represent simplified healthy straight geometries or highly simplified plaques that do not reproduce the characteristic geometry and composition of them. However, there is growing evidence that plaque composition may well have an impact on drug distribution within diseased tissue.

Methods

Therefore, a finite element model of an idealised coronary artery under conditions of atherosclerotic disease between DES and healthy tissue is performed, and the effect of plaque composition and structure on global drug distribution is investigated. Amongst all the geometric factors affecting this problem, we focus on the thickness of the fibrous cap, the total length of the plaque and the length and thickness of the necrotic core and percentage stenosis. The arterial wall includes three different layers: subendothelial space, media and adventitia. Endothelium, internal and external elastic laminae are considered as semipermeable membranes. The device is represented by several circular struts half-embedded in the tissue. Blood flow is modelled using Navier-Stokes equation, while Darcy's law is used to calculate filtration velocity through porous layers. Drug transport within the arterial wall is modelled by means of advection-diffusion-reaction equations. For the media layer, fibrous cap and lipid core, we use a non-linear saturable reversible binding model to describe drug interactions with the cells of the tissue.

Results

A 2D map of the total NLC of sirolimus in the therapeutic domain at different time points after stent implantation for the baseline model is shown in Figure 1. The presence of the plaque leads to a delay on the diffusion of drug in the media; however, the plaque appears to act as source for drug, ensuring that NLC drug levels in the media are maintained for longer time.
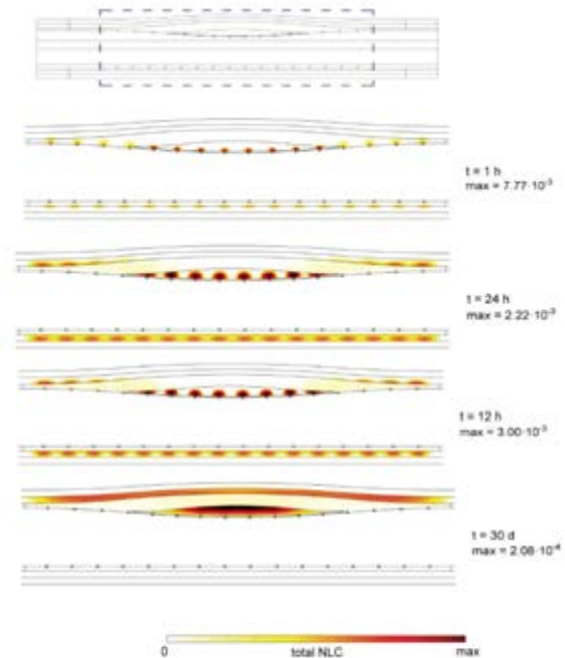
Figure 1: Normalized drug for different time points.

Conclusions

The results demonstrate that the spatio-temporal distribution of drug is highly dependent on the geometrical variables analysed. The composition of the core strongly influences the drug concentrations, due to the different density of binding sites in this region. The results suggest that lipid plaques give rise to higher drug concentrations than fibrotic plaques, while calcified plaques are basically drug-impenetrable. This may act as a significant barrier to drug from reaching arterial tissue.

References

1. Tzafriri A. R, et al. Journal of controlled release,161(3):918–92, .2012.
2. Escuer, J. et al, J. Mech Behav Biomed Mater 104, 103610, 2020.

Acknowledgements

THE EFFECT OF TISSUE PRESERVATION ON THE MECHANICAL BEHAVIOR OF PORCINE AORTA

Heleen Fehervary (1,2), Klaas Vander Linden (1), Maïté Pétré (1,3), Nele Famaey (1,2)
1. Biomechanics, Dpt. Mechanical Engineering, KU Leuven, Belgium;
2. FIBEr, KU Leuven Core Facility for Biomechanical Experimentation, Belgium;
3. Institute of Mechanics, Materials and Civil Engineering (iMMC), UCLouvain, Belgium

Introduction

After harvesting, biological tissues are preferably stored until testing, since the variation in time between harvesting & storage can be made much lower than between harvesting & (fresh) testing. However, literature shows contradicting results on the influence of preservation methods on mechanical behavior. Moreover, methodological concerns can be raised for past studies, such as the fact that tissue is considered 'fresh' up to 24 hours after harvesting [1, 2], while some biological tissues already stiffen three minutes *post mortem* [3]. In this study, we investigate the effect of preservation on the mechanical properties of aortic tissue.

Methods

Samples

34 porcine descending aortas were harvested in a local slaughterhouse to investigate 5 different preservation methods: fresh (G1), slow frozen short-term (G2) and long-term (G3), and fast frozen short-term (G4) and long-term (G5) . Fresh samples were tested within 4 hours after sacrifice; short- and long-term samples were frozen for 1 week and 6 months, respectively; slow frozen samples were placed in a liquid container with Phosphate Buffered Saline (PBS) in a -80°C freezer, and fast frozen samples were snap frozen (dry) using isopentane, also at -80 °C. From each aorta, 10 dogbone samples (5 groups in both circumferential and longitudinal orientation), were excised in a randomized manner.

Mechanical testing

Prior to testing, the dimensions of the samples were measured using a micro-laser-scanner (MLS) (Gocator 2120, LMI technologies, Canada). Afterwards, a speckle pattern was applied to the intimal surface and the sample was mounted using clamps to be tested uniaxially in a MessPhysik biaxial tester (Zwick/Roell, Germany). Throughout the test, samples were immersed in PBS at 37°C and the deformation of the samples was imaged using a Manta G917-B camera (Allied Vision, Germany) and VIC Software (Correlated Solutions, USA), integrated by isi-sys GmbH. The loading protocol consisted of multiple preconditioning cycles and the applied nominal strain was increased stepwise (10%, 25%, 50%, 100%, 150%), at a speed of 5% nominal strain per second. Data and images were captured at 20 Hz.

Data processing

For each sample, the last completed loading cycle of each loading step was analyzed. All data was processed using Matlab (The MathWorks Inc., USA) to calculate the first Piola-Kirchhoff stress and stretch. The thickness and width of the neck region of the samples was extracted from the MLS measurements. VIC-2D (Correlated Solutions, USA) was used for digital image correlation measurements to calculate the sample stretch.

Results

Figure 1 shows some preliminary results: stress-stretch curves of the 50% nominal strain cycle of 3 circumferentially oriented samples for each of the 5 groups. The fresh group is shown in blue and ideally we want a preservation method that approaches the blue curves as closely as possible.
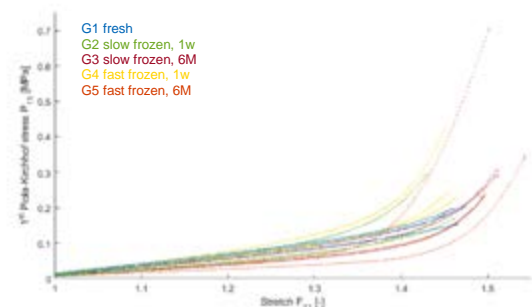
Figure 1: Stress-stretch curves of 50% loading cycle of 3 circumferentially oriented samples of each group.

Discussion

In Figure 1 a large variability between the samples can be observed. This can attributed to the biological variability between subjects, to the preservation method, or to the mechanical testing protocol. The analysis of more samples might give more insight on whether the effects of tissue preservation are significant compared to the biological and testing variability. Future work also includes a statistical analysis using the linearized stiffness & strength of the samples.

References

1. J. O. Virues Delgadillo et al, J. Biomed. Sci. Eng. 337088(07):645-652, 2010.
2. M. Adham et al, J. Surg. Res. 15;64(1):32-4, 1996.
3. J. Weickenmeier et al., J. Mech. Behav. Biomed. Mater. 84:88-98, 2018.

Acknowledgements

NUMERICAL ANALYSIS OF THE HEMODYNAMICS AND PERFORMANCE OF A MINIATURE VENTRICULAR ASSIST DEVICE

Yuval Gabso (1,2), Moshe Rosenfeld (1), Idit Avrahami (2)
1. Tel Aviv University, Israel; 2. Ariel University, Israel

Introduction

Mechanical circulatory support devices have improved the management, survival and prognosis of many patients with acute or chronic heart failure. However, there is still a high mortality and a wide burden of disease, mostly due to related thrombosis, embolization and hemolysis, thus requiring anticoagulation. Most of the current approved percutaneous left ventricular assist devices (p-LVADs) operate far beyond the critical threshold for biological damage which increases those disease [1]. The need for p-LVADs with minimized blood damage is critical. In this study we examine the effect of impeller design on function and hemodynamics of a novel p-LVAD using numerical analysis.

Methods

The suggested p-LVAD contains a straight tube which is located along the left ventricular outflow tract and the aortic root. In the tube, a levitating 2.5mm diameter impeller rotates at high speeds (30000-50000 RPM) to deliver blood from the ventricle to the aorta (Figure 1A). The investigated impeller designs are defined by the area ratio $\gamma = A_{outlet}/A_{inlet}$ of the outlet (A_{outlet}) and inlet (A_{inlet}) areas shown in Figure 1B.

(A)

(B)
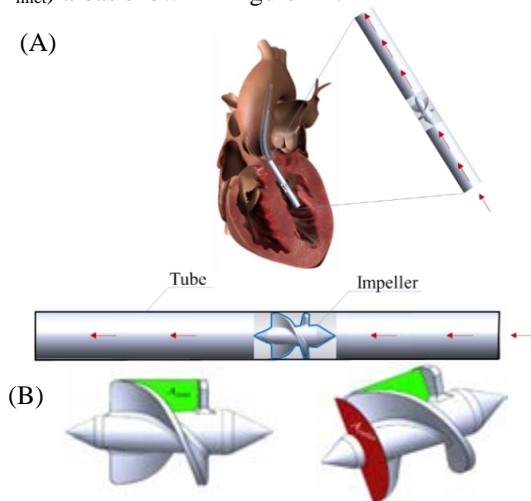
Figure 1 - 1A a schematic description of the p- p-LVAD in the aortic tract; 1B the impeller, with the inlet area marked in green and the outlet area marked in red.

Steady and transient numerical simulations of rotating frame using ANSYS CFX were performed and analyzed to estimate the pump's performance and blood damage for different impeller design, motor speed and working conditions (flow and pressure).
Estimation of RBC hemolysis was conducted according to four different models (based on Kolmogorov length scale [2]; and based on combinations of exposure time to shear stress above 425[Pa] [3]). Probabilities for shear induced platelet activation (PDF) were estimated based on accumulated shear stresses along streamlines [4].

Results and Discussion

The examined parameters included flow patterns, shear stress distribution, estimation of platelets activation and hemolysis index (HI), and global pump performance such as flow rate, pressure head, power and the efficiency.
An example of resulted average PDF, hemolysis index and efficiency for different impeller designs and at different motor speed with the same head pressure and flow rate is shown in Figure 2.
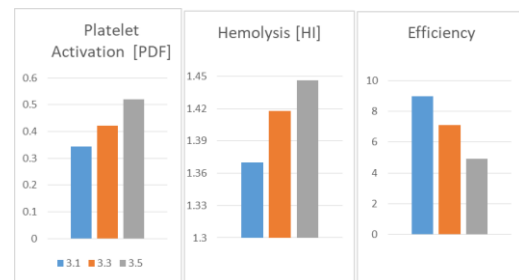
Figure 2 - Resulted average PDF, Hemolysis Index and efficiency for different impeller designs (3.1, 3.3 and 3.5). The motor speed for each model was adjusted to provide the same pump conditions of flow rate 2.75[L/min] and head pressure of 70[mmHg].

The main results show correlation between impeller design and both performance and blood damage parameters. Impellers with lower area ratio exhibit better pump performance, less hemolysis and less PDF. Increase in motor speed increased the obtained flow rate but also increased blood damage parameters (due to higher shear stresses) and reduced pump efficiency.

In cases with lower efficiency and higher HI and PDF, regions of disturbed and recirculating flow are found.
These results may improve p-LVAD design in the pursuit for efficient and safe percutaneous LVAD for longer periods.

References

1. Marcuschamer et al, CAD, 29:344-353, 2018.
2. James et al, Fluids, 4:1-19, 2019.
3. Roberts et al, IJAO, 10:1-9, 2020.
4. Marom. et al, ERMD, 13:113-122, 2016.

Acknowledgements

AN IMPEDANCE PUMP FOR ASSISTING FAILING FONTAN CIRCULATION

Manuel García-Díaz (1), Francisco Castro-Ruiz (1), José Ángel Moneo-Fernández (1), César Barrios-Collado(1), Joaquín Anatol(1), Markus Horvath(2), Ellen T. Roche(2) and José Sierra-Pallares (1)

1. *Departamento de Ingeniería Energética y Fluidomecánica & ITAP, Universidad de Valladolid. Paseo del Cauce 59, 47010 Valladolid (Spain)*
2. *Institute for Medical Engineering and Science, Massachusetts Institute of Technology, Cambridge, MA 02139, USA*

Introduction

Fontan operation is the current standard of care for the palliation of single ventricle defects results in significant late complications in children. The use of a mechanical circulatory device (a pump) to alleviate the missing subpulmonary ventricle could potentially stabilize the failing Fontan circulation [1]. A new alternative to traditional heart pumps is the impedance pump. Also known as Liebau pumps, impedance pumps are valveless pumps that operates based on the principles of wave propagation and reflection [2]. As example, impedance pumping is present in the embryonic heart of zebrafish during the early stages before valve formation. This works aim is to evaluate an impedance pump for assisting Failing Fontan circulation using a simplified in vitro facility.

Methods

We have built an in vitro facility to first test impedance pumping in a simplified way. A test rig similar to the one published in [3], has been constructed replacing with a latex pliant tube a piston pump. The latex pliant tube is compressed by a wave generator or pincher, emulating the work of [4]. In our case, the pincher is a diaphragm actuator like the one used in a traditional photo camera (Fig. 1), able to open and close at controlled frequency. Additionally, the test rig is composed of two reservoirs connected with two tubes of different length, which can be replaced to assess different configurations.

Diaphragm actuator
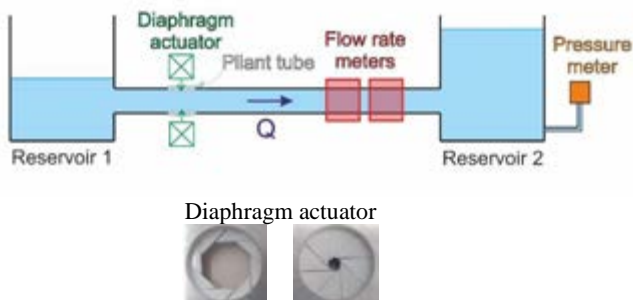
Figure 1: Test rig constructed for asymmetric pumping and a picture of the diaphragm actuator open and closed.

Results

Different pinching frequencies are studied, varying the speed aperture/close of the diaphragm, which lead to different head vs flow rate curves (Fig. 2). Main results show linear experimental curves. Observed heads and flow rates show potential application for developing devices to assist pulmonary circulation in failing Fontan patients [1].
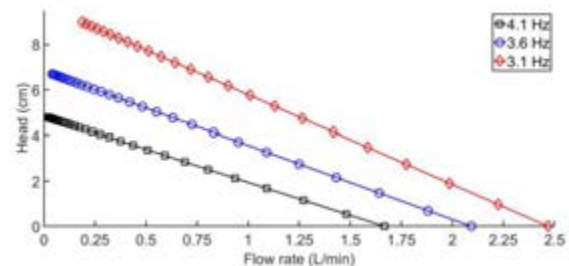
Figure 2: Head vs Flow rate curves at different pinching frequencies.

Discussion

Impedance pumping has revealed itself as a promising technology for assisting in failing Fontan circulation. It shows interesting features like its valveless nature, and it can assist properly under the conditions studied.

Future work will study impedance pumping being used in an in vitro loop which resembles much more precisely Fontan circulation.

References

[1] M. Farahmand, M. N. Kavarana, P. M. Trusty, and E. O. Kung, "Target Flow-Pressure Operating Range for Designing a Failing Fontan Cavopulmonary Support Device," *IEEE Trans. Biomed. Eng.*, vol. 67, no. 10, pp. 2925–2933, 2020

[2] N. M. Pahlevan and M. Gharib, "In-vitro investigation of a potential wave pumping effect in human aorta," *J. Biomech.*, vol. 46, no. 13, pp. 2122–2129, 2013

[3] T. Takagi, S; Saijo, "Study of a Piston Pump, without valves.," *Bull. JSME*, vol. 26, no. 218, 1983.

[4] E. T. Roche *et al.*, "Soft robotic sleeve supports heart function," *Sci. Transl. Med.*, vol. 9, no. 373, p. eaaf3925, 2017

Acknowledgements

A NOVEL FSI FRAMEWORK FOR HIGH-FIDELITY SIMULATION OF HEMODYNAMICS IN INTRACRANIAL ANEURYSMS

Aurèle Goetz (1), Pablo Jeken-Rico (1), Ramy Nemer (1), Philippe Meliga (1), Aurélien Larcher (1), Augusto Sanches (2), Yigit Özpeynirci (2), Thomas Liebig (2), Elie Hachem (1).

1. PSL Mines Paris, CFL Research Group at CEMEF, Sophia Antipolis, 06904, France; 2. Institute of Neuroradiology, University Hospital, LMU, Munich.

Introduction

Intracranial aneurysms (IAs) are responsible for almost 500,000 deaths worldwide each year. These anomalies of the brain vasculature are bulges typically arising on arterial bifurcations, which bear the risk of rupture, leading to subarachnoidal haemorrhage. Mostly detected incidentally on magnetic resonance angiography scans, they represent a substantial source of anxiety for patients. Although it is well-known that most of these bulges never rupture, some still carry a continuous threat and have to be identified. For physicians, assessing the hazard of an IA is a crucial challenge that needs to be addressed in order to evaluate the need for treatment. To date, doctors base their decisions on the size, shape and location of the aneurysm in the brain. However, these criteria have shown their limits and thus require more accurate assessment metrics. Computational Fluid Dynamics (CFD) simulations have arisen as a potential candidates for bridging that gap, allowing to simulate hemodynamics in patient-specific vascular geometries, with tailored modeling conditions. According to literature, rupture of IAs can be associated with abnormal WSS (Wall-Shear Stress) values, be they irregularly high or low [1]. Assessing WSS through CFD simulations has thus become a goal for many research teams to predict the stability of IAs over time. Nevertheless, the interaction of blood flow with arterial walls is almost systematically neglected and walls are modelled as rigid. Only a few publications further mention the influence of the wall thickness and material properties on measured flow characteristics, although biological phenomena involved in the remodelling of IAs have been shown to induce substantial modifications of the arterial structure.

Methods

Inspired by previous works [2,3], we propose to apply a novel FSI framework to model the behaviour of patient-specific aneurysms. This framework stands as a hybrid approach between the traditional monolithic and partitioned methods. The arterial wall geometry is immersed in the fluid-solid mesh at each time iteration while having its independent solid mesh [4]. The fluid dynamics are modelled solving the incompressible Navier-Stokes equation. Adding to the method, the mesh is refined at the boundary between the blood flow and the vessel's wall using anisotropic mesh adaptation and a level-set function. The approach is referred to as the Adaptive Immersed Mesh Method.

Results

Hemodynamics and structural mechanics in several patient-specific aneurysms have been modelled using the method described above. The stability and performance of the method have been evaluated. Differences in flow characteristics between fully-rigid wall simulations and the introduced FSI method are presented. A particular interest of FSI simulations has been assessed in different scenarios, varying arterial wall characteristics. The impact of different wall thickness profiles over the surface of aneurysm domes has also been evaluated.

Discussion

Presented results prove that the relevance of FSI modelling depends on the used arterial walls characteristics. Considering that these vary substantially among different aneurysms and over the surface of a single aneurysm dome, we deem FSI modelling necessary to identify weak points on aneurysm geometries. However, wall characteristics being difficult to measure in-vivo, assumptions still have to be made to model IAs comprehensively. A better grasp of aneurysm growth remodelling phenomena will certainly guide these assumptions in future works. We hope that this study will encourage the research community to pursue the assessment of the rigid-wall assumption validity for modelling intracranial aneurysms.

References

1. H. Meng et al. "High WSS or Low WSS? Complex Interactions of Hemodynamics with Intracranial Aneurysm Initiation, Growth, and Rupture: Toward a Unifying Hypothesis". American Journal of Neuroradiology 35.7 (2014), pp. 1254–1262.

2. Ryo Torii et al. "Fluid-structure interaction modeling of a patient-specific cerebral aneurysm: influence of structural modeling". Computational Mechanics 43 (2008), pp. 151–159.

3. Samuel Voß et al. "Fluid-Structure Simulations of a Ruptured Intracranial Aneurysm: Constant versus Patient-Specific Wall Thickness". Computational and Mathematical Methods in Medicine 2016 (2016), pp. 1–8.

4. R. Nemer et al. "Stabilized finite element method for incompressible solid dynamics using an updated Lagrangian formulation". Computer Methods in Applied Mechanics and Engineering 384 (2021), p. 113923.

ANALYSIS OF THE INFLUENCE OF THE ARTERIAL WALL MECHANICS IN A MECHANOBIOLOGICAL MODEL OF ATHEROSCLEROSIS

Patricia Hernández-López (1), Nicolás Laita (1), Myriam Cilla (1, 2), Miguel Ángel Martínez (1, 2), Estefenía Peña (1, 2)

1. *Aragón Institute of Engineering Research (I3A). University of Zaragoza, Zaragoza, Spain*
2. *Biomedical Research Networking Center in Bioengineering, Biomaterials and Nanomedicine (CIBER-BBN), Spain*

Introduction

Atherosclerosis –a disease that causes the formation of plaques in the arterial wall, decreasing the lumen area for blood circulation- and it consequences are one of the main causes of mortality in developed countries nowadays. It can derive, for example, in heart attacks, ischemia or cerebral strokes. Because of this, it results important to understand the process of atheroma plaques formation, to predict future atheroma plaques and prevent their consequences.

The aim of this work is to study the influence of the mechanics of the arterial wall in the process of atheroma plaques formation, considering his porosity and tortuosity.

Methods

We propose a mechanobiological model to study the development of atheroma plaques in arteries, considering as main substances in the process: LDL, oxidized LDL, monocytes, macrophages, cytokines, foam cells, contractile and synthetic smooth muscle cells and collagen fibbers.

We use a two dimensions axisymmetric model based in coronary artery with a previous atheroma plaque, considering multilayer wall, composed by the intima, media and adventitia layers. The first plaque causes the perturbation of blood flow and thus, the development of another new plaque, whose growth we analyze. The geometry can be seen in Figure 1.

Figure 1: 2D-axisymmetric considered geometry, with lumen, obstacle plaque and the arterial wall layers

We use Navier-Stokes equations to model stationary blood flow along the lumen and consider Wall Shear Stress (WSS) as the main mechanical stimulus to the development of plaques. We model plasma and substances flows across the endothelium with the three-pore model [1], and use Kedem-Katchalsky equations for the flux of substances through the different membranes. We also use convection-diffusion-reaction equations to model substances concentrations in the different layers of the model. Finally, we compute the growth of plaques considering concentrations of foam cells, synthetic smooth muscle cells and collagen fibbers in the intima layer.

We analyze the influence of the arterial wall mechanics with different models, without considering any mechanics in it, considering the porosity of the arterial wall [2], considering its tortuosity [3] and finally, considering a combination of porosity and tortuosity models.

Results

Our results compare atheroma plaques development for the different models analyzed, considering the porosity of the arterial wall, its tortuosity and both or none of them. In Figure 2, we can see an example of plasma flow through all the wall layers in the model and the area in which plaque is going to grow (area of higher plasma flow, in red color), with a detail of the area of growth.
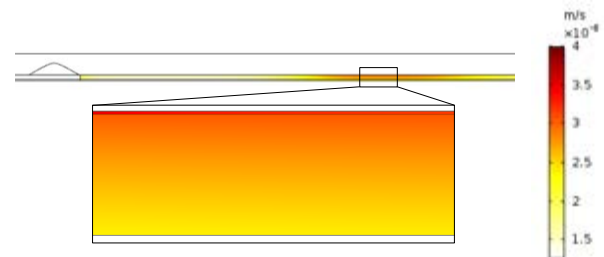
Figure 2. Plasma flow results through the multilayer wall.

Discussion

A computational model of coronary artery with multilayer wall has been developed. It can predict atheroma plaques formation in the artery, considering the influence of the arterial wall mechanics.

References

1. U. Olgac et al. Am. J. Physiol. - Heart Circ. Physiol. 294(2) 909-919, 2008.
2. M. Dabagh et al. Am. J. Physiol. - Heart Circ. Physiol. 297: H983–H996, 2009.
3. W.J. Denny et al. Annals of Biom. Eng. 41(5) 1062-1073, 2013.

Acknowledgements

PATIENT-SPECIFIC SIMULATION AIMED AT EVALUATION OF THE NEOINTIMA GROWTH EFFECT ON ANASTOMOSIS HEMODYNAMICS

Yana Ivanova (1), Andrey Yukhnev (1), Evgueni Smirnov (1), Ludmila Tikhomolova (2), Andrey Vrabiy (2), Andrey Suprunovich (2), Alexander Morozov (2), Gennady Khubulava (2), Valeriy Vavilov (2)

1. Peter The Great St. Petersburg Polytechnic University, Russia; 2. Pavlov First St. Petersburg State Medical University, Russia

Introduction

Femoral-popliteal artery bypass surgery is performed to restore the main blood flow through a popliteal artery by vascular graft implantation. Numerical simulation can help to evaluate the progression of patient's condition in the postoperative period. Known numerical studies of the flow in anastomoses (e.g. [1, 2]) usually don't take into account the change of anastomosis geometry in case of neointima growth in a long term after the bypass surgery. The aim of our study is to analyze hemodynamics changes due to the neointimal growth in the proximal anastomosis of femoral-popliteal bypass with a synthetic graft.

Methods

To perform patient-specific simulations, personalized geometric models of proximal anastomosis have been created based on computer tomography data for three patients.

Definition of the neointima size and its position was performed with two methods: computer tomography and ultrasonography. The ultrasound Doppler method was used to measure flow rates needed to set boundary conditions in blood flow numerical simulation.

Calculations were performed using the ANSYS CFX computational fluid dynamics package. Blood was modeled as an incompressible viscous fluid. The vessels elasticity was not taken into account.

Velocity changes during a cycle were set as the inlet boundary condition, assuming the flat velocity profile. At the graft-section outlet the time-dependent flow rate was specified in accordance with the measurements. The no-slip condition was set on the walls.

Results

For the studied models, the inlet Reynolds numbers at the maximum flow rate instance were 1200 to 2900. In the analysis, a special attention was paid to calculated distributions of the time-averaged wall shear stress (TAWSS) and oscillatory shear index (OSI) [1, 2], as well as to the streamline patterns at the maximum flow. Fig. 1 illustrates some results for one of the studied models at 18 and 28 months after bypass surgery. In this case the model geometry has changed considerably in 10 months, due to neointimal hyperplasia at the proximal anastomosis of femoral-popliteal bypass. In the figure, the gray area marks the vessel wall area with the overgrown neointima. Its maximum thickness was about 4 mm. The flow constriction entails the velocity increase followed by a TAWSS increase and

an OSI decrease in this area. However, within the substantially increased downstream stagnant zone, TAWSS decreases and OSI increases.

Compared to the models without neointima, the TAWSS values averaged over the wall area with the overgrown neointima increased by 50-130%, depending on the patient case studied, and the OSI values decreased by 20-30%.
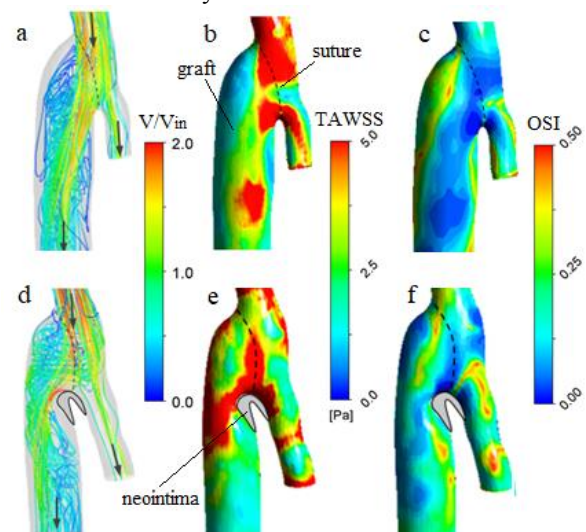
Figure 1: (a,d) Streamlines at the instance of maximum flow rate, (b,e) TAWSS and (c,f) OSI (a,b,c) 18 and (d,e,f) 28 months passed since bypass surgery.

Discussion

The results obtained have pointed to significant changes of the flow structure during the neointimal growth in the proximal anastomosis of femoral-popliteal bypass. Related considerable changes in distributions of the wall shear stresses were evaluated both qualitatively and quantitatively. Further patient-specific calculations aimed at evaluation of the neointima growth effects can provide new knowledge on the relationship of hemodynamic and biological processes that is necessary for development of methods able to predict of increased risk of graft occlusion.

References

1. Can Gokgol et al, Biomechanics and Modeling in Mechanobiology, 18: 10, 2019.
2. Luoding Zhu, Kaoru Sakai, Phys. Fluids, 33: 10, 2021.

Acknowledgements

FLUID-STRUCTURE INTERACTION ANALYSES OF BLOOD FLOWS IN LARGE ARTERIES

Daniel Jodko

Lodz University of Technology, Poland
University of New South Wales, Australia

Introduction

Fluid-structure interaction (FSI) simulations are more and more frequently employed in the modeling of blood flows in particular parts of the human circulatory system and vascular access [1, 2]. However, FSI computations are still time-consuming and expensive, therefore there is a question about the benefits of such an approach. This study shows the influence of the blood vessel wall elasticity on hemodynamic parameters in a simplified model of the artery as well as patient-specific examples.

Methods

In the initial study, a straight tube representing the artery was investigated as an elastic and rigid channel (fig. 1). For compliant models, different materials, damping coefficients, meshes, and fixations were compared.
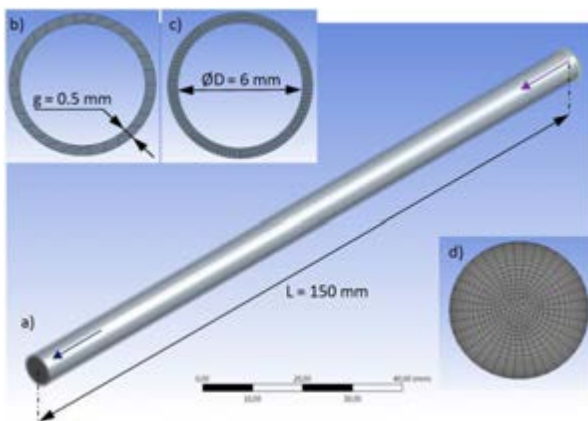
Figure 1: a) Investigated FSI domain; b) and c) two meshes used for the structural domain; d) example of mesh in the fluid domain.

The blood was considered to be a Newtonian fluid ($\mu = 3$ mPa s, $\rho = 1040$ kg/m^3). The blood flow was assumed to be pulsating and typical for the radial artery feeding an arteriovenous shunt. Three cardiac cycles were simulated. Each cardiac cycle was assumed to last 0.84 s. The time step equal to 0.01 s yielding a stable solution in acceptable real-time calculations (4-13 hours) was set in all simulations. As a boundary condition at the inlet of the radial artery, a velocity profile was used, in which the maximal velocity (V_{max}) located in the centreline changes in time. At the outlet cross-section, a pressure waveform was used as a boundary condition [3]. A commercial code, provided by ANSYS v. 17.1, was employed to solve the equations used to describe two-way coupled FSI tasks. A single workstation was used for all the calculations: Intel Core i7-3930K 3.20GHz, 6 cores, 64 GB RAM. Additionally, patient-specific cases were investigated, for which the non-Newtonian behavior of blood was taken into account.

Results

The results concerning max. wall shear stress (maxWSS), area-averaged WSS averaged in time (TAAWSS), the time-averaged pressure drop between the inlet and the outlet (Δp), max. displacement, and max. von Mises stress were extracted only from the third cardiac cycle. An example of the obtained results is presented in Table 1.

Parameter	Rigid material	Linear material
Young's modulus [MPa]	∞	3
damping coeff. ($\alpha = \beta$)	∞	0.01
elastic support coeff. [N/mm^3]	∞	0.1
maxWSS [Pa]	17.39	17.21
TAAWSS [Pa]	2.46	2.32
Δp [Pa]	286	256
max. displacement [mm]	0	0.0668
max. von-Mises stress [MPa]	0	0.0857
calculation time [h]	4	13

Table 1: Example of the obtained results.

Discussion

This study shows quantitative differences between hemodynamics in the rigid and elastic arterial models. Allowing the wall to be resilient, decreased the maxWSS, TAAWSS as well as pressure drop occurring between the inlet and outlet. Moreover, the elastic support on the external wall, which represents the response of the surrounding tissue, also affected hemodynamic parameters. To conclude, the development of FSI approach seems to be necessary to make blood flow simulations more realistic.

References

1. Chen et al., Scientific Reports, 11(1): 1-12, 2021.
2. Kumar et al., Int J Eng Science, 154: 103341, 2020.
3. Jodko et al., Acta Bioeng Biomech, 22(2): 139-153, 2020.

Acknowledgments

HEMODYNAMICS OF AN IDEALIZED MECHANICAL HEART VALVE – PREDICTIONS BY FVM AND SPH

Sumanta Laha (1,2), Georgios Fourtakas (1), Prasanta Kumar Das (2), Amir Keshmiri (1,3)

1. The University of Manchester, UK; 2. IIT Kharagpur, India; 3. Manchester University NHS Foundation Trust, Manchester Academic Health Science Centre, UK

Introduction

The human heart supports the processes of life through its unparalleled performance. To this end, the heart valves need to operate approximately 100,000 times in a day. Failure of the heart valves is common due to several reasons resulting in deterioration of the pumping function of which may ultimately result to a cardiac arrest. Heart valve replacement emerged as one of the most reliable and effective solutions to this problem. In order to investigate the performance, hemodynamics and design of the mechanical heart valves (MHV), computational fluid dynamics (CFD) is ideally suited as a numerical non-intrusive tool.

In the past, several investigations using classical numerical schemes such as the finite volume method (FVM) have been carried out with MHV [1–2]. Nevertheless, shortcomings such as complex geometries, mesh generation and interface tracking are evident. With the emergence on meshless schemes such as smooth particle hydrodynamics (SPH) these limitations resolved own to the meshless and Lagrangian nature of SPH [3]. However, the potential of the SPH scheme is not fully explored.

Methods

In the present study, a preliminary CFD study has been conducted for the bi-leaflet mechanical heart valve (BMHV). Traditional FVM and SPH mesh-free particle based methods have been adopted for the simulations. A pulsatile velocity is considered as the inlet boundary condition and a pressure pulsation is taken at the outlet. Anatomically reasonable aorta fitted with an idealized 25mm St Jude MHV is chosen for the present simulation. In FVM, a polyhedral mesh with the prism layers was chosen for better accuracy and similar particle sizes have been used for SPH for a fair comparison.

Results

It is observed from figure 1 that, a three-jet structure is formed under the full opening condition of the leaflet followed by a strong recirculation zone in the wake of the leaflets and in the aortic sinus region. Under the peak inlet velocity the central jet exhibits its maximum velocity (1.4m/s). Similar results are observed with the SPH simulation which will be examined in detail. From the pressure distribution, it has been perceived that a low-pressure region (72mmHg) is created in between the two leaflets of the valve and that helps the leaflets for their natural closing (figure 1).
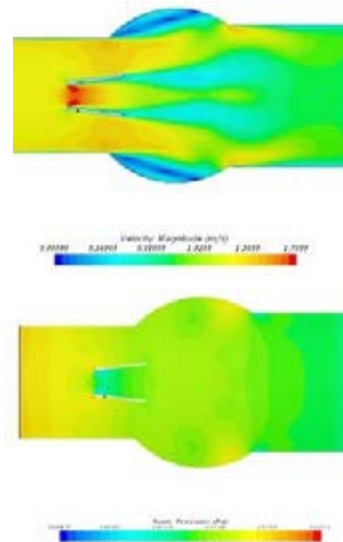
Figure 1: The velocity (top) and pressure (bottom) contour of the blood flow under peak systole condition..

Discussion

Unlike the native heart valves, BMHV act as a bluff body in the flow regime and exhibits flow reversal at the wake of the leaflets. In addition, the recirculation zone in the aortic sinus regions allow the blood to stay longer in a particular space which may initiate thrombus formation. Moreover, the non-biological jet like flow from the BMHV can damage the blood cells and cause severe hemolysis in the aorta. Herein, a direct comparison of the FVM and SPH simulations is performed.

References

1. Xu, X., Liu, T., Li, C., Zhu, L., and Li, S., 2019, "A Numerical Analysis of Pressure PulsationCharacteristics Induced by Unsteady Blood Flow in ABileaflet Mechanical Heart Valve," Processes, 7(232).

2. James, M. E., Papavassiliou, D. V., and O'Rear, E. A., 2019, "Use of Computational Fluid Dynamics to Analyze Blood Flow, Hemolysis and Sublethal Damage to Red Blood Cells in a Bileaflet Artificial Heart Valve," Fluids, 4(1).

3. Shahriari, S., Maleki, H., Hassan, I., and Kadem, L., 2012, "Evaluation of Shear Stress Accumulation on Blood Components in Normal and Dysfunctional Bileaflet Mechanical Heart Valves Using Smoothed Particle Hydrodynamics," J. Biomech., 45(15), pp. 2637–2644.

2D FLUID-STRUCTURE INTERACTION MODELING OF THE LEFT ATRIUM – IMPACT OF MITRAL VALVE STIFFENING

Masoud Meskin (1), Jørgen Arendt Jensen (2), Matthias Bo Stuart (2), Marie Sand Traberg (1)

1. Cardiovascular biomechanics group, Technical University of Denmark, Denmark; 2. Center for fast ultrasound imaging, Technical University of Denmark, Denmark

Introduction

The mitral valve (MV) plays a crucial role in a healthy cardiac function and is associated more to the heart valve diseases amongst the four heart valves. Some MV diseases cause MV leaflets stiffening, and result in malfunctioning MV and disruption of the physiologic performance of the left heart. The impacts of MV stiffening (MVS) on the left atrium (LA) hemodynamics are not completely known. This study presents a 2D simplified fluid-structure interaction (FSI) model of the LA and the MV over a full cardiac cycle to investigate the impact of MVS on the LA hemodynamics.

Methods

To build the 2D model (Fig.1A), it is assumed that the 3D LA has a symmetric spherical shape with four circular pulmonary veins (PVs), and therefore the 2D model would be a circular plane with rectangular PVs. The LA diameter is 45.7 mm, the LA wall thickness is 2 mm, and the PVs diameter is 13.2 mm. Two sets of nearly incompressible hyperelastic material models were prescribed for the MV [1] and the LA [2]:

$$W_{MV} = \frac{1}{2}\,\mu(I_{1c} - 3) + \frac{1}{2}\,k_{MV}(J-1)^2 \qquad (1)$$

$$W_{LA} = C_{NH}\left[I_{1c}(I_{3c})^{-\frac{1}{3}} - 3\right] + \frac{1}{2}k_{LA}(J-1)^2 \quad (2)$$

where W_{MV} and W_{LA} are the strain energy density functions, μ and C_{NH} are the stress like material parameters, I_{1c} and I_{3c} are the first and third invariants of the right Cauchy-Green strain tensor, k_{MV} and k_{LA} are the bulk modulus of the MV and the LA, and J is the determinant of the deformation tensor. To mimic the MVS, four different stress like material parameters, μ_1=150, μ_2=450, μ_3=850 and μ_4=1100 [kPa] were assigned to the MV. A realistic PV flowrate profile was applied at the inlets, and a time dependent pressure profile was considered as the outlet boundary condition. A triangular tension force function was applied to the LA wall to mock the LA contraction. Triangle and quad elements were utilized to generate the mesh. The blood was considered incompressible with a density of 1060 kg/m^3 and a viscosity of 4 mPa·s. The FSI simulations were done in Comsol Multiphysics.

Results and Discussion

The LA pressure (LAP), LA volume (LAV), transmitral velocity (TV) and the MV effective orifice length (EOL) were calculated and the hemodynamics indices, a-peak of the LAP, E/A ratio of the TV, late diastolic velocity time integration (VTI_LD) of TV, the maximum early diastolic EOL (EOL_E), and the LA total emptying fraction (TEF) are reported in Tab.1.

Index	a-peak (mmHg)	EOL (mm)	E/A	VTI_LD (cm)	TEF
μ_1	11.9	16.1	2.42	1.6	0.47
μ_2	16.2	10.6	1.10	3.9	0.43
μ_3	20.0	7.9	0.9	4.9	0.3
μ_4	21.4	6.4	0.86	4.8	0.22

Table 1: FSI-calculated hemodynamics indices.

The results show that the MVS reduces EOL and increases the TEF, resulting in the LAP enhancement, keeping the LAP elevated and amplifying the a-peak of the LAP (Fig.1B). Considering the TV profile (Fig.1C), the E-peak is suppressed, and the A-peak is amplified which is reflected in the calculated E/A ratio and VTI_LD (Tab.1). In conclusion, the MVS dramatically impairs the LA physiologic performance.
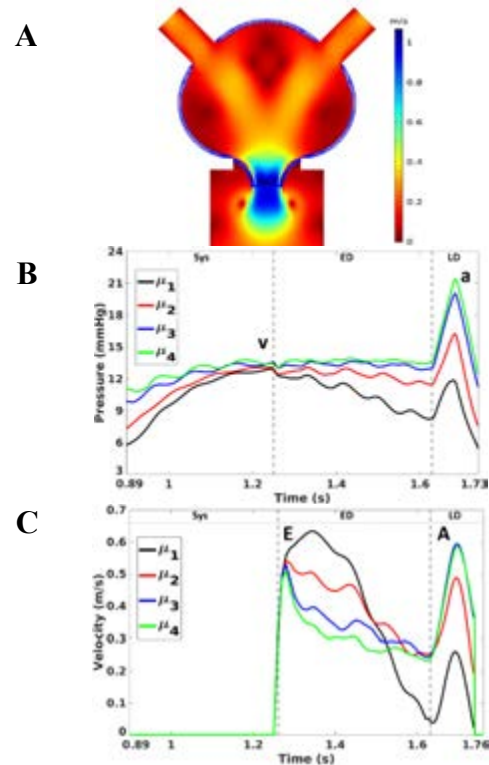

Figure 1: A) Velocity field in ED, B) LAP and C) TV. Sys=systolic ED=early diastolic, LD=late diastolic

References

1. Di Martino et al, J Biomech, 2011,10.1016.
2. Weinberg et al, J Cardiovascular Eng (2005): 37-43.

A NEW TECHNIQUE OF RECONSTRUCTING 3D GEOMETRIES FROM CT IMAGES – A CFD STUDY

Masoud Meskin (1), Rasmus Hvid (1), Marie Sand Traberg (1)

1. Cardiovascular Biomechanics Group, Technical University of Denmark, Denmark

Introduction

Numerical models have become a fundamental tool in cardiovascular studies [1]. The first step in numerical modeling is reconstructing a prototypical 3D geometry of the structure of interest from different medical imaging modalities [2]. A way to reconstruct the 3D geometry of the cardiac components is through segmenting computed tomography (CT) images and generating a mesh. However, the generated mesh may be corrupted during segmentation, resulting in a flawed or discontinuous mesh. Moreover, repairing such a corrupted mesh is a tedious task. In this work, the 3D structure of the left atrial (LA) chamber was generated with a new technique by using the "freeform part modeling" feature in the Autodesk Inventor® (Autodesk, Inc., California, USA). The created 3D LA geometry was then used in a computational fluid dynamic (CFD) study of the LA during left ventricular diastolic phase in STAR-CCM+ (Siemens Industries Digital Software).

Methods

To prepare the 3D LA geometry for the CFD study, first the LA structure at the beginning of systole was segmented, using 3DSlicer, from a 4D CT image data set and imported into Autodesk Inventor as a surface mesh (Fig.1a). Then a freeform cylinder with the approximate dimensions of the LA structure was created and divided into a number of rectangular patches (Fig.1b). Next, each rectangular patch was manipulated and formed individually to be shaped like the area of the LA structure it covers. Afterwards, the pulmonary veins (PVs) are added as cylindrical tubes with circular cross-sectional area, and the mitral valve (MV) was embedded as an oval conduit at the outlet of the LA. The LA structure was imported into STAR-CCM+ and polyhedral-shaped cells along with prismatic cells were utilized to generate volume and boundary layer mesh elements (Fig.1c and 1d). The final mesh consists of 215389 elements. The PVs and MV diameters and the inlet flowrate profiles were taken from Dahl et.al [3]. The MV was connected to a long tube and a zero pressure was set as the outlet boundary condition at the end of the tube. Blood is the working fluid and considered incompressible, with density of 1060 kg/m^3 and viscosity of 4 mPa·s.

Results

The results are mesh independent as the relative difference between the results is less than 3% after conducting mesh convergence analysis. The velocity contour on the MV plane and the intra-atrial flow field streamlines during the diastolic phase are displayed in Fig.2. The maximum transmitral velocity is 0.58 m/s and the maximum intra-atrial velocity is 0.47 m/s. The vortex rings formation is also visible in the LA chamber.

Discussion

The topology of the reconstructed LA geometry resembles the one reported by Dahl et al [3]. The values of maximum transmitral velocity and intra-atrial flow reported by Dahl et al [3] are 0.50 m/s and 0.60 m/s respectively, which are close to the findings of this study. In conclusion, the freeform technique could generate a representative model of the LA geometry.
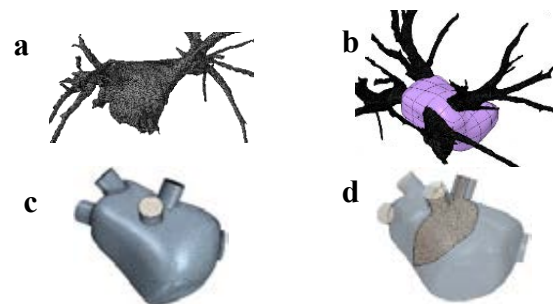

Figure 1: a) 3D surface mesh. b) freeform cylinder. covered the surface mesh. c,d) mesh structure.
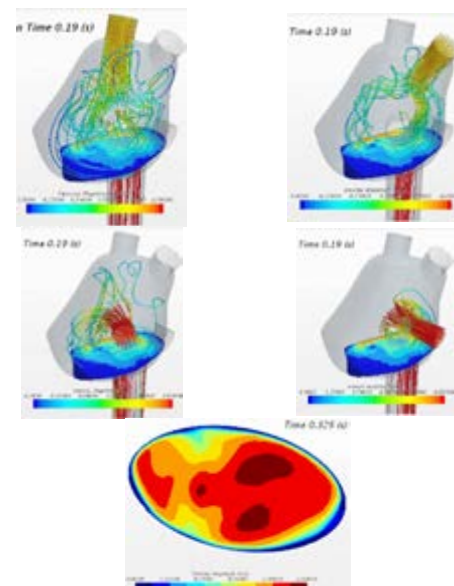

Figure 1: The intra-atrial flow field and transmitral velocity contour.

References

1. Lamata et al, Biophysics and molecular biology,2014
2. Masci et al, J Biomech Eng, 2020.
3. Dahl et al, BMES, 2012.

TRILEAFLET VS BILEAFLET MECHANICAL AORTIC VALVE – ASSESSMENT OF THEIR BLOOD ANTICOAGULATION PERFORMANCE

Anna Nieroda (1), Marek Pawlikowski (1)

1. Institute of Mechanics and Printing, Warsaw University of Technology, Poland

Introduction

The projected number of aortic valve transplants for 2050 is approximately 850 000 [1]. An inherent problem associated with transplantation is the need for anticoagulation therapy in operated patients.

The main subject of the research is the simulation of blood flow through an artificial aortic heart valve using the finite element method (FEM). The studies aim to verify the shear stress occurring behind the valves of two types, i.e. bileaflet (BIL) and trileaflet (TRI) valves. Regions of high shear stress can cause a thrombotic response, specifically through haemolysis and shear-induced platelet activation.

Methods

The geometrical model consisted of the left ventricle and ascending aorta. Our study considered two types of mechanical valves, i.e. BIL and TRI valves. For the TRI valve, we proposed a new leaflet curvature (Figure 1).
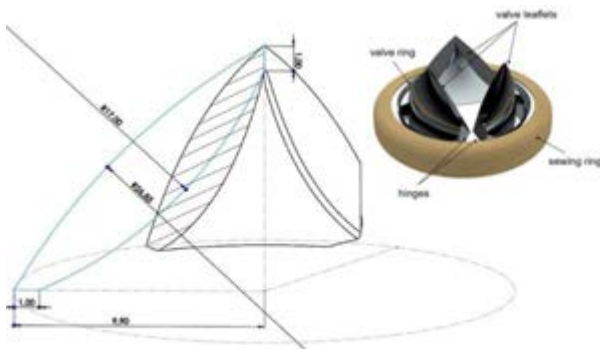
Figure 1: TRI valve model.

In our research, we analyse the blood flow at three positions of the valves' leaflets defined using angle with respect to the vertical plane (passing through the symmetry axis of the valve) 40°, 20° and 0° (fully opened valve).

The correlation of the flow velocity and the leaflets' time opening was determined using the Doppler ultrasound examination in an adult human being [2]. The length of one cycle was assumed to be 0.8 s. Heart rate was 75 beats per minute. The flow velocity values were determined at the inlet, which was defined at the entrance to the left ventricle. A constant pressure of 14 kPa was described at the aortic outlet, corresponding to a healthy human's average pressure of the systolic and diastolic phases. We have assumed turbulent and non-Newtonian blood flow. The dynamics of blood circulation were determined using ANSYS 2020 R2 software.

Results

The effect of using three leaflets in the TRI valve construction on hemolysis was assessed by shear stress occurring in the ascending aorta (Figure 2). Stress distribution in the leaflets of the BIL and TRI valves was calculated as well as the flow through it was characterised.
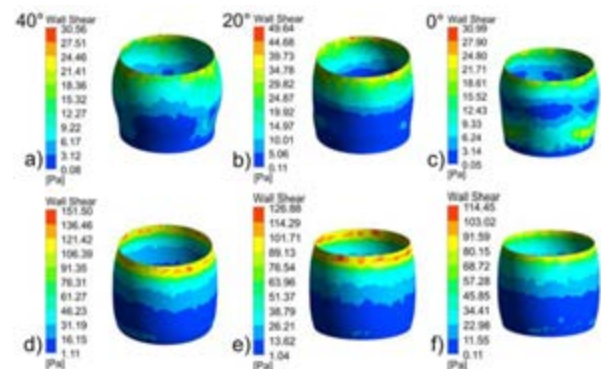
Figure 2: Shear stress distributions in the ascending aorta wall for the TRI valve: a) 40◦, b) 20◦ c) 0◦ and BIL valve d) 40◦, e) 20◦, f) 0◦.

Discussion

Shear stress must be above 150 Pa to cause haemolysis and above 10 Pa to cause platelet activation [3]. A high value of shear stress in the ascending aorta for the BIL valve (i.e. 151.5 Pa, 126.88 Pa and 114.45 Pa) may indicate the possibility of haemolysis. Exceptionally high shear stress (151.5 Pa) occurs at the valve opening. This stress is because the flow runs close to the aortic wall. Furthermore, vortices occur during valve opening, which increases blood's impact on the aortic wall.

The main advantage of the TRI valve design is the central blood flow, contributing to more physiologic blood flow and decreasing the risk of haemolysis (maximum shear stress for the BIL valve is 151.5 Pa, for the TRI valve 49.64 Pa) and, therefore, avoiding anticoagulation therapy in transplant patients. This will increase the possibility of implanting mechanical aortic valves in more patients.

References

1. Yacoub MH et al, Nat Clin Pract Cardiovasc Med, 2:60-61, 2005.
2. Amindari A et al, Inf in Medicine Unlocked, 9:191, 2017.
3. Ge L et al, Ann. Biomed. Eng. 36: 276–297, 2008.

ESTIMATION OF WALL VISCOELASTIC PARAMETERS FROM THE PRESSURE AND DIAMETER CURVE OF A CAROTID ARTERY

Jeongsup Shin, Kyehan Rhee

Department of Mechanical Engineering, Myongji University
Republic of Korea

Introduction

Arterial wall tissue composition changes as atherosclerosis progresses, and it affects the mechanical properties of diseased wall. Arterial wall shows both elastic and viscous behavior, and wall motion under pulsating intraluminal pressure may provide valuable quantitative information on wall viscoelasticity. The aim of this study is to estimate carotid wall viscoelasticity using ultrasound (US) cine images and brachial arterial pressure waveforms.

Method

Data were collected from the patients who underwent both carotid US and brachial to ankle pressure wave velocity (ba-PWV) examination to evaluate atherosclerosis status at Gangnam Severance Hospital, Department of Cardiology. Forty-five CCA segments of the patients with mild and severe atherosclerotic plaque were analyzed. This study was approved by the Institutional Review Board of Gangnam Severance Hospital. Carotid artery US images were used to measure radial wall motion, and a diameter waveform was measured automatically using the CAROLAB software. The diameter waveform was measured ten times at the same location and the averaged waveforms were saved for postprocessing in MATLAB program (MathWorks Inc, MA). Diameter waveforms were filtered with a band-pass filter and detrended by subtracting the mean from the signal. The carotid pressure waveform was reconstructed from the brachial pressure waveform of a patient using a transfer function (TF). TFs were obtained from the virtual subjects whose age, mean and pulse pressure waveforms matched our patient. Diameter and pressure waveforms were synchronized with R wave of electrocardiogram (ECG) and the pressure-diameter (PD) waveform was constructed as shown in Fig. 1. Wall elasticity was estimated using the Peterson elastic modulus (Ep). Wall viscosity was quantified using the energy dissipation ratio (EDR), the viscosity index (Xvis) using a Kelvin Voigt viscoelastic model. The phase lag of the first harmonic of pressure and displacement waves (PL1) was also computed to assess wall viscosity.

Results and Discussion

The mean values of the viscoelastic parameters measured are shown in Table 1. The mean value of Ep of our patients was agreed with that in carotid segments with plaques measured in the previous study using US imaging and brachial artery pressure [1]. It also showed agreement with Ep of hypertensive subjects measured
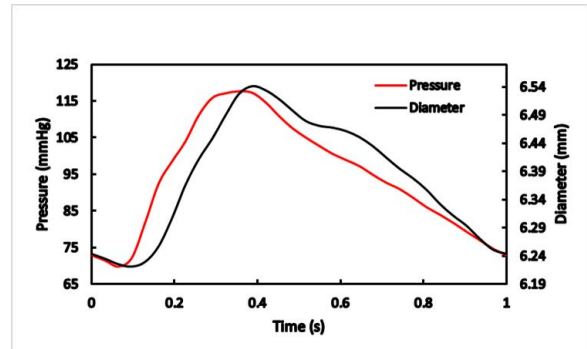
Figure: 1Pressure and diameter waveforms measured separately and synchronized using ECG.

Ep	EDR	Xvis	PL1
735±243	7.89±5.59	5.74±4.61	5.21±8.97
(mmHg)	(%)	mmHg·s/mm	degree

Table 1: Viscoelastic parameters measured (Mean±SD)

from US imaging and carotid applanation tonometry [2]. Three parameters (EDR, Xvis, PL1) were computed to assess the wall viscosity. They show significant positive correlations each other, which implies all three viscous parameters can represent viscous nature of arterial wall. The correlation coefficient between Xvis and EDR, and Xvis and PL1 was 0.92 and 0.80, respectively. The mean value of Xvis of our subjects and the carotid wall viscosity index of hypertensive patient was similar [1]. The mean value of EDR was also agreed with that of carotid artery of healthy subjects [2].

Conclusions

The viscoelastic properties of carotid artery were estimated from PD curves measured from carotid US images and brachial pressure waveform. Albeit from the limitations of non-simultaneous measurement of carotid pressure and diameter, PD relationship was successfully obtained using the transfer function and ECG synchronization. Estimated viscoelastic parameters agreed with those of published data, and all three viscous parameters showed good positive correlations.

References

1. Armentano RL et al, Hypertension, 31: 534-539, 1998.
2. Shau, Y-W et al, Ultrasound in Medicine & Biology, 25: 1377-1388, 1999.

Acknowledgements

ADHESION PROPERTIES OF A MONOLAYER OF ENDOTHELIAL CELLS ON MICROFLUIDICS DEVICES

Itziar Ríos Ruíz (1), Miguel Ángel Martínez (1,2), Estefanía Peña (1,2)

1. Aragón Institute of Engineering Research (I3A), University of Zaragoza, Zaragoza, Spain
2. Biomedical Research Networking Center in Bioengineering, Biomaterials and Nanomedicine (CIBER-BBN), Spain

Introduction

The mechanism of atherosclerosis involves many complex micro- and macroscale processes. The disease is known to start with a dysfunctional endothelium, which implies an increased permeability of the vessel wall. Several experimental tests, especially in the field of microfluidics, have been developed in order to study endothelial cell (EC) response to flow [1], which would help relate the permeability of the endothelium to different blood flow conditions [2]. ECs in general respond to laminar and unidirectional flow by aligning and elongating [3]. And although this response to flow is reported to happen significantly in the first hours of the experiment, microfluidic tests with longer durations have shown that ECs keep on elongating and aligning throughout more than 24 hours [4]. One of the main challenges of these longer microfluidic tests is the adhesion of ECs to the substrate. ECs are delicate and flow tests can be harsh. If ECs detach during a flow experiment, the results are invalid as cells will modify their behaviour.

In this study, we have performed and adhesion study on human umbilical vein endothelial cells (HUVECs), considering the substrate material as well as the adhesion treatment for the surfaces.

Methods

For this study, a microfluidic device previously developed was used to apply the flow conditions in the monolayer of HUVECs. These conditions were computed with fluid-structure interaction simulations. The device is made of PDMS. It is prepared by pouring PDMS in a resin mould and, once polymerised, it is attached to the substrate. In this study, this substrate is either a glass slide, or a PDMS base of around 1.6 mm in thickness.

The adhesion treatment of the microfluidic devices was performed as follows. The hydrophilicity of the substrate was enhanced by a O_2 plasma treatment for 60 seconds. Immediately after, a coating suspension was introduced in the device and kept in the incubator for one hour. Afterwards, the suspension was carefully removed and the device was cleansed three times with PBS, in order to remove all traces of the suspension. Afterwards, HUVECs were seeded in the microfluidic device and left to attach and grow in the incubator overnight.

Before the tests, the formation of a homogeneous monolayer was checked and phase contrast images were taken as initiation of the experiments. Flow was applied with a peristaltic pump and its inherent pulsatility was reduced by the use of a damper. Images were taken at 16 and 24 hours of the experiment. These images were processed afterwards with a self-developed algorithm and cell counting was performed automatically.

Results
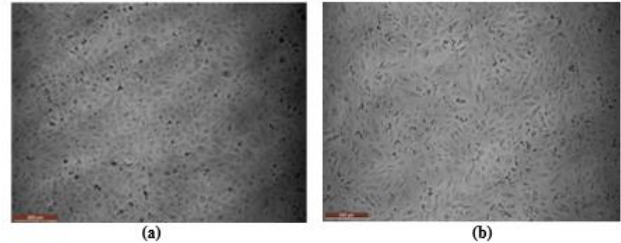
Figure 1. Monolayers of HUVEC before (a) and after (b) the adhesion study with fibronectin coating

The best adhesion treatment for HUVECs was found to be fibronectin, see Fig. 1. Moreover, PDMS as substrate showed better behaviour for cell adhesion than glass slides.

Conclusions

This is the first step needed to be developed before a flow microfluidic test that is to be performed for more than a few hours. Cell adhesion was notably different for the coating treatments we used, highlighting the importance to optimise the adhesion procedures in the experiments. Once the adhesion of ECs is assured, flow tests with different conditions can be performed to obtain cell response in terms of these parameters.

Acknowledgements

References

1. CHIU, J.-J. and CHIEN, S. Effects of Disturbed Flow on Vascular Endothelium: Pathophysiological Basis and Clinical Perspectives. Physiological Reviews. 2011, 91, 327-387.
2.- OLGAC, U., KURTCUOGLU, V. and POULIKAKOS, D. Computational modeling of coupled blood-wall mass transport of LDL: effects of local wall shear stress. Heart and Circulatory Physiology. 2008, 294, H909-H919.
3.- ZHANG, X., HUK, D. J., WANG, Q., LINCOLN, J. and ZHAO, Y. A microfluidic shear device that accommodates parallel high and low stress zones within the same culturing chamber. Biomicrofluidics. 2014, 8, 054106.
5.- HELMLINGER, G., GEIGER, R. V., SCHRECK, S. and NEREM, R. M. Effects of Pulsatile Flow on Cultured Vascular Endothelial Cell Morphology. Journal of Biomechanical Engineering. 1991, 113, 123-131.

USING HYPER- OR LINEAR- PROPERTIES DOES NOT AFFECT PREDICTIVE CAPABILITY OF VULNERABLE CORONARY PLAQUES

Marco Stefanati (1), Gabriele Dubini (1), Martin R Bennett (2), Zhongzhao Teng (3), José Félix Rodriguez Matas (1)

1. Department of Chemistry, Materials and Chemical Engineering "Giulio Natta", Politecnico di Milano, Italy;
2.3. Department of Medicine/Radiology, University of Cambridge, United Kingdom

Introduction

Coronary plaque rupture is a precipitating event in 2/3 of myocardial infarctions [1]. Frequent considered precursors for a lesion are thin overlying fibrous cap separating the core from the lumen (i.e. thin-cap fibroatheroma, TCFA) [2], and large, necrotic, lipid core and superimposed thrombus [1]. Currently, the risk of plaque rupture is computed based on demographic, clinical, and image-based adverse features. However, the absolute event rate per single higher-risk lesion remains low. Hence, additional methods for assessment of plaque vulnerability are required to improve the ability to predict plaque rupture and decide the best intervention and/or treatment for the patient. In this regard, increased plaque structural stress (PSS) could be a potential predictor, and/or classifying feature, for vulnerable plaque rupture [2]. This work studies the potential of PSS as a potential feature for stratifying vulnerable and non-vulnerable coronary plaques.

Methods

Virtual histology intravascular ultrasound (VH-IVUS) data of 55 patients, 29 with unstable angina pectoris (G1 group) and 26 with chronic stable angina (G2 group) were elaborated to reconstruct the two-dimensional (2D) cross-sections of vessels for FEM modeling (ABAQUS® 2019). The FEM model allows the analysis of von Mises stress along the coronary to determine specific thresholds for both groups of patients and identify a risk classifier for atherosclerotic plaque rupture. For each patient, around 10 sections (meshed with triangular elements) distributed equally along the coronary were analysed. In particular, three sets of simulations were performed for each plaque section: (i) a simulation using the mean hyper-elastic parameters, (ii) a Montecarlo simulation considering 100 different hyper-elastic parameters covering the range of stress-strain data reported in the literature [3] for the different plaque constituents, and (iii) a simulation using a linear elastic approximation of the mean stress-strain response for the plaque constituents used in (i). In the analysis, plaque structural stress (PSS) was described using maximum von Mises stress (peak MISES or pMIS) at the dynamic pressure, $P^{dyn} = P^{sys} - P^{dia}$, defined as:

$$pMIS^{dyn} = \max\left(MIS_i^{sys} - MIS_i^{dia}\right), \quad (1)$$

with the subscript $i=i$th centroid node (1 per element). Statistical analyses, performed in MATLAB R2020b, concerned the assessment of normality using the Jarque-Bera test and comparison using the Wilcoxon rank sum test (p-value<0.05 considered statistically significant) of the dynamic peak MISES.

Results

The G1 group is characterized by the higher median peak MISES respect to the G2 group for all three sets of simulations, namely: $pMIS^{dyn}=103.83$ vs 90.73 kPa, p-value=8.0e-04*, for the simulations using the mean hyper-elastic parameters; $pMIS^{dyn}=124.31$ vs 106.35 kPa, p-value<1e-12* for the Montecarlo simulations; and $pMIS^{dyn}=48.81$ vs 41.92 kPa, p-value=3.9e-05*, for the simulations using the mean linear-elastic parameters. The ROC curve (Fig. 1A) with the higher Area Under Curve (AUC), sensitivity (true positive rate, TPR), and specificity (true negative rate, TNR) was obtained for the $pMIS^{dyn} + P^{dyn}$ in both the Montecarlo and mean hyper-elastic parameters simulations (AUC=0.69). However, no significant difference in the ROC curves and AUCs for $pMIS^{dyn} + P^{dyn}$ was found for the simulations using the linear elastic approximation (AUC=0.68, see Fig. 1B).
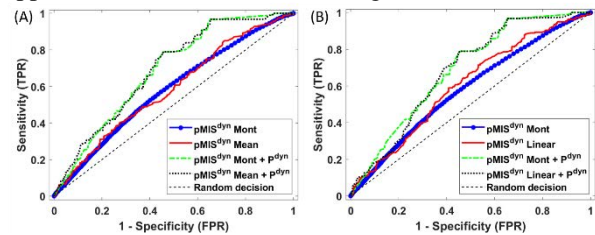
Figure 1: Receiver operating characteristic ROC curves.

Discussion

The results suggest the $pMIS^{dyn}$ as a robust classifier of vulnerable coronary plaques since it is an independent parameter, which takes into account the loading conditions in addition to the geometric features of the atherosclerotic plaques. Last but not least, our study demonstrates that the ability to distinguish between the two populations of atherosclerotic plaques is independent of the mechanical properties, but dependent on the stress state and plaque geometric peculiarities, since considering variable hyper-, mean hyper-, and mean linear-elastic mechanical properties leads to similar ROC curves. This legitimates the choice commonly made in the literature to consider the mechanical average properties of plaque components, and the possibility of using linear-elastic properties for tissue characterization.

References

1. Teng et al, Circ Cardiovasc Imaging, 7:461-470, 2014.
2. Costopoulos et al, Jacc: Cardio Imag, 10: 1472-1483, 2017.
3. Teng et al, Acta Biomaterialia 10:5055-5063, 2014.

MECHANICAL ASPECTS OF DRUG-COATED BALLOON ANGIOPLASTY DETERMINING THE EFFICIENCY OF THE COATING TRANSFER

Efstathios Stratakos, Lorenza Petrini, Giancarlo Pennati

Laboratory of Biological Structure Mechanics, Department of Chemistry, Materials and Chemical Engineering "Giulio Natta", Politecnico di Milano, Italy

Introduction

Computational modeling has been proven a powerful tool and a compelling ally of physicians to confront cardiovascular diseases. In the past decade, there has been an effort by scientists to approach Drug-Coated Balloon (DCB) angioplasty exploiting this numerical tool. Nevertheless, the vast majority of the studies have so far focused on mass transfer and drug-elution kinetics within the arterial wall, neglecting further aspects of the DCB treatment. Literature indicates that the coating transfer onto the arterial wall is to date insufficient and, as evidenced, there is a strong dependence of the coating transfer rates on the local contact pressure values [1,2]. Furthermore, the drug coating on the balloon may experience preliminary loss, during the various manufacturing processes involved. Consequently, the objective of this study is the investigation of, pre- and during-treatment, mechanical processes that could influence the coating transfer rates onto the mural arterial surface, using computational means.

Methods

The DCB thickness was gauged in a number of bare balloons, along their longitudinal axis. An accurate replica for the angioplasty balloon was introduced into the finite element models, reproduced of shell elements on Abaqus software. The realistic folding process of the balloon was simulated, as implemented in a recent study [3], taking into account possible non-uniform balloon thickness. Subsequently, the folded balloon was inflated in peripheral arterial models. The contact pressure with the arterial wall (as an indication of the coating transfer), was evaluated, as a function of oversizing and different vessel features. Simplified models of peripheral arteries were used, considering cylindrical shapes with the addition of different stiffness areas, as occurring *in vivo*.

Results

Our preliminary measurements on real devices suggest a varying thickness along the longitudinal axis of the balloons (thicker at the two ends). This was expected as a direct consequence of the blow molding process during the balloon forming and was implemented in the numerical models. The balloon folding simulations forecasted increased strain values at the crests and the "valleys" of the folds, suggesting a possible risk for microcracks on the coating or delamination during the folding process (Figure 1), as the strain values exceeded the calculated strains at break [4]. Moreover, the expansion of a folded balloon inside an undersized cylindrical arterial model revealed linearly-patterned areas with elevated contact pressure values, due to the irregular contact of the non-distended balloon with the arterial wall (Figure 2). These results could justify the observed drug coating transfer distribution onto the mural surface of porcine femoral arteries [1].
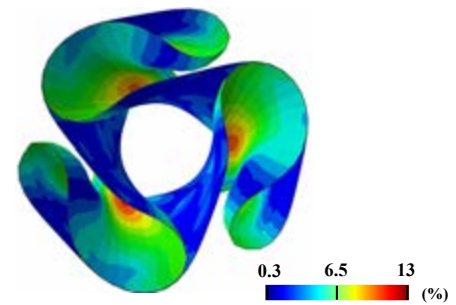
Figure 1: Maximum principal logarithmic strain percentage at integration points of the folded and pleated balloon.
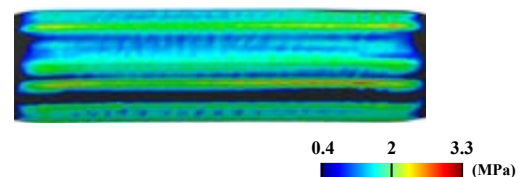
Figure 2: Contact pressure variables at the nodes of the arterial wall during the inflation of a uniform-thickness balloon, inside a slightly undersized simplified artery (black color equals to values below 0.4 MPa).

Discussion

In this study, we aimed to examine the parameters that could impact the coating transfer onto the arterial wall. There are some mechanical effects that arise during the pre- and during-operation processes, which could deteriorate the coating layer. Thus, we regarded the inclusion of the folding process of the balloon as a consequential factor when approaching the DCB treatment computationally. Furthermore, the heavy fluctuation of contact pressure values between the DCB and the vessel could justify the observed inhomogeneous coating transfer on the arterial wall [1]. Effectively, our study concluded that the mechanical aspects of DCB angioplasty can justify the reduced coating transfer rates.

References

1. Tzafriri et al, Biomaterials, 260 ,2020,
2. Chang et al, Sci Rep 9, 6839, 2019
3. Geith et al, International journal for numerical methods in biomedical engineering, 35(11),2019
4. Anderson et al, Acta Biomaterialia, 29: 333-351,2016

A FLUID-STRUCTURE INTERACTION APPROACH FOR PATIENT-SPECIFIC THORACIC AORTIC WALL STRESS ANALYSIS USING SIMVASCULAR

Rodrigo Valente[1,2], André Mourato[1], Moisés Brito[1], José Xavier[1], Stephane Avril[3], José Cesar de Sá[4], António Tomás[4], José Fragata[4]

1. UNIDEMI, NOVA School of Science and Technology, Universidade NOVA Lisboa, Portugal
2. INEGI – Institute of Science and Innovation in Mechanical and Industrial Engineering, Porto, Portugal
3. Mines Saint-Etienne, University of Lyon, Inserm, Sainbiose U1059, France
3. Faculty of Engineering, University of Porto (FEUP), Porto, Portugal
4. Cardiac Surgery Department, Hospital de Santa Marta, Centro Hosp. Univ, Lisboa Central, Portugal

Introduction

The ascending aorta is the first segment of the largest artery in the human body, located at the exit of the left ventricle. Several evidence suggest that aging, environmental factors, lifestyle and pathologies such as Bicuspid Aortic Valve (BAV) or stenosis are responsible for a loss of elasticity in the arterial wall. If this degeneration process yields an increase of 50% in diameter, then it is defined as an Ascending Aorta Thoracic Aneurysm (AATA) [1].

According to the European Society of Cardiology (ESC), surgical intervention is recommended when the aneurysm exceeds 55 mm, but it has been shown that dissection or rupture of the ATAA may occur before reaching this threshold [2]. Hence, the current method of diagnosing AATA is not conservative and more thorough methods need to be developed [3].

The use of computational modelling and simulation tools has proven to be a powerful tool in describing the hemodynamics and structural stresses involved in this pathology, as it may allow leveraging the clinical analysis of the patient without invasive medical exams.

Methods

In this paper, a method was developed to analyze the hemodynamic and structural response of the ATAA from the patient's CT scans. For this purpose, SimVascular [5,6] was used, given its ability to encompass the numerical study from the design of the patient-specific geometric model using a three-dimensional segmentation tool to the Fluid-Structure Interaction (FSI) calculations which incorporate the impact of the aortic wall on the hemodynamics.

The numerical model in the Lumen Domain was defined by using a flow rate variation at the inlet and a three element Windkessel model or RCR model at the outputs since it can predict the pressure distribution downstream over time [6]. Furthermore, the inlet and outlet surface in Anulus Domains were defined with a zero-valued Dirichlet boundary condition.

The hyperelastic behaviour of the aorta was simulated with a Neo-Hookean constitutive model. The fluid was considered Newtonian with laminar flow, as this is an acceptable approximation for largest arteries.

Results

The separation of the geometric model in lumen and solid domains is an important step in the development of FSI numerical models. Although it increases pre-processing complexity, the numerical efficiency is much higher, thus reducing the required computational effort. Furthermore, it was shown that using a prestress analysis improves numerical stability, improving the numerical model.

Discussion

The proposed numerical model proved to be capable of predicting patient-specific hemodynamic and structural parameters. This FSI approach was able to predict the ATAA effect on the hemodynamics. Nevertheless, more data should be incorporated into the analysis in order to calibrate the model for patient-specific evaluation.

References

1. Dieter, R., R. Dieter e R. D. III, Diseases of the Aorta, 2019.
2. Erbel, R. et al, 2014 ESC guidelines on the diagnosis and treatment of aortic diseases, European Heart Journal: 35, 2873–2926, 2014.
3. Youssefi, P. et al, Functional assessment of thoracic aortic aneurysms - The future of risk prediction? British Medical Bulletin 2017: 121, 61–71.
4. Updegrove, A. et al, SimVascular: An Open-Source Pipeline for Cardiovascular Simulation, Annals of Biomedical Engineering 2017: 45, 525–541.
5. Valente, et al. Fluid-structure interaction modelling of ascending thoracic aortic aneurysms in SimVascula. Biomechanics 2(2), 189-204, 2022.
6. Bäumler, K. et al, Fluid–structure interaction simulations of patient-specific aortic dissection, Biomechanics and Modeling in Mechanobiology 2020: 19, 1607–1628.
7. Mourato A. et al, On the RANS modelling of the patient-specific thoracic aortic aneurysm, Advances and Current Trends in Biomechanics 2021, 1, 98-102.

Acknowledgements

COMPARISON OF DIFFERENT TENSEGRITY MODELS OF THE LIVING CELL UNDERGOING COMPRESSION

Alessandro Arduino (1), Sofia Pettenuzzo (1), Alice Berardo (1,2), Valentina Salomoni (3) Emanuele Luigi Carniel (4), Carmelo Majorana (1)

1. Department of Civil, Environmental and Architectural Engineering, University of Padova, Italy
2. Department of Biomedical Sciences, University of Padova, Italy
3. Department of Management and Engineering, University of Padua, Italy
4. Department of Industrial Engineering, University of Padova, Italy

Introduction

The mechanical properties of human cells and their subcomponents play a key role in the mechano-transduction of external stimuli into physiological processes such as proliferation, differentiation, and migration. As a result, the interest in the mechanical behavior of living cells has drawn a lot of attention within the scientific community in recent years. Many possible models of the cell mechanics have been proposed throughout the years and the most used and investigated are continuous models and tensegrity models. Tensegrity models were first introduced to the field of cellular mechanics by the insights of Donald Ingber [1] and have been used to mimic many different types of cells. Although the abundance of works in the literature, there is no clear answer to what type of tensegrity structure better represents most cells.

Methods

To shed some light on the effect of considering different types of tensegrity models, three-dimensional Finite Element (FE) Models (developed with Abaqus/CAE 2019, Dassault Systems) of the cell were created and compared. The used models varied from the usual 12 nodes tensegrity icosahedron [2,3,4] to the 24 nodes cuboctahedron [5,6]. Furthermore, the effect of the introduction of a nucleoskeleton as an inner tensegrity layer has been investigated. Finally, the models have been tested for both rigid and bendable struts.
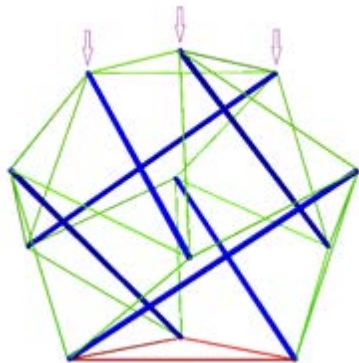
Figure 1: Example of a 12 node tensegrity ichosaedron. Blue lines represent the struts (i.e. the microtubules) while the green lines represent the tensile cables (i.e. the microfilaments). The lines in red are fixed in all degrees

of freedom to simulate adherence to a substrate. A concentrated vertical force or a fixed displacement is imposed on the three upper nodes (purple arrows) to simulate AFM indentation.

Results

These FE models have been used to simulate indentation through atomic force microscopy by applying a constant force or displacement in the upper nodes of the structure. The values of the reaction forces or displacements were then recorded. The resulting data were compared with similar in vitro experiments from the literature [7].

Discussion

The results of this work can help to develop a better understanding of the role of the cytoskeleton in the overall mechanical response of the cell. Furthermore, the addition of a nucleoskeleton structure can be a useful method to quantify how much of an external force is translated into mechanical stimuli to the cell nucleus and thus how they influence the proliferation, differentiation, and migration of living cells.

References

1. Ingber DE, Journal of cell science, 104(3), 613-627, 1993.
2. McGarry JG and Prendergast PJ, European Cells and Material, 7, 27-34, 2004.
3. Coughlin MF, Journal of biomechanical engineering, 120(6), 770-777, 1998.
4. Fraldi M et al, Journal of the Mechanics and Physics of Solids, 124, 299-324, 2019.
5. Wang L & Chen W, Applied Bionics and biomechanics, 2019.
6. Chen, TJ et al, PloS one, 5(12), e14392, 2010.
7. Darling EM et al, Journal of Biomechanics, 41, 454-464, 2008.

Acknowledgements

DYSREGULATED ENERGY PRODUCTION IMPACT THE OUTCOME OF SCAFFOLD-GUIDED BONE REGENERATION IN TYPE 2 DIABETES

Daniela Dias (1), Raphaela Fritsche-Guenther (3), Agnes Ellinghaus (1,2), Georg N. Duda (1,2), Jennifer Kirwan (3), Patrina S.P. Poh (1,2)

1. Berlin Institute of Health at Charité – Universitätsmedizin Berlin, Julius Wolff Institute, Germany;

2. Berlin Institute of Health at Charité – Universitätsmedizin Berlin, Berlin Institute of Health Center for Regenerative Therapies, Germany

3. Berlin Institute of Health – Metabolomics Platform, Berlin, Germany

Introduction

Healing of a large bone defect is generally challenging. Specifically in patients with Type 2 diabetes (T2D) endogenous bone healing capabilities are impaired. Bone regeneration is known to be influenced by various factors [1] and concepts to heal large bone defects have advanced [2]. Scaffolds have been shown to act as a bridge between the bone ends and guide cells to self-organize and fill the defect along the biomaterial [3]. Curvatures of such scaffolds surfaces cause cells to drive cellular migration and eventually phenotype [4]. Scaffold geometry and material properties can be tuned to provide favorable conditions for cells to enable osteogenesis. However, all these cellular activities are energy consuming. Recent advancements in metabolomic research show that patients with T2D have a disrupted gut microbiota composition resulting in increased membrane transport of glucose (leading to high blood glucose) and branched chain amino acid (BCAA) transport but decreases in short chain fatty acid (SCFA) production and metabolism of cofactors and vitamins [5]. These differences in the endogenous substrates' composition associated with T2D disrupt the metabolism homeostasis and potentially contribute to a dysregulated pro-inflammatory response, a lack of anti-inflammatory factors alterations in angiogenesis, and eventually mineralization [6]. All these phenomena have been observed in fracture patients with T2D [7].

Hence, the aim of our work was to investigate metabolism alterations during regeneration in a T2D rat model of scaffold-guided bone healing.

Methods

In vivo: A well-established 5 mm critical-sized femoral defect was used and healing in healthy versus T2D rats was compared. Scaffolds made of polycaprolactone (PCL) designed with 70% porosity and gyroid architecture were press-fit into the defect. At 2, 4 and 5 weeks' time point, in vivo μCT was performed as well as at the time of sacrifice. At 3 and 6 weeks, explants were collected, and flash frozen in liquid nitrogen until further processing.

Metabolomics: Explants of the femur containing the scaffolds were processed following a previously established protocol [8] and central carbon metabolites (CCM) were measured with gas-chromatography mass spectrometry (GC-MS).

Results

Bone regeneration was impaired in T2D compared to healthy animals as evidenced by the lower bone volume from the μCT data at 3 and 6 weeks. Semi-targeted metabolomics revealed that metabolic pathways, such as the tricarboxylic acid (TCA) cycle and glycolysis were differently regulated in T2D compared to healthy animal indicating a disruption in the energy metabolism which facilitates bone regeneration.

Discussion

Metabolism homeostasis plays a pivotal role in maintaining a "healthy" endogenous bone healing potential. This study highlighted the relevance of the central carbon metabolic pathway in bone defect healing and eventually could pave the way to a better understanding of what should be different in metabolically challenging defect healing settings. Patients with T2D may need a more personalized treatment compared to otherwise healthy patients to metabolically reprogram the different cell types towards successful regeneration.

References

[1] B. M. Willie *et al.*, Soft Matter, 6:4976–4987, 2010.
[2] M. Moreno *et al.*, Curr. Pharm. Des., 18:2726–2736, 2016.
[3] A. M. Pobloth *et al.*, Sci. Transl. Med., 423:1-16, 2018.
[4] M. Werner *et al.*, Materials (Basel)., 4:1–18, 2020.
[5] Y. Fan *et al.*, Nat. Rev. Microbiol.,1:55–71, 2021.
[6] C. Hamann *et al.*, Am J Physiol Endocrinol Metab., 17:1220–1228, 2011.
[7] A. V. Schwartz, Bone, 82:2–8, 2016.
[8] R. Fritsche-Guenther *et al.*, Metabolites, 1:1–14, 2020.

Acknowledgements

LARGE-SCALE QUANTIFICATION OF OSTEOCYTE MORPHOMETRY AND PROTEIN EXPRESSION FROM MURINE BONE HISTOLOGY

Francisco C. Marques (1), Dilara Yilmaz (1), Esther Wehrle (1), Ralph Müller (1)

1. Institute for Biomechanics, ETH Zurich, Zurich, Switzerland

Introduction

Osteocytes are cells embedded in the mineralised bone matrix and are regarded as the mechanosensors directing bone formation and resorption in bone adaptation and regeneration [1]. Likewise, immunohistochemistry is a foundational technique applied in bone research to retrieve cellular morphometry and protein expression. However, automated methods that can efficiently analyse histological sections from bone are still lacking, hampering its throughput and integration into correlative multimodal imaging approaches combining cellular data from histological sections with tissue-organ-level information from micro-computed tomography (micro-CT). In this work, we developed a pipeline for large-scale quantification of osteocyte morphometry and protein expression in histological sections in a mouse femur defect model of bone regeneration. We expect this analysis to be generalisable to other preclinical models used in bone research.

Methods

The data used here was collected in a previous study [2]. Briefly, 20-week-old C57BL/6J mice underwent femur defect surgery and were imaged weekly with *in vivo* micro-CT (vivaCT 40) over seven weeks after surgery, revealing bone remodelling regions between images [2]. *Ex vivo* 10-µm thick histological sections were collected from one paraffin-embedded femur from day 49 and stained for Sclerostin (Fast Green counterstain), and individual cells were annotated around the lacunar borders in QuPath [3] by one operator. The pipeline was developed in Python, combining binary cell annotations with original high-resolution histological images (0.39 µm pixel size). For protein expression quantification, the image was converted to HSV space, and the value channel was segmented with a multi-Otsu criterion (for Sclerostin, the third threshold out of 4 classes was found to work best). Next, a median filter was applied to smooth the segmented areas, followed by a binary erosion step, yielding the set of pixels representing stained protein for each cell. The size of this set of pixels over the measured cell area from the annotation gives a normalized mean intensity protein expression per cell. Cell annotations were also used to quantify the perimeter, major and minor axis length, orientation, and eccentricity. Cells were individually labelled, and the data was exported to a table for statistical analysis.

Results

Two Sclerostin slices from the middle of the femur were analysed with this pipeline (Fig. 1B), providing cell-specific data for over 2,500 cells. Mean intensity values
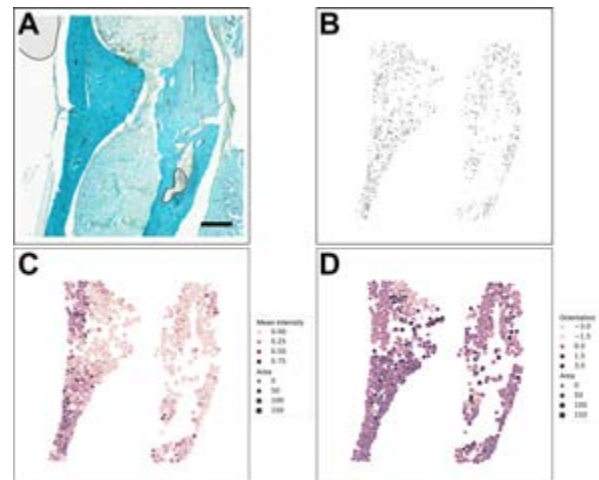
Figure 1: A) Histological section showing Sclerostin staining, around the fracture callus and adjacent cortex (FCR), Scale bar: 400µm; B) Binary mask with annotated Sclerostin$^+$ cells in FCR; C) Mean intensity values per cell as a proxy for Sclerostin expression; D) Cell orientation (in radians).

were significantly lower in formation vs. quiescent regions (Fig. 1C). Cell orientation was also significantly different (p<0.0001) between these regions, while other parameters showed no significant differences.

Discussion

The results agree with existing literature, which indicates an anti-anabolic effect of Sclerostin. Also, osteocyte orientation has been suggested to influence mechanosensitivity [4]. Combined, these results reinforce osteocytes' role in bone mechanoregulation, especially in highly dynamic events, like bone regeneration. Local stretch in some cell clusters and variations in image quality and illumination across the image were the main factors affecting the output of the analysis. Moreover, manual annotation of the cells is the biggest bottleneck in the analysis. Ongoing work aims to investigate the effects of stretch in the histological sections on the analysis and to increase the throughput of cell segmentation by leveraging recent deep learning approaches designed for this task.

References

1. Klein-Nulend et al., FASEB J 9:441–445, 1995.
2. Wehrle et al., Sci Rep 11**,** 23037, 2021.
3. Bankhead et al., Sci Rep 7, 16878, 2017.
4. Wu et al., *Int J Oral Sci* **10,** 2, 2018

Acknowledgements

CULTURE OF PORCINE BONE EXPLANTS UNDER COMPRESSIVE LOADING

Esther E.A. Cramer (1), Linda M. Kock (1,2), Davy Wanders (2), Keita Ito (1), Sandra Hofmann (1)

1. *Orthopaedic Biomechanics, Department of Biomedical Engineering and Institute for Complex Molecular Systems, Eindhoven University of Technology, the Netherlands*
2. *LifeTec Group BV, Eindhoven, The Netherlands*

Introduction

Bone mechanotransduction, a process in which physical forces are converted into biochemical signals, coordinates matrix remodeling to maintain bone mass and evokes changes in bone structure [1]. In this process, complex interactions are required between many cell types, such as osteocytes, osteoblasts, osteoclasts, and their progenitors MSCs and monocytes. The ability of bone explants to preserve tissue specific cells in their native 3D extracellular matrix provides a unique environment to study remodeling [2]. In bone explants, mechanical loading - such as compression - also appears to play an important role by enhancing osteocyte viability [2-4]. This research aims to examine the potential of compressive forces on preserving cell viability and bone formation of porcine bone explants.

Methods

Bone cores (Ø=8 mm, 7 mm height) were isolated from porcine femoral condyles, obtained freshly from the slaughterhouse's left-over material. Bone explants were cultured for 4 weeks in culture medium supplemented with ascorbic acid and ß-glycerophosphate. Samples subjected to compressive loading were cultured in a custom-made bioreactor system (LifeTec Group BV). After an initial preload of 3N, a loading regime of dynamic compressive loading (40N, 1Hz) was applied for 30 min, 5 days a week.

DNA levels were measured in explants both in static and dynamic culture conditions (n=3,4). Micro computed tomography (µCT) was performed to quantify mineralized tissue volume change. Loaded and unloaded samples (n=2 per group) were scanned at the start of the culture period and a follow-up scan was made after 4 weeks of culture.

Results

Similar amounts of DNA per explant (Fig. 1A) were seen for loaded and unloaded samples suggesting comparable amounts of cell numbers and no adverse effects of compressive loading.

When bone volume of week 4 was compared to the bone volume at the start of culture (Fig. 1B) a trend towards a greater increase in bone volume for samples cultured under compressive loading conditions was observed (2.9% vs 5.7%). Nonetheless, only 2 samples were included for analysis at this point. Additional research is in progress to increase sample size which is required for comprehensive comparison.
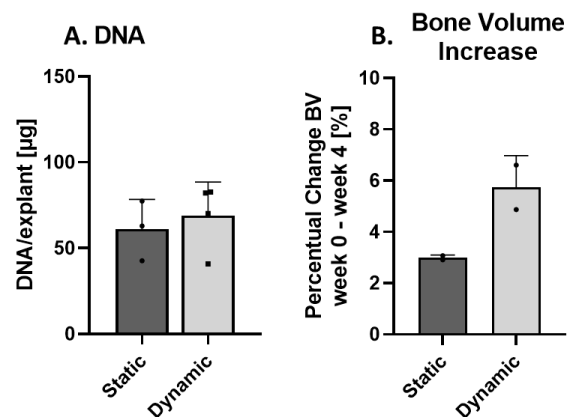
Figure 1: (A) Amount of DNA per explant measured after 4 weeks of culture in static (dark-grey column) and dynamic (light-grey column) culture conditions. (B) Quantitative analysis of µCT scans. Percentual increase in bone volume over 4-week culture period for statically (dark-grey column) and dynamically (light-grey column) cultured samples.

Discussion

These preliminary results demonstrate a first indication of increased bone formation upon compressive mechanical stimulation in bone cores cultured *ex vivo*. Additional analysis of cellular response and bone formation using for example histology and techniques for overlaying µCT images are currently performed to increase sample size and to verify the initial results. Moreover, further optimization of culture and loading conditions together with a larger sample size will give more insight in the effects of compression on bone explants. Taken together, the addition of compressive mechanical loading in bone explant cultures is a step forward in mimicking the natural bone remodeling environment more closely, which might set ground in bridging the gap between *in vitro* and *in vivo* studies.

References

1. Jing et al, FASEB J, 28(4):1582–1592, 2014
2. Cramer et al., Curr Osteoporos Rep, 19(1): 75–87, 2021;
3. Chan et al, Cell Mol Bioeng, 2:405-415, 2009.
4. Lozupone et al, Clin Rheumatol, 15(6):563–572, 1996

CLOSED-LOOP BIAXIAL CELL STRETCHING SYSTEM FOR CONTROLLING CELL MECHANO-TRANSDUCTION PROCESSES

Luigi Crimaldi (1), Valeria Panzetta (2), Carlo Natale (1), Paolo Antonio Netti (1,2)

1. Centre for Advanced Biomaterial for Health Care, Istituto Italiano di Tecnologia, Napoli, Italy; 2. Centro di Ricerca Interdipartimentale sui Biomateriali, Università degli Studi di Napoli Federico II, Napoli, Italy

Introduction

Deformable cell culture systems, such as cell stretcher device, proved to modulate cell behaviour through a fine tuning of mechano-sensing/transduction events occurring at cell-material interface. Although a heterogeneous category of cell stretchers offers high performances and flexibility in modulating cell mechanics [1], nowadays a precise automatized cell stretching system capable to operate in a closed-loop system along with cell biochemical and biophysical response is still missing. Along these lines, the goal of this project is the development of a custom-made biaxial cell stretcher equipped with a feedback loop on cell response for the control of cell mechano-transduction processes.

Methods

The cell stretcher's device consists of two stepper motors connected to stainless steel trapezoidal reverse lead screws. The rotation of these screws is converted into a linear translation of nuts which, in turn, is transferred to a custom-made PDMS cell chamber through a system of linear rods and mechanical bearings. Moreover, the stretching device (Fig.1) is mounted on the top of an inverted fluorescence microscope allowing live-cell fluorescent imaging. A MATLAB algorithm is implemented to interface the microscope and the actuators, creating a closed-loop system. Biophysical (cell and nucleus morphology) and/or biochemical (gene/protein/transcription factor localization and expression) information will be extracted real-time from digital images acquired by microscope camera and once processed by the algorithm, they will provide information concerning the perturbed cellular state following stretching. Based on that, the entity of substrate stretch will be automatically and dynamically adapted by the control algorithm, until the cell reaches the desired controlled state.
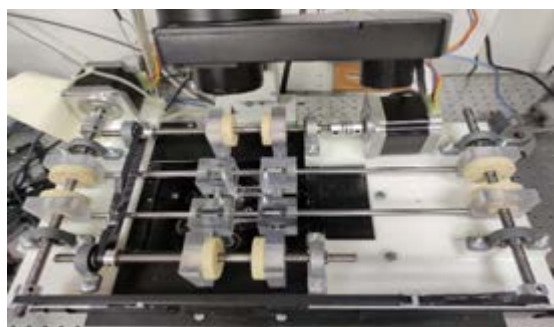
Fig.1: Cell stretcher device placed on an inverted microscope.

Results

To validate the control algorithm, a preliminary test was carried out on micropatterned circular islands (semi-axis of 38.5 µm) of fluorescent fibronectin, realized on the PDMS chamber's substrate through microcontact printing technique. The input provided to the control algorithm was the increase of vertical semi-axis by 30%. During the controlled stretching (Fig.2), the vertical semi-axis reached the reference approximately after 8 iterations and oscillated around it with an average error of 0.2% respect the setpoint (50 µm).
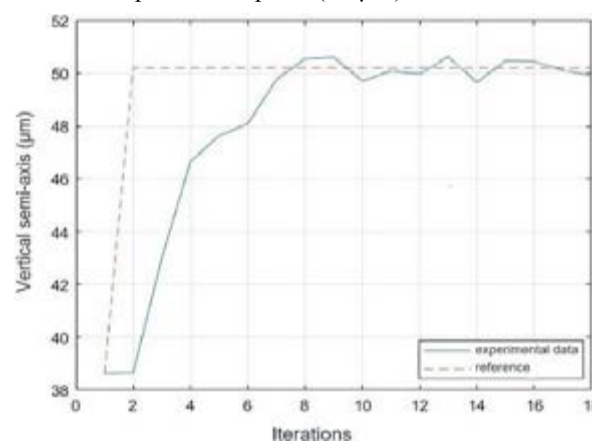
Fig.2: Controlled stretching of circular adhesive islands.

In future, similar experiments will be aimed to precisely control cell/nuclear shape and gene/transcription factor expression to guide mechano-transduction related cell functions in a predictable way.

Discussion

This project presents a custom-made automated biaxial cell stretcher representing a first example of synergy between Mechanobiology and Automation Engineering. The next steps will be the realization of an incubation chamber to perform mechanobiology studies and the use of Machine Learning algorithms for Image Processing. In this way, we expect that such a tool could further elucidate the mechanisms behind cell mechano-transduction processes and give important insights about the mechanical dosing necessary to guide cell functions or fate.

References

1. H. Kamble et al, Lab Chip, 2016,16, 3193-3203.

ACOUSTIC LENS DESIGN FOR *IN-VITRO* CELL STIMULATION: A NUMERICAL STUDY

Elise Doveri (1), Meysam Majnooni (2,3), Carine Guivier-Curien (3), Philippe Lasaygues (1), Cécile Baron (2,3)

1. Aix Marseille Univ, CNRS, Centrale Marseille, LMA UMR 7031, Marseille, France;
2. Aix-Marseille Université, CNRS, ISM UMR 7287, Marseille, France;
3. Aix-Marseille Université, CNRS, IRPHE UMR 7342, Marseille, France

Introduction

In the early 1950s, the first clinical observations on the effect of *Ultrasound Stimulation on Bone Regeneration* (*USBR*), were reported [1]. However, the effects of the mechanotransduction are still unclear and *USBR* remains controversial [2]. To better understand the interaction between ultrasound and bone cells, the development of *in-vitro* experiments is a key step.

One of the first challenges was to characterize and monitor the ultrasound dose delivered to the cells inside a Petri dish. In order to avoid perturbating phenomena such as multiple reflections and standing waves, an innovative experimental set-up including an anti-reflection cover [3], has been proposed: bone cells are seeded in a Petri dish and are stimulated by using a 1 MHz transducer. However, experimental results showed that the intensity distribution is heterogeneous and concentrated in the middle of the Petri dish. In order to enlarge and homogenize the acoustic intensity distribution inside the Petri dish, an acoustic lens is designed. In this study, a numerical model using Finite Element (FE) method is developed to reproduce the experimental set-up, and guide the design of this lens. Different configurations are thus tested in order to optimize the geometrical and material composition of the lens.

Methods

A numerical 2D axisymmetric model (black dashed rectangle on Fig. 1) of the *in-vitro* stimulation experimental set-up is developed under *COMSOL Multiphysics®* v5.5, due to cylindrical nature of experimental set-up (Fig. 1).

The Pressure Acoustics module (transient) is used for the propagation of acoustic wave in the fluid parts (lens and water) and the Solid Mechanics module for the elastic wave propagation in the solid parts (Petri dish).
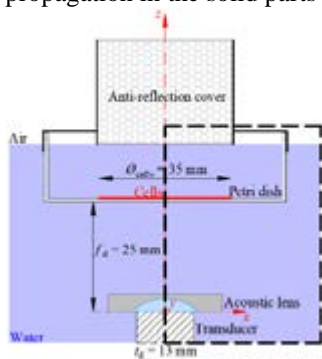
Figure 1: Schematic of the experimental set-up

Results

Figure 2 presents the normalized I_{TA} (*Temporal Average Intensity*) [4] inside the Petri dish (in the *xy*-plane) for three configurations: without the lens, with a lens made only in epoxy and with a lens made in epoxy and PDMS. The black dashed circles (Fig. 2) delimit the covered surface, such that the $I_{TA} \geq 0.25\max(I_{TA})$. This surface is equal to 15.7% without the lens, 70.2% with an epoxy lens and 96.3% with a lens made in PDMS and epoxy.

The homogeneity of the intensity field is quantified by the calculation of the mean value and standard deviation of the absolute value of the gradient of the normalized I_{TA} [4]. The mean I_{TA} gradient is equal to 0.058 ± 0.108 mm^{-1} without the lens, 0.081 ± 0.067 mm^{-1} with an epoxy lens and 0.130 ± 0.117 mm^{-1} with a lens made in epoxy and PDMS.
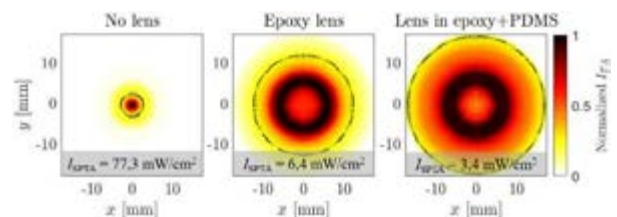
Figure 2: Normalized intensity inside the Petri dish without the lens, with a lens made only in epoxy and with a lens made in epoxy and PDMS.

Discussion

With the lens almost all the surface is covered (96.3%). Nevertheless, the intensity distribution is not homogeneous (the mean gradient is higher than without the lens or than with a lens made only in epoxy) and the maximum intensity is significantly reduced (less than 10 mW/cm² with the lens, 77.3 mW/cm² without the lens). This means that the lens can be used to enlarge the acoustic intensity distribution inside the Petri dish, but not really to homogenize it.

In order to improve that, some parametric studies will be conducted on the size of the lens. Then, once the lens is designed, it will be fabricated and tested in *in-vitro* conditions with murine osteocytes cells.

References

1. Buchtata, Br J Phys Med Its Appl Ind, 15(1):3-6, 1952.
2. Padilla et al, Ultrasonics, 15(5):1125-1145, 2014.
3. Majnooni et al, Ultrasonics (in revision), 2021.
4. Horne et al, Biomed Phys Eng Express, 6(3):035033, 2020.

CELL'S SENSE OF SLOPE

Crescenzo Frascogna (1,2), Valeria Panzetta (1,2), Paolo Antonio Netti (1,2)

1. Centre for Advanced Biomaterial for Health Care, Istituto Italiano di Tecnologia, Napoli, Italy; 2. Centro di Ricerca Interdipartimentale sui Biomateriali, Università degli Studi di Napoli Federico II, Napoli, Italy

Introduction

Cells have developed multiple mechanisms to apprehend and adapt finely to their environment. Signals from the extracellular matrix are known to influence spatio-temporal organization of cells and tissues, guiding many processes such as morphogenesis, pathology, and repair. A physical cue that is gaining importance in the comprehension of cell mechanics is the local geometry [1]. Here, the effects of surface curvature on the focal adhesions (FAs) dynamics and cytoskeletal rearrangement have been investigated by using a molecular-mechanical model.

Methods

Cells probe tissue properties through their contractile and adhesive molecular machinery that is referred to as a "molecular clutch". We developed a modified version of the molecular clutch model [2], as schematized in figure 1, to explain the recent observations of cell response to concave and convex substrates. The master equations governing the dynamic evolution of the system are those introduced by Odde [2] with some modifications that consider the spatial organization of the actin stress fibers and the slope of the substrate. Monte Carlo simulations have been used to predict the clutch binding and unbinding events. The velocity of the clutch is weighted by the probabilities $P_{b,i}$ that the clutch is either bound or unbound. If it is not bound, its end has the same velocity of the substrate dx_s/dt because it has zero extension. Otherwise, if the clutch is bound, its end moves with a velocity that is a fraction of the actin retrograde flow rate v_f as reported in the equation (1).

$$\frac{dx_{c,i}}{dt} = \left(1 - P_{b,i}\right)\frac{dx_s}{dt} + P_{b,i} v_f \cos(\gamma) \qquad (1)$$

where:

$$\gamma = \alpha_{vf} - \beta \qquad (2)$$

is the angle of the stress fibres respect to the tangential plane of the cell (α_{vf}) and the curvature of the substrate (β).

Results

The model has been implemented in MATLAB and we firstly analyzed the actin retrograde flow that can be interpreted as a measure of the cytoskeletal activity. Two different trends have been identified through computational insights. On concave surfaces, the equilibrium condition, corresponding to the minimum of the actin retrograde flow rate, is characterized by a lower number of clutches bounded respect to the planar case.

Specifically, it decreases as the concavity of the substrate increases. Contrariwise, the simulations on convex substrates identify a trend that is completely reversed, in fact, a higher number of clutches is involved in the adhesion process respect to the planar case. In addition, the model predicts that these substrate slope-dependent changes in clutch dynamics lead to substantial differences in the mean traction forces exerted on curved versus flat substrates. Again, we identified two opposite trends. Cells exert a force that increases as the convexity of the substrate increases. Moreover, the simulations were carried out on different substrate stiffness. The trend has the same shape previously discussed but it is shifted, demonstrating that the model is still sensitive to the material stiffness.
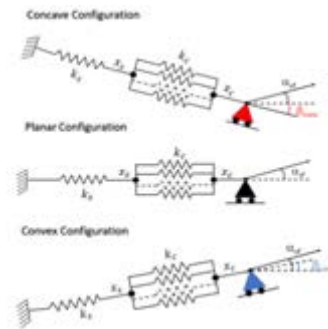
Figure 1 – Molecular Clutch Model in concave, planar and convex configuration.

Discussion

The concavity induces a softening effect in the cellular perception of substrates with cells adopting a spider-like configuration characterized by a lower number of involved clutches than in the planar case. On the other hand, the convexity induces a stiffening effect that results in cells adopting a snail-like configuration with a higher number of clutches involved in the adhesion and exerting a greater force on the substrate [3]. Cell mechanosensing is not mediated only by substrate stiffness but also the curvature plays a key role in the mechanical response of the cell. The model predictions will be tested using an *ad hoc* microfluidic device able to deform a PDMS membrane generating concavity and/or convexity with different radii of curvature. This is really promising because, differently to substrate stiffness, curvature can be changed dynamically according to the real time response of the cell.

References

1. Callens et al, Biomaterials, 232:119739, 2020.
2. Bangasser et al, Cell Mol Bioeng, 6(4):449-459, 2015.
3. Werner M et al, Adv Sci, 4(2):1600347, 2016.

COMPUTATIONAL MODELLING OF CELL RESPONSE TO VARIOUS MECHANICAL STIMULI

Veera Venkata Satya Varaprasad Jakka, Lucie Orlova and Jiri Bursa

Faculty of Mechanical Engineering, Brno University of Technology, Brno, Czech Republic
E-mails: 207437@vutbr.cz, 182631@vutbr.cz, bursa@fme.vutbr.cz

Introduction

Endothelial cells in the arterial wall may play a decisive role in the etiology of atherosclerosis. To improve the understanding of the cell mechanical response, the bendo-tensegrity concept was recently used to describe the characteristic behavior of the cytoskeleton. This helped to overcome the excessive stiffness of microtubules from the previous tensegrity-based cell models. In the presented hybrid model, actin filaments (AFs) serve as tension-supporting cables, while microtubules serve as compression-supporting bended beams. The AFs are prestressed which is essential for the cell shape stability, while the intermediate filaments (IFs) are wavy, thus not bearing any load until straightened.

Methods

A hybrid FE model was created by combining the cytoskeleton model with continuum parts of the cell (nucleus, cytoplasm and cell membrane) taking into consideration different physiological shapes of endothelial cells. Additionally, four different variants of the model were created (regular flat and domed, elongated flat and domed) being even closer to its physiological shape [1]. To validate the described model with experimental results, the model was transformed (by keeping the same volume) into different shapes observed in vitro which were then used in Finite Element (FE) simulations of tension and compression [2].

Results

The objective of this work is to investigate the mechanical response of endothelial cells to different loading conditions (compression, uniaxial and biaxial tension, and shear). The cell model was used for assessment of the impact of wall shear stress acting on the endothelium cells in arteries under their biaxial tensional load corresponding to the physiological conditions in the arterial wall (axial pre-stretch and mean arterial blood pressure causing circumferential stresses and strains). Finally, the model is intended to be used in FE simulations of the cell populations and their debonding from the substrate (basal lamina) under cyclic load corresponding to pulsatile blood pressure. Considerations on the role of the mitochondrial network in cell mechanical responses are also scheduled.

Discussion

The significant contribution of the cytoskeleton and its individual components to overall cell stiffness was assessed and nucleus deformation has been established as a decisive quantity for mechanotransduction.

— **Actin filaments (AFs)**
— **Intermediate filaments (IFs)**
— **Microtubules (MTs)**
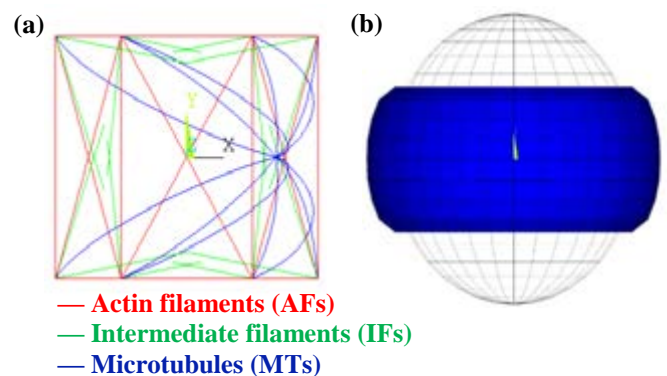
Figure: Suspended cell model for simulation of compression test: (a) unloaded cytoskeleton in front view (b) unloaded model in wireframe and under 50% compression [2].

References

1. Veera Venkata Satya Varaprasad Jakka, Jiri Bursa, "Impact of physiological loads of arterial wall on nucleus deformation in endothelial cells: A computational study" Comput. Biol. Med, Volume 143, 2022.
2. Jakka VVSV, Bursa J. Finite Element Simulations of Mechanical Behaviour of Endothelial Cells. Biomed Res. Int. 2021. Article ID 8847372

Acknowledgments

IN SILICO ULTRASOUND STIMULATION OF OSTEOCYTE IN BONE LACUNO-CANALICULAR NETWORK

Meysam Majnooni (1, 2), Elise Doveri (3), Philippe Lasaygues (3),
Carine Guivier-Curien (1), Cécile Baron (1, 2),

1. Aix-Marseille Université, CNRS, Centrale Marseille, IRPHE UMR 7342, Marseille, France ;
2. Aix-Marseille Université, CNRS, ISM UMR 7287, Marseille, France ;
3. Aix Marseille Univ, CNRS, Centrale Marseille, LMA UMR 7031, Marseille France.

Introduction

Osteocytes are known as the master orchestrator of bone remodeling being the mechanosensors of bone. They are dendritic cells, ubiquituous in the bone extracellular matrix (ECM) forming a complex micrometric 3D network. The space between the osteocytes and the ECM is called the pericellular matrix (PCM) and can be considered as a fluid. To relevantly analyze the mechanical stress induced by external stimulation such as physiological loading or ultrasound (US), this 3D micro-environment need to be taken into account. Several papers have been published on the interaction between lacuno-canalicular network (LCN) and physiological loading, currently represented as a gradient of pressure (30Pa/µm). However, to our knowledge, no study has been published on the action of ultrasound stimulation (USS) on osteocytes in a 3D configuration representative of their *in-vivo* micro-environment while ultrasound stimulation is clinically used in bone healing. To overcome this lack, we propose a first numerical finite-element model to investigate the effect of ultrasound stimulation on an 3D idealized geometry of the PCM.

Material and Methods

As currently admitted in the literature in the case of physiological loading, osteocytes are mainly sensitive to the fluid shear stress induced inside the PCM. Consequently, the goal of this study is to estimate the wall shear stress (WSS) applied on the osteocytes by ultrasound stimulation considered as harmonic acoustic wave. This configuration is modeled in the frequency domain with finite-element commercial software Comsol Multiphysics v6.0. The idealized 2D axisymmetric geometry is inspired from [1] (Figure 1a). The ECM and the osteocyte are considered as rigid bodies and the PCM as water. The boundary condition at the ends of the canaliculi is symmetry condition in order to represent a succession of osteocytes. The US loading is represented by the displacement of the ECM/PCM interface in the radial direction (e_r), with an amplitude U_0 imposed at the frequency f.

Considering the dimensions of the system and the wavelength, the Thermoviscous Acoustics module and the Laminar flow module of Comsol Multiphysics are coupled to take into account the acoustic streaming induced in the PCM and to estimate the WSS at the osteocyte surface [2].

Results

Two parametric studies on U_0 and f were carried out in order to produce a WSS in the range [0.8-3] Pa defined by [3] to trigger the osteocytes remodeling response.
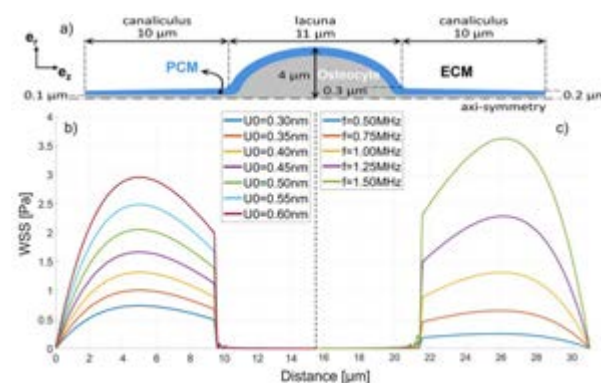
Figure 1: a) Geometrical 2D axisymmetric model; b) WSS at f=1 MHz for different values of U_0; c) WSS for different values of f at U_0=0.4 nm.

Figures 1b and 1c, clearly state that, whatever the amplitude and/or the frequency, WSS is quite zero at the osteocyte body whereas it mainly acts on the processes known as the privileged sites of mechanotransduction in osteocytes. Figure 1c confirms that the WSS increases with the frequency, i.e. the same level of stimulation will be reached for a lower loading by increasing the frequency.

Discussion

These results confirm that USS could reach WSS levels liable to trigger bone remodeling. However, more realistic boundary conditions and geometry will be investigated to be closer to the physiological environment, especially considering a network of osteocytes with irregular shape. In addition, the WSS reference range can be questioned because it was established for a physiological load that has different characteristics from USS (load direction and frequency). A WSS range dedicated to USS has yet to be defined. A better understanding of the interaction between US and LCN, will lead to a better interpretation of experimental and clinical observations on USS of bone regeneration in order to finally achieve an optimized therapeutic protocol.

References

1 Anderson et al., *Ann. Biomed. Eng.*, 33: 52–62, 2005.
2 Muller and Bruus, *Phys. Rev. E*, 90,: 43016, 2014.
3 Weinbaum et al., *J. Biomech.*, 27: 339–360, 1994.

MECHANOBIOLOGICAL COMPUTER MODELING OF MANDIBULAR FRACTURE HEALING

Vincenzo Orassi (1)(2), Carsten Rendenbach (3), Sara Checa (1)

1. Berlin Institute of Health at Charité – Universitätsmedizin Berlin, Julius Wolff Institute, Berlin, Germany; 2. Berlin-Brandenburg School for Regenerative Therapies, Berlin, Germany; 3. Department of Oral and Maxillofacial Surgery, Charité – Universitätsmedizin, corporate member of Freie Universität Berlin, Humboldt-Universität zu Berlin and Berlin Institute of Health, Berlin, Germany;

Introduction

Mechanical cues are known to influence the bone healing process, guiding cell proliferation, differentiation, and migration. Mechanobiological computer models have proven useful to define the optimal biomechanical environment to enhance bone healing in long bones [1]. However, the mechanoregulation of bone regeneration in the fractured mandible remains to be clarified. This knowledge is highly important to replace devices made of clinically used titanium for more advantageous materials, such as biodegradable ones.

This study aims to investigate the biomechanical cues induced by already established and novel fixation devices within the healing region in a mandibular body fracture and their effect on the bone healing process.

Methods

A computer model based on combined finite element (FE) and agent-based modeling techniques was used to quantify the mechanical strains within the healing region and simulate MSCs activity and phenotypical response to those stimuli in time.

A mandibular body fracture fixated with two parallel miniplates was simulated and physiological post-operative loading and boundary conditions were applied (Fig. 1) [2]. Material properties of traditional titanium and novel biodegradable magnesium alloy WE43 were assigned to the fixation devices.

(a) (b)
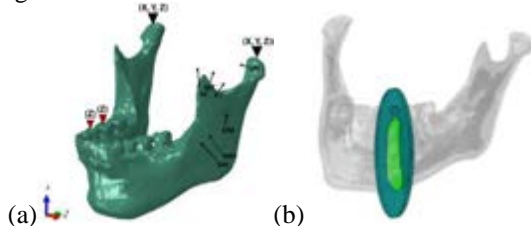
Fig. 1: (a) Loading and boundary conditions of the FE model; (b) Bone callus (dark green); healing region (light green).

In an iterative process, the mechanical conditions at the callus region predicted by the FE model were used as an input for the agent-based model, where the cellular processes of differentiation, proliferation, migration, and apoptosis were simulated according to mechanoregulation rules [1]. MSCs were able to differentiate into osteoblasts, chondrocytes, and fibroblasts, each of them associated with the formation of new bone, cartilage, and fibrous tissue, respectively. The material properties of the healing region were then updated in the finite element model for a new iteration.

Results

Post-surgery, strains within the healing region were between 0.4 and 1% with a clinically used titanium fixation. Higher mechanical strains (0.7-1.5%) were predicted within the healing region for magnesium fixation (Fig. 2).

(a) (b)
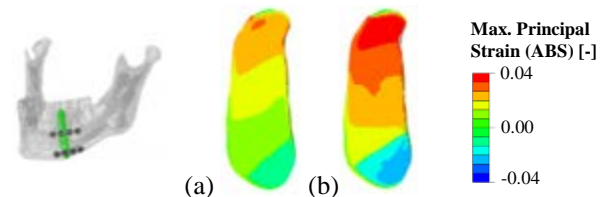
Fig. 2: Distribution of absolute maximum principal strains within the healing region during unilateral clenching induced by (a) titanium and (b) magnesium WE43 fixation devices.

Peak von Mises stresses within the fixation devices were always inferior to the yield strength of both titanium (880 MPa) and magnesium (162 MPa) (Fig. 3).

(a) (b)
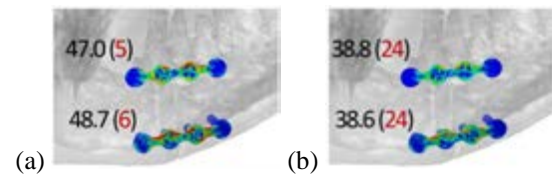
Fig. 3: Stress within the (a) titanium and (b) magnesium WE43 fixation devices. Peak stress [MPa] (in black) and peak stress as a percentage of the yield strength of the material (in red).

Discussion

In this study, the strain ranges within the healing region in a human mandibular body fracture stabilized with two titanium miniplates were determined. These strains were in the range of those reported to induce intramembranous ossification in long bone fractures [1]. Strains induced by novel magnesium fixation devices were only slightly higher than those with titanium, suggesting that magnesium devices are able to support the healing process. No implant failure was predicted. Future studies will aim at optimizing fixation devices to promote bone regeneration.

References

1. Claes and Heigele, Journal of biomechanics, 32.3: 255-266, 1999.
2. Korioth et al., American journal of physical anthropology, 88.1: 69-96, 1992.

Acknowledgments

BIOMECHANICAL MODEL REPRODUCING THE ACTIVE RESPONSE OF A CARDIAC SARCOMERE

Madalena M. A. Peyroteo (1), Jorge Belinha (2), Inês Falcão-Pires (3), Adelino F. Leite-Moreira (3) Renato Natal Jorge (4)

1. Institute of Science and Innovation in Mechanical and Industrial Engineering (INEGI), Portugal; 2. School of Engineering Polytechnic of Porto (ISEP), Portugal; 3. UnIC@RISE, Department of Surgery and Physiology, Faculty of Medicine of the University of Porto, Portugal; 4. Faculty of Engineering, University of Porto, Portugal

Introduction

Sarcomere is the contractile unit of the heart. Its contraction is caused by the interaction between two of its filaments - actin and myosin. The myosin filament has several myosin heads, which attach to the actin filament, forming a crossbridge. Described as the sliding theory, the attachment of several crossbridges leads to the sliding of myosin past actin, causing sarcomere´s contraction.

Since distinct heart pathologies result from contractility impairments, it is important to study sarcomere's functioning. Therefore, this work proposes an extended version of a biological model of sarcomere's contraction [1], as computational tools have become an asset in biomechanical studies. To validate the algorithm, experimental data was also collected to compare the experimental and numerical curves obtained.

Methods

The devised algorithm describes the functioning of each myosin head with a Markov chain. Depending on the Ca^{2+} concentration, each myosin head have two possible states - attached or not attached to the actin filament. The probability associated to each state is determined and correlated with the active force, F_A, generated when the myosin head is attached to the actin filament, forming a crossbridge. Using the nonlinear finite element method (FEM), the active stress is also determined. Assuming isometric conditions, distinct sarcomere lengths (SL's) are tested (from 1.9 to 2.2 µm), obtaining an active stress response at distinct SL's. The model also studies the active response at distinct Ca^{2+} concentration levels, presenting the Ca^{2+} sensitivity curve at 2.2 µm.

Figure 1 presents the numerical model used in the simulations. Sarcomere's geometry is simplified, but carefully designed to respect the dimension of each filament composing this structure.

Figure 1: 2D numerical model of a sarcomere unit of contraction.

Results

In regards to the active stress, σ_A, as SL increased, σ_A also increased. The same behavior occurred when Ca^{2+} concentration increased.

The σ_A levels obtained with this model were validated with experimental data. For instance, at SL = 2.2 µm, σ_A = 37.0 kN/m², corresponding to a 1.1% deviation from the experimental data.

Discussion

The levels of σ_A depends on the Ca^{2+} concentration and SL. Maximum σ_A is attained at 2.2 µm and maximal Ca^{2+} activation, as actin and myosin filaments present an optimal overlap under these conditions.

Active response of the sarcomere was fully described with this model, combining a previously proposed biological model [1] with a nonlinear mechanical analysis.

References

1. Regazzoni F. et al, Biomech Model Mechanobiol 17:1663–1686, 2018.

Acknowledgements

DESIGN AND CHARACTERIZATION OF A FLEXIBLE SUBSTRATE FOR CULTURING ADHERENT CELLS UNDER DEFINED UNIAXIAL STRETCH

Giovanni Putame (1), Marta Tosini (1), Andrea T. Lugas (1), Ilaria Roato (2), Beatrice Masante (1, 2), Federico Mussano (2), Diana Massai (1)

1. Polito^{BIO}Med Lab, Department of Mechanical and Aerospace Engineering, Politecnico di Torino, Italy;
2. Department of Surgical Sciences, CIR-Dental School, University of Torino, Italy

Introduction

Mechanical forces play a key role in the structural organization of multicellular organisms, with consequences in cell differentiation, tissue renewal and homeostasis, as well as in pathogenesis [1]. To investigate in vitro the mechanotransduction pathways triggered by mechanical stimuli, traditional monolayer static cell cultures performed on rigid substrates are unsuitable. Contrarily, dynamic cell cultures, performed by controlled culture devices (i.e., bioreactors) designed for mimicking defined native-like mechanical stimuli, represent a powerful investigation tool. Here, we developed and characterized a customized flexible substrate for exposing adherent cell cultures to defined uniaxial stretch within a tunable bioreactor [2], with the final aim of elucidating the role played by mechanical stretch on cellular behaviour.

Methods

The flexible substrate was designed: (1) to be cytocompatible and autoclavable; (2) to guarantee controlled planar and uniform uniaxial strain; (3) to allow parallelization of experiments; and (4) to be clamped in a uniaxial stretch bioreactor. Based on these requirements, the substrate design was characterized by two parallel rectangular wells (Figure 1A). Substrate size and shape were optimized by finite element analyses (FEA, Comsol Multiphysics), imposing a uniaxial displacement of 2 mm to a substrate side while fixing the opposite one. Once the optimized design was defined, the corresponding mould was designed and 3D printed, and the substrate was manufactured by casting polydimethylsiloxane (PDMS, Sylgard 184). Digital image correlation (DIC) method was adopted to characterize the substrate mechanical behaviour under uniaxial stretch and to validate the simulation outcomes. Finally, the substrate was used, with and without fibronectin functionalization, in preliminary cell experiments to investigate the effect of cyclic uniaxial stretch (90 s, 1 Hz, 15% total strain, every 6 h) on adipose-derived stem cells (ASCs). ASCs were seeded on the substrate and, after 4 days, exposed to static (control) or dynamic (within the bioreactor, Figure 1B) culture for 3 days, and the expression of an osteogenic markers (e.g., osteocalcin (OCN)) was assessed.

Results

Numerical simulations demonstrated that the substrate design allows a uniform strain distribution at the bottom of the wells, with a minimal out-of-plane deflection (Figure 1D). DIC tests showed a very good agreement between simulated and measured strain and displacements values at the wells bottom (Figure 1D). Biological tests revealed that ASCs cultured under uniaxial stretch on PDMS substrates without fibronectin expressed the highest levels of OCN (Figure 1E).
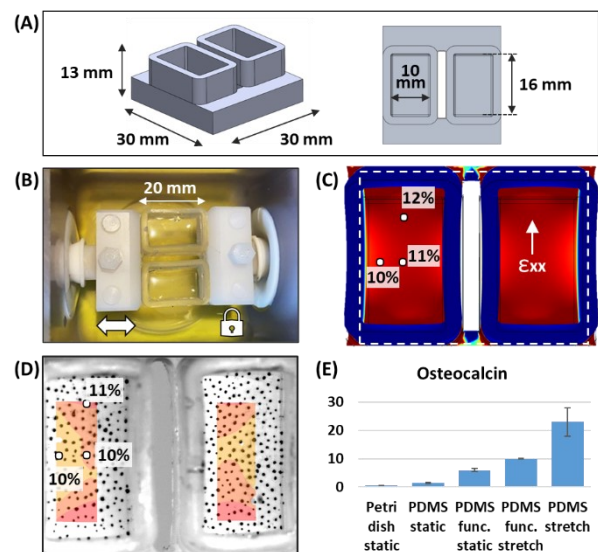
Figure 1: Substrate design, characterization, and application. (A) Technical drawing of the flexible substrate; (B) PDMS substrate clamped in the uniaxial stretch bioreactor; (C) Simulated strain (ε_{xx}); (D) Experimentally measured strain; (E) Biological results showing OCN expressed by ASCs.

Discussion

The adopted engineering design process based on development, modelling, testing and validation of the proposed flexible substrate allowed optimizing the substrate design and accomplishing the design requirements. Indeed, the proposed substrate, to be used in combination with a stretch bioreactor, allows providing controlled uniaxial stretch and guaranteeing uniform uniaxial strain on two parallel wells, supporting process reproducibility and reliability. Further biological tests are ongoing, imposing different stretch patterns and testing different cell types, in order to unravel the cause-effect relationships between mechanical stretch and cellular behaviour.

References

1. Mammoto A. et al, Ann Rev Cell Dev Biol, 29:27–61, 2013
2. Putame G. et al, Med Eng Phys 84:1-9, 2020

MICROFLUIDIC PLATFORM TO STUDY THE ROLE OF DYNAMIC MECHANICAL LOADING ON CELL FATE AND BEHAVIOR

Stefania Saporito (1, 2), Valeria Panzetta (1,2), Paolo Antonio Netti (1, 2)

1 Department of Chemical, Materials and Industrial Production Engineering, University of Naples Federico II, Piazzale Tecchio 80, 80125 Naples, Italy.

2 Center for Advanced Biomaterials for Health Care@CRIB, Istituto Italiano di Tecnologia, Largo Barsanti e Matteucci 53, 80125 Naples, Italy

Introduction

Living cells can sense and respond to mechanical cues through mechanosensing and mechanotransduction, respectively. These signals can be either external forces applied on the cell from the extracellular matrix, or intracellular forces generated in response to extracellular matrix variations [1].

On the cell scale, the geometric form of cells and their biological functions are inherently correlated; particularly, there is increasing evidence of the effects of substrate curvature on cell behavior. In fact, cells can discriminate between planar, convex, and concave surfaces [2]. Then, there is a spatio-temporal dependence in the influence of cell response from its surrounding environment, which has to be analyzed [3].

Methods

A specific microfluidic platform has been designed to dynamically stimulate single adipose derived mesenchymal stem cells along a preferential direction (Figure 1). It is designed choosing the polydimethylsiloxane (PDMS) embedded with fluorescent nanoparticles as cell seeding material, whereas the other layers were made with polymethylmethacrylate (PMMA). Even if PMMA and PDMS are two polymers with characteristics completely different, their combination permits to attach the PDMS substrate to a more rigid polymer, like PMMA, which ensures the mechanical deformation only to the membrane where the cells are seeded. Furthermore, the microfluidic platform can be reused.

This mechanical cue is applied with a pressure controller modifying the curvature of the PDMS substrate. As response, the influence of these signals on single cell behavior has been studied.

Results

The effects of cyclic mechanical stimulation on cell morphology, cell orientation, and focal adhesion organization have been analyzed using the confocal microscopy technology. To visualize in real time the cell response to the dynamic mechanical solicitation, the electroporation technique has been used. Particularly, actin cytoskeleton and focal adhesions are viewed.

Moreover, to quantify stresses and strains developed on substrate surface during the mechanical solicitation, a specific 3D finite element model (FEM) has been formulated. Knowing the mechanical properties of the PDMS membrane and the pressure variations applied during the experiments, the stress/strain on the material surface has been quantified.

Studying the single cell responses to the dynamic mechanical stimulation in short time (1h, 2h), variations of the cell area and the cell orientation with respect to the undeformed configuration have been observed. Particularly, cells tend to reorient along the preferential direction fixed by microfluidic platform.

Discussion

The combination of microfluidic platform, electroporation, pressure controller and FEM models introduces different novelties, such as the possibility to stimulate cells with different pressures, the knowledge of the stresses exerted on cells and their real time visualization.

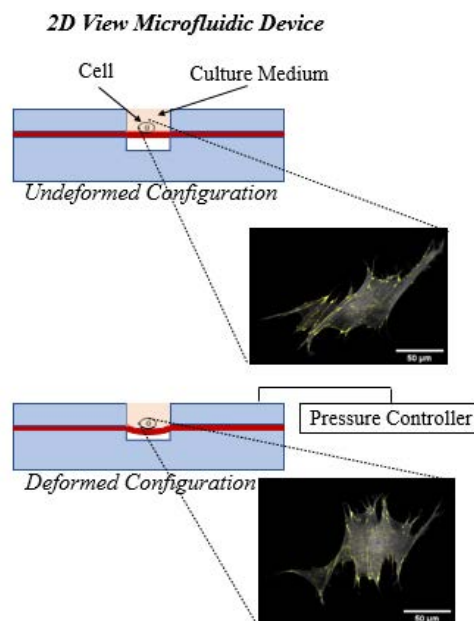*Figure 1: 2D View of the microfluidic device and single cell response into undeformed and deformed configuration (gray actin filaments, yellow focal adhesions). Scale bar: 50 µm*

References

1. Garcia, Alberto et al., Integrative Biology 8.10: 1011-1021, 2016
2. Baptista, Danielle, et al. Trends in biotechnology 37.8: 838-854, 2019.
3. Park, Joong Yull, et al. Lab on a Chip 9.14: 2043-2049, 2009.

COMPUTATIONAL MODELING REVEALS ROLE OF PROXIMITY-DRIVEN, NONCONTACT CELL-CELL INTERACTIONS IN CANCER INVASIVENESS

Marina Tulchinsky (1), Daphne Weihs (1)

1. Faculty of Biomedical Engineering, Technion – Israel Institute of Technology, Haifa 3200003, Israel

Introduction

Solid-tumor cell invasion typically occurs by collective migration of attached cell-cohorts, yet we show here that indirect cell-interactions through the substrate can also drive invasiveness. We have previously shown that well-spaced, invasive cancer cells push-into and indent impenetrable, physiological-stiffness gels to depths of 10 µm [1], while closely adjacent, non-contacting cancer cells may reach up to 18 µm, potentially relying on cell-cell interactions through the gel-substrate [2].

Methods

We developed finite element models of indenting cells, using experimental gel mechanics, cell mechano-structure, and force magnitudes. Forces were applied in two different configurations: in-plane/traction only or combined in-plane and normal [3]. Meshing of the gel-substrate and the cell, and the model simulations were performed using FEBio Studio.

Results

We show that under 50-350 nN of combined traction and normal forces, a stiff nucleus-region is essential in facilitating 5-10 µm single-cell indentations, while uniformly soft cells attain 1.6-fold smaller indentations. We observe that indentation depths of cells in close proximity (0.5-50 µm distance) increase relative to well-spaced cells, due to additive, continuum mechanics-driven contributions. Specifically, 2-3 cells applying 220 nN normal forces gained up to 3% in depth, which interestingly increased to 7.8% when two cells, 10 µm apart, applied unequal force-magnitudes (i.e., 220 and 350 nN). We note that nucleus stiffening or cytoplasm softening by 25-50% increased indentation depths by only 1-7%, while depths increase nearly linearly with force-magnitude even to two-fold levels.

Discussion

We have shown that the stiff nucleus facilitates indentations 5-10 µm, indicating its important mechanical role in invasiveness. In addition, cell-proximity triggered, synergistic and additive cell-interactions through the substrate can drive collective cancer-cell invasiveness, even without in absence of direct cell-cell interactions.

References

1. Kristal-Muscal et al., New J. Phys., 20:1187-1194, 2021.
2. Merkher et al., Ann. Biomed. Eng., 45:1399-1406, 2017.
3. Ben-David & Weihs, Biomech. Model. Mechanobiol., 20:1187-1194, 2021.

CHANGES IN NUCLEAR MORPHOLOGY CORRELATE WITH INVASIVENESS IN BREAST CANCER CELLS

Barbara Zbiral (1), Andreas Weber (1), Maria dM Vivanco (2), José Luis Toca-Herrera (1)

1. Institute of Biophysics, Department of Nanobiotechnology, University of Natural Resources and Life Sciences, Vienna, Austria.

2. Cancer Heterogeneity Lab, CIC bioGUNE, Bizkaia Science and Technology Park, Derio, Spain

Introduction

Cancer cells acquire structural alterations associated with malignancy progression, such as changes in cell morphology and cell elasticity. Such processes are largely due to cytoskeletal remodeling as cell signaling and tissue integrity become disrupted and are linked to metastatic potential [1-3]. Further, nuclear shape and morphology have been found altered in malignant cells. Evidence exists that this process is active, possibly in order to facilitate easier cell migration through tissues during metastatic progression [4-6]. In this work, we correlate cell mechanical parameters of three differently aggressive breast cancer cell lines (MCF10A, MCF-7, MDA-MB-231) to their nuclear morphology and cytoskeletal arrangement.

We use Atomic Force Microscopy (AFM) to study the mechanical properties of the cells and Confocal Laser Scanning Microscopy (CLSM) to image cell nuclei and cytoskeletal compounds such as actin. We found significant differences to exist both mechanically and morphologically.

Methods

Cells were grown on glass slides and measured by AFM in force spectroscopy mode using cantilevers with a spherical particle. The cells were indented at a constant force (1 nN) above the nuclear and cytoplasmic region, then the z-position kept constant for 10 s to perform stress relaxation measurements (see Figure 1). Apparent elasticity and viscoelastic values were determined by fitting a modified Hertz model to the indentation segments, and a Zener model to pause segments of the force-distance curves, respectively [7]. For CLSM, nuclei and cytoskeleton were labeled with fluorophores and 3D-imaging via z-stacks was performed (see Figure 2). Actin arrangement and nuclear aspect ratio was analyzed using ImageJ software.

Figure and Tables
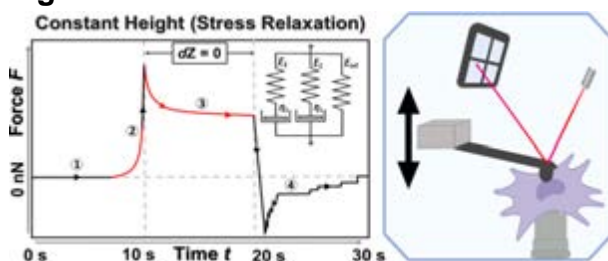
Figure 1: Schematic AFM stress relaxation curve (left) and applied mechanical model (inset, left). Schematic of AFM experimental set-up (left).
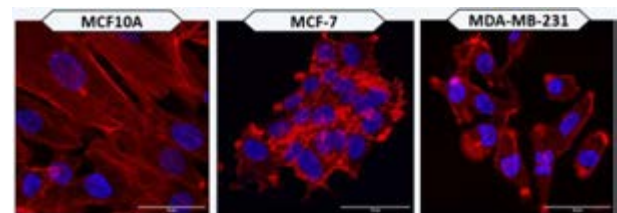
Figure 2: CLSM images of the MCF10A, MCF-7 and MDA-MB-231. Nuclei shown in blue, actin in red. The scale bar indicates 50 µm.

Results and Discussion

MCF10A are non-malignant and non-invasive, MCF-7 are malignant but low-invasive, and MDA-MB-231 are malignant with high invasive potential. The apparent stiffness of the cell lines is inversely correlated to their malignancy (see table 1). With increased invasiveness, cell nuclei appear more deformed and less spherical. CLSM also reveals structural differences in actin arrangement between the cell lines. These results suggest that nuclear morphology contributes to altered mechanics in breast cancer cells, potentially constituting a factor for cancer cell invasiveness.

Cell line	E [Pa]	τ_1 [s]	τ_2 [s]
MCF10A	297	0.13	2.94
MCF-7	249	0.16	3.46
MDA-MB-231	224	0.18	4.21

Table 1: Apparent Young's modulus and relaxation times for the compared cell lines.

References

1. Fletcher D., Mullins D. Nature 463, 485-492, 2010.
2. Plodinec et al, Nat Nanotechnology, 7(11):757-65, 2012.
3. Lekka, M. BioNanoScience 6, 65-80, 2016.
4. Chiotaki, R. et al, BCB, 92(4): 287-295, 2014.
5. Fischer, T. et al, Front Cell Dev Biol, 8:393, 2020.
6. Deville, SS., Cordes, N., Front Oncol, 9: 1376, 2019.
7. Zbiral, B. et al, Materials, 14(11):2897, 2021.

Acknowledgements

VENTRICULAR SEPTAL DEFECT FROM IN SILICO STUDY TO CLINICAL PRACTICE

Myriem Belghiti Alaoui (1) (2), Fedoua El-Louali (1) (2), Morgane Evin (2)

1. Applied Biomechanics Laboratory, Marseille, France; 2. Marseille Public University Hospital, France

Introduction

Ventricular Septal Defect is the most frequent congenital heart disease. Initially, isolated VSD shunt occurs in systole, from Left Ventricle (LV) to Right Ventricle (RV). This is explain by a transventricular pressure gradient for restrictive VSD and by a pulmonary/systemic vascular resistances ratio < 1 for non-restrictive VSD. This shunt leads to pulmonary overflow with an increase of LV End Diastolic Volume (EDV). [1]

VSD hemodynamic profil is easily represented by LV and RV Pressure Volume Loops (PVL). *In vivo* PVL require invasive measures by percutaneous cardiac catheterization. However, there are analytical hemodynamic models that allow access to PVL in a non-invasive way. Digital model Circadapt is the most used to model congenital heart disease in children but is not validated to model VSD.

Our aim is to determine if Circadapt is adapted to model VSD in children based on known pathophysiological and clinical data.

Materiel and Method

Circadapt software aims to represent heart and its circulation with a variable elastance ventricular model coupled to a four elements Windkessel model. The last one models the vascular system by an electrical circuit with impedance, resistance, compliance and inertia properties. Circadapt is a lumped parameters model which source code is implemented in Matlab® 6.5.0 (Mathworks, Natick, MA) with differential ordinary equations. [2]

VSD is simulated as a flow through a valve between the left and the right ventricle, with a variable diameter. The valve is opening and closing gradually depending on pressure gradient.

We simulated two virtual patients populations: infant and children by varying the inlet parameters (venous return, cardiac frequency, mean arterial pressure, atrio ventricular delay and tricuspid insufficiency) based on patient age [3]. Then, we modelled four ventricular septal defect sizes from 1 to 20 mm in infant and children. Our primary endpoints were left and right ventricle EDV.

Results:
Main results are represented in tables.

Infants VSD	EDV LV (mL)	EDV RV (mL)
No VSD	88	98
1 mm	88	99
5 mm	92	117
12 mm	107	177
20 mm	130	234

Table 1: Reference (no VSD) and VSD simulation with Circadapt in infant

Children VSD	EDV LV (mL)	EDV RV (mL)
No VSD	114	133
1 mm	114	134
5 mm	125	158
12 mm	152	252
20 mm	156	266

Table 1: Reference (no VSD) and VSD simulation with Circadapt in children

Discussion

By modelling 10 virtual patients with Circadapt we found an expected LV dilatation but we also found a RV dilatation even more important than the LV one, both increasing on proportion to VSD size. The RV dilatation is not observed in clinical practice and not explained in a pathophysiological way. We believe that model VSD as a valve between the LV and directly the pulmonary artery would be more representative of this LV to RV shunt occurring only in systole when the pulmonary artery valve is opened.

Conclusion

Circadapt, widely used in children, is not adapted to model VSD in children and infants. This preliminary study led us to develop a Circadapt adaptation to model VSD hemodynamic profil on the basis of clinical reference data and known pathophysiologic considerations. This work is on process.

References

1. Penny DJ, Vick GW 3rd. Ventricular septal defect. Lancet. 2011
2. Arts, T., Delhaas, T., Bovendeerd, P., Verbeek, X.; Prinzen FW. Adaptation to mechanical load determines shape and properties of heart and circulation : theCircAdapt model. American Journal of Physiology-Heart and Circulatory Physiology, (2005)
3. Munneke, A.G., Lumens, J., Delhaas, T. Cardiovascular fetal-to-neonatal transition: an in silico model. Pediatr Res (2021)

EDGE LOADING TESTING OF HIP REPLACEMENTS: TECHNIQUES FOR EFFICIENT AND ACCURATE MODELLING

Lee Etchels (1), Ruth Wilcox (1), Alison Jones (1)

1. University of Leeds, UK; 2. DePuy Synthes, UK

Introduction

Edge loading pre-clinical testing of hip replacements reflects the increasing clinical need to evaluate more than just the wear performance of both hard-on-hard bearing combinations and the newer, more wear resistant, highly-crosslinked UHMWPE liners. Understanding how different designs compare in terms of fatigue and fracture resilience necessitates a detailed understanding of the underlying stress/strain state during loading. Computational modelling is particularly well suited to support experimental testing in this regard. Representing testing under ISO 14242:4 conditions, however, involves modelling a dynamic system where inertia plays a role in the kinematics and subsequent loading, where the contact sweeps across different sections of the liner, and where the non-conforming rim contact requires a very refined mesh. The resulting dynamic explicit finite element (FE) models can be infeasibly time consuming to develop and run [1] and therefore a robust, optimised, and well documented approach could speed the adoption and implementation of this technique in industrial practice.

Methods

FE models, matching the ISO 14242:4 test, were created (Abaqus 2019, Dassault Systèmes, France) using the geometry of a 36mm metal-on-polyethylene. Separation translations were allowed at the rigid femoral head rather than the liner, allowing mass-scaling of the UHMWPE elements without changing the translating mass. Elastic-plastic conventional UHMWPE material properties were used [2]. A combined mesh refinement and mass-scaling sensitivity was performed across three different input cases, with model run times from ~5min to ~600h. A 'Recommended Mesh' (RM) model was selected as a reasonable compromise between accuracy and solution time, recommended as a time efficient starting point for model development in new studies.

Results

The RM model had a run time of ~40min using a 1mm linear tetrahedral global liner mesh, 0.075mm linear hexahedral rim mesh, and mass scaling to a target time increment of $1E^{-5}$s. Compared to a 'Best Estimate' (BE) model (0.25mm global, 0.025mm rim, $1E^{-6}$s, ~190h) it underestimated peak and total plastic strain by 7% and 9%. Largest difference was a 25% overestimation of swing phase contact area. For the RM model and ISO input case, peak liner strain was 0.17, swing phase contact area was $1.5mm^2$.
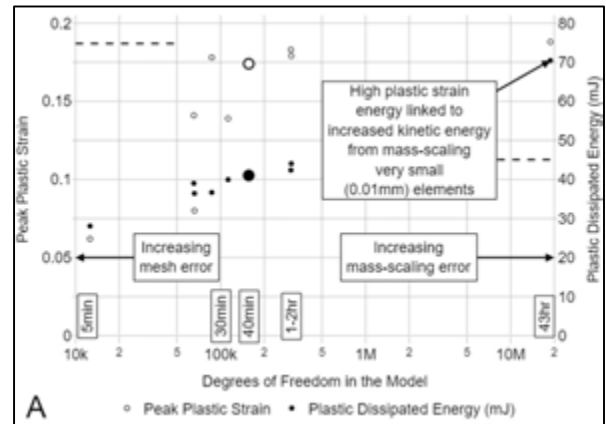
Figure 1: Mesh sensitivity test for effect of element size on the liner peak absolute principal plastic strain and total dissipated plastic strain energy at the end of the cycle. Mass-scaling target time increment of 1E-5s. Larger marker points indicate results from RM model. Approximate model run times given along the x axis. Values from the BE model are shown as dashed horizontal lines from each vertical axis.

Discussion

With mass-scaling, it is possible to drastically reduce the run time of dynamic explicit models of edge loading to a point where the models would be convenient for parameter sweeps and comparison of early-stage product designs. This can allow for mesh refinement improvements that can capture higher localized plastic strains. Compared to previous static, and less refined dynamic, models in the literature, this model generated peak plastic strains ~2x higher. Previously published models therefore may have underestimated the accumulation of plastic strain at the rim.

Although the ideal settings for a particular study will be dependent on the design, materials, and aim, the 'Recommended Mesh' model from this study would be a suitable starting point and would significantly reduce the model development time required.

References

1. Jahani, F. et al, Med Eng & Phys, 95:97-103, 2021.
2. Hua, X. et al, J Biomech, 47(13):3303-3309, 2014.

Acknowledgements

IN SILICO AND IN VITRO TESTS TO ASSESS MECHANICAL HEMOLYSIS IN HEMODIALYSIS CATHETERS

I. Guidetti (1), F. De Gaetano (1), D. Gallo (2), U. Morbiducci (2), M.L. Costantino (1)

1. Department of Chemistry, Material and Chemical Engineering, Politecnico di Milano, Milan, Italy;

2. Department of Mechanical and Aerospace Engineering, Politecnico di Torino, Turin, Italy.

Introduction

Mechanical hemolysis is one of the major issues for cardiovascular devices and the assessment of the induced mechanical blood damage is a key point in their design and optimization. Hemolysis can lead to anemia and tissue hypoxia; therefore, it is necessary to assess the amount of red blood cells (RBCs) damage caused by implantable and blood recirculating devices [1]. Computational fluid dynamics (CFD) models represent a powerful tool for the assessment of the risk of mechanically induced blood damage associated with cardiovascular devices [2]. However, the sole knowledge of the mechanical stress profile in the blood streaming through the device is not sufficient per se to identify the cause-effect relation leading to hemolysis [2]. Currently, there is not a universally accepted computational model of mechanical hemolysis. In this study, a computational model was implemented in order to predict mechanically induced hemolysis in catheters for hemodialysis. In vitro tests were carried out to assess the capability of the in silico model to predict the risk of hemolysis associated to the devices.

Methods

Two different central venous catheters for hemodialysis were considered, namely the Palindrome™ Precision Symmetric Tip (Medtronic, Dublin, Ireland) and the Arrow-ClarkTM VectorFlow® (Teleflex, Wayne, Pennsylvania). The finite volume-based solver Fluent (Ansys Inc.) was used to solve the governing equation of fluid motion. The Lagrangian stress-based blood damage model proposed by Grigioni et al. [3], accounting for the shear history of RBCs, was implemented incorporating the equivalent shear stress formulation proposed by Faghih and Sharp [4]. According to the international standard ASTM F1841, in-vitro tests were performed (Figure 1) to validate the in-silico model. The modified index of hemolysis (MIH) was calculated to compare experimental and computational results.

Results

The Lagrangian representation of the flow fields in the two catheters is presented in Figure 2. Blood elements entering the catheters through the side holes are subjected to a higher equivalent shear stress than those entering through the tip. The in silico approach highlighted a higher degree of hemolysis induced by the VectorFlow® catheter than by the Palindrome™. The in vitro experiments confirmed the results of the in silico model.
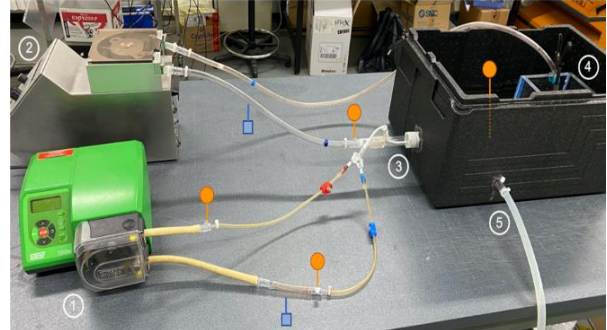
Figure 1: Experimental set-up: 1) pump reproducing the catheter flow, 2) pump reproducing the systemic flow, 3) catheter, 4) reservoir and 5) thermostat bath. In blue and orange are reported the point where flow and pressure were measured, respectively.

Discussion

The in silico - in vitro approach of the present work allows to develop and experimentally validate a computational model capable of predicting the degree of hemolysis in cardiovascular devices. The CFD model correctly predicts the higher degree of hemolysis induced by the VectorFlow® and shows the fundamental importance of carefully choosing the set of parameters for the blood damage model.
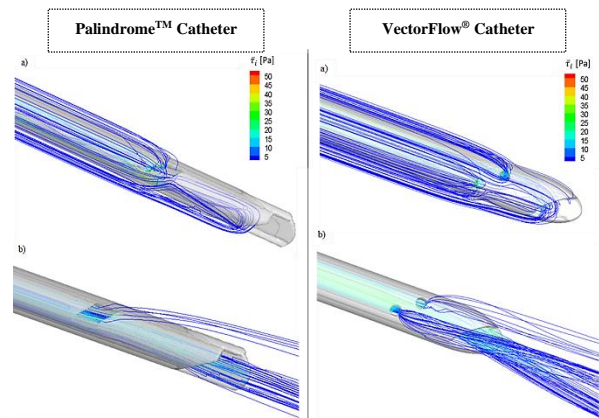
Figure 2: Trajectories of red blood cells entering the arterial lumen (a) and exiting the venous lumen (b) of the catheters.

References

1. O. K. Baskurt et al., Handbook of Hemorheology and Hemodynamics. IOS Press, 2007.
2. H. Yu et al., Artif. Organs, vol. 41, no. 7, pp. 603–621, 2017.
3. M. Grigioni et al., Biomech. Model. Mechanobiol., vol. 4, no. 4, pp. 249–260, 2005.
4. M. M. Faghih and M. K. Sharp, J. Biomech. Eng., vol. 138, no. 12, pp. 6–9, 2016.

INFLUENCE OF TRANSURETHRAL CATHETERS ON URODYNAMICS MEASUREMENTS IN MALE: A COMPUTATIONAL STUDY

Maria Vittoria Mascolini(1), Alice Berardo(2,3), Chiara Giulia Fontanella(1), Emanuele Luigi Carniel(1)

1. Department of Industrial Engineering, Padova, Italy; 2. Department of Civil Environmental and Architectural Engineering, Padova, Italy; 3. Department of Biomedical Sciences, Padova, Italy

Introduction

Urodynamic techniques aim at evaluating urethral resistance throughout micturition in order to correlate this quantity with different disorders and/or pathologies, such as strictures, prostatic hyperplasia, bladder outlet obstruction. The study aims at analysing the effects of a geometric obstruction within the lower urinary tract due to different sized transurethral catheters (1.5-, 3- and 6-Fr) on urodynamics pressure-flow measurements in men. The analyses have been developed by means of Computational Fluid Dynamics (CFD) simulations.

Methods

Four different three-dimensional CFD models of the male lower urinary tract were developed, by varying the diameters distribution along the urethra, according to inter-individual anatomical variability. Average data of bladder and urethra morphometry [1–2] were considered for the models' generation.

The urethra, along its length from the bladder neck to the urinary meatus, was assumed as subdivided into five regions, characterized by different diameters. A fully opened and circular conformation was adopted, so that the lumen resulted in the actual diameter continuously changed all along the urethral axis. Different values of mean intraluminal diameter were considered, from 3.14 mm to 7.72 mm, resulting in the four analysed conformations. For each conformation, the development of the catheterized configurations required the subtraction of a cylindroid swept along the urethral axis. CFD simulations were performed to analyse the urine flow from the bladder up to the urinary meatus, considering both the free urethra and three different catheterized conditions (1.5-, 3-, 6-Fr) for all four models. The fluid characterization of urine assumed incompressible and Newtonian behaviour [3]. With regard to typical micturition conditions, bladder wall pressure defined the inlet condition, while atmospheric pressure provided for the outlet condition at the urinary meatus. Values ranging between 0 and 6 kPa were assumed [4–5] to perform transient CFD simulations. All the simulations have been performed by means of the general-purpose code Comsol Multiphysics 5.4 (Comsol Inc., Burlington, MA, USA).

Results

At the same bladder pressure condition, simulations showed that the voiding phase of micturition was influenced by the urethral configuration considered and the presence of one catheter rather than another of different size. The pressure profiles along the urethra were extracted to quantify the influence of each catheter. In terms of urodynamics parameters, the minimum flow rate and the maximum urethral pressure were obtained in the model with the lowest mean urethral cross-section obstructed by the 6-Fr catheter.
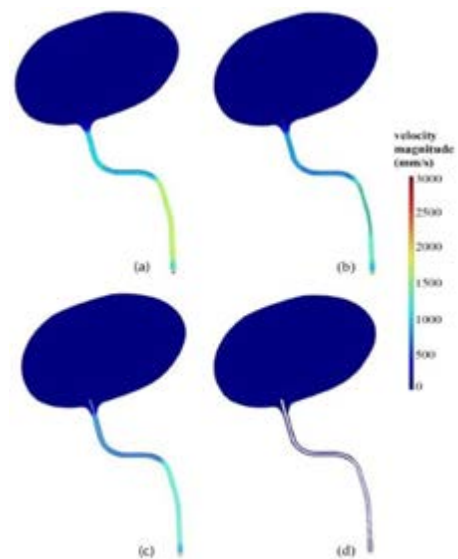
Figure 1: Urine velocity fields at 6 kPa bladder pressure condition for the model with lowest mean urethral diameter in condition of free urethra (a), in presence of 1.5-Fr (b),3-Fr (c) and 6-Fr catheters (d).

Discussion

Transurethral catheterization could lead to an improper interpretation of pressure-flow findings, thus confirming the observations of previous studies [6]. Therefore, with regard to patients needing urodynamics evaluations, these insights could help in reducing the uncertainties on the measured parameters relevant to diagnosis, and consequently provide more efficient clinical assistance.

References

1. Pullan B.R. et al., Br J Urol., 54:399-407, 1982
2. Mahadevan V., Surg., 34:318-325, 2016
3. Inman B.A et al., Int J Hyperth., 29:206-210, 2013
4. Fusco M.A. et al., J Trauma Inj Infect Crit Care, 50:297-302, 2001
5. Clausen I. et al., Sensors, 18:2128, 2018
6. Scaldazza C.V. et al., Urol Int., 75:21-25, 2005

Acknowledgements

PROXIMAL FEMUR BONE MINERAL DENSITY IN OSTEOPOROTIC PATIENTS: A REVIEW OF PLACEBO GROUPS IN CLINICAL TRIALS

Sara Oliviero (1,2), Marco Viceconti (1,2)

1. Department of Industrial Engineering, Alma Mater Studiorum, University of Bologna, Italy; 2. Medical Technology Lab, IRCCS Istituto Ortopedico Rizzoli, Bologna, Italy

Introduction

Osteoporosis (OP) is characterized by low bone mineral density (BMD) and bone architecture deterioration, which is associated with increased fracture risk. Hip fractures are of particular concern given their severe impact on the patient's health. However, one of the major challenges in the development of drug treatments for OP is the need to run large clinical trials, with increased time and costs [1]. Computer modelling and simulation could improve the development of drugs by refining or partially replacing clinical trials using virtual patients (*In silico* clinical trials) [2]. Finite element (FE) models based on Computed Tomography (CT) data have been developed and validated for the prediction of the femur strength [3]. Also, FE models have been integrated in a multiscale approach to predict the current absolute risk of hip fracture (ARF0) [4]. To predict the fracture risk at subsequent years, a similar approach could be applied by adding a disease progression model to account for bone changes over time. The simplest model could be implemented by including a loss of BMD over time, by adjusting the material properties in FE models.

The aim of this study is to perform a systematic review to collect data on BMD variations over time measured in placebo groups of interventional phase III clinical trials for OP drug treatments.

Materials and methods

Clinical trials were searched using a combination of relevant MESH terms and key words in PubMed. The search was built by combining multiple relevant terms related to the population of interest (postmenopausal women), type of study (phase III clinical trial), treatment arm (placebo group), measurement of interest (BMD measured with DXA) and anatomical location (femoral neck or total hip). Inclusion criteria were based on age of participants (55 and older), femoral neck T-score (-1 and lower), number of subjects enrolled (at least 200), duration of the study (at least 1 year). BMD changes from baseline (mean and SD) were collected from each eligible study at each follow up time point. The reported statistical properties were used to artificially generate synthetic data distributions with the same statistical properties to mimic the clinical data. Two sample t-tests were used to evaluate if the distributions were statistically different among studies.

Results

Preliminary results based on three large clinical trials for evaluating the efficacy of alendronate [5], risedronate [6] and denosumab [7] are presented in Fig1. BMD decreased in an approximately linear manner between years 1 to 4. Average BMD variations were $0.08 \pm 0.30\%$ at 1 year, $-0.47 \pm 0.37\%$ at 2 years and $-0.96 \pm 0.46\%$ at 3 years. The BMD loss reported in one of the studies [7] was significantly different from the others ($p<0.001$).
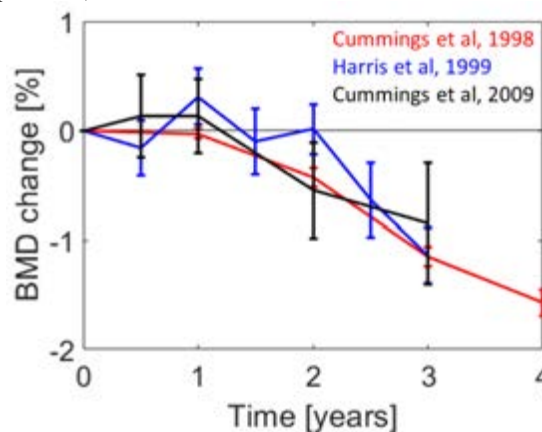
Figure 1: proximal femur BMD over time reported for placebo groups of three different clinical trials.

Discussion

Data collected from previous clinical studies is useful to characterize the BMD loss in OP patients, which can be applied to simulate OP progression in *In Silico* clinical trials. The differences observed for one of the studies suggest that a further stratification of the population may be needed. The BMD variability needs to be included in the model. Future work will include further relevant clinical trials.

References

1. Madrasi et al, J Clin Pharmacol, 58: 572-585, 2018.
2. Viceconti et al, Int J Clin Trials, 3(2):37-46, 2016.
3. Qasim et al, Osteoporos Int, 27:2815-2822, 2016.
4. Bhattacharya et al, Biomech Model Mechanobiol, 18:301-318, 2019.
5. Cummings et al, JAMA, 280:2077-2082, 1998.
6. Harris et al, JAMA, 282:1344-1352, 1999.
7. Cummings et al, N Engl J Med, 361:756-65, 2009.

Acknowledgements

LATERAL MENISCUS ANTERIOR ROOT AVULSION INCREASES CONTACT PRESSURES: A FINITE ELEMENT STUDY

Peña-Trabalón A. (1), Moreno-Vegas S. (1), Estebanez B. (1), Prado-Novoa M. (1), Espejo-Reina A. (1, 2), García-Vacas F. (1), Perez-Blanca A. (1)

1. Clinical Biomechanics Laboratory of Andalusia, University of Malaga, Spain

2. Vithas Malaga Hospital, Spain

Introduction

Deleterious consequences of posterior meniscal root detachment have been related to variations in contact pressure (CP) distribution seen in biomechanical investigations. However, little is known about the biomechanical effects of lateral anterior root avulsions (ARA), despite clinical studies reporting it as a lesion concomitant with anterior cruciate ligament (ACL) injuries and tibial fractures [1,2] and as an iatrogenic injury during ACL reconstructions [3,4]. This work analyzes variations in CP due to lateral meniscus (LM) ARA using a knee finite element model (FEM).

Methods

A human cadaveric specimen was used to create and validate a knee FEM to compute the tibio-femoral CP distribution in three conditions of the LM: intact, with ARA and with posterior root avulsion (PRA).

Meniscus, cartilages, femur and tibia were segmented from MRI data (T1, thickness=3.5mm) using 3D Slicer®. From the point clouds extracted, solid models were built and assembled in Solidworks®. Cartilage models were refined using a 3D Laser Scanner (Picza LPX-1200, Roland DG, Hamamatsu, Japan). From the assembly, a FEM was defined in Abaqus®. Ligament insertions were identified in MRI images (Figure 1).
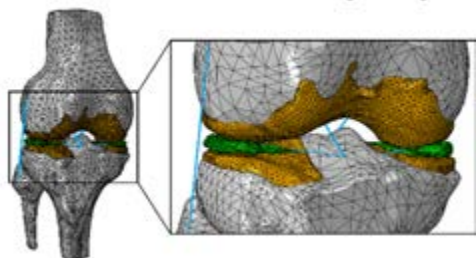
Figure 1: Knee FEM developed in Abaqus®.

Bones were assumed rigid. Meshes of cartilages and menisci were created using 1.5mm second order tetrahedral elements. Linear isotropic elastic materials were applied to the menisci (E = 59MPa) and cartilages (E = 5MPa). Menisci root and ligaments were modelled as nonlinear elastic axial springs with material properties extracted from the literature [5,6]. Surface-to-surface contact was defined at all menisci/cartilage and cartilage/cartilage interfaces.

To validate the model, the same specimen with intact menisci was subjected to an experimental axial compression test with the knee in extension under a 1000N load. A pressure sensor (K-scan 4000, Tekscan Inc., Boston, MA) placed between menisci-tibial cartilage captured the CP.

Boundary conditions were replicated in the FEM and CP given by the two methods were compared. The validated model was used to compute the CP distributions in the three pre-stablished conditions of the lateral meniscus.

Results

In the intact condition, the CP distributions of experimental and FEM methods were similar (Figure 2). In ARA and PRA, the CP increases and the contact area decreases (Table 1).
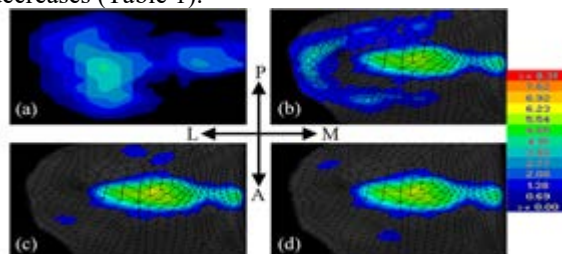
Figure 2: Tibial cartilage CP: (a) Intact experimental; (b) Intact FEM; (c) ARA FEM; (d) PRA FEM.

FEM	Pmax	Pavg	Contact Area
Intact	6.40MPa	1.02MPa	578.28mm^2
ARA	6.92MPa	2.00MPa	387.01mm^2
PRA	6.81MPa	1.98MPa	367.49mm^2

Table 1: FEM contact area, maximum and average pressures in the three conditions of the lateral meniscus.

Discussion

Changes observed in knee contact biomechanics after lateral meniscus ARA indicated potential for similar cartilage damage than observed after a PRA. Since most daily activities and sports are done in low flexion angles in which anterior roots bear most of the load, an ARA could be even more critical. Therefore, special attention should be paid to diagnostic and treatment of this injury.

References

1. Krych A. et al, J Am Acad Orthop Surg, 28:491-9, 2020.
2. Menge TJ. et al, J Orthop Res, 47(5), 2018.
3. Kodama Y. et al, J Orthop Res, 28(11), 2020.
4. Kodama Y. et al, KSSTA, 28:3517-23, 2020.
5. Orozco, G.A. et al, Sci Rep, 8:2323, 2018.
6. Peña, E. et al, Clin Biomech, 20:498-507, 2005.

Acknowledgements

ANALYZING MECHANICAL CIRCULATORY SUPPORT IN PATIENTS WITH SINGLE VENTRICLE PHYSIOLOGY USING A MULTISCALE MODEL

Victoria Yuan (1), Francesco De Gaetano (1), Maria Laura Costantino (1)

1. Laboratory of Biological Structure Mechanics, Politecnico di Milano, Italy

Introduction

Infants with single ventricle physiology (SV) make up the largest cohort of the 8,000 children hospitalized each year for heart failure [1]. These patients undergo a 3-stage palliative surgical procedure. During the first week of life, children undergo the Norwood procedure, which has the highest mortality rate [2]. After this surgery, physicians may place children on mechanical circulatory support to improve outcomes. The Berlin Heart EXCOR (BH) is the only licensed pediatric ventricular assist device (VAD); the device comes in a wide range of volumes, and physicians can control different settings [3]. While the BH has shown promise in supporting SV patients, there is an incomplete understanding of interactions between the device and extra pulmonary flow in the Norwood circulation [4]. Moreover, clinicians struggle to determine the appropriate BH size and settings for each patient. While existing literature analyzes continuous devices in these patients, the models are limited to 0D and they do not investigate the BH, which is pulsatile and the primary device for SV patients [5]. In this work, we present a multiscale model of the Norwood physiology and study the performance of the BH.

Methods

We utilized a closed loop, 1D-0D model in Python to capture the physiology of a 3 month old infant with Norwood circulation and a 4 mm modified Blalock-Taussig shunt [6]. We represented the cardiovascular system in three parts: the heart, the pulmonary circulation, and the systemic circulation (Figure 1). The atrium and ventricle are simulated with the single-fiber model. The pulmonary and systemic circulations are lumped parameter networks, with a shunt connecting the pulmonary artery and ascending aorta. We then virtually "implant" the BH with inflow at the atria and outflow at the ascending aorta. The BH is represented as a lumped parameter network using a novel, mechanistic model [7]. We quantified the cardiac output (CO), the ventricular stroke work (VSW), and the ratio of pulmonary to systemic flow (Q_p:Q_s) in the patient with and without the BH. Finally, we analyzed the relationship between BH volume, rate, and these metrics.

Results

Although we are still tuning our model, our simulations will quantify changes in CO, VSW, and Q_p:Q_s after BH implantation. We will also quantify the relationship between these metrics, device volume, and device rate. Our multiscale model will also quantify how the BH

offloads stress and strain on cardiac sarcomeres, which can provide insight into the molecular effects of mechanical circulatory support.
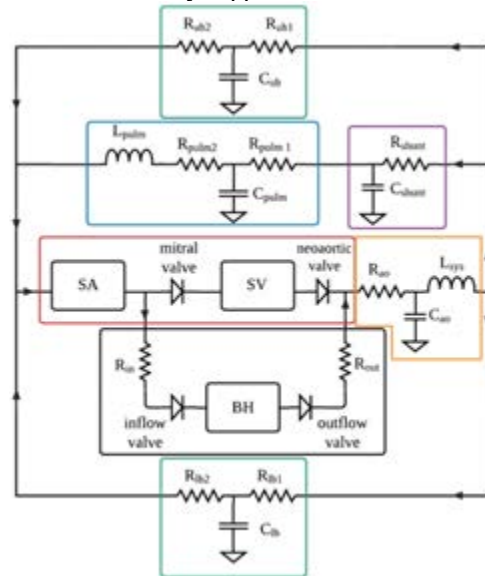
Figure 1: Multiscale model of the Norwood circulation, with the heart in red, BH in black, aorta in orange, systemic circulation in green, shunt in purple, and pulmonary circulation in blue.

Discussion

Our study aims to investigate the impact of pulmonary flow on BH performance and to inform clinical decision-making on device volume and settings for patient. Our results will identify interactions between the atrium and BH, which will provide insight on device output and efficiency. Finally, we will uncover trends in CO, VSW, Q_p:Q_s, and BH performance after device implantation and changes in device volume and rate. These findings can guide clinicians in determining appropriate BH treatments for patients. Future work involves coupling a 3D model of the ascending aorta, pulmonary artery, and shunt to our 1D-0D model to more thoroughly characterize the impact of the BH.

References

1. Reddy, S, et al, JAHA, 9, 2020.
2. Garcia, AM, et al, J Physiol Heart Circ Physiol, 4, 2020.
3. Molfetta, AD, et al, Front Phys, 7, 2016.
4. Weinstein, S, et al, J Thorac Cardiovasc Surg, 2, 2013.
5. Molfetta, A, et al, Artif Organs, 1:34-42, 2015.
6. Pant, S, et al, J Biomech, 49:2162-2173, 2016.
7. Yuan, V, et al, Cardiovasc Eng Tech, 2022.

Acknowledgements

GROWTH ORIENTATION, AND NOT HETEROGENEOUS GROWTH RATES, DOMINATES ZEBRAFISH JAW JOINT MORPHOGENESIS

Josepha Godivier (1), Elizabeth A. Lawrence (2), Chrissy L. Hammond (2), Niamh C. Nowlan (1, 3)

1. Imperial College London, UK; 2. University of Bristol, UK; 3. University of Dublin, Ireland

Introduction

Synovial joints are complex structures connecting skeletal elements. A diverse range of joint shapes allow different body motions. These shapes emerge from a process called joint morphogenesis in which the opposing joint surfaces are moulded into reciprocal and interlocking shapes. Joint morphogenesis remains the least understood aspect of joint formation. Some cellular activities have been identified as being involved, such as cell volume expansion, intercalation, orientation [1], but the cell-level dynamics underlying joint shaping are poorly understood. In this research, we quantify the cellular dynamics involved in growth and morphogenesis of the zebrafish jaw joint and synthesise tracked, cell-level data in a predictive computational simulation of joint development. We use the simulation to test if growth heterogeneity or growth orientation are the dominant influences on joint growth and morphogenesis.

Methods

Confocal image stacks of larval zebrafish jaws labelled with cartilage markers were obtained at twelve-hour intervals from 3.5 to 5.5 days post fertilization (dpf). All zebrafish experiments were approved by the local ethics committee and performed under a UK Home Office Project Licence. Distance and orientation variations between adjacent cell centroids over time were used to calculate the rate and direction of local tissue deformations [2]. These results were then integrated into a finite element model (FEM) of the zebrafish jaw, with which growth for each twelve-hour time window was predicted. The impact of growth characteristics—magnitude and orientation—was explored by successively simulating heterogeneous or homogeneous growth and anisotropic or isotropic growth.

Results

Spatial and temporal patterns of growth in the zebrafish jaw joint were observed from 3.5 to 5.5 dpf with elevated rates of growth at the level of the retroarticular process of the Meckel's cartilage. Integration of the biofidelic, heterogeneous anisotropic growth patterns into the zebrafish jaw FEM resulted in accurate shape predictions (Fig 1). Simulating homogeneous anisotropic growth resulted in very slight shape changes compared to the biofidelic predictions for all time windows (Fig 2). However, the removal of growth orientation resulted in marked shape changes for three of the four time windows (Fig 2), indicating that growth orientation, rather than growth homogeneity, dominates embryonic joint morphogenesis in the zebrafish.
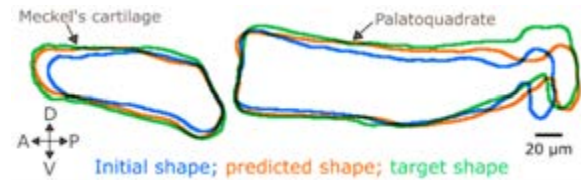
Figure 1: Cell-based data enable accurate growth predictions. Growth predictions of the zebrafish jaw joint from 4 to 4.5 dpf obtained from heterogeneous anisotropic growth fields. A: Anterior, P: Posterior, D. Dorsal, V: Ventral.
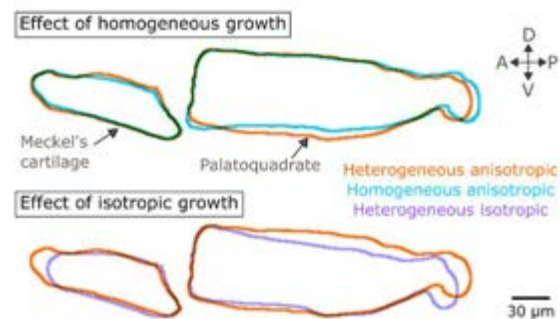
Figure 2: Growth orientation plays a major role in joint shaping whereas growth heterogeneity minorly impacts zebrafish jaw shape predictions. Jaw joint growth predictions obtained from heterogeneous/homogeneous anisotropic/isotropic growth fields (from 3.5 to 4 dpf). A: Anterior, P: Posterior, L: Lateral, M: Medial.

Discussion

Accurate shape predictions in the larval zebrafish jaw joint were obtained from direct quantification of cell rearrangement, volume expansion and ECM deposition, suggesting that these behaviours are the main drivers of zebrafish jaw joint growth and morphogenesis. Proliferation was not an important influence on growth, which may be specific to this stage of zebrafish development. The importance of growth orientation was emphasized when isotropic growth patterns resulted in altered shape predictions, whereas growth heterogeneity was found to play a minor role. This suggests that cell rearrangements and orientation, likely responsible for growth orientation, are dominant influences on joint growth and morphogenesis.

References

1. Shwartz et al, Dev Biol, 370:154-163, 2012.
2. Graner et al, Eur Phys J E Soft Matter, 25:349-369, 2008.

Acknowledgements

PLANTAR PRESSURE DATA RECONSTRUCTION BASED ON REDUCED DATA USING COMPRESSIVE SENSING TECHNIQUE

Zeinab Kamal[1]*, Edsko E.G. Hekman[1], G.J. (Bart) Verkerke[1]
*z.kamal@utwente.nl
1. University of Twente, 7500 AE Enschede, Netherlands

Introduction

Plantar pressure (PP) history of patients can be used as a powerful pathological recognition tool to predict and thus prevent pathologies, such as ulceration in diabetes that is more likely on a foot high-pressure sites and scoliosis progression that results in changes in a foot pressure distribution [1, 2]. The preserve of the history of PP data for many patients costs a massive storage capacity. Recently, the compressive sensing (CS) technique was used to compress high-dimensional data using the sparse selection of the most important information in data and subsequently reconstruct high-dimensional data based on the low-dimensional compressed data [3]. In this paper, we employed CS principles to: 1) compress high-dimensional PP data of a normal foot; and 2) reconstruct the PP data using the compressed data. Results indicated that using the CS method to compress 50% of the original data, the root-mean-square-error (RMSE) between the reconstructed and original data (RRMSE) was found to be about 0.7% of the highest pressure data.

Method

PP data at the midstance phase of a female foot (75kg) were measured using a pressure mat and depicted on a foot model (Fig. 1a). Different percentages of the original data, ranging from 1% to 100%, were sparsely selected to be compressed into low-dimensional data and subsequently reconstructed as the high-dimensional PP data based on the low-dimensional compressed data using the CS method [3] (Fig. 1b,c) (Eq. 1).

$$f(x) = \min_{x}\|\mathcal{P} - \psi x\|_2^2 \qquad (1)$$
$$\nabla f(x) = 2(\psi^T \psi x - \psi^T \mathcal{P})$$

The optimization library PyLBFGS in Python was utilized to calculate the least-squares objective function $f(x)$ which is the L^2 norm of the residual squared between the matrices of random sample pressure data ($\mathcal{P}$), and original high-dimensional pressure data (ψx).

Results

Given sparsely selected data percentage less than 55%, results revealed that the RMSE between the compressed and original data (CRMSE) is less than RRMSE. However, this observation was reversed for the sparsely selected data greater than 55% where the RRMSE reduced as the data percentage increased (Fig. 1d).

Conclusion

In agreement with the data in the literature, The plantar pressure magnitudes during walking occurred under the calcaneus and distal metatarsal ends (Fig. 1a), which showed the most likely positions of the ulceration development [1]. According to the current study, storing the sparsely selected 50% of the original data enables us to recreate the PP distribution using the CS method with an RMSE of 3.4kPa which is about 0.7% of the highest

PP. Despite the RRMSE exceeding the CRMSE for the data percentage less than 55%, the results intuitively signified the viability of the CS technique to depict the highest pressure sites based on sparsely selected 1% of the original data (Fig. 1c). As a crucial tool to evaluate adolescent idiopathic scoliosis effects on PP distribution [2], a finite element analysis can be used to investigate the plantar stresses for scoliotic patients [4].
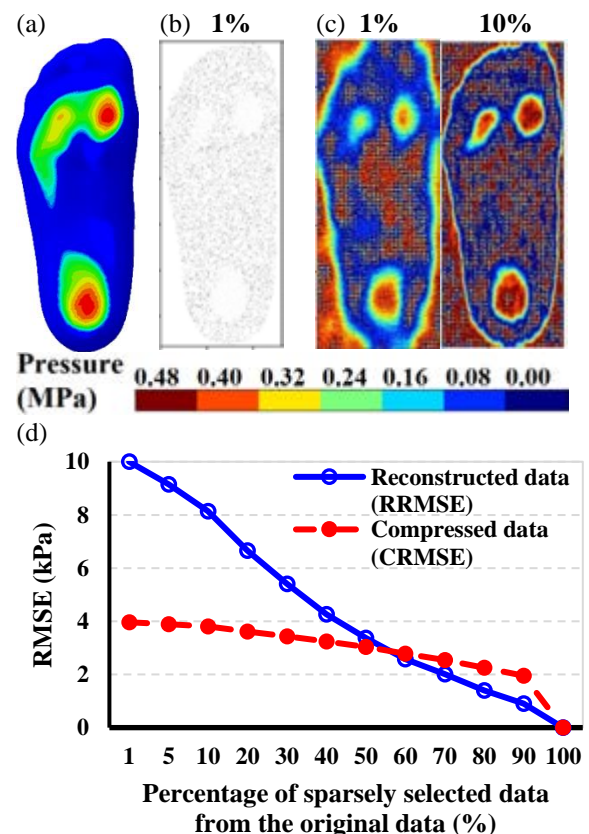
Fig. 1. (a) Original plantar pressure image at the midstance phase. (b) An image showing an example of the sparsely selected data, here 10%, of the original pressure data using CS that is called the compressed data. (c) The reconstructed PP data based on the compressed data using CS. Two images showing examples of the reconstructed data, here 1% and 10%, of the original data. (d) RRMSE compared to the CRMSE for different data percentages.

References

[1] Bus et al., Randomized Controlled Trial (2013)36(12):4109-16. [2] Horng et al., Stud Health Technol Inform (2021) 280:131-135. [3] Brunton, Steven l. and Kutz, J. Nathan. Data Driven Science & Engineering (2017) Book. [4] Kamal et al. Med Eng Phys (2019) 64: 46-55. [5] Kamal and Rouhi. Med Eng Phys (2019) 71: 51-63. [6] Kamal and Rouhi. J Biomech (2020) 111:109997.

EXPLOITING CELL MODULARITY TO CREATE REPURPOSABLE DIGITAL TWINS

Ian Manifacier (1)(2), Karine Anselme (3), Barbara Nebe (4), Jean-Louis Milan (1)(2)

1. Aix Marseille University, CNRS, ISM, Marseille, France
2. APHM, Institute for Locomotion, Department of Orthopaedics and Traumatology, St Marguerite Hospital, Marseille, France
3. Institut de Science des Matériaux de Mulhouse, University of Haute Alsace, 68057 Mulhouse, France
4. Department of Cell Biology, University Medical Center Rostock, 18057 Rostock, Germany

Introduction

Over the years many in silico cell models have been developed to successfully answer very specific scientific questions [1]. However, the repurposability of these models is very poor. For instance, combining the knowledge gained from two different studies into a single model too often requires rewriting a new model. This is a huge problem because the lack of repurposability will prevent us from tackling complex emergent processes, for example, involving a great number of known phenomena. Repurposability is therefore key to efficiently tackle multicellular modeling. In addition, we really need to allow large teams or even a community to work on and update the same model. Otherwise, modeling advanced embryogenic and regenerative processes will remain out of reach.

To solve the problem of model repurposability, we propose to use cell modularity [2] to our advantage. A prime example of cellular modularity is differentiation. A cell type may be viewed as the expression of one or more genes, or proteins. Yet; in the end, what differentiates one cell type from another is the expression of a new module (i.a. podosomes, filopodia, stress fibers, cell-cell contacts) or the change in behavior of a module by adding or removing one or more protein isoforms.

We hypothesize that based on pre-identified cell modules, we can create a functional digital twin that can be upgraded over time. However, this approach differs from already popular cell modeling frameworks that propose the modeling tools as modules, for example, physics library and solvers.

Instead, our aim here is to consider the biological cell as an ensemble of modules and, based on the observed living system, create our cell avatar module by module. Modular design is standard in the software industry; it allows different parts of the software to be designed and upgraded independently by hundreds of programmers.

In this study, we created the basis of a reusable cell avatar based on the modular architecture of adherent cells. We aimed for it to have an emergent behavior that arose from the interactions between autonomous agents defined by each subcellular module. We then tested the ability of the cell avatar to exhibit durotaxy, haptotaxy and to interact with substrate anomalies in free adhesion conditions.

Methods

To allow the cell avatar to spread, migrate and adhere to the substrate, we created the following modules: focal adhesions, protrusion and the cell membrane combined with the actin cortex. Each module is used to create one or more autonomous agents.

Results

The behavior of the cell avatar is emergent. After 10 single cell simulations of free adhesion, 72h each, cells were able to exhibit durotaxis and haptotaxis over a distance ranging between 50 to 100 µm (figure 1). The cell avatar could also interact with the substrate patterns and topological anomalies in a convincing manner.

Discussion

Although this is still preliminary work, we were able to create a model based on cell modularity. The modules could be modified independently as long they did not require new types of interactions with other modules. In the future, this modular approach should allow large teams or even a community to work and update the same model.
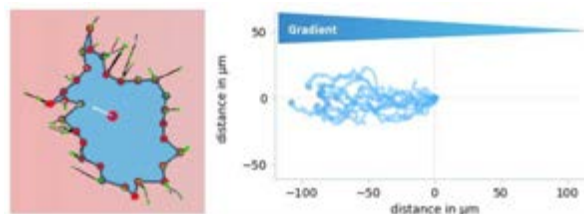

Figure 1: Visualization of the cell avatar (left). Migration results of 10 single cell simulations over a 72h free adhesion run on a substrate with a rigidity and coating gradient (right).

References

1. Szabó et al, J Cell Biol 213 (5): 543–555, 2016.
2. Hartwell et al, Nature 402 (6761): C47–52, 1999.

Acknowledgements

NETWORK MODELLING FOR NUCLEUS PULPOSUS CELL ACTIVITY IN EARLY INTERVERTEBRAL DISC DEGENERATION

Sofia Tseranidou (1), Maria Segarra-Queralt (1), Janet Piñero (2), Jérôme Noailly (1)

1. BCN MedTech (Universitat Pompeu Fabra), Spain;2. IMIM, Spain

Introduction

Low back pain (LBP) is a major cause of disability worldwide. It is often related to intervertebral disc (IVD) degeneration (IDD), characterized by loss of water, proteoglycans, and type-II collagen, in the nucleus pulposus (NP) of the IVD. Extracellular matrix (ECM) degradation results from complex biochemical processes, with redundant and feedback-looped processes that further interact with physical factors. Accordingly, IDD has a strong inertia and might only be tackled if apprehended sufficiently early. While its pathogenesis remains poorly understood, several numerical [1,2] and experimental [3,4] models explore underlying biomechanical and biochemical processes. Yet, the integration of knowledge about IVD cell regulation in health and disease still needs to be improved. Accordingly, a new NP cell (NPC) regulatory network model (RNM) is presented, incorporating critical biochemical interactions in IVD regulation.

Methods

First, a unique corpus of 120 articles was built about the biochemical stimuli in the NP and their activation and/or inhibition effect on the regulation of soluble cytokines, proteases, and ECM proteins by NPC. Due to the limited knowledge about IDD and the lack of experiments with healthy human IVD material, the corpus was enriched through the STRING database, including general protein-protein interactions in Homo Sapiens. In particular, relevant interactions in chondrocyte regulation were retained. To build the RNM, proteins were represented as nodes that interacted among each other through a directed network of inhibition and activation edges. Nodal activations were calculated through a system of ordinary differential equations that semi-quantitatively interpolates Boolean rules and provide the stable steady states (SSS) of the RNM [5]. Finally, two experimental studies, using healthy human [3] and bovine [4] IVD NPC, were simulated to evaluate the model.

Results and Discussion

Fig. 1 shows the topology of the final NPC regulatory network, highlighting the complexity of the system.
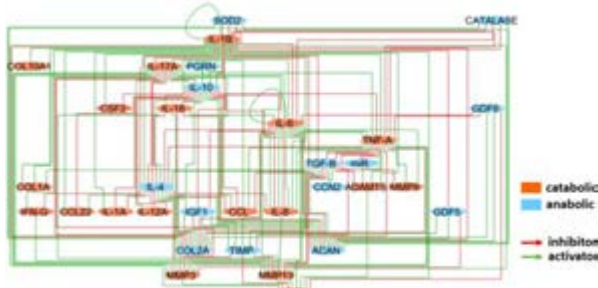
Figure 1: Network topology after enrichment

Simulations revealed an anabolic basal SSS of the RNM (light blue bars in Fig. 2). According to the experimental measurements [3,4] related to the simulated NPC perturbation, initial activation of IL-17A enhanced slightly COL1A and MMP13, while inactivating almost completely the anabolic ECM components, indicating its negative role in the IVD regulation. In contrast, initial activation of GDF5 up-regulated not only the expression of ACAN and COL2A, but also important growth factors and anti-inflammatory cytokines that play an important anabolic role in the IVD. Interestingly though, the increase of MMP-13 activation with IL-17A was very low, which seems to be supported by some evidence that this protease might not play a clear role in IDD, in contrast to osteoarthritis [6].
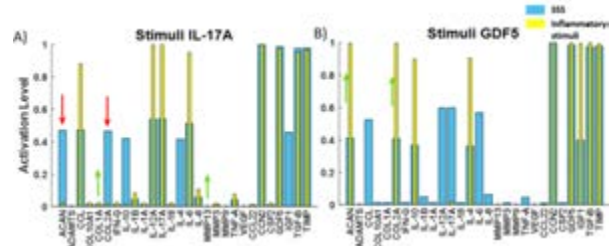
Figure 2: Initial state (light blue) and stimuli-state (yellow) of the IVD NC network with the (A), IL-17A and (B), GDF5.

Further experiments with anti-inflammatory IL-4 and TGF-B showed a significant increase of the anabolic factors and a decrease but not depletion of the catabolic ones, emphasizing the complexity of the IVD regeneration. IL-1B initial activation increased the activation levels of ADAMTs, the primary enzymes that cleave proteoglycans in IDD progression, whereas the activation of MMP3, believed to increase in advanced stages of IDD [6], remained low. Despite, the relatively limited amount of knowledge about IDD, compared to other diseases, e.g., such as osteoarthritis, an enriched RNM was built and successfully assessed against independent experiments. This directed RNM in IDD stands for a unique basis to further integrate both mechano-regulation and biochemical knowledge and enrich existing dose-dependent NPC activity model.

References

1. Ruiz Wills C. et al., Front Physiol 9:1-12, 2018.
2. Baumgartner L. et al, Front Bioeng 10;9:734258, 2021
3. Yao, Zhixiao et al., Inflammation 39,6: 1997–2007, 2016
4. Chujo, Takehide et al., Spine 1;31(25):2909-17, 2006
5. Mendoza et al, Theor Biol Med Model, 3:1-13, 2006.
6. Vo et al, Spine J. 13:331-41, 2013

Acknowledgements

NON-INVASIVE METHOD OF FRACTIONAL FLOW RESERVE ESTIMATION IN PATIENTS SUFFERING FROM ISCHEMIC HEART

Krzysztof Jankowski (1), Anna Nieroda (1), Marek Pawlikowski (1)

1. Institute of Mechanics and Printing, Warsaw University of Technology, Poland

Introduction

The most common cardiovascular condition is coronary artery disease, one of the leading causes of death worldwide [1]. Coronary artery disease is caused by a narrowing or complete occlusion of the coronary artery lumen. Early diagnosis and correct assessment of the existing stenosis is essential.

The main subject of the research is the simulation of blood flow through coronary arteries using the finite element method (FEM). The studies aim to non-invasively define the fractional flow reserve (FFR) ratio based on computed tomography (CT) images and pressure measurements.

Methods

The geometrical model was generated in Mimics software from CT images. The model consisted of the aortic root and coronary arteries (Figure 1).
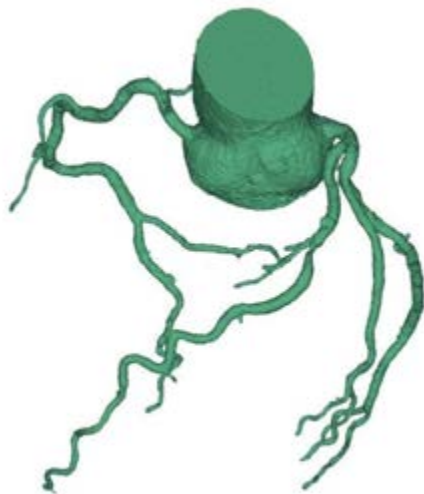
Figure 1: Geometric model of the coronary artery based on CT images.

The blood flow was determined using ANSYS 2020 R2 software. The flow pressure values were determined at the inlet, defined at the aortic root. The length of one heart cycle was assumed to be 0.8 s. Heart rate was 75 beats per minute. We have adopted non-Newtonian blood flow.

Results

FFR is defined as the ratio of mean pressure measured distally behind the stenosis location (P_d) to mean pressure measured in the aorta (P_a) (Equation 1) [2]. FFR < 0.8 determines surgical treatment.

$$FFR \approx \frac{P_d}{P_a} \qquad (1)$$

From the defined flow, we obtained the pressure distribution in the artery (Figure 2). This allowed us to determine the FFR ratio, which gives information on the degree of artery stenosis and to give the medical doctors guidelines for further treatment.
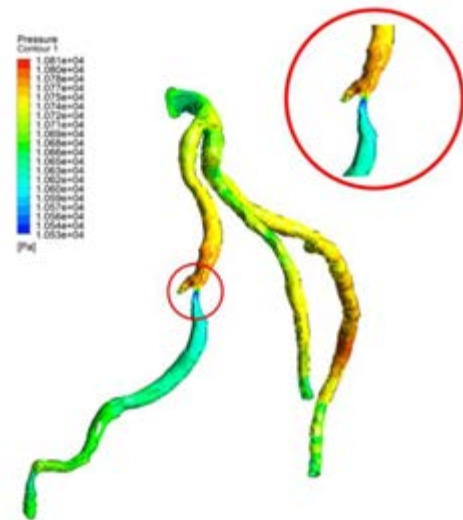
Figure 2: Pressure distribution in the coronary artery

Discussion

Studies so far suggest that geometric parameters of the coronary artery have an essential role in the final hemodynamic results of the simulations performed. This issue is important because coronary branches' number, length, irregularity, and given boundary conditions at the ends influence the pressure value behind the stenosis. Consequently, their underestimation or omission may distort the determined FFR ratio.

Coronary artery imaging using CT may be a reliable, non-invasive method for assessing the degree of coronary artery stenosis [3]. The FFR can be defined based on CT images and pressure measurements. This method would eliminate the need for an invasive coronarography examination. In addition, it would increase accessibility and shorten the waiting time for the test because, by its very nature, it does not require hospitalization of the patient. Currently, there is only commercial software that is not publicly available.

References

1. Carvalho V, et al, Fluids 6:53, 2021.
2. Pijls NH, et al, Circulation 87:1354–1367, 1993.
3. Zhuang B, et al. Eur Radiol 30:712-725, 2019.

COMPARISON BETWEEN TRANSTIBIAL AND ANTEROMEDIAL PORTAL ACL RECONSTRUCTION THROUGH FINITE ELEMENT ANALYSIS

Konstantinos Risvas, Konstantinos Moustakas

Department of Electrical and Computer Engineering, University of Patras, Greece

Introduction

The Anterior Cruciate Ligament (ACL) rupture is a very common knee injury in sport activities. Usually, it requires the total replacement of the native tissue with a graft that is fixed through tunnels, drilled in both tibia and femur bones. This procedure is known as Anterior Cruciate Ligament Reconstruction (ACLR), and it features a plethora of different parameters. In this work, we present a Finite Element (FE) gait simulation study to compare two of the most common ACLR surgery techniques regarding tunnel drilling, the Anteromedial (AM) and Transtibial (TT) portal approaches. The former method usually demonstrates poor ability to place the femoral tunnel in the location of the native ACL insertion site, while the latter one leads to increased graft bending angle around the area of femoral insertion area.

Methods

The MRI data used throughout this work are acquired by the OpenKnee database [1] and processed using tailored segmentation tools [2]. The ACLR modeling pipeline is developed in Blender. The tibia and femur tunnels were drilled using a Boolean operator. The graft was modeled as a cylinder that passed through the tunnels. The results of the modeling workflow are presented in Figure 1.
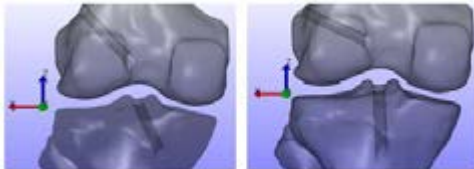
Figure 1: The tunnels in TT (left) and AM (right) portal surgery techniques. In the case of the TT technique the tunnels are placed in a more parallel direction, while the AM is characterized by a femoral tunnel placed in a more horizontal orientation.

The created geometries were used to assembly two FE models utilizing the FEBio software [3], along with meshes that represented the other key anatomical structures, such as the menisci and the cartilages. The ligaments were modelled as non-linear springs and proper contact and material models were established. The knee joint was modelled as a universal joint composed of three cylindrical joints. The final FE models are presented in Figure 2. Regarding boundary conditions, a dynamic simulation of gait using the OpenSim software was performed to acquire knee joint reaction loads and primary knee joint kinematics (knee flexion angle) for the stance phase of a gait cycle. The superior – inferior force and abduction – adduction moment were prescribed and applied to the FE models,

as well as the knee joint flexion angle. Tibia was constraint in all Degrees of Freedom (DoFs), whereas femur was fixed in anterior – posterior and internal – external rotational DoFs. At the end of each simulation, we measured cartilage contact pressures, menisci and graft von Mises stress and graft contact pressure at the femoral and tibial insertion sites.
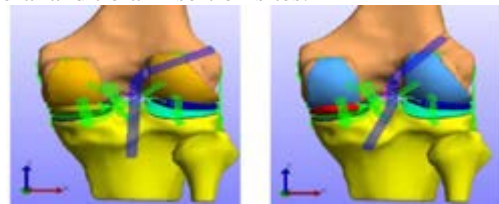
Figure 2: The AM (left) and TT (right) FE models. The graft bending angle around femoral insertion is clearly increased for the AM case.

Results

The AM graft featured a peak contact pressure around the entry point of the femoral tunnel of 16.59 MPa, that was almost the twice of the corresponding value of the TT approach. Additionally, the peak graft von Mises stress in the AM technique was almost 13 MPa higher than in the case of TT. On the other hand, TT exhibited a higher contact pressure on the entry point of the tibial tunnel. The maximum contact pressure in both cases occurred close to knee extension before toe-off. Moreover, the graft von Mises stress was larger in the case of AM compared to TT. Finally, cartilage contact pressure and menisci stress were identical for both cases.

Conclusion

In conclusion, the TT portal technique features smaller graft stress and contact pressure at femoral tunnel insertion compared to the AM approach. Nonetheless, the possible superiority of AM to place the femoral tunnel closer to the anatomical ACL footprint, and thus, further restore knee kinematics after ACLR was not evaluated under the scope of this work and will be addressed in following studies.

References

1. Erdemir A, *J Knee Surg*. 2016;29(2):107-116
2. Nikolopoulos et al, *IEEE Access*, 8:56766-56781, 2020
3. Maas SA et al, Journal of Biomechanical Engineering, 134(1) 2012.

Acknowledgements

THE INFLUENCE OF THE IMPLANT GEOMETRY CONCEPTS IN BONE STRAINS DISTRIBUTION

Cátia Gomes (1), Michel Mesnard (2), António Ramos (1*)

1. TEMA-DEM, Biomechanics Group, University of Aveiro, Portugal, 2. TEMA-DEM, Biomechanics Group, University of Aveiro, Portugal, a.ramos@ua.pt

2. Institut de Mécanique et d'Ingénierie, University of Bordeaux, France, michel.mesnard@u-bordeaux.fr

Introduction

The market of dental implants are growing in the world, to improve the life of patients. The aplications is a stetics changing the personal image or functional in a lack of teeth. Due to their high success rates, although there are still existing reports of biological and technical complications related with implant interface. The success of dental implants depends on several factors [1] as the implant design, the surface topology, the bone quality [2]. The market presents several solutions, with different screw geometries and with support in tissue level and bone level [3]. The present work aims to study the effect of the dental implant design in load transfer on the surrounding bone and the comparison with the tooth.

Materials and methods

The geometric models of the three Comercial dental implants presented in figure 1, was obtained from catalogs, a) Straumann Bone Level implant (SBL), b) Straumann Tissue Level implant (STL), c) Dentatus Anew ® Narrow body implant (DAN). Another model for comparison was the real tooth obtained from a CT scan of a right first premolar d). The model considers the tooth geometry and cancellation of the local cortical bone; the periodontal ligament with 0.2mm of thickness was assumed in the tooth model. The finite element model was expanded to a 3: 1 scale. Each model was built and a convergence study performed .

a)   b)   c)   d)
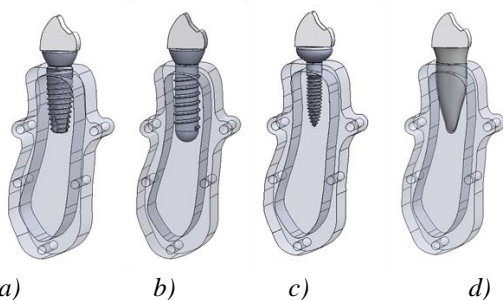
Figure 1: CAD models of three dental implants and one tooth.

The size of each implant was selected according to the recommendation of implantation, considering the 1.5mm of bone thickness. Table 1 presents the geometric properties of each implant and the mechanical properties of tissues and implants made of Titanium alloy. The boundary condition applied in the models considered a fixation in the cortical bone and a 100 N lingual load with an inclination of 30° with the vertical axes of the tooth was applied on the models [3].

Structure/ Model	Diamenter/ Length (mm)	Young's Modulus (GPa)	Poisson 's ratio
Cortical bone		19	0;3
Trabecular bone		0.21	0.3
Ligament		2.55	0.4
Dentin		22.5	0.25
SBL	3.5/10.5	110	0.34
STL	3.5/10	110	0.34
DAN	2.4/11.5	110	0.34

Table 1: Dimensions and material properties.

Results

The results point out the importance of implant design in implant stability. The SBL implant is the most stable (6µm) inducing reduced movement of the crown but it presents a higher stiffness comparable with tooth (90 µm). The distribution of stresses is different from that of the tooth (figure 2), and different between implants. The narrow implant presented the highest values and SBL the lower values, similar to the tooth.
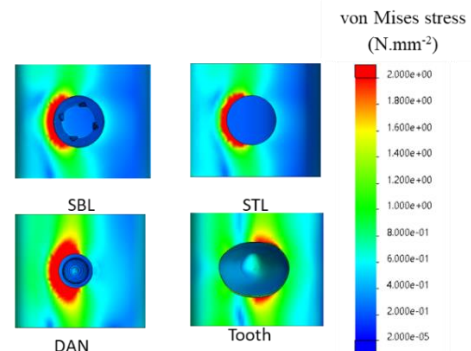
Figure 2: Von Mises stress distributions at the cortical level.

References

1. L. Gaviria, et al. Journal of the Korean Association of Oral Maxillofacial Surgeons, vol. 40, pp. 50-60, 2014...
2. Catia Gomes et al. Comp Methods in Biomech and Biomed Eng, 23:sup1, S133-S135, 2020.
3. J. Londono, et al. Comp Methods in Biomech and Biomed Eng, 23:sup1, S178-S179, 2020
4. D. Robinson, et al. The journal of advanced prostho-dontics, vol. 11, no. 3, pp. 169-178, 2019.

Acknowledgments

STRESS RELAXATION PHENOMENA IN POLYMERIC ORTHODONTIC LIGATURES

Grzegorz Milewski

Department of Applied Mechanics and Biomechanics, Cracow University of Technology, Poland

Introduction

Elastomeric products are applied in orthodontics mainly as the elastic ligatures or chains and have become an alternative to wire ligation made of titanium alloy or stainless steel. Despite their popularity among the dentists and undoubtful advantages some essential warnings are being raised mainly concerning the degree of load loss due to the relaxation phenomenon which seems to be a dominant feature in time-dependent behaviour of those elements in orthodontic procedures as dentition corrections or teeth extrusions. The aim of the paper was to examine and analyse strength and rheological properties of biocompatible orthodontic elastomeric ligatures. The proper assessment of their rheological properties will enable the dentists to predict the degree of load/stress loss due to the relaxation phenomenon in elastomeric ligatures and finally will enable the precise control of the treatment progress in various orthodontic procedures.

Methods

Ligatures and chains are made of polyurethanes, characterized with a rubber-like elasticity, have a long chain and a poorly cross-linked structure. Elastic behavior is the result of reducing the entropy associated with the twisting of the macromolecular chain from its most likely conformation. Nevertheless, the local movements of the chain segments must be limited for the polymer to return to its original shape, since irreversible movement of the chains with each subsequent movement will cause constant distortion of the material. Cross-linkages between the chains must be relatively few in order to facilitate high stretching without any breakage of the base bonds [1, 2]. Elastomeric ligatures are the main element supporting and maintaining wire arch in channel of orthodontic lock. Five different orthodontic ligatures were chosen for the tests - three of them were of chain type (denoted in the experiments as A, B, C); the next two were of string type (D and E) – Fig. 1.
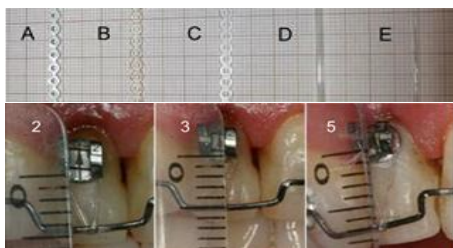
Figure 1: Examples of chain and string elastomeric ligatures and the results of the orthodontic extrusion after 2, 3 and 5 weeks of the treatment.

Results

Fig. 2 presents a comparison of relaxation courses for all types of ligatures plotted in logarithmic time scale. Regardless the type of ligature the basic relaxation time, corresponding to the inflection point of the curve, varies between 50 and 100 seconds, so that is why only the initial parts of the relaxation courses are presented.
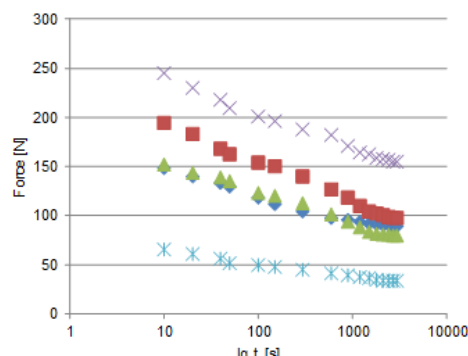
Figure 2: Examples of the relaxation course for each group of the elastomeric ligatures.

Discussion

The proper orthodontic extrusion assumes that the tooth should descend towards the occlusal line about 0.15 mm per day. Correlations between stress-strain curves and stress relaxation characteristics enable to estimate the value of the therapeutic force that should be applied to the treated tooth in order to provide the extrusion phenomenon to follow the recommendations, i.e. at a rate of about 1 mm per week. The most important conclusions from the research are as following: the relaxation process runs most rapidly in the first phase of the phenomenon, after a day, the influence of the extrusion process on the decrease in strength begins to outweigh the influence of the relaxation process, a secondary increase in the tension of the ligature slows down the relaxation process and increases the asymptote value by about a half of the difference between the primary and secondary tightening. The power-law descriptions fit the best the time-dependent behaviour during orthodontic procedures. Power-law model gives the most intensive initial relaxation which is characteristic for elastomeric ligatures.

References

1. Ward J.M., Sweeney J.: Mechanical properties of solid polymers. 3rd Edition, 2012, John Wiley & Sons Inc., New York.
2. Brantley W.A., Eliades T.: Orthodontic material – scientific and clinical aspects, Czelej, Lublin, 2003.

FRACTURE RESISTANCE OF ZIRCONIA REINFORCED LITHIUM SILICATE DENTAL RESTORATIONS AFTER THERMOCYCLING ©

R. D. Vasiliu(1), L. Rusu(2), A. Boloș(3), S. D. Porojan(4), L. Porojan(1)

1Department of Dental Prostheses Technology (Dental Technology), Center for Advanced Technologies in Dental Prosthodontics, Faculty of Dental Medicine, "Victor Babeş" University of Medicine and Pharmacy Timişoara, Eftimie Murgu Sq. No. 2, 300041 Timişoara, RomaniaUniversity of Medicine and Pharmacy Victor Babes, Timişoara, Romania; 2Department Mechanics and Vibrations, Faculty of Mechanical Engineering, Politehnica University, Mihai Viteazu Street, 300222 9 Timisoara, RomaniaPolitehnica University Timişoara; 3: Department of Oral Rehabilitation (Dental Technique), , Faculty of Dental Medicine, "Victor Babeş" University of Medicine and Pharmacy Timişoara, Eftimie Murgu Sq. No. 2, 300041 Timişoara, Romania; 4 Department of Oral Rehabilitation (Dental Technique), Center for Advanced Technologies in Dental Prosthodontics,Faculty of Dental Medicine, "Victor Babeş" University of Medicine and Pharmacy Timişoara, Eftimie Murgu Sq. No. 2, 300041 Timişoara, Romania

Introduction:

All-ceramic materials are considered to be the most esthetical choice of election in restorative dentistry nowadays[1-2]. Although their mechanical structure is constantly improving, these materials still present a brittle character that makes them more prone to fracture. Studies in literature revealed that the first reason for failure of dental restorations is their fracture [3].A new class of improved glass-ceramics that strives to combine the mechanical strength and the aesthetical properties is zirconia reinforced lithium silicate (ZLS). This type of glass-ceramic microstructure is based on a lithium- metasilicate glass ceramic reinforced with 10% zirconium dioxide. ZLS ceramic is part of the new hybrid ceramics that combines both aesthetical properties of glass-ceramic and mechanical resistance of zirconia [4].

Methods:

16 all-ceramic crowns were obtained from zirconia reinforced lithium silicate glass ceramic (ZLS). Half of them were obtained using heat-pressing technique (Celtra Press, Degudent Dentsply, Hanau,Germany) and the other half were milled (Vita Suprinity, Vita Zahnfabrick, Germany) using CAD/CAM technology.
The abutment was an upper premolar typodont tooth. It was prepared with a 6 ° convergence of the axial wall, the reduction of the axial and of the occlusal surface was 1,5 mm. The marginal preparation design was a 1 mm circumferential rounded chamfer. The abutment preparation was digitally scanned using a D2000 3D optical scanner (3Shape, Copenhagen, Denmark). Thermocycling was conducted for 10.000 cycles with a thermocycling equipment in two distilled baths with 5 degrees Celsius and 55 degrees Celsius temperature. The dwelling time was 20 seconds. Tests were conducted after thermal aging using a universal testing machine (Instron 3366, Instron Corp, Norwood MA, USA). Each probe was placed in the testing machine at 0 degrees to the long axis of the tooth. A stainless steel stylus of 15 cm, with a rounded 6 mm tip, was used to express the force, to occlusal surface.

Results:

One-way ANOVA revealed that there were no significant differences ($p < .05$) after thermocycling the samples and static fracture test (Figure 1). The tested crowns suffered fractures that started where the indenter took contact with the sample. Also, radiant cracks were seen all over the ceramic crowns. Some samples fractured in multiple parts for both ZLS materials.
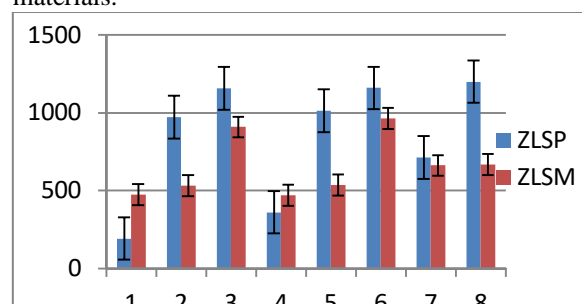
Figure 1: Maximal compression force (N) for every sample of heat-pressed (ZLSP) and milled (ZLSM).

Discussions:

Fracture toughness is used to characterize the fracture resistance of the ceramic materials [5]. Fractographic results determined that the ZLS crowns milled and heat-pressed had a similar fatigue bahaviour after being adhesively luted to resin abutments. The ZLSP restorations had better performance compared to the other material, but without statistically difference. The average fracture load values for the samples in this study ranged from 438 -845 N. These values are lower compared to the forces for the unrestored maxillary premolars-932 N [6].

References:

1. Kelly JR. Dental Clinics of North America 2004;48:513–30.
2. Raigrodski AJ. The Journal of Prosthetic Dentistry 2004;92:557–62.
3. Blatz MB. Quintessence International 2002;33:415–26.
4. Pjetursson BE, Sailer I, Zwahlen M, Hammerle CH. 2007;18(Suppl 3):73–85.
5. Schmidt, K.K., Chiayabutr, Y., J. Prosthet. Dent. 105, 374–382.
6. Ahlers, M.O., Morig, G.Int. J.Comput. Dent. 12, 309–325.

SOFT DESIGN FOR AN REHABILITATION EXOSUIT: A PRELIMINARY APPROACH

António Diogo André (1), Ana Margarida Teixeira (2), Pedro Martins (3)

1. INEGI, Porto, Portugal (a.diogo.andre@icloud.com); 2. INEGI, Porto, Portugal (margarida.t28@gmail.com); 3. INEGI-LAETA, Porto, Portugal (palsm@fe.up.pt); 3. ARAID, i3A, University of Zaragoza, Spain

Introduction

Nowadays, physical impairments are common, and they are caused by different reasons [1]. The normal aging process accentuated by increasing life expectancy, neurodegenerative diseases and finally daily living misfortunes such as accidents (falls, motor vehicle accidents, sport practices and others), all having a significant contribution for this reality.

The resultant mobility deficit has a high and long-term impact on social, economic and financial sphere of communities and health care systems worldwide [2]. Besides, the psychological effect of these life changes on patients may be stressful, painful and in some cases depressive [3].

As an attempt to mitigate the negative effects of these mental and physical conditions, some solutions were already developed. They include wanderers, wheeled vehicles and wheelchairs [4]. However, most devices do not have rehabilitation as primary goal.

Despite the early stages of development, exoskeletons and exosuits [5] already play an important role in a rehabilitation context, as seen in some solutions described on literature [6,7].

Soft Design

The design, being one of the most valuable characteristics, has a direct impact (at different levels) on users' appreciation about the solution . This explains why every design decision must be made carefully.

It is crucial the design adopted can accommodate some natural movements of the user, such as flexion and extension, abduction and adduction and/or some rotations. In summary, it must allow the appropriate degrees of freedom (DOFs) [8].

Also, the aesthetic appearance is a very relevant consideration. The patient should feel comfortable and secure, and that he is using a simple and usable device with practical benefits in his life.

Being a wearable soft solution premises the use of soft, flexible and biomimetic materials, such as some biocompatible polymers [9,10]. This fact contributes for a global solution more adaptable to the user.

As an example of these concepts, figure 1 represents a very early scheme of what could be a soft wearable design for the elbow.

Discussion and Conclusion

Although every important aspect of an exoskeleton or exosuit is well known and well described on literature, from distribution of weight to safety measures or power production and consumption, it is important to keep the design development as a whole.

Having the patient point of view in mind, these devices should be perceived as natural body extensions, instead of strange and exogenous objects. This aspect may become more important than the overall helpfulness of the device, if baseline objectives are achieved through its usage.
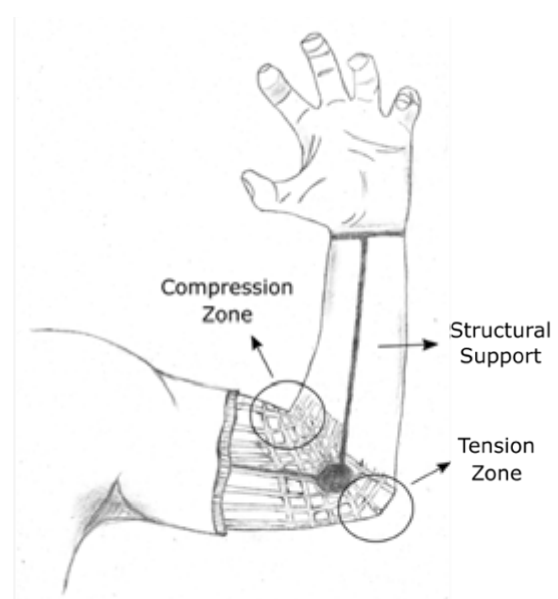
Figure 1: Scheme of an elbow exosuit.

References

1. Miranda et al, 4th IEEE RAS EMBS, 1776-1781, 2012
2. Chen et al, Journal of Orthopaedic Translation, 26-37, 2015
3. Rantanen, JOURNAL OF Preventive Medicine & Public Health, 2013
4. Van den Bogert, Biomedical Engineering Online, 2003
5. Sado et al, Mechatronics, 2019
6. Bae et al, IEEE ICRA, 2820-2827, 2018
7. Bryan et al, The Int J of Robotics Research, 40: 722-746, 2021
8. Hansen et al, Applied Ergonomics, 68: 283-288, 2018
9. Chiaradia et al, Biosystems & Biorobotics, 22: 415-419, 2019
10. Yu et al, Nano Energy, 27: 275-281, 2016

Acknowledgements

ASSESSING INTUITIVE DESIGN OF ASSISTIVE DEVICES TO IMPROVE HUMAN BIOMECHANICAL DEFICIENCIES: AN EYE-TRACKER STUDY

V. Bayarri-Porcar (1), J. L. Sancho-Bru (1), M. Vergara (1)

1. Departamento de Ingeniería Mecánica y Construcción, Universitat Jaume I. Spain.

Introduction

People with upper limb pathologies usually have difficulties to carry out activities of daily living. Assistive devices (ADs) can help to improve their quality of life by increasing their autonomy and facilitating the performance of certain tasks [1]. Occasionally, biomechanical deficiencies are accompanied with cognitive damages, which may hinder the use of the ADs, causing frustration. This work uses Eye-Tracker (ET) technology to assess design aspects of ADs accountable for their intuitive use with the aim of reducing the level of frustration.

Methods

Sixty subjects participated in an ET study in which they were shown images of six models of ADs aimed to open jars (Figure 1, top). The research was approved by the University Ethical Committee and each participant gave his/her written informed consent to take part in the study. The six models were selected to cover different movements be made in the opening action. The grip area and the contact area with the lid in each AD model were defined as areas of interest (AoIs) to be tracked by the ET. Based on the transmitted information by the device through the image and without having previously used the product, each subject was asked what kind of effort they would make during the jar-opening action (Figure 1, bottom). The subject had to select the effort from a list of six answers: (a) pull, (b) push, (c) turn, (d) clench and turn, (e) push and turn, (f) others. After the ET study, the subjects were asked if they were familiar (if they knew it and/or if they had use it) with any of the models observed.

Figure 1: TOP, images used of the six ADs; BOTTOM, examples of the image observed by the subject during the ET study (Spanish version).

Only one of the answers was considered correct for each model, based on customer instructions and tests of use. For each AD, the percentage of subjects that provided an incorrect answer was calculated. The time of decision making by each subject for each AD was also measured as the total duration time until clicking the selected response. In case a subject had used previously a specific AD, the data of this model for this subject was discarded for the posterior analyses. For each AD model, the time spent observing each AoI was computed with the ET. Finally, the percentage of subjects who were familiar with the model, but had never used it, was also computed.

Results

Table 1 shows the different results obtained. Models 4 and 5 show the worst rates of correct effort selection, and model 1 the best one. Model 1 shows the smallest time of decision making, while model 2 the highest one. Model 1 is the only one that is relatively familiar to the interviewed subjects. Time spent looking the lid AoI is larger in all models than that looking the grip AoI, but especially in model 3.

Model	AD1	AD2	AD3	AD4	AD5	AD6
Wrong (%)	19.3	48.3	48.3	60	58.6	37.3
Decision Time (s)	7.42	16.98	12.55	9.81	9.19	11.35
Mean (SD)	(5.11)	(12.91)	(8.86)	(6.87)	(5.95)	(9.93)
Time grip AoI (s)	1.12	1.94	0.64	0.33	0.24	1.52
Time lid AoI (s)	1.94	5.30	3.46	3.52	1.99	2.73
Unknow (%)	52.2	95	91.7	80	87.9	91.5

Table 1: Percentage of subjects who selected a wrong effort, mean (SD) of time of decision making (s), and percentage of subjects who did not know each model.

Discussion

The simplest models (with less elements in their design) (1, 4 and 5) require less time in decision making. Model 1 is the most intuitive one, as it shows the lowest percentage of error in the response, and the least time in the decision making. Its clothespin shape is familiar, and the need of both squeezing and turning has been identified by most of subjects. However, these results may be influenced by the fact that model 1 is also the most familiar to the participants. Simplicity of models 4 and 5 provided a fast response, but with a high failure rate, as the shape of the model only indicates the need of turning, but not the need of pushing (there is not any signifier [2] in the design asking for pushing on it). Models 2, 3 and 6 are the least known models, with the highest time in decision making and trying to understand their mechanism, but they are moderately intuitive, considering that the information transmitted is understood by almost 50% of the subjects. The effort is better understood in those models where the gripping area and the use position are familiar.

References

1. Roda-Sales et al, PeerJ, 7, e7806, 2019.
2. Norman, D., Currency Doubleday, New York, 1988

BALANCE RECOVERY PREDICTION UNDER THE INFLUENCE OF DIFFERENT ACTUATION MODELS

Monika Harant (1), Michael Roller (1), Marius Obentheuer (1), Joachim Linn (1)

1. Fraunhofer Institute for Industrial Mathematics (ITWM), Kaiserslautern, Germany

Introduction

The transition to autonomous driving brings new challenges, but also new opportunities. It enables the application of driving maneuvers that respond faster and more flexibly than a driver could. In addition, new ways are being explored to ensure compliance with safety standards and further reduce the risk of injury in traffic hazards. Especially in public transport, experiments with crash test dummies or crash simulations with complex finite element models of the human body cannot cover all interesting scenarios for passenger cars since both methods do not take into account the active movements of the occupants and only consider a very short time horizon. Optimal control of multibody models is a promising method to address this issue. It has been successfully applied to predict various sports and lifting tasks [1] [2] involving highly dynamic motions and interaction with objects. However, for the calculation of long movements, e.g. during a braking maneuver that lasts several seconds, a balance between model accuracy and calculation time must be achieved, which we want to investigate in this work.

We apply optimal control to predict balance recovery motions of a standing shuttle occupant using a handrail. Furthermore, we analyze the effect of actuation models of different complexity on motion prediction by comparing joint torques (T), muscle torque generators (MTG), and Hill-type muscles (M).

Methods

The human is represented by a rigid multibody system with 40 degrees of freedom. The different actuation models are limited to the arms, since they are the main actors in balance control using a handrail. In case of M, 29 Hill-type muscles [4] (including bi-articular ones) actuate each arm. In case of MTG and T, 14 MTG [3] and 7 simple torque sources actuate each arm, respectively. They neglect the effect of bi-articular muscles. The remaining joints are torque-controlled.

A multiphase optimal control problem using the method of [4] is set up that predicts human behavior during a shuttle deceleration. The outline of the motion is as follows (Fig. 1): After a quiet stance phase, the braking profile is applied. A short phase in which the actuation of the manikin does not change simulates the reaction time of the occupant. In the third phase, it can react to the perturbation. The movement ends when the manikin is at rest in an upright position again after completion of the braking profile. For all three actuation models, the applied constraints are identical or comparable with respect to the actuation system.
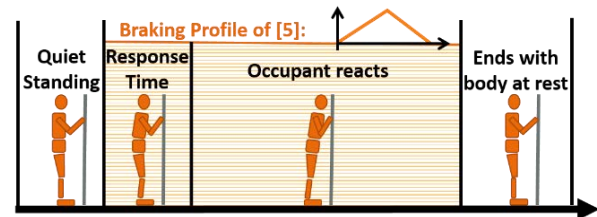
Figure 1: Outline of the optimized motion.

Results

The optimized motion of a short braking maneuver with model M at shoulder height grip is shown exemplarily here (Fig. 2). The braking profile follows that of [5] with a maximum braking acceleration of $2\frac{m}{s^2}$. The manikin is able to counteract the disturbance. Due to the response time, the upper body shifts forward. During the motion, a peak hand force of 96 N and a maximum displacement of the Center of Pressure (CoP) by 10.3 cm occurs.
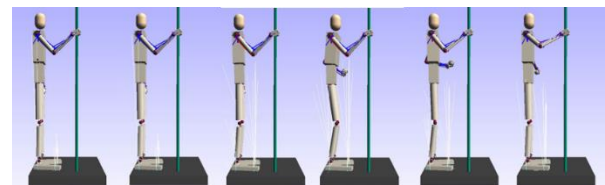
Figure 2: Snapshots of the optimized balance recovery motion with model M. The white lines indicate the ground reaction forces at each contact point.

Discussion

The optimized motion could reproduce key characteristics observed in recorded balance recovery motions. The maximum displacement of the CoP and the peak hand force of the optimized motion agree well with mean values (9.0 cm and 82.9 N) observed in [5]. Furthermore, this approach offers the possibility to estimate the effect of different braking profiles for a variety of occupant positions with comparably low computational effort. This allows defining guidelines for braking profiles, which responds suitably to potential traffic hazards while ensuring occupant safety.

References

1. K.A. Inkol et al, Multibody Syst Dyn, 50:435-452, 2020.
2. M. Sreenivasa et al, J Biomech, 78:118-125, 2018.
3. M. Millard et al, J Biomech, 89:11-20, 2019.
4. M. Roller et al, Adv Transdiscipl Eng, 11:269-276, 2020.
5. T.A. Sarraf et al, Gait & Posture, 39(1):258-264, 2014.

Acknowledgements

EVALUATION OF OPTIMAL PROCEDURES FOR MEDICAL STAFF HANDLING WITH PATIENTS IN NURSING CARE

Zdenek Horak (1), Marie Docekalova (2), Petra Vrsecka (2), Miroslav Hanacek (3)

1. Department of Technical Studies, College of Polytechnics Jihlava, Czech Republic; 2. Department of Health Care Studies, College of Polytechnics Jihlava, Czech Republic; 3. Department of Mathematics, College of Polytechnics Jihlava, Czech Republic

Introduction

The aim of the project was to experimentally measure a load of selected muscle groups on the body of medical staff when handling patients in nursing care in bed. Based on the identified parameters, optimal procedures were designed for medical staff in handled patients in bed so that the physical loading on staff is as low as possible [1,2,3]. Several procedures have been experimentally analyzed to safely lift a lying patient into a sitting position.

Materials and Method

The aim of the project was to experimentally measure the selected muscle groups loading on the body of volunteers who simulated the handling of a patient in bed. Two basic situations were analyzed; the first was lay handling, the second was professional handling according to recommended procedures in nursing. Experimental measurements were realized on volunteers who were instructed to perform which tasks. The volunteer representing the lying patient was utterly passive. The medical staff was instructed on the various methods of handling, which they first tested before their measurement.

Figure 1: Demonstration of the analyzed professional handling of medical staff when lifting a patient from lying down to sitting.

The Qualisys system with 14 IR cameras was used for experimental measurements. The frequency of capturing the movement of the markers by the cameras was 25 Hz. At the same time, sensors measuring the magnitude of muscle intensity using EMG were fixed to the monitored muscle groups of volunteers. Three muscle groups were selected to analyze: straight abdominal muscles left and right, quadriceps femoris left and right, and paravertebral muscles left and right.

Results

The realized experimental measurements obtained complete information on the kinematics (trajectory, speed, and acceleration) of individual segments of the volunteers' bodies. The activation value in individual muscles was measured on selected muscle groups using EMG. The measured values were related to the maximum value of the isometric contraction of muscle so that the magnitude of the muscle activation was standardized. These values were then compared for different types of patient handling. The handling that showed the smallest amount of muscle activity for the shortest possible time was chosen as optimal.
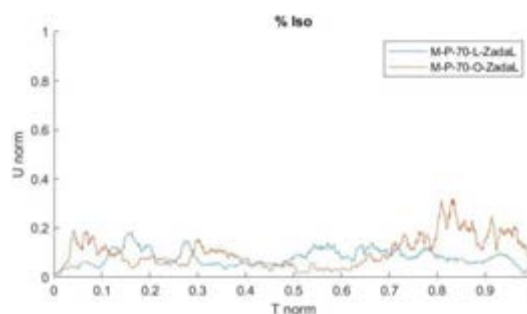
Figure 2: The medical staff demonstrated paravertebral muscle activity (left side) when handling the lying patient to sitting. The blue line is a layman's, and the orange color is a professional design.

Discussion and Conclusion

Based on the realized experimental measurements, the procedure of handling with the lying patient was set so that the selected muscle groups of the medical staff were loaded as low as possible. The measurements were realized on a relatively small group of volunteers (n=5); however, the obtained results have the same trends for each. Therefore it was possible to determine a suitable procedure for patient handling.

References

1. Garzillo et al, Int J Environ Res Public Health, 17:4971, 2020.
2. Hegewald et al, Int J Environ Res Public Health, 15:476, 2018.
3. Koshy et al, J Family Med Prim Care, 9:1397-1402, 2020.

DIABETIC SHOE UPPER PRESSURES: RESULTS OF A PROOF CONCEPT

Sara Lopes (1), Pedro Martins (2), Carolina Silva (3), Arcelina Marques (4), Lino Figueiredo (5)

1. CIETI, ISEP - P. Porto, Portugal; 2. CIETI, ISEP – P. Porto, Portugal; 3. CIETI, ISEP - P. Porto, Portugal; 4. CIETI, ISEP - P. Porto, Portugal; 5. GECAD, ISEP - P. Porto, Portugal

Introduction

The development of peripheral neuropathy, peripheral vascular disease, loss of skin sensitivity and plantar overpressure leads people with diabetes to an increased risk of developing foot ulceration. Foot ulceration in diabetics can cause some form of amputation, either of just a few toes or even the entire foot [1]. One of the factors that leads to ulceration is frequent and repetitive high pressure in the same areas of the foot. The constant monitoring of pressures in high-risk ulceration areas is critical to prevent their formation. Nowadays there are several commercial systems to monitor in-shoe plantar pressures as well as measuring motion characteristics. At the same time, plantar in-shoe pressures monitoring is also an extensively explored topic in scientific literature [2]. Although with a lower prevalence, in-shoe upper pressures are also a concern mainly due to the lack of scientific evidence to establish ulceration thresholds, in a similar way as done for plantar pressures [1].

In this paper, we describe some results obtained with a system developed to monitor plantar and upper pressures incorporated in a shoe specifically built for diabetic patients.

Methods

The system developed to monitor foot pressures (upper and plantar) was defined considering the critical locations for foot ulceration, as defined in literature, which will be the sensors positions. The adopted technology was based on Force-Sensitive Resistors (FSR) sensors and the data acquisition system was based on an ESP32 development kit. Plantar pressures measurements were achieved selecting 8 specific sensors from a commercial pressure insole. Upper pressures were measured with 4 FSR (FSR 402, Interlink Electronics) sensors integrated in the upper shoe, as indicated in Figure 1.
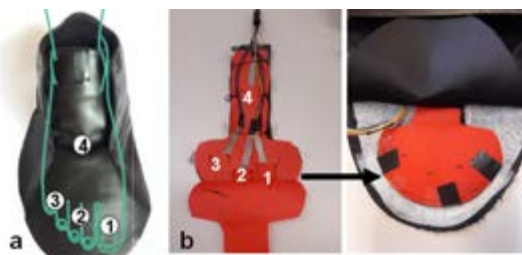
Figure 1: FSR location (a) and FSR inside a textile to attach in the upper shoe (b).

With both sensing layers integrated inside the shoe, the chosen testing procedure was based on the same participant walking approximately 20 meters in a flat surface, with the instrumented shoe in the right foot, during several gait trials. The obtained data was sent to a PC application.

Results

The gait was characterized by a total of 18 right steps, with a gait cycle of 1,03 s and a cadence of 116,8 steps per minute. The results obtained allowed us to plot the graph in Figure 2, which shows the sum of plantar and upper pressures during gait. The average maximum values for plantar and upper pressures are 363±29,5 kPa and 51,1±17,1 kPa, respectively, representing a ratio upper/plantar pressure of 14%. The maximum values for each dorsal sensor are presented in Table 1. The upper pressure average minimum values were 10,1±8,1 kPa.
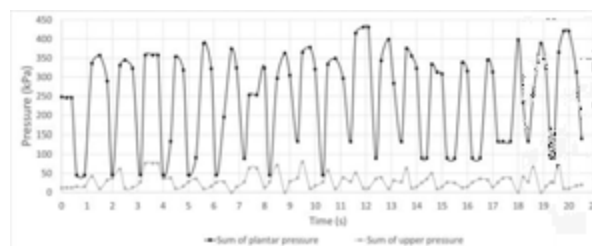
Figure 2: Sum of plantar pressures (8 sensors) and sum of upper shoe pressures (4 sensors) during gait.

	S1	S2	S3	S4
Pressure (kPa)	35,6	30,4	17,6	21,2

Table 1: Maximum pressure detected in upper sensors.

Discussion

From the analysis of Figure 2, we can verify that a maximum of the summed pressures in the dorsal area of the foot precedes the maximum of the summed pressures in the plantar zone, while the minima occur at the same instant as the plantar maxima. The upper pressure values obtained are according to the other authors [3].

References

1. N. Schaper et al., "Practical Guidelines on the prevention and management of diabetic foot disease (IWGDF 2019 update)," *Diabetes Met. Res. Rev.*, 36 (e3266): 1–10, 2020.
2. S. Ahmed et al, "Footwear and insole design features that reduce neuropathic plantar forefoot ulcer risk in people with diabetes: a systematic literature review," *J. Foot Ankle Res.*, 13 (30): 1–13, 2020.
3. A. Herbaut et al., "A reliable measure of footwear upper comfort enabled by an innovative sock equipped with textile pressure sensors", Ergonomics, 59 (10): 1327–1334, 2016.

ON THE PERFORMANCE OF CABLE-DRIVEN MOBILE LOWER LIMB REHABILITATION EXOSKELETON: THREE VERSUS FOUR CABLES

Rajan Prasad (1), Kinda Khalaf (1), Mohammed Awad (1), Irfan Hussain (1), H.F. Jelinek (1), Umer Huzaifa (2), and Marwan El Rich (1)

1. Khalifa University, United Arab Emirates; 2. DePaul University, United States of America

Introduction

Link-based lower limb exoskeletons tend to be heavy, mostly use direct actuation (placing actuator directly at the joint), and thus result in inertial vibration due to induced inertia. Actuating joints via cable can overcome these problems. Furthermore, the exact alignment of the joint with the actuator end is no longer required [1]. However, the cables can be routed in various ways. In this study, we compare the performance of three cable and four cable-driven exoskeletons.

Methodology

A generalized framework for the assessment of cable-driven exoskeleton has been proposed in our recent study [2]. The framework assumes limb as rigid links of equivalent masses and inertias. The reference healthy Gait data is taken from the Fukuchi et al. dataset [3] with a time of 3.5 seconds. Different possible configurations of 3 and 4 cables are selected for analysis (shown in Figure 1).

Case 1 **Case 2** **Case 3** **Case 4**
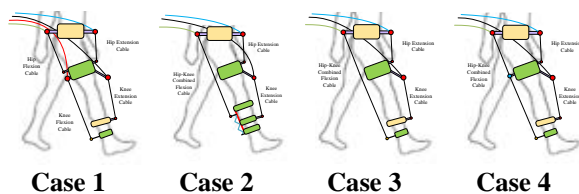
Figure 1. Three and four cable-driven models [Case 1: 4 Cable configuration, Case 2: 3 Cable with spring attached to the long cable at shank cuff, Case 3: 3 Cable configuration, Case 4: 3 Cable with long cable routed via the thigh cuff]

The maximum and minimum allowable cable tension is set to **100N** and **7N** to ensure the tension is within the desired range and always taut. The cable is driven using motors (assumed specification of **5 Nm** torque at **420 RPM** speed with pully of **5 cm** radius. The spring attached to the 3 cable configuration is allowed to slide along the shank with a spring and damping constant of **500N/m** and **10 N-s/m**. The models have been simulated for two Gait Cycles.

Result and Discussion

The trajectory in all the cases has successfully been tracked to the reference trajectory. Case 2 and 3 failed to meet the specified motor characteristics. Case 4 tracked the trajectory within specified motor characteristics, however, required higher cable tensions (in Figure 2) and induced much higher compressive force on the knee joint than 4 cables. Thus, the 4 cable-driven exoskeleton is a preferable design candidate for given motor constraints and exertion of compressive forces.
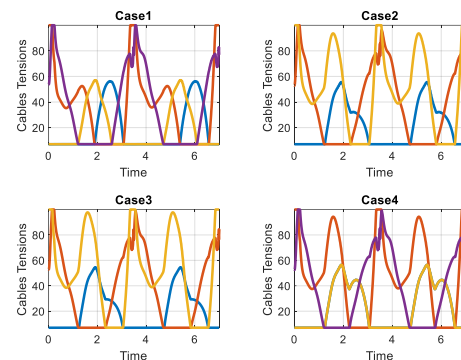
Figure 2. Cable Tensions in each case
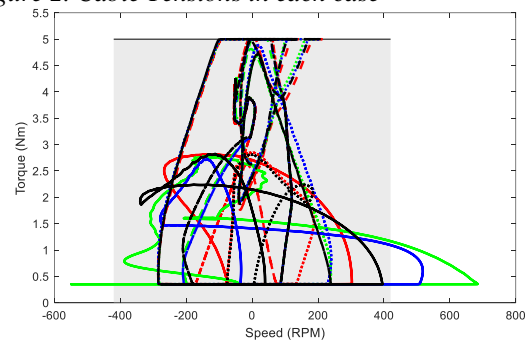
Figure 3. Required Motor Torque-Speed
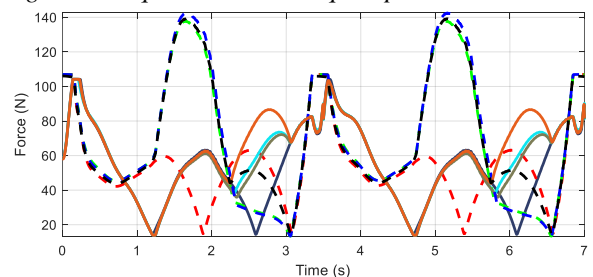
Figure 4. Compressive Force due to Cable on the Joints

In Figure 3 and 4, Red, Green, Blue, and Black represents cases 1 to 4 respectively. In Figure 3, the solid line, dashed line, dot line, and the dash-dotted line represents motors 1 to 4 respectively in each case. The shaded zone is the feasible zone for a given motor configuration. In Figure 4, the Solid and dash lines represent Hip and Knee joints respectively.

References

1. Grosu et al., *Front. Robot. AI*, 5:1–11, 2018
2. Rajan et al., ICBET 2022 (accepted)
3. Fukuchi et al., *PeerJ*, 6: e4640, 2018

PRECISION REHABILITATION: TARGETED ASSISTANCE OF INDIVIDUAL MUSCLES VIA EXOSKELETONS

Tiago Rodrigues (1), Jorge Ferreira (2), Herman van der Kooij (3), Massimo Sartori (3), Guillaume Durandau (3)

1. Department of Physics, *University of Aveiro, Portugal* 2. *Department of Mechanical Engineering, University of Aveiro, Portugal* 3. *Department of Biomechanical Engineering, University of Twente, The Netherlands*

Introduction

Exoskeletons are robotic devices that are coupled in parallel with a joint. Hope has been put in using exoskeleton for rehabilitation of patients after a neural or muscular injury. These injuries can affect groups of synergistic muscles or even individual muscles. Unfortunately, exoskeletons and their controllers are designed to assist at the joint level thus affecting the whole groups of muscles crossing the assisted joint. Being able to assist only a targeted muscle or a sub-group of muscle could open the way to precision rehabilitation using exoskeletons.

Method

We integrated a personalized real-time neuromusculoskeletal (NMS) model [1] with an ankle exoskeleton. In a previous study, we used the computed joint torque multiplied by a gain as a control command to the exoskeleton [2]. Since, in this study, we wanted to target individual muscle and not a joint complex, we approached that by directly using individual gain (G_m) for each computed muscle force (F_m) and then projected it at the joint level by multiplying it by the muscle moment arm (r_m) to compute the assistance torque (τ_a) (eq. 1).

$$\tau_a = (F_m \times G_m)r_m \qquad \text{(eq. 1)}$$

Two tests were conducted on one subject during walking (0.7 m/s) on a treadmill with an ankle exoskeleton. The first test consisted of using a fixed muscle gain (0 for the non-targeted muscles and positive gain for the targeted muscle). The second test consisted on finding a set of muscle gains (one different gains for all considered muscles in the NMS model) that reduce EMG level for a targeted muscle using an online optimizer. The CMAES optimizer was used and the averaged EMG changes in respect with pre-optimization level computed over 50 steps was used as the objectives function. The goal of both experiments was to reduce electromyograms (EMG) level of the targeted muscle while having the EMG of non-targeted muscle being kept at their level pre-assistance.

Results and Discussion
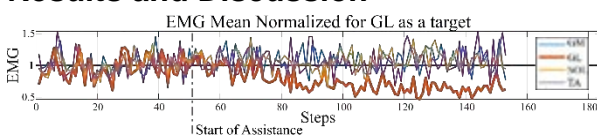
Figure1: EMG reduction for constant assistance (test 1) with the Gastrocnemius Lateral as a target.

Results showed that reduction of the Gastrocnemius Lateral (GL) EMG with minimal change on other muscles was possible. In Fig. 1, results for the first test showed that the basic concept of using individual gain for each muscle allows for the reduction of muscular control level (EMG) of individual muscle with minimal change in other muscles. What we can also see is that the effect on the targeted muscle is not immediate but take around 50 steps to adapt to the new assistive condition. In Fig. 2, results for the second test showed also the possibility to reduce EMG level on only one muscle using online optimization. At the end of the optimization, the assistance was turned to zero and interestingly, EMG level of almost all muscles did not return to their initial value pre-optimization.
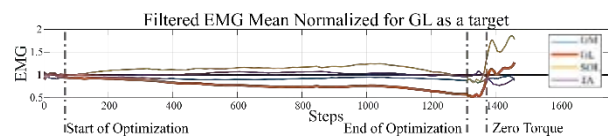
Figure 2: EMG reduction after optimization (test 2) with the Gastrocnemius Lateral as a target.

Those results are encouraging but tests on additional subjects need to be carried out to confirm those results. Effect on other muscle and combination of muscle also needs to be conducted. It was previously shown that the Triceps Surae muscles may have limited common drive [3], which show the possibility to work on other muscle of the ankle. A better understanding of how individual muscles adapt to external mechanical stimuli is also needed to better optimize the assistance, as seen in Fig. 1 quite a large number of steps are required for reduction of EMG level which makes the overall optimization process long. A better understanding of the effect of the optimization is also desirable to explain why muscle activation pattern does not return to their initial pre-optimization value. This may mean that the original objective of the optimization is attained but other undesirable effects (other than EMG level change) are also in play in other muscles.

References

[1] G. Durandau, et al, "Robust Real-Time Musculoskeletal Modeling driven by Electromyograms," *IEEE Trans. Biomed. Eng.*, 2017.

[2] G. Durandau, et al"Neuromechanical model-based control of bi-lateral ankle exoskeletons: biological joint torque and electromyogram reduction across walking conditions," *arXiv2108.00980*, 2021.

[3] F. Hug, et al, "Muscles from the same muscle group do not necessarily share common drive: evidence from the human triceps surae.," *J. Appl. Physiol.*, 2020.

A THUMS BASED MULTIBODY MODEL FOR DRIVING SIMULATIONS WITH SEAT INTERACTION

Michael Roller (1), Daniel Niklas Fahse (2), Monika Harant (1), Marius Obentheuer (1), Jörg Fehr (2), Joachim Linn (1)

1. Fraunhofer Institute for Industrial Mathematics (ITWM), Kaiserslautern, Germany;

2. Institute of Engineering and Computational Mechanics (ITM), University of Stuttgart, Germany

Introduction

To simulate the human driver in early stages of product development, digital human models (DHM) are widely used in automotive industry. Detailed finite element (FE) models of the human body are used to simulate the highly dynamic impact and resulting injuries in the human body in crash scenarios [1]. DHM based on multibody system (MBS) kinematics are widely applied in driver accessibility and ergonomic evaluation studies [2]. These types of models are only used in (quasi-)static scenarios, where the car is stationary or traveling at a constant speed. In dynamic driving maneuvers like cornering, sudden braking or lane change and pre-crash scenarios, neither FE nor simple MBS kinematic models are applicable. On one hand, FE models are comparatively difficult to control and the scenario durations are too long. Simulation times for dynamic driving maneuvers are in the range of seconds, while in crash simulations only milliseconds are computed. On the other hand, purely kinematic MBS models are not able to take dynamic loads and contact forces into account. Furthermore, the motion generation is complicated, because these models are usually based on forward or inverse kinematics.

Methods

In this work, we will present an approach for the enhancement of a multibody based DHM to generate human like motions for a dynamic driving simulation. The human is modelled as a multibody system, where the limbs are rigid bodies and connected via joints. As basis for this the bones of the FEM model THUMS [1] are used. The joint positions and orientations are adopted from the PIPER project [3]. This approach enables us to easily transfer results from the multibody simulation to the FE model and vice versa. An optimal control algorithm, which is able to handle opening and closing of contacts, is developed in order to generate the dynamic human motion. Joint torques are used to control the manikin. This approach has already been successfully applied to simulate dynamic motions of workers [4,5]. This approach is enhanced to be able to handle dynamic interaction with the car seat. Therefore, forces are introduced, which depend on the relative position and orientation of the bones of the multibody system and the seat. This force is based on pre calculated simulation with the THUMS model.

Figure 1: THUMS based MBS model with corresponding coordinate systems at the joints based on PIPER

Results

At the conference we will show first results of an easy sit in process. The manikin is falling into the seat and come to a resting position due to the interaction with the seat and its internal control. Figure 1 visualizes the DHM in start position.

Discussion

The approach presented in this work enables the use of data generated by FEM simulations in MBS. And vice versa the simulation results e.g. posture prediction of the active DHM model can be easily transferred to the THUMS model, due to the use of standardized coordinate systems from PIPER.

References

1. M. Iwamoto et al, Proceedings of the international IRCOBI Conference; 2002.
2. L Hanson et al, Elsevier; 2019. p. 115–124.
3. Piqueras-Lorente et al, IRC-18-31 IRCOBI conference 2018
4. S. Björkenstam et al, Journal of Computational and Nonlinear Dynamics. 2018;13(10):101001.
5. M. Roller et al, IFToMM World Congress on Mechanism and Machine Science. Springer; 2019. p. 26–33.

Acknowledgements

FINITE ELEMENT ANALYSIS OF MECHANICAL BEHAVIOR OF A JAW PLATE DURING THE IMPLANT BIODEGRADATION PROCESS

Pieter Ansoms (1), Mojtaba Barzegari (1), Liesbet Geris (1)

1. Biomechanics section, KU Leuven, Leuven, Belgium

Introduction

The mandible is the second most frequently fractured bone of the face, with common causes being violence, car crashes and sports [1]. The weakest section of the mandible is the angle because there is an abrupt change in direction between the body and ascending ramus in both the sagittal and transverse planes, resulting in the involvement of the mandibular angle in jaw fractures in up to 28.5% of cases. The treatment of a mandible fracture is traditionally done with a bioinert fracture fixation plate. However, biodegradable implant materials have significant advantages over bioinert ones when it comes to a need for second surgery, the occurrence of stress shielding and the presence of metal artifacts on medical images. While there are three popular biodegradable metals (Mg, Zn and Fe), the focus of this study was only on WE43 (Mg alloy) because it shows a suitable biodegradation rate to support the regeneration of bone [2]. When the biodegradation rate of the implant material is well adapted to the tissue regeneration rate, the healing process can be optimally supported while the tissue is gradually being exposed to an increasing portion of the loading. The specific type of fixation considered here is shown in Fig. 1. This is called the 'miniplate fixation technique', also known as 'semi-rigid' or 'functionally adequate fixation', and causes the plate to be under tensile loading when mastication forces are applied [1]. Fig. 1 also shows the jaw plate that was used in the simulation of the biodegradation and the mechanical behavior.
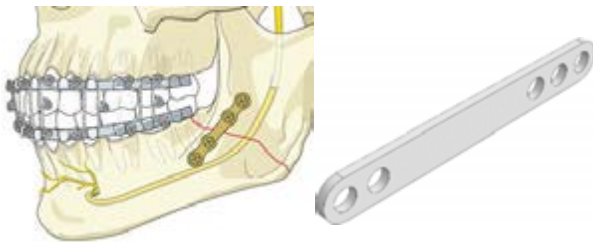
Figure 1: Miniplate fixation by AO Foundation (left) and model for the simulation of biodegradation and mechanical behavior (right)

Materials and Methods

The simulation of the biodegradation of the jaw plate was performed by Barzegari et al. [2]. Their model solved a set of partial differential equations derived from the chemistry of biodegradation, capturing the oxidation of the metallic part, changes in pH, and formation of a protective film on the surface of the implant, slowing down the rate of degradation. Moreover, to track the geometrical evolution of the implant over time and compute the mass loss, the model employed a Level Set formulation to capture the movement of the environment-implant interface. The output of the degradation simulation was then used as an input to the simulation of the mechanical behavior by performing tensile tests in a finite element environment on the jaw plate models with different amounts of biodegradation (Abaqus 6.11, Dassault Systèmes, USA). An explicit/dynamic type of analysis was used to allow for material failure to be modeled. The mechanical behavior of the plate was then compared to the loads occurring in the mandible during mastication. For this, a time-dependent estimation was made by applying beam theory to the mandibular body and the jaw plate. These calculations were performed in MATLAB 2020b (Mathworks, USA) and took into account the geometry changes over time of the jaw plate as a result of biodegradation and the changing material properties of the cortical and trabecular bone during the bone healing process. The magnitude and positioning of the mastication load, as well as the geometry of the mandible, were extracted from literature [3].

Results and Discussion

The results are shown in Fig. 2. The biodegradation rate was initially higher, but decreased to a constant as the protective film was formed. The strength of the jaw plate under tension decreased with the degradation of the implant material, but it remained higher than the tensile loading on the jaw plate for the simulated amount of time. It can therefore be concluded that the mechanical properties of the WE43 jaw plate sufficed in supporting the bone healing process of the mandible fracture.
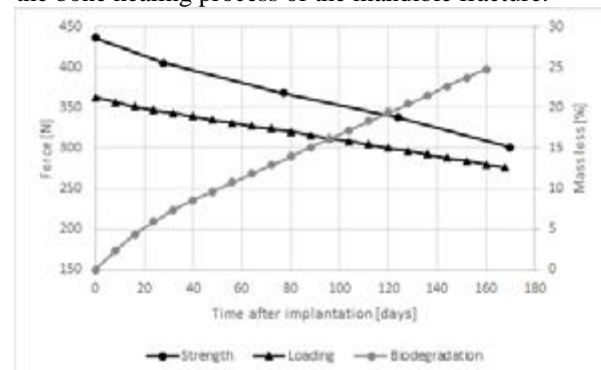
Figure 2: Results for the strength of, loading on and biodegradation of the jaw plate

References

1. Levy et al., AOHNS, 117:149-154, 1991
2. Barzegari et al., Corr. Sc., 190, 2021
3. Mansour, J. Orthod. Sc., 6:136-140, 2017

WHICH POSTERIOR SLOPE SHOULD BE USED WITHIN A MEDIAL STABILISED TKA DESIGNS: AN IN VITRO WEIGHT-BEARING KNEE RIG STUDY

Leandra Bauer, Christoph Thorwächter, Arnd Steinbrück, Volkmar Jansson, Hannes Traxler, Boris Holzapfel and Matthias Woiczinski

Department of Orthopaedics and Trauma Surgery, Musculoskeletal University Center Munich (MUM), University Hospital, LMU Munich

Introduction

Patient satisfaction after total knee arthroplasty (TKA) ends nowadays still with up to 20 % unsatisfied patients and implant position during operation influences the knee movement and therefore is one key factor for a natural knee movement and a satisfied patient. During implementation of TKA, the posterior tibial slope (PTS) is one of the most important factors to pay attention to. The PTS has an influence on the kinematics of the knee joint (1,2). The different design variants of the TKAs also imply an adaptation of the PTS due to the coupling degree. So far, there is hardly any literature with recommendations for the PTS in a medial stabilized (MS) prosthesis (3). The aim of the present study was to investigate the influence of different PTS on a prosthesis with MS design with respect to femorotibial kinematics.

Method

Seven fresh frozen human specimens were used and a MS prosthesis with 0°, 3° and 6° PTS were tested within the same cadaver for a direct comparison. After testing the 3° PTS, a custom-made plate was positioned under the inlay to compensate for the initial 3° PTS and thus represent a 0° PTS in the same specimen. Lastly, for another test, a plate was inserted that increased the initial 3° PTS by an additional 3° to produce a 6° PTS. After implantation, weight-bearing deep knee flexion (30-130°) with an experimental knee rig was performed and kinematics were analysed.

Result

All PTS resulted in femoral rollback. With a 3° PTS, the desired medial rotation point could be achieved better as with the other variants. With increasing PTS, the tibia was shifted more anterior on the lateral side. No difference according to the tibiarotation could be found for the different PTS variants. All PTS lead to an internal rotation of the tibia.

Discussion

The most important findings of the present study was that a 3° PTS showed the least deviation from the native situation and a desired medial rotation point compared to the different PTS variants especially in lower degrees of flexion. However, a continuous femoral rollback on the lateral site and tibial internal rotation were observed in all PTS variants for the medial stabilized TKA design. According to our findings, we recommend a PTS of 3° when implanting the MS prosthesis used in this study.
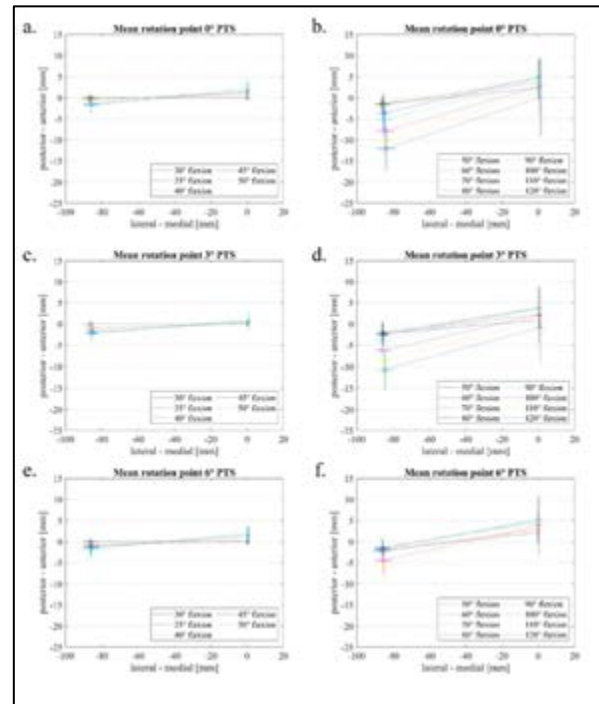
Figure 1: Mean values and vertikal/horizontal standard deviation of medial and lateral femoral condyle points for a. 0° PTS for 30-50° flexion, b. 0° PTS for 50-120° flexion, c. 3° PTS for 30-50° flexion, d. 3° PTS for 50-120° flexion, e. 6° PTS for 30-50° flexion, f. 6° PTS for 50-120° flexion

References

1. Kang KT, Koh YG, Son J, Kwon OR, Lee JS, Kwon SK (2017) Biomechanical Effects of Posterior Condylar Offset and Posterior Tibial Slope on Quadriceps Force and Joint Contact Forces in Posterior-Stabilized Total Knee Arthroplasty. Biomed Res Int 2017:4908639
2. Wittenberg S, Sentuerk U, Renner L, Weynandt C, Perka CF, Gwinner C (2020) [Importance of the tibial slope in knee arthroplasty]. Orthopade 49:10-17
3. Shi W, Jiang Y, Zhao X, Zhang H, Wang Y, Li T (2021) The influence of posterior tibial slope on the mid-term clinical effect of medial-pivot knee prosthesis. J Orthop Surg Res 16:563

APPROACH TO HUMAN JOINT ANALYSIS IMPLEMENTING ACCELEROMETERS FOR OUTDOOR MOTION STUDIES (1)

Jorge Andrés Hinojosa Virviescas (1), David Santiago Pulgarín Castañeda (1), Christian Cifuentes-De la Portilla Ph.D (1)

1.Biomechanics group (IBIOMECH), Department of biomedical engineering, Universidad de los Andes, Colombia.

Introduction

Currently, biomechanical studies implement expensive devices, technology, and specific places to realize different analysis. Therefore, people have limited access to these elements, reducing their interest in the opportunities and impact that these studies can have in their daily life [1]. This study aimed to develop an approach of a low-cost capture system to realize biomechanical analysis of human joints with the same precision as the conventional methods in outdoor activities.

Methods

The capture system was designed from elements of the Arduino system, such as: inertial sensors (MPU9250) and a microcontroller (ESP-32). Initially, this strategy was evaluated by using an artificial arm that allowed to simulate a human joint, such as the knee or elbow (Fig. 1B). It is important to mention that before using the sensors, it was necessary to perform a calibration, which was done using libraries of the Arduino software. The collected acceleration data were converted to angle using the formula shown in Figure 1A [2-3]. Different tests were performed, which consisted of raising the artificial arm to different amplitudes a certain number of times. The validation of the system was done by comparing the experimental data with those yielded by the XSens-dot and Kinovea system for the same tests.

Figure 1. Quantification method for the joint angle evaluation. **A)** Angle equation with the measured accelerations [2-3]. **B)** Experimental design of a joint with the sensors and their respective axis.

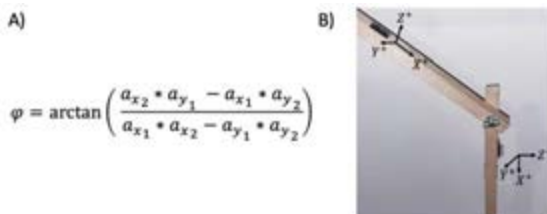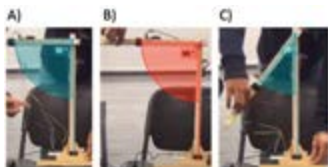$$\varphi = \arctan\left(\frac{a_{x_2} * a_{y_1} - a_{x_1} * a_{y_2}}{a_{x_1} * a_{x_2} - a_{y_1} * a_{y_2}}\right)$$

Results

Figure 2. Tests analysis performed in Kinovea. **A)** One arm rise until 90º. **B)** Three arm rises until 90º. **C)** Five arm rises increasing amplitude until 90º.

Figure 2 shows the analysis performed in Kinovea of the validation tests for system that was built. Furthermore, Figure 3 illustrates the graphic results of the validation tests. Herein, can be seen the similarity between the developed system and current methods that were selected as the point of comparison. Nonetheless, there is a displacement in time of the created system in comparison with the current methods. Finally, there is a reduced amount of data in the created system, making it more discontinuous that the other methods.
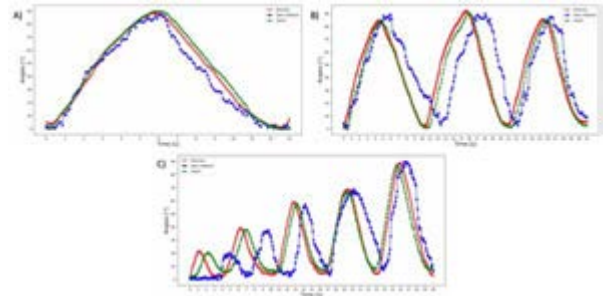
Figure 3. Results obtained for our method and its comparison with conventional methods. **A)** One arm rise until 90º. **B)** Three arm rises until 90º. **C)** Five arm rises increasing amplitude until 90º.

Discussion

The results obtained demonstrate that the low-cost system developed can deliver results similar to traditional methods used in the evaluation of motion analysis in indoor laboratories. Current methods are around thousands and even millions of dollars. In comparison, the cost of our system is less than one hundred dollars. This is a considerable reduce that will help the researchers that use the system developed in this study to perform biomechanical analysis and studies with a precision really close to current methods. There is not a quantitative comparison method since the recollected data is less than the current methods. The cause of this was that the sample rate was not established. Also, the proposed system has different problems related to the hardware, because it has a high sensor-microcontroller relation (1:1), that could be optimized but it will result in many issues related with the calibration of the sensors, causing errors in the raw data that will be recollected.

References

1. "What is the cost of motion capture for the physical therapy clinic?", 2019. [Online]. Available: https://www.eumotus.com/post/what-is-the-cost-of-motion-capture-for-the-physical-therapy-clinic.
2. Nwaizu, H., Saatchi, R., & Burke, D. (2016). Accelerometer based human joints' range of movement measurement. 2016 10th International Symposium on Communication Systems, Networks and Digital Signal Processing, CSNDSP 2016. https://doi.org/10.1109/CSNDSP.2016.7573970
3. S. Kurata, M. Makikawa, H. Kobayashi, A. Takahashi and R. Tokue, "Joint motion monitoring by accelerometers set at both near sides around the joint," Proceedings of the 20th Annual International Conference of the IEEE Engineering in Medicine and Biology Society. Vol.20 Biomedical Engineering Towards the Year 2000 and Beyond (Cat. No.98CH36286), 1998, pp. 1936-1939 vol.4, doi: 10.1109/IEMBS.1998.746978.

DESIGN OF AN *IN VIVO* BIOMECHANICAL CHARACTERISATION DEVICE FOR UNRUPTURED INTRACRANIAL ANEURYSMS: CALIBRATION STUDY ON PHANTOM ARTERIES

Guillaume Plet (1), Jolan Raviol (1), Hélène Magoariec (1), Cyril Pailler-Mattei (1,2)

1. Laboratoire de Tribologie et Dynamique des Systèmes, CNRS UMR 5513, Université de Lyon, Ecole Centrale de Lyon, France.
2. Université de Lyon, Université Claude Bernard Lyon 1, IPSB-Faculté de Pharmacie, France

Introduction

An intracranial aneurysm is an anatomical anomaly resulting from a residual and structural deformation of the wall of a cerebral artery. The estimated prevalence of unruptured intracranial aneurysm is 2-5 % in the world population [1]. Scores exist to assess the risk of rupture [2], but no quantitative information on the biomechanical state of the aneurysm wall is considered, a parameter that is yet predominant in the mechanisms of aneurysm rupture.

In this context, we have developed an original device to measure *in vivo* the mechanical behaviour of the aneurysmal wall and predict the risk of rupture. This work deals with the calibration of the device on polymeric phantoms, which is the necessary stage before testing on animal model.

Materials and Methods

Three saccular intracranial aneurysms phantoms representing a bifurcation of the circle of Willis were 3D-printed by stereolitography. For calibration purpose, dimensions of the phantoms were deliberately not biofidelic: the arteries have a diameter of 8 mm and a thickness of 600 μm, while the aneurysm has a diameter of 16 mm and a thickness of 400 μm. Concerning the mechanical stiffness, Young's modulus of phantoms is 1.57±0.13 MPa. The phantoms were fixed in a tank and a fluid flow of 500 ml/min was controlled using a pump as well as flowmeters at the artery inlet and at both outlets. The device, connected to a syringe pump, was then inserted into the aneurysm in order to stress the wall with physiological fluid at a flow rate between 0 and 150 ml/min.

The aneurysmal domes were speckled in order to use a stereo-correlation system allowing the collection of the displacements as well as the strains generated by the experimental probe. Acquisitions of 45 s at 3 Hz (135 images) were recorded with a load of 6 s (18 images) at 150 ml/min in order to observe the maximum strains and displacements generated by the device in the pulsation area.

Results and Discussion

For the three samples, we consider the point of pulse impact on the aneurysm wall, and we compare the repeatability for the strain norms obtained.

For the same aneurysm wall thickness and the same Young's modulus, the strains tensor norm are comparable and have been observed in Figure 1.
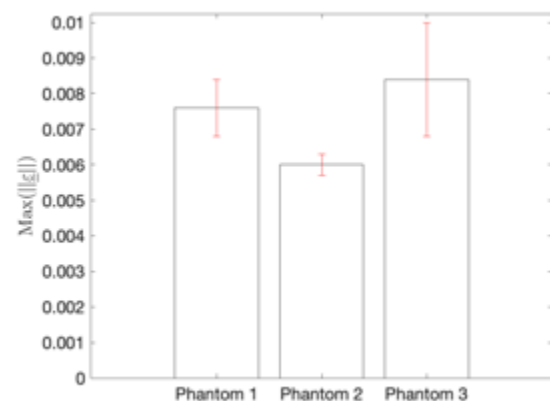
Figure 1: Strains tensor norm at the point of pulse impact on aneurysm wall on three printed polymeric phantoms.

Actually, for the Phantom 1, we obtained for the 6 s of pulsation a mean value of 0.0076±0.0008, for the Phantom 2 a mean value of 0.0060±0.0003 and for the Phantom 3 a mean value of 0.0084±0.0016.

Conclusion

On phantoms of significant elasticity, the strains generated by our stress device are repeatable and of the same order of magnitude. The differences can be caused by different parameters such as the printing resolution, the angle of solicitation of our system or the exact solicitation distance to the aneurysmal wall.

References

1. Rinkel GJ, Djibuti M, Algra A, Van Gijn J. Prevalence and risk of rupture of intracranial aneurysm: a systematic review. Stroke, 1998; 29:251-6.
2. Greving, J.P., Wermer, M.J.H., Brown, R.D., Morita, A., Juvela, S., Yonekura, M., Ishibashi, T., Torner, J.C., Nakayama, T., Rinkel, G.J.E., Algra, A., 2014. Development of the PHASES score for prediction of risk of rupture of intracranial aneurysms: a pooled analysis of six prospective cohort studies. The Lancet Neurology 13, 59–66.

Acknowledgements

A VISCOELASTOPLASTIC MODEL TO INTERPRET DENTAL CEMENTS RESPONSE TO A NANOINDENTATION TEST

Gianpaolo Serino (1,2), Alberto Audenino (1,2)

1. *Department of Mechanical and Aerospace Engineering (DIMEAS), Politecnico di Torino,Italy; 2. PolitoBIOMed Lab, Politecnico di Torino, Italy;*

Introduction

Nowadays employment of dental resins of different types has become a standard procedure. Providing a complete characterization of their mechanical behaviour is mandatory to improve their characteristics, design, and usage. In this study we applied the nanoindentation technique to obtain experimental data to be fitted. Then, a genetic algorithm combined with a gradient algorithm were applied to find the best set of the mechanical parameters that characterize the Burger model in series with a frictional element (figure 1), able to predict the nanoindentation process [1]. Furthermore, with this approach one type of test permits to obtain mechanical parameters useful to characterize the viscoelastoplastic response of these materials.
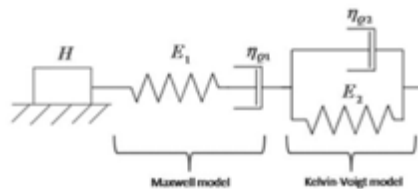
Figure 1: Lumped parameter system used to predict the viscoelastoplastic behavior of the analysed cements.

Materials and methods

Three different commercial cements were tested, i.e., two temporary cements Temp Bond and Telio C.S. and the Harvard cement, the permanent one. Cement samples were produced following the manufacturing guideline, embedded into epoxy resin, cut and, fine polished. All tests were performed with the Nanoindenter XP equipped with a diamond Berkovich indenter. The nanoindentation curves were characterized by a loading phase, and a holding phase of 5 s before the onset of the unloading phase. Different loading condition were explored imposing 4 values of strain rate: 0.5; 1: 5; 10 s^{-1} during the loading and unloading phase. The tests were performed in load control imposing a maximum load value of 10 mN. A total of 40 nanoindentation tests were performed for each cement and strain rate value. However, only few representative curves were analysed for each condition and cement.

A number of 15 sets of the initial parameters were randomly generated and, for each set an iterative application of a genetic algorithm and gradient minimization approach were applied. The convergence criteria were: (1) a value of the cost function lower than 0.0001 (2) or the number of iteration equal to 100. For each iteration 10^4 generation were created through the genetic algorithm refining then, the solution with a

gradient algorithm. As stated in the work of [2,3] only the loading and holding phase (where the contact area increases) ca be analysed.

Results

Representative results of the fitting procedure were reported in figure 2. Although the behaviour of the cement at the microscale strongly depends on the strain rate, as highlighted by the displacement registered during the loading and holding phase, the model was able to fit both the examined phases of the nanoindentation process.
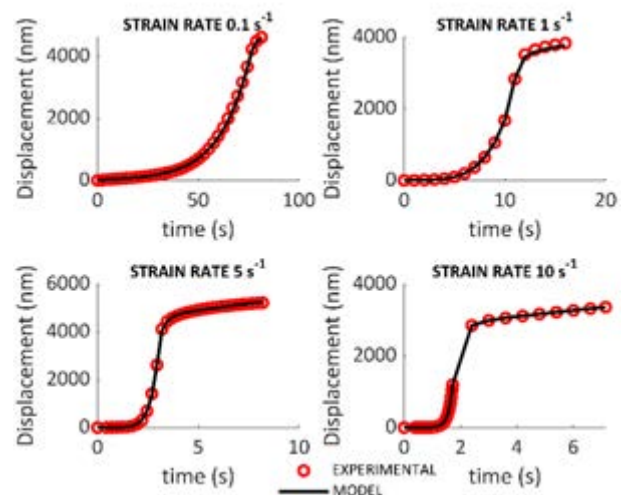
Figure 2: Representative curves of fitting process obtained for the Telio C.S. cement, imposing 4 values of strain rate

Discussion

Performing the tests with a constant strain rate, implied the use of an input loading curve that follows an exponential law over time, making it necessary to fit the experimental curves through a Burgers model [3] in series with a frictional element. Indeed, the elastic and viscous behaviour can be properly explained by the spring and dashpot in the maxwell model; whilst the Kelvin Voigt model and the frictional element take into account respectively the viscoelastic response and dissipative phenomena, related to the plasticization, of the cements.

References

1. L. Chien-Kuo et al, J. Appl. Phys. 100,033503 (2006)
2. J.R.M. Radok et al, Q.Appl. Math. 15,198 (1957)
3. E.H. Lee et al, ASME Trans. J. Appl. Mech. Mater. 30,438 (1960)

DEVELOPMENT AND VALIDATION OF CUSTOM-MADE MARKER SETS FOR MICRO-MOVEMENT ANALYSIS

Matthias Sukopp, Jonas Schwer, Luisa de Roy, Anita Ignatius, Andreas M. Seitz

Institute of Orthopaedic Research and Biomechanics, Trauma Research Center, Ulm University, Germany

Introduction

Marker-based 3D motion analysis are being used to study the human musculoskeletal system [1]. In theory, it is also possible to record and calculate smaller movements, such as those of implants or osteosynthesis material. Regardless of the application, special markers or rigid body marker sets are required for this, which are, unfortunately, only available in certain sizes. The aim of our study was to produce comparable marker sets for different applications and to validate them against commercially available marker sets. Such custom-made solutions would have clear advantages in terms of economic efficiency and quick and easy research-related adaptations to the respective test setups and specimens.

Methods

The customized marker, designed in a CAD (Creo Parametric, PTC) system, were manufactured on a fused deposition modeling 3D printer (i3 Mega, Anycubic). For comparison with a commercially available marker (ReferenceCom), a marker of similar dimensions (MarkerBig) and a smaller marker (MarkerSmall) were used. The reflective layer on the marker sphere was created in a novel customized dip-coating process. The MACH-1 (Biomomentum Inc) measuring machine with three translational stages (resolution accuracy: 0.1-0.5µm) was used for validation (*Figure 1*). To do so, two series of five consecutive cycles each between 0 and 10mm translation were performed in x and y direction. The accuracy (1) of the translation was evaluated according to Stüssi and Müller [2]. An OptiTrack system (NaturalPoint Inc) was used as 3D motion analysis system. The evaluation of the translation was performed in a self-developed MATLAB (The MathWorks, Inc) script.

$$\text{Accuracy } \alpha = \sqrt{\frac{1}{m-1} \sum_{i=1}^{m} (\bar{x}_i - \bar{x}_0)^2} \qquad (1)$$

With $\bar{x}_i$ average Optitrack values at gridpoint i and $\bar{x}_0$ average measuring machine values at gridpoint i, m represents the number of datapoint plateaus.

Results

Accuracy evaluation was performed in two translation planes *(Figure 1, C)*. In the x-direction, the small marker obtained an accuracy of 2.54µm, the large one 5.01µm and the commercially available one 3.62µm. In the y-direction, on the other hand, the accuracies were slightly lower, with 14.34µm for the small marker, 23.92µm for the large marker and 7.92µm for the original marker *(Figure 2)*.
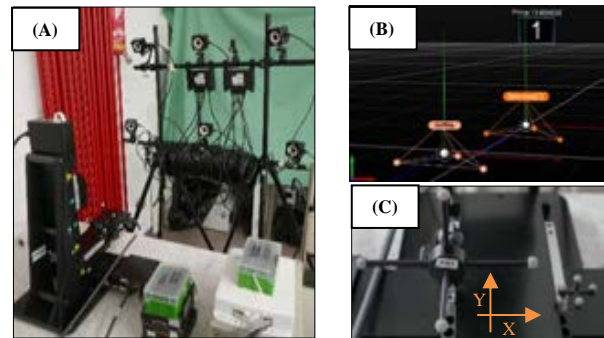
Figure 1: (A) Test setup with 3D motion analysis system and adapted markers on the measuring machine. (B) Recording from the analysis software. (C) Commercially rigid body marker set (KS1, left) and a small custom-made rigid body marker set (right).
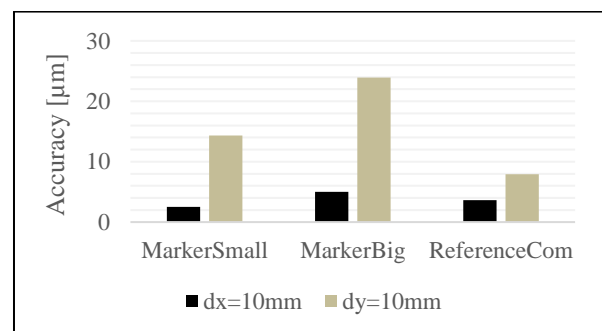
Figure 2: Accuracy analysis comparing three different rigid body marker sets in x/y-direction with 10mm displacement.

Discussion

The results of our study suggest that custom-made, accurate marker sets can be quickly and easily produced with conventional 3D printer. Further, with the here introduced rigid body marker sets, it is possible to adapt them to specific specimens' sizes without influencing them by their own weight and moment of inertia. This could be used, for example, to track and evaluate the position and orientation (six degrees of freedom) of bone fragments as rigid body elements within a fracture. The accuracy of the customized marker sets shows promising results comparing to commercially available marker sets. However, further studies are required to check also the accuracy of the markers along the rotational axes.

References

1. Windolf et al., J Biomech 2776-2780, 2008.
2. Stüssi and Müller, Int. Symposium, Berlin, 1990

IN VITRO OVINE MODEL CONFIRMS IMPORTANCE OF SCREW POSITIONING FOR STABILITY OF BONE-FRACTURE TREATMENT

Thomas Zumbrunn (1), Simon Comtesse (1), Arvind von Keudell (2), Stephen J. Ferguson (1)

1. Institute for Biomechanics, ETH Zurich, Switzerland; 2. Department of Orthopaedic Geriatric Trauma Surgery and Research, Brigham and Women's Hospital, Harvard Medical School, Boston, MA, USA

Introduction

The stability of bone reconstructions following joint fractures is critical in recreating appropriate articular surfaces for a well-functioning joint. It is often unclear how screws and implants shall be positioned for a specific case and outcomes heavily depend on the surgeon's experience.

Knowing the effects of screw positioning on construct stability is expected to be beneficial for achieving bone union and recreation of stable joint articulation.

Our hypothesis is that the stability of bone fractures depends on various patient factors, including specific fracture patterns and bone quality, and that individual screw positioning for each case is critical to achieve a stable reconstruction of bone and joint.

Methods

6 fresh ovine tibias were harvested, and systematic bone cuts were applied, representing a common fracture pattern. Specifically, a unilateral shear fracture of the medial tibia plateau was imitated (**Figure 1**). All specimens were reconstructed with 3 titanium screws (⌀3.5 mm). In 3 specimens the screws were positioned perpendicular to the outer bone surface and in the other 3 specimens the screws were positioned perpendicular to the cut surface of the bone fragment.

Figure 1: Setup of biomechanical testing, including an ovine tibia cemented in a PMMA potting and load application through a mechanical testing machine.

Each bone was cemented with PMMA into a fixture for testing with a mechanical testing machine, using a 10 kN load cell (Instron E10,000; Instron, Norwood, MA, USA), (**Figure 1**). Each specimen was preconditioned with cyclic loading at 2 Hz between 10 N and 50 N, followed by quasi-static load increase until failure of the sample (0.06 mm/s) [1]. At 375 N and 750 N the load was held for 10 s, allowing for specimen evaluation.

Results

Our findings showed that the displacement of loaded bone fragments for a given force is variable depending on the screw positioning, as well as between specimens.

Load \ Screws	Bone-oriented	Cut-oriented
375 N	0.6 - 1.3 mm	0.5 - 1.4 mm
750 N	1.5 - 2.8 mm	1.5 - 3.1 mm

Table 1: Displacement range of 2 load & screw options.

This resulted in a variation of construct stiffness and further, differences in the linear (elastic) force-displacement region (**Figure 2**).
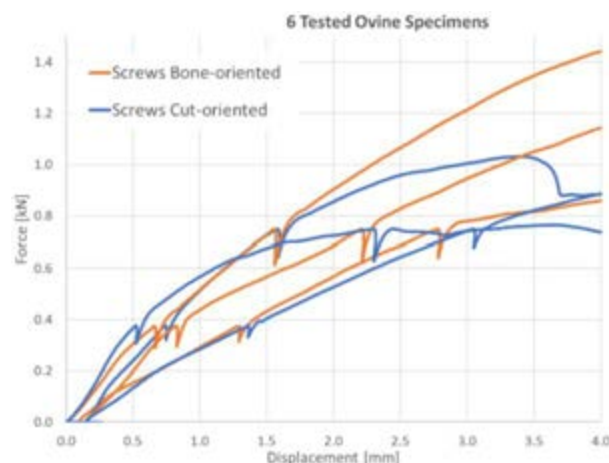
Figure 2: Force-displacement curves of 6 ovine tibia reconstructions under mechanical loading, with two fixation methods (orange: screws perpendicular to bone surface vs. blue: perpendicular to cut surface).

Discussion

Considering the goal to achieve maximum stability in the treatment of joint fractures, displacements beyond 4 mm were considered irrelevant. The displacement of the reconstruction with the lowest stiffness was increased up to 3-fold over that of the highest construct stiffness.

Based on this pilot study, we suggest that achieving biomechanical stability of bone reconstructions is case-dependent with a substantial effect of screw positioning.

References

1. Steiner et al, J Orthop Res, 36(3):954-962, 2018

Acknowledgements

POROSITY AND MATRIX MINERAL CONTENT DETERMINE THE VARIATION OF COMPRESSION STRENGTH OF CORTICAL BONE FROM ELDERLY DONORS

Xiran Cai (1,2), Fan Fan (1,3), Hélène Follet (4), Françoise Peyrin (5), Haijun Niu (3)
Quentin Grimal (1)

1. Sorbonne Université, INSERM UMR-S 1146, CNRS UMR 7371, Laboratoire d'Imagerie Biomédicale, F-75006, Paris, France; 2. School of Information Science and Technology, ShanghaiTech University, 201210, Shanghai, China; 3. Beijing Advanced Innovation Center for Biomedical Engineering, School of Biological Science and Medical Engineering, Beihang University, 100083, Beijing, China; 4. Univ Lyon, Université Claude Bernard Lyon 1, INSERM, LYOS UMR 1033, F-69008, Lyon, France; 5. Univ Lyon, INSA-Lyon, Université Claude Bernard Lyon 1, UJM-Saint Etienne, CNRS, Inserm, CREATIS UMR 5220, U1206, F-69621, Lyon, France

Introduction

Cortical bone strenght is multifactorial [1], in principle depending on composition (mineral, proteins) and microstructure. The relative importance of these different factors is not fully elucidated, in part because of the limited precision of the methods of characterization and the limited availability of bone specimens. In this communication, we report experiments conducted on cortical bone samples to evaluate compression strength, anisotropic elastic properties, microstructure, and composition. The objective was to elucidate the main factors determining strength variations among the different specimens. The relationships between elastic properties, microstructure and composition for the same specimens were previously reported in [2].

Method

We used femur bones from 29 human donors (16 women, 13 men, mean age (SD) 77.8 (11,4)). Specimens of nominal size 3×4×5mm³ obtained from the mid-diaphysis underwent uniaxial compression until failure at a strain rate of 0.1/s, immersed in saline at 37 °C, to assess maximal stress (strength). Before mechanical testing, the vascular porosity network and mineral content were assessed from X-ray computed tomography images with isotropic voxel size of 6.5 µm performed at the European Synchrotron Radiation Facility (ESRF, Grenoble, France). Fourier transformed infrared microspectroscopy (FTIRM) was used to quantify mineral-to-organic phase ratio, mineral maturity, crystallinity, and collagen maturity. Cross-links were quantified from biochemistry. Anisotropic (transversely isotropic) elastic properties were obtained with resonant ultrasound spectroscopy (RUS). Multivariate regression analysis was conducted to determine the factors explaining the variation of strength. Micro-finite element simulations based on the 3D images were also conducted with FAIM (v7.1, Numerics88 Solutions, Calgary, Canada).

Results

Measured strengh varied between about 80 and 180 MPa, porosity between 2 and 20%, and mineral content between 0.95 and 1.07 g/cm³. Porosity was the major determinant of stength (R^2=0.42), and mineral content explained a small part of the variation in addition to porosity (adj-R^2=0.45 for the two parameter model). The variation of the other parameters were not or weaky associated to variations of strength. Micro-finite element simulations based on the 3D images were also conducted, which confirm the major effect of porosity on strength as observed experimentally.

Discussion

The results are in line with previous studies pointing at the major role of porosity variations [1,3] in cortical bone strength variations, and the minor role of material composition. Data was obtained from elderly donors without documented bone pathology. This study provides data at the material level to interpret the variations of macroscopic bone resistance and fracture susceptibility.

References

1. Mirzaali et al., Bone 93:196–211, 2016.
2. Cai et al., Acta Biomater. 90, 254–266, 2019
3. Peralta et al. Ultrasound Med Biol 47(3):799-808, 2021.

Acknowledgements

A BONE CELL POPULATION MODEL DESCRIBING INTERMITTENT ACTIVATION OF BMUS BASED ON CELL AVAILABILITY

J.L. Calvo-Gallego (1), P. Manchado-Morales (1), P. Pivonka (2), J. Martínez-Reina (1)

1. Departamento de Ingeniería Mecánica y Fabricación, Universidad de Sevilla, Seville 41092, Spain;

2. School of Mechanical, Medical and Process Eng, Queensland University of Technology, Australia

Introduction

Bone cell population models (BCPM) simulate the process of bone remodelling by considering cell concentrations and biochemical factors (see Fig. 1). However, BCPMs are continuous in time and do not account for the spatio-temporal nature of the remodeling process, with the latter occuring intermittently and sequentially, through so-called BMUs (Basic Multicellular Units). BMU remodelling follows: activation - resorption - inversion - formation - quiescence. In this work, a previously proposed BCPM [1] has been formulated into a spatio-temporal model of intermittent BMU activation. This model is implemented into a Finite Element (FE) code and interactions between BMUs are taken into account.
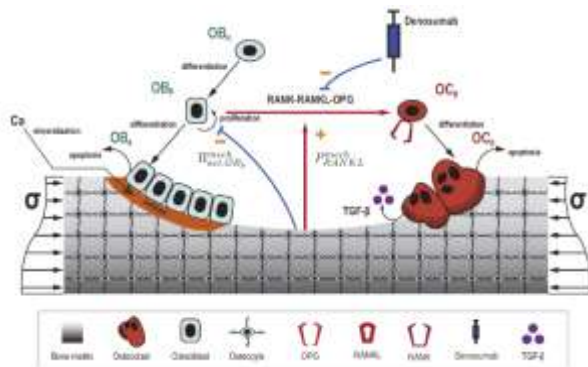
Figure. 1: BCPM [1] basis of the proposed model.

Methods

The new model takes into account the same cell populations and signalling factors as the BCPM (Fig. 1), but is based on the assumption that differentiation of precursors into mature cells can only take place when sufficient precursor cells are available (i.e. differentiation occurs when the precursor concentration exceeds an upper threshold and stops when the concentration falls below a lower threshold). This new model accounts for the lag between resorption and formation processes via TGF-β released from bone matrix during osteoclastic resorption. TGF-β upregulates apoptosis of osteoclasts, promotes the differentiation of pre-osteoblasts, which start to accumulate until the upper threshold is exceeded, when they differentiate into active osteoblasts. Thus, the lag between resorption and formation appears naturally in the new spatio-temporal model of BMU remodelling.
Another important aspect is that remodelling does not occur locally and independently in a bone region, but is affected by its neighborhood (a sphere of radius R).

Thus, for a BMU to be activated at a point, 3 conditions must be met: 1) the population of osteoclast precursors must exceed the activation threshold; 2) this is the point of the neighborhood with the maximum concentration of precursors; 3) there is no other already active BMU, within the neighborhood.

Results and discussion

Fig 2 shows the temporal evolution (in days) of resorbed and formed bone volume in one element. Resorption (red) and formation (blue) occur separately, with the former being very fast, while formation is slow.
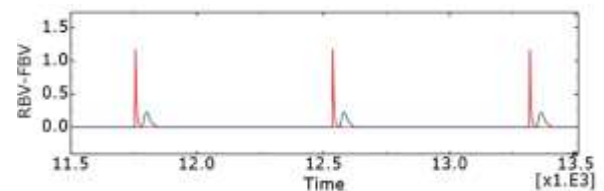
Figure 2: Resorbed (red) and formed (blue) bone volume in an element subjected to uniaxial tensile stress.

The average lengths of the resorption, inversion and formation phases are shown in the following table and compared with the literature [2]. The activation frequency of BMUs is 0.05 BMUs/mm^3/day, identical to that measured in [3].

Phase	Model	Literature [2]
Resorption	22.9	24
Inversion	7.5	8
Formation	63.0	64

Table 1: Average lengths of the phases in days.

Conclusion

A previous BCPM has been adapted to simulate spatio-temporal BMU remodelling. The role of TGF-β has been shown to play a key role in regulating the lag between the resorption and formation phases.

References

1. Martínez-Reina J., Calvo-Gallego J.L. and Pivonka P., Front. Bioeng. Biotechnol, 9: 635056, 2021.
2. Hazelwood S. et al., J. Biomech, 34(3): 299-308, 2001.
3. Frost, H.M. Ed. Charles C Thomas, 1969

Acknowledgements

ASSESSING BONE ULTRASTRUCTURE VIA NANOSCALE X-RAY COMPUTED TOMOGRAPHY AND QUANTITATIVE POLARIZED RAMAN SPECTROSCOPY

**Tatiana Kochetkova (1), Tatiana Kormilina (2), Silvan Englisch (2),
Dominik Drobek (2), Janis Wirth (2), Benjamin Apeleo Zubiri (2),
Oliver Braun (1), Michel Calame (1), Stefan Remund (3), Beat Neuenschwander (3),
Johann Michler (1), Philippe Zysset (4), Erdmann Spiecker (2), Jakob Schwiedrzik (1)**

1. Empa, Swiss Federal Laboratories for Materials Science and Technology, Switzerland; 2. Institute of Micro- and Nanostructure Research (IMN) and Center for Nanoanalysis and Electron Microscopy (CENEM), IZNF, Friedrich-Alexander-Universität Erlangen-Nürnberg, Germany; 3. Institute for Applied Laser, Photonics and Surface technologies (ALPS), Bern University of Applied Sciences, Switzerland; 4. ARTORG Center for Biomedical Engineering Research, University of Bern, Switzerland

Introduction

Bone is a biological hierarchical nanocomposite, combining toughness and strength with a low weight. Similar to other complex composites, the hierarchical organization of mineralized tissues affects drastically their mechanical performance across different scales. The elementary building block of bone at the microscale consists of arrays of parallel mineralized collagen fibrils (MCFs, each 10-300 nm in diameter) embedded in an extrafibrillar matrix. Human cortical bone exhibits a complex structural arrangement of MCF that may be affected by metabolic bone conditions like osteogenesis imperfecta or Paget's disease.

In this study, we explored the capabilities of nano X-ray computed tomography (nano-CT) and quantitative polarized Raman spectroscopy (qPRS) for the correlative structural and compositional analysis of bone.

Materials and Methods

A cortical bone sample was extracted from the femoral neck part of a 52 y.o. female donor with no reported metabolic bone diseases. Four freestanding bone micropillars (~25 µm diameter, ~55 µm height) were fabricated using femtosecond laser ablation (Fig. 1). The recently developed qPRS method [1] allowed us to collect data on the bone composition and MCFs spatial orientation ~5 µm underneath the pillar surface with a spatial resolution of ~$(0.3 \ \mu m)^3$. Laboratory X-ray Zernike phase-contrast tilt series were collected from selected volumes of interest up to 20 µm underneath the surface with an enhanced 3D resolution of ~$(53 \ nm)^3$. The quantitative local orientation of MCFs was estimated after 3D reconstruction and segmentation using Arivis Vision4D with machine learning algorithms.
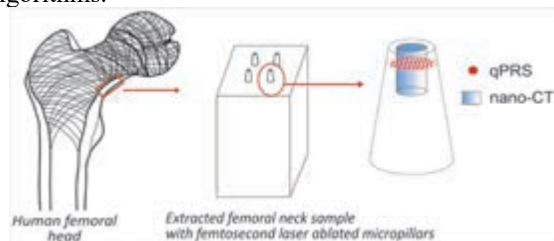
Figure 1: Sample geometry and location of the qPRS and nano-CT measurements.

Results and Discussion

Volumes of interest were located in both osteonal and interstitial zones of cortical bone, as was checked with the light microscope images before laser ablation. According to the nano-CT scans, osteonal bone zones exhibited higher directionality of the lacuno-canalicular network (LCN) in comparison to the interstitial zones. However, MCFs appear to have a consistent orientation within the interstitial zones (Fig. 2 A). For the volume of interest in the osteonal zone, a clear lamellar-interlamellar interface was observed with a ~3 µm step (Fig. 2 B). Within the intersecting volumes of the qPRS and nano-CT measurements [2], the out-of-plane MCFs angle discrepancy between the methods was close to the error of the qPRS (RMSE = 13°).
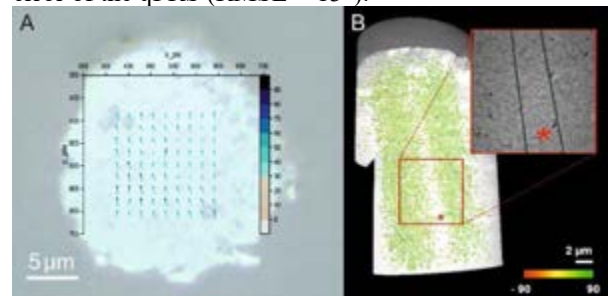
Figure 2: A: qPRS map collected atop the interstitial bone with marked MCF orientations; B: nano-CT scan with MCF segmentation of osteonal bone volume with the distinct interlamellar region (*) (adapted from [2]).

Hereby, we were able to resolve the ultrastructural organization of bone at the level of MCF bundles at a spatial resolution approaching the one of synchrotron CT. The gained information was consistent between the two techniques and may be used to identify novel bone quality biomarkers for clinics, improving bone fracture risk assessment in patients in the future.

References

1. Kochetkova et al., *Acta Biomater.* 119, 390-404, 2020
2. Kormilina et al., *Microsc. Microanal.* 27 (Suppl 1), 2021

Acknowledgements

PRELIMINARY INVERSE ANALYSIS FOR CRACK PROPAGATION MECHANICAL PARAMETERS ON LONG HUMAN CORTICAL BONE

Théophile Kurtz (1), Jean-Louis Tailhan (2), Yves Godio-Raboutet (1)
1. Aix Marseille Univ, Univ Gustave Eiffel, LBA, Marseille, France;

2. Gustave Eiffel University MAST-EMGCU, France.

Introduction

The following paper details the study performed to determine mechanical parameters relative to a transversal crack propagation in mode I in human femoral cortical bone via inverse analysis. In a previous work [1], an experimental test was designed to propagate a macrocrack in notched segments of femur. Results have demonstrated the prominent role of cracking in stiffness decrease and residual deformations. However, the material anisotropy strongly deviates the macrocrack orientation. Then, the test has been modified to avoid this effect and force a transversal propagation of the macrocrack. A complex but original methodology for post-processing the experimental results is developed and assessed. The first results obtained are presented and analyzed.

Methods

The experiment consists of a three-point bending performed on notched shaft segments of human femur (fig.1). The loading, applied with a hydraulic jack, is controlled indirectly by the Notch Opening Displacement (NOD) measured with an inductive sensor. A series of unloading/reloading cycles is performed to assess the effect of the cracking process at the structural level of the bone segment. A semispherical groove is milled on the external surface in the sample mid-section to ensure the macrocrack transversal propagation (fig.1). Experimental results are expressed in terms of curves load vs. NOD.

1. Impactor
2. Fixed support
3. Sliding support
4. Notch & Groove
5. Sensor
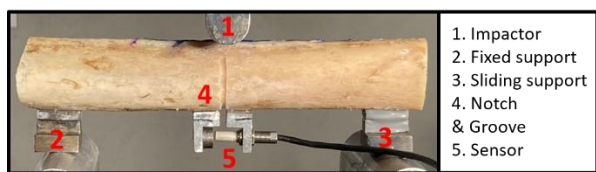
Figure 1: Three-point bending test.

A "realistic" Finite Element model of the experimental setup is performed coupling segmentation methods, 3D modelling and meshing tools. A first simulation is run in elasticity considering the value of the Young modulus E as the unknown and searching it to fit the experimental elastic behavior. In a second step, the compliance method is applied to estimate the critical energy release rate value G_{Ic}. Several elastic simulations with different lengths of a pre-existing equivalent macrocrack are again run. Comparing numerical simulations to mechanical test results allows the compliance calibration and the determination of the crack extension resistance curve [2].

Results

Typical bending test results are shown (fig.2a). The values of elastic moduli are for specimens *6121G and 15017D* respectively: 14628 MPa and 9380 MPa. The obtained R-curves are given (fig.2b).
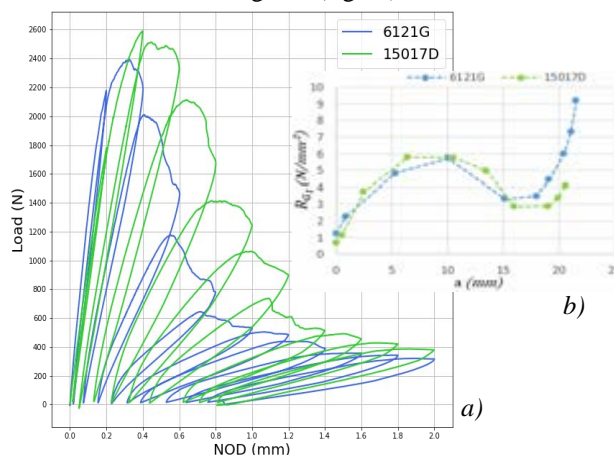
Figure 2: a) Load vs NOD curves, b) Crack extension resistance curves (R_{G_I} vs. crack length a)

Discussion

As a first observation, grooving the samples perfectly maintains the crack orientation in the transversal direction. The first half of R-curves (fig.2b) show a plateau, reached for crack lengths between 2.5 and 10mm. It corresponds to a crack propagation in the medial and lateral bone quadrants only. The corresponding values give the bones' toughness (G_{Ic}) in these zones (similar to values of the literature [3,4]). For longer cracks, sectional geometry and material microstructure variations as well as boundary conditions modify cracking processes, and significantly influence results, making any toughness assessment difficult in this area.

References

1. Tailhan J.-L. et al. (2021). Macrocrack propagation in a notched shaft segment of human long bone: experimental results and mechanical aspects. Journal of the Mechanical Behavior of Biomedical Materials (2021), in reviewing
2. Erdogan, F. (2000). Fracture Mechanics. Int. Journal of Solids and Structures (37):171-183.
3. Behiri, J. C., & Bonfield, W. (1980). Crack velocity dependence of longitudinal fracture in bone. Journal of Materials Science, 15(7), 1841-1849. https://doi.org/10.1007/BF00550605
4. Li S. et al. (2013). Analysis of fracture processes in cortical bone tissue. Engineering Fracture Mechanics.(110):448-458.

HYDROXYAPATITE CRYSTAL THICKNESS AND ORIENTATION AT THE BONE IMPLANT INTERFACE: SPATIAL AND TEMPORAL EVOLUTIONS

Sophie Le Cann (1), Elin Törnquist (2), Isabella Silva Barreto (2), Manon Fraulob (1), Mariana Verezhak (3), Manuel Guizar-Sicairos (3), Hugues Albini Lomani (1), Hanna Isaksson (2), Guillaume Haïat (1)

1. CNRS, MSME UMR CNRS 8208, France; 2. Department of Biomedical Engineering, Lund University, Sweden; 3. Swiss Light Source, Paul Scherrer Institut, Switzerland

Introduction

Bone structure is complex and evolves over time, especially during osseointegration, when bone forms around and onto an implant surface. Sufficient bone ingrowth together with adequate quality, depending on its compositional, structural and mechanical properties, will condition the long-term stability of the implant. The nanoscale arrangement and reorganization is of particular interest since a relationship between mineral crystals thickness and elastic properties of bone tissue has been observed [1]. Thus, characterizing crystal thickness around an implant may help to evaluate the mechanical properties of the interface. but only little work is available [2, 3]. We investigated spatial and temporal evolutions of crystal thickness and orientation close to a metallic implant using small angle x-ray scattering (SAXS); this work has been published [4].

Methods

Samples. Eight New Zealand male rabbits had their tibiae implanted with a standardized implant model (coin-shaped, titanium, Ø5mm, L3mm) composed of a flat interface and a chamber for bone to grow into (Fig. 1 top). After 7 (n=4) and 13 weeks (n=4) of healing time, the rabbits were euthanized and samples were embedded into PMMA, cut transversally and polished to ~100μm-thick slices to expose the interface.

Scanning SAXS was conducted at the cSAXS beamline, SLS, PSI, using a microfocus setup with x-ray energy of 12.4keV and 100ms exposure time. The whole ingrowth chamber and a mature bone region were mapped with a pixel size of 5μm and a step size of 5μm.

Data analysis was conducted using Matlab routines. Crystal thickness was calculated from the radial integration of scattering intensity (I(q)) profiles and orientation from the azimuthal integration (I(ψ)) using established protocols [4]. Thickness and orientation were averaged in 10μm-thick lines from the interface to investigate their spatial evolution.

Figure 1: Standardized implant model (top) and crystal thickness (T) mapping of newly formed bone after 7 and 13 weeks of osseointegration.

Results

Crystal are thinner in the bone chamber compared to mature regions (Table 1). Moreover, within the chamber, crystals are thinner after 7 compared to 13 weeks of healing time (Fig. 1) with a larger variation of the thicknesses at 13 weeks. Close to the implant surface, crystals are thinner and appear more aligned to the surface than further into the chamber.

T (nm)	Chamber	Mature
7w	1.79±0.45	2.52±0.31
13w	2.4±0.57	2.75±0.35

Table 1: Average crystal thickness (T) in nm of newly formed (chamber) and mature bone.

Discussion

Crystal thickness has been shown to be correlated to crystal volume [5] and can thus be used as a representative parameter of the evolution of the crystal size. The increased thickness with osseointegration is coherent with observed increase in bulk bone with maturation [1] and the larger spread of values at 13 weeks may reflect combined processes of bone ingrowth and bone remodeling, with both thin crystals being formed and large crystals being remodeled in more mature regions. Thinner crystals close to the interface confirm previous results [2], and could be linked to reduced mechanical loading, which is in agreement with our model. Further investigation on loaded interfaces and mechanical testing could help clarify if thick crystals at the interface are representative of higher strength. The tendency of crystals to align to the interface is consistent with previous results [3], but will be further investigated in the bone longitudinal direction, where fibers alignment is more pronounced.

References

1. Törnquist et al, J Bone Miner Metab., 1:1-10 2019
2. Bünger et al, European Cells and Materials, 12:81-91, 2006
3. Hoerth et al, J Mater Sci Mater Med; 25:411–422, 2014
4. Le Cann et al, Acta Biomater, 116 : 391-399, 2020
5. Turunen et al, J Structural Biology, 195:337-344, 2016

Acknowledgements

GRAFT POSITIONING DURING THE LATARJET PROCEDURE: COMPUTATIONAL ANALYSIS OF SHOULDER STABILITY AND CONTACT

Rita Martins (1), Carlos Quental (1), João Folgado (1), Ana Catarina Ângelo (2,3), Clara de Campos Azevedo (2,3)

1. IDMEC, Instituto Superior Técnico, Universidade de Lisboa, Portugal; 2. Hospital dos SAMS de Lisboa, Portugal; 3. Hospital CUF Tejo, Lisboa, Portugal

Introduction

When large glenoid bone defects exist, the Latarjet procedure is the recommended procedure for treating anterior shoulder instability. By transferring a section of the coracoid process to the anteroinferior side of the glenoid, this procedure contributes to anterior shoulder stability by three main stabilizing mechanisms: the graft acts as a bone block; the conjoint tendon acts as a sling; and the lowering of the subscapularis muscle makes it work as a hammock [1, 2].

One key factor affecting the efficacy of the Latarjet procedure is the positioning of the graft, especially in the medial-lateral direction; however, no objective recommendations exist on the best graft placement [3]. Considering 3D finite element models of the Latarjet procedure, the objective of this study was to investigate how shoulder stability and articular contact are affected by the medial-lateral positioning of the bone graft.

Methods

Three-dimensional geometries of the right humerus, scapula, and glenoid labrum were generated from the male image data of the Visible Human Project. The articular cartilages of the humeral head and glenoid cavity were modelled in Solidworks (Dassault Systèmes, Waltham, MA, USA) based on anatomical studies. The conjoint tendon was neglected. To simulate the Latarjet procedure, a glenoid bone defect of 20% of the glenoid width was simulated, and the distal section of the coracoid process was resected and was positioned flush with the anterior-inferior surface of the glenoid bone defect, according to the instructions of a shoulder orthopedic surgeon (C.d.C.A.). Considering this position, hereafter denoted as "ML-0mm", as reference, three additional positions were considered by laterally translating the graft 1.5 mm, 3.0 mm, and 4.5 mm from the ML-0mm position. Finite element models were generated in Abaqus (Dassault Systèmes, Waltham, MA, USA) for all graft positions. The glenoid labrum and articular cartilages were modelled as hyperelastic Neo-Hookean materials, and the remaining structures were modelled as linear elastic materials. For the sake of simplicity, the humerus was assumed rigid. The scapula was assigned inhomogeneous material properties based on its density distribution, estimated from the CT data.

The interactions between the articular cartilages, the glenoid labrum and humeral head cartilage, and the bone graft and humeral head cartilage were modelled using a frictionless contact formulation. The remaining interactions were assumed bonded [4,5].

Anterior shoulder instability was simulated by translating the humeral head anteriorly, under a 50N compressive force, until peak anterior shear force was reached. To avoid rigid body motion, scapula regions near the trigonum spinae and inferior angle were fixed in space [6]. Joint stability was evaluated as the ratio between the shear and the compressive components of the glenohumeral joint reaction force [3].

Results

The bone block effect of the Latarjet procedure increased shoulder stability only for the ML-3.0mm and ML-4.5mm positions (Figure 1).
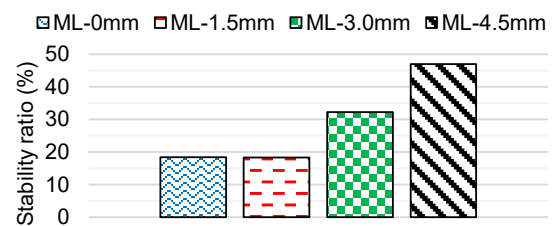
In the ML-0mm and ML-1.5mm positions, the humeral head cartilage never contacted the bone graft. In the remaining positions, peak contact pressures surpassed the failure stress threshold of articular cartilage, assumed 29.5 MPa, especially in the ML-4.5 mm position.

Discussion

Considering shoulder stability and articular contact pressure, preliminary results suggest the best placement of the graft to be between the ML-1.5mm and ML-3.0mm positions. Since the conjoint tendon was neglected, the evaluation of shoulder stability assumed only the bone block effect of the Latarjet procedure.

References

1. Yamamoto et al, J Bone Joint Surg Am, 95:1390-1397, 2013.
2. Goetti et al., EFORT Open Rev, 5:508-518, 2020.
3. Imai, JBJS Open Access, 6:e20.00141, 2021.
4. Favre et al, J Biomech, 45:2248-2255, 2012.
5. Sano et al, J Shoulder Elbow Surg, 29:2632-2639, 2020.
6. Quental et al, Biomech Model Mechanobiol, 13:827-838, 2014.

Acknowledgements

CONCURRENT IMAGING AND DIFFRACTION OF TRABECULAR BONE CONSTRUCTS WITH *IN SITU* SCANNING AND COMPRESSION

Elis Newham (1), Andrew James (2), Hans Deyhle (2), Sharif Ahmed (2),
Gianluca Tozzi (3), and Himadri Shikhar Gupta (1)

1. School of Engineering and Materials Science, Queen Mary University of London, London, UK; 2. DIAD, Diamond Light Source, Harwell, UK; 3. School of Engineering, London South Bank University, London, UK

Introduction

The complex 3D micro- and nanostructure of bone makes the characterisation of *in situ* loading environment in the extracellular matrix (ECM) very challenging. Here, we use the unique technical capacities of the new Dual Imaging and Diffraction (DIAD) beamline at Diamond Light Source to obtain proof-of-concept results toward addressing this question. The ECM of bone consists, at the nanoscale, of anisotropic tough collagen fibrils, incorporating a stiff carbonated mineral component with a crystallographic apatite structure [1]. In this study, we combine microscale X-ray computed tomography (SR-XCT) [2] and molecular-level (spatially-resolved) wide-angle X-ray diffraction (WAXD) [3] mapping of the ECM in trabecular bone. Using WAXD mapping, we are able to study variations in the 3D mineral crystallographic orientation, crystallinity and lattice spacing at different spatial locations in the tissue, potentially allowing pre-strain changes with regeneration to be mapped. By correlating such data with the SR-XCT image on the same sample, these molecular-level changes can be linked to microscale tissue features. Using a manual compressive rig, we also carried out in situ SR-XCT/WAXD mechanics of trabecular cores. Analysis of the regions of high strain using WAXD and SR-XCT can be correlated to understand the development of biomechanical forces in the ECM at the micro- and molecular level.

Materials and Methods

Trabecular bone planar sections from ovine femoral condyle and cores from bovine femoral head were used. Sections were prepared to ~200 μm thickness embedded in PMMA. Cores (~5 mm L x 2 mm D) were prepared with a diamond drill bit. A) For scanning-WAXD/SR-XCT on sections (K11 DIAD beamline, Diamond Light Source, UK), the detector position was adjusted to visualize the (004) apatite peak (parallel to the fibril load-bearing direction). SR-XCT imaging was taken followed by 2D WAXD scans (beam-size 25μm×25μm; 40μm step size; wavelength 0.73 Å) over a size of 600 μm × 600 μm. B) For *in situ* loading, cores were mounted in a manual compressive rig with bespoke PMMA-potted end-cups (3D printed; ABS) to minimize end-artifacts during mechanical testing. SR-XCT and WAXD scans were taken at 0% and 0.5% apparent strain, with similar step size parameters as for sections. CT volumes were reconstructed using single distance phase retrieval algorithms and analyzed using ImageJ with the BoneJ plugin [5]. WAXD patterns were analyzed to determine mineral peak intensity, lattice period (pre-strain), orientational texture and changes in these parameters on loading and tissue location.

Figure 1 shows an example of the microstructure (CT) and ultrastructure of the trabecular bone section. The intensity variation of the (004) peak reflects the orientation difference between mineralized fibrils at different locations in the tissue. 3D models of WAXD diffraction [4] are applied to measure spatially resolved mineralized fibril strain and orientation.
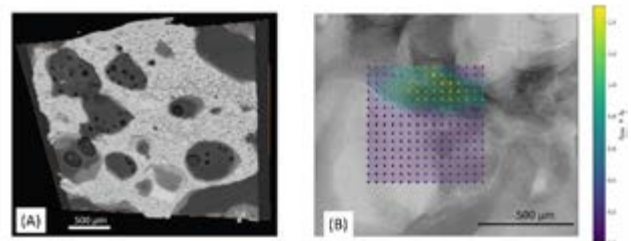
Figure 1: A) 3D CT image of trabecular bone B) WAXD-scanning map overlaid on 2D X-ray radiograph, showing variation in ultrastructural peak intensity, reflecting 3D orientational changes in mineralized fibril [5]. Scale bar is 500 μm in both A) and B).

Discussion

This is the first study performing concurrent tomographic imaging and diffraction of trabecular bone thin sections and, most importantly, cylindrical cores subjected to in situ SR-XCT/WAXD mechanics. The preliminary results here reported show a first glimpse of micro-to-ultra/structural correlation in native bone tissue, which will be further expanded to regenerated bone following action of different biomaterials *in vivo* and *in situ* mechanics with digital volume correlation. The technique has the potential to both produce a breakthrough in bone tissue experimental measurement, and to better inform and refine computational models.

References

1. P. Fratzl et al, *Prog. Mater. Sci.* 52:1263-1334 (2014).
2. M. P. Fernandez et al, *ACS Biomater. Sci. Engg.*, 5:2543-2554 (2019).
3. X. Li et al, *Bone*, 131:115111 (2020)
4. Y. Zhang et al, *ACS Nano*, 14:16535-16546 (2020)
5. M. Doube et al, Bone, 47:1076-1079 (2010)

Acknowledgements

PREDICTING FRACTURE LOCALIZATION IN TRABECULAR BONE

Martino Pani (1), Carlos Ruiz Wills (2), Maria Ballart (2), Simone Tassani (2)

(1) School of Mechanical and Design Engineering, University of Portsmoouth, UK

(2). BCN MedTech, DTIC, Universidad Pompeu Fabra, Barcelona, Spain

Introduction

The mechanics of trabecular bone is of crucial importance for improving diagnosis and treatement of a number of skeletal diseases. Complex histology as well as intricate spatial architecture make it very difficult to initiate reliable numerical models: micro-FE models based in µCT images have been widely used to model the mechanical response of relatively small samples; but when trabecular structure was directly embedded on models at the bigger scale of bone segments advanced High Performance Computing facilities were required. Prediction of fracture is still uncertain for trabecular bone: simple linear models based on a strain-based fracture criterion (successfully applied at organ level) were proven unable to localise the fracture; complex non-linear models, are still characterised by a significant low generality, robustness and accuracy in detecting the structural collapse.

Fracture appears as a chain of events where a local phenomenon triggers a sort of butterfly effect on an increasingly growing surrounding area. The fracture onset appears not related to strain/stress concentration as it emerges from linear models [@]; on the other hand, models embedding constitutive non-linearities are not providing further insights. The complexity of those models, combined with their significant computational cost, makes the identification of a reliable, robust and accurate model still an open challenge.

Skeletonisation is an algorithm able to extract essential features about the topology of a 3D structure from its digital imaging. Using this approach, the intricated trabecular arhitecture can be described as a graph of truss/beam elements. In this study skeletonisation was applied to µCT images of trabecular bone samples; the resulting graph initialised a FE model of beam elements replicating the experimental uni-axial compression test conducted up to failure.

Material and Methods

MicroCT datasets of 8 bone samples (cylinders, D=10mm, h=20mm, BVTV 9.36+/-2.33%) from the LHDL dataset were binarised (fixed global threshold 143) and skeletonised (in-house matlab script, homotopic thinning algorithm [2] algorithm). Trabeculae were identified between the nodes of the resulting graph; each link was modeled as a beam element (homogeneous and isotropic linear material, E=19GPa, ni=0.3); cross sections were defined by computing the average distance between skeletonised links and the surface obtained from dataset binarisation. Nodal constrains were applied to replicate the uni-axial compression (full constrain on bottom region; top region imposed a purely vertical displacement). FE models were solved using Abaqus on a standard laptop. The map of the resulting nodal displacements and rotation were analysed and compared with the map of the fractured areas as identified by comparison between registered pre and post fracture microCTs [3].

Results and Discussion

Nodal rotation magnitude showed an excellent spatial match with fractured areas: all the models presented damaged regions systematically overlapping the highest values of nodal rotations. In particular, specific torsion (i.e. axial nodal rotation difference divided by trabecular length) showed peaks positioned onto damaged areas: peaks were localized on fractured regions within 0.67% and 2.46% of the total length of the sample.
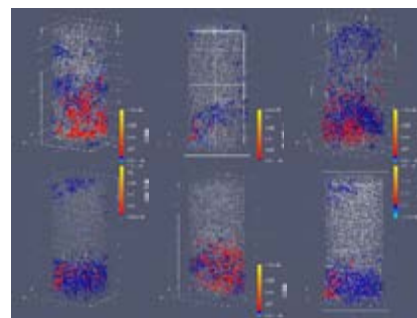
Figure 1: Few examples of FE model (white), Fracture regions (blue), and peaks of specific torsions (red spots).

These preliminary results suggested that beam models based on µCT datasets skeletonisation were able not only to capture the overall mechanical response of the trabecular structure but also to localize the fracture onset. Trabecular torsion (an information not achievable from voxel-based FEM) appeared spatially aligned with fractures on experiments. A strong rationale can lays on the laminar structure of the trabeculae where shear stresses between adjacent lamelleae produced by torsion is likely to result in pack delamination. The simple structure and the light computational cost of this modelling make it possible to easily consider both laminar structure of each beam as well as a non linear model for studying the post-deliamination phase. Both this topic would be problematic and demanding with µFE approach.

References

1. Tassani et al. Frontiers in Materials, Section Mechanics of Materials
2. Ta-Chih Lee et al, Computer Vision, Graphics, and Image Processing, 56(6):462–478, 1994
3. Tassani et al. Bone, 60, 78–86.

BONE REMODELLING ALGORITHM. A VOXEL BASED APPROACH

Jorge Roces-García (1), Víctor Celemín-Mohedano (1,2), Pankaj Pankaj (3)

1. University of Oviedo, Spain; 2. Nanoker Research S.L., Spain; 3. The University of Edinburgh, Scotland

Introduction

The first important reference on bone remodelling dates from 1892 [1]. It describes how any alteration in the stress state of the bone could cause changes in the bone structure. Since the 1980s, techniques and algorithms have been developed to evaluate bone remodelling, based on mathematical models [2] or FE simulations [3]. This work presents a simplified bone remodelling algorithm based on essential constitutive elements of bone.

Methods

Bone properties from CT (HU), patient characteristics (age, gender and physical activity) and stress states (σ) are used as initial data. Bone remodelling in a certain period is evaluated according to the iterative process shown in Figure 1.
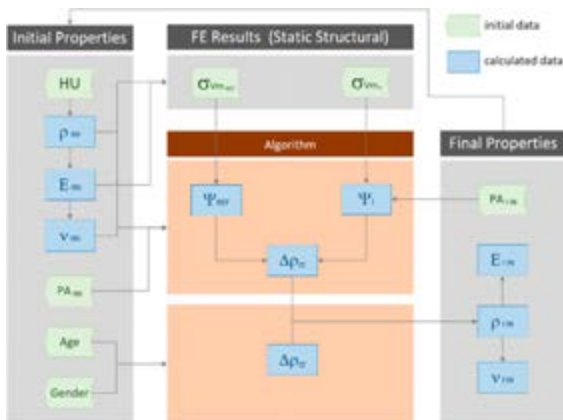
Figure 1: Bone remodelling algorithm

Regular hexahedral elements representing voxels are employed. Hounsfield units are converted to density and then to elastic moduli based on available literature. In this preliminary study density was discretized in ten groups (from 0.3 g/cm^3 to 1.98 g/cm^3 density).

Results

Mechanical properties evolution of elements was assessed by calculating the stress tensors in different scenarios. The elastic modulus (and density) changes and the negative or positive jumps of discretised material were examined in response to different stress states, changes in physical activity, age-related disturbances or the number of iterations (time).

Case Study · Fracture fixation in the central femur
The central region of the femur (male 46 years) was studied. A standard fixation was included and voxelized

[4]. The virtual model consists of 2814 bone voxels and 472 implant voxels (Figure 2A). There were 238 elements with a negative change of material (resorption), in blue, and 306 elements with a positive change of material (densification), in orange/red (Figure 2B). Two layers of voxels were removed and filled with voxels of material 2 representing fracture gap.
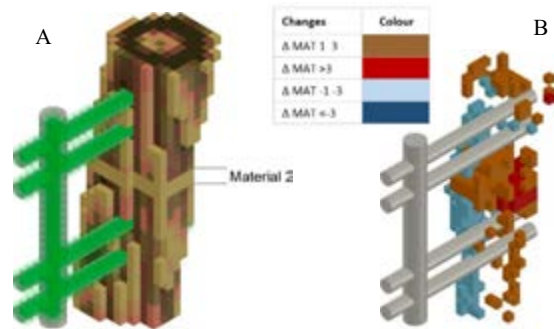
Figure 2: Voxel model (A) and elements with a material jump after the first application iteration (B)

Discussion

This study uses voxel-based models, which allow stress analysis with a lower computational cost. The algorithm allows a complete 3D bone remodelling simulation in multiple scenarios (fractures, prostheses, implants…), in order to evaluate implants (commercial or new designs) or carry out preoperative planning studies. In this preliminary study ten bone materials were used but these can readily be increased in order to improve the precision of the results.

References

[1] J. Wolff, The Law of Bone Remodelling. Berlin, 1986.
[2] C. R. Jacobs, et al, J Biomech, 28-4:449–459, 1995.
[3] I. Levadnyi, et al, Clin Biomech, 50:122–129, 2017.
[4] J. Roces-García, et al, Dyna, 91-1, 2016.

Acknowledgements

CHARACTERISATION OF THE SPECIFIC GEOMETRIC ANISOTROPY OF TRABECULAR PLATES AND RODS.

Nicolas Rogalski (1), Sébastien Laporte (1), Ivan Iordanoff (1), Christophe Cluzel (2)

1.   Arts et Métiers Institute of Technology, Université Sorbonne Paris Nord, IBHGC - Institut de Biomécanique Humaine Georges Charpak, Paris, France
2.   Université Paris-Saclay, Centrale Supélec, ENS Paris-Saclay, CNRS, Laboratoire de Mécanique Paris-Saclay, Gif-Sur-Yvette, France

Introduction

The geometric anisotropy of trabecular bone, composed of plates and rods, plays a crucial role in its mechanical performances. The reference tool for characterizing trabecular microstructure is the Mean Intercept Length (MIL), which defines an orthotropic system within a representative volume [1]. However, it does not discriminate between the specific orientations of plates and rods, which have distinct mechanical roles. The aim of this study is to propose a method for discriminating and quantifying full specific geometrical anisotropies of plates and rods.

Methods

Using triangular surface mesh of trabecular bone, the method relied on two steps: first, a curvature criterion was used to discriminate between plates and rods (figure 1), allowing to extract surface ratios. Then, an angular filter [2] was applied to analyse their specific orientations using triangle normals. The orientations were finally represented on polar plots (figure 2). In addition, principal axis from ellipsoidal approximation of MIL polar plots were compared to our results, as an average angle between directions.
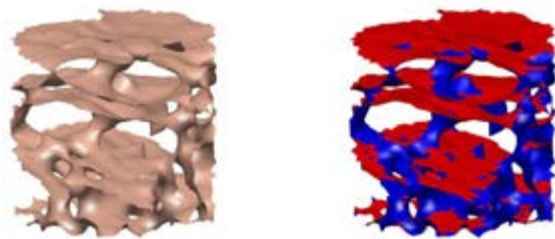
Figure 1: Use of the curvature criterion to discriminate between plates (red) and rods (blue).
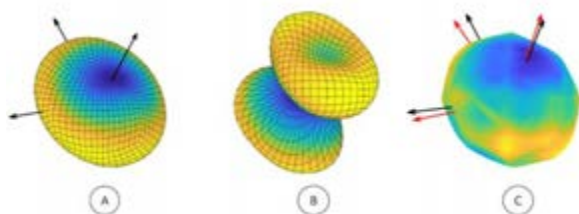
Figure 2: Polar plots of privileged plates (a) and rods (b) orientations. (c) MIL polar plot and comparison of MIL (red) and sample orientations (black).

The method was used on meshes from 32 bovine femoral cylindrical (diameter 10.5mm, height 7.5mm) cancellous bone samples, obtained from binarized CT images (resolution $80\mu m$) [3]. This sample set contained only one plate orientation and was selected to evaluate the method.

Results

The average angle between plates and rods, for all samples, was $\mathbf{51 \pm 5}°$. The average rod to plates area ratio was $\mathbf{0.69 \pm 0.1}$. The average angle between the directions of the ellipsoidal approximation of the MIL polar plots and the directions of the samples polar plots was $\mathbf{4 \pm 4}°$.

Discussion

The proposed method allows the rapid discrimination of plates and rods as well as the identification of their specific directions. The directions obtained were consistent with the MIL, but the method allowed obtaining additional information in terms of orientations, in the case of a mixed plates and rods structure. Another method, based on a skeletonization algorithm, has been proposed [4]. It was found that in the femoral neck, most rods are transverse to the plates while in our study, there are mostly oblique. This difference could come from their use of the mean axis of rods while we analysed their surface orientations. This study [4] also suggests that in the trabecular network, the plates are the primary structures resisting local compressive loads, while the beams serve rather as links between the plates and allow load transfer. The average inclination of the rods with respect to the plate normals obtained here is consistent with this assumption as it allows the structure to be consolidated by limiting their shear loading. It will be interesting to study trabecular structures with several plate orientations to highlight reinforcement directions in these cases. In addition, this method is functional for a pqCT-type of scanner resolution. It could therefore consolidate the clinical diagnosis based on the sole measurement of bone density.

References

1. Whitehouse et al, J. Microsc, 101, 153–168, 1974.
2. Rogalski et al, Structmat, vol 132, 153-162, 2020.
3. Prot et al, J. Biomech, vol 48, 498-503, 2015.
4. Liu et al, J. Biomech, 42, 249–256, 2009.

A PK-PD MODEL OF ALENDRONATE FOR THE TREATMENT OF POSTMENOPAUSAL OSTEOPOROSIS

R. Ruiz-Lozano (1), J.L. Calvo-Gallego (1), P. Pivonka (2), J. Martínez-Reina (1)

1. Departamento de Ingeniería Mecánica y Fabricación, Universidad de Sevilla, Seville 41092, Spain;
2. School of Mechanical, Medical and Process Eng, Queensland University of Technology, Australia

Introduction

Osteoporosis (OP) is a disease caused by an imbalance in bone turnover, with postmenopausal OP being the most common disease type. Alendronate is the most widely used OP drug, which inhibits bone resorption via two mechanisms: a reduction in the resorbing capacity of osteoclasts and inducing their apoptosis [1]. The objective of this work is to develop a pharmacokinetic – pharmacodynamic (PK-PD) model of alendronate able to reproduce: (i) the PK in the short- and long-term; (ii) the PD in a bone cell population model (BCPM) to analyse the effect of the drug on the body. Such model will provide a valuable tool for future research covering the effects of alendronate in different scenarios.

Methods

First, the most suitable PK model was identified, and then the PD model was added. Different compartmental models, like the one depicted in Fig.1, were fitted to reproduce three sets of clinical results (short-term serum concentration [2], short-term [3] and long-term [4] urinary excretion) and the goodness of the fit was jointly evaluated to choose the best PK model.

CC: central compartment
NCT: non-calcified tissues
BC: bone compartment
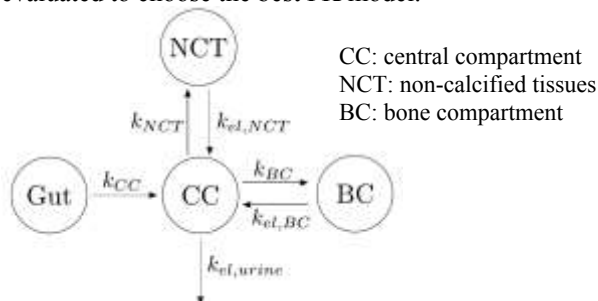
Figure 1: Compartmental scheme of the PK model.

Once a suitable PK model is selected, the effect of alendronate on bone remodelling was modelled using a BCPM [5]. We hypothesized that the BC can be divided in two parts: one termed active, the closest to the bone-marrow interface with an immediate retrieval of alendronate through bone resorption; the second part, termed inactive, corresponds to the innermost regions of bone, where alendronate is buried and, to some extent, inaccessible to bone resorption. In trabecular bone the active part is predominant as most of the tissue is superficial. To distinguish between active and inactive parts, as well as the saturation of the active one, the specific surface per bone tissue volume was introduced. Both effects of alendronate on osteoclasts (i.e., reduction in resorbing capacity and increase of apoptosis) were modelled proportional to the concentration of active alendronate. The model was fitted for the PK clinical results of serum concentration and urinary excretion plus bone density gain (BDG) data in postmenopausal women with osteoporosis treated with alendronate for 2 years [6].

Results

The model configuration shown in Fig.1 was finally selected as the most suitable PK model, since it could fit the clinical results with high accuracy. In Fig.2, the results of the PK-PD model are shown and compared with the clinical results:
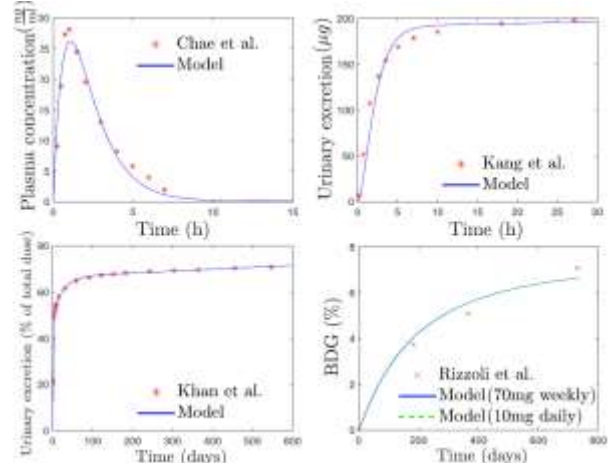
Figure 2: PK-PD model curves and clinical data.

Discussion

The PK-PD model of alendronate proposed in this work was able to reproduce the pharmacokinetics reported in the literature, as well as the BDG in a case of PMO for two different treatment protocols (10 mg administered daily and 70 mg administered weekly) and at two bone sites, i.e. lumbar spine and hip.

References

1. Takagi et al, Microscopy, 70(3):302-7, 2021.
2. Chae et al, Drug Dev Ind Pharm, 40(10):1325-9, 2014.
3. Kang et al, J. Liq. Chr. Relat. Tech., 29(11):1589-600, 2006
4. Khan et al, J. Bone Miner. Res., 12(10): 1700-7, 1997
5. Martin et al, Biomech.Mod.Mechanobiol,18:1475-96,2019
6. Rizzoli et al, J. Bone Miner. Res., 17(11):1988-96, 2002

Acknowledgements

EPIPHYSEAL BONE HEALING WITHIN CONTINUUM BONE REMODELING

Ina Schmidt (1), Paul Steinmann (2), Areti Papastavrou (1)

1. Nuremberg Tech, Germany; 2. Friedrich-Alexander Universität Erlangen-Nürnberg, Germany

Introduction

Bone healing as a consequence of major tissue injury is a highly interesting but also complex process. Especially in view of an aging population, bone fractures and their treatment are gaining importance because they are usually accompanied not only with pain, but also with limited mobility, financial challenges, and sometimes even long-term consequences.

In order to better understand and even predict the bone healing process, computational models have been developed in the last decades. Most of them are based on the assumption of tissue differentiation depending on the state of stress, sometimes also considering cellular activities or fuzzy logic [1,2,3,4,5]. However, they all focus on secondary healing at the shaft of tubular bones. In contrast, this novel approach focuses on healing at the end of long bones, which are mainly composed of cancellous bone. Moreover, in addition to classical fracture healing, this method also considers healing after fixation removal.

Methods

To ensure broad applicability and easy extensibility of the model, it is embedded in a continuum remodeling framework, see [6,7,8,9]. In this, bone is modelled as a continuum, so that the porous material is considered only to a certain extent.

One of the primary variables in this formulation is the (homogenized) bone density ρ_0. Its evolution over time in the classical model is described by the difference between the weighted free energy density Ψ_0 and an attractor stimulus Ψ_0^a that describes the biological equilibrium the system is driving to:

$$\dot{\rho}_0 = c \left[\left(\frac{\rho_0}{\rho_0^*} \right)^{-m} \Psi_0 - \Psi_0^a \right] := S_0^{mech} \qquad (1)$$

As novelty, the mechanical stimulation is complemented by a phenomenological healing stimulation:

$$\dot{\rho}_0 = f_{heal} \, S_0^{heal} + f_{mech} \, S_0^{mech} \qquad (2)$$

Herein, the prefactor functions f_{heal} and f_{mech} regulate the activation and deactivation of the corresponding process time-dependent as well as locally.

Results

To analyze the model, a common 2D finite element model of the proximal femur head is used. A fracture is defined at a certain time, which then heals through different modelling. For example, a dynamic healing process can be simulated by adjusting the healing prefactor as a function dependent on time. Furthermore, the difference between absolute immobility during the healing phase and gradual load increase through physiotherapy can be investigated.

In addition, the removal of a fixation system and the subsequent healing phase can be modelled. Figure 1 shows the results at a 3D proximal humerus model using a fixation system with 6 screws similar to [11,12].
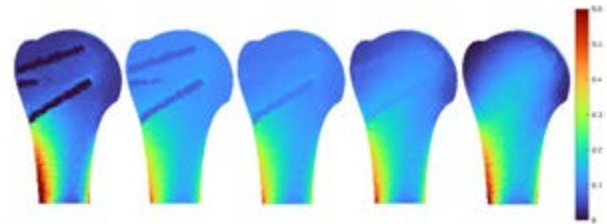
Figure 1: Temporal evolution of the nominal density after fixation removal

Discussion

The results indicate that the presented rather phenomenological approach of modeling bone healing is a first promising attempt to represent the dynamic process. The model proves to be efficient and can be easily extended to include further aspects such as age-dependency and the availability of nutrients.

However, large clinical datasets are needed to validate the model quantitatively. In addition, the model offers opportunities for improvement, for example, by examining patient-specific data and loadings, or by more accurate modelling of the micro- and meso-structure.

References

1. Carter et al, J Orthop Res, 6:736,748, 1988.
2. Geris et al, Biom Model Mechanobiol, 9:713–724, 2010.
3. Ghiasi et al, MC Musculoskelet Disord, 20:562, 2019.
4. Lacroix et al, Med Biol Eng Comput, 40:14–21, 2002.
5. Ament et al, J Biomech, 33:961–968, 2000.
6. Kuhl et al, Int J Numer Meth Engng, 58:1593–1615, 2003.
7. Papastavrou et al, J Biomech. 103: 109701, 2020.
8. Papastavrou et al, CMBBE, 23:432–444, 2020.
9. Schmidt et al, CMBBE, 24:1274–1212, 2021.
10. Carter et al, J Bone Joint Surg Am, 59:954–962, 1977.
11. Acklin et al, BMC musculoskel. disorders, 17:119, 2016.
12. Kirchhoff et al, BMC musculoskel. disorders, 9:138, 2008.

Acknowledgements

A COARSE GRAINED MODEL OF MINERALISED COLLAGEN FIBRIL BIOMECHANICS: UNDERSTANDING THE ROLE EXTRAFIBRILLAR MINERALIZATION

Mahdi Tavakol (1), Ted J. Vaughan (1)

1. Biomechanics Research Centre, School of Engineering, College of Science and Engineering, National University of Ireland, Galway, Ireland

Introduction

Bone is a naturally occurring composite mainly made of Hydroxyapatite mineral phase and a collagenous organic matrix, which are assembled into Mineralized Collagen Fibrils (MCFs) at its lowest level of hierarchy. Even though the higher order structures of bone may vary, MCFs are the universal building that are remain similar across different bone types and species. The mechanical properties of different bone types are dependent on the corresponding characteristics of their constituent MCFs. Collagen molecules in MCFs are arranged according to Hodge-Petruska model, which gives rise to overlap and gap regions. Initially, it was suggested that the gap regions, caused by the staggered arrangement of molecules, were occupied by the HAp minerals [1]. However, bone mineral volume measurements have shown that there was not enough space in these regions to accommodate the overall volume of mineral in bone [2]. Therefore, there must be substantial mineralization in the extrafibrillar space. However, it is not clear how the presence of extrafibrillar minerals affects the MCF mechanical properties. In the current study, the effect of the extrafibrillar mineralization on the mechanical properties of bone is investigated.

Methods

To reach large simulation length and time scales, a mesoscopic model [3] is utilized for collagen according to which atoms are replaced with equidistant beads along the central axis. A collagen fibril with 20 nm diameter is built which has 155 collagen molecules. According to the simulations done by Depalle et al. [3], the ultimate tensile strength and tensile modulus for fibrils with diameters larger than 12 nm are independent of diameter. Thus, the 20 nm diameter fibril is considered to be a suitable representation for biological fibrils with diameters in 20-500 nm range. The mechanical properties of two different systems are studied through uniaxial loading to elucidate the role of extrafibrillar mineralization; a) single MCF with 35% intrafibrillar minerals (Figure 1a), b) four MCFs with 35% intrafibrillar and 75% extrafibrillar mineralization (Figure 1b).

Results and Discussions

The molecular dynamics simulation results show different stress-strain response in the presence of and wihtout extrafibrillar mineralization (Figure 1c). The presence of extrafibrillar mineral increases the Young modulus of the system and coincides with a reduction in overall strength. The presence of extrafibrillar minerals leads to a reduction in the fracture strain owing to the propagation of the cracks initiated from the extrafibrillar minerals. The decreased fracture strain is also due to the restriction imposed on the collagen molecules sliding by the extrafibrillar minerals. However, the reduced ultimate tensile strength is caused by non-uniform stress distribution in the collagen molecules with those in the vicinity of the minerals carrying larger stress owing to their restricted ability of sliding. The Young modulus value of 45 GPa is calculated for the extrafibrillar mineralized MCF, which is in a good agreement with the experimentally measured values of 40±5 GPa [4].
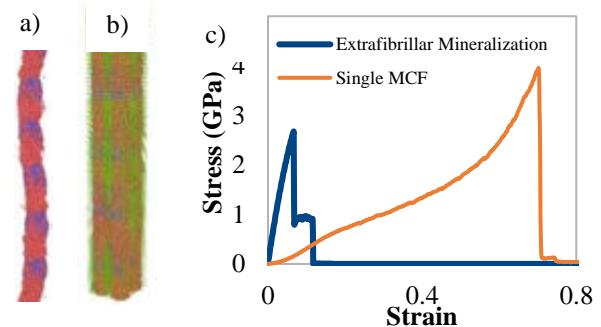
Figure 1 – Simulation box containing a) a single MCF and b) four MCFs with extrafibrillar mineralization. c) The stress-strain response of the mentioned systems.

Conclusions

This study discovered the role of the extrafibrillar mineralization in the mechanical properties of collagen fibrils. Here, it was found that the mechanical properties of bone tissue is likely dominated by the presence of minerals in the extrafibrillar space, highlighting the importance of extrafibrillar mineralization in bone biomechanics.

References

1. Siperko et al, J. Struct. Biol., 135:313-320,2001
2. Su et al, Bone, 32:150-162,2003.
3. Depalle et al, J Mech Behav Biomed Mater, 52:1-3,2015.
4. Karunaratne et al, J Bone Miner Res, 27:876-890,2012.

Acknowledgements

INTERNAL STRAIN FIELD OF A HUMAN TIBIA WITH TITANIUM TIBIAL TRAY DURING STAIR DESCENT: A MICRO-CT AND DVC ANALYSIS

Lauren Wearne (1), Sophie Rapagna (1), Maged Awadalla (1), Mark Taylor (1), Egon Perilli (1)

1. Medical Device Research Institute, Flinders University, Adelaide, Australia.

Introduction

Achieving primary stability of cementless tibial trays is important for their long-term success. Stair descent, coupling high loads at increased flexion, exposes the implant to loading patterns that can jeopardise this stability [1]. However, the immediate post-implantation strain field of cancellous bone is yet to be quantified experimentally. Digital volume correlation (DVC) and time-elapsed micro-CT imaging allows analysis of the internal strain field of bone. Here, this technique is applied to a cadaveric tibia implanted with a titanium tibial press-fit tray, with the aim of quantifying the internal strain field when subjected to a progressive load sequence that replicates stair descent.

Methods

Micro-CT Imaging: One right cadaveric proximal tibia (42yr old male, 67kg) was implanted with a titanium tibial tray (ATTUNE, Depuy Synthes) and loaded in a step-wise manner. Uniaxial loads (Deben CT5000N, with custom-built aluminum tube, permitting a specimen height of 186mm) were scaled to the weight of the donor, for load steps of 0.0BW (preload of 50N), 0.5BW, 1.0BW, 1.5BW and 2.5BW. The load was transferred through two contact points (M: medial, L: lateral), offset posteriorly from the center of the tray by 9.9mm M, and 11.8mm L, to replicate those of a femur on tray during stair descent. Micro-CT scans (Nikon XT H225 ST, isotropic 46µm/pixel, 215kVp, 46W, 2000 projections, 66min scan time) were taken at each load step, after a 20min relaxation period. A repeated scan of the tibia in an unloaded condition (pre-load of 50N) was taken for DVC zero-strain error analysis [2].

DVC Analysis: The second pre-load scan (0.0BW) was considered as baseline, to which subsequent scans were 3D rigidly co-registered and DVC analysis performed (DaVis 8.3.1, LaVision, direct correlation), with a final subvolume side length of 34pix (1.56mm). Masking was applied on the extracted minimum principal strains (P_{min}), to remove subvolumes that contained either the titanium tray or had a trabecular bone volume fraction (BV/TV) < 5%. Eight cylindrical volumes of interest (A:H Fig. 1, 15mm diameter, 15mm height) were virtually selected for analysis. These contained either bone (A, B, C, D), or were centered on an implant peg (E, F, G, H), with surrounding bone.

Results

Across all VOIs analysed, average P_{min} ranged from -822µε (0.5BW, VOI D) to -14,268µε (2.5BW, VOI G), Fig 2. For zero-strain error analysis, accuracy was 531±116µε (ave±SD) with precision 399±198µε. The average correlation coefficient across all VOIs was 0.88±0.03.
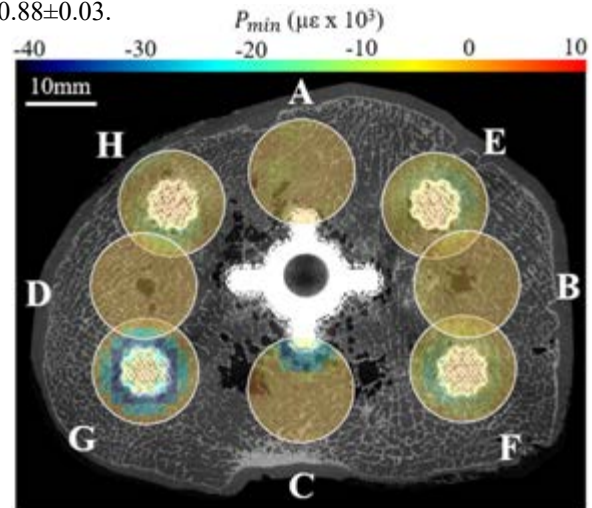
Figure 1: Micro-CT cross section of the right cadaveric tibia with titanium tibial tray, with the DVC computed minimum principal strains (P_{min}) for the VOIs.
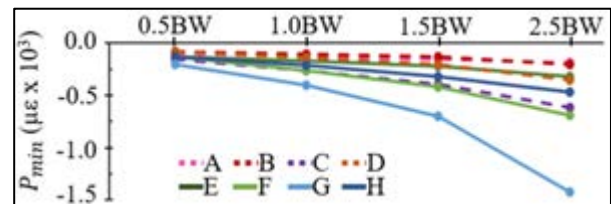
Figure 2: Average minimum principal strain (P_{min}) for each VOI, at progressive loads.

Discussion

For each VOI, progressive loads resulted in increased compressive strains within the cancellous bone. Strain variations were observed across the tibia, with posterior VOIs (G, F, C in descending magnitude) showing higher values compared to anterior. Errors were sufficiently low for strain analysis within bone's elastic region [3]. This study demonstrates that it is possible to extract the immediate post implantation strain field of a cadaveric tibia with a press-fit implant and to quantify the strain of bone in direct contact with the titanium tray. The study is continuing, exploring diverse loading scenarios.

References

1. Taylor, et al., J Orthop Res, 30:1362-1368, 2012.
2. Tozzi, et al., J Mech Behav Biomed, 67:117-126, 2017.
3. Liu, et al., J Biomech, 40:3516-3520, 2007.

Acknowledgements

UNDERSTANDING BONE MATURITY: PROPERTIES AT THE INTERSTITIAL AND OSTEONAL LAMELLAR LEVEL

Andrea Bonicelli (1,2), Hannah McGivern (2), Elena F. Kranioti (3), Bledar Xhemali (4), Peter Zioupos(2)

1. School of Health and Life Science, Northumbria University, UK; 2. Cranfield Forensic Institute, Cranfield University, Defence Academy of the UK; 3. Dept of Forensic Sciences, University of Crete, Heraklion, Greece; 4. Institute of Forensic Medicine, Tirana, Albania.

Introduction

In ontogeny the properties and structure/composition of bone alter continuously according to demands placed upon it. Structural changes are concomitant to composition, architecture and physicochemical changes at the microscale which reflect at properties at the macroscale. We present here the pattern of properties at the osteon and interstitial lamellar level of a large collection of samples of human ribs [1] and clavicles [2] across a wide age range. The implication is that by understanding these pattens at the micro level we may be able to better understand bone physiology in ontogeny, in disease and the developmental pressures exerted upon it.

Methods

Sternal ends of the fourth and fifth ribs from 85 individuals (12-85 yrs) and the clavicle of 55 individuals (12-59 yrs) from the Forensic Institute in Tirana were employed in this study. The material was stored at -20°C and exposed to temperature variation for the least amount of time possible during testing. Experimental procedure involved TGA/DSC3+ (Mettler Toledo®, Indium calibrated) for collagen thermal stability and gravimetric analysis on powdered samples of these specimens and thin transverse sections were metallographically polished for Nano- and Micro-indentation to obtain matrix mechanical properties at osteons and nearby interstitial lamellae by using an CSM-NHT (v.3.75, CSM, 2034 Peseux, Switzerland). Statistical analysis was carried out using the open-source software R 3.6.0.

Results & Discussion

Results show that the two most interesting nanomechanical properties of note, hardness and indentation modulus showed a two-phase behaviour with age. They climbed to a maximum value by the age of 35 and declined thereafter. This behaviour, as expected, was related to the underlying chemistry and composition of the tissue [1]. However, the data has also raised some unanswered questions among which is the following conundrum: why do the interstitial lamellae decline after maturity? Why do the two types of tissue show the same pattern? Do we really understand the osteon mediated remodelling of bone or there are mechanisms by which both matures and remodels in situ? We are in the process of deciphering some of these questions by careful sequencing these tissue areas to define more precisely tissue age across the chronological ages.
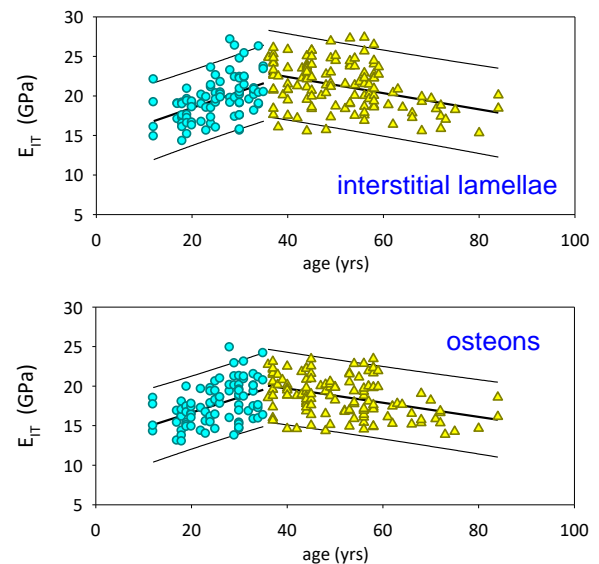
Figure 1: indentation modulus showed a very similar pattern across ages for interstitial and osteon lamellae in the mixed sample of ribs and clavicles with higher values for the interstitial tissue lamellae.
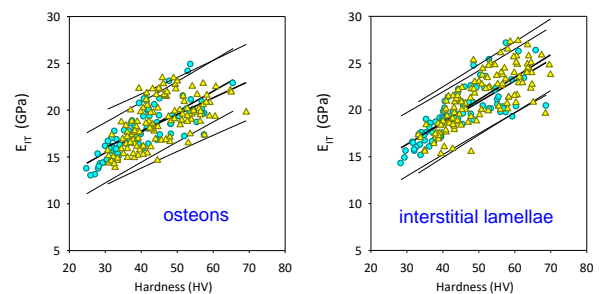
Figure 2: hardness followed modulus closely and as a function of the mineral content throughout and in both the pre-maturity and post-maturity stages of life.

References

1. Bonicelli et al., *Bone,* vol 155, 116265 (2022)
2. McGivern et al., *Front. Bioeng. Biotechnol.* Vol 7:467 (2020)

Acknowledgements

ANALYSIS OF EYE LOAD DURING BALL IMPACT

Tereza Bacova (1,2), Zdenek Horak (2), Vaclav Baca (1)

1. Department of Health Care Studies, College of Polytechnics Jihlava, Czech Republic; 2. Department of Pathophysiology, 3rd Faculty of Medicine, Charles University, Czech Republic

Introduction

The project aims to realize numerical simulations using the finite element method (FEM) for court proceedings. Numerical analyses were carried out to analyze a situation when a baseball ball impact with a velocity of 50 m/s could injure the eye's tissues; if so, to what extent, or whether it was could direct the eye penetrate. Numerical simulations were performed for situation, that ball hits the cornea in the eye axis. The output of the realized numerical analysis was the determination and distribution of the stress, strains, and pressure in individual parts of the human eye model.

Materials and Methods

The eye model was built by the anatomical structure of the human eye, where the basic geometry and dimensions of the eye model were taken from [1]. Per the anatomy of the eye, the computational model of the eye consisted of the following parts: cornea, sclera, ciliary body, suspension apparatus, lens, anterior chamber, posterior chamber, and soft tissues (Figure 1). The eye's tissues were modeled in the FE model mainly as a homogeneous linear isotropic material. The anterior chamber was modeled as a fluid, the sclera was modeled as a hyperelastic material, the posterior chamber and soft tissues were modeled as viscoelastic materials, and the orbits with the ball were modeled as a rigid body [2].
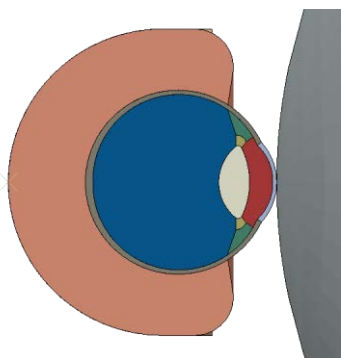
Figure 1: Numerical eye model with ball impact to the eye model.

Numerical simulations were realized in the ABAQUS software when modeled as contact nonlinear dynamic problems with an explicit numerical integration scheme. The ball's impact loaded the eye model when ball weighing of 145.5 g and velocity of 50 m/s.

Results

The results of FE simulations were evaluated by the magnitude of the reduced stress, the equivalent pressure, the principal stresses, strains and kinetic energy. The magnitude of the eye model's deformation during the ball impact is evident in Figure 2.
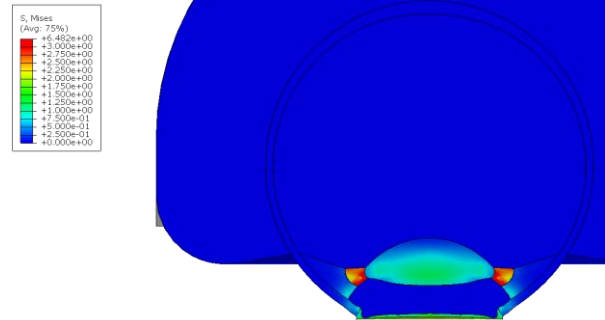
Figure 2: Display the reduced stress distribution of the eye after ball impact to the eye model.

As expected, the impact of the ball moving in the axis of the eye caused permanent damage of anterior and posterior chambers, sclera, and ciliary body. Material limits have been exceeded in all of the above parts of the eye.

Discussion and Conclusions

Biological tissues are generally complicated to establish relevant criteria for failure (due to differences in age, gender, current health status, etc.). However, at least isolated data obtained from experimental cadaveric samples can be found from literature sources. For this assessment, the values of maximum corneal loading [1,3], sclera [1,3], the maximum pressure in the anterior and posterior chambers of the eye [4], and the amount of kinetic energy acting on the eye [1,5]. Based on the results of FE simulations, it can be stated that the human eye impacted by a ball with the velocity at 50 m/s and weighing 145.5 g, then there would be a high probability of serious eye injury (rupture).

References

1. Stitzel et al, Stapp Car Crash J, 46:81-102, 2002.
2. Liu et al, J Biomech, 46:1321-7, 2013.
3. Uchio et al, Br J Ophthalmol, 83:1106-1111, 1999.
4. Dyster-Aas et al, Acta Ophthalmol, 40: 117-119, 1962.
5. Tillett et al, Am J Ophthalmol, 54:675-688, 1962.

APPLICATION OF MARKERLESS POSE ESTIMATION TO RUGBY COLLISION TRACKING

Richard Blythman (1), Manan Saxena (2), Gregory Tierney (3), Chris Richter (4), Aljosa Smolic (5), Ciaran Simms (6)

1. Trinity College Dublin, Ireland; 2. Trinity College Dublin, Ireland; 3. Leeds University, UK; 4 Sports Surgery Clinic, Ireland; 5. Trinity College Dublin, Ireland; 6. Trinity College Dublin, Ireland

Introduction

Participation in sport is important for societal health, but injuries from sporting collisions carry a high societal cost. This is particularly true in collision sports such as rugby. Video analysis is an important pillar of sports injury biomechanics research, but marker-based motion capture is generally only feasible in a laboratory setting, and manual video analysis is slow and frequently inaccurate. Commercial markerless motion capture systems do exist, but these are expensive and require the use of many cameras. Advances in computer vision and artificial intelligence have led to several open-source models for human pose estimation. This work assesses the potential of a recent free-to-use learnable triangulation pose estimation method for integrating multiple calibrated cameras to estimate human pose during rugby collisions.

Methods

We applied the recent Learnable Triangulation (LT) method proposed by Iskakov et al [1] to a set of previously published staged tackles [2]. The dataset includes upper and lower body tackles from four participants recorded using a VICON system with markers placed according to the conventional gait model protocol (both models shown in Figure 1a). Markers were tracked using 10 infrared cameras to provide ground truth, and 3 high-speed video feeds were also available for LT application. The LT model was applied without further training. The LT code takes the three video feeds and the intrinsic and extrinsic camera parameters as inputs (available here from the Vicon system outputs) and provides 3D joint positions as outputs. Joint position errors were computed using Mean Absolute Error (MAE) and mean per joint position error (MPJPE) across frames (F) and joints (J):

$$MAE = \frac{1}{N_J}\frac{1}{N_F}\sum_{j=1}^{N_F}\sum_{i=1}^{N_J}\left\|m_{ij_{LT}} - m_{ij_{GT}}\right\|\dots (1)$$

$$MPJPE = \frac{1}{N_J}\frac{1}{N_F}\sum_{j=1}^{N_F}\sum_{i=1}^{N_J}\left\|m_{ij_{LT}} - m_{ij_{GT}}\right\|^2\dots(2)$$
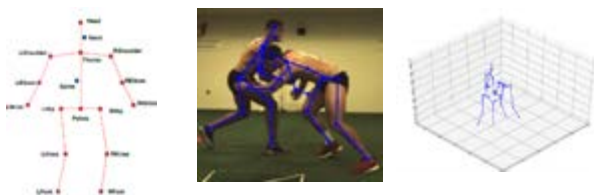
Figure 1: (a) fitted skeleton configurations of the CGM and LT models, (b) sample 2 keypoint overlay of LT model with video still of rugby tackle, (c) 3D spatial LT reconstruction.

Results & Discussion

Figure 1b shows a sample overlay of LT key points. A sample LT reconstruction is shown in Figure 1c. Table 1 shows sample MAE results for one player.

	Knee (L)	Knee (R)	Hip (L)	Hip (R)	Shoulder (L)	Shoulder (R)
X	25	22	19	86	10	36
Y	11	5	33	17	9	14
Z	9	10	14	10	6	22

Table 1: Sample Mean Absolute Error (mm) results

Discussion and Conclusions

We think this is the first study to analyze the validity of rugby tackle kinematics measured using open-source markerless motion capture based on deep learning techniques. The staged tackle dataset constitutes a very challenging scenario for the model containing significant occlusion and self-occlusion of the players. Nonetheless, the results indicate that this novel approach holds promise for providing reliable measurements of sports collision movement outside of the laboratory.

About three quarters of the joint position estimates have a MAE below 25 mm, which may be at an accuracy level suitable for general injury prevention studies. However much larger errors were observed in some cases, especially for the hip, see Table 1. Larger errors occur when the principal camera axis is aligned with the lateral axis of the pelvis. Occlusion during the contact phase also increases the error substantially. This technology has the potential to be widely used on calibrated video footage to provide a measure of whole-body kinematics leading to injuries in sporting collisions. However, future work must assess the degradation in positional accuracy for more ecologically valid settings, i.e. on-pitch. The model needs retraining on data more representative of sporting collisions.

References

1. Iskakov et al, ICCV, 2019.
2. Tierney et al, JBiomech 2018.

Acknowledgements

EVALUATION OF FINITE ELEMENT HEAD MODELS USING 3D PRINTED SURROGATE – PRELIMINARY CONTROL OF BOUNDARY CONDITIONS

François Jonca (1), Sylvain Persohn (1), Léa Chalanqui (1), Sébastien Laporte (1), Baptiste Sandoz (1)

1. IBHGC, Arts et Metiers Institute of Technology, Paris, France

Introduction

Brain concussions are dysfunctions that do not lead to immediate clinical symptoms [1]. Finite element head models (FEHM) were developed to understand mechanical head behavior and define specific injury criteria for brain concussions. However, these FEHMs need to be cautiously evaluated to have validated behavior and outputs.

This preliminary work presents results from an experimental drop mass setup developed to evaluate a parametrized FEHM by applying impacts on its 3D-printed surrogate.

Methods

3D-printed surrogate
Preliminary surrogate was designed as a hollow 50mm-diameter sphere. This surrogate was 3D-printed using Black PLA (Ultimaker 3 Extended).

Drop-mass setup and instrumentation
A drop-mass bench was designed to apply controlled 20cm-height impacts with a 4.15kg mass. Impactor kinematics was captured thanks to targets using a 2,000 fps-high-speed camera (Photronics) and a synchronized accelerometer sampled at 20kHz (PCB Piezotronics).

Surrogates were suspended using stiffness-known springs (0.13N/mm, maximal length 101.5mm). Two impacts were performed. Right after impacting the surrogate, impactor is stopped using a dissipative material (cardboards).

Comparison of the obtained impactor kinematics
Obtained experimental signals were filtered using a CFC1000 filter [3]. Then impactor speed along vertical axis was obtained by both camera (derivation) and accelerometer (integration). These curves were then aligned with respect to the impactor stop. Comparisons were made between the obtained curves and theoretical free-fall.

Preliminary results

Obtained speeds from accelerometer and high-speed camera are presented figure 1. Impactor stop could be identified thanks to a similar slope changing in all curves.

Just prior to the mass stop, at the instant of the theoretical impact speed of 1.98m/s, relative errors for both camera-computed speeds were below 5%. For accelerometer-computed one, it was 15% above theoretical impact speed. However, a specific pattern was observed with oscillations that could correspond to the impact (figure 2).
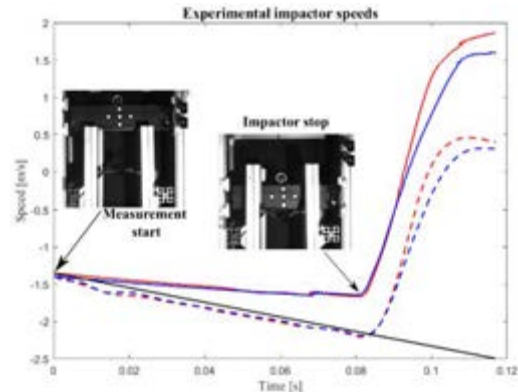
Figure 1: Computed impactor speeds from target-tracking (dashed lines) and accelerometer (solid lines) before the mass stop. Trial 1 is in red and trial 2 in blue. Black line is the theoretical free fall.
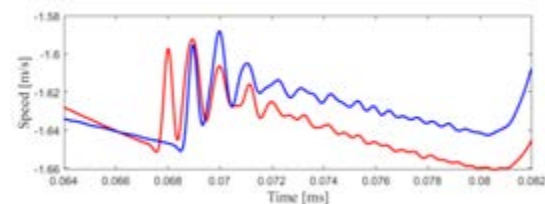
Figure 2: Zoom on oscillations in accelerometer-computed speeds.

Discussion

These preliminary results show promising ways to evaluate a physical surrogate with a geometry driven by a FE model, controlling experimental inputs. Camera-computed speed gave a good accordance with free fall while it could be possible to identify impact time with surrogate using the accelerometer. Then same and controlled boundary conditions could be applied to the numerical model like in animal FEHMs [4]. Observed differences with experimental might be linked, in this method, to modelling hypotheses only. Hence, it will enable a confident understanding of the simulation outputs, mostly head injury parameters such as strain (Cumulative Strain Damage Measurement) and acceleration (Head Injury Criterion).

Further work is still needed on new multimaterial 3D-printed surrogates and head-like parametrized geometries.

References

1. Gardner & Yaffe, Molecular and Cellular Neuroscience 66:75-80, 2015.
2. SAE, J211-1, Surface vehicle recommended practice, 1995.
3. Hajiaghamemar et al., Biomechanics and Modelling in Mechanobiology, 2019.

PREDICTIVE SIMULATION OF SINGLE-LEG LANDING SCENARIOS FOR ACL INJURY RISK FACTORS EVALUATION

Evgenia Moustridi , Konstantinos Risvas , Konstantinos Moustakas

Visualization and Virtual Reality Group, Department of Electrical and Computer Engineering, University of Patras, Greece

Introduction

The Anterior Cruciate Ligament (ACL) rupture is a very common knee injury during sports activities. Landing after a jump is one of the most prominent human body movement scenarios that can lead to such an injury. Traditionally, researchers acquire knowledge about human movement by organizing "in vivo" studies, that feature high complexity, cost, and technical and most importantly physical challenges. Computational modeling and simulation methods overcome these limitations and allow for studying musculoskeletal systems. Specifically, predictive simulation approaches offer researchers the opportunity to predict and study new biological motions without the demands of acquiring experimental data. In this work, we propose a pipeline that aims to predict scenarios of single-leg landing motions and identify key parameters of interest that are related to ACL injury.

Methods

Our analysis was divided in three main parts. First, we predicted the motion of a single-leg landing using the SCONE software [2] with a simplified OpenSim model. Then, we tracked that motion using more complex OpenSim models and the Moco tool [3]. Finally, we predicted multiple single-leg (left side) landing motions using Moco and the previously tracked motion as an initial guess. The key steps of this workflow are presented in Figure 1.
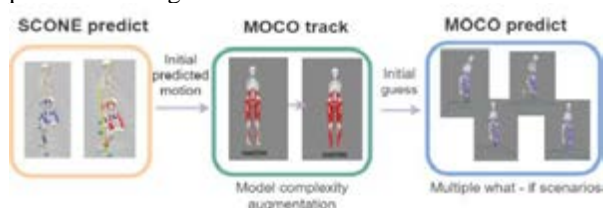
Figure 1: Overview of the proposed simulation pipeline with the implemented methods and software tools.

The model was simplified by removing the muscle-tendon units of the right side to reduce simulation time. The right-side Degrees of Freedom (DoFs) were actuated by ideal torque actuators. Also, foot-ground interaction was enabled using a compliant contact force model. The examined case studies included single - leg landings from six different landing heights, different hip rotation angles and deviations of the trunk orientation (lumbar flexion-extension, medial-lateral bending, and internal-external rotation) leading to a total of 43 simulations. The parameters of interest were muscle forces, Ground Reaction Forces (GRFs) and Knee Joint Reaction Forces (KJRFs), all of which have been associated with ACL injuries based on literature review. Furthermore, we developed scripts to perform post-processing operations on each predicted trajectory to acquire the previously metntioned parameteres.

Results

The outcome of the presented workflow was the prediction of multiple single-leg landing motions. The final states of four of these motions are demonstrated in Figure 2.

Figure 2: Final state of the predicted motion for four case studies with: trunk forward leaning, left bending, internal rotation, and hip external rotation.

The results demonstrated that as the landing height was increased, vertical GRF (vGRF) was also incremented. At time of peak vGRF, the knee joint Anterior Force (AF) was increased for greater heights. Moreover, the cases with internally rotated hip were associated with increased vGRF, while the cases with 10° and 15° of hip external rotation showed lower vGRF, AF, Abduction Moment (AM) and Internal Rotation moment (IRM) compared to the case without rotated hip. Furthermore, the landing with a 25° forward leaning posture, resulted in lower peak vGRF and knee AM compared to landings with other forward leaning angles. On the contrary, landings with trunk leaning backwards, bending, or rotated resulted in greater peak vGRF compared with the landing with an upright posture. These in generally agree with similar research studies. Therefore, by predicting landing motions, GRF and knee forces we can identify scenarios with high ACL injury risk.

Discussion

Our study demonstrated that ACL injury is a rather complicated mechanism with many associated risk factors. Also, it showcased the promising potential of predictive simulations to evaluate such complicated phenomena. As a conclusion, we envision that this work can lead to a set of tools at the disposal of clinicians to adjust rehabilitation and training plans based on subject-specific characteristics to reduce ACL injury risk during single-leg landings.

References

1. Geijtenbeek et al., Journal of Open Source Software, 2019
2. Dembia et al., PLOS Computational Biology, 2020.

BIOMECHANICAL ANALYSIS OF THE CORRELATION BETWEEN MID-SHAFT ATYPICAL FEMORAL FRACTURE AND VARUS DEFORMATION

**Mathieu Severyns (1,2), Dalila Belaid (3), Kevin Aubert (1),
Tanguy Vendeuvre (1,4), Arnaud Germaneau (1)**

1 Institut Pprime, UPR 3346 CNRS – Université de Poitiers – ISAE-ENSMA, France
2 Department of Orthopaedic surgery and Traumatology, University Hospital, Martinique, France
3 Université des Frères Mentouri, Constantine, Algery
4 Department of Orthopaedic Surgery and Traumatology, University Hospital, Poitiers, France

Introduction

Atypical femoral fractures (AFF) are diaphyseal fractures of the elderly that occur as a result of minor trauma and may extend from the small trochanter to the supra-condylar metaphyso-diaphyseal junction [1]. Strict diagnostic criteria have recently been developed by the American Society for Bone and Mineral Research [2]. The concepts of iatrogenic (biphosphonates, glucocorticoids, proton pump inhibitors [3]) or comorbidities (rheumatoid arthritis, chronic kidney failure [4]) are now reduced to minor criteria. Indeed, several scientific studies [5,6] have supported the mechanistic theory that these atypical fractures are linked to an abnormal distribution of stresses on the external femoral cortical. Two major types of AFF now appear to be emerging: medial-diaphyseal fatigue fracture on curved femur and sub-trochanteric fracture [7]. The hypothesis of this work was that an axial varus deformation of the lower limb could explain the occurrence of AFF. The objective of this biomechanical study, using finite element modelling, was therefore to evaluate the variations of the femoral diaphysis fracture indicator according to the variations of the mechanical axis of the lower limb.

Methods

A total of 6 CT scans of femoral segments have been analyzed to identify density and young modulus (Figure 1). Then Finite Element (FE) analyses have been performed considering the following boundary conditions: the distal part of the femur was constrained in all degrees of freedom; an axial compression load was applied on the femoral head to simulate the bipodal configuration in neutral position and in different axial positions in varus/valgus. The atypical diaphyseal femur fracture risk indicator was measured for all malalignment configurations from stress distribution:

$$\eta^C = \frac{\sigma^C_{min,ppal}}{\sigma^C_{y,ppl}}$$

With $\sigma^C_{min,ppal}$ the minimal principal stress and $\sigma^C_{y,ppl}$ elastic stress limit value.

Results

The maximum value of equivalent stress was twice higher (17.96± 4.87 MPa) at a varus angle of -10° than in neutral position conditions. The fracture risk indicator of the femoral diaphysis varies proportionally with the absolute value of the steering angle (Figure 2). The largest simulated varus malalignment (-10°) found a higher risk fracture indicator than in valgus (10°).
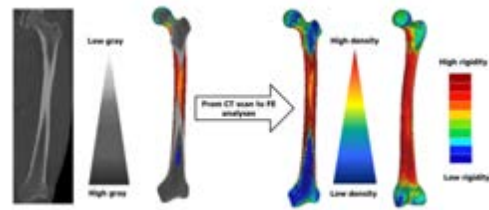
Figure 1. Femur bone density mapping

Discussion

Variations in the mechanical axis of the lower limb influence the stress distribution on the femoral diaphysis and consequently increase the risk of AFF. The axial malalignment in varus is particularly at risk of AFF. The combination of axial malalignment stresses and bone fragility consequently contribute to the creation of an favorable environment to the development of AFF.
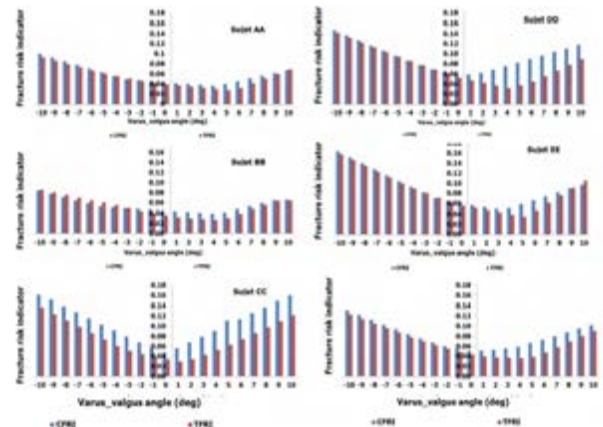
Figure 2. *Femoral diaphysis fracture risk indicators for all subjects in all configurations.*

References

1. Shane et al, E., J Bone Miner Res, 25;2267–2294, 2010.
2. Shane et al, J Bone Miner Res. 29;1–23, 2014.
3. Mahjoub et al, J Bone Miner Res, 31;767–776, 2016.
4. Lo et al, Bone, 51;181–184, 2012.
5. Oh et al, Injury, 45;1764–1771, 2014.
6. Haider et al, Bone, 110;295–303, 2018.
7. Tano et al. Injury, 50;1876–1882, 2019.

COMPARISON OF THE LOWER EXTREMITY DYNAMICS OF THE ELDERLY FEMALE, HIII 50TH MALE AND HIII 5TH FEMALE DUMMIES

Andreas Schäuble (1), Florian Zippel (1), Thilo Wackenroder (1), Peter Rücker (1), Thomas Kinsky (2)

1. DEKRA Automobil GmbH, Germany; 2. Humanetics Europe GmbH, Germany

Introduction

As the world population keeps ageing, these demographic changes are increasingly noticed on the global roads too. Whereas the overall numbers of traffic fatalities continuously decline since 2010, senior citizens form the only age group with an increase in road deaths [1]. For elderly patients, trauma also increases with age, with injuries being more frequent in senior women than men [2]. Currently, this population group is neither represented by crash test dummies nor considered in consumer test protocols and legislation. Therefore, Humanetics is developing the Elderly Female Dummy, an Anthropomorphic Test Device (ATD) which represents elderly females [3]. DEKRA conducted crash tests with a prototype version of the Elderly Female Dummy. Aim of the tests was to compare the performance with the HIII 50th male and the HIII 5th female dummies.

Methods

Three crash tests were conducted with a midsize station wagon based on Regulation UN R137 with the three different ATDs either positioned on the driver, front passenger, or right back seat. In this study, however, we solely focused on the front passenger seat to analyze the influence of both a standardized seating position and a restraint system with double pre-tensioner and load limiter on the lower extremity dynamics. The passenger seat was adjusted in its longitudinal mid-position based on real-world data – a height adjustment was not available.

The HIII dummies were equipped with a standard configuration of sensors, while the Elderly Female Dummy had only sensors for measuring the accelerations of the head, thoracic spine and pelvis, and the thorax compression in the tested development level. To determine the seating position for the front passenger side, DEKRA contacted elderly people in Stuttgart area and measured their vehicles and also conducted a GIDAS-analysis.

Figure 1: Moment of first contact with frontal airbag (left: Elderly Dummy; middle: HIII 50th male; right: HIII 5th female)

Results

The pelvis of the HIII 50th male experienced the largest forward movement with 91 mm, followed by the Elderly Female (53 mm) and the HIII 5th female (48 mm) dummies. However, the HIII 5th female experienced the lowest pelvis acceleration, a_{3ms}, with 41.87 g followed by the HIII 50th male and the Elderly Female dummies with 44.96 g and 49.94 g respectively. Lap belt forces were the highest for the HIII 50th male with 4.96 kN and the lowest for the Elderly Female Dummy with 4.34 kN. The HIII 50th male recorded higher femur forces than the HIII 5th female, while the Elderly Female Dummy currently has no sensors to measure femur forces. Pelvis kinematics differed and influenced the torso kinematics. The Elderly Female recorded substantial submarining, resulting in the torso still leaning backwards at the first moment of contact with the front airbag, while the HIII 5th female dummy's legs flung upwards against the lower part of the dashboard (see figure 1).

Discussion

The chosen seat position showed major variances in occupant kinematics for different sizes and weight distributions. It must be evaluated whether the current pelvis design of the Elderly Female Dummy provided better real-world behavior and biofidelity compared to HIII or THOR dummy designs. Dummy interaction with the restraint system was only acceptable for the HIII 50th male, while the other dummies exhibited less adequate interactions leading to reduced performances. A real-world seating position of passenger occupants should be used to optimize passenger occupant restraints compared to seating positions currently defined in regulations and consumer tests.

The Elderly Female Dummy is still in its prototype phase. To the knowledge of the present authors, this is the first time that a comparison of the lower extremity dynamics is performed between the Elderly Female, the HIII 50th male and the HIII 5th female dummies.

References

1. International Transport Forum, Road Safety Annual Report 2020, 2020.
2. Gioffrè-Florio et al, G Chir, 39(1) :35-40, 2018.
3. Beebe et al, 25th ESV Conference, Michigan (US), 2017.

EFFICACY OF KARTING NECK BRACES IN REDUCING NECK INJURIES IN ROLLOVER ACCIDENTS: A FINITE ELEMENT STUDY

Wei Wei (1,2), Marie-Hélène Beauséjour (1,2), Nicolas Bailly (1,2), Maxime Llari (1), Zhi Xiao (3), Paolo Panichelli (4), Pierre-Jean Arnoux (1,2)

1. Laboratoire de biomecanique appliquee, Aix-Marseille Univ & Univ Gustave Eiffel, France; 2. iLab-Spine, France & Canada; 3. Hunan University, China; 4. Fédération Internationale de l'Automobile, Switzerland

Introduction

Karting rollover is one of the leading causes of death in karting accidents [1]. The neck can sustain serious injuries in karting rollovers due to the direct impact loadings from the head and the inertial loadings from the lower body and kart. Neck braces are usually worn by drivers to mitigate or prevent neck injuries during karting racing. However, little biomechanical research exists on evaluating the efficacy of neck braces in reducing neck injuries during karting accidents especially rollovers, which would be the objective of this study.

Methods

The head (helmet) impact conditions were evaluated in our previous reconstructions of karting rollovers with multi-body simulations. Most collisions were found to occur on the helmet regions 1 and 2 with the normal impact velocities of 3.6m/s and 4.1m/s (figure 1). An effective impact mass of 37kg to hit the helmet was also found to result in similar impact loadings as those in karting rollovers.
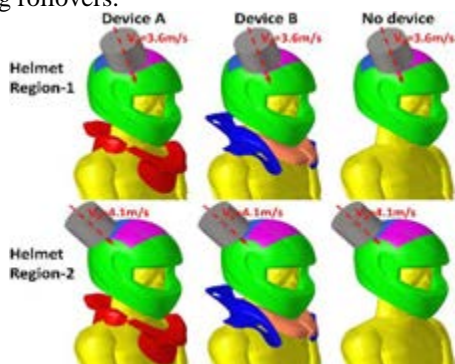
Figure 1: FE simulation setup of head impacts with and without a neck brace

Therefore, finite element (FE) simulations were performed here by applying initial velocities of 3.6m/s and 4.1m/s to a rigid cylinder impactor (mass 37kg, diameter 130mm and guided in its axis direction) to respectively hit on the region 1 and region 2 of the helmet worn on the THUMS v5.03 50th percentile occupant model (figure 1). The helmet FE model was previously validated and optimized for better head protection [2]. To evaluate the efficacy of neck braces, three configurations of device-wearing were considered: 1) wearing device A, 2) device B, 3) and wearing no device. Device A is a prototype only with stiff components while device B consists of stiff components and a foam able to absorb and dissipate energy. The FE models of both devices were previously validated under different impact loadings [3] and are currently worn on the THUMS model (figure 1). The cervical loadings (forces and moments) and the intervertebral range of motions (ROM) were measured and compared among the simulations with and without a neck brace.

Results

The flexion and lateral bending moments were higher at the lower neck (measured at T1) than at the upper (C1) and middle neck (C5) (figure 2). The compression force measured at the middle neck was higher than the upper and lower neck. Although the head-neck (C0-T1) ROMs were always within the physiological ROM thresholds, the ROM of certain functional spinal units (FSUs) exceeded the corresponding thresholds [4]. All these observations did not seem to depend on the device wearing configurations.
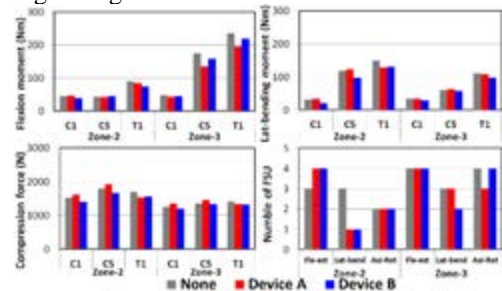
Figure 2: Mechanical loadings measured on C1, C5, and T1, and the number of FSU with ROMs over the physiological ROM thresholds in simulations

Discussion

The two devices showed no considerable reduction in flexion, lateral bending moments, or compression force of the neck. Both devices showed limited reductions in C0-T1 global ROMs to some extent but not in the number of FSUs with excessive ROMs. Therefore, the neck braces of both prototypes do not seem efficient in preventing neck injuries under these impact loadings representing karting rollovers. Further research remains to be done on device optimization for better neck protection in karting accidents.

References

1. Adler, Consumer Product Safety Commission, 48, 2000.
2. Li et al, Int J Mech Sci, 199: 106406, 2021.
3. Sun et al, Int J Crashworthiness, 17(6): 571-581, 2012.
4. Watier et al, ITBM-RBM, 27, 2006.

Acknowledgments

ON MEASURING IMPLANT FIXATION STABILITY IN ACL RECONSTRUCTION

Emir Benca (1,2), Ivan Zderic (2), Jan Caspar (2), Kenneth van Knegsel (2,3), Lena Hirtler (4), Boyko Gueorguiev (2), Reinhard Windhager (1), Harald Widhalm (1), and Peter Varga (2)

1. Department of Orthopedics and Trauma Surgery, Medical University of Vienna, Austria; 2. AO Research Institute Davos, Switzerland; 3. Department of Orthopedics and Trauma Surgery, Cantonal Hospital of Lucerne, Switzerland; 4. Division of Anatomy, Center for Anatomy and Cell Biology, Medical University of Vienna, Austria

Introduction

Numerous methods and devices are available for implant fixation in anterior cruciate ligament (ACL) reconstruction [1]. Their primary stability has been studied biomechanically by calculating fixation stiffness commonly from machine displacements [e.g. 2]. This study aimed to provide a better insight into measuring the structural characteristics and mechanical behavior of ACL implant fixations.

Methods

The ACL was reconstructed in 14 human tibial specimens from 3 female and 8 male donors (age 72.5 ± 5.7 years, range $62 - 79$ years). For the reconstruction, an 8 mm bone tunnel was drilled, a quadrupled semitendinosus and gracilis tendon was pulled through and secured with an 8 x 28 mm BioComposite Interference Screw (Arthrex Inc.) or 8.0 mm Shark Screw ACL (surgebright GmbH). A custom test setup was designed (Figure 1). The specimens (1) distally embedded in PMMA (2) were fixed into an electrodynamic test system (Acumen; MTS Systems Corporation). A D-shackle (3) was secured into tendon graft loop (4) and attached to the machine actuator (5). The spatial motion of the loading frame (6), specimen (7) and tendon graft (4) were tracked using a stereographic optical motion tracking system (Aramis SRX, GOM GmbH). A dial gauge (8) was attached to the distal end of the graft (9) to monitor the migration of the screw in the tunnel (slippage). The specimens were loaded cyclically with a sinusoidal profile at a constant valley load of 50 N and a peak load level starting from 50 N and increasing at a rate of 0.1 N/cycle until failure.
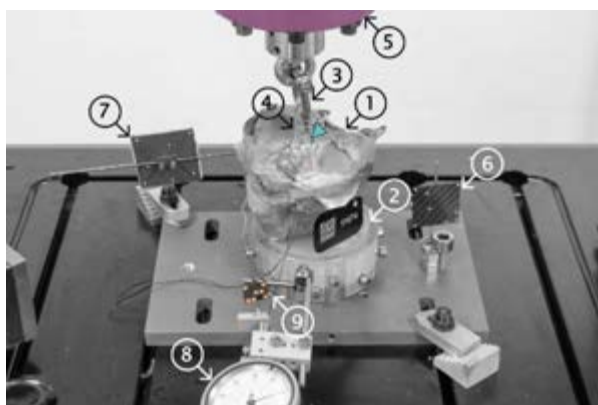
Figure 1: Experimental test setup.

Results

Significant differences were found between the displacement of the proximal and distal graft ends and the machine actuator. Machine displacements were up to 400% higher than the graft displacement and thus caused a significant underestimation of the fixation stiffness (Figure 2). The displacements measured at the different locations at ultimate load were found to correlate with each other ($0.772 < r < 0.893$).
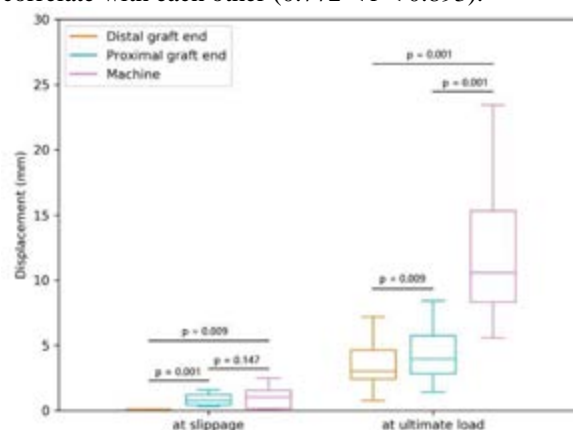
Figure 2: Boxplots for displacements of the proximal and distal graft end, and the machine actuator assessed at slippage initiation and ultimate load.

Discussion

Experimental assessment of the stability following implant fixation methods in ACL reconstruction relies on accurate measurement of relative displacements and deformations of the tendon graft. Machine actuator displacement, commonly used to assess fixation stiffness and graft slippage, leads to significant underestimation of stiffness due to the compliances of various components but allows a qualitative comparison between different fixation methods and devices.

References

1. Pasquali, M., et al., Knee Surg Sports, 2017. 25(5).
2. Scannell, B.P., et al., Am J Orthop, 2015. 44(1).

Acknowledgements

BIOMECHANICAL ANALYSIS OF SEVERAL HINGED TKA FEATURES IN WELL-ALIGNED AND VALGUS/VALGUS KNEE

Edoardo Bori, Federica Armaroli, Lilia Maestripieri, Bernardo Innocenti

1. BEAMS Department, Université Libre de Bruxelles, Belgium;

Introduction

Adequate fixation is an important requisite for hinged Total Knee Arthroplasty (TKA): consequently, several stem solutions are currently available. However, there are no evidence-based biomechanical guidelines for surgeons to determine the appropriate stem length and whether to use cemented or press-fit fixation, considering both physiologically aligned configurations and eventual cases of varus/valgus deformities for such high-constrained design.

The objective of this study is therefore to compare, using a validated finite-element model, bone stresses and implant micromotions in different configurations.

Methods

The 3D bone geometries were obtained from CT-scans reconstruction and the 3D model components of the Endo-Model Rotating Hinge (WALDEMAR LINK GmbH & Co. KG, Hamburg, Germany) were generated from industrial designs provided by the manufacturer. Sixteen configurations were investigated considering four stem lengths (50, 95, 120, 160 mm), cemented and press-fit fixation and physiological and osteoporotic bone properties. A further configuration without stem was analyzed as control. Average Von-Mises stresses, risk of fracture and micromotions were extracted in several regions of interest at 0 °and 90 °of flexion, under physiological load conditions.

Similar approach was followed to then analyze and compare 4 cases of varus and 4 cases of valgus deformities (5°, 10°, 20° and 30°), considering for each of them three different stem lengths (50, 120 and 160 mm) and three different angles of flexion (0°, 5° and 90°); the sought output was then concerning the force distribution on the two compartments, in order to analyze how the deformities were affecting this proportions and consequently which was the optimal stem configuration to maintain a proper distribution.

Results

In well-aligned situation, longer stems returned better results in terms of fixation compared to short ones; however, they induce higher stress-shielding effect in the distal region of the femur (even greater for press-fit stems, with values up to 38.5% greater than cemented ones) (see Figure 1). The cemented configurations, especially in case of 50 mm and 95 mm lengths, induce lower micro- motions (down to 16% lower) compared to their respective press-fit configurations. The osteoporotic RF values were greater than the physiological ones (up to 20.5%), but always below the bone limit of fracture.

Addressing the deformities, it was possible to note that the trend of mediolateral force distribution for 50 mm and 160 mm cementless stem is similar; in particular, the force increased sharply after 10° of Varus and Valgus alignment, with values of 100% of total force in respectively medial and lateral region. The 120 mm stem, instead, returned lower differences among the medial and lateral distribution even with extreme deformities (see Figure 2).
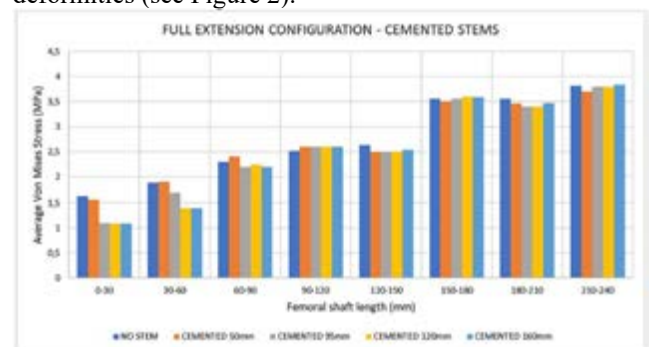
Figure 1:Von Mises Stress in femur bone at different distances from the cut for the four stem lengths analyzed
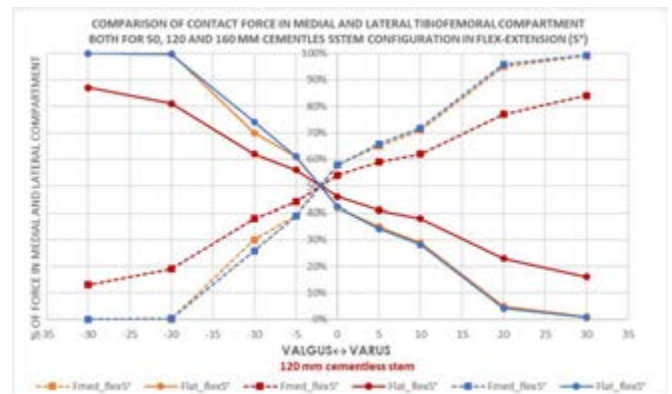
Figure 2: Force distribution between medial and lateral compartments in case of different deformity levels with the three lengths of stem analyzed.

Discussions

According to this study, when surgeons need to select a femoral stem in a hinged TKA aiming to proper stability and bone stress, the preferable option would be short cemented stems in case of physiological joint alignment; in case joint deformities were present, however, a better distribution could be provided with the use of longer stems accordingly to the level of deformity to address.

A PROTOCOL FOR EVALUATING HAND PROSTHESIS CONTROL

J. V. García-Ortiz, M. C. Mora, J. J. Arroyave-Salazar, A. Pérez-González

BE group, Dept. of Mechanical Engineering and Construction, Universitat Jaume I, Spain

Introduction

The development of anthropomorphic and functional hand prostheses is still a difficult engineering challenge, specifically regarding the interaction with the user. Most prostheses only include one or two degrees of freedom (DoF). This lack of dexterity implies its limited use during activities of daily living (ADL) [1]. The increase of the low acceptance rates of advanced prostheses requires a better understanding of the hand performance as well as commonly accepted measures and evaluation protocols [2]. This work presents an experimental protocol to evaluate the performance of the hand prosthesis control in ADL and evaluates the influence of training in the time performance of the control system.

Methods

Experiments were made with a 3D printed prosthetic hand prototype based on the BruJa Hand [3], a 5-finger 6-DoF low-cost prosthesis developed by the BE group. 10 right-handed healthy subjects (5 man/5 women; ages 20-55 years) performed transport tasks with cylindrical -CYL- and pulp pinch -PP- grasps [4] on different objects using the hand, attached to the forearm with a Pro Cuff device (Fig. 1, left). The subjects selected the grasp type with a mechanical switch and closed/opened the hand using a button when required.
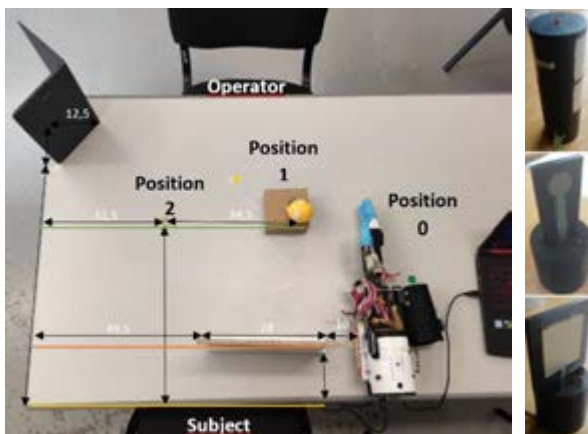
5 subjects were trained with 3D printed objects (Fig. 1, right) specifically designed for CYL and PP grasps. The other 5 subjects were not trained but were able to practice a few minutes with the hand. Finally, all the subjects performed the evaluation protocol with 17 selected objects from the YCB set, where both the objects and the hand were equipped with IMU sensors (Pikkulab) for measuring times and motions. The evaluation protocol was (setup in Fig.1, left): 1) The subject sits on the table and places the hand in Pos. 0

(rest); 2) the operator sticks an IMU sensor to the object and places it on Pos. 1 (hidden from the subject by a board). Then, the operator starts recording the trial (data and video) and, after 3 seconds, removes the board; 3) the subject, in view of the object, selects the grasp and performs the transport task from Pos. 1 to Pos. 2, returning the hand to Pos. 0; 4) the operator ends the recording and returns to step 1 with a new object.

The evaluation of the influence of the training in the hand control has been carried out measuring the total time involved in the transport task (TT). The TT is a summation of times between the following events of the transport task: E1) Decision to grasp; E2) Grip selection; E3) Grip identification by the control system; E4) Start of hand motion; E5) Reach to grasp phase; E6) Grasping posture generation; E7) Grasp execution; E8) Grasp confirmation; E9) Transport phase; E10) Object release decision; E11) Object release execution; E12) Return to rest position. Only events E3, E7 and E11 belong to the control system and the other to the user skills.

Results and Discussion

Figure 2 shows a polar diagram with the mean TT of the subjects to perform the transport tasks of each YCB-set object, with and without training. The results show that non-trained subjects generally spend more time in the transport tasks than trained subjects. A further data analysis will involve differentiating times between events, types of grasps and quality of the grasps in order to establish the performance of the control system.
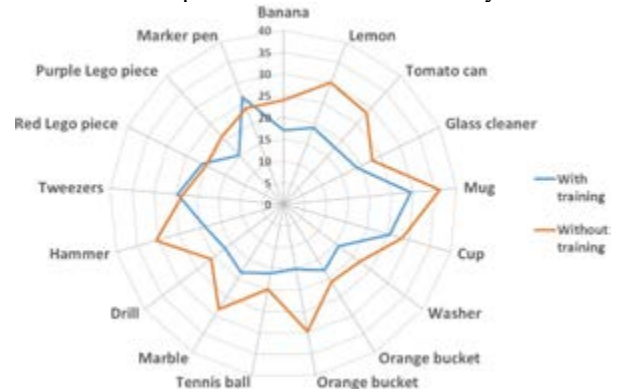
References

1. Liu et al, Ind. Robot. 41: 381-362, 2014.
2. Belter JT et al, J Rehab Res Dev. 50(5):599-618, 2013.
3. Andrés FJ et al, J Mechanisms&Robotics 11(1), 2018.

Acknowledgements

TOPOLOGY OPTIMIZATION OF A UNIVERSAL ARTIFICIAL TALUS IMPLANT

Ahmed Hafez (1), Andreas Schiffer (1), Marwan El-Rich (1)

1. Department of Mechanical Engineering, Khalifa University, Abu Dhabi, 127788, UAE

Introduction

Total talar replacement (TTR) surgeries have been used as an alternative to circumvent the drawbacks and limitations associated with various other talus fracture treatments [1]. Typically, the design of a custom, patient-specific TTR could take up to several months, delaying the surgical procedure. As a result, a universal talus prosthesis has been suggested and had its feasibility demonstrated in a previous study [2]. To further improve the performance of implants, topology optimization (TO) is often involved in their design. However, in the case of talus implants, no studies are known to exist in literature that involve TO in their design. Therefore, this study demonstrates the use of TO in the design process of a universal TTR and compares it against its non-optimized counterpart.

Methods

The universal talus prosthesis used was obtained from a previous study and a similar finite element (FE) approach was employed [3]. The FE model used (figure 1, left) involved a combination of two postures: dorsiflexion (+20°) and neutral standing (0°). For each posture, the simulation took place in three static time-steps: 1) bones surrounding the talus in the ankle joint were displaced towards the fixed talus, 2) the talus bone was allowed to freely adjust itself, 3) the displacement equivalent of a 2000 N compressive force was applied to the tibia. The titanium alloy Ti-6Al-4V ($E = 107$ GPa and $v = 0.323$) was used for the talus implant. For the TO, a volume fraction constraint of 0.3 and a stress constraint of 375 MPa was used for the implant. As an objective, the weighted compliance of the loading step for the two postures (both assigned an equal weight of one) was maximized for the design space (figure 1, right). The FE model was setup in Hypermesh (Altair, Troy, USA) and the TO was carried out using Optistruct solver (Altair, Troy, USA).
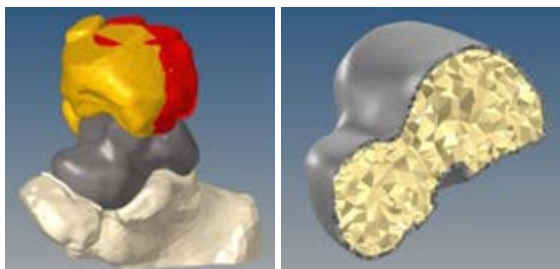
Figure 1: (left) Combined posture setup: dorsiflexion in orange and neutral standing in red; (right) Section view of design space (in yellow) and non-design space (in grey)

Results

Figure 2 shows the contour plot for element densities (ratio of the density of the optimized element to its non-optimized counterpart) ranging from 0 to 1. A 0 value represents a void and a 1 value represent a solid. As for intermediary values, they represent a fictitious material.
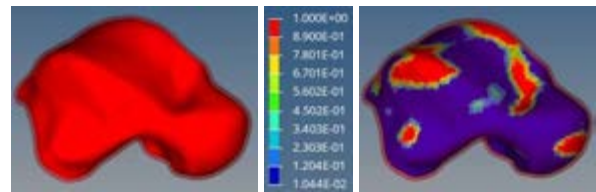
Figure 2: Non-design space made transparent for clarity. (left) Non-optimized; (right) Optimized

As a better illustration of the results, different views of the optimized implant with element densities > 0.3 (with simple averaging) are shown in figure 3.
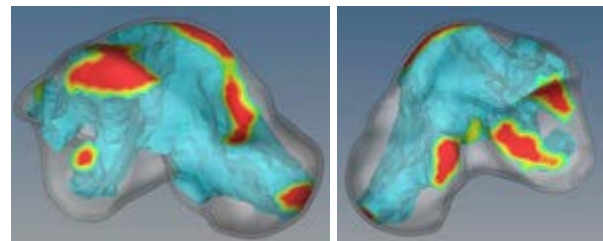
Figure 3: Different views of optimized implant with element densities > 0.3 shown

Discussion

To compare, the non-optimized implant weights approximately 190g while the optimized implant weighs (theoretically) 79g, which amounts to a 58% reduction in total weight. The results shown are a demonstration of the feasibility of using TO methods in talus implant design. A future finite element analysis will be performed to compare the stress distribution on the optimized and non-optimized implants as well as the surrounding bone in both postures

References

1. Hussain, Journal of Foot and Ankle Surgery, 60:1-8, 2020
2. Trovato et al., Foot and Ankle Surgery, 23:89-94
3. Liu et al., ESBiomech, 2022

Acknowledgements

NUMERICAL SIMULATION OF STRESS-SHIELDING
AT THE BONE-IMPLANT INTERFACE UNDER SHEAR LOADING

Yoann Hériveaux (1), Sophie Le Cann (2), Manon Fraulob (2),
Elsa Vennat (1), Vu-Hieu Nguyen (3), Guillaume Haïat (2)

1. *Université Paris-Saclay, CentraleSupélec, ENS Paris-Saclay, CNRS, LMPS, France ;*
2. *CNRS, MSME UMR 8208, France ;*   3. *Université Paris-Est Créteil, MSME UMR 8208, France*

Introduction

Inserting a titanium implant in bone tissue may modify its physiological loading and therefore cause bone resorption, a phenomenon known as stress-shielding [1]. While monitoring and preventing stress-shielding is necessary to ensure the surgical success, it remains difficult to experimentally retrieve information on the properties of the interfacial tissues at the scale of 1-100 µm from the implant surface, where this phenomenon is localized. Numerical modelling represents a complementary tool to better understand phenomena related to the coupled bone-implant system due to the difficulty of measuring the stress distribution *in vivo*. The aim of this study is to investigate numerically the influence of various geometrical and material parameters on the local stress field around a bone-implant interface (BII) subject to shear loading.

Methods

A 2D plane strain finite element model of a sinusoidal BII allowing to vary the bone-implant contact (BIC) and the implant roughness through its periodicity λ and its amplitude 2Δ, was derived from a previous study [2] (Fig.1b). A shear loading was applied at the top of two half-spaces corresponding to a rough implant and to cortical bone tissue respectively, separated from each other by an irregular interphase. The isostatic pressure and the maximum shear stress around the BII were simulated for different (i) implant roughness, (ii) implant materials, (iii) BIC ratios, and (iv) bone Young's moduli. The equivalent stiffness of the BII was also derived from the simulations.
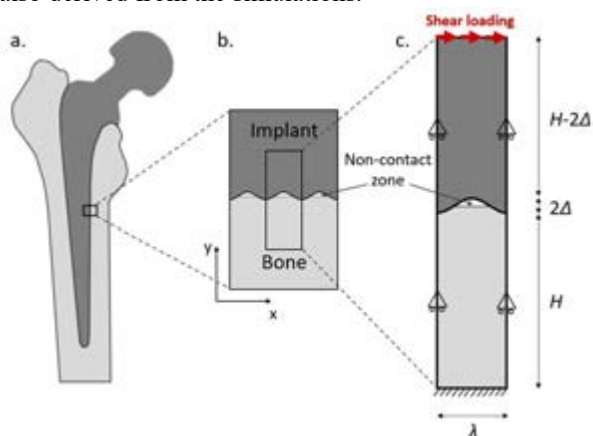
Figure 1: Schematic description of the model at the macroscopic level, with the example of a femoral stem (a). Geometrical description of the sinusoidal BII (b), with the numerical details in (c).

Results

A stress concentration is evidenced at the intersection between the implant, the void and the bone, in particular for lower roughness (Fig. 2). More generally, stress-shielding occurs at a distance lower than around 0.4λ from the BII, and increases (i) when the BIC ratio decreases and (ii) when the implant roughness decreases. Moreover, changing the implant material to get closer to the mechanical properties of bone (*e.g.* using metal-polymer composites) reduces the shear stress and the isostatic pressure.
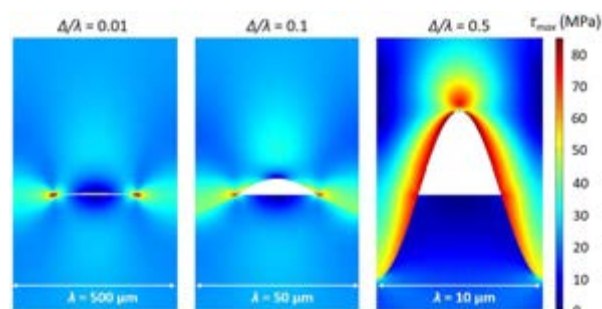
Figure 2: Spatial variation of the maximal shear stress τ_{max} around the BII for BIC = 50% and three values of the implant roughness (Δ/λ = 0.01, 0.1, and 0.5).

Discussion

This study enhances the clinical importance of maximizing the BIC ratio to minimize stress-shielding effects, and suggests that using adapted implant material such as the metal-polymer composite Ti-35BPA [3] could help to minimize stress-shielding effects. Future studies could use the equivalent stiffness of the BII determined herein in order to replace the complex behavior of the BII by a simple analytical model. It would also be of interest to introduce bone remodeling in our model to investigate the temporal changes occurring during healing, after the implant insertion.

References

1. Sumner et al, J Biomech, 48(5):797-800, 2015.
2. Raffa et al, J Orthop Res, 39(6):1174-83, 2021.
3. Okulov et al, Sci Rep, 7(1):20, 2017

Acknowledgments

BIOMECHANICAL ANALYSIS OF SURGICAL ALIGNMENT AND DESIGN IN TOTAL KNEE ARTHROPLASTY

Bernardo Innocenti, Edoardo Bori
BEAMS Department, Université Libre de Bruxelles, Belgium

Introduction

The design of each TKA implant is originally defined by the manufacturers according to a certain alignment philosophy, but its in-vivo performances are however strongly depending on surgeon's decisions in terms of position and orientation together with the relative soft tissue envelope management. Although extremely important, this topic is still highly debated and a clear, standardized approach has not yet been established [1]. Among the different alignment strategies, mechanical alignment [MA] and kinematic alignment [KA] are the most popular [1,2]: in MA, the tibial and femoral components are positioned orthogonally to the tibial and femoral mechanical axis; in KA, instead, the TKA components are re-aligned to the native joint line.

Several studies have attempted to clinically compare the outcomes related to the different alignments, but no definitive results were achieved and long-term unbiased multicenter follow-up studies are still missing. It is furthermore to highlight that sometimes the surgeons establish the surgical alignment approach to perform according to their preferences, which may not always match the rationale behind the TKA implant; this means that components designed according to the traditional mechanical alignment may be implanted with a kinematic alignment, and this discrepancy could therefore affect clinical outcomes and make difficult their interpretation [1].

The aim of this work is therefore to compare the different alignment philosophies in different TKA designs of knee implant, through the use of a validated finite elements model.

Methods

This study is performed using finite element analysis, developing a knee finite element model based on an already validated and published one [3].

To model the bone, the geometry of a Sawbones tibia (right side, size medium) was selected in agreement with previous studies [1,3]; the orthopedic devices were instead based on data coming by an industrial prosthesis.

Four different configurations were analyzed:
-MA with a symmetric polyethylene thickness implant (inducing a joint line orthogonal to the bone cuts);
-MA with an insert having asymmetric thickness (inducing a joint line similar to the physiological);
-KA with a tibial stem orthogonal to the tibial cut;
-KA with the tibial stem aligned with the tibial axis.

Each model underwent a 2500N vertical load simulating the peak force in walking [4]. Polyethylene and bone stress were extracted and compared in several regions of interest.

Results

The stress distribution on the polyethylene in case of a symmetric insert resulted to be more uniform among the medial and lateral compartment, if compared with the asymmetric insert (Figure 1). A similar homogeneous distribution was identified in terms of bone von Mises stress when a symmetric insert is used (Figure 2).

The presence of an aligned tibial stem for the kinematic aligned model induces an increase of the poly stress and of the bone stress in comparison to the orthogonal tibial stem.
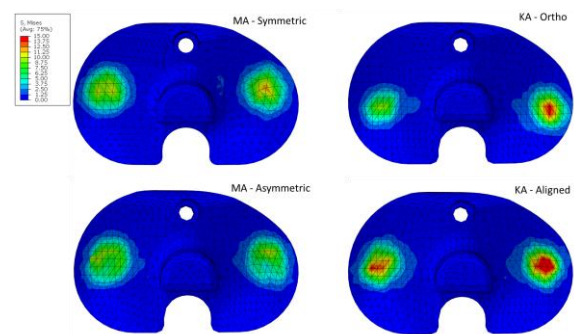
Figure 1 – Von Mises stress in the polyethylene insert for the different configurations.
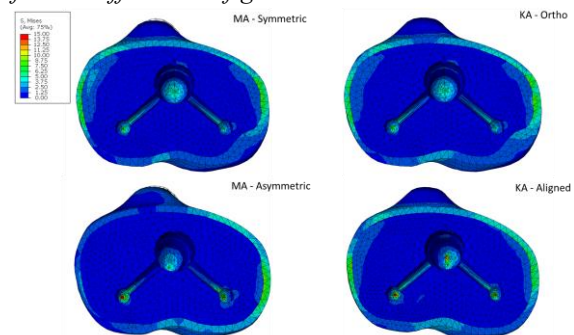
Figure 2 – Von Mises stress in the tibial bone for the different configurations.

Discussions

This study has demonstrated that each combination of alignment approach and prosthesis design induces a specific stress distribution in both the tibio-femoral and the prosthesis-bone interfaces; therefore, surgeons should consider this information when deciding which implant to adopt and the relative alignment approach to follow.

References

1. Innocenti and Galbusera. Human Orthopaedic Biomechanics, 2022.
2. Lustig et al. SICOT J:7:19, 2017.
3. Innocenti, et al., JOA: 29(7): 1491-8, 2014.
4. Innocenti, et al., JOA: 31(1): 295-301, 2016.

POSTERIOR CRUCIATE LIGAMENT TENSION AND TIBIAL COMPONENT MALROTATION IN TOTAL KNEE REPLACEMENT

Kurt Johnson (1), Jan-Oliver Sass (1), Lucas Buerstenbinder (1), Jean Baptiste Darques (1), Iman Soodmand (1), Rainer Bader (1), Maeruan Kebbach (1)

1. Rostock University Medical Center, Department of Orthopaedics, Germany

Introduction

Although total knee replacement (TKR) is an established treatment for advanced osteoarthritis, with more than 1,324,000 operations performed yearly [1], 20% of patients experience unsatisfactory results [2]. Many factors, such as implant alignment and a balanced flexion-extension gap, influence the postoperative result [3, 4]. The posterior cruciate ligament (PCL) controls anterior-posterior translation and joint compression, which affects the flexion-extension gap [4]. Previous studies have examined the impact of PCL tension [4] and implant malrotation [5] on tibiofemoral stresses individually. However, few studies have analyzed the combined impact of these factors. Therefore, the present study aims to utilize a finite element (FE)-model of a cruciate-retaining bicondylar TKR to analyze the impact of tibial malrotation with different PCL properties on the tibiofemoral contact stress and knee kinematics.

Methods

A quasi-static FE-model was created in Abaqus/Standard 6.14 (SIMULIA, Providence, RI, USA). The femoral component (P.F.C. Sigma, DePuy Synthes, Raynham, MA, USA) was modeled as linear-elastic Co-28Cr-6Mo (E = 210 GPa, ν = 0.29) [6] meshed with 37,157 modified tetrahedral elements. The tibial insert made of UHMW-PE was modeled as elasto-plastic (E = 463 MPa, ν = 0.46) [7, 8] meshed with 60,135 modified tetrahedral elements. Amplitudes for knee kinematics and load were imported from a musculoskeletal multibody model during a squat motion [9]. Flexion, internal rotation, medio-lateral and anterior-posterior translation, and compressive load were applied to the femoral component. Abduction-adduction motion was unconstrained. FE-simulations representing neutral alignment and 5˚ tibial internal malrotation combined with normal [9], tight [10], and resected PCL properties were created, and contact stresses and knee kinematics were analysed.

Results

A sample of different tibial rotational alignments for a given PCL is shown in Figure 1. Malrotation had the highest impact on contact stresses, with a ~9 MPa increase for each PCL (Table 1). PCL properties had some impact on contact stress, with increases of ~2-3 MPa between the resected and tight PCL properties for each orientation. Knee motion was similar for each PCL condition, with less femoral rollback for the tight PCL.
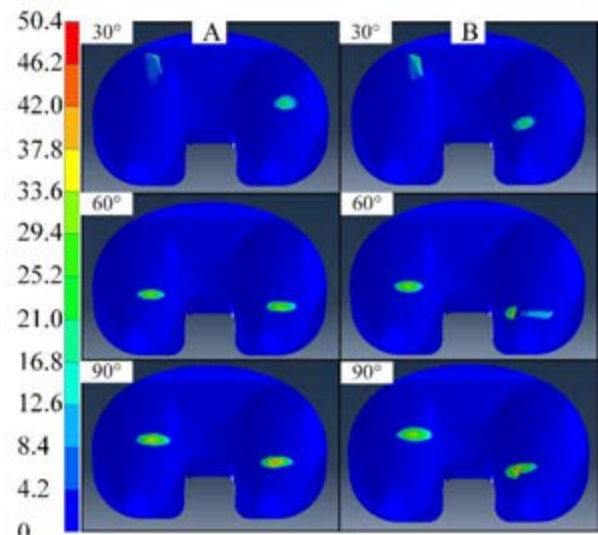
Figure 1: Comparison of contact stress values (MPa) for A) neutral alignment with normal PCL condition, B) 5˚ internal malrotation with normal PCL condition

	No PCL	Norm PCL	Tight PCL
0°	40.39	41.43	43.33
5° IR	50.14	50.38	51.86

Table 1: Maximum contact stresses (MPa) for different PCL conditions in normal and 5˚ internal malrotation

Discussion

This computational study demonstrates that increased PCL tension and tibial internal malrotation of TKR lead to increased contact stresses in articulation during a squat motion. This is comparable to [5], where increased stresses for 4˚ tibial internal malrotation was reported. Therefore, PCL tension and malrotation might increase wear-rate on the tibial insert. A limitation of our study is the lack of experimental validation, but our model design enables the evaluation of different surgical parameter effects on stresses and kinematics in TKR.

References

1. Kurtz, S. et al, Int Orthop, 35:1783-9, 2011.
2. Kahlenberg, C. et al, HSS J, 14:192-201, 2018.
3. Barrack, R. et al, Clin. Orthop. Relat. Res.,392:46-55,2001.
4. Steinbrück, A. et al, Biomed. Eng. Online, 13.1:1-13, 2014.
5. Kang, K.T. et al, Bone Joint Res, 5.11:552-559, 2016.
6. Conlisk, N. Et al, Med. Eng. Phys., 38.9:959-968, 2016.
7. Kurtz, S et al, Biomaterials, 23.9:1907-1919, 2002.
8. Godest, A.C. et al, J Biomech, 35.2:267-275, 2002.
9. Kebbach, M. et al, Materials, 13:2365, 2020.
10. Abubakar, M.S. et al, J. Knee Surg., 29.8:684-689, 2016.

INTRAMEDULLARY NAILS VS. BONE PLATE AT THE PROXIMAL HUMERUS - COMPUTERSIMULATION

Stefan Lehner (1), Uli Schreiber (2)

1. Munich University of Applied Sciences, Germany; 2. OT Medizintechnik. Munich, Germany;

Introduction

Femoral shaft fractures are among the most prevalent fracture type, representing around 13% of total skeleton fractures [1]. For the operative therapy different osteosynthesis techniques are known, e.g. angular locking implants. Locking means a fixed, rigid connection which does not allow any movement between implant and locking screws.

In general the use of locking osteosynthesis implants results in an increase of the connectivity between the bone and the prosthesis as well as a higher stability within the osteoporotic bone. But combined with the angular stability an increased number of metal bone screws cut outs of the head of the humerus bone were observed. Depending on the grade and the type of the fracture and the quality of the bone the impact of the implants on the osteosynthesis at the proximal humerus differs.

Goal of this study was to compare the biomechanics of an angular locking nail ostesynthesis and an angular locking plate ostesynthesis in terms of the risk of a bone screws cut out of the head of the proximal humerus head. Due to the application of measured in vivo loads it was possible to simulate realistic activities and to measure the displacements of the stabilizing interacting bodies).

Methods

For the numerical simulation a detailed multi-body model of the head and the neck was developed using SIMPACK (Dassault Systèmes, Vélizy-Villacoublay, France).

Based on CT data the humerus is modeled as a rigid body describing the exact 3D geometries of three fractured bone parts. An intramedullary nail system as well as a bone plate were modelled as flexible bodies. Both CAD models were created by 3D scans of implants which are well known on the market. Also the bone screws were modelled as flexible bodies. All implants were modelled by using the material properties of medical grade Titanium alloy Ti6Al4V.

Based on the results of experimental 3-point bending tests the verification of the flexible models of the intramedullary nail system and the anatomical bone plate were carried out.

The fixation of the screws within the bone segments was realized by using spring-damper elements. The stiffness of the spring elements can be varied to simulate different bone density respectively bone quality.

To apply realistic loads during two daily activities in-vivo data published in the Orthoload data base (www.orthoload.com) were simulated [2,3].

Results

From the biomechanical perspective the bone plate showed higher deformations than the intramedullary nail in both simulated load cases (fig. 1).
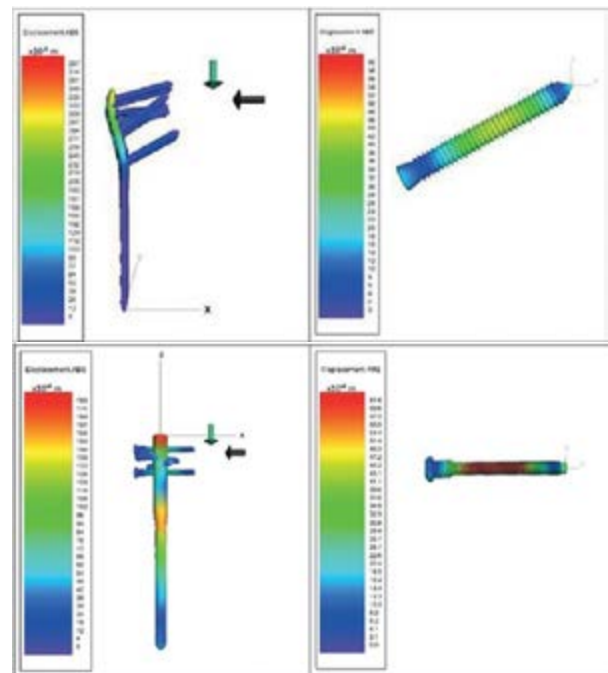
Figure 1: Deformations of the bone plate respectively of the intramedullary nail in a simulated load case

The absolute deformation in the bone plate patient walking with a pair of crutches was 2 times higher as the deformation of the nail. During the lifting of the 10 kg mass the deformation in the bone plate was even 8 times higher as the deformation of the nail.

Discussion

Using flexible models within a MBS model open up further possibilities in biomechanical simulations. With the developed and validated model it is possible to analyse clinical problems with ostesynthesis systems more detailed.

References

1. Gabarre et al, Advances in Biomechanics and Tissue Regenration:215-240, 2019.
2. Westerhoff et al, J Biomech, 25:1840-9, 2009.
3. Westerhoff et al, Clin Biomech, 27:711-18, 2012.

MEASURING SPINAL ROD FORCES FOR SCOLIOSIS AND/OR FRACTURE FIXATION IN VIVO

Meera Mangaleshwaran, Julian Leong, Stephen Taylor

University College London – Division of Surgery and Interventional Sciences, United Kingdom

Introduction

Harrington (1962) developed the first spinal rod for progressive scoliosis correction. Nachemson and Elfstrom (1971) measured the forces acting on a modified Harrington rod during scoliosis correction and measured an axial force up to 350N before the corrective procedure, which then declined over the following days before the next surgery [1]. The forces of distraction have been measured using calipers, with the force increasing with distraction length [2]. The aim of our work is to measure the 6 dof of loading acting upon the central portion of a spinal distraction rod, using sealed strain gauges, and inductively coupling for power supply and telemetry. This force-measurement rod will offer regular readouts and daily progress. Being more sensitive than radiographs, it will aid clinicians in determining optimal time for a second intervention. Another possible use is for fracture stabilisation, the rod will show gradual reduction in load from rod to spine and ultimately show optimal time of removal [3]. This study uses rods of the same geometry and size as regular implants, preserving the same bending stiffness and clinical procedure.

Method

Ti-6-4 tubes of 6.35mm outer diameter are instrumented internally with 9 strain gauges. A concentric load bearing solid outer tube (0.7mm wall thickness) and one semi-circular x-section inner shell on which are pre-mounted strain gauges and electronics are pre-bonded using implant-grade ISO 10993-6 adhesive epoxy. End pieces joining this assembly to the tube for strain transfer will be spot welded or epoxy joined. This cross section is shown in figure 1. This construct allows for instrumentation to be contained entirely within the rod, without welding longitudinally, whilst maintaining adequate bending stiffness at one end will be an implant coil in line with rod. The overall geometry will reduce bending stiffness to that of a 5.65mm rod, an acceptable reduction since rods of 5mm pure Ti are also used routinely. Implant instrumentation is being evaluated for resolution, power, and speed. Strains will be amplified, digitized, telemetered, and powered using inductive coupling between an implanted coil contained at one end of the rod and an external coil [4] The construct will be mechanically tested using a Wohler fatigue machine. The model was finite element analysed using COMSOL™ to validate the choice of strain measurement sites for efficacy of load sensitivity and selectivity.

Results

A model of the proposed rod was created on COMSOL with a fixed constraint on end, boundary loads, and materials assigned respectively. User controlled fine mesh was also applied. Sinusoidal strain profiles and their phase relationships are seen in figure 2 give a good assurance. But further analysis of results is needed and experimental results to validate and verify.

Figure 1: Meshed FE model of sleeves with end stops
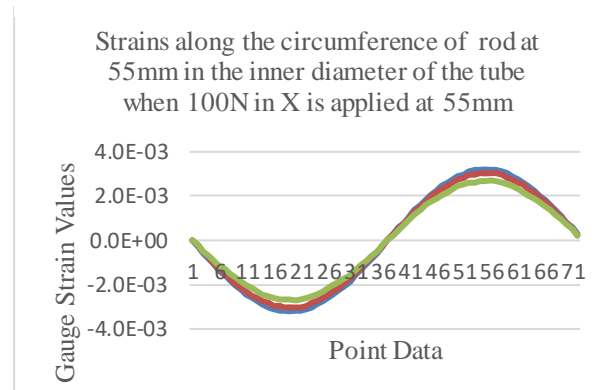
Figure 2: Plot showing strains

Discussion

Analysis of models will find strain sensitivities at various locations for different loads. The study will inform on optimal strain gauge positions by transmitting strain from the outer tube to the inner core. The chosen positions allow measurement of dynamic 3 forces and 3 moments acting across the healing section of the rod.

References

1. Nachemson A, Elfström G. Intravital wireless telemetry of axial forces in Harrington distraction rods in patients with idiopathic scoliosis. J Bone Joint Surg Am. 1971 Apr;53(3):445-65. PMID: 5580005..
2. Teli, M., 2012. Measurement of forces generated during the distraction of growing-rods in early-onset scoliosis. World Journal of Orthopedics, 3(2), p.15.
3. Rohlmann, A., Graichen, F. and Bergmann, G. (2002). Loads on an Internal Spinal Fixation Device During Physical Therapy. *Physical Therapy*, 82(1), pp.44–52.
4. Hao S, Gorjon J, Taylor S. SCIMITAR: subject-carried implant monitoring inductive telemetric ambulatory reader for remote data acquisition from implanted orthopaedic prostheses. Med Eng Phys. 2014 Mar;36(3):405-11.

A COMPUTATIONAL METHODOLOGY FOR THE INVESTIGATION AND COMPARISON OF THE ASSEMBLY EFFECTIVENESS DURING TOTAL HIP ARTHROPLASTY

Ali Cherif Messellek (1), Mohand Ould Ouali (2), Abdelwaheb Amrouche (3)

1. École Militaire Polytechnique, Algeria; 2. University of Tizi Ouzou, Algeria; 3. Université d'Artois, France

Introduction

The assembly of the femoral head and/or the neck onto the femoral stem is achieved by a manual impaction during a Total Hip Arthroplasty (THA). Surgeons use a polymer tipped impactor instrument and an orthopedic mallet to avoid damaging the prosthesis. This surgical procedure is considered to be a critical factor determining the success or failure of THA [1,2]. Surgeons are provided with general guidelines and training by manufacturers on how to assemble the head to a particular stem; however, manufacturers' guidelines are vague for the assembly of the head and stem with statements such as 'slightly' or 'firmly' impacted the norm to describe the magnitude of any impaction force to be used [3]. In reality, the magnitude of the impact used is based on a surgeons' preference, experience, the type of prosthetic femoral head, and the quality of the patients' bone stock. In this study, a computational methodology is proposed for the simulation of the assembly procedure. Using this methodology, two mechanical quantities are introduced to be able to compare the effect of the assembly magnitudes on the initial mechanical state, following a surgical gesture. The comparison is carried out on the most widely used modular tapers in THA, which are the 12/14 scheme and the Type I scheme. This is in the aim to contribute to the standardization of the surgical gesture.

Methods

The first mechanical quantity is the taper axial strength which corresponds to the ability of the taper to resist axial disassembly. It mainly depends on the material Young's modulus, contact geometry, and friction aspect. It is given as follows:

$$\text{Axial Strenght} = \frac{\text{Assembly Force Magnitude}}{\text{Dissassembly Force Magnitude}} \quad (1)$$

The second mechanical quantity is the axial stiffness which is defined as the ability to resist the axial displacement. It mainly depends upon the elastic Young Modulus, area of the cross-section, and size of the design. It is given as follows:

$$\text{Axial Stiffness} = \frac{\text{Assembly Force Magnitude}}{\text{Induced Displacement Magnitude}} \quad (2)$$

Results and discussion

Based on the axial strength and axial stiffness, a comparative investigation between taper designs is carried out considering the design scheme, material coupling, angular mismatch, and friction coefficient (COF). We present here only the result for the case of 'Type I' and '12/14' design scheme (Figure. 1).
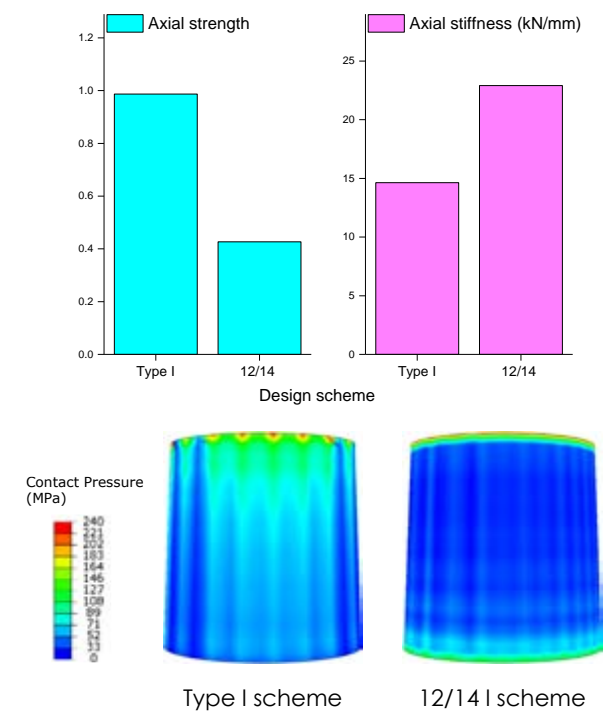
Figure 1: Comparison in terms of the taper design scheme.

As can be shown, the axial strength is largely affected by the design scheme. Type I scheme exhibits a better resistance to disassembly forces, which is twice as high as the 12/14 scheme. This behavior can be explained with the shape of the Type I scheme which offers more perfect contact overlap between the trunnion and bore interfaces. Furthermore, the 12/14 scheme provides a stiffer taper about 1,6 times. This is also explained by the size of the 12/14 scheme which results in significant inertia and therefore high stiffness.

Conclusion

Type I is easier to be assembled by a surgeon during a primary THA and more difficult to be extracted during a revision THA, than a 12/14 design scheme.

References

1. Haschke et al, Proc Inst Mech Eng H, 230:690-699, 2016.
2. Jauch et al, J Biomech, 44:1747-1751, 2011.
3. Rehmer et al, Clin Biomech, 27:77-83, 2012.

NUMERICAL STUDY FOR PRIMARY STABILITY ASSESSMENT IN OSSEOINTEGRATED TRANSFEMORAL PROSTHESES

Agostino Igor Mirulla (1,2), Andrea Valenti (1), Laura Bragonzoni (2), Tommaso Ingrassia (1)

1. Department of Engineering, University of Palermo, Italy; 2. Department for Life Quality Studies, University of Bologna, Italy

Introduction

The bone remodeling is a cyclic and continuous biological process during which bone tissue modifies and adapts its internal structure, stressed by an external load [1].

In the prosthetic field, the bone adaptation is stimulated by the direct interaction between a biocompatible metal component and the surrounding bone tissue. The efficacy of this process is identified by the primary and secondary stability assessment [2].

The aim of this study is to evaluate by finite element (FE) analysis the primary stability in an osseointegrated transfemoral prosthesis, comparing different geometrical shapes.

Methods

A 3D femoral model of an amputee was rebuilt by processing TC images using MIMICS INNOVATION SUITE (Materialise HQ, Leuven, Belgium).

Three different femoral stems, with different geometrical shape (straight, planar curvature and bi-planar curvature), were modeled following the medullary canal morphology and using SOLIDWORKS (Dassault Systèmes, Vélizy-Villacoublay, Francia).

The FE model has been performed using ABAQUS (Dassault Systèmes, Vélizy-Villacoublay, Francia) applying a compression load of 1000N.

Results

The micromotion between metal implant and cortical bone was assessed by CSLIP variable. The latter represents the relative tangential displacement at the bone-implant contact surfaces. The resulting displacement has been calculated using the following formula:

$$CSLIP = \sqrt{CSLIP1^2 + CSLIP2^2} \qquad (1)$$

In the end, the displacement trend has been evaluated for all different femoral stems (figure 1).
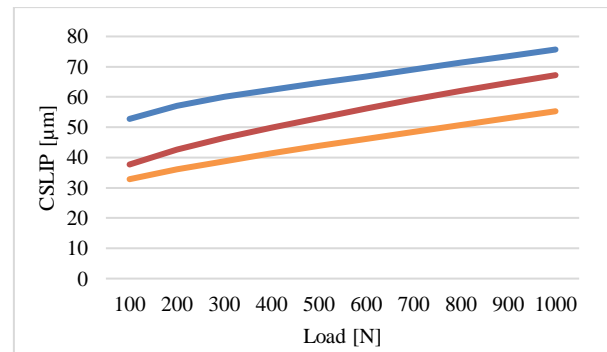
Figure 1: Trend of displacement on the bone-implant contact surface for the straight (blu line), planar curvature (orange line) and bi-planar curvature (red line) stems.

Discussion

The femoral stem modeled following a bi-planar curvature provides the smallest relative displacement. However, the tangential displacements are within the allowable range for the formation of new bone tissue, 50-150 µm [3] in all femoral stems analyzed.

References

1. J. Klein-Nulend et al, Pathol. Biol., vol. 53, no. 10, pp. 576–580.
2. T. Nishii et al, Clin. Orthop. Relat. Res., no. 339, pp. 121–131, 1997.
3. M. Viceconti et al, J. Biomech., vol. 33, no. 12, pp. 1611–1618.

COMPUTATIONAL TOOLS FOR BIO-COMPATIBLE GYROID FOAMS

Ana Pais (1), Jorge Lino Alves (2), Jorge Belinha (3)

1. INEGI, Portugal; 2. FEUP, Portugal; 3. ISEP, Portugal

Introduction

In this work, it is proposed a methodology to obtain gyroid foams for prosthesis or implants. The gyroid foam being considered is a sheet network, which is shown to possess higher stiffness and strength than solid networks [1].

The gyroid surface can be described by Triply Periodic Minimal Surface (TPMS) equation. This surface divides the space into two parts which can be equal is the isosurface value is zero. If we choose the space defined by one of the sides, a gyroid solid network is obtained. On the other hand, if we thicken the surface by translating it an amount of a half-thickness on both sides, defined by the normal vector to the surface in each point, a sheet networks obtained.

It is possible to edit the function point by point and thus, a gradient of density is obtained, which can enhance the mechanical properties of the part. In biomedical implants, stress shielding can be minimized as the stiffness of the implant is optimized according to the bone stiffness [2].

Methods

A bio-inspired remodelling algorithm is used to obtain the optimal density field for some part, whose functioning is shown as a scheme in Figure 1.
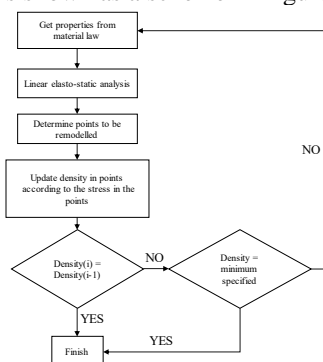
Figure 1: Flowchart of the bio-inspired remodelling algorithm

Transforming a density field into a foam-like solid requires a post-processing phase where the input is the remodeling result and the output is the solid. The post processing is summarized in the following steps:

1) Interpolating the gyroid surface

The gyroid equation has two main editable parameters, namely, the size of the unit cell which can be different in the three axes, and the value of the iso-surface.

If the original discretization in the model is not very fine, the interpolated surface will be inaccurate. So, extra interpolating points are added in between the Gauss points, which inherit the properties of the nearest Gauss point. These properties translate into parameters of the gyroid equation, or later, into thickness of the surface.

2) Thickening the surface into a solid

In order to turn the surface into a solid, the surface is thickened by offsetting the surface t/2 to both sides, where t is the thickness. Since the gyroid is defined through an equation, it is possible to define the thickness of the surface at a given point from the apparent density. An example of the thick surface can be seen in Figure 2.
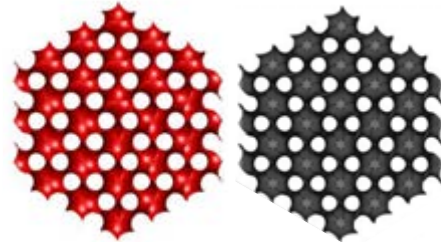
Figure 2: Gyroid surface (on the left) and gyroid foam obtained by thickening the surface (on the right)

3) Trimming and final steps

The need for this stage is to improve the quality of the surface mesh for 3D printing, or for remeshing with a solid mesh. Non-parametric CAD software is used at this stage.

Discussion

The remodelling algorithm does not considers the intricate geometry of the gyroid foam. Instead, and with the advantage of significantly reducing the required computational cost, in the material law, it considers homogenized equivalent mechanical properties of the gyroid, obtained through numerical homogenization. With this post-processing, the geometry is recovered as a solid. Thus, the solid can be 3D printed to obtain a functional prototype or it can be re-meshed for further analysis using FEM software. Therefore, it is possible to validate the material models, by comparing the accuracy of the homogenization model and the accurate representation model.

References

[1] O. Al-Ketan, R. Rowshan, and R. K. Abu Al-Rub, "Topology-mechanical property relationship of 3D printed strut, skeletal, and sheet based periodic metallic cellular materials," *Addit. Manuf.*, vol. 19, pp. 167–183, 2018, doi: 10.1016/j.addma.2017.12.006.

[2] S. Ma, K. Song, J. Lan, and L. Ma, "Biological and mechanical property analysis for designed heterogeneous porous scaffolds based on the refined TPMS," *J. Mech. Behav. Biomed. Mater.*, vol. 107, no. March, 2020, doi: 10.1016/j.jmbbm.2020.103727.

Acknowledgements

NUMERICAL APPROACH TO IMPROVE SOCKET-LINER SYSTEM USING TAILORABLE 3D PRINTED METAMATERIALS

Vasja Plesec (1), Gregor Harih (1)

1. Faculty of Mechanical Engineering, University of Maribor, Slovenia

Introduction

The development of additive technologies has enabled the rapid and detailed fabrication of customised parts that enhance ergonomics through systematic adaptation when interacting with biological tissue. The materials that provide such customisation by manipulating design parameters are metamaterials. The successful use of metamaterials is already evident in applications such as footwear or personal and sports protective equipment [1]. However, they have not yet been used in prosthetics to produce an improved socket-liner system that minimises pressure on the limb surface while ensuring adequate stability. Our research aims to investigate the potential of flexible 3D-printed metamaterials to develop a tailored socket-liner system for lower limb prostheses.

Methods

To develop the socket liner system, we used the established finite element method, which allows us to analyse the biomechanical system. The geometry is based on a previously developed generic 3D model. The residual limb, which was dimensioned based on anthropometric measurements, consists of bones (femur, tibia, fibula, patella) and a bulk soft tissue. Previously performed numerical analyses with commercially available silicone liners in combination with PTB or TSB socket validated the model. The simulation consists of the following two steps:

1. donning of the prosthesis,
2. vertical loading - simulating stance.

To achieve the desired mechanical response, we adjusted design parameters such as wall thickness, type of cellular structure, size of cells and type of base material. The aim was to reduce stress concentrations at the limb-liner interface and conserve stability by minimising relative displacement until the pain pressure threshold (PPT) was reached. The value of PPT was taken from the literature [2].

Results

Initially, metamaterials behave as linear elastic materials with a quasi-rigid stiffness compared to soft tissue. When the contact pressure reaches a certain point, the material starts to deform under almost constant pressure, also known as a plateau in the σ-ε diagram (Figure 1). In the final phase, the structure compresses rapidly, and the elastic modulus increases exponentially [3]. Such a material response can be controlled with the design parameters and customised according to the needs. The results in terms of contact
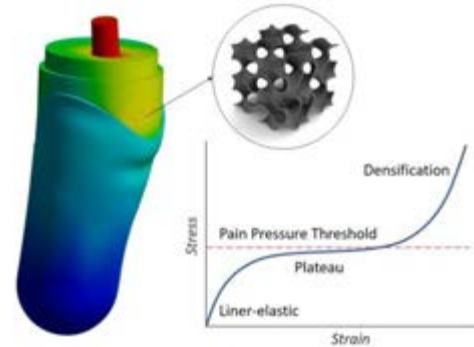
Figure 1: Total deformation of the numerical model and schematic representation of the cellular structure with corresponding σ-ε diagram.

pressures and relative displacements were used to systematically adjust the parameters of the metamaterials to minimise the contact pressure and relative displacements. A direct comparison of different liners has shown that tailored metamaterials redistribute the pressure over a larger area and thus reduce the stress concentration whilst maintaining low displacements of the entire residual limb within the prosthesis for maximum stability.

Discussion

The results have shown that 3D-printed metamaterials can be customized depending on the condition of the residual limb. By changing the design parameters, we obtain a flexible structure that improves biomechanical response and hence comfort, stability, and safety. Using numerical analysis, we have been able to investigate the potential of customised liners and sockets made of metamaterials to improve comfort and preserve stability when wearing prostheses. Future research will include experimental validation and subjective measurements of the proposed 3D-printed socket-liner system.

References

1. Soe et al, Int J Adv ManufTechnol, 79:1975-1982, 2015.
2. Wu et al, J Chinese Institute of Eng, 26:853-860, 2003.
3. Habib et al, Int J of Adv ManufTechnol, 103: 2347-2361, 2019.

Acknowledgements

ASSESSING THE FIRST RESONANCE FREQUENCY OF SCREWS IN BONE BLOCKS FOR ESTIMATION OF SCREW FIXATION.

Maikel Timmermans (1), Quentin Goossens (1), Leonard Pastrav (1), Bart Depreitere (2), Wim Desmet (3), Kathleen Denis (1)

1. KU Leuven, Department of Mechanical Engineering, Campus Group T, Smart Instrumentation Group, Leuven, Belgium; 2. KU Leuven, Department of Neurosciences, Experimental Neurosurgery and Neuroanatomy, Belgium; 3. KU Leuven, Department of Mechanical Engineering, LMSD, Belgium;

Introduction

Pedicle screw loosening is a typical and clinically relevant post-operative complication in spinal fusion surgery which may lead to fixation failure and revision surgery [1]. Many standard methods for the assessment of pedicle screw fixation are either non-repeatable (e.g. insertion torque measurements) or either destructive and not applicable intra-operatively (e.g. pull-out testing). In previous research it has been shown that selected features from vibration analysis can predict implant stability [2]. This research investigates the potential of the first resonance frequency of a screw - bone block system to estimate screw fixation. The methodology is comparable to [3] but with different levels of fixation.

Methods

One solid rigid polyurethane foam block with a density of 160 kg/m³ and one with a density of 240 kg/m³ (1522-01 & 1522-02 resp., Sawbones, Malmö, Sweden) were each cut into 18 cuboid samples of dimensions: 30x40x30mm. This results in a total of 36 bone block samples. For each density, the samples were divided in six groups of three. Every group was drilled with a different diameter pilot hole (3.0, 3.5, 4.0, 4.5, 5.0 and 5.5 mm). A hexagonal head wood screw TBR06 (DIN-571) with a total length of 53.5 mm, was inserted in every sample. The insertion was done with a 3D-printed guide to assure a consistent orientation and insertion depth of 37mm over all samples. After insertion, resonant frequency analysis was performed on all screws. The samples were mounted in a massive vice, while wrapped in soft foam. The vice was always tightened until the gap between the jaws of the vice measured 40mm, this to allow a flexible support of the sample by the foam. The laser spot of a laser vibrometer (IVS-500, Polytec GmbH, Waldbronn, Germany) was focused at the screw head to measure the vibration velocity. The screw was excited on the opposite side of the head by an automatic modal hammer (vImpact-61, Maul-Theet GmbH, Berlin, Germany). Data acquisition was performed with LMS SCADAS LVLIII (Siemens, Leuven, Belgium). Based on the measured frequency response functions, the resonance frequencies were determined in Simcenter Testlab (Siemens, Leuven, Belgium). Then, each sample was placed in a tensile test bench (Universal testing machine 3369, INSTRON, Norwood, MA, USA) for a pull-out test to determine the maximal pull-out force of the screw in the bone block. That maximal pull-out force is considered as a golden standard in the assessment of screw fixation.
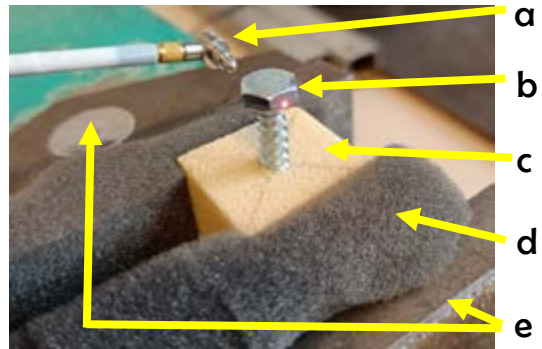
Figure 1: Vibration analysis set-up with a) automatic impact hammer, b) screw with red laser dot, c) PUR block, d) foam, e) vice.

Results

A logarithmic regression model was applied to analyze the relationship between the first resonance frequency and the maximal pull-out force for the acquired datasets. For the dataset of 160 kg/m³ samples, following logarithmic regression equation is found: $y = 667,66 + 369,78 \cdot \ln(x)$ (R²=0.976, p=2.0e-14). For the dataset of 240 kg/m³ samples: $y = 1310,1 + 241,89 \cdot \ln(x)$ (R²=0.786, p=9.5e-7). When the datasets of both densities are combined, the correlation between the first resonance frequency and the pull-out force remains high (R²=0.924, p=1.4e-20).

Discussion

This study suggests that there is a logarithmic relationship between the first resonance frequency of a screw inserted in a bone block and the maximal pull-out force of that screw from the bone block. The material properties of the block heavily influence the value of the first resonance frequency. However, the pull-out force is also sensitive to a change in bone block density and the logarithmic regression model for the combined datasets alludes to the possibility of applying a frequency threshold to predict high or low pull-out force and thus good or bad fixation of the screw in the bone block.

References

1. Galbusera et al., Eur. Spine J. 24(5): 1005-1016, 2015
2. Goossens et al., Med. Eng. Phys. 49: 109-120, 2017
3. Einafshar, M. et al. ESB, 622, 2019.

Acknowledgements

DESIGN AND TRANSLATION OF A MODULAR HIP IMPLANT DEVICE FOR SOFT TISSUE TENSION AND MOTION TRACKING EVALUATED IN A SHEEP MODEL DURING HIP ARTHROPLASTY

Jonathan CJ Wei (1), Nick A White (1), Javier Pérez de Frutos (2), Eva M Pérez Merino (3), Nieves Pastor Sirvent (3), Massimo Santella (3), Bryan J Blaauw (4), Francisco M Sánchez-Margallo (5), David Durán-Rey (5), Isabel López-Agudelo (5), Manuel R González-Portillo (5), Juan A Sánchez Margallo (5), Jenny Dankelman (1), Tim Horeman (1)

1. Technische Universiteit Delft, The Netherlands; 2. SINTEF, Norway; 3. Universidad de Extremadura, Spain; 4. Elkerliek Hospital, The Netherlands; 5. Centro de Cirugía de Mínima Invasión Jesús Usón, Spain

Introduction

In hip arthroplasty operations, surgeons rely on their experience to assess the stability and balance of hip tissues when fitting the implant to their patients[1]. During the trial, surgeons feel the tension in the surrounding soft tissues and adjust the implant configuration (size, length, neck angle, neck offset, head size, liner size, cup size). This process is naturally subjective and therefore depends on the operator. In this study, we designed and manufactured a hip implant neck based on the DepuySynthes Corail® trial component design but scaled to the dimensions of the sheep anatomy. We demonstrated the implant evaluated in a sheep model, where we propose that this is an important and clinically relevant step for the translation of medical devices.

Methods

The instrumented implant integrates Hall effect sensors to measure soft tissue tension, leading to small deformations of a compliant structure (rubber), see Figure 1 (left). This change in displacement is registered as a change in voltage with the Hall sensor which is read using an Arduino® board. An inertial measurement unit (IMU) is used to measure orientation and the acceleration during the range of motion (ROM) tests.
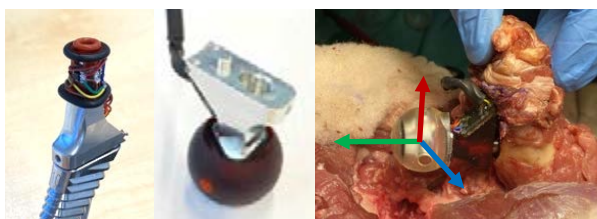
Figure 1: (left) The prototype neck without the head with Hall sensors exposed, (centre) the neck with the head installed, (right) the prototype inserted into the femur of the sheep. Axes correspond Figure 2.

Sheep anatomy was taken from x-ray images, then the implant components were scaled accordingly to the best possible fit. 3D printed components with reinforced metal support were manufactured. The prototype was first tested *ex vivo,* then *in situ* in three sheep for fit. In the latter model the Range of Motion (ROM) tests were performed by hand, and measurements were recorded.

Results

Distinct patterns were observed during the ROM tests, matching the operated leg movements. Peak forces measured are between 30-50 N, as seen in Figure 2.
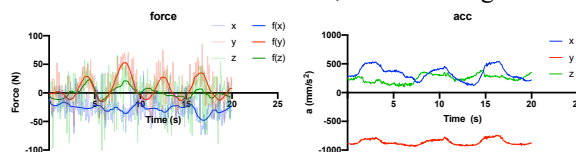
Figure 2: (left) The filtered force data from a flexion-extension ROM; (right) the acceleration data.

Discussion

We designed and tested a low-cost, modular, instrumented hip implant prototype based on the existing DepuySynthes Corail® implant. The device has been proven to successfully measure force and acceleration in the three-dimensional axes, both in a laboratory and a clinical setting (cadaver study).

Carrying out such an experiment in the sheep presents several challenges – such as the musculoskeletal differences between humans and sheep (thus generating different force-response curves). Furthermore, given the limited access to cadaver studies, it is important that the technology is evaluated sufficiently in a suitable model.

Furthermore, the measured data show forces and ROMs on one case study. It is therefore necessary that future investigation focuses on expanding the replicate number, as well as the inter-replicate differences. The device should also undergo optimisation for the model (e.g., to increase force range and measurement resolution). Future research on bridging the differences between species will better discern the interpatient differences, and thus provide a more personalised and more accurate treatment to each patient.

References

1. Wei, J; et al. (2021): Design of an affordable, modular implant device for soft tissue tension assessment and range of motion tracking during total hip arthroplasty. TechRxiv. Preprint. DOI: 10.36227/techrxiv.16942879

Acknowledgements

MECHANICAL PROPERTIES OF GYROID UNIT CELLS FOR BIOMEDICAL APPLICATIONS

Ana Pais (1), Jorge Lino Alves (2), Jorge Belinha (3)

1. INEGI, Portugal; 2. FEUP, Portugal; 3. ISEP, Portugal

Introduction

The gyroid foam presents a large interest for biomedical applications because its highly porous geometry promotes cell growth. Moreover, it has been shown that in comparison to other shapes the gyroid is more permeable than foams based on other triply periodic minimal surfaces (TPMS) [1]. In addition, TPMS based foams built using additive manufacturing technology have been shown to be able to achieve the necessary mechanical properties to replace human bone [2].

Materials and Methods

Models of the gyroid unit cells with different densities were created in MATLAB, exported and meshed into 10-node tetrahedral elements. The edge length of the unit cell is 20mm and the different density is achieved by varying the wall thickness of the foam. The mechanical properties are calculated using the homogenization approach shown in [3], where a unit strain is applied. Thus, using $\boldsymbol{\sigma} = \boldsymbol{C}\boldsymbol{\varepsilon}$ it is possible to calculate the $\boldsymbol{C}$ matrix using 6 FE analyses. The stress values are obtained from the volume average of the stress in the cell. The boundary conditions for the homogenization can be summarized as in Figure 2 which shows a cubic representative volume element. The building material has a Young's modulus of 3000MPa and a Poisson ratio of 0.3. To study the ultimate stress of the foam in comparison to the ultimate stress of the material which constitutes it, the material was modelled as elastic-perfectly plastic with and three values of yield stress were chosen namely 10, 30 and 50MPa. The yield stress was defined as the maximum value in the stress-strain curve from the simulation.

Results

The results of the mechanical properties can be consulted in table 1, which shows the Young's modulus ratio E_h/E_m where E_m is the Young's modulus of the building material and E_h is the homogenized Young's modulus and the yield stress ratio σ^y_h/σ^y_m where σ^y_m is the yield stress of the building material and σ^y_h is the homogenized yield stress. The value of yield stress ratio did not change significantly with different yield stress values of the building material.

Wall thickness	Density	E_h/E_m	σ^y_h/σ^y_m
1	15.54%	0.03792	0.07
3	44.86%	0.18694	0.23
5	70.36%	0.41466	0.52

Table 1: Results of the homogenization

Figure 1: Gyroid models (a) wall thickness 1mm, (b) wall thickness 3mm density, and (c) wall thickness 5mm
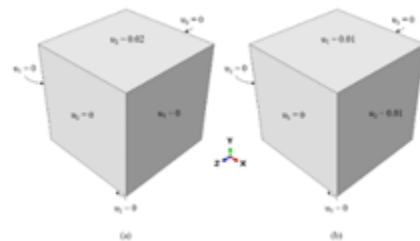
Figure 2: Boundary conditions for the homogenization of the mechanical properties (a) example for normal strain (b) example for shear strain

Discussion

The homogenization model can be used to predict the mechanical properties of 3D printed scaffold. Structurally, it is important that the stiffness and strength of the implant are correctly predicted. Stiffness must not be larger than the stiffness of the surrounding bone to avoid stress shielding, while the implant must still be able to support weight and have enough strength.

References

[1] J. Santos, T. Pires, B. P. Gouveia, A. P. G. Castro, and P. R. Fernandes, "On the permeability of TPMS scaffolds," *J. Mech. Behav. Biomed. Mater.*, vol. 110, no. March, pp. 1–7, 2020, doi: 10.1016/j.jmbbm.2020.103932.

[2] F. S. L. Bobbert *et al.*, "Additively manufactured metallic porous biomaterials based on minimal surfaces: A unique combination of topological, mechanical, and mass transport properties," *Acta Biomater.*, vol. 53, pp. 572–584, 2017, doi: 10.1016/j.actbio.2017.02.024.

[3] D. Li, W. Liao, N. Dai, G. Dong, Y. Tang, and Y. M. Xie, "Optimal design and modeling of gyroid-based functionally graded cellular structures for additive manufacturing," *CAD Comput. Aided Des.*, vol. 104, pp. 87–99, 2018, doi: 10.1016/j.cad.2018.06.003.

Acknowledgements

COMPARING CALCULATED AND MEASURED MUSCLE ACTIVITY OF THIGH MUSCLES IN DYNAMIC MOTION

Simon Auer (1), Lukas Reinker (1,2), Franz Süß (1), Sebastian Dendorfer (1,2)

1. Laboratory for Biomechanics, Ostbayerische Technische Hochschule (OTH) Regensburg, Germany; 2. Regensburg Center of Biomedical Engineering, OTH and University Regensburg, Germany

Introduction

Musculoskeletal models are essential in biomechanics research and provide valuable information on various parameters. In recent years, inertial motion capture gained importance as a new method of generating kinematic input for musculoskeletal models. Some studies investigated the correlation of measured and predicted ground reaction forces of musculoskeletal models driven by inertial motion capture data [1]. However, the validity of muscle activities has only been investigated for optical motion capture [2]. Furthermore, numerical muscle activity depends on the muscle model and muscle recruitment type. However, their influence in dynamic movements is uncertain. Hence, this study examined their effect on calculated muscle activity and furthermore investigated the correlation of measured and calculated muscle activity using inertial motion capture as kinematic input.

Materials & Methods

Twenty subjects performed sprinting tasks of five times 10 m on artificial turf. Kinematics were recorded using inertial motion capture (MVN Link, Xsens Technologies B.V., NL) at 240 Hz. Furthermore, muscle activity was measured at 1111 Hz using ten surface electromyography (EMG) sensors (Trigno IM, Delsys Inc., USA). The investigated muscles were Rectus Femoris (RF), Vastus Medialis (VM), Vastus Lateralis (VL), Biceps Femoris (BF) and Semitendinosus (ST). The motion capture data was used as input for the AnyBody Modeling System (AMS, v. 7.3.3, AnyBody Technology, DK). The numerical muscle activity was calculated using the AnyBody Modeling System (AMS, v. 7.3, AnyBody Technology, DK) with four different configurations. A simple muscle model was used with a quadratic target function for the muscle recruitment (S2) as well as a simple muscle model with composite target function (SC), with composite target function consisting of a polynomial with infinite exponent and an additional quadratic term. Furthermore, a Hill-type muscle model was used with a quadratic muscle target function (H2) and a composite target function (HC). The muscle activities were compared by calculating the Pearson correlation coefficient r and determining the dynamic time warping distance (DTWD) in Python (v. 3.7.6). The correlation was categorised as small ($r \leq 0.3$), medium ($r \leq 0.5$) or strong ($0.5 < r \leq 1$) [3].

Results

The results show a moderate to strong correlation of measured and calculated muscle activity. The strongest correlation with $r=0.68$ is found in the ST muscle for S2 and SC. The lowest correlation with $r=0.27$ is found in the RF muscle for S2 and SC. The simple muscle model has a better agreement of calculated and measured muscle activity (Fig. 1). Additionally, the DTWD is considerably higher when a Hill-type muscle model is used instead of a simple muscle model.
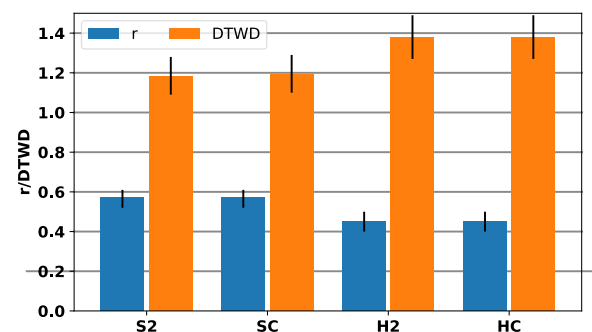
Figure 1: Median r and DTWD values with 95% confidence interval for the different model configurations.

Discussion

This study examined the effect of muscle recruitment and muscle type on calculated and measured muscle activity correlation using inertial motion capture as kinematic input. Overall, the correlation of calculated and measured muscle activity was moderate (H2, HC) to high (S2, SC). The different muscle recruitment criteria of the AMS have little influence on the calculated muscle activity. On the contrary, the simple muscle model shows a higher Pearson correlation and a lower DTWD than the Hill-type muscle model. This is probably caused by the Hill-type muscle model's dependency on the calibration sequence and the muscle wrapping. With the knee joint being modelled as a hinge joint, the dependency on the muscle parameters increases. Nevertheless, the overall Pearson correlation is within the range of literature data for slower movements [2].

Altogether, the results show that inertial motion capture as kinematic input for musculoskeletal models and a simple muscle model are suited for calculating thigh muscle activities in sprinting movements.

References

1. Karatsidis et al., Sensors, 17(1):75, 2016
2. Wibawa et al., J Biomech, 49, 3660-3666, 2016
3. Cohen, Statistical Power Analysis for the Behavioral Sciences. 1988

TOWARDS THE MEASUREMENT OF ELBOW JOINT FORCES IN MAN: A FINITE ELEMENT STUDY

Marim Basiouny[1], Simon Lambert[2], Chin Kuenfoo[3], Stephen Taylor[1]

1. Division of surgery and interventional science, University College London, UK; 2. University College London Hospital, UK; 3. Barking, Havering and Redbridge University Hospitals

Introduction

Elbow Arthroplasty can be a treatment option to restore elbow functions affected by inflammatory, degenerative, or post-traumatic arthritis. In 2020 the National Joint Registry recorded the indications for Total Elbow Replacement as 69% trauma, 9% osteoarthritis and 8% inflammatory arthropathy [1]. The largest systematic review of recent literature showed that aseptic loosening remains the greatest complication in Total Elbow Replacement at 17.5% of cases performed due to trauma requiring revision for aseptic loosening [2]. Mechanical failure can also occur the form of dislocation (4.7%) bushing wear (2.3%) or disassembly (2.3%) [3]. The elbow joint is one of the few remaining major joints in which in vivo joint forces have yet to be measured. Direct measurement of elbow joint forces will give insight into the mechanics of the joint, stress distribution in the constituent bones and soft tissues and how these are affected by activity. This research aims to measure in vivo the forces and moments acting at the hinge of an instrumented humeral component instrumented with strain gauges and embedded electronics.

Methods

A 3D computational model of a modified Discovery humeral component was generated using SolidWorks. The model was created with 3 weld cavities (figure 1) for electronics and strain gauges. Mechanical loading of the model was simulated in a FEA study performed in COMSOL^{TM}. Proposed sites for strain gauges were analysed for sensitivity and selectivity. The loading vectors applied to the humeral component simulated the 6 degrees of freedom loads applied to the joint, whilst fixing the humerus at the stem to compare strains generated accordingly.

A prototype of the humeral implant is being developed through CNC machining, then a fatigue test will be conducted under load. Prototypes will be strain gauged for powering and telemetry. Welding trials followed by trial calibrations will take place to measure sensitivities to all loading modes. Internal electronics will be developed and tested, and implant microcontroller code written for strain sampling and telemetry. Inductive coupling will be developed with external electronics.

Results

Strains at the joint forks have been correlated with applied loads, and calibration matrix techniques used to separate each strain direction. Peak strains are shown

(Table 1) for a 1000N applied load in Fx, y, z and 1 Nm. in Mx, y, z. Peak sensitivities show a reasonable confidence in selecting strain gauge sites. Table 2 shows the selected strain gauge locations.

Discussion
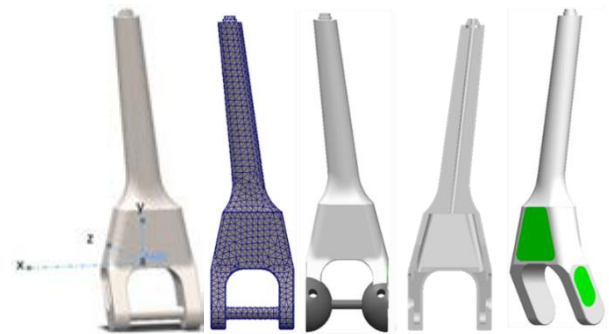
Figure 1: modified humeral FE model with weld cavities, caps, and FE mesh

peak sensitivities					
Fx	**Fy**	**Fz**	**Mx**	**My**	**Mz**
strain/N			strain/Nmm		
4.93E-07	6.99E-07	7.65E-07	9.15E-08	4.46E-06	4.24E-06

Table 1: peak sensitivities at potential strain gauge locations

	X (mm)	Y (mm)	Z (mm)
Cavity 1 (left fork)	11.43	-8.12	-9.70
	11.14	-4.12	-9.70
	8.65	-0.42	-10.00
	4.17	1.02	-6.31
Cavity 3 (Base)	-4.17	1.02	-6.31
Cavity 2 (right fork)	-8.65	-0.42	-10.00
	-11.14	-4.12	-9.70
	-11.43	-8.12	-9.70

Table 2: 8 potential strain gauge sites for bonding the strain gauges

The overall proposed work led to the selection of 8 optimum strain gauge locations which will in turn enable measuring the 6 degrees of freedom acting at the elbow hinge during normal activities of daily living.

References

1. U.K. National Joint Registry: https://reports.njrcentre.org.uk/elbows-reports
2. William J White. Complications of contemporary total elbow arthroplasty: a systematic review. J Shoulder Elbow Surg. 2021, Vol. 13(5) 544–551.
3. Voloshin I. Complications of total elbow replacement: a systematic review. J Shoulder Elbow Surg. 2011 Jan; 20

DEVELOPMENT OF A MUSCULOSKELETAL MODEL FOR THE DETERMINATION OF MUSCLE ACTIVITY IN THE HEALTHY SHOULDER

Leandra Bauer, Erika Raicholt, Matthias Woiczinski, Peter Müller, Ines Santos
Department of Orthopaedics and Trauma Surgery, Musculoskeletal University Center Munich (MUM), University Hospital, LMU Munich

Introduction

The complexity of the shoulder joint has long been a difficulty when trying to investigate implant behavior. This becomes more evident when it is necessary to simulate an active, muscle-controlled shoulder motion since it requires knowledge about the activity ratios of the different muscles involved. As the rotator cuff cannot be completely analyzed with surface electromyography (EMG) [1], using musculoskeletal modelling to estimate muscle and joint loading during upper limb motion could be advantageous, if properly validated. Therefore, the aim of this study was to develop and validate a reliable musculoskeletal shoulder model, based on newly acquired EMG data, in order to determine muscle activity ratios during different movements.

Method

Sixteen healthy subjects were measured during six motions of the upper limb in the scapular plane (abduction/adduction, anteversion/retroversion, external/internal rotation). Joint movements in the scapular plane and kinematics were measured with an inertial motion capture system (Xsens Technologies B.V., An Enschede, The Netherlands), EMG of the deltoid (anterior, middle and posterior heads) and infraspinatus muscles were measured (EMG Bluetooth measuring system, Zebris Medical GmbH, Isny, Germany) for validation of the muscle model. The musculoskeletal shoulder model was created using AnyBody Modeling Software (AnyBody Technology A/S, Aalborg, Denmark) and the AnyMuscleModel3E, a three-element model based on the work by Hill [2], was used. The model included the following muscles: M. deltoid anterior/middle/posterior, M. infraspinatus, M. subscapularis, M. supraspinatus und M. teres minor; and the subject-specific movement data from the Xsens sensors were used. The EMG data was normalized and the joint positions recorded with the Xsens system were used in the Euler rotation sequence ZXY (except for abduction/adduction to avoid gimbal lock). Pearson's correlation of EMG activity and AnyBody muscle activity was calculated to validate the model. In order to calculate the ratio of muscle activation, a main/primary muscle was defined for each movement. The activity of the remaining/secondary muscles was defined as a percentage in relation to the main muscle over the course of the movement.

Result

The model showed moderate to strong correlation for the four measured muscles (r = [0.38; 0.51]). This allowed the muscle activities from the body-muscle model to be subsequently used to determine the muscle ratios. The middle deltoid was defined as the main muscle acting during abduction/adduction (figure 1). Peaks were seen in the ratio to the anterior deltoid, posterior deltoid, infraspinatus, and teres minor at 110 degrees of abduction. Higher ratios were shown by the supraspinatus and the subscapularis in adduction at -10 degrees. During retroversion, the middle deltoid had a higher activity than the anterior deltoid, and the posterior deltoid exhibited a lower activity than both muscles.
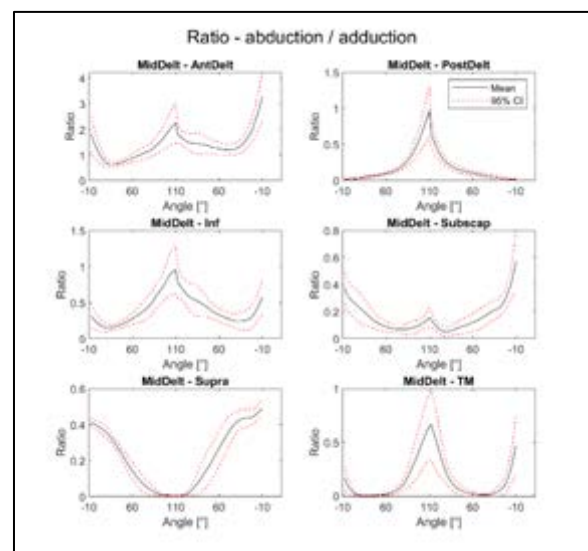
Figure 1: Mean ratio (mean + 95% confidence interval) of the muscles involved in the abduction/adduction movement of the arm in relation to the middle deltoid muscle.

Discussion

A muscle model of the shoulder was successfully created based on subject data. The musculoskeletal model can thus calculate the activity of muscles that would not be accessible with a surface EMG. With the knowledge of the ratios of each individual muscle of the rotator cuff during certain movements, a more accurate in-vitro simulation of the shoulder motion for investigating clinical questions can be achieved.

References

1. De Luca, C. J. (1997). The use of surface electromyography in biomechanics. *Journal of applied biomechanics, 13*(2), 135-163.
2. Hill, A. V. (1938). The heat of shortening and the dynamics constants of muscle. *Proceedings of the Royal Society*, Ser. B. 126(843), pp. 136-195.

HOW DO THE MUSCULOSKELETAL MODELING PARAMETERS AFFECT THE ESTIMATION OF THE TIBIOFEMORAL CONTACT FORCES?

Williane Bernardes (1), Sana Jahangir (1), Amir Esrafilian (1), Mika Mononen (1), Petri Tanska (1), Tine Alkjaer (2,3), Marius Henriksen (3), Rami Korhonen (1), Lauri Stenroth (1,2)

1. Department of Applied Physics, University of Eastern Finland, Finland; 2. Department of Biomedical Sciences, University of Copenhagen, Denmark; 3. The Parker Institute, Copenhagen University Hospital, Denmark

Introduction

Musculoskeletal modeling can be used to estimate joint-level kinematics and kinetics that cannot be measured experimentally. Simulations are based on motion capture data and mathematical and biological principles. However, the outcomes of musculoskeletal modeling can be affected by several factors, for instance, inaccurate marker placement [1] and the muscle activation optimization function [2].

In this study, we investigated how sensitive the estimated knee joint mechanics are to the uncertainty in some of the underlying assumptions of musculoskeletal modeling using a model with 12 degrees of freedom knee joint.

Methods

We used the motion capture data of one participant from the CAROT trial [3] and a musculoskeletal model with 12 degrees of freedom knee joint [4]. Subsequently, we simulated five trials of self-selected walking speed in OpenSim 4.1 with five different models (Table 1). Each model was based on the reference model but with one adjusted parameter that represents different assumptions made during musculoskeletal modeling and simulation.

Model	Adjusted Parameters
Reference model (Model 1)	- Weighted optimization [2] - Knee marker in optimal locations - Nominal cartilage Young's modulus of 20 MPa [5]
Altered optimization function (Model 2)	- Unweighted optimization
Marker misplacement (Model 3)	- Knee marker misplacement 10 mm anteriorly
Marker misplacement (Model 4)	- Knee marker misplacement 10 mm posteriorly
Altered cartilage stiffness (Model 5)	- Half of the nominal cartilage Young's modulus, i.e. 10 MPa

Table 1: The parameter variation of each musculoskeletal model in relation to the reference model.

Results

The different assumptions in musculoskeletal modeling had a modest influence on the simulated tibiofemoral joint contact forces and their distribution between medial and lateral compartments of the knee (Figure 1). The effect was mainly seen on the latter half of the stance.
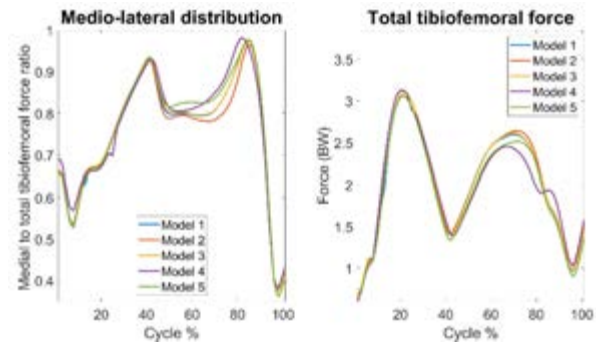
Figure 1: The estimated medio-lateral distribution of tibiofemoral contact forces and the total contact force for each model in five averaged self-selected walking speed trials.

Discussion

The different assumptions in musculoskeletal modeling did not have a great effect on the simulated joint level outcomes (Figure 1). However, previous studies have shown that muscle activation optimization function mainly affects forces around the second half of the stance [2], which also seems to be the case for the other parameters investigated in this study.

Knee marker misplacement posteriorly appeared to have the largest influence on the estimated tibiofemoral joint contact forces (Figure 1, model 4). This highlights the need for careful experimental data collection and model scaling.

The small variations in joint level mechanics observed in this study may have a large impact when utilized in further analysis (e.g. as inputs in finite element modeling). We will investigate this in our future studies.

References

1. McFadden, C. et al, J. Biomech., 101:109635, 2020.
2. Smith, C. et al, J. Biomech., 82:124-133, 2019.
3. Aaboe, J. et al, Osteoarthr. Cartil., 19(7):822-828, 2011.
4. Lenhart, R. L. et al, Ann Biomed Eng, 43(11):2675-2685, 2015.
5. Esrafilian, A. e al, IEEE Trans Neural Syst Rehabil Eng, 29:123-133, 2021.

Acknowledgements

AN INNOVATIVE APPROACH TO INVESTIGATE THE TIBIOFEMORAL ELASTICITY DURING GAIT WITH IN-VIVO 3D COMPLIANCE MATRIXES

Francesca Bucci (1), Mark Taylor (1), Rami Al-Dirini (1), Saulo Martelli (1,2)

1. Flinders University, Australia; 2. Queensland University of Technology, Australia

Introduction

Personalized musculoskeletal models enable studies on individual features of healthy and pathological tibiofemoral motion. As such, the understanding of the separate of effect of tibiofemoral geometry [1] and elasticity [2] on tibiofemoral motion during normal activity is important to both researchers and clinicians. However, complex geometry-based musculoskeletal models embedding tibiofemoral contact surfaces, geometrical and elastic properties of each relevant knee structure are computationally expensive and difficult to identify in vivo [5]. One possibility is to model the effect of tibiofemoral geometry on knee motion using fast rigid-body models [3], and tibiofemoral elasticity using lumped-parameters compliance matrices accounting for the effect of all separate elastic structures [4]. The aim of this work is to demonstrate the use of a compliance matrix for studying tibiofemoral motion during normal physical activity.

Methods

The model by Lenhart *et al.* [5] was used for this work. The healthy 23-year-old female model (height = 1.65 m, mass = 61 kg) is a 25-segments, 52-DOFs multibody dynamic system including tibiofemoral contact surfaces, 14 non-linear springs linking ligament origin footprint to insertions. Active and passive tibiofemoral kinematics, inverse dynamics, muscle activation/force and tibiofemoral contact forces were computed using the OpenSim Joint and Articular Mechanics framework [5]. Active tibiofemoral motion was calculated by simulating a gait trial with Lenhart model [5]. Passive tibiofemoral motion, during the same gait trial, was simulated by removing knee-spanning muscles, with external forces scaled down to 1%, gravity set to zero and ligament stiffness reduced by 50%, to ensure that the ligament force was less than 50N. The compliance matrices (CMs) were defined as 6x6 matrices:

$$[CM] \cdot \{F_a - F_p\} = \{X_a - X_p\}$$
$$\{X_a - X_p\} = (\Delta t_{AP} \quad \Delta t_{SI} \quad \Delta t_{ML} \quad \Delta \theta_{AA} \quad \Delta \theta_{IE} \quad \Delta \theta_{FE})$$
$$\{F_a - F_p\} = (\Delta F_{AP} \quad \Delta F_{SI} \quad \Delta F_{ML} \quad \Delta M_{AA} \quad \Delta M_{IE} \quad \Delta M_{FE})$$

where (a) and (p) stand for active and passive variation (Δ) of tibiofemoral linear (t) and angular (θ) displacements, forces/moments (F) along antero-posterior (AP), superior-inferior (SP), medial-lateral (ML), adduction-abduction (AA), internal-external (IE), flexion-extension (FE) axes. A CM was calculated for each frame of the gait cycle and analyzed along with the stiffness of each individual motion axis, and with passive and active kinematics used to calculate the elastic contribution during the stance phase.

Results

The highest compliance was found in AP direction, with $4065 \pm 1587 (10^{-5})$ mm/N mean$\pm$std during stance phase, while SI, IE, ML, and AA reported $-74 \pm 15 (10^{-5})$, $1750 \pm 905 (10^{-5})$, $22 \pm 41 (10^{-5})$, $-47 \pm 49 (10^{-5})$ mm/N respectively. The 3D CM representations at 0-,15- and 30-degrees of knee flexion were reported (Fig.1). Interestingly, AP compliance reached its peak at the toe-off/pre-swing around 0-degree flexion (Fig.1), while it did not happen at 0-degree flexion heel strike.
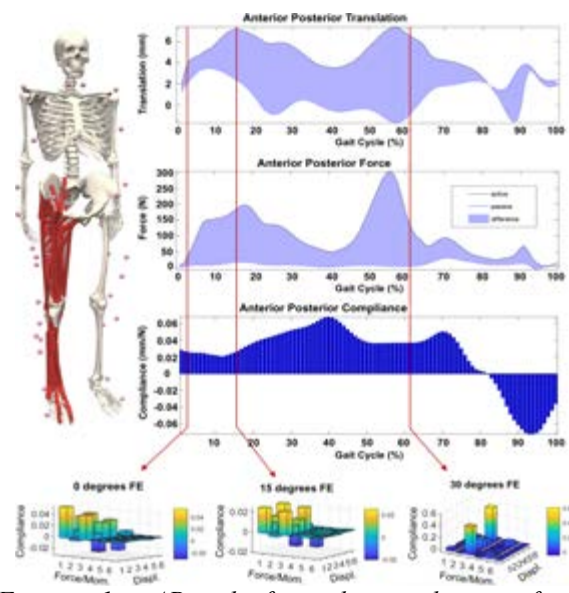
Figure 1: AP tibiofemoral translation, force, compliance during gait with 0/15/30deg 3d in-vivo CMs.

Discussion

Results show that contrary to ex-vivo investigation [4], CMs depend on gait cycle phase, rather than tibiofemoral flexion angle. This methodology offers a viable accurate representation of in-vivo tibiofemoral elasticity and load-dependent behaviour during physical activity with few parameters. However, reducing the number of CMs to describe the gait cycle more efficiently, the accuracy decreases.

References

1. Smoger *et al*, *J.Orthop.Res.*,**33(11)**:1620-1630, 2015
2. Myers *et al., Am. J. Sports Med.,***40(1)**:170-178, 2012
3. Martelli *et al.*, Gait Posture, **80**: 374-382, 2020
4. Lamberto *et al.*, Med. Eng. Phys, **64**: 80-85, 2019
5. Lenhart *et al*., Annu.Rev.Biomed.Eng., **43**: 2675-85, 2015

Acknowledgements

PRIMITIVE-DRIVEN MUSCULOSKELETAL MODELLING OF HUMAN LOCOMOTION: TOWARDS MODEL-BASED CONTROL OF BIONIC LEGS

Federica Damonte (1), Guillaume Durandau(1), Herman van der Kooij(1), Jose Gonzales (2), Massimo Sartori(1)

1.University of Twente, The Netherlands; 2. Ottobock, Germany

Introduction

Powered prostheses have the potential to improve the quality of life of lower limb amputees, by improving their mobility [1]. Myoelectric control systems that employ electromyograms (EMGs) as driving control signal have shown promising performances [2]. However, EMG electrodes are susceptible to noise and movement artefact and may decrease myocontrolled prostheses overall robustness and stability. EMG-dependence in prosthetic controllers can be relaxed by exploiting the concept of muscle synergy and modularity.

We propose a solution based on neuromusculoskeletal modelling including a numerical model that simulates the role of neural synergies in the recruitment of skeletal muscles. The aim is to devise advanced model-based control strategies with minimal EMG-dependence to ultimately improve physical interaction between the user and a powered prostheses during dynamic motor tasks.

Methods

The human neuromuscular system has an inherent redundant nature. It is hypothesized that the nervous system organises motor control by activating fixed groups of muscles as individual units, or muscle synergies, determined by their functionality and/or location [3]. Therefore, in order to generate a specific movement only a low dimensional set of basic patterns of excitations is required for a large number of muscles [3].

We previously analysed EMGs during gait at different speeds and inclinations conditions from which we built a predictive model to estimate leg muscles activation as a linear combination of four basic gaussian primitives.

The generated muscle excitation showed minimal loss of accuracy in estimating EMGs [4].

The aim of the current research is to interface the given primitive model [4] with an existing real-time musculoskeletal model that estimate muscle-tendon units forces and joint moments with no need for EMG sensing [5]. We call this primitive-driven modelling.

To assess the ability of the primitive-driven model to predict accurately joint moments, data from dynamic trials on healthy subjects walking on a treadmill was recorded. The subject walked at different speeds (3 km/h, 4 km/h, 5 km/h). In order to measure joint angles and moments, Inertial Motion Capture system, markers and Force plates were employed. At each timestep the primitive-driven model requires an accurate gait phase estimation. For that, ground reaction forces together with speed and elevation information were used. Results from the primitive-driven model were validated in comparison with estimated joint moments from inverse dynamics (ID) and angles from inverse kinematics.

Results

The ankle torques from the ID and the primitive-driven model were compared for one leg (left) using the root mean square error (RMSE) and correlation factor. At medium speed the RMSE is 0.175 Nm/Kg with a correlation coefficient of 0.971 (*Figure 1*) , at 4 km/h the RMSE is 0,254 Nm/Kg and at 5 km/h is 0,367 Nm/Kg with a correlation coefficient of 0,956 and 0,926 respectively.
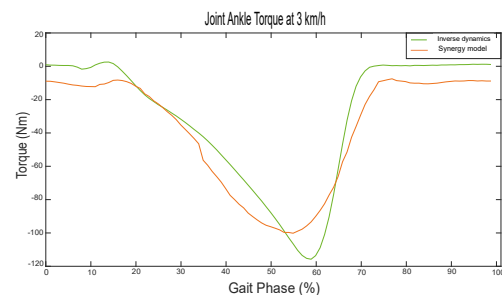
Figure 1: - Joint ankle moment of the left leg during one gait cycle . The green moment represents the result of the inverse dynamics from motion capture systems. The orange line is the output of the model for a given speed and gait phase information

Discussion

Results showed a good correlation between reference and estimated joint moments, however errors might be reduced optimizing the synergies model to a specific subject instead of using an averaged model. We assume that the proposed approach as biomimetic feedforward control will improve the physical interaction between the user and a powered lower limb device, yielding to a more natural and robust control.

References

1. M. R. Tucker et al., J. Neuroeng. Rehabil.,1, 2015
2. M. Sartori et al., J. Neural Eng., 6,2018
3. F. Lacquaniti et al., J. Physiol.,10:2189-2199, 2012
4. J. Gonzalez-Vargas et al., Front. Comput. Neurosci., SEP: 1-14, 2015
5. G. Durandau et al, IEEE Trans. Biomed. Eng., 3:556-564, 2018

THE EFFECT OF SUBSTRATE SIZE ON GRIP AND PULL FORCES IN PARROTS

Edwin Dickinson[1], Melody W Young[1], Charles J Kim[1], Michael Hadjiargyrou[1], Michael C Granatosky[1]

[1] *New York Institute of Technology College of Osteopathic Medicine, Old Westbury, NY, USA.*

Introduction.

The ability to generate and maintain a secure grasp is critical to maintain stability on small arboreal substrates. Using *in vivo* experiments, gripping and pulling performance has been measured in many arboreal primates and lizards [1,2]. However, despite the broad functional and morphological diversity of the avian foot, few studies have considered the functional capabilities of this limb in birds.

Methods.

In this study, we collected *in vivo* gripping and pulling forces at a range of perch sizes (0.5 – 17.5 mm) from a captive colony of rosy-faced lovebirds (*Agapornis roseicollis*). These perches were custom designed using CAD software and 3D printed to specification, then covered in sand to provide a naturalistic texture. To measure intrinsic grip strength, these perches were connected to an AMTI small load force plate, while pull strength was measured by attaching each perch to a BIOSEB-GS3 portable strength tester.

Results.

We conducted 1,943 grip trials and 1,430 pull trials, respectively. Grip forces peaked at 72 g on a 5mm diameter perch, and were generally highest between 5 and 10 mm. Forces were equivalent at the two sizes bracketing this range (2.5 and 12.5mm) and lowest at the largest sizes (15 and 17.5 mm). We found no differences between left and right foot forces. Pull forces peaked at 440 g at a 2.5 mm perch and decreased at all subsequent size increments. Again, no bilateral differences were observed.

Discussion.

Grip and pull forces were extremely high in parrots, registering 1.5x and 10x body mass respectively. These forces match or exceed the highest relative gripping forces observed in any taxon. We suggest that a major contributor to the incredible pulling strength of parrots is the ability to activate a tendon-locking mechanism, in which the digital flexor tendon interlocks with its sheath to provide a strong, passive anchor [3].

Figure and Tables
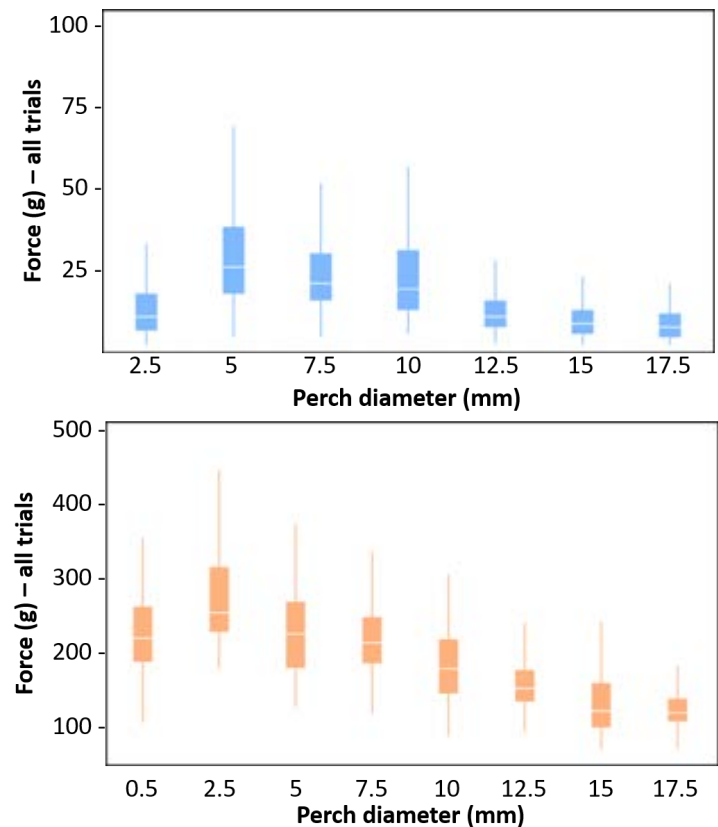
Figure 1 Gripping (top, blue) and pulling (bottom, orange) forces measured in *A. roseicollis* at a range of substrate sizes.

References

[1] da Silva et al. 2014. *Functional Ecology* 28.3: 702-713.
[2] Thomas, P., et al. 2016. *Journal of Zoology* 298.2: 77-81.
[3] Quinn TH and Baumel JJ 1990. *Zoomorphology* 109.5: 281-293.

THE RELATIVE BITE FORCE AND GAPE POTENTIAL OF PSITTACIFORMES

Edwin Dickinson[1], Melody W Young[1], Michael C Granatosky[1]

[1] *New York Institute of Technology College of Osteopathic Medicine, Old Westbury, NY, USA.*

Introduction.

Bite force and gape are critical ecological variables that determine which foods an animal may consume from its environment. As such, these variables have been widely analyzed in the context of ecology and body size across numerous vertebrate lineages. Among avians, bite force potential has been comprehensively quantified in finches; however, no *in vivo* data has been reported within parrots (order Psittaciformes), and an anatomical estimate of bite force has been calculated for only two species [1,2]. Nevertheless, parrots represent one of the most functionally interesting avian orders, exhibiting numerous adaptations towards tree climbing that include the exaptation of the beak into a functional limb when scaling vertical substrates [3]. Parrots are also generally considered to possess relatively high bite force capabilities, though, as noted above, this is yet to be evaluated empirically.

Methods.

Using a small load force plate in combination with an adjustable mouthpiece, we collected *in vivo* bite force data from six rosy-faced lovebirds (*Agapornis roseicollis*) at a range of gapes (2.5, 5.0, 7.5, and 10mm). To contextualize the biting performance of our parrots, we also compiled a comprehensive catalog of all *in vivo* and anatomically-estimated bite forces in other avian species. Phylogenetically adjusted RMA (pRMA) regressions were used to assess the scaling of bite force relative to body size across *Aves* as a whole, and determine the extent to which the bite forces are relatively increased within Psittaciformes.

Figure 1. Demonstration of experimental setup.

Results.

A total of 896 trials were measured across the four gape sizes. Our highest forces were registered at the 2.5 mm gape, with an average of 10.59 N and a peak value of 19.44 N. Registered bite forces decreased iteratively with each increase in size. At the largest (10 mm) size, we measured a rotational gape of 52°, closely according to biomechanical estimates of maximum gape potential in parakeets. Using our pRMA regressions to compare bite force across avians, we report positive residuals in all psittaciform species (+0.29 in *Psittacus erithacus*, +0.21 in *A. roseicollis*, +0.10 in *Myiopsitta monachus*) suggesting that parrots demonstrate a strong bite force for their body size.
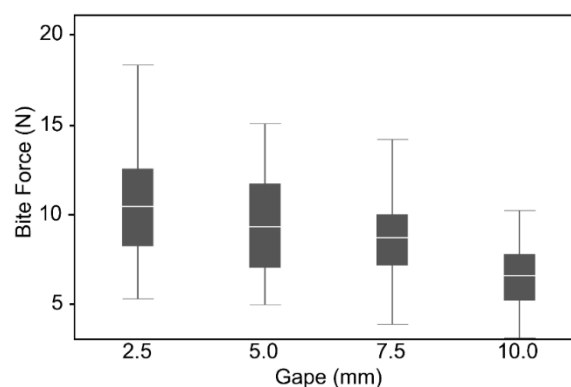
Figure 2. In vivo bite forces measured across a range of gape sizes in *Agapornis roseicollis*.

Discussion.

Bite forces in *A. roseicollis* decline as gape increases, a trend previously reported both experimentally and biomechanically in mammals and lizards. Such data suggests functional consequences for food processing and acquisition. Our data further demonstrate that, among birds, Psittaciformes appear to exhibit relatively high bite forces for their body size. Interestingly, all species demonstrating stronger positive residuals– i.e., greater relative bite force potential – than *A. roseicollis* were also strongly granivorous, suggesting a strong influence of dietary niche on biting potential across the avian class.

References

[1] Carril et al. 2015. Journal of Anatomy 227(1):34-44.
[2] Cost et al. 2020. The Anatomical Record 303(4):999-1017. [3] Young et al. 2022. SICB 2022 Annual Meeting, Poster Presentation.

A NOVEL METHOD FOR ARTIFICIAL INTELLIGENCE BASED GROUND REACTION FORCE MEASUREMENT FROM VIDEO

Travis Eliason (1), Tylan Templin (1), Nathan Louis (1), Omar Medjaouri (1), David Chambers (1), Kase Saylor (1), Daniel Nicolella (1)

1. Southwest Research Institute, United States

Introduction

Traditionally, inverse dynamics analyses have required sophisticated and expensive lab-based sensors, preventing adoption outside of the laboratory. To address this limitation, several studies have leveraged artificial intelligence by using videos to estimate kinematic [1] and kinetic [2] data. While innovative, these studies have not offered a solution that exclusively uses video data to measure all the movement components needed to perform an inverse dynamics analysis. Therefore, the purpose of this study was to develop and quantify the accuracy of a video-based methodology to measure kinematics, 3D ground reaction forces (GRFs), and 2D center-of- pressure (COP) utilizing deep neural networks.

Methods

Video data was recorded using four Imaging Development Systems cameras at 100Hz from eight subjects performing countermovement jumps. All video data was synchronized with a Vicon motion capture system (100Hz) and Bertec force plates (600Hz), which were used to capture ground truth data. Six of the eight subjects were used for training, and the two left out subjects were used for evaluation. The evaluation videos were first processed through a pre-trained convolutional neural network that creates 2D pose estimates of 29 virtual markers. Next, an outlier-aware triangulation process was used to estimate the 3D locations. Finally, an inverse kinematic fit was applied to transform marker locations into the kinematic parameters. The predicted 3D virtual marker locations were used as input to a bi-directional long-short term memory (LSTM) network, similar to previous work [3], to predict GRFs and COP. The accuracy of the neural networks was evaluated against the ground truth data kinematic and kinetic data using the root mean squared error (RMSE).

Results

The predicted kinematic values showed a high level of agreement Vicon data with the average RMSE values of 9.94, 4.99, 6.80 degrees for hip, knee, and ankle flexion angles respectively. A representative plot of the predicted and force plate measured GRFs (normalized by mass) and COP are shown in Figures 1 and 2. The normalized GRFs values had an average RMSE of 0.22, 1.6, 0.42 N/kg for medio-lateral, vertical, anterior-posterior directions respectively, and COP values had an average RMSE of 1.1 and 2.9 cm for medio-lateral and anterior-posterior directions.
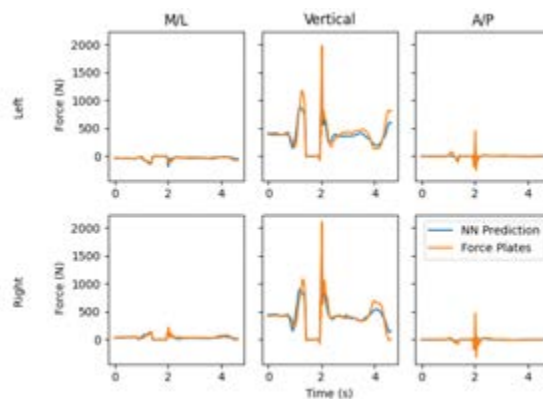
Figure 1: Example 3D GRF comparison between force plates and neural network
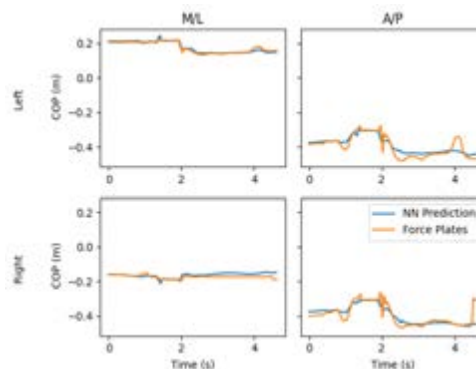
Figure 2: Example COP comparison between force plates and neural network

Discussion

A comprehensive system that is capable of tracking kinematics and associated kinetic data from video has the potential to bring traditional biomechanics analyses out of the lab. These preliminary results show considerable promise and the potential of using a solely video-based tracking system for biomechanical analyses. Future work will focus on predicting a more diverse set of motions and utilizing these results to perform an inverse dynamics analysis and validate against current gold standard methodologies.

References

1. Desmarais et al. *Comp. Vision and Image Und.* ,*212*, 2021.
2. Morris et al. .*ISBS Proceedings* 39:77, 2021.
3. Alcantara et al.. *bioRxiv*, 2021

Acknowledgements

REPRODUCIBILITY OF MUSCLE FORCES ESTIMATION DURING POST-STROKE GAIT USING OPENSIM

Georgios Giarmatzis (1), Erasmia Giannakou (1), Styliani Fotiadou (1), Athanasios Gkrekidis (1), Christos Kokkotis (1), Konstantinos Vadikolias (2) Nikolaos Aggelousis (1)

1. Physical Education and Sport Science Department, Democritus University of Thrace, Greece; 2. Department of Medicine, Democritus University of Thrace, Greece

Introduction

Musculoskeletal (MSK) modelling software Opensim has been extensively used to study healthy and pathological locomotion, and it is used both for assessment and planning of interventions. Despite its widespread application on muscle function and joint loading, its reproducibility on muscle force estimation during walking in pathological populations has never been addressed.

Thus, the aim of this study was to assess the within-session reproducibility of major lower limb muscle group forces, as calculated from Opensim, in chronic post-stroke patients for the paretic side.

Methods

Twelve chronic stroke patients (6 males, mean (std) BMI: 29.9 (3.4), mean (std) age: 64.5 (3.1) years), were recruited from a database of the General Hospital of Komotini, Thrace, Greece. Three-dimensional motion capture (6 cameras, Vicon) and two ground-embedded force plates (Kistler) were used to record position-time data during walking and ground reaction forces, sampling at 100 and 1000 Hz respectively.

A generic musculoskeletal model [1] was linearly scaled to each patient based on a static trial and individual mass. Joint angles and muscle forces for the paretic side were calculated using the Residual Reduction Algorithm, and Static Optimization analyses in Opensim respectively, during single leg support of stance phase.

To quantify reproducibility, coefficient of multiple correlation (CMC) was calculated for each variable using all successful trials within the session per patient. CMC values >0.9 are excellent, 0.8-0.9 are good, 0.65-0.8 are moderate and <0.65 are poor. Inter-trial variability was calculated as root mean squared error (RMSE) between each trial and the mean curve over all trials, for each calculated variable per patient.

Results

Mean (standard deviation) values of CMC and RMSE for all trials and muscle groups across subjects are shown in Table 1. Hip flexors (iliacus and psoas), rectus femoris, gluteus maximus (three portions of gluteus maximus), hamstrings (semitendinous, semimembranosus and biceps femoris—short and long heads), vastii muscles (vastus intermedius, vastus lateralis and vastus medialis), ankle dorsi-flexors (extensor digitalis longus, extensor hallucis longus and tibialis anterior), gastrocnemius (medial and lateral heads) and soleus-tibialis posterior were analysed by summation of individual muscle forces over time. Good reproducibility was found for gluteus maximus, gastrocnemius and vastus group. Moderate reproducibility was found for iliopsoas, rectus femoris and soleus-tibialis posterior. Poor reproducibility was found for gluteus medius, biceps and ankle dorsiflexors.

Muscles	CMC	RMSE
Glut. Med	0.59 (0.25)	60.07 (13.17)
Glut. Max	0.88 (0.15)	35.01 (16.20)
Biceps	0.64 (0.23)	13.80 (11.22)
Iliopsoas	0.78 (0.27)	57.09 (26.40)
Rectus Fem	0.71 (0.16)	71.32 (18.26)
Gastro	0.86 (0.13)	107.68 (25)
Vastus	0.83 (0.22)	68.9 (34)
Ankle dorflex	0.47 (0.32)	14.28 (13.99)
Sol-Tib post	0.74 (0.16)	134.9 (29.5)

Table 1: Mean (sd) values of CMC and RMSE for each muscle group across subjects.

Discussion

Findings from this study show for the first time that reproducibility varies considerably between muscle group forces across trials for each subject, when calculated from static optimization during walking in chronic stroke patients. This can be attributed to the effective changes in muscle moment arms and consequently individual muscle force calculation during static optimization due to small between trials variations in kinematics/kinetics seen in the same patient group [2]. For example, small incremental variations in highly variable hip rotation angle could lead to substantial changes in moment arm of gluteus medius group and affect the instantaneous solution of the muscle redundancy problem during walking. Therefore, conclusions on effect of intervention on muscle force production should be drawn based upon the inherent variability of calculations.

References

1   Rajagopal, A. *et al. IEEE Trans. Biomed. Eng.*, 2016, 63 (10).

2   Fotiadou, S. *et al. NeuroRehabilitation*, 2018, 42 (1).

Acknowledgements

FEASIBILITY STUDY TO TRANSFER MUSKULOSKELETAL MODEL DATA TO A 6 DOF JOINT SIMULATOR

Paul Henke (1), Leo Ruehrmund (1), Maeruan Kebbach (1), Jan-Oliver Saß (1), Iman Soodmand (1), Eric Kleist (2), Christoph Woernle (2), Rainer Bader (1)

1. Rostock University Medical Center, Germany; 2. University of Rostock, Germany

Introduction

Musculoskeletal modeling has proven to be an efficient method to rapidly vary and analyze the effects of different aspects of total knee replacement (TKR), such as malalignment or ligament balancing, on the knee joint dynamics [1] during different active movements. Data of the joint dynamics can be implemented in experimental testing beyond standard test conditions.

Therefore, this feasibility study aims to transfer data from a musculoskeletal multibody model for active knee movement into an experimental test setup for total knee replacements utilizing a six degree of freedom (DOF) joint simulator.

Methods

An inverse kinematic multibody model of an active movement was built using marker trajectories and telemetrically acquired force data from an instrumentalized TKR (P.F.C. Sigma, DePuy Synthes, Warsaw, IN, USA) [2]. On this basis, a forward dynamic multibody model was generated, consisting of muscles, distributed contacts, and ligaments implemented as 1-dimensional nonlinear force elements [1]. Data for tibiofemoral flexion, abduction and internal rotational moment as well as the three translational force vectors were extracted and transferred to the 6 DOF VIVO™ joint simulator (Advanced Mechanical Technology, Watertown, MA USA) as shown in Figure 1. Therefore, the dynamic data of the multibody model given in xyz-cardan coordinates were transformed in Grood and Suntay [3] coordinates used by the VIVO™ joint simulator. Forces and moments were reduced to 25% to prevent damage from the simulator. The dataset is tested with a cruciate-retaining TKR (Multigen Plus, Lima Corporate, San Daniele, Italy).
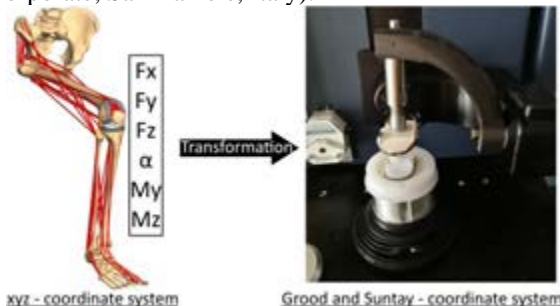
Figure 1: Input parameters were extracted from multibody model (left), transformed and transferred to the VIVO™ joint simulator (right).

Results

The data of the musculoskeletal model of the lower extremity could be successfully transferred to the joint simulator with only minimal control errors (Table 1).

Table 1: Root mean square error of the joint forces F_x, F_y, F_z, abduction M_y and rotational moment M_z and the flexion angle α between measured and target values.

F_x [N]	F_y [N]	F_z [N]	α [°]	M_y [Nm]	M_z [Nm]
3.4	7.5	2.63	0.008°	0.54	0.53

In particular, the parameters flexion angle α and joint forces F_x, F_y and F_z showed good agreement between the model data and experimental results.
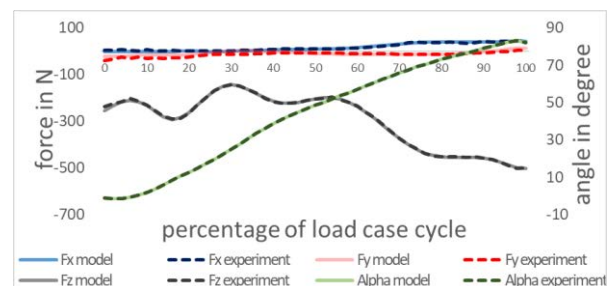
Figure 2: Comparison of the model and experimental joint forces F_x, F_y and F_z and the flexion angle α.

Discussion

In the presented feasibility study, data from a forward dynamic multibody model, which was built from in-vivo kinematic and dynamic measurements, was successfully transferred to a 6 DOF joint simulator. The measured error regarding the flexion angle and joint forces were considerably low. Currently we virtually implement the ligaments to the VIVO™ joint simulators to simulate the transferred load case with an even higher level of detail by using the same ligament apparatus in both multibody model and experimental setup. Subsequently, the input parameters of individual ligaments (e.g., stiffness) will be modified to evaluate the direct effects on the dynamic joint behavior.

References

1. Kebbach et al. Materials, 13(10):2365, 2020.
2. Fregly et al, J Orthop Res, 30(4):503-13, 2012.
3. Grood et al, J Biomech Eng, 105(2):136-44, 1983.

Acknowledgements

IMPLEMENTATION OF AN AUTOMATED METHOD FOR THE SELECTION OF SUBJECT-SPECIFIC MUSCLE INSERTION POINTS

Vera Maioli (2), Giorgio Biesso (1), Ingmar Fleps (1), Stephen J. Ferguson (1), Pasquale Vena (2), Benedikt Helgason (1), Alexander Baker (1),

1. Institute for Biomechanics, ETH Zurich, Zurich, Switzerland
2. Politecnico di Milano, Milan, Italy

Introduction

Fragility fractures due to falls in the elderly population decrease quality of life and burden the healthcare system. While muscle activation likely plays a role in fracture risk, there are very few studies investigating this topic. Existing work on muscle activation in Finite Element (FE) sideways fall models often required substantial effort in order to choose muscle insertion points in the model building process [1]. In addition, the placement of insertion points is often subjective and, thus, not reproducible.

The aim of this study was to implement an automated method of insertion point placement using the Advanced Normalization Tools software (ANTs) [2], and subsequently integrate these into existing biofidelic FE sideways fall models for fracture risk determination [3].

Methods

The bone segmentations from CT scans of 6 female specimens were registered to a template (the TLEM 2.0 [4]) using a symmetric normalization transformation within ANTs. From these registrations, 130 muscle insertion points were determined for each specimen (780 in total) without any manual intervention.

The quality of these insertion points was evaluated by calculating the distance of the insertion point to the bony surface, as each insertion point should lie directly on the bone as in the template TLEM 2.0.
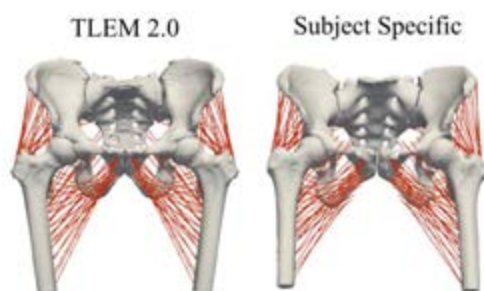
Figure 1: Left, the template TLEM 2.0. Right, the specimen with muscle created based on the TLEM 2.0 using ANTs

The muscles were implemented in the biofidelic FE simulations as discrete pre-tensioned spring elements. The forces were determined by minimizing the squared muscle stress while keeping a target 1 body weight joint contact force at the hip joint. Attachment regions were chosen based upon distance to the insertion point. In addition, biofidelic FE simulations without any muscles

were simulated as a reference and the peak contact force between the acetabular cup and femoral head were measured.

Results and Discussion

Across 780 muscle insertion points, insertion points for the femur stayed closer to the bone (mean = 0.82 mm) than insertion points for the pelvis (mean = 3.38 mm).

In the 12 FE simulations, the peak acetabular contact force increased (mean = 3.03 kN with the muscles; mean = 2.68 kN without the muscles) when 1 body weight muscle activation was added (Fig 2).
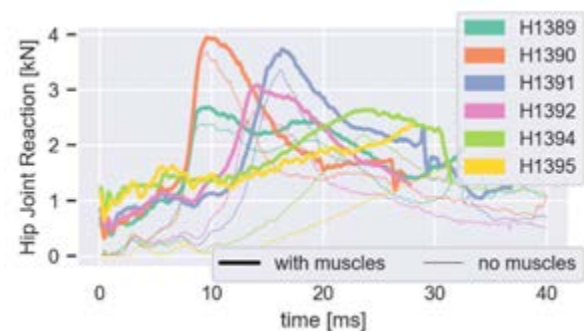
Figure 2: Variation of reaction force at the left acetabulum for 6 specimens with and without the effect of the muscle activation

Discussion

Generally, insertion points on the femur were more accurately placed than on the pelvis, as shown by the distance of the points to the bone surface. This may be because pelvis geometries are more difficult to register. Nevertheless, attachment points were still successfully integrated into FE models and results showed that the acetabular contact force increased under muscle activation. This would indicate a possible increase of fracture risk under this level of muscle activation.

In this study, a reproducible and quantitative method for automatic determination of muscle insertion points was demonstrated. This method may be used to rigorously investigate the role of muscle contraction in future computational fracture risk studies.

References

1. G. Biesso ESB2021, 302, 2021
2. Avants BB, Neuroimage, 2011
3. I. Fleps *et al* , *J. Bone Miner*, 1837–1850, 2019.
4. Carbone, Vincenzo, et al.," Journal of biomechanics, 734-741, 2015

ESTIMATION OF THE FREE ENERGY BARRIER OF THE STEP OF PI RELEASE IN MYOSIN VI CYCLE

Robin Manevy (1), Matthieu Caruel (2), Fabrice Detrez (1), Isabelle Navizet (1)

1. Univ Gustave Eiffel, Univ Paris Est Creteil, CNRS, UMR 8208, MSME, F-77454 Marne-la-Vallée, France;
2. Univ Paris Est Creteil, Univ Gustave Eiffel, CNRS, UMR 8208, MSME, F-94010 Creteil, France

Introduction

Physiologically relevant multiscale models of muscle contraction should include the description of the molecular scale force generation mechanisms.

At this molecular scale Myosin and Actin proteins interact in a cycle and form a molecular motor at the origin of muscular contraction.

During this metabolic process the energy comes from the hydrolysis of adenosine triphosphate (ATP):

An ATP molecule, initially coordinated to a magnesium cation, is broken into ADP and inorganic phosphate (Pi) inside the active site of the Myosin molecule (see Figure 1).

The release of the Pi product outside of the active site is in direct relation with the working-stroke conformational change of the Myosin motor from which the macroscopic force originates.

The mechanisms behind this key biochemical-mechanical coupling are still under intense investigation both experimentally and with simulation. In the present work we used Molecular Dynamics and Umbrella Sampling simulation to study the energetics of the departure of the Pi from the active site and describe the associated structural pathways.

The goal is to quantify the associated energy barrier for further use in coarse-grained models of molecular motors.

Methods

After preparation of the relaxed all atoms' models hydrated in explicit water boxes and using appropriate forces field, we performed Umbrella Sampling simulations with AMBER to obtain the associated free energy barrier with two different initial conformations preceding phosphate release, called Pre-Powerstroke (PPS) and Pi-Release (PiR). For each state, the simulations were also started with 2 different hydrations of Magnesium, resulting in four initial conditions. The potential of mean force (PMF) as well as the different interactions along the release of the Pi along the protein cavity are compared.

Results

The comparison of the structural motion within the active site along the four trajectories was done in parallel with the study of the PMF. For this, new analytical tools to extract information on most important interactions are proposed. Important residues involved in the trajectory are highlighted.

Our simulations suggest that the release of phosphate is favored in PiR compared to PPS which is in accordance with previous studies on Pi release. [1]

Moreover, all escapes were observed along the backdoor exit, which is the most probable escape route, without explicit bias.

Finally, our detailed analysis of the molecular interactions along this escape route brings new elements to explain the difference between the energetic costs in each process. [2]

Discussion

Our results confirm the role of the hydration of magnesium for an easier release of phosphate which was proposed using unbiased simulations. [3]

However the coupling between Pi release and working stroke remains debated. [4]

Figure

Figure 1: Cartoon representation of the myosin, with ADP and Pi represented in balls in the active site.

References

1. M. Cecchini, Y. Alexeev and M. Karplus, Structure, 18.4:458-470, 2010.
2. Manuscript in preparation
3. M. L. Mugnai and D. Thirumalai, J. Phys. Chem. A B, 125.4:1107-1117, 2021
4. M. Caremani, et al., J. Physiol 591.20:5187-5205, 2013

EXPERIMENTAL AND NUMERICAL CHARACTERIZATION OF THE ACTIVE BEHAVIOUR OF MOUSE ROTATOR CUFF MUSCLES

P. Martins (1, 2), A. Pérez(3, 4), G. Abanza (3, 4), B. Calvo (1,5), J. Grasa (1,5)

1 Aragón Institute of Engineering Research (i3A), University of Zaragoza, Spain; 2 Fundación Aragonesa para la investigación y desarrollo (ARAID); 3 Regenerative Medicine Program, Foundation for Applied Medical Research (FIMA), University of Navarra (UNAV); 4 Instituto de Investigación Sanitaria de Navarra (IdiSNA), 5 Bioengineering, Biomaterials and Nanomedicine Networking Biomedical Research Centre (CIBER-BBN), Zaragoza, Spain.

Introduction

Tendon injuries are frequent among musculoskeletal lesions, affecting almost all tendons within the human body. In chronic lesions, in addition to repair tendon discontinuity, it is essential to avoid muscle degeneration, a consequence of tendon retraction and shortening, leading to muscle atrophy. Muscle fatty infiltration after tendon rupture is responsible for muscle atrophy, and consequently, muscle function loss. This scenario remains a challenge for orthopaedic surgeons, as there is no optimal solution capable of restoring the initial traction capacity once that muscle degeneration is present. This problem is common in rotator cuff injuries [1]. The rotator cuff is the group of muscles and tendons that act to stabilize the shoulder and allow for its extensive range of motion. This work establishes a new framework based on an animal model and computational simulation to understand the biomechanics of the joint and to test new treatments. To achieve this goal, the active behaviour of the Infraspinatus and Supraspinatus muscles of a mice model has been analyzed as a first step.

Methods

The experimental study was conducted in accordance with the provisions of the European and Spanish legal normatives (RD53/2013). Isolated supraspinatus (n=3) and infraspinatus (n=3) mouse (wild-type (WT, C57BL/6J)) muscles were prepared to measure their maximum active isometric force. The Aurora Scientific Inc. 1200A system for isolated muscle tests was used. After optimal length was fixed by conducting single twitch stimulations, the force frequency response was analyzed varying the frequency activation signal: 10, 80, 100, 120 and 140 Hz. Then, tensile tests were conducted in all the samples to obtain the passive behaviour of the tissue. This experimental protocol was adapted from previous works [2] where the experiments were designed to obtain different parameters of interest to develop the computational model.

Results

The experimental results obtained in the force-frequency protocol are presented in Figure 1. The mean maximum force registered for the *Supra* group was $F(supra) \pm SD = 115.20 \pm 52.76$ mN at 140 Hz and $F(infra) \pm SD = 15.51 \pm 7.39\ mN$ at the same frequency.
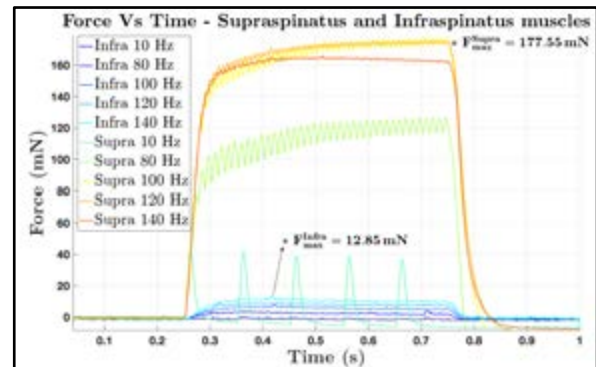
Figure 1: Force vs time response of one the samples of the infraspinatus and supraspinatus muscles.

All *Supra* samples showed higher maximum forces when compared to their *Infra* counterparts (both muscles from the same mouse). This difference is shown in Figure 1 where $F(supra)$ is approximately 14 times higher than $F(infra)$. Despite this coherent behavior, expected due to the supraspinous higher mass, the results dispersion was significant - ~46% for **Supra** and ~48% for **Infra**.

The passive and active behaviour of these muscles were fitted by an hyperelastic material model formulated using a strain energy density function based on a previous model [2].

Discussion

The results show the difference in maximum force between both muscles and the contractile properties according to time to achieve maximum force in twitch stimulation. The data and fittings will be used to develop FEM simulations of the rotator cuff muscles to investigate the biomechanics and damage effects.

References

1. Shirasawa et al, Sci Reports, 7:1, 2017
2. Grasa et al, J Mech Behav Biomed Mater, 61:444-454, 2016

Acknowledgements

MUSCULOSKELETAL ANALYSIS OF ELBOW STABILITY FOR COMMON INJURY PATTERNS

Maximilian Melzner (1,2), Christian Pfeifer (3), Franz Süß (1,2), Sebastian Dendorfer (1,2)

1. Laboratory for Biomechanics, Ostbayerische Technische Hochschule (OTH) Regensburg, Germany
2. Regensburg Center of Biomedical Engineering, OTH and University Regensburg, Germany
3. Orthopaedics, Trauma and Hand Surgery, Innklinikum Altötting, Germany

Introduction

The elbow is the most and second most commonly dislocated joint in children and adults, respectively [1]. An elbow trauma can cause injury to the bony, ligamentous, and muscular stabilizers of the elbow joint, which interact in complex ways and are distinguished in primary and secondary stabilizers. The stability of the joint is an important decision criterion for the subsequent treatment (e.g. non-operative vs operative). The stability assessment, however, depends on the expertise of the practicing physician. Therefore, the aim of this study is to use numerical simulation models to recreate different injury patterns of the elbow and to provide an objective basis for the assessment of elbow stability.

Materials and Methods

For the numerical assessment of the elbow joint after trauma, a detailed model of the elbow was developed in the AnyBody Modeling System (AnyBody Technology, DK), which includes the medial and lateral ligaments of the elbow and additionally the cubital angle is determined based on the acting forces. Experimentally collected data from the literature were used to validate the model [2-4].

In close collaboration with experienced practicing physicians, various scenarios of ligament injuries, muscle and osseous damages that occur in everyday clinical practice were identified (see Table 1). For the realization of each scenario, the stiffness of the corresponding ligaments or the maximum muscle forces of the extensor/flexor muscles were set to zero, respectively.

	LL	RH	ML-P	ML	EM	FM
Scen. 1	x					
Scen. 2	x	x				
Scen. 3	x	x			x	
Scen. 4			x			
Scen. 5				x		
Scen. 6				x		x
Scen. 7	x	x	x			
Scen. 8	x	x		x		
Scen. 9		x				

Table 1: Overview of the nine scenarios, with "x" indicating which of the injuries are included – lateral ligament failure (LL), radial head fracture (RH), posterior medial ligament failure (ML-P), complete medial ligament failure (ML), extensor muscle failure (EM), and flexor muscle failure (FM).

The acting varus and valgus moments (low (2 Nm) and high (4 Nm)) were applied under 0°, 45° and 90° flexion for intact and injured scenarios. Cubital angle was determined for the intact cases. For injured cases the corresponding valgus and varus moments which result in the same angle were analyzed. This resulted in a total of 5.790 simulations.

Results

Table 2 shows the average stability loss of every scenario according to the musculoskeletal simulations in ranked order from low to high. The higher the stability loss for the particular scenario, the more unstable the elbow joint becomes when the respective injury occurs.

	average stability loss
Scen. 4	1.3 %
Scen. 9	10.1 %
Scen. 1	10.6 %
Scen. 6	20.3 %
Scen. 2	20.7 %
Scen. 3	20.7 %
Scen. 5	21.1 %
Scen. 7	22.4 %
Scen. 8	35.0 %

Table 2: Average stability loss of every scenario according to the musculoskeletal simulations in ranked order from low to high.

Discussion

The purpose of this study was to evaluate elbow stability to varus and valgus forces based on the calculations of a musculoskeletal model. Different contribution behaviors to elbow stability are revealed depending on the failure of different stabilizers. Thus, it could be shown that scenario 8 has by far the highest joint instability. The results of this study will be correlated to clinical findings. In future this simulation might be useful to assist physicians in assessing elbow stability and allow for the derivation of appropriate treatment procedures.

References

1. Litin, Scott C. "Mayo Clinic Family Health Book." Mayo Clinic, 2018.
2. Morrey & An, Clinical orthopaedics and related research, (201), 84-90, 1985
3. Regan et al., Clinical orthopaedics and related research, (271), 170-179, 1991
4. Morrey, The Elbow and Its Disorders. Elsevier Health Sciences, 2009

A PROCEDURE TO PERSONALIZE A MUSCLE FATIGUE MODEL FOR SOLVING THE MUSCLE RECRUITMENT PROBLEM

Florian Michaud (1), Francisco Romero-Sanchez (2), Urbano Lúgris (1), Javier Cuadrado (1)

1. Lab. of Mechanical Engineering, University of La Coruña, Spain; 2. Lab. of Mechanical Engineering, University of Extremadura, Spain;

Introduction

Determination of muscle forces is of great interest to extract the principles of the central nervous system control (diagnosis of neuromuscular disorders), or to estimate the loads on bones and joints (prevention of injuries in sports/work tasks, surgical planning to reconstruct diseased joints) [1]. The redundancy problem of the muscle recruitment, the uniqueness of each human being and the difficulty to extract some subject-specific parameters are the main issues to solve for obtaining good results. The aim of this study is to propose a procedure to include a personalized muscle fatigue model in the optimization-based solution of the muscle recruitment problem.

Methods

Muscle activation, fatigue, and recovery under a variety of loading conditions can be represented by a three-compartment model, fully explained in [2], corresponding to the three muscle states: resting, activated, or fatigued. This model can be implemented to constraint the muscle forces within the optimization problem, thus offering a valid approach for the calculation of the redundant muscle forces in the presence of muscular fatigue, as stated in [3].

However, in [3], the authors did not apply the resulting model to a real case, and consequently did not address some issues. In order to use the full muscle model considering fatigue, it is required to calibrate some subject-specific parameters. While some parameters depend directly on the musculoskeletal geometry (musculotendon length, musculotendon velocity, and moment arms), and others can be indirectly scaled from it (optimal muscle fiber length and slack tendon length), maximum isometric force (*Fm0*) as well as fatigue and recovery coefficients (*F* and *R*, respectively) require additional calibration measurements. The latter play an essential role for an accurate fatigue simulation because they introduce muscle force constraints. If they are not calibrated, the task-related loss of force will not be reflected.

For this reason, to assess muscles forces considering fatigue, the authors propose a protocol consisting of two main steps (Figure 1):

1. Muscle force and fatigue calibration.
2. Determination of muscle forces with fatigue.

A right upper extremity model of the elbow joint with seven muscles adapted from [4] was used in an inverse dynamics analysis perspective for two subjects (one male and one female).
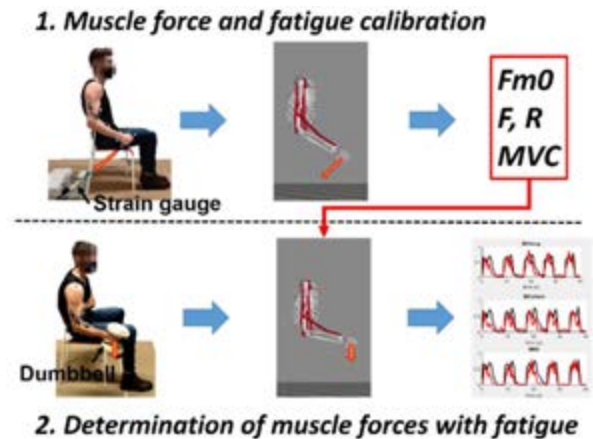
Figure 1: Protocol steps (MVC: Maximum Voluntary Contraction).

Results

In this work, the process is applied to a benchmark case: the force quantification of the elbow flexor and extensor muscle sets engaged in weightlifting and performing cycles of forearm flexion/extension. Results are compared to those obtained without considering fatigue, showing good correlation with experimental measurements (surface electromyography).

Discussion

Results were observed for two subjects, and subject-specific parameters showed differences. In order to highlight the inter-subject variability and validate the procedure, the approach will be applied to more subjects in a future work.

References

1. F. Michaud et al., J. Neuroeng. Rehabil., 18:1, 2021.
2. T. Xia and L. A. Frey Law, J. Biomech., 41:3046–3052, 2008.
3. A. F. Pereira et al., Proc. Inst. Mech. Eng. Part K J. Multi-body Dyn., 225:359–370, 2011.
4. K. R. Saul et al., Computer Methods in Biomechanics and Biomedical Engineering, 18:1445–1458, 2015.

COMPARING THE EFFICIENCY AND ACCURACY OF SEVERAL CONTACT METHODS FOR HUMAN-ENVIRONMENT INTERACTION

Francisco Mouzo, Florian Michaud, Urbano Lugris, Javier Cuadrado

Lab. of Mechanical Engineering, University of La Coruña, Spain

Introduction

Contact with the ground is common in typical activities, as gait, running, weightlifting, etc. But additional contacts may also appear in others, either with the environment, as in bag boxing or parkour, or between humans in partnering or opposing exercises, as duet dancing or martial arts. In the context of predictive simulation, inclusion of contact encompasses collision detection and contact force modeling, which may be computationally costly. In this work, several methods for considering human-environment contacts are compared in terms of efficiency and accuracy, seeking to provide criteria for their use in human motion simulation.

Methods

The case study is an exercise consisting of a subject kicking the half of a foam ball attached to a force plate hung from the roof by means of two cables. In the experiment, shown in Fig. 1 left, reflective markers were placed on the subject and on the force plate, their motions being captured by infrared cameras. Moreover, the contact force between the kicking foot and the ball was measured by means of the force plate shown in the figure, while the foot-ground contact force of the supporting leg was measured by a second force plate. The same system was modeled in the computer, as illustrated in Fig. 1 right. A multibody model featuring 18 anatomical segments connected by 17 spherical joints, leading to 57 degrees of freedom, was used for the human [1], while a simple rigid body undergoing two constraints of constant distance to represent the effect of the cables was used for the force plate. In the human model, a CTC-type controller was in charge of tracking the captured joint trajectories, and the force measured by the force plate on the floor was applied to the supported foot. The geometries of foot and ball were represented either as triangular meshes or sets of spheres, and the corresponding collision detection method provided the contact parameters. With this information, the contact model (several were tested) yielded the impact force, which was applied to both the kicking foot of the human model and the rigid body representing the hanging force plate. The approximation introduced by considering the force plate measurement as the contact force was also investigated.

Two trials of the experiment were performed by the same subject, trying to kick the ball in the same way in both cases, the corresponding data being measured and stored. Then, for each combination of geometric representation of the contacting surfaces and contact force model, the following procedure was carried out.

First, data from the first trial were used to calibrate the parameters of the contact model by optimization, seeking to minimize the discrepancy between the contact force measured by the force plate and calculated in the simulation. Second, data from the second trial were used to run a simulation in which the parameters of the contact model adopted the values obtained in the previous calibration process. The efficiency of this simulation was measured, and the accuracy was evaluated as the discrepancy between the contact force measured by the force plate and calculated in the simulation.
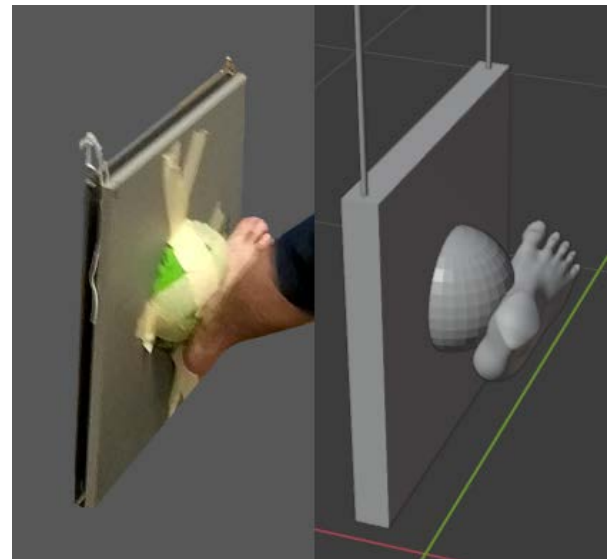
Figure 1: Experiment and simulation.

Results

A table was generated gathering the values of efficiency and accuracy obtained for each couple of geometric representation of contacting surfaces and contact force model.

Discussion

Based on the data gathered in the table mentioned in the previous section, conclusions were drawn, and criteria were provided for the use of the different alternatives to model contact between humans and environment in the context of predictive simulations.

References

1. F. Mouzo, U. Lugrís, R. Pamies-Vila and J. Cuadrado, "Skeletal-level control-based forward dynamic analysis of acquired healthy and assisted gait motion," Multibody Syst Dyn 44(1):1-29, 2018.

MUSCLE TORQUE GENERATORS FOR DIGITAL HUMAN MODEL CONTROL - MEASUREMENT PROTOCOL FOR DATA AQUSITION

Marius Obentheuer (1), Monika Harant (1), Eva Bartaguiz (2), Carlo Dindorf (2), Joachim Linn (1), Michael Fröhlich (2)

1. Fraunhofer ITWM, Germany; 2. University of Kaiserslautern, Germany;

Introduction

In several branches of industry, digital human models (DHM) are meanwhile an integral part of the simulation tools used for product design and workplace layout [1]. They allow to consider human aspects already at an early stage of development, when physical prototypes do not yet exist, and help to create safe and ergonomic workplaces and products.

For the ergonomic evaluation of work processes on a (future) assembly line, posture-related criteria and workload-related criteria are assessed. To consider the anthropometric variance of different people, large databases of anthropometric measurements are available. For the evaluation of loads and forces using a DHM, look-up tables describing the permissible loads for a specific task (e.g. pick and place) are common. There is still no direct way to evaluate simulated forces (such as joint torques or muscle forces) simply due to the lack of data to parameterize DHMs.

As human muscle force generation is complex and muscle forces cannot be estimated directly and in vivo, there is still no standard procedure for data acquisition for e.g. Hill muscle models. The concept of muscle torque generators (MTG) [2] is a promising compromise between human like actuation and the possibility for parameter identification. MTG transfer the characteristics of human force generation from muscle (force-length and force-velocity relationship) to joint level (torque-angle and torque-angular velocity relationship), and in contrast to muscle forces, the resulting joint torque as summarized output of agonist and antagonist muscular activation can be directly measured.

We perform measurements in the motion lab, which we process and analyze, with the goal to define a minimum set of tests that are needed to parametrize a DHM actuated via MTG, and capable to perform task independent simulations. We further on want to derive a standard test protocol, which can be applied to a larger set of subjects, to acquire comparable data. In this presentation we focus on first results for MTG parametrization of an arm model and the general challenges at data acquisition and parametrization.

Methods

We perform isokinetic measurements using an *ISOMED 2000 by D. & R. Ferstl (Germany)*. For each kinematical degree of freedom (DOF) of each joint, we measure **1:** maximum joint torques for a multitude of different (constant) angular velocities over the whole range of motion **2:** both motion directions (e.g. flexion & extension) as well as concentric and eccentric motions

3: maximum isometric torques for a set of discrete joint angle values **4:** the passive torques to get parameters for joint stiffness β^{PE} (see (1)). By performing these measurements for different joint configurations (e.g. measuring elbow flexion at different forearm rotations and shoulder angles), we investigate the effect of muscles, whose activation influences more than one kinematical joint DOF as well as bi-articular muscles.
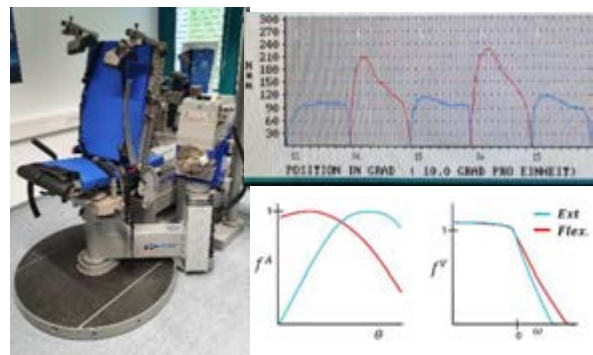
Figure 1: The Isomed 2000 (left) allows to measure torque-angle dependency at constant angular velocity (right-top), which are used to parametrize muscle torque generators (right-bottom) for DHM actuation.

In a post-processing step, we define a minimum set of necessary measurements for each joint DOF to estimate adequate parameters for our used MTG model

$$\tau^{MTG} = \alpha\tau_{max}^{MTG}f^A(\theta)\cdot f^V(\omega) + f^{PE}(\theta)(1 - \beta^{PE}\left(\frac{\omega}{\omega_{max}}\right)\ (1),$$

where τ^{MTG} is the resulting joint torque for a given activation α, depending on the torque-angle relationship $f^A(\theta)$, the torque-velocity relationship $f^V(\omega)$, the passive elasticity and the maximum voluntary joint torque τ_{max}^{MTG} [3].

Results and Discussion

We give an overview of the challenges of parameter identification for MTG, used for task independent DHM simulations. As example, we show the influence of forearm rotations (pronated, neutral, supinated) to the resulting torque measurements for elbow flexion and extension, and give an advise for MTG parametrization of the elbow joint, including measurement protocol (joint angles (θ) for isometric measurements, angular velocities (ω) for isokinetic measurements) as well as procedures to process raw data. And we point out limitations of a MTG actuation, in comparison to a DHM actuated via Hill muscles.

References

1. Högberg et al, IJDH.2016.077413: 132-152, 2016.
2. Anderson et al, J Biomech, 40(14): 3105–3113, 2007.
3. Millard et al, J Biomech, 89:11-20, 2019.

FINITE ELEMENT MANDIBLE MODEL OPTIMIZATION FOR LARGE MANDIBULAR DEFECT REGENERATION

Ana Rita Reis (1,2), Vincenzo Orassi (3,4), Sara Checa (3), Renato Natal (1,2), Marco Parente (1,2)

1. INEGI, Portugal; 2. FEUP, Portugal; 3. Berlin Institute of Health at Charité – Universitätsmedizin Berlin, Julius Wolff Institute, Berlin, Germany; 4 Berlin-Brandenburg School for Regenerative Therapies, Berlin, Germany

Introduction

Large mandibular bone defects, due to tumour resections, and consequent mandibular reconstruction represent a clinical challenge for orthopaedic surgeons. The gold standard treatment includes the use of microvascular free flaps, however, the high complication rate and donor site morbidity [1] make it necessary to find alternative treatments. Scaffold-supported bone regeneration has been investigated [2], however, it is still unsure if it can generate optimal biomechanical conditions to enhance the bone healing process in the mandible.

The present study aims to use a computer modelling approach to design a large mandibular defect for the insertion of a mechanobiologically optimized scaffold.

The aim is to create a scaffold site for further evaluation of the bone healing process as well as if it provides sufficient strength to withstand the mechanical loads generated by common clenching tasks.

Eventually, the biomechanical performance of the scaffold can be evaluated in terms of both mechanical strains induced within the healing region and mechanical stresses within the scaffold and relative fixation system.

Methods

Using tomography scans, a finite element model of a healthy adult mandible was simulated (figure 1). By applying physiological muscular loads [3] and boundary conditions, intercuspal, incisal, and unilateral biting were simulated.

Then, using the same methodology, a finite element model of a mandibular body defect of ca. 20 mm width was simulated (figure 2). Different scaffold structures will be tested in terms of their biomechanical behaviour.
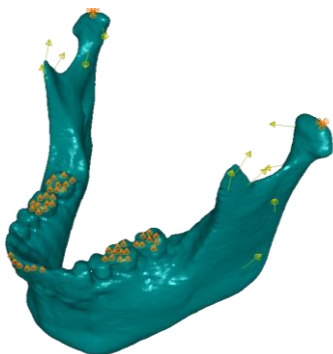
Figure 1: Finite element model of a healthy adult mandible with boundary conditions and muscle forces directions.

Figure 2: Finite element model of a mandibular body defect of ca. 20 mm width.

Results

The values in table 1 show the intercuspal, incisal, and unilateral resulting biting forces of the healthy mandible.

Intercuspal	Incisal	Unilateral
415 N	192 N	546 N

Table 1: Reaction forces in Newton of the intercuspal, incisal, and unilateral superior dental planes.

Discussion

The validation results of the healthy mandible are within the real occlusal mandible forces as measured by Hallie M Edmonds and Halszka Glowacka [4]**.**

The results show that the same muscle forces and occlusal boundary conditions can be used in the mandibular body defect model and further scaffold biomechanical performance can be carried out.

References

1. JS Brown et al, Mandibular reconstruction with vascularised bone flaps: a systematic review over 25 years, British Journal of Oral and Maxillofacial Surgery, 55:113-126, 2017
2. Hui Gao et al, Mechanobiologically optimization of a 3D titanium-mesh implant for mandibular large defect: A simulated study, 104:109934, 2019
3. Korioth and Hannam, Mandibular forces during simulated tooth clenching. J. Orofacial Pain 8:179–189, 1994
4. Hallie M Edmonds and Halszka Glowacka, The ontogeny of maximum bite force in humans, Journal of anatomy, 237: 529-542, 2020

Acknowledgements

MONITORING LOWER LIMB ASYMMETRY DURING REHABILITATION OF ACL RECONSTRUCTED PATIENTS USING DINABANG DEVICE

Dario Santos (1-2-4), Bernardo Articardi (2), Jimena García (2)
Marcelo Bonilla (2), Juan Comesaña (2), Martha Arriola (1-2), Fernando Motta (3) & Franco Simini (4)

1. Departamento de Rehabilitación, Hospital de Clínicas, Universidad de la República, Uruguay
2. Department of Rehabilitation & Physiotherapy, British Hospital, Uruguay; 3. Department of Orthopaedic Surgery, British Hospital, Uruguay 4. Núcleo de Ingeniería Biomédica de las Facultades de Medicina e Ingeniería, Universidad de la República, Uruguay

Introduction

Usual practice of Anterior Cruciate Ligament (ACL) rehabilitation concentrates on quadriceps development with minor concern on hamstring. The aim of the present study is to measure the strength of quadriceps and hamstring during rehabilitation of ACL reconstructed (ACLr) patients. We used DINABANG®, capable of dynamic torque measurement [1].

Methods

Four male subjects, $42,5 \pm 11,2$ years, 179 ± 23 cm, $79,3 \pm 8,6$ kg who had an ACLr according to the hamstring tendon graft technique, were recruited. All subjects provided written informed consent prior to participation. Patients followed an "ACL ligamentization" protocol [2]. Three times during rehabilitation (week 11, 16, 21) quadriceps and hamstring strength was measured (60º) using DINABANG® (Fig. 1).

Figure 1: Quadriceps strength measurement as the patient extends the lower limb, with DINABANG secured just above malleolus to a rear fixed point.

Results

Maximal Voluntary Isometric Strenght (N)				
Week after ACLr	Quadriceps		Hamstring	
	Operated Leg $\bar{x} \pm$ SD	Uninvolved Leg $\bar{x} \pm$ SD	Operated Leg $\bar{x} \pm$ SD	Uninvolved Leg $\bar{x} \pm$ SD
11	210.0 ± 81.2	395.0 ± 70.5	152.5 ± 47.9	235.0 ± 48,0
16	300.0 ± 75.3	480.0 ± 62.7	210.0 ± 27.1	287.5 ± 32.0
21	395.0 ± 98.8	525.0 ± 31.1	267.5 ± 59,1	335.0 ± 67.6

Table 1: Mean maximum strength of four ACL operated male individuals, at 11, 16 and 21 weeks after surgery.

Table 1 shows the mean value and standard deviation (SD) of the four subjects at different times. Table 2 shows the limb strength asymmetry, measured for both quadriceps and hamstring as rehabilitation progresses.

Asymmetric Strength: Operated/univolved (%)			
Week after ACLr	Week 11	Week 16	Week 21
Hamstring	46	32	23
Quadriceps	64	48	30

Table 2: Mean quadriceps and hamstring asymmetry.

Discussion

DINABANG® measures torque and angular velocity of lower limbs with elastic bands [1]. DINABANG® is used here to isometrically measure hamstring during flexion and quadriceps strength during extension. During rehabilitation, strength increases in muscles of both limbs (Table 1), the operated side more so. Since the imbalance of strength is an indicator of possible injury [3], DINABANG® calculates the asymmetry index (Table 2). Rehabilitation from week 11 to week 21 roughly halves the asymmetry, because our rehabilitation program concentrates on both.

Acknowledgements

References

1. D. Santos *et al.*, "Hamstring Torque, Velocity and Power Elastic Band Measurements during Hip Extension and Knee Flexion," *Appl. Sci.*, vol. 11, no. 22, p. 10509, 2021.
2. S. Claes et al., "The 'ligamentization' process in anterior cruciate ligament reconstruction: What happens to the human graft? A systematic review of the literature," *Am. J. Sports Med.*, vol. 39, no. 11, pp. 2476–2483, 2011.
3. S. Yeung et al., "A prospective cohort study of hamstring injuries in competitive sprinters: Preseason muscle imbalance as a possible risk factor," British Journal of Sports Medicine, vol. 43, no. 8. pp. 589–594, 2009.

VALIDATION OF REMOTE METHODS FOR MEASURING FOOT ARCH HEIGHT AND SHAPE

Jerneja Uhan (1,2), Alpesh Kothari (1,2), Amy Zavatsky (1), Julie Stebbins (1,2)

1. University of Oxford, United Kingdom; 2. Oxford Gait Laboratory, United Kingdom

Introduction

Foot arch height and shape parameters are generally quantified using equipment such as pressure plates and callipers. In recent years, remote/telemedicine techniques have become more prolific, with the Covid-19 pandemic accelerating this trend. Recording characteristics of foot arch shape remotely could be useful for both clinical and research purposes. Therefore, the aim of this study was to validate remote measures of arch height index (AHI, Fig. 1) and arch index (AI, Fig. 2) against measures collected in person in a clinical gait laboratory setting.
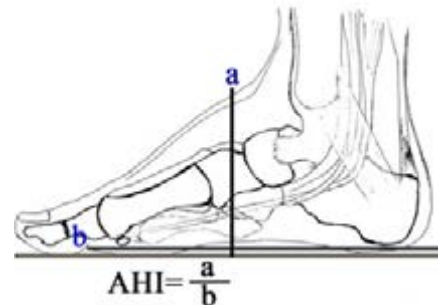
Methods

The data was collected on 40 feet (mean age = 38 years, age range 21-75 years, 10 males and 10 females). For in-person measurement of AHI, calibrated callipers and a standardised technique were used across two different days by the same tester. For in-person AI measurements, an EMED pressure plate (novel gmbh, Germany) and a standardised technique for data collection during standing were used. For remote measurement of AHI, participants were asked to photograph their feet using a smartphone camera and to follow a specific protocol on how to position their feet, to allow for consistency in camera distance and angulation (Fig. 3a). For collecting remote AI measurements, Invisible Ink paper (NEKOOSA, USA) and the same protocol as that for in-person measurements were utilised (Fig. 3b). Intra-tester reliability of each measurement method was evaluated by calculating the intraclass correlation coefficient (ICC) and mean error. Validity of each of the remote measures was determined by calculating the Pearson correlation coefficient between the in-person measurement and its remote counterpart.

Results

Both the in-person and remote AHI measurement methods demonstrated excellent intra-tester reliability with an ICC of 0.988 ($p<.001$ and mean error of 0.008 for the former method, and an ICC of 0.986 ($p<.001$) and mean error of 0.0004 for the latter method). There was a strong Pearson correlation coefficient of 0.738 ($p<.001$) and a linear regression gradient of 0.791 ($p<.001$) when comparing the in-person and remote AHI techniques. In addition, there was a strong Pearson correlation coefficient of 0.996 ($p<.001$) and a small absolute difference of 0.01 mm between both AI measurement techniques.

Figure 1: Calculation of AHI

$$AHI = \frac{a}{b}$$

Figure 2: Calculation of AI

$$AI = \frac{b}{a+b+c}$$

(a) AHI   (b) AI

Figure 3: Demonstration of remote AHI measurement
Figure 3: Demonstration of remote AI measurement

Discussion

The demand for remote data collection methods has increased in light of the pandemic, as well as carrying the benefit of routine monitoring of patients without costly visits to a clinic. The results obtained from this study indicate that remote measurement methods of standard foot arch indices are reliable and valid alternatives to in-person assessment methods for measuring AHI and AI. However, further research on validating other measures of foot health is recommended to facilitate broader remote data collection for diagnostic or therapeutic purposes.

ENHANCING DYNAMIC CONSISTENCY OF MULTIMODAL MOTION DATA IN MUSCULOSKELETAL SIMULATION

Iris Wechsler, Alexander Wolf, Sandro Wartzack, Jörg Miehling

Friedrich-Alexander-Universität Erlangen-Nürnberg (FAU), Engineering Design, Martensstraße 9, 91058 Erlangen, Germany

Introduction

Digital human models can be used to determine biomechanical parameters (e.g. muscle or joint reaction forces) virtually and in a non-invasive way [1]. Hereby, subject-specific models lead to more reliable simulation results in this context [2]. Moreover, even though current sensor and measuring systems can achieve high-quality data, the measurements are still error-prone and subject to uncertainties such as noise or jumps. Furthermore, kinematic and dynamic inconsistencies between the measured data and the motion capabilities of the human body can occur. We assume that motion tracking accuracy and consistency will be increased when multimodal data, e.g., some combination of position, orientation, EMG, or surface data, is considered. Therefore, our goal is to research and develop methods for filtering and analysing multimodal motion measurement data in conjunction with individualized digital human models. In this paper we want to discuss available approaches.

Methods

Subject-specific individualization of the applied musculoskeletal human models in multiple domains (anthropometry, mobility, strength) is to be achieved through a combination of subject-specific manual measurements and population data [3]. Further, we aim to develop a method for kinematically consistent and precise motion tracking. The standard method, Inverse Kinematics, minimises the difference between measured and virtual marker and coordinate positions in a least squares approach to compute generalized coordinate trajectories [4]. The novel tracking algorithm should include different types of data, which are weighted in relation to each other. This way the observed movement information from different data sources should be transferred to the digital model in order to get the most accurate and consistent simulation results possible. Nevertheless, the problem regarding the dynamic consistencies between the motion of the model and the measurements still remains. For this we also want to investigate methods to enhance dynamic consistency and further develop a dynamic tracking method that is able to generate kinematically and also dynamically consistent motion data. Therefore, dynamic components (e.g. muscle activation, accelerations) are to be included in the tracking method.

Results

There are various approaches available in literature for enhancing dynamic consistency (cf. figure 1). The EMG-informed forward simulation approach, for example, tracks measured marker trajectories while replicating EMG measurements to obtain dynamic consistency [5-7]. Controller-based solution approaches optimise measured trajectories through forward simulation with a time-limited observation interval to enhance dynamic consistency [8]. Also, trajectory optimization using direct collocation and a Kalman filter have already been used to achieve dynamically consistent movement simulations [9,10].
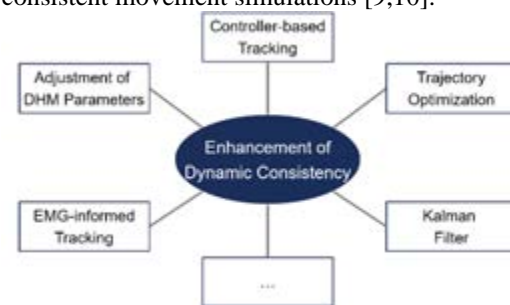
Figure 1: Selected solution approaches

Discussion

In the next step, a systematic literature review will be conducted based on the mentioned results, in order to identify and analyse all relevant dynamic tracking solutions regarding multimodal motion data. Main focus will be the classification into different solution approaches. Moreover, input and output variables, the used model and the regarded dynamic component will be explored. Based on these results the solution approach for our application of multimodal motion data is to be set up. This new musculoskeletal simulation approach is then to be evaluated regarding accuracy and usability and to be benchmarked against the standard methods of biomechanical motion capture and analysis.

References

1. Seth et al, Computational Biol, 14(7), 2018.
2. Lund et al, Internat Biomech, 2:1-11, 2015.
3. Miehling, Comput Methods Biomech Biomed Engin, 22(15):1209-1218, 2019.
4. Delp et al, IEEE Trans Biomed Eng, 54: 1940-1950, 2007.
5. Sartori et al, PLoS One, 7(12), 2012.
6. Bailly et al, Front Bioeng Biotechnol, 2021.
7. Moissenet et, Front. Neurorobot, 2019.
8. Thelen et al, J Biomech, 39:1107-1115, 2006.
9. Dembia et al, PLoS Comput Biol, 16(12), 2020.
10. Bonnet et al, J Biomech, 62:140-147, 2017.

Acknowledgements

BIOMECHANICAL ANALYSIS OF STRESS CHANGES IN MEDIAL ANKLE LIGAMENTS CAUSED BY ADULT ACQUIRED FLAFOOT DEFORMITY

Nicolás Yanguma Muñoz (1), Brayan David Solorzano(1), Christian Cifuentes-De la Portilla Ph.D (1)

1. Biomechanics group (IBIOMECH), Department of biomedical engineering, Universidad de los Andes, Colombia

Introduction

Adult Acquired Flatfoot Deformity (AAFD) is an illness related to, between others, the dysfunction/failure of passive stabilizers of the foot, plantar fascia (PF), and spring ligament (SL) [1]. The consequence of this condition is an increased loss of arch integrity and forefoot pronation, as well as a possible overload in ankle ligaments, especially medial ankle ligaments [2]. Thus, this study aimed to analyse how to change the stress forces in some ligaments: tibiocalcaneal, tibiotalar and calcaneofibular when the main passive stabilizers of the foot arch lost their mechanical properties, which is a common characteristic in patients with flatfoot.

Methods

The analysis was performed using a new version of the model proposed by Cifuentes-De la Portilla et al. [1]. This model reconstructs a human unloaded foot, but it can simulate a flatfoot deformation. Tissues were considered as elastic-linear materials except for the cartilage in the foot. The biomechanical properties were taken from the literature: cortical bone (E = 17,000 MPa, v = 0.3), trabecular bone (E = 700 MPa, v = 0.3), ligaments (E = 250 MPa, v = 0.28), plantar fascia (E = 240 MPa, v = 0.28), and cartilage of tibia and fibula (E=10, v=0.49) [1]. Meshing was performed in ICEM CFD V. 19.2. Also, a trial error approach was employed to optimize the mesh size of each segment [3]. Simulations were performed constraining the model by fixing nodes at the lower part of the calcaneus and blocking the Z-axis displacement of the lower nodes of the metatarsals. The load was applied in a descending vertical direction in the fibula and tibia. Simulations were performed in ABAQUS/CAE V. 6.14, and evaluations were based on maximum principal stress. The complete model can be seen in figure 1.
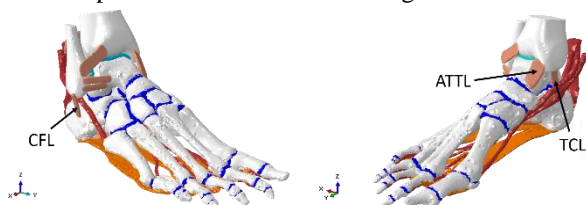
Figure 1. Model based on Cifuentes-De la Portilla et al. including some medial ankle ligaments design for this research.

Results

In figure 2 can be seen obtained results of maximum principal stress in medial ankle ligaments in some flatfoot development scenarios. Herein an increase of more than 100% in the stress forces in tibiocalcaneal ligament (TCL) can be seen when both passive stabilizers were dysfunctional. Additionally, the stress in the anterior tibiotalar ligament (ATTL) grows approximately 12% when PF and SL do not perform correctly. Finally, maximum principal stress in the calcaneofibular ligament (CFL) goes up to 9% when SL and PF lost their mechanical properties.
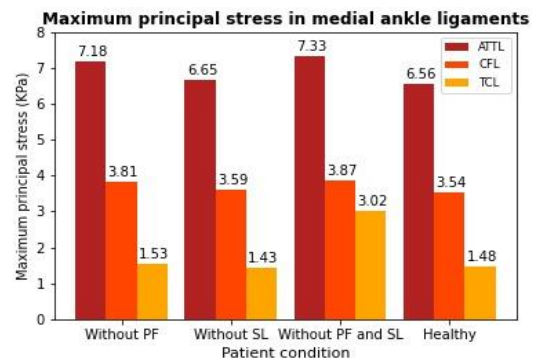
Figure 2. Maximum principal stress in some ankle ligaments in AAFD situations and in a healthy patient.

Discussion

According to the obtained results, there is a good possibility that AAFD has a notable effect on medial ankle ligaments because it increases their stress forces. These results are interesting because they explain why occurs the pain, in this region of the ankle joint, when a patient has a flatfoot, as well as the reported injuries around the deltoid and medial ankle ligaments [2]. Moreover, the stress and risk of injury in ligaments are more considerable when PF and SL lose their mechanical properties. Our results are a first approximation about the stress forces changes in the medial ankle ligaments. As work in the future, simulations will continue including the action of active stabilizers, such as the long and short peroneal tendon, and the traction generated by the Achilles tendon to simulate a closer scenario to that of a human foot in a dynamic activity.

References

1. Cifuentes-De la Portilla, C., Pasapula, C., Gutiérrez-Narvarte, B., Larrainzar-Garijo, R., & Bayod, J. (2021). Peroneus Longus overload caused by soft tissue deficiencies associated with early adult acquired flatfoot: A finite element analysis. *Clinical Biomechanics*, *86*, 105383.
2. Flores, D. V., Mejía Gómez, C., Fernández Hernando, M., Davis, M. A., & Pathria, M. N. (2019). Adult acquired flatfoot deformity: anatomy, biomechanics, staging, and imaging findings. *Radiographics*, *39*(5), 1437-1460.
3. Burkhart, T. A., Andrews, D. M., & Dunning, C. E. (2013). Finite element modeling mesh quality, energy balance and validation methods: A review with recommendations associated with the modeling of bone tissue. *Journal of biomechanics*,*46*(9), 1477-1488.

KNEE EXTENSORS' RATE OF FORCE DEVELOPMENT MEASUREMENT USING A HAND-HELD DYNAMOMETER AND A 3D PRINTED ADAPTER

Tomer Yona[1], Arielle Fischer[1]

[1] *Department of Biomedical Engineering, Technion, Israel Institute of Technology, Israel*

Introduction

The importance of lower limb muscle strength in the rehabilitation and performance fields are well documented. An equally important but less common measurement is the Rate of Force Development (RFD), defined as the ability to generate muscle force quickly. Recent reviews have highlighted the importance of RFD assessment after an anterior cruciate ligament injury [1] and among people suffering from knee osteoarthritis [2]. Deficits in RFD can last for years after an injury [1]. They might be more pronounced than the differences in peak force [3], emphasizing the importance of knee RFD assessment in different pathologies.

Measuring RFD is commonly done in the lab using stationary and expensive isokinetic dynamometers. However, measuring RFD using handheld dynamometers (HHD) enables testing in different environments such as the lab, the field, and the clinic, with lower costs.

However, the use of HHD is prone to strength discrepancies between the tester and the participant, that might bias the results. A previous study evaluated the reliability of the knee extensors RFD using a HHD and reported that the reliability of the knee extensors' muscles was the lowest compared to the hips and ankles, as the extensors are much stronger than the examiner's hand holding the HHD, leading to lower reliability [3].

Therefore, our objectives were to a) design a 3D printed adapter to attach the HHD to a fixed belt, and b) Investigate the intra-tester, within-session, and between-session reliability of the RFD (early phase-100ms and late phase-200ms) and peak force of the knee extensors using a 3D adapter attached to the fixed HHD.

Methods

After providing informed consent, 35 healthy participants enrolled in the study: Males and females, aged 18-50.

Using a fixed MicroFET2 HHD (Hoggan Scientific, LLC, Salt Lake City, UT) and a printed 3D adapter, we assessed the knee extensor muscles in a seated position at the edge of a treatment bed (Figure 1). Each participant had a standardized warm-up, followed by three maximum isometric knee extension trials. One minute of rest was given between trials.

Outcome measures were peak force and early and late phase of the RFD (0-100ms and 0-200ms, respectively). Test-retest reliability was measured within sessions (30 minutes) and between sessions (one week).

Test-retest reliability was assessed by two-way random, single measures, absolute agreement, Intraclass Correlation Coefficient (ICC 2.1).

Additionally, we report on each outcome's standard error of measurement (SEM), calculated as:

$$SEM = SD * \sqrt{(1-ICC)}$$
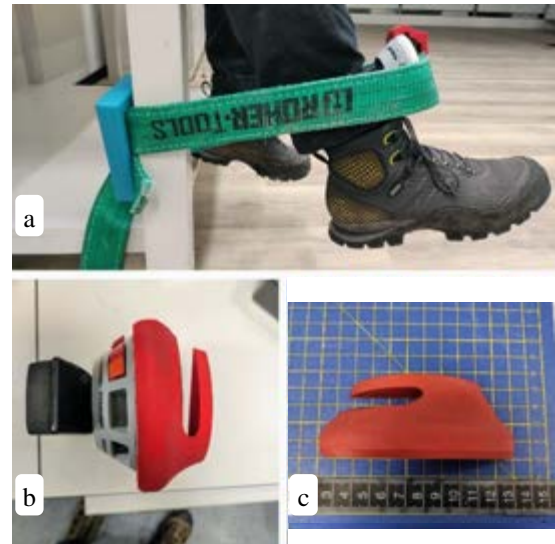
Figure 1. (a) Test position. (b) Adapter attached to HHD (c) Adapter size.

Results

The ICC for the early phase RFD was 0.85-0.93 [95% CI, 0.75-0.95] and the late phase RFD was 0.89-0.94 [95% CI, 0.80-0.96]. The peak force's ICC was 0.95-0.96 [95% CI, 0.92-0.98].

Lastly, the SEM ranged from 28.9-29.4 (N) for the peak force, 243.4-280.7 (N/s) for the early phase RFD, and 131.1-145.6 (N/s) for the late phase RFD.

Discussion

Combining a HHD, fixed belt, and a 3D printed adapter allowed to evaluate the knee extensors RFD with high reliability.

Our results are on par with previous results describing the measurement of the hip muscles RFD [4] and are better than the previously described method for assessing the knee RFD using a HHD [3].

We provide a reliable, feasible, and cost-effective approach for clinicians and researchers for assessing the knee extensor RFD and peak force.

References

1. Turpeinen et at, Scand J Med Sci Sports, 30:1572-1585, 2020
2. Maffiuletti et al, Clin Orthop Relat Res, 468:191-198, 2010
3. Mentiplay et al, PloS One, 10:10, 2015
4. Ishøi et al, Int J Sports Phys Ther, 14:715-723, 2019

NORMATIVE DATA SET OF THE KNEE EXTENSORS' RATE OF FORCE DEVELOPMENT USING A FIXED HAND-HELD DYNAMOMETER

Tomer Yona[1], Arielle Fischer[1]

[1] *Department of Biomedical Engineering, Technion, Israel Institute of Technology, Israel*

Introduction

Retraining lower limb strength is an essential part of many lower limb injuries rehabilitation protocols [1,2,3]. Limited data have been published regarding the Rate of Force Development (RFD) of the knee extensors, defined as one's ability to quickly generate muscle force.

Recently, many papers have stressed the importance of RFD in various conditions such as anterior cruciate ligament injury, osteoarthritis, and stroke [4,5,6].

The knee force can easily be assessed in and outside of the lab, clinic, or the field using hand-held dynamometers (HHD) since assessing RFD requires stationary and expensive isokinetic devices. Moreover, using a HHD might cause strength discrepancies between the tester and the participant, hence lowering the reliability of the measurement.

This study used a recently developed method to reliably assess RFD using a HHD (MicroFET2, Hoggan Scientific, LLC, Salt Lake City, UT), a fixed belt, and a 3D printed adapter (ICC$_{2.1}$ = 0.85-0.96]. We aim to examine the knee extensor RFD and provide a normative data set among a cohort of healthy participants.

Methods

We used a fixed HHD (MicroFET2) and a 3D printed adapter to assess the knee extensor muscles in a seated position at the edge of a treatment bed (Figure 1).

After providing informed consent, participants completed a standardized warm-up which included self-paced walking for one minute followed by two submaximal seated knee extension trials.

Participants performed three maximum isometric knee extension trials with one minute of rest between attempts.

All the verbal cues were standardized: The participants were first instructed to do three trials of the following: "Push as fast and as hard as possible" and "keep pushing until instructed to relax" (approximately 1-2 s).

The outcome measures of interest were the early and late phase RFD (0-100ms and 0-200ms, respectively), and the peak force.

We averaged the result of each trial and presented the data using median [range], as the data was not normally distributed.

Results

Thirty-five healthy participants, males (n=18) and females (n=17), aged 18-50, enrolled to our study.

The early phase RFD median was 1647.51 N/s [421.69-5638.82], and the late phase RFD median was 1152.28 N/s [353.04-3182.26]. Lastly, the peak force median was 354.02 N [211.82-926]. Differences between male and female participants are presented in Table 1.

Figure 1. (a) *Testing position.* (b) *3D printed adapter.*

Discussion

In the study, we described the normative values of the knee extensors' late and early phase RFD and peak force among healthy participants.

While Mentiplay et al. [7] previously described the knee RFD using a HHD, their experimental setup lacked a fixed HHD, leading to lower reliability. By utilizing a reliable way to assess the knee extensors RFD, our data provides a feasible way to evaluate the knee extensors RFD. This study's results offer clinicians, coaches, and researchers a tool for comparing their injured patients and athletes' RFD measures to a normative data set.

	Males (n=18)	Females (n=17)
Age (years)	29 [22-39]	29 [23-54]
BMI	22 [19-28]	21 [17-29]
Early RFD (N/s)	1623 [379-4671]	899 [471-2576]
Late RFD (N/s)	1220 [307-2489]	727 [351-2120]
Peak Force (N)	476 [206-866]	295 [200-610]

Table 1: Demographic data, Rate of Force Development, and peak force of the participants. Data is presented as median [range].

References

1. Chaput et al, Int J Sports Phys Ther, 16:145-155, 2021
2. Whittaker et al, Osteoarthritis Cartilage, 29:190-207, 2021
3. Na et al, Orthop J Sports Med, 9, 2021
4. Turpeinen et at, Scand J Med Sci Sports, 30:1572-1585, 2020
5. Maffiuletti et al, Clin Orthop Relat Res, 468:191-198, 2010
6. da Silva et al, Clin Biomech, 91, 2022
7. Mentiplay et al, PloS One, 10:10, 2015

EFFECT OF CORACOACROMIAL LIGAMENT RELEASE IN SHOULDER BIOMECHANICS: A PRELIMINARY IN-VITRO STUDY

Inês Santos (1), Katharina Borst (1), Simon Hoffmann (1), Yan Chevalier (1), Hannes Traxler (2), Peter E. Müller (1), Matthias Pietschmann (1)

1. Department of Orthopaedics and Trauma Surgery, Musculoskeletal University Center Munich (MUM), University Hospital, LMU Munich, Germany; 2. Center for Anatomy and Cell Biology, Medical University of Vienna, Austria

Introduction

Subacromial decompression is a common shoulder procedure to treat shoulder impingement that includes release of the coracoacromial ligament (CAL). Previous studies have shown that CAL release causes significant increases in superior and anterosuperior translation of the humeral head [1,2]. How the compromise of the CAL and force production by the rotator cuff (RC) act to maintain baseline glenohumeral biomechanics is still unclear. The aim of this preliminary study was to investigate the effect of CAL excision, combined with different degrees of supraspinatus (SSP) strength, in glenohumeral kinematics, subacromial pressure and deltoid force recruitment during shoulder abduction.

Methods

Four fresh-frozen cadaveric glenohumeral joints were dissected, retaining only scapula, humerus, CAL, glenohumeral capsular and coracohumeral ligaments, and RC tendons. The subacromial bursa was removed to fix a pressure sensor (ST2042, Novel GmbH, Munich, Germany) under the acromion and CAL. Cables were attached to the RC tendinous insertions on the humeral head and constantly loaded (subscapularis = 10N, infraspinatus/teres minor = 10N) through their physiological lines of action. The deltoid (pars acromialis) was replaced by a stainless-steel cable attached to the deltoid tuberosity and guided to a linear electric actuator (EletroPuls E10000, Instron, Norwood, MA, USA). The humeral shaft was transected proximal to the elbow joint and embedded into a pot fixed with a rod to simulate the weight and length of the complete arm. Optical tracking markers (GOM GmbH, Braunschweig, Germany) were attached to the humerus and scapula, and anatomical landmarks were digitized to create bone fixed local coordinate systems [3]. Glenohumeral abduction in the scapular plane was simulated until 60° by loading the deltoid cable at 2 mm/s. Five cycles of abduction/adduction were simulated with an intact CAL and varying loads applied to the SSP tendon (5N, 15N and 25N). After complete release of the CAL, the same loading protocol was repeated. Shoulder kinematics was evaluated with the software ARAMIS Professional (GOM GmbH, Braunschweig, Germany) using the bone geometry acquired by manual segmentation from computed tomography scans of each specimen.

Results

Increasing the strength of the SSP muscle resulted in a decrease in mean deltoid force. CAL release led to a significant decrease in subacromial pressure (p<0.05). Increasing SSP strength together with CAL resection also had a positive effect in reducing subacromial pressure. A reduction in anterior translation due to increasing SSP load was observed in two specimens. Nonetheless, CAL resection increased both anterior and superior translation of the humeral head in all specimens.

Figure 1: Experimental setup: shoulder specimen positioned at 60° of abduction in the scapular plane.

Discussion

This preliminary study shows that CAL release alters baseline glenohumeral kinematics, specially increasing superior and anterior translation of the humeral head during abduction. The results suggest that resection of the CAL with postoperative physiotherapeutic increase of SSP strength may be superior to isolated measures in the treatment of impingement. However, further studies must show whether and how different acromion shapes influence subacromial pressure.

References

1. Payne et al, Am J Sports Med, 25:801-8, 1997.
2. Su et al, Arthroscopy, 26:578-86, 2010.
3. Wu et al et al, J Biomech, 38(5):981-992, 2005.

HUMAN BRAIN AND MUSCLE ACTIVITIES COUPLING DURING ISOKINETIC CONTRACTIONS WITH INCREMENTAL MOTOR OUTPUT

Dorian Glories (1), Mathias Soulhol (1), David Amarantini (1), Julien Duclay (1)

1. Toulouse NeuroImaging Center, Université de Toulouse, Inserm, UPS, France.

Introduction

Corticomuscular coherence (CMC), which directly assesses the frequency coupling between cortical and muscle electrophysiological oscillatory activities recorded between electroencephalography (EEG) and electromyography (EMG), is considered a promising tool to analyze the motor cortical oscillatory fluctuations [1]. While incremental contraction intensity may modulate CMC, its influence has only been investigated during isometric contractions, and its underlying mechanisms are still unclear. Since we recently highlighted an effect of the contraction type on CMC associated with neural modulations at the spinal level [2], we seized the opportunity provided by the specific neural drive of anisometric contractions to deepen our understanding of the neural mechanisms involved in this contraction intensity induced CMC modulation. Hence, CMC and spinal excitability were concurrently measured at three intensity levels during both isometric and anisometric contractions.

Methods

Fifteen participants performed submaximal voluntary plantar flexions on an isokinetic ergometer, at 25, 50, and 70% of the maximal soleus (SOL) EMG activity measured during maximal isometric voluntary contractions. SOL and medialis gastrocnemius (MG) EMG and 64-channel EEG were recorded. For each contraction intensity, isometric, shortening and lengthening contractions were performed in a randomized order. CMC was computed in the time–frequency domain [3] between Cz EEG and unrectified EMG SOL (CMC SOL-Cz) or MG (CMC MG-Cz) signals in the beta-band (13-32 Hz). Spinal excitability was quantified through normalized H-reflex amplitude.

Results

Beta-band CMC was decreased in the SOL only between 25 and 50-70% contractions, independently from the contraction type (p<0.01) but remained similar for all contraction intensities in the MG (p>0.05). Spinal excitability was similar for all contraction intensities in both muscles (p>0.05).
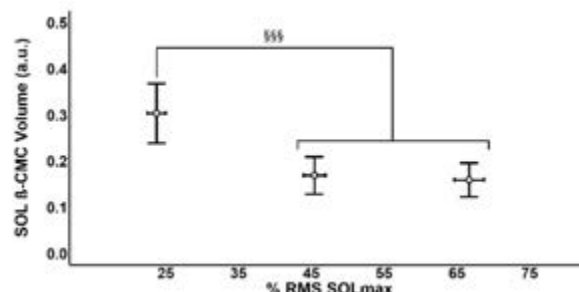
Figure 1: Effects of the contraction intensity on the soleus beta-band CMC. Modulations are shown during 25, 50 and 70% MVIC contractions, averaged across all contraction types. Vertical error bars represent the 95% CI of the mean beta-band CMC. Horizontal error bars represent the 95% CI of the mean % of maximum RMS. 25% vs 50-70%: §§§ p < .01

Discussion

Collectively, these results confirm an effect of the contraction intensity on beta-band CMC, although it may depend on the contraction intensity level and differ between agonist synergist muscles. Furthermore, the current findings provide new evidence that the observed modulations of beta-band CMC with the contraction intensity does not depend on the contraction type or on spinal excitability variations.

References

1. Bourguignon M. et al, *NeuroImage* **203,** 116177, 2019.
2. Glories D. et al, Sci. Rep, **116,** 11, 6322, 2021.
3. Bigot J. et al, *NeuroImage* **55,** 1504–1518, 2011.

DIFFERENT MUSCLE EXCITATION PATTERNS AND MODEL-BASED MUSCLE FORCES IN PARKINSON'S DISEASE

Marco Romanato (1), Daniele Volpe (2), Zimi Sawacha (1)
1. Department of Information Engineering, University of Padova, Padova, Italy; 2. Fresco Parkinson Center, Villa Margherita, S. Stefano, Vicenza, Italy

Introduction

Gait alterations are one of the most disabling symptoms in Parkinson's disease (PD). Indeed, reduced stride length, stride velocity and lower limb joint have been documented as hallmarks of parkinsonian gait [1]. Recently, differences in muscle excitations profile have been documented when grouping the participants per excitation patterns (i.e., number of bursts within gait cycle) [2]. Moreover, the authors identified an impaired magnitude on leg muscle forces in PD during locomotion when compared with healthy control subjects (CS) [3]. The aim of our work was to explore if differences in the excitation patterns are accompanied by differences in muscle forces.

Methods

A convenient sample of ten CS (age=60.2±4.3 years, BMI=26.0±3.6 kg/m2) and ten PD subjects (age=62.8±11.4 years, BMI=27.1±2.9 kg/m2) were acquired with a 6-cameras motion capture system (60Hz, BTS), synchronized with 2 force plates (960Hz, Bertec) and a 8-channels EMG system (1000Hz, BTS) that recorded bilaterally the activities of 4 lower-limb muscles: Biceps Femoris, Rectus Femoris, Gastrocnemius Lateralis and Tibialis Anterior. A double-threshold statistical detector [2] was chosen to retrieve the onset and the offset (burst) of muscle activity. Based on this, trials were divided in three modalities with respect to the number of detected bursts. Then, inverse kinematics, inverse dynamics, and muscle analysis were performed in OpenSim using a muscle-optimized scaled model [4], including 24 lower limb muscles. Muscle-tendon parameters were calibrated to the individual using CEINMS [3]. EMG-assisted neuromusculoskeletal modelling was executed to extract muscle forces acting on the ankle and knee joints. Differences between muscle forces produced by the two groups were compared using two-sample nonparametric t-test with statistical parametric mapping (SPM) (p<0.05, Bonferroni post-hoc) [5].

Results

Envelope and simulated muscle forces time series for the modalities that appeared with the highest frequencies are reported in Figure 1.
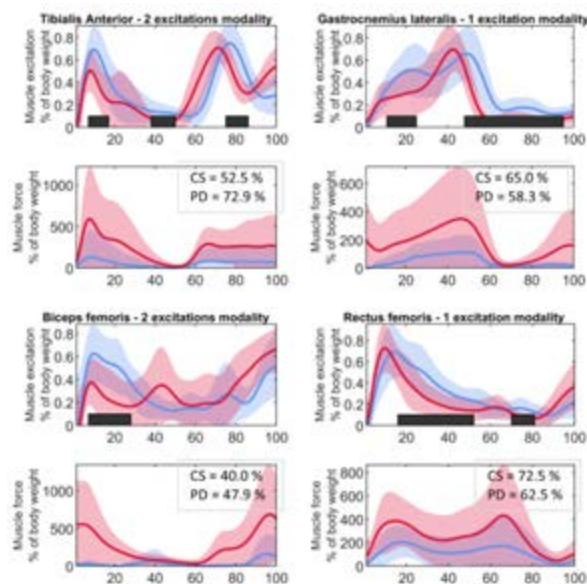
Figure 1: Envelope and simulated muscle forces time series for the patterns that appeared with the highest frequencies. Bands are reported as mean (solid line) ± standard deviation (shaded area). PD in blue, CS in red. Percentages of the occurrence of each pattern over the total trials are reported. ■ = SPM statistically significant differences (p<0.05)

Discussion

It was interesting to notice that statistically significant differences in the excitations profile were not linked with statistical differences in the muscle forces when data are grouped by excitations patterns. Increasing the sample size would be helpful to enhance the statistical power of the results and significance on the alterations might be reached. However, to understand how different patterns of muscle excitations are linked with the muscle force production might be helpful to evaluate the disease assessment and the treatment planning when rehabilitating people with PD.

References

1. Morris et al. Mov. Disord. 2005. 1(20):40–50.
2. Romanato et al. JEK. Under review (2nd round).
3. Romanato et al. CMBBE. 2021. 17;1-13.
4. Pataky et al. J Biomech. 2013.

Acknowledgements

A PIPELINE TO CONVERT OPENSIM MUSCULOSKELETAL MODELS INTO MUJOCO PRESERVING ANATOMICAL CONSISTENCY

Huawei Wang* (1), Vittorio Caggiano (2), Guillaume Durandau (1) Vikash Kumar (2) Massimo Sartori (1)
1. University of Twente, the Netherlands; 2. Meta AI, USA;

Introduction

Machine learning (ML) has shown its massive power in domains such as vision, natural language, and speech processing. However, its potentials have not been widely explored in the neuro-bio-mechanical systems. Despite progress, there still are knowledge gaps between biomechanics and ML community that prevent full cross-fertilization. ML researchers largely use dynamic engines such as MuJoCo to build plants and training environments due to its rich contact and the fast execution features. Whereas, biomechanical fellows rely on platforms such as OpenSim, providing accurate musculoskeletal formulations. To connect these two communities and integrate ML and neuromechanical studies, we developed an automated pipeline to convert OpenSim musculoskeletal models into MuJoCo models while maintaining the accurate musculo-skeletal properties.

An open-access conversion code was previously created by Ikkala et al [1] that parsed OpenSim bodies, joints, and muscles into MuJoCo modelling format. However, muscle-tendon wrapping objects and the muscle parameters were not handled. In this study, we extended Ikkala's code to convert musculo-skeletal geometrical and force-generating properties into MuJoCo.

Methods

Figure 1 shows the extended pipeline. We first added two new features in the conversion scheme including: 1) markers information and 2) wrapping surfaces for muscle-tendon units to achieve correct muscle paths (avoid collisions with bones) during movements (Cvt1). The forward kinematics (Vlt1) checks the model geometry differences by comparing the selected marker locations at different joint postures. The pipeline then optimizes the wrapping sites in the converted MuJoCo model (Cvt2), so that the moment arms that MuJoCo model's muscle-tendon unit generate on the joints best fit with OpenSim model's values; given the fact that OpenSim and MuJoCo have different wrapping objects and different ways of defining the wrapping methods. Movement arms comparisons were used as the validation for this step (Vlt2). Lastly, the muscle force-generating parameters in the converted MuJoCo models were optimized to generate similar active and passive force-length relationships as the referencing OpenSim models (Cvt3), due to the fact that MuJoCo uses stiff tendons and specific ways of defining muscle operating ranges. The muscle force maps were used as the converting validation for this last step (Vlt3).

Results

This pipeline was used to convert an elbow model [2] and a full hand model [3]. Segment kinematics (Vlt1) were identical between the referencing OpenSim models
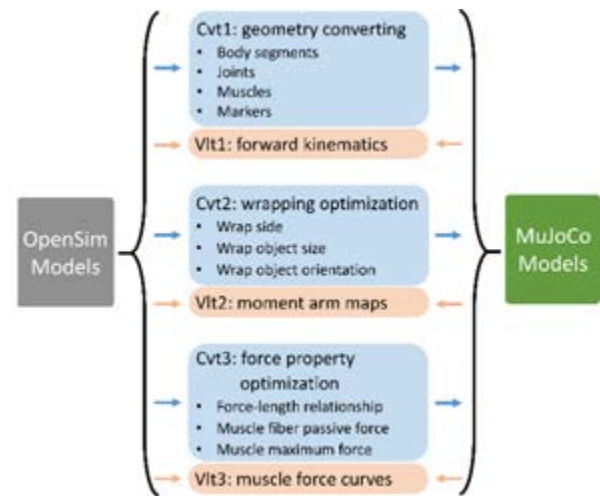
and the converted MuJoCo models. Muscle moment arm root mean square (RMS) differences between them were $0.044 \pm 0.09\%$ for the elbow model and $0.38 \pm 0.57\%$ for the hand model. The RMS error in forces was $2.2 \pm 1.4\%$ Fmax (OpenSim peak force) for the elbow model and $4.1 \pm 2.0\%$ Fmax for the hand model.

A speed test was conducted with the OpenSim and converted MuJoCo elbow models. Ten repetitions of 5000 seconds simulations showed that the MuJoCo model is around 170 times more efficient.

An elbow soft exoskeleton (cable driven for example) was also modeled in the MuJoCo elbow model with a weight of 0.101 Kg for the upper arm and 0.111 Kg on the forearm. Trained ML control law generated similar muscle activation reductions in the assisted lifting tasks that has been shown in the experimental study [4].

Discussion & Conclusion

In conclusion, the developed pipeline was able to generate physiological accurate musculoskeletal models in MuJoCo, which can contribute both the ML and biomechanical communities.

Force-velocity property of the muscle model inside MuJoCo can be optimized also to achieve better fit in the dynamic properties. In addition, The converting pipeline has the potential to generate musculoskeletal models directly from anatomical data that collected from cadaver studies.

References

1. Ikkala et al, arXiv, 2020 (*2006.10618 [1-bio.QM]*).
2. Seth et al, PLOS computational biology, 14:1-28, 2018
3. Lee et al, PLOS ONE, 10(4):1-28, 2015.
4. Lotti et al, IRRR RAM, 27(1): 43-53, 2020.

Acknowledgements

EFFECTS OF CORNEAL PRESERVATION ON THE MECHANICAL PROPERTIES OF PORCINE CORNEAS

Shima Bahramizadeh-Sajadi (1,2), Hamid R. Katoozian (1), Miguel A. Ariza-Gracia (2), Jiri Nohava (3), Philippe Büchler (2)

1. Dept. of Biomedical Engineering, Amirkabir University of Technology (Tehran Polytechnic), Tehran, Iran;
2. ARTORG Center for Biomedical Engineering Research, University of Bern, Bern, Switzerland;
3. Anton Paar TriTec, Les Vernets 6, 2035 Corcelles, Switzerland

Introduction

The biomechanics of the cornea plays an essential role in vision. It is involved in the underlying mechanisms of major ophthalmic disorders [1], and consequently in current treatment procedures [2]. Quantification of the overall biomechanical behavior has been extensively studied [3-4]. In a few of these studies, corneal properties have been characterized using mechanical indentation [5]. An interesting feature of this measurement approach is that it provides a local assessment of the tissue.

However, the effects of preservation medium and storage time on corneal mechanical properties has not been well studied [6]. In addition, there is a need for a practical solution to preserve corneal mechanical properties that both meets the requirement of being available in any clinical practice and preserves corneal biomechanics for several days. Therefore, the aim of this study was to investigate the effects of two preservation methods that are readily available for tissue storage and transport.

Methods

This study assessed the effects of two easily accessible preservation methods on the viscoelastic properties of porcine corneas measured using nano-indentation: 1) freezing at -20°C (Frz), and 2) preservation of the tissue in culture medium (TiC, AL.CHI. MI.A. S.r.l., Italy). We compared the viscoelastic behavior of the samples preserved by both techniques for 6 days with the properties of fresh samples (Fsh). The mechanical response was evaluated by the elastic modulus calculated by applying Hertz's equation for the contact of sphere with a plane (EHz) at different loading rates (1, 10, and 30 seconds) by nano-indentation. The measurements were performed at 9 locations near the cornea's optical axis, with the samples immersed in a Dextran solution. The mechanical response was measured 567 times, corresponding to 7 samples per group, 3 loading rates, 9 measurement sites, and 3 preservation methods. The mixed-effects model was fitted to the EHz collected in this study. Samples were weighted immediately after dissection and before measurements.

Results

No statistical difference was found between the different preservation methods and the fresh samples, nor between the different measurement locations. However, different loading rates caused significant differences for EHz (p<0.0001). As expected, faster loading speeds increased EHz (Figure 1). The weight of the samples in the different groups showed no statistical difference after dissection (P>0.05). After 6 days of preservation, the samples in the Frz group showed a slight weight loss (<3.5%) compared to the fresh samples, while the TiC group became significantly heavier (+38%). The change in sample weight was statistically different between the Frz and TiC groups (p = 0.006) (Figure 2d).
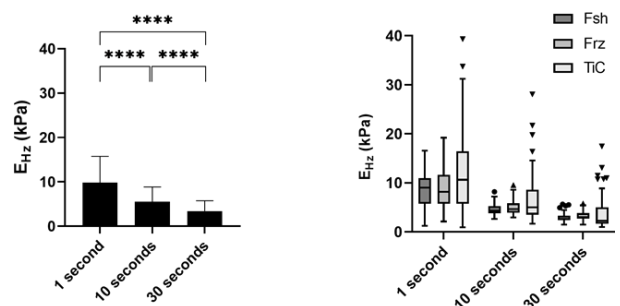
Figure 1: Elastic modulus of porcine corneas measured for different loading rates (left) and preservation methods (right) (**** indicates p<0.0001).

Discussion

While the loading rate had a significant effect on the mechanical response (p<0.0001), the results showed that the mechanical properties were not altered by any of the preservation methods (p>0.270). However, the standard deviation was up to 4.9 times larger when the samples were preserved in the culture medium compared to the fresh and frozen samples. In conclusion, while both preservation techniques provide equivalent mechanical properties measured by nano-indentation, freezing the samples prevents swelling and provides more stable measurements.

References

1. Girard, MJA et al, Curr Eye Res, 40:1–18, 2015.
2. Piñero, DP et al, Clin Exp Ophthalmol, 38:154–167, 2010.
3. Elsheikh, A et al, J R Soc Interface, 7:1475–1485, 2010.
4. Abass, A et al, J Biomech, 87:93–99, 2019.
5. Nohava, J et al, J Biomed Mater Res A, 106:1413–20, 2018.
6. Chaurasia, S et al, Indian J Ophthalmol 68:1363, 2020.

Competing interests

Jiri Nohava is an employee of Anton Paar TriTec.

ANALYSIS OF THE CILIARY MUSCLE MOVEMENT DURING ACCOMMODATION USING ARTIFICIAL INTELLIGENCE

Iulen Cabeza-Gil (1), Marco Ruggeri (2,3), Yu-Cherng Chang (2,3), Begoña Calvo (1,4), Fabrice Manns (2,3)

1 Aragón Institute of Engineering Research (i3A), University of Zaragoza, Spain; 2 Ophthalmic Biophysics Center, Bascom Palmer Eye Institute, University of Miami Miller School of Medicine, Miami, FL, USA; 3 Department of Biomedical Engineering, University of Miami College of Engineering, Coral Gables, FL, USA; 4 Bioengineering, Biomaterials and Nanomedicine Networking Biomedical Research Centre (CIBER-BBN), Zaragoza, Spain.

Introduction

The ciliary muscle can be considered the engine of accommodation, the ability of the eye to focus on near objects. Ciliary muscle contraction results in an inward movement of the apex of the ciliary processes towards the lens equator, what loosens the zonular tension at the lens equator and allows the lens to become rounded, resulting in accommodation. For this reason, analyzing the ciliary muscle movement during accommodation might be key to approach potential presbyopia therapies. The ciliary muscle can be imaged in-vivo using optical coherence tomography (OCT), but quantifying the ciliary muscle shape from these images has been challenging both due to the low contrast of the images at the apex of the ciliary muscle and the tedious work of segmenting the ciliary muscle geometry. To address this issue, we propose an automatic segmentation tool for transscleral OCT images of the ciliary muscle using fully convolutional networks (FCN).

Methods

1,039 images obtained from a database of transscleral Spectral-Domain OCT (SD-OCT) images of the ciliary muscle were used to develop the FCN [1-2]. The database contained dynamic recordings of human subjects subjected to a step stimulus of accommodation. The images were acquired using a system that was described previously [1-2] and all studies were approved by the Institutional Review Board at the University of Miami Miller School of Medicine and followed the tenets of the Declaration of Helsinki. 716 images (69%) were used for training, 164 (16%) for validation and 159 (15%) for testing.

The FCN performed a multi-class segmentation differentiating between the background, the ciliary muscle and other ocular structures, see Fig. 1. To develop a robust FCN, a real-time augmentation code including rotation, translation, noise and brightness was implemented. This resulted in more than 100,000 different images introduced in each training.
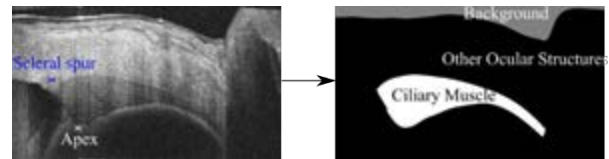
Figure 1: The raw image (left) is introduced into the FCN and the multi-class segmentation is performed (right). The distortion and aspect ratio are corrected using the boundaries of the image segmentation, resulting in the actual ciliary muscle shape.

Results

UNet and LinkNet architectures were trained with different backbones (ResNet34, EfficientNetb2, Vgg19) to select the outperforming network. UNet-EfficientNetb2 achieved the highest performance with an IoU score of 94.54%, 97.37% and 90.23% for the background, other ocular structures and ciliary muscle, respectively, resulting in a mean IoU of 94.04%, and an F-Score of 97.33%. Fig. 2 shows the biometry of the ciliary muscle for a step stimulus of 2 diopters (D) for a specific subject of 45 yo.

Discussion

The results show that the trained FCN can successfully segment ciliary muscle images and quantify the biometry of the ciliary muscle during accommodation. The study also shows that EfficientNet outperforms other current backbones of the literature.

References

1. Ruggeri et al., Ophthalmic Technologies XXIV. 2014
2. Ruggeri et al., Biomed Opt Express, 7(4):1351-1354. 2016
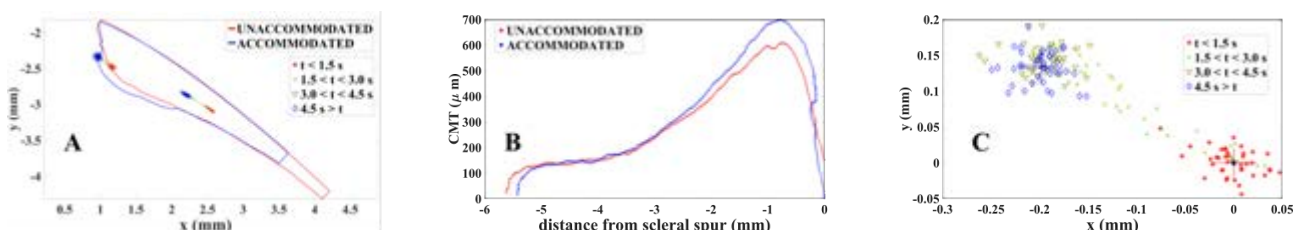
Figure 2: Results for a 45 yo subject subjected to a 2D stimulus. (A) Unaccommodated and accommodated geometry of the ciliary muscle, together the movement of the ciliary muscle centroid and apex during the accommodation response. (B) Ciliary muscle thickness profiles on both states. (C) Dynamic change of the ciliary muscle apex during accommodation

CHARACTERIZATION OF CORNEAL VISCOSITY USING TORSIONAL WAVES

1. José M. Cortés Cortés (1), Antonio M. Callejas Zafra (1), Inas H. Faris (2), Guillermo R. Carlborg (1)
1. Department of Structural Mechanics, University of Granada, Spain; 2. IBS Institute for Biosanitary Research, Granada, Spain.

Introduction

The cornea is the front transparent part of the eye that covers the iris and allows light to enter the eye. The thickness of the porcine cornea is 2 to 3 millimeters. The thickest part is the stroma, formed by collagen fibrils, these fibrils are distributed unevenly parallel to the surface of the cornea giving it a certain degree of anisotropy [1,2]. We have designed a device that applying torsional waves can quantify the mechanical parameters of the cornea, the shear wave velocity, and the modulus of rigidity at different angles on the corneal surface by completing 360 degrees. A Kelvin-Voigt rheological model [4] is used to perform a viscoelasticity calculation.

Methods

The experimental setup consists of a signal generation and acquisition system consisting of a Tascam US-20x20 audio card with 8 input channels, two phono preamplifiers, and a third high fidelity amplifier to which the probe coupled to the motion system is connected, all interconnected through a PC with MATLAB as user interface. The automated system is capable of controlling the pressure at which the measurement is made, measurements have been made in increments of 7.2 degrees to complete a full rotation. Four pig eyes have been tested with an intraocular pressure of 15 mmHg and a pressure of 60 grams between the probe and the cornea. For each measurement, the shear wave velocity was calculated for a frequency range of 400-1200 Hz in increments of 200 Hz, then using this dispersion curve the viscosity was calculated.

Kelvin-Voigt adjustment equation used for viscosity calculation

$$C_s(\omega) = \sqrt{\frac{2(\mu^2 + \omega^2\eta^2)}{\rho(\mu + \sqrt{\mu^2 + \omega^2\eta^2})}}$$

where μ is the shear elasticity in Pa and η is the shear viscosity in Pa·s and the density ρ is considered 1000 kg/m^3.

Results and discussion

Figure 1 shows a polar plot of the shear wave velocity values for the frequency range 400-1200 Hz rotating the probe over the cornea.
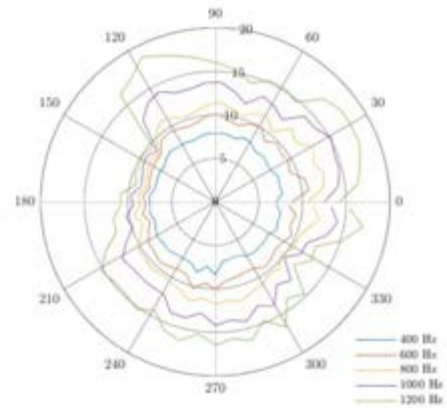
Figure 1: Polar plot of dispersion shear wave velocity

Figure 2 shows a polar plot of how corneal viscosity is distributed, showing a preferred direction, similar to that found in other studies on elasticity [3].
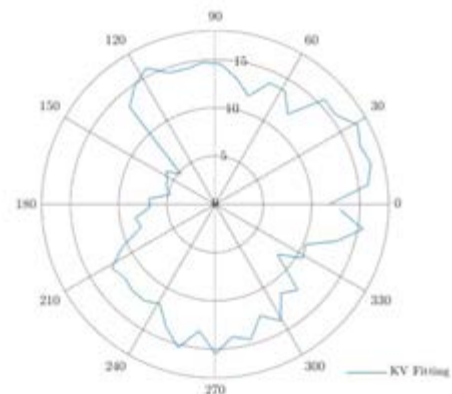
Figure 2: Polar plot of viscosity after KV fitting.

References

1. Komai, Yoshiko, and Tatsuo Ushiki. "The three-dimensional organization of collagen fibrils in the human cornea and sclera." *Investigative ophthalmology & visual science* 32.8 (1991): 2244-2258.
2. Beer, Florian, et al. "Conical scan pattern for enhanced visualization of the human cornea using polarization-sensitive OCT." *Biomedical optics express* 8.6 (2017): 2906-2923.
3. Singh, Manmohan, et al. "Assessing the effects of riboflavin/UV-A crosslinking on porcine corneal mechanical anisotropy with optical coherence elastography." *Biomedical optics express* 8.1 (2017): 349-366.
4. Callejas, Antonio, et al. "Kelvin–Voigt Parameters Reconstruction of Cervical Tissue-Mimicking Phantoms Using Torsional Wave Elastography." *Sensors* 19.15 (2019): 3281.

HOW REFRACTIVE POWER OF THE EYE MAY EFFECT THE CHANGE OF FOCUS

Fabian Dębowy, Barbara Pierścionek

Faculty of Health, Education, Medicine and Social Care, Medical Technology Research Centre, Chelmsford Campus, Bishops Hall Lane, Chelmsford CM1 1SQ, UK

Introduction

The accommodative system in the eye which is responsible for allowing the eye to alter its focus has classically been considered as being the result of an adjustment of the shape of the eye lens mediated by forces that emanate from the ciliary muscle movement. However, there are opponent theories [1-2] about the mode of shape change and, in addition, anecdotal suggestions that the accommodative system may alter ocular focus not only by changing shape of the lens but also by translatory movement of the lens. This is not implausible given observations post-cataract surgery that in some individuals, the attempt to accommodate results in a translational shift of the lens, while in others this does not happen [3-5].

Methods

The data introduced in this work was simulated in Zemax OpticStudio based on different eye models [6].

By looking at the components of the accommodative mechanism, lens thickness and shape, zonular insertions and possibly even the axial length of the eye as well as other biometric parameters that affect the optics of the eye, differing modes of accommodation including shape change and/or translation may be feasible. If this is linked to optical properties of the eye and refractive status, it may explain why accommodation is considered to predispose to development and progression of certain refractive errors. This has never been fully investigated.
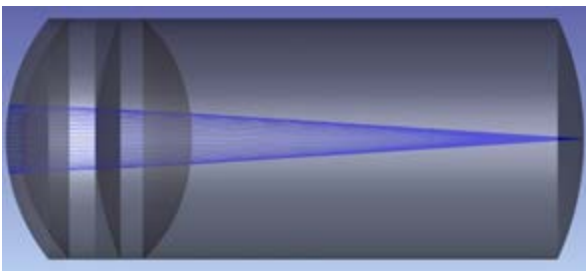
Figure 1: Liou Brennan human eye model based on [6] used to analysis.

Results

This work considers the range of ocular components and their combinations by creating a range of different models that represent the refractive error range. The potential modes of accommodation across the refractive error range were investigated and compared to literature results from clinical investigations.

Discussion

There are some suggestions that translatory movement of the lens may occur in accommodation; this may be related to the refractive status of the eye. Greater insights into the accommodative response in eyes with different refractive errors will be beneficial to developing a personalised approach to treating accommodative problems in children and young adults and inform optical design to produce novel and effective accommodating implant lenses.

References

1. Schachar, R. A. (2006). The Mechanism of Accommodation and Presbyopia. International Ophthalmology Clinics, 46(3), 39–61. doi:10.1097/00004397-200604630-00006
2. Burd, H. J., Judge, S. J., & Flavell, M. J. (1999). Mechanics of accommodation of the human eye. Vision Research, 39(9), 1591–1595. doi:10.1016/s0042-6989(98)00298-3
3. Koeppl, C., Findl, O., Kriechbaum, K., Sacu, S., & Drexler, W. (2005). Change in IOL position and capsular bag size with an angulated intraocular lens early after cataract surgery. Journal of Cataract & Refractive Surgery, 31(2), 348–353. doi:10.1016/j.jcrs.2004.04.063
4. Lesiewska-Junk, H., & Kałużny, J. (2000). Intraocular lens movement and accommodation in eyes of young patients. Journal of Cataract & Refractive Surgery, 26(4), 562–565. doi:10.1016/s0886-3350(99)00407-1
5. Findl, O., Kiss, B., Petternel, V., Menapace, R., Georgopoulos, M., Rainer, G., & Drexler, W. (2003). Intraocular lens movement caused by ciliary muscle contraction. Journal of Cataract & Refractive Surgery, 29(4), 669–676. doi:10.1016/s0886-3350(02)01652-8
6. D. A. Atchison, G. Smith, Optics of the Human Eye, Butterworth-Heinemann, 2000, ISBN 9780750637756

Acknowledgements

CORNEAL STIFFNESS – IMPORTANT PARAMETER IN INTRAOCULAR PRESSURE MEASUREMENT

Branislav Hučko (1), Patrik Grossinger (1), Jan Rybář (2), Stanislav Ďuriš (2), Alena Furdová (3), Pavol Veselý (4)

1. Faculty of Mechanical Engineering, STU in Bratislava, Institute of Applied Mechanics and Mechatronics, Bratislava, Slovakia;2. Faculty of Mechanical Engineering, STU in Bratislava, Institute of Automation, Measurement and Applied Informatics, Bratislava, Slovakia; 3. University Hospital Bratislava, Ophthalmology Clinic LFUK and UNB, Bratislava, Slovakia; 4. VESELY Očná klinika, s.r.o, Bratislava, Slovakia

Introduction

The cornea itself represents the prestressed structure. The prestressed state arises due to intraocular pressure (IOP). Subsequently the load is applied to the prestressed cornea by the tonometer. The stiffness of prestressed cornea is naturally higher. Therefore we can conclude that the influencing factors of cornea stiffness are:

- geometrical parameters – for example the central corneal thickness (CCT), etc.;
- mechanical parameters - Young´s modulus, Poisson´s ratio, etc.;
- prestressed state – as the initial state.

The influence of prestressed state on stiffness has been presented in [1]. This influence varied from 4% to 7%. The next step is to find the correlation between other factors and the corneal stiffness. We started with CCT. The basic data about geometrical parameters of cornea are in [2].

Methods

For finding the correlation between CCT and the stiffness we applied methodology presented in [1]. The sample of cornea is placed between two plates. The compressive force is applied on the upper plate and on the lower plate is placed the force sensor. And the extensometer measures the distance between plates, see Figure 1.
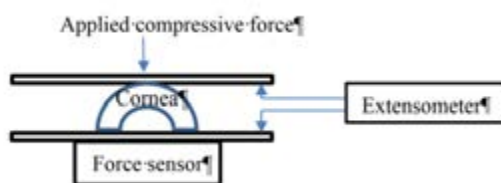
Figure 1:The experimental setup

Thus we obtained several curves load vs. deflection. Using the least squares method and with the linear approximation we got the linear representation of them. The stiffness of cornea has been calculated for a simple spring model: applied force / deflection.

Results

A group of 10 corneal samples was tested. The mean value of CCT was 477 µm. This value is little bit smaller than one can expected. The min. value was 419 µm and the max. value was 530 µm. The mean stiffness reaches value of 0,0045 mN/mm. The lower and upper bounds are 0,0034 mN/mm and 0,0050 mN/mm.

Discussion

We worked with the relatively wide range group of corneal samples. Using classical statistical approach to correlation factor of CCT we found out it with the value of 0,47.

The explanation is that stiffness is the complex variable containing CCT, mechanical properties and the initial state. The CCT is only one of influencing factor.

References

1. Rybář, J. et al, sc – Journal of Mechanical Engineering, 70, 133-140, 2020
2. Hučko, B. et al, Measurement: Sensors, 18, 100281, 2021

Acknowledgements

BIOMECHANICAL CHARACTERIZATION AND MODELING OF HUMAN LENTICULES

Malavika Nambiar (1), Layko Liechti (1), Harald Studer (2), Abhijit Sinha Roy (3), Theo G. Seiler (4,5,6), Philippe Büchler (1)

1.University of Bern, Switzerland; 2. Optimo Medical AG, Switzerland. 3. Narayana Nethralaya Eye Clinic, India; 4. Institut für Refraktive und Ophthalmo-Chirurgie (IROC), Switzerland; 5. University Hospital Bern, Switzerland; 6. Universitätsklinikum Düsseldorf, Germany

Introduction

Patient-specific numerical models have been proposed to improve the planning of refractive procedures such as LASIK, CLEAR, and PRK. While tomographs are used to accurately measure patient anatomy, determining patient-specific biomechanical properties is challenging. Now, a new device is available to ophthalmologists to quantify tissue biomechanics based on Brillouin scattering in vivo. However, the relationship between frequency shift and nonlinear corneal biomechanical properties remains poorly characterized, especially for in vivo measurements. Therefore, this study proposes a technique to quantify corneal biomechanical properties on tissue samples from patients undergoing CLEAR surgery. The harvested tissue, which is usually discarded, is uniaxially tested in different orientations, which allows us to 1) gain insight into the biomechanics of the young cornea and 2) directly evaluate Brillouin measurements in the future.

Methods

Experimental: Corneal lenticules extracted from CLEAR surgeries (KEK approval 2021-00145) were tested by uniaxial extension in the nasal-temporal (NT) direction or at an angle 45° to it. The tissue was pre-stretched with a force of 10mN and preconditioned with 4 cycles of 15 % strain. The last cycle of force displacement data was recorded for analysis.

Computational: The lenticules were numerically reconstructed using an in-house algorithm that can accurately build a finite element mesh from the elevation maps obtained from the pre-operative Pentacam data. These lenticules were modelled with orthogonal collagen fibers. The material behaviour was described using the HGO material model[2]:

$$U = C_{10}(I_1 - 3) + \frac{k_1}{2k_2}\sum_{\alpha=1}^{2}\{\exp[k_2 < E\alpha >^2] - 1\} \quad (1)$$

A Bayesian optimization procedure was used to identify the material parameters that best fit the experimental data.
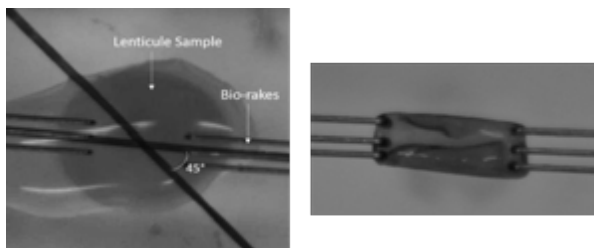
Results

The experimental setup for a lenticule tested in the NT direction is shown in Fig 1. Although the lenticles were thin ($< 50\mu m$), it was possible to perform repeated measurements without damaging the tissue. Parameter identification was performed simultaneously on three patients and in different tissue orientations. The results of the identification with four parameters showed that the model was able to reproduce the experimental data (figure 2).
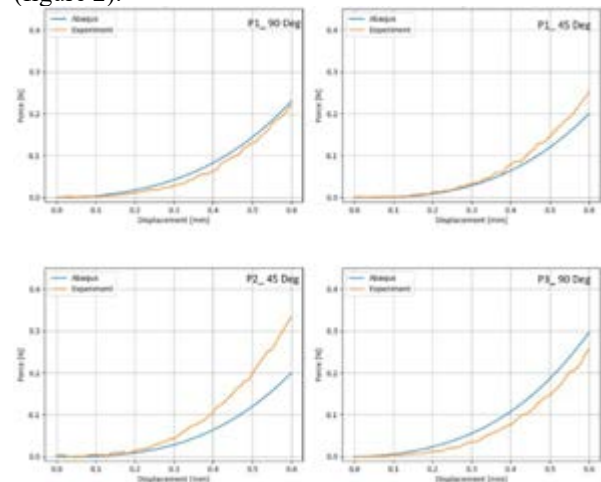
: HGO model fit (blue) obtained on experimental data of 3 patients in two orientations (red)

Discussion

Corneal geometry can be accurately replicated, and mechanical characterization of the CLEAR lenticules leads to good parameter estimates across all patient data. The current limitation of the characterization is that it was performed only on 3 patients. However, it indicates that the study is feasible. From the current data, only small differences in orientation can be noted. Further measurements are needed to confirm whether the anisotropy of the human cornea is located more in the posterior cornea than the anterior cornea of CLEAR treatment. The numerical model needs to be calibrated on more patients and eventually these results need to be complemented *by* in vivo biomechanical measurements with Brillouin scattering to develop a predictive surgical planning tool that takes into account patient-specific corneal biomechanics.

References

1. Holden BA et al, J. Opthalmology 2016.
2. Holzapfel G.A. et al, J Elasticity, vol. 61, pp.1–48, 2000.

MODELLING THE EYE LENS: INFLUENCE OF CAPSULAR THICKNESS ON LENS ACCOMMODATION

Lin Ye, Barbara K. Pierscionek

Faculty of Health, Education, Medicine and Social Care, Medical Technology Research Centre, Anglia Ruskin University, Chelmsford Campus, United Kingdom

Background

Ocular biomechanics is still a very new field and many fundamental aspects of this field are poorly understood. This project aims to look at one aspect of this in relation to the eye lens, the way it changes to alter focus of the eye, a process called accommodation and the loss of accommodative ability with age. The project is based on development of appropriate opto-biomechanical models. There are no models to date that correctly consider the component structures in the accommodative system that mediate and control the forces of accommodation, notably the zonule and the ciliary muscle. The zonule is constituted by a range of ligaments that are inserted at one end into the capsule of the lens around the lens equator and join the ciliary muscle at the other end. Previous models were not based on biological lenses, and therefore did not properly represent the biological lens, the capsule or the zonule which has been modelled as a single element or as an element with two or three components that meet at the same point [1].

Recent advances

Recent modelling work has indicated that the insertion points of the zonule in the lens and in the ciliary muscle have a significant impact on the forces mediated to the lens and the consequent shape [2,3]. The angle of the zonule also has a significant effect on the optical power of the lens [4]. The thickness of the capsule may have a great impact on eye accommodation [2] and can change with age [5]. The thickness of the capsule and the distribution of the ciliary body are also highly significant and need to be properly modelled together with the zonular insertions in order to produce physiologically accurate models that are optically and biomechanically viable.

Methods

Models were developed using Finite Element Analysis software (SolidWorks2021, Abaqus2022) based on anatomical and physiological parameters from the literature. Fourteen lens sagittal images have been used from the literature [6]. The lens in the image was extracted and the spline curve were used to depict the lens material properties in SolidWorks. The lens capsule was modelled with constant thickness and with varying thicknesses.

Findings

The capsular thickness has an effect on the lens and this is also based on lens age and shape. The force distribution of the capsule and the effect of the zonule and the combined influence on accommodation are described. These have important implications for understanding accommodation and its loss with age as well as for optical design of implant lenses.

References

1. Wilde, G.., Burd, H.. and Judge, S.., 2012. Shear modulus data for the human lens determined from a spinning lens test. Experimental eye research, 97(1), pp.36–48.
2. Wang, K., Pierscionek, B.K. 2019. Biomechanics of the human lens and accommodative system: Functional relevance to physiological states Progress in Retinal and Eye Research 17, 114-131
3. Wang, K., Venetsanos, D.T., Hoshino, M., Uesugi, K., Yagi, N. Pierscionek, B.K. 2019. A modelling approach for investigating opto-mechanical relationships in the human eye lens. Transactions on Biomedical Engineering. 10.1109/TBME.2019.2927390
4. Wang, K., Venetsanos, D., Wang, J. and Pierscionek, B.K., 2016. Gradient moduli lens models: How material properties and application of forces can affect deformation and distributions of stress. Scientific reports, 6(1), pp.31171–31171.
5. Barraquer, R.I., Michael, R., Abreu, R., Lamarca, J. and Tresserra, F., 2006. Human Lens Capsule Thickness as a Function of Age and Location along the Sagittal Lens Perimeter. Investigative ophthalmology & visual science, 47(5), pp.2053–2060.
6. Pierscionek, B., Bahrami, M., Hoshino, M., Uesugi, K., Regini, J. and Yagi, N., 2015. The eye lens: age-related trends and individual variations in refractive index and shape parameters. Oncotarget, 6(31), pp.30532–30544.

MECHANICAL FRACTURE ENVIRONMENT IN LOWER EXTREMITY NON-UNIONS – AN INDIVIDUALIZED SIMULATION-BASED STUDY

A. Andres (1), M. Roland (1), K. Wickert (1), S. Diebels (1), T. Histing (2), B. Braun (2)

1 Saarland University, Chair of Applied Mechanics, Germany, 2 University Hospital Tuebingen on Behalf of the Eberhard-Karls-University Tuebingen, Faculty of Medicine, BG Hospital Tuebingen, Germany

Introduction

Interfragmentary movement (IFM) is a key quantity for healing in mechanically compromised non-union situations. Based on the clinical workflow for patient monitoring presented in [1], we have generated high-resolution computational models for several patients with fracture non-unions of the lower extremity. These models are used to simulate and to analyse patient-specific issues of healing parameters, local micro-mechanics inside the fracture gap and personalized implant strategies both before and after surgical non-union revision.

Methods and Results

Our established clinical workflow consists of the following steps: (1) Monitoring of the patients during the planning and follow-up visits with a motion capturing system (Xsens™), (2) transfer of the motion data into the musculoskeletal simulation system AnyBody™ to achieve the corresponding individual muscle and joint forces, as well as moments. (3) Clinical imaging of the patients if available via post-operative computed tomography (CT) scans ideally combined with a six-rod bone density calibration phantom. (4) Segmentation of the CT images and generation of the corresponding adaptive finite element (FE) meshes of the bone-implant-systems, including the material parameters based on the Hounsfield units and the calibration phantom via the software ScanIP™ (Synopsys, US). (5) All information from the musculoskeletal simulation were passed as patient-specific boundary conditions to our biomechanical FE simulation process based on the patient-specific meshes. This workflow (Figure 1) allows us to simulate individual patient models based on their respective real motion data over their treatment course. This enables us to analyse questions about mechanical influences during primary and revision surgery contributing to non-union development, as well as consecutive healing. Based on the described workflow, different motion patterns were analysed and compared with respect to the effects on the micromechanics of the non-union situation. Thereby, it is shown that both the individual motion parameters and the individual fracture morphology have a lasting influence on the local healing parameters. In addition, such simulations allow an investigation of the von Mises stress distribution of the implant systems during the movement of the individual patient, which allows various conclusions for future design optimizations. The results allow a first estimation of the individual non-union healing capability based on fracture gap

mechanics. However, additional studies and larger patient cohorts are needed to further substantiate the conclusions. A limitation of this study also lies in the definition of the mechanically meaningful healing window for fractures. Here, further factors will certainly have to be included in future simulations and virtual studies.
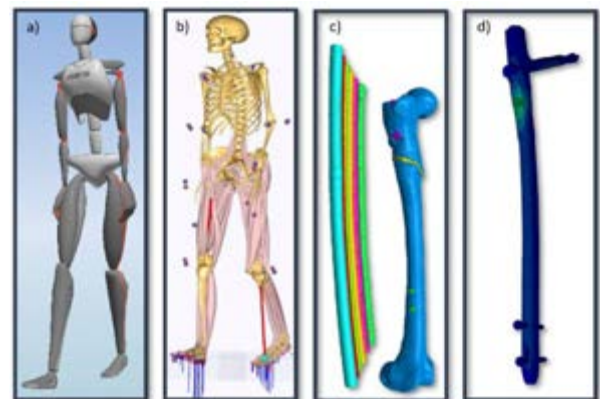

Figure 1:
   a) *Digital Avatar of Xsens™*
   b) *Musculoskeletal simulation with AnyBody™*
   c) *Segmentation with ScanIP™*
   d) *Simulation with finite element analysis software*

References

1. B.J. Braun, et al. Individualized Determination of the Mechanical Fracture Environment After Tibial Exchange Nailing-A Simulation-Based Feasibility Study. *Front. Surg.*, **8**:749209, 2021.

UNCERTAINTIES QUANTIFICATION ON ARTERIES RECONSTRUCTED FOR CORONARY STENT DEPLOYMENT SIMULATIONS

Luca Antonini (1), Federico Lotrecchiano (1), Gianluca Poletti (1), Lorenza Petrini (2), Giancarlo Pennati (1)

1. LaBS – Dept. of Chemistry, Materials and Chemical Engineering, Politecnico di Milano, Milan, Italy;
2. Dept. of Civil and Environmental Engineering, Politecnico di Milano, Milan, Italy.

Introduction

The recent conceptualization of in silico clinical trials has dictated an increasing demand for highly reliable computational analyses. Concerning stent deployment simulations, this involves the use of a validated description of the devices and rigorous patient-specific models of the arteries to be treated [1, 2]. The simulation reliability is evaluated on the comparison of the post-treatment geometry predicted in silico with the one detected in vivo after the stenting procedure through slices of the artery acquired with OCT catheter. In this study, a fully computational method was proposed to address the uncertainties that affect the validation process derived from the pre-treatment vessel reconstruction based on data from OCT (for vessel slices) and angiography (to reconstruct the centerline). It was investigated how the positioning of slices obtained with the OCT catheter and therefore orthogonal to it, can distort the geometry of the reconstructed patient-specific vessel when realigned along the centerline. Moreover, it was evaluated how using measurements acquired on OCT slices for the post-treatment comparison could introduce additional uncertainties in the simulation reliability assessment.

Methods

Different types of arteries, from simplified to more realistic geometries, were developed and taken as a reference for the evaluation of uncertainties. The process of acquiring OCT images and reconstructing the vessel was simulated using a fully automated procedure. The first step consisted in simulating the insertion of the catheter and generating slices of the artery orthogonal to the catheter itself (Figure 1a). These slices were then processed through a code that oriented them along the centerline of the artery to be used as a reference for the creation of the lumen surface and the external wall. The reference vessel and the reconstructed vessel were then involved in stent deployment simulations. The comparison of the output of the computational analyses was made by considering the slices of the reference vessel obtained again by inserting a catheter inside it and repeating the procedure carried out in the reconstruction phase. This was done to replicate the method of clinical analysis by OCT of the post-treatment artery.

Results

Differences between reference and reconstructed arteries were assessed in terms of cross-sectional areas. Figure 1b shows the outcome of the deployment simulations of a selected case in which the comparison between the areas of the cross-sections belonging to the reference lumen (black) and the reconstructed one (red) revealed differences of up to 10%.
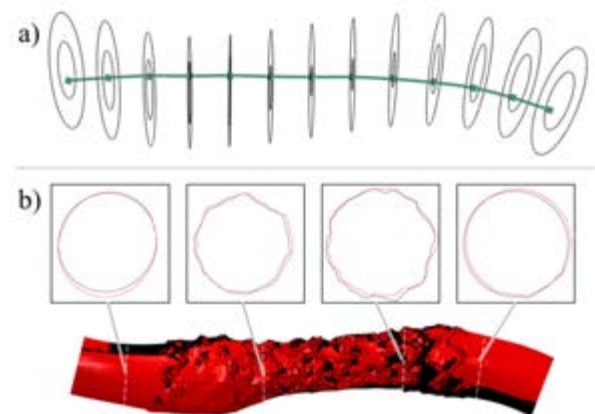
Figure 1: a) catheter (depicted with a green beam) inserted into the reference vessel and used to obtain orthogonal slices; b) superimposition of the post-deployment lumen of the reference vessel (black) and the reconstructed vessel (red) with detail of differences in four cross-sections.

Discussion

Through direct comparison between the reference vessel and the reconstructed one, it was possible to evaluate the uncertainties related to the input data of the stenting simulation and observe their dependence on the geometric peculiarities of the artery (e.g., curvatures and localized stenosis). Moreover, the influence of these uncertainties was also assessed by comparing the results of deployment simulations considering that in vivo, the method of the investigation again involves the acquisition of images with the insertion of a catheter and therefore introduces new uncertainties.

References

1. Antonini et al, JMBBM, 122:104644, 2021.
2. Berti et al, Front. Med. Technol., 3:702656, 2021.

Acknowledgements

SIMULATING THE IMPACT OF DIABETIC FOOT INSOLES: A FINITE ELEMENT ANALYSIS

Alfredo Ciniglio (1), Annamaria Guiotto (1), Mattia Palladino (1), Michele Faccin (1), Fabiola Spolaor (1), Elisa Bertoncello (2), Eleonora Meggiato (3), Zimi Sawacha (1,4)

1. Dept. of Information Engineering, University of Padova, Italy; 2. Orthomedica S.r.l., Padova, Italy;
3. Podartis S.r.l., Crocetta del Montello, Treviso, Italy; 4. Dept. of Medicine, University of Padova, Italy

Introduction

The diabetic foot ulceration process is due to neuropathy, trauma, and peripheral vasculopathy. Diabetic neuropathy results in biomechanical alterations [1] leading to increase in both skin pressure and plantar soft tissues internal stresses while walking [2]. A multidisciplinary approach to the diabetic foot care is recommended, which includes also off-loading therapy to reduce plantar pressure (PP) during gait and unload critical areas [3]. The common practice for the design and production of plantar orthotics for subjects with diabetic foot is represented by custom made insoles which mainly rely on the expertise of the orthotic technician. In this context, finite element modeling simulation represents a valid method for quantitatively estimating the effect of plantar foot insoles on plantar pressures and internal stresses with respect to the insole design and prior to insole's production [4]. The purpose of the study was to develop a methodology, applicable at the manufacturer site, able to quantify the insole effectiveness in reducing excessive plantar pressure (PP) and internal stresses on the foot of diabetic subjects.

Methods

Nine diabetic neuropathic subjects (mean(SD) age 60.9(17.4) years and BMI 29.4(5.4) Kg/m²) were tested at the orthotic manufacturer site, during the routine assessment for plantar insoles production with and without the insoles. The Each subject foot geometry and insole were captured by a 3D scanner (Structure3D) in unloaded conditions and PP data were acquired (PedarX, Novel gmbh) while walking both over ground and on a treadmill (2 km/h). Then a finite element model was created in Abaqus [2] by including: foot and insoles geometries meshed from the scanned foot volume, foot bones of a previously developed model based on MRI scans [2] scaled on subjects' foot morphology. Insole material properties were assigned according to the manufacturer's declared characteristics. Simulations were run in four critical instants of the stance phase of gait [2], both with and without the insole. Ground reaction forces and ankle plantar dorsiflexion angle during gait were applied as boundary conditions. Simulated PP distribution was compared with the experimental PP with and without insole. Simulated PP and Von Mises stresses in plantar soft tissues were compared across the different conditions.

Results

Encouraging results were obtained from the comparison between simulated and experimental PP thus supporting the validity of the approach. For what regards the simulations run with the insole, it can be noticed that excessive PPs were not completely redistributed by means of the insoles, however, Von Mises stresses at the internal soft tissues of the plantar aspect of the foot were reduced (Figure 1).
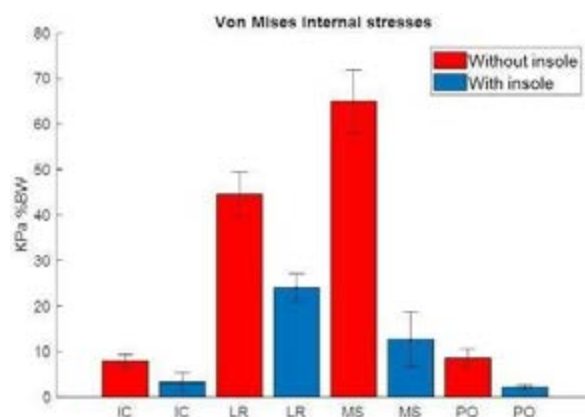
Figure 1: Von Mises stresses, at the plantar soft tissues. with (blue) and without (red) insoles, in four istants of the stance phase of gait: Initial Contact (IC), Loading Response (LR), Midstance (MS) and Push Off (PO).

Discussion

According to the designed methodology, it was possible to successfully simulate the effect of the insole.
This procedure could be used to optimize the plantar insole prior to production by changing both insole shape and material in order to obtain a better PP redistribution.

References

1. Armstrong et al, SAGE, 47:145-171, 2017.
2. Guiotto et al, J Biomech, 47:3064-3071, 2014.
3. Bandyk et al, Semin Vasc Surg, 31:43-48, 2018.
4. Telfer et al, J Biomech, 60:157-161, 2017.

Acknowledgements

COMPUTATIONAL METHOD FOR EVALUATING FRACTURE-FIXATION STABILITY OF COMPLEX BONE FRACTURES

Simon Comtesse (1), Arvind von Keudell (2), Stephen J. Ferguson (1), Thomas Zumbrunn (1)

1. Institute for Biomechanics, ETH Zurich, Switzerland; 2. Department of Orthopaedic Geriatric Trauma Surgery and Research, Brigham and Women's Hospital, Harvard Medical School, Boston, MA, USA;

Introduction

Bone fractures cause about two million hospitalizations per year just in the US. Some of them are highly complex with complication rates up to 28% [1]. It is often unclear how the screws and plates shall be positioned for a specific fracture case and outcomes heavily depend on the surgeon's experience.

This implies that there is no objective measure, how a clinically accomplished reconstruction will perform biomechanically under loading.

Hence, our goal is to introduce a method for quantitative evaluation of fracture-fixation stability, by means of finite element analysis and musculoskeletal modelling.

Methods

Based on a pre-operative computed tomography (CT) scan, ten fractured bone fragments of a right proximal tibia were segmented and aligned to achieve adequate fracture reduction. According to the post-operative CT scan, 3D models of the used stainless-steel screws were designed and aligned to the bone fragments to reverse-engineer the clinical reconstruction.

Bone material properties for each fragment were derived from Hounsfield Units (HU) of the preoperative CT scan, based on internal density calibration with air, fat, muscle, and cortical bone [2,3]. The stainless-steel screws were modelled linear elastic with a Young's Modulus of 180 GPa and a Poisson's Ratio of 0.27.

Knee joint reaction forces and muscle forces were imported from a subject-specific musculoskeletal gait model during mid-stance phase (AnyBody Technology, A/S, Denmark) and implemented in the Finite Element Model (FEM) through pressure forces across the designated attachment surface (**Figure 1**). The distal part of the tibia was fixed in space.
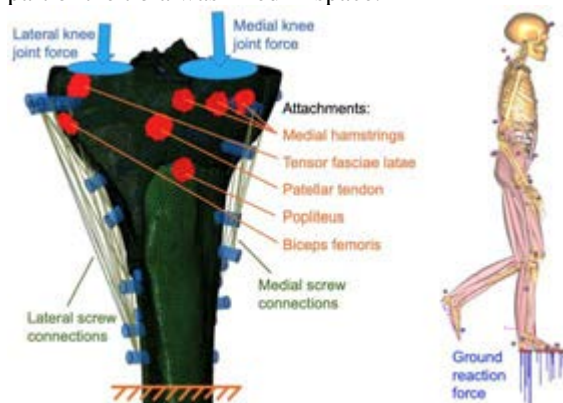
Figure 1: Setup of the FEM (left) with bone fragments (green) and screws (blue); mid-stance phase of the musculoskeletal model (right).

Respective screw heads (medial/lateral) were connected through beam elements representing the plate and the screw-bone interface was modelled with a tie constraint. A total of 994'399 linear tetrahedral elements were used, corresponding to a volume mesh density of 9.98. The Finite Element Simulation was run in Abaqus 6.14 (Simulia, Dassault Systemes, France).

Results

A maximum displacement of 1.62 mm was found at the top of the lateral fragment. The maximum von Mises stress of 423 MPa is located on the most distal screw on the lateral side (**Figure 2**).
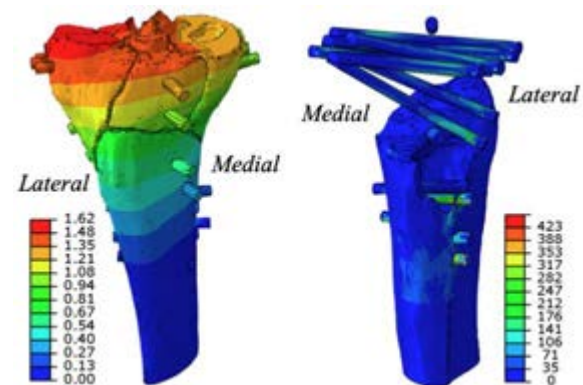
Figure 2: Displacement (left) and von Mises stress (right) of the simulated bone-screw construct.

Discussion

The method presented herein represents an objective process for the quantitative evaluation of fracture fixation stability. Our results allow prediction of bone fragment motion during daily activities, and if screws may be loaded beyond material capabilities.

After validation of the model, fragment movement could be related to fracture healing and serve as a predictive tool for clinical outcome. Possible hardware failure could be predicted by means of von Mises stresses in the screws. Furthermore, this process will enable development of patient-specific implants in the future.

References

1. Ruffolo et al, J Orthop Trauma, 29(2):85-90, 2015
2. Helgason et al, Med Eng Phys, 38(7):679-689, 2016.
3. Winsor et al, Bone, 143:115759, 2021.

Acknowledgements

Biomechanical modeling of the Anomalous aortic origin of the coronary artery

Michele Conti[1], Giovanni Maria Formato[2], Valentina Ceserani[1], Antonio Rosato[1], Mauro Lo Rito[3]

[1]*DICAr, University of Pavia, Italy*

[2] *3D and Computer Simulation Laboratory, IRCCS Policlinico San Donato, San Donato Milanese, Italy.*

[3] *Department of Congenital Cardiac Surgery, IRCCS Policlinico San Donato, San Donato Milanese, Italy*

Background. Anomalous aortic origin of the coronary artery (AAOCA) could be related to sudden cardiac death and ischemic events, especially in young athletes. The indication for surgical intervention is mainly based on static anatomical characteristics. However, adverse events occur during dynamic physical effort suggesting a strong coupling between the anatomical anomaly and the cardiac physiology. Unfortunately, routine medical stress tests showed a low prognostic ability to detect alteration or predict adverse events, calling for novel approaches. Motivated by such a need, we developed a computational model able to simulate anomalous coronary behavior to investigate coronary characteristics at increasing loading stress conditions [1].

Methods. Structural finite element analysis (FEA) is performed by Abaqus/STD (Dassault Systemes FR) using a 3D patient-specific model derived from medical image analysis. Computed tomography angiography (CTA) is used for the 3D model generation. Five patients with the anomalous right coronary artery (AAORCA) and 5 control subjects were studied. For each of them, we construct a 3D resembling the aortic root and coronary arteries, with intramural segment) based on 25 geometrical parameters automatically measured from CTA using Rhino v5 (Robert McNeel & Associates, USA). FEA simulations were run to simulate pressure increasing in the aortic root during exercise and investigate coronary lumen changes.

Results. In control subjects, the right coronary artery had a more significant lumen expansion at loading conditions than anomalous RCA. In AAORCA, the lumen expansion during effort was impaired, especially within the intramural segment [2] (see Figure 1).

Conclusions and Future Directions. The proposed AAOCA model can investigate the pathogenic disease mechanism related to the anatomical anomaly based on patient-specific data. Furthermore, the model allows the evaluation of a process that cannot be quantified in any clinical setup, especially in a non-invasive manner. This promising result in assessing the AAOCA pathological behaviour may help in patient-specific risk stratification. Current developments are tackling the improvement of many model features. Automatic segmentation of the CTA scan is performed by U-net; integration of IVUS and CT scan is foreseen to improve the accuracy of luminal reconstruction within the intramural segment. The coupling of the structural analysis with the fluid-dynamic modeling is under development to assess the impact of lumen narrowing of the artery on cardiac perfusion.

Figures
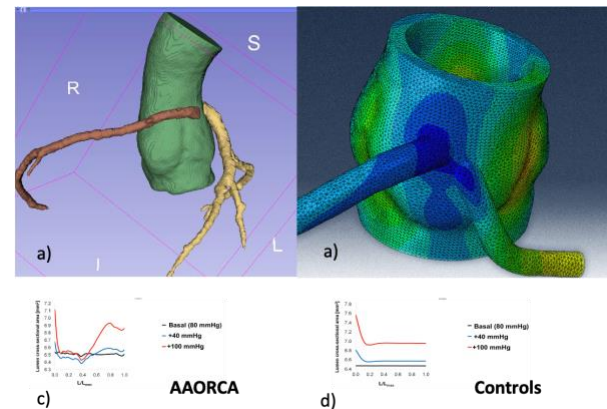
Figure 1: a) segmentation of CTA scan where aortic root and coronary arteries are identified. b) result of structural FEA simulating aortic root and coronary inflation during effort. c) lumen cross-sectional area of the AAORCA in three working conditions (basal and two effort phases); c) as d) fpr a control subject.

References

1. Formato, G. M., Lo Rito, M., Auricchio, F., Frigiola, A., & Conti, M. (2018). Aortic expansion induces lumen narrowing in anomalous coronary arteries: a parametric structural finite element analysis. *Journal of biomechanical engineering*, *140*(11).
2. Rito, M. L., Romarowski, R. M., Rosato, A., Pica, S., Secchi, F., Giamberti, A., ... & Conti, M. (2021). Anomalous aortic origin of coronary artery biomechanical modeling: toward clinical application. *The Journal of Thoracic and Cardiovascular Surgery*, *161*(1), 191-201.

ESTIMATION OF TIBIA AXES ON PARTIAL DISTAL SCANNER IMAGES : A NOVEL APPROACH IN THREE DIMENSIONS

Maryama Dufrénot (1)(2)(3), Sorin Siegler (4), Mélanie Donnez (3), Mathias Donnez (3), François Lintz(5), Patrick Chabrand (1)(2)

1. Aix-Marseille University CNRS, ISM UMR 7287, Marseille, France ; 2. APHM Institute for Locomotion, Department of orthopedics and traumatology Sainte-Marguerite Hospital, Marseille, France ; 3. Newclip Technics, Haute-Goulaine, France ; 4. Department of Mechanical Engineering, Drexel University, Philadelphia, Pennsylvania, USA ; 5. Department of foot and ankle surgery, union private hospital, Saint-Jean, France

Introduction

Scanner imaging for orthopedics has allowed to develop 3D surgical planning and cutting guides for many applications. These guides have improved surgery precision and reproducibility[1]. In order to plan surgeries and design devices, 3D coordinate system must be used to define anatomical planes and measure bones deformity. When procedures on distal tibia are performed, the entire tibia is not always available on scanner images. Thus, definition of tibia axis using common methods in not possible. In this work, we proposed different methods based on different 3D geometric objects to estimate tibia diaphyseal axis (DA) and mechanical axis (MA) when only distal tibia is available. The purpose was to identify for each methods what was the minimum amount of diaphysis to have an invariant angle between partial axis and real axis.

Methods

We used 15 tibias scanner images from cadavers which were segmented using Mimics and 3-Matic (Materialize, Belgium).Coding was done using MATLAB (MathWorks, USA). Three types of methods were tested, based on spheres, planes, or cylinders. Details are presented in table 1. Statistics were made using RStudio. Kruskal-Wallis and Kruskal-Nemenyi post-hoc tests were performed. Alpha was set to 5%.

Method	3D object	Reference axis	3D line fitting	Incrementation
SV1a	Sphere fitted to distal tibia epiphysis	D		Factor of 0.1 time the initial sphere radius
SV1b			X	
SV2a	Sphere enclosing dTP and center on dTPC	M		
SV2b			X	
IPC1	Plane orthogonal to tibia 1st PIA	D	X	Diaphysis length : ratio from 2% to 100% of diaphysis. Plane translation by step of 1 mm
		M	X	
IPC2	Plane fitted to dTP	D	X	
		M	X	
CylinderPIA	Cylinder fitted to tibia diaphysis. Initialized with tibia 1st PIA	D		Diaphysis length : ratio from 2% to 100% of diaphysis.
		M		
CylinderPN	Cylinder fitted to tibia diaphysis. Initialized with dTP fitted plane normal	D		
		M		

Table 1 – Details about the tested methods. SV : sphere variation, IPC : incremental plane centroid, PIA : principal axis of inertia, dTP : distal tibia plafond, dTPC : distal tibia plafond centroid; D : diaphyseal, M : mechanical

Results

Results are presented in the table below. All p-values for KW test were < 0.05. Kruskal-Nemenyi post-hoc test allowed to identify limit scaling factor (SF) or diaphysis ratio (DR) and corresponding diaphysis length (DL). Minimum SF were 5 for SV1a (DL=68-99mm); 3.8 for SV1b (DL=49-68mm). SV2a and SV2b methods were reproductible from SF=1, no minimum DL were needed. Minimum DR were 30% for DA estimation using IPC1, IPC2, CylinderPIA and CylinderPN (DL=58-95mm). For MA estimation, minimum DR were 10% for IPC1 and IPC2 (DL=24-31mm) and 6% for CylinderPIA and CylinderPN (DL=15-19mm).

Discussion

Our results highlighted that, independently from the methods, at least 49-68mm of diaphysis should be available on scanner images in order to estimate DA. To estimate MA, the only methods that would not nictitate a minimum amount od diaphysis are SV2ab methods. However, as dTP sphere did not cross tibia diaphysis, it would be important to determine what could be a reasonable minimum amount of diaphysis to scan in clinical routine. Recommendations from ISB can be found about definition of bones[2] axes and some papers are available about knee bones 3D coordinate systems [3]. Our work is the first to our knowledge proposing methods to estimate tibia axes when proximal tibia is not available. One limit of our work that should be considered is the small number of bones used for analysis. This work could help in designing scanner imaging protocols for patient-specific instrumentation companies when only distal tibia in concerned. It could lead to lessen patients radiations exposure.

References

1. Cerciello et al, Knee Surg Sports Traomatol, Epub ahead of print, doi: 10.1007/s00167-020-06253-5, 2020
2. Wu et al, J Biomech, 35:543–8 ; 2002
3. Renault et al, J Biomech, 80:171–8, 2018

AN ULTRASOUND-BASED MODELING FRAMEWORK FOR THE ASSESSMENT OF PERIPHERAL ARTERIAL DISEASE

Milan Gillissen[1], Frans N. van de Vosse[2], Marc van Sambeek[1,3], Richard Lopata[1]

1. Photoacoustics and Ultrasound Laboratory, University of Technology, Eindhoven, The Netherlands
2. Cardiovascular Biomechanics group, University of Technology, Eindhoven, The Netherlands
3. Catharina Hospital, Eindhoven, Noord-Brabant, The Netherlands

Introduction

Cardiovascular diseases (CVDs) are a leading cause of death worldwide. Peripheral artery disease (PAD) represents an estimated 32% of all global deaths in 2019, affecting over 230 million people worldwide. Currently, the length of the occlusion is used as criteria for endovascular therapy or surgical bypass [1]. However, main challenges of endovascular therapy include the durability of stents in the femoro-popliteal region where the artery is very mobile, and the more typical restenosis, which can occur within six to twelve months [2]. Several studies have shown that finite element analysis (FEA) can predict restenosis regions in different arteries [3, 4]. Despite promising results, these patient-specific models are not used in the clinical setting yet. The current computed tomography (CT) or magnetic resonance (MR) approaches suffer from several drawbacks, e.g., ionizing radiation and high cost. We propose a framework based on time-resolved two-dimensional ultrasound (US), which tackles the aforementioned disadvantages as well as acquire the vessel's motion during the cardiac cycle. A new screening method is proposed in this study which is based on multiple sweeps of the entire upper leg using a two-dimensional ultrasound probe in combination with a probe-tracker. An in-house developed framework is demonstrated, which segments US images automatically, and meshes the geometries obtained for computational fluid dynamics analysis.

Methods

Ultrasound (US) scans were made using a MyLab70 scanner (Esaote Europe B.V., Maastricht, The Netherlands). The images were automatically segmented by an in-house developed framework, created in Matlab (2020b, Mathworks Inc., Natick, MA, USA). These segmentations were extended to ensure flow was fully developed at the measured inlet. The final coordinates encapsulating the geometry were imported into Python (3.7, Python Software Foundation, Wilmington, DE, USA) where the Visualisation Toolkit (8.1.2, Kitware Inc., Clifton Park, NY, USA) was used to construct a surface from the scattered coordinates. The extended geometry was converted to a 3D tetrahedral volume mesh in Ansys (Fluent 19.2, Ansys Inc., Canonsburg, PA, USA) by using the built-in Fluent meshing tool. Finally, a computational fluid dynamics (CFD) simulation is performed in Ansys Fluent 19.2.
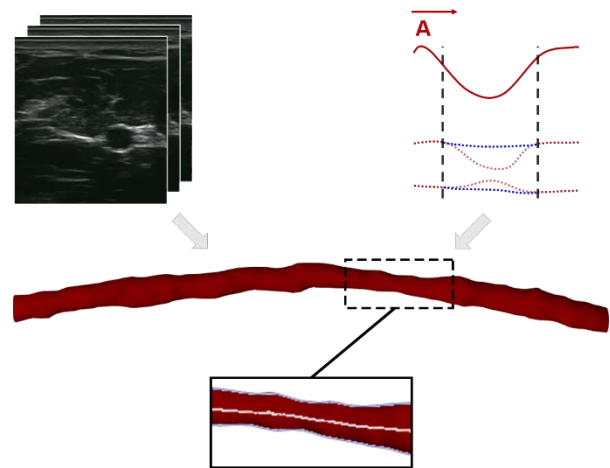
Figure 1: Automatically segmented geometry based on multiple sweeps of the femoral artery of a patient suffering from PAD. By using an in-house developed automatic stenosis detection algorithm, the stenotic area is found (highlighted by the dashed box).

Results

Figure 1 shows an automatically segmented geometry from a patient suffering from PAD. In this geometry, the stenotic area is found automatically with a stenosis detection algorithm.

Discussion

First results show the feasibility of the technique in healthy volunteers and patients with PAD. In the future, the CFD models can be used for intervention planning, due to the fact that these models will be extended so that a procedure can be applied to the 'virtual patient'. The stenosis could be virtually removed and tested to see if there are any other anomalies in the circulatory system.

References

[1] Victor Aboyans et al, European Journal of Vascular and Endovascular Surgery, 55(3):305–368, March 2018.
[2] Dario Buccheri et al, Journal of Thoracic Disease, 8(10), October 2016
[3] Nicolas Benard et al, Journal of Biomechanics 39, December 2006.
[4] Jonathan Murphy and Fergal Boyle. Computers in Biology and Medicine, 40(4):408–418, April 2010.

IN SILICO STUDY ON ALLOGRAFT-BASED ACETABULAR RECONSTRUCTION

Ajay Goyal, Zafar Haider, Anoop Chawla, Kaushik Mukherjee

Department of Mechanical Engineering, Indian Institute of Technology Delhi, New Delhi, India 110016

Introduction

Surgeons have always struggled to reconstruct severe acetabular defects during hip replacement/revision surgeries [1]. Bone substitute materials like autografts, allografts, and artificial bone grafts, have usually been considered for treating such severe acetabular defects [2]. Among all these various bone substitute materials, allografts are usually preferred to treat such acetabular defect. However, the post-operative stability of such reconstruction has always been a case of concern [3]. The objective of this finite element (FE) study is to investigate the immediate post-operative load bearing capacity of the allograft-based reconstruction of a severe acetabular defect as compared to that of a defect-free implanted hemi-pelvis.

Methods

The defect-free 3D CAD model of right hemi-pelvis was generated from CT scans of a 74 year old female (76kg weight) using biomedical image processing software (Mimics 23.0, Materialize, Leuven, Belgium © 2021). Acetabular cup and femoral head were designed and virtually placed in acetabulum using Hypermesh (Altair Engineering Inc. 2020). The defect-free implanted pelvis model was discretized using Hypermesh (Fig.1). Linear elastic and homogeneous material properties were assumed for the cortical bone and cancellous bone [4]. The acetabular component and the femoral head were assumed to be made of steel. Twenty one muscle patches were developed at surface of pelvic bone to prescribe loading conditions. Fixed boundary conditions were assigned for pubis symphysis and sacroiliac joints. A static frictional contact was defined between cup-bone ($\mu=0.3$) and cup-head ($\mu=0.02$). In order to simulate the reconstruction of a severe acetabular defect, a cavity of $\Phi15$mm was virtually created at the center of the implanted acetabulum model and was filled with allograft. The allograft was also assumed to be homogeneous, linear elastic, and isotropic. The right single support stance (13% of cycle) was considered as the loading condition. The FE models were solved using Optistruct (Altair Engineering Inc. 2020).

Results

The von Mises stress distributions, shown in Fig. 2, at the ilium and pubis of the pelvic bone are higher in defect-free implanted hemi-pelvis model as compared to the other one. There were significant differences in the distribution of stresses and strains around the acetabulum (Fig. 2). The defect-free implanted pelvic bone exhibited a maximum von Mises stress of 57.9MPa near the front rim of the acetabulum. In comparison, the allograft-based acetabular reconstruction model exhibited a lower peak von Mises stress level (47.6MPa).
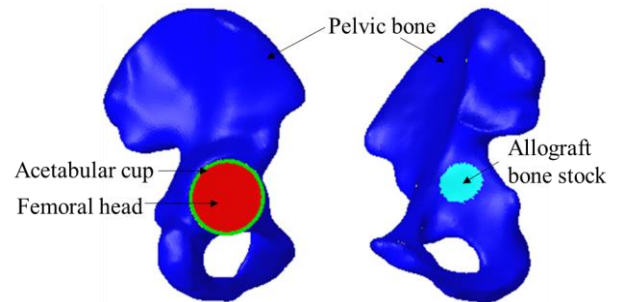
Figure 1. FE model for pelvic bone with bone allograft stock in acetabulum
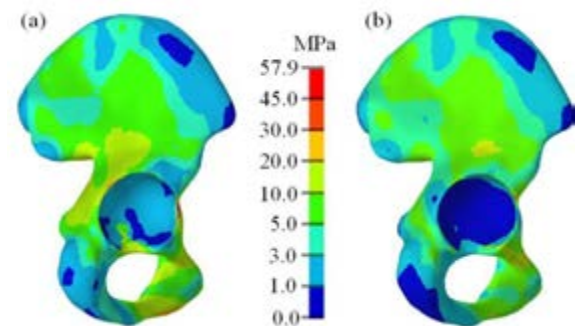
Figure 2. von-Mises stress distribution in pelvic bone exposed to a walking cycle condition:(a) without allograft, (b) with allograft

Discussion

This computational study evaluated the feasibility of using bone allografts as possible substitute to fill in the severe acetabular defects during reconstruction surgery. This study shows that there is reduction in stresses and strain distribution in case of allograft-based acetabular reconstruction as compared to defect-free hip reconstruction. It should, however, be noted that the allograft component itself is exposed to high strain values which further warrants detailed investigations for allograft-based acetabular reconstructions.

References

1. Paprosky et al., Clinical orthopaedics and related research; 298: 147-155, 1994.
2. Brewster et al., J Bone Joint Surg Br; 81: 118–124, 1999.
3. Haaren et al. J Bone Joint Surg Br; 89(3): 296–300, 2007.
4. Ghosh et al., J of Biomechanical Engineering, 134: 1-9, 2012.

EFFECT OF SUBJECT-SPECIFIC MASS DISTRIBUTION ON JOINT BIOMECHANICS DURING GAIT

Abdul Aziz Vaqar Hulleck (1) , Marwan El Rich (1), Tao Liu (2), Kinda Khalaf (1)

1. Khalifa University, United Arab Emirates; 2. University of Alberta, Canada

Introduction

Body segment parameters, particularly mass distribution, center of mass (CoM) and moment of inertia, significantly affect musculoskeletal (MSK) model predictions, hence limiting their clinical applications [1]. Our previous trunk mass distribution and CoM prediction model, which considers both external body shape and relevant internal structures [2], has proven its capability of predicting subject-specific body shapes. The current study compares joint reaction forces obtained based on subject-specific mass distribution with a linearly scaled model during gait in subjects with different body mass index (BMI).

Method

Gait motion capture was performed for three healthy male subjects (normal weight BMI: 23.8, over-weight BMI: 27.3 and obese BMI: 31 kg/m^3) using IMU sensors (Xsens Technologies BV, Enschede, The Netherlands). IRB approval and informed consent were obtained prior to data collection. Fifteen anthropometric measurements in addition to the subject's height and weight, were recorded and a full body MSK model (AnyBody) was used to predict joint reaction forces. The model was scaled using two methods: 1- linearly using the default approach implemented in AnyBody based on total body mass and segment mass ratio values extracted from literature [3] and 2- using our recently developed subject-specific trunk segment mass (T1-S1) and CoM locations prediction model which accounts for the subject body shape and internal tissue distribution in addition to subject's body weight and height [2]. The model utilizes 15 anthropometric measurements of a male subject to predict the body shape, and a scalable cross-section template created based on the Visible Human (VHP) male subject (age: 38 yrs; body height: 180.34 cm; body weight: 90.24 kg; BMI: 27.75 kg/m2) images to compute the bone, fat and lean tissues volumes. The model then computes the subject trunk segment mass and CoM locations using the fat, bone, and lean tissue densities of 0.94 g/cc, 1.5 g/cc and 1.06 g/cc [4] respectively. The resultant joint reaction forces normalized to body weight at toe-off (TO) and heel strike (HS) were averaged over three gait cycles for each subject at hip, knee, ankle, and T12-S1 intervertebral discs. One-way ANOVA was performed on the joint reaction forces to compare the results using the two different mass distribution approaches.

Results
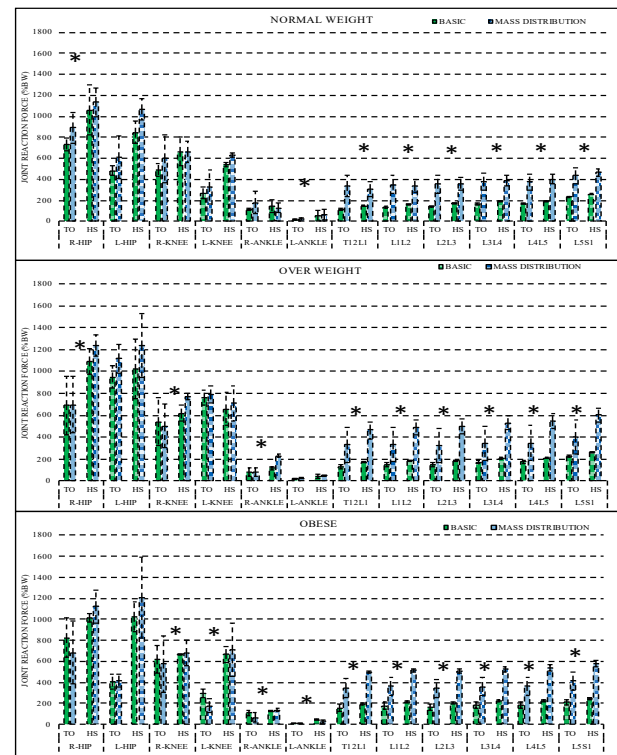
Figure 1: Joint reaction forces at T12-S1 intervertebral discs, hip, knee, and ankle joints at toe-off (TO) and heel strike (HS) of gait cycle for 2 scaling techniques. (* denotes p<0.05, one-way ANOVA)

Discussion

The two scaling techniques demonstrated significant difference (p<0.05) in almost all joints of the 3 subjects and its occurrence increased with BMI (i.e. number of joints with significant difference was higher in the obese subject as compared to other subjects). The linear scaling approach underestimated the reaction forces at all joints and the magnitudes at L5-S1 discs were less than half the values predicted by the body shape-based approach.

This study confirmed the limitation of the linear scaling approach when used in subject specific MSK models and the importance of including the body shape in segmental mass and CoM determination [5].

References

[1] Lund M et al. International Biomechanics 2015
[2] Liu T et al. J Biomech 2021
[3] Karatsidis A et al. Med Eng Phys 2019
[4] Pearsall D et al. Ann Biomed Eng 1996
[5] Ghezelbash, A. et al. Ann Biomed Eng 45, 2017.

PATIENT-SPECIFIC DESIGN OF HIGH TIBIAL OSTEOTOMY PLATES USING DENSITOMETRIC CALLIBRATION

Shafath Chowdhury[1], Sanjeevan Kanagalingam[1], Lorenzo Grassi[2], Tarek Boutefnouchet[3], Lauren E. J. Thomas-Seale[1],

[1] *Department of Mechanical Engineering, School of Engineering, University of Birmingham, United Kingdom*
[2] *Department of Biomedical Engineering, Lund University, Sweden*
[3] *University Hospitals Birmingham NHS Trust*

Introduction

High Tibial Osteotomy (HTO) is a surgical procedure used to treat unicompartmental osteoarthritis of the knee through load redistribution. HTO can also be used to treat varus knee alignment by positioning the tibial plateau in line with the transverse plane. Current HTO procedures are limited due to the indeterminability of optimal correction angles prior to surgery in addition to having no tangible methods to evaluate the effect of plate stiffness and load redistribution on callus formation, interfragmentary motion (IFM), and bone union [1]. These limitations lead to inconsistent results post-surgery.

The authors have developed a novel design framework for patient-specific HTO plates using Generative Design. This approach creates a custom fit that conforms to variability in both patient anatomy and biomechanics. This study extends this work by integrating densitometric calibration of patient computerised tomography (CT) scans. Densitometric calibration is used map patient specific mechanical properties, taken from a CT scan, onto a discretised finite element model. This calibration allows accurate modelling of mechanical properties based on density variation in cortical and cancellous bone. This new approach greatly increases patient specificity; combining an accurate anatomical and biomechanical approach to supersede current plate designs. This approach will offer optimised IFM, promote efficient bone healing and prevents stress shielding.

Methods

The workflow requires the generation of a proximal tibia STL file. This file was produced using a donor CT scan and 3D Slicer [2]. Once a refined geometry was achieved, an STL file was exported. OpenFlipper 4.1 [3] was used to closely control the element size of the tibial geometry. The osteotomy was performed computationally to create an open wedge, apply screws, and fixate a T-plate. Altair Hypermesh was used to create a surface mesh, and then converted into a volumetric mesh using Ansys Workbench. Finally, Bonemat 3.2 [4] applied the densitometric calibration to create a patient specific mechanical property map. This density specific osteotomy model was analysed within FEA to determine the forces induced on the screws and to measure the IFM of the fracture compared to generic material properties from an idealised sawbone model.

Results
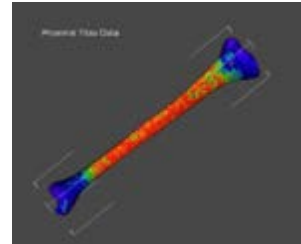
Figure 1: Proximal Tibia produced in Bonemat 3.2 using densitometric calibration for a tibia [5].

Figure 1 portrays the variation of Young's Modulus (E) in a donor tibia. Red is indicative of higher E values of cortical bone and blue regions indicate low E values of trabecular bone.

The osteotomy plates obtained through generative design are evaluated to measure plate stiffness and IFM through FEA. These parameters are used to determine the clinical efficacy of the plate designs.

Discussion

This study aims to increase the mechanical specificity of a patient-specific HTO fixation plate design. This is achieved through the integration of densitometric calibration, thus increasing the accuracy of the biomechanical analysis, which is integral to the design process. This approach to HTO fixation plates offers better outcomes due to patient variability accountability.

References

1. X. Lui et al, "High Tibial Osteotomy: Review of Techniques and Biomechanics", *Journal of Healthcare Engineering*, 2019.
2. R. Kikinis et al, "3D Slicer: a platform for subject specific image analysis, visualization, and clinical support". *Intraoperative Imaging Image-Guided Therapy, 2014.*
3. L. Kobbelt, OpenFlipper, 4.1, *RWTH Aachen University, 2019*
4. F. Taddei et al, "The material mapping strategy influences the accuracy of CT-based finite element models of bones: an evaluation against experimental measurements", *Medical Engineering & Physics, 2007.*
5. E. Morgan et al, "Trabecular bone modulus-density relationships depend on anatomic site", *Journal of Biomechanics, 2003.*

Acknowledgements

MORPHOLOGICAL AND HAEMODYNAMIC CHARACTERISATON OF TURNER SYNDROME AORTAE

**Lauren Johnston (1), Ruth Allen (2), Pauline Hall-Barrientos (2),
Avril Mason (2) and Asimina Kazakidi (1)**

1. University of Strathclyde, UK

2. Royal Hospital for Children, Queen Elizabeth University Hospital, UK

Introduction

Turner syndrome (TS) is a genetic disorder affecting 1 in 2000 to 2500 females worldwide, with an increased prevalence of cardiovascular disease [1]. The spectrum of congenital heart disease ranges from minor abnormalities to severe and highly complex disorders. Despite European and American guidelines, cardiovascular risk assessment in Turners syndrome is challenging [2-3]. This research aims to characterize the morphology and haemodynamics in the aortae of Turner syndrome children, to improve our understanding of cardiovascular disease in this population.

Methods

Retrospective MRI data was obtained from Turner syndrome girls, and three-dimensional patient-specific geometries of the aorta (including the major branches) were reconstructed. Morphometric analysis was performed for all aortic geometries within Vascular Modelling Toolkit (VMTK) (www.vmtk.org) software. Quantitative values and statistical analysis were obtained for the following parameters: aortic diameter, volume, and surface area; arch length, height, and width; and curvature, torsion, and tortuosity. Numerical simulations were then performed for each geometry within the open-source software OpenFOAM®, using patient-specific MRI-obtained boundary conditions. Velocity streamlines, time-averaged wall shear stress (TAWSS), and oscillatory shear index (OSI) were computed for all models. This methodology was repeated for a cohort of healthy (non-Turner syndrome) girls and used for comparison.

Results

Morphometric analysis revealed greater aortic diameters, arch height and arch width in TS girls compared to their healthy counterparts. Also, for the TS group, a significant association between body surface area and (1) systolic blood pressure, (2) arch height, (3) arch height to width ratio, and (4) arch diameter was found. Computational fluid dynamic (CFD) analysis revealed an increase in vortical flow in the arch, supra-aortic vessels, and descending aorta, and a correlation between the presence of aortic abnormalities and disturbed flow [4]. Most interestingly, the Turner syndrome group exhibited markedly elevated TAWSS values compared to the age-matched healthy group [4].

Discussion

In this study, the anatomical abnormalities observed in the aortae of young TS girls, the majority of which were obese or overweight, were accompanied by abnormal flow patterns and highly non-uniform distribution of wall shear stresses, which may promote the development of cardiovascular diseases earlier in life. Considering the excess of morbidity and mortality seen in TS, the analysis presented in this study could be applied clinically to cardiovascular risk stratification.

References

1. Nielsen and Wohlert, Hum Genet, 87:81-83, 1991.
2. Gravholt et al., Eur J Endocrinol, 177, 2017.
3. Silberbach et al., Circ, 11, 2018.
4. Johnston et al., Front Cardiovasc Med, 2021.

Acknowledgements

INFLUENCE OF MODIFIED MUSCULOSKELETAL MODEL ON THE HIP LOADING IN CEREBRAL PALSY PATIENT

Justyna Skubich (1), Szczepan Piszczatowski (2)

1. Bialystok University of Technology, Poland; 2. Bialystok University of Technology, Poland

Introduction

Spastic form of cerebral palsy (CP) is the reason for abnormal muscle activity. Morphological changes in muscle structure [1], an improper value of muscle forces and finally deformity of the musculoskeletal system are the results of such pathology [2]. Biomechanical analysis of the spastic hip joint in CP is a challenge because of the complexity of the locomotor system and the multi-faceted influence of the disease on its functioning. What's more, a standard musculoskeletal model used in dynamic analyses of human movement neglects specific musculoskeletal geometry occurring in CP patients (i.e. improper femoral neck-shaft angle) or real parameters of spastic muscles. The aim of presented study was to estimate the influence of the musculoskeletal model modification, taking into account changes occurring in the spastic cerebral palsy, on the loadings acting in the hip joint.

Methods

The analyses of the musculoskeletal system were performed in the AnyBody Modeling System, using motion-capture data recorded for CP patient as input. In the first step, a kinematic analysis based on the marker trajectories was conducted to calculate joint kinematics. Secondly, an inverse dynamic analysis with complement of optimization based on a polynomial, third power muscle recruitment criterion [3], was performed to calculate required muscle forces and hip joint reaction force during gait of CP patient. The results obtained with the use of a standard musculoskeletal model (*M0*) were compared with the results of a simulation conducted on models with modified: morphological parameters of selected muscles (*MI*), pattern of muscle excitation for selected muscles (*MII*), femoral bones geometry (*MIII*) or passive parameters of selected muscles (*MIV*).

In the first variant of the model (*MI*) the fibre length and the muscle volume belly of selected muscles were decreased on the basis of results of the research on spastic muscle available in the literature [1, 4]. In the second variant (*MII*), the pattern of muscle excitation was modified to reconstruct some features of the spastic muscle and its abnormal activity. This variant assumed that the minimum excitation of the muscle is associated with the velocity of muscle elongation. In the third variant (*MIII*) the geometrical modification of the skeletal model was performed. In the last analysed model (*MIV*) the passive parameters of selected muscles were modified to reflect increased stiffness of the spastic tendon-muscle unit.

Results

The muscle force patterns generated by particular actons as well as the hip joint reaction force (value and direction) during gait cycle for the spastic patient were evaluated. The exemplary results of the reaction force acting in the right hip joint during gait cycle (fig. 1.) obtained using all analysed variants of the model (*MI, MII, MIII, MIV*) have been compared with each other, and presented against results calculated with use of the unchanged, standard model (*M0*).
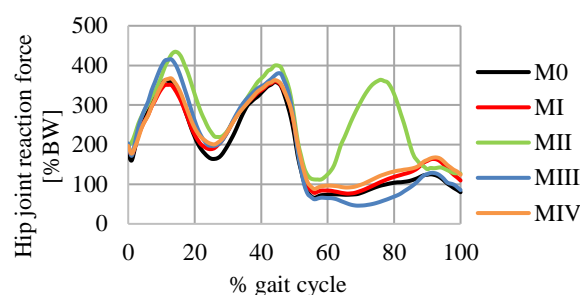
Fig. 1. Total joint reaction force in the right hip joint as a function of the gait cycle

Discussion

Modification of the musculoskeletal model allowed to demonstrate the influence of pathological changes occurring in CP patients on biomechanical parameters (muscle forces, joint reaction force) during gait. What's more, the inclusion in the model deformities of particular bones and spastic characteristics of selected muscle, has significant influence on the results of the simulation obtained for the entire musculoskeletal system.

The obtained results of the simulation present influence of particular aspects of pathology separately. In fact, all analysed phenomena occur simultaneously, then in further research, model including all of them should be elaborated. It would allow to obtain more realistic biomechanical parameters of the CP patient during gait simulation.

References

1. Barrett et al, Dev Med Child Neurol, 52(9):794-804, 2010.
2. Miller, Cerebral palsy, Springer, 2006.
3. Damsgaard et al, Simul Model Pract Th, 14:1100–1111, 2010.
4. Handsfield et al, Muscle Nerve, 53(6):933–945, 2016.

Acknowledgements

A MESHLESS METHOD TO STUDY THE EFFECT OF VEGF DIFFUSION IN CAPILLARY NETWORK MORPHOLOGY

Tomás Sousa (1), Ana Guerra (2), Jorge Belinha (1), Renato Natal Jorge (3,4)

1. School of Engineering, Polytechnic of Porto (ISEP), Portugal; 2. Institute of Science and Innovation in Mechanical and Industrial Engineering (INEGI), Portugal; 3. Associated Laboratory in Energy, Transport and Aeronautics (LAETA – INEGI), Portugal; 4. Faculty of Engineering of the University of Porto (FEUP), Portugal.

Introduction

Angiogenesis is the formation of new capillaries from pre-existent vasculature and it is an essential event in tumorous growth and wound healing. To develop new cancer and wound healing therapies it is pivotal to understand the mechanisms by which angiogenesis is regulated. Biomaterials are strong candidates for future therapies [1]. Nonetheless, studying the biomaterial's effect in angiogenesis using only experimental approaches is financially expensive and present many variables that are extremely difficult to control. The development of *in silico* models allows to test different hypothesis, in a completely manipulative environment, and to present results comparable with experimental studies.

Methods

In this work, a 2D numerical method that simulates sprouting angiogenesis in a wound healing context is proposed. In this model, endothelial cells migrate according to a reaction-diffusion equation, which governs the Vascular Endothelial Growth Factor (VEGF) diffusion and uses a meshless method, the Radial Point Interpolation Method (RPIM), to establish its governing equations [2]. Capillary networks obtained from the chick chorioallantoic membrane (CAM) assay were used to achieve parameters to implement in the model in order to simulate capillary branching. The proposed model was used to study the influence of VEGF concentration and constant and variable VEGF diffusion rates in the capillary network morphology during wound healing.

Results

Endothelial cells migrate according to chemotaxis effect, towards the highest VEGF concentration. Moreover, morphologically realistic capillary networks were obtained. The VEGF releasing from biomaterial influenced the capillary network pattern in a way that, the more the VEGF concentration in the biomaterial increased, the more the capillary network was dragged towards the biomaterial. In the simulations with variable VEGF diffusion rate, the obtained capillaries were not as attracted towards the biomaterial as in the constant diffusion rate (Figure 1). Nevertheless, the capillary network density increased with an increase in the VEGF concentration released from the biomaterial.
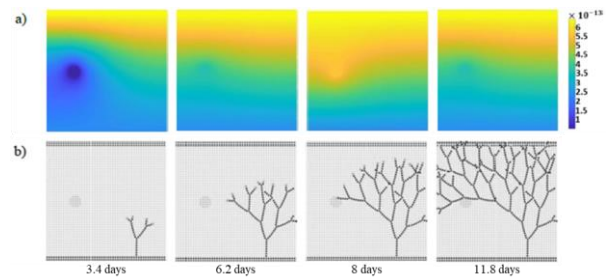
Figure 1: Capillary network formed with variable VEGF diffusion rate. Biomaterial loaded with a VEGF concentration of 87% of the wound's concentration. a) VEGF diffusion gradient throughout time (VEGF concentration in $g\ mm^{-3}$). b) Vascular network pattern evolution throughout time in a regular nodal discretization mesh. The tip cell is located at $x = 3.8\ mm$.

Discussion

The developed model presented promising results and demonstrated the value of using meshless methods for biological problems' applications. In this work, an experimental assay was used to model the branching occurrence, allowing to obtain realistic capillary networks. However, the obtained results for the biomaterial's influence in the capillary networks formation still requires experimental validation.

References

1. Liu W et al., J Nanobiotechnology, 18(1):1–22, 2020.
2. Guerra A et al., Int J Numer Method Biomed Eng, 36(11):e3393, 2020.

Acknowledgements

UNUSUAL PHALANGEAL PROPORTIONS IMPROVE GRASPING POTENTIAL IN BIRDS, MAMMALS, AND BIOINSPIRED DESIGN

Michael C. Granatosky (1, 2), Melody W. Young (1) , Nicholas D. Flaim (1), Lukas Faltings (1), Manrose Singh (1), Edwin Dickinson (1)

1. *New York Institute of Technology College of Osteopathic Medicine, United States of America; 2. Center for Biomedical Innovation, United States of America*

Introduction

Among tetrapods digital proportions are highly constrained in a large-to-small proximodistal gradient [1]. However, some mammals and birds have broken this pattern, elongating the distal phalanx and shortening its proximal counterpart [1, 2] (Figure 1). The convergent morphology among these distantly related taxa suggests a biomechanical advantage to this configuration [3]. Yet, beyond simple associations with substrate use, no biomechanical explanation for this aberrant morphology has been proposed.

Figure 1: Micro-CT scan of a fat-tailed dwarf lemur (Cheirogaleus medius; A) demonstrating the large-to-small proximodistal phalangeal gradient contrasted with a colugo (Galeopterus variegatus; B) showing distal elongation of the penultimate phalanx and a shortening of the proximal phalanx. Bioinspired models (C-E) can be developed to test the functional consequences of varying phalangeal proportions within the digital ray.

Methods

In this study, we collect linear measurements of phalangeal length, width, and depth along digital ray three from a broad phylogenetic sample of birds and mammals (~10-20 representative species per order). We use phylogenetic generalized least squares to assess whether aspects of locomotor behavior and limb loading influence phalangeal morphology and proportions. From these measurements, we estimate force production at each of the interphalangeal joints by modelling the digital ray as a series of pullies and levers [4]. Further, we developed a set of bioinspired three-dimensional robotic rays that vary in relative proportions of the phalanges but retain total digit length (Figure 1). Peak forces were collected at the interdigital pads along the ray of our bioinspired models.

Results

In a broad phylogenetic sample of birds and mammals, we demonstrate that distal elongation of the penultimate phalanx and a shortening of the proximal phalanx is associated with scansorial and raptorial birds and suspensory non-primate mammals. Modelling the digital ray as a series of pulley and levers reveals that shortening the proximal phalanx reduces out-lever lengths, theoretically increasing the mechanical advantages of the digital flexor musculature. When this condition is replicated in our bioinspired robot, this theoretical relationship is empirically confirmed.

Discussion

These data demonstrate that shortening the proximal phalanges serves to increase the force generating potential of extrinsic flexor musculature at more proximal interdigital pads, but not the claw tip. As such, we propose that shortening the proximal phalanges evolves when high grip forces are required. Assuming the legitimacy of this hypothesis, elongation of the penultimate phalanx has no influence on the force generating potential of digital musculature. Instead, such elongation serves to maintain overall ray length to accommodate for the short proximal phalanges.

References

1. K. D. Kavanagh et al., PNAS. 110, 18190–18195 (2013).
2. K. C. Beard, Nature. 345, 340–341 (1990).
3. M. W. Hamrick, B. A. Rosenman, J. A. Brush, Am. J. Phys. Anthropol. 109, 397–413 (1999).
4. M. C. Granatosky, C. F. Ross, Journal of Anatomy. 237, 1072–1086 (2020).

THE FEASIBILITY OF BESPOKE REHABILITATION ROBOT HANDGRIPS TO MEET THE SPECIFIC NEEDS OF STROKE PATIENTS

Lutong Li (1), Qiang Fu (1), Sarah Tyson (2), Andrew Weightman (1)

1. Department of Mechanical, Aerospace and Civil Engineering, School of Engineering, University of Manchester, United Kingdom; 2. School of Health Sciences, University of Manchester, United Kingdom

Introduction

Stroke is the main cause of morbidity [1]. Upper limb robotic-assisted therapy can s improve motor control (P <0.05) [2, 3]. However to be effective, the tasks practiced with the robot need to replicate those used in real life. Most upper limb rehabilitation provide only a single handgrip [4], which cannot accommodate the range of weakness found and variety of grips needed in everyday life. We have previously identified that providing handgrips that are used in everyday life is an important requirement for rehabilitation robots [5]. Bespoke handgrips (e.g. size, shape and type) could meet this need. This research investigates the feasibility of bespoke handgrips to meet stroke survivors' needs by analyzing the frequency of different grip in Activities of Daily Living (ADLs) and their priority for upper limb rehabilitation.

Methods

This research had two parts. Firstly, two experienced stroke physiotherapists identified the frequency with which different grips were used in daily living. The tasks assessed were drawn from the ABILHAND (a comprehensive clinical assessment in which the ability to perform 21 common ADLs is assessed) [6]. The frequency with which each grip was used was summed. The second part was an online questionnaire with a further 15 experienced stroke therapists (4 occupational therapists and 11 physiotherapists) to prioritize the grip types (grasp grip, pinch grip, pencil grip and hook grip) according to their importance for upper limb rehabilitation.

Results

Type of grip	Image of grip	Frequency in daily life (%)	Importance for rehabilitation
Grasp grip		7 (33%)	1
Pinch grip		14 (66.7%)	2
Pencil grip		3 (14.3%)	3
Hook grip		1 (4.8%)	4

Table 1: The frequency and importance of grips in daily life (importance level from high to low is from 1 to 4).

Of the 17 therapists involved in this study, 76% had more than 10 years' experience in stroke rehabilitation. Table 1 illustrates the frequency and importance of four grips in daily living activities. Pinch grip was most commonly used (66.7%, 14/21 activities), followed by grasp grip (33.3%, 7/21 activities).

Thus a single generic (grasp) handgrip is not fit-for-purpose to facilitate ADLs-based practice, especially for those who are too weak to grip.

Discussion

This study engaged experienced stroke therapists to identify and prioritise the handgrips used in everyday life and the specification for bespoke hand grips to meet the patients' needs for upper limb rehabilitation robots. Analysis of ADLs showed the most prevalent grip was the pinch grip but rehabilitation robots also needed to accommodate a grasp grip. Pencil and hook grips were lower priority. This shows that single grip robots (which are currently the norm) are not fit-for-purpose and limit access for those with severe disabilities. Robotic-assisted rehabilitation may be enhanced by developing bespoke (e.g. size, shape and type) handgrips based on stroke survivor need (e.g. impairment and rehabilitation goal). Further research is needed to investigate the benefit of bespoke handgrips of rehabilitation robot.

References

1. Krinock MJ, Singhal NS. Diabetes, stroke, and neuroresilience: looking beyond hyperglycemia. Annals of the New York Academy of Sciences. 2021;1495(1):78-98.
2. Veerbeek JM, Langbroek-Amersfoort AC, van Wegen EEH, Meskers CGM, Kwakkel G. Effects of Robot-Assisted Therapy for the Upper Limb After Stroke: A Systematic Review and Meta-analysis. Neurorehabilitation and Neural Repair. 2017;31(2):107-21.
3. Duret C, Grosmaire A-G, Krebs HI. Robot-Assisted Therapy in Upper Extremity Hemiparesis: Overview of an Evidence-Based Approach. Frontiers in Neurology. 2019;10(412).
4. Qassim HM, Wan Hasan WZ. A Review on Upper Limb Rehabilitation Robots. Applied Sciences. 2020;10(19):6976.
5. Li L, Fu Q, Tyson S, Preston N, Weightman A. A scoping review of design requirements for a home-based upper limb rehabilitation robot for stroke. Topics in Stroke Rehabilitation. 2021:1-15.
6. Penta M, Tesio L, Arnould C, Zancan A, Thonnard J-L. The ABILHAND questionnaire as a measure of manual ability in chronic stroke patients: Rasch-based validation and relationship to upper limb impairment. Stroke. 2001;32(7):1627-34.

ANALYSIS OF THE EFFECT OF SKINFOLD THICKNESS ON MYOTONOMETRIC SIGNAL CHARACTERISTICS

Shib Sundar Banerjee (1), Arockiarajan Arunachalakasi (1), Ramakrishnan Swaminathan (1)

1. Department of Applied Mechanics, Indian Institute of Technology Madras, India

Introduction

Myotonometry is a novel method for the non-invasive estimation of viscoelastic parameters of the muscle. An instantaneous actuation is generated on the skin surface and the resulting free oscillation signal is acquired using an accelerometer for material characterization in this method [1]. It involves a superficial measurement technique and suffers interception from the soft tissue cover of the muscle [2]. The impact of the soft tissue cover on the characteristics of the myotonometric signal is investigated in the present study.

Methods

Eight healthy young participants (age: 25 ± 4.21, height: 169.18 ± 5.17, weight: 65.25 ± 5.31) have participated in this study. Myotonometric signals have been acquired from the relaxed biceps brachii muscles from both of the hands ($n = 2 \times 8$). The recorded acceleration signals are further processed using a low-pass filter to remove high-frequency noise. A cut-off frequency of 70 Hz is set to eliminate both the transient modes of vibrations and movement artifacts [3]. The exponential order of decay (b) is computed by fitting the oscillation peaks with the decay envelope given by the following expression:

$$y(t) = ae^{bt} \tag{1}$$

where $y(t)$ is the decay envelope corresponding to time instance t, and a is the magnitude parameter.

The triceps skinfold thickness values are also acquired from the hands using a skinfold caliper. Pearson correlation analysis has been performed between the exponential order and skinfold thickness.

Results

Table 1 demonstrates the variation in the fitted exponential order of decay separately for the right and left hands. No significant difference in the values between the hands is observed.

Hand	b (s⁻¹)	95% CI	
		Minimum	Maximum
Right	-12.72	-13.97	-11.48
Left	-12.30	-13.66	-10.93

Table 1: Mean exponential order of decay with 95% confidence interval for right and left hand

The variation of exponential order of decay with skinfold thickness is plotted in figure 1. A Significant negative correlation with an R-value of -0.81 is noted between exponential order and skinfold thickness ($p < 0.001$).
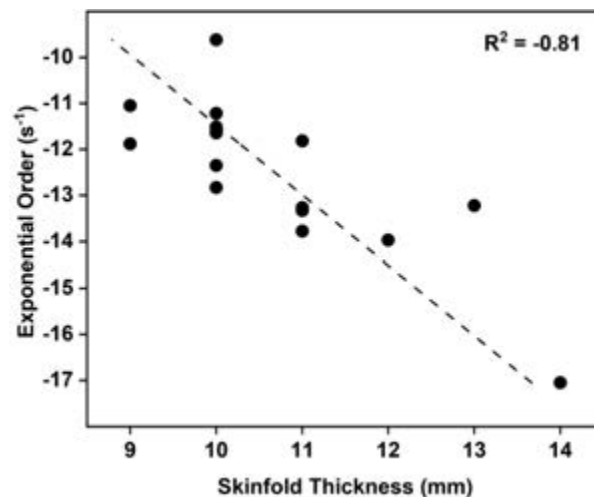
Figure 1: Variation of exponential order of decay with skinfold thickness

Discussion

The exponential order of decay of the myotonometric signal is the measure of the viscous damping of the mechanical oscillation due to the presence of the soft tissue cover [2]. In this study, the magnitude of the decay parameter is observed to be linearly proportional to the skinfold thickness. Therefore, this parameter can be used to determine the effect of soft tissue cover on the myotonometric signal, and the overestimation in the dynamic measurement of muscle stiffness [4].

References

1. Schneider et al, Med Biol Eng Comput, 53:57-66, 2015.
2. Feng et al., Sci Rep, 8:17064, 2018.
3. Banerjee et al., J Med Device, 14:2-7, 2020.
4. Sohirad et al., PLoS One, 12:1-9, 2017.

FINITE ELEMENT MODELING OF THE COUPLING BETWEEN THE EARCANAL AND THE TEMPOROMANDIBULAR JOINT

Michel Demuynck[1], Aidin Delnavaz[1], Jérémie Voix[1]

[1]*Department of Mechanical Engineering, École de technologie supérieure, Université du Québec, Montréal, QC H3C 1K3, Canada*

Introduction

The movements of the jaw induce earcanal (EC) deformations through the mandibular condyle displacement. Studies have shown that a significant amount of energy can be harvested from the resulting EC dynamic motion. The power capability of the earcanal has been studied experimentally [1] and analytically [2]. However, the relationship between EC and the temporomandibular joint (TMJ) is still unknown and is not included in these studies. Hence, it is still difficult to evaluate accurately the maximum amount of harvestable energy. The objective of this study is to develop a parametric numerical model reproducing the biomechanical coupling between EC and TMJ in order to assess the maximum reachable amount of in-ear harvestable energy.

Methods

Earcanal impressions were taken in the closed-mouth (CM) and open-mouth (OM) position in the left ear of a healthy male test subject. Both earmolds were later digitally scanned.

The OM earmold was used to model the finite-element (FE) EC core. It consists of a perforated cylinder whose inner surface corresponds to the outer surface of the earmold. The mechanical properties of a homogeneous, isotropic and linear silicone rubber material were attributed to the EC core. The TMJ kinematic path synthesized in a previous study [3] was used to reproduce the EC dynamic motion. The path was set to the center of the TMJ condyle which is modeled by an ellipsoid [4] and considered as a rigid body. It was assumed that there is a bonded contact between the two parts. While the medial surface of the EC core was assumed fixed as it is in contact with the EC bony part, the remaining surfaces were considered as free. Four parameters were considered in the FE model as shown in Fig. 1: outer EC core diameter (D), soft tissues length from lateral to medial plane (L), orientation of the medial plane corresponding to the soft tissues/bone transition plane (θ), position of the TMJ condyle center regarding to the EC core lateral plane (x).

The least squares criterion (LSC) was computed to evaluate the similarity between the FE-deformed OM-EC and the CM-EC, where the latter is considered as the reference. A trial-and-error method based on minimizing the LSC was used to find the optimal values of four geometrical parameters that ensure the best coupling between EC and TMJ condyle.

Results and Discussion

The FE model setting leading to the lowest LSC value was $D = 50$mm; $L = 18$mm; $\theta = 12°$; $x = 8$mm. The best set of parameters locates the TMJ condyle center between the two EC bends. This result is consistent with assumptions made in previous studies focused on EC dynamic motion [5,6]. As the transition between soft and bony part of the EC is very complex, it is difficult to accurately model their border from the anatomical point of view. However, the orientation parameter θ enables to model the isthmus, the narrowest part of the EC considered as the anatomic landmark to locate the transition plane.

Although the human EC anatomy is far from unique and this study was carried out only on one subject, the proposed model represents an important step for future research aiming at understanding the EC-TMJ coupling.
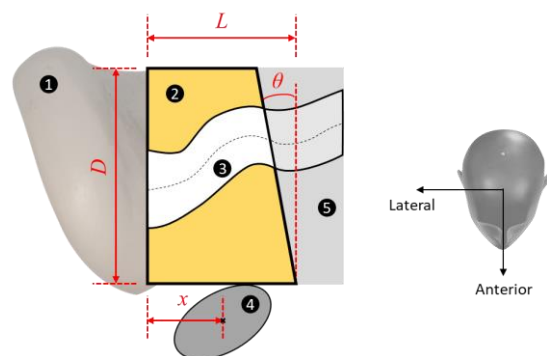
Figure 1: Schematic representation of the ear in the transverse plane with the pinna (1), the soft tissues (2) surrounding the EC cavity (3), the TMJ condyle (4) and the bony part of the EC (5). The 4-parameters FE model includes the EC cavity, its surrounding soft tissues and the TMJ condyle in contact.

References

1. Bouchard-Roy et al., IEEE Sensors J, 20 (12): 6338–45, 2020.
2. Carioli et al., AIP Advances, 6 (12): 125203, 2016.
3. Demuynck et al., J of Mechanisms and Robotics, 13 (6): 065001, 2021.
4. Peck et al., Archives of Oral Biology, 45 (11): 963-982, 2000.
5. Pirzanski, Hearing Review, 13(5), 39, 2006.
6. Oliveira et al., Hearing Review 12 (2): 18-19, 2005.

Acknowledgements

27th Congress of the European Society of Biomechanics, June 26-29, 2022, Porto, Portugal

ADAPTIVE QUASI-LINEAR MODEL – UNIVERSAL MATERIAL PARAMETERS OF LIVER TISSUE FOR DIFFERENT LOAD CASES?

Martin Frank (1), Othniel J. Aryeetey (1,2), Sarah-Jane Esterman (1,2), Dieter H. Pahr (1,2)

1. Division Biomechanics, Karl Landsteiner University of Health Sciences, Austria;

2. Institute of Lightweight Design and Structural Biomechanics, TU Wien, Austria

Introduction

The adaptive quasi-linear (AQLV) model is able to accurately predict the visco-elastic behavior of porcine liver tissue for ramp and hold experiments at multiple strain levels [1]. Since several closed loop solutions exist analytically for the AQLV model [2] it can potentially predict the stress response of different loading scenarios, like triangular and sine wave excitation. Further, the model should compensate for differences in strain rate between calibration and prediction. However, this assumption will only be valid if the AQLV model parameters, calibrated on ramp-hold experiments, are indeed material properties, independent of the loading scenario. Goal of the current study was to use experimental strain data from different loading scenarios to predict stress with the AQLV model and to compare the output to experimental stresses.

Methods

AQLV model parameters for porcine liver tissue were taken from a previous study on tensile ramp-hold experiments, with a slow pulling speed of 0.1 mm/s (n=8) [1]. Further, experimental results (stress/strain-time) of liver samples loaded in tensile mode with fast ramp-hold (pulling speed of 12.5 mm/s, n=10), sine wave excitation (at frequencies of (0.5, 1.0, 1.5, 2.0) Hz, n=12), and slow triangular load-unload (pulling speed of 0.08 mm/s, n=10) were obtained from a previous study [3]. All loading tests (calibration and prediction) were performed in the very same test set-up, but with different samples. The equations for stress prediction of the AQLV model were adapted for ramp unloading and sine wave excitation analytically. Three different aspects were investigated for all three load cases: (1) Usage of original AQLV model parameters obtained from [1], (2) re-scaling of model stress by multiplication with the ratio of amplitudes of model stress to experimental stress (A_{AQLV}/A_{data}), and (3) additionally re-calculation of relaxation times (τ) based on ramp time or excitation frequency.

Results

Usage of the original AQLV model parameters (1) could not properly predict the stress of any load case (see Figure 1, left). Even rescaling of the stress amplitude still indicated a pronounced deviation from experimental results (see Figure 1, middle, red ellipses). However, adaptation of amplitudes and relaxation times resulted in a very accurate prediction of the stress responses of all load cases. As such, also the loss tangent (phase shift between stress and strain for sine wave excitation) could be predicted accurately.

Discussion

AQLV model parameters, obtained in ramp-hold mode, are no universal material constants, e.g. they are not valid for different loading scenarios or strain rates. However, rescaling of the stress amplitude and adaption of the relaxation times by the ramp time or the sine wave excitation frequency resulted in satisfying model outcomes. The dependency of relaxation times on strain rate is in accordance with previous findings about Fung's QLV model [4]. Taken together, the AQLV model can be used to predict different loading scenarios properly, but only if the model parameters are adapted.
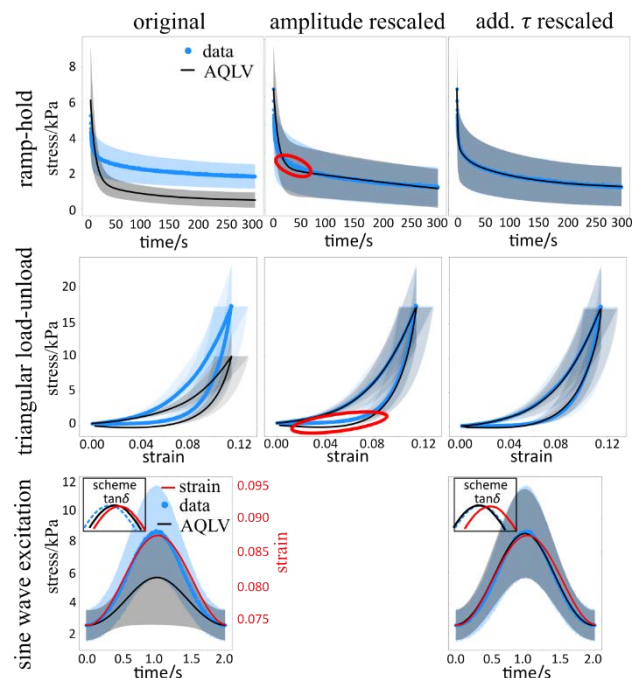
Figure 1: Average experimental stress data (blue) and AQLV model predictions (black) for different load cases, based on original model parameters (left), amplitude rescaled (middle), and additionally τ rescaled (right). Curves show mean ± standard deviation.

References

1. O. J. Aryeetey et al., J Mech Behav Biomed Mater. 2022, 126: 104999
2. A. Nekouzadeh et al, J Biomech. 2007; 40(14): 3070–3078
3. S.-J. Esterman et al., J Mech Behav Biomed Mater. 2020, 112(3):104038
4. B. Babei et al., Mech Behav Biomed Mater. 2018; 84: 198–207

Acknowledgements

NUMERICAL AND EXPERIMENTAL EVALAUTION OF THE BULGE TEST IN THE CHARACTERISATION OF THE BIOLOGICAL SOFT TISSUES

Emanuele Gasparotti (1,2), Stefano Quartieri (3), Emanuele Vignali (1), Francesco Bardi (4), Roberta Lazzeri (3), Simona Celi (1)

1. Fondazione Toscana Gabriele Monasterio, Italy; 2. Information Engineering Department, University of Pisa, Italy; 3. Civil and Industrial Engineering Department, University of Pisa, Italy; 4. ISERM University of Lyon University Jean Monnet, Italy;

Introduction

The ascending thoracic aortic aneurysm (aTAA) is one of the most serious heart diseases leading to sudden death in case of abrupt rupture. Correct modelling of mechanical anisotropic behavior is essential for studying disease progression. As far as biaxial mechanical assessment is concerned, the bulge test is a technique used to study soft tissues [1]. It involves the applying a pressure to square specimens through a circular cavity. The resulting strain field is extracted from Digital Image Correlation (DIC) [2], while the stress field is evaluated with inverse analysis (IA) [3]. The aim of this study is to develop a new bulge testing machine by evaluating the influence of material properties and cavity shapes on IA accuracy to predict the bulge test stresses in aTAA specimens.

Methods

The machine design consists in a first phase of finite element analysis to simulate the bulge test steps. Firstly, a flat specimen, was bulged during the baseline simulations. The dimensions of the specimen were defined on the basis of average dimension recorded a database of 40 aTAA specimens previously tested with a biaxial tensile machine [4]. The model was constrained at the lateral surfaces and subjected to bulge test pressure at the bottom surface. Regarding the material properties, an established hyperelastic, anisotropic, two fiber-based model was used [4]. Elliptical mask cavities were simulated, related to the different shapes of the bulge cavity to be studied. In the second phase, the IA was used to evaluate the stress fields during the bulge test by elaborating the deformed shapes resulting from the baseline simulations. For each bulge configuration, the stress error (δ) committed by the IA was evaluated via baseline stresses comparison. The influence of material and geometrical parameters on IA accuracy was assessed by varying the collagen fiber direction angle (λ), the angle (α) between the ellipse major axis and the circumferential axis ($\theta\theta$) and the ellipse eccentricity (ρ). After defining the best elliptical contour mask design on the basis of δ, the bulge test machine was developed and realized. The machine was realized to meet the requirements of gripping, sealing and referencing of the specimen, while allowing rapid exchange of cavities. Pressure connections were included to control e measure the load during the test. Stereolithography additive manufacturing technique was adopted to realize the machine.

Results

Figure 1a shows the error of IA in the analysis of the circular cavity ($\rho=1$). The error δ depends on the degree of anisotropy and shows values above 45% when the material properties are strongly anisotropic ($\lambda<10°$ and $\lambda>80°$). The results of the simulations of the elliptical cavity (Figure1 b-c) show the dependence of the δ on the α-angle for the same degree of anisotropy of the material. The introduction of angled elliptical cavities leads a reduction of δ values also on highly anisotropic materials down to 10%. The realized bulge tests setup is showed in Figure 1d with the magnification of the bulge machine developed for testing elliptical bulge cavities.
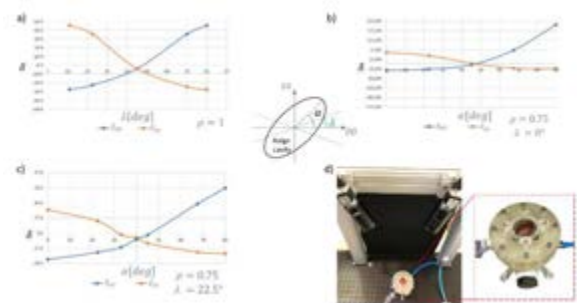
Figure 1: IA error related to circular (a) and elliptical shapes (b-c) and developed bulge setup (d).

Discussion

A new bulge test machine was developed by evaluating the accuracy of IA for predicting the stress field induced by the bulge test on aTAA specimens using a numerical approach. The results show that the circular bulge is unsuitable for testing highly anisotropic tissues due to the high error of IA in stress evaluation. On the contrary, the introduction of elliptically angled mask cavities reduced the stress error. This opens new ways to develop a bulge testing machine capable of analysing anisotropic tissues without accuracy degradation and forcing different strain ratios.

References

1. Davis et al, Biomech. Model. Mechanobiol., 2015
2. Machado et al, Exp. Mech., 2012
3. Lu et al, Biomech. Model. Mechanobiol., 2008
4. Vignali et al, Electronics, 2021

Acknowledgements

DESIGN AND EXPERIMENTAL STUDY OF ULTRASONIC WAVE BIOREACTOR TO EVALUATE EFFECT ON TUMORS

Manuel Hurtado[*15], Carmen Griñán-Lisón[245], Gema Jiménez[245], Elena Lopez[245], Daniel Martínez-Moreno[245], Juan A. Marchal[245], Juan M. Melchor[345], Guillermo Rus[145].

1 UGR Department of Structural Mechanics, University of Granada, Politécnico de Fuentenueva, Granada E-18071, Spain. hurtadoestevez@correo.ugr.es
2 UGR Biopathology and Regenerative Medicine Institute (IBIMER), Biomedical Research Centre, University of Granada, Granada E-18100, Spain
3 UGR Department of Statistics and Operations Research, University of Granada, E-18071 Granada, Spain.
4 Excellence Research Unit "Modeling Nature" (MNat), University of Granada, Granada, Spain
5 Biosanitary Research Institute of Granada (ibs.GRANADA), University Hospitals of Granada, Spain

Introduction

Malignant melanoma has become the most common neoplasm wordwide, it has a significantly higher morbidity and mortality, resulting in 65% of all skin cancer deaths. Cancer stem cells (CSCs) possess many traits of tumor-initiating or tumor stem cells including self-renewal capacity, high tumorigenicity, and differentiation. In this study we have designed and manufactured a bioreactor that allows to study the effect of ultrasonic mechanical waves on a population of melanoma (CSCs) as a potential alternative cancer treatment. Stimulation is produced by these ultrasonic waves by the propagation of compression and rarefaction through a continuous medium. The strain in the cells produced by this mechanical stimulation of the wave generates a chemical response between the internal part and the cell surface (1). Many studies have focused in the use of low-intensity US for diagnostic of several cancer types such as breast or prostate cancer (2). However, few studies have been centered in their use as therapeutic agent targeting CSCs (3).

Methods

The main objective is to evaluate the effect of the ultrasonic mechanical wave on a CSCs culture. In order to accommodate a wider range of experimentation, a device has been designed with the purpose of evaluating various frequencies and acoustic pressure levels. Frequencies from 50 KHz to 5 MHz have been applied, and different pressures have been evaluated for each frequency to test whether mechanotransduction is more affected by frequency or pressure. To avoid additional variability in proliferation due to external factors (humidity, temperature, pass, etc.) the mentioned device allows to evaluate and compare 15 different configurations of the same cell line and population simultaneously.

To make the design of the bioreactor, it has followed certain guidelines due to the different ultrasonic transducers used and the different frequencies and characteristics of those.

Acoustic waves properties have been analyzed and characterized as the near field, attenuation or impedance to achieve a standard geometry between the different ultrasonic beam and develop it adapted to the dimensions of the incubator.

Results and conclusion

An Ultrasound bioreactor has been developed, that allow the application of the ultrasonics mechanical waves. The configuration of different frequencies and acoustic level pressure used in this work is a contribution in itself. The experiment was performed for 72 hours, where proliferation pattern was affected after waves application. Figure 1 shows one of the experiments, the cells treated with ultrasound (1MHz and 5MHz) have a lower growth rate. In conclusion, our results strongly proved that acoustic waves affected to CSCs which allows establishing a targeted therapy against each tumor cell. Ultrasonics waves could constitute a new non-invasive treatment against melanoma that could be applied in clinic in monotherapy or with those already existing as a combined treatment.
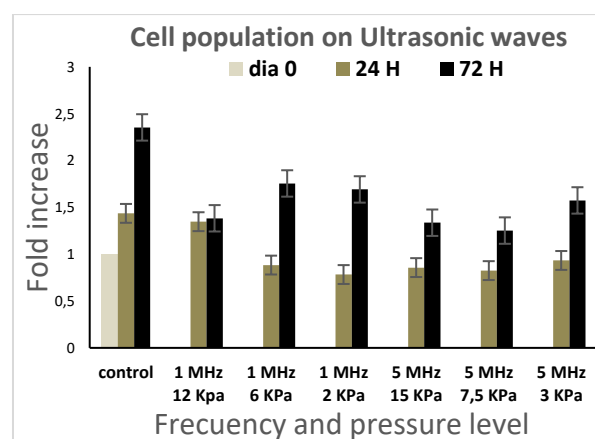
Figure 1: Proliferation assay in cancer stem cells, Control (day 0), 24 hours and 72 hours.

References

1. Lijun Kang, Jingwei Gao, William R Schafer, Zhixiong Xie, and XZ Shawn Xu. C. elegans trp family protein trp-4 is a pore-forming subunit of a native mechanotransduction channel. Neuron, 67(3):381{391, 2010.
2. Shieh AC. Biomechanical Forces Shape the Tumor Microenvironment. Ann Biomed Eng [Internet]. 2011 May
3. J. Y. Hwang et al., "High-frequency ultrasound microbeam induced calcium elevations in cancer cells: Discrimination between invasive and non-invasive breast cancer cells," 2012 IEEE International Ultrasonics Symposium, 2012.

EXPERIMENTAL PROCEDURE AND FINITE ELEMENT ANALYSIS TO MAP MECHANICAL CONSTITUTIVE PARAMETERS OF ARTIFICIAL MENISCUS

Gregorio Marchiori (1), Matteo Berni (1), Massimiliano Zingales (2), Caterina Mannone (2), Stefano di Paolo (1), Stefano Zaffagnini (1), Nicola Francesco Lopomo (3), Massimiliano Baleani (1), Milena Fini (1)

1. IRCCS Rizzoli Orthopaedic Institute, Italy; 2 University of Palermo, Italy; 3 University of Brescia, Italy

Introduction

The role of the menisci in the knee homeostasis is well recognized. Since partial or total meniscectomy still represent the most performed surgeries, to avoid "post-meniscectomy syndrome" it is fundamental to replace the resected tissue with allograft or artificial scaffold [1]. In the latter approach, an ideal artificial implant should mimic the mechanical behaviour of the native tissue [2]. In this regard, literature often reports generic/partial information [3], which are not even sufficient to implement the basic constitutive model (i.e., isotropic linear elastic). Therefore, aim of this study was to design a procedure able to describe the mechanical performance of meniscal material without imposing *a priori* hypotheses about constitutive parameters, by combining experiments and Finite Element Modelling (FEM) of indentation testing.

Methods

An artificial meniscus (95% bovine collagen fibers, 5% glycosaminoglycans by dry weight) was soaked in PBS for 24h to reach a steady rate of fluid sorption. Subsequently, the sample was placed in a testing chamber filled with PBS. Indentation was performed by a multi-axis mechanical tester (Biomomentum, Canada) equipped with a multi-axis load cell and with a spherical indenter (Ø = 2 mm) (*Fig.1*, left), using a displacement control [4]. Displacement-force curve was collected. In parallel, a FEM model of the indentation test was implemented (*Fig.1*, right); meniscus geometry was obtained by microtomography.
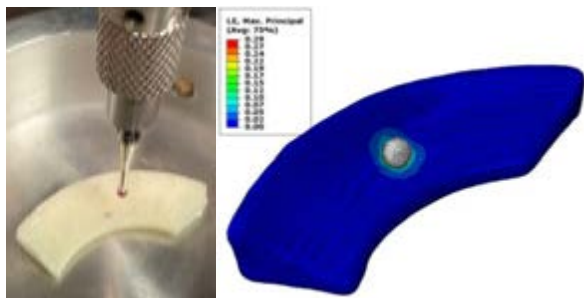
Fig.1: artificial meniscus experimental indentation (left) and corresponding Finite Element Model mapping max principal logarithmic strain LE (right)

Boundary conditions were the same of the experimental testing. Meniscus tetrahedral mesh and bottom fixing underwent a convergence analysis. The indenter was rigid; the meniscus was isotropic linear elastic. Meniscus constitutive parameters, Young's modulus E and Poisson's ratio v, assumed seven values in the range 0.1-1 MPa [5] and 0.20-0.48 [6], respectively. For each point of this (E, v) grid, simulation was run, displacement-force curve extracted and compared to the experimental one to calculate the Root Mean Square Error (RMSE). A Response Surface was fitted on the Error grid; the minimum of this Surface gives the optimal (E, v) for the material in the indented point.

Results & Discussion

Response Surface (*Fig.2*) provided 0.44 MPa and 0.43 as best E and v, respectively, for the artificial meniscus. E is in the range of the native meniscus Indentation Modulus [4]. Nevertheless, the here presented value has been obtained for a long PBS bath before testing. The procedure adopted by the clinician to implant the scaffold, which starts from a dry situation, should be considered as well.
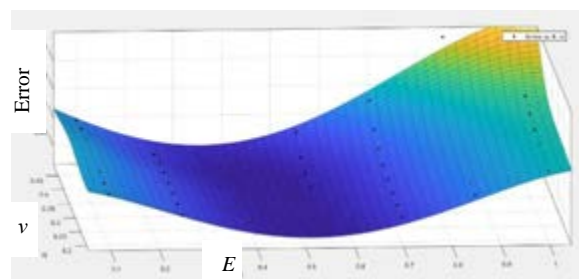
Fig.2: Response Surface fitted on the RMSE of the simulated (E, v) grid

Conclusions

Integrated experimental-numerical approach can be adopted to map constitutive parameters of the artificial meniscus and assess regional inhomogeneity (internal-external, horns-pars intermedia [7]). Moreover, authors are working to relate those parameters to microarchitecture information revealed by microtomography on the corresponding zones, thus providing important feedback to the scaffold design.

References

1. Grassi et al, Ann Joint, 2021.
2. Pietrzak et al, 978-1-59745-239-7, 2008.
3. Sandmann et al, Musculoskelet Disord, 14(324), 2013.
4. Seitz et al, Front Bioeng Biotechnol, 9:659989, 2021.
5. US 2014/0296980 Patent
6. Danso et al, J Biomech, 77:233-237, 2018.
7. Berni et al, Acta Biomater, 135:393-402, 2021

Acknowledgements

EX-VIVO HUMAN TONGUE MUSCLE MECHANICAL CHARACTERIZATION

M. A. Nazari[1,4], P. Perrier[2], C. Jeanin[3], S. Veyre[3], C. Masri[4], Y. Payan[4]

1: University of Tehran, Iran; 2: UGA, Grenoble INP, France; 3: Université Claude Bernard, Faculté d'odontologiem France; 4: Université Grenoble Alpes, CNRS, France

Introduction

Mechanical characterization of human tongue has a great influence on modelling of its complex behaviour. The strong nonlinearity and also anisotropy make this characterization more difficult. The non-invasive methods like indentation or aspiration tests usually need a presumption of the underneath layers beneath the measurement probe. The elastography methods also suffer from small displacement assumption which is not sufficient for soft tissue accounting large deformations. Moreover, all of these methods cannot eliminate the effect of initial stresses in the tissues. For this reason, the invasive tests are preferred [1] which for living human subjects is implausible. For this purpose, a cadaver study (ex-vivo) is a step forward to have better identification of the mechanical properties of human tissues.

Method

Tongue of a human cadaver with signed consent of its donor was extracted in Lyon Hospital anatomy laboratory and transferred in zero-degree saline solution. Specimen from tongue musculature both along fibre direction and orthogonal to it were extracted. The specimens were installed in a warm bath with temperature set equal to 37°C in uniaxial testing machine to simulate human body condition. After some loading and unloading cycles for preconditioning purpose, loading cycles were performed at different strain rates to measure viscoelastic properties as well. The last cycle continued up to complete rupture of samples.

Results

The elastic portion of the last loading cycle with a small strain rate were fitted with different hyperelastic models assuming isotropy and full incompressibility. Two linear regions connected with a middle toe region are observed, which is a typical behavior of soft materials (figure). The hyperelastic models range from low order ones such as 2 parameter Mooney-Rivlin to high order ones such as Ogden, Yeoh and Gent models. The fitted constitutive laws show significant differences (figure). None of them is able to follow the behavior for whole strain region simultaneously. By playing on the inclusion of the second or third order term in the Yeoh model strain energy density:

$$\psi = (c_1 (I_1 - 3) + c_2 (I_1 - 3)^2 + c_3 (I_1 - 3)^3)$$

it was possible to get flexibility to reach a satisfactory approximation of the toe region. The obtained results with the second order term are given in Table. 1.

c_1 (kPa)	c_2 (kPa)	c_3 (kPa)
0.357	90.17	0
0.357	0	409.05

Table 1: Parameters for Yeoh Constitutive law

The fitted curves with these values are shown along with experimental data in Figure 1. As it can be seen none of these models predict the full behavior of experimental data. Fitting the initial linear portion deviates the model to fit the second linear portion corresponding to collagen straightening.
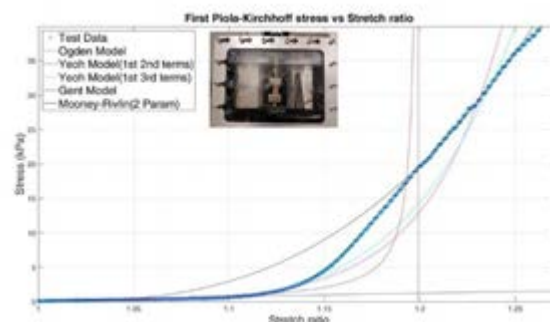
Figure 1:Constitutive Law for Human Tongue (experimental data with two different Yeoh hyperelastic models and Gent model).

Discussion

Presumably due to the collagen straightening phenomenon in soft tissues the tensile force creates a toe region which usually gets fitted with a piecewise function. These types of functions confront the 3D modelling with the problem of convergence due to needed order of continuity between regions at different loading conditions. The results suffer from the lack of anisotropy assumption but they provide a good estimate for the mechanical properties of tongue muscle matrix [2].

References

1. Yousefi, A.A.K., Nazari, M.A., Perrier, P., Panahi, M.S. and Payan, Y., 2018. A visco-hyperelastic constitutive model and its application in bovine tongue tissue. *Journal of biomechanics*, *71*, pp.190-198.
2. Nazari, M.A., Perrier, P. and Payan, Y., 2013. The distributed lambda (λ) model (DLM): a 3-D, finite-element muscle model based on Feldman's λ model; assessment of orofacial gestures. *JASA*.

TRACHEOBRONCHIAL MATERIALS COMPUTATIONAL DEFINITION

Rui B. Ruben (1,2), Jairson C. Dinis (1), João Brites Pinto (1), Carlos A. Campos (1), Mário S. Correia (1,3), Henrique Almeida (1,4)

1. ESTG, Polytechnic of Leiria, Portugal; 2. CDRsp, Polytechnic of Leiria, Portugal;
3. CEMMPRE, University of Coimbra, Portugal; 4. CIIC, Polytechnic of Leiria, Portugal

Introduction

Tracheal stenosis leads to breath and eating difficulties. Stents are a common procedure in patients with stenosis. However, silicone stents have some performance limitations related with implant migration, development of granulation tissue and accumulation of secretions. To understand stents performance and the influence of geometry and stiffness, a computational model must be defined, in order to simulate full swallowing movement. However, this is a complex computational analysis, starting with materials definition that should include airway cartilage rings, annular ligaments and smooth muscle. Computational model should also include adventitia and mucosa and submucosa membranes.

Based on an experimental materials characterization from Teng et al. [1], an optimization model was defined to computational characterize all materials. Later, equivalent material properties were obtained with homogenization. This step, can reduce the swallowing analysis time significantly without a substantial loss of detail.

Methods

Based on experimental work from Teng et al. [1], an optimization method was defined in order to obtain the best parameters to computationally define all materials. So, mucosa and submucosa membrane, tracheal muscle and adventitia membrane and cartilage rings, experimental curves were fitted to Holzapfel anisotropic hyper-elastic material. Annular ligaments were modeled as a neo-Hooke material [2] (Figure 1).

Figure 1: Materials at tracheal airway system: muscle (red), ligament (white) and cartilage (green).

To reduce complexity and running time, cartilage rings, ligaments, muscle and membranes were considered as an equivalent material obtained with homogenization [3].

Results and Discussion

Swallowing movement analysis is a very complex computational analysis. Using Abaqus software, all movement analysis takes more than 6 hours in a Xeon E3-1240v6 3.70GHz 8MB computer. With equivalent properties obtained with homogenization a significant reduction is obtained for less than 1 hour. Is, more or less, 1/6 of the time, for the same swallowing analysis. With a silicone stent, computational times are even bigger. Is possible to reduce from 12 hours analysis to less than 2 hours. Equivalent properties are the reason to have a substantial computational time reduction, however the contact results between stent and trachea are almost the same, like the example in Figure 2, where is possible to observe tangential relative displacement.
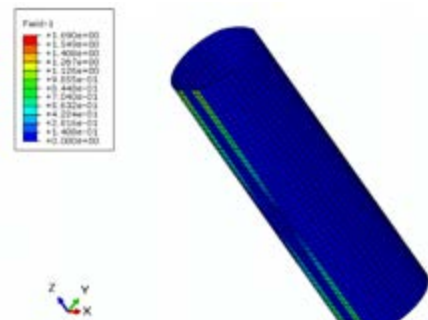
Figure 2: Maximum tangential relative displacement (mm) between stent and trachea. Without equivalent properties.

Computational time reduction is essential to the next stage in the present project. Stent in Figure 2 is only a silicone shell, but in fact stents have small studs that are essential for the performance of stents. So, the study of several stud's geometries and number are important to understand tracheal stents performance.

References

1. Teng et al, J Biomech, 45:1717-1723, 2012.
2. Trabelsi et al, Applied Mathematical Modelling, 35:4902-4912, 2011.
3. Guedes and Kikuchi, Computer Methods in Applied Mechanics and Engineering, 83(2), 143-198, 1990.

Acknowledgements

STUDY OF TORSIONAL WAVE BEHAVIOR DUE TO DEPTH CHANGE IN HYDROGEL PHANTOMS

Hirad Shamimi Noori (1), Jorge Torres (1), Guillermo Rus (1,2)

1. Department of Structural Mechanics, University of Granada, 18071 Granada, Spain, 2. Excellence Research Unit "ModelingNature" (MNat), Universidad de Granada, 18071 Granada, Spain.

Introduction

To overcome the obstacles in early diagnosis and prognosis of various diseases and injuries, numerous elastography techniques have been introduced and examined. Elastography techniques which are based on mapping the stiffness of the tissue follow two different methods, namely, Static elastography (SE) and Dynamic Elastography (DE). In (SE) tissue is subjected to the maximum deformation and will be observed through B-mode. On the other hand, in (DE) the stiffness of tissue will be evaluated by propagation of shear wave through the medium [1]. Among all the elastography methods only shear wave elastography is suitable for quantitative analysis. Shear waves propagate towards the tissues perpendicularly to the primary wave. These waves propagate in transverse planes [2]. Torsional waves which are shear elastic waves able to propagate radially in the soft tissue also have the ability of quantitative analysis. In this study propagation of torsional wave in two homogeneous and inhomogeneous mediums has been studied to understand the behavior of this wave in while penetrating in depth.

In order to conduct the tests, gelatin phantoms with different concentration of gelatin were made as single layer and bi-layer phantoms.

Materials and Methods

Two homogeneous gelatin phantoms with 15% and 25% gelatin were fabricated. A bi-layer gelatin phantom was also fabricated with the same concentration of gelatin for the two layers. Top layer was made of 15% gelatin and thickness of 3mm, and bottom layer was made of 25% gelatin and thickness of 7mm. Measurements were conducted using a torsional wave emitter which propagated the wave in burst as 1-cycle sinusoidal frequency of 1kHz and amplitude of 500mV [3], and Verasonics research system L22-14vX transducer with center frequency of 18 MHz as the receiver. First measurements were conducted by placing the emitter on top of the phantoms and the transducer vertically to receive the wave emitted with the excitation frequency of 1 kHz in both homogeneous and bi-layer phantoms. For the second measurement the emitter was placed in the same spot and the transducer was placed horizontally close to the phantom to receive the waves in the horizontal plane.

Results

Mean values for shear wave velocity acquired from 3 tests on each phantom in horizontal and vertical planes are presented in table 1.

Phantoms	Vertical (m/s)	Horizontal (m/s)
15% Gelatin	3.782±0.017	6.58±0.012
25% Gelatin	6.407 ±0.026	8.462±0.012
Bi-Layer (25%)	6.652±0.015	7.854±0.014
Bi-Layer (15%)	3.495±0.011	5.951±0.015

Table 1: Shear wave Velocity in vertical and horizontal placement of transducer

It is observed that the shear wave speed by using the torsional emission is slower while the transducer is placed vertically and the torsional wave is penetrating in depth, and the velocity is higher when the transducer is placed horizontally next to the phantom and waves are propagated radially in horizontal planes.

Discussion

In this study we measured shear wave velocity while placing the transducer vertically and horizontally next to the phantom, by emitting torsional wave with the excitation frequency of 1kHz in two mediums, i.e., homogeneous gelatin phantoms and a bi-layer phantom composed of two layers with different thicknesses and stiffness. Further studies using different combinations of frequencies and amplitudes are suggested to fully understand the behavior of torsional wave while penetrating in depth. Moreover, different parameters such as displacement amplitude and phase velocity as should be considered for future studies.

References

1. Callejas, A., et al. 2017. Performance Study of a Torsional Wave Sensor and Cervical Tissue Characterization. Sensors 17/ 2078; doi:10.3390/s17092078Somebody et al, J Biomech, 45:1-10, 2014.
2. Mihra S. Taljanovic, et al. 2017. Shear-Wave Elastography: Basic Physics and Musculoskeletal Applications. Radiographics. 2017; 37(3): 855–870.
3. G.Rus, M.Riveiro, F.S.Molina. 2018. Effect of Contact Conditions of Torsional Wave Elastographic Probe on Human Cervix. Mathematical Problems in Engineering Volume 2018, Article ID 6494758, 6 pages https://doi.org/10.1155/2018/6494758

DETERMINING TIP RADIUS IN AFM NANOINDENTATION

Stylianos-Vasileios Kontomaris[1], Anna malamou[2], Andreas Stylianou[3]

1. Metropolitan College, Greece; 2. National Technical University of Athens, Greece; 3. European University of Cyprus, Cyprus

Introduction

Atomic Force Microscopy (AFM) nanoindentation is the most commonly used technique for the determination of the mechanical properties of soft samples at the nanoscale. In this paper an approximate method to determine the tip radius when using pyramidal indenters is presented.

Sneddon's equations

Assume an axisymmetric indenter that can be described by an arbitrary function Z=f(r) which is rotated about z-axis to produce a solid of revolution. The function is selected under the condition, f(0)=0. According to Sneddon's analysis, the equations that relate the indentation depth (h) and the applied force on an elastic half space (F) with respect to the shape of the indenter are provided below [1]:

$$h = \int_0^1 \frac{f'(x)}{\sqrt{1-x^2}} dx \qquad (1)$$

$$F = \frac{2Er_c}{(1-v^2)} \int_0^1 \frac{x^2 f'(x)}{\sqrt{1-x^2}} dx \qquad (2)$$

In equations (1) and (2), x is a non-dimensional parameter defined as $x = r/r_c$ where r_c is the radius at contact depth between the indenter and the sample ($0 \leq x \leq 1$). In addition, E, v are the Young's modulus and the Poisson's ratio of the half space respectively.

An indenter with shape described by the function f(r)=ax^n, n>1.

Usually, in AFM indentation experiments the pyramidal indenters' shape can be approximately described by the following function [2]:

$$f(r) = Br^n \quad \text{or} \quad f(x) = ax^n, \quad n \geq 1 \qquad (3)$$

Using equation (1), (2) and (3) the applied force on the elastic half space is related to the indentation depth with the equation below [2]:

$$F = \frac{n}{n+1} \frac{2Er_c}{(1-v^2)} h \qquad (4)$$

In addition, it has been previously experimentally shown that the applied force on the elastic half space is provided by the following equation [3]:

$$F = const. h^m \qquad (5)$$

According to Oliver & Pharr analysis [3],

$$m = 1 + \frac{1}{n} \qquad (6)$$

Thus, by combining equations (4) and (6) it is concluded:

$$F = \frac{1}{m} \frac{2Er_c}{(1-v^2)} h \qquad (7)$$

Determining indenter's tip radius

Equation (7) is important because the function $h = f\left(\frac{F}{h}\right)$ can reveal the dimensions of the AFM tip radius since the ratio $\frac{F}{h}$ is directly proportional to r_c. To provide an example regarding the application of this method, open access simulated data on an elastic half space with Young's modulus equal to E=20kPa and Poisson's ratio v=0.5 were used. The data can be found in Atomic J repository [4]. The simulated force-indentation data were created using a pyramidal tip with θ=35°, and tip radius R=0.1 μm. As presented in Figure (1) the $h = f\left(\frac{F}{h}\right)$ graph reveals approximately the indenter's shape and tip radius (the transition depth between the spherical and the conical parts of the indenter was ~80nm).
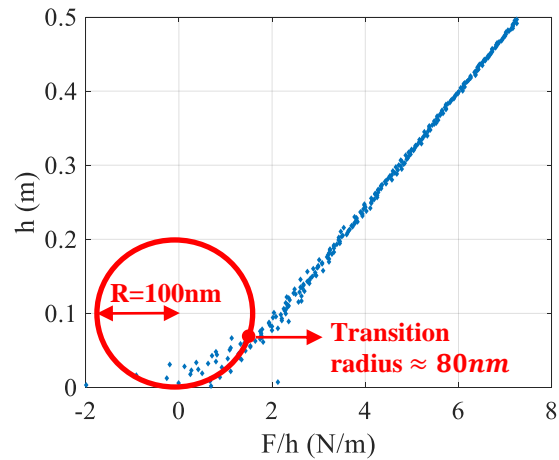
Figure 1: The tip radius determination.

Discussion

The significant advantage of the presented method is that it does not require additional equipment or experiments for the AFM tip calibration. It only requires the same force indentation data used for the determination of the samples' mechanical properties (under the condition that the sample behaves like an elastic half space).

References

1. Sneddon I N, Int. J. Engng Sci., 3, 47-57, 1965.
2. Kontomaris S V et al, Eur. J. Phys. Eur. J. Phys. 43, 2022
3. Oliver W C and Pharr G M Mater. Res. **19** 3–20, 2004
4. Hermanowicz P et al. Rev. Sci. Instrum. 85 063703, 2014

HIS ANGLE, FOOD VISCOSITY AND LSG: HOW THEY AFFECT GASTROESOPHAGEAL REFLUX. A FLUID-STRUCTURE STUDY

Ilaria Toniolo (1,2), Alice Berardo (2,3), Michel Gagner (4), Mirto Foletto (5), Emanuele Luigi Carniel (1,2)

1. *Department of Industrial Engineering of the University of Padova, Italy; 2. Centre for Mechanics of Biological Materials, University of Padova, Italy; 3. Department of Civil, Environmental and Architectural Engineering, University of Padova, Italy; 4. Department of Surgery, Hôpital du Sacré-Coeur de Montréal, Canada; 5. Department of Surgery, Oncology and Gastroenterology, University of Padova, Italy*

Introduction

Gastro-esophageal reflux disease (GERD) affects quality of life [1]. Laparoscopic Sleeve Gastrectomy (LSG) could induce *ex novo* GERD and worsen pre-existing GERD because of the higher gastric pressure due to the great reduction of the stomach capacity and the wider His angle [2]. Fluid-Structure Interaction (FSI) computational models which couple the solid mechanics of the gastric wall, and the fluid domain of the bolus, could highlight the biomechanical aspects that vehiculate GERD after LSG.

Materials and Methods

A 2D stomach model was created by means of Solidworks® program (Dassault Systemes, 2018) which included a 20mm-widht and 138mm-long esophageal tract (Fig. 1). Post-surgical geometries simulating the LSG procedure, were created by varying His angles (the angle between the fundus of the stomach and the esophageal tract). A displacement equal to a closed LES region of 95 % was imposed to mimic the closing action that takes place after food intake to prevent reflux events, while the intragastric pressures were imposed as those reported in [3] and equal to 2800 and 4466 Pa for pre- and post-surgical configurations, respectively. The FSI simulations were performed by means of the general-purpose code Comsol Multiphysics 5.4 (Comsol Inc., Burlington, MA, USA) by imposing a laminar flow.
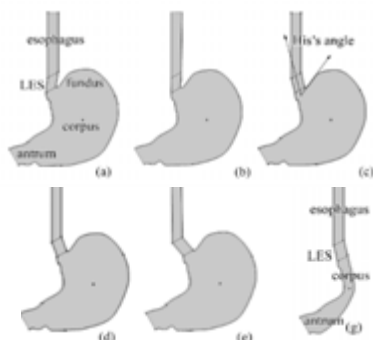
Figure 1: 2D models of pre-surgical configurations considering different His angles: 25 ° (a), 30° (b), 45° (c), 50° (d) and 65° (e) and 2D post-surgical model with His angle of 25° (f).

Average mechanical behaviours were derived by combing the circumferential and longitudinal behaviour of the different regions composing the stomach (fundus, corpus and antrum) in order to simplify the gastric tissues as an isotropic hyperelastic material [4].

Results

The flow values were computed by integrating the velocity on the distal line of the esophagus and applying the Pappo-Guldino theorem. Pre-surgical configurations recorded the lowest value of the reflux compared to post-surgical ones (Fig. 2).
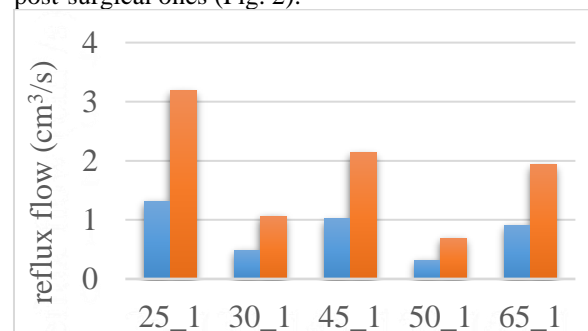
Figure 2: Reflux flow values expressed in cm³/s. Viscosity was imposed equal to 1 Pa·s and the internal pressure to 4466 Pa. The blue bars are related to pre-surgical configuration and the orange ones to post-surgical one.

Conclusion

The preliminary results could be a starting point to analyse the link existing between anatomical features apported by bariatric surgery and reflux events. Further studies able to deep interpreter the reflux insurgence concerning 3D geometries must be performed.

References

1. El-Serag et al, Gut, 63, 2014.
2. Itani et al, Curr Treat Options Gastroenterol, 18, 2020.
3. Quero et al, Obes. Surg., 30, 2020.
4. Toniolo et al, J Mech Behav Biomed Mater, 125, 2021.

Acknowledgements

VERTEBRAL BODY TETHERING VS SPINAL FUSION: LOOKING BEYOND THE RADIOGRAPHICAL OUTCOME

Thijs Ackermans (1), Sebastiaan Schelfaut (1, 2), Pieter Severijns (1), Anja Van Campenhout (2), Lieven Moke (1, 2), Pierre Moens (2), Lennart Scheys (1, 2),

1. Institute for Orthopaedic Research and Training (IORT), Faculty of Medicine, KU Leuven, Leuven, Belgium; 2. Division of Orthopaedics, University Hospitals Leuven, Leuven, Belgium

Introduction

Adolescent Idiopathic Scoliosis (AIS) is a growth defect of the spine that primarily occurs in pre-pubertal children and is surgically treated when a curve exceeds 50° [1]. Presently, spinal fusion (SF) surgery is established as the gold-standard treatment modality for patients with AIS [1]. Although, SF is associated with successful long-term outcomes in terms of deformity correction, it is also associated with a loss of spinal motion at the fused levels [1]. Therefore, fusionless treatments of progressive curves might be appealing, especially in the skeletally immature. Vertebral Body Tethering (VBT) is a fusionless growth-modulating technique for skeletally immature AIS patients with good curve control in selective indications [2]. Although the radiographic outcome, in the form of curve correction, is usually inferior to modern SF [2], potential advantages over spinal fusion have been reported in terms of function [1]. Nevertheless, comparative objective measurements of the degree of preservation of motion associated with both techniques are as of yet scarce. The aim of the present study is, therefore, to objectively measure and compare the postoperative trunk mobility, activity levels and functional outcome scores between VBT patients and SF patients.

Methods

From our prospective study sample (N=32) we matched 5 VBT patients based on curve type (Lenke classification), gender and follow-up duration with 5 SF patients. Preoperatively (Pre-OP) and at three months post-operatively (Post-OP) patients completed the following patient reported outcome measures (PROMs): SRS-22 (scored from 0-5), International Physical Activity Questionnaire (IPAQ) (scored from 0-5) and pain intensity scale (scored from 0-10). In addition, the daily step count (SC) obtained through a wrist-worn activity tracker (Xiaomi Mi Band, version 5) was averaged over a period of seven consecutive days. Furthermore, at both timepoints the patients performed a spinal deformity-specific motion analysis [3] that was captured using a 10-camera motion capture system (VICON Motion systems Oxford, UK) and consisted of a seated maximal trunk flexion in three directions (forward and laterally to the left and right side) and, additionally, all patients walked on a split-belt treadmill (Motek, Amsterdam, NL) at 1.25m/s. Maximal trunk flexion (°) was calculated using the markers placed on C7 and the pelvis. During walking the range of motion (RoM) of the shoulder and pelvis (°) in the frontal and transverse plane was determined from the relevant marker positions. A one-way ANOVA ($p<0.05$) was performed to identify differences between groups.

Results

Radiographically, the main cobb angle correction from Pre-OP to Post-OP was significantly ($p<0.05$) greater for the SF group (Pre-OP = 51.2°; Post-OP = 12.4°) compared to the VBT group (Pre-OP = 48.6°; Post-OP = 20.4°).

In terms of the PROMs, the VBT group showed Post-OP a greater (p=0.19) overall score in SRS-22 (Mean SRS-22 score: VBT = 4.1 vs. SF = 3.6), predominantly caused by the significantly ($p<0.05$) greater Post-OP scores in the subdomain 'function' (SRS-Function: VBT = 4.4 vs. SF = 3.4). Both groups had little to no pain Post-OP (VAS-score: VBT = 0.1 vs. SF = 0.2). In addition, no significant differences in Post-OP physical activity levels were identified on the IPAQ (VBT = 1.8 vs. SF = 1.7) and daily SC (VBT = 4698 steps/day vs. SF = 5089 steps/day).

In terms of trunk flexion, the loss of forward flexion from Pre-OP to Post-OP was significantly ($p<0.05$) greater for the SF group (Pre-OP = 82.9°; Post-OP = 47.1°) compared to the VBT group (Pre-OP = 93.6°; Post-OP = 87.0°). No significant differences in lateral flexion were found from Pre-OP to Post-OP between groups. In addition, the SF group had a greater (p = 0.37) overall reduction from Pre-OP to Post-OP in trunk motion during walking compared to the VBT group (RoM: VBT = -0.7% vs. SF = -9.3%).

Discussion

The present study aimed to integrate a radiographical comparison with an objective comparison of VBT and SF on the functional level. Even though SF patients have a superior radiographic outcome, this contrasts with improved spinal mobility (especially during forward flexion) and better PROMs (especially, in SRS-22 functional scores) in the VBT patients. These advantages of VBT should be further investigated in view of treatment selection in skeletally immature AIS patients whose curves progressed beyond the range of bracing.

References

1. Pehlivanoglu et al, Spine Deformity, 9:1175-1182, 2021.
2. Rushton et al, Spine Deformity, 21:1461-1467, 2021.
3. Severijns et al, Spine J, 20:934-946, 2020.

MECHANICAL CHARACTERIZATION OF THE NERVE ROOTS BY TENSILE TESTING

Audrey Berriot (1,2,3,4), Eric Wagnac (2,3,4), Elisabeth Laroche (2,3,4), Morgane Evin (1,2)

1. Laboratoire de Biomécanique Appliquée, UMRT24 AMU/IFSTTAR, Marseille, France ; 2. iLab-Spine – Laboratoire International en Imagerie et Biomécanique du Rachis, Marseille, France & Montréal, Canada ; 3. Department of Mechanical Engineering, Ecole de Technologie Supérieure, 1100 Notre-Dame Street West, Montréal, Québec H3C 1K3, Canada ; 4. Research Center, Hôpital du Sacré-Coeur de Montréal, 5400 Gouin blvd, Montréal Québec, H4J 1C5, Canada

Introduction

Cerebro-spinal fluid dynamics in the spinal subarachnoid space has been studied through numerical models. It was highlighted that the presence of nerve roots (NR) has an important impact in term of velocity field and flow pattern [1]. To improve the mechanical behaviour of the NR in existing models, this study intends to mechanically characterise those structures under quasi-static loading conditions at different spinal levels.

Methods

Eighteen (6 cervical, 6 high thoracic and 6 lumbar) samples of NR were collected on a porcine spinal cord (80kg, 6 months, landrace mixed with Yorshire). The anterior NR, the posterior NR and bundles of fibers were tested. Tensile tests with a preload of 0.1 N, 10 sinusoïdal cycles of preconditioning and by a ramp at a strain rate of 0.1 s^{-1} (quasistatic) were performed up to failure, on a Mach-1 V500cst mechanical tester (Biomomentum, Canada) equipped with a 17 N load cell (Fig. 1A). Maximum stress (σ_f), strain at maximum stress (ε_f) and modulus of elasticity for the toe and linear regions (E1 and E2 respectively) (Fig. 1B) were calculated from the load-displacement curves [3].
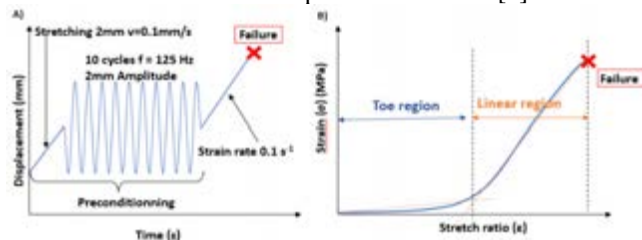

Figure 1: A) Test protocol B) Typical mechanical response of a sample subjected to uniaxial stretch.

Results

Elastic moduli were found to be higher for the bundle samples than for the posterior and anterior NR. Higher elastic moduli were found for the anterior NR than for the posterior (Table 1, Fig. 2). For every spinal region, higher maximum stress and strain were observed for the anterior and posterior NR.

Discussion

Under similar conditions, the literature reports an elastic modulus of 1.3 MPa (SD : 0.8) at lumbar level [2] which

seems consistent with our result of 0.96 MPa. Results from our pre-study seems to indicate that the behaviour of the spinal nerve roots is stiffer compared to a simple bundle of nerves. Further testing will enable a statistical analysis to confirm these observations.

		n	E1 (MPa)	E2 (MPa)	ε_f	σ_f (MPa)
C	Anterior	2	0.018	0.99	0.34	0.18
	Posterior	2	0.014	0.34	0.41	0.067
	Bundle	2	0.084	1.4	0.19	0.56
T	Anterior	2	0.20	0.69	0.25	0.090
	Posterior	2	0.015	0.097	0.29	0.053
	Bundle	1	0.066	4.3	0.20	0.70
L	Anterior	2	0.013	0.37	0.31	0.066
	Posterior	2	0.085	0.23	0.27	0.050
	Bundle	2	0.12	0.96	0.14	0.12

Table 1: Representative mechanical parameters obtained at each spinal level (mean). C : Cervical region ; T : thoracic region ; L : lumbar spinal region. n : number of specimen.
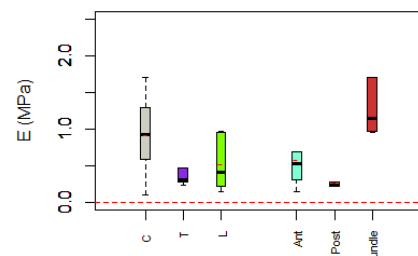
Figure 2 : E2 between spinal levels and location.

References

1. Heidari Pahlavian, Soroush, Theresia Yiallourou, R. Shane Tubbs, Alexander C. Bunck, Francis Loth, Mark Goodin, Mehrdad Raisee, et Bryn A. Martin. 2014. « The Impact of Spinal Cord Nerve Roots and Denticulate Ligaments on Cerebrospinal Fluid Dynamics in the Cervical Spine » édité par K. Sleegers. PLoS ONE 9(4):e91888. doi: 10.1371/journal.pone.0091888.
2. Singh, Anita, Ying Lu, Chaoyang Chen, et John M Cavanaugh. 2006. « Mechanical Properties of Spinal Nerve Roots Subjected to Tension at Different Strain Rates ». Journal of Biomechanics 39(9):1669-76. doi: 10.1016/j.jbiomech.2005.04.023.
3. Tamura, Atsutaka, et Mizuki Sakaya. 2018. « Dynamic Tensile Behavior of Fiber Bundles Isolated From Spinal Neve Roots: Effects of Anatomical Site and Loading Rate on Mechanical Strength ». *Journal of Engineering and Science in Medical Diagnostics and Therapy* 1(3):031001. doi: 10.1115/1.4039560.

EVALUATION OF TRUNK MUSCLE ANTAGONISM PREDICTIONS BY MULTI-BODY MODELS

Alice Caimi (1), Stephen J. Ferguson (1), Dominika Ignasiak (1)
1. Institute for Biomechanics, ETH Zurich, Zurich, Switzerland

Introduction

Musculoskeletal models are widely used in spine biomechanics research, but their ability to predict activation of antagonist muscles, and the validity of such predictions remain questioned. Optimization-based simulations minimize muscle effort in the system, therefore are not expected to predict antagonism. However several spine models (e.g., AnyBody model) do predict it, likely because they fulfill conditions suggested in the literature to facilitate it [1,2,3]. Considering the complexity of current models and the lack of available comprehensive analysis, model-predicted trunk muscle antagonism is still poorly understood. Therefore, the aims of this study were to demonstrate the influence of individual factors enabling and modulating predicted antagonism, and to validate these predictions.

Methods

To demonstrate under which conditions optimization-based models can predict muscle antagonism, simple models (2 or 3 segments) were created to study 2D vs. 3D problem, with simple vs. multi-joint muscles, solved using an activity-based muscle optimization function. The AnyBody lumbar spine model [4] was then used to investigate the effects of acceleration profile and modeling intra-abdominal pressure (IAP) on predicted antagonism during several simulated tasks: sagittal, frontal and transverse motion of the spine (Table 1), with and without 20kg hand load. The predicted coactivation ratio was compared to EMG-based experimental results reported in the literature.

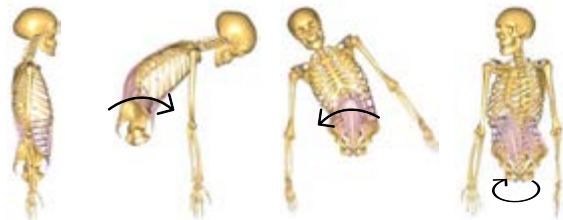| Upright standing	Forward flexion 60°	Lateral bending 30°	Axial rotation 45°

Table 1: Illustrations of the simulated posture and dynamic tasks.

Results

Simulations of simplified models demonstrated that antagonism was predicted when multi-joint muscles were present in the model, for both planar and three-dimensional models, unless muscles were symmetrical.

In the three-dimensional models, antagonism was predicted also with only single-joint muscles. No antagonism was predicted by a planar model with single-joint muscles only. The activation of muscles antagonist to various simulated motions, as predicted with the lumbar spine model, was generally in accordance with electromyographic data reported in the literature, for all considered muscle groups except for the rectus abdominis. The coactivation ratio of abdominal and extensor muscles at different flexed body postures was negligibly influenced by the acceleration of movement and generally reduced with the exclusion of IAP from the model (Fig. 1). In the upright standing posture, antagonism was markedly overpredicted.
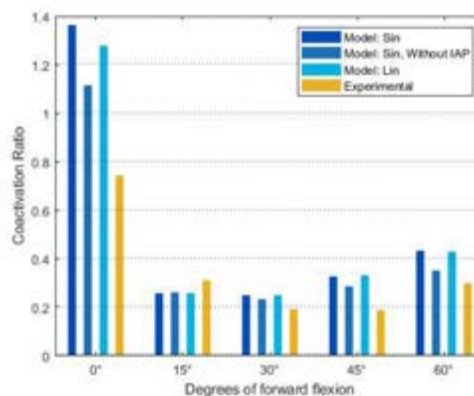
Figure 1: Predicted coactivation ratios (abdominal muscles activity/extensor muscles activity) for different positions of forward flexion using sinusoidal (Sin), linear (Lin) kinematic patterns and excluding the IAP (Without IAP).

Discussion

The analysis of simplified models demonstrated the conditions needed for antagonism predictions (as previously suggested by the literature): 3D models or multi-joint muscles. This provides an explanation why some current models predict antagonism. The antagonist activations predicted with the AnyBody lumbar spine model for several various tasks compared well with available experimental data, suggesting model validity in this respect. The findings of this study contribute to building confidence in the use of musculoskeletal models of the spine for future clinical and ergonomic investigations.

References

1. Herzog and Binding, Mathematical Biosciences, 111: 217-229, 1992.
2. Jinha et al., Mathematical Biosciences, 202: 57-70, 2006.
3. Stokes and Gardner-Morse, 28 : 173-186, 1995.
4. de Zee et al., J Biomech, 40: 1219-1227, 2007

INTRA-OPERATIVE MEASUREMENT OF THE SPINE: TOWARDS IN VIVO BIOMECHANICAL DATA OF PATIENTS WITH IDIOPATHIC ADOLESCENT SCOLIOSIS

Felix Erb (1), Nicolas Gerig (1), Daniel Studer (2), Philippe Büchler (3), Carol Hasler (2) and Georg Rauter (1)

1. Department of Biomedical Engineering, University of Basel, Switzerland; 2.Orthopaedic Department, University Children's Hospital Basel (UKBB), University of Basel, Switzerland; 3. ARTOG Center for Biomedical Engineering Research, University of Bern, Switzerland

Absence of Data

Adolescent idiopathic scoliosis (AIS) is among the most frequent deformities, with an overall prevalence of 0.47-5.2% [1]. In severe cases that would otherwise result in a progression of the scoliosis and thus endanger a patient's mobility and health, different surgical strategies are performed: posterior fusion (75%), anterior fusion (18%), or a combination thereof (7%) [1]. Currently, the main challenge of surgical strategies is to find a balance between the patient's mobility and structural stability while minimizing the risk of complications and follow-up treatments.

Currently, the decision on the treatment is based on empirical data of clinical studies and the surgeon's experience.

Another option to gain deeper insight into the underlying biomechanics of spine deformities are in ex vivo cadaveric studies using a spinal loading simulator. However, in general, the donor spines do not represent the pathology of interest since they originate from elderly individuals. Additionally, spinal loading simulators require isolating the spine or spine segments from the supportive neighboring tissue (muscles, ligaments). Accordingly, the lack of in vivo biomechanical data on patients with AIS, limits the development of novel treatment strategies and surgical approaches.

To overcome the issues of acquiring in vivo data on the intervertebral spine stiffness in three planes in the target population, a 6 Dof parallel robot (SpineBot) has been developed [2]. The design of the SpineBot was based on first intra-operative force assessments in AIS patients to establish force requirements for sufficient relative vertebra displacements [3].

Towards a SpineBot 2.0 System

Through requirement analysis taking into account safety, workspace volume, and weight/load ratio, the current SpineBot showed significant limitations that prevent its use in a clinical context. A parametrized kinematic model able to induce a flexion of [-5°: 5°] in 3 planes on a spinal segment is constructed based on the design by Büchler et al. [2].

We are currently building up a Pre-interventional planning and visualization tool to evaluate robot configuration and motion during the interoperative stiffness measurement procedure. Such a tool will further enable rapid prototyping for the SpineBot 2.0, reducing measurement time intra-operatively, and facilitating the integration of biomechanical simulation of the data.

Current Work

Due to our analysis, we decided to revise the current SpineBot. Furthermore, we propose an absolute force/torque sensor-actuator concept to achieve pure bending moments. As a first step in concept realization, we realized a tool of volumetric spine rendering and pedicle screw placement in VR (Unity Software).
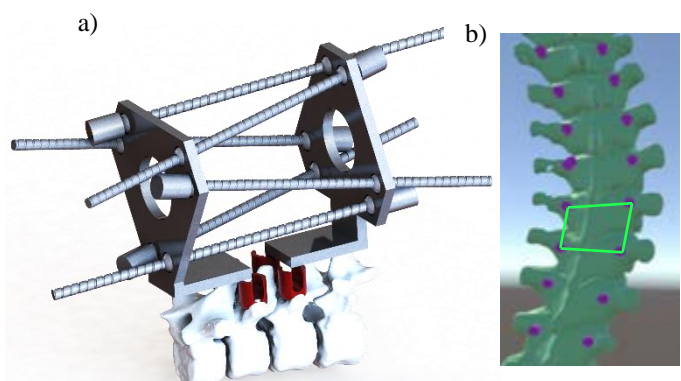
Figure 1: a) Concept SpineBot 2.0 attached to vertebra (T09-T11) via pedicle screws (red) b) VR tool of pedicle screw placement and orientation (spinal segment highlighted in green).

Outlook

Knowledge gained from instrumented in vivo spine manipulation to obtain spine impedance/stiffness, stability, and mobility of scoliotic and non-scoliotic segments will foster the development of realistic Musculoskeletal simulations, novel treatment strategies, and novel implant design that can revolutionize the way AIS patients are treated in future.

References

1. Mohrej et al, A. of Medicine and Surgery, 52:19-23, 2020.
2. Buechler et al, J. of Medical Devices, 15(1):011111, 2021.
3. Reutlinger et al., European Spine J. 21:860-867, 2012

Acknowledgements

FORWARD DYNAMIC SIMULATION OF A DETAILED THORACOLUMBAR SPINE MODEL UNDER GRAVITATIONAL LOAD

Maria Hammer (1,2), Julia M. Riede (1), Laura Meszaros-Beller (3), Syn Schmitt (1,2,3)

1. *Institute for Modelling and Simulation of Biomechanical Systems, University of Stuttgart, Germany*
2. *Stuttgart Center for Simulation Science (SC SimTech), University of Stuttgart, Germany*
3. *School of Mechanical, Medical and Process Engineering, Queensland University of Technology, Brisbane, Australia*

Introduction

Computer modelling and simulation is a key technique for research in spine biomechanics, to gain insight into the biomechanical interplay of soft tissue elements. In order to study the response, such as damage or degeneration, of biological tissue to mechanical loads, the load distribution among all compartments of the spine must be known. Recently, the load sharing of muscles, ligaments and intervertebral discs (IVDs) was investigated for passive, externally driven spine movements [1]. With the help of a detailed spine model, we here continue this work and examine the contribution of the main structures to active spine motions like forward flexion starting from an upright posture using a forward-dynamic approach.

Methods

We developed a state-of-the-art generic neuro-musculoskeletal model of a healthy thoracolumbar spine in the multibody simulation framework demoa (https://get-demoa.com). It bases on the lumbar spine model of [2], revised and validated for passive motions in [1], and is fully articulated in the spinal column from pelvis to the first thoracic vertebra (T1), i.e. with free intervertebral joints (six degree of freedom joints) on every spinal level. The relative motion of two adjacent vertebrae is only restricted by IVDs, ligaments and muscles. While IVDs are represented by Bushing elements, the 192 ligament strands and 294 muscles fascicles are implemented as line actuators, partly redirected using the via-ellipse method [3].

Using a simple hybrid controller as in [4] and keeping the pelvis spatially fixed, we let the model settle under gravity and initiate purely muscle-driven flexion-extension movements.

Results

In the simulated settling process of our spine model, we observe that a low level of muscle activity (below 5% of maximum isometric force) is sufficient to balance the spinal column in an upright position while the weight of the upper body is fully borne by IVDs. Afterwards, the model performs a controlled bending movement with capability to hold the flexed position and to return to an upright posture – solely actuated by muscles. The analysis of the bending moment in the lumbar spine shows similar shares of ligaments and IVDs - with increasing influence of ligaments for large flexion angles - whereas passive and active muscle forces contribute only 25-30% to the total joint moment. During the entire movement, we achieve realistic activation levels for all muscles and also the overall stiffness of all passive compartments is in good agreement with experimental findings from [1].

Figure 1: Forward-dynamic, muscle-driven simulation of a spine movement. Starting from an equilibrated upright posture (left), the model performed a forward flexion (center and right), held the peak (right) and lifted itself back into the upright position.

Discussion

The presented spine model is capable of withstanding gravitational loads and equilibrating in an upright position without any further joint constraints. Moreover, it enables us to study the dynamic inter-action of all four sub-structures – rigid vertebral bodies and the three soft tissue types – during muscle-driven, forward-dynamic bending movements and to predict the load distribution among soft tissue elements as well as their contribution to the joint stiffness.

References

1. Mörl et al. , *Biomech Model Mechan*, 19(6):2015-2047, 2020;
2. Rupp et al., *Biomech Model Mechan*, 14(5):1081-1105, 2015;
3. Hammer et al, *Math Biosci,* 311:68-81, 2019;
4. Bayer et al., *CMBBE,* 20(8):803-821, 2017.

Acknowledgements

THE INFLUENCE OF THE GRADE OF DISC DEGENERATION ON THE BIOMECHANICAL RESPONSE OF LUMBAR SPINE

Kinda Khalaf (1), Zahra Khoz (2), Mohammad Nikkhoo (2)

1.Department of Biomedical Engineering, Khalifa University, Abu Dhabi, UAE; 2.Department of Biomedical Engineering, Science and Research Branch, Islamic Azad University, Tehran, Iran.

Introduction

Various studies have shown that intervertebral disc degeneration, lumbar stability, motion segment flexibility and low back pain are all interrelated [1]. Hence, the impact of different grades of disc degeneration on lumbar spine flexibility and other biomechanical attributes is of great interest both to research and clinical communities, alike. Finite element (FE) modeling remains an advantageous time and cost-effective approach to investigate detailed spinal biomechanics elusive to clinical studies. Therefore, the objective of this work was to evaluate the influence of disc degeneration on the biomechanical response of the lumbar spine using geometrically patient-specific FE modelling.

Materials and Methods

Using a validated parametric poroelastic FE model of the human spine [2], six subject-specific pre-operative models were developed based on the images of 6 patients. The geometry of the lumbar spine (L1-S1) was automatically updated by inputting 125 independent parameters with user-defined code based on geometrical constraints obtained from lateral and AP X-Ray images. The FE models consisted of 5 vertebrae, sacral component, 5 IVDs, 7 ligaments and 5 pairs of facet joints. The validity of the models was assessed based on *in-vitro* [3] and FE studies [4] from literature. Furthermore, parametric FE models of the lumbar spines were developed simulating L4-L5 disc degeneration with different grades (i.e., healthy, mild, moderate, and severe degeneration), in which disc height reduction and increasing the compressibility of the nucleus pulposus were considered. Biomechanical responses, including motion patterns, intradiscal pressure (IDP) and stress in different components were analysed under the same loading and boundary conditions. The extracted ranges of motion (ROM) were compared using one-way ANOVA, where differences were considered significant at $p<0.05$.

Results

The results of the intersegmental ROMs for the healthy models were consistent with available experimental data in literature [3].Similarly, the estimated IDP was in alignment with reported data [4]. The ROM was significantly decreased in moderate and severe degenerated discs (i.e., L4-L5) in all directions. However, the ROMs at the adjacent levels were only altered in severe degeneration (Fig 1). The IDP was also significantly decreased in severely degenerated discs during flexion and extension, while relevant experienced stress significantly increased in all directions (Table1).
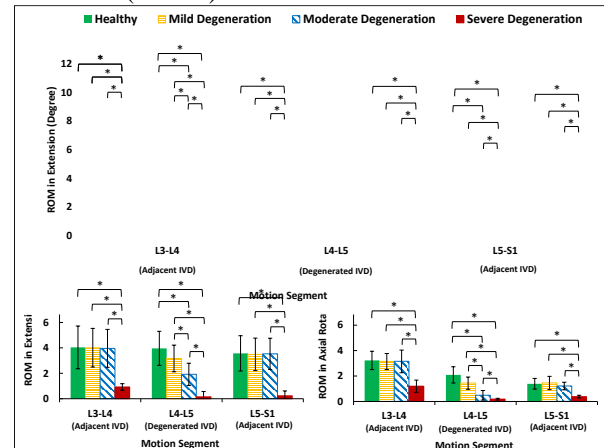

*Figure 1: Variation of segmental range of motions in degenerated and adjacent levels. *p value <0.05.*

	Flexion			Extension		
	Mild	Moderate	Severe	Mild	Moderate	Severe
Intradiscal Pressure	-5.7 (±2.2) %	-8.3 (±2.9) %	-24.1 (±5.3) %	-3.7 (±1.8) %	-6.4 (±3.5) %	-18.5 (±4.0) %
Von-Mises Stress	+4.1 (±1.6) %	+13.4 (±3.8) %	+33.6 (±7.1) %	+3.3 (±1.8) %	+11.1 (±3.2) %	+28.5 (±7.4) %
	Lateral Bending			Axial Rotation		
	Mild	Moderate	Severe	Mild	Moderate	Severe
Intradiscal Pressure	-3.8 (±2.2) %	-8.0 (±2.9) %	-24.9 (±5.3) %	-0.9 (±0.8) %	-8.9 (±3.6) %	-18.5 (±4.0) %
Von-Mises Stress	+4.1 (±1.6) %	+13.4 (±3.8) %	+33.6 (±3.1) %	+3.3 (±0.9) %	+11.1 (±3.2) %	+28.5 (±5.8) %

Table 1: Averaged IDP and Von-Mises stress in L4-L5 IVDs with different degrees of degeneration (% of healthy ones) under different lumbar motions.

Discussion

This study provided a validated FE model for investigating the effect of the degree of disc degeneration on spinal biomechanics. The results show that increased severity of disc degeneration leads to decreased ROM for both degenerated and adjacent levels. The results also reveal that higher degrees of disc degeneration reduce IDP but increase stress distribution. However, these variations are highly dependent on the degree of degeneration and the direction of movement. Importantly this work confirms that moderate and severe degeneration alter both intersegmental motion and load-sharing of the lumbar spine, hence shedding light on spinal stability towards improved clinical outcomes.

References

1. Mimura et al., Spine, 19: 1371-80, 1994.
2. Nikkhoo et al., J. Biomech, 102:109722, 2020.
3. Panjabi et al., J. Bone Joint Sur, 76:413-424, 1994.
4. Dreischarf et al., J. Biomech, 47: 1757–1766, 2014.

ASSESSMENT OF SAGITTAL BALANCE IN THE DISTAL JUNCTIONAL PATHOLOGY IN THE LUMBAR SPINE: A RETROSPECTIVE ANALYSIS

Sara Montanari (1), Cristiana Griffoni (2), Luca Cristofolini (1), Giovanni Barbanti Brodano (2)

1. Department of Industrial Engineering, Alma Mater Studiorum – Università di Bologna, Italy
2. Spine Surgery Unit, IRCCS Istituto Ortopedico Rizzoli, Bologna, Italy

Introduction

Mechanical failure of spinal posterior instrumented arthrodesis in the lumbar region is suspected to occur more frequently when sagittal balance is not adequately restored [1]. While failures at the proximal instrumented extremity have been well described, the lumbar distal junctional pathology has received less attention [2]. The aim of this work was to investigate if the spinopelvic parameters which characterize the sagittal balance are correlated with mechanical failure.

Methods

All spine surgeries performed in 2017-2019 at Rizzoli Institute were retrospectively analysed to extract all cases of junctional pathology. Lumbar distal fixation failures were included in the junctional group (JUNCT) if, in the last instrumented level, or immediately below, a revision surgery was required due to:

    i.   Pedicle screws pullout and/or
    ii.   Breakage of rods or screws and/or
    iii.   Vertebral fracture and/or
    iv.   Degenerative disc disease.

A total of 83 cases were identified as JUNCT group. All the lumbar fixation surgeries which to date have not failed (n=241) were used as control group (CONTROL). Demographic and clinical data were extracted. The software Surgimap (Nemaris) was used to assess the pelvic incidence (PI), sagittal vertical axis (SVA), pelvic tilt (PT), T1 pelvic angle (TPA), and lumbar lordosis (LL) from the preoperative (Pre-op) and postoperative (Post-op) standing lateral X-rays.

Results

Distal lumbar junctional pathology onset was observed within two years on the first vertebral fixation in 51.8% of cases. In JUNCT, the main failure cause was the screw pullout (45%). Cases with arthrodesis at 7 or more levels were the most common in JUNCT (51.8%) in contrast to CONTROL (14.1%). In JUNCT, in 71% of cases the Post-op SVA was outside the recommended range for good stability (SVA<±40mm [3]) despite the correction. Before revision surgery (Pre-rev), in 65.4% of patients suffered an increased imbalance. Conversely, in 63.1% of CONTROL, a good spine alignment was observed Post-op. In JUNCT, the worsening of the balance was also confirmed by the increase in PT and TPA by comparing Post-op and Pre-rev values (p=0.004, p= 0.0003, *Wilcoxon test*) (Table 1). Comparison of regression models of PT versus PI, SS versus PI and LL versus PI (Figure 1) between JUNCT and CONTROL showed different trends without statistically significant differences (p = 0.57, 0.46 and 0.35 respectively, *Z-test*) in Post-op.

	Pre-op	**Post-op**	**Pre-rev**	
PT [°]	17.6 (8.5)	20.3 (7.7)	-	**CONTROL**
	25.9 (12.8)	21.5 (9.3)	26.1 (11.0)	**JUNCT**
TPA [°]	14.3 (9.5)	15.9 (7.5)	-	**CONTROL**
	23.4 (15.6)	18.7 (10.2)	25.2 (14.3)	**JUNCT**

Table 1: Comparison of spino-pelvic parameters PT and TPA before the first fixation (Pre-op), after fixation (Post-op) and before revision surgery (Pre-rev). For each group mean (st. dev.) are indicated.
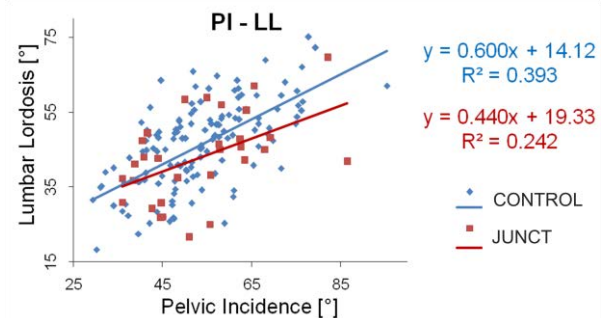
Figure 1: Regression models of LL versus PI from Post-op x-rays for the JUNCT and CONTROL groups.

Discussion

These preliminary results showed that failure is most common in long fused segments, likely due to long lever arms leading to screw pullout or implant failure. This effect was confirmed by the worsening of PT and TPA before the revision surgery compared to Post-op. The PT increase (increased pelvic retroversion) indicates a compensatory mechanism for the altered mechanical balance. Additionally, in cases of fixation failure the increase of the TPA (a measure of deformity over the whole spine) confirms changes of the load distribution. Our results show also that SVA is a reliable parameter to monitor the patient balance over time. The surgical planning using PT, SS and LL related to PI is important to restore the sagittal balance, but it does not seem to prevent mechanical failure.

References

1. Lau et al, Spine, 39:2093-2102, 2014.
2. Berjano et al, Eur. Spine J, 29:86-102, 2020.
3. Schwab et al, Spine, 37:1077-1082, 2012.

DEVELOPMENT OF A FULLY-PARAMETRIC THORACOLUMBAR SPINE MODEL AND CALIBRATION OF T6-T7-R7 FSU

Alice Perego (1), Alice Pezzinga (1), Luigi La Barbera (1)

1. Laboratory of Biological Structure Mechanics, Dept. of Chemistry, Materials and Chemical Engineering "Giulio Natta", Politecnico di Milano, Italy

Introduction

Spine pathophysiology is often investigated using very detailed patient-specific biomechanical models, often including few functional spinal units (FSUs), which can be hardly generalized. Fully-parametric spine models easy-to-adapt to any patient promises to be a more efficient strategy to scale up biomechanical problems by including entire populations featuring a desired range of spinal morphologies and alignments. Therefore, the present study aimed at: i) developing a fully-parametric thoracolumbar spine model based on few independent parameters, ii) calibrating the kinematic response of a representative thoracic FSU assigning adequate mechanical properties to subcomponents.

Material and Methods

Regression analysis and CAD model. Mean anatomical data describing 38 dependent parameters for each vertebra [1,2], were plotted as a function of the posterior height of the vertebral bodies (VBHP, assumed as the only independent parameter) and best-fitted with a third order polynomial regression line. The coefficient of determination (R^2) and the Root Mean Square Error (RMSE) were used to quantify the validity of these equations for each vertebral level. The regression equations were implemented in Solidworks 2020 (Waltham, MA, USA), where the morphology of each vertebra, approximated through elementary geometrical structures, was fully defined. T1-T12 thoracic kyphosis (*TK*), L1-L5 lumbar lordosis (*LL*), and sacral slope (SS) were implemented as additional independent parameters [3], allowing to assemble the vertebrae and to set the desired sagittal alignment (Figure 1). Rib cage description relied on average values [4,5].
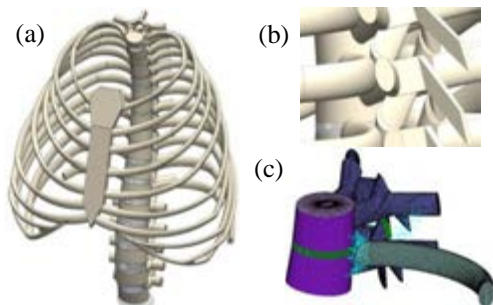

Figure 1: Developed parametric model representing the average spine of a healthy adult (a), and meshed T6-T7-R7 FSU model including the costovertebral joint and ribs (b).

Calibration of T6-T7-R7 FSU FE model. One FSU was meshed in Abaqus 2020 (Simulia). A backward stepwise reduction approach was adopted and FSU components (from the nucleus up to ribs and sternum) were sequentially added to the model calibrating the mechanical properties of each component by comparison with the available *in vitro* kinematic data (RoM, range of motion) for FSU [6], FSU+left rib [7], and FSU+ribs+sternum [8].

Results

Regression analysis and CAD model. The RMSE of the predicted values with respect to the anatomical measurements was much lower than the mean experimental dispersion (8 vs. 20%).

Calibration of T7-T8-R7 FSU. Calibration ensured an accurate description of the kinematics behavior in each loading direction by assigning adequate mechanical properties (Figure 2).
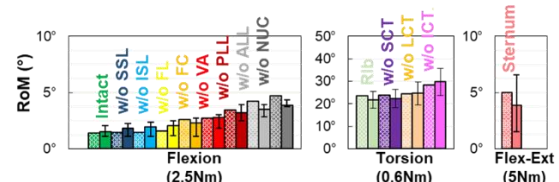

Figure 2: Examples of range of motion (RoM) calibrated using the backward stepwise reduction strategy applied on T6-T7-R7 FSU.

Discussion and Conclusions

The result of the regression analysis supported a satisfactory and overall accurate description of the 38 dependent parameters simply using VBHP as a single independent parameter. The additional independent parameters (TK, LL, SS), which are widely used in clinical practice, potentially allow to easily describe other global sagittal alignment, both in the physiological and pathological ranges. The proposed thoracolumbar spine model is based on few independent parameters, which make the proposed model much simpler than any other available to date. Based on the proposed approach, finite element models can be promptly developed and calibrated, providing useful biomechanical information.

References

1. Panjabi et al, Spine (Phila Pa 1976), 16(8):888-901, 1991.
2. Panjabi et al, Spine (Phila Pa 1976), 17(3):299-306, 1992.
3. Pesenti et al, Clin Orthop Relat Res, 476(8):1603-11, 2018.
4. Holcombe et al, J. Anat, 231(2):229-427, 2017.
5. Selthofer et al, Coll Antropol, 30(1):43-47, 2006.
6. Wilke et al, Eur Spine J, 29(1):179-185, 2020.
7. Lemosse et al, Eur Spine J, 7(1):16-23, 1998.
8. Liebsch et al, Spine J, 20(3):488-498, 2020.

Acknowledgements

AN INVERSE DYNAMIC ACTIVE HYBRID MODEL TO PREDICT EFFECTS OF THE INTRA-ABDOMINAL PRESSURE ON THE LUMBAR SPINE

Robin Remus (1), Andreas Lipphaus (2), Alina Hoffmann (1), Marc Neumann (1), Beate Bender (1)

1. *Chair of Product Development, Dept. of Mechanical Engineering, Ruhr-University Bochum, Germany*
2. *Biomechanics Research Group, Dept. of Mechanical Engineering, Ruhr-University Bochum, Germany*

Introduction

Although low back pain is a major health concern, many cause-effect relationships are still poorly understood. However, many lower back problems can be associated with excessive loads during lifting activities. At the same time, there is a multitude of studies, guidelines, and measures for prevention and treatment. With the aim of protecting the spine, an often pursued approach involves stiffening the trunk and increasing the intra-abdominal pressure (IAP) [1]. The IAP can be increased intrinsically by activating the abdominal muscles or extrinsically by an enclosing spinal orthosis. The effects of elevated IAP on lumbosacral spine loads and muscle activities while holding a heavy load in different positions were simulated.

Methods

We used a validated model of the ligamentous lumbosacral spine [2] built in ArtiSynth [3] and enhanced with pelvis, thorax, and a muscle set (Figure 1A). The rigid vertebrae L1-S1 are interconnected with hyperelastic fiber-reinforced finite element intervertebral discs, ligaments, and facet joints. Lumped masses and moments of inertia were applied to all movable segments. Applied muscle datasets [4,5] were geometrically [6] and materially scaled. To reduce the number of individual activations to be optimized the muscles were grouped in 22 excitation components. Simplified as a central force acting on the diaphragm, the IAP was calculated assuming an ideal cylinder with constant volume compressed by the forces acting perpendicularly on the abdominal plate. All abdominal muscles were attached to the abdominal plate, which, like the muscle wrapping bodies, were kinematically driven by the vertebrae, pelvis, and thorax. Intradiscal pressure (IDP), muscle excitations, and IAP were predicted by inverse static simulations while keeping the chest upright. Three load cases *C* and three forms of IAP influence *P* were investigated: To replicate holding a heavy crate with arms close at chest level (*C2*) and extended (*C3*) in upright standing position a 20 kg load [7] was applied to the center of both hands. For reference, no load was lifted (*C1*) and the IAP was not manipulated (*P1*). Also, IAP was set to 25 mmHg (*P2*) and transversus abdominis muscles were activated by 60% (*P3*).

Results

All results depended on the predicted IAP, external loads, and muscle activity. For *C1-3* at *P1*, the L4/5 IDP were 0.68, 1.02, and 1.78 MPa, which agreed well with

values measured in vivo [7]. Increasing the IAP without a lifted load barely changed the IDP (Figure 1B). In case of C1, the IAP for *P1-3* were 9.1, 35.2, and 20.8 mmHg, respectively. For C3 all latissimus dorsi muscle excitations varied by less than 10% and were below 52%.
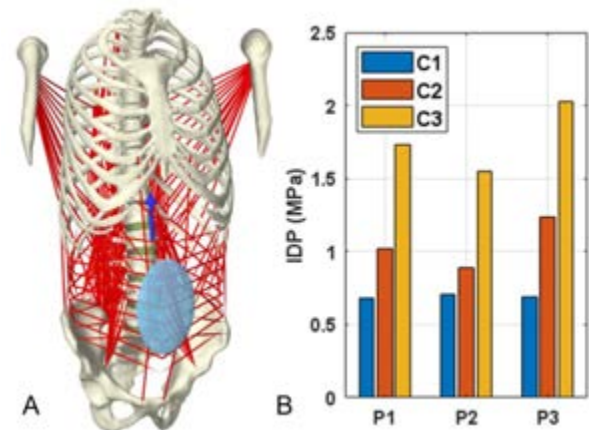

Figure 1: A) Active hybrid model with muscles in red, abdominal plate in transparent blue, and IAP force. B) Comparison of L4/5 IDP for evaluated load cases C.

Discussion

Different load cases and boundary conditions in upright standing were investigated. Without manipulating the IAP, the loads on the intervertebral discs showed very high agreement with in vivo data [7]. Further postures like leaning forward and load cases need to be investigated. The compressive influence of lumbar orthoses could only be simulated to a limited extent by increasing the IAP. Influences of the load-transmitting soft tissues must be considered in the future. Abdominal muscle contraction resulted in an increased IDP and a stabilization of the spine was assumed. Nevertheless, the generation of the IAP was simplified and could lead to erroneous assumptions. Only increasing the IAP relieved disc pressure during load lifting, but barely reduced posterior muscle activity. Overall, by combining classical finite element and multibody methods, the active hybrid model used demonstrated its potential for further studies on the lumbar spine.

References

1. Stokes et al., Clin Biomech, 26(8): 797–803, 2011
2. Remus et al., PloS One, 16(4): e0250456, 2021
3. Lloyd et al., 978-3-642-29014-5, 355-394, 2012
4. Christophy et al., Biomech MM 11(1):19-34, 2012
5. Bayoglu et al., J Biomech, 53:111-119, 2017
6. Modenese et al., J Biomech, 73:108-118, 2018
7. Wilke et al., Clin Biomech, 16(1):111-126, 2001

IN VITRO STUDY OF THE INFLUENCE OF VERTEBRAE GEOMETRY ON THE BEHAVIOUR OF LUMBAR ARTHROPLASTY PROSTHESES

François ZOT (1), Arnaud GERMANEAU (1), Med Amine LARIBI (1), Juan SANDOVAL (1), Laëtitia CAILLÉ (1), Yann LEDOUX (3), Michel MESNARD (3), Estelle BEN BRAHIM (1, 2), Mathieu SEVERYNS (1, 4), Valéry VALLE (1), Tanguy VENDEUVRE (1, 2)

1. Institut Pprime, UPR 3346 CNRS – Université de Poitiers – ISAE ENSMA, Poitiers, France; 2. Department of Orthopaedic Surgery and Traumatology, University Hospital, Poitiers, France; 3. Institut de Mécanique et d'Ingénierie, UMR 5295 CNRS – Université de Bordeaux, Bordeaux, France; 4. Department of Orthopaedic Surgery and Traumatology, University Hospital, Martinique, France.

Introduction

The management of degenerative phenomena of the spine, particularly the lumbar spine, is a major health issue. Indeed, degenerative discopathies of the lumbar spine are frequent and disabling (low back pain, radiculalgia, etc.). Surgical arthrodesis procedures (TLIF, ALIF, OLIF, etc.) have provided a relevant response to this problem [1]. Nevertheless, the significant hindsight of these techniques has revealed mechanical complications in the medium and long term (adjacent syndromes, dislocations, etc.). This can be explained by the transfer of stress from the treated disc to the adjacent levels [2]. From this observation, a new approach to the treatment of disc disease has emerged: arthroplasty. The advantage being the preservation of physiological mobility. However, the majority of prostheses available on the market seem to offer a uniform design for a multitude of patients with varying spinal anatomy. These geometric variabilities probably have an influence on the biomechanical behaviour of the implants. The objective of this work is to study the influence of vertebral geometries on the biomechanical behaviour of prostheses during physiological loads.

Methods

To perform these tests, we used a 7DoF Franka Emika robot to apply pure moments to our samples and to reproduce physiological loads (Figure 1). The robot was positionally controlled for each direction: flexion/extension, lateral bending and axial rotation. Maximum amplitudes were imposed in accordance with the literature [3] with a moment limit set at +/- 5N.m.

Two lumbar interbody prostheses were studied: Prodisc-L (Centinel Spine) and Mobidisc-L (Zimmer Biomet). The tests were performed on two types of spine segments:
- Two demonstrators of spinal units (3D printed, ABS) with flat endplates
- Real geometry of 10 spinal units printed from 3D models obtained from segmentations of CT-scans of 5 anatomic lumbar spinal segments (2F/3M). For each spinal unit, the lower vertebra was fixed, while the upper vertebra was linked to the robot end effector.

Moment data was provided by the robot's internal sensors, and ranges of motion were measured by an Optitrack V120 Trio camera system.
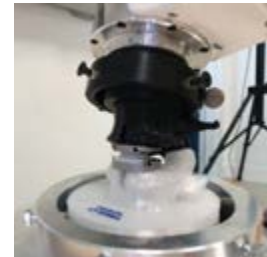

Figure 1: Loading setup with 2 vertebrae (L4 and L5) and the Prodisc-L (Centinel Spine) prosthesis.

Results

Ranges of motion were measured for each type of demonstrator specimen and for the different studied prostheses. Table 1 presents the results obtained on the prosthesis Prodisc-L for both types of plate geometry.

Spinal unit	Flat endplates	Real geometry
Flexion/Extension	+19.1 / -19.1	+18.5 /-12.6
Lateral Bending	+18.9 / -18.9	+14.2 / -17.5
Axial Rotation	+180 / -180	+0.24 / -0.78

Table 1: Ranges of motion (degrees) measured for the three simulated physiological movements offered by the prosthesis Prodisc-L (Centinel Spine)

Discussion

This study provides objective data of ranges of motions given by lumbar interbody prostheses fixed on realistic geometries and under physiological loadings. This studied did not considered interface with bone and supposed a perfect joint with endplates. Tests on healthy anatomical segments will have to be carried out in order to compare the behaviour of the prostheses (i) with mechanical response given by intact discs and (ii) by considering a real joint with bone tissues in a case of primary stabilisation. Furthermore, it will be relevant to analyse the influence of the prostheses on the mechanical behaviour of adjacent discs.

References

1. Tarpada et al, Journal of Orthopaedics, 14:134–136, 2017
2. Lee and Park, Asian Spine J,10:593,2016
3. Kapandji, The Physiology of the Joints, p. 129-133. Handspring Publishing Limited, 2019

Acknowledgements

MECHANICAL CHARACTERIZATION OF THE DENTICULATE LIGAMENTS BY TENSILE TESTING

Audrey Berriot (1,2,3,4), Eric Wagnac (2,3,4), Elisabeth Laroche (2,3,4), Morgane Evin (1,2)

1. Laboratoire de Biomécanique Appliquée, UMRT24 AMU/IFSTTAR, Marseille, France ; 2. iLab-Spine – Laboratoire International en Imagerie et Biomécanique du Rachis, Marseille, France & Montréal, Canada ; 3. Department of Mechanical Engineering, Ecole de Technologie Supérieure, 1100 Notre-Dame Street West, Montréal, Québec H3C 1K3, Canada ; 4. Research Center, Hôpital du Sacré-Coeur de Montréal, 5400 Gouin blvd, Montréal Québec, H4J 1C5, Canada

Introduction

The spinal cord is attached in the spinal canal thanks to microstructures such as nerve roots (NR) and denticulate ligaments (DL). It has been shown that the presence of these structures help maintaining the spinal cord and prevents it from non-physiological extensions [1]. For a more accurate understanding and modelling of these phenomenon, better identification of the material properties of the DL needs to be done. This study intends to mechanically characterise those structures under quasi-static loading conditions at cervical, thoracic, and lumbar levels.

Methods

Six (2 cervical, 2 low thoracic and 2 lumbar) samples of DL were collected on a porcine spinal cord (80kg, 6 months, landrace mixed with Yorshire). Tensile tests with a preload of 10 sinusoidal cycles of preconditioning and by a ramp at a strain rate of 0.1 s^{-1} and 0.5 s^{-1} (quasistatic) were performed up to failure, on a Bose mechanical tester (GRIP ASST, T/C, 3200, Bose Corporation, Framingham, Massachusetts, US) equipped with a 17 N load cell (Fig. 1A). Maximum stress (σ_f), strain at maximum stress (ε_f) and modulus of elasticity for linear region (E) (Fig. 1B) were calculated from the load-displacement curves [2,3].
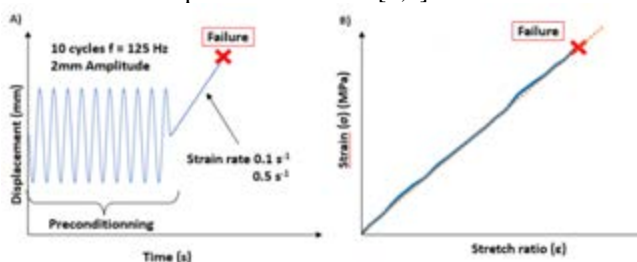

Figure 1: A) Test protocol B) Typical mechanical response of a sample subjected to uniaxial stretch.

Results

Elastic moduli were found to be higher for the thoracic and lumbar samples than for the cervical ones. Higher elastic moduli were found for a strain rate of 0.5 s^{-1} at all spinal levels (Table 1, Fig. 2).

Discussion

Under similar conditions, the literature reports an elastic modulus between 3.26 MPa (SD : 1.45) and 4.42 MPa (SD : 2.27) at cervical level [3] which seems consistent with our results of 3.65 MPa (SR : 1 s^{-1}) and 4.67 (SR : 0.5 s-1) MPa. Results from our pre-study seems to indicate that the behaviour of the denticulate ligaments might depends on its location. Further testing will enable a statistical analysis to confirm these observations.

	n	Strain Rate (s^{-1})	E (MPa)	ε_f	σ_f (MPa)
C	2	1	3.65	0.139	0.467
	2	0,5	4.67	0.108	0.465
T	2	1	6.65	0.0713	0.769
	2	0,5	8.71	0.0759	0.808
L	2	1	6.17	0.0741	0.430
	2	0,5	6.95	0.0770	0.399

Table 1: Representative mechanical parameters obtained at each spinal level (mean). C : Cervical region ; T : thoracic region ; L : lumbar spinal region. n : number of specimen.
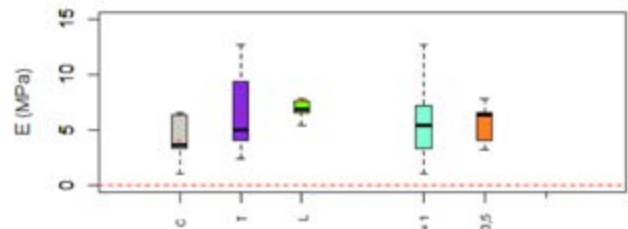

Figure 2 : E between spinal levels and strain rates.

References

1. Tani, Satoshi, Shokei Yamada, et Robert S. Knighton. 1987. « Extensibility of the Lumbar and Sacral Cord: Pathophysiology of the Tethered Spinal Cord in Cats ». *Journal of Neurosurgery* 66(1):116-23. doi: 10.3171/jns.1987.66.1.0116.
2. Polak, Katarzyna, Marcin Czyż, Krzysztof Ścigała, Włodzimierz Jarmundowicz, et Romuald Będziński. 2014. « Biomechanical Characteristics of the Porcine Denticulate Ligament in Different Vertebral Levels of the Cervical Spine—Preliminary Results of an Experimental Study ». *Journal of the Mechanical Behavior of Biomedical Materials* 34:165-70. doi: 10.1016/j.jmbbm.2014.02.010.
3. Polak-Kraśna, Katarzyna, Sandra Robak-Nawrocka, Sylwia Szotek, Marcin Czyż, Daniel Gheek, et Celina Pezowicz. 2019. « The Denticulate Ligament – Tensile Characterisation and Finite Element Micro-Scale Model of the Structure Stabilising Spinal Cord ». *Journal of the Mechanical Behavior of Biomedical Materials* 91:10-17. doi: 10.1016/j.jmbbm.2018.11.017.

THE EFFECT OF CRYOTHERAPY ON BALANCE RECOVERY AT DIFFERENT MOMENTS AFTER LOWER EXTREMITY MUSCLE FATIGUE

Yuqi He[1,2], Zixiang Gao[1,2], Gusztáv Fekete[3], Dusan Mitic[4], Yaodong Gu[2]

1. University of Pannonia, Hungary; 2. Ningbo University, China; 3. Eötvös Lorand University, Hungary; 4. University of Belgrade, Serbia;

Abstract

Cryotherapy as an emerging physiotherapy gradually accepted and used by more athletes and coaches. The purpose of this study was to investigate the influence of cryotherapy on the balance ability after lower extremity muscle fatigue. Twelve table tennis players were selected in this research, all participant have to join the cryotherapy intervention (CI) at first experimental and the control group (CON) at second experimental. The static and dynamic balance abilities of the participants at six different moments (post warm up, post fatigue, post intervention, 24h post intervention, 48h post intervention and 72h post intervention) were collected by a 1000 HZ Kistler force platform and Y balance test system. SPSS19.0 software was used to analyze the results of experimental indicators by selecting two-factor repeated measurement ANOVA. The result shows that: 1) From the moment of 24h post intervention, the effect of cryotherapy on dynamic balance recovery was significantly better than no cryotherapy; 2) Except for the COP (Center of Pressure) maximum displacement on ML (Medium-Lateral axis) at the moment of 72h post intervention, the cryotherapy had no positive effect on the recovery of static balance ability; 3) Cryotherapy has a significant negative impact on the COP maximum displacement in ML and AP (Antero-Posterior axis) at the moment of post cryotherapy, which may lead to the decline of static balance ability. The conlusion of this study was that it was not recommended to use cryotherapy for balance recovery if the competition was on the same day or within 24h. The cryotherapy was recommended to use if the competition was in the next day or after the next day.

Figure 1: The comparison of balance ability recovery between CI and CON intervention at each moment. Note: "A" indicates the difference of dynamic balance. "B" indicates the difference of COP area. "C" indicates the difference of COP displacement velocity in ML. "D" indicates the difference of COP displacement velocity in AP. "E" indicates the difference of COP maximum displacement in ML. "F" indicates the difference of COP maximum displacement in AP. The "a" indicates that there is a significant difference between the moment of post warm up and other moments (post fatigue, post intervention, 24h, 48h and 72h). The "b" indicates that there is a significant difference between the moment of post fatigue and other moments (post intervention, 24h, 48h and 72h). The "c" indicates that there is a significant difference between the moment of post intervention and other moment (24h, 48h and 72h). The "d" indicates that there is a significant difference between the moment of 24h and other moment (48h and 72h). The "e" indicates that there is a significant difference between the moment of 48h and the moment of 72h. The "" indicates that there was a significant difference between the CI and the CON.*

Acknowledgements
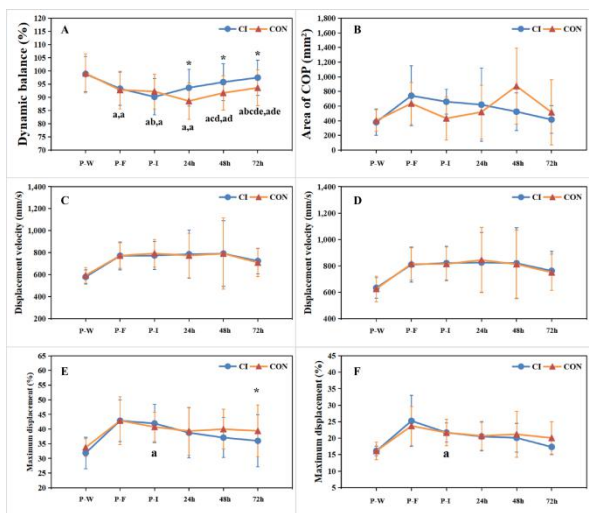
FORCE AND SWIMMING PERFORMANCE: POOL AND OPEN WATER

Phornpot Chainok (1), Radomyos Masjuir (1), Natthaphol Phewkham (2)
Piyaporn Tumnark (3), Rodrigo Zacca (4,5)

1. Faculty of Sport Science, Burapha University, Thailand; 2. Faculty of Allied Health Sciences, Thammasat University, Thailand; 3. Faculty of Sports Science, Kasetsart University, Thailand. 4. Research Center in Physical Activity, Health and Leisure (CIAFEL), Faculty of Sports, University of Porto (FADEUP), Portugal; 5. Laboratory for Integrative and Translational Research in Population Health (ITR), Porto, Portugal

Introduction

The tethered swimming test has been used by coaches and researchers to evaluate sprinting performance, aerobic and anaerobic (power and capacity), and propulsive force [1,2]. We estimated the propulsive force contributions and its relationships with swimming performance over sprinters (SP), middle distance (MD), open water (OW) and recreational (RS) swimmers.

Methods

Main physical, performance characteristics and 400-m swimming performance (T400) are present in table 1. Maximal tethered swim tests (30-s) were measured during the competitive period with load-cell system connected to the swimmer, recording at 100 Hz with a measurement capacity of 1,000 N (Swimforce V1.0.0, Germany). All swimmers performed the tethered swim tests, in randomized order, (i) with arm stroke or (ii) with leg kicking or (iii) with full front crawl (whole body). The T400 was obtained 24-h after tethered swim tests. Analysis of variance and Pearson product-moment correlation coefficients (r) were calculated.

Variables	SP (M=6,F=4)	MD (M=4,F=6)	OW (M=5,F=5)	RS (M=10)
Age (yrs)	18.7 ± 1.9	19.8 ± 1.2	17.1 ± 1.6	19.8 ± 0.6
Weight(kg)	68.0 ± 9.6	53.8 ± 2.6	53.8 ± 5.8	60.9 ± 6.9
Height (cm)	176.7 ± 7.6	169.7 ± 6.3	163.5 ± 5.2	170.2 ± 6.1
Body fat (%)	20.9 ± 6.4	18.8 ± 2.3	12.3 ± 1.7	17.4 ± 3.5
Grip strength(kg)	43.7 ± 5.4	42.9 ± 4.6	25.4 ± 5.7	35.3 ± 2.9
Jump height(cm)	50.2 ± 10.4	37.4 ± 3.9	33.9 ± 4.3	36.8 ± 2.8
T400 (s)	288.9 ± 1.4	280.4 ± 2.8	290.5 ± 2.1	483.0 ± 2.1

Table 1: Main physical and performance characteristics of the swimmers. sprinters (SP), middle distance (MD), open water (OW) and recreational (RS) swimmers.

Results

Faster T400 was identified for middle distance (F 3, 36 =19787.48; p = 0.001). Higher maximal (F 3, 37 =16.41; p = 0.001) and mean force (F 3, 37 =13.68; p = 0.001) were observed for sprint swimmers. The relative contributions of the mean force of the whole body were 66.7, 69.1, 81.6 and 114.2%; arm stroke were 55.4, 54.4, 76.0 and 80.4%, and leg kicking were 44.5, 45.5, 23.9 and 19.5% for sprinters, middle distance, open water and recreation swimmers, respectively (Table 2). No significant correlations were observed between the maximal and mean force vs. T400.

Variables	SP	MD	OW	RS
Maximum force (N)				
Whole body	438.5 ±182.5	244.6 ± 64.3	208.5 ± 8.4	157.9 ± 31.1
Arm stroke	248.6 ± 86.1	178.9 ± 87.5	175.1 ± 59.6	136.6 ± 27.7
Leg kicking	128.4 ± 33.5	119.1 ± 27.0	84.7 ± 29.9	97.5 ± 36.0
Mean force (N)				
Whole body	88.9 ± 39.7	56.2 ± 18.7	39.2 ± 20.5	34.0 ± 14.3
Arm stroke	73.9 ± 23.2	44.3 ± 16.6	36.6 ± 15.5	23.9 ± 10.4
Leg kicking	59.4 ± 11.6	37.0 ± 23.0	11.5 ± 4.5	5.8 ± 3.4

Table2: *Data collected from the 30 s fully tethered front crawl swimming tests. sprinters (SP), middle distance (MD), open water (OW) and recreational (RS) swimmers.*

Discussion

The arm stroke force produced is moderately to highly related to swimming speed in sprint distance. These findings support the idea that high-intensity front crawl swimming demand seems to be strongly influenced by the effective application of force during the arm stroke [1,2]. Mean leg kicking and arm stroke force plays an important role over short duration but is not well related to T400.

References

1. Morouço, P. G., Marinho, D. A., Keskinen, K. L., Badillo, J. J., & Marques, M. C. (2014). Tethered swimming can be used to evaluate force contribution for short-distance swimming performance. The Journal of Strength & Conditioning Research, 28(11), 3093-3099
2. . Morouço, P. G., Marinho, D. A., Izquierdo, M., Neiva, H., & Marques, M. C. (2015). Relative contribution of arms and legs in 30 s fully tethered front crawl swimming. BioMed research international, 2015.

BIOMECHANICAL ANALYSIS OF RUNNING AND ASSOCIATED INJURES BASED ON A LITERATURE REVIEW

Marcela Lucía Martínez Pinedo(1), Laura Daniela Parra Gómez(1),Christian Cifuentes-De La Portilla(1)

1. *Biomechanics group (IBIOMECH), Universidad de los Andes, Bogotá, Colombia*

Introduction

Running is one of the most common sports around the world. However, it is also associated with a high incidence of running related injuries (RRI), especially for lower limb injuries [1]. Due to differences in factors studied such as gender, footwear and technique, and methodology used in the published studies mainly because of the differences between chosen population. Currently, little consensus is found between the relationship and importance of these factors and the RRI. Thus, the objective of this review is to identify and synthesize the most commonly found injuries and the risk factors related to them in order to offer useful information for the design of RRI prevention strategies.

Methods

Four electronic databases were used: Google Scholar, PubMed, Scopus and Web of Science. Two reviewers independently screened studies for eligibility and subsequently reviewed to include a total of 63 articles. In the final selection of articles, it was only included those published since 2015 which were in English or Spanish and those that were far from the subject matter were discarded. These were divided into 4 proposed categories: most common running injuries, risk factors of running, running technique and footwear. Some of the articles were used in more than one of the categories.

Results

Injury incidence can range from 10 to 79%, the most common injuries are tendinitis (43%), muscle tears (22%) and sprains (21%) [1]. These are more frequently presented in lower limbs. Injury distribution could vary as shown in Table 1.

Lower limbs	Upper limbs
Knee (17.4%)	Lower back (8.7%)
Feet (17.7%)	Hand (0.8%)
Ankle (16.6%)	Shoulder (0.5%)

Table 1: Most common injured sites [2]

Running risk factors can be classified into intrinsic factors and extrinsic factors. Among the most reported intrinsic factors are gender, strike pattern, training, and previous injuries. Less experience, fatigue, previous injuries, a higher body mass index, and higher weight were consistently classified as risk factors. There is inconsistency about gender and age. On the other hand, the main extrinsic factors reported were footwear, surface, intensity and training distance. A higher intensity of training, as well as bad habits during it, are considered risk factors. There is no agreement about footwear, surface, and training distance.

Footwear is a risk factor extensively studied in running. However, literature is inconsistent about the benefits and risks of each footwear (conventional, minimalist, and barefoot running). The last two types cause other types of injuries that did not occur with conventional footwear. Some studies suggest that a gradual transition could reduce RRI [3]. Instead, some articles argue that there are no benefits between different footwear [4].

Regarding running technique, strike pattern the most studied factor due to its relevance in force absorption and distribution. Different advantages and disadvantages were related to each pattern, however, runners presenting a rearfoot strike were consistently more prone to RRI [5].

Discussion

Evidence in relation to risk factors for RRI is limited and highly dependent on the population, methodology, type of study, and lesions studied. Populations studied among deferent studies varied in terms of age and gender distribution, geography, type of runner, etc. Other considerations to which differences in results can attributed are the follow up time used to assess the RRI, investigations focusing on particular of RRI or factors and the criteria used to define an injury. Future research is needed to confirm above risk factors and determine whether modifying these variables can help in injury prevention and treatment. It is suggested to standardize methods in order to prevent the sources of incongruence.

References

1. Z. Noriega Barneond, M. Aguilera Cuevas, and M. Nicole, "Factores de riesgo asociados a lesiones en corredores de 16 a 68 años de edad," *Rev. médica (Colegio Médicos y Cir. Guatemala)*, vol. 158, no. 1, pp. 37–40, 2019.
2. J. P. Warne, A. H. Gruber, R. Cheung, and J. Bonacci, "Training and technique choices predict self-reported running injuries: An international study," Phys. Ther. Sport, vol. 48, pp. 83–90, Mar. 2021.
3. I. S. Davis, H. M. Rice, and S. C. Wearing, "Why forefoot striking in minimal shoes might positively change the course of running injuries," *J. Sport Heal. Sci.*, vol. 6, no. 2, pp. 154–161, Jun. 2017.
4. D. van Poppel, J. de Koning, A. P. Verhagen, and G. G. M. Scholten-Peeters, "Risk factors for lower extremity injuries among half marathon and marathon runners of the Lage Landen Marathon Eindhoven 2012: A prospective cohort study in the Netherlands," *Scand. J. Med. Sci. Sports*, vol. 26, no. 2, pp. 226–234, Feb. 2016.
5. M. A. Thompson, S. S. Lee, J. Seegmiller, and C. P. McGowan, "Kinematic and kinetic comparison of barefoot and shod running in mid/forefoot and rearfoot strike runners," *Gait Posture*, vol. 41, no. 4, pp. 957–959, May 2015.

VECTOR CODING ASSESSMENT OF LOWER LIMB JOINT ANGULAR COORDINATION ON LONG, SHORT AND NO COUNTERMOVEMENT

Carlos Rodrigues (1,2), Miguel Correia (1,2), João Abrantes (3)
Marco Benedetti (4), Jurandir Nadal (5)

1. FEUP, Portugal; 2. INESC TEC, Portugal; 3. MovLab - ULHT, Portugal
4. PPGEE - UFPE, Brazil; PEB - COPPE/UFRJ

Introduction

Muscle stretch shortening cycle (SSC) is a natural phenomenon associated with eccentric action preceding concentric contraction for powerful muscle action [1]. Despite muscle SSC can be observed at gait and run [2], its higher expression and accessibility can be observed on standard maximum vertical jump (MVJ) with long and short countermovement (CM) and SSC on countermovement (CMJ) and drop jump (DJ) for comparison with squat jump (SJ) and no CM [3]. Nevertheless, when we think about a specific movement, we do not think on muscle contraction or inhibition, with movement intention converted under central nervous control and proprioceptive system feedback for joint angular coordination [4]. In order to address lower limb joint angular coordination, linear methods have been applied [5] with an open issue on joint angle-angle nonlinear coordination assessment.

Methods

To assess lower limb joint angle-angle nonlinear variability during impulse phase at SJ, CMJ and DJ, vector coding was applied to the hip, knee, and ankle joint sagittal angle diagrams. Best MVJ trial with higher flight time was selected for each subject from 3 SJ, CMJ and DJ repetitions on a small sample of six heathy higher education sports students without specific train or sport modality, ages (21.5 ± 1.4) years, (76.7 ± 9.3) kg mass and (1.79 ± 0.06) m height. Inverse kinematics was performed from lower limb joint reflexive marks at selected anatomical points using SIMI Motion 3D. Angle-angle diagrams were plotted for the hip, the knee, and the ankle joint sagittal angle during impulse phase on each SJ, CMJ and DJ trials. Vector code was obtained for each angle-angle plot based on consecutive data points, determining coupling angle γ_i from vector projection and vector length r_i from its magnitude. Mean coefficient of correspondence was obtained for each trial by the product of the radial mean coupling angle and magnitude of directional concentration.

Results

Coupling angle presented at SJ trials initial instability with steady state convergence at the end of the impulse phase, whereas CMJ and DJ present at the start of the impulse phase negative γ with gradual transition on CMJ and sharp transition on DJ to positive values at the upward impulse phase. Vector lengths presented at SJ increasing amplitudes during entire impulse phase, with CMJ and DJ increasing values at the start of the impulse phase followed by its decrease to null values and increase amplitude at upward impulse phase with final decrease.
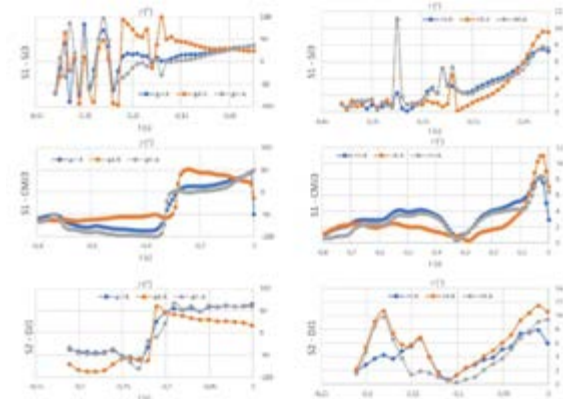

Figure 1: Coupling angle γ_i and vector length r_i time profiles of SJ, CMJ and DJ representative trials.

$\mu \pm \sigma$	H – K	A – K	H – A
SJ (γ)	46.00 ± 0.07	56.34 ± 0.13	34.33 ± 0.13
CMJ (γ)	$-48.68 \pm 0,84$	-0.62 ± 0.66	-74.86 ± 0.57
DJ (γ)	89.98 ± 0.66	56.64 ± 0.39	$-89,1 \pm 0.84$
SJ (r)	2.56 ± 0.23	2.23 ± 0.26	2.17 ± 0.27
CMJ (r)	0.61 ± 1.26	0.69 ± 0.60	0.81 ± 0.91
DJ (r)	$0.90 \pm 0,44$	0.88 ± 0.54	0.80 ± 0.33

Table 1: Hip, knee, ankle vector coupling angle, length.

Discussion

Lower limb joint coupling angle and vector length allowed detection of nonlinear coordination differences during impulse phase at SJ, CMJ and DJ. Circular mean and standard deviation of the hip, the knee, and the ankle joint coupling angles presented statistical significative differences on SJ, CMJ and DJ with lower mean and higher dispersion on CMJ. SJ presented higher mean vector length and lower standard deviation with CMJ opposite lower mean and higher standard deviation, the same trend presented by the correspondence coefficient.

References

1. Zatsiorsky, VM, Kraemer, WJ, "Science and Practice of Strength Training", Human Kinetics, Champaign, 2006.
2. Komi et al, Portuguese J Sport Sc., 11(2):31-34, 2011.
3. Asmussen, E, Acta Physiol. Scand., 91(3):385-392, 1974.
4. Latash, ML, Zatsiorsky, VM "Classics in Movement Science", Human Kinetics, Champaign, 2001.
5. Rodrigues et al, VipIMAGE 2019, LNCVB, 34:29-40, 2020.

A METHODOLOGY TO DETERMINE THE EFFECTS OF THE PITCHER-GROUND INTERACTION ON FASTBALL PITCH VELOCITY

Noelle Tuttle (1), Marco A Avalos (2), Melanie Meek (1), Young-Hoo Kwon (1).

1. Texas Woman's University, United States of America; 2. Rosalind Franklin University of Medicine and Science, United States of America.

Introduction

Baseball is one of the most popular sports worldwide and participation continues to grow each year. The number of pitchers per team is also rising, with pitchers accounting for more than half of the team roster at the Major League level [1]. With the number of pitchers increasing, so are the number of injuries [2], most of which target the pitching arm. One of the most common pitches is the fastball, which is also the highest velocity pitch type. Faster balls are harder to hit, so higher velocity pitches are desired in a game. However, players who throw repetitively at high velocities are more susceptible to injury [3]. Ground reaction forces (GRF) have been determined to be an important component of the kinetic chain and have been found to be related to pitch velocity [4]. However, the contributions of the ground reaction moments (GRM), including ground reaction force moments, foot contact moments, and pivoting moments, to pitching velocity have not yet been determined. Knowing the effects of the entire pitcher-ground interaction could allow for more effective use of the kinetic chain and result in higher velocity fastballs. The purpose of this study was to validate a methodology that could be used to determine the effects of the pitcher-ground interaction on fastball velocity.

Methods

One male baseball pitcher (age: 22 yrs, height: 185.5 cm, weight: 80.4 kg) with 15 years of fastball pitching experience was recruited for this methodology validation. The participant wore spandex shorts, normal practice shoes, and a baseball hat, and 58 retroreflective markers were placed on the body. An additional marker was placed on a standard baseball. A 10-camera motion capture system sampling at 500 Hz and 2 force plates, covered with artificial turf, sampling at 1,000 Hz were used to capture kinematic and kinetic data. The force plates were installed in a custom pitching mound, with one force plate on top of the mound and the other within the slope of the mound (Fig 1). Data was collected for 10 successful fastball pitches and was processed using Kwon3D.

Results

This methodology provided information regarding the pitcher-ground interaction and pitch velocity. The average maximum GRF for the drive foot was 1.12 ± 0.01 BW vertically and 0.48 ± 0.03 BW anteriorly; the average maximum GRF for the stride foot was 2.12 ± 0.07 BW vertically and 0.87 ± 0.05 BW posteriorly (Fig

2). The average velocity of the pitching wrist, used as an indirect indicator of ball velocity [4], was 13.86 ± 0.13 m/s.

Figure 1. Pitcher model and instrumented pitching mound.
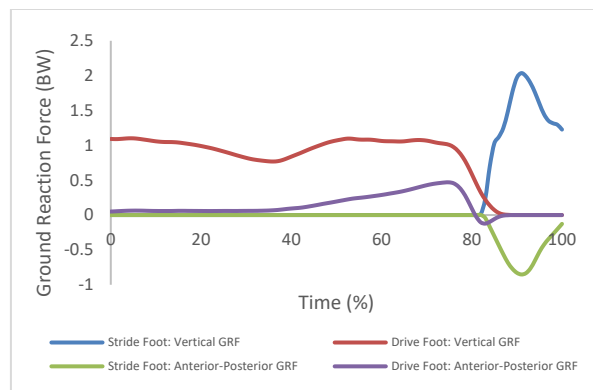

Figure 2. Vertical and anterior-posterior GRF patterns for the drive and stride feet. GRF values have been normalized by body weight.

Discussion

This methodology was able to successfully determine variables related to the pitcher-ground interaction and measures of pitch velocity. As a result of this validation study, a few changes were made to improve the methodology: camera positions were adjusted to better view the hands during the wind-up phase; the start of each trial was modified to have the hands start at the sides instead of together at the chest to avoid missing markers at the beginning of a trial; and a second force plate was added within the slope of the mound to create a larger area in which the stride foot could land. Using this methodology, future studies aim to investigate the relationship between the pitcher-ground interaction (GRFs and GRMs) and fastball pitch velocity.

References

1. Armour & Levitt, Baseball Demographics, 2021.
2. Platt et al, Orthop J Sports Med, 9(3), 2021.
3. Anz et al, Am J Sports Med, 38(7), 1368-1374, 2010.
4. MacWilliams et al, Am J Sports Med, 26(1), 66-71, 1998.

POROUS GEOMETRY OF TISSUE ENGINEERING SCAFFOLD INFLUENCES ITS INTERNAL MICROFLUIDIC ENVIRONMENT

Matthew Bedding, Feihu Zhao

Biomedical Engineering, Zienkiewicz Centre for Computational Engineering, Faculty of Science and Engineering, Swansea University, United Kingdom

Introduction

Porous scaffolds play an important part in tissue engineering experiments in vitro, they are used for the housing of cells and facilitating the application of micro-physical/chemical environment to cells during 3-dimensional (3D) cell culturing. The scaffolds have porous structures which can affect the micro-mechanical environment that the cells undergo within a bioreactor (e.g., based on perfusion flow) [1]. Therefore, the ability to tune the micro-mechanical environment on cells can be achieved via scaffold porous geometric design. This study aims to investigate the effect of pore size and porosity on the scaffold permeability and fluid-induced wall shear stress (WSS) using a combination of computational and experimental approaches. With the outcome of this study, it is anticipated to provide a reliable basis for achieving efficient design of scaffold porous geometry.

Methods

We have proposed 2.5D scaffold struts (cylindrical shape in Figure 1a), which should allow for accurate controlling of the porosity and pore size, moreover the visualisation of the internal flow path under perfusion in the experiment. The investigated pore size and porosity are in the range of 300 – 1000 μm and 50% - 90%, respectively. The struts are placed within a custom-made microfluidic device, which are fabricated with Poly(methyl methacrylate) (PMMA) by 3D printing (Figure 1a). A corresponding CFD model is set up for this microfluidic device system for calculating the scaffold permeability and WSS. In the experimental measurement, a peristaltic pump is connected to the microfluidic device for delivering the perfusion flow through the struts. The flow rate of the medium is altered using the pump to achieve an inlet velocity of 0.1 mm/s. Dyed water is used for visualizing the flow path within the struts, which will be compared to the CFD simulations.

Results

For the uniform struts, pore size was the more dominant independent variable for affecting WSS and permeability. As pore size decreased the WSS increased parabolically (Figure 1b), whilst permeability was linearly increased through increasing pore size.
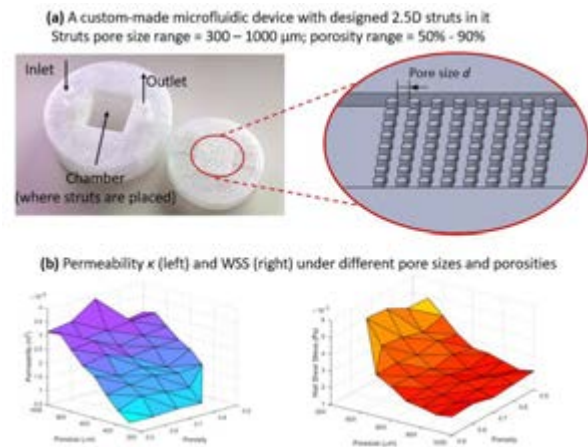

Figure 1 (a) Custom-made microfluid device with 2.5D struts; (b) results of permeability and WSS as functions of porosity and pore size.

Discussion and Conclusion

Pore size and porosity have shown to directly effect WSS and permeability conspicuously. The permeability of porous solid can be calculated by Kozeny-Carman equation [2], while in our study it is beyond the capability of Kozney-Carman equation as the pore size and pore shape are not explicitly considered in Kozeny-Carman equation. In the future, the database of geometry-dependent permeability and WSS will be updated with more experimental data. Afterwards, a surrogate model, which describe the relationship between geometric parameters and permeability as well as WSS will be developed for facilitate efficient scaffold design.

References

1. Pires et al. (2022) *Proc. R. Soc. A* 478(2257).
2. Kruczek B. (2014) Carman–Kozeny Equation. Encyclopedia of Membranes.

Acknowledgements

DESIGN AND EXPERIMENTAL STUDY OF TORSIONAL WAVE BIOREACTOR TO EVALUATE EFFECT ON MELANOMA STEM CELL

Manuel Hurtado[*15], Carmen Griñán-Lisón[245], Gema Jiménez[245], Elena Lopez[245], Daniel Martínez-Moreno[245], María J. Jiménez[2], Juan A. Marchal[245], Juan M. Melchor[345], Guillermo Rus[145]

1 UGR Department of Structural Mechanics, University of Granada, Politécnico de Fuentenueva, Granada E-18071, Spain. hurtadoestevez@correo.ugr.es
2 UGR Biopathology and Regenerative Medicine Institute (IBIMER), Biomedical Research Centre, University of Granada, Granada E-18100, Spain
3 UGR Department of Statistics and Operations Research, University of Granada, E-18071 Granada, Spain.
4 Excellence Research Unit "Modeling Nature" (MNat), University of Granada, Granada, Spain
5 Biosanitary Research Institute of Granada (ibs.GRANADA), University Hospitals of Granada-University of Granada, Granada, Spain

Introduction:

In this study we have designed and manufactured a bioreactor that allows to study, for the first time, the effect of torsional shear mechanical waves on a population of melanoma CSCs (MEL-1) and differentiated cells over tumor and non-tumor cells as a potential alternative cancer treatment.

There is no previous information on the scientific literature explaining the use of torsional waves in the treatment of cancer. The stimulation is produced by these elastic shear waves that propagate through soft tissue radially and in depth with a curved geometry.

Malignant melanoma is the most aggressive skin cancer with poor prognosis; contributes to 90% the mortality of skin cancers. The main problem of melanoma therapies is the lack of effectiveness treatments, due to the presence of the cancer stem cells (CSCs), cells responsible for tumor initiation, metastasis and cancer recurrence.

Cancer Stem cells (CSCs) are a small subpopulation of cells present in tumors and they are considered as tumor initiating cells (TICs). They also are capable of maintaining the heterogeneity. Tumor growth is related to diverse changes in biomechanical structure of microenvironment such as matrix stiffness, growth-induced solid stresses, high fluid pressure and increased interstitial flow. All those changes are controlled by mechanical forces that contribute and promote to tumorigenesis and tumor cell invasion (1)(2)(3).

Methods:

Torsional waves, with different configurations were employed in diverse types of tumor cells, aggregates of differentiated tumor cells, and healthy cells (fibroblasts).

Incorporated motors in this device were tailored in such a way that exerting contact pressure was optimiezed modifying the motor height to ensure proper rotation. Each well-plate was carefully filled with a mixture of alginate hidrogel. Those ones were stimulated with different frequencies and amplitudes: from 10 Hz to 1000 Hz and from 2 volt to 10 volt. Control samples were same conditions but without motor movement.

Results and conclusion:

A bioreactor has been developed that allows the application of novel torsion waves. These waves have been shown to affect differently depending on the cell type.

In a first experiment, torsion waves decreased the proliferation of tumor cells during the first 72 hours; with the 10 Hz resulted in the most attenuated CSCs proliferation. On the other hand, the 1000 Hz frequency also affected isolated differentiated cells. For healthy cells, such as fibroblasts, the tendency was mostly to grow. Next, we increased the stimulation time up to 7 days with 10 Hz, focusing on CSCs and monolayer cultures, again, torsional waves decreased the proliferation of tumor cells (Figure 1). Our results of this pilot study allow us to observe the effect of torsional waves with various frequencies on CSCs. In conclusion, torsion waves could have the potential to constitute a new non-invasive treatment against melanoma that can be applied in clinic in monotherapy or with existing ones as a combined treatment.
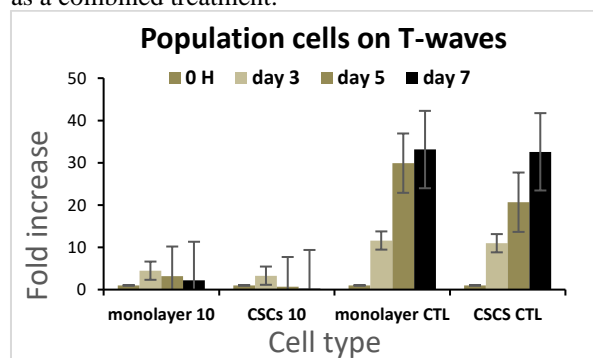

Figure 1: Proliferation assay in cancer stem cells and control for 7 days.

References

1. Shieh AC. Biomechanical Forces Shape the Tumor Microenvironment. Ann Biomed Eng [Internet]. 2011 May
2. Suresh S. Biomechanics and biophysics of cancer cells. Acta Biomater [Internet]. 2007 Jul
3. House M, Kaplan DL, Socrate S. Relationships Between Mechanical Properties and Extracellular Matrix Constituents of the Cervical Stroma During Pregnancy. Vol. 33, Seminars in Perinatology. 2009. p. 300–7.

BIOMECHANICAL CHARACTERIZATION OF TPMS SCAFFOLDS FOR BONE AND CARTILAGE TISSUE ENGINEERING

J. Santos (1), A. Lombard (2), T. Pires (1), A. P. G. Castro (1, 3), P. R. Fernandes (1)

1. IDMEC, Instituto Superior Técnico, Universidade de Lisboa, Portugal; 2. ENSTA ParisTech, France; 3. Escola Superior de Tecnologia de Setúbal, Instituto Politécnico de Setúbal, Portugal

Introduction

Scaffolds created with the TPMS (triply periodic minimal surfaces) method have been developed to be used as bone and cartilage substitutes. For both applications, tissue engineering (TE) scaffolds must provide appropriate mechanical support and allow for convenient tissue regeneration [1]. To verify these properties, parameters such as the permeability and the stiffness of the structure must be characterized.

The aim of this work was to determine the mechanical and fluidic properties of different TPMS scaffolds, varying not only the basic structure and the porosity, but also the length of the basic cubic unit. The goal was to understand the behavior of the scaffold when built with growing cell sizes, as this will add to pore size as a determinant factor for additive manufacturing.

Methods

The TPMS scaffolds considered here are Schwartz D, Gyroid and Schwartz P, with 70 and 80% porosity (ahead referred from SD70 to SP80). For the computational fluid dynamics (CFD) simulations, each basic cubic unit was made of 40 elements per side. All the meshes were generated by an existing Python code [2]. In this script, the parameters to be changed are the scaffold geometry, the porosity and the length of each cubic unit of the scaffold. As so, 5 cell sizes were studied: 1mm, 2.5mm, 5mm, 7.5mm and 10mm.

The CFD simulations were performed with FLUENT ANSYS (Ansys Inc., Canonsburg, Pennsylvania, USA). As the aim is to study the fluid flow through the scaffold, the geometry used with the software was the inverse of the scaffold. The computational cost was too high for the entire scaffold to be simulated; thus, a simpler configuration was adapted, i.e., 1x1x4 instead of 4x4x4 cubic unit configuration previously designed for experimental permeability studies [2].

In the simulations, the fluid flows along the y direction, while the other directions (x and z) are constrained by a periodic boundary condition. This periodic model does not consider the effects at the walls in the calculation of the pressure drop, but a correction factor as previously been studied to account for the effects of the walls [3]. No slippage on the walls and a zero-pressure outlet were also considered. The flow regime must be laminar and not turbulent to get correct results under Darcy's law [2]. Thus, two different flow velocities were studied (0.0005 m/s and 0.001 m/s), in order to verify that this criterion is respected (i.e., that the calculated permeability, which is the main output here, is the same for both velocities).

Results

The permeability for each square size and for each level of porosity was calculated, considering each type of TPMS scaffold, meaning that 6 different curves of the permeability as a function of the cell size were plotted. Fig. 1 shows an example for the SG scaffolds. The SP scaffolds presented the steepest increase of permeability (74%) for an increase of 10% of porosity, while SD presented the lowest variation (32%). These values were constant across the different cell sizes.
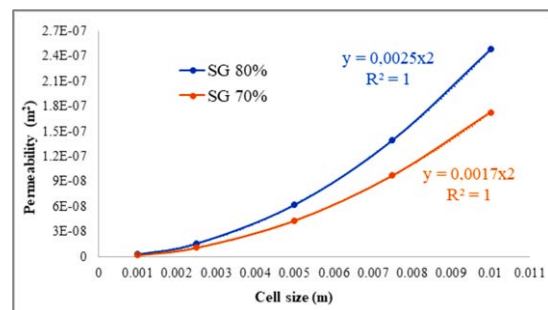

Figure 1. Permeability as a function of the cell size for SG70 (in orange) and SG80 (in blue).

Discussion

Permeability has increased with the cell size as theoretically expected. However, the way it increases depends on the type of TPMS structure. Whatever the cell size of the TPMS scaffold, the increase of permeability with the porosity occurred in the same proportion. Moreover, the CFD simulations revealed that the increase of permeability with the increase of the cell size of the basic unit of the scaffold follows a square function for all the TPMS structures. This means that higher permeability can be achieved without increasing the porosity of the scaffold, allowing for the maintenance of the equivalent mechanical properties of the scaffolds. Experimental verification will be a continuation of this study, but these results are promising for the development of tailored scaffolds for TE applications, as they help to define appropriate volume fraction/pore size relationships.

References

1. Feng et al., CMAME, 336:333-352, 2019.
2. Santos et al, JMBBM, 110, 103932, 2020.
3. Pires et al, J Biomech, 110263, 2021.

Acknowledgements

RECREATING ARTICULAR CARTILAGE'S ZONAL FIBRE ALIGNMENT IN 3D ELECTROSPUN SCAFFOLDS

Ângela Semitela (1), Andreia L. Pereira (1), Ana Capitão (2), Alexandrina F. Mendes (2), Paula A.A.P. Marques (1) and António Completo (1)

1. TEMA, University of Aveiro, Portugal; 2. CNC, University of Coimbra, Portugal

Introduction

Cartilage tissue engineering (TE) strategies for repairing and regenerating articular cartilage have struggled to mimic the biochemical and biomechanical microenvironment of native articular cartilage, particularly the collagen fiber alignment, progressing from parallel in the superficial zone, to radial or random in the middle zone, and finally orientating perpendicular in the deep zone [1]. In this regard, electrospinning has been widely used for cartilage repair due to the similarity between the fabricated and the collagen fibers of the native tissue [2]. Recently, it has been reported the development of three-dimensional (3D) electrospun scaffolds by means of post-processing strategies of the electrospun meshes [1,3]. However, these strategies are not automated, resulting in low reproducibility. To overcome this limitation, a new 3D electrospinning platform has been developed, that allows not only the fabrication of 3D aligned electrospun scaffolds with specific fiber alignments, but also the incorporation of cells within the fibrous layers [4,5]. Thus, in this work, the zonal fiber alignment was replicated in 3D electrospun scaffolds laden with chondrocytes using this platform in a fully automated manner.

Methods

All experiments were performed on a newly patented electromechanically 3D electrospinning platform [4,5], in which fibers are collected and deposited in a collector in accordance with a predetermined fiber alignment (Figure 1b). All equipment and materials used in these experiments were sterile or thoroughly sterilized. A polymeric blend of polycaprolactone (PCL) and Gelatin (GEL) in 2,2,2-trifluoroethanol mixed in a proportion of 6:4 was used to fabricate the 3D scaffolds. An immortalized human chondrocyte cell line C28/I2 was incorporated within the 3D scaffolds in an alternated manner with the polymer electrospinning, after which chondrocyte metabolic and distribution within the fibers and extracellular matrix production was assessed after 7 days of culture.

Results

3D electrospun scaffolds were successfully fabricated with the fiber alignments observed in native articular cartilage: aligned parallelly in the top layer, radially in the middle layer and perpendicularly in the bottom layer, as depicted in Figure 1. Chondrocytes were able to survive the layering process and proliferate over time.

Scanning electron microscopy and hematoxylin and eosin staining revealed cells dispersed between the fibrous layers, suggesting that chondrocytes were retained in the fibrous structure. Small amounts of collagen and glycosaminoglycan were visually detected by sirius red/fast green and alcian blue staining.
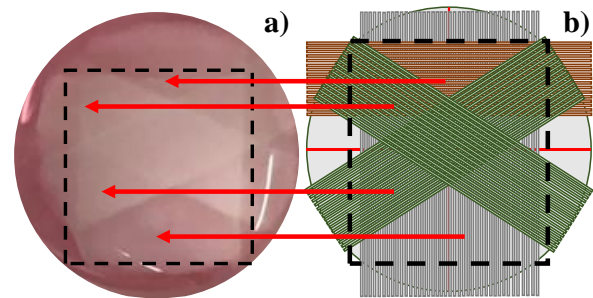

Figure 1: Resulting 3D scaffold (a) and the programmed fiber alignment (b) with the respective zonal layers.

Discussion

It was possible to fabricate 3D scaffolds with zonal fibrous alignments in a fully automated manner. Furthermore, chondrocytes survived and retained their proliferative capacity after the layering process, and synthesized extracellular matrix, implying a potential beneficial impact of the zonal fibrous alignment on chondrocyte behavior.

References

1. A. Semitela et al, J. Mech. Behav. Biomed. Mater., 117: 104373, 2021.
2. A. Semitela et al, J. Biomater. Appl., 35:471-484, 2020.
3. A.F. Girão et al, J. Mater. Sci. Mater. Med., 31: 69, 2020.
4. E. Silva et al, J. Comput. Artif. Intell. Mech. Biomech., 1: 81-91, 2021.
5. A. Semitela et al, in: Adv. Curr. Trends Biomech, 187-190, 2022.

Acknowledgements